

Lecture Notes in Mechanical Engineering

Basant Singh Sikarwar
Bengt Sundén
Qiuwang Wang *Editors*

Advances in Fluid and Thermal Engineering

Select Proceedings of FLAME 2020

 Springer

Lecture Notes in Mechanical Engineering

Series Editors

Francisco Cavas-Martínez, Departamento de Estructuras, Universidad Politécnica de Cartagena, Cartagena, Murcia, Spain

Fakher Chaari, National School of Engineers, University of Sfax, Sfax, Tunisia

Francesco Gherardini, Dipartimento di Ingegneria, Università di Modena e Reggio Emilia, Modena, Italy

Mohamed Haddar, National School of Engineers of Sfax (ENIS), Sfax, Tunisia

Vitalii Ivanov, Department of Manufacturing Engineering Machine and Tools, Sumy State University, Sumy, Ukraine

Young W. Kwon, Department of Manufacturing Engineering and Aerospace Engineering, Graduate School of Engineering and Applied Science, Monterey, CA, USA

Justyna Trojanowska, Poznan University of Technology, Poznan, Poland

Lecture Notes in Mechanical Engineering (LNME) publishes the latest developments in Mechanical Engineering—quickly, informally and with high quality. Original research reported in proceedings and post-proceedings represents the core of LNME. Volumes published in LNME embrace all aspects, subfields and new challenges of mechanical engineering. Topics in the series include:

- Engineering Design
- Machinery and Machine Elements
- Mechanical Structures and Stress Analysis
- Automotive Engineering
- Engine Technology
- Aerospace Technology and Astronautics
- Nanotechnology and Microengineering
- Control, Robotics, Mechatronics
- MEMS
- Theoretical and Applied Mechanics
- Dynamical Systems, Control
- Fluid Mechanics
- Engineering Thermodynamics, Heat and Mass Transfer
- Manufacturing
- Precision Engineering, Instrumentation, Measurement
- Materials Engineering
- Tribology and Surface Technology

To submit a proposal or request further information, please contact the Springer Editor of your location:

China: Ms. Ella Zhang at ella.zhang@springer.com

India: Priya Vyas at priya.vyas@springer.com

Rest of Asia, Australia, New Zealand: Swati Meherishi at swati.meherishi@springer.com

All other countries: Dr. Leontina Di Cecco at Leontina.dicecco@springer.com

To submit a proposal for a monograph, please check our Springer Tracts in Mechanical Engineering at <http://www.springer.com/series/11693> or contact Leontina.dicecco@springer.com

Indexed by SCOPUS. All books published in the series are submitted for consideration in Web of Science.

More information about this series at <http://www.springer.com/series/11236>

Basant Singh Sikarwar · Bengt Sundén ·
Qiuwang Wang
Editors

Advances in Fluid and Thermal Engineering

Select Proceedings of FLAME 2020

 Springer

Editors

Basant Singh Sikarwar
Amity University Uttar Pradesh
Noida, India

Bengt Sundén
Lund University
Lund, Sweden

Qiuwang Wang
Xi'an Jiaotong University
Shaanxi, China

ISSN 2195-4356 ISSN 2195-4364 (electronic)
Lecture Notes in Mechanical Engineering
ISBN 978-981-16-0158-3 ISBN 978-981-16-0159-0 (eBook)
<https://doi.org/10.1007/978-981-16-0159-0>

© The Editor(s) (if applicable) and The Author(s), under exclusive license to Springer Nature Singapore Pte Ltd. 2021

This work is subject to copyright. All rights are solely and exclusively licensed by the Publisher, whether the whole or part of the material is concerned, specifically the rights of translation, reprinting, reuse of illustrations, recitation, broadcasting, reproduction on microfilms or in any other physical way, and transmission or information storage and retrieval, electronic adaptation, computer software, or by similar or dissimilar methodology now known or hereafter developed.

The use of general descriptive names, registered names, trademarks, service marks, etc. in this publication does not imply, even in the absence of a specific statement, that such names are exempt from the relevant protective laws and regulations and therefore free for general use.

The publisher, the authors and the editors are safe to assume that the advice and information in this book are believed to be true and accurate at the date of publication. Neither the publisher nor the authors or the editors give a warranty, expressed or implied, with respect to the material contained herein or for any errors or omissions that may have been made. The publisher remains neutral with regard to jurisdictional claims in published maps and institutional affiliations.

This Springer imprint is published by the registered company Springer Nature Singapore Pte Ltd. The registered company address is: 152 Beach Road, #21-01/04 Gateway East, Singapore 189721, Singapore

Preface

This book brings together the collection of cutting-edge research articles on fluid and thermal engineering from the 2nd International Conference on Future Learning Aspects for Mechanical Engineering (FLAME), which was organized by Amity University, Noida, Uttar Pradesh, India, from August 5 to 7, 2020. Owing to pandemic COVID-19, this conference was held virtually. The primary mission of this conference was to lay a platform that brings together academicians, scientists, and researchers across the globe to share their scientific ideas and vision in the areas of thermal, design, industrial, production, and interdisciplinary areas of mechanical engineering. FLAME 2020 played a key role to set up a bridge between academia and industry.

The conference hosted almost 600 participants to exchange scientific ideas. During 3 days of the conference, researchers from academics and industries presented the most recent cutting-edge discoveries, went through various scientific brainstorming sessions, and exchanged ideas on practical socioeconomic problems. This conference also provided a scope to establish a network for joint collaboration between academia and industry. Major emphasis was focused on the recent developments and innovations in various fields of mechanical engineering through plenary and keynote lectures.

In particular, this volume discusses selected topics of fluid and thermal engineering in eighty chapters such as heat transfer enhancement, thermodynamics, heat transfer in nuclear engineering, microscale and nanoscale, two-phase flow, phase change process, advancement in numerical methods, computational fluid dynamics, refrigeration and air conditioning, advancement in aerospace engineering, flow through porous media, condensation, evaporation, hybrid vehicles, passive cooling method, thermal management of various devices, theoretical fluid mechanics, flow measurement techniques, and fluid machinery and fluid power with special emphasises on renewable energy. The contents of this book will be useful for researchers as well as industry professionals.

We would like to acknowledge all the participants who have contributed to this volume. We also deeply express our gratitude for the generous support provided by Amity University, Noida. We also thank the publishers and every staff of the

department and institute who have directly or indirectly helped to accomplish this goal. We are highly thankful for the encouragements from our respected chancellor, Dr. Atul Chauhan, and valuable guidance of our Vice-Chancellor, Prof. (Dr.) Balvinder Shukla. Finally, we would also like to express our gratitude to Respected Founder President, Amity University, Dr. Ashok K. Chauhan, for providing all kinds of support, and this book is not complete without his blessings.

Prof. Basant Singh Sikarwar
Amity University Uttar Pradesh, Uttar Pradesh, India

Prof. Bengt Sundén
Lund University, Lund, Sweden

Prof. Qiuwang Wang
Xi'an Jiaotong University, Shaanxi, China

Contents

Numerical Investigation of Swirl and Tumble Motion in the Cylinder and Their Effect on Combustion of Gasoline–Methanol Blends in SI Engine	1
Neeraj Kumar Yadav and Rakesh Kumar Maurya	
An Experimental Analysis of the Thermal Performance of Solar Air Heater (SAH) Having Two Different Absorber Plate Along with (PCM)-Based Energy Storage	11
Arvind Kumar Singh and Nitin Agarwal	
Comparative Study of the Fluid Interface-Capturing High-Resolution Algebraic Schemes	23
Ashish Arote, Mukund Bade, and Jyotirmay Banerjee	
Performance Investigation of Atmospheric Water Generating Device for Hot and Humid Conditions	33
Vishakha Baghel and Basant Singh Sikarwar	
Vortex Dynamics in Near Wake Region Behind a Triangular Cylinder at Intermediate Reynolds Number	43
Namit Agrawal and Maharshi Subhash	
Numerical Study of Gas Turbine Type Continuous Combustion Unit Burning LPG Mixture	55
Shah Shahood Alam, Sanaur Rehman, and Anchal Varshney	
Soot Formation Characteristics of Homogeneous Supercritical Fuel Spray of Dieseline Blend	67
Sanaur Rehman and Shah Shahood Alam	
A Review on Thermal Barrier Coatings (TBC) Usage and Effect on Internal Combustion Engine	77
Priyanka Sharma, Vijay K Dwivedi, and Dipak Kumar	

Evaluation of Emission Characteristics of Diesel Engine Fueled with Blends of Biodiesel Obtained from Waste Sesame Oil and Its Blends with Pure Menthe Oil	87
Sanjay Kumar Yadav, Manoj Kumar, and Niraj Kumar	
Liquid Film Thickness Measurement: A Critical Review	101
Sagar G. Nayak, Nishant M. Shah, and Jyotirmay Banerjee	
Modelling and Simulation of Evaporation on Porous Surface	113
Jyoti Prakash, Basant Singh Sikarwar, Basant Kumar Agarwal, and Rajesh Kumar	
Effect of Ageing on Emission Levels of a Gasoline Vehicle: A Case Study in Indian Context	127
Manu Bindra and Devendra Vashist	
Comparison of Free Convection Around Heated Square Plate in a Square Enclosure Enclosing Air, Water, and Ag-Water Nanofluid	141
Parth Patpatiya, Isha Pandey, and Ananya Gupta	
Numerical Study of Heat Exchanger Having Protrusion and Dimple Roughened Conical Ring Inserts	151
Bhanu Pratap Singh, Vijay Singh Bisht, and Prabhakar Bhandari	
Futuristic Approaches of Low-Grade Industrial Waste Heat Recovery	163
Prasanta Majumder, Abhijit Sinha, and Rajat Gupta	
Generation of Temperature Profile by Artificial Neural Network in Flow of Non-Newtonian Third Grade Fluid Through Two Parallel Plates Under Noisy Data	173
Vijay Kumar Mishra, Auritro Samanta, Sumanta Chaudhuri, and Daya Shankar	
Impact of Thermal Contact Resistance on Thermal-Hydraulic Characteristics of Double Fin-and-Tube Heat Exchanger	187
Shobhana Singh and Navin Kumar Dwivedi	
Heat Dissipation Characteristics of a FSAE Racecar Radiator	199
Shreyas Padmaraman and N. Rajesh Mathivanan	
Fabrication and Analysis of Evaporative Water Reclamation Plant Using Waste Water from Different Sources	209
Anil Kumar and Arindam Kumar Chanda	
Techno-Economic Feasibility Analysis of Parabolic Solar Cooker in Tropical Environment of India	219
Harshita Sawarn, Pushpendra Kumar Singh Rathore, and Shailendra Kumar Shukla	

Computational Analysis of EMHD Flow of Nanofluid Over a Rotating Disk with Convective Boundary Conditions: Buongiorno’s Model 231
 Rajnish Kumar and Srishti Singh

CFD Analysis of Mixed Convection in an Enclosure with a Floor-Mounted Step-Like Heat Source 249
 Venkata Reddy Poluru

An Experimental Study on Performance Parameters of Diesel Engine Fueled with Blends of Diesel Fuel and Linseed Biodiesel 261
 Brahma Nand Agrawal, Shailendra Sinha, Sudhir Kumar Singh, Kaushlendra Kumar Dubey, and Manoj Kumar

Study of Natural Convection Heat Transfer in a Closed Wall with Thermal Conditions 271
 S. J. Yaksha, E. Akash, U. Sanjay, K. N. Seetharamu, and Balesh Babali

CFD Analysis of Tube Type Heat Exchanger of a Split Air Conditioner 283
 Rimi Sinha and Basant Singh Sikarwar

Effect of Strip Orientations and Geometry on the Critical Heat Flux in Pool Boiling 293
 Bikash Pattanayak, Harsh Deswal, Vivek Saxena, and Hardik Kothadia

Effect of Velocity Variation on the Rate of Erosion Wear at the Elbow of the Slurry Pipe by Using CFD 305
 Pardeep Bishnoi, Satish Kumar, Abhijeet Singh, Virender Chahal, and Vikrant

Computational Study of the Effect of Cold Orifice Dimension on the Temperature Variation in the Counter Flow Vortex Tube 313
 Ravi Kant Singh, Achintya Kumar Pramanick, and Subhas Chandra Rana

Modeling and Simulation of the Load Governing System of Steam Turbine 327
 Jagannath Hirkude, Sharven Kerkar, and Mrinal Borkar

Modeling and Optimization of Piezoelectric Energy Harvesting System Under Dynamic Loading 339
 Mohit Yadav, Dinesh Yadav, Ramesh Kumar Garg, Ravi Kant Gupta, Surendra Kumar, and Deepak Chhabra

Improving Physio-Chemical Properties of Biodiesel by Using Blending 355
 Gaurav Pathak and S. Kennedy

Slurry Pressure Drop Through Horizontal Mitre Pipe Bend Using CFD 367
 Om Parkash, Arvind Kumar, and Basant Singh Sikarwar

Development of Characteristic Equation for Evacuated Tubular Collector Under Constant Collection Temperature Mode of Operation	377
R. K. Mishra, Siddarth Gupta, Rajesh Tripathi, and Rajendra Prasad	
Simulation Studies on the Transition from Simple Expansion Chamber Muffler to Tapered Expansion Chamber Muffler	389
S. K. Vishwakarma and S. J. Pawar	
Comparison of Supersonic Flow Regime for Two Different Symmetric Biconvex Circular-Arc Aerofoil	399
Rakesh Prasad, Sandeep Agarwal, Devendra Singh, and Manipl Singh	
Effects of Surface Geometries and Fin Modifications on the Thermal Performance of Solar Air Heaters: A Review	409
Rahul Khatri, Shyam Sunder Sharma, Shlok Goswami, Shubham Sharma, and Mohd. Anas	
Numerical Modelling and Simulation of Wind Turbine Blade Aerofoil for Performance Enhancement	423
Pankaj Negi, Tarun Kumar Dhiman, Gagan Bansal, and Neeraj Panwar	
Hydrophobicity Enhancement of Mesh-like Surface for Moist Air Condensation	435
Punj Lata Singh and Basant Singh Sikarwar	
Studies on Flow Past Surface Cooled Circular Cylinder at Low Reynolds Number	443
Sujith Stephen and S. Ajith Kumar	
Design and Thermal Analysis of Pipe Insulation	455
Shwetank Avikal, Reena Devi, Arjun Singh Bisht, and K. C. Nithin Kumar	
Efficiency Analysis of Aerospike Nozzle by Comparison with a de-Laval Nozzle Using Computational Fluid Dynamics	467
Clavin Wilton Sequeira and M. V. Sanjay	
Vortex Formation in Liquid Columns During Draining: Influence of Drain Port Geometry	477
M. R. Harikrishnan, Mahadev Prabhu, and R. Ajith Kumar	
A Study for the Effect of Antioxidant EDA and Aluminium Hydroxide Additives to Mitigate CO and NO_x Emissions in Biodiesel–Diesel Blend Fuelled CI Engine	487
Ajai Prasad Nigam and Shailendra Sinha	
Thermal Performance Optimization of Heat Pipe Using Taguchi Method	499
Naveen Kumar Gupta	

Effects of Hybrid Nanofluids on the Thermal Performance of Heat Pipe: An Experimental Investigation	509
Naveen Kumar Gupta	
Energy Saving Technique for Separation of a Fuel Additive	519
Asma Iqbal and Syed Akhlaq Ahmad	
Opportunities and Issues with Clean Renewable Energy Development in India: A Review	527
Prakarti Sharma, Anbesh Jamwal, Nidhi Sharma, and Rajeev Agrawal	
A Review on Scramjet Engine	539
Riyan Cyriac Jose, Rhitik Raj, Yogesh Dewang, and Vipin Sharma	
Numerical Simulation of Ribbed Solar Air Heater	549
Anil Singh Yadav and Sanjay Kr Sharma	
The Coatings Developed by Thermal Spraying Technique for Hydroturbine Applications—A Brief Review	559
Purusharth Bhati, Vishal Shrama, Raghav Jha, Sujeet Gupta, Mohit Vishnoi, and T. G. Mamatha	
Study on Tribological Behavior of HVOF Developed Coatings Especially for Hydroturbine Runner Application—A Concise Review	575
Adheesh Tripathi, Aman Pandey, Aakash Rathore, Abhishek Singh, and Mohit Vishnoi	
Emission Characteristics of Renewable Diesel and Its Comparison with the Diesel Fuel on Single-Cylinder Diesel Engine	597
Rashi Koul, Naveen Kumar, and R. C. Singh	
Effect of Tyre Inflation Pressure on Fuel Consumption and Vehicle Handling Performance	607
Nigatu Belayneh, Ramesh Babu Nallamothe, Anantha Kamal Nallamothe, and Seshu Kishan Nallamothe	
CFD Analysis on Aerodynamic Drag Reduction of Pickup Vehicles Using Rear Spoiler	619
Engidayehu Wotango, Ramesh Babu Nallamothe, Surafel Kebede, Natnael Bekele, Anantha Kamal Nallamothe, and Seshu Kishan Nallamothe	
Simulation of Performance and Emission of SI Engine Fuelled with Ethanol–Gasoline Blend (E15)	629
Tamiru Tesfaye Gemechu and Ramesh Babu Nallamothe	

CFD Studies on the Modified Laparoscopic Instrument Used in Minimally Invasive Surgeries	643
Md. Abdul Raheem Junaidi, Gourabh Pandey, K. Ram Chandra Murthy, and Y. V. Daseswara Rao	
Study of Existing Systems to Control Inside Temperature of Car Compartment and Factors Influencing the Rise of Temperature Within the Car Compartment—A Review	653
Alok Bharti, P. Mathiyalagan, and Pawan Kumar Singh Nain	
Air-Conditioning System in Surgical and Critical Care: A Review	661
Triyank Mishra, Ravneet Singh, Vikas Giri, Joydeep Chakraborty, and Sorabh	
Static Analysis of Euler–Bernoulli Beam by Using Bond Graph	673
Anandit Wadhera, Bhuwandeeep, Harsh Vishwakarma, Jatin Mahato, and Anuj Kumar Jain	
Design Optimization and Computational Analysis of Heat Transfer Through IC Engine Fins	683
Ashish Kumar, Amit Kumar Gupta, Banti, and Samsher	
Energy Utilization Reduction of Domestic Refrigerator Using Phase Change Materials	695
Anand Pavithran, Meeta Sharma, and Anoop Kumar Shukla	
Flutter and Modal Analysis of Gas Turbine Compressor Blades	707
Priya Singh, V. K. Chawla, and N. R. Chauhan	
Biomass Thermochemical Processing in Fixed Bed Downdraft Gasifier: A Review	721
Praveen Kumar	
Utilization of Nanofluids as Coolant—A Review	731
Aashray Sharma, Preeti Joshi, and Jaspreet Hira	
Biodiesel in India—A Review	741
Sanjay Mohite and P. K. Rohtagi	
Numerical Analysis of Turbulent Heat Exchanger Tube Using Novel Para-Winglet Tape	753
R. Thejaraju, K. B. Girisha, S. H. Manjunath, and B. S. Dayananda	
Identification of Gas-Liquid Two-Phase Flow Patterns Using Various Experimental Techniques: A Review	767
Dhiren Makwana and Jignesh Thaker	
Fuzzy Grey Relational-Based Risk Analysis of Steam Generating Unit	777
Priyank Srivastava Srivastava, Yash Sharma, Prikshit Rana, Rohit Gupta, Melfi Alrasheedi, and Naveen Kumar	

Development and Testing of Binary Organic Eutectic Mixture for Thermal Energy Storage 787
 Alok Kumar Ansu, Pooja Singh, and Ravi Kumar Sharma

A Review of Natural Gas—Diesel Dual Fuel Engines 795
 Manoj Gwalwanshi and Gaurav Mittal

Effect of Wall Fin Aspect Ratio in a Suddenly Expanded Micro-Combustor 805
 Arees Qamareen, Shah Shahood Alam, and Mubashshir Ahmad Ansari

Mathematical Modeling of Drying Kinetics of Garlic Clove in Forced Convection Evacuated Tube Solar Dryer 813
 Santanu Malakar and Vinkel Kumar Arora

Numerical Analysis of Regenerator for Pulse Tube Refrigerator 821
 Sahil Variya, Dhruvil Joshi, Nikunj Rohit, Rutvik Brahmabhatt, and Chetan O. Yadav

Waste Heat Management in Hybrid Vehicles for Cabin Cooling 831
 George Hawkins, Meeta Sharma, and Anoop Kumar Shukla

Effect on Performance and Emission of IC Engine Using Mahua Oil and Yellow Grease—A Simulation-Based Study Using Diesel-RK 847
 Shiv Kumar Sonkar, Pushyamitra Mishra, and Prashant V. Baredar

Comparative CFD Analysis of Straight and Helical-Shaped Earth Air Pipe Heat Exchanger (EAPHE) System 857
 Mahendra Kumar Verma and Vikas Bansal

Application of Taguchi Method and ANOVA in Parameters Optimization for Fluidization Characteristic of Pine Needles in Fluidized Bed 869
 Vishal Sharma and Rajeev Kamal Sharma

A Study on Agglomeration Behaviour of Cotton Stalk Under Fluidized Bed Conditions 879
 Rajeev Kamal Sharma, Rajneesh Kaushik, and Rajesh Kumar

Effect of Fuel Composition on Thermoacoustic Instability in a Turbulent Combustor 891
 Nikhil A. Baraiya and Satyanarayanan R. Chakravarthy

Experimental Investigation of Combustion Instability in Syngas Turbulent Combustor 901
 Nikhil A. Baraiya and Satyanarayanan R. Chakravarthy

About the Editors

Dr. Basant Singh Sikarwar completed his Post Doctorate from Iowa State University, Ames, Iowa (USA) and PhD from Indian Institute of Technology, Kanpur, India. He did his Master of Technology from the Indian Institute of Technology Roorkee, India. Dr. Sikarwar is heading the Department of Mechanical Engineering at Amity School of Engineering and Technology, Amity University, Noida, Uttar Pradesh, India. His research interest involves thermal energy storage, energy systems, condensation, boiling, two-phase heat transfer, bioengineering, biological fluid flow, modeling of blood flow, and flow visualization. He is having 15 years of working experience in teaching UG and PG courses in mechanical engineering. He is working as Principal Investigator (PI) in three projects funded by the Government of India, Science Engineering Research Board (SERB) India, MSME, and Department of Atomic Energy through IPR, Ahmedabad. He has industry consultancies from Advance Valve Pvt. Ltd, Noida; Amber Pvt. Ltd., Rajpur; and Tex Pvt. Ltd, Gurugram, India. He has published 50 research articles in refereed international journals and 70 articles in conference proceedings. He edited the book titled “Advances in Fluid and Thermal Engineering.” Dr. Sikarwar has guided 3 PhDs and currently supervising 7 PhD candidates. He has delivered many guest lectures in national/international conferences and workshops. He has also been the author/ co-author of 2 books, and he has obtained 10 Indian Invent Patents.

Dr. Bengt Sundén received his M.Sc. in 1973, Ph.D. in 1979 and became Docent in 1980, all from Chalmers University of Technology, Gothenburg, Sweden. He was appointed Professor of Heat Transfer at Lund University, Lund, Sweden in 1992 and served as Head of the Department of Energy Sciences, Lund University for 21 years, 1995–2016. He has served as Professor Emeritus and Senior Professor since 2016. The research activities mainly include various heat transfer enhancement techniques, gas turbine heat transfer, computational modeling and analysis of multiphysics and multiscale transport phenomena for fuel cells, nano-and micro-scale heat transfer, boiling and condensation, aerospace heat transfer, thermal management of batteries. He has supervised 51 PhD students and many post docs as well hosted many visiting scholars and PhD students. He serves as Guest or

Honorary Professor of several prestigious universities. He is a Fellow of American Society of Mechanical Engineers (ASME), a regional editor for Journal of Enhanced Heat Transfer since 2007, an associate editor of Heat Transfer Research since 2011, ASME Journal of Thermal Science, Engineering and Applications in 2010–2016 and ASME Journal of Electrochemical Energy Conversion and Storage 2017–2023. He was a recipient of the ASME Heat Transfer Memorial Award 2011 and Donald Q. Kern Award 2016. He received the ASME HTD 75th Anniversary Medal 2013. He has edited more than 30 books and authored three major textbooks. He has published more than 500 papers in well-established and highly ranked journals. The h-index is 47 and the number of citations is more than 10000.

Dr. Qiuwang Wang is a full Professor of School of Energy and Power Engineering, Xi'an Jiaotong University. He is also the executive director of International Joint Research Lab of Thermal Science and Engineering, MOE of China. He is a recipient of National Funds for Distinguished Young Scientists by NSF of China (2010), the Changjiang Scholarship Chair Professor by Ministry of Education of China (2013), the Leader of Innovation Team in Key Areas of Ministry of Science and Technology (2016), the Director of National International Joint Research Center (2017), and the People Plan of Science and Technology Innovation Leading Talents (2018). His research team obtained the 2nd Grade National Award for Technological Invention of China (2015) and National Science and Technology Progress Award of China (Innovation Team, 2017). Dr. Wang is now a Fellow of ASME, the China Delegate of Assembly for International Heat Transfer Conferences (AIHTC), a member of Scientific Council of the International Centre for Heat and Mass Transfer (ICHMT), an Associate Editor of Heat Transfer Engineering Journal, and Editorial Board Members for several international journals such as Renewable and Sustainable Energy Reviews, Energy Conversion and Management, Applied Thermal Engineering, Energy etc. In China, he is a vice president of Chinese Society of Engineering Thermo-physics in Heat and Mass Transfer. Dr. Wang's research interests include heat transfer enhancement and its applications to engineering problems, high temperature/high-pressure heat transfer and fluid flow, transport phenomena in porous media, numerical simulation, prediction & optimization, etc. He has delivered more than 40 Plenary/Keynote/Invited lectures in international conferences or foreign universities. He has also been authors or co-authors of 4 books and more than 200 international journal papers. He has obtained more than 30 China Invent Patents and 3 US Patents.

Numerical Investigation of Swirl and Tumble Motion in the Cylinder and Their Effect on Combustion of Gasoline–Methanol Blends in SI Engine



Neeraj Kumar Yadav and Rakesh Kumar Maurya

Abstract Two-wheeler vehicles are having challenges in adopting advanced after-treatment devices due to their compactness and lightweight. Swirl and tumble motion inside the cylinder is considered to be the desired way to improve combustion efficiency and reduce engine emissions. The present study investigates the effect of swirl and tumble motion on combustion characteristics of gasoline–methanol blend in the SI engine. This study presents a new approach to calculate the motion of the flow, including swirl and tumble during both the intake and the compression strokes using 3D-CFD simulation. The effects of the swirl and tumble variations were evaluated in terms of the swirl and tumble ratios, the turbulent kinetic energy, and the vortex motion characteristics at intake valve closing (IVC). The numerical simulations are conducted at different engine speed, and the effect of engine speeds on the in-cylinder fluid motions are analyzed and presented. Four different methanol–gasoline blends (M05, M10, M15, and M20) are used to investigate the effect of different blends on engine performance and emission. A model of 2D cylinder piston cavity is used for combustion simulation at different speeds of the engine for different swirl and tumble ratios. It was found that the swirl and tumble ratios mainly vary with the position of crank angle. The cylinder pressure increases with the increase in methanol percentage. Additionally, the turbulent kinetic energy increases with the increase of speed and swirl and tumble ratio, which leads to the completeness of combustion and improves the performance of the engine.

Keywords Swirl · Tumble · Gasoline · Methanol · Ignition · Combustion engine

N. K. Yadav · R. K. Maurya (✉)
Indian Institute of Technology Ropar, Ropar, India
e-mail: rakesh.maurya@iitrpr.ac.in

N. K. Yadav
e-mail: 2018mez0024@iitrpr.ac.in

1 Introduction

To deal with surpassing petroleum prices, alternative fuels are highly reliable substitutes. Presently government and automotive industries are showing great interest in alternative fuels, which motivates the researchers to work on them. Among all alternative fuels recommended globally, alcohols have become a stronger alternative because alcohol can be produced from renewable materials such as biomass. Among all accessible alcohols, mainly methanol, ethanol, and butanol have higher potential for use in the automobile industry due to their cost being lower than other higher alcohols and their combustion properties being comparable with gasoline [1].

Several studies have been conducted globally for using gasoline and their blends in the SI engine. A study showed that the gasoline–methanol blend operation shortened the fast-burning phase of combustion and flame development period during cold start and warm-up conditions [2]. The peak in-cylinder pressure (P_{\max}) of the methanol–gasoline blends in the SI engine was observed higher than pure gasoline [2, 3]. The start of combustion (SOC) was advanced due to an increase in methanol percentage in the blend, and the rapid burn phase was shortened at higher engine speeds [3]. Another study showed that combustion duration and ignition delay were shortened for a blend with 85% methanol compared to gasoline [4]. El-Emam and Desoky [5] demonstrated that NO_x and carbon monoxide (CO) emissions could be reduced significantly using alcohol in SI engines. Another study reported similar results, but they also reported a slight increase in HC emission [6]. Falfari et al. [7] investigated that the swirl and tumble ratios are especially very useful because they govern the flow characteristic of charge, which leads to the efficient combustion and increased the flame velocity. Lee et al. [8] investigated the effect of flow patterns in the combustion chamber experimentally, and the effect of swirl and tumble on early flame propagation was studied in a four-valve spark-ignition engine using lean mixture conditions for different inlet ports entry angles. The propagating flames were captured with an image-intensified CCD camera. The flame images taken during the experiment give visual evidence on the effect of tumble motion on flame propagation in the SI engine. This experimental result showed that turbulent flame could be deformed and convected by the tumble/swirl flow field. Shaikh and Shukla [9] concluded that the inlet velocity of flow must be very high for the high swirl, which means inlet velocity directly affects the flame propagation and flow inside the cylinder. The study also shows the tumble and swirl ratios that are directly dependent on the engine speed, and it can be increased by changing a valve and port design. Königsson et al. [10] found that with an increase in the swirl from 0 to 6.5, the heat transfer to the coolant increases by 50%, and the HC emission is reduced due to higher mixing. Li et al. [11] showed that tumble motion in the SI engine reduced the instability in the combustion due to fast mixing of fuel and air, and also extend the EGR limit, which is typically used for NO_x reduction. Hu and Lokhande [12] have performed the numerical simulation for swirl and tumble motion and showed that the hybrid

approach has convincing results for both swirl and tumble motion in layering and different meshes. In this study, a hybrid approach was used to investigate the in-cylinder flow motion of charge in the SI engine. The effect of initial swirl and tumble on combustion of methanol–gasoline has not been found in the literature, which motivates the present study. The present study provides an insight of effect of swirl and tumble on combustion in SI engine. The investigation of flow motion is very important for the IC engine as the flow motion governs the charge preparation, turbulence, and heat transfer inside the combustion chamber. This study focused on the in-cylinder swirl/tumble variation during intake and compression stroke and their effect on the combustion of gasoline–methanol blends.

2 Methodology and Validation

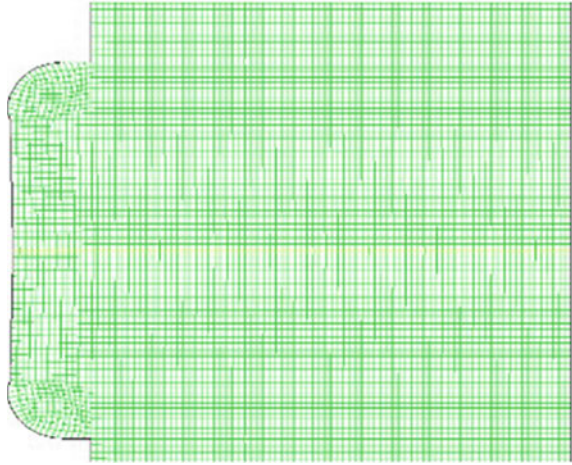
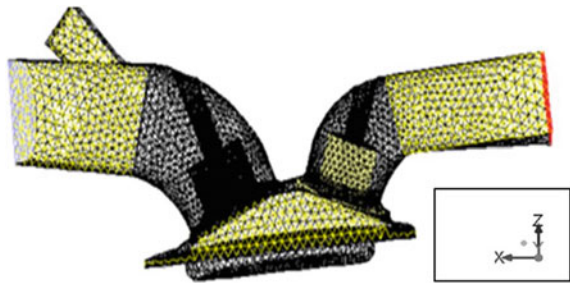
In this section, the methodology of both the simulations was discussed briefly for cold flow as well as combustion simulation.

2.1 Flow and Combustion Simulation

Cold flow simulation has been performed in the following model for the calculation of swirl and tumble and different flow characteristics inside the cylinder. The presented research had been done to study the physical phenomena associated with flow inside the combustion chamber of the spark ignition engine. ANSYS FLUENT was preferred in this study to take benefit of its capability to simulate general flow problems. The first step of the simulation was to set up an in-cylinder case involving only a part of suction and compression stroke and then setting up IC cold flow simulation in ANSYS FLUENT with user-defined function (UDF) to specify the flow characteristics. A 3D symmetric geometry of the configuration of an IC engine cylinder is shown in Figs. 1 and 2. Tumble and swirl usually quantified as tumble ratio (R_t) and swirl ratio (R_s) are the ratio of the rotational velocity of charge (ω) to piston speed (N) about a given axis in which, the swirl is around the z -axis, and tumble is around x - and y -axis, and the expression is given as,

$$R_s = \frac{\omega_s}{2\pi N}, \quad R_t = \frac{\omega_t}{2\pi N} \quad (1)$$

In the given mesh, X and Y are the tumble axis, and Z is the axis of swirl. After this mesh reading and scaling, a dynamic mesh motion was performed to check the mesh motion, which was the reason for flow simulation that began at 360 CA for cold flow simulation. Calculation activities for combustion were done for M05 (5% Methanol with 95% gasoline), M10, M15, M20 fuel blends with 2000, 2500 rpm with variable tumble and swirl ratio. For combustion analysis, ANSYS FLUENT

Fig. 1 Combustion mesh**Fig. 2** Cold flow mesh

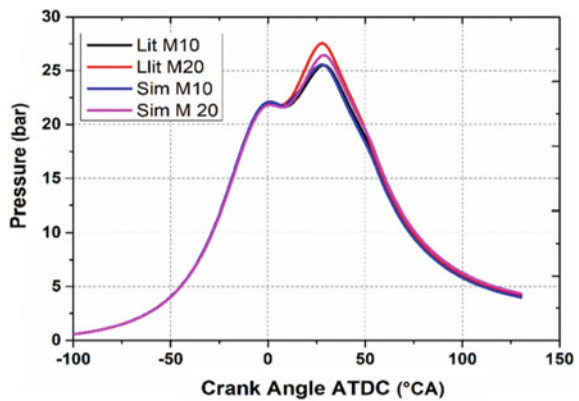
had been used, which was equipped with a premix model in which only the fuel species and the mechanism of reaction from coupled Chemkin module were to be defined. Premixed combustion model in ANSYS FLUENT predicted equilibrium composition and had been used for premixed combustion, which had a better prediction for peak temperature and pressure. There were no valves involved because the simulation started when the inlet valve closed and ended when the exhaust valve was about to open. A pure layering approach was used on a 2D axisymmetric geometry. Methanol and gasoline were used as boundary species, and their properties can be seen in reference [1]. Engine operating parameters for current simulations are provided in Table 1.

2.2 Model Validation

Validation was made by comparing the in-cylinder pressure for M10 and M20 fuels and is shown in Fig. 3. The first peaks in the cylinder at pressures of 25 bars and 28 bars for M10 and M20, respectively, were obtained from literature, while in the case

Table 1 Engine parameters and boundary conditions for simulation

Parameter	Value
Initial swirl and tumble ratio	1.0, 1.5, 2.0
Crank speed (rpm)	2000, 2500
Start cold flow crank angle (°)	360
Crank period (°)	720
Step size crank angle (°)	0.25
Piston stroke (mm)	80
Connecting rod (mm)	140
Start of combustion simulation (°)	570
End of combustion simulation (°)	850
Piston temperature (K)	300
Cylinder wall temperature (K)	300
Turbulent intensity	0.1
Turbulent length scale constant	0.37
Turbulent flame speed constant	0.6

Fig. 3 Model validation from literature [1, 4]

of simulation, they were 24.6 bar and 27.8 bar, and on the other hand, the experimental second peak pressure is higher than those obtained from simulation. The maximum deviation in the peak cylinder pressure was found to be less than 5%.

3 Result and Discussion

In this section, the in-cylinder variation of flow and combustion findings were discussed.

3.1 Swirl and Tumble Inside the Cylinder with Flow Visualization

The variation of swirl and tumble motion inside the cylinder is plotted in Fig. 4 with respect to the crank angle; velocity contour for few cases is also shown in Fig. 5.

It is observed that tumble and swirl began with a decreasing tendency. The maximum swirl ratio was achieved around 160° CA after TDC when the piston attained the maximum instantaneous speed, and the inlet valve was fully opened, as

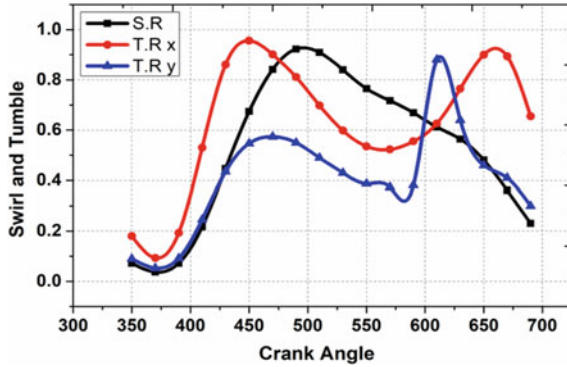


Fig. 4 Swirl and tumble versus crank angle

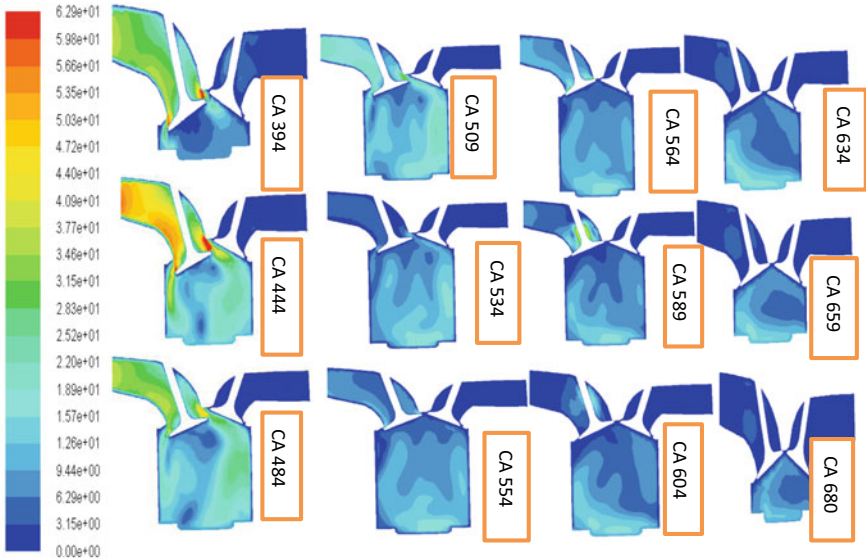


Fig. 5 Velocity contour during flow simulation

seen in Fig. 4. Beyond this point, the swirl and tumble gradually decreased toward the end of the suction stroke because air velocity decreased with valve closing. During the compression stroke, the swirl ratio or swirl velocity was declining because of viscous drag due to cylinder walls. The tumble ratio in the oblique direction (about the x -axis) can be seen in Fig. 4. The graph shows variation inside the engine cylinder of the sidelong tumble ratio. The effect of tumble was very low at the beginning of suction stroke as the fluid had not gained enough momentum. It then increased progressively and reached the highest value in the compression stroke. A foremost tumbling motion had developed at this stage because of the sideways tumbling action. Tumble slowly decreased as the compression stroke ended. Near the TDC, because of compression of circumferential charge, the tumble got squished and then broke into small vortices that led it to a sudden rise in the tumble near TDC after that the tumble again decreasing because of low kinetic energy

In velocity contour, during suction, the lumps of eddies were seen, and during compression, the compressed fluid layers were seen at CA 604, which then broke into small vortices at CA 608.

3.2 Effect of Tumble and Swirl on in-Cylinder Pressure

In-cylinder pressure with various swirl and tumble ratio is plotted in Figs. 6 and 7. Cylinder pressure and temperature increased with increasing engine speeds and tumble and swirl motion; the reason being the observation which suggested that with an increase in speed, the fuel also increased to keep the power constant; there is a small pressure variation observed in the gasoline blends with respect to the gasoline. The peak rise in pressure can be seen in the 2500 rpm with swirl and

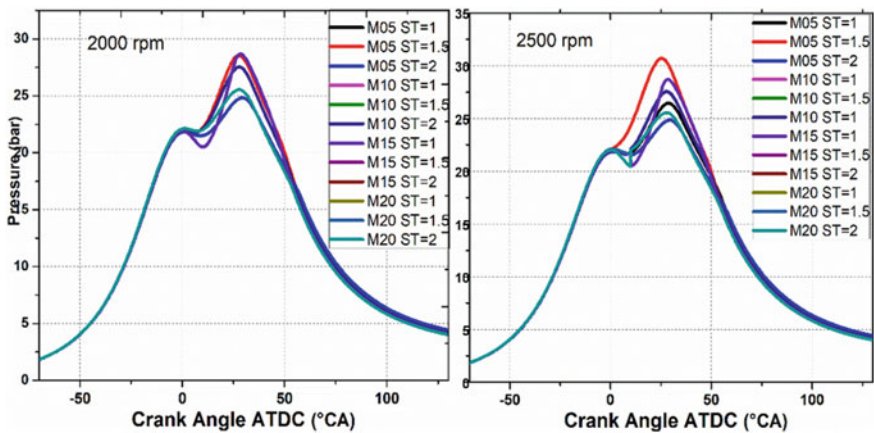


Fig. 6 In-cylinder pressure variation with swirl and tumble ratios

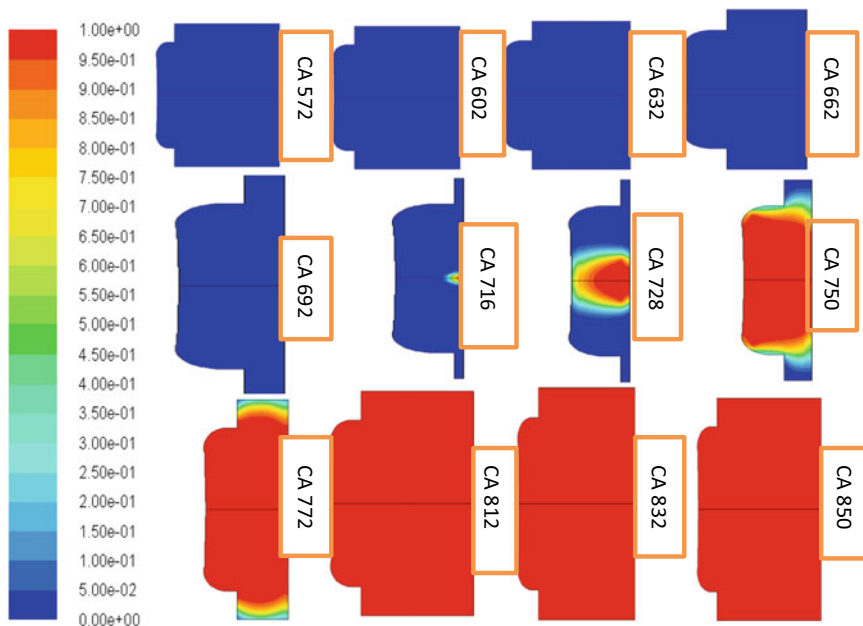


Fig. 7 Contours of premix combustion during compression and power stroke

tumble of 1.5 as more the fuel, the more the heat release, and so the increase in pressure was observed. At lower swirl and tumble, the flame velocity associated with laminar was comparatively lower as the turbulence decreased. Therefore, the fuel burnt slowly that gave two times a rise in pressure in a small fluctuation. The peak pressure in gasoline also occurred slightly before than blends because the flame speed in blends was lower than gasoline. It could be seen that by using different blends, the pressure developed in the cylinder was more when we used the blend of gasoline and alcohol; the temperature was also increased. From this, it could be said that the increase in pressure and temperature increased the power, and also the heat added increased the BTE of the engine. Methanol burns very cleanly because it already has oxygen content within it, which helps in pure burning. The results also showed that beyond 1.5 tumble, there is a slight decrease in temperature because of high turbulence that increased the heat transfer rate and also gave better mixing than lower tumble. High swirl also affected the flame speed as in blend, the flame speed is lower, but the swirl compensates that speed with an increase in turbulence.

3.3 *Contours of in-Cylinder Progress Variables During Combustion*

In the given figure, the premix combustion progress variable is shown at different crank angles saved during the simulation.

4 Conclusions

The complete in-cylinder tumble flows are mainly dependent on the crank angle position, regardless of the engine speed; very slight variation is observed with speed. A variable swirl and tumble have shown an effect that suggests that with the increase in swirl and tumble, increases the value of in-cylinder pressure and temperature as the fuel and air get mixed together, and tumble increases the value of in-cylinder pressure and temperature. Complete combustion takes place because of oxygen content in methanol and also increases in volumetric efficiency because of its latent heat of vaporization that gives the cooling effect to the charge and leads to an increase in density.

References

1. Agarwal AK, Karare H, Dhar A (2014) Combustion, performance, emissions and particulate characterization of a methanol–gasoline blend (gasohol) fuelled medium duty spark ignition transportation engine. *Fuel Process Technol* 121:16–24
2. Hu T, Wei Y, Liu S, Zhou L (2007) Improvement of spark-ignition (SI) engine combustion and emission during cold start, fueled with methanol/gasoline blends. *Energ Fuels* 21(1):171–175
3. Liu S, Clemente ERC, Hu T, Wei Y (2007) Study of spark ignition engine fueled with methanol/gasoline fuel blends. *Appl Therm Eng* 27(11–12):1904–1910
4. Yanju W, Shenghua L, Hongsong L, Rui Y, Jie L, Ying W (2008) Effects of methanol/gasoline blends on a spark ignition engine performance and emissions. *Energ Fuels* 22(2):1254–1259
5. El-Emam SH, Desoky AA (1985) A study on the combustion of alternative fuels in spark-ignition engines. *Int J Hydrogen Energ* 10(7–8):497–504
6. Cetinkaya S, Celik B (1997) The use of methanol–gasoline blends as fuel in spark ignition engine. In: Fifth international combustion symposium, Uludag University, pp 21–23
7. Falfari S, Brusiani F, Bianchi GM (2014) Numerical analysis of in-cylinder tumble flow structures–parametric 0D model development. *Energy Procedia* 45:987–996
8. Lee K, Bae C, Kang K (2007) The effects of tumble and swirl flows on flame propagation in a four-valve SI engine. *Appl Therm Eng* 27(11–12):2122–2130
9. Shaikh MA, Shukla AH (2016) Optimization of natural gas mixture design by computational method for improving swirl effect to obtain enhancement of SI engine performance: a review. *Int J Curr Eng Technol* 6(5):1509–1514

10. Königsson F, Dembinski H, Angstrom HE (2013) The influence of in-cylinder flows on emissions and heat transfer from methane-diesel dual fuel combustion. *SAE Int J Engines* 6 (4):1877–1887
11. Li Y, Zhao H, Peng Z, Ladommatos N (2001) Analysis of tumble and swirl motions in a four-valve SI engine. *SAE Trans* 2226–2241
12. Hu X, Lokhande B (2006) Simulation and validation of IC engine swirl/tumble using different meshing strategies (No. 2006-01-1195). SAE technical paper

An Experimental Analysis of the Thermal Performance of Solar Air Heater (SAH) Having Two Different Absorber Plate Along with (PCM)-Based Energy Storage



Arvind Kumar Singh and Nitin Agarwal

Abstract This work aims to examine the thermal output of a solar air heater (SAH) with flat plate absorber and an absorber having flat plate with conical extended geometry; along with the phase change material (PCM). During the investigation, the PCM was placed under the absorber plate. During this inquiry, paraffin was taken as a PCM. The thermal output of the newly developed absorber plate by means of conical extended geometry has been analyzed in this work, and it has been compared to a flat plate absorber of conventional SAH. The integrated solar air heater (SAH) including paraffin wax as a PCM is developed and tested in Moradabad city under normal weather conditions (Latitude—28.84° N, and 78.79° E), Uttar Pradesh. The various thermal performance parameters have been evaluated for the established SAH. These parameters are solar radiation, instant thermal efficiency, the difference in temperature around the heater, and the PCM effect. Constant rate of mass flow 0.01 kg/s has been used to test the parameters for the thermal efficiency. The average thermal efficiency of 55–60% has been obtained at the constant rate of mass flow 0.01 kg/s. The uppermost thermal efficiency was acquired when utilizing absorber plate with conical extended geometry filled with PCM at operation condition. As the result obtained during experiment, it is clear that, utilizing PCM, the air exit temperature for flat plate SAH with extended conical geometry is above the ambient temperature of 2–10 °C for 4.5 h after nightfall compared to 1–6 °C for 2.7 h after sunset for the flat plate absorber SAH when constant rate of mass flow 0.01 kg/s has been maintained. It also comes to the conclusion that, utilizing extended geometry, the charging and discharging time of PCM is much lower than without utilizing extended geometry.

Keywords Solar air heater (SAH) · Solar energy · Energy storage · Phase change material (PCM)

A. K. Singh (✉) · N. Agarwal
Department of Mechanical Engineering, MIT, Moradabad, India
e-mail: arvindmit230144@gmail.com

N. Agarwal
e-mail: nitin23757@gmail.com

1 Introduction

Energy comes from solar is a source of renewable energy, it could be used effectively for various solar thermal applications, and SAH is one of its applications, and the use of this technology plays a significant role. Solar air heaters (SAH) are used primarily to dry cereals, timber seasoning, house heating, and agricultural product drying, and [1]. Wazed et al. [2] studied a cost-effective, simple in design, maintenance, and less expensive solar air heater (SAH). The collector in the solar air heater (SAH) absorbs the incident energy that comes from solar, and this energy is converted into heat energy after absorption and the converted into the energy in the form of heat and that energy is taken over to the fluid which flows through the SAH [3]. Due to seasonal and regional variation of solar irradiation, collector performance in SAH is varied in nature. This requires an efficient thermal energy storage system to accommodate this variability. Previous research shows that a unit to store thermal energy could be divided into three separate categories, specifically storage with chemical energy, latent heat storage, and sensible energy storage [4–10]. Alkilani et al. [11] analyzed a solar air collector filled with PCM in cylindrical container at eight different rate of mass flow. Karim and Hawlader [12] studied solar air heaters with flat plate, using fin and corrected in V shape sheet both in experimental terminology and in theory. They found that the corrugated collector in V shape was 10–15% greater performance than the flat plate and 5–11% greater performance than the collector using pate with fins. When the rate of air flow was 0.04 kg/s, Kabeel et al. [13] experimentally analogized the SAH with a flat plate and V-corrugated absorber with and without PCM. This was noticed that the solar air heater with corrugated plate in V shape, the exit temperature was 1.5–7.2 °C for 3.5 h after nightfall, as compared to 5.5 °C for 2.5 h at sunset for a flat plate SAH at a given rate of mass flow. Mettawee and Assassa [14] integrated SAH with paraffin wax as a latent energy storage medium been analyzed after experiment. After investigation, it has been found that the PCM layer thickness tends to increase the coefficient of heat transfer due to convection and the discharging time increases. Alta et al. [15] analyzed and compared with three diverse designs of a SAH with flat plate, two with extended geometry and one without extended geometry. After calculation of the energy output rates, the SAH with double vents are more powerful. However, they also said that air circulation time is more essential than glazing. Alkilani et al. [16] manufactured a domestic SAH by integrating series of copper pipes PCM filled in and mixed with aluminum to increase PCM conductivity. On the basis of an experimental study, they concluded that the system remained in operation for 8 h after sunset at a rate of 0.05 kg/s. Saxena et al. [17] conducted an experimental investigation of four different configurations of the SAH and found that the thermal performance of all new configurations had improved compared to conventional configurations for both natural and force convection. Saxena et al. [18] also discuss an article describing the detailed advances in SAHs together with several novel SAHs patents. They also addressed the various methods that can be used to make improvements in efficiency of SAHs, as with the

incorporation of photovoltaics with heaters, the use of sensitive or latent storage media, the using concentrator in heaters, dimensions optimization, etc. During design and construction of flat plate solar air heater, the ASHRAE guidelines 93-77 [19] are taken care.

The use of absorber having flat plate with conical extended geometry filled with PCM in solar air heater is not studied so far. So in this investigation, a SAH having flat plate having conical extended geometry filled with PCM beneath the absorbing surface is taken into consideration for analysis. As the result obtained by investigation, it has been accomplished that the performance of SAHs is improved by utilizing conical extended geometry filled with PCM. According to this study, the result was that not only the use of PCM boosts the routine performance but also reduces the working time of the SAH. It is also concluded that utilizing extended geometry with PCM, the charging and uncharging time of PCM reduces and by which, we can melt more volume of PCM that means store more energy for specified area of collector, and it will increase the performance of SAH during hours off sunlight.

2 Thermal Performance Evaluation of SAHs

The impact of various parameters on developed solar air heater utilizing experimental data have been analyzed. The essential equations of various factors to measure solar air heater (SAH) output are shown in this portion.

Flow of the air mass is calculated by;

$$\dot{m} = \rho_a A_a V_a \quad (1)$$

Valuable thermal gain (Q_u) is given by the;

$$Q_u = \dot{m} c_p \Delta t_a \quad (2)$$

where A_c is collector's cross-sectional area in m^2 , ρ_a is the air density in kg/m^3 , and V_a is the speed of air at exit of collector in m/s . The amount of heat energy stored at any time within the PCM is given by [20, 21];

$$Q_s = \frac{m_{pcm}}{\Delta t} c_{p,s} \Delta T_{pcm}, \quad T_{pcm} < T_m \quad (3)$$

$$Q_s = \left(\frac{m_{pcm}}{\Delta t} \right)_{pcm} c_{p,s}, \quad T_{pcm} = T_m \quad (4)$$

$$Q_s = \frac{m_{\text{pcm}}}{\Delta t} c_{p,L} \Delta T_{\text{pcm}}, \quad T_{\text{pcm}} > T_m \quad (5)$$

where Δt is the time interval in second, ΔT_{PCM} is the increase in temperature of phase change material (PCM) in $^{\circ}\text{C}$, m_{pcm} is the mass of PCM in kg, L is PCM latent heat in J/kg, T_{pcm} is the PCM average temperature in $^{\circ}\text{C}$, T_m is the temperature at which PCM melts in $^{\circ}\text{C}$, and $c_{p,L}$, $c_{p,s}$ are the liquid and solid PCM specific heat in (J/kg $^{\circ}\text{C}$). The heat transfer coefficient due to convection between the absorber plate and air is determined by [22, 23];

$$h = Q / (A_p \cdot (T_{\text{ab}} - T_{\text{air}})) \quad (6)$$

where T_{ab} is average temperature of absorber plate in $^{\circ}\text{C}$, T_{air} is the mean air temperature inside the collector (in $^{\circ}\text{C}$), and Q is the valuable heat received by air in (W).

The collector's average output can be determined by cumulative heat gain from the air to the accumulated incident radiation that is dropping during the whole day at the solar air heater, that is given by [22];

$$\eta_{\text{avg}} = \frac{Q_u}{I \cdot A_p} \quad (7)$$

The solar air heater's instantaneous thermal efficiency (η_{ins}) is measured as the helpful heat transfer from the air within the collector to the solar energy falling on the surface of heaters, which is given by [24];

$$\eta_{\text{ins}} = \frac{Q_u}{I \cdot A_p} \quad (8)$$

where I is the total radiation energy falling at the air heater (W/m^2) and A_p is projected area of the heater.

3 Experimental Setup

The experimental setup has been designed, constructed, and tested with absorber plate having conical extended geometries surrounded by PCM fitted at the base of the air heater and an experimental setup having simple flat absorber plate as shown in Fig. 1. This figure shows the solar air heater with absorber plate having conical extended geometries surrounded by PCM fitted at the base. When we remove the conical extended geometry from Fig. 1, the construction and all dimensions are exactly same for second configuration. Comparisons and validation of the thermal performance of these heaters are discussed in result and analysis part.

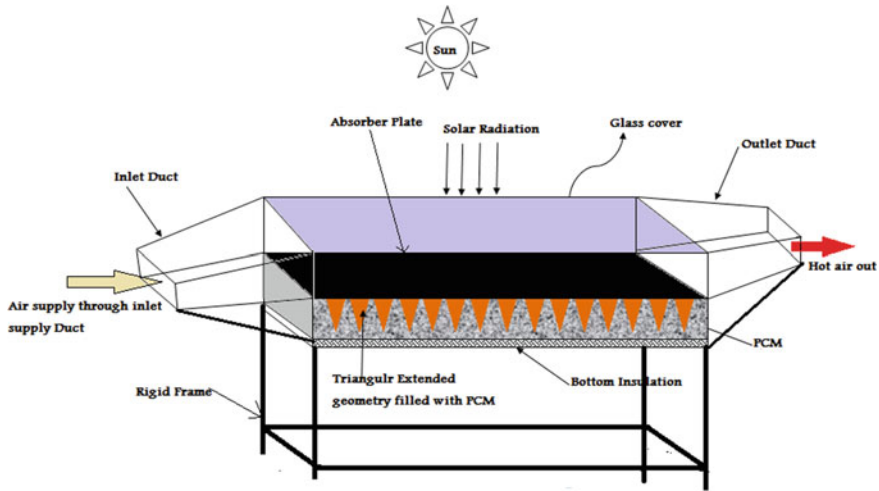


Fig. 1 Experimental setup

The solar collector taken during this experimentation has a gross collector area of 5775 cm². The total height of collector has been taken 95 mm from the glazing to underside of PCM. The developed solar air heater (SAH) has been constructed as an overflow type. Fabricated supporting structure of the collector is made of mild steel. A flat absorber plate consists of 70 conical extended geometries in seven columns. The glass wool insulation is properly packed at the sides and underside of the collector to minimize loss of collector’s heat. The wooden layer is used to encapsulate the whole set up and 4 mm toughed glass is used as glazing material. A rectangular tapered duct of diverging in nature at inlet and converging in nature at outlet is formed in between the absorber plate and glazing. The height of extended geometries has been taken 5 cm, the height of extended geometry is 5 cm, and the base diameter of conical extended geometries has been taken 40 mm each.

Figure 2 shows the sectional view of the SAH with absorber plate having conical extended geometry. The air flow passage through collector with conical extended geometries (filled with and without PCM) as given in Fig. 2, and the conical extended geometries are positioned vertically downward pointing to base of PCM. The height of the extended geometries is 50 mm. All the leakage from the side and bottom of the collector are prevented utilizing silicon sealant.

Table 1 [25] displays the properties of phase change material (paraffin wax) taken in this experimental analysis. Each experiment has been conducted in such a way that leakage can be prevented during the melting of paraffin wax.

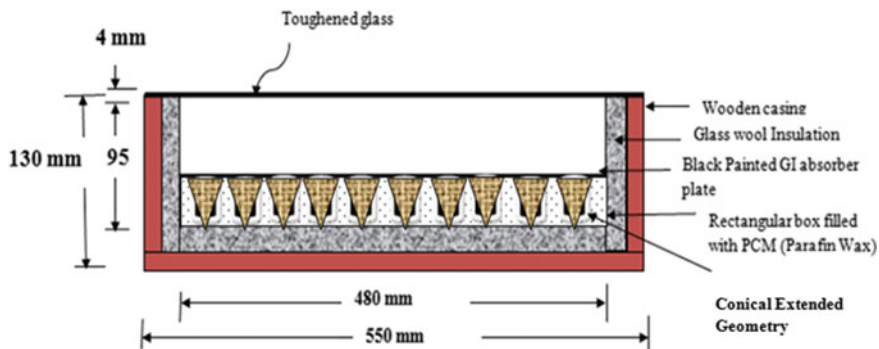


Fig. 2 Sectional view of overflow SAH having flat absorber plate with conical extended geometry

Table 1 PCM thermo-physical properties [25]

Property	Value
Thermal conductivity	0.21 W/m °C
Heat capacity	2.1 kJ/kg °C
Latent heat of fusion	190 kJ/kg
Melting temperature	46 °C
Solid density	876 kg/m ³
Liquid density	795 kg/m ³

4 Experimental Procedure and Measurement

The solar air heater has been tested utilizing PCM for flat plate as an absorber and also integrated with conical extended geometry. Before conducting the experiments, it has been ensured that there should not be any leakage of air and PCM from all joints, fittings, links, etc., of the heater. It is also ensured that all instruments used to measure different parameters works properly. All tests were carried out in perfect heavenly days during May and June 2019 at Moradabad Institute of Technology (Moradabad, Latitude—28.84° N, and 78.79° E). The various measured variables in all experiments include intensity of radiation normal to the absorber surface, inlet and outlet temperature, ambient air temperature, glass temperature, as well as the absorber plate temperature at various points. Rate of mass flow of air has been calculated from the velocity of outlet of air at heater. Air velocity has been measured by a digital anemometer (Model AM 4201) having range of 0.4–30 m/s. Accuratness of anemometer used was 0.1 m/s. The solar intensity of radiation has been measured with ‘Solarimeter’, which has a minimum count of 2 mW/cm² with 2% accuracy on the full-scale range of 0–120 mW/cm². Digital multipoint calibrated temperature sensors with the range of temperature from 10 to 125 °C and with an accurateness of ± 0.5 °C has been used to compute the temperature at various locations in the air heater.

5 Results Analysis and Discussion

Thermal output of the designed SAH, taking two unlike configurations of the absorbing surface, first, a flat plate, and, second, a flat plate with conical extended geometry have been analyzed with and without utilizing PCM at constant mass flow rate, i.e., 0.01 kg/s. All the experiment has been conducted when the PCM thickness below the absorber plate is taken 5 cm. Initially, the solar air heater has been tested taking flat plate absorber arrangement without utilizing PCM.

The Fig. 3 demonstrates the hour by hour fluctuations in the temperatures measured at various parts of heater without the use of PCM in May 2019. It is evident from Fig. 3 that the radiation intensity increases with time, along with the temperature of different elements also increases with time and the maximum intensity, and temperature at 1:00 p.m. is obtained. The value of the $T_{a,out}$, T_p , $T_{a,avg}$ maximum measured temperatures was found to be 58 °C, 81 °C, 44 °C, respectively. It is also obtained that at 1:00 p.m., the average solar intensity is 760 W/m², and the ambient temperature rises first and then decreases from 30 to 44 °C, as seen in the Fig. 3.

The SAH is then tested when a flat plate with incorporated conical extended geometry is replaced without the use of PCM. Figure 4 represents the hourly variations of temperature achieved by various elements of solar air heater with flat plate with conical extended geometry without utilizing PCM on May 2019 at constant rate of mass flow, i.e., 0.01 kg/s. Utmost temperature value measured in the plate (T_p), average air temperature ($T_{air,avg}$), and outlet temperature of air ($T_{air,out}$) has been achieved to be 75 °C, 41 °C, and 65 °C, correspondingly.

The thermal performance of the above two configurations have been tested utilizing the PCM taking 5 cm PCM thickness at constant rate of mass flow 0.01 kg/s. The above Fig. 5 shows the hourly variability in ambient temperature, temperature of the various elements, and solar radiation intensity for solar air

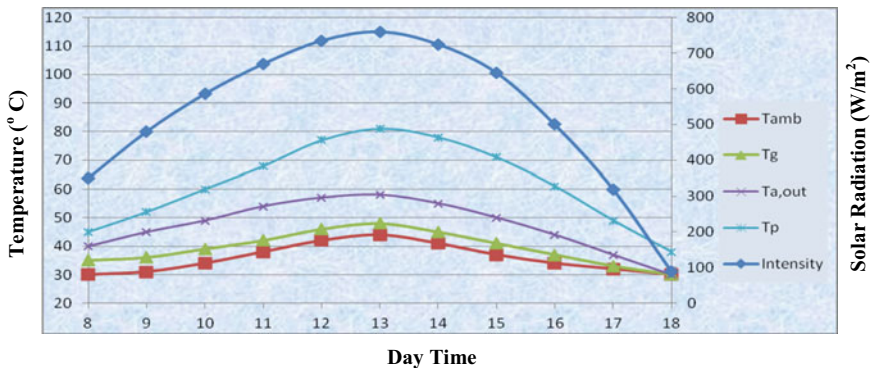


Fig. 3 Temperatures assessed in components of the SAH with flat absorber plate without the use of phase change material versus time

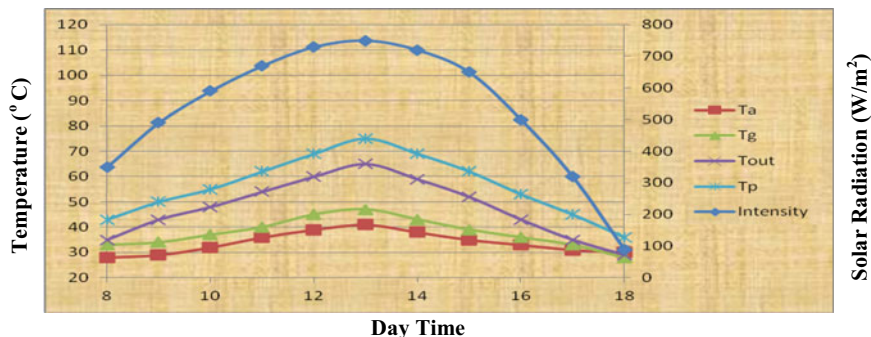


Fig. 4 Temperatures assessed in various parts of SAH with conical extended geometry in flat absorber plate without phase change material versus time

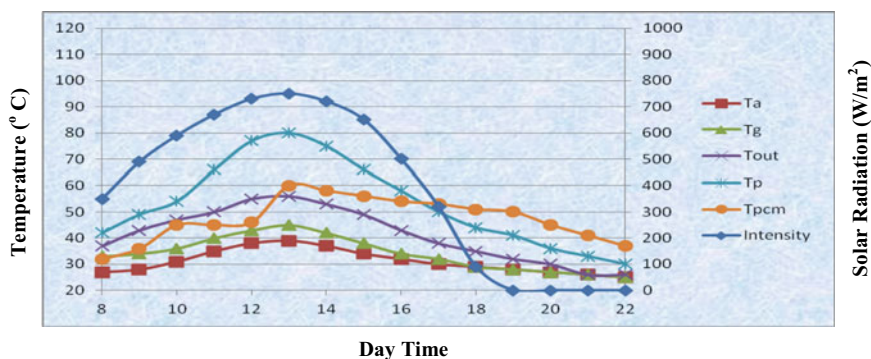


Fig. 5 Measured distributions of temperatures of different flat absorber plate SAH components by the use of PCM, versus time

heaters having flat plate absorber with the thickness of phase change material which is 5 cm in June 2019. From the analysis as indicated in Fig. 5, the utmost temperature of ambient (T_{amb}) and the maximum intensity of radiation intensity (I_{max}) are 39 °C and 750 W/m², respectively, at 1:00 p.m. The utmost temperature of phase change material (T_{pcm}) and air outlet temperature (T_{air}) values were measured to be 60 °C and 56 °C, respectively. The above figure also indicates that the PCM begins to melt at 10:30 a.m., and it takes about 1.75 h to fully melt at a steady temperature at 46 °C, later than which the PCM temperature begins to rise to the maximum strength. The effect of integrating PCM has been seen in the above Fig. 5 that the exit air temperature is superior than the environmental temperature by 1.4 °C to 8 °C during 2.6 h after off sunshine.

Similarly, Fig. 6 shows the hourly deviation in temperatures of the various elements in solar air heater absorbing the surface as a flat plate with conical extended geometry at 5 cm PCM thickness and variability in radiation strength,

PCM temperature and ambient temperature at constant rate of mass flow, i.e., 0.01 kg/s on June 2019. Testing reveals that the maximum radiation intensity (I_{max}) and maximum ambient temperature (T_{amb}) values at 1:00 p.m. are 750 W/m^2 and $46 \text{ }^\circ\text{C}$, respectively. The maximum temperature of air outlet and PCM temperature, respectively, was obtained at $66 \text{ }^\circ\text{C}$ and $73 \text{ }^\circ\text{C}$. It was also found that, as a flat plate with conical extended geometry, solar air heater absorption surface is more effective than the absorption surface as a flat plate. Figure 6 clearly indicates that, after introduction of conical extended geometry, phase change material provides good backup to outlet air. From Fig. 6, it is clearly shown that in 4.5 h after off sunlight, air outlet temperature is above average temperature by $2 \text{ }^\circ\text{C}$ to $10 \text{ }^\circ\text{C}$.

Figure 7 displays evaluation of the thermal efficiency SAHs with flat absorber plate and flat absorber plate with conical extended geometry over time, using paraffin wax and without the use of paraffin wax, the rate of mass flow remained constant, i.e., 0.01 kg/s. Figure 7 clearly shows that the thermal efficiency of the integrated SAH with extended geometry is superior to that of the without extension geometry. It was also evident that, with flat plate and flat plate combined with conical extended geometry without the use of paraffin wax, thermal efficiency of the SAH increases as time rises before it enters a peak at 1:00 p.m. and then reduces to zero gradually at sunset. Therefore, if the phase change material is used, thermal efficiency then grows with increasing time and reaches their peak value at 1:00 p.m. and slowly decreases to 4:00 p.m. then increases dramatically due to the large PCM heat supply during phase of discharge.

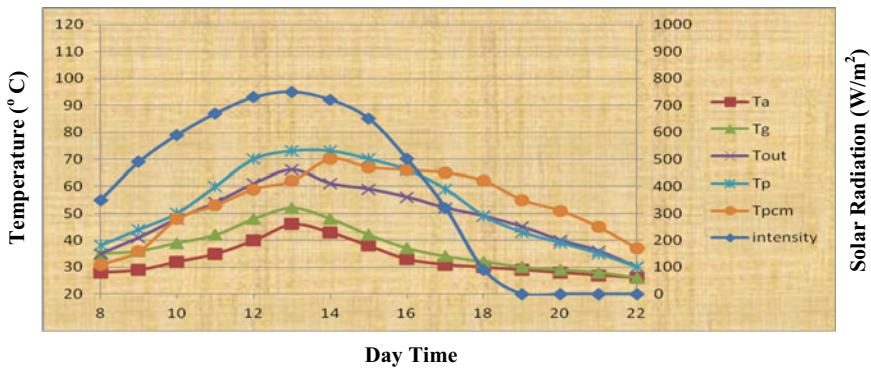


Fig. 6 Measured distributions of temperatures at various parts in SAH with flat absorber plate integrated with conical extended geometry utilizing PCM, versus time

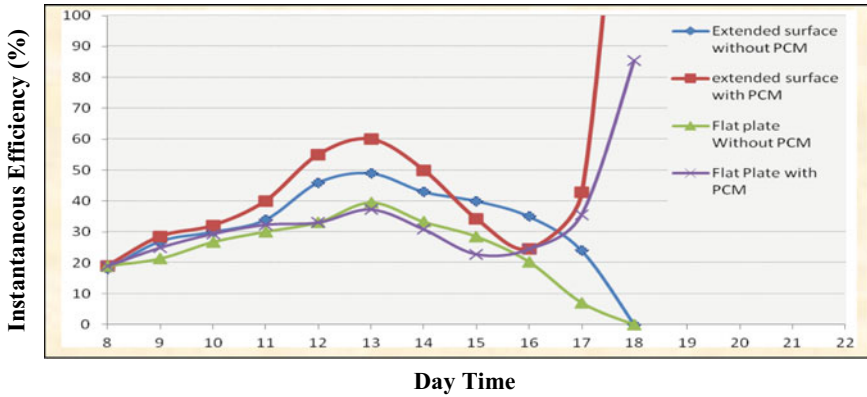


Fig. 7 Comparison of SAH thermal efficiency between absorber plate as a flat absorber plate with conical extended geometry and just a flat absorber plates, without and with phase change material when 0.01 kg/s is available

6 Conclusions

In this study, first, a flat absorber plate and, second, a flat absorber plate with conical extended geometry combined with paraffin wax, have been analyzed. Paraffin wax is used as the medium to store latent heat. Solar air heater having extended conical geometry filled with PCM is usually more effective than the SAH with flat absorber plate. The results taken from the experimental study are as follows:

- The intensity of solar radiation increases as the time increases; it reaches maximum at 1:00 p.m.; then, it reduces to zero approximately at 7:00 p.m.
- The temperature of each element in the solar air heater increases as the intensity of solar radiation increase, and it also decreases as the intensity of solar radiation decreases.
- PCM acts as thermal energy storage and provides backup of the exit fluid temperature on the SAH, especially during off-sunshine periods.
- With use of conical extended geometry, the outlet temperature of a flat plate is above the ambient temperature of 2–10 °C for 4.5 h after sunset compared to 1–6 °C for a flat plate absorber for 2.7 h after sunset while rate of mass flow of air was held constant, i.e., 0.01 kg/s.
- Often, this happens that due to the use of extended geometry with phase change material, phase change material PCM begins discharging 1–1.3 h before the SAH has flat absorber plate filled with paraffin wax, and it also takes less time to discharge completely than flat plate by means of PCM. Because of this, it can also help with bad atmospheric conditions.

- Using PCM with conical extended geometry, the thermal efficiency obtained is higher than the respective without phase change material maintaining a constant rate of mass flow 0.01 kg/s.
- It was thus concluded too; from this study that conical extended geometry filled with PCM is the more efficient means of improving the solar air heater thermal efficiency.
- From this study, it is clear that the solar air heater fitted with conical extended geometric absorber is more efficient than flat plate absorber when using PCM.

References

1. El-Sebaei AA, Aboul-Enein S, Ramadan MRI, Shalaby SM, Moharram BM (2011) Thermal performance investigation of double pass-finned plate solar air heater. *Appl Energy* 88 (2011):1727–1739
2. Wazed MA, Nukman Y, Islam MT (2010) Design fabrication of a cost effective solar air heater for Bangladesh. *Appl Energy* 87(2010):3030–3036
3. Rajaseenivasan T, Srinivasan S, Srihar K (2015) Comprehensive study on solar air heater with circular and V-type turbulators attached on absorber plate. *Energy* 88(2015):863–873
4. Li W, Zhang R, Jiang N, Tang XF, Shi HF, Zhang XX, Zhang Y, Dong L, Zhang N (2013) Composite macro capsule of phase change materials/expanded graphite for thermal energy storage. *Energy* 57(2013):607–614
5. Jurinak JJ, Abdel-Khalik SI (1979) On the performance of air-based solar heating systems utilizing phase-change energy storage. *Energy* 4(1979):503–522
6. Duffie JA, Beckman WA (1991) *Solar engineering of thermal processes*, second edn. John Wiley and Sons, New York
7. Sokhansan S, Schoenau GJ (1991) Evaluation of a solar collector system with thermal storage for preheating ventilation air in farm buildings. *Energ Convers Manage* 32(1991):183–189
8. Domanski R, El-Sebaei AA, Jaworski M (1995) Cooking during off-sunshine hours utilizing PCMs as storage media. *Energy* 20(1995):607–616
9. Farid MM, Khudhair AM, Razack SAK, Al-Hallaj S (2004) A review on phase change energy storage: materials and applications. *Energ Convers Manage* 45(2004):1597–1615
10. Zhou D, Zhao CY, Tian Y (2012) Review on thermal energy storage with phase change materials (PCMs) in building applications. *Appl Energy* 92(2012):593–605
11. Alkilani MM, Sopian K, Mat S, Alghoul MA (2009) Output air temperature prediction in a solar air heater integrated with phase change material. *Eur J Sci Res* 27(2009):334–441
12. Karim M, Hawlader M (2006) Performance investigation of flat plate, v-corrugated and finned air collectors. *Energy Convers Manage* 31:452–470
13. Kabeel et al (2016) Experimental investigation of thermal performance of flat and v-corrugated plate solar air heaters with and without PCM as thermal energy storage. *Energy* 113:264–272
14. Mettawee EB, Assassa GMR (2006) Experimental study of a compact PCM solar collector. *Energy* 31:2958–2968
15. Alta D, Bilgili E, Ertekin C, Yaldız O (2010) Experimental investigation of three different solar air heaters: energy and exergy analysis. *Appl Energy* 87(2010):2953–2973
16. Alkilani MM, Sopian K, Mat S, Alghoul MA (2009) Output air temperature prediction in a solar air collector integrated with phase change material. *Eur J Sci Res* 27(3):334–434
17. Saxena A, Agarwal N, Srivastava G (2013) Design and performance of a solar air heater with long term heat storage. *Int J Heat Mass Transf* 60(2013):8–16

18. Saxena A, Varun, El-Sebaei AA (2015) A thermodynamic review of solar air heaters. *Renew Sustain Energy Rev* 43(2015):863–890
19. Standard A (1977) *Methods of testing to determine thermal performance of solar collectors*, 345. Ashrae, New York
20. Radhwan AM (2004) Transient performance of a steeped solar still with built-in latent heat thermal energy storage. *Desalination* 171:61–76
21. El-Sebaei AA, Al-Ghamdi AA, Al-Hazmi FS, Faidah AS (2009) Thermal performance of a single basin solar still with PCM as a storage medium. *Appl Energy* 86:1187–1195
22. Kays WM, Crawford ME (1980) *Convective heat and mass transfer*, second edn. Mc Graw-H, New York
23. Kabeel AE et al (2017) Improvement of thermal performance of the finned plate solar air heater by using latent heat thermal storage. *Appl Therm Eng* 546–553
24. Gao W, Lin W, Liu T, Xia C (2007) Analytical and experimental studies on the thermal performances of cross-corrugated and flat-plate solar air collectors. *Appl Energy* 425–441
25. Zalba B, Marin JM, Cabeza LF, Mehling H (2003) Review on thermal energy storage with phase change materials, heat transfer analysis and applications. *Appl Therm Eng* 23:251–283

Comparative Study of the Fluid Interface-Capturing High-Resolution Algebraic Schemes



Ashish Arote , Mukund Bade, and Jyotirmay Banerjee

Abstract The present work demonstrates the qualitative and quantitative comparison between high-resolution algebraic interface-capturing schemes applied to volume of fluid (VOF) method. *Basic Compressive Interface-Capturing Scheme for Arbitrary Meshes* (B-CICSAM), *Modified Compressive Interface-Capturing Scheme for Arbitrary Meshes* (M-CICSAM), *Flux-Blending Interface-Capturing Scheme* (FBICS) and *Cubic Upwind Interpolation Based Blending Scheme* (CUIBS) are compared in the present study. Comparisons are based on the L_2 norm of the mass loss and topological accuracies shown by the above schemes when subjected to the known flow field causing shearing and deformation of the fluid interface. The present study also demonstrates the performance of these schemes when applied to real-life problems such as Rayleigh–Taylor instability. It is observed that FBICS is accurate and robust as compared to other methods, whereas M-CICSAM displays comparatively similar accuracy at lower Courant values but by being computationally efficient. On the other hand, it was observed that CICSAM and CUIBS display strong dependency over the Courant values.

Keywords VOF · Interface capturing · Rayleigh–Taylor instability · Algebraic VOF

1 Introduction

The shear flow modelling involving multiple fluids is an intriguing and challenging problem. The accurate depiction of the surface topology with minimal distortion has been the prime objective for the researchers involved in the simulation of such

A. Arote (✉) · M. Bade · J. Banerjee
Sardar Vallabhbhai National Institute of Technology, Surat 395007, India
e-mail: ashisharote4@gmail.com

M. Bade
e-mail: mukundbade@gmail.com

J. Banerjee
e-mail: jbaner@med.svnit.ac.in

flows. Algebraic VOF methods provide better platform for such simulations. These methods make use of the blend between a bounded and higher order schemes to obtain an accurate and monotonic solution.

The initial attempt towards development of algebraic VOF methods was made by Ubbink and Issa [1] and Muzafferija [2] in the form of *Compressive Interface-Capturing Scheme for Arbitrary Meshes* (CICSAM) and *High-Resolution Interface-Capturing* (HRIC) scheme, respectively. These methods had a shortcoming which required the *Courant* (Co) condition to be lowered so as to avoid the interface distortion. Thus, improvement came in the form of *Switching Technique for Advection and Capturing of Surface* (STACS) [3], *High-Resolution Artificial Compression* (HiRAC) [4] and *modified-CICSAM* (M-CICSAM) [5] which used hybrid limiters to tackle the co-conditions. Furthermore, there are methods such as *Cubic Upwind Interpolation-based Blending Scheme* (CUIBS) [6] and *Flux-Blending Interface-Capturing Scheme* (FBICS) [7] that attempted completely co-independent scheme where the solution does not get distorted as co-value is increased. Here, M-CICSAM performs better than CICSAM, HRIC and STACS by preserving mass and being efficient.

The qualitative and quantitative comparison between M-CICSAM, CUIBS, FBICS and CICSAM has not been performed yet in the literature. Such comparison is important in view of the applicant as it makes it easy to decide the method needed for a particular problem. Also, it becomes important to identify the shortcomings of certain methods when compared with others as it will lay down the foundation for the improved methods.

The present study compares the algebraic VOF methods using standard test cases based on the interface topology and their mass preserving capabilities.

2 Governing Equations

The VOF method designates the colour function as the volume fraction (ϕ) of each phase in a cell. This colour function takes up value 0 for secondary fluid and 1 for primary fluid, whereas for interface, value lies between 0 and 1.

The volume fraction in each cell is obtained after the solution of general scalar transport Eq. (1).

$$\iiint_{cV} \frac{\partial \phi}{\partial t} dV + \iint_{cS} (\vec{V} \phi) d\vec{A} = 0 \quad (1)$$

where scalar ϕ is advected across each cell of volume \forall over a given time by the velocity vector \vec{V} . The discretized version of Eq. (2) can be written as,

$$\frac{\phi_p^{n+1} - \phi_p^n}{\Delta t} \nabla_p = - \sum_{\text{faces}} \left(\frac{\phi_f^{n+1} + \phi_f^n}{2} \right) F_f^n \quad (2)$$

Here, the right-hand side of the Eq. (2) is treated by a Crank–Nicolson scheme with F_f^n being the flux ($F_f^n = \vec{V}_f \vec{A}_f$) through face f . The above equation needs the velocity field to advect the volume fraction ϕ over the domain. This velocity field is provided by the equations governing the physical system. In this case, we choose the Navier–Stokes equations as given below in their non-dimensional form.

$$\frac{\partial u_j}{\partial x_j} = 0; \quad \frac{\partial u_i}{\partial t} + \frac{\partial u_i u_j}{\partial x_j} = - \frac{1}{\rho^*} \frac{\partial p}{\partial x_i} + \frac{\mu^*}{\rho^* \text{Re}} \nabla^2 u_i - \frac{1}{\text{Fr}^2} + \frac{F_{ST}}{\text{We}} \quad (3)$$

where Re and Fr being the *Reynolds number* and *Froude number*, while ρ^* and μ^* represent the non-dimensional fluid density and viscosity, respectively, which can be determined based on the volume fraction as,

$$\rho^* = \phi + (1 - \phi) \frac{\rho_{\text{gas}}}{\rho_{\text{liquid}}}, \quad \mu^* = \phi + (1 - \phi) \frac{\mu_{\text{gas}}}{\mu_{\text{liquid}}} \quad (4)$$

The face volume fractions (ϕ) are estimated through the blending between two bounded (BD) and high-resolution (HR) scheme based on the interface orientation (θ) given by

$$\theta = \left| \frac{(\nabla \phi)_D \cdot \vec{d}}{|(\nabla \phi)_D| \cdot |\vec{d}|} \right| \quad (5)$$

where subscript D denotes donor cell, while \vec{d} represents the distance vector connecting two adjacent centroids of the donor and acceptor cells. The blending factor (γ) is a function of interface orientation θ , and its function varies for each method shown in Table 1. Thus, the face flux for each method demonstrated in Table 1 can be obtained by using Eq. (6),

$$\tilde{\phi}_f = \tilde{\phi}_{\text{BD}} \cdot \gamma + \tilde{\phi}_{\text{HR}} \cdot (1 - \gamma) \quad (6)$$

The $\tilde{}$ terms denote the normalized variables, and the face flux that breaks the bound ($\tilde{\phi}_D > 1$ or $\tilde{\phi}_D < 0$) is assigned with donor values. The subscript SUP represents the flux obtained through *Superbee* limiter.

Table 1 Scheme formulations for various algebraic VOF methods

Method	HR-Scheme (ϕ_{HR})	Bounded-Scheme (ϕ_{BD})
CICSAM	$\min \left\{ \frac{8Co_D \tilde{\phi}_D + (1-Co_D)(6\tilde{\phi}_D + 3)}{8}, \phi_{BD} \right\}$	$\min \left\{ \frac{\tilde{\phi}_D}{Co_D}, 1 \right\}$ $0 \leq \tilde{\phi}_D \leq 1$ $\tilde{\phi}_D > 1, \tilde{\phi}_D < 0$
CUIBS	$\frac{3\tilde{\phi}_D}{5/6\tilde{\phi}_D + 0.25}$ $0 \leq \tilde{\phi}_D \leq 2/13$ $2/13 \leq \tilde{\phi}_D \leq 4/5$ $4/5 \leq \tilde{\phi}_D \leq 1$	$3\tilde{\phi}_D$ $0 \leq \tilde{\phi}_D \leq 1/3$ 1 $1/3 \leq \tilde{\phi}_D \leq 1$
FBICS	$\frac{3\tilde{\phi}_D}{\tilde{\phi}_D + 0.25}$ $0 \leq \tilde{\phi}_D \leq 1/8$ $1/8 \leq \tilde{\phi}_D \leq 3/4$ $3/4 \leq \tilde{\phi}_D \leq 1$	$3\tilde{\phi}_D$ $0 \leq \tilde{\phi}_D \leq 1/3$ 1 $1/3 \leq \tilde{\phi}_D \leq 1$
M-CICSAM	$\frac{2\tilde{\phi}_D}{\tilde{\phi}_D + 0.25}$ $0 \leq \tilde{\phi}_D \leq 1/4$ $1/4 \leq \tilde{\phi}_D \leq 3/4$ $3/4 \leq \tilde{\phi}_D \leq 1$	$\min \left\{ \frac{\tilde{\phi}_D}{Co_D}, 1 \right\}$ $0 \leq Co \leq 0.3$ $\min \left\{ \frac{\tilde{\phi}_D}{0.3}, 1 \right\}$ $0.3 \leq Co \leq 0.6$ $\frac{0.7-Co}{0.1} \min \left\{ \frac{\tilde{\phi}_D}{0.3}, 1 \right\} + \frac{Co-0.6}{0.1} \tilde{\phi}_{SUP}$ $0.6 \leq Co \leq 0.7$ $Co \geq 0.7$ $\tilde{\phi}_{SUP}$

3 Test Cases with Known Velocity Field

The algebraic VOF methods mentioned above are tested against the standard test cases with known velocity fields. The results in the form of L_2 norm of the mass loss and interface topologies are compared at different *Courant* numbers. Thus, the error during the advection is calculated as

$$\|\text{Mass Loss}\|_2 = \frac{1}{N} \int_0^N \sqrt{|\phi_{\text{initial}} - \phi_{\text{final}}|^2} dV$$

The test cases for the advection algorithm are based on the cases taken by Saincher and Banerjee [8] and Ahn and Shashkov [9] in which case of single vortex and superman flow is covered.

3.1 Single Vortex

In single vortex test, the circular fluid patch of radius 0.15 is placed in a unit sized domain at [0.5, 0.75], and the velocity field described by Saincher and Banerjee [8] is applied until $T = 3.0$. The interface topologies at *Courant* number 0.25, 0.6 and 0.9 are compared in Fig. 1.

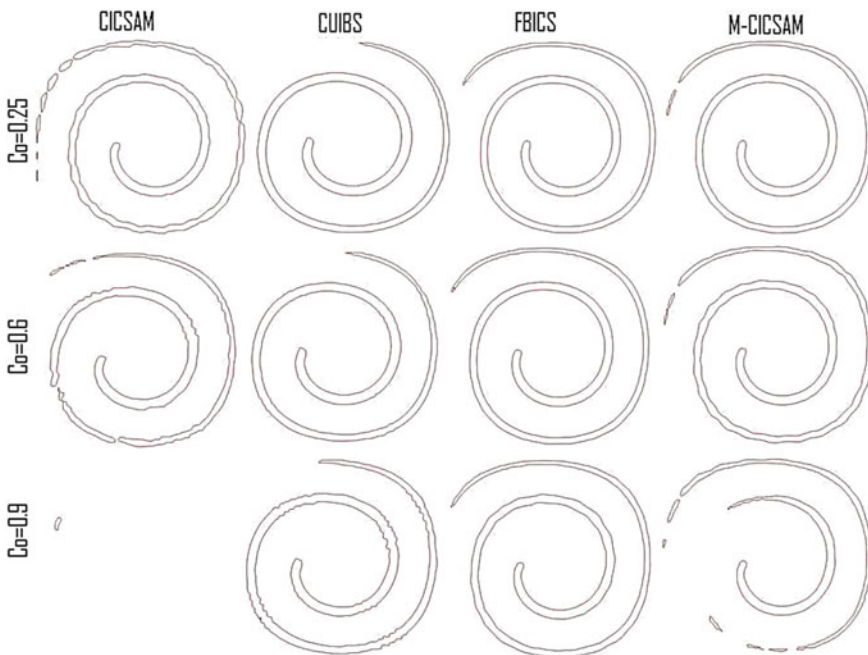


Fig. 1 Interface at $t = 3$ during single vortex test case at *Courant* number 0.25, 0.6 and 0.9

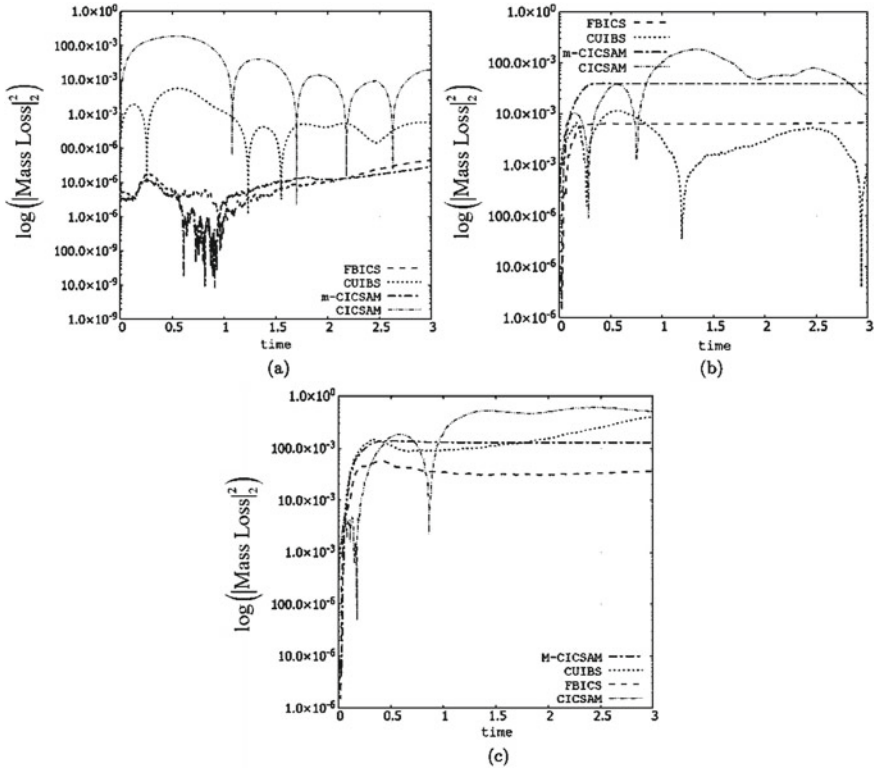


Fig. 2 L_2 norm of mass loss at **a** $Co = 0.25$ **b** $Co = 0.6$ and **c** $Co = 0.9$

It can be depicted from Figs. 1 and 2 that FBICS demonstrates better overall accuracy and robustness as compared to the other schemes. It is found to be the only method that is less affected by the *Courant* condition. M-CICSAM on the other hand provides better results at low *co*-values and can be considered when *Courant* condition required is strict. Also, it was observed during the simulations that M-CICSAM is computationally efficient as compared to others due to its blending function which does not involve *arccos* and *cos* evaluation.

3.2 Superman Flow

In superman flow test, the circular fluid patch of radius 0.25 is placed in a unit sized domain at $[0.5, 0.5]$, and the velocity field described by Saincher and Banerjee [8] is applied until $T = 2.0$. The interface topologies at *Courant number* 0.25 and 0.9 are compared in Fig. 3, while the mass loss over the time is compared in Fig. 4.

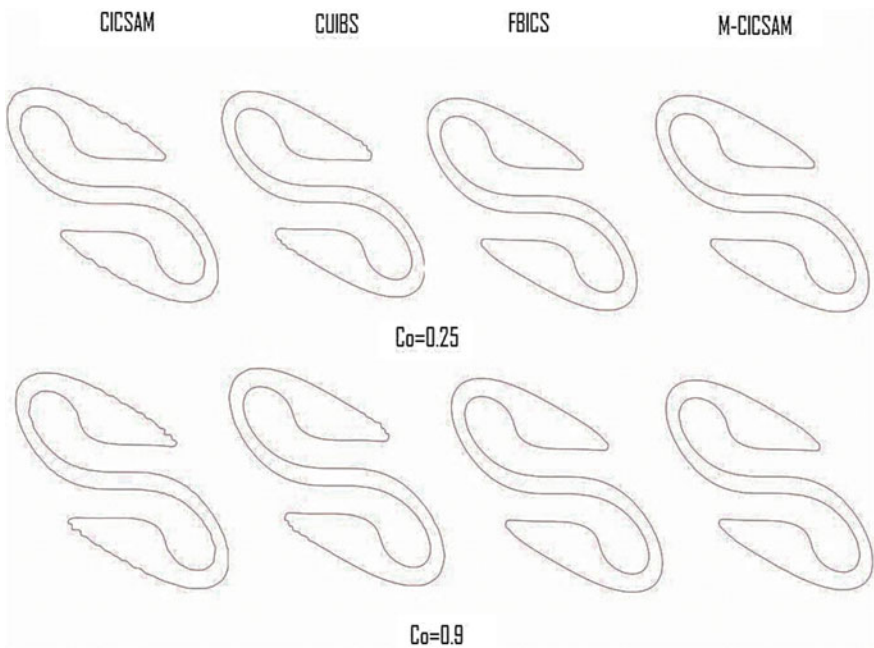


Fig. 3 Interface at $t = 2$ during superman flow test case at Courant number 0.25 and 0.9

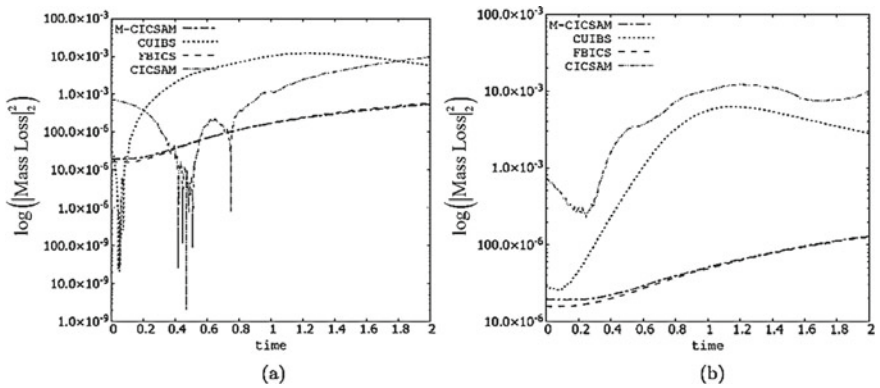


Fig. 4 L_2 norm of mass loss at **a** $Co = 0.25$ and **b** $Co = 0.9$

Similar observations can be made in the superman flow test as in Sect. 3.1. The interface gets distorted at higher Co values in CUIBS and CICSAM, whereas FBICS and M-CICSAM show better results.

4 Test Case with Unknown Velocity Field: Rayleigh–Taylor Instability

In this basic flow instability, the heavier fluid is placed on top of the lighter fluid. When a small disturbance is given on the interface, it grows to evolve as mushroom shapes in order to attain the natural equilibrium in the system. The results are compared with Rudman [10] and found to be in agreement with their results as evident from Fig. 5.

The simulations are performed with the resolution of 96×288 and maintaining the Courant value at 0.1. Figure 5 demonstrates the results obtained using FBICS method and advection term treated with blended QUICK scheme [11].

It can be observed through Fig. 6 that both the methods are equally capable and show the order of accuracy slightly ($p \sim 1.74$) less than 2.

5 Summary and Conclusions

The comparative study between the existing algebraic VOF methods on the basis of interface topology and L_2 norm of the mass loss was performed in the present study. These methods were applied to both known as well as unknown velocity fields.

It is found that FBICS method shows less distortion at the fluid interface at higher *Courant* values as compared to others. In terms of the mass preserving capability, both M-CICSAM and FBICS do well as compared to CICSAM and CUIBS.

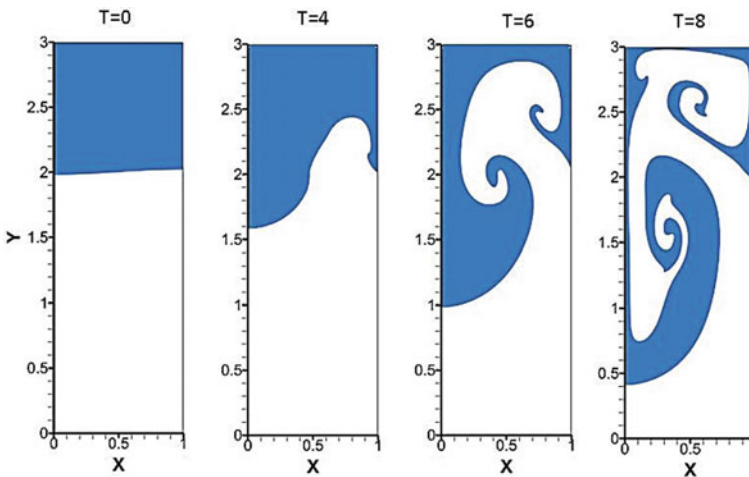
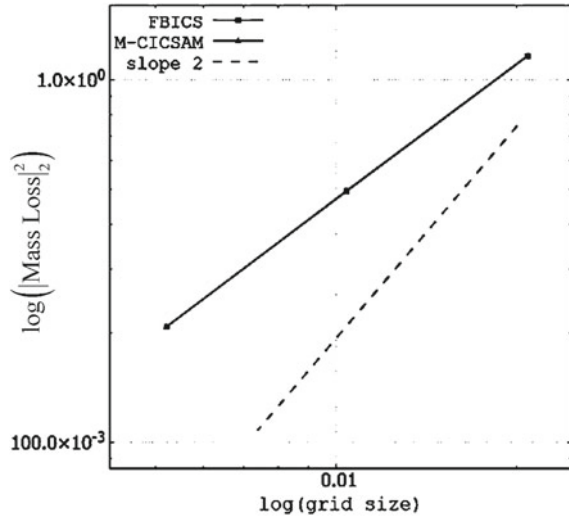


Fig. 5 Flow topology with heavy fluid represented in blue at non-dimensional time $t = 0$, $t = 4$, $t = 6$ and $t = 8$

Fig. 6 Convergence rates for FBICS and M-CICSAM methods based on L_2 norm



When these methods are coupled with Navier–Stokes equations, both M-CICSAM and FBICS show better accuracies than others and display same order of accuracy ($p \sim 1.74$) when tested for order of convergence. Even though FBICS and M-CICSAM produce overall equivalent results, M-CICSAM is computationally efficient than others due to its blending function.

References

1. Ubbink O, Issa RI (1999) A method for capturing sharp fluid interfaces on arbitrary meshes. *J Comput Phys* 153(1):26–50
2. Muzafariza S (1998) A two-fluid Navier-stokes solver to simulate water entry. In: *Proceeding of the 22nd symposium of naval hydrodynamics*. Washington, DC
3. Darwish MI, van Beek VM, Bruining J (2006) Convective schemes for capturing interfaces of free-surface flows on unstructured grids. *Numer Heat Transf Part B: Fundam* 88(1-3 SPEC. ISS.):19–23
4. Heyns JA, Malan AG, Harms TM, Oxtoby OF (2013) Development of a compressive surface capturing formulation for modelling free-surface flow by using the volume-of-fluid approach. *Int J Numer Meth Fluids* 71(6):788–804
5. Zhang D, Jiang C, Liang D, Chen Z, Yang Y (2014) A refined volume-of-fluid algorithm for capturing sharp UID interfaces on arbitrary meshes. *J Comput Phys* 274:709–736
6. Patel JK, Natarajan G (2015) A generic framework for design of interface capturing schemes for multi-fluid flows. *Comput Fluids* 106:108–118
7. Tsui Y, Lin S, Cheng T, Wu T (2009) Flux-blending schemes for interface capture in two-fluid flow. *Int J Heat Mass Transf* 52(23–24):5547–5556
8. Saincher S, Banerjee J (2015) A redistribution-based volume-preserving PLIC-VOF technique. *Numer Heat Transf Part B: Fundam* 67(4):338–362
9. Ahn HT, Shashkov M (2009) Adaptive moment-of-fluid method. *J Comput Phys* 228(8):2792–2821

10. Rudman M (1997) Volume-tracking methods for interfacial flow calculations. *Int J Numer Meth Fluids* 24(7):671–691
11. Jha R, Arote A, Banerjee J (2019) Advection stabilization using lower order scheme blending: a case study of Rayleigh Taylor instability. In: 46th National conference on fluid mechanics and fluid power (FMFP)

Performance Investigation of Atmospheric Water Generating Device for Hot and Humid Conditions



Vishakha Baghel and Basant Singh Sikarwar

Abstract Despite of the fact that Earth's atmosphere has abundant freshwater inform of moisture, water scarcity is one of the crucial problems especially in humid, hot, and drought prone regions. The conventional systems which extracts atmospheric water are very bulky, incompatible with the existing system, energy intensive, impractical, low water yield and expensive. These adverse effects hinder their deployment for large scale applications. In this manuscript, a water harvesting device is deigned and fabricated for extracting water from moist air. The device uses vertical copper pipes entrenched in horizontal Al fins as the condensing surfaces. All the components of the device functions on solar powered energy. The proposed device is environment friendly, compact, lightweight, low manufacturing, and maintenance cost. The device generate water with turbidity of 40 PPM. Results shows that condensation rates strongly depend on the relative humidity, saturation temperature of the moist air, and degree of subcooling. In this device, the cost of water is estimated as Rs. 10 per liter. This device is efficient for providing drinkable water in hot and humid, water scare regions globally.

Keywords Condensation · Water harvesting · Moist air · Copper · Condensation rate · Potable water

Nomenclature

A	Cross-sectional area of rectangular duct (mm^2)
\bar{C}	Cost of solar energy in India (Rs.)
C	Cost of producing 1 L of water from the proposed device (Rs.)
C_p	Specific heat capacity (J/kg K)
dp	Total pressure increased in the fan (N/m^2)
ΔT	Degree of subcooling ($^{\circ}\text{C}$)

V. Baghel (✉) · B. S. Sikarwar
Department of Mechanical Engineering, Amity School of Engineering and Technology,
Amity University, Noida, Uttar Pradesh, India
e-mail: vbaghel@amity.edu

B. S. Sikarwar
e-mail: bssikarwar@amity.edu

E_{total}	Total energy requirements of the device (kWh)
m	Condensation rate (l/h)
m_{cond}	Amount of condensed water collected during the experiment (l)
\dot{m}	Mass flow rate of water-cooling unit (kg/s)
M_a	Mass of air (28.963 kg/Kmol),
M_v	Mass of water vapor (18.02 kg/Kmol),
N_{max}	RPM of the fan at maximum speed
N_{req}	RPM of the fan at required speed
P_0	Total atmospheric pressure (bar)
P_{fan}	Power requirement of fan modules (kW)
P_{sat}	Pressure corresponding to saturation temperature (bar)
P_{total}	Total energy requirement of the water harvesting device (kW)
P_{WC}	Power requirement of water-cooling unit (kW)
Q_N	Flow rate of moist air at the required speed (m^3/s)
Q_{max}	Flow rate of moist air at the maximum speed (m^3/s)
RH	Relative humidity (%)
t	Total time of condensation experiment (hours)
T	Moist air temperature ($^{\circ}\text{C}$)
V_{max}	Maximum speed (m/s)

Subscripts

- a Properties of dry air
- m Properties of moist air
- v Properties of water vapor
- w Properties of water

Abbreviation

- CFM Cubic feet per minute
- PPM Parts per million
- RPM Revolutions per minute

1 Introduction

Water crisis is particularly severe challenge in hot, humid, arid, and drought prone region of the world. However, enormous amount of freshwater is present in atmospheric air in form of moisture. Harvesting water from atmospheric air is an innovative technology which have strong potential to combat the problem of potable water crisis by producing liquid water from atmospheric air. In literature, three variation of this technology is reported for instance; generating drinkable

water by cooling the atmospheric air onto/underneath a cold solid or mesh like surfaces below than the dew point temperature, concentrating water vapor by using liquid or solid desiccants, or by inducing and controlling convection in tower like structure [1, 2]. Out of these variations, the desiccant and condensation on solid and mesh like surfaces methodologies are predominantly implemented for extracting atmospheric water [3]. However, the common problem typically associated with the desiccant methods is, this system includes corrosion and the carryover of desiccant solution into the air stream [4]. Therefore, the condensation technique is more practically viable as it has ability to exploit huge amount of water from atmospheric air, it is safe for human consumption and environment as it does not produce any hypersaline waste discharge.

Various authors [5–12] have developed technologies for generating water from moist air. Ming et al. [5] designed and developed a freshwater harvesting system from moist air using solar chimney power plant. They implemented 1-D compressible fluid transfer model and estimated condensation level and rates, efficiency, and output power of the system. Eslami et al. [6] reported a holistic thermodynamic analysis of condensed water from moist air using Peltier modules. Jradi et al. [7] combined a moist air dehumidification system with solar distiller system and enhanced the distillate output to 10 l/day of fresh water from moist atmospheric air. Bamisaye and Oke [8] developed an empirical relation for estimating the water produced from moist air in an conventional room air conditional systems specially for Nigeria regions. Suryaningsih and Nurhilal [9] developed an atmospheric water generator using thermo-electric cooler and performed a CFD analysis for the same to optimize the design process. Also, several devices for generating water from moist air are commercially available [10–12]. However, these systems are very bulky, incompatible with the existing system, energy intensive, impractical, low water yield, and expensive. These adverse effects limit their implementation for large scale industrial and domestic applications.

In this background, the device for harvesting water from atmospheric air is designed and fabricated to investigate its performance parameters for enhancing its efficacy. The proposed device presents a modified alternative to the state-of-the-art available technologies. The study incorporated an experimental procedure for evaluating the effect of various parameters on the condensation rate. The effect of relative humidity, degree of subcooling, and saturation temperature are addressed. The device comprises of Cu pipes embedded in Al fins as the condensing unit and solar powered fan module for moist air intake. The device generates pure water with turbidity of 40 PPM which after mineralization and UV filtration is fit for human consumption. The proposed device has wide application in providing potable water in hot and humid regions worldwide. The results of study are useful for engineers and designers while optimizing the performance parameters of the atmospheric water harvesting devices.

2 Experimental Study

In this experimental study, moist air is condensed on extended surface (Al fins) which are attached with the series of array of Cu tubes. Cu and Al has higher thermal conductivity as compared to other metallic surfaces. However, Cu is expensive and more corrosive in nature than Al. Therefore, in this work, the condensing surfaces were selected as the Cu tubes entrenched in the Al fins, where fins house the major portion for the condensation process and significantly helps in optimizing the cost of condenser unit. Such condenser designs are also widely used in conventional household air-conditioning unit. Hence, the study is also helpful for optimizing the performance parameters of the room air conditioners.

Atmospheric moist air is a combination of dry air and water vapor. The quantity of water vapor present in moist air depends on the environmental temperature and pressure. The water vapor can be either in saturated or unsaturated state in the moist air. This state defines the difference between moist air temperature and dew point temperature. Moist air is a binary fluid whose thermophysical properties are strong function of temperature and pressure; the properties are estimated as [13].

$$\bar{M}_m = \left[\frac{\bar{R}\rho_m T_d}{P_0} \right] \quad (1)$$

In this expression, \bar{M}_m is the molecular weight of moist air, P_0 is the total pressure of moist air ($P_0 = 1$ atm) for moist air at atmospheric condition and the density (ρ_m) and specific heat of moist air (C_{pm}) are determined as;

$$\rho_m = \frac{P_0}{R \times T} \times M_a \left[1 - \text{RH} \times \left(1 - \frac{M_v}{M_a} \right) \times \left(\frac{P_{\text{sat}}}{P_0} \right) \right] \quad (2)$$

$$C_{pm} = \frac{C_{pa} \left[1 - \text{RH} \times \frac{P_{\text{sat}}}{P_0} \right] \times M_a + C_{pv} \times \text{RH} \times \frac{P_{\text{sat}}}{P_0} \times M_v}{M_a \left[1 - \text{RH} \times \frac{P_{\text{sat}}}{P_0} \right] + M_v \times \text{RH} \times \frac{P_{\text{sat}}}{P_0}} \quad (3)$$

Here, T is the moist air temperature, RH is the relative humidity, M_a is the mass of air (28.963 kg/Kmol), M_v is the mass of water vapor (18.02 kg/Kmol), P_{sat} is the pressure corresponding to saturation temperature, C_{pm} , C_{pa} , and C_{pv} is the specific heat capacity of moist air, dry air, and water vapor in J/kg K.

The experimental setup used in this study is as shown in Fig. 1a, b. Figure 1a shows the schematic diagram, and Fig. 1b shows the photograph of the device for atmospheric water harvesting. It consists of a condenser unit and solar fan module mounted inside a rectangular duct of cross-sectional area $A = 420 \text{ mm} \times 390 \text{ mm}$ and solar powered customized water-cooling unit. The condenser unit incorporates vertical copper pipes entrenched into number of horizontal thin aluminum fins in

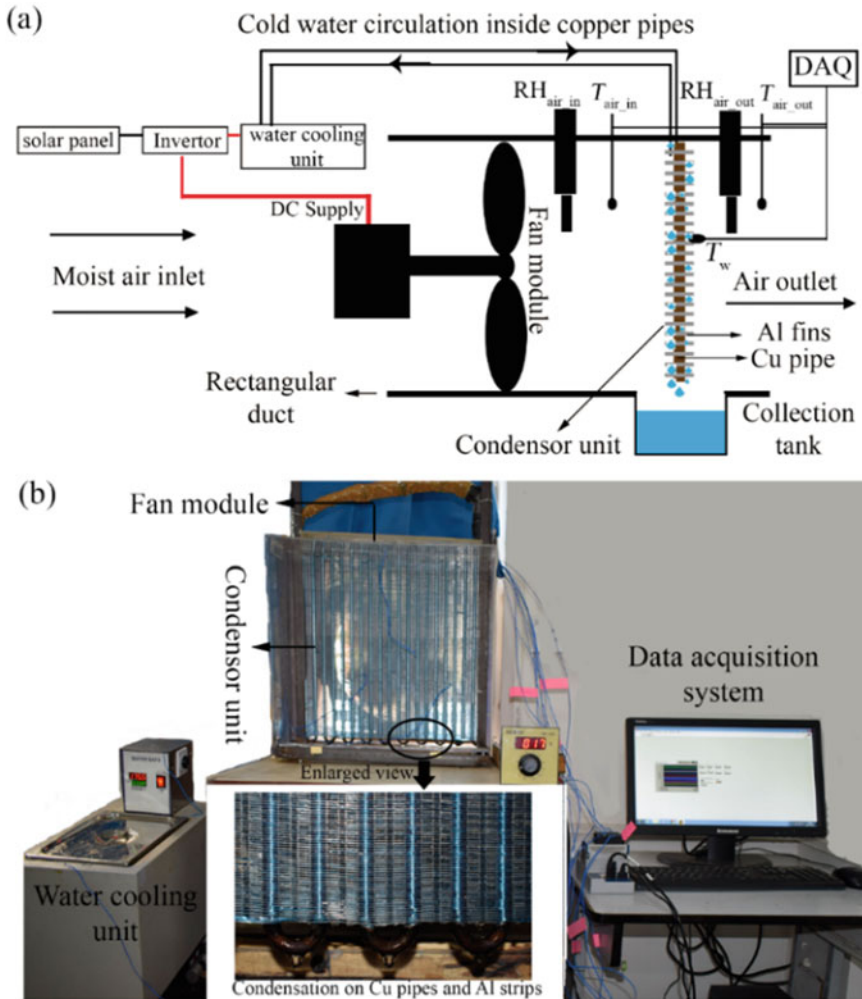


Fig. 1 Experimental setup for device for water harvesting from moist air. **a** Schematic diagram of the device for atmospheric water harvesting and **b** photograph of the experimental setup along with enlarged view of the moist air condensation on the condenser unit

order to ensure maximum area for condensation. The solar powered fan is used for moist air intake inside the condensing chamber. The fan was operated at required speed to ensure optimal mass flow rate of the moist air onto the condenser unit. In order to measure the CFM at required speed (Q_N), initially, the maximum velocity (V_{max}) was measured using digital hot wire anemometer, Kusum Mecro (KM-734). The velocity was measured perpendicular to the direction of motion of moist air at 20 different location across the height of the duct of cross section area (A). In addition, the revolutions per minute (RPM) of the fan at maximum speed (N_{max})

and required speed (N_{req}) was measured via a digital tachometer in non-contact mode (ESCORP). The required speed of the fan is set such that the viscous dissipation of moist air flow is negligible. The flow rate of moist air at the required speed is evaluated as;

$$Q_N = \frac{N_{req}}{N_{max}} Q_{max} \quad (4)$$

$$\text{where } Q_{max} = V_{max} \cdot A \quad (5)$$

In this device, the solar energy is converted to electrical energy using custom built-in inverter unit and used for powering water-cooling unit. This unit flows cold water into copper pipes of the condenser unit at constant temperature. As soon as the temperature of the condenser unit reaches a temperature below than the dew point temperature of ambient moist air, the water vapor present in the moist air condenses on the copper pipes and aluminum fins of the condenser unit. The condensed water gradually grows by direct condensation and coalesce mechanism and subsequently fall-off from horizontal aluminum strips and slide-off from the vertically oriented copper pipes. The condensed water is further collected into the collection tank and used for analyses.

Experiments were carried out in month of July and August at controlled moist air temperature and relative humidity during daytime. The moist air condensation experiment was repeated 5 times for ensuring the repeatability of the results. Throughout the experiment, humidity and temperature of moist air at inlet and outlet of condenser unit and temperature of the condenser unit were measured at various locations. The real-time data acquisition of the temperature was carried out using T-type thermocouples attached with National Instruments LabVIEW controlled NI-9211(National Instruments) temperature card, and humidity was measured via hygrometer, Kusum Mecro (KM-918). The uncertainty in the temperature and humidity of moist air were measured as 1.5% and 2.3%, respectively. The amount of condensate collected was measured in calibrated collection tank and TDS meter, Wellon (TDS-3) was used for measuring the turbidity of the condensed water to quantitatively and qualitatively analyzes the condensed water and ensure its consumption for human use.

3 Results and Discussion

The results of the experimental study carried out for the atmospheric water harvesting device is detailed in this section. Moist air condensation experiment was carried out for various values of moist air temperature, relative humidity, and degree of subcooling. The temperature and humidity were directly measured from the environment at inlet and outlet locations. Various set of degree of subcooling was achieved by supplying cold water at desired temperature using constant

temperature water cooling unit. In this study, all the experiments were conducted for total duration of 3 h. The values of parameter under study was recorded using respective sensors, further the acquired data was averaged to obtain the final value of the parameters. The efficiency of the device was estimated by analyzing the mass of condensate collected from experimental studies.

Figures 2 and 3 show the condensation rate as a function of relative humidity, degree of subcooling and moist air temperature. Results shows that as the relative humidity, moist air temperature, and degree of subcooling increase, the condensation rate linearly increases for the proposed device. Hence, the device is efficient for curing water scarcity especially in hot and humid regions with humidity and temperature ranging from 50–90% and 20–50 °C, respectively.

Fig. 2 Condensation rate (m) versus relative humidity (RH) at various values of moist air temperature at $\Delta T = 10$ °C and $P_0 = 1.01$ bar

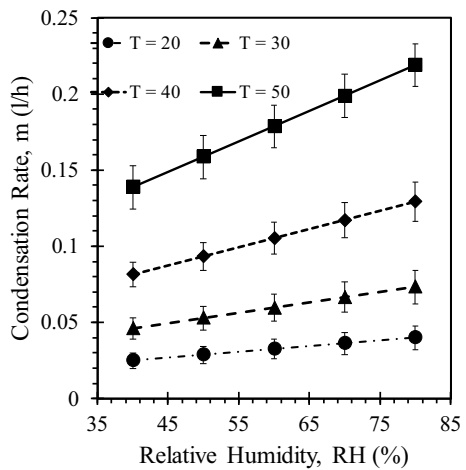
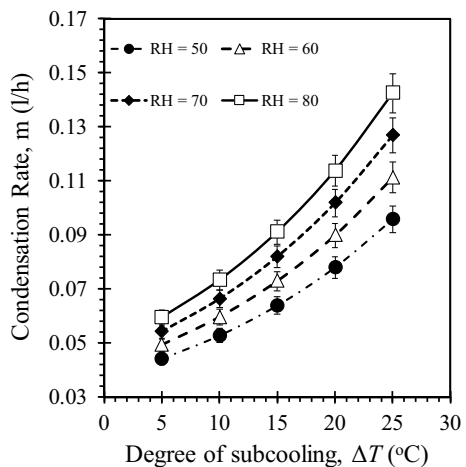


Fig. 3 Condensation rate (m) versus subcooling (ΔT) at various values of inlet moist air relative humidity. The experiments were carried out for moist air temperature (T) = 20 °C and $P_0 = 1.01$ bar



In addition, the quality of condensed water was also examined to investigate that the water is fit for consumption or not. According to WHO, the permissible limit of TDS in India is <500 PPM [14]. In the present work, the turbidity of the condensed water was measured using sensor as 40 PPM. Apparently, the water collected from the proposed water harvesting device is fit for human consumption.

The cost of a liter of water produced by the proposed water harvesting device was estimated for operating conditions inlet moist air temperature = 40 °C, degree of subcooling (ΔT) = 10 °C, relative humidity = 80%. In this device, solar energy was converted to electrical energy and was supplied to fan module and water-cooling unit. This cooling unit cools the water at desired temperature and flows the water at constant temperature using preinstalled pump. The power requirement of water-cooling unit, P_{WC} (kW) is estimated as;

$$P_{WC} = \dot{m}C_{pw}\Delta T \quad (6)$$

where \dot{m} (= 0.0105 kg/s) is the mass flow rate of water-cooling unit and C_{pw} is the specific heat of water. Further, the power requirement of fan modules P_{fan} (kW) was estimated as;

$$P_{fan} = dp \times Q_N \quad (7)$$

where dp is the total pressure increased in the fan (N/m^2) and Q_N is the volumetric flow rate of moist air through fan (m^3/s). Finally, the total energy requirement of the water harvesting device P_{total} (kW) is;

$$P_{total} = P_{WC} + P_{fan} \quad (8)$$

Further, total energy requirements of the device are E_{total} (kWh)

$$E_{total} = P_{total} \times t \quad (9)$$

where t (hours) is the total time for which the condensation experiment was performed. It is well acquainted that the cost of solar energy in India is \bar{C} = Rs. 3.5 per kWh. So, the cost of producing 1 L of water C (Rs.) from the proposed device is estimated as,

$$C = \frac{\bar{C} \times E_{total}}{m_{cond}} \quad (10)$$

Here, m_{cond} (liters) is the amount of condensed water collected during the experiment. Hence, from above formulation, the cost of water produced from proposed device is estimated as Rs. 10 per liter.

4 Conclusion

A solar-based device for generating water from moist atmospheric air is designed and fabricated. Device generates portable water for hot and humid water scare regions. In this work, moist air condensation experiments were performed in controlled ambient conditions and investigated the effect of various parameter on the performance of proposed atmospheric water harvesting device. Parameter under consideration were relative humidity, moist air temperature, and degree of sub-cooling. In addition, analysis was done on the quality of water which is obtained from moist air condensation. The present study concluded that the design of condenser unit, i.e., Al fins entrenched into series of array of Cu tubes enables more surface area, therefore increases condensation rates onto the surface. Condensation rates increases with increasing relative humidity, moist air temperature and degree of subcooling. The quality assessment of the atmospheric water harvesting device shows that the device generate water with turbidity of 40 PPM which is suitable for human consumption. Finally, the cost of water from present device is estimated as Rs. 10 per liter, which is reasonable price, however, the present cost can be further decreased by improving the chemo-physical properties of the condensing surface.

Acknowledgements The authors acknowledge the financial support from Science and Engineering Research Board (SERB), Department of Science and Technology (DST), Govt. of India (Project No. ECR/2016/000020).

References

1. Wahlgren RV (2001) Atmospheric water vapour processor designs for potable water production: a review. *Wat Res* 35(1):1–22
2. Hamed AM, Kabeel AE, Zeidan ESB, Aly AA (2010) A technical review on the extraction of water from atmospheric air in arid zones. *JP J Heat Mass Transf* 4(3):213–228
3. El-Ghonemy AMK (2012) Fresh water production from/by atmospheric air for arid regions, using solar energy: review. *Renew Sustain Energ Rev* 16(8):6384–6422
4. Liu XH, Yi X, Jiang Y (2011) Mass transfer performance comparison of two commonly used liquid desiccants: LiBr and LiCl aqueous solutions. *Energ Convers Manag* 52:180–190
5. Ming T, Gong T, de Richter RK, Wu Y, Liu W (2017) A moist air condensing device for sustainable energy production and water generation. *Energ Convers Manag* 138:638–650. <https://doi.org/10.1016/j.enconman.2017.02.012>
6. Eslami M, Tajeddini F, Etaati N (2018) Thermal analysis and optimization of a system for water harvesting from humid air using thermoelectric coolers. *Energ Convers Manag* 174:417–429. <https://doi.org/10.1016/j.enconman.2018.08.045>
7. Jradi M, Ghaddar N, Ghali K (2012) Experimental and theoretical study of an integrated thermoelectric-photovoltaic system for air dehumidification and fresh water production. *Int J Energ Res* 36(9):963–974. <https://doi.org/10.1002/er.1848>
8. Bamisaye OS, Oke PK (2019) Modelling the condensed water discharge rate in air conditional system in south west, Nigeria. *Curr J Appl Sci Technol* 32(3):1–13
9. Suryaningsih S, Nurhilal O (2016) Optimal design of an atmospheric water generator (AWG) based on thermo-electric cooler (TEC) for drought in rural area

10. Gerard RD, Worzel JL (1972) Atmospheric water extraction over the ocean, beneficial modifications of the marine environment. In: Symposium sponsored by national research council and department of the interior, Washington DC, 11 Mar, 1968. National Academy of Sciences, Washington, DC, pp 66–84
11. Harrison LG (1996) Water recovery device for reclaiming and refiltering atmospheric water. Patent Appl 5,553,459
12. Rosenthal RA (1999) Atmospheric water extractor and method. Patent Appl 5,857,344
13. Tsilingiris PT (2008) Thermophysical and transport properties of humid air at temperature range between 0 and 100 °C. *Energ Convers Manag* 49(5):1098–1110. <https://doi.org/10.1016/j.enconman.2007.09.015>
14. Kumari M, Mudgal LK, Singh AK (2013) Comparative studies of physico-chemical parameters of two reservoirs of Narmada river, MP, India. *Curr World Environ J* 8(3):473–478. <https://doi.org/10.12944/cwe.8.3.18>

Vortex Dynamics in Near Wake Region Behind a Triangular Cylinder at Intermediate Reynolds Number



Namit Agrawal and Maharshi Subhash

Abstract The vortex dynamics of near wake region of 75 degree triangular cylinder with apex pointing upstream (UP) configuration at $Re = 520, 640, 840$ and 1040 in the intermediate range is studied numerically in this paper. It was discovered that twin shear layers result in formation of two alternating primary vortices. These primary vortices result in formation of a set of alternating secondary vortices that remain attached to the base of the triangular cylinder at fixed positions irrespective of the Reynolds number. Reynolds number affected only the strengths of secondary vortices. Moreover, it was found that alternating secondary vortices bear a relationship with Reynolds number and vortex shedding frequency. Based on these observations, a statistical relationship between secondary vortex strength and Reynolds Number and an analytical relationship between secondary vortex strength and vortex shedding frequency have been proposed.

Keywords Secondary vortex · Vortex dynamics · Intermediate reynolds number

1 Introduction

Flow past sharp-edged bluff bodies are categorized as passive flow control technique that has wide range of applications due to constant flow structure irrespective of Reynolds number. Moreover, the flow depends on several controllable parameters like apex angle, geometrical shape, cylinder orientation, etc. Flame holders, landing gear, periscopes, pitot static tube errors, hot wire anemometry (HWA) probe errors, cross-flow heat exchangers, vortex flow metres, bridge piers, high rise towers, non-aerodynamic vehicles, etc., require a deep understanding of physics of this flow.

N. Agrawal · M. Subhash (✉)

Department of Mechanical Engineering, Graphic Era Deemed to Be University,
Dehradun, Uttarakhand 248 002, India
e-mail: marharshisubhash@gmail.com

N. Agrawal

e-mail: mailbox.namit@gmail.com

A regular von Kármán vortex street behind circular cylinders is observed in the range of $Re = 60-5000$ (based on cylinder diameter, d) [12] unlike sharp-edged bluff bodies. Because of this common flow structure, it can be argued that some similarities must exist between the near wake region mechanics of both these cylinders. However, it is observed that this similarity is limited only to von Kármán vortex street due to forced free shear layer separation in sharp-edged bluff bodies.

Kovácsznay [6] measured regular vortex street pattern formed behind a circular cylinder at low Reynolds number using HWA technique, thereby determining a critical $Re = 40$. The author found that the vortices shed at some distance downstream from the cylinder and not directly from the cylinder. The author showed existence of a near wake region and concluded that this phenomenon is a laminar wake instability that dies prior to becoming turbulent.

Later, Roshko [11] classified periodic wake phenomenon behind circular cylinder in two distinct Reynolds number ranges, stable range ($40 < Re < 150$) and irregular range ($300 < Re < 10000+$), combined with a transition range ($150 < Re < 300$). Building on Roshko's [11] work, Gerrard [5] observed that near wake region behind a circular cylinder plays a significant role in determination of vortex shedding frequency. Fluid entrainment from interior of formation region and its replenishment by reversed flow was found fundamental in determining vortex shedding frequency.

Bearman [4] validated vortex street stability criteria of von Kármán and Kronauer by making a comparison between measured vortex street parameters and results predicted by existing theories. It was found that von Kármán's idealized potential flow model predicted accurate values of longitudinal spaces between vortices. However, the value of Roshko's universal wake Strouhal number was affected by the introduction of wake interference elements.

An experimental study of flow behind circular cylinder in sub-critical regime was performed by Nakagawa [8] to find the reason behind asymmetry of vortex formation region with respect to the wake axis. This asymmetry was attributed to increase in strength and scale of vortex pair until one vortex comes in contact with other vortex. At this stage, the vortex pair and vortex formation region becomes asymmetrical with respect to wake axis, and a third vortex is also formed.

Thompson et al. [14] provided evidence of applicability of the initial transition phenomenon to three dimensionality of flow past a circular cylinder to other two-dimensional cylinder cross sections.

Previous studies on flow past circular cylinder divide the wake region into two distinct regions, near wake region and an alternate vortex shedding region well known as von Kármán vortex street. It is also evident that the mechanism involved in small near wake region is responsible for the generation and properties of vortex street. However, pure von Kármán vortex street regime exists for a particular range of Reynolds number suggesting that the physics in this region depends on the Reynolds number and friction between fluid and the curved surface is responsible for boundary layer separation and hence formation of twin shear layers.

Nakagawa [9] proposed a vortex shedding mechanism behind a 53° triangular cylinder with apex pointing upstream (UP) configuration on the basis of experimental study at high Reynolds number of 1.73×10^5 . It was concluded that the vortex shedding is maintained by the unstable system of three vortices generated in the vortex formation region. Only main vortices (upper and lower) and a third vortex were observed in this configuration.

Structure of flow past triangular cylinder at high Reynolds number ($= 4.5 \times 10^4$) was studied numerically by Zhang and Perot [17]. An almost perfect periodicity, stream function sinusoidal in nature, was found to exist.

Prasath et al. [10] numerically studied wake characteristics of different triangular cylinders (Aspect ratio = 0.5, 0.866, 1, 2, 3, 4, 5) in both UP and apex pointing downstream (DOWN) configurations at low Reynolds numbers ($Re = 10, 20, 30, 40$ and 50). Recirculation bubble length was found to be directly proportional to Reynolds number in sub-critical range for UP configuration, which decreases exponentially with increase in aspect ratio.

Flow characteristics around 60° triangular cylinder were studied by Yagmur et al. [16] using both experimental and numerical methods. All particle image velocimetry (PIV) experiments were performed at $Re = 2.9 \times 10^3$ to 1.16×10^4 , while all numerical experiments were performed at $Re = 2.9 \times 10^3$ to 1.16×10^5 . PIV was used for experiments, and large eddy simulation (LES) was used for numerical experiments. The cylinder was kept in UP configuration. The authors observed shrinkage in wake region with increase in Reynolds number.

Ahlborn et al. [3] proposed a statistical model of wake kinematics for calculation of bluff body drag. They focussed on the fact that von Kármán vortex street is independent of both geometry and Reynolds number. The non-existence of this flow regime for a particular Reynolds number range in case of circular cylinder was not considered. The role of near wake region in vortex street formation and difference in mechanics of near wake in different geometries was also not considered.

Unlike circular cylinders, the free shear layers get forcefully separated due to the abrupt absence of cylinder surface in case of triangular cylinders. As a result, friction does not play a significant role in boundary layer separation. This indicates that the vortex formation region behind triangular cylinders must have mechanics different than that of a circular cylinder. Apart from several other parameters that are affected by the change in Reynolds number, changes in flow of this region are expected.

Previous studies suggested the phenomenon to be independent of Reynolds number. On the other hand, most of the mechanics proposed are of qualitative nature. Experimental techniques like PIV have a drawback of limited spatial and temporal resolutions. This limitation suggests that smaller flow structures might exist that play a role in mechanics of vortex formation region. High temporal and spatial resolutions are possible with numerical methods allowing for a deeper insight into the mechanism of a flow.

2 Problem Statement

The objective of current study is to closely examine the vortex dynamics of the vortex formation region behind 75° triangular cylinder in UP configuration at intermediate Reynolds numbers. The study aims at finding smaller flow structures that play a role in formation of von Kármán vortex street. The study also aims at finding relationship between these flow structures. Numerical technique has been used for the present study as high temporal and spatial resolutions required for resolving smaller flow structures are possible with these techniques in comparison with PIV technique. The study is performed at $Re = 520, 640, 840$ and 1040 in the intermediate range as the flow is in transition phase instead of being fully turbulent.

3 Governing Equations

For an unsteady, three-dimensional mass conservation equation for incompressible fluid for the mean flow according to Versteeg and Malalasekera [15] is as follows:

$$\text{div}\mathbf{U} = 0 \quad (1)$$

While the Reynolds-averaged Navier–Stokes equations as per Versteeg and Malalasekera [15] are as follows:

$$\frac{\partial U}{\partial t} + \text{div}(UU) = -\frac{1}{\rho} \frac{\partial P}{\partial x} + \nu \text{div}(\text{grad}(U)) + \frac{1}{\rho} \left[\frac{\partial(-\rho \overline{u'^2})}{\partial x} + \frac{\partial(-\rho \overline{u'v'})}{\partial y} + \frac{\partial(-\rho \overline{u'w'})}{\partial z} \right] \quad (2)$$

$$\frac{\partial V}{\partial t} + \text{div}(VU) = -\frac{1}{\rho} \frac{\partial P}{\partial x} + \nu \text{div}(\text{grad}(V)) + \frac{1}{\rho} \left[\frac{\partial(-\rho \overline{u'v'})}{\partial x} + \frac{\partial(-\rho \overline{v'^2})}{\partial y} + \frac{\partial(-\rho \overline{v'w'})}{\partial z} \right] \quad (3)$$

$$\frac{\partial W}{\partial t} + \text{div}(WU) = -\frac{1}{\rho} \frac{\partial P}{\partial x} + \nu \text{div}(\text{grad}(W)) + \frac{1}{\rho} \left[\frac{\partial(-\rho \overline{u'w'})}{\partial x} + \frac{\partial(-\rho \overline{v'w'})}{\partial y} + \frac{\partial(-\rho \overline{w'^2})}{\partial z} \right] \quad (4)$$

The standard $k-\varepsilon$ model by Launder and Spalding [7] was used in the study. The following transport equations are used in this model for k and ε :

$$\frac{\partial(\rho k)}{\partial t} + \text{div}(\rho k \mathbf{U}) = \text{div} \left[\frac{\mu_t}{\sigma_k} \text{grad} k \right] + 2\mu_t S_{ij} \cdot S_{ij} - \rho \varepsilon \quad (5)$$

$$\frac{\partial(\rho \varepsilon)}{\partial t} + \text{div}(\rho \varepsilon \mathbf{U}) = \text{div} \left[\frac{\mu_t}{\sigma_\varepsilon} \text{grad} \varepsilon \right] + C_{1\varepsilon} \frac{\varepsilon}{k} 2\mu_t S_{ij} \cdot S_{ij} - C_{2\varepsilon} \rho \frac{\varepsilon^2}{k} \quad (6)$$

The values, $C_\mu = 0.09$, $\sigma_k = 1.00$, $\sigma_\varepsilon = 1.30$, $C_{1\varepsilon} = 1.44$ and $C_{2\varepsilon} = 1.92$, are used for the five unknown constants employed in equations.

4 Methodology

The numerical results were compared with experimental results published by Agrawal et al. [1, 2]. The same results were used by Yagmur et al. [16] as reference for their own investigation. Figure 1 shows the photograph of the PIV system. The acrylic test section used for PIV measurements was 1500 mm long, 160 mm wide and 100 mm in height. The experimental study was completed using a triangular cylinder with 6 mm base. The aspect ratio was 26.7 (160/6) with a blockage ratio of 6%. Reynolds numbers based on base length were 520, 640, 840 and 1040 in the intermediate range. This range of intermediate Reynolds numbers was selected due to the existence of few studies for flow in this range [1, 2].

The PIV system consisted of double pulsed Nd-YAG laser (New Wave lasers; wavelength = 532 nm; 50 mJ). Seeding of olive oil particles was achieved through a six-jet atomizer (TSI model 9306). Images were captured using Powerview Plus 4MP CCD camera (2048 × 2048 effective pixels). Minimum frame straddling time for PIV capture was 200 ns.

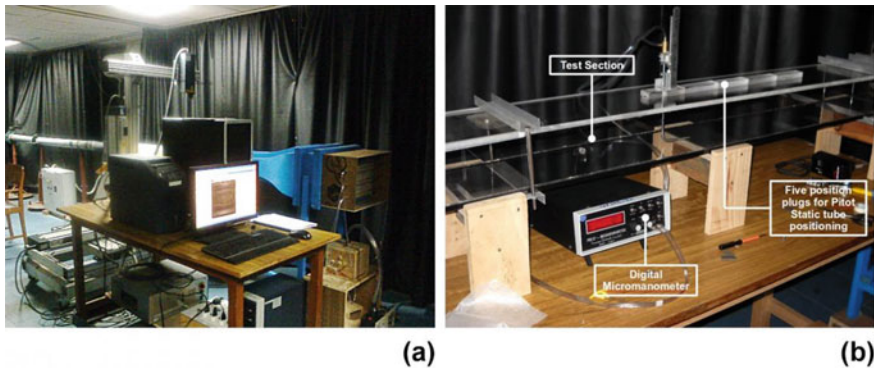


Fig. 1 **a** PIV set-up, **b** calibrated digital micro-manometer (Furness Controls; 19.99 mm H₂O) with wind tunnel

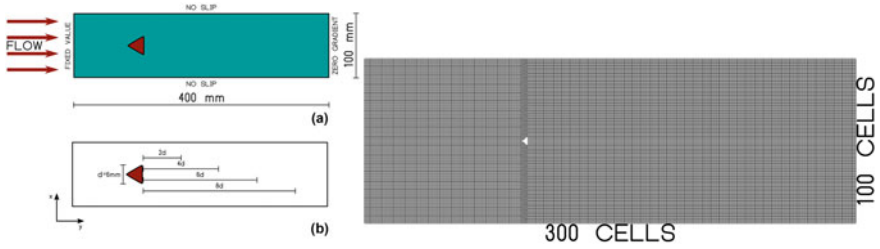


Fig. 2 Flow domain, boundary conditions and mesh used in numerical simulations

A pitot static tube and digital micro-manometer were used for validation of the velocity measured by PIV. The velocity signal from HWA, by Dantec Streamline pro, was used for measuring the Strouhal number and the power spectra. The single wire straight probe was used for the velocity signal measurements. The sampling frequency was 1000 Hz, and the signal length was 20 s.

All numerical simulations were performed on a mesh of 300×100 cells with dimensions corresponding to wind tunnel test section used in PIV experiments. Figure 2 shows the flow domain, boundary conditions and mesh used in numerical simulations. The standard k -epsilon model was implemented in OpenFOAM v5.0 running on a dual-core computer with 6 GB RAM running Linux operating system.

5 Results and Discussions

Figure 3 compares numerical and experimental data of x -velocity component for UP configuration at $Re = 520$. An excellent agreement between numerical and experimental data was observed at $2d$ and $4d$ downstream. The slight discrepancy at $6d$ and $8d$ is attributed to presence of high mean shear rate in these regions as the standard k - ϵ model is not suitable for flows with a high mean shear rate [13].

In Fig. 4, the formation of an alternating secondary vortex above and below the mid-point of the cylinder base at fixed position irrespective of the Reynolds number can be observed. The vortex strength increases with increase in Reynolds number. In Fig. 5, the vortex dynamics is explained using instantaneous z -component of

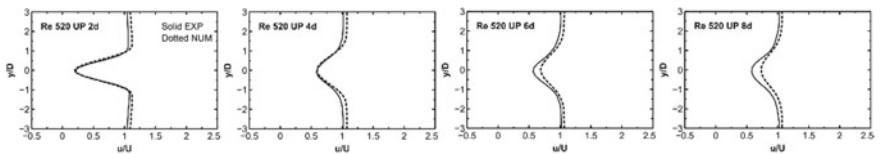


Fig. 3 Comparison of numerical data with experimental data. Time-averaged x -component of velocity (u) at $Re 520$ with apex facing upstream

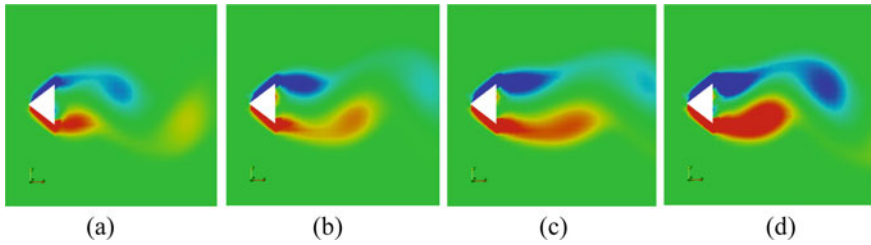


Fig. 4 Instantaneous z -vorticity component strengths at **a** $Re = 520$, **b** $Re = 640$, **c** $Re = 840$ and **d** $Re = 1040$ at 1.96 s

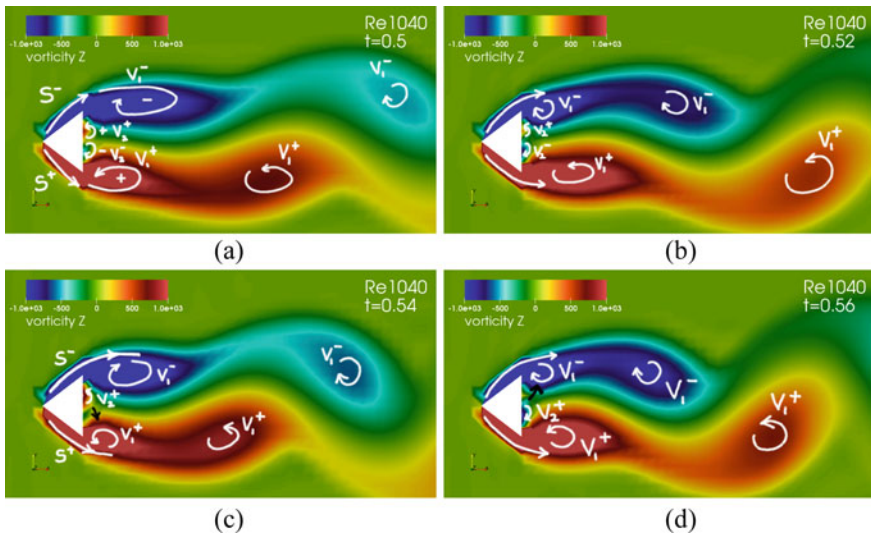


Fig. 5 Vortex dynamics using instantaneous z -vorticity component strengths at $Re = 1040$ **a** $t = 0.50$ s, **b** $t = 0.52$ s, **c** $t = 0.54$ s, **d** $t = 0.56$ s

vorticity. The symbol “ S ” represents shear layers, and “ V ” represents vortices, respectively. Superscripts “+” and “-” represent positive and negative vorticity strengths, respectively. Subscripts “1” and “2” represent primary and secondary vortices, respectively. Therefore, “ S^- ” and “ S^+ ” represent upper and lower shear layers, respectively.

In Fig. 5a, the two shear layers, S^- (upper) and S^+ (lower), turn inwards towards the wake axis forming two primary vortices, V_1^- (upper) and V_1^+ (lower), and transfer energy to these vortices. Nakagawa [9] also observed these two vortices and referred them later as first and second vortices while referring shed vortex as the third vortex.

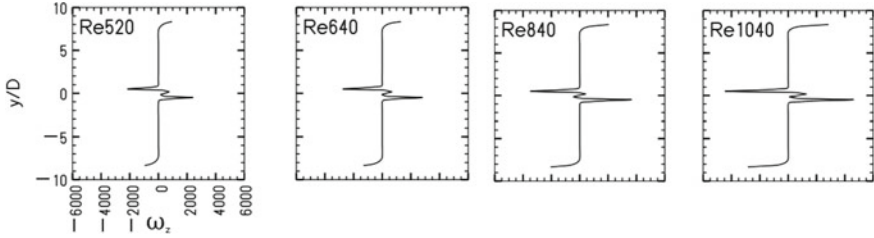


Fig. 6 Transverse time-averaged z -vorticity strengths at triangular cylinder base showing fixed positions of secondary vortices with increasing strengths

V_1^- and V_1^+ form two secondary vortices, V_2^+ (upper) and V_2^- (lower), attached to the base of the cylinder and transfer energy to these small secondary vortices. These secondary vortices in turn transfer extra energy from the new primary vortex formed after shedding a vortex to the opposite primary vortex as shown in Fig. 5c. The process of shedding V_1^- vortex can be observed in this figure. The new V_1^- vortex results in formation of V_2^+ secondary vortex. This secondary vortex is entrained by the lower V_1^+ vortex which grows in size while reducing the size of the secondary vortex. Simultaneously, the size of upper primary vortex grows which separates the lower primary vortex forcing it to shed. The process repeats as shown in Fig. 5d. The secondary vortices alternatively grow and reduce in size but do not vanish completely. Only their strengths increase and decrease.

The vortex dynamics become prominent at higher Reynolds numbers. However, same vortex dynamics are applicable to other Reynolds numbers, as shown in Fig. 4.

Figure 6 shows fixed location of secondary vortex formed at the cylinder base irrespective of the Reynolds number and an increase in the vortex strength with increase in Reynolds number. It is also worth noting that the alternating secondary vortices does not vanish completely.

5.1 Statistical Relationship Between Secondary Vortex Strength and Reynolds Number

The inflection points of time-averaged z -component of secondary vortex strengths are shown in Table 1. The position of upper secondary vortex is found to be $y/D = 0.25$ and that of lower secondary vortex is found to be $y/D = -0.25$. A linear correlation is fitted on both upper and lower secondary vortex inflection point data.

The R^2 values and the plots in Fig. 7 show excellent agreement between the empirical relationship and the numerical results. The following empirical relationship (Eq. 7) is proposed after slight adjustment of the dimensional constant before the Re:

Table 1 Inflection points of z -component of secondary vortex strengths at $y/D = \pm 0.25$

Re	y/D	$-\omega_z$ (upper sec. vortex)	ω_z (lower sec. vortex)	$\omega_z = 4.1\text{Re} + 100$
520	± 0.25	2399.5	2144.7	2232
640	± 0.25	2790.5	2736	2724
840	± 0.25	3643.4	3466.9	3544
1040	± 0.25	4598.9	4436.4	4364

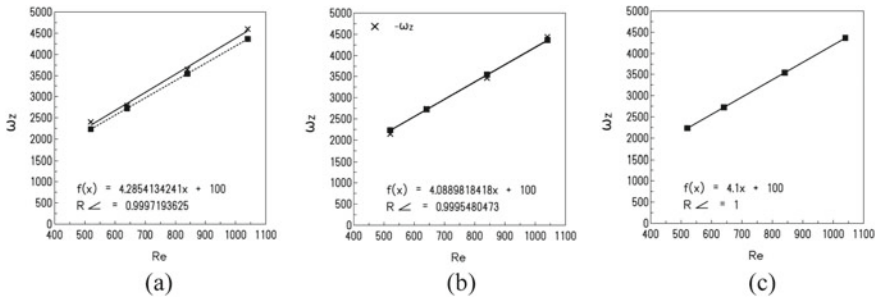


Fig. 7 **a** Comparison between calculated and numerically obtained upper secondary vortex strengths, **b** comparison between calculated and numerically obtained lower secondary vortex strength and Reynolds number, **c** calculated secondary vortex strength

$$|\omega_z| = 4.1\text{Re} + 100 \tag{7}$$

5.2 Analytical Relationship Between Secondary Vortex Strength and Vortex Shedding Frequency

Figure 8 shows periodic variation of secondary vortex strengths over time. The upper and lower vortex variation is alternating in nature due to non-intersecting crests and troughs. The standard deviation given in Table 2 gives this cosine function’s amplitude. Thus, the following cosine function (Eq. 8) is proposed for the secondary vortices:

$$f(\omega_z) = |A \cos(2\pi f)\omega_z| \tag{8}$$

where A = amplitude = minimum/maximum value of the secondary vortex strength over time; f = Vortex shedding frequency = time between two crests or troughs in Fig. 8 (function of Strouhal number).

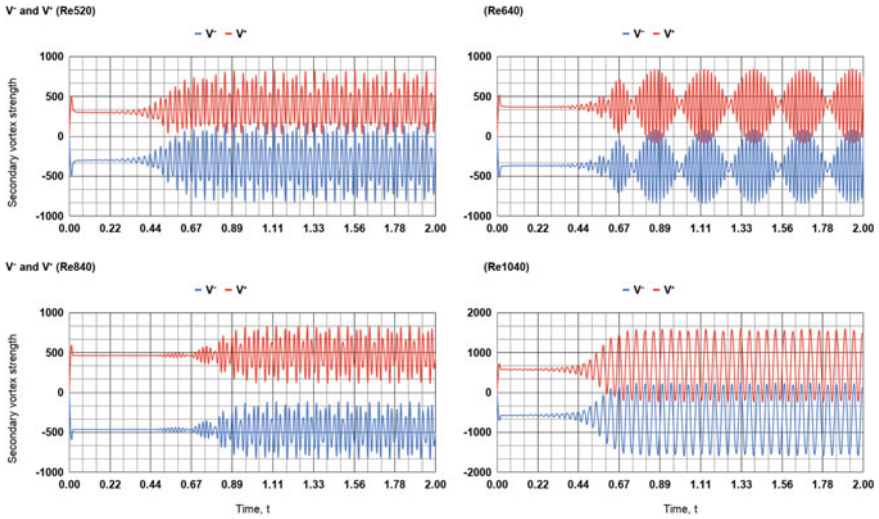


Fig. 8 Instantaneous secondary vortex strengths plotted over time at Re = 520, 640, 840 and 1040

Table 2 Statistical data of secondary vortex strengths at $y/D = \pm 0.25$ at Re = 1040

Re		Mean	Min.	Max.	Std. Dev.
520	V^-	-324.1106119	-824.97	169.4	297.6305286
	V^+	367.7833731	0	825.1	244.7454628
640	V^-	-381.5154378	-841.29	83.401	274.5099992
	V^+	383.4073358	-82.316	843.32	274.4948473
840	V^-	-471.5165174	-838.82	0	197.4504978
	V^+	470.9398507	0	838.71	197.4110128
1040	V^-	-647.541	-1588.1	246.13	550.243
	V^+	654.251	-242.53	1595.6	550.22

6 Conclusions

A near wake region vortex dynamics behind 75° triangular cylinder was studied numerically. It was observed that secondary vortices attached to the cylinder base play a role of intermediary vortices in transfer of extra energy from opposite shear layer to the primary vortex and hence vortex shedding in triangular cylinders. Two relations, one statistical and one analytical, showing relationship of time-averaged and instantaneous vortex strengths with Reynolds number and Strouhal number have also been proposed.

Current study is focussed on single geometry over a limited range of Reynolds numbers. Despite of the fact that the flow is Re independent, it was observed that

few parameters are affected by change in Re . As a result, there is a scope of extensive studies on wider range of apex angles, Reynolds numbers, etc. Furthermore, effect of higher turbulence levels, size of similar geometries, etc., on flow are few more aspects that can be explored in future.

Acknowledgements The authors would like to acknowledge Graphic Era deemed to be University for providing all the research facilities and its continuous support for the present research work.

References

1. Agrawal N, Dutta S, Gandhi B (2013) An experimental study on flow past an equilateral triangular prism at intermediate Reynolds number and the effect of its orientation. In: ASME FEDSM2013, pp V01BT13A005–V01BT13A005. Incline Village, Nevada, USA
2. Agrawal N, Dutta S, Gandhi B (2016) Experimental investigation of flow field behind triangular prisms at intermediate Reynolds number with different apex angles. *Exp Thermal Fluid Sci* 72:97–111
3. Ahlborn B, Seto ML, Noack BR (2002) On drag, Strouhal number and vortex-street structure. *Fluid Dyn Res* 30(6):379
4. Bearman P (1967) On vortex street wakes. *J Fluid Mech* 28(4):625–641
5. Gerrard J (1966) The mechanics of the formation region of vortices behind bluff bodies. *J Fluid Mech* 25(2):401–413
6. Kovásznyai L (1949) Hot-wire investigation of the wake behind cylinders at low Reynolds numbers. *Proc Roy Soc London Ser A, Math Phys Sci* 198(1053):174–190
7. Launder BE, Spalding DB (1974) The numerical computation of turbulent flows. *Comput Meth Appl Mech Eng* 3:269–289
8. Nakagawa T (1986) A formation mechanism of alternating vortices behind a circular cylinder at high Reynolds number. *J Wind Eng Ind Aerodyn* 25(1986):113–129
9. Nakagawa T (1989) Vortex shedding mechanism from a triangular prism in a subsonic flow. *Fluid Dyn Res* 5(2):69
10. Prasath SG, Sudharsan M, Kumar VV, Diwakar S, Sundararajan T, Tiwari S (2014) Effects of aspect ratio and orientation on the wake characteristics of low Reynolds number flow over a triangular prism. *J Fluids Struct* 46:59–76
11. Roshko A (1954) On the development of turbulent wakes from vortex streets
12. Schlichting H, Gersten K (2016) *Boundary layer theory*. Springer
13. Shih T-H, Liou WW, Shabbir A, Yang Z, Zhu J (1995) A new $k-\epsilon$ eddy viscosity model for high Reynolds number turbulent flows. *Comput Fluids* 24(3):227–238
14. Thompson MC, Lewke T, Williamson CHK (2001) The physical mechanism of transition in bluff body wakes. *J Fluids Struct* 15:607–616
15. Versteeg HK, Malalasekera W (2010) *An introduction to computational fluid dynamics*, 2nd edn. Pearson Education Ltd, India
16. Yagmur S, Dogan S, Aksoy MH, Goktepe I, Ozgoren M (2017) Comparison of flow characteristics around an equilateral triangular cylinder via PIV and large eddy simulation methods. *Flow Meas Instrum* 55:23–36
17. Zhang X, Perot B (2000) Turbulent vortex shedding from triangle cylinder using the turbulent body force potential model. In: FEDSM2000. Boston, Massachusetts, USA

Numerical Study of Gas Turbine Type Continuous Combustion Unit Burning LPG Mixture



Shah Shahood Alam, Sanaur Rehman, and Anchal Varshney

Abstract In the present work, burning of LPG mixture (50% each of propane C_3H_8 and butane C_4H_{10}) in a gas turbine type environment is simulated and validated against the benchmark continuous combustion unit (P. A. Hilton) experiment. Ansys Fluent[®] has been used to carry out the numerical study with major validation parameters limited to axial profiles of exhaust gas temperature and adiabatic flame temperature with equivalence ratio. It is observed that both exhaust gas and flame temperatures follow the theoretical trend of increasing with equivalence ratio, achieving their peak values at equivalence ratio near to unity and then subsequently decreasing. A pressure-based steady-state solver based on finite volume approach has been used to model the fluid flow with eddy dissipation limiters and realizable $k-\epsilon$ equations defining the combustion and turbulence phenomenon respectively. Axial profiles of important combustion parameters like temperature, pressure, and component mass fractions are obtained to draw out conclusions. The developed numerical methodology has been further extended to study the behavior of CNG in place of LPG and effect of air preheating on combustion. The study focuses on robustness of the solver and can be further expanded to include burning of liquid fuel sprays and their blends, variation of NO_x , and study of flame characteristics in a continuous combustion-type environment.

Keywords Continuous combustion unit • Gas turbine • LPG • CNG • Adiabatic • Numerical simulation • Flame temperature

S. S. Alam · S. Rehman · A. Varshney (✉)
Combustion and Pollution Control Laboratory, Department of Mechanical Engineering,
ZHCET, AMU, Aligarh, India
e-mail: anchalvarshney@zhcet.ac.in

S. S. Alam
e-mail: sshahood2004@yahoo.co.in

S. Rehman
e-mail: sanaur.rehman@zhcet.ac.in

1 Introduction

In modern gas turbine engines, basic performance parameters are thermal efficiency and emissions [1, 2]. For improvement, various experimental and numerical solutions have been tried and tested for given operating conditions, for example designing of modern gas turbine combustors may employ advanced technologies such as catalytic reduction and RQL, etc. [1]. Another option for controlling NO_x emissions is the employment of steam injection [3]. Retrofitting technologies (inlet evaporative cooling system and steam-injected gas turbine) have been applied on simple gas turbine cycle for performance improvement followed by parametric analysis. The performance improvement has been thermodynamically analyzed and discussed for retrofitted techniques. The parametric study predicts that retrofitting technique (STIG) improves net power output, thermal efficiency, power generation efficiency, first law efficiency, and exergy efficiency (Second law efficiency) while heat rate falls with a considerable increment in fuel consumption. Exergy analysis further showed that combustion chamber and turbine are most sensitive components of retrofitted system. The power output, thermal efficiency, exergy efficiency, and fuel-air ratio improved using STIG technology [4].

Numerical simulation of gas turbine combustor is a challenging task due to inherent complex processes taking place simultaneously [1–3]. Hence, the prime objective of the present study aims at numerically simulating a realistic ‘continuous combustion unit’ (experimental set up provided by P. A. Hilton, UK) and to validate the experimental results with those obtained through simulation. The study involves validation of a basic experimental setup moving onto inclusion of advanced variables. The information generated can be further used to analyze modern gas turbine combustion units. For present simulation, grid independency test and use of proper turbulence and chemical kinetics model becomes important. Furthermore, optimization of the solver to account maximum possible flow physics, heat transfer, and collision phenomena with an efficient CPU time [5] has been ensured.

2 Problem Formulation

2.1 Experimental Setup

Figure 1 shows the continuous combustion unit setup at Combustion Lab of the Department of Mechanical Engineering, Aligarh Muslim University. It comprises of an air and fuel compression system, a preheater, a gas turbine combustion chamber, and an exhaust outlet. Compressed air is injected into the combustion chamber followed by fuel injection. A stable burning flame is observed which can be witnessed through watch glass on the walls of chamber. There is heat loss inform of convection and radiation. A water jacket running around the walls of the chamber cools the combustion products before they are vented out into the



Fig. 1 Experiment CCU setup at combustion lab, AMU

atmosphere through an exhaust system. The experimental setup is meant to study the energy balance, effect of equivalence ratio on combustion characteristics, and the effect of preheating, compression ratio, and fuel type on flame characteristics.

2.2 Numerical Setup

A numerical methodology based on commercial code of Fluent® has been developed to validate the experimental setup. The intent is to diversify the effect and choice of variables on combustion phenomenon beyond the capacity of experimental setup with the help of a robust numerical solver. A pressure-based semi-implicit formulation has been used to solve the dynamics of the flow. Due to axisymmetric properties of the flow and gas turbine chamber, only half section is considered as the computational domain. Figure 2 shows the symmetry in the complete domain and Fig. 3 shows a structured grid that has been generated using ICEM CFD comprising of 65 K elements and least non-dimensional height of $1e-04$. A grid independence study was used to arrive at the number of cells (65 K) appropriate for this simulation. The equations for conservation of momentum, energy, and species have been solved with $k-\epsilon$ turbulence model. SIMPLE coupling scheme has been used with second and third-order spatial discretization of evolution equations. Eddy dissipation model is used to inhibit turbulence chemistry interaction. Details of geometrical parameters of combustion chamber are given in Table 1.

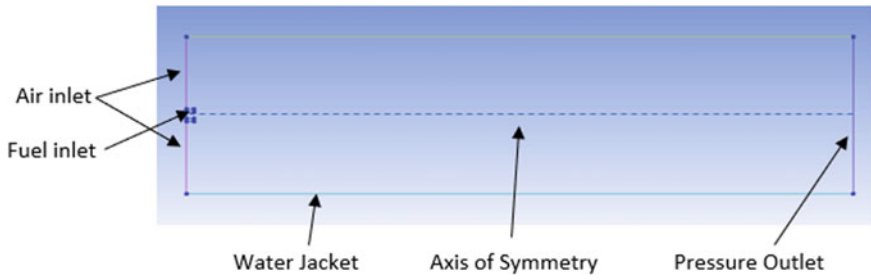


Fig. 2 Geometry

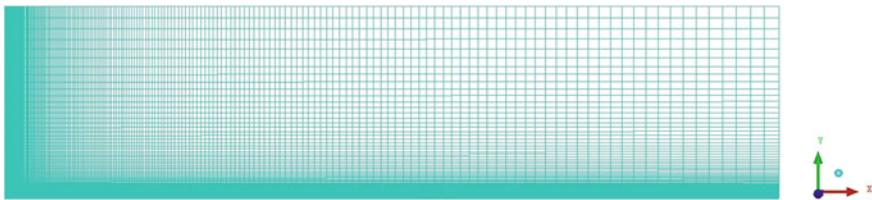


Fig. 3 Mesh

Table 1 Geometrical details of the chamber

Parameters	Typical values (mm)
Length of the combustor	1000
Height of the combustor	500
Size of fuel inlet	10
Size of air inlet	490

The species transport model predicts the transport of all species along with their consumption and production in the combustion zone. It solves conservation equation for every chemical species in the reaction. The eddy dissipation model is suitable for reactions which occur in short time; the flow is turbulent and non-premixed. The progress of elementary reaction is to determine reactant and products limiter, based on conservation equation for mass fraction. Major advantage of eddy dissipation model is that it calculates Arrhenius rate once and thus provides early results than other models. Boundary conditions for species are given in Table 2. The top wall is modeled as a mixed heat transfer (convection and radiation) boundary condition, while the outlet is given a pressure outlet BC averaging the gauge pressure to zero.

Table 2 Boundary conditions

Zone	Air	Fuel inlet
Temperature (K)	300	300
Pressure (atm)	1	2
Species mass fractions	0.033	0.00194
Hydraulic diameter	0.128	0.01
Temperature (K)	300	300

3 Simulation Results of the Present Study for LPG-Air Mixture Combustion Along Combustion Chamber Length (Axial Profile)

A continuous combustion unit (gas turbine type) is simulated with respect to the initial conditions of fuel (LPG) and air mass fractions, temperature, and pressure. Figure 4 shows the contours of total temperature in the computational domain, and Fig. 5 indicates the variation of temperature along the axis of combustion chamber. The profile obtained is a standard for constant pressure-type gas turbine combustion chambers. The decrease in the magnitude can be attributed to convection and radiation heat losses from the chamber to water jacket and surroundings. A flat pressure profile in Fig. 6 validates the constant pressure assumption taken for the model, with a minor bump near 0.2 m position arising due to turbulence created from fuel injection and combustion. Figures 7 and 8 show reactant mass fractions, and Fig. 9 shows product mass fractions along the axis of combustion chamber. The values in these figures are in accordance with rate kinetics of the chemical reactions.

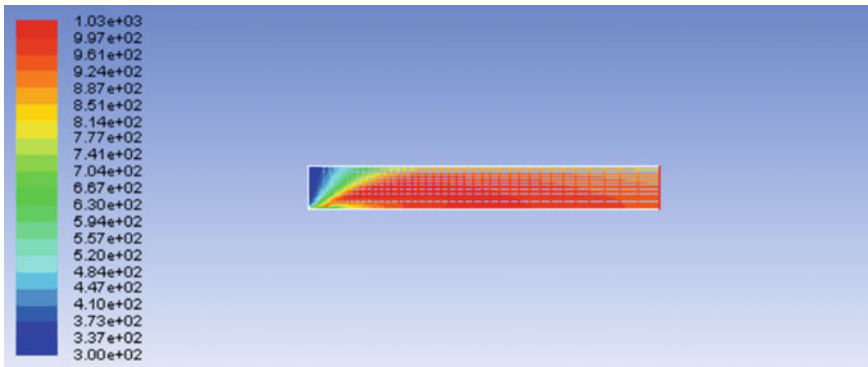


Fig. 4 Contour of total temperature

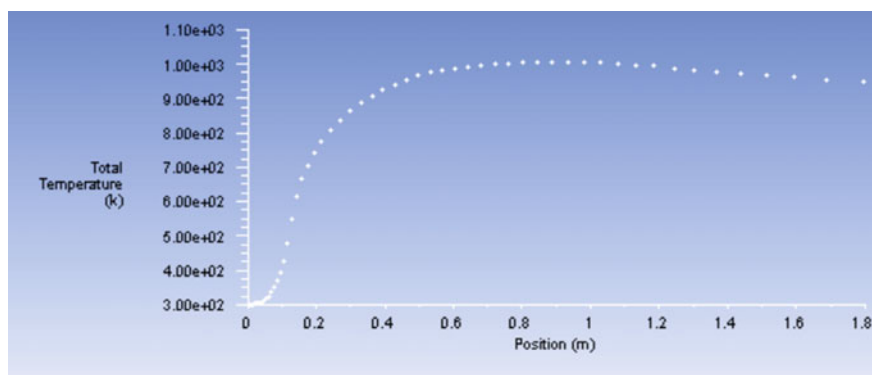


Fig. 5 Plot of total temperature

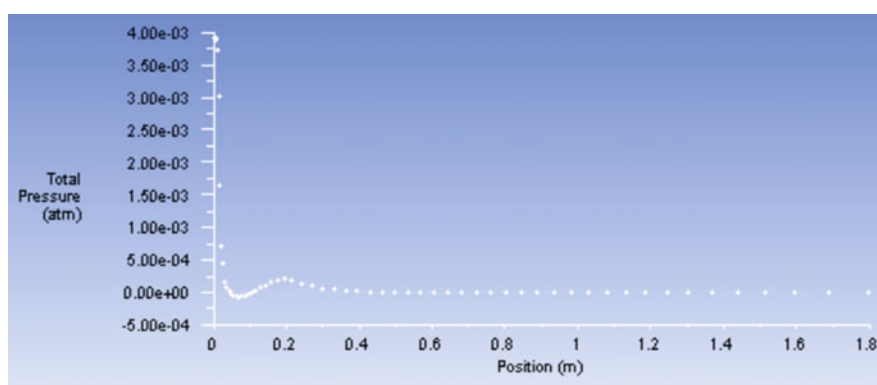


Fig. 6 Plot of pressure

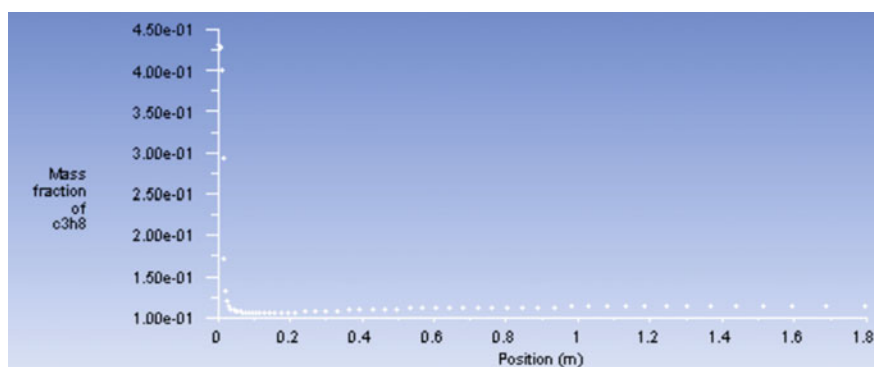


Fig. 7 Mass fraction of C_3H_8

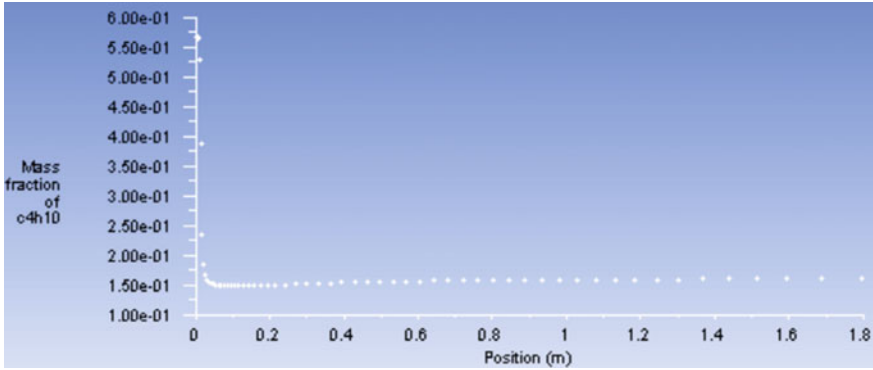


Fig. 8 Mass fraction of C₄H₁₀

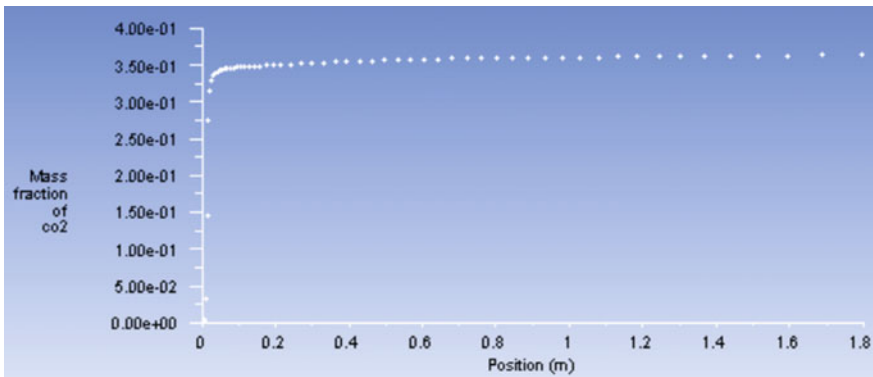


Fig. 9 Mass fraction of CO₂

3.1 Validation of Adiabatic Flame Temperature (AFT) Versus Equivalence Ratio for Air-Propane Mixture

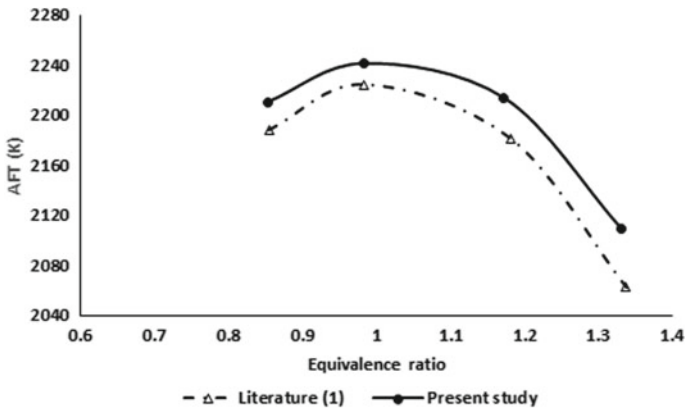
Tables 3 and 4 show results of present study and study [1] for validation purpose (Fig. 10).

Table 3 Present simulation study

Equivalence ratio	AFT (K)
0.85	2210
0.98	2240
1.17	2210
1.33	2120

Table 4 Reference data [1]

Equivalence ratio	AFT (K)
0.85	2189
0.98	2222
1.17	2175
1.33	2052

**Fig. 10** AFT versus equivalence ratio (propane)

3.2 Simulation Result for Combustion of CNG-Air Mixture (Axial Profile)

Density of CNG = 0.8 kg/m^3 , mass flow rate of fuel = 0.00194 kg/s , mass flow rate for air at equivalence ratio $0.91 = 0.0368 \text{ kg/s}$, hydraulic diameter for fuel inlet = 0.01 , hydraulic diameter for air inlet = 0.128 .

The adiabatic flame temperature of air-propane combustion achieves its maximum value near to equivalence ratio 1 (Fig. 11). The temperature first increases till equivalence ratio 1 and then decreases gradually which is similar to AFT versus equivalence ratio plot of [1], thus results obtained show a good validation.

3.3 Comparison of Experimental Data (Hilton Continuous Combustion Unit) with Respect to Exhaust Gas Temperature and Present Simulation Study for Different Equivalence Ratios (E. R)

Table 5 show results of experimental and simulation studies in terms of exhaust gas temperature as a function of equivalence ratio. Figure 12 illustrates the comparison

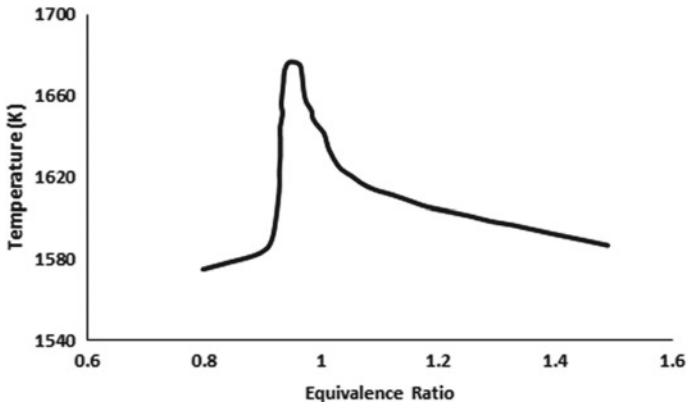


Fig. 11 Temperature versus equivalence ratio

Table 5 Comparison of experimental and simulation results

Equivalence ratio	Experimental results (CCU)	Simulation results
0.85	793	749
0.937	813	977
0.98	833	1009
1.17	833	950
1.33	813	761
1.56	731	749

of exhaust gas temperature in the experiment with the numerical study. The polynomial curves fit obtained for both of the data sets helps in realization of validation studies within predefined numerical certainty.

3.4 *Effect of Preheating of Air on Exhaust Gas Temperature of LPG-Air Mixture*

Table 6 shows values of exhaust gas temperature in cases of air preheating and with no preheating.

As expected, due to preheating of air, the exhaust gas temperature increases as compared to the case of without preheating (Fig. 13). Also, the flame temperature increases with air preheating in the same proportion. The temperature is maximum at equivalence ratio near to unity. Preheating air before it reaches the combustion chamber can improve mixture fuel economy and efficiency. Preheating the intake air can be used for different purposes such as anti-icing, low temperature operations, and problems caused by the low load operations can be avoided or at least significantly reduced among other positive effects [6].

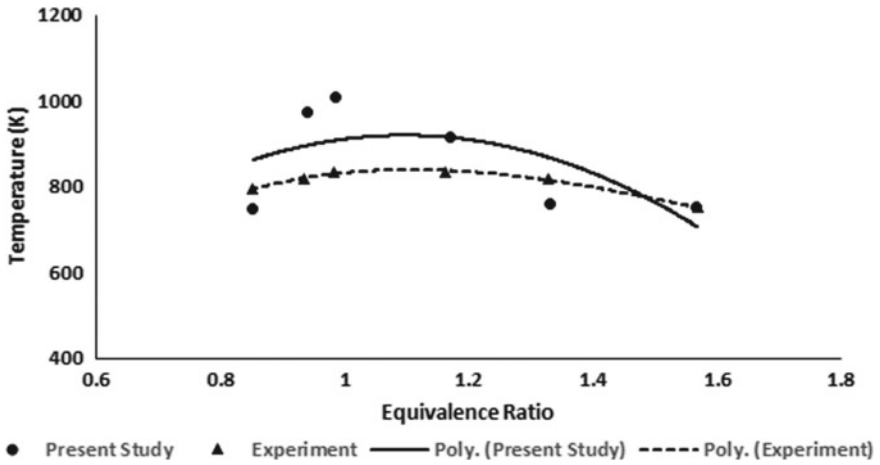
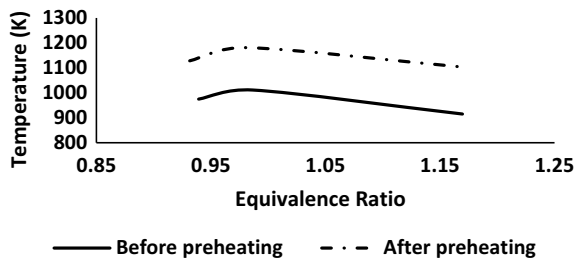


Fig. 12 Exhaust gas temperature versus equivalence ratio

Table 6 Effect of preheating of air on exhaust gas temperature

Equivalence ratio	Exhaust gas temperature (K) before preheating	Exhaust gas temperature (K) after preheating
0.93	974	1127
0.98	1010	1180
1.17	914	1102

Fig. 13 Equivalence ratio versus temperature for both cases



4 Conclusions

A numerical study is performed on a state-of-the-art experimental setup comprising of ‘continuous combustion unit’ (more detailed versions of which are employed in gas turbine engines). The simulation results are obtained with respect to adiabatic flame temperature and exhaust gas temperature as a function of equivalence ratio. Both these performance parameters play a vital role in the design of gas turbine combustion chamber. Literature review indicates that past studies [1–3] have used

complex CFD models to evaluate the performance parameters requiring large CPU time. The same results are obtained in the present study requiring relatively less CPU time. A 3D model of the CCU used in the present study can be evolved which could help study the flame characteristics and compare schlieren images from that of experiment. Some important conclusions drawn from the study are listed below:

- Numerical study of LPG-Air combustion in a continuous combustion unit (P. A. Hilton) is carried out using Ansys Fluent®. Results indicate that both flame temperature and exhaust gas temperature become maximum near the stoichiometric equivalence ratio. The results are compared with experimental and theoretical data and are found to be in a good agreement.
- Profiles of temperature, pressure, reactants, and products mass fractions have been used to draw out conclusions for both LPG-Air and CNG-Air mixtures.
- Effect of inlet air preheating shows that both the flame temperature and exhaust gas temperature increase with an increase in equivalence ratio peaking at equivalence ratio of about unity.
- Future scope of this study involves studying the behavior of liquid fuel (kerosene) in similar conditions by employing discrete phase models. The rate of heat release and NO_x variation with air-fuel ratio, preheating, and change of fuel (including blends) can also be quantified.

References

1. Turns SR (2012) An introduction to combustion concepts and applications. McGraw Hill International Edition
2. Lefebvre AH (2010) Gas turbine combustion, Second edn. Taylor and Francis group
3. Moore RPGD. Gas turbine emission and control, GE Energy Services Atlanta, GA
4. Agarwal S, Mishra RS (2012) Thermodynamic analysis for improvement in thermal performance of a simple gas turbine cycle through retrofitting techniques. In: Proceedings of the national conference on trends and advances in mechanical engineering, YMCA University of Science & Technology, Faridabad, Haryana, Oct 19–20
5. Khodabandeh A (2011) CFD modelling of generic gas turbine combustor, Master thesis, ISSN 1652-8557
6. Droubot P, Denhez M (2015) Gas turbine with intake air preheating. European patent application, EP2881562A1

Soot Formation Characteristics of Homogeneous Supercritical Fuel Spray of Dieseline Blend



Sanaur Rehman and Shah Shahood Alam

Abstract In present experimental work, comparative study between supercritical (SC) spray combustion and normal diesel impinging spray combustion is done at direct injection diesel engine-type operating conditions inside cylindrical constant volume combustion chamber. Ranges of hot surface temperature (623–723 K), cylinder air pressure (20–40 bar) and 200 bar fuel injection pressure are chosen. Commercial diesel fuel is used for normal spray combustion study. Dieseline blend having 50% diesel and 50% gasoline by volume is used for producing homogeneous SC sprays. Quantitative study is done between normal diesel spray combustion (non-supercritical) and homogeneous SC spray combustion in terms of soot formation characteristics. Photo transducer (sensor) is employed to indicate whole combustion process on digital four channel scopometer. Soot formation is estimated as time integrated natural luminosity with the help of scopometer's image. Soot formation is characterized through time integrated natural luminosity values. In case of normal diesel impinging spray combustion, soot formation is found to reduce with increase in hot surface temperature and cylinder air pressure. Soot formation decreases with increase in hot surface temperature and cylinder air pressure in SC fuel spray combustion. Soot formation in SC fuel spray combustion is found to be substantially smaller as compared to soot formation in normal diesel spray combustion (percentage reduction is more than 80% at all operating conditions). SC spray combustion system is observed to be a clean combustion for future automotive engines.

Keywords Supercritical fuel spray • Constant volume chamber • Dieseline • Soot formation

S. Rehman (✉) · S. S. Alam

Department of Mechanical Engineering, ZHCET, AMU, Aligarh, India
e-mail: sanaur.rehman@zhcet.ac.in

S. S. Alam

e-mail: sshahood2004@yahoo.co.in

1 Introduction

Continuous increasing demands of energy consumptions in transportation sector globally along with depleting fossil fuel resources and stringent emissions regulations lead to the need of development of new efficient and clean utilization methods of available energy resources. In transportation sector, diesel engines have significant advantages due to high conversion efficiency and vast on-road and off-road applications. Traditional diesel engine suffers from high emissions problem especially smoke and NO_x (oxides of nitrogen) [1]. One interesting solution to this problem of diesel engine was proposed and investigated [2–7]. In this solution, DF in SC state is injected into cylinder of diesel engine instead of in liquid form. Due to the elimination of fuel droplet formation and vaporization processes, fuel–air mixing enhances and consequently improves engine efficiency and reduces emissions drastically [8, 9]. In order to achieve SC state of DF, it has to be heated to higher temperatures above its critical temperature. But at elevated temperatures, DF decomposes, and coke formation occurs in DF [4, 10]. Coke formation causes injector and fuel lines choking problem, and hence, inert diluents such as CO_2 , H_2O , EGR, natural gas or gasoline are added in DF to avoid coke formation at elevated temperatures. These diluents are also called as anticoking agents. Anticoking agents can be mixed with DF before injection [8]. Gasoline as a diluent is a good choice for DF [8]. DL blend is defined as a mixture of gasoline and DF [8]. CVCC is generally used for studying combustion process of diesel engines [11–13]. Also, trends towards smaller engine sizes with high pressure fuel injection systems cause extensive fuel impingement on piston bowls and walls [14–16]. Table 1 shows nomenclature used in present work.

On the basis of above discussion, present work focuses on studying soot formation characteristics of SC spray combustion. Further comparison is made between soot formation characteristics of SC spray with conventional impinging diesel spray combustion under same operating conditions. This work assists in developing new SC spray combustion technology for future diesel engines for reducing harmful emissions.

Table 1 Nomenclature

Acronyms	Meaning
AG	Automotive gasoline
CVCC	Constant volume combustion chamber
CP	Cylinder air pressure
DF	Diesel fuel
DL	Dieseline blend
HST	Hot surface temperature
IP	Injection pressure
PM	Particulate matter
SC	Supercritical
SF	Soot formation
TINL	Time integrated natural luminosity

2 Experimental Set-up

Present experimental set-up and its components are shown in Fig. 1a. The specifications of setup are provided in Table 2. The set-up is fabricated to measure SF characteristic of normal and SC fuel spray combustion under different experimental conditions. Cylindrical chamber having fuel injector on one side and hot surface plate of stainless steel on opposite side of chamber is used. Fuel injector has pintle nozzle for developing sprays, which impinge on hot surface/plate. Bosch fuel

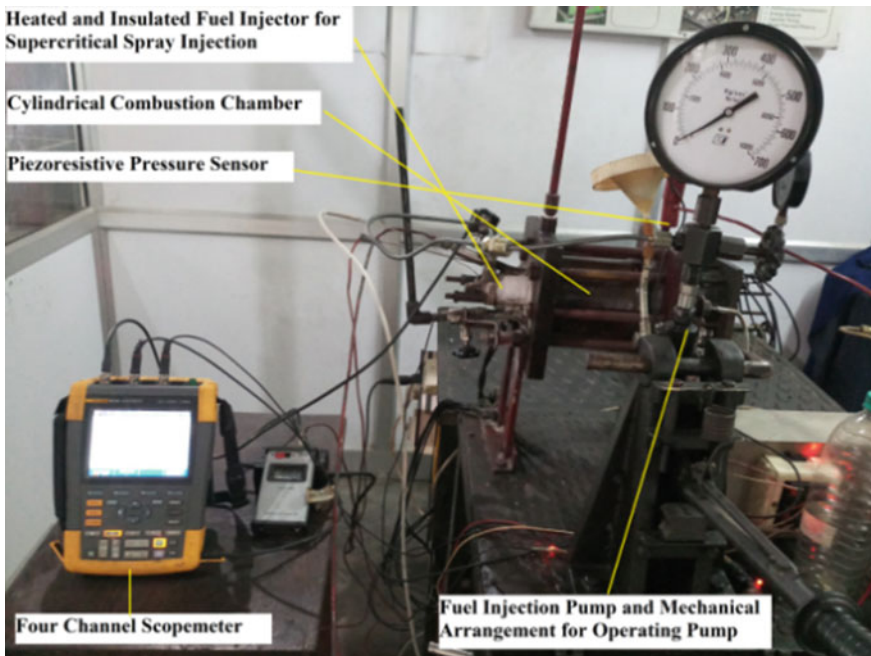


Fig. 1 Experimental set-up and its components

Table 2 Specifications of set-up

Components	Typical values
Dimensions of combustion chamber	Diameter = 9.5 cm, Length = 17.3 cm
Hot plate diameter	7.3 cm
Hot plate thickness	5.7 cm
Hot plate distance from nozzle tip	8 cm
Nozzle hole dia	0.15 mm
Maximum fuel delivery per stroke	0.2 mm
Fluke scopemeter	4 Channel, 100 MHz

injection pump is connected to heated and insulated fuel injector through high pressure fuel line. Fuel injection pump is operated manually by hand. Fuel IP is measured through pressure gauge mounted on pump as shown in Fig. 1. CP is measured with pressure gauge mounted on one side of combustion chamber. Temperature controller and indicator show HST and DL50 blend's critical temperature measured through thermocouples. Thermocouple is inserted in fuel return valve of injector for measuring DL50 blend's critical temperature.

2.1 Experimental Methodology

Commercially available DF and DL50 blend (50% gasoline and 50% diesel by volume) are used in impinging diesel spray and SC spray combustion, respectively. Experimental conditions are shown in Table 3. At same operating condition, average of five repeated readings is taken to reduce errors in measurement. In case of SC spray combustion of DL50 blend, initially HST inside the combustion chamber is increased and maintained at 623, 673 and 723 K. The fresh compressed air supplied by reciprocating compressor is introduced into chamber through inlet valve at various CP (20, 30 and 40 bar). CP is varied from 20 to 40 bar in steps of 10 bar for fuel IP 200 bar at constant HST. Temperature of DL50 is increased through heating of fuel injector, and then, measuring DL50 blend's temperature is done continuously. The thermocouple is placed in fuel return valve of the injector for measuring DL50 blend's temperature. The critical point of DL50 blend is nearly 629.3 K and 17.75 bar as estimated using Zhou correlation [17]. The critical temperature for DL50 is estimated by Kay's rule [18], and critical pressure was estimated by Thompson's relation [19]. Critical point of various fuels is listed in Table 4. After achieving critical temperature of DL50 blend (above 356.3 °C) in injector, pressure of DL50 blend is increased through injection pump till 200 bar IP, (which is above critical pressure, i.e. 17.75 bar), and hence, SC spray condition of DL50 blend is achieved. After achieving SC spray condition, DL50 blend is

Table 3 Experimental conditions

Operating parameters	Typical values
IP	200 bar
Fuel injection quantity	0.14 ml@200 bar
CP	20, 30 and 40 bar
HST	623, 673 and 723 K

Table 4 Critical Point of DF, DL50 blend and AG

Fuels	Critical temperature (K)	Critical pressure (bar)
DF	714.71	19.23
DL50	629.30	17.75
AG	543.9	25.7

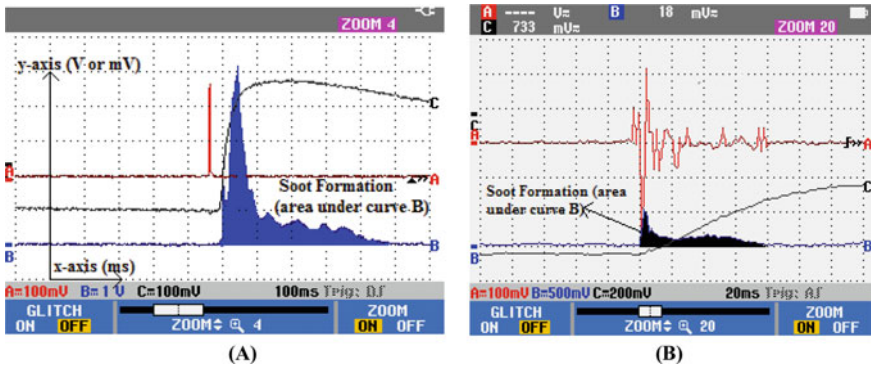


Fig. 2 a Images showing SF measurement during normal diesel impinging spray combustion, b images showing SF measurement during SC fuel spray combustion

injected into combustion chamber. At each operating condition, injection, ignition and combustion events sprays are recorded on scopemeter with the help of various transducers. Photo sensor indicates combustion event on channel B of scopemeter at various experimental conditions as shown in Fig. 2. SF is calculated as area under the curve on channel B (blue colour) shown in Fig. 2. Area of one small pixel box is calculated first, and then, number of small pixel boxes under curve are evaluated using image software. Total area is calculated by multiplying area of one small pixel box with total number of small boxes under curve B. After saving image of scopemeter, purging of combustion chamber is done by fresh compressed air. Above procedure is repeated again for other sets of readings. In case of impinging diesel spray combustion, above procedure is repeated, but difference is that fuel injector is not electrically heated, and DF is injected at room temperature.

3 Results and Discussion

In present work on SC fuel spray combustion of DL50 blend, time integrated natural luminosity (TINL) values are calculated for both combustion systems to quantify and compare SF levels under similar operating conditions. TINL values are indicators of soot formation [20]. Plots in Fig. 3a show the variation of SF with HST and at different CP (20, 30 and 40 bar) for both impinging (normal) and SC spray combustion. It is observed that SF in SC spray combustion is significantly lower than SF in liquid diesel impinging spray (non-supercritical) combustion in all cases. The reduced SF of SC sprays is due to significant changes in thermophysical properties of fluids in SC state [4, 5] such as density, volatility, diffusivity, surface tension, thermal conductivity and viscosity. In SC spray combustion, fuel is injected into cylinder air inside combustion chamber in SC state. SC sprays are injected as homogeneous single-phase fluid [2–4] into combustion chamber and has

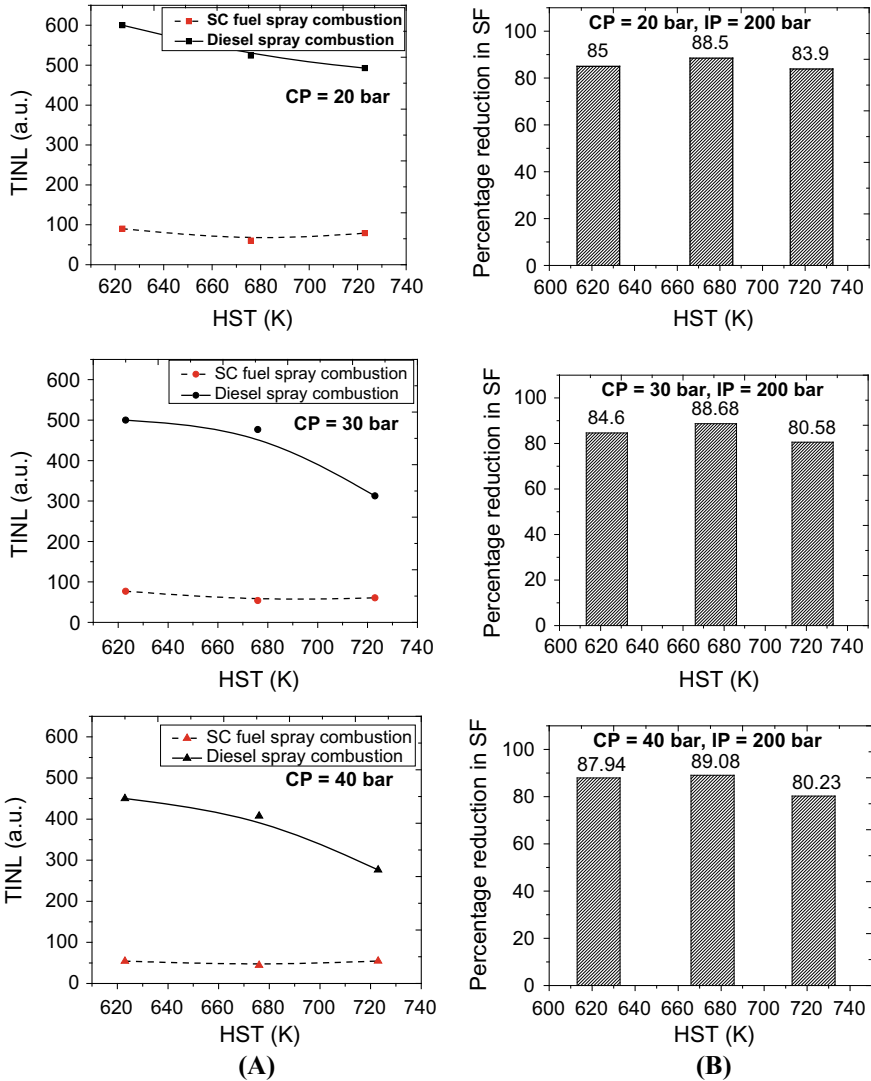


Fig. 3 a Variation of SF with HST at various CP (20, 30 and 40 bar) in both combustion processes, b variation of percentage reduction in SF with HST and at various CP values

reduced penetration length [8], wider spray cone angles [8], higher volatility due to more lighter/volatile components from gasoline, higher diffusivity and reduced surface tension [8]. All these desirable changes in thermophysical properties of SC fluids cause homogeneous, faster and quick mixing of SC spray with cylinder air. In case of SC sprays, hot air combustion seems to occur rather than hot surface ignition due to reduced penetration length of SC sprays.

Figure 3b shows the variation of percentage reduction in SF under SC fuel sprays of DL50 blend as compared to diesel impinging sprays with HST at various CP and at constant IP of 200 bar. Similarly, Fig. 4b indicates variation of percentage reduction in SF fuel sprays of DL50 blend as compared to normal diesel impinging sprays with CP at different HST values. It can be noticed from Figs. 3 and 4 that at a given IP and at all CP and HST, SF levels (TINL values) in case of SC fuel spray combustion are greatly reduced to much lower levels than SF levels in normal diesel spray combustion process. It is observed from Figs. 3b and 4b that in all cases, percentage reduction in SF in SC sprays than liquid diesel impinging sprays is above 80%. Similar reduction in SF is also reported by researchers in SC spray injection and combustion system [6, 9, 21]. It is reported that heated fuel injection results in reduced soot emissions [21].

Simultaneous reduction of both NO_x and PM during SC fuel spray combustion occurred in engines or in other combustors is reported [6, 9, 21]. In present work, only SF is quantified and compared by TINL values. However, on the basis of previous studies [6, 9] it can be stated that simultaneous reduction of NO_x will occur in SC spray injection and combustion. NO_x formation will be significantly smaller in SC spray combustion of DL50 blend because of the fact that SC fuel spray combustion occurs at lower combustion temperature than diesel droplet spray combustion temperature [22]. Temperature spikes and fuel-rich regions are absent due to homogeneous single-phase SC fuel spray combustion [9, 22, 23] as compared to conventional diesel spray combustion, and hence, significant reduction of both major diesel engine emissions (NO_x and soot) is ensured in SC fuel spray combustion [24, 25]. It can be observed from Fig. 4a that for SC fuel spray combustion of DL50 blend, SF reduces with increase in pressure of cylinder air from 20 to 40 bar. The reduction in SF with increase in CP may be attributed to the fact that increasing CP increases density of cylinder air and this causes enhancement in SC DL50 blend spray-air mixing process. Also, fuel-air mixture becomes more homogeneous and therefore avoids local fuel-rich mixtures regions. All these factors may contribute to a reduction in SF at higher CP. Moreover, it can be noticed from Fig. 3a that with increase in HST, SF slightly reduces in SC fuel spray combustion. The decrease in SF with increase in HST may be due to the reason that increase in HST results in corresponding increase in temperature of compressed cylinder air and therefore oxidation of fuel-rich regions increases with rising compressed cylinder air temperature. It is also found that effects of CP and HST on SF in normal diesel impinging sprays are significant. The reduction in SF with increase in HST is due to the enhancing fuel-air mixing rates at higher HST results in more homogeneous and complete combustion at higher HST. Reduced SF at higher CP attributed to the increased oxidation of fuel-rich regions as a result of fuel-air mixture becomes more leaner at high CP values and absence of local fuel-rich regions.

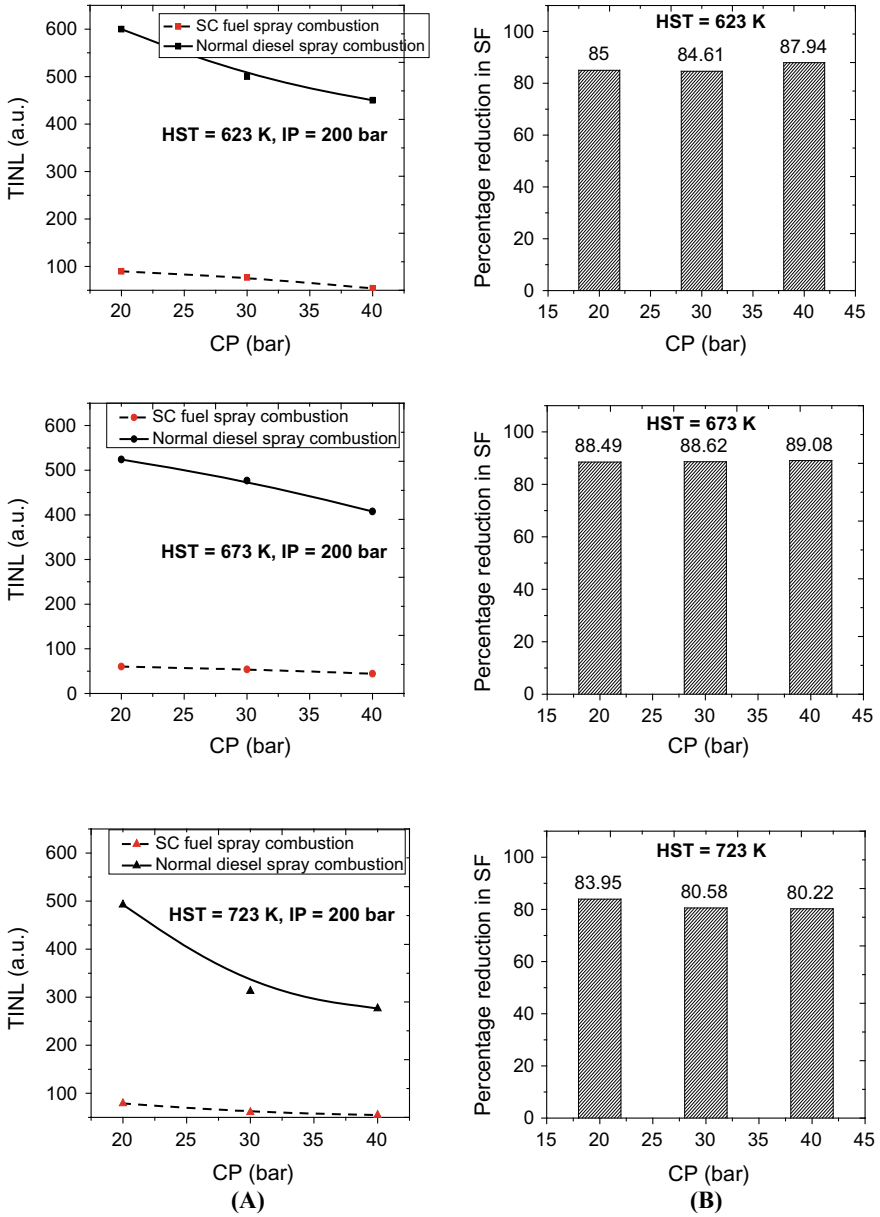


Fig. 4 a Variation of SF with CP at various HST (623, 673 and 723 K) in both combustion systems, **b** variation of percentage reduction in SF with CP at HST values

4 Conclusions

In present study, SC fuel spray combustion and conventional combustion of impinging sprays are analysed and compared at same operating conditions inside CVCC under very lean burning conditions in terms of soot formation. Following conclusions are drawn from present study:

- SF in case of SC spray combustion is significantly smaller than SF in normal diesel impinging spray combustion at all operating conditions.
- In all cases, percentage reduction in SF of SC sprays than normal diesel impinging sprays is above 80%.
- Drastic reduction in SF in SC fuel spray combustion is due to the single-phase and homogeneous combustion nature of SC fuel spray combustion and desirable properties of SC fluids.
- Lowest percentage reduction (nearly 80%) is achieved at HST of 723 K and CP of 40 bar.
- Hot air combustion nature of SC spray combustion is found rather than hot surface ignition of SC sprays.
- It is noted that SF marginally decreases with increase in HST but reduces significantly with increase in CP in SC fuel spray combustion.
- SC spray injection is observed to be a homogeneous, faster and cleaner combustion technology than normal diesel spray combustion for automotive engines.

Acknowledgements This work is supported by (TEQIP-II) project, MHRD, Govt. of India.

References

1. Heywood JB (2011) Internal combustion engines, 2nd edn. McGraw Hill International, New York
2. Tavlarides LL, Anitescu G (2009) Supercritical diesel fuel composition, combustion process, and fuel system. US Patent 7488357, Feb 10
3. Anitescu G, Lin RH, Tavlarides LL (2012) Preparation, injection and combustion of supercritical fuels, poster P-2. In: Directions in engine-efficiency and emissions research (DEER) conference; Dearborn, MI, 3–6 Aug, 2009. http://www1.eere.energy.gov/vehiclesandfuels/pdfs/deer_2009/poster1/deer09_anitescu.pdf
4. Anitescu G, Tavlarides LL, Geana D (2009) Phase transitions and thermal behavior of fuel-diluent mixtures. *Energy Fuels* 23(6):3068–3077
5. Anitescu G (2008) Supercritical fluid technology applied to the production and combustion of diesel and biodiesel fuels. Ph.D. thesis, Syracuse University
6. Canter N (2010) Tech. Beat, *Tribol Lubr Technol* 10–11
7. Anitescu G, Bruno TJ (2012) Volatility of gasoline and diesel fuel blends for supercritical fuel injection, poster P-2. In: Directions in engine-efficiency and emissions research (DEER) conference, Detroit, MI, 3–6 Oct, 2011. http://www1.eere.energy.gov/vehiclesandfuels/pdfs/deer_2011/wednesday/posters/p-02_anitescu.pdf

8. Anitescu G, Bruno T, Tavlarides LL (2012) Dieseline for supercritical injection and combustion in compression ignition engines: volatility, phase transitions, spray/jet structure and thermal stability. *Energ Fuels* 26:6247–6258
9. Ahern B, Djutrisno I, Donahue K, Haldeman C, Hynek S, Johnson K, Valbert J, Woods M, Corp SC, Taylor J, Tester J (2001) Dramatic emissions reductions with a direct injection diesel engine burning supercritical fuel/ water mixtures. SAE Tech Pap 2001-01-3526, p 6
10. Lin R, Tavlarides LL (2013) Thermal stability and decomposition of diesel fuel under subcritical and supercritical conditions. *J Supercrit Fluids* 75:101–111
11. Rehman S (2016) Sensors based measurement techniques of fuel injection and ignition characteristics of diesel sprays in direct injection combustion system. *Alexandria Eng J* 55 (3):2391-2403, ISSN: 1110-0168
12. Lapuerta M, Sanz-Argent J, Raine RR (2014) Ignition characteristics of diesel fuel in a constant volume bomb under diesel-like conditions. Effect of the operation parameters. *Energ Fuels* 28:5445–5454
13. Kuszewski H, Jaworski A, Ustrzycki A, Lejda K, Balawender K, Wos P (2017) Use of the constant volume combustion chamber to examine the properties of autoignition and derived cetane number of mixtures of diesel fuel and ethanol. *Fuel* 564–575
14. Ladommatos N, Xiao Z, Zhao H (2005) The effect of piston bowl temperatures on diesel exhaust emissions. *Proc Inst Mech Eng Part D: J Autom Eng*, vol 219 , pp 371–388
15. Rehman S (2018) Hot surface ignition and combustion characteristics of sprays in constant volume combustion chamber using various sensors. *Cogent Eng*, ISSN: 2331–1916. <https://doi.org/10.1080/23311916.2018.1464879>
16. Feng L, Chen B, Liu H, Yao M et al (2017) Combustion characteristics of wall-impinging diesel fuel spray under different wall temperatures. SAE Tech Paper 2017-01-2251. <https://doi.org/10.4271/2017-01-2251>
17. Zhou P (1984) Correlation of the average boiling points of petroleum fractions with pseudocritical constants. *Int Chem Eng* 24:731–741
18. Kuo KK (2005) Principles of combustion, 2nd ed. John Wiley and sons
19. Thomson GH, Brobst KR, Hankinson RW (1982) An improved correlation for densities of compressed liquids and liquid mixtures. *AIChE J* 28:671–676
20. Wu H, Nithyanandan K, Lee TH, Lee CF, Zhang C (2014) Spray and combustion characteristics of neat acetone-butanol-ethanol, n-butanol, and diesel in a constant volume chamber. *Energ Fuels* 28:6380–6391
21. De Boer C, Bonar G, Sasaki S, Shetty S (2013) Application of supercritical gasoline injection to a direct injection spark ignition engine for particulate reduction. SAE Int 2013-01-0257
22. Supercritical dieseline as an optimized fuel for low temperature combustion. In: Green Car Congress, August 2012
23. Ihme M, Ma PC, Bravo L (2018) Computational modeling and analysis of diesel-fuel injection and autoignition at transcritical conditions. In: THIESEL 2018 conference on thermo- and fluid dynamic processes in direct injection engines, pp 1–13
24. Sens M, Michael R (2018) Fundamental investigations about heated fuel injection on SI engines. SAE Int 2018-37-0003(May 2018):1–16
25. Rehman S, Alam SS (2020) Rate of heat release characteristics of supercritical sprays of dieseline blend in constant volume combustion chamber. *Results in Eng* 100121. <https://doi.org/10.1016/j.rineng.2020.100121>. (April 2020)

A Review on Thermal Barrier Coatings (TBC) Usage and Effect on Internal Combustion Engine



Priyanka Sharma, Vijay K Dwivedi, and Dipak Kumar

Abstract A growing number of vehicles polluting the environment and are also responsible for the fossil fuel depletion. To overcome these problems, the efficiency of an internal combustion engine needs to be increased. Many types of research have been carried out on decreasing the polluting gases from the engine by treating them with chemicals or by trapping them with some means. But some advanced methods are also dominating the automobile industry to overcome such problems. The use of thermal barrier coating (TBC) on the surface of the components of engine (piston crown, cylinder head, and combustion chamber) is one of the advanced technologies to increase the engine power and efficiency which means decrement in the harmful exhaust gases from the engine. This technology is the advancement in the material of the components of the diesel IC engine by coating it with the layer of ceramic material and making it more insulating to trap the heat within the chamber. As the operating temperature of the engine increases, it is in turn helpful in burning the maximum fuel and hence decreasing the ratio of particulate matter, smog, and other harmful gases. This will result in less pollution and better engine efficiency. The objective of this paper is to present a review report on the usage of the thermal barrier coating on the engine components like piston crown, cylinder head, combustion chamber, and effect of the thermal barrier coating in the internal combustion engine parameters.

Keywords Thermal barrier coating · Engine efficiency · Exhaust

P. Sharma (✉) · V. K. Dwivedi
GLA University, Mathura, Uttar Pradesh 281406, India
e-mail: priya24ipecc@yahoo.in

V. K. Dwivedi
e-mail: vijay.dwivedi@gla.ac.in

D. Kumar
RKGIT, Ghaziabad, Uttar Pradesh 201003, India
e-mail: dipakmnnit@gmail.com

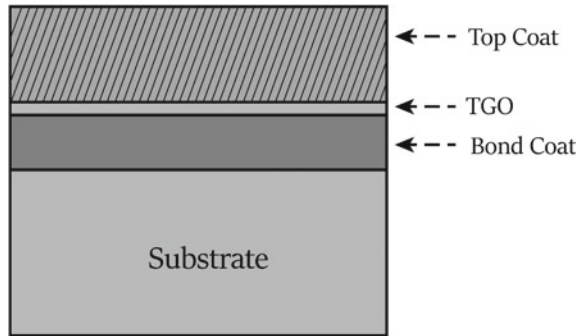
1 Introduction

In 1980s, the thermal barrier coating was first used for the internal combustion engines (diesel engines) [1] due to the low temperature capabilities of IC engines, turbines in automotive, power industry and aerospace, and the researches were carried out to tackle the problem. Thermal barrier coating was found to be an efficient and effective method to fulfil requirements that is mainly to increase the operating temperature in the various mechanical operations. The use of thermal barrier coating also helps in decreasing the depletion of the fossil fuels as by increasing the efficiency and power of the engine (by reducing the heat penetration), and the use of fuel also becomes low that improves the fuel consumption. In case of turbines, it is required that it must work on the temperature at which the fuel leaves the engine (turbine entry temperature) but due to heat penetration from the components and losses, the temperature lowers and hence reaches the turbine below the temperature at which it leaves. This also decreases the turbine efficiency. To increase the temperature, the thermal barrier coating is used on the inlet guide vanes, blades and afterburners, and hence, a huge difference was examined in the temperature that is TET increases by 1700 °C [2], which in turn increments the efficiency of the turbine. Thermal barrier coating has proved to be very beneficial in the automobile industry as it not only making engine efficient by reducing the exhaust emission and smoke density but also making is economical by reducing the specific fuel consumption, fuel efficiency. For the coating, mainly ceramic material is used based on the thermal conductivity of the material. The review shows the various materials that can be used of the thermal barrier coating and studies the related researches to the types of coatings used, and their effect on the engine parameters is presented in the review. Also, the applications of the thermal barrier coating are being reviewed.

1.1 Structure of TBC

Two metallic layers and two ceramic layers are there in the thermal barrier coating. The metallic layers include: substrate and base metal of the components on which the coating has to be obtained. It is mainly of nickel or cobalt super alloy in the single crystal or polycrystalline form [3] (Fig. 1).

Top coat The topmost layer of thermal barrier coating is named as top coat which is a ceramic layer, and yttria-stabilized zirconia (YSZ) is mainly used as the ceramic material for the coating to create insulation due to low thermal conductivity of the range of $2.3 \text{ Wm}^{-1} \text{ K}^{-1}$ and has high thermal expansion coefficient [3]. As the top coat comes in direct contact with the temperature, so its spallation starts due to very high temperature and thus the thermal cyclic behavior of the coating plays a vital role that it must resist the thermal cyclic loads [4, 5].

Fig. 1 Structure of TBC

Bond coat The second layer in TBC is the metallic bond layer. This layer is also known as the oxidation-resistant layer as it protects the oxidation and corrosion of top layer. The thickness of bond layer is 100 μm . It provides the adherence between the substrate and the top coat [3]. The damage of the top coat and the substrate also decreases due to the presence of bond coat.

Thermally grown oxide (TGO) The layer developed due to the high temperature at bond coat is named as the thermally grown oxide (TGO) layer [3]. The main composition of the TGO is alumina, and it extends approximately up to 10 μm .

2 Materials for TBC

The main criteria for using a material in the thermal barrier coating are: (i) low thermal conductivity, (ii) high thermal expansion coefficient, (iii) high thermal shock resistance, (iv) high corrosion resistance, and (v) economical [6].

Yttria-stabilized zirconia (YSZ) Mainly, zirconates (ZrO_2 , 3YSZ, 8YSZ, 18YSZ) (IX) are being used as the top coat material in the thermal barrier coating due to their following properties: (a) low thermal conductivity, (b) low sintering, and (c) high thermal expansion coefficients.

Alumina Though alumina is having high thermal conductivity when compared with YSZ and comparatively low coefficient of thermal expansion, its phase transformation at comparatively low temperature (1273 K) makes it unsuitable for the top coat.

Mullite Mullite has relatively low thermal expansion coefficient ($5.3 \times 10^{-6} \text{ K}^{-1}$) [6] but has very high thermal conductivity. But this leads to bad adhesion to the substrate as the thermal expansion coefficient does not match with the thermal expansion coefficient of the substrate.

Table 1 Coating materials and usage

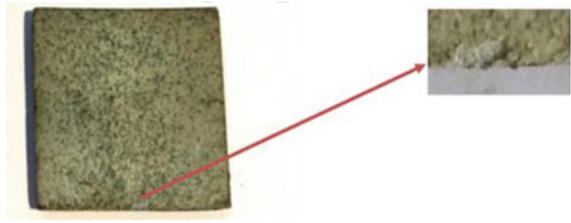
Name of the material	Spray process	Usage
Amdry 962	APS	Gas turbine and diesel engine (Bond coat)
CO-210-1	APS	Gas turbine and diesel engine (Bond coat)
9620AM	APS	Gas turbine and diesel engine (Bond coat)
Amdry 995C	APS	Gas turbine and diesel engine (Bond coat)
Diamalloy 4700	HVOF	Gas turbine and diesel engine (Bond coat)
9950AMF	HVOF	Gas turbine and diesel engine (Bond coat)
2008P	APS	Gas turbine and diesel engine (Top coat)
204NS-G	APS	Gas turbine and diesel engine (Top coat)

The coating deposition methods that are widely used are atmospheric (air) plasma spray method [7–10] and high-velocity oxygen fuel coating method. From these two methods, APS is more widely used due to the fact that it produces dense coating on the substrate and material with very high melting point can also be used for coating due to this method. Another advanced method which is used for the coating to obtain more corrosion resistance coating is MAO coating that is micro-arc oxidation coating which is mainly used to obtain the adhesive coating with porous microstructure. It is done on various substrate materials like AZ31B magnesium alloy, 2024 aluminium alloy and titanium alloys [11–13] (Table 1).

3 Thermal and Mechanical Properties of TBC

The material for the thermal barrier coating is done on the basis of following parameters: thermal expansion coefficient of the coating should be in accordance with the substrate, it should have low thermal conductivity, high melting point of the coating material is also considered, there should not be any phase transformation, it should be chemically inert, and it must be adhesive and have low sintering rate [1]. The properties of ZrO_2 are as follows: melting point is (2973 K), thermal conductivity is $2.17 \text{ Wm}^{-1} \text{ K}^{-1}$ (1273 K), thermal expansion coefficient is $15.3 \times 10^{-3} \text{ K}^{-1}$ (1273 K)¹¹ [14]. These properties make it suitable for the thermal barrier coating. Also, the thermal expansion coefficient for 8YSZ (APS) is $10.7 \times 10^{-6} \text{ K}^{-1}$ (293–1273 K) [14]. The fracture of the thermal barrier coating occurs in between the top coat and the bond coat when the specimen is tested for the tensile test and fatigue test [8]. The surface hardness, surface roughness and thermal fatigue of the coating also play a vital role in deciding the material and the shape of the specimen [15].

Fig. 2 Structure of TBC in diesel engine components [15]



4 Applications of TBC

Figure 2 shows the top coat of the thermal barrier coating that can be used in diesel engine components. The specimen is coated with YSZ-8 as the top coat, and for the bond coat, NiCoCrAlY is used as the bond coat [15]. The coating can be used in the piston crowns of the diesel and gasoline engines [16]. 0.1–0.2 mm layer of partially stabilized zirconia (PSZ) over the turbine blades decreases the surface temperature of the blades by 170° which in turn increases the thrust, and hence, efficiency of the turbine has been incremented [2]. This results in the increment in the TET for the further process [3, 14]. In engine, thermal barrier coating is used on the cylinder liners, head, piston crown, and inlet and exhaust valves [3, 17–21] not only to reduce thermal fatigue and heat rejection but also to reduce the exhaust emissions [22].

Thermal barrier coating on combustion chamber leads to the increment in the fuel burning rate and thus increases fuel economy at low engine power (4%) [14, 23–27]. The pollutants like hydrocarbons and CO also decrease due to the complete burning of the fuel, but oxides of nitrogen increase comparatively.

5 Related Work

Alumina-titania or yttria partially stabilized ZrO_2 is used as the top coat with the thickness of less than 0.5 mm, and NiCrAl is used as the bond coat for the coating on the piston crown diesel and gasoline engine [16]. The desirable results were observed that 15–20% decrement in the specific fuel consumption, also 8% and 6% increment in the power and brake moment of the engine [16]. The increased efficiency of the engine and improved fuel consumptions were noted on using the $CaZrO_3$ and $MgZrO_3$ as the top coat and NiCrAl as the bond coat on coating the piston crown, cylinder head and combustion chamber of a diesel engine. [28]. Alumina-titania is used as the top coat and nickel chromium as the bond coat on the piston, and the cylinder head of a diesel engine was done to improve the performance of engine [29, 30]. The coating on piston crown and cylinder head is shown in the following Fig. 3.

Fig. 3 Thermal barrier coating on the piston and cylinder head [29]



YSZ coating on the cylinder liner and piston crown of the diesel engine were useful in obtaining the 5% increase in the specific fuel consumption, 7.5% improvement in the brake thermal efficiency, and 20% increment in the mechanical efficiency of the engine [31–33].

6 Result (Effect on Internal Combustion Engine)

Brake-specific fuel consumption is seen to be decremented up to 3 to 13.4% when coating is deposited on the combustion chamber, but in some of cases, it increases. For diesel, the brake-specific energy consumption was seen to be reduced by 7.4%, and if biofuel was used in the engine, then the reduction reaches up to 15.4% [3, 30]. Thermal barrier coating along with the use of biofuel gives better results as compared to the use of gasoline and diesel fuel. The heat transfer to the coolant also get reduced owing to the insulation provided by the thermal barrier coating up to 19% due to reduction in the emission up to 80% [3]. But due to increase in the temperature, the emission of oxides of nitrogen (NO_x) increases, but by decrementing the injection timing along with the TBC [34–36], it can also be reduced up to 2.44% (Table 2).

The decrease in the various harmful exhaust gases (like smoke, CO, and hydrocarbons) emitted from the diesel engine is seen on applying the YSZ coating with different thicknesses [37, 38]. The improvement in the engine's efficiency and decrement in the energy-related losses is noted by using the coating

Table 2 Effect of thermal barrier coating on engine [3]

Properties	Effect	Percentage
Oxides of nitrogen	Decrement	14
Unburned HC	Decrement	23
CO	Decrement	48
Fuel consumption	Decrement	11
Engine noise	Decrement	3 (db)
Engine life	Increment	20
Cost	Increment	20

($ZrO_2-Al_2O_3$ and SiC). The SiC coating proved to be more effective in decreasing the emission of NO_x as compared to $ZrO_2-Al_2O_3$ [39]. There is slight increment in the smoke density of the engine seen due to the coating [39]. But the coating of fused zirconia (40FZA) reduces the smoke density and other harmful gases as compared to the other coating materials ($ZrO_2 + Al_2O_3$) [40]. The reduction up to 37.93% in the smoke density of the engine for the compression ratio of 19 is observed in the study; also for compression ratio of 20, there is reduction of 37.5% noted in the smoke density [41].

7 Conclusion

The power and mechanical efficiency of the internal combustion engine have been remarkably improved due to the deposition of thermal barrier coating on the engine parts (piston crown, cylinder head, and combustion chamber). Many engine parameters (specific fuel consumption, fuel efficiency, exhaust emission, and brake moment) have been seen to be improved significantly, and there has been a great improvement in the exhaust emission of the engine that will contribute to reduce the pollution in the environment. The lifetime of the engine components has seen to be incremented after using thermal barrier coating. Also, the variation in the smoke density is also noted in many researches. Hence, the paper serves for the applications and the effect of thermal barrier coating on the internal combustion engine to make it more efficient.

References

1. Thiruselvam K (2015) Thermal barrier coating in internal combustion engine. *J Chem Pharm Sci* 7:413–418
2. Saini AK, Das D, Pathak MK (2012) Thermal barrier coatings—applications, stability and longevity aspects. *Procedia Eng* 38:3173–3179
3. Nitin P (2018) Padture, Maurice Gell, Eric H Jordan: thermal barrier coatings for gas-turbine engine applications, *Material. Science* 296:280–284
4. Kumar D, Pandey KN, Das DK (2015) Thermal cyclic resistance behavior of INCONEL 800 superalloy substrate with thermal barrier coatings by plasma spraying. *Mater Today: Proc* 2:3156–3160
5. Buyukkaya E, Demirkiran AS, Cerit M (2004) Application of thermal barrier coating in a diesel engine. *Key Eng Mater* 264–268:517–520
6. Winkler MF, Parker DW, Bonar JA (1992) Thermal barrier coating for diesel engines: ten years of experience. *SAE, Paper no* 922438
7. Kumar D, Pandey KN, Das DK (2016) Microstructure studies of air plasma spray deposited CoNiCrAlY coating structure before and after thermal cyclic loading for high temperature application. *Int J Miner Metall Mater* 23(8):934–942
8. Kumar D (2018) Study on the tensile and the fatigue behavior of air plasma sprayed YSZ TBC systems. *J Met Mater Res* 1(1):27–31

9. Vibha, Dwivedi VK, Kumar D (2019) Nano-microstructural characterization of IN718 with thermal barrier coatings after thermal shock tests. *Int J Inno Technol Explor Eng (IJITEE)* 8 (5):36–41
10. Kumar Dipak (2019) Comparison of thermal fatigue of superni 718SGTBCs and APS TBCs. *Trans Indian Inst Metals* 72(7):1927–1939
11. Wang Y, Yu H, Chen C, Zhao Z (2015) Review of the biocompatibility of micro-arc oxidation coated titanium alloys, 85:640-652
12. Ezhilselvi V, Nithin J, Balaraju JN, Subramanian S (2016) The influence of current density on the morphology and corrosion properties of MAO coatings on AZ31B magnesium alloy, 288:221–229
13. Shchedrina I, Rakoch AG, Henrion G, Martin J (2014) Non-destructive methods to control the properties of MAO coatings on the surface of 2024 aluminium alloy, 238:27–44
14. Cao XQ, Vassen R, Stoever D (2004) Ceramic materials for thermal barrier coating. *J Eur Ceram Soc* 24:1–10
15. Sharma P, Dwivedi VK, Kumar D (2020) Effect of shape on the mechanical properties of thermal barrier coating of YSZ 7–8. *Mater Today: Proc*
16. Hejrowski T, Weronki A (2002) The effect of thermal barrier coatings on diesel engine performance. *Vacuum* 65:427–432
17. Yonushonis TM (1997) Overview of thermal barrier coatings for diesel engines. *J Therm Spray Technol* 6(1):50–56
18. Stover D, Funke C (1999) Directions of the development of thermal barrier coatings in energy applications. *J Mater Process Technol* 195–202:92–93
19. Pierz PM (1993) Thermal barrier coating development for diesel engine aluminum pistons. *Surf Coat Technol* 61:60–66
20. Lakshmanan S, Ranjith Babu G, Sabesh S, Manikandan M (2014) Investigation of thermal barrier coating on ic engine piston. *Int J Res Appl Sci Eng Technol*. ISSN: 2321-9653
21. Vishal NS, Mandar RT, Amol RW (2013) Thermal barrier coatings on ic engines: review. *Int J Res Aero Mech Engi* 1:134–139
22. Kumar D, Pandey KN, Das DK (2014) Thermal barrier coatings on aluminum-based alloy 2024 for high temperature protection subjected to thermal cyclic loading. *Procedia Mater Sci* 5:1075–1080
23. Patel BD, Mevada RN, Patel DP (2014) Review of literature survey on effect of thermal coating on cylinder and piston crown. *Int J Eng Res Gen Sci* 2. ISSN 2091-2730
24. Karthikeya Sharma T (2014) Performance and emission characteristics of the thermal barrier coated SI engine by adding argon inert gas to intake mixture. *J Adv Res*
25. Rajasekaran J, Gnanasekaran BM, Senthilkumar T, Kumaragurubaran B, Chandrasekar M (2013) Effect of thermal barrier coating for the improvement of SI engine performance and emission characteristics. *Int J Res Eng Technol*. eISSN: 2319-1163, pISSN: 2321-7308
26. Chan HS (2001) Performance and emissions characteristics of a partially insulated gasoline engine. *Int J Therm Sci* 40:251–255
27. Barbezat G (2006) Application of thermal spraying in the automobile industry. *Surf Coat Technol* 201:2028–2031
28. Taymaz Imdat (2007) The effect of thermal barrier coatings on diesel engine performance. *Surf Coat Technol* 201:5249–5252
29. N. Santosh Arjun: The effect of thermal barrier coatings on diesel engine performance, 212579040, (2013)
30. Masera K, Hossain AK (2018) Biofuels and thermal barrier: a review on compression ignition engine performance, combustion and exhaust gas emission. *J Energ Inst* 1–19 (2018)
31. Raghu, Chandrashekara K (2018) Experimental study of the effect of thermal barrier coating on diesel engine performance, 212530414
32. Kumar S, Kant S (2016) Effects of thermal barrier coatings on diesel and gas turbine engines: a review, 212486676
33. Meier SM, Gupta DK (1994) The evolution of thermal barrier coatings in gas turbine applications. *J Eng Gas Turbines Power* 116:25–257

34. Buyukkaya E, Cerit M (2008) Experimental study of NO_x emissions and injection timing of a low heat rejection diesel engine. *Int J Therm Sci* 47:1096–1106
35. Cerit Muhammet, Coban Mehmet (2014) Temperature and thermal stress analyses of a ceramic-coated aluminum alloy piston used in a diesel engine. *Int J Therm Sci* 77:11–18
36. Chan SH, Khor KA (2000) The effect of thermal barrier coated piston crown on engine characteristic. *J Mater Eng Perform* 9:103–109
37. Das D, Majumdar G, Sen RS, Ghosh BB (2014) The effects of thermal barrier coatings on diesel engine performance and emission. *J Inst Eng (India): Ser C*, 95:63–68
38. Palaniswamy E, Manoharan N (2008) Ceramic coated combustion chamber for improving IC engine performance. *Int J Des Manuf Technol* 2
39. Ramu P, Saravanan CG (2009) Effect of ZrO₂-Al₂O₃ and SiC coating on diesel engine to study the combustion and emission characteristics, 0148-7191
40. Mohamed Abbas S, Elayaperumal A (2019) Experimental investigation on the effect of ceramic coating on engine performance and emission characteristics for clear production, 214:506–513
41. Beg RA, Bose PK, Ghosh BB, Banerjee TK, Ghosh AK (1997) Experimental investigation on some performance parameters of a diesel engine using ceramic coating on the top of the piston, 0148-7191

Evaluation of Emission Characteristics of Diesel Engine Fueled with Blends of Biodiesel Obtained from Waste Sesame Oil and Its Blends with Pure Menthe Oil



Sanjay Kumar Yadav, Manoj Kumar, and Niraj Kumar

Abstract Air pollution produced from the combustion of diesel fuel is a very serious problem especially in India; therefore, it is necessary to develop an alternative fuel which must be environmental friendly. Emissions of hydrocarbon, carbon dioxide, carbon mono oxide, nitrogen oxides, and particulate matter from exhaust of diesel engine are very important as per as air pollution is concern. As the cost of diesel fuel is also increasing day by day at the same time it is polluting the environment too. The biodiesel derived from pure vegetable oil and waste vegetable oil has become an alternating fuel up to some extent as per emissions concern for compression ignition engine. This alternating fuel can be used without any further modification in diesel engine. In present research work, biodiesel has derived from waste sesame oil and various blends of it with menthe oil have been prepared. The blends (B20, B40, B60, B80, and B100) have been used to find out the emission characteristics at various loads like 0%, 25%, 50%, 75%, and 100%. As per the testing and result analysis, it is found that emissions of hydrocarbon, carbon dioxide, carbon mono oxide, nitrogen oxides, and particulate matter for blend B20 are very close to the diesel fuel. It is also observed that except B20, other blends shows higher rate of emissions. The results also show that blend B20 is very much suitable fuel, which gives better result in concern with the emission and environment friendly. Also, the cost of the derived biodiesel is reasonable in comparison with the diesel.

Keywords Waste vegetable oil · Biodiesel · Diesel engine · Sesame oil · Menthe oil · Fuel

S. K. Yadav (✉) · M. Kumar
IFTM University, Moradabad, Uttar Pradesh 244001, India
e-mail: sanjay.atulya@gmail.com

M. Kumar
e-mail: manoj_kumar@iftmuniversity.ac.in

N. Kumar
Amity University, Noida, Uttar Pradesh 201313, India
e-mail: kniraj2006@gmail.com

1 Introduction

Nowadays, we cannot think about living on this earth without diesel engine. Diesel engines are very essentials and useful machines for transportation of goods for various purposes. Specialties of compression ignition engines are robust design, easy to use and maintain but air pollution is very serious problem. Availability of diesel fuel is also very limited. Therefore, many researchers are working to find out a suitable alternative fuel of diesel. It will serve twin purposes: reduction in air pollution and reduction in dependency on the import of diesel. Biodiesel obtained from different source may be an alternative fuel of diesel fuel. Biodiesel is oxygenated fuel and hence provides better combustion and reduces emission [1]. The use of biodiesel-diesel blends will reduce the greenhouse gas emissions and other pollutants. Blends of biodiesel with a small content by volume can be used in existing CI engines without any major modifications [2]. Hydrocarbon, carbon monoxide, carbon dioxide, nitrogen oxides, and particulate matter are the important emission characteristics of compression ignition engine, by observing these characteristics we can find the suitability of any alternative fuel for diesel engine. Hydrocarbon emission was found to be decreased for most of the biodiesel operated engine [3, 4]. HC emission does not depend on types of feedstock; however, it was reported that ethyl ester of pure oil produced less HC than corresponding methyl ester [5]. Quality of combustion, fuel spray pattern, and fuel properties affect the HC emission of compression ignition engine. With increasing amount of biodiesel in blends, cetane number, content of oxygen in biodiesel increases which lead better combustion. Hence, complete combustion ensures lesser unburned HC emission and other emission. More air flow inside the engine cylinder at high speed created more homogenous mixture and reduces HC emission. Incomplete combustion always shows higher emission of carbon monoxide for biodiesel [6]. Many researchers concluded that less CO emission for biodiesel was the indication of complete combustion of biodiesel [7–9]. Carbon monoxide is the result of incomplete combustion of fuel. Carbon dioxide emissions were observed higher for biodiesel [10, 11]. On the other hand, some researchers observed lower CO₂ emission for biodiesel than diesel. Presence of more oxygen leads to better combustion, hence reduction in CO emission but increase in CO₂ emission. However, relatively low content of carbon in biodiesel for the same volume of fuel was investigated the reason for lower emission of CO₂ [10]. An increase in NO_x emission was observed by the researchers [7, 8]. It was investigated that NO_x emission for biodiesel and their blends depend on number of factors. All types of biodiesel contain some additional amount of oxygen compared to diesel. In addition to inducted air inside the engine cylinder, oxygenated biodiesels add some more oxygen which may affect the formation of NO_x. Higher combustion temperature increases the NO_x formation by supporting the NO_x formation reactions. NO_x emission was directly related to degree of molecular saturation [12]. In most of the research work, it has been found that the use of biodiesel reduces smoke opacity and exhaust emission (PM) at full load [13, 14]. Soot particles were found to be

Table 1 Properties of vegetable oil [16]

Properties	Diesel	Sea lemon oil	Jatropha oil	Cotton seed oil	Tobacco see oil	Waste sesame oil
Density(KG/M ³)	840	927	918	874	920	878
Calorific value (KJ/KG)	42,390	39,650	39,774	39,648	39,400	35,207
Cetane number	45–55	–	45	45	38	53
Viscosity (cst)	4.59	49.7	49.9	50	27.7	4.3
Flash point (°C)	75	158	240	210	220	128.2
Carbon residue (%)	0.1	0.46	0.44	0.55	0.57	0.006

increased in lower blends [15]. In the present work, the effects of biodiesel obtained from waste sesame oil and its blends with menthe oil are experimentally analyzed for emission characteristics of single cylinder direct injection diesel engine using as a fuel. Table 1 compares some of the important properties of different vegetable oil, which are used as fuel in diesel engine.

2 Material and Method

A single cylinder four-stroke water-cooled diesel engine developing 3.5 KW at 1100 RPM used for this work. Eddy current dynamometer with a control system is coupled with engine. The specification of the selected diesel engine is shown in Table 2. Composition of blends of biodiesel obtained from waste sesame oil and menthe oil are shown in Table 3. Emission of hydrocarbon, carbon monoxide, carbon dioxide, nitrogen oxides, and particulate matter was recorded at 0, 25, 50, 75, and 100 load for each and every blend at steady state operation of engine.

Table 2 Technical specification of the engine

Make	KirloskarTAF1
Rated brake power (kW)	3.5
Rated speed (rpm)	1500
Number of cylinder	1
Bore × stroke (mm)	87.5 × 110
Displacement volume (cc)	661 cc
Compression ratio	17.5:1
Cooling system	Water cooled
Starting system	Manual hand start (with handle)

Table 3 Compositions of different blends

S/N	Sample	Biodiesel from waste sesame oil (ml)	Menthe oil (ml)	Diesel (ml)	Blends
1	Sample 1	200	800	00	B20
2	Sample 2	400	600	00	B40
3	Sample 3	600	400	00	B60
4	Sample 4	800	200	00	B80
5	Sample 5	1000	000	00	B100
6	Sample 6	00	000	1000	D100

3 Result and Discussion

Blends of waste sesame oil biodiesel and menthe oil have significant effects on the emission characteristics of diesel engine. Emission of hydrocarbon, carbon monoxide, carbon dioxide, nitrogen oxides, and particulate matter at different load depends upon the quantity of biodiesel present in the particular blend. Emission of hydrocarbon, carbon mono oxide, carbon dioxide, nitrogen oxides, and particulate matter of diesel engine fueled with blend B20, B40, B60, B80, and B100 D100 are shown in Figs. 1, 2, 3, 4, 5, respectively. Emission characteristics of DIC I engine are directly related to fuel properties such as oxygen content, viscosity, density, HHV, and fuel injection system [17]. Generally, fuel property affects combustion process and hence emission characteristics of engine [18].

3.1 Hydrocarbon (HC)

All the blends were tested under similar steady state condition of diesel engine. Variation in hydrocarbon of different blends at various loads is shown in Fig. 1. Emission of hydrocarbon at any load is maximum for blend B20 and minimum for

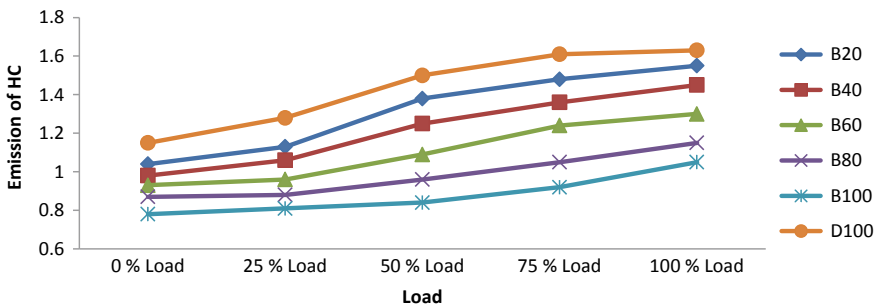


Fig. 1 Variation in the emission of HC of different blends at various loads

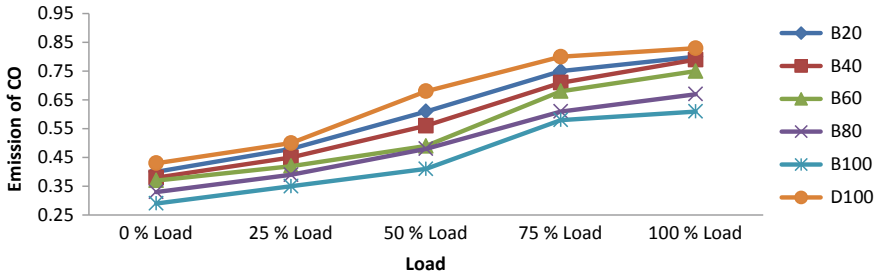


Fig. 2 Variation in emission of carbon monoxide of different blends at various loads

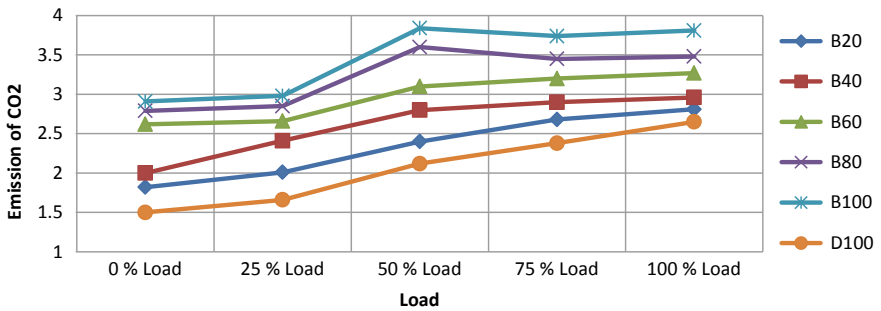


Fig. 3 Variation in emissions of carbon dioxide of different blends at various loads

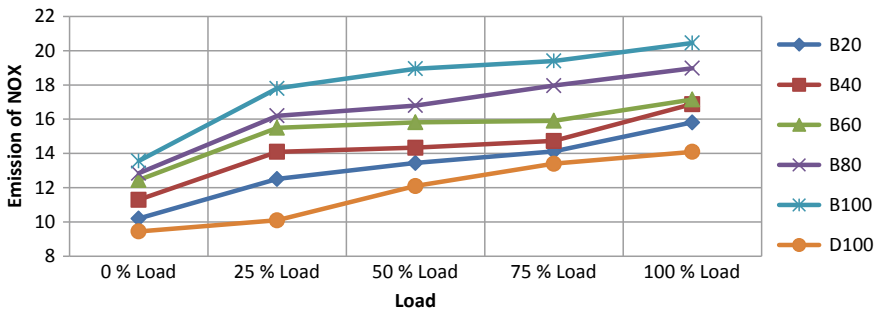


Fig. 4 Variation in emission of nitrogen oxides of different blends at various loads

blend B100. Ruhul et al. reported in his work that HC emission can be reduced by 9%, by the use of biodiesel blends [19]. Above-mentioned Fig. 1 shows that level of hydrocarbons increases from blend B100 to blend B20 and intensity of hydrocarbons in exhaust gases increases approximate linearly irrespective of load. Level of hydrocarbon for blend B20 and D100 is almost same at any load. Hydrocarbon emitted by blend B40 is little less than blend B20 at any load.

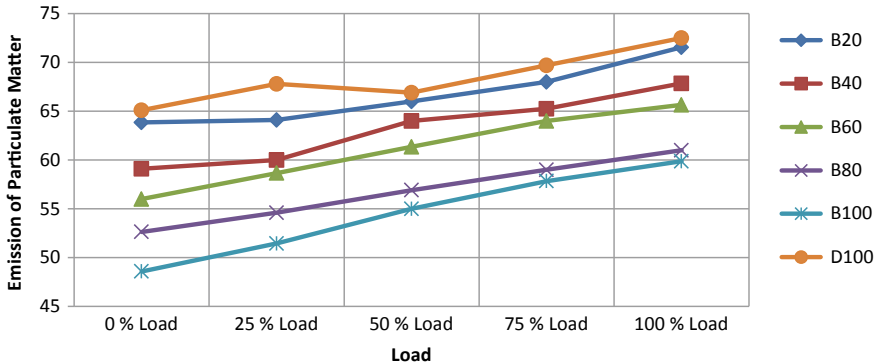


Fig. 5 Variation in emission of particulate matter of different blends at various loads

Blends like B60, B80, and B100 show a low level of hydrocarbon at any load. Blends having more quantity of biodiesel in the fuel also have low level of hydrocarbon in the emission at any load. The unburned hydrocarbon emission of the engine fueled with biodiesel and its blends were lower than diesel fuel [1]. Now if we consider blend B20 than hydrocarbon released in exhaust by blend B20 is minimum at 0% load and maximum at 100% load, level of hydrocarbon increases linearly (approximately) from 0% load to 100% load. A similar result has been observed for hydrocarbon emission for other blends (B40, B60, B80, B100, and D100) too from 0 to 100% load. Quantity of hydrocarbon emission present in the exhaust of engine for different blends changes from minimum to maximum when load changes from minimum to maximum for any blend. Hydrocarbon emissions for any blends are minimum at 0% load and maximum at 100% load. Every blends show maximum level of emission of hydrocarbons at 100% load and minimum level of hydrocarbons at 0% load. Every blend also shows a linear increment in emission of hydrocarbon when load increases. The HC emissions can be reduced to a great extent by the use of biodiesel blends [2].

It could be concluded that HC emission increases as load increases and HC emission also increases as quantity of biodiesel decreases in the blend. There are several reasons behind this rise in HC emission in exhaust. Some reasons are low calorific value of blends, more fuel consumption for producing same power as that of lower blend for higher blends, incomplete combustion which is generally associated with higher blends. Hydrocarbons in the exhaust are the principal cause of the unpleasant smell of diesel engine, though the lubricating oil also makes a small contribution. There are three main reasons for this. First, at low temperature and light loads, the mixture may be too lean for efficient burning so the pre-combustion process during the ignition delay period is partially inhibited. This is why some of the mixture subsequently fails to burn.

Second reason, because of low volatility of fuel relative to diesel or petrol, and the short period time available for it to evaporate before combustion begins, HC is generated during starting warming up from the cold. In these circumstances, fuel

droplets, together with water droplets produced by the burning of hydrogen content of the remainder of fuel remains present in the exhaust. At about 10%, load and rated speed HC and CO output are specially sensitive to fuel quality and, in particular, cetane number.

Third reason, after cold starting and during warm up, a higher than normal proportion of the injected fuel, failing to evaporate, is deposited on the combustion chamber wall. This further reduce the rate of evaporation of the fuel, so that it fails to be ignited before the contents of the chamber have been cooled, by expansion of gases, to a level such that ignition can no longer occur.

Another potential cause of HC is the fuel contained in the volume between the pintle needle seat and spray hole. HC emission decreases slightly as cetane number increases and fuel density decreases and relationship with volatility inconsistent.

3.2 Carbon Monoxide (CO)

Figure 2 represents the relationship in between the emission of carbon monoxide and load for different blends at various load. Blend B20 has maximum emission of carbon monoxide and blend B100 has minimum emission of carbon monoxide at any load. The carbon monoxide of the engine fueled with biodiesel and its blends were lower than diesel fuel [1]. Above-mentioned Fig. 2 shows an approximately linear growth in the emission of carbon monoxide for any load as we change blend from B100 to B20. Level of carbon monoxide for blend B20 and D100 is almost same at any load. The CO emissions were reduced to a great extent [2]. Carbon monoxide emitted by blend B40 is little less than blend B20 at any load. Fuels like B60, B80, and B100 are producing less carbon monoxide in the exhaust emission at any load. Blends having more quantity of biodiesel in the fuel also have low level of carbon monoxide in the emission at any load. Emission of carbon monoxide for blend B20 is almost similar as that of emission of carbon monoxide for D100. Carbon monoxide released in exhaust by blend B20 is minimum at 0% load and maximum at 100% load. Level of carbon monoxide increases linearly (approximately) from 0% load to 100% load. A similar result has been observed for carbon monoxide emission for other blends (B40, B60, B80, B100, and D100) too from 0 to 100% load. Quantity of carbon monoxide emission presents in the exhaust of engine for different blends changes from minimum to maximum when load changes from minimum to maximum for any blend. Shivramakrishnan [20] reported that CO emission increases as the quantity of biodiesel increases in blend. Carbon monoxide emissions for any blends are minimum at 0% load and maximum at 100% load. Every blends show maximum level of emission of carbon monoxide at 100% load and minimum level of carbon mono oxide at 0% load. Every blend also shows a linear increment in emission of carbon monoxide when load increases. It can be summarized that CO emission increases as load increases and CO emission also increases as quantity of biodiesel decreases in the blend. There are several reasons behind this rise in CO emission in exhaust. Some reasons are low calorific value of

Blends B40, B60, B80, and B100, more fuel consumption for producing same power as that of lower blend for higher blends, incomplete combustion which is generally associated with higher blends. Cramble biodiesel resulted in a reduction in emission of CO as a function of the increase in cramble oil in the proportion [21]. Carbon monoxide emissions for waste cooking oil biodiesel blends were lower than diesel [22].

Even at maximum power output, there is as much as 38% of excess air in the combustion chamber. However, although carbon monoxide should not be formed, it may be found in small quantities in the exhaust. The reason is partly that, in local areas of the combustion chamber, most of the oxygen has been consumed before injection ceases, and therefore, fuel injected into areas cannot burn completely to CO₂.

3.3 Carbon Dioxide (CO₂)

Relationship between carbon dioxide and load for various blends at different load is shown in Fig. 3. Emission of carbon dioxide at any load is minimum for blend B20 and maximum for blend B100. Results of emissions demonstrated that B5 has little low CO₂ emissions [23]. It is clear from above-mentioned figures that the level of carbon dioxide increases from blend B20 to blend B100 and intensity of carbon dioxide in exhaust gases increases approximate linearly irrespective of load. Level of carbon dioxide for blend B20 and D100 is almost same at any load. CO₂ emission was reduced by 18.6% when millettia pinnata-based biodiesel blends were used as a fuel in C.I. engine [19].

Carbon dioxide emitted by blend B40 is little more than blend B20 at any load. Blends like B60, B80, and B100 show a high level of carbon dioxide at any load. Blends having more quantity of biodiesel in the fuel also have high level of carbon di oxide in the emission at any load. Cramble biodiesel resulted in a reduction in emission of CO₂ as a function of the increase in cramble oil in the proportion [21]. Now if we consider blend B20 than carbon dioxide released in exhaust by blend B20 is minimum at 0% load and maximum at 100% load, level of carbon dioxide increases linearly(approximately) from 0% load to 100% load. A similar result has been observed for carbon dioxide emission for other blends (B40, B60, B80, B100, and D100) too from 0 to 100% load. Quantity of carbon dioxide emission present in the exhaust of engine for different blends changes from minimum to maximum when load changes from minimum to maximum for any blend. Carbon dioxide emissions for any blends are minimum at 0% load and maximum at 100% load. Every blends show maximum level of emission of carbon dioxide at 100% load and minimum level of carbon dioxide at 0% load. Every blend also shows a linear increment in emission of carbon dioxide when load increases. CO₂ emissions for waste cooking oil biodiesel blends were higher than diesel [22].

Therefore, it can be concluded that CO₂ emission increases as load increases and CO₂ emission also increases as quantity of biodiesel increases in the blend. There

are several reasons behind this rise in CO₂ emission in exhaust. Some reasons are low calorific value of blends B40, B60, B80, and B100, more fuel consumption for producing same power as that of lower blend for higher blends, incomplete combustion which is generally associated with higher blends.

3.4 Nitrogen Oxides (NO_x)

Variation in nitrogen oxides (NO_x) for different blends at various loads is shown in Fig. 4. Blend B20 has minimum emission of nitrogen oxides and blend B100 has maximum emission of nitrogen oxides at any load. Cramble biodiesel resulted in a reduction in emission of NO_x as a function of the increase in cramble oil in the proportion [21]. Above-mentioned Fig. 4 shows an approximately linear growth in the emission of nitrogen oxides for any load as we changes blend from B20 to B100. Level of nitrogen oxides for blend B20 and D100 is almost same at any load. Less NO_x emission was reported as compared for blend B20 [23]. Nitrogen oxides emitted by blend B40 are little more than blend B20 at any load. NO_x emission was increased by 17.15% when the blends of biodiesel obtained from *milletia pinnata* were used as a fuel in diesel engine [19]. Fuels like B60, B80, and B100 are producing more nitrogen oxides in the exhaust emission at any load. Blends having more quantity of biodiesel in the fuel also have high level of nitrogen oxides in the emission at any load. The oxides of nitrogen and smoke emission increased while using the fuel blends and biodiesel [1, 2]. Emission of nitrogen oxides for blend B20 is almost similar as that of emission of nitrogen oxides for D100. As per as performance of blend is concern, than nitrogen oxides released in exhaust by blend B20 are minimum at 0% load and maximum at 100% load. Level of nitrogen oxides increases linearly(approximately) from 0% load to 100% load. A similar result has been observed for nitrogen oxides emission for other blends (B40, B60, B80, B100, and D100) too from 0 to 100% load. Quantity of nitrogen oxides emission present in the exhaust of engine for different blends changes from minimum to maximum when load changes from minimum to maximum for any blend. Nitrogen oxides emissions for any blends are minimum at 0% load and maximum at 100% load. Every blends show maximum level of emission of nitrogen oxides at 100% load and minimum level of nitrogen oxides at 0% load. Every blend also shows a linear increment in emission of nitrogen oxides when load increases. It can be summarized that NO_x emission increases as load increases and NO_x emission also increases as the quantity of biodiesel increases in the blend. There are several reasons behind this rise in NO_x emission in exhaust. Some reasons are low calorific value of blends B40, B60, B80, and B100, more fuel consumption for producing same power as that of lower blend for higher blends, incomplete combustion which is generally associated with higher blends.

Emission of nitrogen oxides does not depend only on the peak temperature of combustion but also on the rate of rise and fall to and from it. Secondly, the combustion temperature depends on primarily the quantity and to a lesser degree,

the cetane number of the fuel injected. Increasing the cetane number reduces the delay period, so that fuel starts to burn earlier, so higher temperature and therefore more NO_x . Increasing fuel volatility reduces NO_x because fuel injected is reduced and the engine is therefore de rated. Consequently, combustion temperature is lowered. Unfortunately, most of the current conventional method of reducing NO_x also impair efficiency and therefore increase fuel consumption and the output of CO_2 . In general, NO_x tends to form most readily in fuel lean zones around the injection spray. Reduction of the rate of swirl is another way of reducing the output NO_x but it reduced thermal efficiency. Delaying the start of injection has the effect of reducing peak temperature, and therefore NO_x . This is because the combustion process builds up its peak later in the cycle. NO_x emission decreases as aromatic content is lowered. Measure taken to reduce NO_x tends to increase the quantity of particulates and HC in the exhaust. This is primarily because while NO_x is reduced by reducing the combustion temperature, both soot and HC are burned off by increasing it.

3.5 *Particulate Matter (PM)*

Particulate matter is an important emission characteristic of diesel engine; variation in the emission of particulate matter of different blends at various load is shown in Fig. 5. Smoke and particulate matter for blend B20 is minimum at 0% load; it increases as load increases and becomes maximum at 100% load. The PM emissions are reduced to a great extent [2]. Soot emission for blend B20 was little more than diesel [23]. Smoke and particulate matter for blend B40 is less than the smoke and particulate matter of blend B20. The blends which have higher volume of biodiesel in blend shows lower value of smoke and particulate matter. B100 blend has minimum value of smoke and particulate matter at each and every load. B20 blend has maximum value of smoke and particulate matter, and it is close to the value of smoke and particulate matter of D100 at corresponding load. If we consider the load than at any load, blend B20 has minimum smoke and particulate matter than any blend at a particular load and blend B20, smoke and particulate matter for D 100 is almost similar to blend B20. Smoke opacity emissions for waste cooking oil biodiesel blends were lower than diesel [22]. At any load, higher blends (B40, B60, B80, and B100) show reduced value of smoke and particulate matter. Particulates may be anything that is retained, at an exhaust gas temperature of 52 °C, by a filter having certain specified properties. Very low soot emissions (<0.01 g/kWh) were also reported by the authors [24].

They therefore include liquids as well as solids. Particle sizes range from 0.01 to 10 μm , the majority being well under 1.0 μm , while black smoke comprises mainly carbon, the heavier particulates comprise ash and other substances, some combined with carbon. The proportions depend on types of engine, fuel, and lubricants. Measures appropriate for reducing the fuel and oil content of the particulates are same as with HC emission. The overall quantity of particulates can be reduced by

increasing the injection pressure and reducing the size of the injector holes, to atomize the fuel better. Increasing the combustion temperature helps to burn the loose soot deposited on the combustion chamber wall. Reduction of sulfur content of the fuel also reduces particulates. A small proportion of the particulates is ash, most of which come from burning the lubrication oil. Reduction of sulfur in the fuel reduces the need for including, in lubricating oils, additives that neutralize the acid products of combustion, these additives that are responsible for a significant proportion of the ash content.

Smoke and particulates matter increases as load increases and quantity of biodiesel increases in the blend; the reasons behind this rise of smoke and particulates are high volatility of fuel, high cetane number of fuel, and more sulfur content in fuel.

4 Conclusion

A single cylinder diesel engine was fueled with the blends of waste sesame oil biodiesel and pure menthe oil B20, B40, B60, B80, B100, and D100. Emission characteristics were recorded at 0, 25, 50, 75, and 100% at constant speed of 1500 RPM. Emission of hydrocarbon, carbon monoxide, carbon dioxide, nitrogen oxides, and particulate matter were recorded and compared with pure diesel oil. The following conclusions could be summarized as:

1. Blend B100 has minimum emission of HC, CO, and PM at all loads, while the emissions of HC, CO, and particulate matter increase as load increases.
2. Emissions of HC, CO, and PM increase as the quantity of biodiesel decreases in blend.
3. Blend B20 has maximum emission of HC, CO, and PM at all load but less than diesel. It has been seen that emissions of HC, CO, and particulate matter increase as load increases.
4. Emission of nitrogen oxides and carbon dioxide is minimum for blend B20. Emission of CO_2 and NO_x increases as load increases.
5. Emission of nitrogen oxides and carbon dioxide is maximum for blend B100. It increases as load increases.
6. This study concludes that pure biodiesel obtained from waste sesame oil is suitable for diesel engine since it has minimum emission at all load.

Cost of biodiesel obtained from waste sesame oil is more in comparison with other biodiesel; therefore, efforts can be focused to reduce the cost. Further, performance characteristics (brake thermal efficiency, fuel consumption, brake power, and other properties) of diesel engine may be evaluated with waste sesame oil biodiesel.

References

1. Raman LA, Deepanraj B, Rajakumar S, Shivasubramanian V (2019) Experimental investigation on performance, combustion and emission analysis of a direct injection diesel engine fuelled with rapeseed oil biodiesel. *Fuel* 246:69–74
2. Hasan MM, Rahman MM (2017) Performance and emission characteristics biodiesel-diesel blend and environmental and economic impact of biodiesel production: a review. *Renew Sustain Energy Rev* 74:938–948
3. Canakci M, Erdil A, Arcaklioglu E (2006) Performance and exhaust emission of a biodiesel engine. *Appl Energy* 83:594–605
4. Payri F, Bermudez VR, Tormos B, Linares WG (2009) Hydrocarbon emission speciation in diesel and biodiesel exhaust. *Atmos Environ* 43:1273–1279
5. Canakci M, Van Gerpen H (2003) Comparison of engine performance and emission for petroleum diesel fuel, yellow grease biodiesel and Soybean oil biodiesel. *Trans ASAE* 46:937–944
6. Kalam MA, Masjuki HH (2004) Emissions and deposits characteristics of a small diesel engine when operated on pre heated crude palm oil. *Biomass Bio Energy* 27:289–297
7. Ozesen AN, Canakci M (2010) The emission analysis of an IDI diesel engine fuelled with methyl ester of waste frying palm oil and its blends. *Biomass Bio Energy* 34:1870–1878
8. Canakci M, Ozsezen AN, Arcaklioglu E, Erdil A (2009) Prediction of performance and exhaust emission of a diesel engine fuelled with bio diesel produced from waste frying palm oil. *Exp Syst Appl* 36:9268–9280
9. Das L, Babu MKG (2008) Performance of mixed biodiesel fuelled diesel engine. *J Sci Ind Res* 67–73
10. Chauhan BS, Kumar N, Cho HM (2012) A study on the performance and emission of a diesel engine fuelled with *Jatropha* biodiesel oil and its blends. *Energy* 37(1):616–622
11. Mbarawa M (2008) Performance emission and economic assessment of clove stem oil-biodiesel blended fuel as alternative fuel for diesel engine. *Renew Energy* 33:871–878
12. Navi MN, Rahman MM, Akthar MS et al (2009) Bio diesel from cotton seed oil and its effect on engine performance an exhaust emission. *Appl Therm Eng* 29:2265–2270
13. Enweremadu CC, Rutto HI (2010) Combustion emission and performance characteristics of used cooking oil biodiesel: a review. *Renew Sustain Energy Rev* 14:2863–2873
14. Ramadhas AM, Murleedharan C, Jayaraj S (2005) Performance and evaluation of a diesel engine fuelled with methyl ester of rubber seed oil. *Renew Energy* 30:1789–1800
15. Omidvarvorna H, Kumar A, Kim DS (2016) Variation of soot characteristics by different types and blends of biodiesel in laboratory combustion chamber. *Sci Tot Environ* 544:450–459
16. Hariharan VS, Reddy Vijay kumar K (2011) Effect of injection pressure on diesel engine performance with sea lemon oil. 4(8):907–909
17. Habibullah M, Rizwanul Fattah IM, Masjuki HH, Kalam MA (2015) Effects of Palm-Coconut biodiesel blends on the performance an emission of single cylinder diesel engine. *Energy Fuels* 29(2):34–43
18. Murillo S, Miguez J, Porteiro J, Granda E, Moran J (2007) Performance and exhaust emission in the use of biodiesel in outboard diesel engine. *Fuel* 86(12):1765–1771
19. Ruhul AM, Kalam MA, Masjuki HH, Sahahir SA, Alabdulkareem A, Teoh YH, How HG, Reham SS (2017) Evaluating combustion, performance an emission characteristics of *Millettia Pinnata* and *Croton Megalocarpus* biodiesel blend in a diesel engine. *Energy* 141:2362–2376
20. Shivramakrishnan K (2017) Investigation on performance and emission characteristics of a variable compression multi fuel engine fuelled with Karanga biodiesel-diesel blends. *Egypt J Petrol*

21. Leite D, Santos RF, Bassegio D, de Souza SNM, Seco D, Gurgacz F, Bentoli e Silva TR (2019) Emission and performance of a diesel engine affected by soyabean, linsee and cramble biodiesel. *Ind Crop Prod* 130:267–272
22. Abed KA, EI Morsi AK, Sayed MM, EI Shaib AA, Gad MS (2018) Effect of waste cooking oil biodiesel on performance and exhaust emission of a diesel engine. *Egypt J Petrol*
23. Hajlari SA, Nazafi B, Aradabili SF (2019) Castor oil, a source of biodiesel production and its impact on the diesel engine performance. *Renew Energ Focus* 28(00)
24. Liu H, Ma X, Li B, Chaen L, Wang Z, Wang Z (2017) Combustion and emission characteristics of direct injection diesel engine fueled with biodiesel and PODE/biodiesel fuel blends. *Fuel* 209:62–18

Liquid Film Thickness Measurement: A Critical Review



Sagar G. Nayak, Nishant M. Shah, and Jyotirmay Banerjee

Abstract There is a growing demand for high-performance cooling. Two-phase flow through microchannels involving phase change (thin-film evaporation) is one of the prospective techniques for high-performance cooling. Liquid film thickness is a prominent parameter in the study of thin-film evaporation. Measurement of film thickness in macro-, mini-, and microscale channels has drawn many researchers' attention from the past few decades. Many numerical techniques, analytical models, and experimental methods have been proposed in this regard. In the present study, an attempt is made to present a comprehensive literature review of the methods used so far for the measurement of liquid film thickness. Further, image processing technique is demonstrated as a potential candidate for the measurement of liquid film thickness.

Keywords Two-phase flow · Liquid film thickness · Image processing

1 Introduction

Natural and forced cooling has been in use since long time. These systems are highly reliable, financially affordable, and cheap in terms of operational and maintenance cost. There are certain problems of these systems such as low heat flux removing capacity, noise and operational difficulty. Out of these, low heat flux removal becomes a major limitation in many applications where there is an incredibly high heat dissipation. This is because of low specific heat value of air

S. G. Nayak · N. M. Shah (✉) · J. Banerjee
Department of Mechanical Engineering, National Institute of Technology Surat, Surat,
Gujarat 395007, India
e-mail: nishantmshah93@gmail.com

S. G. Nayak
e-mail: nayaksagar226@gmail.com

J. Banerjee
e-mail: jbaner@med.svnit.ac.in

which demands high mass flow rates to achieve desired cooling which further increases pumping costs. Microchannels which possess high surface area-to-volume ratio ranging from 10,000 to 50,000 m^2/m^3 are found to be potential candidates for high-performance cooling. Since the hydraulic diameter of the microchannels is very small, they possess a very high heat transfer coefficient giving an excellent heat transfer mechanism.

Flow through microchannels with the phase change further contributes in making the heat transfer further effective. Flow boiling can increase the thermal performance of microchannels further by providing high heat transfer coefficient than pool boiling or a simple single-phase flow (Table 1). In the literature, one can find that there is an ambiguity about the dominating heat transfer mechanism in flow boiling that whether it is the nucleate boiling that dominates or the convective boiling. Nucleate boiling is independent of the quality of the vapor and flow rate of the liquid but those are the determining parameters for convective boiling. Experiments reveal that dominance of these mechanisms depends on the dimensions or scale of the system; i.e., in macroscale systems, it is the nucleate boiling that dominates and in microscale systems *thin liquid film* around the vapor bubble (see Fig. 1) plays the major role in the heat transfer. Therefore, for better understanding of heat transfer mechanism in microchannels, studying the formation and structure of thin film is necessary.

Additionally, incorporation of the microchannel brings flexibility to spread out the cooling network that can provide better temperature uniformity. Owing to its wide and obvious necessity, thin-film evaporation, particularly formation, and structure of thin film has attracted many researchers' attention from last few decades. There are numerous theories proposed, experiments conducted, and numerical models presented with the intention of capturing the liquid film in a much better manner. Present study aims at summarizing the works that have been carried out till date. Further, an attempt has been made to demonstrate image processing as a

Table 1 Range of heat transfer coefficients for different heat transfer mechanisms [1]

Heat transfer mechanism	Heat transfer coefficient ($\text{W}/\text{m}^2 \text{K}$)
Natural convection	$5-10^3$
Forced convection	$20-10^4$
Pool boiling	$10^3-5 \times 10^4$
Flow boiling	10^3-10^6

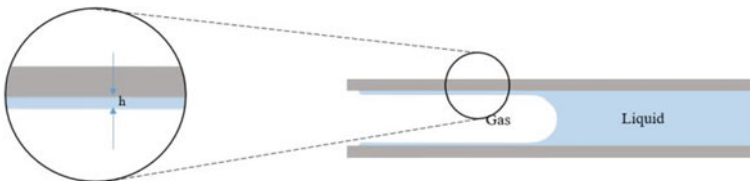


Fig. 1 Liquid film surrounding the gaseous phase

promising tool for film thickness measurements. Height of the liquid phase in a two-phase flow through a macro-channel (25 mm diameter) is measured for demonstration purpose which can be extended for micro- and mini-channels.

2 Experimental Work on Liquid Film Thickness Measurement

Tibirica et al. [2] reviewed research on experimental techniques for the liquid film thickness till 2008. For the sake of brevity, those techniques are not repeated. Film thickness measurement techniques can be classified in many ways, such as the type of fluid used, flow characteristics or physical principle behind the method. Figure 2 shows the detailed classifications of experiments based on the underlying principle [2].

Henkel et al. [3] applied novel optical technique to film thickness measurement on the liner of the gasoline direct engines. This technique is able to measure two-dimensional distribution of film thickness with respect to time.

Alekseenko et al. [4] studied the film thickness (range from 0.05 to 0.15 mm) of wavy flow in the channel using high-speed laser-induced fluorescence (LDF). Further, they investigated the influence of gas velocity, liquid velocity, and viscosity of liquid and diameter of test section on the wave frequency.

Seshadri et al. [5] characterized and measured the liquid film thickness for the various two-phase flow regimes in mini and conventional channels having diameters 0.6, 1.5, 2.6, and 3.4 mm using a non-intrusive technique. The liquid and gas superficial velocities are in the range between 10^{-2} –3 and 10^{-2} –50 m/s, respectively. They proposed correlation between the measured liquid film thicknesses and capillary number based on the analysis.

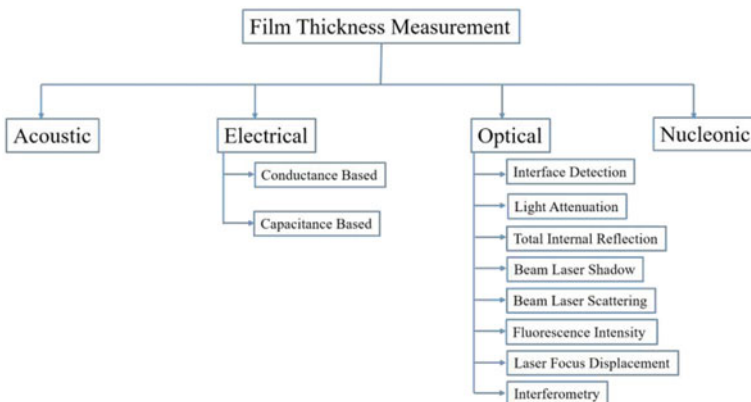


Fig. 2 Classification of film thickness measurement techniques. Adapted from [2]

$$\frac{h}{d} = 2.03Ca^{0.13}We^{0.52} \quad \text{for } Bo > 1$$

$$\frac{h}{d} = 1.08Ca^{0.40}We^{0.35} \quad \text{for } Bo < 1$$

Han et al. [6] measured the variation of film thickness of annular flow with respect to time using laser confocal displacement meter (LCDM). The liquid–gas interface profile was visualized by the high-speed camera in acrylic tubes with different diameters of $D = 1.0, 0.5,$ and 0.3 mm.

Okawa et al. [7] measured liquid film thickness in steam water two-phase flow in SUS tube of 12 mm ID. Laser confocal microscopy was used for the measurement. For the flow oscillation, heat flux and mass flux were varied. They noticed an increase in the film thickness with the decrease in oscillation period.

Kanno et al. [6] investigated behavior of variation of film thickness of FC40 fluids for different mass flow rate varied from $G = 100\text{--}500$ kg/m²s. Average film thickness plotted versus the tube diameters and different flow rates. Liquid film thickness was estimated by laser confocal displacement meter (LCDM). Liquid–gas interface was captured using high-speed camera.

Mac Giolla Eain et al. [8] developed of small-scale medical diagnostic equipment. A non-intrusive optical technique was introduced to determined magnitude of the film. The effects of slug length and primary fluid properties on the magnitude of the liquid film were examined over different capillary numbers.

Wang et al. [9] proposed a new method named by ultrasonic echo resonance main frequency (UERMF) method to measure liquid film thickness to overcome the issues related the measurement of thin thickness and noise. The experiment was carried out in a horizontal 50 mm diameter tube, and the range of superficial velocities was 0.006–0.1 m/s for water and 10–30 m/s for air, and pressure is 0.1–0.5 MPa.

Yu et al. [10] designed new capacitive sensor with a dielectric film coating to measure the liquid film thickness on a flat surface.

3 Analytical Models on Liquid Film Thickness

Wilhem Nusselt in 1910 gave an expression for the film thickness of the vapor condensing on a vertical flat plate as a function of thermal conductivity, viscosity, density, and latent heat of the liquid, the density of the vapor and length of the plate. This model under predicts the film thickness due to its assumptions [11].

Bretherton [12] derived an expression for the liquid film thickness theoretically as a function of capillary number for the long bubble moving in a tube filled with a fluid with considerably large viscosity compared to that in the bubble at low Reynolds number. This theory used the approximation of lubrication theory that film thickness is very small compared to channel radius. Bretherton's correlation predicted film thickness quite accurately for $10^{-4} < Ca < 10^{-2}$ but deviated from experimental results beyond this range.

Stephan and Busse [13] presented a model for the radial heat transfer from a grooved heat pipe evaporator. Through the model, it was proved that assuming interface temperature to be equal to the saturation temperature of the vapor leads to the over prediction of the heat transfer coefficient. They also emphasized on the importance of interface temperature variation on the thin-film evaporation.

Schonberg and Wayner [14] studied the thin-film evaporation theoretically and presented expressions for film slope, curvature, and flow in terms of film thickness. Also, an expression for film thickness as a function of the position is presented.

Hanlon and Ma [15] theoretically calculated the maximum superheat allowable for thin-film evaporation, in their model for predicting heat transfer capability of porous media. It was proposed that by decreasing the particle size of the porous media, the heat transfer coefficient can be increased.

Shkariah et al. [16] proposed physical and mathematical models for the prediction of evaporative heat transfer in microchannels. Analytical solutions for the heat flux distribution, total heat transfer, and liquid film thickness were presented neglecting capillary pressure. The proposed model for film thickness and heat flux shows considerable agreement with numerical solutions at high superheat but is deviating for low superheat.

4 Numerical Techniques for Liquid Film Thickness Estimation

Mukherjee and Kandlikar [17] numerically studied the growth of the vapor bubble in the microchannel of 200 μm square cross section. They observed a constant growth rate of the bubble until it fills the cross section after which there was rapid growth. Also, it was found that bubble growth is proportional to the superheat of the incoming liquid and inversely proportional to Reynolds's number. Level-set algorithm was used to capture the interface and SIMPLER algorithm for solving Navier–Stokes equations.

Okajima and Stephan [18] studied the expansion process of a single vapor bubble through evaporative heat transfer in a microchannel of diameter 200 μm . It was found that when the superheat was low most of the heat transfer was through liquid film, whereas when superheat was high no evaporative heat transfer took place through the vapor bubble due to the rapid expansion of the vapor bubble.

Magnini et al. [19] opined that “*multiple bubble simulations are necessary to capture the essential features of the heat transfer process of slug flow.*” In their work, thermal and hydrodynamic interactions of leading and sequential bubbles were shown. Finally, multiple bubble heat transfer coefficient was proposed for the heat transfer coefficient prediction. VOF for capturing the interface, HF for surface tension, and evaporation model for computing phase change were used. Magnini and Thome [20] also emphasized the importance of modeling multiple bubbles while studying the dynamics and heat transfer in slug flow for flow boiling in microchannels.

Pattamatta et al. [12] investigated the phase change characteristics of Taylor-Bubble during flow boiling numerically. Nucleation, growth, and coalescence of multiple Taylor-Bubbles were modeled along with respective heat transfer mechanisms.

Ling et al. [21] modeled flow boiling in rectangular channels in three dimensions. A CLSVOF algorithm was used to track the interface. The results of the work are showed temporal growth in heat flux when bubbles merge with each other.

Liu et al. [22] studied slug to the annular transition of convective boiling under high heat flux conditions in a channel of 0.4 mm diameter. A novel method for initialization is proposed in order to reduce computational time. Li et al. [11] studied the effects of thermo-capillarity for flow boiling in microchannels and showed that for high Marangoni numbers, change in surface tension effects bubble shape. Ferrari et al. [23] studied the slug flow boiling in the square microchannel to evaluate the effect of liquid film on heat transfer under constant heat flux condition.

5 Image Processing as a Promising Tool

In a two-phase system, there exists an intensity gradient between two phases because light reflected by solids, liquids, and gases possess intensity that is unique to that phase. Each intensity gradient signifies the completion of one phase and the starting of another. This idea can be used to measure the thickness of the liquid film. Further, colored liquids and fluorescent dyes can be used to ease the process of interface detection. For the present study, an image processing algorithm written on MATLAB is used for capturing the intensity variations and thereby measuring liquid film thickness.

An image is nothing but a matrix of color functions or light intensities. Each pixel of the image is an element of the matrix. The magnitude of the color function that a pixel possesses is called as pixel value. Pixel values vary from 0 to 255 on an RGB color range, with 0 and 255 representing white and black colors, respectively. An RGB image or colored image is a three-dimensional matrix with three planes (red, green, and blue) in the z -direction. The pixel value at a particular pixel on each plane signifies the contribution of that plane (R, G, or B) in the final color at that point. A grayscale image is a two-dimensional matrix with a single plane in the third dimension.

MATLAB reads the image as a matrix of pixel values. Figure 3 shows the flowchart of instructions and operations done during the image processing using MATLAB. Idea is to detect the intensity gradients (that signify interfaces between two phases) and count the number of pixels between two such gradients. Then by knowing the size of each pixel, the distance between the two gradients can be calculated which gives the film thickness.

During the image processing, unwanted areas of the images are eliminated in order to avoid the ambiguity. This can be done either by cropping the image or by assigning some constant value to the pixels present in those regions. Edge detection

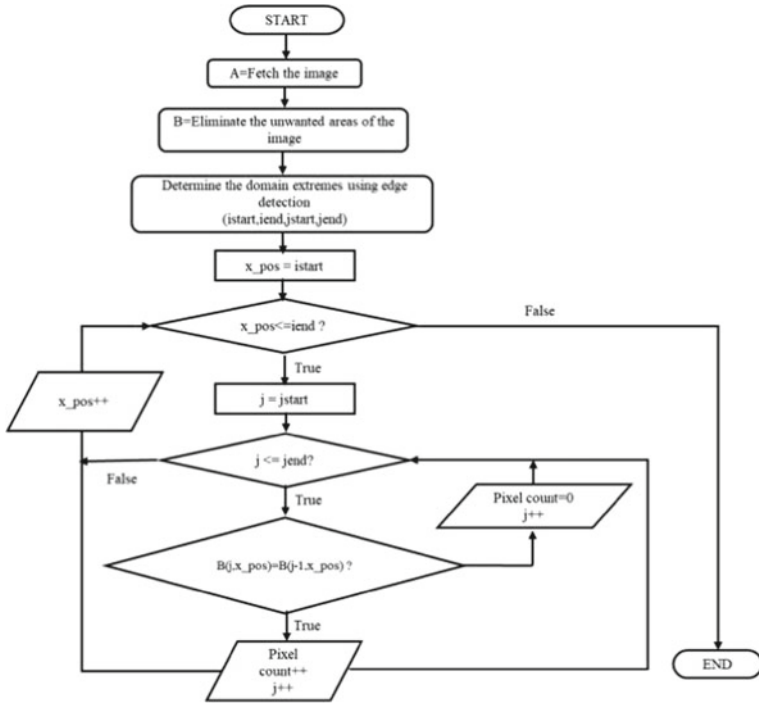


Fig. 3 Algorithm of image processing code

is an optional step that is used to detect the boundaries of the domain so as to restrict the calculations within the domain. In the present study, Robert’s algorithm is used for edge detection. Now, at any point along the length of the pipe pixel values is plotted against the number of pixels in the radial direction. From the plot, the number of pixels that lie between two intensity gradients can be counted.

Figure 4 shows photograph of slug flow captured using high-speed camera (Photron fastcam). Figure 5 shows a plot of pixel count versus intensity at a certain point along the length of the pipe shown in Fig. 4. Going from top to bottom, the first intensity gradient corresponds to the interface between the pipe wall and air, the constant intensity part that succeeds corresponds to pure air, then follows intensity gradient due to air–water interface, constant intensity due to the pure water phase and lastly gradient due to water–pipe wall interphase. It is clear from the figure that the liquid height in the pipe is “the number of pixels between second and third gradient multiplied by the size of each pixel.” The size of each pixel is simply the ratio of the pipe diameter to the total number of pixels in the radial direction. In the present study, there were 148 pixels on the diameter of 25 mm leading to a pixel size of 0.1689 mm.

Figure 6 shows result of spatial measurement of film thickness. The above-mentioned procedure for film thickness calculation is repeated for every

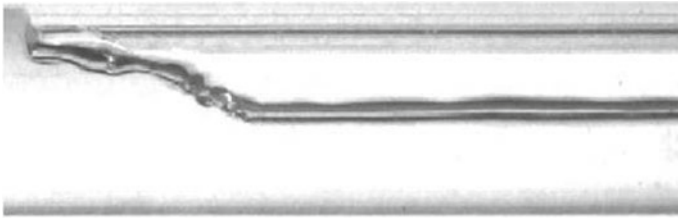


Fig. 4 Photograph of air–water two-phase slug flow captured using high-speed camera [24]

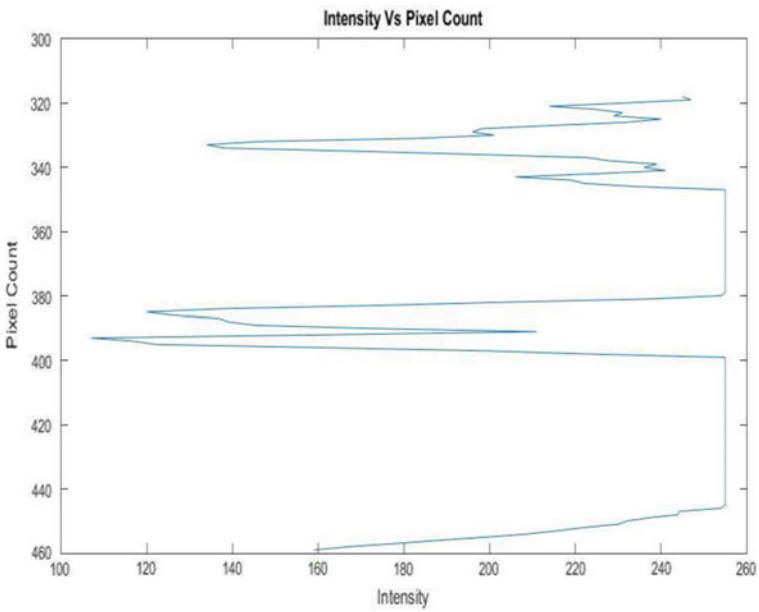


Fig. 5 Plot of pixel count versus x intensity

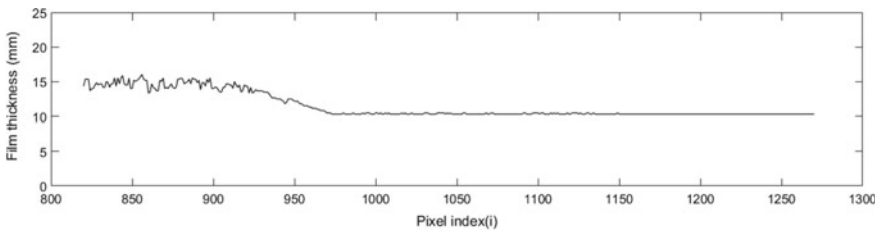


Fig. 6 Plot of film thickness versus pixel index

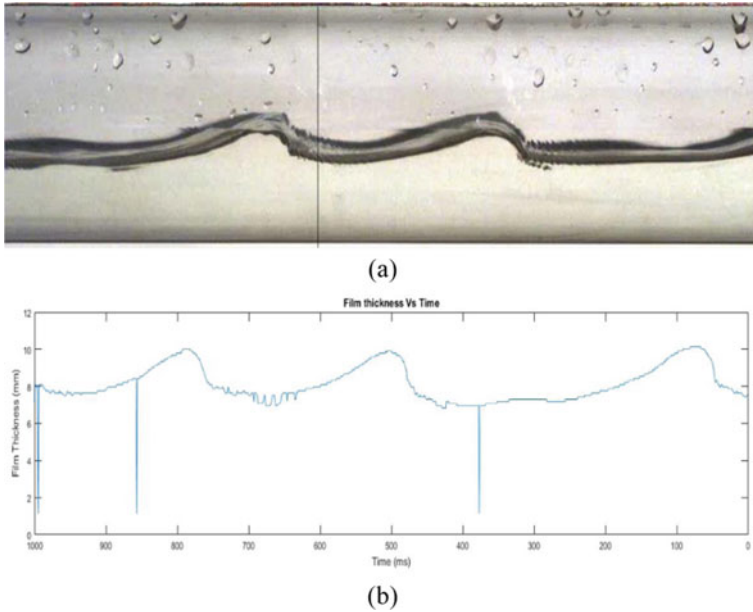


Fig. 7 Dynamic measurement of liquid film thickness: **a** one of the frames of two-phase flow video captured using high-speed camera [24], **b** variation of film thickness with respect to time

point along the longitudinal direction and film thickness are plotted against the length of the pipe or pixel index (i). The resulting plot must resemble the air–water interface throughout the pipe (Fig. 4).

In many of the practical applications, film thickness at a point varies with respect to time. In such cases, there is a need for the dynamic measurement. In such scenario, above-mentioned procedure is repeated at a certain point but on different photographs captured at different time intervals. A video of the two-phase flow is captured using the high-speed camera. Figure 7a shows one of the frames of the video at some instant of time. The black-colored line shows the position at which film thickness is measured at different time intervals. Figure 7b shows plot of film thickness variation with respect to time. Fluctuations in the film thickness are due to external intensity variation.

Along with the non-intrusive nature of the technique, measurement through image processing shows no dependency on the size of the system, i.e., micro-, mini, and macroscale systems can be handled with the equal ease. Additionally, this technique can be easily automated.

6 Summary and Conclusion

A brief review of experimental, numerical and analytical works that have been carried out in the area of liquid film thickness measurement are presented. Image processing is demonstrated as a potential tool for the measurement of film thickness. Further, procedure for the spatial and temporal measurements is briefly explained.

Acknowledgements The authors gratefully thank Mr. Sunny Saini of Advanced Fluid Dynamics Laboratory, National Institute of Technology, Surat, for his technical support and for providing the necessary photographs for image processing.

References

1. Tullius JF, Vajtai R, Bayazitoglu Y (2011) A review of cooling in microchannels. *Heat Transf Eng* 32(7–8):527–541
2. Tibiriçá CB, do Nascimento FJ, Ribatski G (2010) Film thickness measurement techniques applied to micro-scale two-phase flow systems. *Exp Therm Fluid Sci* 34(4):463–473
3. Henkel S, Beyrau F, Hardalupas Y, Taylor AMKP (2016) Novel method for the measurement of liquid film thickness during fuel spray impingement on surfaces. *Opt Express* 24(3):2542
4. Alekseenko S, Cherdantsev A, Heinz O, Kharlamov S, Markovich D (2013) Analysis of spatial and temporal spectra of liquid film surface in annular gas-liquid flow. *Exp Fluids* 54(9)
5. Seshadri A, Mahadevan S, Muniyandi V (2015) Measurement of liquid film thickness in air—water two phase flows in conventional and mini channels using image processing. *Korean J Chem Eng* 32(5):826–836
6. Han Y, Kanno H, Ahn YJ, Shikazono N (2015) Measurement of liquid film thickness in micro tube annular flow. *Int J Multiph Flow* 73:264–274
7. Okawa T, Goto T, Yamagoe Y (2010) Liquid film behavior in annular two-phase flow under flow oscillation conditions. *Int J Heat Mass Transf* 53(5–6):962–971
8. Mac Giolla Eain M, Egan V, Punch J (2013) Film thickness measurements in liquid-liquid slug flow regimes *Int Heat Fluid Flow* 44:515–523
9. Wang M, Zheng D, Xu Y, Cui Z (2019) Two phase flow using ultrasound. In: 2019 IEEE international instrumentation and measurement technology conference, pp 1–6
10. Yu Y, Ma L, Ye H, Zheng Y, Ma Y (2017) Design of instantaneous liquid film thickness measurement system for conductive or non-conductive fluid with high viscosity. *AIP Adv* 7(6)
11. Li W, Luo Y, Zhang J, Minkowycz WJ (2018) Simulation of single bubble evaporation in a microchannel in zero gravity with thermocapillary effect. *J Heat Transf* 140(11):1–9
12. Pattamatta A, Freystein M, Stephan P (2014) A parametric study on phase change heat transfer due to Taylor-Bubble coalescence in a square minichannel. *Int J Heat Mass Transf* 76:16–32
13. Stephan PC, Busse CA (1992) Analysis of the heat transfer coefficient of grooved heat pipe evaporator walls. *Int. Heat Mass Transf.* 35(2):383–391
14. Schonberg JA, Wayner PC (1990) An analytical solution for the integral contact line evaporative heat sink. *AIAA/ASME 5th Jt Thermophys Heat Transf Conf* 6(1):128–134
15. Hanlon MA, Ma HB (2003) Evaporation heat transfer in sintered porous media. *J Heat Transf* 125(4):644–652
16. Shkarah AJ, Bin Sulaiman MY, Bin Hj Ayob MR (2015) Analytical solutions of heat transfer and film thickness with slip condition effect in thin-film evaporation for two-phase flow in microchannel. *Math Probl Eng* 2015

17. Mukherjee A, Kandlikar SG (2005) Numerical simulation of growth of a vapor bubble during flow boiling of water in a microchannel. *Microfluid. Nanofluidics* 1(2):137–145
18. Okajima J, Stephan P (2019) Numerical simulation of liquid film formation and its heat transfer through vapor bubble expansion in a microchannel. *Int J Heat Mass Transf* 136:1241–1249
19. Magnini M, Pulvirenti B, Thome JR (2013) Numerical investigation of the influence of leading and sequential bubbles on slug flow boiling within a microchannel. *Int J Therm Sci* 71:36–52
20. Magnini M, Thome JR (2016) Computational study of saturated flow boiling within a microchannel in the slug flow regime. *J Heat Transf* 138(2):1–12
21. Ling K, Son G, Sun DL, Tao WQ (2015) Three dimensional numerical simulation on bubble growth and merger in microchannel boiling flow. *Int J Therm Sci* 98:135–147
22. Liu Q, Wang W, Palm B (2017) A numerical study of the transition from slug to annular flow in micro-channel convective boiling. *Appl Therm Eng* 112:73–81
23. Ferrari A, Magnini M, Thome JR (2018) Numerical analysis of slug flow boiling in square microchannels. *Int J Heat Mass Transf* 123:928–944
24. Saini S (2017) Measurement of flow characteristics of stratified flow using laser doppler velocimetry and flow visualization

Modelling and Simulation of Evaporation on Porous Surface



Jyoti Prakash, Basant Singh Sikarwar, Basant Kumar Agarwal,
and Rajesh Kumar

Abstract Moisture evaporation on porous surface has grown into a dynamic research due to the advancement in building technologies, wooden frames, water purification, baking and cooling purpose. Evaporation on a porous surface involves complex multiphysics coupling heat and moisture transport concurrently. In the present work, numerical simulation of evaporation on the porous surface is carried out on the basis of heat and moisture transport theory. Simulations are carried out using COMSOL Multiphysics software. The simulation result of this model is validated against the analytical solution ensuing good agreement. Post-validation, a parametric analysis of the evaporation on porous surface is done to compute temperature variation, relative humidity variation, mass transfer coefficient and heat transfer coefficient at various regions on the porous surface. These results are useful for sensitivity analysis of various porous materials in the mathematical modelling of evaporation on the flat surfaces.

Keywords Numerical modeling · Moisture · Heat · Porous media · Capillary pressure

J. Prakash (✉) · B. S. Sikarwar
Department of Mechanical Engineering, ASET, Amity University, Noida
Uttar Pradesh, India
e-mail: jprakash@amity.edu

B. S. Sikarwar
e-mail: bssikarwar@amity.edu

B. K. Agarwal
Amity Institute of Aerospace Engineering, Amity University, Noida, Uttar Pradesh, India
e-mail: bkagarwal@amity.edu

R. Kumar
Delhi Technological University, New Delhi, India
e-mail: rajesh.kumar@dtu.ac.in

Nomenclature

c	Concentration (mol/m^3)
t	Time (s)
T	Temperature (K)
c_p	Heat capacity ($\text{J}/(\text{kg K})$)
k	Thermal conductivity ($\text{W}/(\text{m-K})$)
Q_b	Heat of vaporisation (J/mol)
D	Diffusion coefficient (m^2/s)
M_{mass}	Molecular weight (kg/mol)
m	Evaporation rate (kg/s)
H_{vap}	Latent heat of vaporisation (J/kg)
H	Relative humidity (%)
ρ	Density (kg/m^3)

Subscripts

sat	Saturated condition
a	Air domain
l	Liquid phase

1 Introduction

Application of two-phase flow with phase change in porous medium is evidenced in many daily life appliances like building material, water purification, baking and cooling of electronic devices. Although numerous research articles are available in the literature investigating liquid transport through porous media, still control and prediction of liquid dynamic within these complex media is still need to be improved [1]. The proposed mathematical model is simulated to explain the process of evaporation on porous surface. Woloszyn and Rode [2] carried out various simulations for heat and mass transfers in porous material. Le Tran et al. [3] revealed the impact of temperature-dependent sorption curve on the hygrothermal behaviour of a hemp concrete envelop. Steeman et al. [4] developed a mathematical model to study heat and moisture transport through porous materials using commercial CFD package. General analytical solution for the liquid dynamic of evaporation in porous medium is controlled by the combined effect of capillary imbibition, gravity and evaporation. Hence, liquid dynamic in porous medium can be calculated by two dimensionless numbers: a gravity–capillary number and an evaporation–capillary number [5]. Liu et al. [6] calculated the temperature of inner wall surface of different materials to introduce the cooling effect on the flowing air. Van Belleghem et al. [7] presented a coupled heat and moisture model to study capillary moisture transport and the vapour diffusion through porous material.

Litavcova et al. [8] derived a numerical model to explain liquid and moisture diffusion in a porous material as two separate processes. Many other mathematical models are also developed to define the coupled model on liquid and gas phase transport in wood [9–11]. There are many variables that control the rate of evaporation like temperature [10], humidity of environment [13], velocity of air [12, 14], relative humidity in the porous medium [15] and porosity [16].

It is very difficult to perform each and every research problem of evaporation on porous surface as it consumes plenty of resources. Moreover, experimental parametric study is a complex process for the optimisation of the system. Mathematical modelling of evaporation on porous surface is recommended for cost and time saving, and to figure temperature, concentration, cooling effect on the evaporating surface and evaporation rate with time. In the present study, a mathematical model is proposed that explains the physics governing the evaporation on a porous substrate. For the mathematical model, an exhaustive literature survey is mandatory to figure out the discrepancies and to enhance precision and accuracy of the numerical code. Numerical model is successfully validated with the analytical solution of boundary layer theorem. Post-validation, parametric study is performed to calculate the variation of temperature, evaporation rate, mass transfer coefficient, heat transfer coefficient and relative humidity.

2 Mathematical Modelling and Simulation

Figure 1 represents the schematic diagram of evaporation on porous surface. Mathematical modelling of the evaporation on porous surface involves several steps. In the proposed mathematical model, a porous domain containing water is exposed to free airflow to study the multiphase flow in evaporation process.

Evaporation in a porous material is a complex phenomenon as it involves heat and mass transfer concurrently. In this process, the moisture transport in porous domain comprise liquid and vapour phase. Motion of vapour phase in porous domain is driven by diffusion and convection. Diffusion in vapour is due to vapour

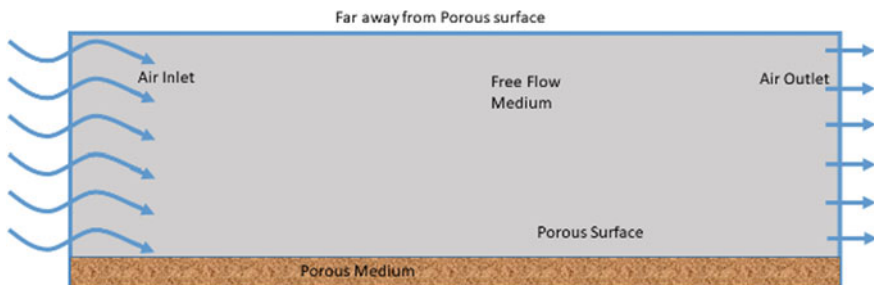


Fig. 1 Schematic diagram of porous surface in the free flow medium

pressure gradient, whereas convection in vapour flow is due to moving air. For the motion of liquid in porous medium, capillary effect and the concentration gradient is the governing medium.

In the mathematical model for evaporation in a porous medium, transport equations and appropriate boundary conditions are required to solve the coupled equations. Motion of vapours in the porous domain is represented by Brinkman equation, whereas liquid flow in porous domain is governed by Darcy's law to compute flow field and pressure distribution.

The continuity equation to govern liquid phase in porous media,

$$\frac{\partial c}{\partial t} + (u \cdot \nabla)c = \nabla \cdot (D \nabla c) \quad (1)$$

To calculate the flow field in the porous and free flow domains, incompressible Navier–Stokes equation is coupled with transports equations.

$$\rho \left(\frac{\partial u}{\partial t} + (u \cdot \nabla)u \right) = \nabla \cdot [-p \cdot I + \mu(\nabla u + \nabla u^T)] + F \quad (2)$$

$$\nabla \cdot (\rho u) = 0 \quad (3)$$

The solution of Navier–Stokes equation and the continuity equation will yield velocity and pressure field inside the porous domain. Energy equation is used to calculate temperature distribution in the porous and free flow domain.

$$\rho c_p \left(\frac{\partial T}{\partial t} + (u \cdot \nabla)T \right) = \nabla \cdot (k \nabla T) \quad (4)$$

2.1 Two-Phase Flow in Porous Media

The fundamental physics governing the multiphase flow in porous domain is identical for most of the applications. Two-phase flow in porous domain comprise of vapour and liquid phase.

$$\alpha_g + \alpha_l = 1 \quad (5)$$

Vapour flow in porous domain is governed by diffusion and convection

$$S_g = -\delta_p \nabla P_v + \rho_v v \quad (6)$$

Liquid flow in porous domain is governed by Darcy's law

$$S_l = -K_l \nabla P_c \quad (7)$$

Evaporation of liquid through porous domain is governed by various transport mechanisms like pressure gradient, capillary effect and vapour diffusion. Motion of vapours in the porous domain is driven by Brinkman equation, whereas liquid flow in porous domain is governed by capillary effect ($P_c = P_g - P_l$) and pressure gradient. Brinkman equation contributes to compute flow field and pressure distribution of the humid air in porous domain, whereas water velocity is computed with the help of Darcy's law. Velocity of liquid is very small as compared to the high wet air velocity. So, Darcy's law is characterised to compute liquid velocity,

$$u_l = -\frac{\kappa_l}{\mu_l} \nabla P_g \quad (8)$$

In the porous domain, the interface will dissipate the latent heat of vaporisation in the environment. This phenomenon is responsible for the cooling of the interface in the evaporation process.

2.2 *Liquid Phase in Porous Domain*

Saturation of the liquid phase is the portion of pore volume filled with the liquid phase.

$$\alpha_l = \frac{c_w M_w}{\rho_w \varepsilon} \quad (9)$$

But, the pores of the porous medium are not completely filled with liquid. Thus,

$$u_l = \frac{\kappa \kappa_{rl}}{\alpha_l \varepsilon \mu_w} \nabla P_g \quad (10)$$

The capillary effect is introduced as the diffusion coefficient D_{cap} which depends on the moisture content

2.3 Vapour Phase in Porous Domain

The transport of vapour phase is due to diffusion of vapour and air in the gaseous phase. Effective diffusivity D_{eff} for both the phases is given by Millington and Quirk equation

$$D_{\text{eff}} = D_{\text{va}} \varepsilon^{4/3} \alpha_g^{10/3} \quad (11)$$

Velocity field due to diffusion of vapour and air in the gaseous phase,

$$u = \frac{u_g}{\alpha_g \varepsilon} - \frac{M_a D_{\text{eff}}}{M_{\text{ma}} \rho_{\text{ma}}} \nabla \rho_{\text{ma}} \quad (12)$$

2.4 Evaporation

m_{evap} is the mass of amount of water evaporates into air. m_{evap} helps to calculate the reduction in the amount of liquid via evaporation and growing moist air proportion in the air,

$$m_{\text{evap}} = K(a_w c_{\text{sat}} - c) \quad (13)$$

Porous domain contains both the liquid and gaseous phase to contribute in the overall velocity and pressure field.

$$\rho_{\text{tot}} = \alpha_g \rho_{\text{ma}} + \alpha_l \rho_w \quad (14)$$

$$C_{p,\text{tot}} = \frac{\alpha_g \rho_{\text{ma}} C_{p,\text{ma}} + \alpha_l \rho_w C_{p,w}}{\rho_{\text{tot}}} \quad (15)$$

$$k_{\text{tot}} = \alpha_g k_{\text{ma}} + \alpha_l k_w \quad (16)$$

Then the overall velocity can be expressed as the average of dry air, water vapour and liquid water velocity, which is:

$$u_{\text{mean}} = \frac{n_a C_{p,a} + n_v C_{p,v} + n_w C_{p,w}}{\rho_{\text{tot}} C_{p,\text{tot}}} \quad (17)$$

Table 1 Thermophysical properties of water

Thermophysical properties	Water
Density	997 kg/m ³
Molecular weight	18 kg/kmol
Thermal conductivity	0.6 W/m-K
Specific heat capacity	4178 J/kg-K
Latent heat of vaporisation	2442 kJ/kg
Surface tension	0.07 N/m
Vapour diffusion coefficient	2.4×10^5 m ² /s
Saturation pressure at 25 °C	3178 Pa

The heat of evaporation is inserted as a source term in the heat transfer equation according to:

$$Q = -H_{\text{vap}} \cdot m_{\text{vap}} \quad (18)$$

Thermophysical properties of water used for calculation in this paper are listed in Table 1.

2.5 Numerical Procedure

Primarily, the geometry of porous domain is constructed to relate the real boundary conditions on the geometry model in COMSOL Multiphysics. Appropriate physics is prudently selected and coupled concerning to the real condition encompassing aforementioned Eqs. (1–18).

In the present work, laminar flow is considered in the free flow medium. Heat transfer in fluid and transport of dilute species physics is used for the evaporation of fluid on the porous surface. The geometric model is discretised into numerous small elements and the suitable PDE's are solved on each discretised element. Figure 2

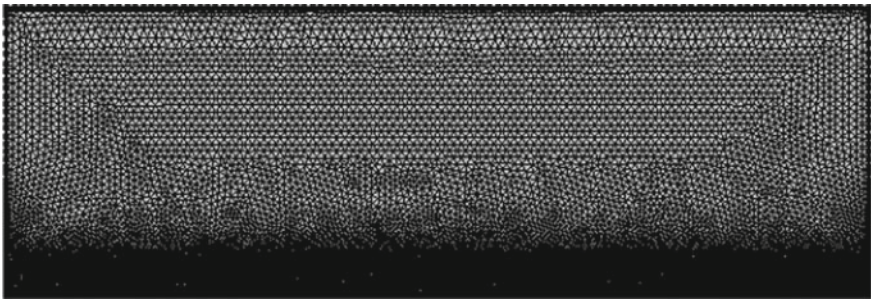


Fig. 2 Meshing of the porous surface placed in free flow domain **a** fine mesh in porous domain, **b** transitional mesh near to the porous surface, **c** coarse mesh in the air domain

shows the triangular meshing of the porous domain placed in dry air. The 8 lakh elements size of grid is chosen in the present study. Meshing inside the porous domain is taken as extremely fine to avoid the singularity error. Meshing adjacent to the porous surface active in evaporation process is taken as 50 times finer to evaluate heat and mass transfer more precisely. The proposed mathematical model is explained by the finite element approach using COMSOL Multiphysics software. The governing equations, the associated initial conditions and the boundary constraints are solved by adding diffusion term to the transport equation. Tolerance of 0.001 is considered to converge the dependent variables in the time-dependent solver.

To develop the moisture flow inside the porous domain towards the evaporating surface involves high computational efforts as it comprises very fine meshing and long simulation time. During the evaporation in porous domain, cooling effect due to evaporation controls the temperature distribution in porous domain, and therefore, this coupled structure is resolved by nonlinear solver in COMSOL Multiphysics. Evaporation of water from porous domain involves continuous mass loss across the porous interface from the porous domain to the dry air.

The proposed mathematical model is used to compute temperature, evaporation rate, heat and mass transfer coefficient during the course of the evaporating water from porous domain. To verify the mathematical model, the simulation results are validated with the analytical solution in the same controlled environment in Figs. 3 and 4.

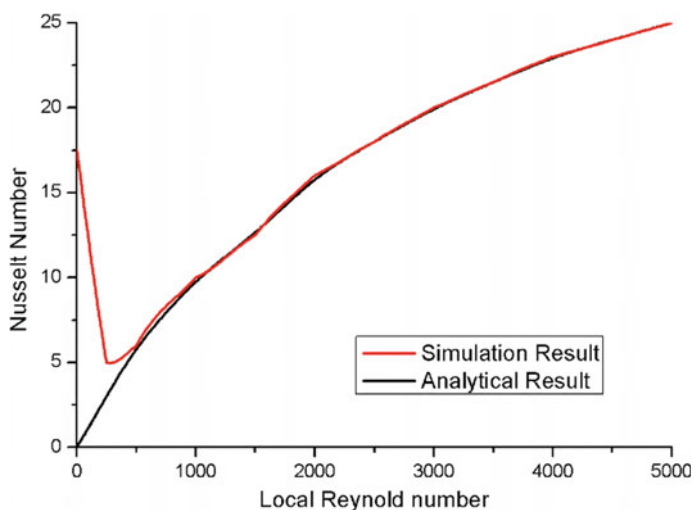


Fig. 3 Comparison of local Nusselt number versus local Reynold number from present mathematical model with the analytical solution

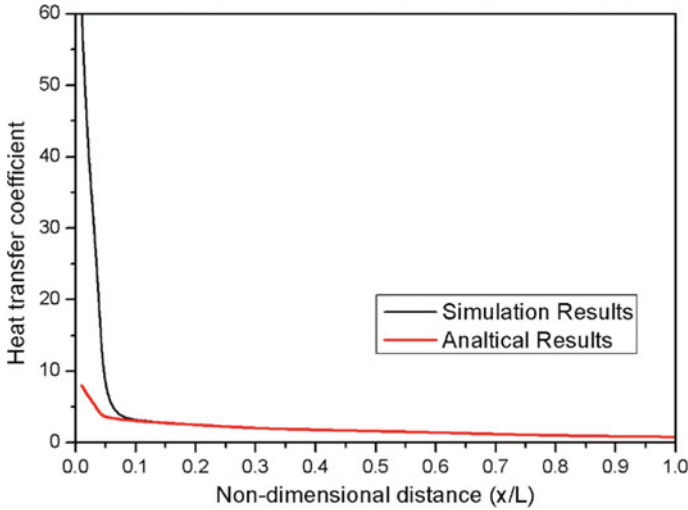


Fig. 4 Comparison of heat transfer coefficient versus dimensionless distance from present mathematical model with the analytical solution

3 Result and Discussion

Parametric study is performed to predict the evaporation behaviour of liquid on a porous surface. Air flowing over the porous medium containing moisture constitutes boundary layer problem. A porous material of porosity 0.9 is placed horizontally under the exposure of laminar dry air, i.e. 0% humid air at 293.15 K at a velocity of $0.18 \times 10^{-3} \text{ms}^{-1}$ as shown in schematic diagram Fig. 1. Porous material contains the water vapour and water liquid. Simulation results obtained are compared with the analytical solutions for the validation of the mathematical model. Post-validation, parametric study is discussed to read temperature profile, mass transfer coefficient, heat transfer coefficient and evaporation rate with respect to the free flow of dry air.

The present work involves the boundary layer flow over the flat porous surface. The analytic value of local Nusselt number for laminar flow over a flat plate at a distance x from the edge of the plate is given in Eq. 19,

$$\text{Nu}_x = 0.332 \text{Re}_x^{\frac{1}{2}} \text{Pr}^{\frac{1}{3}}, \quad (\text{Pr} > 0.6) \tag{19}$$

Free flow over a porous surface with similar geometry, governing equations and initial and boundary conditions for the air domain is simulated and compared against available analytical solution for a boundary layer theorem. Schematic of the proposed work is shown in Fig. 1, with $u = 0$ at $x = 0$. Figure 3 validates the mathematical model of the composed problem with the analytical solution from

boundary layer theory by comparing local Reynold number versus local Nusselt number. Analytical solution and the simulation results evidenced a good agreement except for low Reynold number showing the accuracy of the mathematical model [17]. Figure 4 validates the trend of heat transfer coefficient along the porous surface. The analytical solution and the numerical simulation results obtained in this study show very good agreement except adjacent to the foremost edge of porous surface [17].

Figure 5 shows the temperature profiles at various times during evaporation on the porous surface. Temperature on the porous surface starts decreasing as the evaporation process initiates. This phenomenon of dropping down of temperature is explained in detail later in the figure. Temperature of porous surface is slightly lower than the environmental temperature of the flowing air and thereby cools the porous surface active in evaporation process. Figure 6 shows the variation of relative humidity due to evaporation at various times. Initially dry air is streamed over the porous domain which is filled with liquid as shown in Fig. 6. As the evaporation takes place, water evaporates from the porous domain into the dry air, causing increase in pressure in free flow domain that causes moisture inside the porous domain to move towards the evaporating surface. This is the unceasing evaporation process from porous domain to the dry air over the surface.

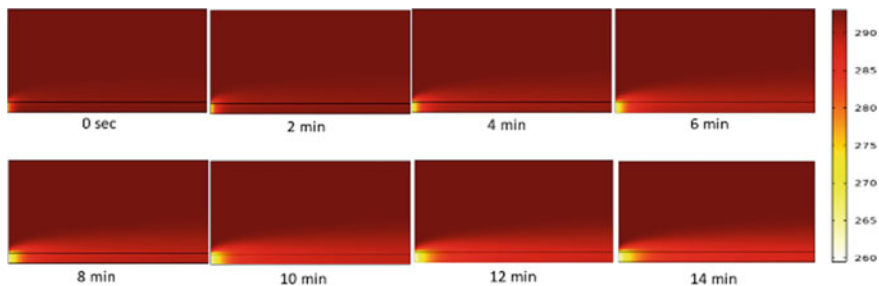


Fig. 5 Temperature profile on porous domain at various time

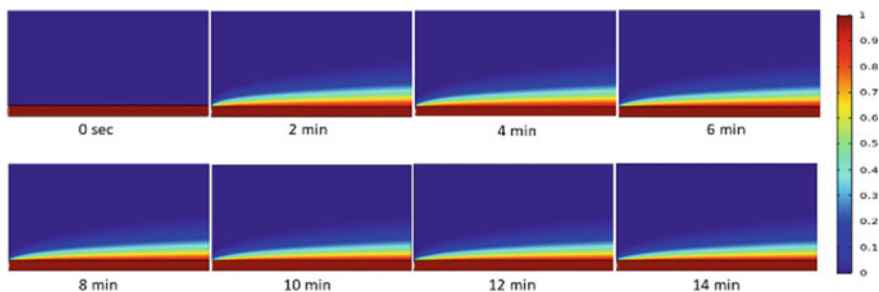


Fig. 6 Relative humidity profile on porous domain at various time

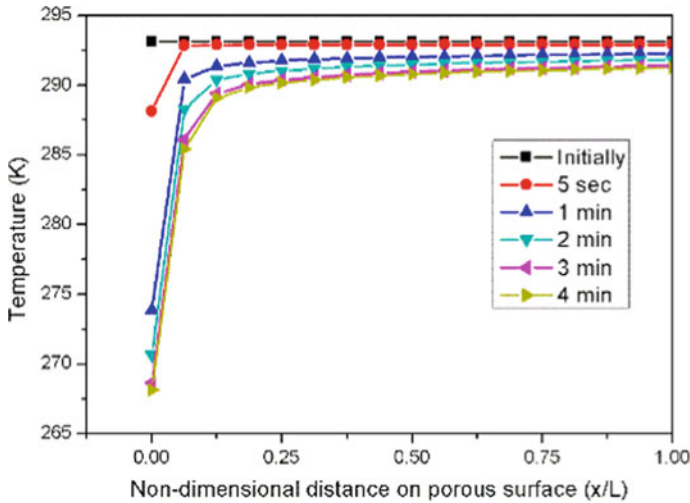


Fig. 7 Local temperature versus dimensionless distance on porous surface

Figure 7 shows the temperature variation with time when the moisture in porous media is exposed to dry air. Initially temperature at the porous surface is taken same as that of the environment. After 5 s, the evaporation phenomena will drag down the surface temperature from 293.15 to 288.15 K. This decrease in temperature with time brings forth the interesting fact that evaporation causes cooling at the surface of concentration gradient. This cooling effect will sustain till the evaporation phenomena will take place. After 1 min, temperature at the surface of porous media is decreased to 273.85 K at the initial point ($x/L = 0$) of porous surface. Temperature at the $x/L = 0$ position is decreased from 293 K to 270.64 K, 268.67 K and 268.17 K after 2 min, 3 min and 4 min, respectively. At $x/L = 0.25$, temperature is decreased from 293.15 K to 291.77 K, 291.06 K, 290.4 K, 290.18 K after 1 min, 2 min, 3 min and 4 min, respectively. At all the position ($x/L = 0.25, 0.5, 0.5$ and 1) on porous surface similar cooling effect is observed, and the temperature gradient is decreased with time at every particular position on porous surface. After 4 min temperature gradient will be very small that it can be considered that quasi steady state is achieved.

Rate of change of temperature at the porous surface is highest in the beginning stage of evaporation. At a particular moment x/L is inversely proportional to change in temperature. After 1 min of evaporation process, temperature varies from 273.85 to 291.77 K on moving from $x/L = 0$ to 0.25 , i.e. 17.92 K temperature difference is observed. Similarly, 0.28 K temperature difference is observed between $x/L = 0.25$ and 0.5 ; 0.14 K temperature difference is witnessed between $x/L = 0.5$ and 0.75 ; 0.07 K temperature difference is detected between $x/L = 0.75$ and 1 . Hence, temperature difference is inversely proportional to dimensionless distance on porous surface (x/L).

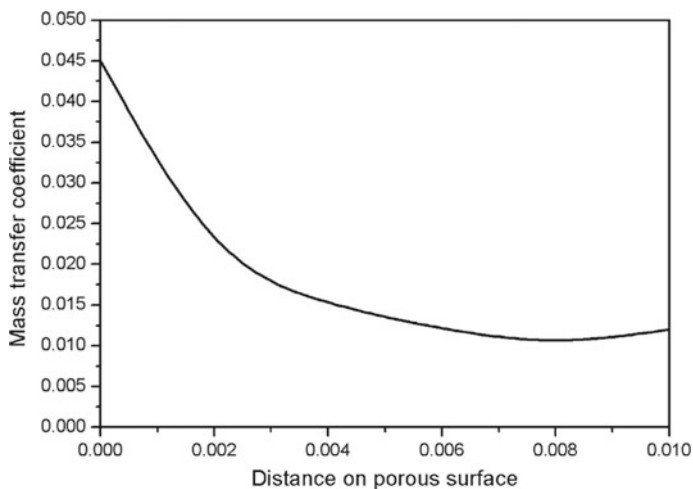


Fig. 8 Mass transfer coefficient versus distance on porous surface from leading edge

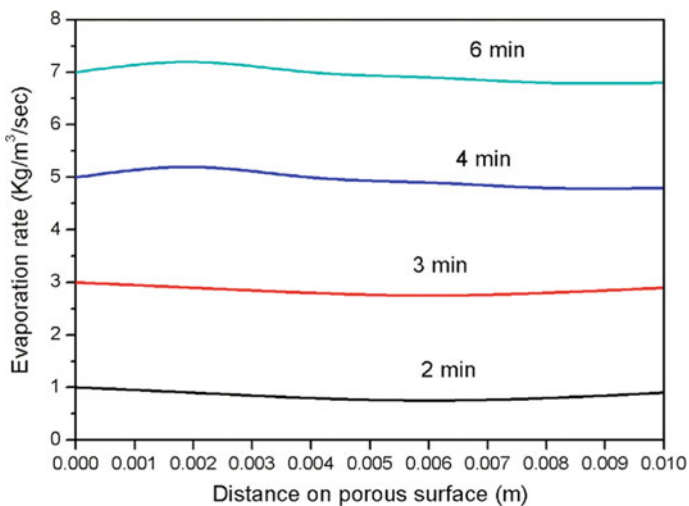


Fig. 9 Evaporation rate versus distance on porous surface from leading edge

Figure 8 shows the mass transfer coefficient on the porous surface due to evaporation. At the leading edge, high mass transfer coefficient is observed, and it decreases along the length of the porous surface. This is because of high evaporation rate near the leading edge and the evaporation rate constantly decreases as we move away from the leading edge on porous surface which is shown in Fig. 9. As the air velocity is increased from 0 to 0.0018 m/sec, evaporation rate also increases significantly as shown in Fig. 9.

4 Conclusion

The proposed mathematical model of evaporation on porous surface is simulated in COMSOL Multiphysics software. In this study, the coupled Navier–Stokes equation and the energy equations were solved for two domains simultaneously. This numerical code is very helpful for the parametric study and sensitivity analysis of evaporation on the porous surface for the thorough study of the system. Also, temperature variation, heat transfer coefficient, mass transfer coefficient and variation in relative humidity are analysed during the evaporation phenomena on porous surface.

Following conclusions have been drawn from the study.

1. The temperature profiles during evaporation on the porous surface are revealed at various time steps. Temperature on the porous surface decreases as the evaporation process continues. Hence, cooling effect in the whole domain is observed.
2. The variation of relative humidity due to evaporation is revealed at various time steps.
3. The temperature gradient decreases with time at every particular position while evaporation of water on porous surface.
4. At the leading edge, high mass transfer coefficient is observed, and it decreases along the length of the porous surface.
5. Evaporation rate constantly decreases as we move away from the leading edge on porous surface.

References

1. Singh K, Jung M, Brinkmann M, Seemann R (2019) Capillary-dominated fluid displacement in porous media. *Annu Rev Fluid Mech* 51(1):429–449
2. Woloszyn M, Rode C (2008) Tools for performance simulation of heat, air and moisture conditions of whole buildings. *Build Simul* 1:5–24
3. Le Tran AD, Samri D, Rahim M, Douzane O, Promis G, Maalouf C, Lachi M, Langlet T (2016) Effect of temperature-dependent sorption characteristics on the hygrothermal behavior of a hemp concrete building envelope submitted to real outdoor conditions. *J Appl Fluid Mech* 9(2):245–252
4. Steeman HJ, Janssens A, Carmeliet J, De Paepe M (2009) Modelling indoor air and hygrothermal wall interaction in building simulation: comparison between CFD and a well-mixed zonal model. *Build Environ* 44(3):572–583
5. Van Engeland Charlotte, Haut Benoît, Spreutels Laurent, Sobac Benjamin (2020) Evaporation versus imbibition in a porous medium. *J Coll Interface Sci* 576:280–290
6. Liu Y, Wang Y, Wang D, Liu J (2013) Effect of moisture transfer on internal surface temperature. *Energ Build* 60:83–91
7. Van Belleghem M, Steeman M, Janssen H, Janssens A, De Paepe M (2014) Validation of a coupled heat, vapour and liquid moisture transport model for porous materials implemented in CFD. *Build Environ* 81:340–353

8. Litavcova E, Korjenic A, Korjenic S, Pavlus M, Sarhadov I, Seman J, Bednar T (2014) Diffusion of moisture into building materials: a model for moisture transport. *Energ Build* 68:558–561
9. Torres SS, Jomaa W, Puiggali JR, Avramidis S (2011) Multiphysics modeling of vacuum drying of wood. *Appl Math Model* 35(10):5006–5016
10. Torres SS, Ramirez JR, Mendez L (2011) Modeling plain vacuum drying by considering a dynamic capillary pressure. *Chem Biochem Eng Q* 25(3):327–334
11. Warning A, Datta AK, Dhall A, Mitrea D (2012) Porous media based model for deep-fat vacuum frying potato chips. *J Food Eng* 110(3):428–440
12. Davarzani H, Smits K, Tolene RM, Illangasekare T (2014) Study of the effect of wind speed on evaporation from soil through integrated modeling of the atmospheric boundary layer and shallow subsurface: effect of wind speed on evaporation from soil. *Water Resour Res* 50(1):661–680
13. Haghghi E, Shahraneeni E, Lehmann P, Or D (2013) Evaporation rates across a convective air boundary layer are dominated by diffusion: diffusion-dominant evaporation rates. *Water Resour Res* 49(3):1602–1610
14. Shahraneeni E, Lehmann P, Or D (2012) Coupling of evaporative fluxes from drying porous surfaces with air boundary layer: characteristics of evaporation from discrete pores. *Water Resour Res* 48(9):1–15
15. Griend A, Owe M (1994) Bare soil surface-resistance to evaporation by vapor diffusion under semiarid conditions. *Water Resour Res* 30:181–188
16. Mahfouf JF, Moilhan J (1991) Comparative study of various formulations of bare soil using in situ data. *J Appl Meteorol* 30(9):1354–1365
17. Halder A, Datta AK (2012) Surface heat and mass transfer coefficients for multiphase porous media transport models with rapid evaporation. *Food Bioprod Process* 90:475–490

Effect of Ageing on Emission Levels of a Gasoline Vehicle: A Case Study in Indian Context



Manu Bindra and Devendra Vashist

Abstract This paper discusses the observations of a study conducted for analysis of emission levels of vehicles manufactured over different years, to ascertain the effect of ageing of vehicle on its emission levels. For this study, Maruti Wagon R was selected as representative sample of Indian four wheeler passenger car market because of its share of approximately 12% of the total passenger vehicle sold in the year 2017. In total, 520 samples were collected during the period of study during year 2018 which included both, gasoline and CNG, driven vehicles. Out of the various regulated vehicle emission components of gasoline IC engines in BS-IV norms, carbon monoxide CO emission values of the vehicles were measured as per the standards notified by Government of India. CO emission values were recorded from vehicles manufactured between years 2004 and 2018. The data was grouped into BS-III and BS-IV vehicles, which was further segregated on the basis of their age, i.e. 0–4 years (manufacturing years 2015–18), 5–9 years (years 2010–14) and 10 years or more (year 2004–9). Within these sub-groups, the CO emission levels thus recorded in this study show a normal distribution with 88% of the samples falling between CO levels of 0.0 and 0.149, well within the maximum limit of 0.3% v/v as per BS-IV norms. Another finding of the study of collected data shows improvement in emission levels of vehicles from year 2001 model to year 2018 models. Also the measured values of CO emission of gasoline vehicle, Wagon R, showed that emissions were well within the emission norms even after vehicle being in use for 10 or more years. Findings in this study imply that due to improvement in engine technology and fuel, the emission levels of modern vehicles remain well within the stipulated emission norms, possibly during full lifecycle of the vehicle. Based on these findings in this study which were conducted with warm engine idling condition, it is recommended that more such studies be undertaken to

M. Bindra (✉) · D. Vashist
Automobile Engineering Department, Manav Rachna International Institute
of Research and Studies, Sector 43, Faridabad, India
e-mail: manubindral@gmail.com

D. Vashist
e-mail: devendra.fet@mriu.edu.in

ascertain variance in CO emission levels of vehicles during real driving conditions due to externalities such as terrain, traffic, ambient temperature, driving habits, etc.

Keywords Carbon monoxide · Vehicle emission · Wagon R · Emission norms · Gasoline vehicle

1 Introduction

Air pollution is now a major health concern in metro cities around the world. India also is equally affected because of deteriorating air quality in major cities like Delhi, Kolkata, Kanpur, Faridabad, etc. A major challenge for the developing country like India is to maintain a critical balance between rapid industrialization, economic growth and environmental preservation of which air quality being an important aspect. The deteriorating quality of air in the metro cities due to rapid urbanization and industrial development is a cause of concern and is creating a number of problems.

Growing air pollution has been mainly attributed to various sources involving hazardous emissions into the environment. Among all sources of emission, vehicular emissions from an internal combustion engine running on fossil fuels are considered a major source of harmful Green House Gases (GHG) and air quality pollutants in the form of emissions in the atmosphere [1, 2]. Direct, i.e. generated during operation of vehicles (Tail pipe emissions and evaporative losses), or as indirect, i.e. as generated during the production of fuel, manufacturing and disposal of vehicle. Various studies undertaken have shown that out of total transport life-cycle emissions, the share of tail pipe emissions is quite significant, i.e. more than 50% of total lifecycle emissions [3].

Tailpipe emissions and exhaust gas flows were measured on-board the vehicle, using a portable emissions measurement system over the European type-approval driving cycle (NEDC) by Kousoulidou et al. [4] The testing of gasoline vehicles showed that emissions are well below the emission standards and are not cause of any concern. Dabbas [5] investigated the inter-correlations between vehicle emissions within a controlled dataset to test the hypothesis of vehicle emissions inter-dependencies. His study presents the relationships between the urban transport system and vehicle emissions. Particularly, it summarizes different types of emissions and the contributory factors of the urban transport system to such emissions along with the emission responses to changes in the other factors. But his study does not account for quantum of tailpipe emission of a vehicle. Hickman [6] reviews information on emissions from road vehicles in service and how they are related to the vehicle's condition and state of maintenance. His findings are rendered irrelevant in current scenario of advancement in engine technology compared to his study of vehicles of 1980–1990 make. A comprehensive study of vehicular emission by using remote sensing technique was done in Auckland, New Zealand in the year 2015 which reported significant reduction in emission levels corresponding to improvement in vehicle engine technology. The study found that EURO IV vehicles were

consistent in their emission levels irrespective of mileage done [7]. In another study, in Beijing in the year 2013, a theoretical model was proposed based on relationship between vehicle exhaust emission and traffic flow [8]. It was found that with increase in average speed, the emission level of vehicles reduces.

2 Vehicle Emission Control and Regulations

Automobile manufacturing is one of the most important industrial activities as it offers millions of jobs and accounts for billions of investment worldwide. There is no denying that road transport has taken the position of an engine for economic growth. Its share in facilitating movement of people and goods is very significant. But, owing to the tremendous growth in vehicle population in urban areas, the vehicle emission density per unit area has reached alarming high levels such that it is now considered as a health hazard.

During the years from 2004 to 2011 in India, there has been an annual growth of about 10% in the number of new vehicles registered. The production of vehicles in India is steadily increasing over the years as shown in Fig. 1. The overall vehicles growth reflected here is at CAGR 4.4% [9], whereas passenger vehicles have grown at a whopping 25% during the same period. In India, passenger vehicles sales were 26.65 lakh in year 2012–13 and increased to 32.88 lakh in year 2017–18 [10]

Such an alarming trend in transportation growth has led to increased consumption of fossil fuel resulting in tremendous growth in harmful green house gas emission in the environment. The rate of increase in carbon dioxide emissions in India over the years as shown in Fig. 2 is of serious concern [11].

Such rapid growth in on road vehicle population in India has resulted into increased consumption of fossil fuel implying increased emission of harmful vehicular emissions. However, very little information is available on the emission

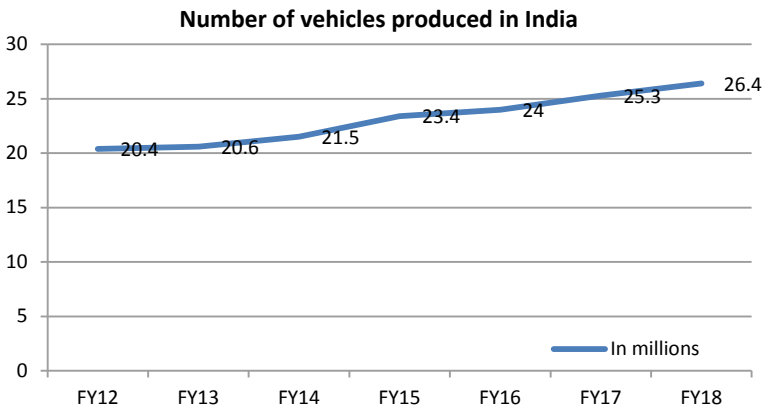


Fig. 1 Trend in automobiles production in India [9]

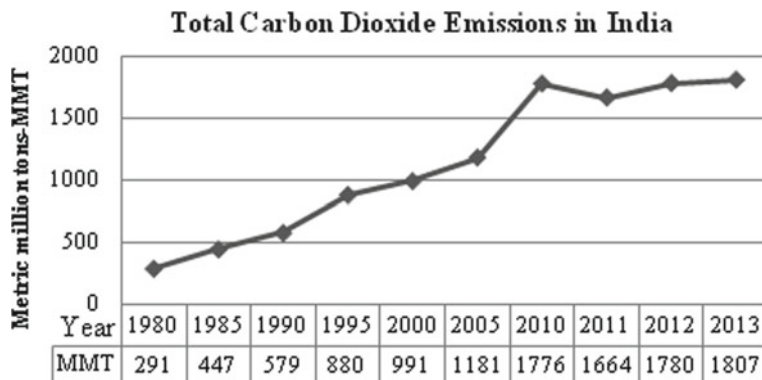


Fig. 2 Increase in CO₂ emission over the years [11]

load which is a factor of operating conditions, maintenance and upkeep of the vehicle.

Historically, we find that focus of reduction in harmful vehicle emissions varied over time as per locally prevailing circumstances but environmentally, CO₂ emission continued rising due to ever increasing population of vehicles using fossil fuels like petrol and diesel [12]. The Bharat stage emission standards are norms/standards framed by Indian Government to control/check the levels of air pollutants from internal combustion engines. However, the enforcement of pollution norms by regulatory authorities in India has been done in a phased manner varying from place to place (Fig. 3). The stricter norms were implemented earlier in metros and larger cities due to higher density of vehicle population. Some metropolitan cities were vying to be in line with EURO emission norms of the date. India is about six years behind in comparison to the European nations in following the emission standards. Euro 6 [13] was implemented in Europe in the year 2014, whereas Government of India has declared its intent to enforce Bharat stage 6 (similar to EURO VI) from the year 2020 in India. Figure 3 below gives an overview of the slow progress in implementing emission norms in India.

India is on an ambitious journey of rapid economic growth and industrialization led by dynamic government policies and technological development. Due to its sheer size and volume of energy requirements, it has a major stake in the future of global emissions.

3 Objectives of the Study

Government has adopted various measures to control and contain air pollution attributed to exhaust emission of vehicles running on internal combustion engines, fuelled by gasoline and diesel. These measures include adopting stricter exhaust

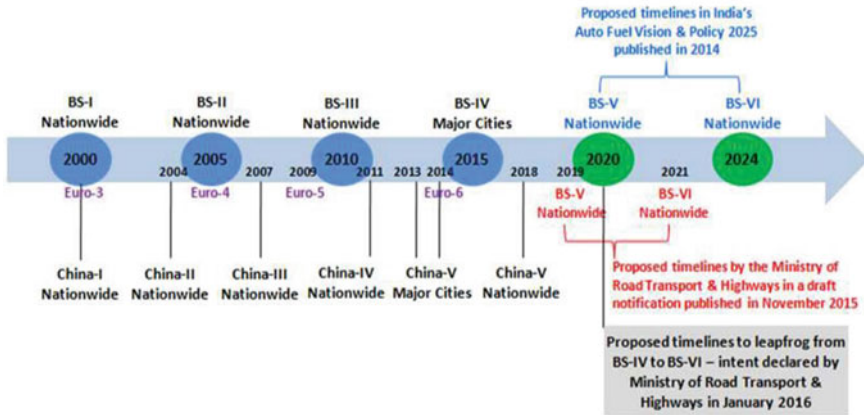


Fig. 3 Comparative timeline of incremental implementation of emission standards [14]

emission standards by planning to leapfrog to Bharat stage VI norms from BS-IV by skipping BS V norms, ensuring supply of lead and sulphur free fuel for vehicles, limiting number of vehicles on roads based on odd-even registration numbers, allowing only petrol/CNG commercial vehicles to ply in metros, limiting/reducing the number of years for which a vehicle is allowed to ply on roads, i.e. 10 years/ 15 years for diesel/gasoline vehicles, etc.

A diesel engine powered vehicle is not allowed to run in Delhi after completing 10 years. Similarly for a gasoline engine vehicle, it is allowed to run only for 15 years. This is done on the pretext/assumption that such aged vehicles' exhaust emission levels increase beyond the stipulated norms, whereas earlier government used to allow vehicle to be tested and recertified fit for next 5 years to ply on Delhi roads. This regulation of the government has limited the lifespan of a vehicle, thereby putting costly burden on public to purchase new vehicles even if their vehicles are fit and performing well.

This study is conducted to ascertain whether a vehicle becomes unfit to ply after stipulated 10 or 15 years in case of gasoline vehicles with the exhaust emission as the sole parameter. The study evaluates whether a vehicle starts polluting more with age or emission levels remain same within government regulated norms.

4 Methodology

4.1 Sample Selection

The volume of vehicles has been increasing over the years from 12 million in year 2000 to 35 million in the year 2018. Figure 4 shows total segment-wise sales

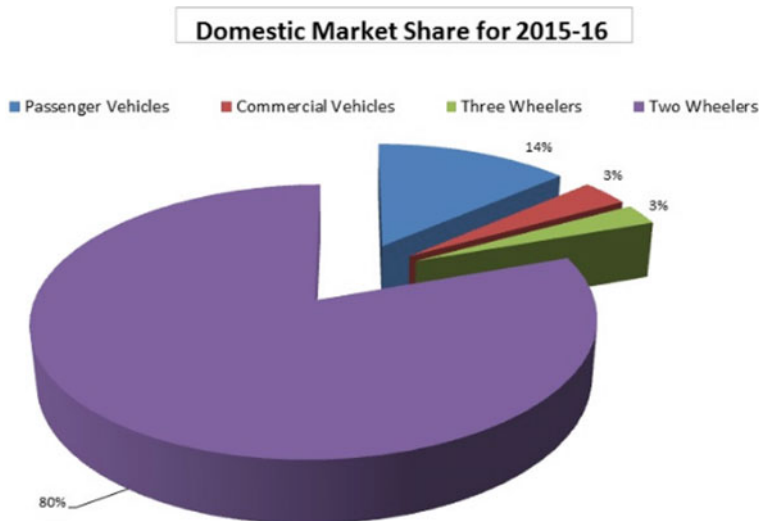


Fig. 4 Market share of vehicles in India for the year 2015–16 [10]

comprise of passenger car vehicle PCV 14%, commercial vehicle CV 3%, three wheelers 3% and two wheelers 80% [10].

Taking into consideration the larger four-wheeler segment of PCVs, the market share of various OEMs in India is as follows:

Figure 5 above shows Maruti Suzuki vehicles which represent 47.38% of total PCVs in Indian market for year 2017. Further breakup of MSIL vehicle sales shows that their model Wagon R accounts for almost 25% of the total sales of all MSIL brand vehicles put together [10]. So Wagon R represents almost 10% of total four-wheeler population in India and is, therefore, selected to be the fair representative sample/subject population of this study.

4.2 Collection of Data

The exhaust emission of a gasoline vehicle consists of mainly CO, HC, CO₂, O₂ and NO_x. As per government notified emission norms (Table 1), CO and HC levels are regulated strictly, whereas NO_x levels remain insignificant for a gasoline engine.

Therefore, in this study, CO emission levels of Wagon R (as selected above) are measured and analysed.

A four-gas analyzer of AVL make is used to measure CO and HC emission levels at a government authorized PUC certification centre. The pollution control readings tell us the health/efficiency of the vehicle engine. It is directly related to the quality of fuel combustion process of the engine as well as the condition/efficiency

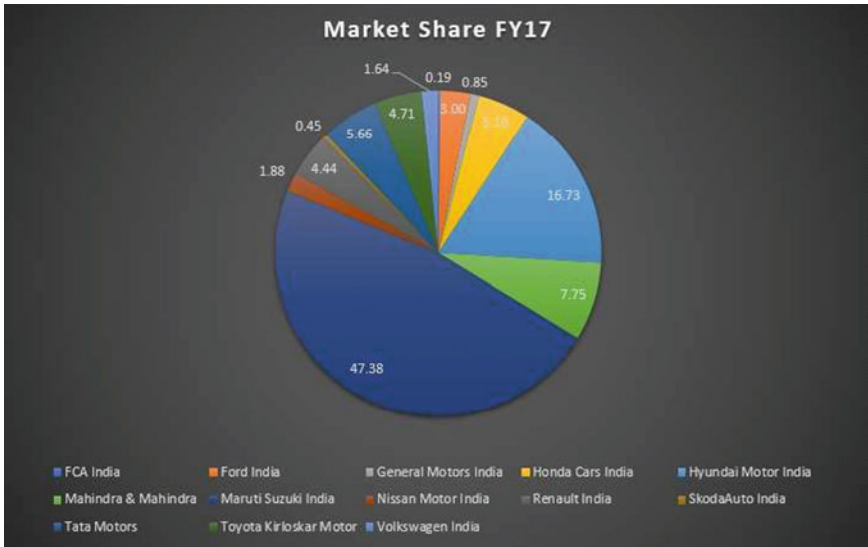


Fig. 5 Market share of four-wheeler vehicles in India for the year 2017 [10]

Table 1 Emission norms for gasoline passenger cars in India [16]

Norms	CO (g/km)	HC + NO _x (g/km)
1991 norms	14.3–27.1	2.0 (only HC)
1996 norms	8.68–12.40	3.0–4.36
1998 norms	4.34–6.20	1.50–2.18
Bharat stage I (2000)	2.72	0.97
Bharat stage II (2005)	2.2	0.5
Bharat stage III (2010)	2.3	0.35 (combined)
Bharat stage IV (2015)	1	0.18 (combined)

of exhaust emission after treatment devices like catalytic converters, filters, SNCR, etc. on-board as readings are taken downstream of the tailpipe. A decently tuned engine with a bad catalytic converter can give high-emission readings. If engine gives good mileage and power but emissions show increased values, then it indicates that vehicle’s exhaust emission after treatment devices are not working properly and efficiently. An inefficient engine will not burn fuel cleanly, and apart from loss in power and mileage, the emission levels would be on higher side in spite of treatment devices like catalytic converters, etc. After treatment devices are supposed to play a critical role during enriched fuel cycles during cold starting, acceleration, etc. The readings of CO and HC, thus measured, give a fair evaluation of vehicles emission levels.

5 Test Procedure

5.1 Test Instrument

A four-gas analyzer of AVL make is used to measure CO and HC emission levels. The instrument used in this study for the measurement of CO is approved by Government of India regulatory authority [15]. The standard specifications of AVL four-gas analyzer are as follows:

Data Measurement Specifications

	Measurement	Resolution
CO	0–10% vol.	0.01% vol.
HC	0–20,000 ppm	1 ppm/10 ppm
CO ₂	0–20% vol.	0.1% vol.
O ₂	0–22% vol.	0.01% vol.
Lambda	0–9.999	0.001

Technical Specifications

Engine speed	400–6000 rpm
Operating voltage	100–300 VAC, 50–60 Hz
Power consumption	Max. 25 W
Approvals	OIML Class 1/CE/ISO 3930:2000/PTB, ARAI Pune

A total of 520 samples were collected for Wagon R vehicles for one year (i.e. from Jan 2018 to Dec 2018). The information thus collected includes; CO (% vol.), HC (ppm), O₂% (vol.), Lambda, vehicle's year of manufacturing, fuel used (Petrol/CNG).

5.2 Data Analysis Methodology

The sample of CO emission data is collected from Maruti Wagon R along with the age of subject vehicle (i.e. year of manufacturing). Samples are collected from vehicles manufactured between year 2004 and year 2018. This spread of vehicles includes BS-III as well as BS-IV vehicles. The data is thus grouped into BS-III and BS-IV vehicles, which is further classified into sub-groups on the basis of their age, i.e. 0–4 years (manufacturing years 2015–18), 5–9 years (years 2010–14) and 10 years or more (year 2004–9). Within these sub-groups, vehicles running on CNG were further segregated. There are many cases, where multiple samples were collected for the same vehicles at different times during the year 2018. Following flow chart (Fig. 6) explains the selection of representative data for analysis.

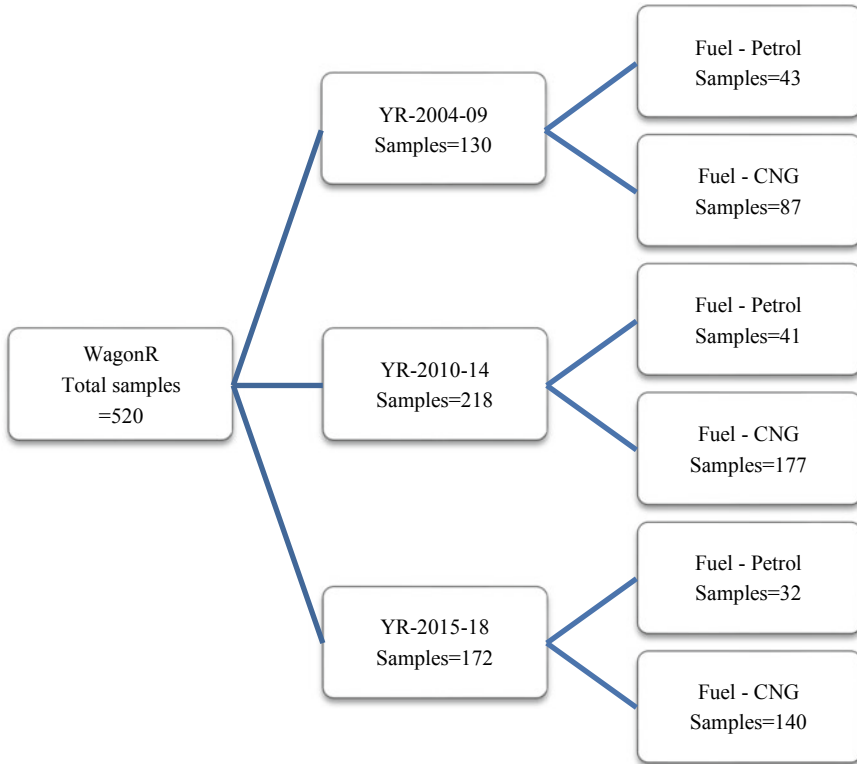


Fig. 6 Flow chart for selection and grouping of samples

6 Results and Discussion

The data thus collected of measured values of CO for the above mentioned 520 vehicles over the year 2018 is analysed in this study, and results are presented as follows.

Table 2 and Fig. 7 show the trend of CO emission level averages for the year of manufacturing as measured for all the vehicles. The average values were calculated for all the vehicles of same year of manufacturing. It clearly indicates the continual improvement in emission levels of vehicles from year 2001 model to year 2018 models. CO emission levels as measured in this study underlines the fact that improvement in engine technology along with availability of better quality of fuel (gasoline) over the years has resulted in lowering of CO emissions of in use vehicles.

Table 3 and Fig. 8 show spread of samples with respect to the measured values of CO emission of all the vehicles. The trend shows a normal distribution with 88% (466 out of 530) of the samples falling between CO levels of 0.0 and 0.149.

Table 2 Year-wise average values of CO measured

Year	2001	2003	2004	2005	2006	2007	2008	2009	2010	2011	2012	2013	2014	2015	2016	2017	2018
CO avg. for year (% volume)	0.181	0.117	0.141	0.116	0.102	0.106	0.093	0.138	0.099	0.083	0.091	0.099	0.092	0.093	0.082	0.077	0.067

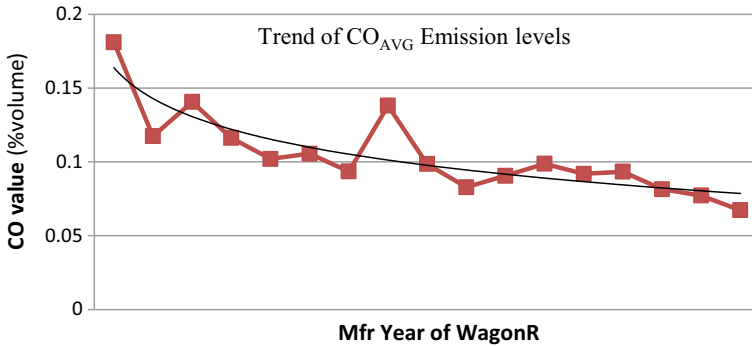


Fig. 7 Improvement in performance of vehicles over the years (CO emission levels)

Table 3 Number of vehicles falling within range of values of CO measured

CO-measured value range (%volume)	0–0.049	0.05–0.099	0.1–0.149	0.15–0.199	0.2–0.249	0.25–0.299	0.3–0.349
Frequency	86	286	94	24	22	10	6

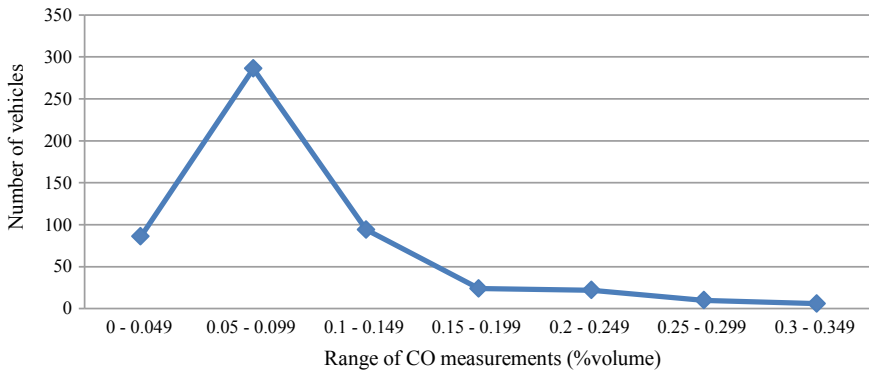


Fig. 8 Spread of vehicles across CO levels

Further analysis of data of CO emission levels as measured in this study is shown in Figs. 9, 10, and 11. There are clear indicators that vehicles manufactured in recent years (year 2015–2018) show markedly better CO emission levels as compared to older vehicles. But another important point which comes out in this study that even older vehicles (manufactured years 2004–2009) are well compliant as far as government stipulated emission norms of the date are concerned.

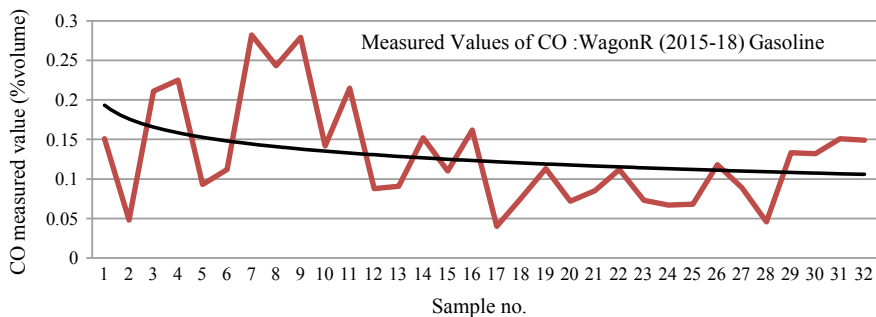


Fig. 9 CO-measured values for Wagon R (2015–18) gasoline

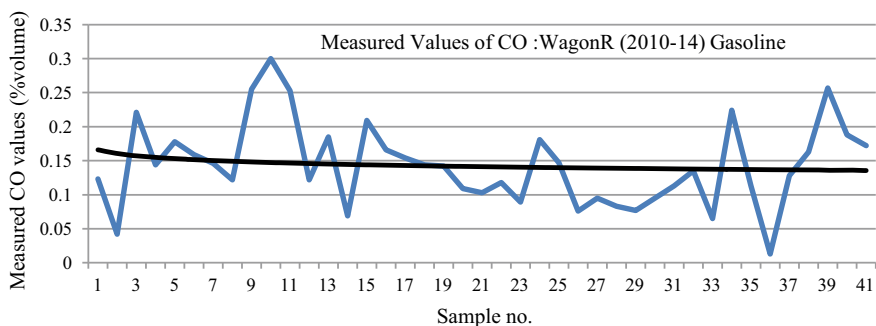


Fig. 10 CO-measured values for Wagon R (2010–14) gasoline

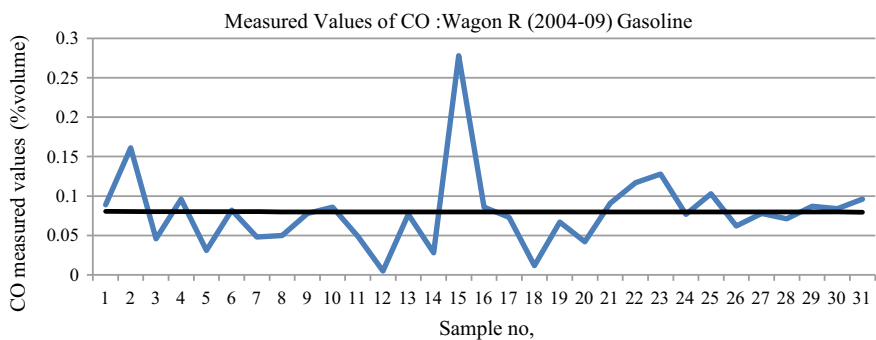


Fig. 11 CO-measured values for Wagon R (2004–09) gasoline

7 Summary and Conclusion

Whereas the improvement in engine technology like fuel injection, EGR, multiple injections, retarding of timing, etc., the electronic control module/on-board diagnostic devices continuously monitor and control air/fuel mixture in the combustion chamber closer to stoichiometric ratio, thereby containing engine exhaust emission under control as prescribed in BS emission norms of the day. The data as observed in this study clearly supports this positive improvement in the emission level of the vehicles over the years due to technological advances in this field. Even 10 years old vehicles (manufactured years 2004–2009) are well compliant as far as government stipulated emission norms of the date are concerned.

This study was conducted on the basis of emission values as measured in warm engine idling conditions, whereas emission values may vary during actual on road running use of vehicles depending on external factors like terrain, ambient temperature, traffic conditions, driving habits, etc. Also during cold starting of engine, emission levels also tend to vary due to rich priming of combustion chamber of an IC engine. Therefore, to ascertain the level of variance in vehicle emission during in use conditions, further analysis on similar lines need to be conducted to reiterate the findings in this study that due to improvement in engine technology and fuel, the emission levels of modern vehicles remain well within the stipulated emission norms, possibly during full lifecycle of the vehicle.

In summary, the many vehicle modifications and fuel changes in the last 20 years have greatly reduced levels of toxics emissions from vehicles. New cars today are capable of emitting 90% less pollution on a per km basis than the uncontrolled models of earlier years. Overall vehicle tailpipe emissions will continue to decrease through the twenty-first century as older vehicles leave the fleet and as new stricter regulatory emission norms like BS-VI take effect. However, the number of vehicles on the road and the number of kilometres they travel are continuing to grow. Without additional controls, growth in vehicle travel will offset progress in reducing net vehicle emission in absolute terms. An effort in reduction of harmful emissions from the tailpipe of vehicles shall contribute substantially in reducing total inventories of global green house gases.

References

1. Rossner P Jr, Cervena T, Vojtisek-Lom M, Vrbova K, Ambroz A, Novakova Z, Elzeinova F, Margaryan H, Beranek V, Pechout M, Macoun D, Klema J, Rossnerova A, Ciganek M, Topinka J (2019) The biological effects of complete gasoline engine emissions exposure in a 3D human airway model (MucilAirTM) and in human bronchial epithelial cells (BEAS-2B). *Int J Mol Sci* 20(22). Available at <https://doi.org/10.3390/ijms20225710>
2. Yilmaz A, Guvendik G (2003) The blood carboxyhemoglobin levels of individuals occupationally exposed to exhaust pollution. *J Fac Pharm, Univ Ankara* 2003(32):213–219
3. Quebec (2006) Available at http://www.hydroquebec.com/sustainable-development/documentation/pdf/options_energetiques/transport_en_2006.pdf

Comparison of Free Convection Around Heated Square Plate in a Square Enclosure Enclosing Air, Water, and Ag-Water Nanofluid



Parth Patpatiya, Isha Pandey, and Ananya Gupta

Abstract This paper compares the behavior of steady state and laminar buoyancy-driven flow consisting of three different working fluids (air, water, and (Ag-water) nanofluid) around a heated square plate placed eccentrically along horizontal central plane in a square enclosure. The aspect ratio of the enclosure is kept constant. The volume fraction of Ag-water nanofluid induced in water is 2% by volume. Two-dimensional numerical analysis is accomplished for single cylinder with different eccentricity ratios (0.15, 0.25, and 0.35) and is computed at three different Rayleigh number (10^4 , 10^5 , and 10^6), respectively. The enclosure and the inner body are kept at a constant temperature variance (i.e., temperature of inner body is conserved high as compared to the enclosure). The analysis is extended to a pair of square plate by placing another plate kept at the same temperature symmetrically opposite to the initial plate. The effect of changing the orientation of the plates (tilting the plates by 45° clockwise) is also observed on the heat transfer performance. This work has been validated with other experimental setup and was observed in finest reconciliation. The entire analysis is performed on licensed version simulation software. Results are arranged in such a way that the response of the Rayleigh number and the location of cylinder are analyzed with the help of analogous flow field and temperature distribution. The distortion of flow lines is much higher in case of nanofluid than with the other two fluids. When compared to other fluids, convective terms were noticeable on introduction of nanofluid. Variation in local Nusselt number is also observed simultaneously with the surface of square plate and simultaneously with the wall of the square enclosure.

Keywords Buoyancy-driven flow · Square plate · Square enclosure · Air · Water · Ag-water nanofluid · Nusselt number · Rayleigh number

P. Patpatiya · I. Pandey (✉) · A. Gupta
School of Automation, Banasthali Vidyapith, Newai, Jaipur, Rajasthan 304022, India
e-mail: ishapandey446@gmail.com

P. Patpatiya
e-mail: paarth.1098@gmail.com

© The Author(s), under exclusive license to Springer Nature Singapore Pte Ltd. 2021
B. S. Sikarwar et al. (eds.), *Advances in Fluid and Thermal Engineering*,
Lecture Notes in Mechanical Engineering,
https://doi.org/10.1007/978-981-16-0159-0_13

1 Introduction

Heat transmission involved in natural convective flow from a frame to a confined zone enclosing it has acknowledged augmented attention in recent years. The flow features and heat transmission involved in natural convection are vital for designing several thermal setups. Heat transmission in natural convection inside enclosure has relevancy to abundant engineering and manufacturing applications like heat exchangers, nuclear powered security systems, solar hoarders, apparatus preservation, etc. An outsized range of investigation is being involved for observation of fluid flow and heat transmission in diverse formed arenas with speckled enveloped fluids levying dissimilar boundary conditions. In the recent years, nanofluid has secured significant responsiveness due to the modest construction customs and inexpensive rate. Adding to the context, nanofluids are the liquid diffusions of submicron substantial subdivisions or nanoparticles in untainted fluent. Comparatively nanofluids have higher value of thermal response or conductivity. Thus, nanofluids can be functional in countless vitalities allied system. Glorious assessments proceeding the motive are constituted in literature [1–4]. Davis [5] was first to numerically examine the paralleling of free transmittal heat transmission within inclusion that was adopted as the standard response of various enclosure issues. The comparisons for truncated momentum compressible flow to affect buoyancy-propelled flow within a square field which was given by Navier–Stokes was totally solved by Vierendeels et al. [6] while not addressing to low Mach number calculation or J. V. Boussinesq calculation. Observable fact in reference to free convection amid centrally positioned isothermal and spherical inner frames was investigated by Warrington and Powe [7] by research. Evaluations were done to get bulkier value of Nusselt range in reference to various sets of intrinsic body-enclosure consolidations. Investigation conducted by Ghaddar [8] for a consistently positioned heated cylinder within an oblong inclusion which discussed about heat transmission is caused due to the effect of natural convection. A comparative study was carried out by Moukalled and Acharya [9] who evaluated uniform transmittal among square and circular cylinders and presented its consequences relating to Rayleigh range and also the height and width magnitude relation on the dissemination of temperature and flow field. Cesini and others [10] assumed of a situation in reference to horizontally located cylinder positioned within an exceedingly oblong cavity and how the response of natural convection will affect it. Zhang and others [11] observed free transmittal rate in the circular inclusion numerically with an inclined plate located asymmetrically. Heat transmission rate was attained through standardized mass degree of movement against the cylinders.

2 Problem Statement

The problem that has been considered in this study is described in Fig. 1. It comprises of a square enclosure of side L , within which a single or a pair of square cylinders is placed. In the case of a single cylinder, it is positioned eccentrically at a

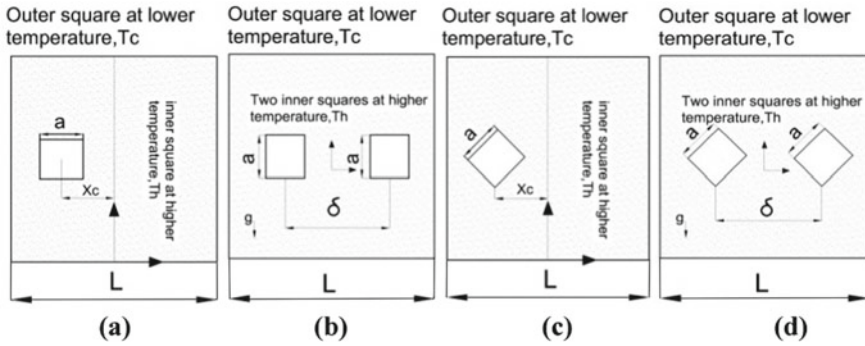


Fig. 1 Layout of plate in the computational region

distance x_c (0.15, 0.25, 0.35) from the center along the horizontal axis of the cross section as shown in Fig. 1a. In case of a pair of cylinders, the distance between the centers of both the inner cylinders has been taken as δ as shown in Fig. 1b. The tilt angle of the square in Fig. 1c is 45° so that one of the diagonals of the square is parallel to the base of the enclosure. Second cylinder is placed symmetrically in the opposite side of the center as shown in Fig. 1d. The distance in the case of a pair of cylinders has been taken as 0.30, 0.50, and 0.60 for Rayleigh number 10^4 , 10^5 , and 10^6 , respectively. Square configuration as per Fig. 1a, c will be referred as case-1 and Fig. 1b, d will be referred as case-2. The side of square cylinder is fixed as a . The square enclosure walls are kept at a relentless low temperature T_c and the inner cylinder is kept at a relentless high temperature T_h .

Boussinesq approximation is applied. With these conventions, the non-dimensional foremost equations are portrayed in the following form:

$$\frac{\partial R}{\partial X} + \frac{\partial S}{\partial Y} = 0 \tag{1}$$

$$R \frac{\partial R}{\partial X} + S \frac{\partial R}{\partial Y} = -\frac{\partial P}{\partial X} + \frac{\partial^2 R}{\partial X^2} + \frac{\partial^2 R}{\partial Y^2} \tag{2}$$

$$R \frac{\partial S}{\partial X} + S \frac{\partial S}{\partial Y} = -\frac{\partial P}{\partial Y} + Gr \cdot \theta + \frac{\partial^2 R}{\partial X^2} + \frac{\partial^2 S}{\partial X^2} \tag{3}$$

$$R \frac{\partial \theta}{\partial X} + S \frac{\partial \theta}{\partial Y} = \frac{1}{Pr} \left(\frac{\partial^2 \theta}{\partial X^2} + \frac{\partial^2 \theta}{\partial Y^2} \right) \tag{4}$$

3 Results and Discussion

The aim of the analysis is to compare the heat transfer performance accomplished by active fluids, i.e., air, water, and (Ag-water) nanofluid on operating parameters such as Rayleigh number, eccentricity (center-to-center distance between the cylinder) and orientation of square plate (tilting the plate). Thermophysical properties are kept steady except density.

3.1 Temperature Distribution and Flow Pattern

A numerical analysis is executed at three distinct Rayleigh numbers (10^4 – 10^6) and at three distinct arrangements. These patterns reflect the conclusion of cylinder location, orientation of the inner square plate, and the Rayleigh number on the buoyancy-driven flow. Figure 3 shows the comparison of isotherms of natural convective flow for $Ra = 10^4$ for a single cylinder allocated internally in a square enclosure at $x_c = 0.15$ for air, water, and Ag-water nanofluid as the working fluid. At lower Rayleigh number, i.e., at 10^4 , a mild effect of convection is seen by the flow pattern, where conduction is dominant than convection. At higher Rayleigh number, convection dominates the conduction in the flow in the enclosure.

3.1.1 Enclosure with Single Plate

Introduction of nanofluid changes the thermal performance to a great extent. Figures 2, 3, 4, 5, 6, 7, 8 and 9 show that average value of Nusselt number increments drastically along the walls of the enclosure and along the wall of plate. Nanofluid (Ag-water) has intense effect on the flow lines and temperature contour lines. In Fig. 3i, a comparison of heat transfer characteristics on changing the working fluid for same Rayleigh number is shown. At high eccentricity ratio, left portion clusters are stretched abruptly on the vertical side and the right portion clusters slightly moves toward left as shown in Fig. 3ii, iii. At distance of $x_c = 0.25$ and 0.35 between the center of the plates as shown in Fig. 4ii, the eddy formation takes place in two phases, i.e., major eddies and minor eddies. Maximum slope in temperature is seen when value of x_c equals 1.2 as shown in Fig. 4iii. Figure 5i demonstrates the patterns of streamlines for all fluids when eccentricity is maximum for $Ra = 10^5$. As the eccentricity ratio increments to 0.15 – 0.35 , the plate shifts more closer to the enclosure wall. The passage between the bodies gets smaller at the right-hand side of the enclosure. The number of recirculating cells increases at the upper half. This effect is observed maximum in case of high Rayleigh numbers when active fluid is Ag-water nanofluid. It indicates the greater strength of convection as shown in Fig. 5ii, iii. The darker part of isotherms also shows grown strength of convection. A slight shift in the pattern is observed in temperature lines

Fig. 2 Isotherms of natural convective flow for working fluid air, water, and nanofluid for $Ra = 10^4$ for a single plate allocated internally in a square enclosure at $x_c = 0.15, 0.25,$ and 0.35 respectively

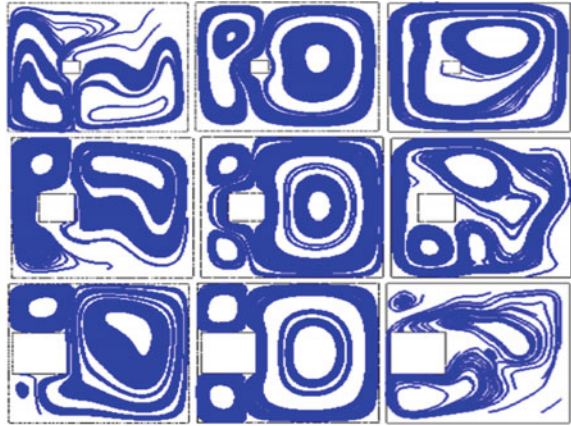


Fig. 3 Isotherms of natural convective flow for working fluid air, water, and nanofluid for $Ra = 10^5$ for a single plate allocated internally in a square enclosure at $x_c = 0.15, 0.25,$ and 0.35 respectively



Fig. 4 Isotherms of natural convective flow for working fluid air, water, and nanofluid for $Ra = 10^6$ for a single plate allocated internally in a square enclosure at $x_c = 0.15, 0.25,$ and 0.35 respectively

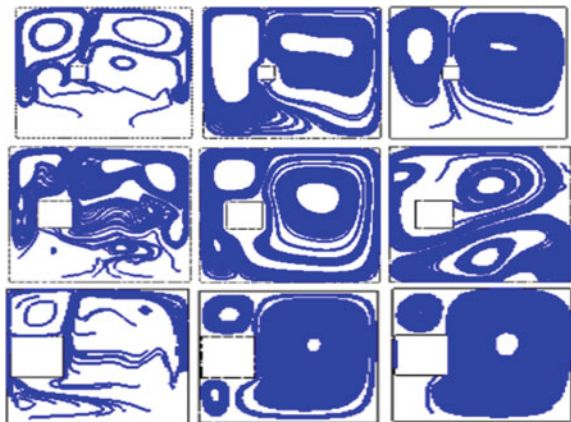


Fig. 5 Isotherms of natural convective flow for working fluid air, water, and nanofluid for $Ra = 10^4$ for a pair of plate allocated internally in a square enclosure at $\delta = 0.3$, 0.5, and 0.6 respectively

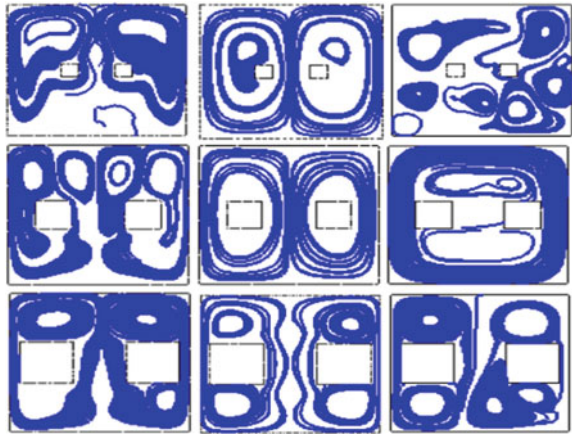


Fig. 6 Isotherms of natural convective flow for working fluid air, water, and nanofluid for $Ra = 10^5$ for a pair of plate allocated internally in a square enclosure at $\delta = 0.3$, 0.5 and 0.6 respectively



Fig. 7 Isotherms of natural convective flow for working fluid air, water, and nanofluid for $Ra = 10^6$ for a pair of plate allocated internally in a square enclosure at $\delta = 0.3$, 0.5, and 0.6 respectively

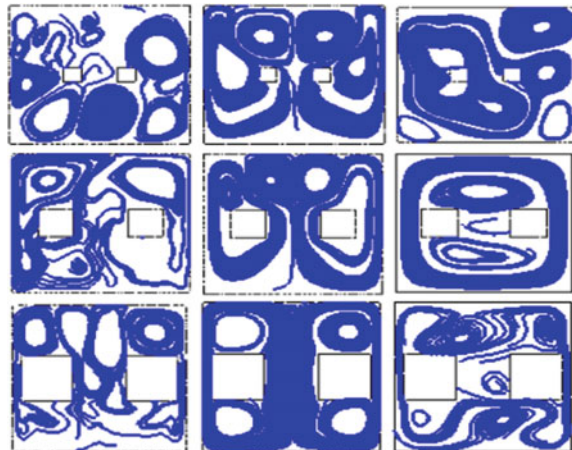


Fig. 8 Isotherms of natural convective flow for working fluid air, water, and nanofluid for $Ra = 10^4$ for a single tilt plate allocated internally in a square enclosure at $x_c = 0.15, 0.25,$ and 0.35 respectively



Fig. 9 Isotherms of natural convective flow for working fluid air, water, and nanofluid for $Ra = 10^5$ for a single tilt plate allocated internally in a square enclosure at $x_c = 0.15, 0.25,$ and 0.35 respectively



for $Ra = 10^6$ for a single cylinder allocated internally in a square enclosure at $x_c = 0.25$. The shape of the flow field changes due to insignificant convection at the lower portion of the enclosure.

3.1.2 Enclosure with a Pair of Plate

It is evident from Fig. 3 as the Rayleigh number increments the Nusselt number increments. Hence, the effect of Rayleigh number on Nusselt number is clear and becomes more significant in case of wider obstacle. This can be easily observed when another plate is placed at the same temperature symmetrically opposite to the initial plate. The same convection dominant conduction effect can be seen in case of

a pair of plate placed inside the enclosure. Strength of convection amplifies on introduction of Ag-water nanofluid in the enclosure. Three distinct values of δ (center-to-center distance), i.e., 0.3, 0.5, and 0.6 are taken for locating plates symmetrically around the vertical plane. Conduction-type arrangement is noticed at low Rayleigh number $Ra = 10^4$ as shown in Fig. 6i. As the distance between the plates reaches at greatest the number of rotating eddies increases from two to four, but it leaves hardly any effect on the pattern of isotherms due to weak convection. On moving from top to bottom, the effect of increasing Rayleigh number is observed. Figure 6ii depicts the motion of the convection cells, i.e., it ascends upward, and its profile also varies. Nanofluid (Ag-water) has intense effect on the flow pattern and temperature distribution. For $Ra = 10^6$, two cells are formed when $\delta = 0.3$, grows to four in number for $\delta = 0.5$ but again negotiates with two cells only for $\delta = 0.6$ as the passage between inner cylinders and the vertical walls of the enclosure is narrowed down considerably which is clearly seen in Fig. 8i–iii. The consequence of placement of cylinders is evident from development of boundary layer and flow separation. Extent of asymmetry in Fig. 7i is more than Fig. 7ii, iii. Entire flow activity shifts toward the upper part of enclosure on increasing the Rayleigh number. There is rarely any flow in the vicinity of the enclosure near the bottom side at the maximum value of Rayleigh number.

3.1.3 Introduction of Similar Tilt Plate

Introduction of similar tilt plate makes the heat transfer rate more clear under the influence of changing Rayleigh number and enclosed working fluid. The effect is similar to the one obtained for Rayleigh number 10^4 when plates are not tilted. The plumes formed in Fig. 9 in case of water as the working plate is symmetric about y-axis. Two overlapping clouds are formed for Rayleigh number 10^4 . As the Rayleigh number drifts toward higher side, the number of clouds becomes more and denser. Six plume structures are generated at $\delta = 0.5$. Diagonal symmetry is observed for $Ra = 10^5$ in case of Ag-water nanofluid as the working fluid for a pair of tilt plate allocated internally in a square enclosure at $\delta = 0.6$. Rising thermal clouds are generated at higher Rayleigh number because of cylinder gets positioned nearer to the cold enclosure.

4 Conclusion

The main motive of performing the numerical analysis is to study the changes in flow pattern and the heat characteristics due to inclination, eccentricity ratio, Rayleigh number, and introduction of working fluids in the square plate. The following conclusions are drawn.

Enclosure with single and a pair of plate

- As the Rayleigh number increases, convection dominates the conduction the flow in the enclosure for all the working fluid.
- Enclosed working fluid has a great effect in development of streamlines and counter lines. Flow and thermal field with asymmetric structure forms when enclosed working fluid changes from air to water and to (Ag-water) nanofluid, respectively.
- As the eccentricity of the square plate increases, heat transfer rate increases with the highest observed for Ag-water nanofluid as working fluid.
- Placing another hot plate symmetrically has a great effect in development of streamlines and counters. Flow and thermal field with asymmetric structure forms when enclosed working fluid changes from air to water and to (Ag-water) nanofluid, respectively.
- For similar conditions of the Rayleigh number and cylinder to cylinder distance, highest eddy formations are observed in case of (Ag-water) nanofluid.
- Distance between the cylinders plays an important role in the formation of circulation cells which determines the rate of heat transfer. As the distance between the plates increases, the density of the field lines decreases for air, water, and (Ag-water) nanofluid as the convective medium.

Enclosure with tilted plate

- It is seen from every table made for single and double plate that the value of local Nusselt number increases as the plate's inclination increases to 45° .
- This pattern is seen for all working fluid. As it is the ratio of convective heat transfer rate to conductive heat transfer rate, conduction is more dominant than convection in that region.
- This is due to the fact that fluid circulation is comparatively more intense when plate is given inclination.
- The temperature flow lines become more symmetric in nature in case of water as enclosed fluid. The effect is more at the lower Rayleigh number.
- The number of vortices (unicellular, bicellular, tricellular), recirculating eddy formation are mainly dependent on tilt of the plate, Rayleigh number, and enclosed working fluid.

References

1. Kamiyo OM, Angell D, Barozzi GS, Collins MW, Olunloyo VOS, Talabi SO (2010) A comprehensive review of natural convection in triangular enclosures. *Appl Mech Rev* 63 (6):060801 (13 pages)
2. Saha SC, Khan MMK (2011) A review of natural convection and heat transfer in attic-shaped space. *Energ Build* 43:2564–2571

3. Bairi A, Zarco-Pernia E, Garcia de Maria J-M (2014) A review on natural convection in enclosure for engineering applications. The particular case of the parallelogrammic diode cavity. *Appl Therm Eng* 63:304–322
4. Hussein AK, Awad MM, Kolsi L, Fathinia F, Adugun IK (2014) A comprehensive review of transient natural convection flow in enclosures. *J Basic Appl Sci Res* 4(11):17–27
5. Davis GDV (1983) Natural convection of air in a square cavity: a benchmark numerical solutions. *Int J Numer Meth Fluids* 3:249–264
6. Vierendeels J, Merci B, Dick E (2003) Benchmark solutions for the natural convective heat transfer problem in a square cavity with large horizontal temperature differences. *Int J Numer Meth Heat Fluid Flow* 13:1057–1078
7. Warrington RO, Powe RE (1985) The heat transfer by natural convection between bodies and their enclosures. *Int J Heat Mass Transf* 28:319–330
8. Ghaddar NK (1992) Natural convection heat transfer between a uniformly heated cylindrical element and its rectangular enclosure. *Int J Heat Mass Transf* 35:2327–2334
9. Moukalled F, Acharya S (1996) Natural convection between concentric horizontal circular and square cylinders. *J Thermophys Heat Transf* 10:524–531
10. Cesini G, Paroncini M, Cortella G, Manzan M (1999) Natural convection from a horizontal cylinder in a rectangular cavity. *Int J Heat Mass Transf* 42:1801–1811
11. Zhang W et al (2018) Partitioning effect on natural convection in a circular enclosure with an asymmetrically placed inclined plate. *Int Commun Heat Mass Transf* 90:11–22

Numerical Study of Heat Exchanger Having Protrusion and Dimple Roughened Conical Ring Inserts



Bhanu Pratap Singh, Vijay Singh Bisht[✉],
and Prabhakar Bhandari[✉]

Abstract Heat transfer rate augmentation in heat exchangers with least pressure drop is one of the important fields for research in research fraternity. The different types of inserts have been used in the tube to fulfill the objective. In the present model, a conical-ring turbulators with protrusion and dimple roughness from inside has been used as an insert. These turbulators were placed inside the heat exchanger tube, and tube was applied with uniform heat flux condition. A parametric study has been performed for different diameter (3, 6 and 9 mm) and pitch space (60 and 240 mm) of protrusion and dimple. The Reynolds number has been varied from 5000–30,000, and heat flux of 1200 W/m² was used. It was concluded that as pitch space and Reynolds number increases, Nusselt number also increases. The protrusion shaped roughness has better thermal performance factor than dimple shape. The diameter of 6 mm has performed better than 3 and 9 mm for both the cases of roughness.

Keywords Computational fluid dynamics · Dimple shaped roughness · Protrusion roughness · Heat exchanger · Thermal performance factor

Nomenclature

c_p Specific heat
 D Diameter (mm)
 D_h Hydraulic diameter(mm)
 k Thermal conductivity

B. P. Singh
Tulas Institute, Uttarakhand Technical University, Dehradun 248007, India
e-mail: erbhanupractap1987@gmail.com

V. S. Bisht
Faculty of Technology, Uttarakhand Technical University, Dehradun 248007, India
e-mail: vsinghbisht5@gmail.com

P. Bhandari (✉)
IFTM University, Moradabad 244001, India
e-mail: prabhakar.bhandari40@gmail.com

P	Pitch space
f	Friction factor
Nu	Nusselt number
V	Velocity matrix

Greek

ρ	Density (Kg/m^3)
μ	Dynamic viscosity (Kg/m-s)

Subscript

c	Channel
o	Plain tube
Cu	Copper
air	Air

1 Introduction

The heating and cooling systems have one of the essential components, i.e., heat exchanger. The application of heat exchanger are in various industries like oil organizations, residential areas, and solar applications [1, 2]. While designing a good heat exchanger, one has to analyze the parameters like heat transfer rate, fluid flow, pressure drop, etc. The passive techniques for heat transfer augmentation in heat exchanger have gained lot of attention nowadays because there is no extra power needed in that. The passive techniques includes surface treatment, i.e., hydrophobic and hydrophilic surface, roughened the surfaces, use of extended surfaces like fins and inserts, introduction of devices like displaced enhancement devices, and vortex generation devices. Other methods are also used by researchers like introducing foreign element in the coolant like nanofluids [3] and using phase change material, etc.

There are various inserts used by different authors for heat transfer augmentation in heat exchangers.

ThianPong et al. [4] uses insert in the form of twisted tape having perforations (PTT) in their study for heat transfer rate improvement. They observed that heat transfer rate has been significantly increased using PTT and also concluded with decrease in pitch ratio and twisted-tape ratio, there is increase in heat transfer rate.

Promvong and Eiamsa-ard [5] use conical-ring and twisted-tape insert in a circular tube and concluded that this combination has over 10% enhancement in heat transfer rate from conical-ring alone case.

Promvong [6] uses heat exchanger tube fitted with arrays of following conical-ring turbulator: Converging conical ring (CR), diverging conical ring (DR),

and converging-diverging conical ring (CDR). He concluded that DR array has highest efficiency, CR has least and while CDR has in between them. Many researchers [5, 6] have performed studies on conical turbulator inserts in the heat exchanger tube for improvement of heat transfer rate and hot shortness problem.

To further enhance the performance of heat exchanger having conical turbulator, two different types of roughness has been investigated. The roughnesses implemented in the present study are:

1. Conical ring with protrusion roughness
2. Conical ring with dimple roughness.

2 Simulation Model

In present work, a heat exchanger tube has been analyzed numerically. The present heat exchanger tube model was modeled in commercial code ANSYS V14.0. The fluent module has been used to solve the present problem. The presented model has used conical ring with different roughness as a way to improve heat exchanger thermal performance. The conical-ring roughnesses used were protrusion roughness and dimple roughness.

The cone rings which were roughened with protrusion and dimple were shown in Figs. 1 and 2, respectively. In Fig. 1a, b, the side and isometric view were shown, respectively. These conical rings were placed inside the heat exchanger tube. The heat exchanger tube was shown by light gray color in these figures. These conical-ring roughnesses helps in heat transfer augmentation between tube surface and working fluid because of formation of turbulent eddies in the tube and disturbances in the boundary layer. The different type of protrusion roughness was shown in Fig. 1c–e and while different dimple roughness in conical ring was shown in Fig. 2a–c. In the present numerical study, *k- ϵ* turbulence RNG– enhanced wall treatment model has been used. Various researchers like Alam and Kim [7] and Li et al. [8] have used similar models in their numerical study.

The total length (L) of heat exchanger tube is 1500 mm and is being divided into three section (i) Entrance section ($L_1 = 100$ mm) (ii) test section ($L_2 = 1300$ mm) where conical ring with roughness were inserted in the heat exchanger tube and (iii) exit section ($L_3 = 100$ mm). The conical-ring insert are having base radius of 15 mm, top radius of 12 mm, and length of 40 mm. These conical rings were of same sizes and having same orientation, i.e., along the tube axis. The different design and working parameters used in the present numerical study were shown in the Table 1. The term pitch space (P) has been used to define the distance between two consecutive inserts and pitch ratio (PR) was the ratio of pitch space to the hydraulic diameter (D_h). The two sets of pitch space has been used, i.e., PR = 2 and PR = 8. The different inlet conditions were achieved by applying different Reynolds number (Re). The Re has been varied from 5000 to 30,000.

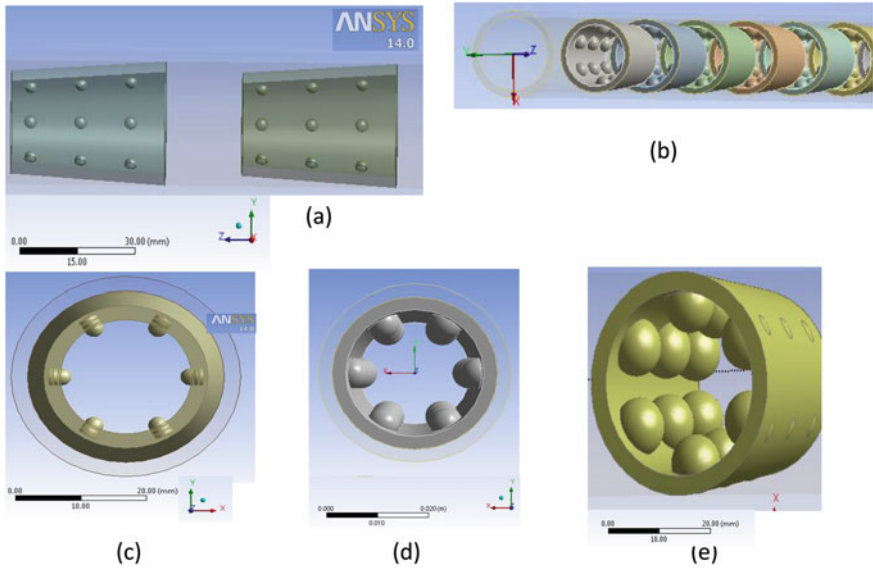


Fig. 1 Geometry of conical-ring insert roughened with protrusion inside of heat exchanger tube, **a** side view, **b** isometric view, **c** protrusion diameter $d = 3$ mm, **d** protrusion diameter, $d = 6$ mm, **e** protrusion diameter $d = 9$ mm

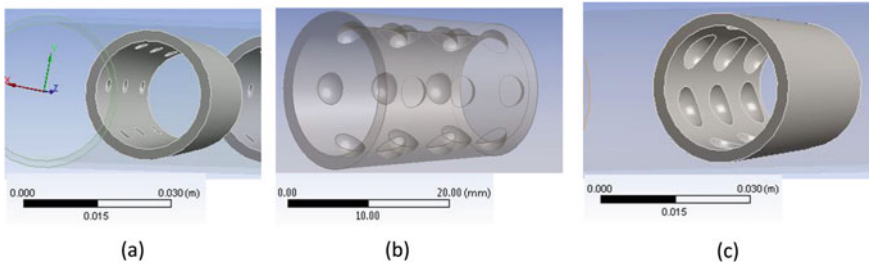


Fig. 2 Geometry of conical-ring insert roughened with dimple inside of heat exchanger tube, **a** dimple diameter, $d = 3$ mm, **b** dimple diameter, $d = 6$ mm, **c** dimple diameter, $d = 9$ mm

2.1 Assumption

To further simplify the numerical simulation, the following assumptions have been incorporated.

- (1) Steady and incompressible fluid flows
- (2) Pressure variation in Y direction is zero.
- (3) Neglecting body forces like gravity forces.

Table 1 Details of different geometric and working parameters of the present heat exchanger tube model

S. No.	Parameters	Values
1	Inner diameter of the tube (D_1)	30 mm
2	Outer diameter of the tube(D_2)	35 mm
3	Thickness of cone roughness	2.5 mm
4	Protrusion and dimple diameter (d)	3, 6 and 9 mm
5	Hydraulic diameter (D_h)	30 mm
6	Pitch space (P)	60 and 240 mm
7	Uniform heat flux (I)	1200 W/m ²

- (4) There is no variation in properties of air and copper with pressure and temperature, i.e., constant properties.
- (5) At the wall of the tube, no slip boundary conditions prevail and turbulence intensity was taken at 5%.

Based on the above listed assumptions, conservation of mass, momentum, and energy (Eqs. 1–3) equations have been solved.

$$\nabla \vec{V} = 0 \tag{1}$$

$$\rho_f(\vec{V} \cdot \nabla \vec{V}) = -\nabla p + \nabla \cdot (\mu_f \nabla \vec{V}) \tag{2}$$

$$\rho_f C_{p,f}(\vec{V} \cdot \nabla T_f) = k_f \nabla^2 T_f \tag{3}$$

where \vec{V} is the velocity vector matrix. The conical-ring insert and heat exchanger tube have been made of copper because it has high thermal conductivity and working fluid used is air. The thermo-physical properties of both tube and working fluid are shown in Table 2.

Table 2 Thermo-physical properties of heat exchanger tube and working fluid air

Air		Copper	
Properties	Value	Properties	Value
Density (ρ_{air})	1.225 kg/m ³	Density(ρ_{Cu})	8978 kg/m ³
Specific heat ($c_{p,air}$)	1006.4 kJ/kg	Specific heat ($c_{p,Cu}$)	381 kJ/kg
Viscosity(μ_{air})	1.7894e-05 kg/(ms)	Thermal conductivity (k_{Cu})	387.6 W/(m ^o K)
Thermal conductivity (k_{air})	0.024 W/(m ^o K)		

2.2 Mesh Generation and Grid Independence Test

The present model has been discretized in two different fashions. From outside of the tube, coarse meshing while at inside, fine meshing has been used. The grid independence test has been performed, and it was observed that after the 1,207,624 numbers of elements, Nusselt number does not increases much. Hence, in further analysis, the same grid size has been used.

3 Results and Discussion

3.1 Validation

The smooth plain tube model has been compared to check the accuracy of present model. On comparing the smooth tube model with Dittus-Boelter equation, the variation in Nu number is in range of 1–7%. The trend is observed for friction factor in smooth plain tube and Blasius friction equation. The present conical inserts inside the tube are also compared with Promvonge [6]. Figure 3 shows the variation plot of Nu with Re for present model and Promvonge [6]. It was founded that deviation of Nu was in acceptable range (4–8%).

3.2 Heat Transfer

The Nusselt number (Nu) value gives a proper overview of heat transfer rate in any heat exchanging device. The Nu number variation with Re for different protrusion

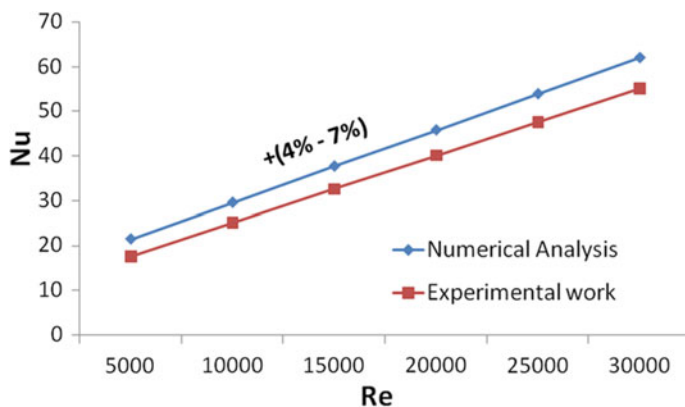


Fig. 3 Validation of present numerical model with Promvonge [6]

diameter was plotted in Fig. 4. The two sets of pitch have been used. In Fig. 4a, the value of P is 60 mm while in Fig. 4b, P is 240 mm.

It has been observed that with increase in Re , heat transfer rate also increases and highest Nu was achieved at maximum Re , i.e., ($Re = 30,000$). This was because as Re increases, more fluid flows through the tube and heat carried by it increases. It was also founded that higher pitch space has high heat transfer rate. The Nu value for $P = 240$ mm was higher than $P = 60$ mm for all the cases. This may be because more flow disturbance was created by pitch space of 240 mm. The $d = 6$ mm has shown highest Nu than $d = 3$ mm and $d = 9$ mm. There was significant improvement that can be seen in heat transfer rate in heat exchanger tube with conical ring with roughness when compared with smooth tube.

The similar trend has been also observed for dimple shape roughness as can be seen in Fig. 5. Here, also dimple diameter, $d = 6$ mm has shown highest value of Nu than compared to $d = 3$ mm and $d = 9$ mm.

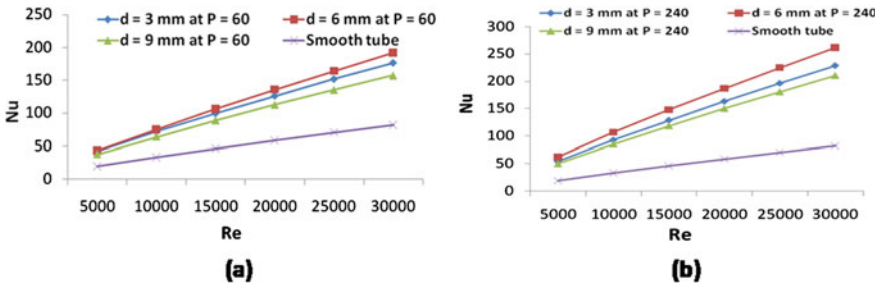


Fig. 4 Variation of Nusselt number with respect to Reynolds number for heat exchanger tube with conical-ring insert roughened with protrusion at a $P = 60$ mm, b $P = 240$ mm

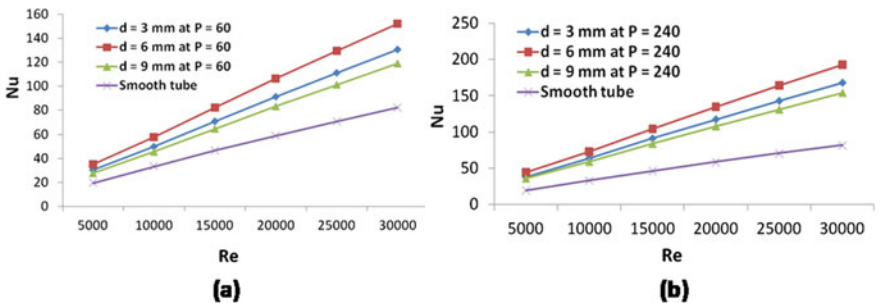


Fig. 5 Variation of Nusselt number with respect to Reynolds number for heat exchanger tube with conical-ring insert roughened with dimple at a $P = 60$ mm, b $P = 240$ mm

3.3 Fluid Flow

The variation of friction factor with Re for protrusion roughness in conical-ring insert inside of heat exchanger tube at $P = 60$ mm and $P = 240$ mm was presented in Fig. 6. The friction factor decreases with increases in Re. The maximum pressure drop is obtained for $d = 6$ mm, while least is obtained in $d = 9$ mm. The pressure drop was more for all the cases of inserts than compared to the smooth tube because inserts present in the tube obstructs the fluid flow.

The similar trends can be seen in heat exchanger tube with dimple shape roughness in conical inserts. Figure 7 shows that for both pitch space ($P = 60$ and 240 mm), the same trend has been observed for dimple roughness as it was observed earlier for protrusion case.

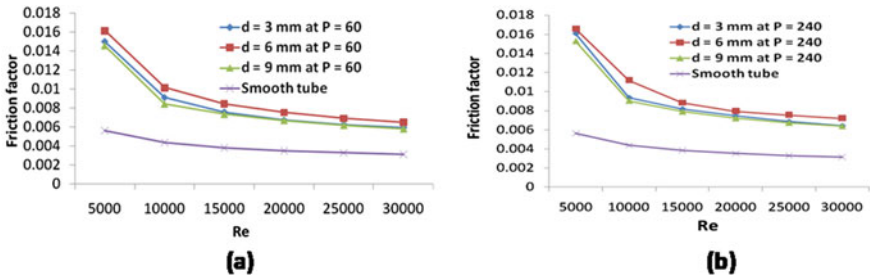


Fig. 6 Variation of friction factor with Re for heat exchanger tube with conical-ring insert roughened with protrusion at **a** $P = 60$ mm, **b** $P = 240$ mm

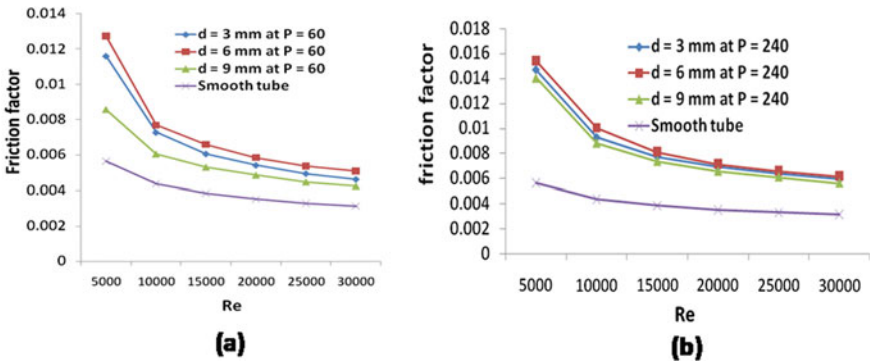


Fig. 7 Variation of friction factor with Re for heat exchanger tube with conical-ring insert roughened with dimple at **a** $P = 60$ mm, **b** $P = 240$ mm

3.4 Thermo-Hydraulic Factor

The thermo-hydraulic factor (THF) is a parameter which depicts the overall working performance of the heat exchanger tube. Generally, different method incorporated to enhance the heat transfer rate has an inherent disadvantage of increased pressure drop. The parameter THF shows that whether the modification done to achieve heat transfer augmentation was feasible or not. A particular design was considered a good design when THF value was greater than 1. Its expression was given by Webb and Eckert [9] which was shown in Eq. 4.

$$THF = \frac{Nu/Nu_o}{(f/f_o)^{1/3}} \tag{4}$$

The variation of THF with Re for all the case has been plotted in Fig. 8. The protrusion roughness has shown higher value of THF than dimple roughness in conical ring for all sets of diameters. The thermal hydraulic performance was found highest for 6 mm diameter for both the roughnesses.

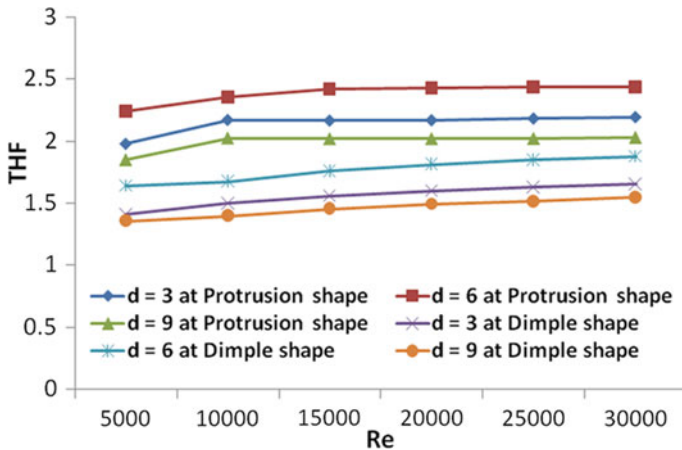


Fig. 8 Variation of thermal hydraulic factor (THF) with Re

4 Conclusion

The heat exchanger tubes with inserts in shape of conical ring were used, and these conical rings are having roughness in the form of protrusion and dimples to further enhance the heat transfer rate. In the present numerical study, two parameters were studied, i.e., pitch space and protrusion/dimple diameter. The modification has been done with the objective to enhance heat transfer rate without significant increase in pressure drop. From the study, the following conclusion has been drawn:

1. With the increase in Re , heat transfer rate increases and friction factor decreases for all the cases.
2. Nu numbers increases from 1.45 to 3.19 times and friction factors increase from 1.36 to 1.96 times of plain tube case in the Re ranging from 5000 to 30,000.
3. The Nu number increases with the pitch space between the conical rings inserts inside of the tube.
4. The highest Nu has been obtained for protrusion roughness in conical ring with diameter of 6 mm.
5. The lowest friction factor was founded for dimple roughness case in tube with diameter of 9 mm.
6. The protrusion shaped roughness has better thermal performance factor than dimple shape for all the cases, and highest THF of 2.44 was obtained at $Re = 30,000$ for protrusion roughness case having diameter of 6 mm and pitch space of 240 mm.

References

1. Bhandari P, Varshney L, Bisht VS (2018) Numerical analysis of hybrid solar water heating system using wire screen packed solar air heater. In: 1st International conference on new frontiers in engineering, science & technology, vol 1, pp 415–1422
2. Varshney L, Bhandari P, Bisht VS (2014) Performance evaluation of hybrid solar water heating system using wire screen packed solar air heater. *Int J Eng Res Appl (IJERA)*:311–316
3. Kumar N, Singh P, Redhewal AK, Bhandari P (2015) A review on nanofluids applications for heat transfer in micro-channels. *Procedia Eng* 127:1197–1202
4. Thianpong C, Eiamsa-ard P, Eiamsa-ard S (2012) Heat transfer and thermal performance characteristics of heat exchanger tube fitted with perforated twisted-tapes. *Heat Mass Transf* 48:881–892
5. Promvong P, Eiamsa-ard S (2007) Heat transfer behaviors in a tube with combined conical-ring and twisted-tape insert. *Int Commun Heat Mass Transf* 34:849–859
6. Promvong P (2008) Heat transfer behaviors in round tube with conical ring inserts. *Energ Convers Manag* 49:8–15
7. Alam T, Kim MH (2016) Numerical study on thermal hydraulic performance improvement in solar air heater duct with semi ellipse shaped obstacles. *Energy* 112:588–598

8. Li JL, Tang HW, Yang YT (2018) Numerical simulation and thermal performance optimization of turbulent flow in a channel with multi V-shaped baffles. *Int Commun Heat Mass Transf* 92:39–50
9. Webb RL, Eckert ERG (1972) Application of rough surfaces to heat exchanger design. *Int J Heat Mass Transf* 15(9):1647–1658

Futuristic Approaches of Low-Grade Industrial Waste Heat Recovery



Prasanta Majumder , Abhijit Sinha , and Rajat Gupta

Abstract Energy deficiency and environmental deterioration are crucial challenges in the current world. About 50% of energy is being wasted due to inefficient energy conversion processes and a lack of execution of reliable recovery technologies. With rapid industrialization and improvement in the standard of life, there exists the enormous potential for recovery of waste heat from industrial processes and transportation systems. The transition of 10% waste heat into electrical power can enhance fuel efficiency by 20%. Apart from enhancing the overall efficiency with the economic outlook, waste energy recovery also helps to mitigate CO₂ emission from thermal systems. In this context, a circular energy management strategy can be applied for effective utilization of waste heat in the form of heat and electrical energy. The effective harnessing of abundant renewable energy sources viz. solar thermal, photovoltaic (PV), biomass, etc., can reduce the dependency on primary energy sources and lead towards sustainable greener future. This review also emphasizes two prominent waste heat recovery technologies viz. Organic Rankine Cycle (ORC) and thermoelectric generator (TEG). While integrating TEG, ORC or other additional features in moving vehicles, the weight has to be taken into account to secure the mass retribution within 5%.

Keywords Low-grade waste heat · Energy conversion · Drying · Organic rankine cycle (ORC) · Thermoelectric generator (TEG)

P. Majumder · A. Sinha (✉) · R. Gupta
Department of Mechanical Engineering, National Institute of Technology Mizoram,
Aizawl 796012, India
e-mail: abhijit.mech@nitmz.ac.in

P. Majumder
e-mail: prst91@gmail.com

R. Gupta
e-mail: rguptanitsri@gmail.com

1 Introduction

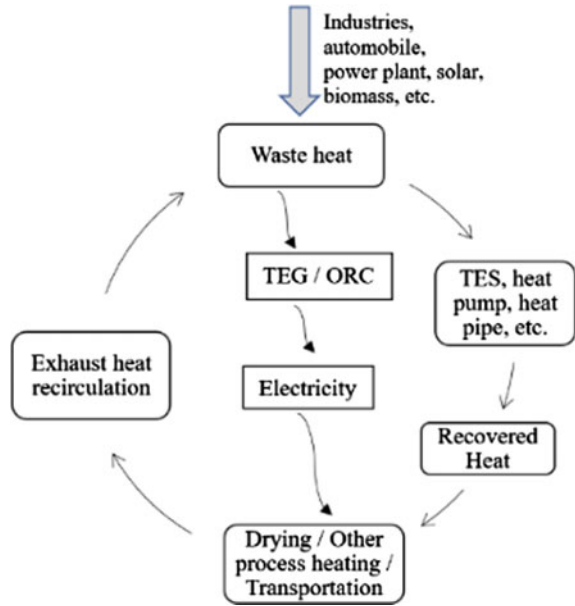
Conventional fossil fuels contribute more than 85% of total energy consumption, out of which 40% is used for space heating and process heating. Inefficient generation, inadequate storage facility, and transmission losses are responsible for 30–40% wastage of low-grade energy. Waste heat utilization is an alternative approach for improving gross efficiency by as much as 20% and is considered a technological wedge, playing a significant role in emission reduction [1]. While designing any heat recovery system one should consider the quantity and quality of waste heat, composition and phase of the waste stream, materials and minimum allowable temperature to prevent corrosion and oxidation in heat exchanger materials, accessibility and transportability of waste heat stream. The operating schedule between the waste heat source and user demand also has a great concern to prevent the fatigue failure of heat exchanger materials occurred by thermal cycling [2, 3]. Waste heat can be differentiated as low grade (<100 °C), medium grade (100–400 °C) and high grade (>400 °C) [4]. About 63% of total unused heat is contributed by low-grade sources like dehydration or drying, solar, biomass, welding process, casting, cement clinkers, pump, ingot, refrigeration and air conditioning, etc. However, there is not much technological evolution in the cost-effective way of recovering this energy [5]. The main constraints for low-grade waste heat recovery are likely uses, prolonged payback period, and irreversible losses due to temperature equivalent to ambient.

Waste heat recovery can be classified into direct or indirect heating and conversion into electrical power, acoustic energy, or other mechanical energy. Direct or indirect heating is done by adiabatic mixing, heat exchanger, heat pump, recuperator, heat pipe, thermal energy storage, etc. The recovered heat is used for process heating, air conditioning and warm water in domestic or small-scale industries [6–8]. Thermoelectric generator (TEG) and organic Rankine cycle (ORC) have the versatile utility for recovering higher to lower ranges of exhaust heat and generation of electricity, which have potential demand in automobile, aircraft, satellites, and decentralized domestic power supply [9–11]. Though several kinds of research have been conducted in this field, it is worth exploring the potential sources and utility of low-grade waste heat, particularly in drying and other process heating applications, solar photovoltaic-thermal and biomass conversion. A circular waste heat management strategy is depicted to show the state of the art technologies on recovery and applications of low-grade waste heat. The recent advancement in performance improvement of TEG and ORC has also been emphasized in the current work.

2 State of the Art Applications of Recovered Waste Heat

Most of the industrial thermal systems using conventional fossil fuels or renewable energy sources work with very low thermodynamic performance due to greater loss of heat through the exhaust and side wall. Circular strategy for waste heat

Fig. 1 Circular strategy for waste heat management



management (Fig. 1) can be a reliable option for recovery of waste heat from industry, automobiles and effective harnessing of renewable energy sources.

The cycle is diverted into two: one is recovery/storage of heat and another one is electricity generation. Recovered heat can be used for drying, other process heating or room air conditioning and generated electricity can be used for operating the electrical appliances. The exhaust heat from the dryer or other processes can be recirculated again to enhance the thermodynamic efficiency. Advanced materials like hybrid metal-polymer composite to be chosen in low-temperature heat exchanger tubes for enhancing the overall heat transfer coefficient, to reduce materials cost and withstand internal pressure [12].

2.1 Industrial Drying

Thermal drying is a process of removing the excess water content inside and outside of the products in the presence of hot drying medium, mostly air and steam. Drying is considered as the highly energy-intensive process for consuming 12–15% of total industrial energy usage in the form of heat energy and electrical energy [13]. Dryer shows relatively low thermal efficiency as 25–40% due to significant heat loss (15–40%) with the exhaust air and from dryer walls (3–10%) to the atmosphere [14]. Partial recovery of heat from exhaust air and utilizing for preheating the drying air can accomplish energy saving up to 30% in any type of industrial dryer [15]. Jokiniemi et al. [16] reported about 18% energy saving by incorporating a parallel

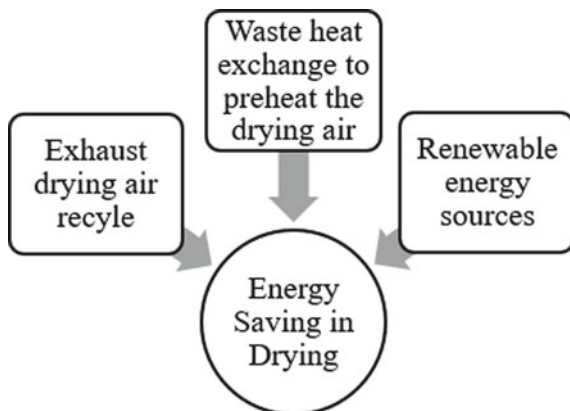


Fig. 2 Potential energy saving techniques in industrial drying

plate heat exchanger in the dryer exhaust which could be further improved by up to 40% by increasing the flow rate of hot drying air. Recirculation of exhaust air with a higher recirculation ratio exhibited a significant increase in thermodynamic efficiency and reduction of energy consumption in a spray dryer [17]. Potential energy saving techniques with efficient drying system are illustrated in Fig. 2.

2.2 Transport Sector

For moving an automobile, only 25% of the total consumed fuel energy is utilized. Except for the engine cooling, a major portion (40%) of the remaining energy is wasted through the exhaust gases in the form of heat (Fig. 3a). This exhaust heat energy can be recovered by converting into electrical energy and utilize for charging of the battery and operating the electronic devices, lightning or air conditioning system [9].

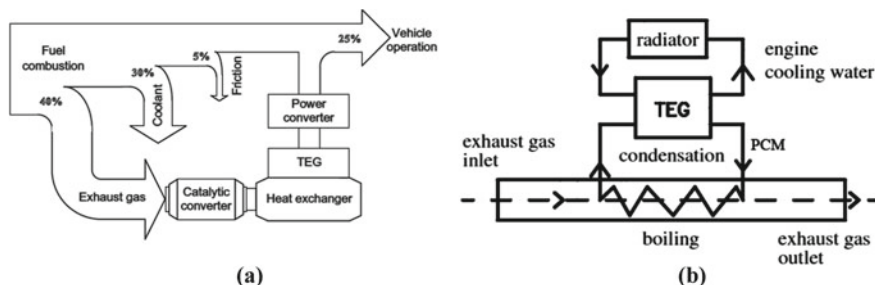


Fig. 3 **a** Typical energy path and waste heat recovery using TEG in gasoline fuelled IC engine [18], **b** schematic of PCM integrated TEG [19]

Lower convective heat transfer coefficient in the exhaust duct and backpressure of the engine are the main constraints in the efficient recovery of vehicles exhaust heat using TEG. By increasing the heat transfer coefficient and adjusting lower internal resistance, maximum TEG power and efficiency can be attained. By introducing the phase change materials (PCM) in the exhaust line (Fig. 3b), a remarkable improvement in output power and efficiency can be observed due to a higher heat transfer coefficient. Different materials with different phase change temperatures in cascade manner along the flow direction of exhaust gases can be used to overcome the problem of quality degradation of waste heat [19]. The integration of porous structure at the exhaust gas flow channel facilitates well-distributed flow and uniform temperature distributions which increases the power output and conversion efficiency. However, Choia et al. [20] reported that porosity should be greater than 0.32 to avoid backpressure in a diesel engine equipped with porous media assisted thermoelectric (Bi_2Te_3) modules. Saufi Sulaiman et al. [21] found that a hybrid TEG-heat pipe-heat sink system can effectively recover ultra-low waste heat (37 °C) from a proton exchange membrane fuel cell operated vehicle.

In order to obtain the desired performance and thermodynamic efficiency, precise control is necessary for on-board ORC of moving vehicle due to transient characteristics. Endo et al. [22] reported that at steady state speed (100 km/h) of a vehicle using ORC exhibited a net electric power output of 2.5 kW with improvement in a thermal efficiency of up to 32.7%. Zhang et al. [23] reported the performance of using R245fa and R134a-based dual loop ORC in diesel engine light vehicles. The output power increased by up to 16% in the maximum thermodynamic efficiency region while in the light loading region up to 43% enhancement was attained. By introducing ORC with the exhaust in the dual-fuel IC engine, energy conversion efficiency increased by 7%, while about an 18% reduction in NO_x and CO_2 emissions was accomplished [24].

Shipping is significantly responsible for greenhouse gas emissions. European Commission has imposed a stringent rule that each ship using European Union ports should report verified emission w.e.f. 2018. In heavy ships, the incinerator is generally used intermittently for combustion of the slime of heavy fossil oil. Installing a steam generator embedded with an incinerator is useful for producing electricity. Therefore, incinerators integrated with the boiler may be a good option for the TEG recovery system in shipping [25]. Aircraft engines release a huge amount of heat into the atmosphere. If this is recovered by converting into electricity using TEG, about a 1% reduction in aviation fuel consumption is possible [26].

2.3 Renewable Energy Sources

Renewable energy resources (solar, biomass, geothermal, etc.) increase the economic viability of TEG, ORC or heat pipe regardless of their lower efficiency as these energies are abundant, completely free of cost and waste. Sun is the ultimate source of energy that can be utilized by directly concentrating solar irradiation or by

using TEG. Combining thermal energy storage or TEG at the rear portion of the solar thermal or Photovoltaic (PV) panel can improve the overall efficiency by combined heat and power (CHP) manner. Recovery of heat from PV panel also increases the electrical efficiency of the PV cell by reducing its temperature. The selection of advanced thermoelectric materials for the low-temperature difference is a crucial factor as it was found that the gross electrical efficiency of the PV-TEG using Bi_2Te_3 as thermoelectric material was reduced and having toxicity [9]. To improve the effectiveness of PV-TEG system, the integration of heat pipe can be a futuristic approach. It was found that heat pipe integrated PV-TEG improved the power output by 1–2% [27]. Ahiska and Mamur [28] experimentally studied the influence of TEG with solar pond having salinity differences at the top and bottom layer. The temperature gradient between the top and bottom layer was recorded as 40–60 °C and produced the power of approximately 34 W.

Biomass, including solid waste, is a tremendous energy source in rural as well as urban areas. Wood is burned in rural kitchen and small-scale village industries like brick manufacturing, parboiling of paddy, etc., with only 7–9% thermal efficiency which is responsible for rapid deforestation. Moreover, fumes coming out from conventional oven is more toxic according to the World Health Organization. The integration of TEG or ORC can be a solution to overcome these problems along with rural off-grid electrification. Liu et al. [29] studied a micro-scale biomass-fired hybrid thermal power system with basic ORC using three different fluids. The electrical efficiency was reported as 8–14% with a gross efficiency of 80%.

3 Prospective Approaches for Performance Enhancement of TEG and ORC

The conversion efficiency of TEG and ORC mainly depends upon thermoelectric materials and working fluid, respectively.

3.1 Thermoelectric Materials of TEG

The performance of thermoelectric materials is measured by the thermoelectric figure of merit, $ZT = s^2\alpha T / (k_e + k_l)$, where, s , α , T , k_e and k_l represents Seebeck coefficient, electrical conductivity, average absolute temperature, electronic thermal and lattice thermal conductivity, respectively. The figure of merit should have greater value for higher conversion efficiency [30].

The materials having lower lattice thermal conductivity like glass and high electrical conductivity like crystal are considered as superior thermoelectric materials. Lattice thermal conductivity can be reduced by introducing phonon scattering that can be obtained by mixing of multiphase composites with low-dimensional materials

and using nanostructured materials. Several techniques are applied to enhance ZT such as doping, alloying, the formation of nanocomposites, nano inclusions, thin films and superlattices, etc. Alternatively, two-dimensional electron gas (2DEG) is used to improve the Seebeck coefficient and power density without reducing thermal conductivity. Bismuth-telluride (Bi_2Te_3)-based materials are mostly used for thermoelectric conversion due to flexibility in use for low to high-grade heat (-100 to 250 °C) with power factor ($s^2\alpha$) about $40\text{--}50 \mu\text{Wcm}^{-1} \text{K}^{-2}$ at ambient condition [31]. The presence of band gap increases the power factor and figure of merit of thermoelectric materials. Markov et al. [32] found that there are several semi-metals (TaAs_2 , $\text{Y}_2\text{Ir}_2\text{O}_7$, Cd_3As_2 , HgCr_2Se_4 , Pt_3Sn) with large asymmetry between conduction and valence band which also hold better thermoelectric properties without introducing band gap. Silicon-based nanocomposites are getting attention in research for better thermoelectric properties at room temperature due to a large difference in mean free path lengths between electrons and phonons. Transition metal dichalcogenides (MoS_2 , MoSe_2 , WS_2) is the potential thermoelectric materials due to their phonon transport properties, less covalent nature and low electronegativity which enhance the power factor. The lower electrical conductivity of MoS_2 can be significantly improved by doping of copper, vanadium, etc. [33].

3.2 Working Fluid of ORC

Saturated vapour profile of working fluids in a temperature-entropy diagram characterizes its applicability in a particular system with better possible efficiency and work output. The system performance and reliability also depend upon thermal-fluid properties and metallurgical aspects of working fluids like Jacob's number, the figure of merit, freezing point, specific volume, critical temperature, thermal stability, molecular weight, material compatibility, viscosity, cost, environmental impact, etc. [10]. For low-grade waste heat recovery, dry and isentropic fluids having lower latent heat of vaporization are preferable. The fluctuation in the temperature of the waste heat source is an obvious phenomenon. In this case, the use of mixture fluid having a different boiling point is advantageous rather than a single fluid because better heat interaction occurs even at fluctuating temperatures. There is a trend towards the use of the zeotropic mixture to curb the flammability, which otherwise reduces the net work output [11]. For low-temperature waste heat recovery, the optimal working fluids in terms of net power output, thermodynamic efficiency and environmental safety are listed in Table 1.

Table 1 The optimal working fluids for low-temperature sources

Waste heat temperature (°C)	Working fluids	References
50–60	R23	[34]
65–70	Ethane	[34]
70–85	R365mfc, isobutane	[10]
75–90	R7146	[34]
≥ 80	R227ea	[35]
<90	R134a, R152a, R600, R600a, R290	[36]
90–100	R143a, R218	[10, 37]
~ 100	Novec649	[38]

4 Conclusion

The paper presents an overview of low-grade waste heat sources viz. industrial drying, solar, biomass, automobile, etc., and its recovery by direct heating or conversion technologies (TEG, ORC). The possible net power output, power density and efficient energy conversion are greatly influenced by the working conditions, particularly waste heat temperature and consistent flow rate. Circular waste heat management strategy can be an effective solution for increasing the efficiency of thermal systems by maximum utilization of recovered heat in drying and other process heating applications, transportation, etc. TEG could play a significant role in energy conservation if this is used on a macro-scale. However, advanced materials with a higher thermoelectric figure of merit (at least ≥ 3) over a wide range of temperatures needed to be explored to become a competitive technology. ORC with a binary mixture of working fluid has better prospects for reducing thermodynamic irreversibility. Binary mixture has the capability of evaporating and condensing over a wide range of temperature, which in turn inevitably reduces the exergy destruction. However, the selection of mixture composition with optimum proportion necessitates further research. Bimetallic thermally-regenerative ammonia-based flow battery and other thermo-electrochemical systems may be another future prospect for harvesting low-grade thermal energy to overcome the limitations of TEG and ORC such as low power density, lower thermoelectric conversion efficiency and higher operating cost.

References

1. Wise M, Calvin K, Thomson A, Clarke L, Bond-Lamberty B, Sands R, Smith SJ, Janetos A, Edmonds J (2009) Implications of limiting CO₂ concentrations for land use and energy. *Science* 324(5931):1183–1186
2. Xu ZY, Wang RZ, Yang C (2019) Perspectives for low-temperature waste heat recovery. *Energy* 176:1037–1043
3. Johnson I, Choate WT, Davidson A (2008) Waste heat recovery-technology and opportunities in US industry. BCS, Inc., Laurel, MD (United States)

4. Thermopedia website. file:///G:/paper%20writing/Waste%20heat%20recovery/WASTE%20HEAT%20RECOVERY.html. Last accessed 30 Mar 2020
5. Forman C, Muritala IK, Pardemann R, Meyer B (2016) Estimating the global waste heat potential. *Renew Sustain Energy Rev* 57:1568–1579
6. Mumith J-A, Makatsoris C, Karayiannis TG (2014) Design of a thermoacoustic heat engine for low temperature waste heat recovery in food manufacturing: a thermoacoustic device for heat recovery. *Appl Therm Eng* 65(1–2):588–596
7. Delpech B, Milani M, Montorsi L, Boscardin D, Chauhan A, Almahmoud S, Axcell B, Jouhara H (2018) Energy efficiency enhancement and waste heat recovery in industrial processes by means of the heat pipe technology: case of the ceramic industry. *Energy* 158:656–665
8. Jouhara H, Khordehghah N, Almahmoud S, Delpech B, Chauhan A, Tassou SA (2018) Waste heat recovery technologies and applications. *Therm Sci Eng Prog* 6:268–289
9. Champier D (2017) Thermoelectric generators: a review of applications. *Energy Convers Manag* 140:167–181
10. Rahbar K, Mahmoud S, Al-Dadah RK, Moazami N, Mirhadizadeh SA (2017) Review of organic rankine cycle for small-scale applications. *Energy Convers Manag* 134:135–155
11. Mahmoudi A, Fazli M, Morad MR (2018) A recent review of waste heat recovery by organic rankine cycle. *Appl Therm Eng* 143:660–675
12. Rajagopal MC, Chang HC, Mana T, Kuntumalla G, Meng Y, Sundar S, Zhao H, Salapaka S, Shao C, Ferreira P, Miljkovic N, Sinha S (2019) Materials-to-device design of hybrid metal-polymer heat exchanger tubes for low temperature waste heat recovery. *Int J Heat Mass Transf* 143:118497
13. Kudra T (2004) Energy aspects in drying. *Drying Technol* 22:917–932
14. Danilov OL, Leontchik BI (1986) Energy economic in thermal drying. *Energoatomizdat, Moscow, Russia*
15. Moraitis CS, Akritidis CB (1997) Energy saving in industrial drying plants by partial recovery of the latent heat of the exhaust air. *Drying Technol* 15(6–8):1931–1940
16. Jokiniemi T, Hautala M, Oksanen T, Ahokas J (2016) Parallel plate heat exchanger for heat energy recovery in a farm grain dryer. *Drying Technol* 34(5):547–556
17. Golman B, Julklang W (2014) Analysis of heat recovery from a spray dryer by recirculation of exhaust air. *Energy Convers Manag* 88:641–649
18. Yu C, Chau KT (2009) Thermoelectric automotive waste heat energy recovery using maximum power point tracking. *Energy Convers Manag* 50(6):1506–1512
19. Wang Y, Dai C, Wang S (2013) Theoretical analysis of a thermoelectric generator using exhaust gas of vehicles as heat source. *Appl Energy* 112:1171–1180
20. Choia Y, Negashb A, Kimc TY (2019) Waste heat recovery of diesel engine using porous medium-assisted thermoelectric generator equipped with customized thermoelectric modules. *Energy Convers Manag* 197:111902
21. Saufi Sulaiman M, Singh B, Mohamed WANW (2019) Experimental and theoretical study of thermoelectric generator waste heat recovery model for an ultra-low temperature PEM fuel cell powered vehicle. *Energy* 179:628–646
22. Endo T, Kawajiri S, Kojima Y, Takahashi K (2007) Study on maximizing exergy in automotive engines. *SAE Int* 116:347–356
23. Zhang HG, Wang EH, Fan BY (2013) A performance analysis of a novel system of a dual loop bottoming organic rankine cycle (ORC) with a light-duty diesel engine. *Appl Energy* 102:1504–1513
24. Srinivasan K, Mago P, Krishnan S (2010) Analysis of exhaust waste heat recovery from a dual fuel low temperature combustion engine using an organic rankine cycle. *Energy* 35:2387–2399
25. Kristiansen N, Snyder G, Nielsen H, Rosendahl L (2012) Waste heat recovery from a marine waste incinerator using a thermoelectric generator. *J Electron Mater* 41(6):1024–1029

26. Kousksou T, Bedecarrats JP, Champier D, Pignolet P, Brillet C (2011) Numerical study of thermoelectric power generation for an helicopter conical nozzle. *J Power Sources* 196(8): 4026–4032
27. Makki A (2017) Innovative heat pipe-based photovoltaic/thermoelectric (PV/TEG) generation system. PhD Thesis, The University of Nottingham, UK
28. Ahiska R, Mamur H (2014) A review: thermoelectric generators in renewable energy. *Int J Renew Energy Res* 4(1)
29. Liu H, Shao Y, Li J (2011) A biomass-fired micro-scale CHP system with organic rankine cycle (ORC)—thermodynamic modelling studies. *Biomass Bioenerg* 35(9):3985–3994
30. Nandihalli N, Wijethunge D, Kim K, Kim J, Gayner C (2019) High efficient nanostructured $\text{PbSe}_{0.5}\text{Te}_{0.5}$ exhibiting broad figure-of-merit plateau. *J Alloy Compd* 785:862–870
31. Ravindra NM, Jariwala B, Bañobre A, Maske A (2019) Thermoelectrics: fundamentals, materials selection, properties, and performance. Springer Nature, Singapore
32. Markov M, Hu X, Liu HC, Liu N, Poon SJ, Esfarjani K (2018) Semi-metals as potential thermoelectric materials. *Nature Sci Report* 8:9876
33. Joseph D, Navaneethan M, Abinaya R, Harish S, Archana J, Ponnusamy S, Hara K, Hayakawa Y (2019) Unveiling the thermoelectric performance of Cu-doped MoS_2 layers for low grade waste heat recovery. *Appl Surf Sci* 144066
34. Hærvig J, Sørensen K, Condra TJ (2016) Guidelines for optimal selection of working fluid for an organic rankine cycle in relation to waste heat recovery. *Energy* 96:592–602
35. Lakew AA, Bolland O (2010) Working fluids for low-temperature heat source. *Appl Therm Eng* 30(10):1262–1268
36. Tchanche BF, Papadakis G, Lambrinos G, Frangoudakis A (2009) Fluid selection for a low-temperature solar organic rankine cycle. *Appl Therm Eng* 29(11–12):2468–2476
37. Hsieh J-C, Fu B-R, Wang T-W, Cheng Y, Lee Y-R, Chang J-C (2017) Design and preliminary results of a 20-kW transcritical organic rankine cycle with a screw expander for low-grade waste heat recovery. *Appl Therm Eng* 110:1120–1127
38. Cataldo F, Mastrullo R, Mauro AW, Vanoli GP (2014) Fluid selection of organic rankine cycle for low-temperature waste heat recovery based on thermal optimization. *Energy* 72:159–167

Generation of Temperature Profile by Artificial Neural Network in Flow of Non-Newtonian Third Grade Fluid Through Two Parallel Plates Under Noisy Data



Vijay Kumar Mishra, Auritro Samanta, Sumanta Chaudhuri,
and Daya Shankar

Abstract Artificial neural network (ANN) is explored to generate temperature profile for a non-Newtonian third grade fluid flowing through two parallel plates. Both the plates are supplied with a constant and uniform heat flux. A semi-analytical approach (Least Square Method LSM) is used to solve the governing equations under with required boundary conditions. The velocity and the temperature profile obtained from the LSM are perturbed by different levels of noise to mimic error in measurement. Thus, velocity and temperature profiles are fed into ANN for training. In ANN, scaled conjugate gradient (SCG) algorithm is used for training the neurons. Once training of ANN is completed, an unknown velocity profile is fed as input, and the temperature profile is obtained as output. The temperature profile obtained from ANN found to be in very good agreement with the LSM results. This approach is suitable to solve the present problem with small alterations, and removing the need to solve such problems by LSM. This leads to time saving and useful for industries involved in non-Newtonian fluid like polymer, paints, blood, grease, etc.

Keywords Non-Newtonian fluid · Artificial neural network · Scaled conjugate gradient · Noisy data · Temperature generation

V. K. Mishra (✉) · A. Samanta · S. Chaudhuri
School of Mechanical Engineering, KIIT Deemed to be University, Bhubaneswar 751024,
India
e-mail: mishra.vdm@gmail.com

A. Samanta
e-mail: 1802230@kiit.ac.in

S. Chaudhuri
e-mail: sumanta.chaudhurifme@kiit.ac.in

D. Shankar
Department of Mechanical Engineering, ICFAI University Tripura, Agartala, India
e-mail: dayashankar@iutripura.edu.in

Nomenclature

A	Third grade fluid parameter
A_c	Cross sectional area
A_1, A_2, A_3, A_n	Kinematic tensor
a_0, a_2, a_4, a_6, a_8	Constants
Br	Brinkman number
$b_0, b_2, b_4, b_6, b_8, b_{10}, b_{12}$	Constants
c_p	Specific heat at constant pressure
c_1, c_2	Constants
c_i	i th constant
d	Differential operator
d/dt	Material derivative
f	Body force per unit volume
g	Function
h	Half depth of channel
k_{th}	Thermal conductivity of the fluid
L	Length of the channel
l_1, l_2	Constants
N	Non-dimensional pressure gradient
Nu	Nusselt number
p^*	Dimensional pressure
Q	Dimensional flow rate
q	Heat flux ratio
q_1, q_2	Heat fluxes at lower and upper walls
R	Residual
S	Sum of square of residual
T^*	Dimensional temperature
T_m^*	Bulk mean temperature
$T_{w_1}^*$	Temperature of the lower wall
u	Non-dimensional velocity along axial direction
u_N	Non-dimensional velocity for Newtonian fluid
u^*	Dimensional velocity along axial direction
u_0	Average velocity
V^*	Velocity vector
v, \tilde{v}	Functions
x, y, z	Non-dimensional coordinates
x^*, y^*, z^*	Dimensional coordinates
w_i	i th weight function

Greek symbols

α_1, α_2	Material constants
β	Constant
$\beta_1, \beta_2, \beta_3$	Material constants

ρ	Density of the fluid
μ	Dynamic viscosity of the fluid
θ	Non-dimensional temperature
θ_N	Non-dimensional temperature for Newtonian fluid
Φ_i	Base function
τ	Stress

Abbreviations

ANN	Artificial neural network
LSM	Least square method
SCG	Scaled conjugate gradient

1 Introduction

ANN is very novel approach to solve complicated engineering problems [1–3]. It is a computational way to simulate the biological process in the human brain. It consists of, simple but highly interconnected processing elements called neurons are present in series. The neurons are very powerful device when interconnected and are capable of approximating any arbitrary functions. This capability of universal approximation makes the neural networks a useful tool for handling nonlinear problems such as: to solve third grade fluid problems. Various industries need proper solution of problems involving third grade for proper functioning of different devices [4–7]. Heat exchanger, mixer, pump, etc., handling thick slurries in industries dealing with polymer solutions, blood, paints, certain oils, and greases, etc. Such problems are very complicated, and in some situations, exact nature of the relation between input and out variables is also not known mathematically. Because of these limitations, analytical and computational approaches are not suitable to handle such problems. In ANN, lots of data with input and target pair are used for training of neurons. ANN generates a mapping between the input and target variables. Once ANN is trained, input variable corresponding to any new case can be fed to get the output.

Here, an ANN approach is explored for solving a non-Newtonian third grade fluid problem. The governing equations are solved by semi-analytical approach least square method (LSM) [8, 9]. Appropriate boundary conditions are used in the LSM. Once velocity and temperature profiles are obtained by LSM; perturbation is induced to mimic experimental measurements. The pairs of velocity and the temperature profiles are fed into ANN for training purposes. In ANN, SCG algorithm is used for training the neurons. After training of ANN, a new velocity profile is supplied (not part of the training data) as input, and temperature profile is obtained as output. Temperature profiles for different levels of noise (error in input data) in input data are obtained and compared. This approach is useful to solve small

variants of the present problem by ANN model, without needing to solve the new problem by complicated LSM method. Thus, lots of time and computing resources can be saved by ANN. So far, use of LSM in conjunction with ANN, is not reported in open literature, for solving a non-Newtonian fluid flow problem.

2 Formulation

Two parallel plates with a third grade fluid flowing through them is shown schematically in Fig. 1a. Both the plates are supplied with a constant and uniform heat flux but different in magnitude. Dimension in flow direction is very large as compared to other two dimensions; i.e., length (L) is much larger than height (H) and width (W). The analysis is done with constant fluid properties and following assumptions for fluid flow: laminar, incompressible, steady, fully developed (hydro-dynamically and thermally).

The governing equations are summarized below:

Continuity Equation:

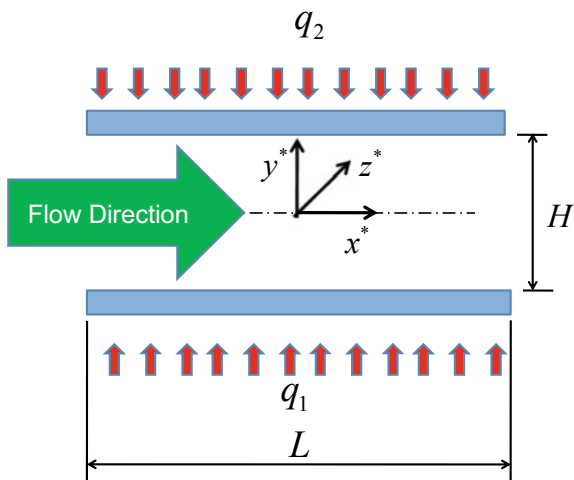
$$\nabla \cdot V^* = 0 \tag{1}$$

where V^* is the velocity vector.

Momentum Equation:

$$\rho \frac{dV^*}{dt} = \nabla \cdot \tau + f \tag{2}$$

Fig. 1 Schematic of third grade fluid flowing through two parallel plates



Here, body forces are neglected.

For Newtonian fluids, stress tensor varies linearly with the strain rate tensor. But in case of non-Newtonian fluid, stress tensor varies non-linearly with the change in strain rate tensor. In case of a third grade fluid, the relation between stress tensor and strain rate tensor can be written as

$$\tau = -pI + \mu A_1 + \alpha_1 A_2 + \alpha_2 A_1^2 + \beta_1 A_3 + \beta_2 (A_1 A_2 + A_2 A_1) + \beta_3 (\text{tr} A_1^2) A_1 \quad (3)$$

$$A_1 = (\text{grad} V^*) + (\text{grad} V^*)^{\text{Transpose}} \quad (4)$$

$$A_n = \frac{dA_{n-1}}{dt} + A_{n-1}(\text{grad} V^*) + (\text{grad} V^*)^{\text{Transpose}} A_{n-1}, \quad n = 1, 2, 3 \quad (5)$$

Energy Equation:

$$\rho c_p \frac{dT^*}{dt} = \tau : \text{grad}(V^*) - \nabla \cdot (-k_{th} \nabla T^*) \quad (6)$$

Because of the assumption of hydro-dynamically developed flow, the velocity vector can be simplified as:

$$v^* = [u^*(y^*), 0, 0] \quad (7)$$

After substitution of above velocity vector into momentum conservation equation, we get simplified form of momentum conservation equation:

$$\frac{\partial p^*}{\partial x^*} = \mu \frac{d^2 u^*}{dy^{*2}} + 2(\beta_2 + \beta_3) \frac{d}{dy^*} \left(\frac{du^*}{dy^*} \right)^3 \quad (8)$$

$$\frac{\partial p^*}{\partial y^*} = (2\alpha_1 + \alpha_2) \frac{d}{dy^*} \left(\frac{du^*}{dy^*} \right)^2 \quad (9)$$

$$\frac{\partial p^*}{\partial z^*} = 0 \quad (10)$$

Similarly, after the substitution of assumed velocity profile in energy conservation equation, we get simplified energy equation as:

$$\rho c_p u^* \frac{\partial T^*}{\partial x^*} = k_{th} \left(\frac{\partial^2 T^*}{\partial x^{*2}} + \frac{\partial^2 T^*}{\partial y^{*2}} \right) + \mu \left(\frac{du^*}{dy^*} \right)^2 + 2(\beta_2 + \beta_3) \left(\frac{du^*}{dy^*} \right)^4 \quad (11)$$

Here, thermal conductivity of the third grade fluid is represented by k_{th} and viscous dissipation is represented by second term. The parameters of third grade

fluid leads to the third term in Eq. (11). Substitute of zero values for β_2 and β_3 in Eq. (11) will the results for Newtonian fluid in the same problem. Under thermally developed condition, the temperature profile can be non-dimensionalized as:

$$\theta = \frac{T^* - T_{w1}^*}{T_m^* - T_{w1}^*}$$

Here, the temperature of bulk fluid and the upper plate is represented by T_m^* and T_{w1}^* , respectively. For constant and uniform heat flux through the wall give rise to following expressions:

$$\frac{\partial T^*}{\partial x^*} = \frac{dT_m^*}{dx^*} = \text{constant}, \quad \frac{\partial^2 T^*}{\partial x^{*2}} = 0 \quad (12)$$

By substituting the relations from Eq. (12) into Eq. (11), we get modified form for energy equation

$$\rho c_p u^* \frac{\partial T^*}{\partial x^*} = k_{th} \left(\frac{\partial^2 T^*}{\partial y^{*2}} \right) + \mu \left(\frac{du^*}{dy^*} \right)^2 + 2(\beta_2 + \beta_3) \left(\frac{du^*}{dy^*} \right)^4 \quad (13)$$

Boundary conditions: At the surface of both the plates, no-slip boundary conditions are used

$$u^*(-h) = 0, \quad u^*(h) = 0 \quad (14)$$

Because of constant and uniform heat flux on both the plates, the boundary conditions for energy equation can be written as

$$k_{th} \left(\frac{\partial T^*}{\partial y^*} \right)_{-h} = \mp q_1, \quad k_{th} \left(\frac{\partial T^*}{\partial y^*} \right)_h = \pm q_2 \quad (15)$$

A non-dimensional temperature scale is considered, because of the absence of the knowledge of the plate temperature and is expressed as follows:

$$\theta = \frac{T^* - T_{w1}^*}{q_1 h / k_{th}} \quad (16)$$

Following non-dimensional velocity and distance are used in momentum equation:

$$u = \frac{u^*}{u_0}, \quad y = \frac{y^*}{h} \quad (17)$$

After non-dimensionalization, the momentum and energy equation can be written as:

$$\frac{d^2u}{dy^2} + 6A \left(\frac{du}{dy}\right)^2 \frac{d^2u}{dy^2} = N \tag{18}$$

$$\beta u = \frac{d^2\theta}{dy^2} + Br \left(\frac{du}{dy}\right)^2 + 2ABr \left(\frac{du}{dy}\right)^4 \tag{19}$$

$$A = \frac{\beta_2 + \beta_3}{\mu} \left(\frac{u_0}{h}\right)^2, \quad Br = \frac{\mu u_0^2}{q_1 h}, \quad u_0 = \frac{1}{N} \frac{dp^*}{dx^*} \frac{h^2}{\mu}, \quad \beta = \frac{\rho c_p u_0}{q_1} \frac{dT^*}{dx^*} \tag{20}$$

The non-dimensional velocity in the momentum equation has following boundary conditions:

$$u(-1) = 0, \quad u(1) = 0 \tag{21}$$

In non-dimensional form, the boundary conditions for energy equation, becomes:

$$\theta(-1) = 0 \tag{22}$$

$$\frac{d\theta}{dx}(-1) = \mp 1 \tag{23}$$

$$\frac{d\theta}{dx}(1) = \pm \frac{q_2}{q_1} = q \tag{24}$$

It is to be noted here, Eqs. (18) and (19) are highly non-linear and difficult to solve. If any further complicated cases need to be solved, the problem will become even more difficult to handle by analytical or computational methods. The ANN model comes very handy in these types of situations. ANN for any simple problem can be trained by getting data from any means such as: experimental, analytical or computational. Once ANN is trained for a simple problem, it can be used to get the results for some complicated problems also.

2.1 Solution by LSM

In LSM, any function $v(y)$ can be differentiated to give $g(y)$. The function $v(y)$ can be approximated by combination of linearly independent base function ϕ_i , as:

$$v \cong \tilde{v} = \sum_{i=1}^n c_i \phi_i \quad (25)$$

Now, residue can be calculated as:

$$R(y) = D\{\tilde{v}(y)\} - g(y) \neq 0 \quad (26)$$

Then, the average residue over the domain is made to zero.

$$\int_x R(y)w_i(y)dy = 0; \quad i = 0, 2, 3, \dots n \quad (27)$$

Weight becomes equal to residue in LSM, thus, Eq. (27) becomes,

$$S = \int_y R(y)R(y)dy = \int_y R^2 dy \quad (28)$$

S needs to be minimized as

$$\frac{\partial S}{\partial c_i} = 2 \int_y R(y) \frac{\partial R}{\partial c_i} dy = 0 \quad (29)$$

The relevant governing equations together with the boundary conditions are solved by semi-analytical method LSM.

3 Results and Discussions

The solution of LSM is validated with the exact solution available in the literature [10]. The validation is presented in Fig. 2a, the velocity profile from both the method matches well. Two different values of third grade fluid parameter are considered here for validation purpose. In the present solution of LSM, the equivalent results for Newtonian fluid are also obtained and validated in Fig. 2b.

Solving the problem by LSM constitutes the first part of the problem. In the next part, ANN is used to solve the problem. It is very useful tool for solving problems where the relationship between the input variable is not known or very complicated such as highly non-linear, etc. The schematic of the ANN model used in the solution of present work is shown in Fig. 3. In present problem, the velocity profile and the temperature profile (obtained from LSM) are used in the training of ANN.

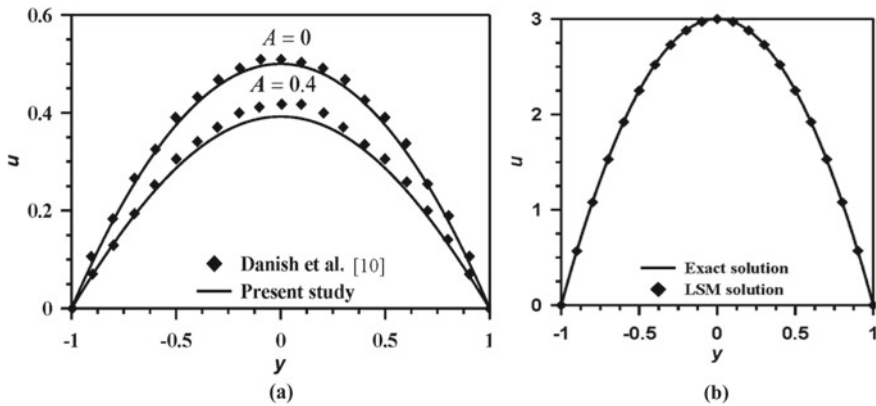


Fig. 2 Validation of the results from LSM with the exact solution available in literature [10]. **a** Velocity profile for third grade fluid for two different values of third grade fluid parameter A , **b** velocity profiles for equivalent conditions for Newtonian fluid

The data used in the ANN is perturbed by different levels (0, 0.1, 0.5, 1, 2%) to mimic error in measurement of data. This data with error/noise is used to train another ANN model. Once ANN is trained for different cases, an unknown velocity profile is fed into it, and the temperature profile is obtained as output. In the ANN, SCG algorithm is used for training of neurons. The input data used in the training of ANN consists of velocity and the temperature profiles for various values of third grade fluid parameter A . Temperature profiles corresponding to different levels of error/noise in the input data is generated by ANN. When noise of 0.1% is used in the input data (velocity and temperature profiles for 14 different values of third grade fluid parameter A), results of the ANN model are presented in the below section. For other levels of noise, only a consolidated temperature plot and comparative table is given. In Fig. 4, histogram of the input data in the training of the ANN is shown. Most of the data in the zero error line indicates proper learning of the ANN. While significant amount of data gradually spread on both sides of the zero error line indicates that the ANN is not over trained, and it can handle the cases for which input data is not given.

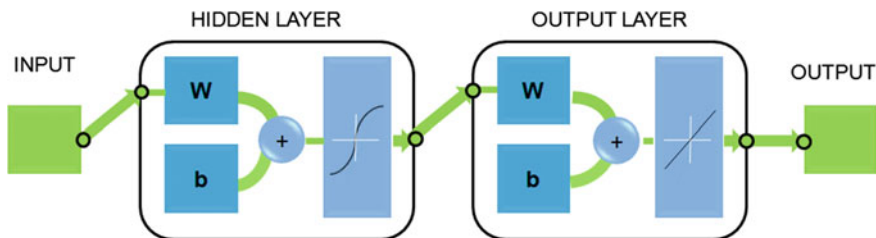
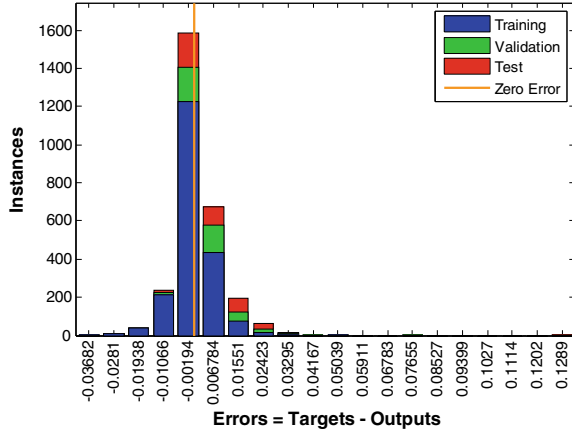


Fig. 3 ANN model for generation of temperature profile under noisy data

Fig. 4 Histogram of input data in ANN model with SCG algorithm and 0.1% noise



The performance of the training stage is shown in Fig. 5. It is observed that during the training, convergence reaches at 244th iteration. This indicates SCG algorithm is suitable for training of neurons, as the convergence is neither too early nor too delayed. If best validation occurs very late, it indicates over fitting case. Whereas, early occurring of the same, indicates under fitting. The robustness of ANN model is very necessary for good results. The regression analysis of the present ANN model is shown in Fig. 6. The near one values or regression coefficient indicates the ANN model is suitable to get accurate results. The temperature profile obtained for input data corresponding to 0.1% noise is compared with the solution of LSM in Fig. 7. The overall pattern of the ANN generated temperature profile follows the trend of the LSM solution.

Fig. 5 Performance curves in present ANN model with SCG algorithm and 0.1% noise

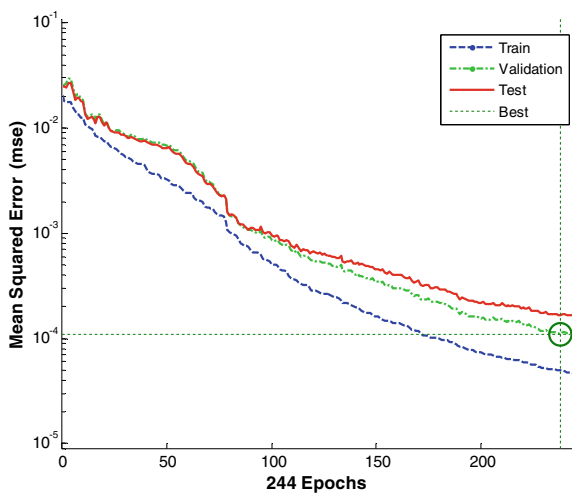


Fig. 6 Regression analysis of the ANN model

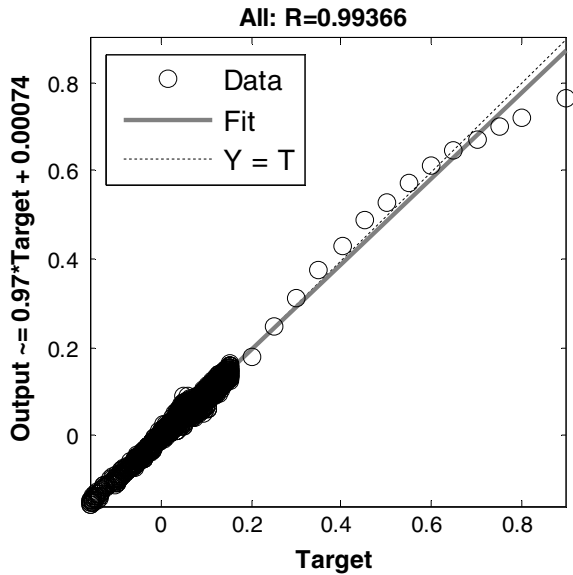
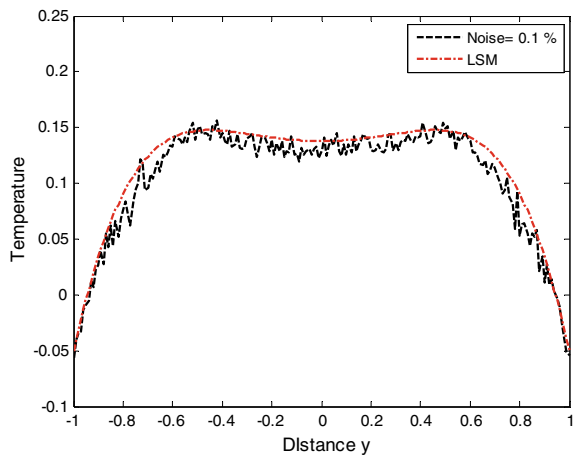


Fig. 7 Comparison of temperature profile obtained from the ANN model with that obtained from LSM (semi-analytical) for 0.1% noise



The zig-zag nature of the ANN generated temperature profile depends on various factors such as: number of test cases, number of neurons, training algorithm, division of data among training, validation, and testing [11, 12].

Temperature profiles for different levels of noise are compared with the LSM solution and are shown in Fig. 8. Except for 2% noise, all other ANN generated temperature profile follow the trend of LSM generated temperature. For 2% noise, the zig-zag is very high. The third grade fluid parameter A is also generated by the present ANN model. For $A = 0.85$, the ANN generates value of A for different cases of noise and is presented in Table 1. Up to 0.5% noise, present ANN model gives

Fig. 8 Comparison of ANN generated temperature with LSM generated temperature, for different noise levels

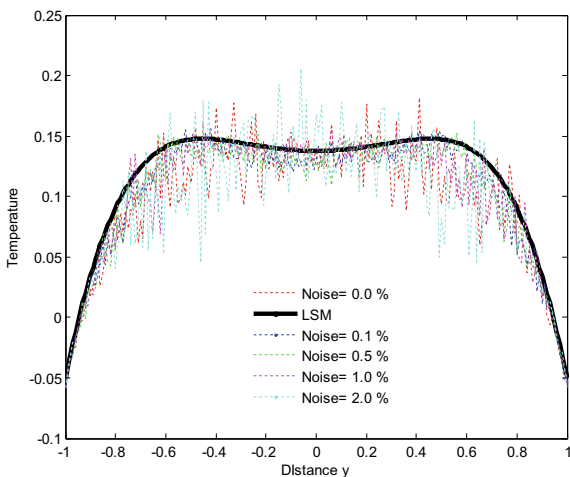


Table 1 Comparison of estimation of A under different levels of noise

S. No.	% Error in input	Exact value A_{act}	Estimated value A_{est}	% Error in estimation
1	0.0	0.85	0.866	1.8824
2	0.1	0.85	0.8733	2.7412
3	0.5	0.85	0.8288	2.4941
4	1.0	0.85	0.8065	5.1176
5	2.0	0.85	0.8707	2.4353

good result, after that the error in estimation increases. Better results for higher levels of noise can be obtained by varying the attributes of ANN such as: number of neurons, training algorithm, number of input cases, etc.

4 Conclusions

ANN is explored to solve complicated problem involving third grade fluid and with noisy data. LSM is a semi-analytical method which is used to solve the equations governing flow of third grade fluid through two parallel plates. The temperature and the velocity profiles for different values of third grade fluid parameter (A) are obtained by LSM, and this constitutes the input data for the ANN. The input data is perturbed by different levels (0, 0.1, 0.5, 1, 2%) of noise to mimic error in measurement. These input data are used for training the ANN. In the training stage, SCG algorithm is used for training of neurons. Once ANN is trained, an unknown velocity profile is fed as input, and the corresponding temperature profile is

obtained as output. The temperature profiles for different levels of noise is obtained by ANN and is compared with those obtained by LSM. Except for very high level of noise (2%), the temperature obtained by ANN follows very good trend with that obtained by LSM. The third grade fluid parameter A is also generated by ANN for different levels of noise. The value of A obtained by ANN is found to be highly accurate when noise is kept below 1%. Since ANN is able to give highly accurate temperature profiles for unknown velocity profiles, it can also be used for small variants of the present problem. This will lead to solve such problems without LSM, thus saving time and computational effort.

References

1. Dumek V, Druckmuller M, Raudensk, Woodbury KA (1993) Novel approaches to the ICHP: neural networks and expert systems, inverse problems in engineering: theory and practice. In: Proceedings of the first international conference on inverse problems in engineering, ASME no. I00357, pp 275–282
2. Jambunathan K, Hartle S, Ashforth-Frost S, Fontama VN (1996) Evaluating convective heat transfer coefficients using neural networks. *Int J Heat Mass Transf* 39:2329–2332
3. Sablani SS (2001) A neural network approach for non-iterative calculation of heat transfer coefficient in fluid-particle systems. *Chem Eng Process* 40:363–369
4. Al Mukahal FHH, Wilson SK, Duffy BR (2015) A rivulet of a power-law fluid with constant width draining down a slowly varying substrate. *J Non-Newtonian Fluid Mech* 224:30–39
5. Jalil M, Asghar S (2013) Flow of power-law fluid over a stretching surface: a lie group analysis. *Int J Non-Linear Mech* 48:65–71
6. Tso CP, Sheela Francisca J, Hung YM (2010) Viscous dissipation effects of power-law fluid flow within parallel plates with constant heat flux. *J Non-Newtonian Fluid Mech* 165:625–630
7. Hatami M, Ganji DD (2013) Heat transfer and flow analysis for SA–TiO₂ non-Newtonian nano fluid passing through the porous media between two co-axial cylinders. *J Mol Liq* 188:155–161
8. Pourmehran O, Rahimi-Gorji M, Gorji-Bandpy M, Ganji DD (2015) Analytical investigation of squeezing unsteady nanofluid flow between parallel plates by LSM and CM. *Alexandria Eng J* 54:17–26
9. Fakour M, Vahabzadhe A, Ganji DD, Hatami M (2015) Analytical study of micro polar fluid flow and heat transfer in a channel with permeable walls. *J Mol Liq* 204:198–204
10. Danish M, Kumar S, Kumar S (2012) Exact analytical solutions for the Poiseuille and Couette-Poiseuille flow of third grade fluid between parallel plates. *Commun Non Linear Sci* 17:1089–1097
11. Amani M, Amani P, Bahiraei M, Wongwises S (2019) Prediction of hydrothermal behavior of a non-Newtonian nanofluid in a square channel by modeling of thermophysical properties using neural network. *J Therm Anal Calorim* 135:901–910. <https://doi.org/10.1007/s10973-018-7303-y>
12. Hemmat Esfe M, Bahiraei M, Mahian O (2018) Experimental study for developing an accurate model to predict viscosity of CuO–ethylene glycol nanofluid using genetic algorithm based neural network. *Powder Technol* 338:383–390. <https://doi.org/10.1016/j.powtec.2018.07.013>

Impact of Thermal Contact Resistance on Thermal-Hydraulic Characteristics of Double Fin-and-Tube Heat Exchanger



Shobhana Singh  and Navin Kumar Dwivedi 

Abstract In the present work, the thermal contact resistance in a double fin-and-tube heat exchanger is investigated using multiphysics numerical approach. A three-dimensional (3D) Computational Fluid Dynamic (CFD) model is constructed in commercial software COMSOL Multiphysics® by coupling steady-state conjugate heat transfer and turbulent fluid flow. The impact of contact resistance at the fin and tube interface is analyzed by quantitatively evaluating the thermal-hydraulic characteristics. It is found that contact resistance of 3.3×10^6 Km²/W can reduce the overall performance by approximately 6% when compared without thermal resistance at the contact interface. The developed model can predict the effectiveness of the fin-and-tube heat exchanger design with or without thermal contact resistances. Furthermore, the model can be employed to improve the overall heat exchanger performance used in various applications.

Keywords Heat exchanger · Thermal contact resistance · Contact interface · Conjugate heat transfer

Nomenclature

Symbols

- A_t Available heat transfer surface area [m²]
 C_p Specific heat capacity [J/kg K]
 D_h Hydraulic diameter [m]
 d Thickness of a thin resistive layer [m]
 f Flow friction factor [-]

S. Singh (✉)

Department of Mechanical Engineering, Indian Institute of Technology Jodhpur, Rajasthan 342037, India

e-mail: shobhana@iitj.ac.in

N. K. Dwivedi

Institut Für Weltraumforschung, Österreichische Akademie der Wissenschaften, 8042 Graz, Austria

e-mail: navin.dwivedi@oeaw.ac.at

© The Author(s), under exclusive license to Springer Nature Singapore Pte Ltd. 2021

B. S. Sikarwar et al. (eds.), *Advances in Fluid and Thermal Engineering*,

Lecture Notes in Mechanical Engineering,

https://doi.org/10.1007/978-981-16-0159-0_17

F	Body force vector [N/m ³]
<i>h</i>	Convective heat transfer coefficient [W/m ² K]
<i>j</i>	Colburn <i>j</i> -factor [-]
<i>k</i>	Thermal conductivity [W/m K]
<i>k_e</i>	Turbulent kinetic energy [m ² /s ²]
<i>K_{pl}</i>	Pressure loss coefficient [-]
<i>L</i>	Length [m]
Nu	Nusselt number [-]
<i>p</i>	Pressure [Pa]
Δp	Pressure difference across gas domain [Pa]
Pr	Prandtl number [-]
q	Heat flux vector [W/m ²]
<i>Q_t</i>	Total power exchanged [W]
Q	Heat source or sink [W/m ³]
Re	Average Reynolds number [-]
<i>T</i>	Temperature [K]
ΔT	Log mean temperature difference [K]
<i>u</i>	Flow velocity at the inlet [m/s]
u	Average velocity vector [m/s]
<i>U</i>	Overall heat transfer coefficient [W/m ² K]
ρ	Density [kg/m ³]
μ	Dynamic viscosity [Pa · s]
ε	Turbulent dissipation rate [m ² /s ³]

Subscripts

<i>d</i>	Downside
<i>g</i>	Gas or gas domain
in	Inlet
rl	Resistive layer
<i>u</i>	Upside
<i>w</i>	Inner tube wall

1 Introduction

Extended surface heat exchangers are widely used in many commercial heat processing applications, for example, waste heat recovery engine exhaust, power generation plants, heating and cooling, etc. However, thermal performance of these heat exchangers is typically limited by the heat transfer resistance on the gas flow side [1]. Fins are used to minimize this problem by enhancing the overall heat transfer surface area; however, they require a careful designing as well as perfect thermal contact with tubes in order to have good thermal performance. Depending

on the type of application, different methods are used to attach fins and tubes. Impaired or rough contact can cause high penalty in loss of heat transfer capacity or pressure. Therefore, ensuring a perfect thermal contact between fins and tubes at extreme temperature and fluid flow environments is critical to deliver the desired system performance.

Research and development on fin-and-tube heat exchangers have gained tremendous attention over the past few decades. Investigations ranging from development of new designs to improvement of the existing ones are available [2–12]. Contemporary development methods are focusing more on the numerical methods such as using CFD to describe the thermal-hydraulic behavior. Numerous experimental and numerical studies on measuring thermal contact resistance in fin-and-tube heat exchangers, in particular, can be found in the literature. Sheffield et al. [8] carried out a study to experimentally evaluate the contact conductance by measuring several design parameters and proposed correlation for predicting contact conductance in plate finned tubes. Jeong et al. [9] employed experimental–numerical method and investigated new factors affecting the thermal contact conductance in multiple cases of the fin-and-tube heat exchanger with tube diameter of 7 mm. Authors reported that there is an increase in the thermal contact conductance as the number of fins and the tube expansion ratio increases. Taler and Oclon [10] estimated the mean value of thermal contact resistance based on the experimental data and CFD simulations and reported that it reduces overall heat transfer rate in plate fin-and-tube heat exchangers. Singh et al. [11] conducted a CFD analysis to investigate various degrees of thermal contact in a heat exchanger by changing the physical contact area of the fin and tube interface. The results indicated that as the measure of thermal contact area decreases, the flow resistance increases. In 2019, Junjie et al. [12] experimentally studied the contact gap in tube fin heat exchanger under different hydraulic pressure expansion and observed that the contact gap between the tube and fins is basically completely eliminated when hydraulic pressure of 10 MPa is applied. Another experimental investigation on staggered configuration of finned tubes with transverse flow of air calculated the mean value of the thermal contact resistance to be 2.13×10^{-4} Km²/W within the temperature range 79–95 °C of the contact surfaces [13]. With the complexity in the fin-and-tube heat exchanger design, effective heat management becomes even more important. Improper mechanical contact at the fin and tube interface often deviates from their original purpose of improvement in heat transfer to heat dissipation to the ambient. Thus, the thermal contact resistance cannot be disregarded in the process of designing a heat exchanger with externally finned tubes [14].

The scope of this study is to simulate the double fin-and tube heat exchanger of liquid-gas type and to study the impact of thermal contact resistance by numerically modeling the conjugate heat transfer and turbulent flow mechanism. Because fins attached external to the tube can alter the flow field, and influence the heat transfer rate only on the gas-side, heat exchanger with gas-side flow is simulated in this work. Moreover, thermal-hydraulic characteristics, namely overall heat transfer

coefficient, Colburn j -factor, Nusselt number, flow friction factor, and efficiency index are evaluated.

2 Model Development

2.1 Double Finned-and-Tube Heat Exchanger Configuration

The heat exchanger geometry studied in this paper is conceived from the available prototype of a double fin-and-tube heat exchanger, where the cold water flows inside in-lined circular tubes, and hot gas flows outside across the tubes. Double fins are attached by point welding method on tubes as shown in Fig. 1. Often CFD analyses reckon fin-and-tube surfaces as constant temperature boundaries. In this paper, the model simulates the convective heat transfer between the fluid flow and the solid surface and the conductive heat transfer within the solid simultaneously. This inclusion for the conjugate heat transfer enhances the accuracy of simulation results.

2.2 Computational Model

Figure 2 shows the 3D geometry simulated in present work. It consists of distinct fluid/solid domains and models only one half of the repetitive unit from the entire heat exchanger configuration. It helps reducing the model size, thereby resulting in shorter computational time. The dimensions of the geometry are listed in Table 1. The planes of symmetry are utilized to simulate mirrored geometric configuration.

Fig. 1 Double fin-and-tube heat exchanger

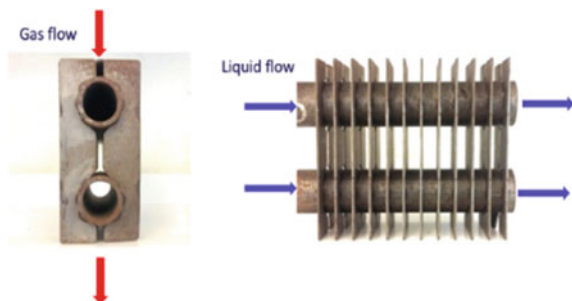


Fig. 2 Computational geometry

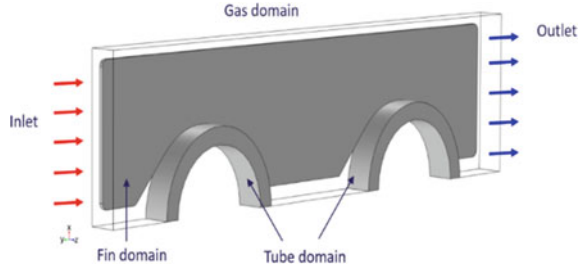


Table 1 Dimensions of computational geometry

Geometric parameter	Value [m]
Fin length	0.145
Fin width	0.032
Fin thickness	0.002
Double fin width	0.006
Fin pitch	0.015
Outer tube diameter	0.038
Inner tube diameter	0.030
Tube pitch	0.075
Fluid domain length	0.150
Fluid domain width	0.075
Fluid domain thickness	0.015

The hot gas inflow and outflow are through the inlet and outlet boundary planes. The solid fin and tube domains are simulated using specific properties of material steel while the gas domain is simulated by applying temperature dependent air properties.

2.3 Governing Equations

Averaged velocity and pressure fields are solved using Reynolds-Averaged Navier-Stokes (RANS) equations. The mass balance and momentum balance equations are:

$$\nabla \cdot \mathbf{u} = 0 \tag{1}$$

$$\rho(\mathbf{u} \cdot \nabla)\mathbf{u} = \nabla \cdot [-p\mathbf{I} + \mu(\nabla\mathbf{u} + (\nabla\mathbf{u})^T)] + \mathbf{F} \tag{2}$$

The $k-\varepsilon$ turbulence model is used to solve for the turbulent flow regimes in the gas domain. The transport equations describing the k_e and ε are:

$$\rho \mathbf{u} \cdot \nabla k_e = \nabla \cdot \left[\left(\mu + \frac{\mu_T}{\sigma_k} \right) \nabla k_e \right] + P_k - \rho \varepsilon \quad (3)$$

$$\rho \mathbf{u} \cdot \nabla \varepsilon = \nabla \cdot \left[\left(\mu + \frac{\mu_T}{\sigma_\varepsilon} \right) \nabla \varepsilon \right] + C_{\varepsilon 1} \frac{\varepsilon}{k_e} P_k - C_{\varepsilon 2} \frac{\varepsilon^2}{k_e} \quad (4)$$

The production and turbulent viscosity can be defined as:

$$P_k = \mu_T [\nabla \mathbf{u} : (\nabla \mathbf{u} + (\nabla \mathbf{u})^T)] \quad (5)$$

$$\mu_T = \rho C_\mu \frac{k_e^2}{\varepsilon} \quad (6)$$

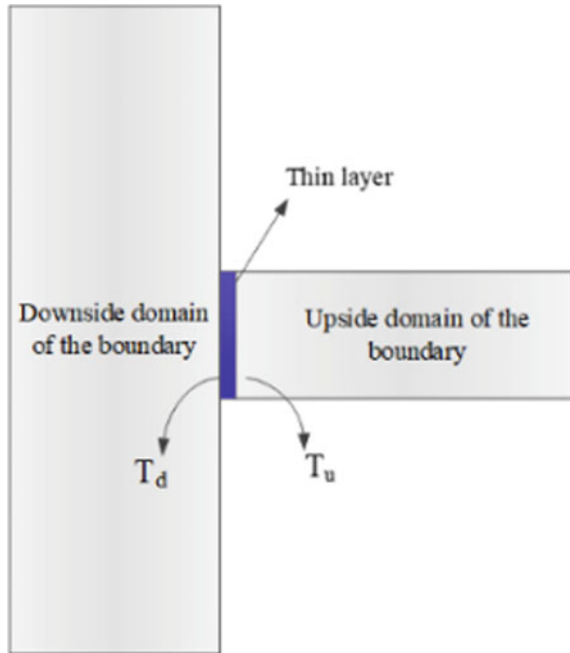
The values of the model constants σ_k , σ_ε , C_{s1} , C_{s2} , and C_μ are taken as 1.0, 1.3, 1.44, 1.92, and 0.09 [15], respectively.

The heat transfer governing equation ruled by convection and conduction is:

$$\rho C_p \mathbf{u} \cdot \nabla T + \nabla \cdot (-k \nabla T) = Q \quad (7)$$

where the radiative heat transfer is neglected.

Fig. 3 Thin layer contact resistance



COMSOL Multiphysics® [16] provides a thin layer functionality that accounts for specific thermal properties in thin layers. The thin layer approximation causes temperature to change and solves for the heat transfer through the layer without actually creating a physical layer at a surface while modeling the computational geometry. Figure 3 depicts the thin layer as blue zone distributing the temperature at upside and downside boundaries. With this approximation, mesh density can be minimized significantly which in turn can reduce the computational time by an order of magnitude than that of high fidelity model.

The thermal contact resistance is simulated as a thin resistive layer of thickness d_{rl} at the fin and tube interface, which can be defined through the thermal resistance:

$$R_{rl} = \frac{d_{rl}}{k_{rl}} \quad (8)$$

The resulting heat flux across the thin layer can be expressed as:

$$-\mathbf{n}_d \cdot (-k_{s,d} \nabla T_d) = -k_{rl} \frac{T_u - T_d}{d_{rl}} \quad (9)$$

$$-\mathbf{n}_u \cdot (-k_{s,u} \nabla T_u) = -k_{rl} \frac{T_d - T_u}{d_{rl}} \quad (10)$$

2.4 Numerical Solution

The governing equations along with boundary conditions as shown in Table 2 are solved numerically using finite element method (FEM) solver in COMSOL Multiphysics® software. Inlet gas temperature and velocity are held at 573.15 K and 9.6 m/s, respectively. Since the change in fluid temperature inside the tube is

Table 2 Boundary conditions

Boundary	Expression
Inlet	$T = T_{in}; u = 0, v = -u_{in}, w = 0$
Outlet	$p = p_{out}; -\mathbf{n} \cdot \mathbf{q} = 0; \nabla k \cdot \mathbf{n} = 0; \nabla \varepsilon \cdot \mathbf{n} = 0$
Inner tube wall	$T = T_w$
Wall	$\mathbf{u} \cdot \mathbf{n} = 0; \nabla k \cdot \mathbf{n} = 0; \nabla \varepsilon \cdot \mathbf{n} = 0$
Symmetry	$\mathbf{u} \cdot \mathbf{n} = 0; -\mathbf{n} \cdot \mathbf{q} = 0; \nabla k \cdot \mathbf{n} = 0; \nabla \varepsilon \cdot \mathbf{n} = 0$

small, inner wall temperature of the tubes is set at 453.15 K. The outlet pressure is kept 0 Pa. Mesh sensitivity study is carried out, and mesh size of 185,212 elements is used. The fine mesh is capable of resolving essential physical phenomena with better accuracy in results. Boundary layers are finely meshed, especially at the fin and tube interface to apprehend high temperature gradients in this region.

3 Results and Discussion

3.1 Temperature and Velocity Distribution

Figure 4a, b show velocity and temperature distributions in the gas domain, respectively. As the hot gas enters with higher temperature at the inlet, it cools down in the downstream of the gas domain. High-velocity region clearly has higher temperature. However, lower temperature region develops between the tubes in the downstream due to relatively lower velocities adversely affecting the heat transfer between gas and fin. The flow pattern in the gas domain is further illustrated using velocity streamlines in Fig. 4c. Low or zero velocity zones can be observed in the downstream of the tubes, which prevent the effective heat transfer between gas and

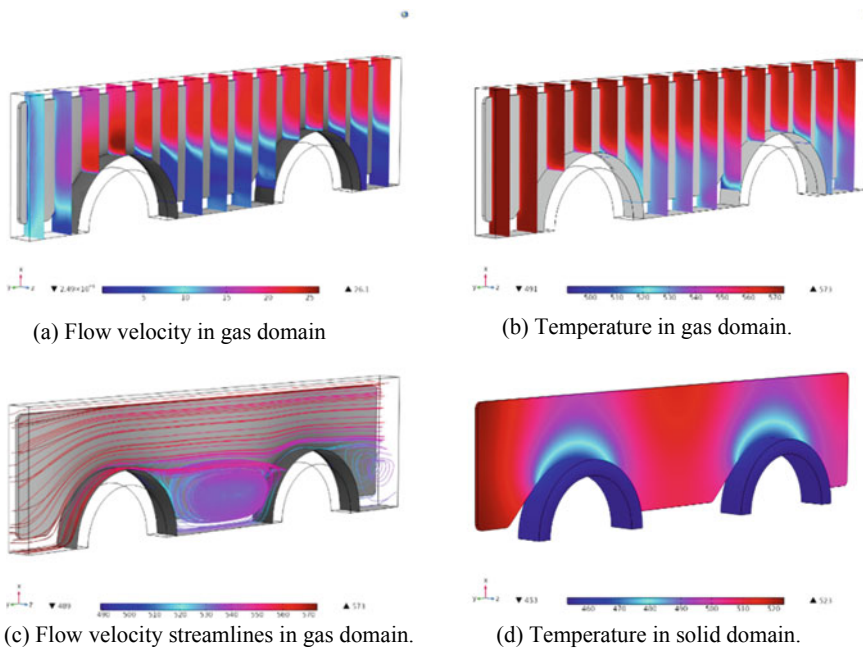


Fig. 4 Steady-state flow velocity and temperature fields

fin surface as indicated from the temperature distribution (Fig. 4b). The temperature gradients on fin and tube surface are shown in Fig. 4d. The fin surface temperature is higher close to the inlet boundary, which decreases gradually along the length up to the outlet boundary due to the conjugate heat transfer. High temperature gradients are observed near to the fin base, where the fin is in thermal contact with the tubes, which is due to the sudden change in the temperatures across the thin resistive layer. Moreover, temperature gradient at the corner and middle edge of the fin surface depicts that these areas are not relatively effective in transferring the heat.

The impact of thin layer thermal resistance at the fin and tube interface on the velocity and temperature distribution is not shown as the results are not visually discrete than what shown in Fig. 4a–d. However, the effect on the performance has been analyzed quantitatively in terms of various parameters.

3.2 Thermal-Hydraulic Performance

The performance is assessed by quantifying overall heat transfer coefficient, Colburn *j*-factor, friction factor, and efficiency index. The obtained solution is compared with the model assuming a thermal contact resistance of 3.3×10^{-6} Km²/W between the fin and tube and is summarized in Table 3. Almost all parameter values drop by approximately 6% compared to the values obtained

Table 3 Performance parameters calculated from the numerical model

Performance parameter	Expression	Without thermal contact resistance	With thermal contact resistance
Overall heat transfer coefficient	$U = \frac{Q_c}{A_i \Delta T_{lm}}$	39.91 [W/m ² K]	37.49 [W/m ² K]
Nusselt number	$Nu = \frac{hD_h}{k_g}$	11.37	10.66
Colburn <i>j</i> -factor	$j = \frac{Nu}{RePr^{1/3}}$	0.00945	0.00889
Friction factor	$f = \frac{\Delta p}{\frac{1}{2} \rho_g u_{in}^2 \left(\frac{L_g}{D_h} \right)}$	0.1614	0.1614
Efficiency index	$\frac{Nu}{K_{pl}} = \frac{Nu}{\left(\frac{\Delta p}{\frac{1}{2} \rho_g u_{in}^2} \right)}$	5.87	5.50

from the model without thermal resistance, whilst the flow friction factor remained constant, which further affirms that thermal contact resistance does not have an impact on flow field. The results clearly indicate that the overall performance devaluates because of the thermal resistance between the fin and tube; hence, careful measures should be taken while designing the fin and tube heat exchanger and to ensure perfect thermal contact between the fin and tube surfaces. The results from this study renew interests in future works in improving the structural designs for enhanced performances.

4 Conclusion

Present paper analyzed the impact of thermal contact resistance in a double fin-and-tube heat exchanger using a 3D multiphysics heat transfer and turbulent flow model. Heat exchanger performance characteristics are determined with and without thermal contact resistance between fin and tube interface. The parameters, namely overall heat transfer coefficient and efficiency index measured without the contact resistance reduced by approximately 6% with a thermal contact resistance of 3.3×10^{-6} Km²/W is assumed at the interface of fin and tube. Developed model provides an opportunity to better understand and further develop a fin-and-tube heat exchanger design. Furthermore, it helps identifying efficient heat transfer areas that are highly critical in practical applications. The study delivers vital information on the impact of thermal contact resistance to consider during mechanical design and manufacturing process.

References

1. Cengel YA, Cimbala JM, Turner RH (2012) Fundamentals of thermal-fluid sciences, 4th ed. in SI units. McGraw-Hills
2. Rocha LAO, Saboya FEM, Vargas JVC (1997) A comparative study of elliptical and circular sections in one- and two-row tubes and plate fin heat exchangers. *Int J Heat Fluid Flow* 18 (2):247–252
3. Chen Y, Fiebig M, Mitra NK (2007) Conjugate heat transfer of a finned oval tube part a: flow patterns. *Num Heat Transf Part A: Appl, An Int J Comput Meth* 33(4):371–385
4. Ereğ A, Özerdem B, Bilir BL, İlken Z (2005) Effect of geometrical parameters on heat transfer and pressure drop characteristics of plate fin and tube heat exchangers. *Appl Therm Eng* 25:2421–2431
5. Ibrahim TA, Gomaa A (2009) Thermal performance criteria of elliptic tube bundle in crossflow. *Int J Therm Sci* 48(11):2148–2158
6. Singh S, Sørensen K, Condra T (2019) Investigation of vortex generator enhanced double-fin and tube heat exchanger. *J Heat Transf* 141(2)
7. Singh S, Sørensen K, Simonsen AS, Condra TJ (2017) Implications of fin profiles on overall performance and weight reduction of a fin and tube heat exchanger. *Appl Therm Eng* 115:962–976

8. Sheffield JW, Wood RA, Sauer HJ (1989) Experimental investigation of thermal conductance of finned tube contacts. *Exp Therm Fluid Sci* 2:107–121
9. Jeong J, Kim CN, Youn B (2006) A study on the thermal contact conductance in fin-tube heat exchangers with 7 mm tube. *Int J Heat Mass Transf* 49:1547–1555
10. Taler D, Oclon P (2014) Thermal contact resistance in plate fin-and-tube heat exchangers, determined by experimental data and CFD simulations. *Int J Therm Sci* 84:309–322
11. Singh S, Sørensen K, Condra TJ (2016) Influence of the degree of thermal contact in fin and tube heat exchanger: a numerical analysis. *Appl Therm Eng* 107:612–624
12. Junjie H, Lianfa Y, Jinjie H, Jingyu J, Yulin H (2019) Experimental study on hydraulic expansion of tube-fin heat exchanger. *IOP Conf Ser Mater Sci Eng* 544:012035
13. Kuntysh VB, Sukhotskii AB, Farafontov VN, Dudarev VV, Sidorik GS (2019) Experimental study of heat exchange and aerodynamic and thermal contact resistance of staggered bundles of tubes with spiral rolled fins of air-cooled devices. *Chem Petrol Eng* 55:22–32
14. Borrajo-Peláez R, Ortega-Casanova J, Cejudo-López JM (2010) A three-dimensional numerical study and comparison between the air side model and the air/water side model of a plain fin-and-tube heat exchanger. *Appl Therm Eng* 30(13):1608–1615
15. Wilcox DC (1998) *Turbulence modeling for CFD*, 2nd ed. DCW Industries
16. COMSOL Multiphysics® (2020) <https://www.comsol.co.in/documentation>

Heat Dissipation Characteristics of a FSAE Racecar Radiator



Shreyas Padmaraman and N. Rajesh Mathivanan

Abstract In recent times, the rise in performance and power output of internal combustion engines has resulted in an increased demand for more efficient cooling systems. Specifically, engineered coolants, coolant additives, thermal properties of radiator materials, redesigned coolant pumps and radiators help meet these increased demands. For any Formula Society of Automotive Engineers (FSAE) racecar, designing a radiator is an important part of controlling the operating temperature of an engine and increasing the effectiveness of the cooling system. In this work, an attempt is made to develop a simple yet reasonably accurate analytical model to calculate the effectiveness of a radiator. This was used to predict the operating temperature of the engine, under the desired running conditions, which are crucial considering the resources and time required to execute complex CFD and multi-physics models which compute the same. Experimental investigations were performed with a customized radiator test rig to replicate field test conditions. The rate of heat dissipation through the radiator with respect to the inlet temperature was analyzed by changing the area of the radiator.

Keywords Heat exchanger · FSAE racecar · Analytical modeling · Heat transfer

Nomenclature

- A Cross-sectional area of the fin, m^2
- C Heat capacity, J/K
- c_p Specific heat capacity of the coolant water at constant pressure, $J/kg\cdot K$
- h Convective heat transfer coefficient at the fin surface, W/m^2K
- k Thermal conductivity of the fin material, W/mK
- L Length of the fin, m

S. Padmaraman (✉) · N. Rajesh Mathivanan
Department of Mechanical Engineering, PES University, Bangalore 560085, India
e-mail: 3459shreyas@gmail.com

N. Rajesh Mathivanan
e-mail: rajesh.mathivanan@pes.edu

\dot{m}_w	Mass flow rate of coolant water through the radiator, kg/s
P	Perimeter of the fin cross section, m
\dot{Q}	Rate of heat transfer, W
T	Temperature, K
U	Overall heat transfer coefficient of the radiator, W/m ² K

Greek Letters

ε	Effectiveness of the radiator
η_{fin}	Fin efficiency

Acronyms and abbreviations widely used in text and list of references

NTU Net transfer units

Subscripts

c	Cold fluid
h	Hot fluid

1 Introduction

The control of the operating temperature of an engine is crucial to its performance, emission generation, life span, and durability of its components [1, 2]. Automobile radiators, typically categorized as cross-flow heat exchangers, wherein the flow of cool air and hot coolant are mutually perpendicular, are responsible for maintaining the operating temperature within the desired range. Patel and Deshmukh [3] indicate that in an internal combustion engine, around 26% of the input energy is converted to useful mechanical work, harnessed at the crankshaft of the engine, and the remaining is converted to heat energy. Roughly, 44% of the total energy is lost through exhaust gases, 29% is dissipated through the cooling system, and a small fraction is lost via convection and conduction through various engine components and lubricants. Since commercial automobiles are not keen on delivering maximum performance at all times, their cooling systems, unlike a well-designed racecar cooling system, are designed to prevent the engine from overheating, without much emphasis on maintaining the engine temperature within a narrow range. The fluctuations in the operating temperature of an engine will be reduced, if the difference between the heat dissipated by the radiator and the heat absorbed by the coolant is maintained minimal. In a bid to reduce the overall size and weight of cooling systems and radiators, it is beneficial to use coolants with a host of additives over plain coolant. As a result of this, there has been continued research that has gone into synthesizing and evaluating new additives [4–7]. Advanced coolant additives

provide greater control over the rate of heat transfer, control over corrosion, fouling, and scaling as well as other physical properties. With recent research focusing on the addition of thermal nanoparticles to the coolant mixtures [5], radiators will only become more effective without significant increase in size and weight. However, with regard formula student [8] competitions, it is mandate to use only distilled water as coolant barring the development and application of additives. Furthermore, the use of OEM radiators for cooling of their respective engines can prove to be inadequate due to their reduction in size. As a result, the design and development of cooling systems for FSAE racecars focus on the radiator fan [9], fan duct, coolant pump, radiator material, location, and size. The nature of air flow through a radiator core has a significant impact on radiator performance as investigated by Zhang et al. [10]. In addition to simulating air flow through the radiator, Bahuguna et al. [2] analyzed the effect on heat transfer using CFD tools such as Siemens' Star CCM+ and predicted the temperature gradient and overall rate of heat transfer across the radiator. Radiators are usually manufactured from aluminum even though materials such as copper and brass offer lesser resistance to heat transfer. Conversely, copper-brass radiators are considerably heavier and more expensive when compared to aluminum radiators [9].

Many FSAE teams incorporate an external electric pump into the cooling system [11] based on design requirements as the coolant pumps integrated into commonly used FSAE engines which have limited scope for improvement. External pumps are also advantageous in cooling an engine that is not running, compared to integrated pumps which do not circulate coolant through the system. This causes the engine temperature to surge past the operating range before cooling down. The downside is that such pumps add weight to the racecar which is not justified for the marginal gains it offers. Hence, it is of greater importance to design and optimize the size of a radiator core when considering cost effectiveness, weight, feasibility, and reliability.

There are two critical operating conditions to be considered when designing a cooling system. The first critical condition is when the engine is idling and the car is at a standstill. The second is when the engine is running under maximum load at a low vehicle speed [12]. However, for an FSAE racecar, the former scenario of the vehicle at a standstill is considered for design purposes as the engine is not frequently subjected to reach peak load conditions [1]. The computational power and time required to achieve reasonable results using complex CFD models are significant when considering the operation of a FSAE team. Conversely, there are few analytical models that do not require the knowledge of any specific software, yet still deliver representative results. It is hence imperative to characterize the performance of a radiator using analytical models based on standard heat transfer relations, which do not require prohibitive computational power or resources.

An attempt is made in this paper to experimentally validate the results of an analytical model for a FSAE racecar radiator setup and hence predict the operating temperature of the engine for different working conditions based on the effectiveness of the radiator as calculated using the analytical model.

2 Experimental Setup and Procedure

FSAE teams conduct radiator experiments and test on their racecars at specific race tracks to evaluate or validate the performance of the radiator. However, when working to validate a model, the ability to create a steady state conditions becomes advantageous and can be achieved on a test rig. Nevertheless, it is important to compare field testing results with experimental and analytical results to understand the model's limitations. The test rig, shown in Fig. 1, consists of an electric water pump, radiator, cooling fan, fan duct, and electric heater. A rotameter, anemometer, and four thermometers connected to digital readouts were used to measure inlet and outlet temperatures of the radiator, air temperature after flowing through the core of the radiator, and ambient air temperature, respectively. The advantage of this specific rig is that crucial variables such as inlet temperature; volume flow rates of air and water can be independently controlled. The outlet of the radiator was connected to a reservoir tank with an electric heating element, used to heat the coolant to the desired temperature. Heated coolant was circulated through the system using the external electric pump at a volume flow rate of 9 lpm, controlled by a rotameter connected to the outlet of the pump. The value of the input variables was decided based on full car testing results.

Fig. 1 Radiator test rig



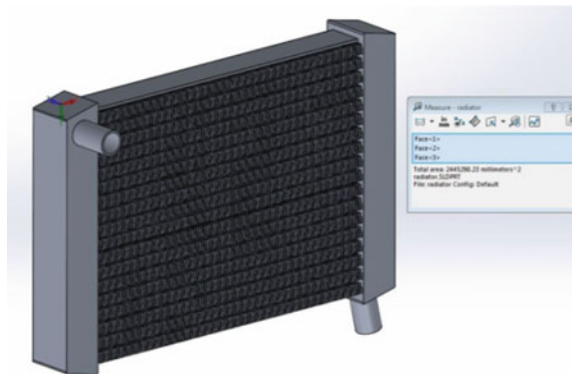
The volume flow rate of coolant was measured across the range of engine speeds which will be encountered on track. The coolant inlet temperature was varied from 70 to 100 °C, based on the temperature at which the thermostat valve of the racecar’s cooling system is designed to open and by the heating capacity of the electric heater being used on the rig, respectively. The speed of the fan positioned behind the radiator on the test rig was set to replicate the suction generated by the radiator fan used on the racecar. The average velocity of air downstream of the radiator was used as an indication of the suction effect and was found to be 1.2 m/s on the racecar as measured using an anemometer. Once steady state conditions were achieved, the heat dissipated by the radiator can be calculated using Eq. (1):

$$\dot{Q}_{\text{radiator}} = \dot{m}_w c_p (T_{h,\text{in}} - T_{h,\text{out}}) \quad (1)$$

3 Analytical Calculations

The performance of a radiator is characterized usually by one of two methods, ε -NTU relations and logarithmic mean temperature difference (LMTD). The LMTD method can be used when the inlet and outlet temperatures of both fluids are known, without which the effectiveness of the radiator cannot be calculated. In this work, efforts are made to predict the inlet temperature of the radiator from its effectiveness; hence, the LMTD method of evaluation cannot be adopted, and therefore, the ε -NTU relations, based on radiator geometry, fluid flow rates, and overall heat transfer coefficient, are used. Measurements of the radiator were used to create a 3D CAD model (Fig. 2) from which the surface area of the radiator core, across which heat transfer occurs, was calculated. Based on operating conditions, the radiator fins were classified as “short fins with insulated ends” for which the efficiency was calculated using Eqs. (2) and (3) and its effective area of heat transfer ($A_{\text{fin-effective}}$) using Eq. (4).

Fig. 2 CAD model of the radiator



$$m = \sqrt{\frac{hP}{kA}} \quad (2)$$

$$\eta_{\text{fin}} = \frac{\tan(mL)}{mL} \quad (3)$$

$$A_{\text{fin-effective}} = A_{\text{fin}}\eta_{\text{fin}} \quad (4)$$

The total effective area of heat transfer ($A_{\text{effective}}$) was calculated using Eq. (5). The effectiveness of the radiator was calculated using the following set of standard relations:

$$A_{\text{effective}} = A_{\text{ducts}} + A_{\text{fin-effective}} \quad (5)$$

$$NTU = \frac{UA_{\text{effective}}}{C_{\text{min}}} \quad (6)$$

$$\varepsilon = 1 - e^{-\left\{ \left(\frac{C_{\text{min}}}{C_{\text{max}}} \right)^{-1} (NTU)^{0.22} \left[e^{\left[-\frac{C_{\text{min}}}{C_{\text{max}}} (NTU)^{0.78} \right]} - 1 \right] \right\}} \quad (7)$$

The effectiveness of a radiator is defined as the ratio of the actual rate of heat rejection to the maximum possible rate of heat rejection (Eq. (8)). Since the engine operating temperature is indicated by the radiator inlet temperature, the terms from Eq. (8) can be rearranged to calculate the radiator inlet temperature (Eq. (9)).

$$\varepsilon = \frac{\dot{Q}_{\text{radiator}}}{\dot{Q}_{\text{radiator, max}}} = \frac{C_h(T_{h,\text{in}} - T_{h,\text{out}})}{C_{\text{min}}(T_{h,\text{in}} - T_{c,\text{in}})} = \frac{C_c(T_{c,\text{out}} - T_{c,\text{in}})}{C_{\text{min}}(T_{h,\text{in}} - T_{c,\text{in}})} \quad (8)$$

$$T_{\text{engine}} = T_{h,\text{in}} = \frac{\dot{Q}_{\text{radiator}}}{\varepsilon C_{\text{min}}} + T_{c,\text{in}} \quad (9)$$

The rate of heat energy lost during the combustion process for the KTM® 390 cc engine across rpm-throttle combinations was obtained using Ricardo WAVE, using which the operating temperature of the engine was predicted for each rpm-throttle combination using Eq. (9).

4 Results and Discussion

4.1 Accuracy of the Model at Design Conditions

The desired operating temperature of the engine on a KTM Duke 390 is between 95 °C and 102 °C, based on data obtained from the engine manufacturer. The rate of heat dissipation through the radiator was calculated from the experimental data as

well as the ε -NTU method across different radiator inlet temperatures corresponding to an engine speed of 3300 rpm and plotted against inlet/engine temperature as shown in Fig. 3. The engine operating temperature, at which the rate of heat dissipated by the radiator (\dot{Q}_r) is equal to the rate of heat generated by the engine (\dot{Q}_e), was calculated to be 107.43 °C from experimental data and 104.64 °C from ε -NTU method. The maximum deviation between the analytical and experimental results was calculated to be 15%. Using this analytical model, the operating temperature of the engine for various engine speeds and throttle positions was predicted. Figure 4 shows the temperature profile when the racecar is driven in first gear across different engine speeds for various throttle positions. The deviation of the analytical results from the experimental results can be explained by the effect of a few unaccounted variables as well as assumptions made in order to simplify the model for the desired operating conditions.

Convection across the surface of the engine and other heated powertrain elements such as the exhaust often contribute to cooling in FSAE racecars as they are not isolated from air flow when the car is in motion. However, due to the engine's irregular surface geometry, it is challenging to accurately estimate the extent of convective cooling using standard heat transfer relations. At a standstill, the heat loss due to free convection is known to be negligible; however, when the vehicle is in motion, the cooling due to forced convection begins to have a considerable impact on the cooling of the engine. The second assumption made in order to efficiently estimate the mass flow rate of air through the radiator was that the effect of the wake and turbulence caused by components upstream of the radiator on the racecar was neglected. The mass flow rate of air was calculated based on the average measured discharge coefficient of the radiator core and the free stream velocity of air relative to the racecar. The discharge coefficient of the radiator core was found to be 0.75 across a wide range of free stream air velocities under laboratory test conditions. This finding is applicable for low vehicle speeds as are commonly encountered in FSAE competitions.

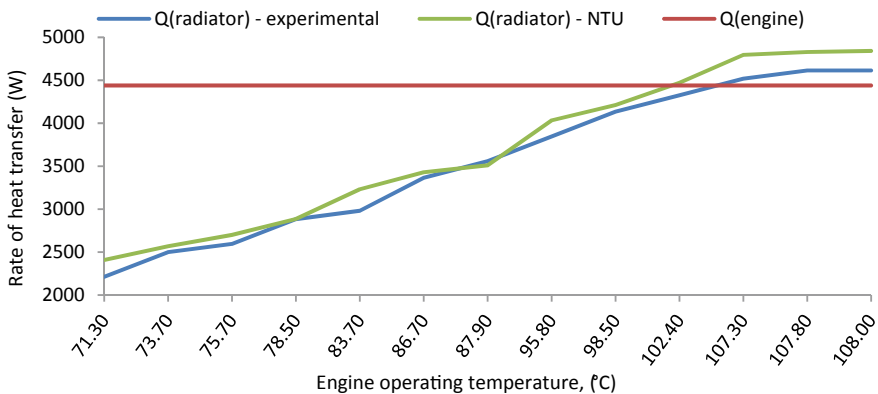


Fig. 3 Radiator heat rejection curves for different inlet temperatures

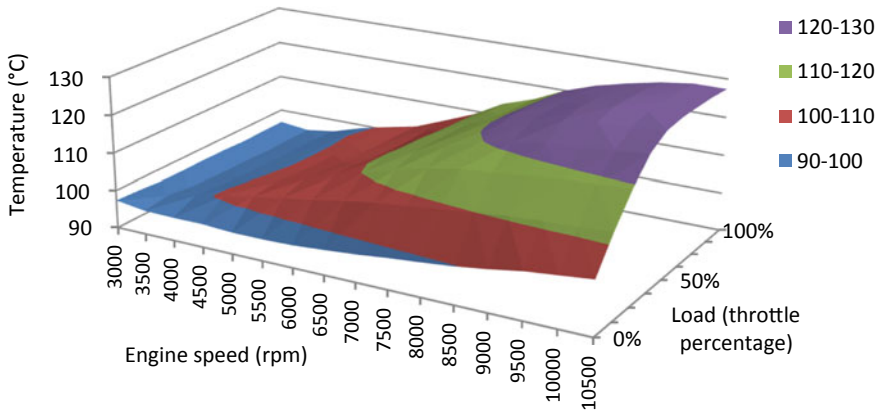


Fig. 4 Variations of engine temperature with engine speeds and throttle percentage for the OEM radiator

A common source of losses in cooling effectiveness which is often difficult to account for is due to the induction of air bubbles in the cooling system. Improper bleeding technique and leakages in the coolant lines results in the formation of such air bubbles. Air having a low specific heat capacity makes it a good insulator, thereby reducing the heat absorption and dissipation capability of the radiator and hence its effectiveness.

Since racecars in FSAE competitions run at vehicle speed between 20 and 70 kmph and operate predominantly in an engine speed range of 5000–9000 rpm, the critical condition for the cooling system of FSAE racecars lies in the low rpm-load conditions for which the assumptions stated are effective. The analytical model can hence be considered reasonably accurate within these operating conditions and can be used for predictive purposes.

4.2 Accuracy of the Model at Extreme Operating Conditions

Although a drastic rise in operating temperature of the engine in the region of high engine speed and high load conditions is observed (Fig. 4), these conditions are often evaded as a result of the track layout commonly encountered at FSAE competitions. As can be observed in the contour plots, the coolant inlet temperature is predicted to exceed 110 °C, at high engine speeds and high throttle positions. At these elevated temperatures, past the boiling point of water at 1.4 bar, it is complicated to model the heat exchanger using the ϵ -NTU method as a fraction of the coolant is in the vapor state and remaining in liquid state. The physical properties such as heat capacity and mass flow are problematic to estimate for such a system.

The deviations at higher engine speeds and load conditions can be explained by the following, in addition to the effect of the assumptions described previously. Difference between the true air-fuel ratio of the engine and the 1D engine model can result in different values of heat generation of the order of hundred watts, as the true air-fuel ratio is affected by the life of the engine, local temperatures within the cylinder, health of the spark plug, and other parameters which are difficult to model. The heat lost due to convection through the engine oil and conduction through engine parts in the 1D engine model is accurate but not exact as the software limits the input of the geometry of engine parts and properties of engine fluids. It is important to realize these limitations without which the results can be misinterpreted.

5 Conclusions

The validation of the radiator analytical model was experimentally conducted using a custom built radiator test rig and comparison with field testing results. In predicting the engine, operating temperature for a specified engine speed has led to the following conclusions:

- The effectiveness of the radiator was analytically calculated to be 0.80 and had a deviation of less than 10% when compared to the experimental results.
- The operating temperature of the engine using the stock radiator was successfully predicted to be 104.64 °C at an engine idling speed of 3300 rpm and had a deviation of less than 5% when compared to the experimental results.
- An increase in the area of the radiator core by 10% from the stock radiator is predicted to result in an average of 12 °C reduction in the operating temperature of the engine across different rpm-load conditions.

From these results, it is concluded that the analytical model is accurate for the operating conditions commonly encountered at FSAE competitions. It is also concluded that OEM radiators do not provide sufficient cooling for their respective engines when restricted by the rules and regulations of FSAE competitions.

References

1. Kuntzer G, Mario ES, Martins Bayer FM, Soliman PA, Sangaletti M (2015) Development of a FSAE racecar cooling system. SAE technical paper series, No. 2015-36-0409
2. Bahuguna R, Prasad T, Khanna R, Kumar AB, Gopal KN, Srivastava S, Mishra A (2018) Design and development of cooling system for a formula SAE race car. SAE Technical Paper, No. 2018-01-0079
3. Patel S, Dr. Deshmukh SP (2017) Analytical design and verification of automotive radiator using 1-D simulation. Int J Res Appl Sci Eng Technol 5(6):2349–2360

4. Sathyanarayanan PL, Ramprabhu R (2005) Study on the effect of different combinations of engine coolant additives on the heat dissipation rate of radiators. *J Automobile Eng* 219 (10):1173–1179
5. Elias MM, Mahbul IM, Saidur R, Sohel MR, Shahrul IM, Khaleduzzaman SS, Sadeghipour S (2014) Experimental investigation on the thermo-physical properties of Al_2O_3 nanoparticles suspended in car radiator coolant. *Int Commun Heat Mass Transfer* 54:48–53
6. Afrand M (2017) Experimental study on thermal conductivity of ethylene glycol containing hybrid nano-additives and development of a new correlation. *Appl Therm Eng* 110:1111–1119
7. Devireddy S, Mekala CSR, Veeredhi VR (2016) Improving the cooling performance of automobile radiator with ethylene glycol water based TiO_2 nanofluids. *Int Commun Heat Mass Transfer* 78:121–126
8. Formula Bharat Rules Booklet (2020)
9. Selim AB, de Lyra B (2016) Cooling package selection through radiator area/material and fan blade angle variation. *SAE Technical Paper*, 2016–36-0370
10. Zhang C, Uddin M, Robinson AC, Foster L (2018) Full vehicle CFD investigations on the influence of front-end configuration on radiator performance and cooling drag. *Appl Therm Eng* 130:1328–1340
11. Ribeiro EG, de Andrade Filho AP, de Carvalho Meira JL (2007) Electric water pump for engine cooling. *SAE Technical Paper*, 2007-01-2785
12. Beard RA, Smith GJ (1971) A method of calculating the heat dissipation from radiators to cool vehicle engines. *SAE Technical Paper*, 710208

Fabrication and Analysis of Evaporative Water Reclamation Plant Using Waste Water from Different Sources



Anil Kumar and Arindam Kumar Chanda

Abstract Nature has blessed us with large ocean bodies, thousands of rivers, beautiful waterfalls and a number of lakes. Unfortunately, all these sources of water are getting polluted due to large production industries' wastes and urbanization. Due to this, water pollution has become havoc in the lives of common people. Taking account of this environmental problem, 'The Zero Liquid Discharge philosophy' has been utilized, which aims at reusing the wastewater by converting it into the pure one. However, as noble as the concept may sound, its economics has been a major deterrent in its implementation in different developing countries, where regulations are not strict enough. In this research, the analysis of the unit cost associated with the purification of wastewater by means of evaporation has been made. This has been done by fabricating a model that resembles the evaporation apparatus in ZLD assemblies. Then, samples from different sources have been collected and purified and tested in the designed apparatus. Then, the efficiency of the apparatus has been calculated, and the relationships between the energy consumed, initial TDS and final TDS of the water samples have been established. After analysis, it has been found that the average thermal efficiency of the apparatus is 75.042%, and the average cost of purifying of water came out to be INR 8.692.

Keywords Water pollution · Purification of waste water · Zero liquid discharge · Reuse of waste water

1 Introduction

For healthy and smooth functioning of the environment, pure water is one of the most important aspects. It is the basic life supporting system and plays a prominent role in balancing of the ecosystem. But nowadays, almost all regions of the world

A. Kumar (✉) · A. K. Chanda
G B Pant Government Engineering College, New Delhi 110020, India
e-mail: anilapmae@gmail.com

A. K. Chanda
e-mail: akcped@yahoo.com

are suffering with the shortage of clean and pure drinking water. Despite being aware of this shortage of pure water, the people continue to contaminate water bodies.

The nature has blessed us with large ocean bodies, thousands of rivers, beautiful waterfalls and a number of lakes. Unfortunately, all these sources of water are getting polluted due to large production industries' wastes and urbanization. Due to this, water pollution has become havoc in the lives of common people [1].

Causes and Effects of Water Pollution:

Most of the primary causes of water pollution are:

1. Sewage water dropped in the fresh water resources—Main source of production of waste water.
2. Polluted river banks.
3. Waste form industries—it is very dangerous source of fresh water pollution and requires more attention.
4. Oil pollution [2].

Zero liquid discharge (ZLD) is as an emerging technique for minimizing waste, treat toxic industrial waste streams and mitigate potential water quality impacts in receiving water streams. Conventional effluent treatment plants

- Do not remove pollutants sufficiently.
- Nutrients and nutrients and salts are not well separated.
- Recycling of water not possible.

Although the prime benefits of ZLD system are not only conservation of water by its reuse as feed water but also the subsequent abstinence from the need to discharge contaminated water into clear sources of water (water bodies like rivers and lakes), thereby avoiding its pollution and conserving fresh water for other consumption purposes [3].

An efficient and well-designed ZLD treatment system should be able to:

- Control variations in waste contamination and flow
- Recover around 95% of the liquid waste for reuse
- Treat and retrieve valuable byproducts from your waste
- Produce a dry, solid cake for disposal [4].

2 Problem Formulation

According to World Wide Fund for Nature (WWF), five rivers in Asia serving over 870 million people are among the most threatened in the world, as dams, water extraction and climate change all take their toll.

In this perspective, Zero Liquid Discharge (ZLD) is thought to be an emerging technique to minimize waste.

So availability of 'Fresh' water scarcity is a growing problem faced by many parts of the world. To remove such a huge problem, purification and reuse of waste water are very important solution.

So the problem statement is '**Analysis of Evaporative Water Reclamation Plant Using Waste Water from Different Sources**'.

3 Objective

- To give an overview of our water reclamation concept and to add a utility concept to the pre-existing ZLD system.
- To find the thermal efficiency of the fabricated set-up.
- To determine the per litre cost of purified water.
- To determine the TDS of waste and purified water.

4 Methodology

The utilization of the pre-existing ZLD system will be made to analyse the cost related aspects by fabrication of a model for required observations [5].

A model will be fabricated which will evaporate the water from the waste water, and then, the purified water condensed from the evaporators will be collected. The energy consumption will then be calculated for the unit water mass.

Also the TDS of waste and purified water will be calculated and analysis, and it will be checked that whether the TDS has been improved or not.

5 Experimental Work

5.1 Fabricated Model

Due to complexities in the ZLD concept, our focus is concentrated on the energy and cost calculations of the fabricated model that is based on distillation. The fabricated model consists of the following components:

- Container (Tin can)
- Overhead condensate guide
- Heating element
- Extraction container
- Base

1. **Container (Tin Can)**—it is used to boil the sample water collected from different sources.
 - Material—Tin coated steel
 - Shape—Cylinder with double friction cover
 - Dry weight—50 g
 - Dimensions—Height—129 mm
Diameter—99 mm (Fig. 1)
2. **Overhead Condensate Guide.**
 - Material—Galvanized iron sheet
 - Thickness—0.5 mm
 - Processes—Shearing and bending

This sheet metal is folded in the form of a cylinder bridge that is used to condense and transport distillate from tin can to the extraction container.
3. **Heating element**—it is used to heat up the sample water to convert it into steam.
 - Type—Immersion type
 - Power—500 W (Fig. 2)
4. **Base**—it is used to support the entire setup and to balance the equipment.
 - Material—Plywood
 - Dimensions—295 mm × 175 mm
5. **Extraction container**—extraction container is a simple plastic container which collects water dripping from the end of condensate guide.

The set-up is mounted on the base via nuts and bolts (Fig. 3).

Fig. 1 Primary container vessel



Fig. 2 Heating element



Fig. 3 Final assembly



5.2 Challenges in Operation of Fabricated Apparatus

1. **Overflow of waste water:** When water is heated in the container, formation of bubbles take place that results in agglomeration of solid particles and increases surface tension of the top layer. This layer moves up due to energy supplied by the heating element, and hence, water overflows before reaching its boiling point.

Solution—this problem can be solved by decreasing surface tension of the waste water sample. The surface tension can be reduced by two methods: **Physical and Chemical**; here, physical method has been used, i.e. a wooden stick has been used as shown in figure below to prevent overflow of water by rupturing the agglomerated layer of solid particles (Fig. 4).

Fig. 4 Bubbling prevention by used of wooden stick



2. **Water vapour leakage:** Due to generation of water vapour in an open container, there is a chance of leakage through joints and container-guide interface. These results in escaping of water vapour that decreases the amount of distillate extracted at the other end.

Solution—Using Aluminium tapes and electrical tapes, temporary sealing is done on the apparatus, and by using resin-based adhesives like Araldite, Bondtite and M-Seal, permanent sealing is done.

3. **Pungent smell from container:** Due to the presence of various solvents like ammonium hydroxide, hydrogen sulphide, ethanethiol, etc., waste water has a characteristic smell that amplifies when exposed to heat from heating element. This results in vaporization of these compounds that result in pungent odours.

Solution—Proper ventilation should be provided near the apparatus to allow escaping of gases.

6 Results

Every design criterion starts with preliminary data for all parameters that are not affected by the variables of the study [6]. The method used for the purpose of fabrication and analysis of present solution required a number of considerations to be followed such as:

- Weight of the container: 40 g
- Maximum allowable volume of test liquid: 500 ml
- Range of initial temperature of test liquid: 27–31 °C
- Rate of electricity per unit (1 kWh)—INR 4.5.

6.1 Observations and Calculations

Five samples were collected from different sources of waste water for the purpose of our calculations. The tables show the initial and final TDS levels for these five samples. Along with these observations, calculations for efficiency and cost have been provided (Table 1).

For sample 1

Initial temperature of sample: $-27.8\text{ }^{\circ}\text{C}$

Calculated heat given (Q) = $M_c\Delta T (Q_C) + mL (Q_L)$

Specific heat of sample (c) = $4.179\text{ J g}^{-1}\text{ }^{\circ}\text{C}^{-1}$

$\Delta T = (100 - 27.8)\text{ }^{\circ}\text{C} = 72.2\text{ }^{\circ}\text{C}$

$Q_C = 500 * 4.179 * 72.2\text{ J} = 150861.9\text{ J} = 150.862\text{ kJ}$

Table 1 Observations of five samples

Sample number	Initial TDS ppm	Initial volume ml	Power supplied w	Duration min.	Final TDS ppm	Final volume ml	Volume of water extracted ml
1	139	500	500	11.15	77	450	31
2	704	500	500	11.37	77	450	33
3	1050	500	500	11.45	112	450	30
4	1220	500	500	11.31	159	450	28
5	2451	500	500	11.43	153	450	33

Latent heat of vaporization (L) = 2264.705 Jg⁻¹

Q_L = 50 * 2264.705 J = 113235.25 J = 113.235 kJ

Heat supplied theoretical (Q) = Q_C + Q_L = 150.862 + 113.235 = 264.097 kJ

Heat supplied by rod = Electrical energy given to rod = Power rating * Time of operation = 500 * 675 = 337500 J = 337.5 kJ

Energy efficiency (η) = Calculated energy (Sensible + Latent Heating)/Heat supplied * 10, η = 264.097/337.5 * 100 = 78.25%

Cost of extraction of clean water (50 mL) = 0.422 Rs

Cost of extraction of clean water = 8.44 Rs per litre.

Similarly for all samples the different values obtained are summarized as under in the Table 2.

Analysis of observations (Fig. 5).

The histogram shown above represents the TDS in water collected from different sources. TDS is varying as the sources are different such as tap water, drain water, sewage water, etc. (Fig. 6).

The sample 4 utilized less amount of energy as compared to 2nd, 3rd and 5th sample as the impurities present in the sample water behaved as insulators and heated the waste water in a faster manner as compared to other 3 samples (Fig. 7).

Table 2 Calculations of different values using formulas for five samples

Initial temp. °C	Δt °C	Q _C kj	L jg ⁻¹	Q _L kj	Q = Q _C + Q _L kj	Qs By Rod kj	H%	Clean water extrac. cost rs/l
27.8	72.2	150.86	2264.70	113.23	264.09	337.5	78.25	8.44
27.8	72.2	150.86	2264.70	113.23	264.09	348.5	75.78	8.8
27.5	72.5	151.48	2264.70	113.23	264.72	352.5	75.1	8.8
30.8	69.2	144.59	2264.70	113.23	257.82	345.5	72.73	8.64
30.8	69.2	144.59	2264.70	113.23	257.82	351.5	73.35	8.78

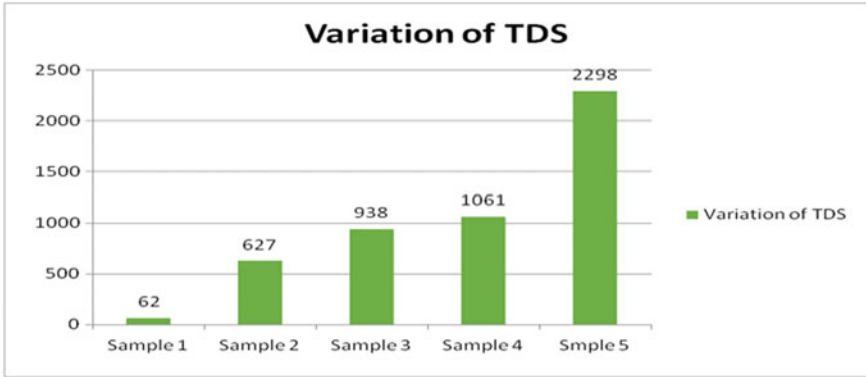


Fig. 5 Variation of TDS in different samples

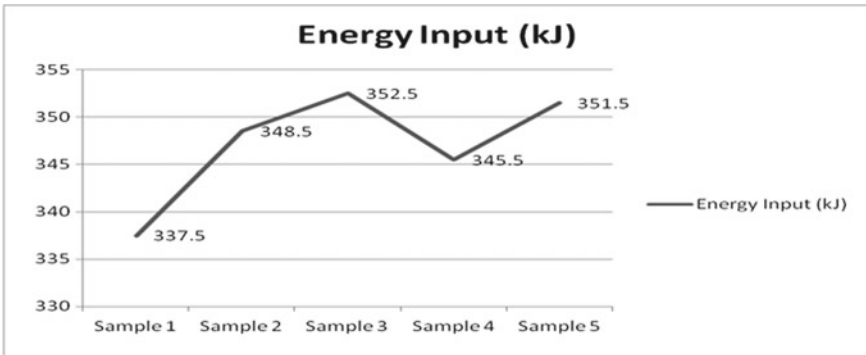


Fig. 6 Energy input for different samples

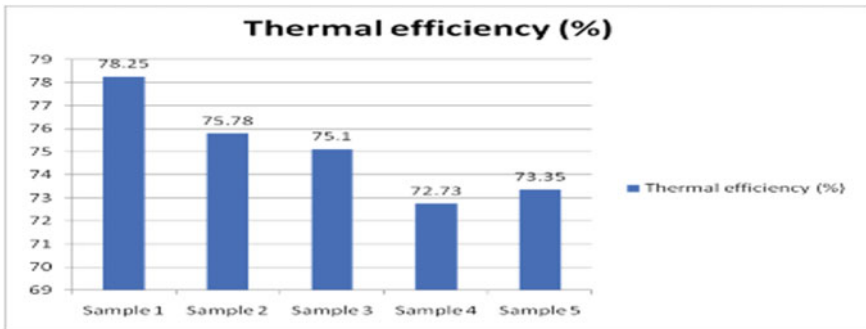


Fig. 7 Thermal efficiency of fabricated system for different samples

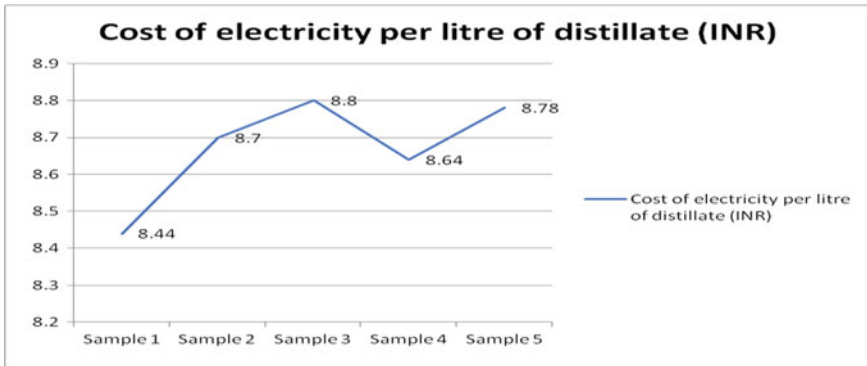


Fig. 8 Cost calculated per litre of distillation

The histogram shown above represents the thermal efficiency of the fabricated system for different water samples. It can be seen that the thermal efficiency of the system is maximum for the sample 1, i.e. for the sample which has lowest TDS (Fig. 8).

The graph above represents the cost of collection of per litre of water from the different sources of waste water. It has been observed that the cost of collection of per litre of water from sewage waste water is 8.78 rupees.

7 Conclusion

In this research, analysis of the unit cost associated with purification of waste water by means of evaporation has been made. This has been done by fabricating a model which resembles the evaporation apparatus in ZLD assemblies. The samples from different sources have been collected and purified and tested in the designed apparatus. Then, the efficiency of the apparatus has been calculated, and the relationships between the energy consumed, initial TDS and final TDS of the water samples have been established. After analysis, it has been found that the average thermal efficiency of the apparatus is 75.042%, and the average cost of purifying of water came out to be INR 8.692.

References

1. Tong T, Elimelech M (2016) The global rise of zero liquid discharge for wastewater management: drivers, technologies, and future directions
2. Murty MN, Kumar S. Book on water pollution in india: an economic appraisal

3. Deng C, Feng X, Bai J (2007) Graphically based analysis of water system with zero liquid discharge author links open overlay panel
4. International and Indian case studies on Zld: Leif Ramm-Schmidt, Ramm-Schmidt Consulting Ltd, Finland, representing Arvind Envisol Private Limited Ahmedabad India Presented at: Seminar and Training Workshop on Zero Liquid Discharge, Ahmedabad 28 Jan 2014
5. Darros-Barbosa R, Balaban MO, Teixeira AA (2007) Temperature and concentration dependence of heat capacity of model aqueous solutions
6. Japan Sewage Works Association (2002) Book on design standard for municipal wastewater treatment plants, 2nd Edn

Techno-Economic Feasibility Analysis of Parabolic Solar Cooker in Tropical Environment of India



Harshita Sawarn, Pushpendra Kumar Singh Rathore,
and Shailendra Kumar Shukla

Abstract The work presented in this article consists of evaluating the techno-economic feasibility of parabolic solar cooker using energy, exergy and overall thermal efficiency for technological feasibility. In addition, useful energy required for cooking, using the solar cooker has also been calculated in this article. For evaluation of economic feasibility capital cost, maintenance costs and payback period have been calculated. Also, to estimate the annual energy saved and costs of energy saved, cooking power of the parabolic solar cooker and the estimated energy content of LPG cylinder used in BHU hostel is calculated. The practical experiment on parabolic solar cooker at Centre for Energy and Resources Development, IIT BHU, and face-to-face interview by cooks of Triveni Girls Hostel, BHU, has been conducted to collect the required experimental data.

Keywords Energy · Exergy · Solar

1 Introduction

The three basic areas where energy is required are cooking, power generation (electricity) and transportation. In India, cooking is one of the major consumer of energy, In India, to feed 1.35 billion, energy requirements is very high, and at the same time, energy affordability is very low forcing them to use conventional energy sources. According to the primary survey report in of Petroleum Planning and

H. Sawarn

Faculty of Arts, Department of Economics, Banaras Hindu University, Varanasi, India
e-mail: harshita.sawarna7@gmail.com

P. K. S. Rathore (✉) · S. K. Shukla

Center for Energy and Resources Development, Department of Mechanical Engineering,
Indian Institute of Technology (BHU), Varanasi, India
e-mail: rathoresamurai@gmail.com

S. K. Shukla

e-mail: skshukla.mec@itbhu.ac.in

© The Author(s), under exclusive license to Springer Nature Singapore Pte Ltd. 2021

B. S. Sikarwar et al. (eds.), *Advances in Fluid and Thermal Engineering*,

Lecture Notes in Mechanical Engineering,

https://doi.org/10.1007/978-981-16-0159-0_20

Analysis Cell (PPAC), 2016, an average of 35% of the total households in India uses firewood, biomass and cow dung as a cooking fuel because it is freely and easily available [1]. The use of these conventional fuels leads to carbon and other pollutants' emission which also causes serious health hazards because of continuous inhaling the gases generated from the burning/or incomplete burning of these fuels. Furthermore, the availability and refilling of the liquefied petroleum gas (LPG) in the remote areas is very difficult because of poor transportation infrastructure. In 2017, 47% of the world population were exposed to household air pollution due to the use of solid energy fuel for cooking. As per the estimation, 846 million people in India are exposed to the household pollution in 2017 [2], primarily consisting of the pollution generated from cooking. In India 2014, 66.69% and 4.141% of total carbon dioxide emission were emitted due to the consumption of solid and gaseous fuels, respectively. The emission of carbon leads to many respiratory diseases and is an indirect cause of other life threatening diseases. Taking global scenario, in 2016, 3.8 million deaths occur due to chronic respiratory disease. Also the cause of 7 million deaths in 2016 was due to indoor and outdoor pollution and 3.8 million deaths alone due to indoor pollution. In India, 1.2 million deaths in 2017 occurred due to air pollution burden. Household air pollution contributes 9% to the loss of life expectancy in India.

Therefore, to mitigate this and to increase the dependency on renewable energy, it is required to promote the use of clean cooking technology. Under these circumstances the solar energy can be one of the sustainable sources of energy that is easily available, pollution free and zero cost [3]. In recent years, the growth and development of solar energy for sustainable technology development [4] in India has increased with a high rate [5]. The geographical location of India makes it a paradise for the development of all type of solar energy technologies. The solar profile of India is very rich, and most of the Indian states receive annual average direct normal irradiance in the range of 4.5–5.0 kW h/m²/day [6]. This much of solar energy is sufficient to produce temperature range required for cooking, i.e., 60–130 °C.

This study shows the utilization of the solar energy for the purpose of cooking. In this study, experiment has been performed at the Centre for Energy Resources and Development, IIT BHU, in the year 2019 to estimate the energy efficiency, overall thermal efficiency, of parabolic solar cooker and estimation of useful energy required for cooking the give quantity of rice. The economic and financial feasibility of solar cooker has also been analysed. The economic feasibility of parabolic solar cooker is analysed here by taking concept of externality.

2 Methodology

The experimental set-up is as shown in the image given at CERD, IIT BHU, which is located at 25.2623° North, 82.9894° East situated in Varanasi, India. The observations were taken once in a week in February, 2019, on experimental set-ups

of parabolic solar heat collector. The observations were taken at an interval of every 15 min on the day of experiment performed to evaluate the energy efficiency and cost analysis of parabolic solar cooker. Six litres of water was filled into the aluminium tank (cooker), placed at the plate and provided with solar insolation. During the experiment, the apparatus mentioned below was used. The initial temperature of water, i.e., temperature of water when put into the cooker, and the final temperature at the completion of the experiment were measured. The first step in performing the experiment was keeping the water tank filled with 6 L of water on the plate attached on the centre of the parabolic solar cooker such that the solar radiations fall directly on the base of the tank after reflected from the aluminium reflector. The angle of the reflector was to be adjusted throughout the experiment as day passed. The second step followed the recording of the required readings with the help of above-mentioned devices. The reading for the ambient temperature, humidity, solar flux/radiation, surface temperature of the thermal tank, surface temperature of top aluminium plate and solar temperature were taken. In addition, initial temperature of the water at 12:15 PM and final temperature at 3:25 PM were taken using digital thermometer.

The parabolic mirror in the solar cooker is so adjusted after certain interval of time such that the solar radiation gets reflected to the exact bottom surface of the tank containing water. This time interval may vary for different days.

For the economic and financial feasibility of the parabolic solar cooker, the cooks working in BHU Hostel have been interviewed to analyse the economic and financial feasibility of parabolic community solar cooker. To analyse the financial feasibility, calculations have been done to estimate the capital cost, maintenance cost, cooking power of the solar cooker, annual energy saved, costs of energy saved and payback period.

3 Experimental Set-up

The experimental set-up consists of parabolic dish collector having an aperture area of 6 m^2 and the aluminium tank (cooker). The base of the aluminium tank is blackened because black body is a good absorber of heat and hence reduces the cooking time by fast absorption of heat. The given parabolic dish collector is made up of multiple aluminium anodized sheets joined together in such a manner that they form a parabolic mirror which reflects the solar radiations to the bottom of the tank which was placed on the plate at the centre of the set-up. Also, Table 1 shows the devices that have been used to take the required readings for the calculation to analyse the technical feasibility of the parabolic solar cooker used in the experiment (Fig. 1).

Table 1 Sensors used for measurement

S. No.	Device	Range	Accuracy	Company
1.	Digital thermometer	-50 to 300 °C	±1.0 °C	Mextecxh DT9
2.	Digital thermo hydrometer	Temperature: -50 °C to +70 °C Humidity: 10% RH to 99% RH	Temperature: ± 1.0 °C Humidity: ±5%	HTC Instruments 288-CTH
3.	Infrared thermometer	20 to 530 °C	±2.0% + 2 °C	HTC MT4
4.	Solar power meter	1999 W/m ² 634 BTU/(ft * h)	±10 W/m ²	Tenmars TM-207

**Fig. 1** Set-up of solar cooker at centre for energy resource and development, IIT BHU

4 Results and Discussions

4.1 *Energy Efficiency and Overall Thermal Efficiency of Solar Cooker*

The energy efficiency of a solar cooker can be defined as the ratio of the energy gained by solar cooker (energy utilized for cooking) to the incident energy.

The total input incident energy to the tank (cooker) can be determined by:

$$Q_{\text{incident}} = I_S \times A_{SC} \quad (1)$$

where

I_S Insolation falling on cooker aperture

A_{SC} Aperture area of collector

And energy gained by the solar cooker i.e. energy utilized for cooking is given by:

$$Q_{\text{cooking}} = (M \times C \times \Delta T) / \Delta t \tag{2}$$

where

- M Mass of cooked food (here water)
- C Specific heat capacity of food (here water)
- Δt Time interval
- ΔT Total time required to cooking food

Energy efficiency:

$$\eta_{\text{energy}} = Q_{\text{cooking}} / Q_{\text{incident}} \tag{3}$$

$$\eta_{\text{energy}} = \frac{(M \times C \times \Delta T) / \Delta t}{I_s \times A_{SC}} \tag{4}$$

Overall thermal efficiency:

$$\eta_{\text{overall}} = (M \times C \times \Delta T_f) / I_s \times A_{SC} \times \Delta T \tag{5}$$

4.2 Calculation of Exergy Efficiency

Exergy is the maximum amount of useful work that can be obtained from a system. Exergy analysis of the system is based on the separate quantification theory and accounting for the usable energy from the system, called exergy or available energy, and unavailable energy, called irreversibility. The energy utilization efficiency of an energy conversion system is found out by means of exergy analysis.

Exergy Input (E_{xi}) [7]: The exergy of solar radiation, i.e., maximum amount of heat that can be obtained from the solar radiation.

$$E_{xi} = I_s \left[1 + 1/3(T_a/T_s)^4 - 4/3(T_a/T_s) \right] A_s \tag{6}$$

where

- T_a Ambient Temperature
- T_s Solar Temperature

Exergy output (E_{xo}): The exergy gained by the solar cooker, i.e., maximum amount of heat that can be obtained from the solar radiation and gained by the solar cooker to attain maximum temperature of water in the solar cooker.

Table 2 For energy efficiency, overall thermal efficiency and exergy of the solar cooker used

Day	Date	Initial temperature	Final temperature	Energy efficiency (%)	Overall thermal efficiency (%)	Exergy
1	05.02.2019	11.7	63.7	28.3	2.36	0.064
2	12.02.2019	23.2	78.5	25.5	2.12	0.238
3	19.02.2019	38.8	91.9	22.9	1.91	0.224

$$E_{xo} = M \times C[\Delta T - T_a \ln T_f/T_i]/\Delta t \quad (7)$$

where

T_f Final temperature of water in the tank

T_i Initial temperature of water in the tank

Exergy Efficiency of Solar Cooker (η_{exergy}): The ratio of total output exergy to total input exergy is called exergy efficiency (Table 2).

$$\eta_{\text{exergy}} = E_{xo}/E_{xi} \quad (8)$$

i.e.

$$\frac{M \times C[\Delta T - T_a \ln T_f/T_i]}{\Delta t} \quad (9)$$

$$I_S \left[1 + 1/3(T_a/T_s)^4 - 4/3(T_a/T_s) \right] A_s$$

4.3 Estimation of Useful Energy Required for Cooking

If the solar cooker is deployed in hostels and schools for cooking mid-day meal, then the most common meals served are rice, pulses and vegetables. These food items are prepared through boiling type cooking. In the experiment performed, 6 L of water has been taken. The cooks in Triveni Complex, BHU, have been interviewed to estimate the quantity of rice that can be cooked in 6 L of water. According to them, rice of approximately half the weight of water can be cooked in the given quantity of water. So in 6 L (1 L = 1 kg), approximately 3 kg of rice can be cooked.

The expression for the useful energy requirement for cooking a food item which can be prepared by boiling is given as [8]:

Table 3 For useful energy requirement

Day	Initial temperature (°C)	SH _C (KJ)	Useful energy requirement (KJ)
1	11.7	2705.15	3381.44
2	23.2	2352.84	2941.05
3	38.8	1874.93	2343.65

$$\text{Useful energy requirement, SHC} = 1.25 [(M_f \times C_{p,f} + M_{w,f} \times C_{p,w})(T_{\text{boil}} - T_{\text{initial}})] \tag{10}$$

where

- M_f Mass of food item to be cooked (kg)
- $M_{w,f}$ Mass of water required for cooking food item loaded to be cooked
- $C_{p,f}$ Specific heat (KJ/kg °C) of food item loaded to be cooked
- $C_{p,w}$ Specific heat (KJ/kg °C) of water
- T_{boil} Boiling temperature of water under atmospheric condition
- T_{initial} Initial water temperature used in cooking

The energy required during the simmering phase of cooking is taken as 25% of the energy required during sensible heating of respective food [9]. Thus, the total useful energy required to cook one batch of food item loaded to be cooked can be estimated as 1.25 times the useful energy required during the sensible heating of food.

- Specific heat of rice [8] = 1.84 kJ/kg °C
- Specific heat of water [10, 11] = 4.186 kJ/kg °C
- Mass of rice to be cooked (kg) = 3 kg
- Mass of water required for cooking food item loaded to be cooked = 6 kg
- Boiling temperature of water = 100 °C (Table 3)

Therefore, average useful energy required for cooking 3 kg rice is 2888.7195 kJ.

5 Financial Feasibility of Parabolic Solar Cooker

5.1 Estimation of Capital Cost and Maintenance Cost

Investments in buying and installing solar energy equipment are important factors in solar process economics. Table 4 summarizes the capital cost of the solar cooker.

The routine maintenance of solar cooker includes assembling and tightening of aluminium reflectors together with the help of binding wires, castor wheels and painting of steel body and other miscellaneous cost which includes labour cost. Table 5 shows the maintenance cost incurred.

Table 4 Cost break-up of parabolic solar cooker

Serial no.	Materials	Total cost (in ₹)
1	Steel structure	5930
2	Aluminium structure	3712
3	Labour	400
4	Castor wheel	100
Total		10,142

Table 5 Estimation of annual maintenance cost of a given parabolic solar cooker (6 L capacity)

Components	Type of repair	Frequency of repair	Estimated cost (₹)	Annual cost (₹)
Steel frame body	Repainting	Once in a year	72	72
Castor wheels	Replacement	Once in 4 years	100	25
Aluminium reflector	Tightening	Once in a year	60	60
Total				157

The maintenance cost is expressed as a fraction (μ) of capital cost of solar cooker.

$$C_m = \mu C_c \quad (11)$$

where

C_m maintenance cost

C_c Capital Cost

μ Fraction of capital cost of solar cooker for maintenance.

5.2 Estimation of the Cooking Power of Solar Cooker

The cooking power of the solar cooker can be calculated using the following expression:

$$P = \frac{(T_f - T_i) \cdot M_{w,f} \cdot C_{p,w}}{t} \quad (12)$$

where

P Cooking Power,

T_f final temperature,

T_i initial temperature,
 t cooking time,
 $M_{w,f}$ mass of water and
 $C_{p,w}$ specific heating capacity of water

The cooking time may vary from the place of cooking, i.e., restaurant, hostel mess or other community cooking place depending on the number of people to be surveyed and other related variables. At the experimental site, average sunshine hours [12] are 7 h or 25200 s.

Mass of water = 6 kg

Specific heating capacity of water = 4.186 kJ/kg °C

Using Eq. 12, the cooking power of the parabolic solar cooker at initial temperature of 11.7 °C, 23.2 °C and 38.8 °C and at final temperature of 63.7 °C, 78.5 °C and 91.9 °C will be evaluated as 51.82 J/s, 55.12 J/s and 52.92 J/s, respectively.

According to the cooks of the BHU Hostel mess, approximately 66 cylinders of weight 14.2 kg are consumed per month for cooking four meals a day. The cost of each unit of LPG cylinder used is ₹680, and this cost varies on monthly basis. They also informed that approximately 100 gm of rice per person per day and 50 gm of pulses per person per day are prepared by them for two meals for 200 people including hostel residents and workers. Total number of days when they prepare full meal for is complete 365 days and quantity of food prepared varies based on holidays.

5.3 Estimation of Energy Content of LPG Cylinder [13]

The calorific value of HP cylinders used is 49789.6 kJ per kg. In BHU Hostel mess, 14.2 kg of cylinder is used. So, the total energy content of a full cylinder is 707012.32 kJ per cylinder. According to calculations done above (refer Table 3), average useful energy required for cooking 3 kg of rice is 2888.7195 kJ. For calculation of unit value from the available multiple values (and vice versa), a very basic mathematical method is used called unitary method. So using unitary method, for 1 kg cooking of rice, average useful energy requirement will be 962.90 kJ/kg.

5.4 Estimation of the Annual Energy Saved and Costs of Energy Saved

Quantity of rice prepared in mess per day = 20 kg

Quantity of rice that is to be prepared in the day light = 10 kg

Useful energy required for 10 kg rice per day = 9629.065 kJ

Useful energy required for 10 kg rice per year = 3514608.73 kJ

The experiment was performed on solar cooker of capacity 6 L and can prepare 3 kg rice in one round of cooking. So to prepare 10 kg of rice, it requires three-round cooking per day saving energy of 9629.065 kJ per day.

From the interview, as mentioned in above two paragraphs, unit LPG used in mess weights 14.2 kg, hence containing 707012.32 kJ of energy per cylinder and costing ₹680 per cylinder. So, we can conclude here that for producing 707012.32 kJ of energy, it costs ₹680. Then again, using an unitary method, 1 kJ of energy produced by LPG costs ₹0.001. So the annual cost that can be saved for 3514608.73 kJ of energy will be ₹3514.

5.5 Calculation for Payback Period

The length of time required for an investment to recover its initial outlay in terms of profits or savings is called payback period.

$$\begin{aligned} \text{Payback period} &= \frac{\text{Cost of Solar Cooker}}{\text{Cost of Energy saved by using solar cooker per year}} \\ &= \$10142 / \$3514 = 2.9 \text{ years} \end{aligned}$$

6 Conclusion

In order to evaluate the performance of parabolic solar cooker, energy, exergy and overall thermal energy of the solar cooker has been calculated. The energy efficiency of solar cooker has been compared with the exergy efficiency and following conclusions have been made:

- The energy efficiency is found to be higher than the exergy efficiency.
- Overall thermal efficiency of solar cooker was 2.36, 2.12 and 1.91% for the first, second and third day of the experiment.
- Payback period for solar cooker used in the experiment is 2.9 years.

Financial feasibility analysis was also shown in the paper. The cost break-up for the capital cost of solar cooker has been done which gives the result that total cost for the construction of solar cooker is Rs 10142 and annual maintenance cost is Rs 157 which is 1.55% of total cost of production of the solar cooker given. These results suggest that the parabolic solar cooker can be potential substitute of fossil fuels used for cooking. In addition, support from government in the form of subsidy can play a vital role for the growth and development of the solar based cooking.

References

1. Petroleum planning and analysis cell, ministry of petroleum and natural gas, Government of India. assessment report: primary survey on household cooking fuel usage and willingness to convert to LPG, June 2016. Available from: <http://ppac.org.in/WriteReadData/Reports/201710310449342512219 PrimarySurveyReportPPAC.pdf>
2. State of global air, a special report on global exposure to air pollution and its disease burden (2019) Available from: https://www.stateofglobalair.org/sites/default/files/soga_2019_report.pdf
3. Rathore PKS, Rathore S, Singh RP, Agnihotri S (2018) Solar power utility sector in india: challenges and opportunities. *Renew Sustain Energy Rev* 81:2703–2713
4. Rathore PKS (2019) An experimental study on solar water heater integrated with phase change material. *Adv Fluid Therm Eng* 347–356
5. Rathore PKS, Chauhan DS, Singh RP (2019) Decentralized solar rooftop photovoltaic in India: on the path of sustainable energy security. *Renewable Energy* 131:297–307
6. Rathore PKS, Das SS, Chauhan DS (2018) Perspectives of solar photovoltaic water pumping for irrigation in India. *Energy Strategy Rev* 22:385–395
7. Panwar NL, Kaushik SC, Kothari Surendra (2012) State of the art of solar cooking: an overview. *Renew Sustain Energy Rev* 16:3776–3785
8. Sunil Indora, Tara Kandpal C (2018) Institutional and community solar cooking in India using SK 23 and scheffer solar cookers: a financial appraisal. *Renewable Energy* 120(2018):501–511
9. Shinde YH, Amogha V, Aniruddha AB, Jyestharaj JB (2014) Kinetics of cooking rice. *J Food Eng* 123:113–129
10. Khalilov MT, Manirov YT, Bekkulov BR, Aliyev RU, Jalolova ZX (2018) Experimental research for paddy and rice. *Int J Adv Res Sci Eng Technol* 5(7)
11. Akoy Elamin OM (2015) Design Construction and Performance Evaluation of Solar Cookers. *J Agri Sci Eng* 1(2):75–82
12. Shukla SK (1998) Comparison of energy and exergy efficiency of community and domestic type parabolic solar cookers. *Int J Green Energy* 437–449
13. Karadnde PD, Kumbhar SV, Songe BK (2017) Experimental study on collection efficiency of solar cooking system. *Int Res J Eng Technol* 04(02)

Computational Analysis of EMHD Flow of Nanofluid Over a Rotating Disk with Convective Boundary Conditions: Buongiorno's Model



Rajnish Kumar and Srishti Singh

Abstract In this investigation, numerical approach has been adopted to address the problem of convective boundary layer flow of nanofluid by an infinitely rotating disk. The phenomena of electrical magneto hydrodynamics (EMHD) and thermal radiation have also been analyzed. The nanofluid manifests the impact of Brownian motion and thermophoresis. The governing partial differential equations are transfigured into nonlinear coupled ordinary differential equation by employing appropriate self-similarity transformation. These ODEs are solved by utilizing shooting technique and RK-4 method. In this article, the impact of different pertinent parameters for velocity, temperature, and concentration profile have been studied. It is observed that the temperature and concentration profiles of nanofluid decline with increasing electric field parameter. The consequences obtained from the postulated method are contrasted with previously published results and manifest remarkable agreement with them.

Keywords EMHD · Nanofluid · Brownian motion · Shooting scheme · Runge–Kutta Method · Rotating disk

1 Introduction

Buongiorno [1] propounded salient features of convective heat transportation in nanofluids where he stated that reasonable explanation for the anomalous enhancement in thermal conductivity and viscosity of nanofluids were yet to be discovered then. He had considered ‘Seven Slip’ mechanisms namely Brownian diffusion, dif-

R. Kumar (✉)

Department of Mathematics, Birla Institute of Technology, Mesra, Ranchi, India
e-mail: rajnish.kumar@bitmesra.ac.in

S. Singh

Department of Electrical and Electronics Engineering, Birla Institute of Technology, Mesra, Ranchi, India
e-mail: srishti.singh1996@gmail.com

fusiophoresis, thermophoresis, the inertia, Magnus, gravity, and fluid drainage. From his examination, he identified that thermophoresis and Brownian diffusion were the only significant mechanism among the other mechanisms in nanofluids.

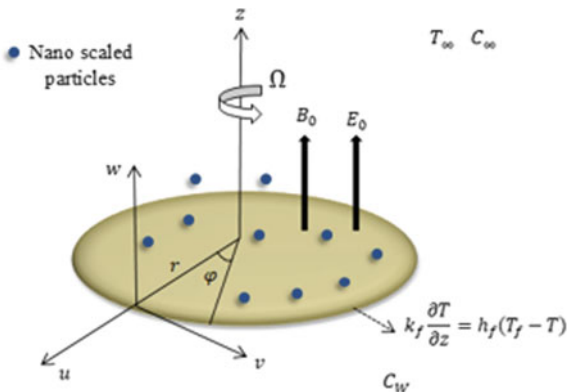
In recent times, the phenomenon of nanofluid flow over rotating disk has gained popularity among researchers particularly because of its numerous applications in diverse field of engineering, biomedical instruments, electronics devices, computer storage devices, and various others [2–4]. In order to get proper insight, various studies have been performed for decades. Von Karman [5] in his article analyzed the fluid flow over a spinning disk. In his conducted study, he adopted momentum-integral technique to analytically solve the problem. His study was further extended by Cochran [6] in which he came up with an asymptotic solution to solve such mathematical model. A series solution comprising exponentially decaying coefficients was designed by Ackroyd [7] for Von Karman problem under the influence of suction/injection. Miclavcic and Wang [8] also investigated the Von Karman model by introducing slip effects at the boundary of the rotating disk. Crank–Nicolson scheme was implemented by Attia [9] to analyze fluid flow over a rotating disk in porous medium. Millsaps and Pohlhausen [10] discussed the heat transfer problem for spinning disk which was subjected to isothermal property. Mustafa [11] performed numerical analysis of nanofluid flow over a rotating disk. In his examination, he considered the impact of partial slip at the boundaries in presence of MHD. Many researchers [12–17] have examined the fluid flow problem of rotating disk under the influence of various parameters and have designed efficient methods to solve such problems. Khan et al. [18] implemented a combination of shooting technique and finite difference to solve the problem of steady nanofluid flow over flat plat. Several other pioneering studies [19–21] have been examined which manifests the advancement in nanofluid technology

In our current study, RK-4 order method with shooting method is deployed to solve the governing equation of steady electrical MHD flow of viscous nanofluid exhibiting effect of Brownian motion and thermophoresis over a rotating disk. The impact of thermal radiation, thermophoresis, and Brownian motion is also incorporated. The results obtained are well illustrated graphically.

2 Mathematical Model

Figure 1 illustrates the geometrical configuration of flow. In our study, we have observed cylindrical co-ordinate arrangement (r, φ, z) for analyzing steady three-dimensional laminar flow of viscous nanofluid by a rotating disk in presence of phenomena electrical magneto hydrodynamics and thermal radiation. The infinitely rotating disk is located in plane $z = 0$ which rotates with consistent angular velocity Ω . Moreover, the incompressible nanofluid occupies the region $z > 0$. The impact of thermophoresis and Brownian motion is also taken into account. A constant magnetic field B_0 and uniform electrical field E_0 act perpendicularly to the direction of flow. It is assumed that magnetic Reynold number is very small, and

Fig. 1 Physical model of the flow



therefore, the impact of induced magnetic field is considered negligible. Electric and magnetic field follows Ohm’s law stating $J = \sigma(E + V \times B)$ where J is Joule current, σ is electrical conductivity, and V is fluid velocity. The temperature and concentration of the ambient liquid are given as T_∞ and C_∞ , respectively. In addition to it, the thermal boundary layer is subjected to convection, and the partial slipping effects are neglected. By applying Boungiorno’s model, the proposed boundary layer expressions are mentioned below:

$$\frac{\partial u}{\partial r} + \frac{u}{r} + \frac{\partial w}{\partial z} = 0 \tag{1}$$

$$u \frac{\partial u}{\partial r} - \frac{v^2}{r} + w \frac{\partial u}{\partial z} = \frac{\mu_f}{\rho_f} \left(\frac{\partial^2 u}{\partial r^2} + \frac{1}{r} \frac{\partial u}{\partial r} - \frac{u}{r^2} + \frac{\partial^2 u}{\partial z^2} \right) - \frac{\sigma_f B_0^2}{\rho_f} u + \frac{\sigma_f B_0 E_0}{\rho_f} \tag{2}$$

$$u \frac{\partial v}{\partial r} + \frac{uv}{r} + w \frac{\partial v}{\partial z} = \frac{\mu_f}{\rho_f} \left(\frac{\partial^2 v}{\partial r^2} + \frac{1}{r} \frac{\partial v}{\partial r} - \frac{v}{r^2} + \frac{\partial^2 v}{\partial z^2} \right) - \frac{\sigma_f B_0^2}{\rho_f} v + \frac{\sigma_f B_0 E_0}{\rho_f} \tag{3}$$

$$u \frac{\partial w}{\partial r} + w \frac{\partial w}{\partial z} = \frac{\mu_f}{\rho_f} \left(\frac{\partial^2 w}{\partial r^2} + \frac{1}{r} \frac{\partial w}{\partial r} + \frac{\partial^2 w}{\partial z^2} \right) \tag{4}$$

$$u \frac{\partial T}{\partial r} + w \frac{\partial T}{\partial z} = \alpha_f \left(\frac{\partial^2 T}{\partial r^2} + \frac{1}{r} \frac{\partial T}{\partial r} + \frac{\partial^2 T}{\partial z^2} \right) - \frac{1}{(\rho c)_f} \frac{\partial q_r}{\partial z} + \tau \left[D_B \left(\frac{\partial T}{\partial r} \frac{\partial C}{\partial r} + \frac{\partial T}{\partial z} \frac{\partial C}{\partial z} \right) + \frac{D_T}{T_\infty} \left\{ \left(\frac{\partial T}{\partial r} \right)^2 + \left(\frac{\partial T}{\partial z} \right)^2 \right\} \right] \tag{5}$$

$$\begin{aligned}
 u \frac{\partial C}{\partial r} + w \frac{\partial C}{\partial z} &= D_B \left(\frac{\partial^2 C}{\partial r^2} + \frac{1}{r} \frac{\partial C}{\partial r} + \frac{\partial^2 C}{\partial z^2} \right) \\
 &+ \frac{D_T}{T_\infty} \left(\frac{\partial^2 T}{\partial r^2} + \frac{1}{r} \frac{\partial T}{\partial r} + \frac{\partial^2 T}{\partial z^2} \right)
 \end{aligned}
 \tag{6}$$

It is to be marked that u, v, w represents radial, tangential, and axial velocity, respectively, τ is the ratio of effective heat capacity of the nanoparticles to the effective heat capacity of the base fluid, C represents concentration, T represents temperature, D_B implies Brownian diffusivity, D_T is thermophoresis diffusion coefficient, α_f is the thermal diffusivity of the fluid, ρ_f is the density of the fluid, μ_f corresponds to dynamic viscosity, σ_f denotes electrical conductivity, T_f stands for temperature of hot fluid, and $(\rho c)_f$ denotes heat capacity of fluid.

As per Rosseland’s approximation, radiative heat flux q_r which is applied to Eq. (5) has the form

$$q_r = - \frac{4\sigma^*}{3k^*} \frac{\partial T^4}{\partial z}
 \tag{7}$$

In Eq. (7), k^* signifies coefficient of mean absorption and σ^* represents Stefan–Boltzmann constant. Further assuming that the difference in temperature inside the flow is adequately very small such that T^4 can be expressed as a linear function of temperature. Thus, expanding T^4 using Taylor series about T_∞ and discarding higher order terms, we obtain

$$T^4 \cong 4T_\infty^3 - 3T_\infty^4
 \tag{8}$$

Using Eqs. (7) and (8), Eq. (5) can be rewritten as:

$$\begin{aligned}
 u \frac{\partial T}{\partial r} + w \frac{\partial T}{\partial z} &= \alpha_f \left(\frac{\partial^2 T}{\partial r^2} + \frac{1}{r} \frac{\partial T}{\partial r} + \frac{\partial^2 T}{\partial z^2} \right) - \frac{1}{(\rho c)_f} \frac{16\sigma^* T_\infty^3}{3k^*} \frac{\partial^2 T}{\partial z^2} \\
 &+ \tau \left[D_B \left(\frac{\partial T}{\partial r} \frac{\partial C}{\partial r} + \frac{\partial T}{\partial z} \frac{\partial C}{\partial z} \right) + \frac{D_T}{T_\infty} \left\{ \left(\frac{\partial T}{\partial r} \right)^2 + \left(\frac{\partial T}{\partial z} \right)^2 \right\} \right]
 \end{aligned}
 \tag{9}$$

The boundary conditions are expressed as:

$$\begin{aligned}
 u = 0, v = r\Omega, w = 0, -k_f \frac{dT}{dz} &= h_f(T_f - T), C = C_W \text{ at } z = 0 \\
 u \rightarrow 0, v \rightarrow 0, T \rightarrow T_\infty, C \rightarrow C_\infty &\text{ at } z \rightarrow \infty
 \end{aligned}
 \tag{10}$$

Hereby, self-similarity transformations are introduced which are expressed as:

$$u = r\Omega f'(\eta), v = r\Omega g(\eta), w = -\sqrt{2\Omega v_f} f(\eta)$$

$$\theta(\eta) = \frac{T - T_\infty}{T_f - T_\infty}, \phi(\eta) = \frac{C - C_\infty}{C_w - C_\infty}, \eta = z\sqrt{\frac{2\Omega}{v_f}} \tag{11}$$

By employing the transformation, governing partial differential equations are reduced to:

$$f''' + ff'' - \frac{1}{2}f'^2 + \frac{1}{2}g^2 - M(f' - E_1) = 0 \tag{12}$$

$$g'' + fg' - f'g - M(g - E_1) = 0 \tag{13}$$

$$\theta'' + \frac{\text{Pr}}{(1 + \frac{4}{3}\text{Nr})} \{f\theta' + N_b\phi'\theta' + N_t\theta'^2\} = 0 \tag{14}$$

$$\phi'' + \text{Sc}f\phi' + \frac{N_t}{N_b}\theta'' = 0 \tag{15}$$

The boundary conditions (10) are expressed as:

$$f = 0, f' = 0, g = 1, \theta' = -\text{Bi}(1 - \theta), \phi = 1 \text{ at } \eta = 0$$

$$f' \rightarrow 0, g \rightarrow 0, \theta \rightarrow 0, \phi \rightarrow 0 \text{ at } \eta \rightarrow \infty \tag{16}$$

In the above- transformed equations, M symbolizes magnetic field factor, E_1 represents electric field factor, Pr denotes Prandtl number, Nr indicates radiation factor, Sc represents Schmidt number, Bi stands for Biot number, and N_b and N_t implies Brownian and thermophoresis factor, respectively. These non-dimensional factors are illustrated below:

$$M = \frac{\sigma B_0^2}{2\rho_f\Omega}, E_1 = \frac{E_0}{B_0v}, \text{Pr} = \frac{v_f}{\alpha_f}, \text{Sc} = \frac{v_f}{D_B},$$

$$N_t = \frac{\tau D_T(T_f - T_\infty)}{T_\infty v_f}, N_b = \frac{\tau D_B(C_w - C_\infty)}{v_f}, \text{Nr} = \frac{4\sigma^* T_\infty^3}{kk^*}, \text{Bi} = \frac{h_f}{k_f} \sqrt{\frac{v_f}{2\Omega}}$$

The physical quantities of significance are skin friction, local Nusselt number, and Sherwood number. These parameters defined in non-dimensional expressions are mentioned below where local rotational Reynolds number is given as $\text{Re}_r = \frac{2(\Omega r)}{\nu}$

$$\begin{aligned}
 \text{Re}_r^{\frac{1}{2}} C_f &= f''(0) \\
 \text{Re}_r^{\frac{1}{2}} C_g &= g'(0) \\
 \text{Re}_r^{-\frac{1}{2}} \text{Nu} &= -\left(1 + \frac{4}{3} \text{Nr}\right) \theta'(0) \\
 \text{Re}_r^{-\frac{1}{2}} \text{Sh} &= -\phi'(0)
 \end{aligned}
 \tag{17}$$

3 Result and Discussions

A rational union of shooting scheme and RK-4 method has been formulated and implemented in MATLAB to solve the reduced nonlinear coupled ordinary differential Eqs. (12–15) subjected to boundary conditions Eq. (16) for different values of governing parameters namely Prandtl number Pr, magnetic field factor M, electric field factor E_1 , radiation parameter Nr, Brownian motion factor Nb, thermophoresis factor Nt, and Schmidt number Sc. Primarily, shooting technique has been employed to reduce boundary conditions Eq. (16) to initial value problem. The I.V.P is then solved by systematic approximation of $f''(0)$, $g'(0)$, $\theta'(0)$, and $\phi'(0)$ until proper convergence has been achieved. Subsequently, RK-4 method is employed with step size equal to 0.001 to solve the nonlinearly coupled ordinary differential equations. The outcomes obtained from the adopted technique are well depicted in tabular and graphical format. The behavior and impact of pertinent governing factors over non-dimensional profile of velocity, temperature, and concentration are portrayed.

Table 1 represents that by varying magnetic field factor rate of heat transfer coefficient $-\theta'(0)$ decreases significantly. It is also noted that Sherwood number $\text{Re}_r^{-\frac{1}{2}} \text{Sh}$ declines with growing value of M . A comparison has been carried out in Table 2 for different values of M .

Figures 2, 3, 4, 5, and 6 demonstrate the effect and behavior of various governing factors over velocity profile $f'(\eta)$ and $g(\eta)$. Figure 2 illustrates the impact of magnetic field parameter over the radial velocity $f'(\eta)$ when $E_1 = 0$. It is observed that as the magnetic field magnifies, the radial velocity profile reduces considerably.

Table 1 Effect of varying values of M over skin friction number, heat transfer coefficient, and Sherwood number when $N_b = N_t = \text{Bi} = \text{Nr} = 0.5$ $\text{Sc} = 1$ $\text{Pr} = 2.5$ $E_1 = 0.1$

M	$f''(0)$	$-g'(0)$	$-\theta'(0)$	$-\phi'(0)$
0.1	0.3426	0.4995	0.1442	0.2236
0.2	0.3269	0.5592	0.1409	0.2210
0.3	0.3138	0.6159	0.1378	0.2177

Table 2 Contrast of present study and previous analysis for various values of M at Velocity Slip $\gamma = 0$

M	Mustafa [11]		Present study	
	$f''(0)$	$-g'(0)$	$f''(0)$	$-g'(0)$
0.2	0.2895	0.5688	0.2895	0.5688
0.3	0.2594	0.6335	0.2594	0.6335
0.5	0.218678	0.755935	0.2187	0.7559

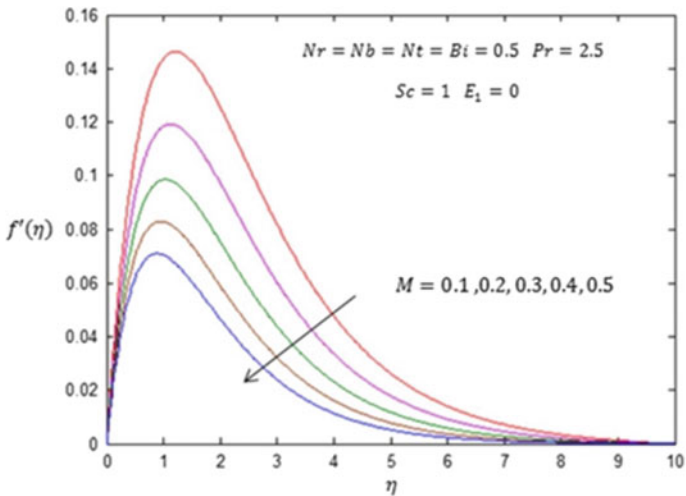


Fig. 2 Impact of M over radial velocity in absence of E_1

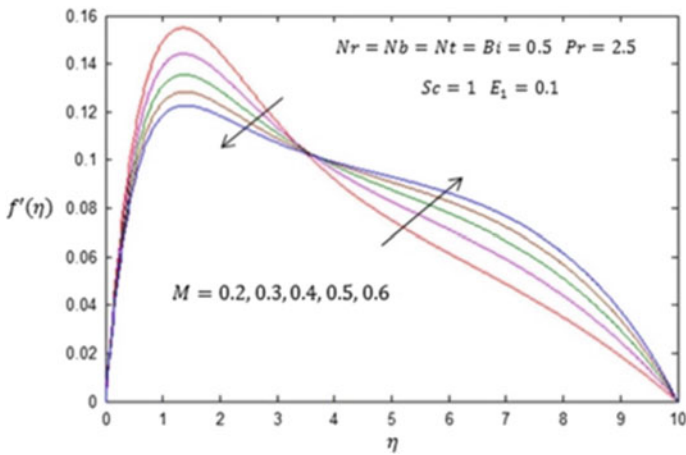


Fig. 3 Impact of M over radial velocity in presence of E_1

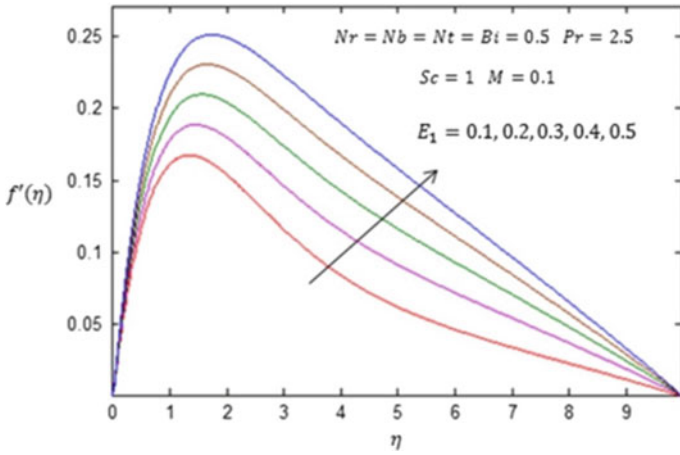


Fig. 4 Impact of E_1 over radial velocity

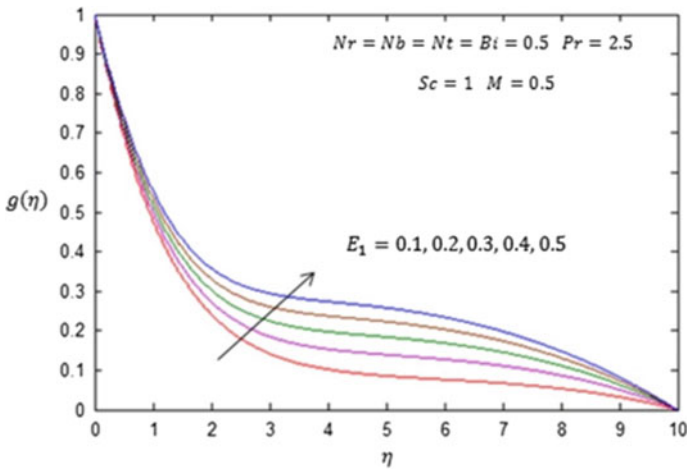


Fig. 5 Impact of E_1 over tangential velocity

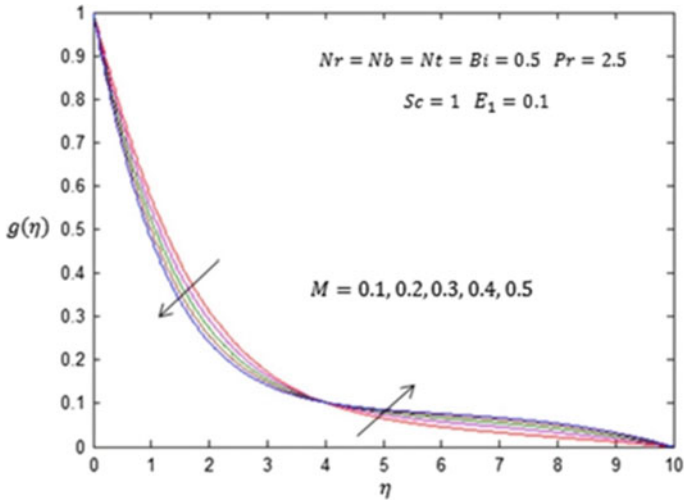


Fig. 6 Impact of M over tangential velocity in presence of E_1

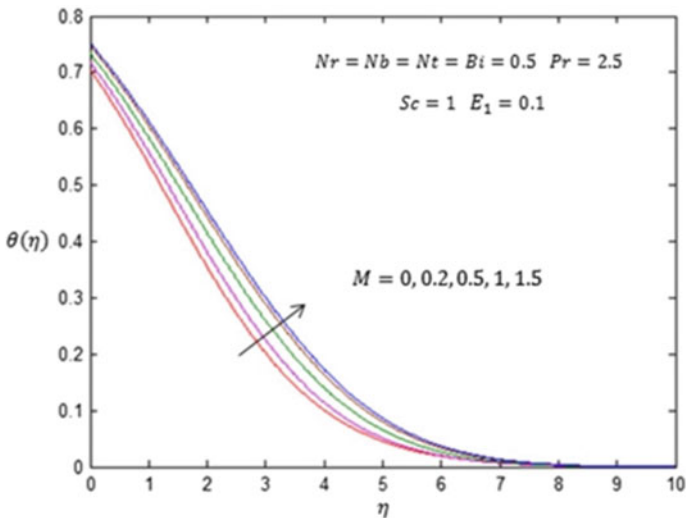


Fig. 7 Influence of M over temperature

This indicates that the Lorentz force intensifies the force of friction that behaves like a decelerating force which opposes the flow of nanofluid over rotating disk. Figure 3 demonstrates influence of magnetic field factor over $f'(\eta)$ in presence of electric field parameter. It is observed that radial velocity initially decreases to a certain distance from wall as magnetic field strengthens while afterward it enhances

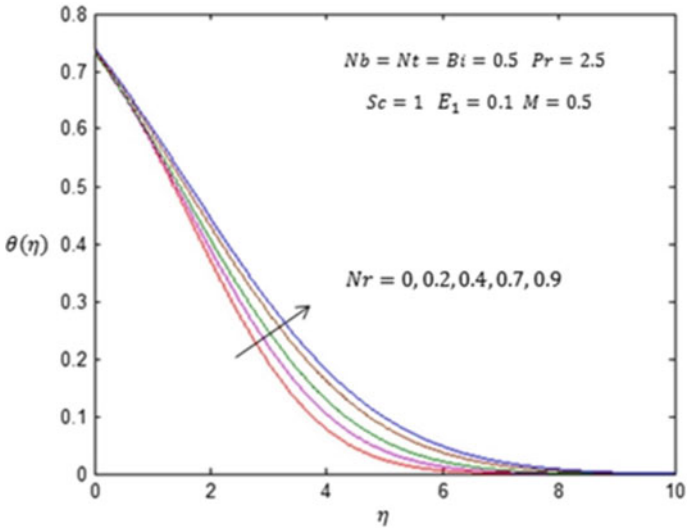


Fig. 8 Impact of Nr over temperature

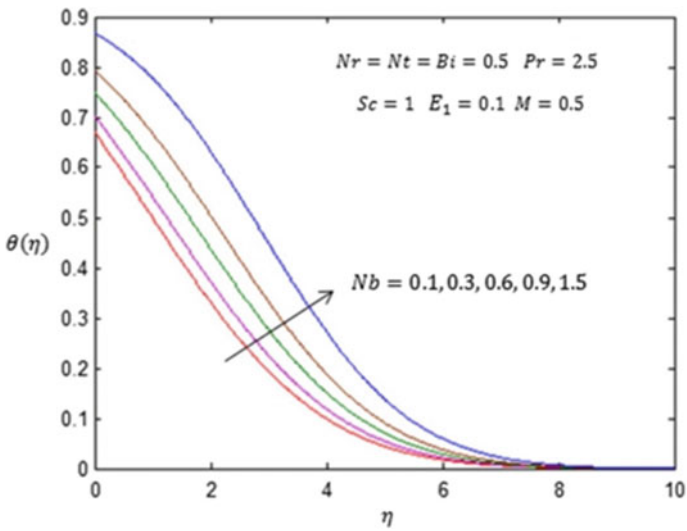


Fig. 9 Impact of Nb over temperature

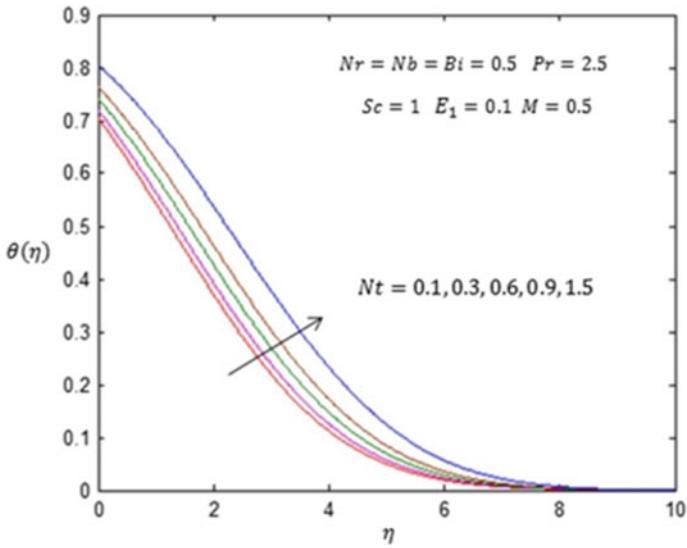


Fig. 10 Impact of N_r over temperature

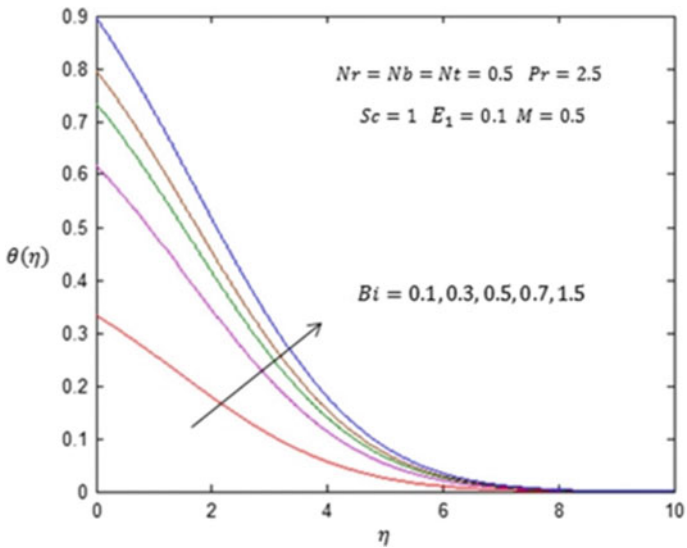


Fig. 11 Impact of Biot number over temperature

with increasing value of M . The reason for this behavior is that the electric field acts like an accelerating force which supports the flow of nanofluid. Similar impact is observed in tangential velocity profile $g(\eta)$ which is depicted in Fig. 6. The

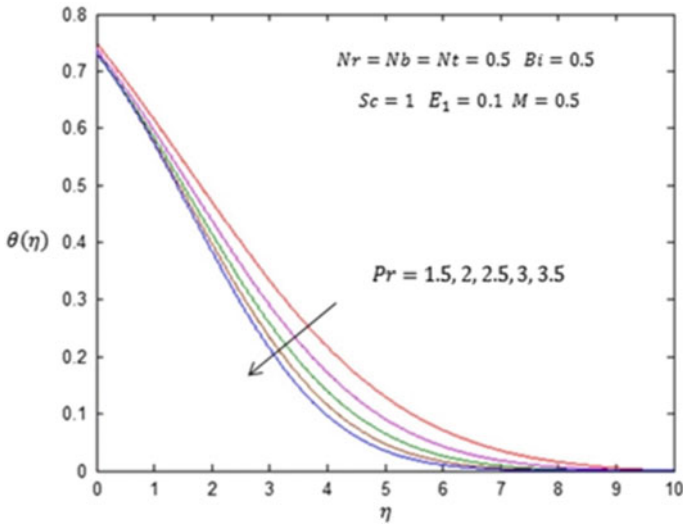


Fig. 12 Impact of Pr number over temperature

influence of electric field parameter over radial and tangential velocity profile is well illustrated in Figs. 4 and 5, respectively. It is perceived that as electric field magnifies, flow of nanofluid enhances radially as well as tangentially.

The effect and behavior of various governing factors over temperature profile $\theta(\eta)$ are portrayed in Figs. 7, 8, 9, 10, 11, 12, and 13. It is noticed in Fig. 7 that as the magnetic field magnifies, the thickness of thermal boundary layer enhances. This is because Lorentz force escalates the nanofluid resistance which corresponds to increase in temperature of fluid. It is shown in Fig. 8 that as the radiation parameter N_r enhances, the temperature of nanofluid also intensifies. Larger values of radiation factor correspond to reduction in the rate of heat transfer. The influence of Brownian motion factor N_b and thermophoresis factor N_t over temperature profile is presented in Figs. 9 and 10, respectively. It is identified that enhancement in N_t leads to thicker thermal boundary layer and significant increase in temperature profile. It is marked that with increase in N_b , the random motion of nanoparticle species also rises. Consequently, the particles collide with one another, and thus, the acquired kinetic energy is converted to heat energy which corresponds to adequate rise in thickness of thermal layer and increment in temperature profile. It is displayed in Fig. 11 that with enlargement in Biot number, there is increment in nanofluid temperature and thickness of thermal layer. It is depicted in Fig. 12 that as Prandtl number enhances, the temperature profile declines thereby yielding inadequate thermal diffusivity that leads to reduction in thickness of thermal boundary layer. It is revealed in Fig. 13 that the temperature and the related thickness of thermal layer decrease with rising value of electric field parameter.

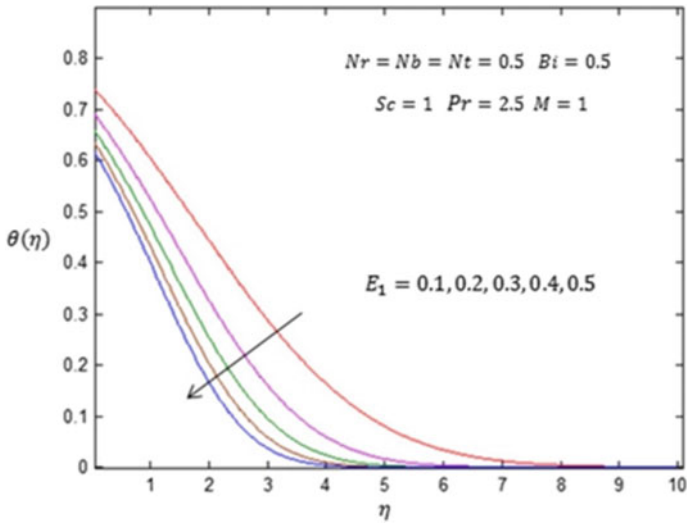


Fig. 13 Impact of E_1 over temperature

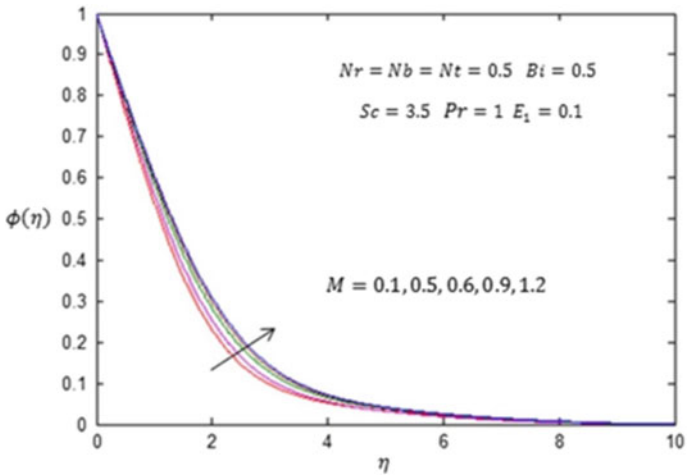


Fig. 14 Impact of M over concentration

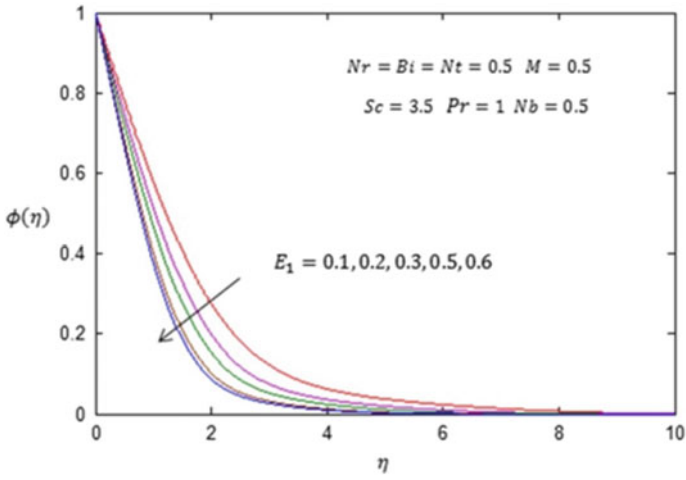


Fig. 15 Impact of E_1 on concentration

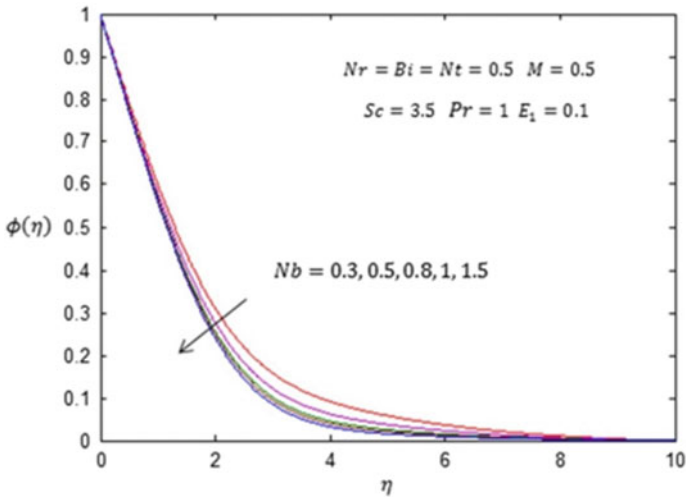


Fig. 16 Impact of N_b over concentration

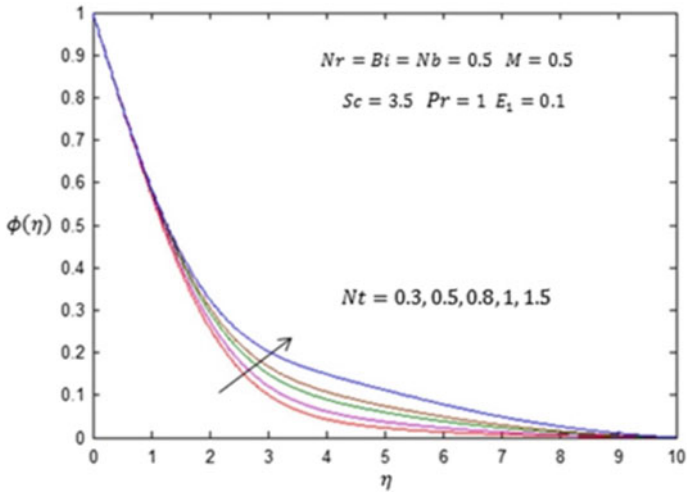


Fig. 17 Impact of N_t over concentration

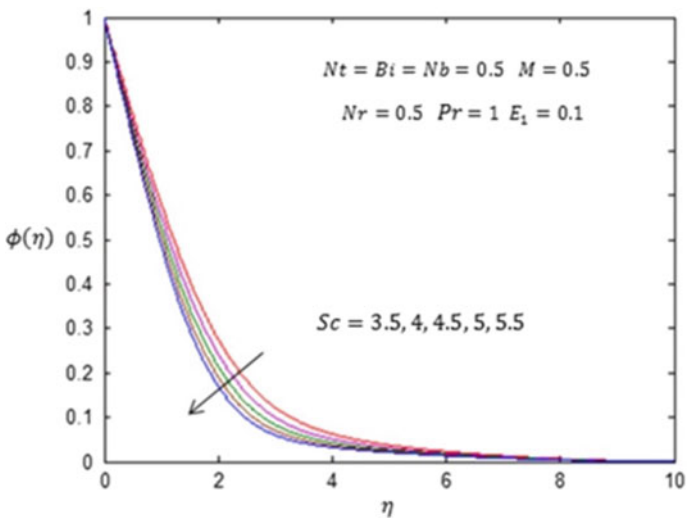


Fig. 18 Impact of Sc over concentration

The impact and behavior of different governing factors over concentration profile $\phi(\eta)$ are depicted in Figs. 14, 15, 16, 17, and 18. It is observed that with increment in M thickness of concentration profile enhances. Figure 15 designates the effect of E_1 over concentration profile. Higher values of electric field lead to decline in concentration of nanofluid at the boundary as well as there is significant reduction in thickness of concentration profile. It is noticed in Fig. 16 that enlargement in Brownian motion factor N_b results in lower concentration profile and increment in rate of mass transfer at the boundary. Figure 17 demonstrates the influence of thermophoresis factor N_t over concentration profile. As N_t magnifies, the thickness of concentration boundary layer also increases. Moreover, the rate of mass transfer at the boundary enhances for larger thermophoresis factor. Figure 18 illustrates the influence of Schmidt number Sc over the concentration profile. It is marked that larger values Sc corresponds to inadequate Brownian diffusivity thereby yielding reduced concentration profile and lower thickness associated with the concentration layer. Consequently, the rate of at which mass transfer occurs at the boundary intensifies.

Figures 2–18 are illustrated.

4 Conclusions

Our present perusal explores computational scheme to compute convective flow of nanofluid over rotating disk subjected to electrical MHD and radiation factor. The problem also involves the aspects of thermophoresis and Brownian motion. The prominent observations of the evaluation are summarized as follows:

- With increment in magnetic field parameter in absence of electric field, the radial velocity reduces.
- As electric field parameter strengthens, both radial and tangential velocity profiles enhance.
- Magnetic field, radiation parameter, and Biot number exhibit similar impact over temperature profile. By enlarging their values, thickness of temperature boundary layer magnifies.
- Larger N_b and N_t results in increment of nanofluid temperature and the related thickness of thermal surface.
- Temperature and concentration profile demonstrates similar impact for higher electric field factor.
- It is noticed that N_b and N_t demonstrate opposite effect over concentration profile.
- For growing values of Schmidt number, it is marked that rate of mass transfer at the concentration regime intensifies.
- Heat transfer coefficient and Sherwood number decline with increasing value of magnetic field factor.

References

1. Buongiorno J (2006) Convective transport in nanofluids. *ASME J Heat Transf* 128:240–250
2. Hu Z, Lu W, Thouless MD (2015) Slip and wear at a corner with Coulomb friction and an interfacial strength. *Wear* 338:242–251
3. Hu Z, Lu W, Thouless MD, Barber JR (2016) Effect of plastic deformation on the evolution of wear and local stress fields in fretting. *Int J Solids Struct* 82:1–8
4. Wang H, Hu Z, Lu W, Thouless MD (2017) The effect of coupled wear and creep during grid-to-rod fretting. *Nucl Eng Des* 318:163–173
5. Von Karman T (1921) Überlaminare und turbulente Reibung. *Zeitschrift für Angew Math Mech ZAMM* 1:233–252
6. Cochran WG (1934) The flow due to a rotating disk. *Proc Camb Philos Soc* 30:365–375
7. Ackroyd JAD (1978) On the steady flow produced by a rotating disk with either surface suction or injection. *J Eng Math* 12:207–220
8. Miclavcic M, Wang CY (2004) The flow due to a rough rotating disk. *Z Angew Math Phys* 54:1–12
9. Attia HA (2009) Steady flow over a rotating disk in porous medium with heat transfer. *Nonlinear Anal Model Control* 14:21–26
10. Millsaps K, Pohlhausen K (1952) Heat transfer by laminar flow from a rotating disk. *J Aeronaut Sci* 19:120–126
11. Mustafa M (2017) MHD nanofluid flow over a rotating disk with partial slip effects: Buongiorno model. *Int J Heat Mass Transfer* 108:1910–1916
12. Turkyilmazoglu M, Senel P (2013) Heat and mass transfer of the flow due to a rotating rough and porous disk. *Int J Therm Sci* 63:146–158
13. Rashidi MM, Kavyani N, Abelman S (2014) Investigation of entropy generation in MHD and slip flow over a rotating porous disk with variable properties. *Int J Heat Mass Transf* 70:892–917
14. Turkyilmazoglu M (2014) Nanofluid flow and heat transfer due to a rotating disk. *Comput Fluids* 94:139–146
15. Hatami M, Sheikholeslami M, Ganji DD (2014) Laminar flow and heat transfer of nanofluid between contracting and rotating disks by least square method. *Powder Tech* 253:769–779
16. Mustafa M, Khan JA, Hayat T, Alsaedi A (2015) On Bödewadt flow and heat transfer of nanofluids over a stretching stationary disk. *J Mol Liq* 211:119–125
17. Sheikholeslami M, Hatami M, Ganji DD (2015) Numerical investigation of nanofluid spraying on an inclined rotating disk for cooling process. *J Mol Liq* 211:577–583
18. Khan WA, Khan ZH, Rahi M (2014) Fluid flow and heat transfer of carbon nanotubes along a flat plate with Navier Slip boundary. *Appl Nano Sci* 4:633–641
19. Garmroodi MRD, Ahmadpour A, Talati F (2019) MHD mixed convection of nanofluids in the presence of multiple rotating cylinders in different configurations: a two-phase numerical study. *Int J Mech Sci* 150:247–264
20. Abbassi MA, Safaei MR, Djebali R, Guedri K, Zeghmami B, Alrashed AAAA (2018) LBM simulation of free convection in a nanofluid filled incinerator containing a hot block. *Int J Mech Sci* 148:393–408
21. Farshad SA, Sheikholeslami M (2019) FVM modeling of nanofluid forced convection through a solar unit involving MCTT. *Int J Mech Sci* 159:126–139

CFD Analysis of Mixed Convection in an Enclosure with a Floor-Mounted Step-Like Heat Source



Venkata Reddy Poluru

Abstract The objective of this work is to study the two-dimensional mixed convection flow and heat transfer over an isoflux step projecting from the floor of an enclosure. The inflow into the enclosure takes place through two inlets placed at either end of the floor and the outflow occurs through an outlet provided in the ceiling of the enclosure. The walls of the enclosure are insulated. Convective heat transfer from the step surfaces to the fluid occurs due to the combined action of forced and free convection effects. The heat transferred to the fluid is carried away by the fluid leaving the enclosure. A mathematical formulation is developed by setting up the conservation equations for mass, momentum and energy, and the initial and boundary conditions. The density variation is taken into account only in so far as it gives rise to a buoyancy force. The equations are non-dimensionalised so that the results will have applicability to wide-ranging practical conditions. A numerical formulation is developed by discretising the primitive variable equations on a staggered mesh, using the ultra-sharp strategy for convection terms with donor-cell differencing scheme option, the modified strongly implicit procedure (MSIP) as the equation solver and the Simplified Marker and Cell (SMAC) method as the pressure-velocity coupling algorithm. Parametric studies are performed by varying the Archimedes number Ar and Reynolds number Re (while Prandtl number Pr is chosen as 0.71 corresponding to air as the working medium), and results are presented in the form of streamline and isotherm maps, graphs, and tables.

Keywords Two-dimensional mixed convection • Cooling of electronic components

V. R. Poluru (✉)
Amity University Campus, Dubai, UAE
e-mail: vreddy@amityuniversity.ae

© The Author(s), under exclusive license to Springer Nature Singapore Pte Ltd. 2021
B. S. Sikarwar et al. (eds.), *Advances in Fluid and Thermal Engineering*,
Lecture Notes in Mechanical Engineering,
https://doi.org/10.1007/978-981-16-0159-0_22

249

1 Introduction

Combined free and forced convection (also referred as a mixed convection) plays an important role in several practical applications like cooling of electronic components, thermal environmental control of dwellings, thermal storage tanks, thermal discharges into lakes and rivers, electric ovens and furnaces [1], and air distribution in ventilated/air-conditioned spaces [2]. But relatively less work is done in the area of mixed convection in enclosures. This is because when low-velocity forced convection occurs the buoyancy effects may compete with forced convection effects.

In general, buoyancy effects cannot be fully separated from forced convection effects. Objective of the present work is to perform a numerical study of this mixed convection in a rectangular enclosure resulting from forced flow and buoyancy effects generated by heat generating equipment present in the enclosure.

2 Literature Overview

The following conclusions are reached from a study of the relevant literature [1–7]:

- A considerable amount of work is done in respect of mixed convection in external flow and mixed convection in channels and tubes. Generally, the opposing mixed convection case is less studied. For external flows, boundary-layer approximations are often made for simplicity for opposing mixed convection. However, the boundary-layer approximations are likely to break down when the buoyancy and forced flow effects compete with each other. Hence, numerical studies employing complete equations need to be carried out in order to determine the flow separation effects. There is also a need for experimental data in the area of opposing external flow mixed convection to verify the numerical solutions.
- The standard thermal boundary conditions like isothermal and isoflux walls are generally difficult to achieve in practice because of conduction through substrates and walls. However, very less work is done in the area of conjugate mixed convection in case of both external and internal flows.
- Mixed convection in enclosures has so far received considerably less attention. The reason could be that while Archimedes number becomes an extra parameter (compared to Reynolds number in pure forced convection and Grashof number in pure natural convection), the geometric parameters like the sizes and placement of inflow and outflow openings also add significantly to the number of governing parameters. The placement of inflow and outflow openings also renders each problem rather unique and makes it difficult to draw general conclusions about mixed convection in enclosures. Despite these facts, applications involving mixed convection in enclosures abound in our daily life.

Hence, there appears to be very wide scope for numerical and experimental investigations in this area.

3 Physical Model

Figure 1 shows the physical model and the coordinate system. Here, x^* and y^* are the dimensionless Cartesian coordinates. The origin is placed at the bottom left corner of the enclosure with the positive direction of the x^* -axis towards right and the positive direction of the y^* -axis vertically upwards. A non-inclined enclosure is considered in the present work by choosing $\theta_x = 90^\circ$ and $\theta_y = 180^\circ$, which are the angles between the gravity vector and the coordinate axes.

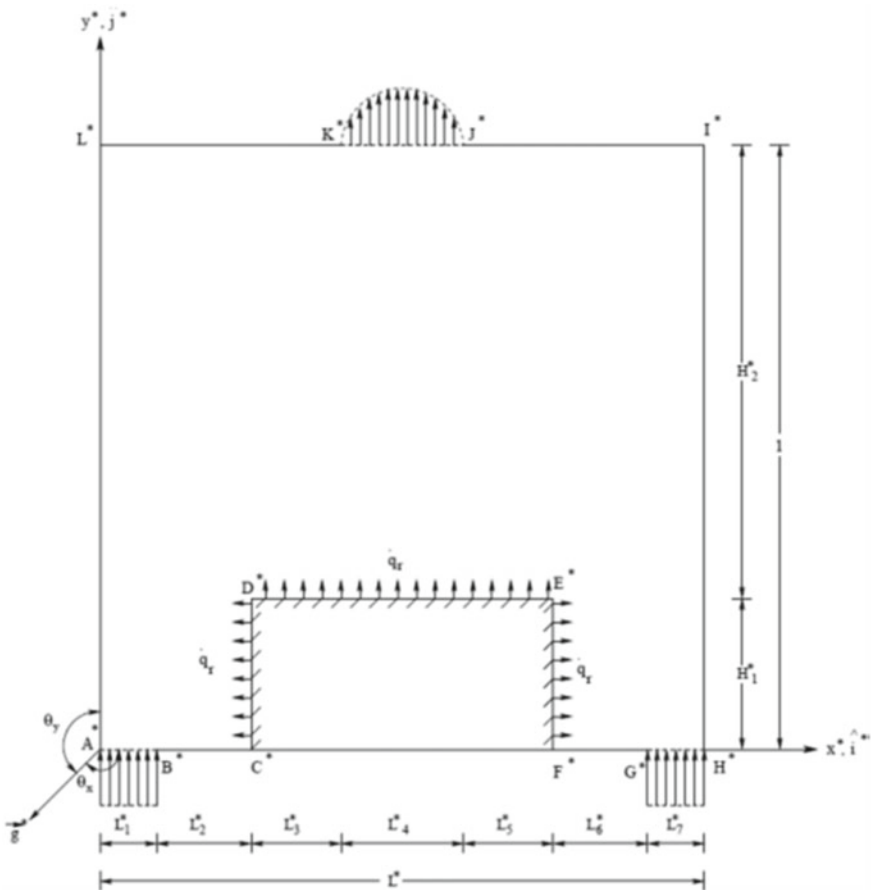


Fig. 1 Physical model mapped on to the non-dimensional coordinate system

The flow and temperature fields are taken as two-dimensional in the $x^* - y^*$ plane. The inlets on the floor of the enclosure are of width L_1^* and L_7^* and the width of the outlet on the ceiling of the enclosure is L_4^* . The width and height of the step (or rib) are $L_3^* + L_4^* + L_5^*$ and H_1^* , respectively, L_2^* and L_6^* being the distances between the inlets and the step. The overall width and height of the enclosure are L^* and H^* , respectively.

At times, less than or equal to zero, the fluid inside the enclosure is quiescent and the temperature is uniform throughout. For times greater than zero, the fluid begins to enter the enclosure through the inlets with a time-invariant velocity profile, which in the present problem is assumed to be rectangular for simplicity. Simultaneously, a constant heat flux with respect to time and position is generated on the left, top and right faces of the step and is transferred to the fluid.

4 Mathematical and Numerical Formulations

A mathematical formulation is developed by setting up the time-dependent conservation equations for momentum and energy and the initial and boundary conditions. The density variation is taken into account only via the Boussinesq approximation. The equations are cast in dimensionless form. A numerical formulation is then developed by discretising the time-dependent primitive variable equations on a staggered mesh. The convection terms are treated by the ultra-sharp strategy of Leonard and Drummond [3]. The pressure-velocity coupling is taken into account by the Simplified Marker and Cell (SMAC) method [4]. The modified strongly implicit procedure (MSIP) is used as the equation solver [5]. The non-dimensional governing equations are as follows:

Continuity Equation

$$\frac{\partial u^*}{\partial x^*} + \frac{\partial v^*}{\partial y^*} = 0 \quad (1)$$

x^* -Direction Momentum Equation

$$\begin{aligned} \frac{\partial u^*}{\partial t^*} + \frac{\partial}{\partial x^*} (u^{*2}) + \frac{\partial}{\partial y^*} (u^* v^*) = - \frac{\partial p^*}{\partial x^*} \\ + \frac{1}{\text{Re}} \left(\frac{\partial^2 u^*}{\partial x^{*2}} + \frac{\partial^2 u^*}{\partial y^{*2}} \right) - \text{Ar} T^* \cos(\theta_x) \end{aligned} \quad (2)$$

y^* -Direction Momentum Equation

$$\frac{\partial u^*}{\partial t^*} + \frac{\partial}{\partial x^*}(u^*v^*) + \frac{\partial}{\partial y^*}(v^{*2}) = -\frac{\partial p^*}{\partial y^*} + \frac{1}{\text{Re}} \left(\frac{\partial^2 v^*}{\partial x^{*2}} + \frac{\partial^2 v^*}{\partial y^{*2}} \right) - \text{Ar}T^* \cos(\theta_y) \quad (3)$$

Energy Equation

$$\frac{\partial T^*}{\partial t^*} + \frac{\partial}{\partial x^*}(u^*T^*) + \frac{\partial}{\partial y^*}(v^*T^*) = \frac{1}{\text{Re Pr}} \left(\frac{\partial^2 T^*}{\partial x^{*2}} + \frac{\partial^2 T^*}{\partial y^{*2}} \right) \quad (4)$$

Initial and Boundary Conditions

The dimensionless forms of the initial and boundary conditions are given below:

At $t^* \leq 0$ (initial conditions): $u^* = 0$; $v^* = 0$; $T^* = 0$, inside the region $A^*B^*C^*D^*E^*F^*G^*H^*I^*J^*K^*L^*A^*$ and on its boundary.

At $t^* > 0$ (boundary conditions): $u^* = 0$; $v^* = 0$, on the boundaries $B^*C^*D^*E^*F^*G^*$, $H^*I^*J^*$ and $K^*L^*A^*$.

On the boundaries A^*B^* , G^*H^* : $v^* = 1$, and on the boundary J^*K^* : $\frac{\partial u^*}{\partial y^*} = 0$ and $p^* = 0$.

As mentioned earlier, v^* on J^*K^* should be determined in such a way that mass conservation is satisfied.

On B^*C^* , F^*G^* , I^*J^* and K^*L^* : $\frac{\partial T^*}{\partial y^*} = 0$, and on H^*I^* and L^*A^* : $\frac{\partial T^*}{\partial x^*} = 0$.

On the boundary C^*D^* : $\frac{\partial T^*}{\partial x^*} = 1$, and on the boundary E^*F^* : $\frac{\partial T^*}{\partial x^*} = -1$.

On the boundary D^*E^* : $\frac{\partial T^*}{\partial y^*} = -1$, and on the boundary J^*K^* : $\frac{\partial T^*}{\partial y^*} = 0$.

On the boundaries A^*B^* and G^*H^* : $T^* = 0$.

5 Results and Discussion

Parametric studies are performed by varying the Reynolds number Re in the range 5–5000 and the Archimedes number Ar in the range 0–100. The characteristic dimension in the definition of Re and Ar is the enclosure height. The characteristic temperature difference is based on the enclosure height and the heat flux from the step. The geometrical parameters shown in Fig. 1 are chosen as $L_1^* = 0.1$, $L_2^* = 0.15$, $L_3^* = 0.15$, $L_4^* = 0.2$, $L_5^* = 0.15$, $L_6^* = 0.15$, $L_7^* = 0.1$, $H_1^* = 0.25$, and $H_2^* = 0.75$. The Prandtl number Pr is chosen as 0.71 corresponding to air as the working medium. A 62×62 mesh is chosen for the parametric study. Results are

presented for the time variation of the step average temperature, variation of the steady-state local Nusselt number and temperature distributions along the step, and variation of the pressure drop across the enclosure and the average step temperature with Ar for various values of Re . The streamline and isotherm maps are generated for all the sets of parameters. However, a typical streamline and isotherm map is shown in Fig. 2 for Reynolds number, $Re=500$, and Archimedes number, $Ar=100$.

The variation of the average step temperature with respect to time at various Reynolds numbers is shown in Fig. 3. From this graph, it can be seen that the temperature rises rapidly initially. The rate of variation then decreases, and finally, the temperature stabilises at a steady value. In no case is there any oscillatory approach to steady state. A small increase at the lower end of the Reynolds number range brings about a rapid fall in the steady temperatures of the step.

When the Reynolds number is increased through the middle range, there is still a drop, but a gradual one, in the steady temperatures. The time–temperature variation for the right vertical face will be identical to that of the left vertical face due to the symmetry about the vertical centre line of the enclosure.

The steady-state temperature distribution along the step for $Re = 500$ and various Archimedes numbers is shown in Fig. 4. It may be noted that the temperature is depressed at the centre of the horizontal face at lower Archimedes numbers and is elevated at higher Archimedes number, showing more clearly the increasing effect of natural convection on the horizontal face.

Consider now the left and the right vertical faces of the step which are uniform heat flux surfaces. A vertical flat plate with uniform heat flux has generally an increasing temperature with distance measured from the leading edge, in forced, free and aiding mixed convection regimes.

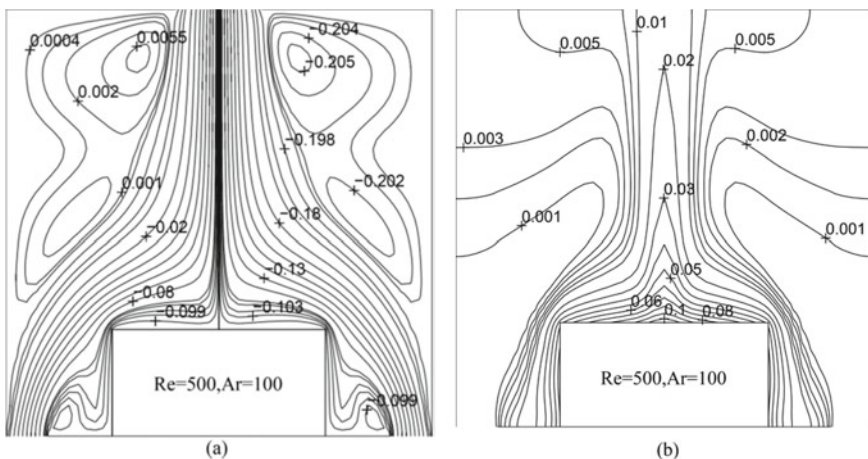


Fig. 2 a Streamlines and b isotherms, for $Re = 500$ and $Ar = 100$

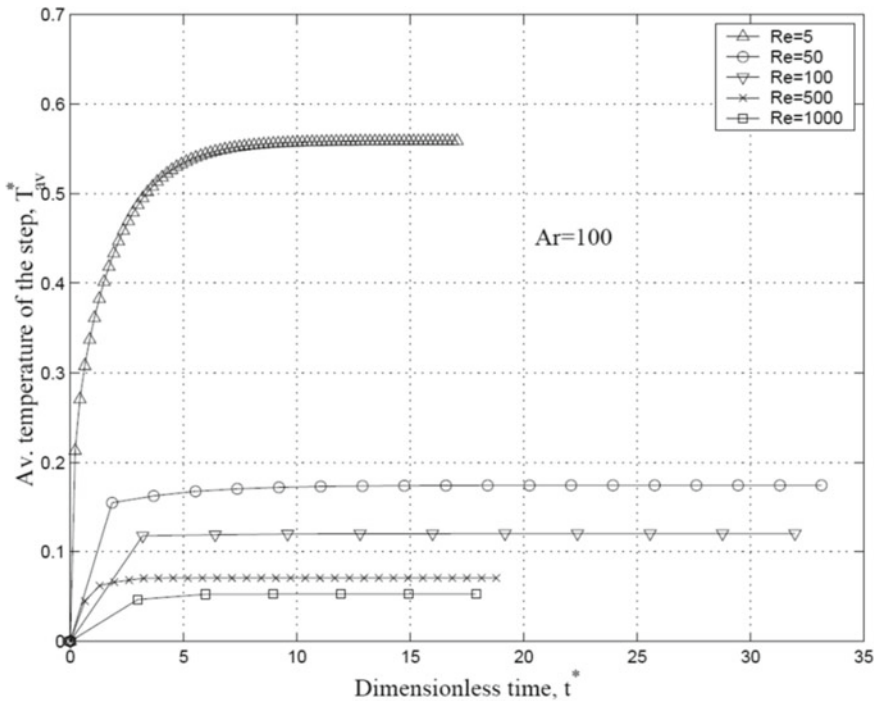


Fig. 3 a Time variation of the average temperature of the step for Ar = 100

The local Nusselt number Nu_s^* at any location on the step is defined in terms of heat transfer coefficient α_s^* and thermal conductivity λ as:

$$Nu_{s^*} = \frac{\alpha_{s^*} H}{\lambda} = \frac{\dot{q} H}{(T_{s^*} - T_r) \lambda} = \frac{\Delta T}{(T_{s^*} - T_r)} = \frac{1}{T_{s^*}}$$

According to which the local Nusselt number is the reciprocal of the local non-dimensional temperature. For this reason, the distribution of the local Nusselt number will be just opposite to that of the local non-dimensional temperature as shown in Fig. 5.

Figure 6 shows the variation of the pressure drop Δp^* across the enclosure against the Archimedes number for Re = 5, 50, 100 and 500. For lower Reynolds numbers, it may be seen that Δp^* is a linear function of Ar. The variation becomes slightly nonlinear at higher Reynolds numbers. More importantly, at any Reynolds number, as the Archimedes number is increased, the pressure drop across the enclosure decreases, passes through zero and even becomes negative. When the pressure drop is exactly zero, the fluid flow and heat transfer mechanism inside the enclosure can be called natural convection.

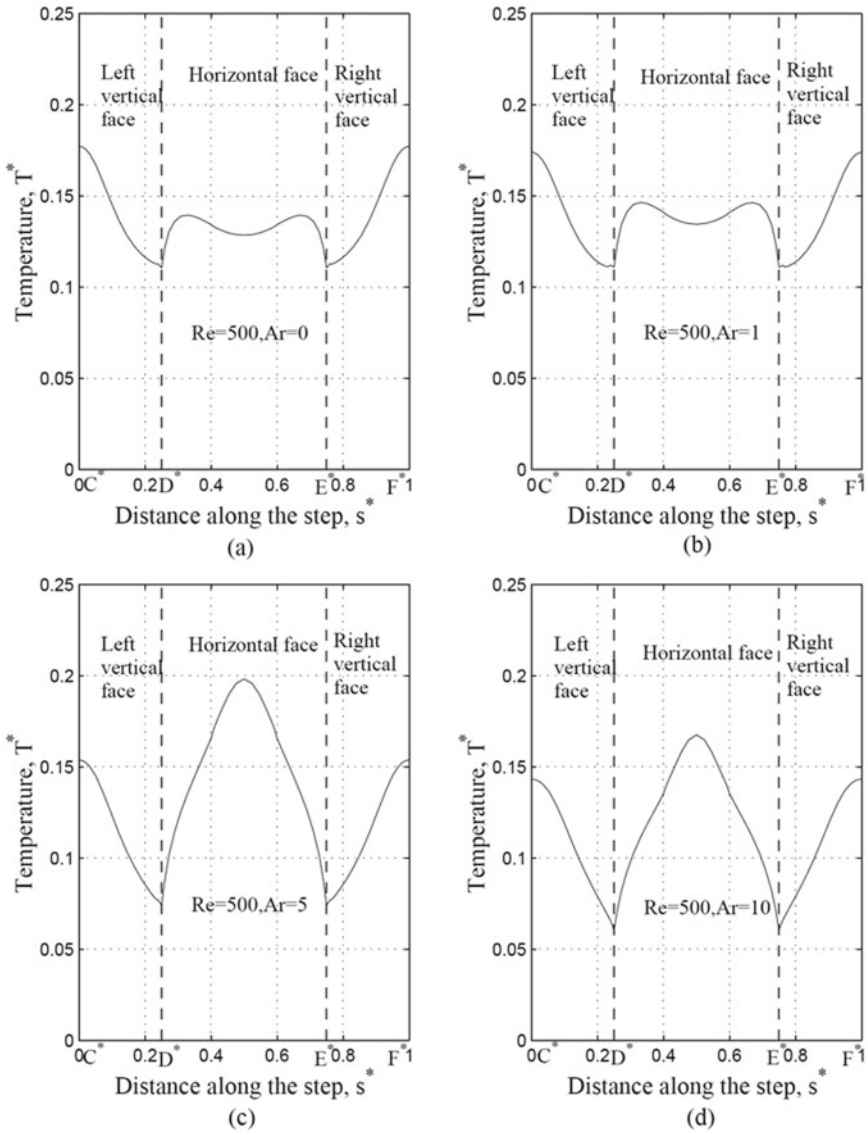


Fig. 4 Steady-state temperature distribution along the step **a** $Re = 500, Ar = 0$. **b** $Re = 500, Ar = 1$. **c** $Re = 500, Ar = 5$. **d** $Re = 500, Ar = 10$

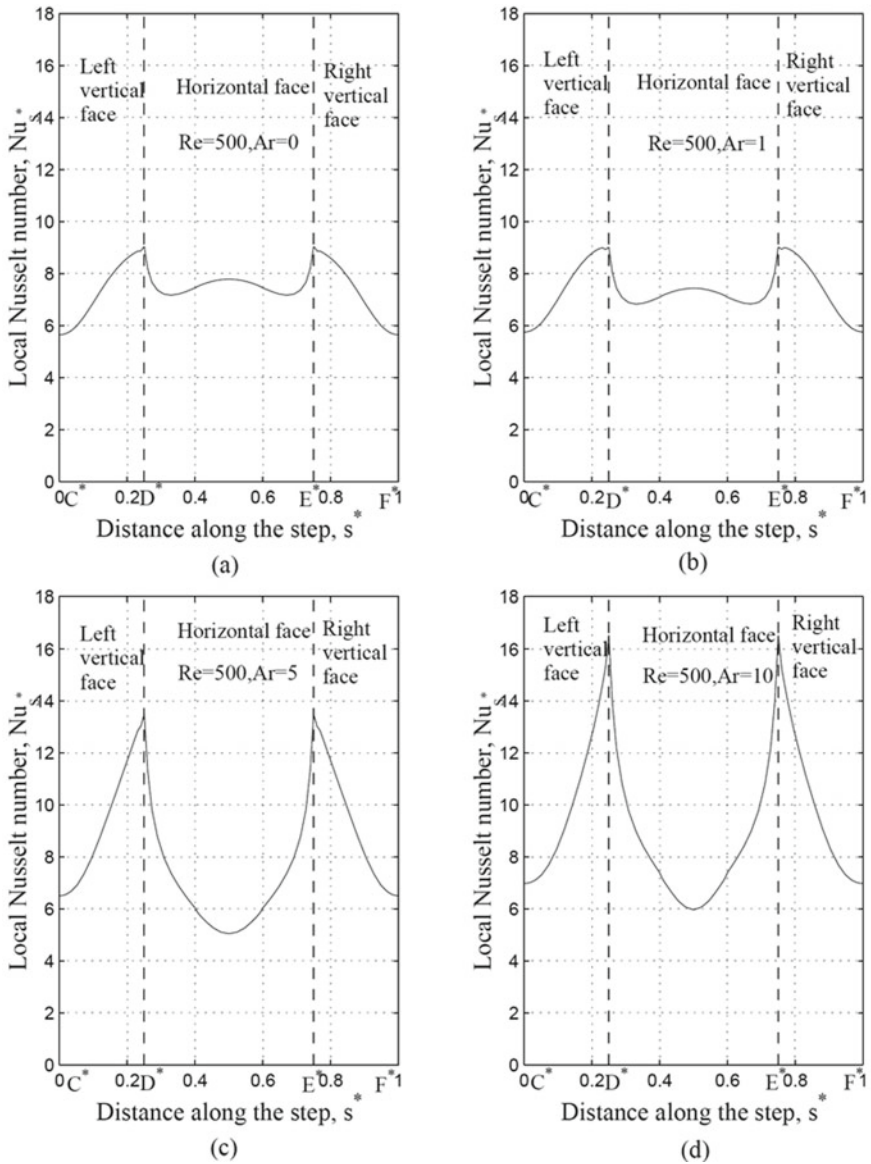


Fig. 5 Local Nusselt number distribution along the step **a** $Re = 500, Ar = 0$. **b** $Re = 500, Ar = 1$. **c** $Re = 500, Ar = 5$. **d** $Re = 500, Ar = 10$

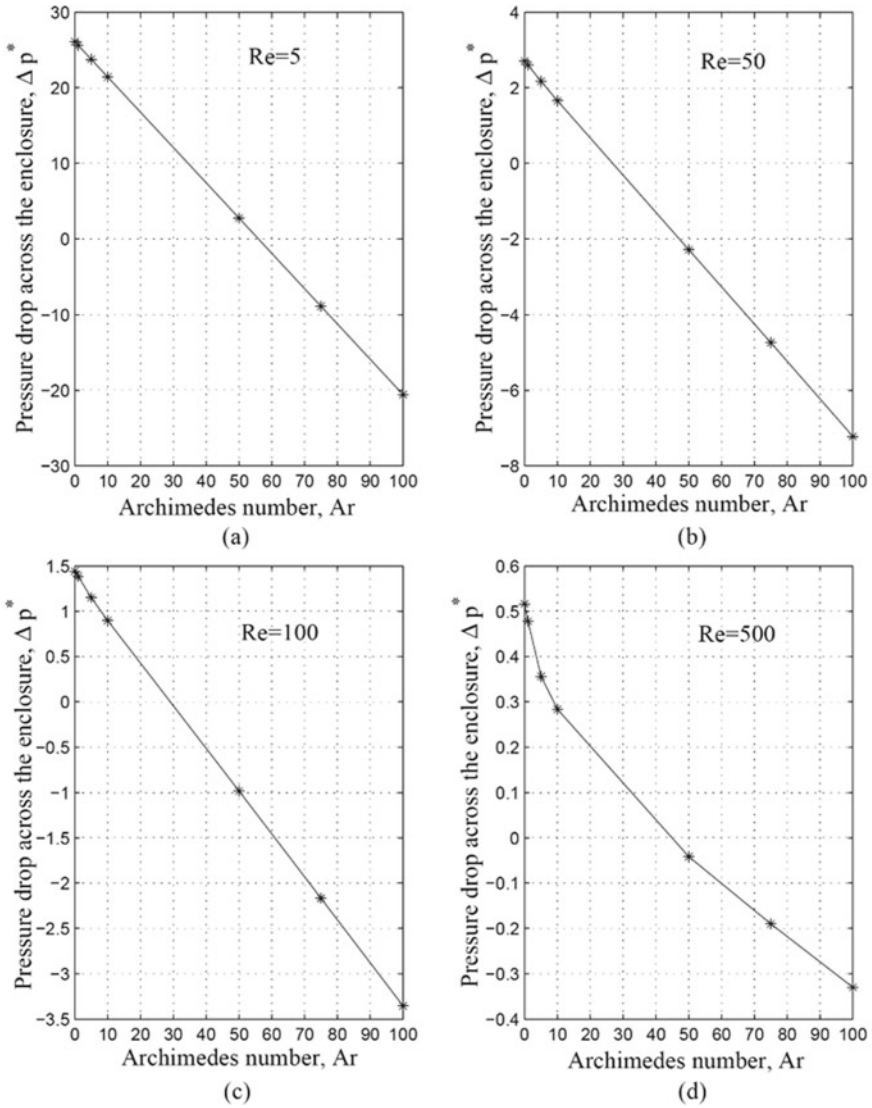


Fig. 6 Variation of the pressure drop across the enclosure with Archimedes number **a** $Re = 5$. **b** $Re = 50$. **c** $Re = 100$. **d** $Re = 500$

6 Conclusions

The effect of natural convection is to prevent the formation of eddies above the horizontal face of the step and to promote the same at the top right and left corners of the enclosure. At any Reynolds number, the pressure drop across the enclosure decreases with increase in Archimedes number, passes through zero and becomes negative thereafter. The positive and negative pressure drops separate the Archimedes number range into aiding mixed convection and opposing mixed convection regimes. At an Archimedes number resulting in zero pressure drop, the Reynolds number should be considered as a dimensional flow rate inducted by the enclosure due to pure buoyancy effect. The buoyancy effect is found to be significant at moderate Reynolds numbers. For instance at Reynolds number of 500, the dimensionless average step temperature is likely to be overpredicted by a maximum of 60 per cent in the aiding mixed convection regime, if analysis is performed assuming forced convection without taking the buoyancy effects into account.

References

1. Papanicolaou E, Jaluria Y (1994) Mixed convection from simulated electronic components at varying relative positions in a cavity. *Trans ASME J Heat Trans* 116:960–970
2. Nielsen PV (1982) Some aspects of the air distribution in ventilated rooms. *Int J Refrig* 5 (2):79–85, March
3. Leonard BP, Drummond JE (1995) Why You should not use ‘Hybrid’, ‘Power-Law’ or related exponential schemes for convective modelling—there are much better alternatives. *Int J Numer Methods Fluids* 20:421–442
4. Amsden AA, Harlow FH (1970) A simplified MAC technique for incompressible fluid flow calculations. *J Comput Phys* 6:322–325
5. Schneider GE, Zedan M (1981) A modified strongly implicit procedure for the numerical solution of field problems. *Numer Heat Transf* 1(4):1–19
6. Hsu S (2000) Mixed convection in a rectangular enclosure with discrete heat sources. *Numer Heat Transf Part A: Appl* 38:627–652
7. Bhoite MT, Narasimham GSVL, Krishna Murthy MV (2005) Mixed convection in a shallow enclosure with a series of heat generating components. *Int J Therm Sci* 44(2):121–135

An Experimental Study on Performance Parameters of Diesel Engine Fueled with Blends of Diesel Fuel and Linseed Biodiesel



Brahma Nand Agrawal, Shailendra Sinha, Sudhir Kumar Singh, Kaushlendra Kumar Dubey, and Manoj Kumar

Abstract An experimental study has been performed to investigate the various performance parameters of a direct injection compression ignition engine fuelled with linseed biodiesel blend share 10–50% with diesel fuel. Furthermore, the empirical relationship has been developed for every performance parameter in terms of engine load and percentage of linseed biodiesel by using regression technique. It could be helpful to determine the values of different performance parameters at any value of engine load and also any blend share of linseed biodiesel. The results indicate that the performance parameters of a diesel engine while using blends deliver results which are better to diesel fuel in terms of brake-specific fuel consumption, indicated mean effective pressure, and indicated power and comparable in term of mechanical efficiency and brake thermal efficiency. The results revealed that L50D50 achieves better outcomes among diesel fuel and all other blends for engine performance of a direct injection compression ignition engine.

Keywords Linseed biodiesel · Diesel fuel · Blended fuel · Performance parameters

B. N. Agrawal (✉) · S. K. Singh · K. K. Dubey · M. Kumar
Department of Mechanical Engineering, Galgotias University, Greater Noida, India
e-mail: agrawalbrahma@gmail.com

S. K. Singh
e-mail: sudhirkumar.singh@galgotiasuniversity.edu.in

K. K. Dubey
e-mail: kaushalendra.dubey@galgotiasuniversity.edu.in

M. Kumar
e-mail: manojkumar@galgotiasuniversity.edu.in

S. Sinha
Department of Mechanical Engineering, Institute of Engineering and Technology, Lucknow, India
e-mail: ssinhaet@gamil.com

Nomenclature

L10D90	10% linseed biodiesel, and 90% diesel
L20D80	20% linseed biodiesel, and 80% diesel
L30D70	30% linseed biodiesel, and 70% diesel
L40D60	40% linseed biodiesel, and 60% diesel
L50D50	50% linseed biodiesel, and 50% diesel
C20D80	20% castor biodiesel, and 80% diesel
K50D50	50% karanja biodiesel, and 50% diesel
IP	Indicated power
BSFC	Brake specific fuel consumption
IMEP	Indicated mean effective pressure
BTE	Brake thermal efficiency
H20	Common rail direct injection
DEE	Di-ethyl ether
MGT	Mean gas temperature

1 Introduction

The prompt depletion of petroleum fuels has made it inescapable to search for unconventional fuel. A notable performance characteristic of vegetable oils seems to be the better option among the several renewable fuels [1]. The diesel system develops to investigate the ignition delay while fueled with di-ethyl ether (DEE) and n-pentane blends with diesel fuel. The results revealed that at lower temperatures, effectively reduces the ignition delay while using DEE blends [2]. The results of power output and fuel consumption are closed to diesel fuel while using vegetable oil and its blends [3, 4]. The engine performance of fuel blend H20 (20% honne oil and 80% diesel) is close to diesel fuel [5].

The blend K50D50 achieved higher peak cylinder pressure (2.21 bar) compared to diesel at maximum load. The higher rate of net heat release, rate of pressure rise, and the mean gas temperature have been achieved at blended fuel while compare with diesel fuel [6]. The thermodynamic cycle has been developed, and study the combustion characteristics for different blend shear of linseed biodiesel and diesel fuel was investigated. An optimum blend shear was obtained for combustion characteristics at 80% diesel fuel with 20% linseed biodiesel [7]. A study has been conducted on the performance parameters of a diesel engine fueled with castor oil blends with pure diesel. The results show that the higher indicated power and IMEP was noticed at blend C20D80. The higher value of BSFC has been achieved at blend C20D80. It is concluded that among all blends, the best results were shown at blend C20D80 for performance parameters of the diesel engine [8].

The authors noticed that limited literature are available which deals with the empirical relations for different performance parameters. So, keeping this perspective, this paper aims to develop the empirical relations and to investigate the influence of blend share 10–50% of linseed biodiesel with diesel fuel for performance parameters of diesel engines. In present study, the empirical relation is developed for every performance parameter. This experimental analysis is discovered to observe the practical feasibility of linseed biodiesel blends in the engine without any modification in the hardware of the engine.

2 Experimental Methodology

2.1 Experimental Set-up

The present study deals with the investigation of various engine performance parameters of the diesel engine fueled with blended diesel fuel and linseed biodiesel. Table 1 shows the engine specification. The line diagram of the set-up is shown in Fig. 1. A computer is connected to the engine. The engine-soft-LV has been used to analyze the engine performance. In the diesel engine, this software is used to evaluate test widely. The dynamometer is connected with the engine for applying various loads. Measurements of temperature, pressure, and crank angle are done by the temperature sensors, piezo sensor, and crank angle sensor, respectively.

2.2 Procedure of Experiment

During the present study, at first, the blends of linseed biodiesel were prepared in different shares by volume 10–50% such as L10D90, L20D80, L30D70, L40D60, and L50D50. The unit ml was used for preparing the blends. Further, the diesel engine has been kept in running state for 45 min to make it stable functionally while fueled with diesel fuel and at a constant speed, before starting the analysis of the engine performance. The data acquisition device collected the data through the various sensors, which are attached to different locations of the engine. All readings

Table 1 Engine specification

S. No.	Parameter	Value
1	Type	Four-stroke, DI engine
2	Rated power	3.5 kW
3	Compression ratio	18
4	Speed	1500, rpm
5	Bore × stroke	87.5 × 110, mm × mm
6	Dynamometer	Eddy current

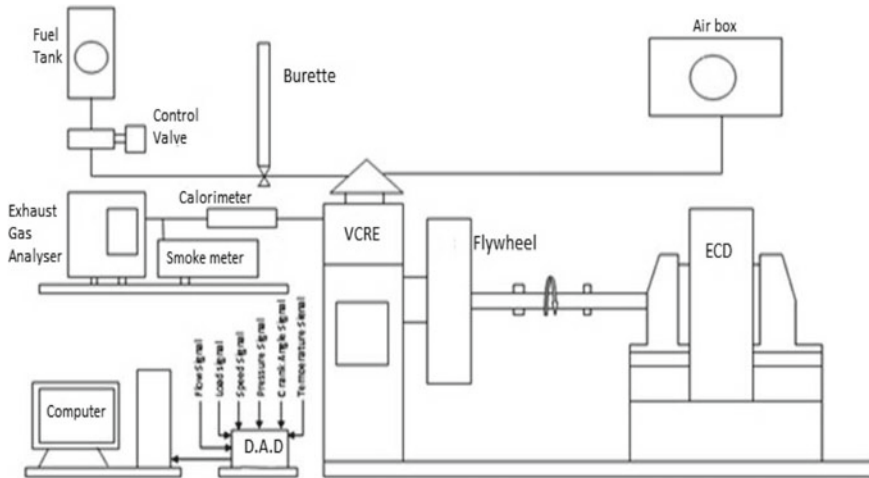


Fig. 1 Line diagram of set-up

have been taken and stored into the hard disk of the computer for diesel fuel as conveyed by engine-soft-LV at various engine loads. The previous step was repeated for all blends as L10D90, L20D80, L30D70, L40D60, and L50D50. Finally, the comparative outcomes have been plotted in graphical form for engine performance.

2.3 *Experimental Errors*

In this study, the total percentages of uncertainty 1.26% are considering during the experiments. It should be undoubtedly noted that estimated errors in the measurements of the elementary and derived quantities do not significantly impact the overall uncertainty in the results [7, 9].

3 **Results and Discussion**

3.1 *Performance Parameters*

The analysis and the comparisons of performance parameters of diesel fuel and linseed biodiesel blends are discussed in this section. The effect of linseed biodiesel share with diesel fuel on performance parameters has been investigated in this study.

Indicated Power (IP)

The various indicated power at different engine loads has been depicted in Fig. 2. The trends curves of indicated power have been almost the same as that of variation in IMEP at various engine load (Fig. 3). It is observed from Fig. 2, from a zero load to top load condition, the blend L50D50 notices more indicated power than diesel fuel and all blends of linseed biodiesel. At top load, the blend L50D50 notices maximum indicated power by amount 520 W to diesel fuel followed by 160 W, 250 W, 230 W, and 160 W, for blend L10D90, L20D80, L30D70, and L40D60, respectively. However, at no-load condition, the blend L50D50 also gives maximum IP by amount 950 W. From 32 to 100% of engine load, all five blends achieved higher indicated power than diesel fuel. That can be attributed to the better content of oxygen in biodiesel blends while compared with diesel [10]. Similar results are achieved by many researchers [7].

Empirical relation among indicated power, engine load, and percentage of linseed biodiesel.

The empirical relation is developed for indicated power in terms of engine load and percentage of linseed biodiesel. The empirical relation obtained by the regression technique to the best fit for indicated power is shown in Eq. (1). This empirical

Fig. 2 Variation of indicated power

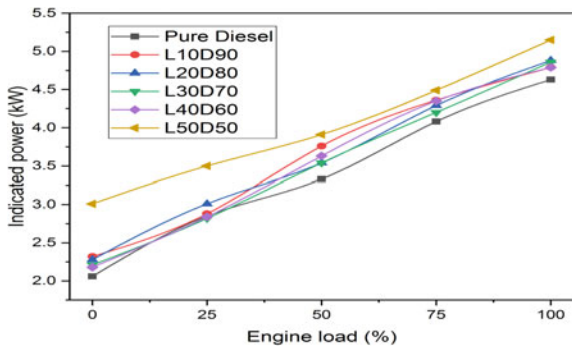
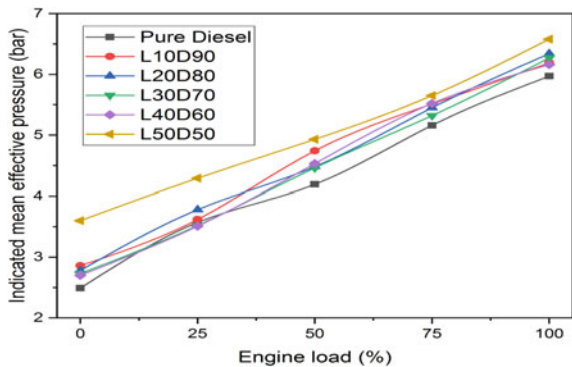


Fig. 3 Variation of IMEP



relation helps to find indicated power at different engine loads and different percentage of linseed biodiesel.

$$\begin{aligned} \text{IP} = & 2.1499 + 0.025300 \text{ Engine load} \\ & + 0.00813\% \text{ of Linseed biodiesel} \end{aligned} \quad (1)$$

$$R^2 = 96.82\% \quad (2)$$

Indicated Mean Effective Pressure (IMEP)

Figure 3 portrays the IMEP at various engine load. It is noticed from Fig. 3 that at zero engine load, the blend L50D50 gives higher IMEP while compare to diesel fuel by amount 1.11 bar. And, at full load, 0.61 bar greater IMEP is noticed while compare to diesel fuel at the blend L50D50. At blend L50D50, higher IMEP is noticed than diesel fuel and all blends irrespective of all loads. Figures 2 and 3 depict that the nature of the graph of IMEP and IP is similar for all blends as well as diesel fuel. However, diesel fuel and all the blends indicate an increasing value of IMEP while an increase in engine load, but the diesel fuel shows comparatively lesser values. The other blends L10D90, L20D80, L30D70, and L40D60 have greater IMEP while compare to diesel fuel by 0.22 bar, 0.37 bar, 0.3 and 0.19 bars at top engine load, respectively. Similar kinds of results have been obtained in the previous study [8].

Empirical Relation among IMEP, engine load, and percentage of Linseed biodiesel.

Empirical relation is developed for IMEP in terms of engine load and percentage of linseed biodiesel. The empirical relation obtained by the regression technique to the best fit for IMEP is shown in Eq. (3). This empirical relation helps to find IMEP at different engine loads and different percentage of linseed biodiesel.

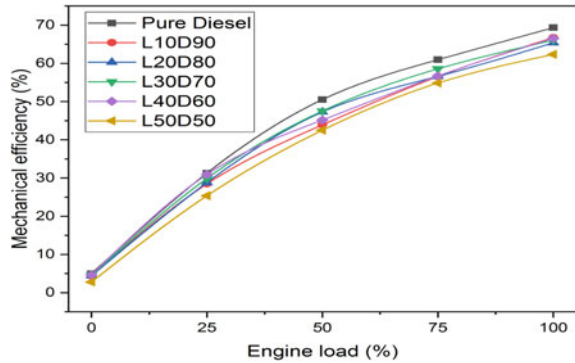
$$\begin{aligned} \text{IMEP} = & 2.6295 + 0.03401 \text{ Engine load} \\ & + 0.00933\% \text{ of Linseed biodiesel} \end{aligned} \quad (3)$$

$$R^2 = 97.57\% \quad (4)$$

Mechanical Efficiency

The mechanical efficiency at various engine loads is shown in Fig. 4. From the experiment result, it is noticed that from Fig. 4 at higher load conditions, higher mechanical efficiency is achieved at diesel fuel than all other blends. For each quarterly growth in the engine load, the increment in load is directly proportional to the speed of the engine directly. However, at all various engine loads, the mechanical efficiency of the L30D70 blend is near to that of diesel fuel. The diesel fuel gives 3.27% higher mechanical efficiency than that of blend L30D70 at full load. It happens due to the linseed biodiesel which has dissimilar properties of fuel

Fig. 4 Variation of mechanical efficiency



in comparison to diesel fuel. The blended fuel provides lesser mechanical efficiency than diesel fuel because density is higher and the cetane number is lower for blended fuel as compared to the diesel fuel [6].

Empirical Relation among mechanical efficiency, engine load, and percentage of Linseed biodiesel.

The empirical relation is developed for mechanical efficiency in terms of engine load and percentage of linseed biodiesel. The empirical relation obtained by the regression technique to the best fit for mechanical efficiency is shown in Eq. (5). This empirical relation helps to find mechanical efficiency at different engine loads and different percentage of linseed biodiesel.

$$\text{Mechanical efficiency} = 12.10 + 0.6073 \text{ Engine load} - 0.0744\% \text{ of Linseed biodiesel} \tag{5}$$

$$R^2 = 95.16\% \tag{6}$$

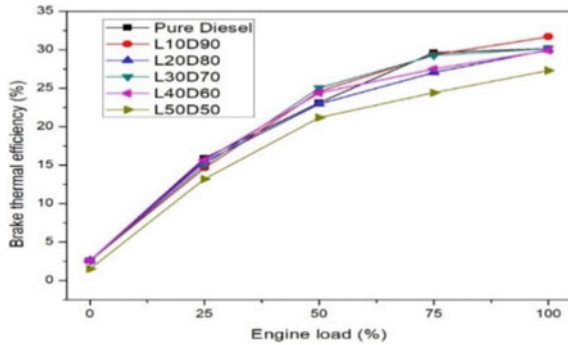
Brake Thermal Efficiency

The variation of brake thermal efficiency (BTE) of an engine at various engine loads highlighted for each cycle in Fig. 5. It is noticed that the blend L10D90 has more BTE than other blends and pure diesel at full load condition. However, from 0 to 75% of load, all blends except L50D50 gave close results to diesel fuel in terms of BTE. The percentage of BTE is constantly increasing from 0% to 100% of engine load, in almost the same trends. The blend L10D90 has been achieved maximum BTE by amount 1.54% than that of diesel fuel at top load. The BTE reduces due to lesser calorific value while an increase in BSFC of fuel mixture [9].

Empirical Relation among BTE, engine load, and percentage of Linseed biodiesel.

The empirical relation is developed for BTE in terms of engine load and percentage of linseed biodiesel. The empirical relation obtained by the regression

Fig. 5 Variation of brake thermal efficiency



technique to the best fit for BTE is shown in Eq. (7). This empirical relation helps to find BTE at different engine loads and different percentage of linseed biodiesel.

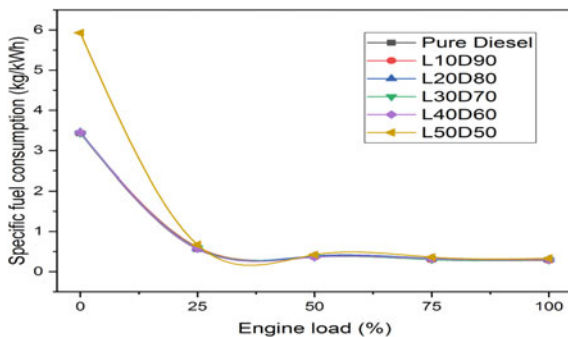
$$BTE = 7.22 + 0.2713 \text{ Engine Load} - 0.0420\% \text{ of Linseed biodiesel} \tag{7}$$

$$R^2 = 89.97\% \tag{8}$$

Brake-Specific Fuel Consumption (BSFC)

The effective combustion of fuel is identified in terms of BSFC. Figure 6 depicts the BSFC of the linseed biodiesel blends with diesel fuel at various engine loads. As shown in the figure that the blend L50D50 has more BSFC than diesel fuel and other blends irrespective of load except 32%. However, at top load conditions, diesel fuel and all blends have the same results in terms of BSFC. At no-load condition, higher specific fuel consumption has been achieved by blend L50D50 by amount of 2.5 kg/kWh than that of diesel fuel. The diesel fuel noticed the minimum value of BSFC 3.43 kg/kWh at no engine load condition. The values of BSFC indicate a drastic drop as the engine load rises to 25% from no-load condition. After

Fig. 6 Variation of specific fuel consumption



25% of engine load, it is to be noted here that all linseed biodiesel blends with diesel fuel give almost similar values of BSFC. The similar trends of result is found in a previous study [11].

Empirical Relation among BSFC, engine load, and percentage of Linseed biodiesel.

The empirical relation is developed for BSFC in terms of engine load and percentage of Linseed biodiesel. The empirical relation obtained by the regression technique to the best fit for BSFC is shown in Eq. (9). This empirical relation helps to find BSFC at different engine loads and different percentage of linseed biodiesel.

$$\text{BSFC} = 2.373 - 0.02958 \text{ Engine Load} + 0.0078\% \text{ of Linseed biodiesel} \quad (9)$$

$$R^2 = 53.99\% \quad (10)$$

4 Conclusion

The concluding remarks are as follows;

- It has been shown in the research that at blend L50D50 the indicated power noticed highest than all blends and diesel fuel at full range of engine load.
- At blend L50D50, 0.61 bar higher IMEP noticed than diesel fuel and also greater than other blends irrespective of all loads.
- The mechanical efficiency noticed higher by amount 3.27% at diesel fuel than that of blend L30D70 at top load.
- Blend L10D90 has higher BTE than diesel fuel and other blends at top load. At other loads from 0 to 75%, the blend L10D90 gives close or higher values of BTE than that of diesel fuel.
- The blend L50D50 noticed more BSFC than diesel fuel and other blends at full range of engine load except 32%.

So, the present study concluded that for performance parameters a 50% blend share of linseed biodiesel in 50% diesel fuel, i.e., the blend L50D50, is an optimal ratio.


References

1. Vijayaraj K, Sathiyagnanam AP (2017) Combustion characteristics of a DI diesel engine fuelled with blends of methyl ester of cottonseed oil. Int J Ambient Energy 0750(June):2016
2. Nand Agrawal B (2017) Combustion characteristics of diesel combustion system using blended diesel: an experimental study. Am J Mech Appl 5(4):34

3. Wang YD (2006) An experimental investigation of the performance and gaseous exhaust emissions of a diesel engine using blends of a vegetable oil. *Appl Therm* 26:1684–1691
4. Kumar NV, Chauhan SR (2016) Evaluation of the effects of engine parameters on performance and emissions of diesel engine operating with biodiesel blend. *Int J Ambient Energy* 37(2):121–135. Sep 2014
5. Venkanna BK, Reddy CV (2015) Performance, emission, and combustion characteristics of a diesel engine running on blends of honne oil and diesel fuel performance, emission, and combustion characteristics of a diesel engine running on blends of honne oil and diesel fuel. *Int J Green Energy* 12:728–736
6. Agrawal BN, Sinha S (2019) Influence of various blends of Karanja oil with pure diesel on performance, emission and combustion characteristics of diesel engine: an experimental investigation 1:1245–1250
7. Agrawal BN, Sinha S, Kuzmin AV, Pinchuk VA (2019) Effect of vegetable oil share on combustion characteristics and thermal efficiency of diesel engine fueled with different blends. *Therm Sci Eng Prog* 14(June):100404
8. Nand B, Sinha S, Bandhu D, Bansal G (2020) Materials today: proceedings effects of blends of castor oil with pure diesel on performance parameters of direct injection compression ignition engine. *Mater Today Proc* (21):1462–1466
9. Rajak U, Nashine P, Nath T (2020) Effect of spirulina microalgae biodiesel enriched with diesel fuel on performance and emission characteristics of CI engine. *Fuel* 268(Jan):117305
10. Naik NS, Balakrishna B (2017) A comparative study of B10 biodiesel blends and its performance and combustion characteristics. *Int J Ambient Energy*:1–21
11. Srihari S, Thirumalini S, Prashanth K (2017) An experimental study on the performance and emission characteristics of PCCI-DI engine fuelled with diethyl ether-biodiesel-diesel blends. *Renew Energy*

Study of Natural Convection Heat Transfer in a Closed Wall with Thermal Conditions



S. J. Yaksha , E. Akash, U. Sanjay, K. N. Seetharamu, and Balesh Babali

Abstract In this study, conjugate natural convection in a square cavity filled with fluids under steady-state condition is numerically investigated with the finite element method. The left side wall is considered as hot wall, and the right wall is considered to be cold. The top and bottom walls are assumed to be adiabatic. Different boundary conditions are introduced on the walls, and a thorough investigation is done in the present study. Numerical simulations have been done for different parameters of Grashof number (10^3 – 10^7) and Prandtl number. The graph of Nusselt number versus Grashof number and Nusselt number versus Prandtl number is plotted. It is observed that the buoyant forces developed in the cavity due to thermally induced density gradients vary as the value of acceleration due to gravity (g) differs, due to the change in temperature and stream function.

Keywords Conjugate natural convection heat transfer · Square cavity

Nomenclature

AR aspect ratio (H/L)
 g acceleration due to gravity (m s^{-2})
 H height of square cavity (m)
 K thermal conductivity ($\text{W m}^{-1} \text{K}^{-1}$)
 L length of the square cavity (m)

S. J. Yaksha (✉) · E. Akash · U. Sanjay · K. N. Seetharamu · B. Babali
Department of Mechanical Engineering, PES University, Bangalore, India
e-mail: yakshasj1999@gmail.com

E. Akash
e-mail: akashelangovan99@gmail.com

U. Sanjay
e-mail: sanjayu0023@gmail.com

K. N. Seetharamu
e-mail: knseetharamu@yahoo.com

B. Babali
e-mail: baleshbabali@pes.edu

Nu	local Nusselt number
P	dimensional pressure (Pa)
Pr	Prandtl number
Ra	Rayleigh number
T	temperature(K)
U	x-component of velocity (m s^{-1})
V	y-component of velocity (m s^{-1})

Greek Symbols

α	thermal diffusivity ($\text{m}^2 \text{s}^{-1}$)
β	volume expansion coefficient (K^{-1})
ρ	density (kg m^{-3})
Ψ	stream function ($\text{m}^2 \text{s}^{-1}$)

Subscripts

b	bottom wall
s	side wall

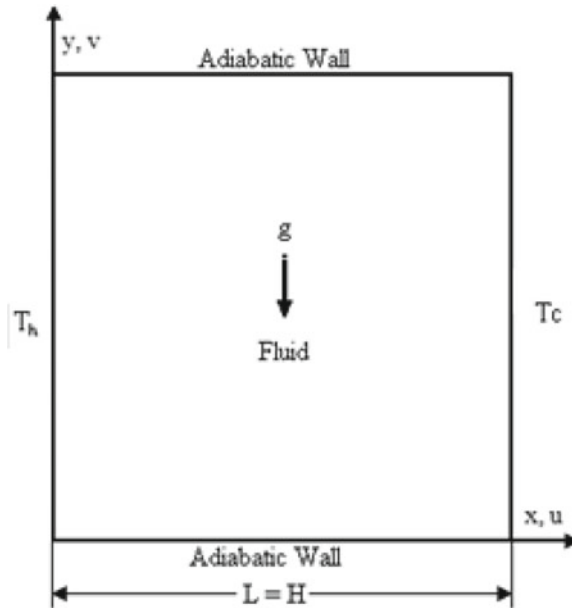
1 Introduction

Laminar, steady, natural convection flow was analyzed for a square closed cavity. Natural/free convection in square enclosures has been the spotlight in heat transfer analysis for more than a decade. Moreover, convection in a closed cavity with different boundary conditions is a paradigm for many practical applications like heat exchangers, cryogenic storage, furnace design, solar panels, and others.

The main purpose of this study is to examine natural/free convection in a closed cavity (square) with zero wall thickness. The configuration is shown in Fig. 1. The cavity is filled with fluids (air and water) with bottom and top walls perfectly insulated while the right and cold walls are differentially cooled and heated.

The objective of this paper is to report the heat transfer characteristics in enclosures exposed to uniform, linearly varying temperatures at the right and left walls while the horizontal walls are perfectly adiabatic. The left wall is maintained at a temperature of 305 K, and the right wall is at 295 K. Heat transfer characteristics have been studied for Grashof numbers varying from 10^3 to 10^7 . The cavity shown in Fig. 1 is elected for simulating natural convective heat transfer attributes.

Fig. 1 Geometry of the enclosure with all walls having zero thickness



1.1 Motivation

As shown in the literature survey, problems has been examined by Catton [1], Ostrach [2], and Hoogendoorn [3]. A cumulative study on the effects of temperature boundary conditions on free convection inside square cavities has been studied by Basak, Roy, and Balakrishnan [4].

November and Nansteel [5] and Valencia and Frederick [6] studied the natural convection in rectangular cavities where the bottom and top walls are heated and cooled differentially. Further, the case of cooling from top and heating on one side has been studied by Aydin [7], who also explored the effect of aspect ratio for rectangular cavities.

In the open literature, a definite analysis of free convection in cavities was dealt with by Ostrach [2]. Aydin and Yang [7] studied natural convection in a rectangular cavity, with one side heated and top wall cooled. The effect of sinusoidal temperature variation on the top wall in a square enclosure was studied by Sarris et al. [8]. Xia and Murthy [9] recognized that considerable attempts had been made to perceive how natural convection develops in closed enclosures. These studies made by various researchers triggered us to take up this problem and to add more value to it

1.2 Reason of Study

The natural convection in enclosures has engaged a great deal of consideration from researchers because of its wide range of applications. Researchers are conducting experiments in the same field by changing the heated plate and incorporating various boundary conditions. This natural convection in cavities has been classical, a standard problem for numerous industrial and technological applications like solar panels, nuclear reactors, electronic components, etc.

In Fig. 1, a square cavity is repleted with a fluid of $Pr = 0.7$ and $Pr = 10$. The left wall is kept hot at a temperature of about 305 K, and the right wall is kept cold at a temperature of 295 K.

The top wall and bottom wall are well insulated to study the heat transfer properties of different fluids with the variation of Grashof number (10^3-10^7).

2 Mathematical Formulation

A cavity, as demonstrated in Fig. 1, is chosen for simulating heat transfer characteristics and free convective flow. The enclosure of length (L) has a hot left wall with hot sinusoidally varying temperatures T_h , and the right cold wall is at consistent temperature T_c while the top surface and bottom surface are perfectly insulated. The gravitational force is acting in the downward direction. Due to the density gradient that arises due to the change in the thermal conditions, a buoyant flow is thus developed. Therefore, heat is transferred from a wall at a higher temperature to the wall at a lower temperature.

The equations that govern the natural convective flow are conservation of energy, mass, and momentum [4] which are penned as:

Continuity:

$$\frac{\partial u}{\partial x} + \frac{\partial v}{\partial y} = 0 \quad (1)$$

X-momentum:

$$u \frac{\partial u}{\partial x} + v \frac{\partial u}{\partial y} = -\frac{1}{\rho} \frac{\partial p}{\partial x} + \gamma \left(\frac{\partial^2 u}{\partial x^2} + \frac{\partial^2 u}{\partial y^2} \right) \quad (2)$$

Y-momentum:

$$u \frac{\partial v}{\partial x} + v \frac{\partial v}{\partial y} = -\frac{1}{\rho} \frac{\partial p}{\partial y} + \gamma \left(\frac{\partial^2 v}{\partial x^2} + \frac{\partial^2 v}{\partial y^2} \right) + g\beta(T - T_c) \quad (3)$$

Energy:

$$u \frac{\partial T}{\partial x} + v \frac{\partial T}{\partial y} = \alpha \left(\frac{\partial^2 T}{\partial x^2} + \frac{\partial^2 T}{\partial y^2} \right) \quad (4)$$

The changes in variables are shown as follows:

$$\theta = \frac{T - T_c}{T_h - T_c} \quad \text{Pr} = \frac{\nu}{\alpha} \quad \text{Ra} = \frac{g\beta(T_h - T_c)L^3 \text{Pr}}{\nu^2} \quad (5)$$

In this examination, the geometry has been designed and discretized the use of Gambit 2.2.3, while to simulate the natural convection of fluid in cavities, Fluent 6.2.16 CFD software is used. The consequence of distinct temperature boundary conditions at the left surface with constant temperature and top adiabatic walls is studied for different Grashof numbers. It was observed that at the corner of the bottom wall, there was a finite discontinuity in the temperature distribution during uniform temperature bottom wall boundary condition.

3 Stream Function and Nusselt Number

3.1 Stream Function

The stream function Ψ , which is realized from x and y components of the velocity, is used to study the fluid motion. For two-dimensional flows, the below equations show the relationship among velocity component (u, v) and stream function Ψ ;

$$u = \frac{\partial \psi}{\partial y} \quad \text{and} \quad v = -\frac{\partial \psi}{\partial x} \quad (6)$$

This can be further simplified to a single equation and can be re-written as:

$$\frac{\partial^2 \psi}{\partial x^2} + \frac{\partial^2 \psi}{\partial y^2} = \frac{\partial u}{\partial y} - \frac{\partial v}{\partial x} \quad (7)$$

Hence, from the stream function equation shown above, we can infer that anti-clockwise circulation is denoted by a positive sign of Ψ , whereas the clockwise circulation is denoted by a negative sign of Ψ .

3.2 Nusselt Number

The temperature profiles are fitted with quadratic, bi-quadratic, and cubic polynomials in order to determine the local Nusselt number and their gradients at the walls. It has been noted that for all the polynomials considered, the temperature gradients at the surface are almost the same. Therefore, only a quadratic polynomial is fitted in the temperature profiles for deriving the local gradients at the walls, which are then used to calculate the local heat transfer coefficients. By this, the local Nusselt number is calculated. The average Nusselt number for each side is calculated by integrating the local Nusselt number over each side. The equations for the same are shown below:

$$\overline{Nu}_b = \int_0^L Nu_b dx \quad (8)$$

$$\overline{Nu}_s = \int_0^H Nu_s dy \quad (9)$$

4 Numerical Procedure

In the current study, the set of governing equations for natural convection has been converted to the algebraic equation by integrating over the control volume. The coupled system of governing equations is determined by Pressure-Implicit with Splitting of Operators (PISO). ADI has been employed to sequentially solve these sets of algebraic equations. The formulation of the convection contribution to the coefficients in the finite-volume equations has been studied using second-order upwind differential scheme. Central differencing is formulated to discretize the diffusion terms. The computation is continued till all the residuals reach 10^{-5} using the FLUENT 6.2.16.

5 Results and Discussion

A 41×41 grid point domain is used for all computations in the present study. Before the simulations, a grid refinement analysis has been conducted to estimate the optimum mesh size. It can be observed that the selected grid size provides a grid-independent solution. Hence, the simulations are all performed with a 41×41 spaced grid system. To determine the accuracy of this numerical procedure, the results obtained with the 41×41 grid-sized square cavity were compared and are in

agreement with the work of Tanmay Basak a, S. Roy b, A.R. Balakrishnan for $Ra = 10^3-10^7$. Computations are carried out for Grashof number ranging from 10^3 to 10^7 and $Pr = 0.7$ and $Pr = 10$ with invariably heating of the left vertical wall while maintaining bottom and top walls at a well-insulated condition. In particular, the left wall needs special attention. As the mesh distribution at the corners is reduced, the Nusselt number is likely to increase. The Nusselt number for finite-volume and finite-difference method is calculated using various interpolation. This has been neglected in the current study.

In the current study, the calculations have been made for domains with different grid sizes (21×21 , 31×31 , 41×41 and 61×61) as well as Biasing Ratios (BR). Figure 2a shows the convergence of the average (mean) Nusselt number at the heated surface with grid refinement for $Ra = 10^5$ of Lo et al. (2004). The grid 41×41 biasing ratio (BR) of 2 (the ratio of the maximum cell to the minimum cell is 2, thus making cells finer near the wall) gave results identical to that of 61×61 uniform mesh.

A 41×41 grid with $BR = 2$ is used in all further calculations. However, in the present case, the study has been made for Grashof number ranging from $Gr = 10^3-10^7$. The average Nusselt numbers are computed by the present methodology for the same values. Figure 2b shows the graph of local Nusselt number versus the Rayleigh numbers and hence can be inferred that local Nusselt number is directly proportional to the Rayleigh number for given Prandtl number (Fig. 3).

Figure 4a and b shows the temperature plot and stream function for the square cavity for Grashof number varied from 10^3 to 10^9 , respectively. It is clearly visible from the isotherm plot that the maximum non-dimensional temperature is present at the top of the cavity, whereas the minimum non-dimensional temperature is present at the bottom. The stream function plot shows that a lower magnitude of stream function will occupy the extreme ends of the cavity, whereas the stream function with a higher magnitude will occupy the center of the cavity. Figures 4a and b shows the temperature plot and stream function for the square cavity for Grashof

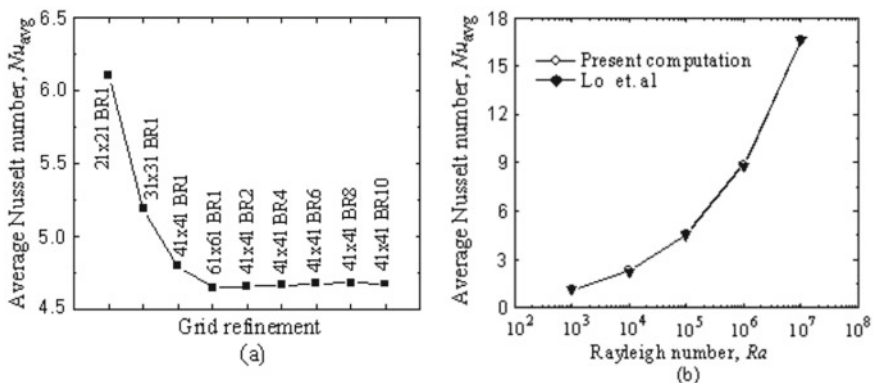
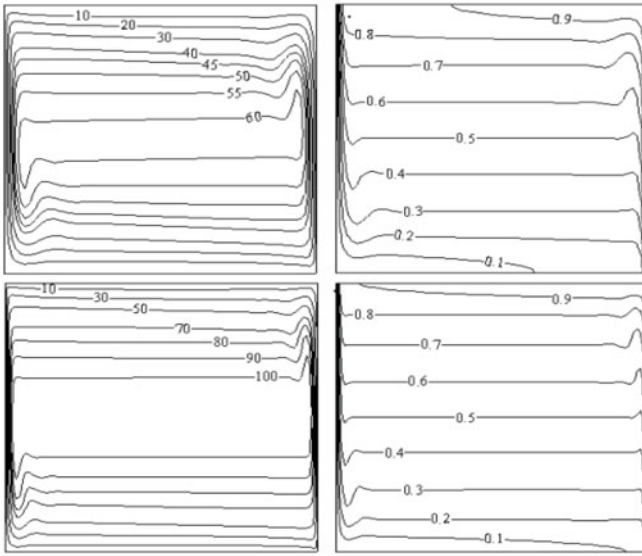
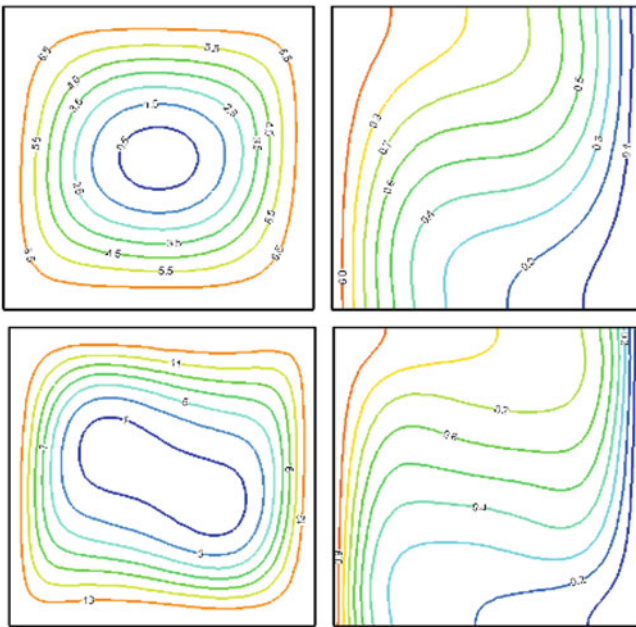


Fig. 2 Convergence of average Nusselt number with (a) grid refinement (b) Lo et al



(a)



(b)

Fig. 3 Comparison of local nusselt number with rayleigh number for given prandtl number

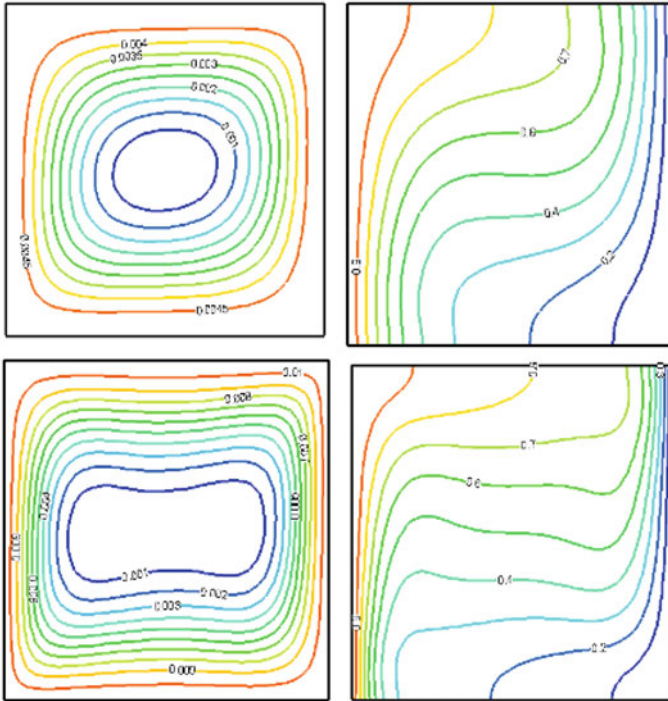


Fig. 4 showing the stream function and temperature profile for conductivity ratio $K = 5$, $Pr = 0.7$, Rayleigh number 10^3-10^9

number 10^9 , respectively. The magnitude of stream function increases, and also, the area occupied by the stream function with a higher magnitude is more compared to the case of Grashof number 10^8 . The thermal boundary layer is thinner compared to the case of Grashof number 10^9 .

In Fig. 5, modest variation in local Nusselt number is noticed up to Rayleigh number 10^3 owing to conduction pre-eminence and significantly varied from Rayleigh number 10^4-10^7 due to convection pre-eminence in the characteristics of heat transfer.

In Fig. 6, it is noted that the heat transfer rate decreases to a minimum value and later increases with distance for different Rayleigh numbers.

Fig. 5 showing the variation in local Nusselt number versus Rayleigh Number for different values of Prandtl number (17,7,0.7)

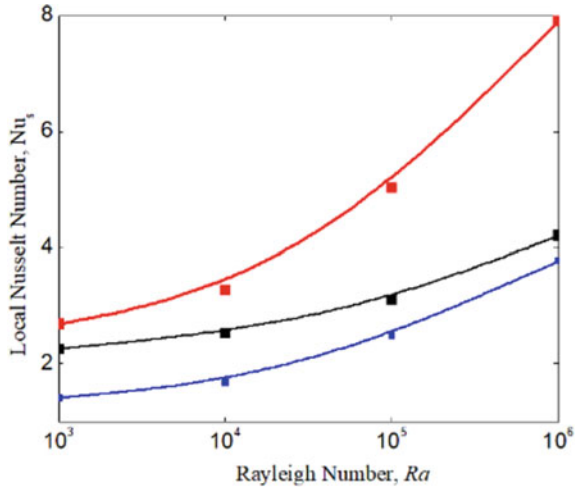
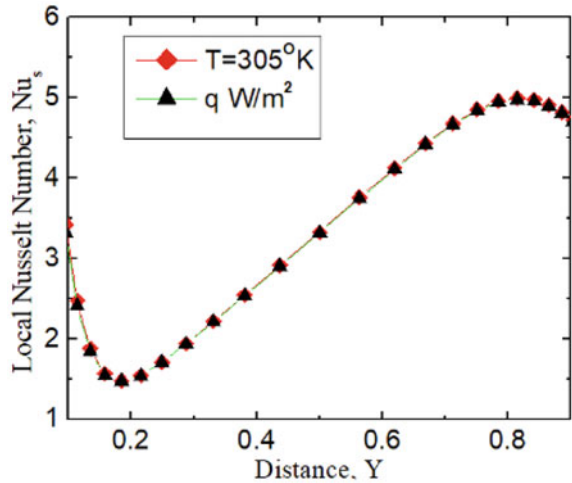


Fig. 6 showing the variation of temperature and heat flux



6 Conclusions

The main intention of the existing study is to analyze the transfer of heat in a square enclosure containing air and water during free convection. For obtaining continuous solutions with regard to isotherms and stream functions, finite element analysis was used for extensive magnitudes of Grashof number varying from 10^3 to 10^7 .

The convection equations of fluids (air and water) along with continuity, energy, and momentum equations have been solved using finite element analysis.

In Fig. 6, it is observed that as the magnitude of Grashof number reaches higher values, the temperature lines tend to constrict against the left hot wall which intern

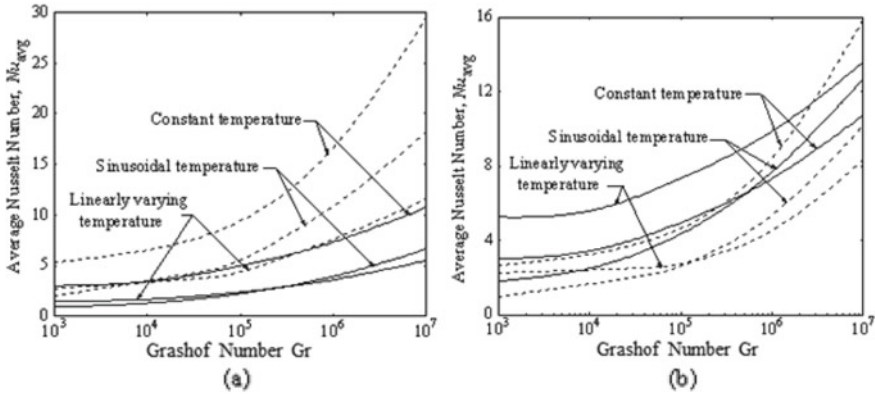


Fig. 7 Variation of average Nusselt number with Grashof number for (a) $Pr = 0.7$ (b) $Pr = 10$

increases the rate of transfer of heat at the corners of the hot wall. The heat transfer gradually decreases to a minimum value at the center.

This examination shows that the temperature distribution remains uniform for a broad spectrum of parameters. Under uniform heating conditions, because of the temperature difference among the vertical walls, the fluid flows toward the wall from the center of gravity in a clockwise direction.

The variations in Nusselt number with changes in the magnitude of Grashof number is shown in Fig. 7a and b.

The present study can be accounted for various real-time applications like solar panels, heat exchangers, and others with cavities filled with different types of fluids.

References

1. Catton I Natural Convection in enclosures. In: Proc. 6th Int. Heat Transfer Conference, Toronto, Canada
2. Ostrach S (1972) Natural Convection in enclosures Advances in Heat Transfer, vol VIII, New York
3. Hoogendoorn CJ (1986) Natural Convection in enclosures. In: Proc. Eighth Int. Heat Transfer Conf. vol I, San Francisco
4. Basak T, Roy S, Balakrishnan AR (2006) Natural convection within a square Cavity, Indian Institute of Madras, Chennai
5. November M, Nansteel MW (1987) Natural Convection in rectangular enclosures from below and cooled along one side. Int J Heat Mass Transfer
6. Valencia A Frederick RL (1989) Heat Transfer in square cavities with partially active vertical walls. Int J Heat Mass Transfer
7. Aydin O, Unal A, Ayhan T (1999) Natural Convection in rectangular enclosures heated from one side and cooled from the ceiling. Int J Heat Mass Transfer
8. Sarris et al (2002) Natural Convection in a 2D enclosure with sinusoidal upper wall temperature
9. Xia C, Murthy JY Buoyancy-driven flow transitions in deep cavities heated from below

CFD Analysis of Tube Type Heat Exchanger of a Split Air Conditioner



Rimi Sinha and Basant Singh Sikarwar

Abstract Crossflow multi-tube type heat exchanger is very popular as a condensing unit of a split air conditioner. In this unit, high-temperature superheated refrigerant vapor flows inside the tubes, which are arranged in a staggered manner in two rows. Atmospheric air drawn through a fan flows over these tubes and cools down the refrigerant. Circular fins in circular shaped tubes are embedded for enhancing the heat transfer rate. The shape of tubes plays an important role for enhancing the heat transfer coefficient and decreasing the coefficient of friction. In this manuscript, CFD simulation is carried out for thermal and fluid analysis of various cross section tubes like circular and elliptical. Simulations have been carried out in the in-house CFD solver for various Reynold numbers and various Prandtl numbers. Our simulation shows that the tube has high Nu/C_f for elliptical cross section as compared to the other shapes. Other insights of fluid flow and heat transfer inside the tubes have been discussed to optimize the heat transfer rate in various environmental conditions.

Keywords Pressure drop · Transport coefficient · Elliptical tube · Circular tube · Simulation · FVM

1 Introduction

The major challenge faced by us in the twenty-first century is the energy crisis. We must conserve energy by judiciously using advanced equipment and application of energy-efficient technologies. The evaporating unit and condenser unit are heat exchangers in air conditioning unit, and these units' thermal performance plays an important role in enhancing the thermo-hydrodynamic performance of air-condensing systems in the Indian environment. Many studies [1–3] reported that the coefficient of

R. Sinha (✉) · B. S. Sikarwar
Department of Mechanical Engineering, Amity University NOIDA, Noida, India
e-mail: rimisinha08@gmail.com

B. S. Sikarwar
e-mail: bssikarwar@amity.edu

performance (COP) of a split air conditioner depends upon the performance of the heat exchangers. As per the literature [4, 5], the transport coefficients of flow inside the condensing tubes depend on the environmental condition and shape of tubes. Outside conditions of condensing tubes are generally hot and humid. However, forced convection is used for the flow of atmospheric air over the condensing tubes. The shape of the tubes used in the condensing unit is circular. Nemati et al. [4] reported that the shape of the tube plays a very crucial role in determining the rate of heat transfer in crossflow heat exchangers. This is because different shape has different cross-sectional area exposed to the cooling fluid, which is an important factor for convective heat transfer. Talukdar [5] replicated numerically the natural and forced convection heat transfer in laminar flow across the triangular duct at constant wall temperature and tried to study the impact of apex angle on mean temperature and Nusselt number. Sayed Ahmed [2] analyzed the heat transfer rate for laminar thermally developing flow in a square duct. Adachi [1] investigated the stability factor of natural convection heat transfer in a square duct. Ting and Hou [6] numerically examined the heat transfer through convection in a nano-fluid flowing across a square duct. As per the author's understanding, the elliptical tubes' hydrothermal performance for condensing unit is an unexplored area of research. Against this background, CFD simulation of a varying cross section is carried out. We have taken circular and elliptical tube and Navier–Stokes equations coupled with energy equations. The flow is considered 1D, incompressible, and steady. The authors extended the present CFD code for turbulent flow. The complete description of the in-house CFD solver is presented in authors elsewhere [7, 8]. However, the turbulent flow is modeled as a standard $k - \varepsilon$ model with wall enhanced function [9, 10]. The code is validated against the data available in the literature [11, 12], and post validation, heat transfer coefficient, and skin friction of single u-tube bend pipe for various flow regimes are presented for single-phase flow. The thermo-hydraulic performance of a heat exchanger is generally enhanced by increasing the ratio Nu/C_f . The higher the value of Nu/C_f , the higher is the heat transfer rate by convection for a given condition. Conventionally, circular cross sections have been used in heat exchangers because of ease of construction and good heat transfer properties due to turbulence. However, they are not suitable for all the applications as they result in a high-pressure drop, and the power input is also high. Ideally, the phase change in condenser occurs at a constant temperature and pressure, but using circular tubes increases the pressure drop, thereby decreasing the overall performance of the equipment.

2 Mathematical Modeling and Solver Models

2.1 Governing Equations

The numerical approximation starts with the following three-dimensional Navier–Stokes (NS) equations, which govern the mass as well as momentum conservation:

$$\frac{\partial(\rho)}{\partial t} + \frac{\partial(\rho u_i)}{\partial x_i} = 0 \quad (1)$$

$$\frac{\partial(\rho u_i)}{\partial t} + \frac{\partial(\rho u_i u_j)}{\partial x_j} = -\frac{\partial p}{\partial x_i} + \frac{\partial}{\partial x_j} \left(\mu \frac{\partial u_i}{\partial x_j} \right) + \frac{\partial R_{ij}}{\partial x_j} \quad (2)$$

$$\frac{\partial(\rho T)}{\partial t} + \frac{\partial(\rho u_i T)}{\partial x_j} = \frac{k}{\rho C_p} \frac{\partial}{\partial x_j} \left(\frac{\partial T}{\partial x_j} \right) \quad (3)$$

For turbulent flow, ensemble (time) averaging may be used to extract the mean flow properties from the instantaneous velocities. The Reynolds stresses are additional unknowns introduced by the averaging procedure. Hence, they were modeled to close the system of governing equations. The term $\frac{\partial R_{ij}}{\partial x_j}$ in Eq. 2 only comes for turbulent flow, and u_i and u_j is the mean velocity of flow in a turbulent flow.

$$R_{ij} = -\overline{\rho u'_i u'_j} = \mu_T \left(\frac{\partial u_i}{\partial x_j} + \frac{\partial u_j}{\partial x_i} \right) \quad (4)$$

The value of eddy viscosity is $(\mu_T) = f(\rho\kappa/\varepsilon)$. The details of κ - ε modeling is the same as given in FLUENT® documentation [9]. However, the ε equation contains a term which cannot be calculated at the wall. Therefore, wall functions were used for knowing the insights of fluid mechanics and heat transfer close to wall. Navier–Stokes equations along with the continuity equation and energy (Eqs. 1–4) were solved using finite volume method (FVM) discretization because they are coupled and highly nonlinear. In FVM, the governing equation is first integrated over a cell volume and an integral form of the governing equation is obtained. The integral is replaced by summation, and the required algebraic equation for the cell quantity is derived. In FVM derived on an unstructured grid, the mass balance and momentum Eqs. (1–2) were to be decoupled first, so that the velocity components and pressure are determined from explicit equations. Pressure–velocity decoupling is an extension of the SIMPLE algorithm and, except for a few differences in implementation, has been followed in the present study. In this approach, pressure (p) is determined via a pressure-correction equation that indirectly satisfies mass-conservation. On an unstructured mesh, it is most convenient to employ collocated variables, so that scalar and vector variables are defined at the same location. For such a collocated arrangement, Date [13] has derived an equation for pressure correction to eliminate spatial fluctuations in the predicted pressure field. All the geometric parameters for all control volumes are calculated in the pre-processing stage and stored for use during time-stepping. Volume-weighted linear interpolation is used to find the face value, whenever required. Convective terms of the Navier–Stokes are discretized using a higher-order upwind scheme, as proposed by Frink et al. [14]. The discretized system of algebraic equations is solved by the stabilized bi-conjugate

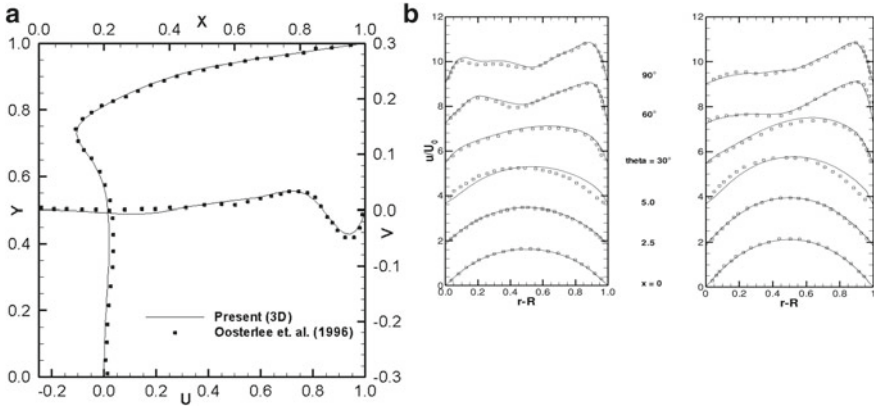


Fig. 1 **a** Centerline velocity components for skew angle 30, $Re = 1000$ at the plane of symmetry $z = 0.5$ for a skew-driven cavity. The present result is compared with published data of Oosterlee et al. [11]. The present results show excellent agreement with their result. **b** Comparison of streamwise velocity profiles at $z = 0.25$ and 0.5 with experimental results of, Humphrey, et al. [12] the code validated against 3D channel flow problem in a 90° bending square duct. The Reynolds number is based on the mean entrance velocity and the duct width. A fully developed inflow velocity profile is imposed at the inlet boundary. At the outflow boundary, Neumann boundary conditions are prescribed. A very satisfactory agreement is found at all the six stations with experimental results

gradient method (biCGStab) with a diagonal pre-conditioner. The overall numerical algorithm used in the present study is quite similar to that presented by Barth and Jespersen [15]. Points of difference are related to the use of certain invariant properties of the tetrahedral element and a powerful linear equations solver. Iterations within the code are executed till an absolute residual convergence criterion of $< 10^{-7}$ for all the computed variables is achieved. The finite volume code is parallelized on shared memory architecture using the Open-MP model, and computations are carried out on the high-performance computing system available at AUUP (India). Code is validated against many experimental and simulation data available in literature. Its validation results were shown in Fig. 1, and they have very close agreement with data available in the literature.

2.2 Simulation of Various Cross-Section Tubes

The computational domain of various cross section tubes of the condensing unit was formed by ICEMCFD®. The computational domain with appropriate boundary conditions is shown in Fig. 2.

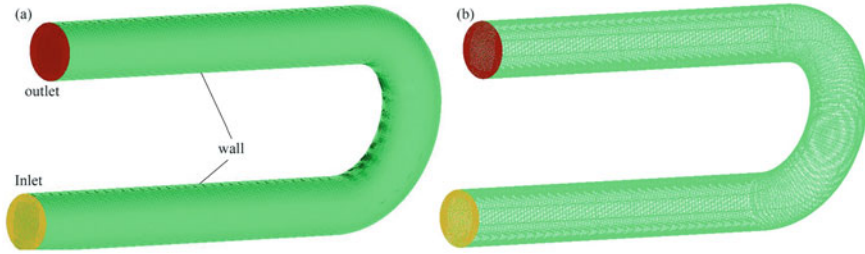
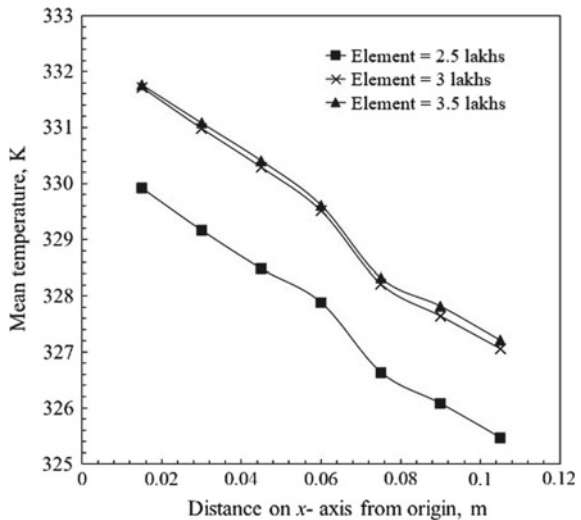


Fig. 2 a Computational domain of condensing tube with appropriate boundary conditions: Fully developed velocity and the temperature are specified at the inlet. However, pressure outlet boundary is specified at the outlet, and no-slip boundary condition is specified at the wall. b The meshing of the domain

Circular and elliptical cross sections were used for comparing the hydrothermal performance of the condensing tube. The hydraulic diameter was kept constant for all the designs, so that the tube shape effect on the performance of the condenser could be studied properly. In previous studies, the tube shape effect has been observed mostly on the airside. However, it does affect the tube side as well since any change in the tube shape will result in a change in thermo-physical properties and thereby impacting the overall performance of the condenser. Based on the grid independence results, all simulation were carried out on 3.5 lakhs cells on the body of domain. Close to wall, the grid size is considered on the basis of wall enhancement criteria [9]. The grid independence result is shown in Fig. 3.

Fig. 3 Grid independence. The results show that there is no effect on the solution after 3.0 Lakhs cell on the body



3 Result and Discussion

After validation, the simulation is carried out for various Reynold numbers (50–5000) and various shapes (circular and elliptical) of tube for specific Prandtl number (1.32) of fluid at optimized grid size (3.5 Lakhs). At the wall, various convective heat transfer coefficients are applied to know the effect on the cooling rate of fluid.

Figure 4 shows the fluid and thermal insights of circular shape tube for laminar flow. However, Fig. 5 shows same for elliptical tubes. The streamline shows that the flow is disturbed in circular pipe close to bend in pipe.

Figure 6 shows the flow and thermal insights for turbulent flow in circular pipe. However, Fig. 7 shows turbulent flow insights for elliptical shape of tube. As it can be seen, the streamlines tend to move away from the wall and deviate from their regular path in case of the circular and triangular tubes. This is because of the flow separation near the wall. The streamline for them is also not regular and does not follow the contour of the body; eddies and vortices are observed near the wall of the joint, which increases the frictional losses.

Flow separation occurs when the boundary layer travels such a distance against an adverse pressure gradient that the velocity of boundary layer relative to the object becomes almost zero. This effect can be observed more clearly near the walls as the momentum is lower than the region of free stream. As the fluid moves in the adverse pressure gradient, the continuous retardation of the flow results in a zero-shear stress near the wall, and it is observed that the flow no longer follows the contour of the body. The point where the wall shear stress becomes zero is known as point of separation. Here, in the elliptical tubes, the streamlines follow the general trend as expected and hence results in the least pressure drop. For turbulent

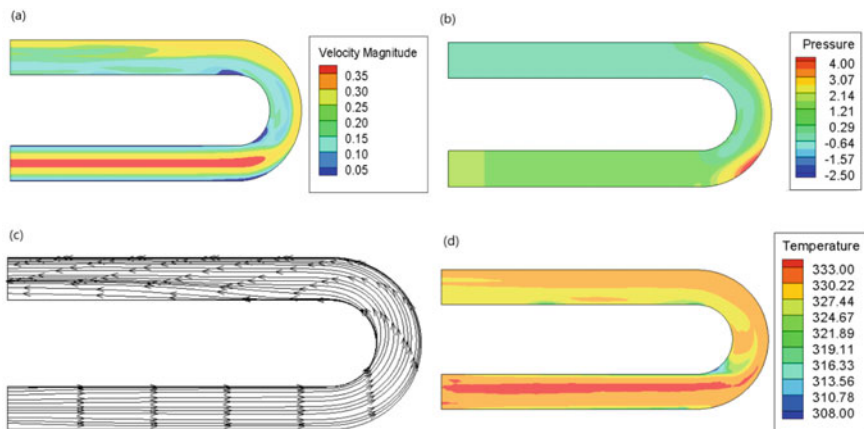


Fig. 4 a Velocity contour, b pressure contour, c streamline pattern, and d temperature contour for Reynolds Number 1000 in a circular tube. The heat transfer coefficient $h = 200 \text{ w/m}^2\text{-K}$, the inlet temperature of the fluid is 333 K, and the hydraulic diameter of the tube is 7 mm

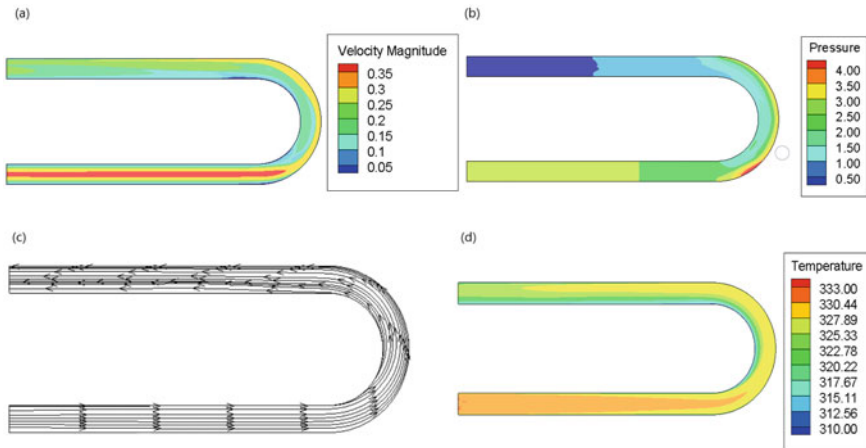


Fig. 5 a Velocity contour, b pressure contour, c streamline pattern, and d temperature contour for Reynolds Number 1000 in elliptical tube. The heat transfer coefficient $h = 200 \text{ w/m}^2\text{-K}$, inlet temperature of fluid is 333 K, and hydraulic diameter of tube is 7 mm

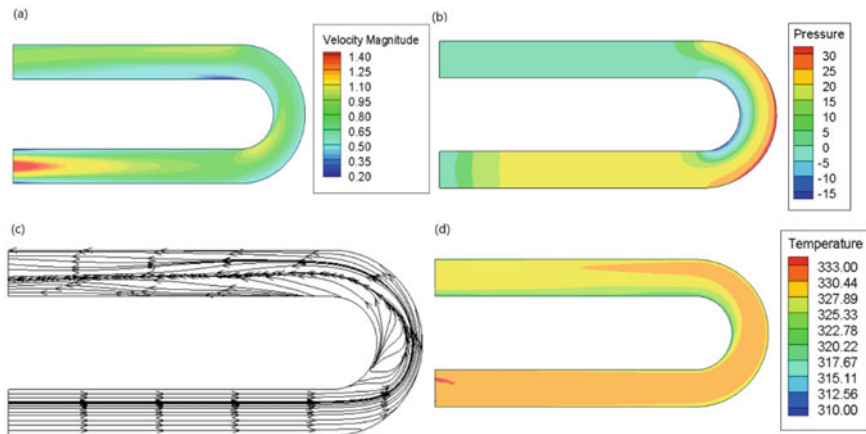


Fig. 6 a Velocity contour, b pressure contour, c streamline pattern, and d temperature contour for Reynolds Number 4000 in a circular tube. The heat transfer coefficient $h = 4000 \text{ w/m}^2\text{-K}$, the inlet temperature of the fluid is 333 K, and the hydraulic diameter of the tube is 7 mm

flow, we used k-epsilon model, which is the most widely used turbulent model. It is a two-equation model, which means it contains two extra transport equations to represent the turbulent flow properties. The first transported variable is turbulent kinetic energy, denoted by k , and the second one is turbulent dissipation rate, denoted by ϵ . k determines the energy in turbulence, and ϵ determines the scale of

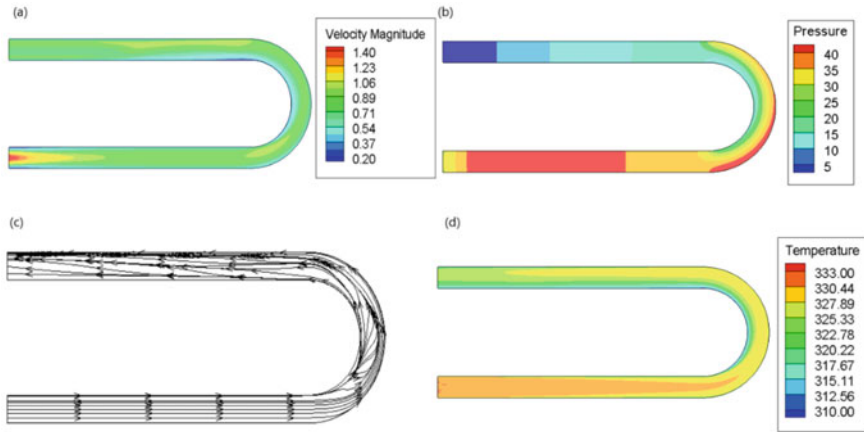


Fig. 7 (a) Velocity contour, (b) pressure contour, (c) streamline pattern, and (d) temperature contour for Reynolds Number 4000 in the elliptical tube. The heat transfer coefficient $h = 4000 \text{ w/m}^2\text{-K}$, the inlet temperature of the fluid is 333 K, and the hydraulic diameter of the tube is 7 mm

turbulence. It emphasizes on the mechanism that affects the turbulent kinetic energy.

After carrying out simulations on these tubes, we calculated the value of heat transfer coefficient (h) and coefficient of friction (C_f). These quantities are the deciding factors for effectiveness of the tube (Fig. 8).

Figure 9 shows variation of heat transfer coefficient with respect to Reynolds number for elliptical shape and circular shape of pipe. It shows the heat transfer coefficient is higher for elliptical shape tube.

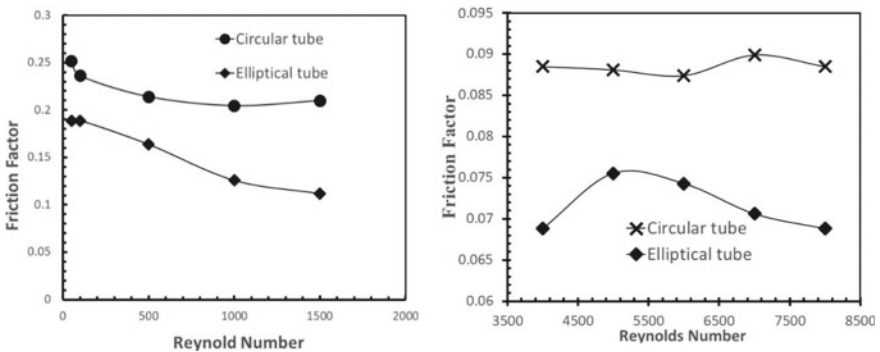


Fig. 8 Friction factor versus Reynold number of tubes for circular and elliptical shape of tube (a) laminar flow and (b) turbulent flow

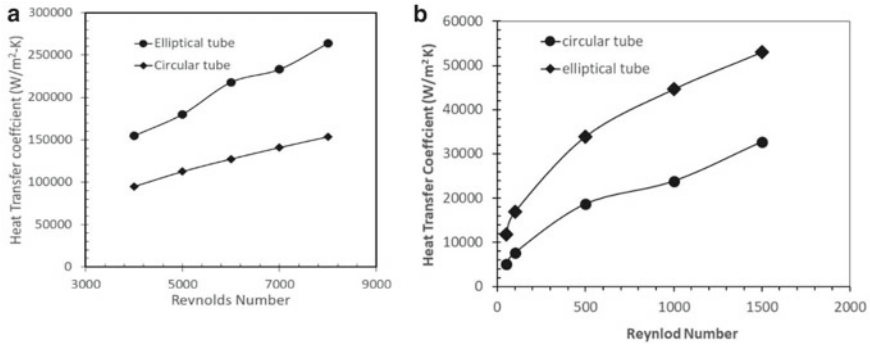


Fig. 9 Heat transfer coefficients versus Reynold number of tubes for circular and elliptical shape of tube **a** laminar flow and **b** turbulent flow

4 Conclusion

The in-house CFD solver is developed for knowing the hydrothermal performance of condensing tube. The simulations were carried out for various Reynold numbers and various shapes of tube for a specific Prandtl number of fluid. From the study, the pressure drop has been observed to be the minimum in elliptical as compared to circular shape of the tube. The heat transfer rate is also the maximum for the elliptical tube as compared to circular. In turbulent flow, these results are more pronounced. On comparing the circular and elliptical shapes, from the above simulations, it has been observed that the elliptical tubes provide least pressure drop among all the shapes. The temperature drop is maximum for the elliptical tubes. Moreover, the turbulence was also observed to be lower. Apart from that, increased work input is required for circular tubes according to many research papers studied. The heat dissipation was more uniform in the elliptical cross section tube, and the frictional losses were observed to decrease. Since the aerodynamic shape is better for elliptical shape, the pressure drop is found to be lesser, which in turn increases the performance of the condenser. Therefore, a pronounced change in COP of the air conditioner can be observed if the ellipse-shaped tubes are installed in the condenser.

References

1. Adachi T (2006) Stability of natural convection in an inclined square duct with perfectly conducting sidewalls. *Int J Heat Mass Transf* 49(13–14):2372–2380
2. Sayed-Ahmed ME, Kishk KM (2008) Heat transfer for Herschel-Bulkley fluids in the entrance region of a rectangular duct. *Int Commun Heat Mass Transfer* 35(8):1007–1016

3. Lavasani AM, Bayat H (2016) Numerical study of pressure drop and heat transfer from circular and cam-shaped tube bank in cross-flow of nanofluid. *Energy Convers Manag* 129:319–328
4. Nemati H, Moghimi MA, Sapin P, Markides CN (2020) Shape optimization of air-cooled finned-tube heat exchangers. *Int J Therm Sci* 150:106233
5. Talukdar P, Shah M (2008) Analysis of laminar mixed convective heat transfer in horizontal triangular ducts. *Numer Heat Transf, Part A: Appl* 54(12):1148–1168
6. Ting H-H, Hou Shuhn-Shyurng (2015) Investigation of Laminar Convective Heat Transfer for Al₂O₃-Water Nanofluids Flowing through a Square Cross-Section Duct with a Constant Heat Flux. *Materials* 8:5321–5335. <https://doi.org/10.3390/ma8085246>
7. Sikarwar BS, Khandekar S, Agrawal S, Kumar S, Muralidhar K (2012) Dropwise condensation studies on multiple scales. *Heat Transfer Eng* 33(4–5):301–341
8. Sikarwar BS, Khandekar S, Muralidhar K (2013) Simulation of flow and heat transfer in a liquid drop sliding underneath a hydrophobic surface. *Int J Heat Mass Transf* 57(2):786–811
9. FLUENT 16 documents, modelling of turbulent flow, <http://www.pmt.usp.br/academic/martoran/notasmodelosgrad/ANSYS%20Fluent%20Users%20Guide.pdf>
10. Open-Foam, <https://www.openfoam.com/documentation/tutorial-guide/>
11. Oosterlee CW, Ritzdorf H (1996) Flux difference splitting for three-dimensional steady incompressible navier-stokes equations in curvilinear coordinates. *Int. J. Num. Meth. Fluids* 23:347–366
12. Humphrey JAC, Taylor AMK, Whitelaw JH (1977) Laminar flow in a square duct of strong curvature. *J Fluid Mech* 83:509–527
13. Date AW (1993) Solution of Navier-Stokes equation on non-staggered grid. *Int. J. Heat Mass Transfer* 36:1913–1922
14. Frink NT, Paresh P, Shahyar P (1991) A Fast-Upwind solver for the Euler equations on three-dimensional unstructured meshes. AIAA paper 91-0102
15. Barth TJ, Jespersen DC (1989) The design and application of upwind schemes on unstructured meshes. AIAA paper 89-0366

Effect of Strip Orientations and Geometry on the Critical Heat Flux in Pool Boiling



Bikash Pattanayak , Harsh Deswal, Vivek Saxena,
and Hardik Kothadia 

Abstract The objective of this research work is to experimentally determine and analyze the effect of geometry and orientation of strips (heating element) on critical heat flux (CHF) in pool boiling under atmospheric pressure. Studies concerning the effect of geometry, orientation, and thermophysical properties of the heating element on CHF are limited. In the present work, Stainless Steel 304 is used as strip material. The experiments are conducted with strips of length 50, 75, 100, and 150 mm each having width 5, 10, and 15 mm. The experiments are performed with strips of two thicknesses 0.1 and 0.2 mm. For each of the aforementioned combination of dimensions, the experiment is conducted by orienting it in horizontally, vertically over width and vertically over length, respectively. DC power supply is used to supply controlled amount of heat accurately. K-type thermocouples are used to measure the temperature of fluid. Datalogger is used to record the current, voltage, and temperature values. DSLR video camera is used to record the boiling mechanism as well as the location of critical heat flux on strips. The experimental setup was tested for repeatability, and it was observed that under same experimental conditions, CHF value obtained was within a relative deviation of $\pm 6\%$. It is observed that thickness of strip has negligible effect on CHF for given dimensions and orientation. However, for a fixed length of strip, the magnitude of CHF decreases with increase in its width.

B. Pattanayak · H. Deswal · V. Saxena · H. Kothadia (✉)

Department of Mechanical Engineering, Indian Institute of Technology Jodhpur, Jodhpur
342037, India

e-mail: hardikothadia@iitj.ac.in

B. Pattanayak

e-mail: pattanayak.1@iitj.ac.in

H. Deswal

e-mail: deswal.1@iitj.ac.in

V. Saxena

e-mail: saxena.3@iitj.ac.in

© The Author(s), under exclusive license to Springer Nature Singapore Pte Ltd. 2021

B. S. Sikarwar et al. (eds.), *Advances in Fluid and Thermal Engineering*,

Lecture Notes in Mechanical Engineering,

https://doi.org/10.1007/978-981-16-0159-0_26

It is observed that CHF decreases with increase in the length of strip for a fixed width irrespective of orientation. Out of the three orientations of strip, vertical over width has maximum CHF followed by horizontal and vertical over length, respectively.

Keywords Critical heat flux · Pool boiling · Bubble nucleation · Strip orientation

Nomenclature

CHF	Critical heat flux (MW/m^2)
L	Length (mm)
W	Width (mm)
T	Thickness (mm)
I	Current (A)
V	Voltage (V)
Q	Power input (W)
A	Surface area of heater strip (m^2)
Ver	Vertical over width
Hor	Horizontal
VerN	Vertical over length

1 Introduction

Nukiyama [1] identified that the pool boiling process includes various stages such as natural convection, nucleate boiling, CHF, and film boiling. Nucleate pool boiling regime is employed widely because it acts as a potent region for heat transfer in super computers, hybrid power vehicle electronics, avionics, nuclear reactors, as evaporator fins in electronic chipset cooling, plate fin heat exchangers, etc. [2–4]. Nowadays, two-phase cooling schemes are being deployed to obtain more heat dissipation rate so as to provide better performance of the equipment. This is achieved by utilizing both the sensible as well as latent heat of the coolant. Nishikawa et al. [5] investigated the effect of surface orientation and concluded that at higher heat flux, the impact of surface orientation is less as compared to lower heat flux magnitude. Elvira et al. [6] performed saturated pool boiling experiment on printed circuit board heater (PCB) and stated that surface orientation affects CHF, CHF location, vapor behavior, and vapor thickness. Yang et al. [7] concluded from their experiment on effect of orientation and size of small plate heater on CHF in pool boiling that CHF decreases with decrease in inclination angle and is lower for higher width of plate. Research articles explaining the effect of length, width, thickness, and orientation of heater surface on CHF are limited. The primary focus of this research work is to analyze the effect of strip orientation and geometry on critical heat flux during pool boiling under atmospheric pressure.

2 Experimental Analysis

2.1 Heater Strips Fabrication and Setup for the Experiment

Figure 1a shows the schematic diagram of the setup used for pool boiling experiment. A transparent hardened glass tank is used in order to visually inspect the boiling process. It has a base with length 700 mm, width 200 mm, and its height is 700 mm. The glass used for tank has a thickness of 12 mm. Water level is maintained at uniform height and temperature in all the experiments at the starting of the experiment. For all the performed experiment, the water level in tank is kept at 500 mm from the tank base and after each experiment some water is replaced with fresh water so that the water temperature remains uniform. Copper strips of length 1000 mm, width 50 mm and thickness 5 mm are used as electrodes. They are connected to the DC power supply using heavy duty copper wires as can be seen in Fig. 1b. DC power supply has a maximum capacity of 15 kW. Power supply is

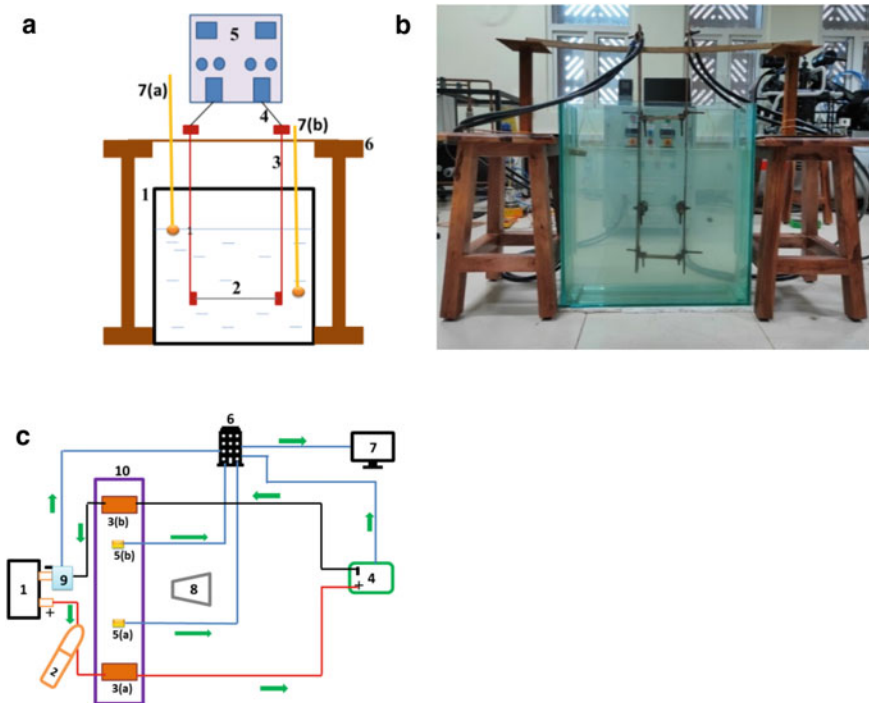


Fig. 1 a Schematic experimental setup, 1—Glass tank, 2—Heater strip, 3—Copper electrodes, 4—Single core wire, 5—DC power supply, 6—Wooden stand, 7(a) and 7(b)—Thermocouples b Experimental setup c Circuit diagram of setup, 1—DC power supply, 2—Clamp meter, 3 (a) (b)—Copper electrodes, 4—Multimeter, 5 (a) (b)—K-type thermocouples, 6—Datalogger, 7—Computer, 8—Camera, 9—DC shunt, 10—Glass tank

coupled with DC shunt to measure the current in datalogger. Multimeter and clamp meter are used for verification of the values displayed by DC power supply. Datalogger is used to record voltage across the electrodes and temperature of the water pool using K-type thermocouples. A DSLR video camera is used to capture the images and video of the boiling phenomenon. Figure 1c shows the electric circuit diagram for the experiment. Thermocouple 5(a) measures the temperature of water near surface and 5(b) measures the temperature of water near the heater strip. Sheets of SS304 with thicknesses 0.1 and 0.2 mm are used for strip preparation. Strips of lengths 50, 75, 100, and 150 mm and each with width 5, 10, and 15 mm are cut. Each strip is then welded to GI strips of length 30 mm, width 20 mm, and thickness 1 mm on both ends in order to minimize the sparks at the clamping junction. Moreover, this will maintain sufficient distance between electrode junction and heater strip for vapor bubble movement without disturbance. It is easy to weld GI with SS compare to copper; hence, GI strip is welded with SS304 heater strip. Heater strip and GI strip is clamped with a copper block and assembly which is further attached to the copper electrode using SS bolts. During the experiment, it is observed and verified that there is no bubble formation at the copper electrodes, copper blocks, and GI strips because the resistance of Cu and GI is less as compared to SS 304. So, the supplied current does not generate the magnitude of heat to cause bubble formation. Figure 2a–c shows the horizontal, vertical over width, and vertical over length orientations of strip, respectively. The water level above the heater strip is kept constant of 250 mm for horizontal strips. For vertical over width and vertical over length strips, the water level above the top most heater surface is kept constant of 250 mm.

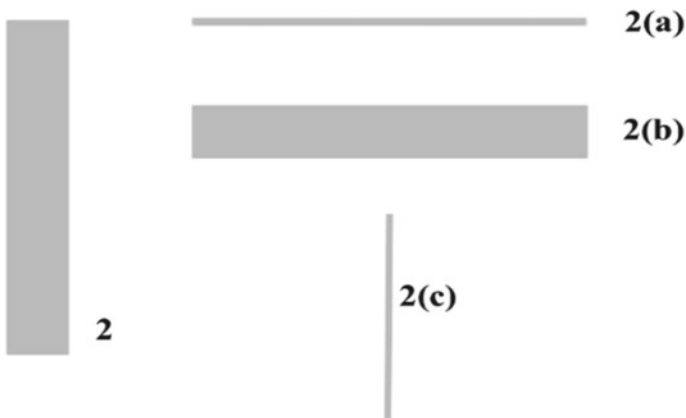


Fig. 2 SS 304 heater strip orientations, 2(a) Horizontal, 2(b) Vertical over width, 2(c) Vertical over length

2.2 CHF Identification

Hardik and Prabhu [8] discussed about CHF detection methods in literature. CHF can be detected by four methods. They are:

1. Heat flux at which temperature rise breaks the heater strip or turns it to red.
2. Heat flux corresponding to maximum heat transfer coefficient.
3. Heat flux corresponding to first temperature jump observed in camera recording.
4. Heat flux at which there is a sharp increase in wall temperature with a small increase in heat flux.

Most of the research articles used CHF identification method as mentioned in point 3 or 4. This method deteriorates heating element's strength and microstructures. So, using the same for multiple experiments may not provide the same repeatability. In this experiment, the CHF is identified by the heat flux at which the heater strip breaks due to rise in temperature.

2.3 Experimental Procedure

The water tank is filled with tap water and electrodes are then inserted in it. Datalogger, DC power supply, and camera are switched on subsequently. Power input to the heater strip is increased gradually, and various regimes of pool boiling are observed. Initially, the natural convection is observed, where due to density difference motion of water occurs without any bubble formation. With further increase in power, bubbles form on the surface of the heater strip. As power is increased, bubble depart and bubble nucleation starts from the heater surface. When the power is further increased, the frequency of bubble detachment increases, and soon bubbles start to coalesce together to form larger bubble and start forming vapor pockets around the heater strip which lead to its burnout. Above-mentioned stages of nucleate pool boiling are depicted in Fig. 3a–h for vertically over width-oriented strip of length 50 mm, width 10 mm, and thickness 0.1 mm. The same procedure is repeated for all geometries and orientations. For every individual experiment, a new strip is prepared.

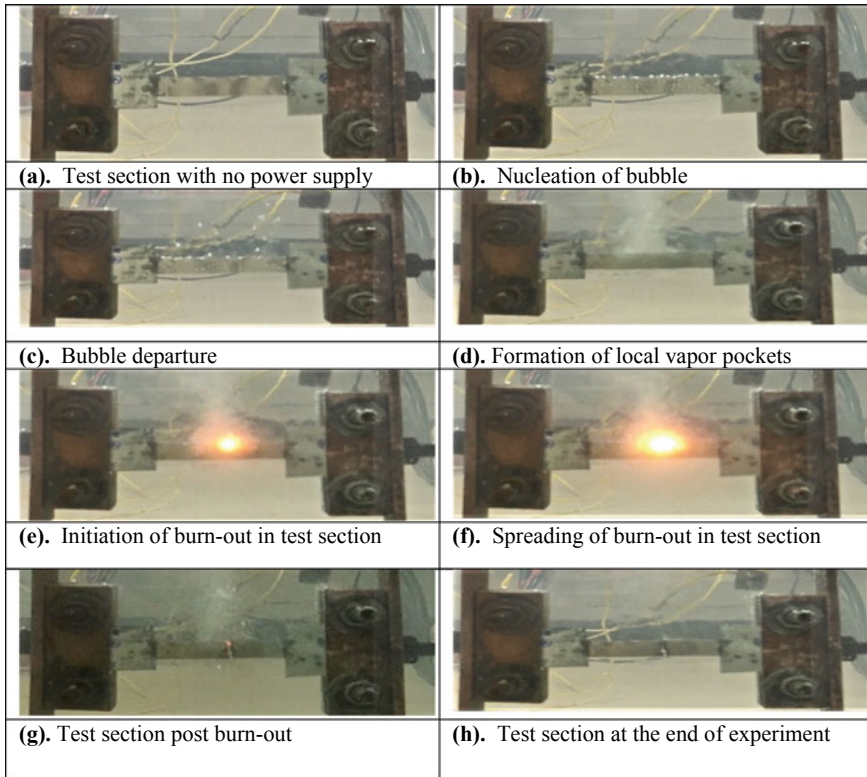


Fig. 3 Occurrence of critical heat flux for heater strip; **a** Test section with no power supply **b** Nucleation of bubble **c** Bubble departure **d** Formation of local vapor pockets **e** Initiation of burnout in test section **f** Spreading of burnout in test section **g** Test section post burnout **h** Test section at the end of experiment CHF = 5.76473 MW/m²

3 Results and Discussion

3.1 Data Reduction

The magnitude of total power input is calculated by Eq. (1). The voltage is measured across the copper electrodes. The current flow through copper electrode to copper block to GI strip to heater strip. The heat generated in copper electrode and copper block is very small due to large current flow area. The heat generated in GI strip is much less than heater strip due to its higher thickness compared to heater strip. The heat loss in GI strip, copper block, and electrode is calculated theoretically according to Joule heating (I^2R) by calculating resistance and supplied current. This heat loss is subtracted from total heat input as given in Eq. (2). The amount of heater area of strip available for heat transfer is given by Eq. (3), and the CHF calculation is carried out as per Eq. (4).

$$Q_{total} = VI \tag{1}$$

$$Q_{total} = Q + Q_{loss} \tag{2}$$

$$A = 2LW \tag{3}$$

$$CHF = (Q)/(2LW) \tag{4}$$

In the calculation for strip area available for heat transfer, a factor of two is used in order to account for two faces of the strip that is subject to heat transfer simultaneously.

3.2 Repeatability Test

To establish repeatability, experiment was performed multiple times under same conditions. Figure 4 shows the plots for data obtained from twenty-six different experiments in thirteen different strip combinations namely 1, 2, ..., 13. For each of

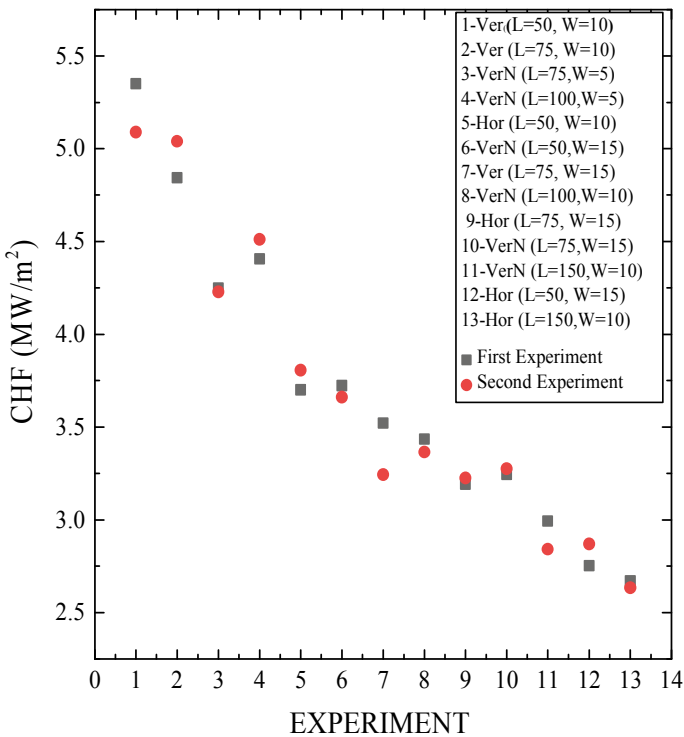


Fig. 4 Repeatability test

the thirteen different strip combinations, two experiments were performed. It was observed that the CHF values obtained are comparable. Data points lie within $\pm 6\%$ relative deviation for each of the thirteen sets.

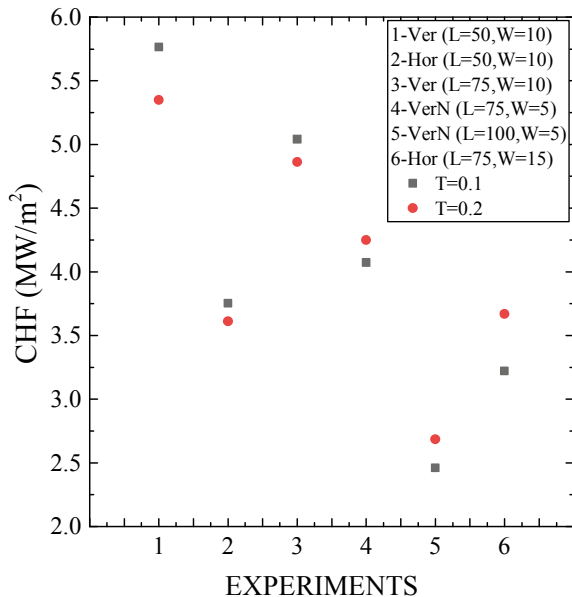
3.3 Effect of Strip Thickness on CHF

Figure 5 shows that for a given length, width, and orientation of strip, the CHF value is comparable for both 0.1 and 0.2 mm thicknesses. Among the performed experiments, six sets of length, width, and orientations are randomly selected and are mentioned as 1, 2, ..., 6. It is inferred that the strip thickness has negligible effect on the CHF value. The maximum relative deviation in CHF values are found to be $\pm 8\%$.

3.4 Effect of Strip Length and Width on CHF for Different Orientations

The effect of width and length on CHF for horizontal, vertical over width, and vertical over length orientations are shown in Fig. 6a–c. The widths of 5, 10, and 15 mm were tested for four different lengths 50, 75, 100, and 150 mm. The CHF value is observed to follow a decreasing trend with increase in the width. Length of

Fig. 5 Effect of thickness on CHF



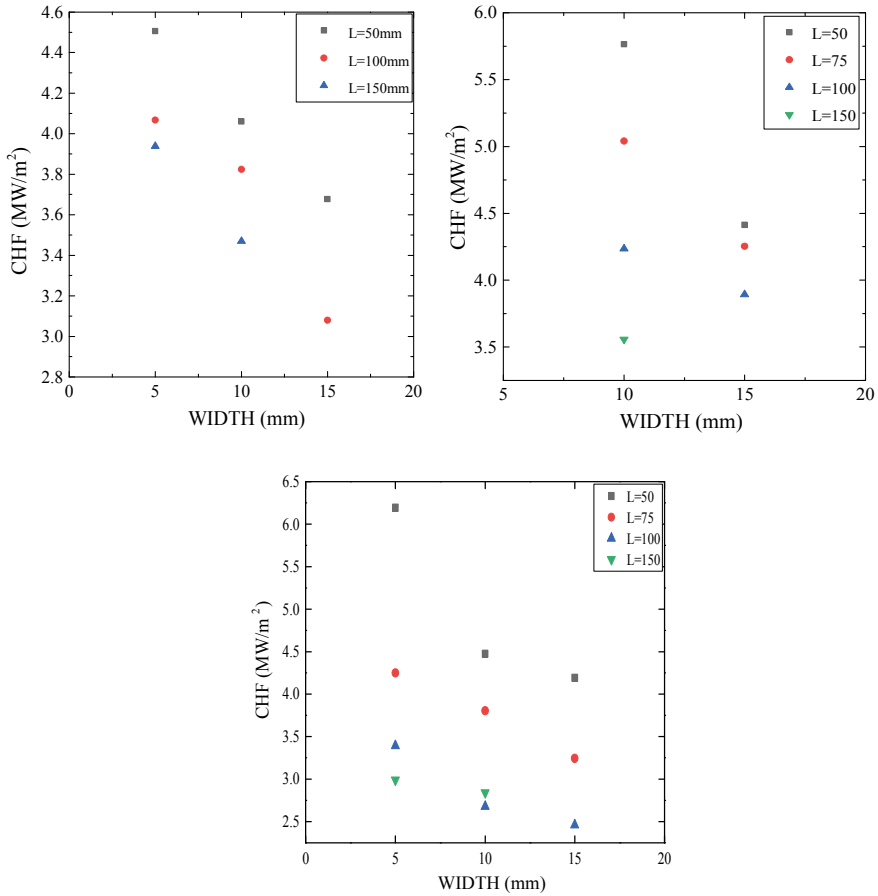
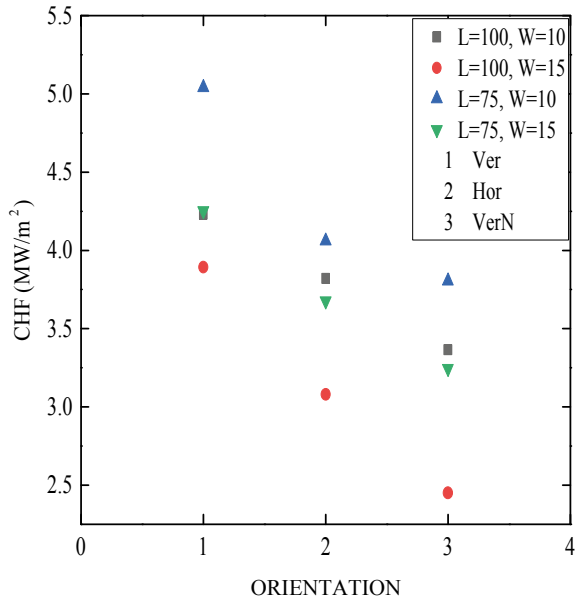


Fig. 6 a Effect on CHF in horizontal orientation b Effect on CHF in vertical over width orientation c Effect on CHF in vertical over length orientation

150 mm with width 15 mm is not included in the plot as CHF was not observed for this configuration due to maximum power limit of the DC supply. In order to avoid buckling, the strips are kept in tension. So, for 50 mm length in horizontal orientations, premature failure of the strips occurs for different widths. Therefore, the experiments were not conducted successfully, and data are not analyzed. Observing the results from Fig. 6a–c, it can be inferred that irrespective of the strip orientation, CHF value follows a decreasing trend with increase in the strip width as well as strip length.

Fig. 7 Effect of orientation on CHF



3.5 Effect of Different Orientation on CHF

The comparative study of CHF for all three orientations is plotted in Fig. 7. The values of CHF obtained for strip of length 75 and 100 mm with width 10 and 15 mm is analyzed. It is observed that heater strip in vertical over width orientation has maximum CHF followed by horizontal and vertical over length orientations, respectively. In the vertical over width orientation, the bubble slides properly over the width of the strips. Therefore, at higher value of heat input to the strip, local vapor pockets initiate, and CHF is observed. However, in horizontal orientation, bubble departs freely from the upward facing surface, but bubble coalesces and departs from the downward face of the strip. The formations of local vapor pockets are observed earlier as compared to vertical over width orientation. For vertical over length orientation, bubble from both the faces slides along the length and makes large vapor pockets, so that location becomes the common site for the inception of burnout. Therefore, at lower power supply, CHF is observed in compared to above two orientations.

4 Conclusion

The nucleate pool boiling experiment is carried out for SS 304 strips of lengths 50, 75, 100, and 150 mm each having width 5, 10, and 15 mm with two thicknesses 0.1 and 0.2 mm. The experimental setup was tested for repeatability, and it was

observed that under same experimental conditions, CHF value obtained was within a relative deviation of $\pm 6\%$. On analyzing the experimental data, it is observed that thickness of strip has negligible effect on the CHF value for given dimensions and orientation. However, for a fixed length of strip, magnitude of CHF decreases with increase in its width. Also, it is observed that CHF decreases with increase in the length for a fixed width irrespective of orientation. Out of the three orientations of strip, i.e., horizontal, vertical over width, and vertical over length, strips that are kept vertical over width have maximum CHF, followed by orientation with strip horizontal and vertical over length, respectively.

References

1. Nukiyama S (1966) The maximum and minimum values of the heat Q transmitted from metal to boiling water under atmospheric pressure. *Int J Heat Mass Transf* 9(12):1419–1433
2. Liang G, Mudawar I (2019) Review of pool boiling enhancement by surface modification. *Int J Heat Mass Transf* 128:892–933
3. Pulvirenti B, Matalone A, Barucca U (2010) Boiling heat transfer in narrow channels with offset strip fins: Application to electronic chipsets cooling. *Appl Therm Eng* 30(14–15):2138–2145
4. Feldman A, Marvillet C, Lebouché M (2000) Nucleate and convective boiling in plate fin heat exchangers. *Int J Heat Mass Transf* 43(18):3433–3442
5. Nishikawa K, Fujita Y, Uchida S, Ohta H (1984) Effect of surface configuration on nucleate heat transfer. *Int J Heat Mass Transf* 27(9):1559–1571
6. Tanjung EF, Jo D (2019) Surface orientation effects on bubble behaviors and critical heat flux mechanism in saturated water pool. *Int J Heat Mass Transf* 133:179–191
7. Yang SH, Baek WP, Chang SH (1997) Pool-boiling critical heat flux of water on small plates: Effects of surface orientation and size. *Int Commun Heat Mass Transf* 24(8):1093–1102
8. Hardik BK, Prabhu SV (2017) Critical heat flux in helical coils at low pressure. *Appl Therm Eng* 112:1223–1239

Effect of Velocity Variation on the Rate of Erosion Wear at the Elbow of the Slurry Pipe by Using CFD



Pardeep Bishnoi, Satish Kumar, Abhijeet Singh, Virender Chahal, and Vikrant

Abstract In this manuscript, the rate of erosion wear in a 90° bend pipe has been investigated with the help of computational fluid dynamics code FLUENT 15.0. Erosion of the surfaces is one of the biggest industrial problems where the solid particles are transported. This manuscript highlights the effect of flow velocity on the solid particle erosion rate on the fluid-carrying pipe. The size of the sand particles and their concentration is kept constant, i.e., 200 μm and 5%, respectively, which are injected from the inlet surface at flow velocity ranging from 2.5 to 20 m/s. The computational modeling proves its importance in demonstrating the erosion rate of the solid particles as well as its complex flow behavior.

Keywords Solid particle erosion · Elbow · Computational flow dynamics · Discrete particle mode (DPM)

1 Introduction

The erosion due to the solid particle is a matter of anxiety in many industries which includes the oil and gas industry, mining industry because the deterioration of pipe material caused by erosion wear may result in failure of the pipeline and leads to

P. Bishnoi (✉) · S. Kumar · V. Chahal · Vikrant
Department of Mechanical Engineering, Chandigarh Engineering College, Mohali, India
e-mail: Pardeep.4318@cgce.edu.in

S. Kumar
e-mail: satish.4310@cgce.edu.in

V. Chahal
e-mail: virender.4311@cgce.edu.in

Vikrant
e-mail: vikrant.4341@cgce.edu.in

A. Singh
Department of Mechanical and Automation Engineering, Amity University Jharkhand,
Ranchi, India
e-mail: abhijeetsingh315@gmail.com

economic loss and raises the issue of safety. So, for the design process as well as product sustainability, it is mandatory to analyze the rate of erosion and its pattern precisely. Various parameters which affect the rate of solid particle erosion in the pipe are fluid properties, particle properties, the material of the impinging wall, and the flow path geometry. Focusing on each of the effective parameters, many studies have been done to predict erosion behavior for different operational conditions.

The solid particle erosion is a complex phenomenon to understand. Also, it is difficult to conduct experiments on the multiphase flow. However, the evolution of computational fluid dynamics (CFD) is found to be very useful in simulating such flow. The multiphase models in CFD are generally based on the Euler–Euler approach and Euler–Lagrange approach [1]. Solid particulate (generally sand/coal particles) dispersed in the fluid strikes on the target wall and removes the inner coated material of the pipe wall. The removal of material by solid particles is labeled as erosion. A few studies utilized computational strategies to analyze the erosion behavior at various affecting parameters [2–6]. Habib et al. [7] studied the erosive flow in the pipe section having a sudden contraction. The influence of impact velocity, particle size, and concentration was evaluated. The numerical part was performed by using commercial CFD code FLUENT with DPM to track the particles by using the *k-c* RNG turbulence modeling scheme. They examined that erosion mainly occurs at the contraction plate. The impact of particles was significant on the contraction plate and insignificant on the pipe wall also the particle with higher size has a higher tendency to erode the material. Zhang et al. [8] developed a probability model to calculate the erosion caused by the solid particles in a straight pipe. They investigated erosion rate using CFD code FLUENT for different particle sizes (50–400 μm), pipe diameter (50.5–203.2 mm), and flow velocity (3.048–15.240 m/s). Later, the model was verified with the experimental results. They described that the penetration rate initially increases to a large extent with the particle size, and then, the increment is limited in extent. The influence of pipe diameter was found to be having an inverse relation with the erosion rate. A low value of penetration rate was reported on the pipe having big diameters. Their study also reports a significant increase in penetration rate with velocity. The penetration rate was increased to 6.4 times at the velocity shift from 3.048 to 6.096 m/s. Safaei et al. [9] studied the effect of copper particle diameter on the erosion rate in a 90° pipe bend. The size of the copper particle was varied from 10 nm to 100 μm at three different velocities of range 5–20 m/s. The most significant effect on erosion rate was observed with the change in impact velocity. For the same concentration, the erosion caused by an impact velocity of 20 m/s was 7.5 times higher than that caused by 10 m/s. Shahata et al. [10] investigated the erosion rate on carbon steel of pipe by varying both flow rates of seawater and sand concentrations (1–11 gm/liter) and observed more erosion rate at higher concentration of sand. Singh et al. [11] computationally explored the impact of particle flow velocity and solid particles concentration on the erosion rate in the bend pipe. Also, observed that the maximum erosion is in the curved section of the pipe.

In this manuscript, the effect of the discrete particle model (DPM), erosion rate on the elbow part of the pipe is investigated at different flow velocities.

2 Governing Equations and Erosion Model

The DPM erosion rate of the water having sand particle is being studied using the numerical simulation techniques. The domain is developed in the Autodesk Fusion 360 software. The simulation is performed on the ANSYS 15.0 (FLUENT) computational tool. The tetrahedral meshing is performed on the model with a high number of cells, so that the result which we get through the simulation is accurate. The k - ϵ viscous model is used for the simulation. The SIMPLEC scheme is used as a pressure velocity coupling model.

2.1 Euler–Lagrange Approach

One-way coupled Eulerian–Lagrangian model was used for the simulation. In this approach, the fluid is assumed as a continuous phase and solves it by the time averaged N-S equation and the solution of dispersed phase obtained by tracking each particle.

The single-phase equations for conservation of mass and momentum are:

$$\frac{\partial \rho}{\partial t} + \nabla \cdot (\rho \mathbf{v}) = 0, \quad (1)$$

$$\left(\frac{\partial \rho \mathbf{v}}{\partial t} + \nabla \cdot (\rho \mathbf{v} * \mathbf{v}) \right) = \nabla \cdot \tau \quad (2)$$

$$\tau = \mu_{\text{eff}} [\nabla \mathbf{v} + (\nabla \mathbf{v})^T] \quad (3)$$

The turbulence is solved by using the standard k - ϵ model. The equation is in the form:

$$\nabla \cdot (\rho \mathbf{v} \phi) - \nabla \cdot \frac{\mu_{\text{eff}}}{\sigma_\phi} = D_\phi \quad (4)$$

Here, k or ϵ , σ_ϕ represents the turbulent diffusivity of ϕ and D_ϕ .

As the particle concentration is low, one-way coupling was applied in this study. Firstly, the solution of continuous phase is obtained, and after that particle trajectories are determined using Lagrangian approach by using Newtonian equation of motion:

Momentum:

$$m \cdot \frac{d\mathbf{v}_p}{dt} = F \quad (5)$$

where F = Force, i.e., a combined effect of drag force and the buoyancy force.

2.2 Erosion Model

A simplified erosion model of Finnie was implemented in this study. The implementation of the Finnie's model in CFX is given as:

$$E = kV^n f(\gamma) \quad (6)$$

$$f(\gamma) = \frac{1}{3} \cos^2 \gamma \quad 18.5^\circ \leq \gamma \leq 90^\circ \quad (7)$$

where E = Erosion rate, k , and n are erosion parameters, and for this study constant, k was set to 1.0 while n was set to 2.0, $f(\gamma)$ is a function that relates wear and impact angle, and γ is the impact angle with respect to normal to the surface. By implementing this model on CFX, the overall erosion rate at every point on the surface of bend is calculated by multiplying erosion rate (E) with the mass flow removed by the particles that are impacting on the surface, after then adding for all the particles. This leads to a variable called erosion rate density ($\text{Kg s}^{-1} \text{m}^{-2}$).

3 Domain Description and Boundary Conditions

A horizontal elbow pipe of mild steel was used in this study. The pipe has diameter $D = 10$ mm and length $L = 100$ mm as shown in Fig. 1. The inlet is the velocity inlet, whereas the outlet is considered as a pressure outlet. The velocity of slurry flow is initially taken as 2.5 m/s which will be changed from 2.5 to 10 m/s for further simulations. The flow is considered as fully developed flow at the inlet. The turbulent intensity at the inlet is 'medium', i.e., 5%.

In this work, tetrahedral type of meshing was done to discretize the domain into smaller cells. The higher grid cell increases the accuracy of the results. Table 1 shows the details of the grid independency test of the meshing. It can be easily visualized from Table 1 that after 2,580,273 cells, the variation in the DPM erosion rate due to meshing cells has become zero. For further simulation purposes, we consider this as our standard meshed domain.

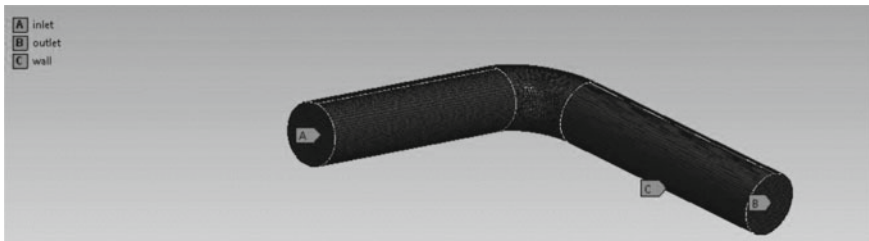


Fig. 1 Physical model of slurry pipeline

Table 1 Grid sensitivity test for meshing

S. no	Number of cells	Change in DPM erosion rate
1	1,012,466	Yes
2	1,195,872	Yes
3	2,246,481	Yes
4	2,580,273	No
5	2,850,692	No

4 Results and Discussion

The effect of flow rate on the erosion rate is studied at the elbow part of the model by keeping all other factors constant, i.e., concentration of solid particle, the diameter of the pipe, and the roughness of the pipe.

4.1 Influence of Velocity

The contour of flow velocity is shown in Fig. 2. The flow is laminar and streamlines up to the elbow point, but after the elbow location, the liquid–solid particle flows on the zig-zag path. The elbow portion can be considered as the transition part of the flow regimes. Also, at elbow region, all solid particle strikes the wall of the pipe and develops the erosion of the pipe material. The momentum of solid particles is more in the transition and turbulent flow region as shown in Fig. 2.

Figure 3a shows the contour of DPM erosion at the elbow region of the pipe. The contour shows that the erosion rate is higher at the point where the solid

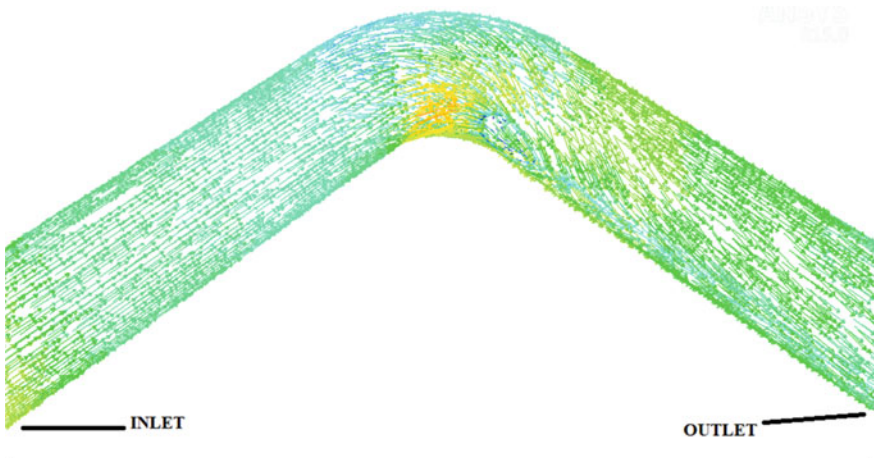


Fig. 2 Velocity contour in the pipe flow

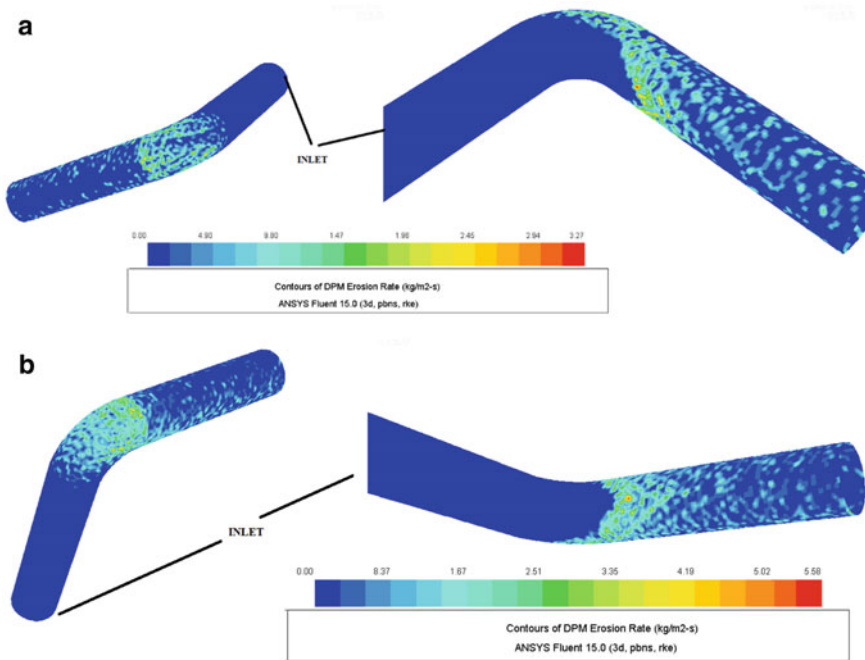


Fig. 3 a Contour of DPM erosion rate for 2.5 ms^{-1} . b Contour of DPM Erosion rate for 10 ms^{-1}

particle collides with each other when they entered the turbulent motion. The higher the turbulence, more will be the erosion rate. The contour profile is symmetric about the flow axis. The distribution of erosion rate is very similar in Fig. 3b; however, the magnitude DPM erosion rate is 2.45 times higher for the 10 ms^{-1} as compared to the 2.5 ms^{-1} .

Figure 4 demonstrates the variation of the DPM Erosion rate at different flow velocity. At the low velocity of 2.5 m/s , erosion rate of solid particle has a very low value. The value of erosion rate density varies linearly and gets enhanced with the increase in the velocity. About six times increment in erosion rate is reported when the velocity gets to step up from 2.5 to 20 m/s . The increase in velocity increases the turbulence in the solid particles. These high momentum particles strike the elbow wall of the pipe hardly and thus cause more erosion.

5 Conclusion

With the help of the CFD model, the investigation of the solid particle erosion rate in a 90° elbow bend pipe is easily be visualized and predictable. Based on the simulation results, it can be concluded that the flow velocity plays a significant role

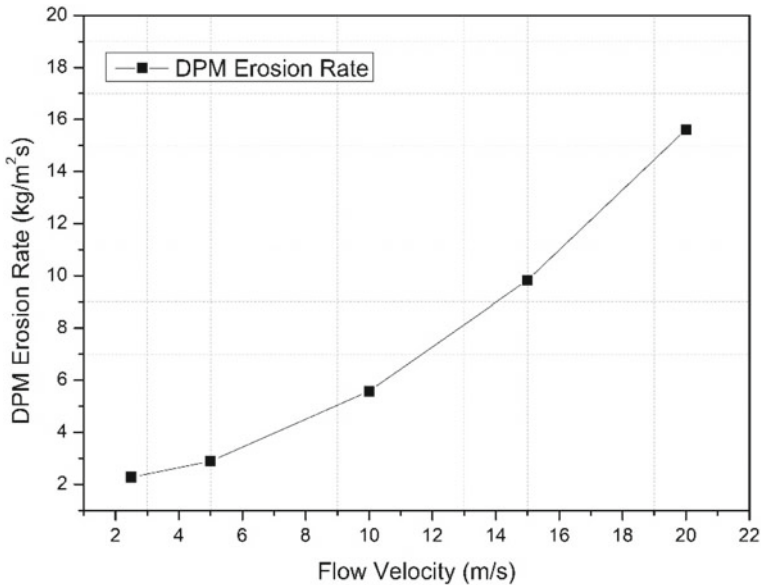


Fig. 4 Variation of DPM erosion rate and flow velocity of the solid particle in the slurry pipeline

in the erosion decay in the pipeline especially at the elbow location. An increment of about six times in the value of erosion rate density is observed when the velocity is shifted from 2.5 to 20 m/s at 200 μm particle size. Based on the main results of this analysis, it is expected that the erosion rate in other geometries can be predicted accurately with the help of computational tools.

References

1. Canonsburg TD (2009) ANSYS CFX Tutorials 15317:724–746
2. Ansari MR, Mohammadi S, Oskouei MK (2012) Two-phase gas/liquid-solid flow modelling in 90 bends and its effect on erosion. *Glob J Res Eng Mech Mech Eng* 12(1):35–44
3. Singh MK, Kumar S, Ratha D (2017) Computational analysis on disposal of coal slurry at high solid concentrations through slurry pipeline. *Int J Coal Prep Util*, 116–130. <https://doi.org/10.1080/19392699.2017.1346632>
4. Kannojiya V, Kumar S, Kanwar M, Mohapatra SK (2016) Simulation of erosion wear in slurry pipeline using CFD. *Appl Mech Mater* 852:459–465
5. Mansouri A, Arabnejad H, Shirazi SA, McLaury BS (2015) A combined CFD/experimental methodology for erosion prediction. *Wear* 332–333:1090–1097. <https://doi.org/10.1016/j.wear.2014.11.025>
6. Pereira GC, de Souza FJ, de Moro Martins DA (2014) Numerical prediction of the erosion due to particles in elbows. *Powder Technol* 261:105–117
7. Habib MA, Badr HM, Kabir ME (2007) Erosion and penetration rates of a pipe protruded in a sudden contraction. *Comput Fluids* 37:146–160

8. Zhang R, Liu H, Zhao C (2013) A probability model for solid particle erosion in a straight pipe. *Wear* 308(1–2):1–9
9. Safaei MR, Mahian O, Garoosi F, Hooman K, Karimipour A, Kazi SN (2014) Investigation of micro- and nanosized particle erosion in a 90 pipe bend using a two-phase discrete phase model. *Sci World J* 740578:12
10. Shahata AI, Youssef MT, Saqr K, Shehadeh M (2014) CFD investigation of slurry seawater flow effect in steel elbows. *Int J Eng Res Technol* 3:364–370
11. Singh V, Kumar S, Mohapatra SK (2019) Modeling of erosion wear of sand water slurry flow through pipe bend using CFD. *J Appl Fluid Mech* 12(3):679–687

Computational Study of the Effect of Cold Orifice Dimension on the Temperature Variation in the Counter Flow Vortex Tube



Ravi Kant Singh, Achintya Kumar Pramanick,
and Subhas Chandra Rana

Abstract The cold orifice is a part of the counter flow vortex tube, and its dimension can control the cold exit temperature of the inlet fluid. Although the geometry of counter flow vortex tube is very simple, it has no moving part, but the flow physics inside the vortex tube is very complex. The purpose of the present paper is to optimize the diameter of cold orifice and study its effect on the performance enhancement of the counter flow vortex tube using CFD analysis. The computational analysis has been performed on an axisymmetric 3D, steady-state, compressible, and turbulent flow vortex tube (VT) with the effect of different orifice dimension. The simulation is done with ANSYS17.1 FLUENT software. Realizable $k - \varepsilon$ model with standard wall function has been used for simulating the turbulence in the flow field in the present problem. This model is best suited for predicting the flow features inside the counter flow vortex tube. It is proposed that the rate of cooling is optimum between 5 and 6 mm diameter of the cold orifice.

Keywords Rate of cooling · Counter flow vortex tube · ANSYS17.1 fluent · Cold orifice diameter

Nomenclature

VT Vortex tube
 T_s Static temperature, K
 d_c Cold exit diameter, mm
 \dot{m}_{in} Mass flow rate at Inlet, Kg/sec
 ΔT Total temperature gradient, K
 ΔT_c Cold temperature gradient, K

R. K. Singh (✉) · A. K. Pramanick · S. C. Rana
National Institute of Technology Durgapur, Durgapur West Bengal, 713209, India
e-mail: ravikantsingh941@gmail.com

A. K. Pramanick
e-mail: achintyakumar.pramanick@me.nitdgp.ac.in

S. C. Rana
e-mail: subhas.rana@me.nitdgp.ac.in

k	Thermal conductivity of air (W/m K)
ΔT_h	Hot temperature gradient, K
D	Vortex tube diameter, mm
C_p	Specific heat of fluid, J/Kg K
T_o	Total temperature, K
\dot{m}_c	Mass flow rate of cold fluid, Kg/sec
L	Length of vortex tube, mm

Greek symbols

ρ	Density of the fluid, kg/m ³
μ_c	Cold mass fraction
γ	Specific heat ratio

1 Introduction

The vortex tube (VT) device, which is also acknowledged as the Ranque–Hilsch vortex tube (RHVT), is having simple mechanism but a complex flow physics which detached a compressed gas stream into two exit streams i.e. hot and cold. The vortex tube (VT) is effective device to accomplish expeditious spot cooling, using compressed fluid such as input source. It has no moving parts. The VT which breaks up a high-pressure inlet fluid, which enters tangentially into low-pressure and high-pressure outlet fluids, flows simultaneously, thereby resulting in the temperature gradient. In most of the cases, it has a circular main tube having a different number of nozzles and a controlling valve called throttle. High-pressure gaseous fluid enters the VT in tangential direction through different nozzles which helps in increasing the angular velocity of fluid and assists to produce a swirling effect. It has two outlets. The location of the hot outlet is at the far end from the inlet nozzle near the outer radius but the location of cold outlet is nearer to the inlet and at the centerline of the tube. The fluid (gas) breaks up into two different layers, one is close to the VT centerline axis having a lower temperature which is obtained through the cold outlet. The other is nearer to the periphery (near wall) of the tube possessing a higher temperature attained by the hot outlet. The temperature gradient in the VT is maintained due to the swirling effect was first discovered by Ranque–Hilsch et al. [1].

The specifications used to assess the effectiveness of the VT are as follows

Cold mass fraction (μ_c): It is given as the ratio of mass flow rate of cold fluid to mass flow rate of inlet fluid, and is expressed as,

$$\mu_c = \frac{\dot{m}_c}{\dot{m}_{in}} \quad (1)$$

Cold exit temperature gradient (ΔT_c): This fluid temperature is given as the difference of temperature at inlet and the temperature of the cold end,

$$\Delta T_c = T_{in} - T_c \quad (2)$$

Hot exit temperature separation (ΔT_h): This fluid temperature is given as the difference of temperature at hot exit and the temperature at the inlet,

$$\Delta T_h = T_h - T_{in} \quad (3)$$

Total temperature separation (ΔT): This fluid temperature is given as the difference of temperature at hot exit and the temperature at cold end,

$$\Delta T = T_h - T_c \quad (4)$$

The discovery of vortex tube was by Ranque [1], since then the researchers have made efforts to improve the vortex tube performance. Skye et al. [2] both experimentally and numerically studied the geometry of VT such as the diameter of 106 mm and length of an Exairs 708 slpm (25 scfm). They found that maximum separation of power occurred for 0.65 of the cold mass fraction. Anish et al. [3] explored the cause of energy separation inside the VT and found that the cause of heating near the VT chamber periphery is mainly due to the work done by the viscous forces. Khazaei et al. [4] uses a 2D vortex tube model to study different gases as working fluid and found that using helium as a working fluid which generates the highest energy separation. Farouk and Farouk [5] studied large Eddies simulation (LES) in VT and indicated that the region of minimum swirl velocity and minimum total temperature are the same. Pourmahmoud et al. [6] analyzed computationally the number of nozzles effect as well as shapes on VT performance. They observed that the helical shaped nozzles produce higher swirling velocity which led to the more temperature gradient, as compared to straight nozzles. Lewins and Bejan [7] proposed that the frictional coupling which occurred between the layers of rotating fluid is due to the angular velocity gradient in the vortex tube.

In the present study, the focus is on attaining one of the important parameters such as optimum cold exit diameter of the VT, according to best of author's knowledge the present problem is seldom addressed. So, the present analysis is mainly executed on this parameter.

2 Mathematical Modeling

Swirling flow of the fluid in VT is governed by nonlinear partial differential equations of momentum balance, mass balance, turbulence, and ideal gas. In the mathematical form, these equations is given as follows:

Continuity equation:

$$\frac{\partial}{\partial x_i}(\rho u_i) = 0 \quad (5)$$

Momentum balance equation:

$$\frac{\partial}{\partial x_i}(\rho u_i u_j) = -\frac{\partial P}{\partial x_i} + \frac{\partial}{\partial x_j} \left[\mu \left(\frac{\partial u_i}{\partial x_i} + \frac{\partial u_j}{\partial x_i} - \frac{2}{3} \delta_{ij} \frac{\partial u_k}{\partial x_k} \right) \right] + \frac{\partial}{\partial x_i} \left(-\overline{\rho u_i' u_j'} \right) \quad (6)$$

Energy balance equation:

$$\frac{\partial}{\partial x_i} [u_i(\rho E + P)] = \frac{\partial}{\partial x_j} \left[\left(k_e + \frac{c_p \mu_t}{Pr_t} \right) \frac{\partial T}{\partial x_j} + u_i(\tau_{ij})_{\text{eff}} \right] + S_h \quad (7a)$$

$$(\tau_{ij})_{\text{eff}} = \mu_{\text{eff}} \left(\frac{\partial u_j}{\partial x_i} + \frac{\partial u_i}{\partial x_j} \right) - \frac{2}{3} \mu_{\text{eff}} \frac{\partial u_k}{\partial x_k} \delta_{ij} \quad (7b)$$

Ideal gas equation:

$$P = \rho RT_s \quad (8)$$

For simulating the turbulence in the flow field, the realizable $k - \varepsilon$ turbulence model is used considering the standard wall function for the present problem. It is noted from Liu et al. [8] both the turbulence model, realizable $k - \varepsilon$ and RSM model produce almost same result but due to higher computational cost and simulation timing of the RSM turbulence model the $k - \varepsilon$ model is preferred; therefore, the present simulation is performed with $k - \varepsilon$ model. The transport equations related to turbulent dissipation (ε) and turbulent kinetic energy (k) in standard realizable $k - \varepsilon$ turbulence model along with the Reynolds average Navier–Stokes (RANS) and energy equations are given below.

$$\frac{\partial}{\partial x_i}(\rho k u_i) = \frac{\partial}{\partial x_j} \left[\left(\mu + \frac{\mu_t}{\sigma_k} \right) \frac{\partial k}{\partial x_j} \right] + G_k + G_b - \rho \varepsilon + Y_M \quad (9)$$

$$\frac{\partial}{\partial x_i}(\rho \varepsilon u_i) = \frac{\partial}{\partial x_j} \left[\left(\mu + \frac{\mu_t}{\sigma_\varepsilon} \right) \frac{\partial \varepsilon}{\partial x_j} \right] - \rho C_2 \frac{\varepsilon^2}{k + \sqrt{v \varepsilon}} + C_{1\varepsilon} \frac{\varepsilon}{k} (G_k + C_{3\varepsilon} G_b) \quad (10)$$

The additional terms $-\overline{\rho u'_i u'_j}$ in the momentum Eq. (6) are known as the Reynolds stresses. These stresses are modeled by Boussinesq hypothesis which is given below:

$$-\overline{\rho u'_i u'_j} = \mu_t \left(\frac{\partial u_i}{\partial x_j} + \frac{\partial u_j}{\partial x_i} \right) - \frac{2}{3} \left(\rho k + \mu_t \frac{\partial u_k}{\partial x_k} \right) \delta_{ij} \quad (11)$$

$$\mu_t = \rho C_\mu \frac{k^2}{\varepsilon} \quad (12)$$

where μ_t is turbulent viscosity or eddy viscosity, k is the turbulent kinetic energy, ε is the turbulent dissipation rate is $\alpha_t = \mu_t / \rho \sigma_t$ turbulent diffusivity, and σ_t is turbulent Prandtl number. In standard $k - \varepsilon$ model $C_\mu = 0.09$ but in the realizable $k - \varepsilon$ model, C_μ is variable which provides improved predictions. T is mean temperature, and u_i and u_j are mean velocity. u'_i and u'_j are fluctuating velocities above mean velocity.

In Eq. (9), Y_m is used for the fluctuating dilatation in compressible turbulence to the overall dissipation rate, G_k , G_b is the generation of turbulence kinetic energy due to the mean velocity gradients and buoyancy, respectively, σ_ε and σ_k are the turbulent Prandtl numbers for ε and k , respectively. The convergence criteria are taken by applying the residuals for the energy of the order of 10^{-6} and it is 10^{-3} for the rest of quantizes. In standard realizable $k - \varepsilon$ turbulence model, the values of the constants are as follows:

$$\sigma_t = 0.9, \sigma_k = 1.0, \sigma_\varepsilon = 1.2, \sigma_{1\varepsilon} = 1.44, \text{ and } C_2 = 1.9$$

3 Boundary Condition

A proper physics-based boundary condition has taken for the successful completion of the solution of the governing equation. In the present work, compressed air is passed through the different nozzles of the VT at the inlet and gets detached into two fluid streams such as cold and hot and comes out with the two different outlets. Adiabatic boundary condition is applied at the wall, due to quick separation of energy inside the vortex tube (VT). In the present model, no-slip boundary condition is suitable near rigid wall, and tangential velocity at inlet is sub-sonic.

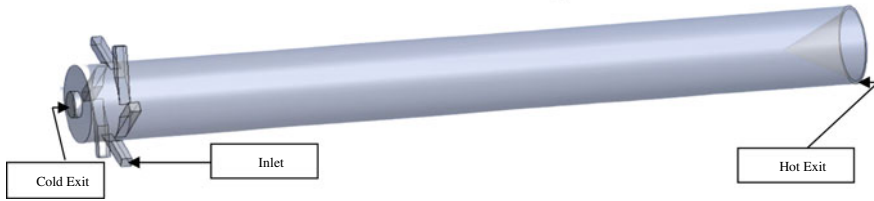


Fig. 1 Three-dimensional model of vortex tube

Table 1 Geometrical measurements of the vortex tube

Parameters	Dimension
Tube main diameter (D)	12 mm
Nozzle number (N)	6
Tube length (L)/diameter (D)	8.33
Cold exit diameter, d_c	5 mm

Table 2 Thermo-physical properties of the working fluid

Working Fluid	Air
Specific heat (C)	1.00643 kJ/kg-k
Density (ρ)	Ideal gas equation
Thermal conductivity of air (K)	0.0242 W/m-k

Pressure-inlet boundary condition is applied at nozzle inlet such as 3–5.5 bar and temperature 294.15 K. Similarly, pressure-outlet boundary condition is taken at cold exit as 1.0132 bar (absolute) and hot exit at 0.5 bar (absolute). The cold and hot exits with six nozzles inlets are shown in Fig. 1. The geometrical specification of the vortex tube has been mentioned in the Table 1 and the thermo physical property of working fluid (air) has been noted from Table 2.

4 Grid Independence Test

The unstructured tetrahedral mesh is used for the present model with inflation layer boundary condition near wall as shown in Fig. 2. The front view, cold exit, and the hot exit of the VT model are presented in Fig. 2. To reduce the errors due to unmapped grids, the study has been performed for different unit cell from 19,587 to 110,000 on a vortex tube of $L/D = 8.33$ and cold mass fraction $\mu_c = 0.35$. The variation of parameter such as cold exit temperature is obtained by varying different grid size as plotted in Fig. 3. It is seen that there is no significant advantage in increasing the grid size above 110,000 unit cell. Thus, for the present model, the simulation is performed at 110,000 unit cell to reduce the extra computational time.

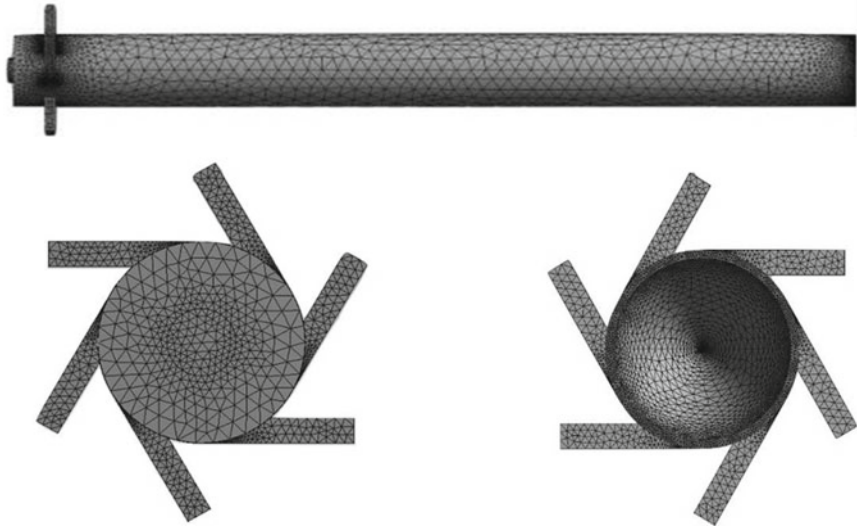
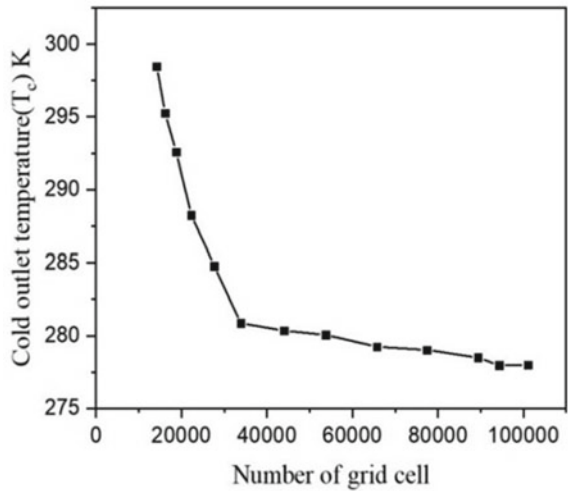


Fig. 2 Vortex tube with unstructured mesh

Fig. 3 Grid size independence study



5 Validation

In the present study, the $k - \epsilon$ turbulence model along with Navier–Stokes equations is adopted by the FLUENT™ software. The quick schemes and second-order upwind are used for energy, momentum, and turbulence equations. For validation of the present study, the temperature separation is calculated and correlated by

Fig. 4 Comparison of similarity relations obtained by different works

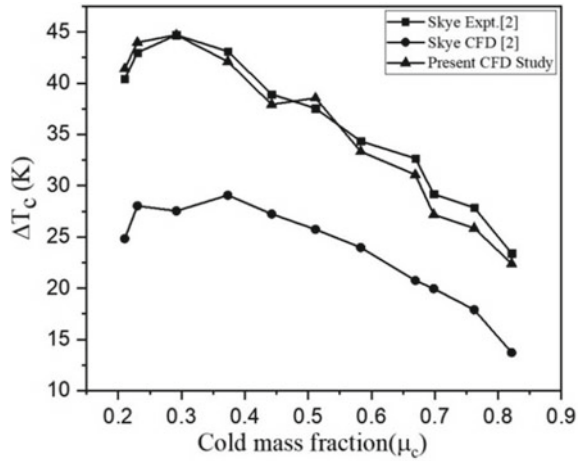
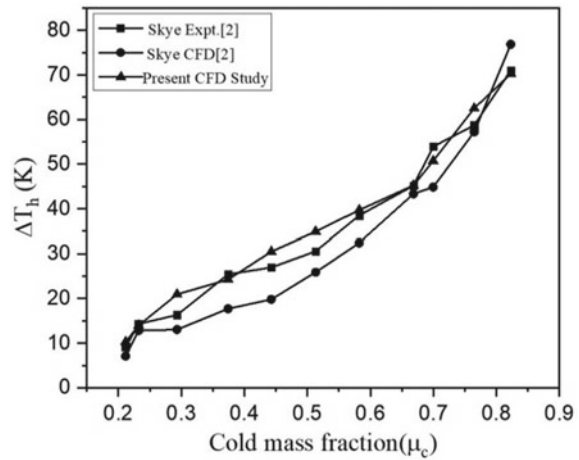


Fig. 5 Comparison of similarity relations obtained by different works



experimental result of Skye et al. [2] as depicted in Figs. 4 and 5. It can be observed in Fig. 4, the predicted result for the cold temperature difference (ΔT_c) is in close agreement with the experimental study. The result of the present study for cold temperature difference is observed between computational and experimental results of Skye et al. [2]. Although, the result of the temperature difference of hot end (ΔT_h) is close to the experimental result.

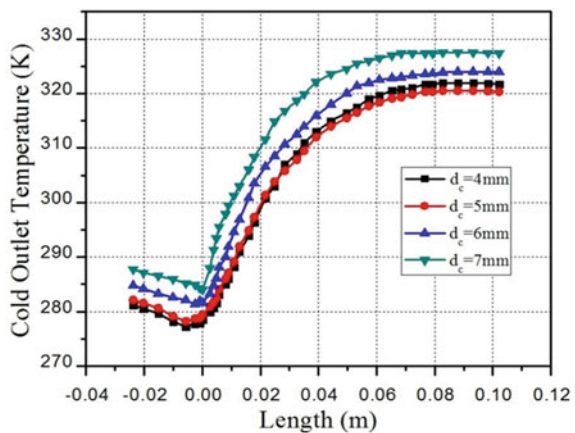
It signifies that the methodology for simulating present work is appropriate, it is seen from Fig. 4 with the increment in the cold mass fraction of air the cold temperature gradient is first increases and attains the maximum value between 0.21 and 0.3 and then decreases. Figure 5 represents the variation of a hot temperature gradient with mass fraction of cold fluid and also observed that by increasing the mass fraction of cold fluid, value of hot temperature gradient increases continuously.

6 Results and Discussion

The computational fluid dynamics simulation has been performed on the VT to analyze the flow physics and temperature for varying cold outlet diameter and to optimize the number of nozzles.

Cold exit diameter: In the present analysis, the variation in cold exit diameter of VT has been studied with four cold exit diameters such as 4, 5, 6, and 7 mm, with a constant VT diameter as 12 mm. Cold exit diameter has an influence on hot as well as on cold mass flow rates. If the diameter of cold exit increases, the rate of flow at the cold exit also increases. It is seen from Fig. 6 that with an increase in cold exit diameter, the hot and cold exit temperatures increases, while the flow rate at the hot exit decreases and at the cold exit increases. To differentiate the end result of cold exit diameter with the temperature gradient, the graph of cold outlet temperature along VT length has been shown in Fig. 6. By increasing cold exit diameter from 5 to 6 mm (or increasing cold exit to VT main diameter ratio of the VT from 0.4167 to 0.50), temperature increases by 2 K in cold exit and also the mass fraction increased with 40%, which is diminishing the effect of 2 K increase of cold exit temperature on the performance of the VT. By increasing the cold exit diameter from 6 to 7 mm (or increasing the cold exit diameter to VT diameter ratio from 0.50 to 0.5833), the temperature of cold exit and the mass fraction of cold exit show increment of near 5 K and 20%, respectively. It can be observed, by increasing diameter of cold exit from 6 to 7 mm, the temperature rise effect is much higher than the mass fraction of cold exit gain, which has been diminishing the performance of the VT in comparison to the previous case (diameter of 6 mm at cold exit). By studying both the parameters such as mass fraction of cold exit and its temperature, it is observed from Fig. 6 performance of VT increases as the cold exit diameter increases from 5 to 6 mm, and increment in the cold exit diameter over 6 mm shows the reduction of the VT performance.

Fig. 6 Variation of cold outlet temperature with cold exit diameter across length



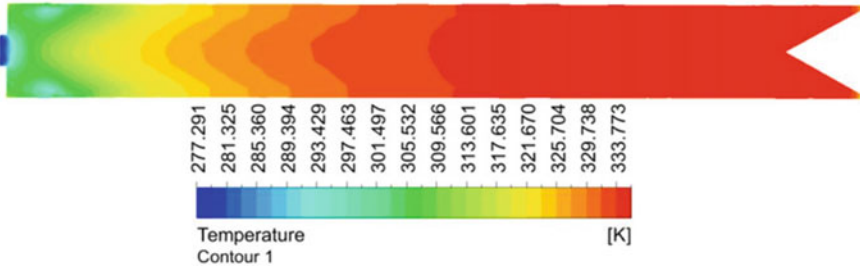


Fig. 7 Temperature contour along the length in the VT

Figure 7 shows the temperature contours distribution of the optimum cold exit diameter of 5 mm case at $P_{in} = 5.5$ bar. From the contour plot in Fig. 8, the temperature separation phenomenon is clearly observable. It is evident from the contour plot that the core axial fluid which is exiting through the cold exit end is having very low temperature and the peripheral fluid which is exiting through the hot exit is having higher temperature in comparison with the fluid entering at the inlet of the VT. Figure 8 depicts the axial velocity variation with radius of vortex tube, and it can be noticed from the graph that the axial velocity of air is continuously decreasing as the flow move toward the hot exit side. The air which is in outer periphery progress in the direction of hot exit side and is observed as positive axial velocity, and the air which is in the core zone of the VT is progress in the direction of cold exit side and is observed as negative axial velocity. The negative axial velocity of air is due to the pressure gradient between flow field and cold exit in the VT. The pressure difference on the air particle is continuously acting while flowing in the direction of hot exit side. When the momentum of the air particle reaches to zero, due to this the flow of air is not able to continue its motion toward hot exit side and by which there is flow reversal takes place. The pressure difference on the air particle is acting continuously which leads to expansion of air particle and this result on an additional increase of the axial velocity of air.

The energy content of the flow also depends upon the specific heat and mass of the substance along with the temperature. Thus, the magnitude of cooling power performance must be calculated to optimize the vortex tube for any application. The cooling power performance is given as,

$$\dot{Q}_c = m_c C_p (T_{in} - T_c) \quad (13)$$

It can be seen from Fig. 9, the result of cooling power performance of vortex tube considering air as working fluid agree well with the experimental result of Skye et al. [2] studied with various value of cold mass fraction. The study shows that the maximum cooling power performance of vortex tube is observed near the cold mass fraction of about 0.65–0.70. However, the temperature separation of cold exit is lower at this cold mass fraction due to higher mixing of hot and cold fluid owing to the interference face by the control valve at hot end. As seen from Fig. 9, the cooling power performance for the lower cold mass fraction is insignificant.

Fig. 8 Variation of axial velocity with radius

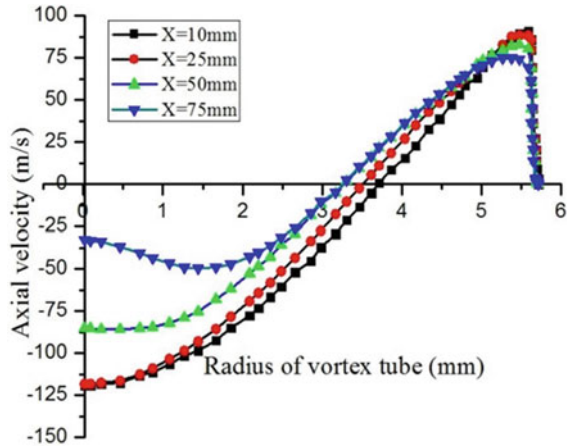
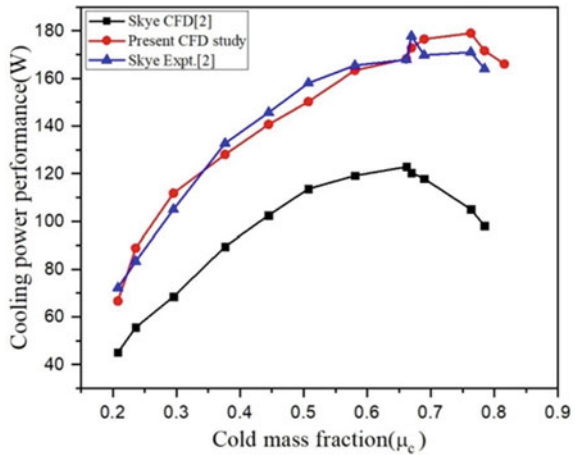


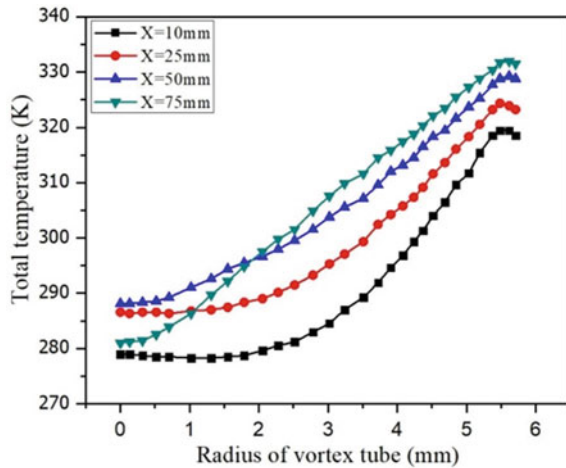
Fig. 9 Cooling power performance of vortex tube



The total temperature consists of kinetic energy component and static temperature in it. As a result of higher kinetic energy component and the nozzle configuration, there is higher swirl velocity in the radial direction. The temperature separation effect in the vortex tube is due to combined effort of variation of kinetic energy as well as the expansion of air due to pressure gradient in the radial direction. The shear work transfer by core axially flowing air on the peripheral layers which result in decrease of their total temperature as well as kinetic energy as shown in Fig. 10. Total temperature (T_o) for a compressible fluid is stated as [9],

$$T_o = T_s + \frac{V^2}{2C_p} \tag{14}$$

Fig. 10 Variation of total temperature radially



7 Conclusion

With the increase in cold outlet diameter of vortex tube, the temperature of the fluid and the mass flow rate at cold exit will be increased but beyond 5 mm the cold outlet temperature increases which are not desired. So the critical cold outlet diameter lies between 5 and 6 mm. The results obtained with the present CFD simulation is agree well with the results of Skye. The study of axial velocity gives the idea about the flow reversal. The 3D axisymmetric vortex tube model can predict the separation of temperature and behavior of fluid flow inside the VT. The cooling performance maximum value is observed for the range of 0.65–0.7 of cold mass fraction.

References

1. Joseph RG (1934) Giration Des Fluides Sarl. Method and apparatus for obtaining from alpha fluid under pressure two currents of fluids at different temperatures. U.S. Patent 1,952,281
2. Skye HM, Nellis GF, Klein SA (2006) Comparison of CFD analysis to empirical data in a commercial vortex tube. *Int J Refrig* 29(1):71–80
3. Anish S, Setoguchi T, Kim HD (2014) Computational investigation of the temperature separation in vortex chamber. *J Mech Sci Technol* 28(6):2369–2376
4. Khazaei H, Teymourtash AR, Malek-Jafarian M (2012) Effects of gas properties and geometrical parameters on performance of a vortex tube. *Sci Iran* 19(3):454–462
5. Farouk T, Farouk B (2007) Large eddy simulations of the flow field and temperature separation in the Ranque-Hilsch vortex tube. *Int J Heat Mass Transf* 50(23–24):4724–4735
6. Pourmahmoud N, Zadeh AH, Moutaby O, Bramo A (2012) Computational fluid dynamics analysis of helical nozzles effects on the energy separation in a vortex tube. *Therm Sci* 16 (1):151–166

7. Lewins J, Bejan A (1999) Vortex tube optimization theory. *Energy* 24(11):931–943
8. Liu X, Liu Z (2014) Investigation of the energy separation effect and flow mechanism inside a vortex tube. *Appl Therm Eng* 67(1–2):494–506
9. Cengel YA (2003) *Heat transfer: a practical approach* (2nd ed). McGraw-Hill, p 23. ISBN 0072458933

Modeling and Simulation of the Load Governing System of Steam Turbine



Jagannath Hirkude, Sharven Kerkar, and Mrinal Borkar

Abstract The paper report describes the simulation of the load governing system of steam turbine. The turbine governing system is vital for the safety and availability of a power plant. It consists of a hydraulic governing in which there are servo valve components. The dynamic characteristics of this system are nonlinear and difficult to predict. The paper report presents mathematical modeling, parameter determination, model validation, simulation and optimization of control valve action of the high and intermediate pressure turbine, speeder gear and throttle governing. The model takes into account flow force effect such as spring rate, viscous damping coefficient and compressibility of oil. The proposed model is simulated using Simulink package in MATLAB. The system has been optimized by using MATLAB. The input parameters for the simulator are load reference, main steam pressure and temperature, condenser pressure, extraction temperatures and governing mode selection nozzle/throttle/hydraulic. The output of the simulation is actual load response, secondary oil pressure, control valve displacement, etc. Governing simulator is useful for better understanding of the governing system, and it can be used as a training simulator.

Keywords Steam turbine · Governing system · Simulation · MATLAB

1 Introduction

Any power-producing turbine generator set has to work in coordination with a grid. A generator delivers power to the grid, and the grid supplies it to an end user. As the generator is connected to a grid, the frequency of the generator has to be equal to

J. Hirkude (✉) · S. Kerkar
Goa College of Engineering, Goa 403401, India
e-mail: jbh@gec.ac.in

S. Kerkar
e-mail: sharven1998@gmail.com

M. Borkar
Padre Conceicao College of Engineering, Goa 403722, India
e-mail: mrinalvardeborkar@gmail.com

that of a grid. The frequency of a grid is controlled ideally by the user. Hence, a person operating a power plant has no control over the frequency. He can keep track of frequency and adjust other parameters for a trouble-free operation [1].

Steam turbine governing is the route of scheming the flow rate of steam to a steam turbine so as to achieve rotation speed constant. Load variation can have considerable impact on performance of steam turbine. In actual case, there always exists a considerable deviation from the desired performance of the turbine [2]. The flow rate of steam is monitored and controlled by interposing valves between the boiler and the turbine [3].

The turbine governor has to perform a basic function of running a turbine at a synchronous speed. In our Indian context, our system has a frequency of 50 Hz; hence, the governor has to keep a turbine speed near the 3000 rpm mark. The conventional governor can achieve this function. However, we have other parameters such as steam pressure and steam flow which has to be controlled. As any turbine speed varies, these parameters vary. Any variation in these parameters has a cascading effect over other equipment. The steady state of this equipment is disturbed. If steps are taken within certain time interval, then the equilibrium or the steady state can be restored. For taking these steps under various situations, one must first determine the behavior of a governor. Hence, one has to have predicted the performance of a governor under dynamic conditions. The grid frequency is an external parameter, but all other are internal parameters and are inter-related with each other. We cannot have a control over an external parameter. Hence, taking it as a variable, we have to relate it with the other parameters. Steady operation is important for an uninterrupted and reliable supply of the power. It is very critical in Indian scenario, as we are deficit in the power. Many of our villages are not yet electrified. The governor is a very critical system. It has a direct effect on the power generation. Proper operation of a governor is necessary for a reliable and a safe operation of any plant.

2 Modeling and Simulation

Governing system or governor is the main controller of the steam turbine. The governor varies the steam flow through the turbine to control its speed or power output. Generating unit speed and system frequency may be adjusted by the governor [4].

Objectives of this paper are

- (i) Modeling and simulation of mechanical hydraulic governing system.
 - (a) Starting device,
 - (b) Speeder gear,
 - (c) Auxiliary follow-up piston.

(ii) Modeling and simulation of control valve and throttle governing.

The turbine governor needs to perform several functions, which can be broadly classified as safety of plant operation, security of generation supply and flexibility of plant response. The function of the governing system is vital under start-up conditions, under emergency conditions and normal operation [5, 6]. The functions are

- (a) To trip turbine whenever turbine protections operate,
- (b) To control speed, load or pressure by regulating steam flow into turbine,
- (c) To avoid turbine over speed either during rolling up or load throw off,
- (d) Unloading in response to low inlet pressure, high back pressure.

To assist the user, we perform the simulation of the governing system How It Assists?

- a. By predicting the behavior of the system,
- b. By simulation fault location is easy [7].

2.1 Turbine Governing System

The turbine governing system used works on mechanical hydraulic control (MHC) [1]. The MHC comprises the starting device, speeder gear, hydraulic speed governor and hydraulic amplifier. The block diagrams of these components with their respective inputs and outputs are given in Fig. 1.

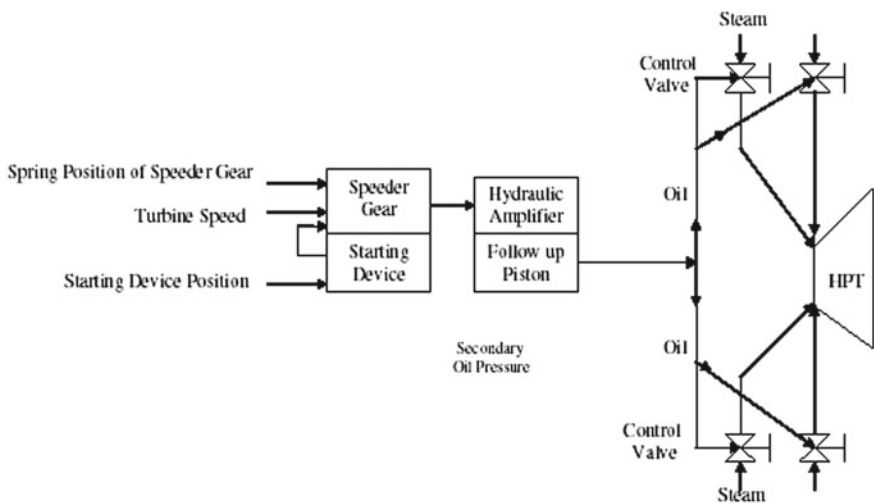


Fig. 1 Control mode selection and governing action

(i) Starting device

See Fig. 2.

(ii) Speeder gear and auxiliary follow-up piston valve

See Fig. 3.

(iii) Hydraulic amplifier and follow-up piston valve

See Fig. 4.

(iv) Control valve mechanism

See Fig. 5.

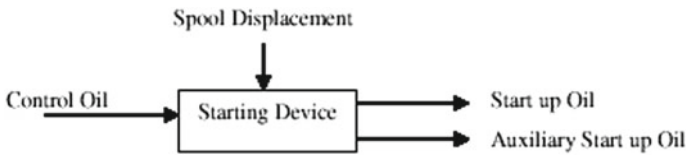


Fig. 2 Block diagram of starting device

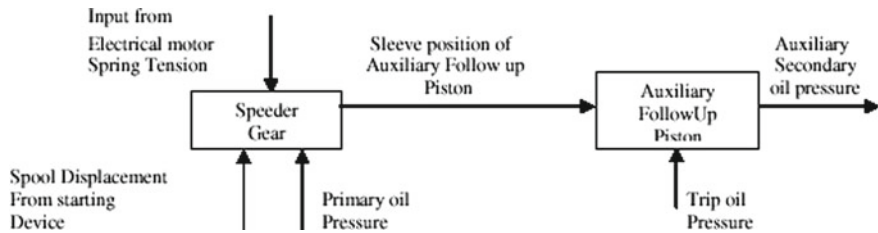


Fig. 3 Block diagram of speeder gear and auxiliary follow-up piston valve

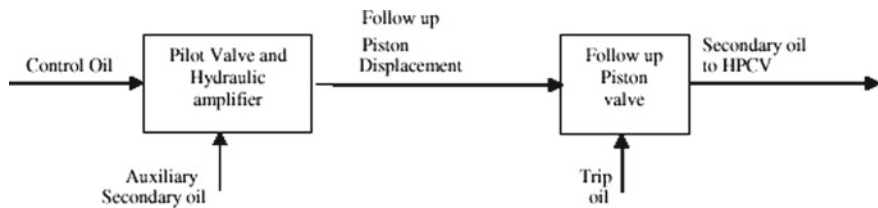


Fig. 4 Block diagram of hydraulic amplifier and follow-up piston valve

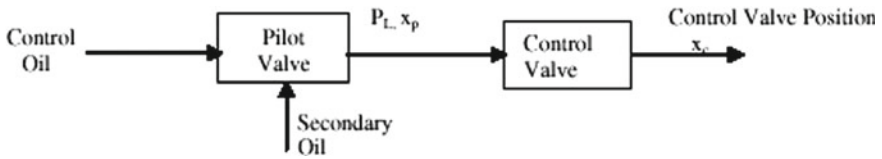
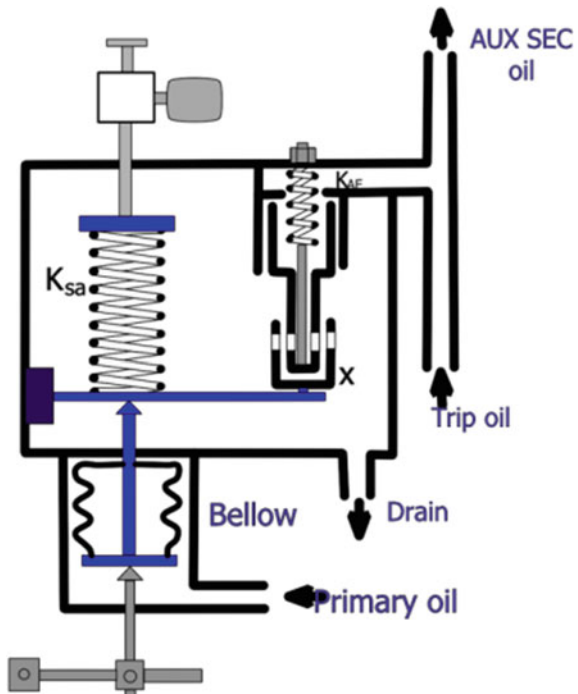


Fig. 5 Block diagram of control valve mechanism

2.2 Modeling and Simulation of Speeder Gear and Auxiliary Follow-up Piston

The speeder gear is an assembly of a bellow and spring, the tension of which can be adjusted by hand wheel or by electric motor. The bellow and spring is rigidly linked to the sleeves of auxiliary follow-up piston valves. The sleeve position changes with the equilibrium position of the bellow. Input to the speeder gear is given by electrical motor in the form of tensioning of spring. Thus, spring load and primary oil are acting on the speeder gear. Output of speeder gear is sleeve position of auxiliary follow-up piston. The data required for modeling of speeder gear is (i) spool position of starting device of speeder gear through lever linkage, (ii) spring load of speeder gear, (iii) primary oil pressure acting on bellow, (iv) input from electrical motor and (v) bellow properties (Fig. 6).

Fig. 6 Block diagram of speeder gear and follow-up piston



2.3 Modeling of Speeder Gear

The schematic of the speeder gear can be represented by Fig. 7.

The forces acting on the lever are.

F_1 = Spring force acting on the lever of speeder gear

$$F_1 = K_{SG} * y + F \tag{1}$$

K_{SG} = Speeder gear spring load, N/m,

y = Compression of spring in m,

F = Preload of speeder gear spring,

F_2 = Force acting on bellow due to primary oil pressure,

$$F_2 = P_p S_e \tag{2}$$

P_p = Primary oil pressure, bar _ N 2,

N = Turbine speed,

S_e = Effective surface of bellow,

F_3 = Force due to weight of sleeve of auxiliary follow-up piston acting on the lever,

$$X = \frac{F_3 l^3}{3EI} + \frac{(F_1 - F_2) C^3}{3EI} + \frac{(F_1 - F_2) C^3 (l - C)}{2EI} \tag{3}$$

X = Sleeve displacement, m,

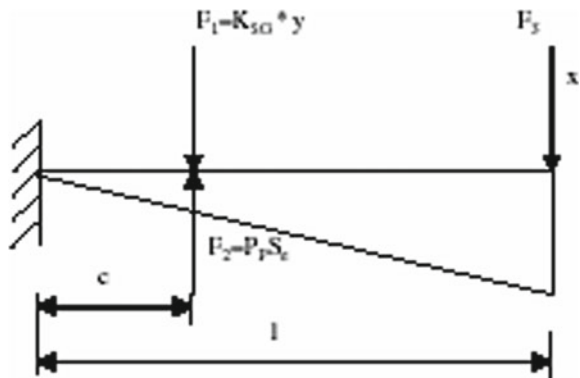
l = Lever length between cantilever fixed point and sleeve position,

C = Lever length between cantilever fixed point and speeder gear spring,

E = Modulus of elasticity of lever material of speeder gear, N/m²,

I = Moment of inertia of lever of speeder gear, m⁴.

Fig. 7 Block diagram of speeder gear



2.3.1 Modeling of Auxiliary Follow-up Piston

For auxiliary follow-up piston modeling, the following data is required

- (1) Trip oil pressure,
- (2) Auxiliary secondary oil pressure,
- (3) Sleeve position of auxiliary follow-up piston,
- (4) Drain oil pressure.

Equilibrium between tension spring and auxiliary secondary oil pressure is

$$K_{AF} * X = P'_d * A_{AF} \quad (4)$$

$$P'_d = \frac{K_{AF} * X}{A_{AF}} \quad (5)$$

where

P_d = Auxiliary secondary oil pressure,

K_{AF} = Spring gradient of auxiliary follow-up piston, N/m,

A_{AF} = Piston area of auxiliary follow-up piston, m^2 ,

X = Sleeve displacement, m.

Auxiliary secondary oil pressure is

$$P_d = P'_d + 2.3 \quad (6)$$

where 2.3 bar is auxiliary secondary oil pressure when the auxiliary follow-up displacement is at a maximum of 8.3 mm.

2.3.2 Modeling of Control Valve

Pilot valve:

Pilot valve is critical center spool valve. Assuming mass and spring load, force equation for pilot valve is,

$$\frac{M_p dx_p^2}{dt^2} + \frac{B_{pv} dx_p}{dt} + K_{pv} X_p + F_{pv} = PA_o \quad (7)$$

where

M_p = Mass of pilot valve, kg,

x_p = Pilot valve displacement, m,

B_{pv} = Viscous damping coefficient of pilot valve, Ns/m,

K_{pv} = Load spring gradient of pilot valve, N/m,
 p = Secondary oil pressure, bar,
 A_o = Area of piston on which secondary oil acts,
 F_{pv} = Preload on pilot valve, N.

Control valve:

The modeling of CV gives you the following equation:

$$X_C = \frac{\frac{K_q x_p}{A_c} - \frac{K_c F_p}{A_c^2}}{\frac{l S^3}{\omega_h^3} + \frac{2 \delta_h S^3}{\omega_h} \left(l + \frac{K_{cv}}{K_h} \right) S + \frac{K_c K_{cv}}{A_c}} \quad (8)$$

where

X_c = Control valve displacement, m,
 K_q = Flow gain, $m^3/s/m$,
 K_c = Flow pressure coefficient, $m^3/s/bar$,
 F_p = Preload on control valve, N,
 A_c = Piston area of control valve, m^2 ,
 ζ_h = Damping ratio,
 ω_h = Hydraulic natural frequency, rad/s,
 K_{cv} = Spring gradient of control valve, N/m,
 K_h = Hydraulic spring rate, N/m (Fig. 8).

2.4 Throttle Governing

In throttle governing, steam is delivered to the turbine through four control valves placed along the periphery at one end and at the same time. The steam flow rate is controlled by the degree of opening of the throttle valves. Hence, for a given load, all four valves open simultaneously. Analysis of nozzle box pressure for throttle governing: Let W be the steam flow rate through valve, P_1 the pressure before valve, P_0 the pressure after valve and v_1 the specific volume of steam before the control valve.

Total effective area of nozzle

$$A = DL \quad (9)$$

where D = Valve diameter,

L = Valve lift length,

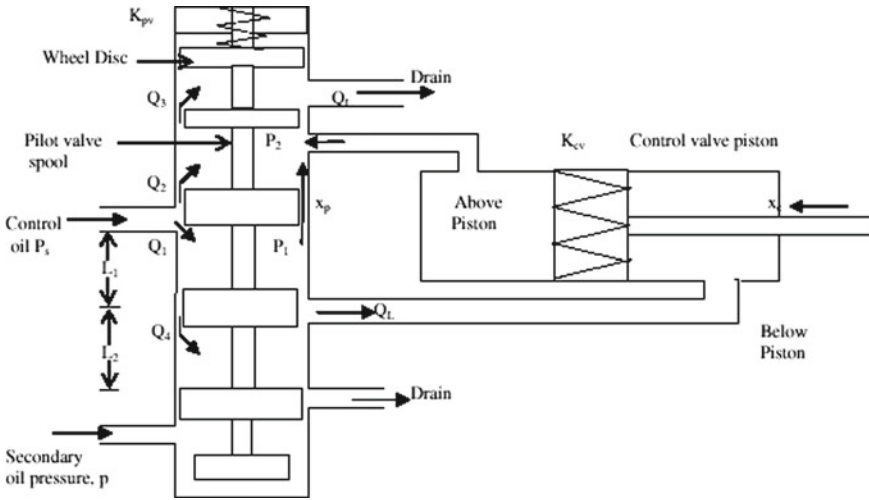


Fig. 8 Control valve mechanism showing details

$$W = CA\sqrt{\frac{P_1}{V_1}} \tag{10}$$

where C = Coefficient of discharge of superheated steam through throttle valve.

$$C = \sqrt{\frac{2g\eta m}{m-1} \left(r^{2/m} - r^{m+\frac{1}{m}} \right)} \tag{11}$$

where m = Adiabatic index,

η = Efficiency of valve.

Nozzle box pressure, i.e., pressure after control valve

$$P_0 = r * P_1 \tag{12}$$

3 Results

3.1 Speeder Gear and Auxiliary Follow-up Piston

The turbine has to be run on a speed of 3000 rpm. For this speed, the optimized value of the sleeve displacement has been found out for various values of speeder gear position. The speeder gear position is constrained to a maximum value if

32 mm. The final output is auxiliary secondary oil pressure. These optimized results were obtained using Simulink package in MATLAB and are shown in Fig. 9.

3.2 Control Valve

Using the optimum values of secondary oil pressure as input, the pilot valve displacement and control valve displacement values were obtained. The plotted results were calculated in MATLAB and are shown in Fig. 10.

3.3 Throttle Governing

The mathematical model of throttle governing has been used for finding the final nozzle box pressure for various values of steam flow rate. The results are given in Table 1.

The optimized results were obtained at the rated speed of 3000 rpm.

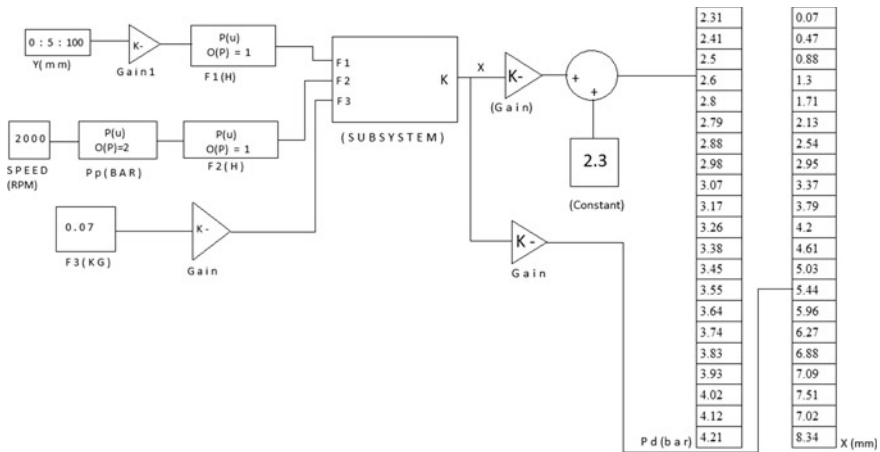


Fig. 9 Simulink model of speeder gear with optimized values of sleeve displacement and auxiliary secondary oil pressure

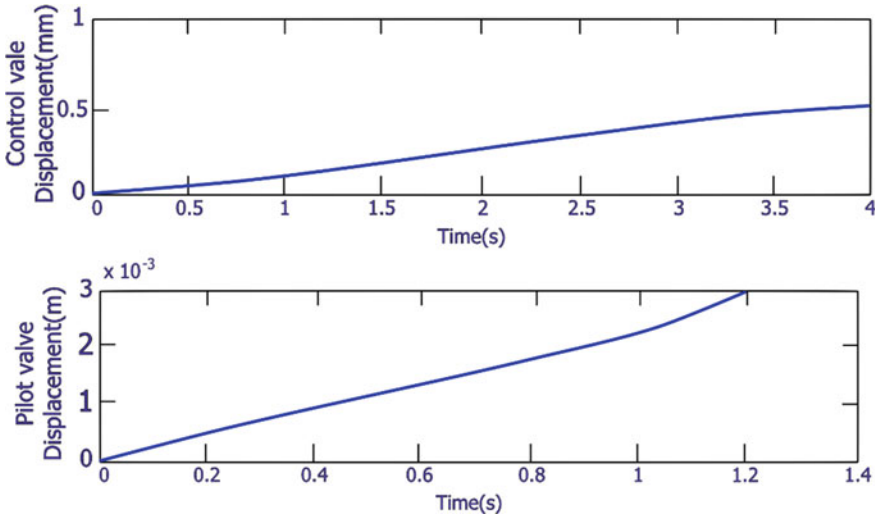


Fig. 10 Pilot valve and control valve displacement

Table 1 Throttle governing

Steam flow Kg/s	Value of coefficient C	Pressure ratio r	Nozzle box pressure P_o bar
54	0.2963	0.297	41.6
105	0.2963	0.603	70.37
145	0.2754	0.603	97.05
160	0.2488	0.693	109.73
170	0.2199	0.784	119.90
180	0.2055	0.856	123.71
185	0.1785	0.884	129.06
192	0.1690	0.922	130.46
195	0.1543	0.944	132.19
200	0.1473	0.949	132.87
204	0.1333	0.957	133.96
208	0.1308	0.958	134.13
210	0.1013	0.968	135.58
220	0.0992	0.969	135.65

4 Conclusion

1. For turbine speed of 3000 rpm, optimum values of sleeve displacement for various speeder gear positions in terms of auxiliary secondary oil pressure were obtained using Simulink package in MATLAB.

2. Using the optimum values of secondary oil pressure as input, the pilot valve displacement and control valve displacement values were obtained.
3. Finally, mathematical model of throttle governing has been applied for analyzing the final nozzle box pressure for various values of steam flow rate.
4. The output of the simulation is actual load response, secondary oil pressure and control valve displacement. Governing simulator is useful for better understanding of the governing system, and it can be used as a training simulator.

References

1. Singh KK, Agnihotri G (2001) Control system design through simulink®. In: System design through matlab®, Control toolbox and simulink®, pp 253–270. Springer, London
2. Jachens WB (1966) Steam turbines: their construction, selection and operation. In: Proceedings of the South African sugar technologists association
3. Rathore MM (2010) Thermal engineering. Tata McGraw-hill, p 739
4. Yahya SM (2010) Turbines, compressors and fans. Tata McGraw-hill, p 393
5. Sohl G, Bobrow JE (1999) Experiments and simulations on the non-linear control of a hydraulic servo system. *IEEE Trans Control Syst Technol* 7(2)
6. Meritt HE (1967) Hydraulic control systems. Wiley, New York
7. Shlyakhin P (2001) Steam turbines theory & design. Foreign Languages Publishing House, Moscow

Modeling and Optimization of Piezoelectric Energy Harvesting System Under Dynamic Loading



Mohit Yadav, Dinesh Yadav, Ramesh Kumar Garg,
Ravi Kant Gupta, Surendra Kumar, and Deepak Chhabra

Abstract In this work, energy is harvested from circular piezoelectric materials with different boundary conditions under dynamic loading. The output of the proposed system is investigated by connecting piezo with full wave bridge rectifier (FWBR) and voltage doubler (VD) circuits. The proposed setup can be used to apply dynamic load with varying magnitude. The boundaries of the circular piezoelectric material are 3D printed using Acrylonitrile butadiene styrene (ABS) material with FDM 3D printing machine to fabricate its simple support (SS), fixed support (FS) and circular support (CS). The proposed setup utilizes a stepper motor, a display unit, a load sensor, eccentric mechanism to convert rotary motion into reciprocating motion, power supply and a compatible circuit on the printed circuit board. It is observed experimentally that the energy harvested is maximum, in case of circular support among the three applied boundary conditions and validated mathematically. The output response of the circular support boundary condition is analyzed using various combinations of three input parameters, i.e., varying dynamic load, number of strokes, two circuits and a total number of 120

M. Yadav · S. Kumar

Department of Applied Sciences, Maharshi Dayanand University, Rohtak 124001, India
e-mail: mohitmathematics@gmail.com

S. Kumar

e-mail: skymathmdu@rediffmail.com

D. Yadav · R. K. Garg

Department of Mechanical Engineering, DCRUST, Murthal Sonipat 131039, India
e-mail: dineshkoslia91@gmail.com

R. K. Garg

e-mail: romeshkgarg@gmail.com

R. K. Gupta

Department of Mechanical Engineering, Manipal University Jaipur, Jaipur, India
e-mail: ravikant.gupta@jaipur.manipal.edu

D. Chhabra (✉)

Department of Mechanical Engineering, Maharshi Dayanand University, Rohtak 124001, India
e-mail: deepaknit10@gmail.com

experiments were performed. Artificial neural network has been applied for modeling and training between input three parameters and one output response, i.e., energy harvested. Further, genetic algorithm is applied on the ANN model to maximize the output of the system w.r.t input parameters and experimentally validated. As number of strokes (26) at dynamic load of 44 N with circular supported piezo patch connected with voltage doubler circuit gives the maximum output of 16.09 V further, when the system is tested on these parameters experimentally, it gives the 15.26 V.

Keywords Dynamic load · Experimental work · Mathematical modeling · Genetic algorithm · FDM 3D printer

1 Introduction

Energy harvesting is a phenomenon of conversion of available energy from surroundings into electricity with the help of transducers which can be reserved in storage devices for future purposes [1–4]. As a consequence of energy crises, the universe shifts from electrical appliances to electronic devices, it causes to a drastic reduction in consumption of electricity which gives birth to nano- and micro-low powered electronic circuits [5–7]. Various researchers have emphasized in the application of piezoelectric energy harvesting (PEH) as individual energy sources rather than saving electricity in batteries, due to the disadvantages of voltage drop in batteries [8, 9]. A dynamic load can be applied by various means like mechanical, hydraulic, and pneumatic for piezoelectric energy harvesting [10, 11]. Harvesting of energy using dynamic load from flowing of unsteady fluid with the help of piezoelectric material is also discussed [12–14]. The authors have applied hybrid optimization tools to optimize the process parameters and to maximize the output of the system [15–17]. The boundary conditions of piezoelectric material play a significant role in energy harvesting. And also, as the number of strokes/impact increases on the piezoelectric material, it will result into more power output up to certain limit. The power output is increased due to the connected circuit condensers, as it goes on storing the energy of the circuits. No work has been done by considering all above factors to maximize the piezoelectric energy harvesting. Therefore, in the present work, an experimental setup has been developed which can be utilized to apply dynamic load; various boundary conditions have been fabricated with FDM 3D printer, and connecting FWBR and VD circuits have also been taken into consideration to investigate the output of circular piezo patch. Mathematical modeling has been done to validate the experimental setup with circular boundary condition. Further, GA-ANN modeling has been done to find out the maximum output of the system w.r.t input parameters and experimentally validated.

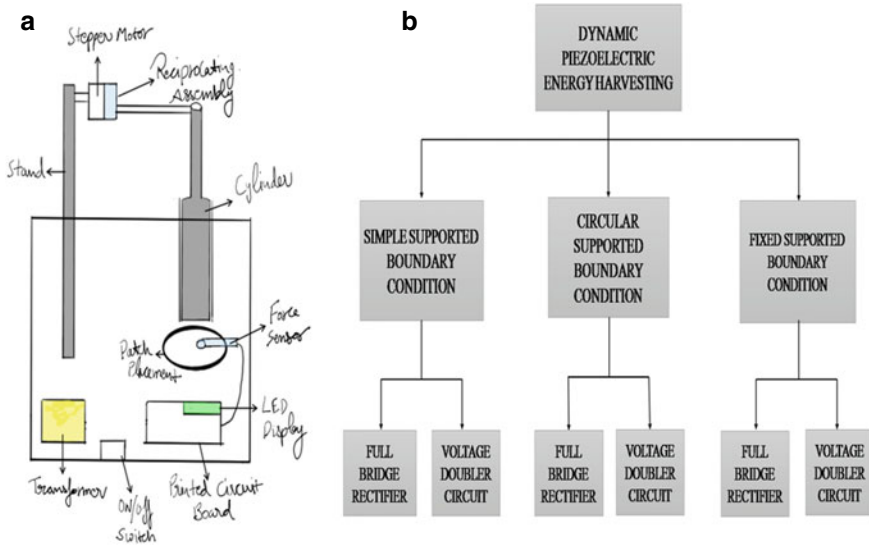


Fig. 1 a Constructional features of mechanism, b Boundary conditions for purposed setup

2 Proposed Setup

The proposed setup has been developed using a stepper motor, a display unit, a 9 V battery, a load sensor, an eccentric mechanism to convert rotary into reciprocating motion, power supply, and a compatible circuit on the printed circuit board as shown in Fig. 1a. The force sensor is mounted on the piezo patch, and its value is displayed on LCD panel, when it is hit by vertical reciprocating arm. The input force can be varied by maintaining the gap between piezo patch and vertical arm. The present setup has been investigated by using different supports and different circuits as shown in flow diagram [18–20]. The boundary supports for circular piezo patch have been fabricated using FDM [21] 3D printer as shown in Figs. 2, 3 and 4.

2.1 Mathematical Modeling of Proposed Setup

The present work consists of three basic phenomenons (1) the impact load on piezoelectric material with DC motor, (2) piezo electricity, and (3) piezo patch circuits connections [22, 23]. The force due to impact load on the piezo patch is calculated by below equation.

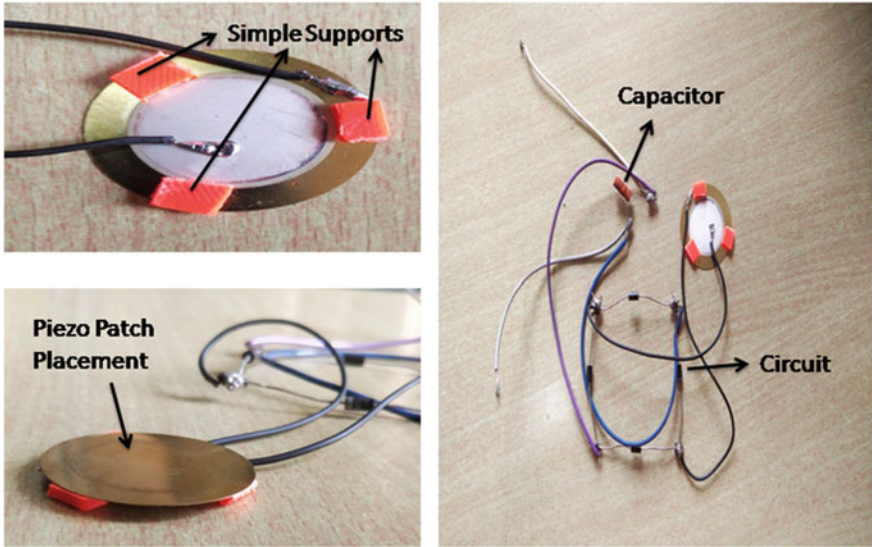


Fig. 2 Piezo patch with SS boundary condition

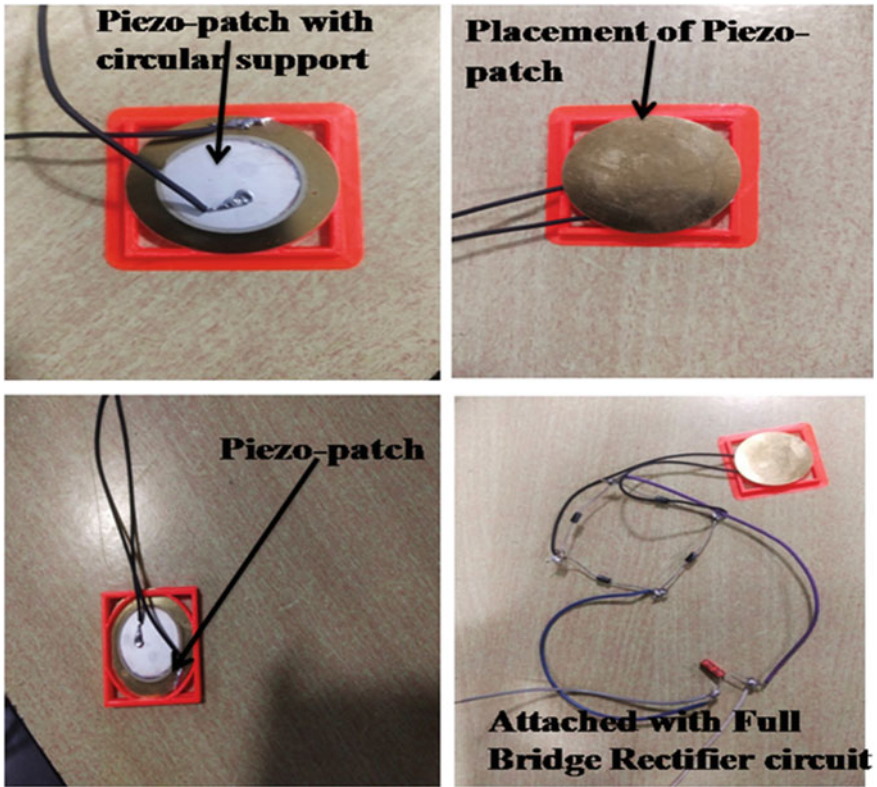


Fig. 3 Piezo patch with CS boundary condition

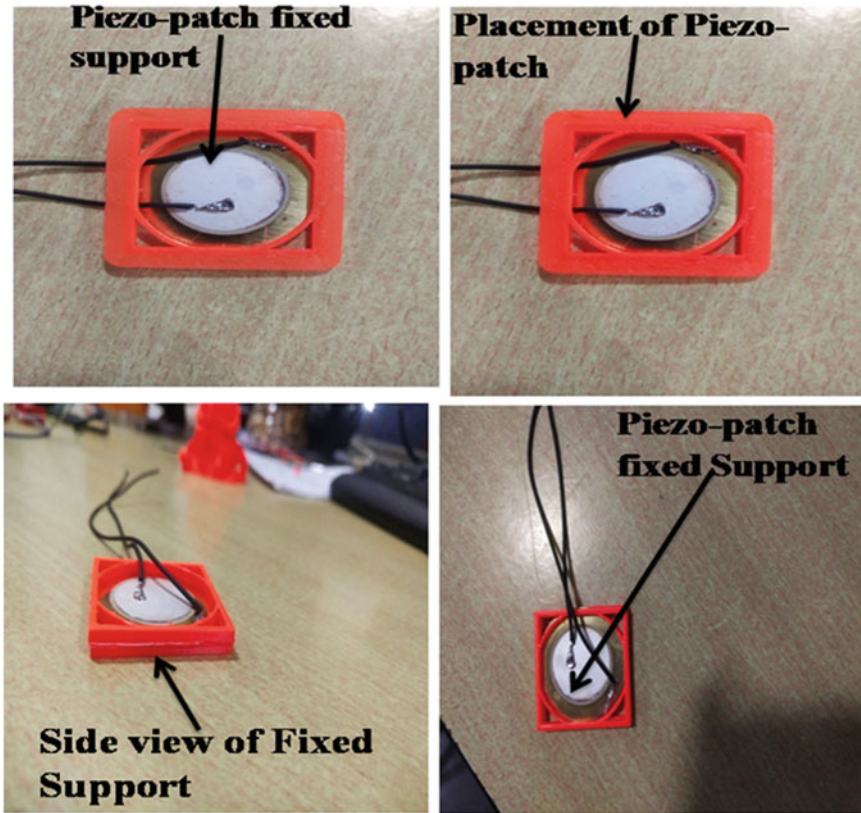


Fig. 4 Piezo patch with FS boundary condition

$$mu''(t) + \gamma u'(t) + ku(t) = F_0 \cos(\omega t) \tag{1}$$

where

- m mass of arm
- $u''(t)$ acceleration of arm
- $u'(t)$ velocity of arm
- $u(t)$ displacement of arm
- F_0 Force applied by arm
- ω angular velocity of arm
- γ damping coefficient
- k stiffness constant
- t time

It follows the basic piezo Electric equations.

$$D_E = e^E(S) + \epsilon^S(E) \quad (2)$$

where

- D_E Electric displacement vector
- e^E Piezoelectric constant matrix at electric field E
- S Constant mechanical strain
- ϵ^S Dielectric permittivity constant matrix
- E Electric field vector

As piezoelectric patch is connected with FWBR and VD circuits, the power output equation for both the circuits are discussed below [24–27].

$$P_{FWBR} = 4C_p V_r f_h (V_0 - V_r - 2V_d) \quad (3)$$

$$P_{VD} = C_p V_r f_h (2V_0 - V_r - 2V_d) \quad (4)$$

where

- C_p Piezoelectric plate capacitance,
- V_0 Open circuit output voltage
- f_h Frequency of excitation of system,
- V_d Voltage drop across the diode
- V_r Rectifier circuits output voltage

The output response voltage and the proposed model can be calculated by below equation [21, 28].

$$V_h = \frac{K_{33}F}{\epsilon D_p} \quad (5)$$

where

- F Force applied on the patch,
- D_p Diameter of patch,
- ϵ Dielectric permittivity,
- K_{33} Electromechanical coupling coefficients,
- V_h Harvested Voltage.

3 Optimization of the Input Parameters to Maximize Response Voltage Using GA-ANN

The load applied, placement of patch under different boundary conditions, and the numbers of strokes are the three input parameters which are used to measure the output of the system. Experimental results obtained for inputs and outputs are

trained, tested, and validated with the help of ANN and further optimized with GA-ANN in MATLAB R2016a.

3.1 Designing of ANN Model with Experimental Data

ANN is a hybrid statistical tool that includes a assigned weight for paths inter connection of inputs to the neurons and then outputs alters constantly unless specific design is predicts efficiently to yield energy consequences. The data interpretation streaming includes a variety of phases as matrices for input-output should be loading, choosing the proportion of division of data among training, validation, testing, and judging mysterious layers neurology and finally selecting a most suitable algorithm for data's training tracked by saving regression-performance consequences. Subsequently the variation in designing, correlation between dataset and mean square error are observed from the ANN model. The proposed algorithm optimise the output by analyzing the all the effective factors.

3.2 Designing of GA-ANN Model with Experimental Data

An evolutionary GA-ANN model has been designed to optimize the process parameters for obtaining highest voltage by using integration of one technique ANN into another technique GA as a fitness function. The population of individual solutions has been successively modified by GA. Since, it is an evolutionary technique, so the parents of present population has been used for generating offspring of the coming generation. After some iteration, the optimized result has been achieved by the population. The lower bound and upper bound of process parameters have been provided in the GA-ANN model along with objective function.

4 Result and Discussion

4.1 Experimental Result Interpretations

Output response voltage obtained from piezo patch with two different circuits due to application of periodic dynamic load with different boundary conditions, i.e., SS, CS, and FS with 30 strokes.

SS Boundary Condition: The Fig. 2 shows the piezo patch with SS boundary condition, in which FDM 3D printer fabricated three supports are provided to the piezo patch on its edges at an angle of 120° each. Both the FWBR and VD circuits are utilized to generate the voltage at these boundary conditions for two loads, i.e., 36 N and 44 N respectively.

CS Boundary Condition: The Fig. 3 shows the piezo patch with CS boundary condition, in which FDM 3D printer fabricated circular support with 35 mm diameter, is attached to the piezo patch on back side of surface of piezo patch. Both the FWBR and VD circuits are utilized to generate the voltage at CB condition for two loads, i.e., 36 N and 44 N respectively.

FS Boundary Condition: The Fig. 4 shows the piezo patch with the FS boundary condition, in which FDM 3D printer fabricated base support with 40 mm diameter, is attached to the piezo patch on the back side of surface of the piezo patch. Both the FWBR and VD circuits are utilized to generate the voltage at CS boundary condition for two loads, i.e., 36 N and 44 N respectively.

4.2 Experimental Result Evaluation with Full FWBR Circuit

In case of FS boundary condition, the output voltage increases w.r.t. number of strokes. The test is performed on two load values, i.e., 36 and 44 N. As the load increases from 36 to 44 N, the generated voltage is also increase, but in a small proportional. The output can be investigated from the graph as shown in Figs. 5 and 6. The maximum voltage generated by FS piezo patch is 4.55 V at 44 N dynamic loads at 30th stroke as illustrated in Fig. 6.

In case of SS boundary condition, the output voltage increases w.r.t. number of strokes. The test is performed on two load values, i.e., 36 and 44 N. As the load increases from 36 to 44 N, the generated voltage is also increasing. The maximum voltage is generated at 30th stroke in both the cases, but there is a huge difference of 3.05 V in both the generated voltage. A maximum of 5.01 V can be generated at 36 N loads at 30th stroke and an 8.15 V at 44 N. The data can also be analyzed from the graph as shown in Figs. 5 and 6. The maximum voltage generated by simply supported piezo patch is 8.15 V at 44 N dynamic loads at a 30th stroke as illustrated in Fig. 6.

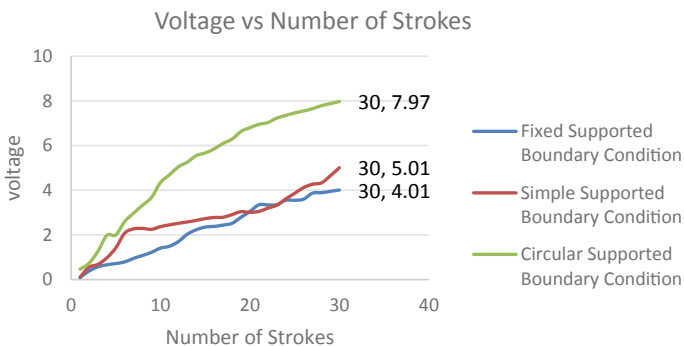


Fig. 5 Variation of voltage with respect to the number of stroke at all boundary conditions with FWBR circuit at 36 N load

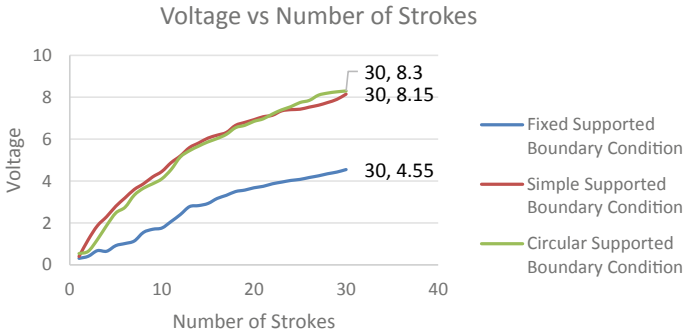


Fig. 6 Variation of voltage with respect to the number of stroke at all boundary conditions with FWBR circuit at 44 N

In case of CS boundary condition, the output voltage increases w.r.t. number of strokes. The test is performed on two load values, i.e., 36 and 44 N. As the load increases from 36 to 44 N, the generated voltage is also increasing. The maximum voltage is generated at 30th stroke in both the cases, but there is a very small difference of 0.33 V in both the generated voltage at 36 and 44 N. A maximum of 7.97 V can be generated at 36 N loads at 30th stroke and 8.30 V at 44 N. The data can also be analyzed from the graph as shown in Figs. 5 and 6. The maximum voltage generated by circular supported piezo patch is 8.30 V at 44 N dynamic loads at 30th stroke as illustrated in Fig. 6 among all boundary conditions.

4.3 Experimental Result Evaluation with VD Circuit

In case of FS boundary condition, the output voltage increases w.r.t. number of strokes up to the 22nd stroke for 36 N and 44 N, respectively. At 22nd stroke, the system produced maximum voltage of 4.25 V corresponding to a load value of 36 N. When we increase the load value to 44 N, voltage increases with a very high rate and at 30th stroke we got the maximum value 9.08 V. The output can be investigated from the graph as shown in Figs. 7 and 8. The maximum voltage generated by FS piezo patch is 9.08 V at 44 N dynamic loads at a 30th stroke as illustrated in Fig. 8.

In case of SS boundary condition, the output voltage increases w.r.t. number of strokes. The test is performed on two load values, i.e., 36 and 44 N. As the load increases from 36 to 44 N, the generated voltage is also increasing. The maximum voltage is generated at 30th stroke in both the cases, but there is a small difference of 1.04 V in both the generated voltage. A maximum of 5.22 V can be generated at 36 N loads at 30th stroke and a 6.70 V at 44 N. The data can also be analyzed from the graph as shown in Figs. 7 and 8. The maximum voltage generated by simple supported piezo patch is 6.70 V at 44 N dynamic loads at a 30th stroke as illustrated in Fig. 8.

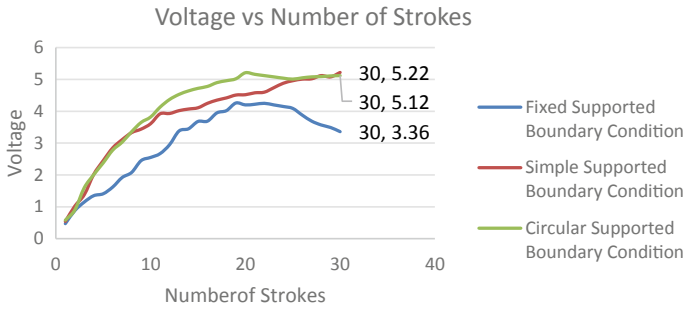


Fig. 7 Variation of voltage with respect to the number of stroke at all boundary conditions using VD circuit at load 36 N

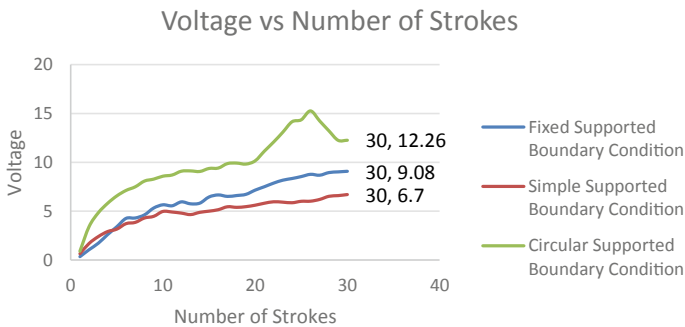


Fig. 8 Variation of voltage with respect to the number of stroke at all boundary conditions using VD circuit at 44 N load

In case of CS boundary condition, the output voltage increases w.r.t. number of strokes. The test is performed on two load values, i.e., 36 and 44 N. As the load increases from 36 to 44 N, the generated voltage is also increasing. The voltage increases up to 20th stroke at a load of 36 N and attained maximum 5.21 V, as we increase the load from 36 N to 44 N, the system attained maximum voltage 15.26 V at 26th stroke and after that voltage start decreasing. The data can also be analyzed from the graph as shown in Figs. 7 and 8. The maximum voltage generated by CS piezo patch is 15.26 V at 44 N dynamic loads at 26th stroke as illustrated in Fig. 8 among all boundary conditions.

It is observed that circular piezo patch with purposed setup produce maximum voltage 15.26 V with circular supported boundary condition and voltage doubler circuit. It is observed that the voltage value increasing up to a certain number of strokes after that it start decreasing.

4.4 ANN Result Interpretation

Training and testing of ANN model with experimental statistics: The input and output data have been utilized for training and testing of the ANN. Output voltage is observed in correspondence to each set of input data. With the help of learning functions (`trainlm`) and sequential order increment, training is executed. Testing yield an autonomous standard of model performance and causes no dependency on training. Repetitions of training algorithm are carried out since it takes different data of each interaction of neurons for each run. While running the training algorithm, corresponding to each run diverse value of correlation coefficient (R) has been obtained.

The value of correlation coefficient 'R' represents the relationship between output values and the value which is illustrated in Fig. 9. The value of 'R' is near to 1 signifies that close relationship and prediction accuracy of network and value of 'R' near to 0 signifies the random relationship. The value of R is 0.9963 which is observed in regression plot as depicted in Fig. 9. The obtained result has been further used in the genetic algorithm for optimizing the parameters [29].

The response output voltage has been compared experimentally and mathematically to validate the present work as shown in Table 1. The voltage generated at first stroke has been considered for validation, when the patch has circular support and connected with a FWBR circuit. From the Table 1, it is observed that the mathematical model and experimental results are good in agreements.

5 Optimization of Output Response Voltage Using GA-ANN Hybrid Algorithm

Genetic algorithm is heuristic approach which generates the random chromosome length according to input factors range and evaluates the fitness function. Crossover and mutation function produce the new child chromosome from the parent chromosome. In the present work, ANN model has been fed into the genetic algorithm as a fitness function, and ANN model has been trained using the data. The tangent sigmoid activation function with feed forward back propagation network has been created. 70% sample has been used for training, 15% sample for testing and 15% sample for cross-validation. The training between input and output data has been tried with various training algorithms like Levenberg-Marquardt back propagation, Resilient back propagation, Scaled Conjugate Gradient, etc., and best value of R is obtained with 0.99638 using Levenberg-Marquardt back propagation as shown in Fig. 9. This trained model of ANN has been fed as objective function into the genetic algorithm to form hybrid GA-ANN. GA-ANN further maximizes the output response up to 16.099 V, resulted on new input parameters, and its convergence is shown in Fig. 10. The new factors have been tested experimentally also that generates the output of 15.26 V and shows the 5.15% error.

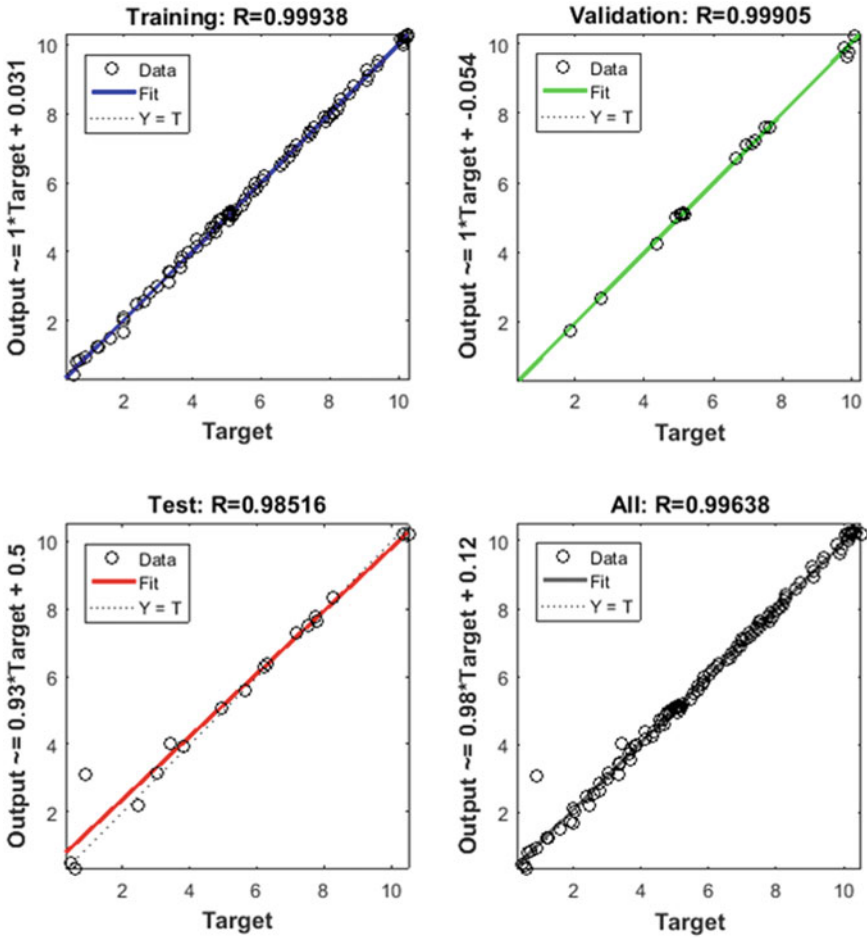


Fig. 9 Correlation plot between outputs and targets fitting results for training and optimization in ANN

6 Conclusions

The experimental setup of energy harvesting using PZT materials under dynamic loading with three boundary conditions and investigation with two circuits, i.e., FWBR and VD has been successfully developed. The following results have been concluded during piezoelectric energy harvesting.

1. It is also observed that in circular boundary condition, output response voltage increases more rapidly with the number of strokes in full wave bridge rectifier and voltage doubler circuitry systems.

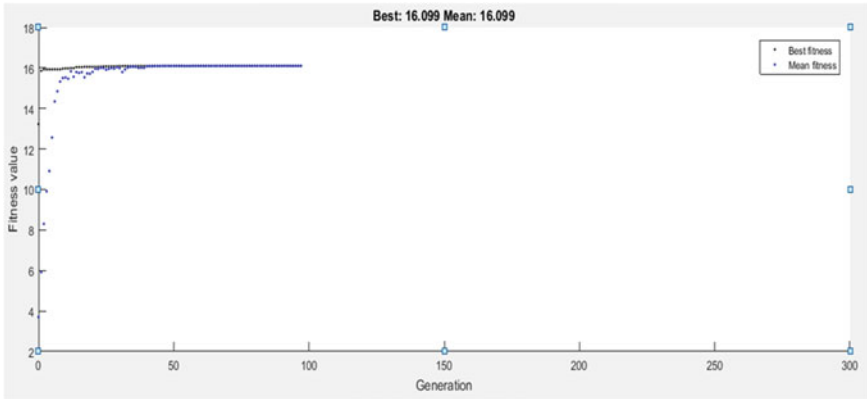


Fig. 10 Convergence of GA-ANN for best fitness

Table 1 Output voltage response

Sr. No.	Boundary conditions	No. of strokes	Load applied	Experimental output voltage	Mathematical output voltage	Percentage error
1	Circular supported with FWBR circuit at 36 N	1	36	0.47	0.4824	2.63
2	Circular supported with FWBR circuit at load 44 N	1	44	0.57	0.5896	3.43

2. The proposed setup is validated using mathematical modeling which shows a 3.43 percentage error.
3. Artificial neural network has been applied for modeling and training between three input parameters and one output response, i.e., energy harvested.
4. Further, GA-ANN is applied on the experimental data which results in optimized input parameters as number of strokes (26) at dynamic load of 44 N with circular supported piezo patch connected with voltage doubler circuit gives the maximum output of 16.09 V.
5. When the system is tested on these parameters experimentally, it gives the 15.26 V which result in 5.15% error.

References

1. Gaudenzi P (2009) Smart structures: physical behaviour, mathematical modelling and applications. *J VibAcoust*
2. Srinivasan AV, McFarland DM (2001) Smart structures, analysis and design 105(1050):458
3. Martinez T, Pillonnet G, Costa FA (2017) 15-mV inductor-less start-up converter using a piezoelectric transformer for energy harvesting applications. *IEEE Trans Power Electron* 33(3):2241–2253
4. Siddiqui S, Lee HB, Kim DI, Duy LT, Hanif Lee NE (2018) An omni directionally stretchable piezoelectric nanogenerator based on hybrid nanofibers and carbon electrodes for multimodal straining and human kinematics energy harvesting. *Adv Energy Mater* 8(2):1701520
5. Xu S, Shi Y, Kim SG (2006) Fabrication and mechanical property of nano piezoelectric fibres. *Nanotechnology* 17(17):4497
6. Zhao T, Fu Y, He H, Dong C, Zhang L, Zeng H, Xing L, Xue X (2018) Self-powered gustation electronic skin for mimicking taste buds based on piezoelectric enzymatic reaction coupling process. *Nanotechnology* 29(7):07550
7. Jin W, Wang Z, Huang H, Hu X, He Y, Li M, Li L, Gao Y, Hu Y, Gu H (2018) High-performance piezoelectric energy harvesting of vertically aligned Pb (Zr, Ti)O₃ nanorod arrays. *RSC Adv* 8(14):7422–7427
8. Anton SR, Sodano HA (2007) A review of power harvesting using piezoelectric materials (2003–2006). *Smart Mater Structures* 16(3)
9. Kim HS, Kim JH, Kim J (2011) A review of piezoelectric energy harvesting based on vibration. *Int J Precision Eng Manuf* 12(6):1129–1141
10. Yadav M (2020) A review on piezoelectric energy harvesting systems based on different mechanical structures. *Int J Enhanced Res Sci Technol Eng* 9(1):1–7
11. Kim H, Tadesse Y, Priya S (2009) Piezoelectric energy harvesting. In *Energy Harvesting Technologies*. 3–39, Springer, Boston, MA.
12. Akaydin HD, Elvin N, Andreopoulos Y (2010) Energy harvesting from highly unsteady fluid flows using piezoelectric materials. *J Intell Mater Syst Struct* 21(13):1263–1278
13. Yadav D, Yadav J, Vashistha R, Goyal DP, Chhabra D (2019) Modeling and simulation of an open channel PEHF system for efficient PVDF energy harvesting. *Mech Adv Mater Struct* 1–15
14. Yadav J, Yadav D, Vashistha R, Goyal DP, Chhabra D (2019) Green energy generation through PEHF—a blueprint of alternate energy harvesting. *Int J Green Energy* 16(3):242–255
15. Kumar V, Chhabra D, Shukla P (2017) Xylanase production from *Thermomyces lanuginosus* VAPS-24 using low cost agro-industrial residues via hybrid optimization tools and its potential use for saccharification. *Biores Technol* 243:1009–1019
16. Kumar V, Kumar A, Chhabra D, Shukla P (2019) Improved biobleaching of mixed hardwood pulp and process optimization using novel GA-ANN and GA-ANFIS hybrid statistical tools. *Biores Technol* 271:274–282
17. Dhankhar R, Kumar A, Kumar S, Chhabra D, Shukla P, Gulati P (2019) Multilevel algorithm and evolutionary hybrid tools for enhanced production of arginine deiminase from *Pseudomonas furukawaii* RS3. *Biores Technol* 290:121789
18. Yadav M, Yadav D (2019) Micro energy generation in different kinds of water flows on lead zirconium titanite/PVDF. *Int J R&D Eng Sci Manage* 9(5):1–8
19. Yadav M, Yadav D, Kumar S, Garg RK, Chhabra D (2019) Experimental and mathematical modeling and analysis of piezoelectric energy harvesting with dynamic periodic loading. *Int J Recent Technol Eng* 8(3):6346–6350
20. Yadav J, Yadav D (2017) Design of an open channel fluid flow system for piezoelectric energy harvesting. *Int J Latest Trends Eng Technol* 8(4–1):244–249
21. Deswal S, Narang R, Chhabra D (2019) Modeling and parametric optimization of FDM 3D printing process using hybrid techniques for enhancing dimensional preciseness. *Int J Interact Des Manuf* 13:1–18

22. Benjeddou A (2004) Modeling and simulation of adaptive structures and composites: current trends and future directions. *Prog Comput Struct Technol* 251–80
23. Hong SR, Choi SB, Choi YT, Wereley NM (2005) A hydro-mechanical model for hysteretic damping force prediction of ER damper: experimental verification. *J Sound Vib* 285(4–5):1180–1188
24. Junior CD, Erturk A, Inman DJ (2009) An electromechanical finite element model for piezoelectric energy harvester plates. *J Sound Vib* 327:9–25
25. Kim HS, Kim JH, Kim J (2011) A review of piezoelectric energy harvesting based on vibration. *Int J Precis Eng Manuf* 12(6):1129–1141
26. Le TT, Han J, Jouanne AV, Mayaram K, Fiez TS (2006) Piezoelectric micro-power generation interface circuits. *IEEE J Solid-State Circuits* 41(6):1411–20
27. Mehta VK, Mehta R. *Principles of electronics*. S. Chand & Co. Ltd., India
28. Dineva P, Gross D, Müller R, Rangelov T (2014) Dynamic fracture of piezoelectric materials. *AMC* 10:12
29. Chhabra D, Bhushan G, Chandna P (2014) Multilevel optimization for the placement of piezo-actuators on plate structures for active vibration control using modified heuristic genetic algorithm. *Ind Commercial Appl Smart Struct Technol* 9059:90590

Improving Physio-Chemical Properties of Biodiesel by Using Blending



Gaurav Pathak and S. Kennedy

Abstract With the constant increase in the demand for alternative sources of power and the fuel, reserves are now in virtue of near depletion (Thapa et al. in *Environmental Technology and Innovation* 9:210–219 [1]). Experiments have been carried out to find alternative fuels with improved physio-chemical properties in order to meet the demands of the era. In this paper, the seeds of jatropha and mahua plants are used to create a biodiesel fuel using the transesterification process. Parameters such as kinematic viscosity, specific gravity, flash point, fire point, acid value, density, pour point and cloud point are obtained by through the experimental method. Improvements are seen in the physicochemical properties of jatropha oil with the use of blends. The yield of 440 ml (i.e. 88%) was obtained in this experimental investigation. Also, biodiesel was extracted from raw jatropha oil and mahua oil using a two-step transesterification process and by using potassium hydroxide as a base catalyst. The free fatty acid content for the jatropha oil was found to be 4.084% which reduced to 0.422% by the addition of 5% of concentrated sulphuric acid that resulted in acid esterification of the oil. The acid value for jatropha oil that was 8.12 was reduced to 0.84, and in the case of mahua oil, acid value that was 26.6 was reduced to 0.448. The kinematic viscosity of jatropha oil which lies between 50 and 55 cst was reduced to 5.78 centistokes (CST). The blended fuels have depicted some marvellous properties as compared to the individual biodiesel.

Keywords Biodiesel · Blends · Cloud point · Fire point · Kinematic viscosity · Transesterification

G. Pathak (✉)

Automobile Engineering, Galgotias University, Greater Noida, India

e-mail: pgaurav832@gmail.com

S. Kennedy

Mechanical Engineering, Galgotias University, Greater Noida, India

e-mail: edysar@gmail.com

© The Author(s), under exclusive license to Springer Nature Singapore Pte Ltd. 2021

B. S. Sikarwar et al. (eds.), *Advances in Fluid and Thermal Engineering*,

Lecture Notes in Mechanical Engineering,

https://doi.org/10.1007/978-981-16-0159-0_31

1 Introduction

Industrial technology is advanced so much in recent years that the world is getting close to the depletion of our reserved fossil fuels [2]. With increasing demands of eco-friendly fuel, biodiesel is one of the best choices available to us. These fuels are non-pollutant and non-toxic in nature. These fuels can be made with vegetable oils like soya bean oil, palm oil, corn oil, etc. [3]. Diesel engines can be operated with pure biodiesels and their blends [4]. Biodiesel which is easily formed with cheaper raw materials such as non-edible vegetable oil, jatropha oil and mahua oil is used for the production of biodiesel and jatropha oil. These are one of the best options available for making biodiesel, as the properties of this oil are nearly identical to those of mineral diesel and can be used as an alternative fuel with some modifications [5]. Biodiesel is a more preferable choice over conventional fuels because of its significant properties and fewer emissions to the environment [6]. As biodiesel is a biodegradable fuel, it is more environmentally friendly, and on burning, it produces less toxic products compared to a mineral diesel [7]. Biodiesel with high flash point makes it easily transported as well as less volatile [8]. It has a significant increase of its lubrication properties as being the mixture of two vegetable oils proclaiming its effects on the engine performance and working of its moving parts with less wear and tear [9].

Jatropha plant is used for making biodiesel through transesterification process. It belongs to the euphorbiaceous family which also had 175 other species in it, and this species of plant is more than almost 60 million years old. These plants are said to be originated from Central America and the southern parts of South America. Now, these jatropha can also be found in south-east Asia, Indian subcontinents, Africa and some countries with sub-Sahara [10]. Jatropha plant is said to be like a shrub which is approximately 6 m in height, but in some countries, such as South America, these are said to have 12 m of height, and these plants have a lifespan of approximately 50 years and are also categorized as the monoecious plant, i.e. these plants have male and female reproductive organs. The seeds of these plants are of length ranging between 2.5 to 3 cm, and these seeds are used for taking out the jatropha oil [11]. As the jatropha has great adaptability to suit itself according to different climatic conditions, it can be grown anywhere like soil with low-fertility, high-fertility areas, stony regions, shallow and dry regions, and these plants can absorb the nutrition from the soil very effectively no matter the state of the soil.

Mahua is a rapid growing tree that can reach up to the height of 20 m to be exact with a life span of 60 years; it can be found in central and north Indian plains and forests. It is a tree that is well suited to arid environments being a prominent tree in tropical mixed deciduous forests of India. These trees can be found in Chhattisgarh, Uttar Pradesh, Bihar, Maharashtra, etc.

Blends of biodiesel have significant advantages over diesel fuel such as higher lubrication content, biodegradable, non-toxic in nature, less harmful to human health and are much more affordable.

Blends of biodiesel have significant advantages over pure biodiesel such as lower viscosity, improved lubrication, low wax formation temperatures and low ignition point.

2 Experimental Procedure

See the Fig. 1.

2.1 Parameters

The sample was initially heated, and the temperature was maintained (70–90 °C). The sample was prepared under normal atmospheric temperature with 500 ml of jatropha oil and 350 ml of mahua oil; 5 ml of sulphuric acid was taken. For obtaining a methoxide solution, use 150 ml of methanol. 5 gm of potassium hydroxide was taken.

SAMPLES

B10 = (5% of jatropha oil + 5% of mahua oil + 90% mineral diesel)

B20 = (10% of jatropha oil + 10% of mahua oil + 80% mineral diesel)

B30 = (15% of jatropha oil + 15% of mahua oil + 70% mineral diesel)

Jatropha biodiesel

Mahua biodiesel

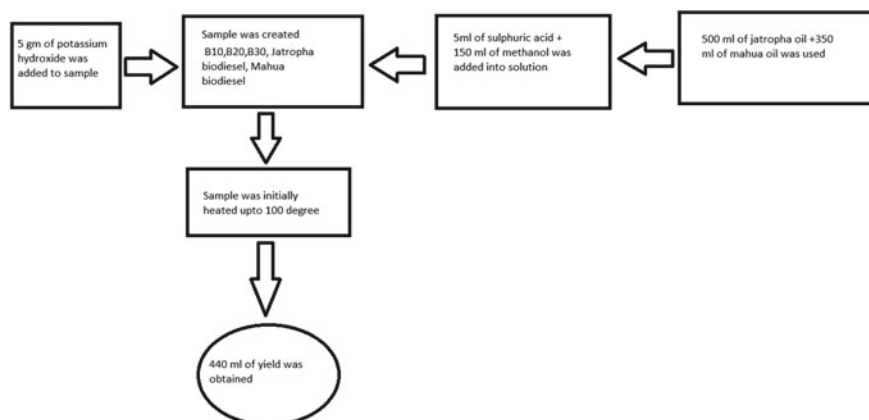


Fig. 1 Schematic diagram

Kinematic viscosity can be calculated by the following formula:

$$\text{Kinematic viscosity} = (At) - b/t \quad (1)$$

where A and B are instrument constants.

The sample was tested under atmospheric pressure. Kinematic viscosity was measured in centistokes (CST) at 40 °C.

Temperature is measured with the help of Redwood Viscometer. Similarly, all other physio-chemical properties such as specific gravity, density, flash point, cloud point, pour point, free fatty acid concentration and fire point were experimentally determined and using a standard formula.

$$\text{Specific gravity} = (\text{weight of the sample} - \text{weight of the bottle}) / \text{Volume of the sample} \quad (2)$$

$$\text{Density} = \text{Specific gravity of sample} * \text{Density of water} \quad (3)$$

Pensky Martin apparatus was used for obtaining the flash and fire point for different samples and the observations obtained under normal atmospheric pressure with 50% input voltage being used for the experimentation, while cloud point and pour point were observed with the help of the cloud and pour point testing apparatus with 50 ml of samples tested under normal atmospheric pressure. For obtaining the values of FFA, 10 ml of the sample was mixed with 50 ml of absolute ethanol which was heated up to 70 °C under normal atmospheric pressure; then, three drops of phenolphthalein were added to the mixture, and KOH of 0.1 normality was taken for titration. FFA content was found with the help of litmus titration.

3 Results and Discussions

From the experiments and formulas, the physio-chemical values were obtained for the blends, and during the comparison with normal biodiesels, it is found that the blends of two biodiesels have significantly affected the physio-chemical properties of the biodiesel.

3.1 *Effect of Kinematic Viscosity (CST) at 40 °C on Engine Performance*

Biodiesels are much more viscous (thicker) than the normal gasoline and having 10% lower power content than that of petroleum biodiesel. Biodiesel can replace the compression ignition in diesel engines without changing engine structure, and

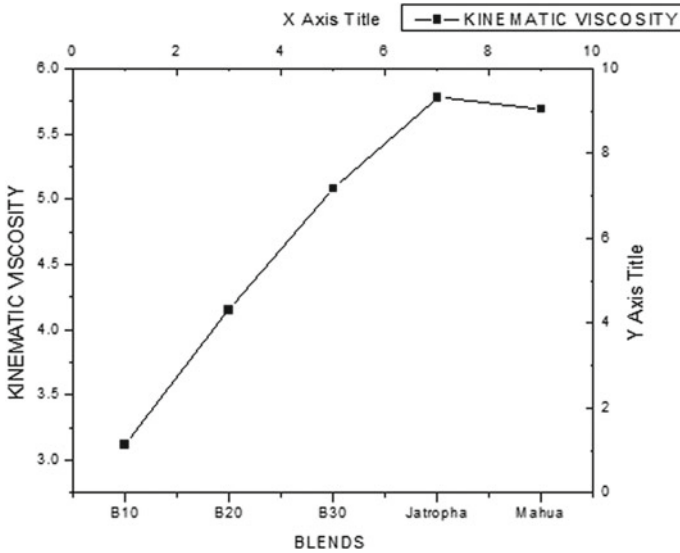


Fig. 2 Kinematic viscosity for blends

the kinematic viscosity of biodiesel was higher which causes engine problems such as sludge formation due to insufficient fuel for atomization and incomplete combustion. Lowering the viscosity of the fuel blending procedure was used in order to lower the viscosity of the fluid. Upon comparison of the results, the blending procedure on biodiesel has significantly changed the viscosity of fuels as B10 with the lowest viscosity of 3.12 CST and jatropa biodiesel with 5.8 CST; here, the kinematic viscosity of jatropa that lies between 50 and 55 CST was reduced to 5.8 CST. The lower viscosity of fuel helps in the proper flow of fuel and improves the start and lowers the wear and tear of the moving parts. Therefore, on the basis of the above comparison, B30 blend is an adequate choice (Fig. 2).

3.2 Effect of Density on Engine Performance

The density of fuel affects the engine power, and the performance characteristics of fuel with higher density of fuels may result in higher emissions of carbon particles, but with the use of blending, the value of density obtained in Fig. 3 of biodiesels from 0.88 to 0.84 for the B10 blend as particle pollution (PP) emissions increases with the rise in fuel density; therefore, the value obtained upon comparison of the blends the B30 was found effective as it has requirements that can help in the proper functioning of the engine as it has relatively power output similar to diesel engines and produces less emissions.

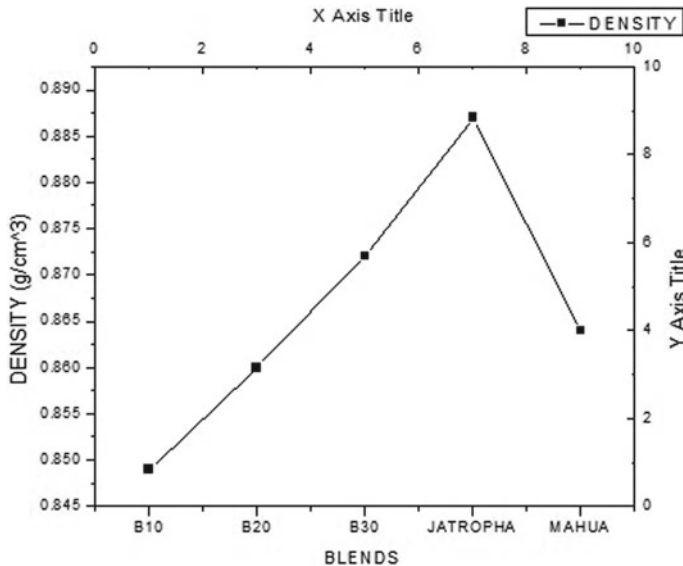


Fig. 3 Density of samples

3.3 Effect of Specific Gravity on Engine Performance

The specific gravity of the fuels affects the fuel consumption characteristics; specific gravity generally depends upon the free fatty acid content, as specific gravity of biodiesel generally lies between 0.903 and 0.92,1 but with the use of blending procedure, values for specific gravity which are shown in Fig. 4 have significantly helped in optimizing the blended fuel properties. The lowest specific gravity for the B10 blend was found to be 0.851, but for the proper working of the engine components as on the basis of comparison based on the experimental results obtained, we gradually choose the B30 blended fuel over the jatropha and mahua fuel because the fuel consumption rate for the B30 blended fuel was less when compared to other samples and blends.

3.4 Effect of FFA and Acid Value Content in Biodiesel

Vegetable oil which is used for the production of biodiesel constitutes various contaminants that can increase the FFA content and reduce the efficiency of the process of removing the contaminants from the oil use of 5% concentrated H₂SO₄ this helped in the acid esterification of the oil. The result is shown in Figs. 5, and 6 shows that FFA has a preponderant effect in acid esterification which reduced the FFA content of jatropha biodiesel from 4.084% to 0.42.

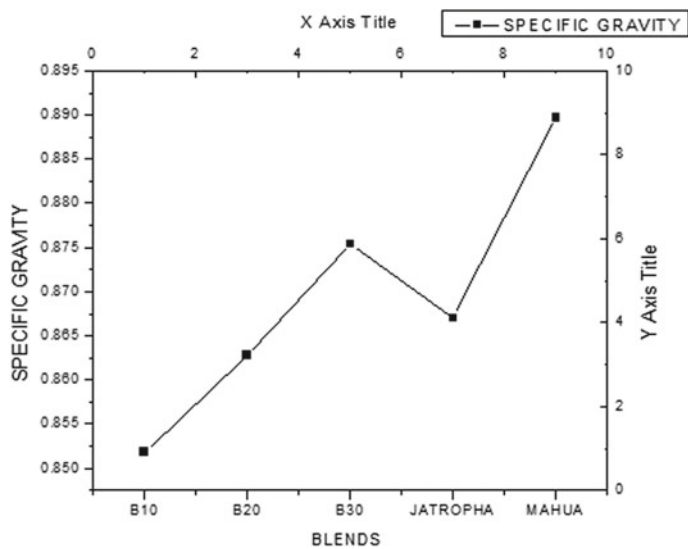


Fig. 4 Specific gravity of blends

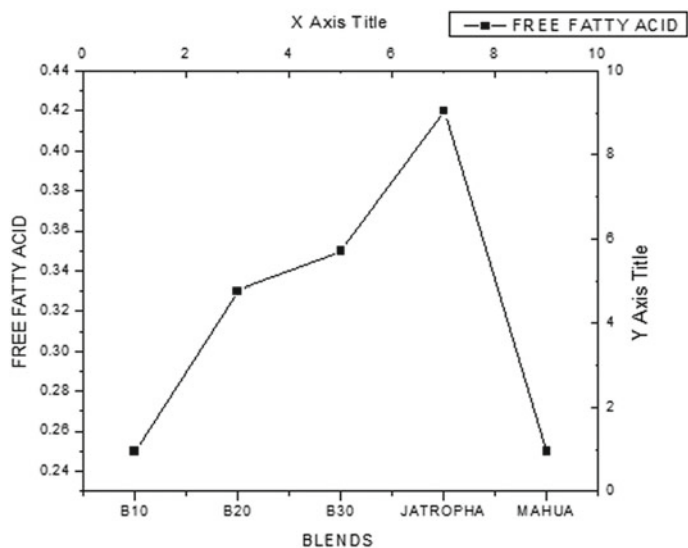


Fig. 5 FFA for blends

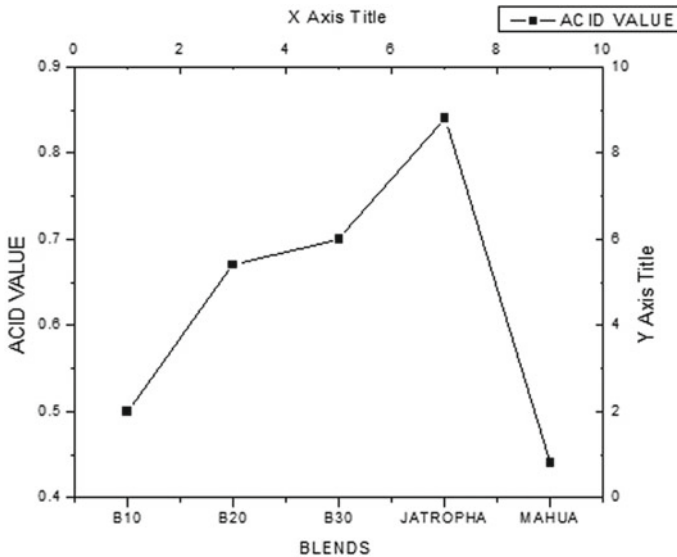


Fig. 6 Acid value for blends

3.5 Effect of Flashpoint and Fire Point of Biodiesel

Flashpoint refers to the lowest point of temperature at which the fuel ignites, In the below, Figs. 7, 8 values obtained for the lowest ignition temperature of 73 °C from B10 blend and the highest ignition temperature of 240 °C for mahua biodiesel but for the optimum working of fuel that can easily ignite under optimum working conditions. Fire point of fuel refers to the lowest temperature at which combustible liquid keeps on burning in the air even after its vapours have been ignited with the lowest temperature of 83 °C from B10 blend and the highest temperature of 244 °C for mahua biodiesel, but for the optimum working condition of fuel and based on the blending procedure used, it can be seen that B30 blend is the best choice.

3.6 Effect of Cloud Point and Pour Point

Cloud point for the fuel is referred to as the temperature under which wax in diesel is formed. As these wax can clog the fuel filters and injectors, pour point for the fuel is referred to as the minimum temperature of fluids at which they lose their flow properties. Figures 9, 10 shows the value of B30 blend that has cloud point temperature of 5 °C and a pour point temperature of 0 °C which is effective for the use in areas of cold climatic conditions.

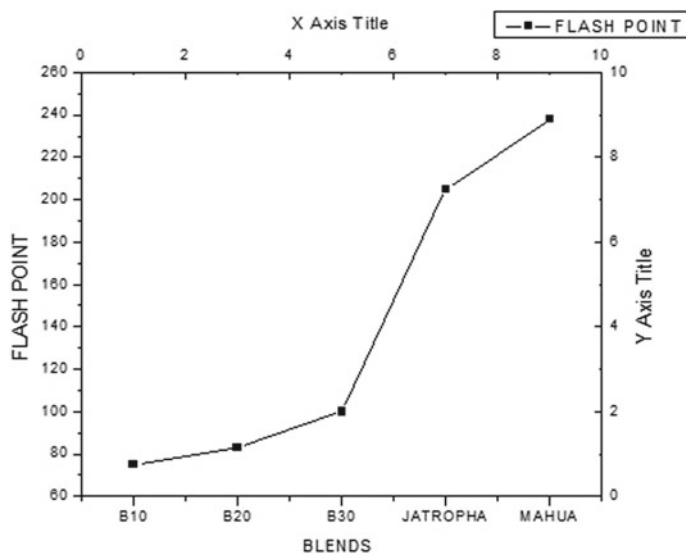


Fig. 7 Flashpoint for blends

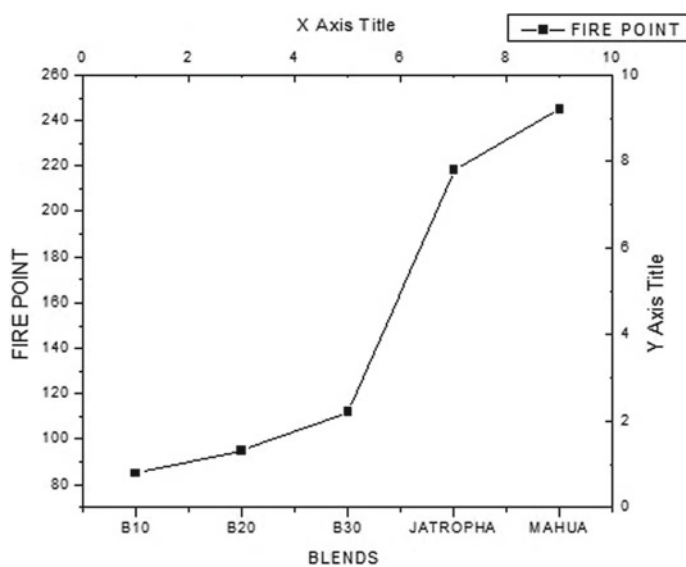


Fig. 8 Fire point for blends

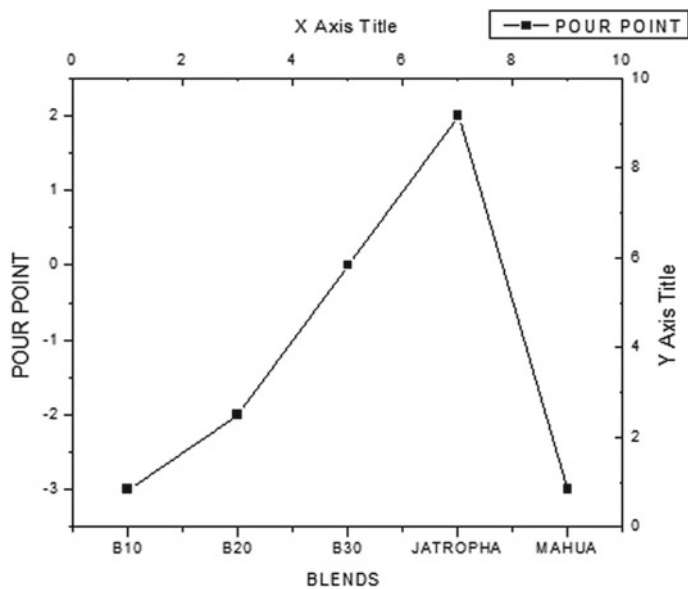


Fig. 9 Cloud point for blends

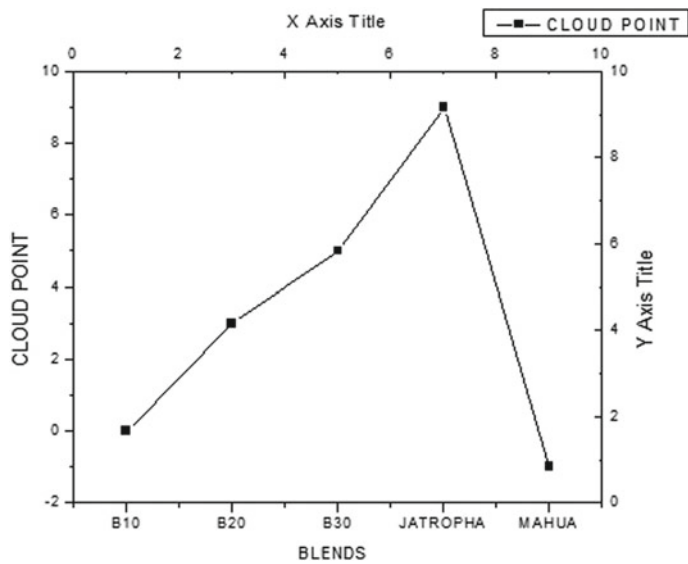


Fig. 10 Pour point for blends

4 Conclusion

Biodiesel is an environment-friendly fuel which will be gaining acceptance in the upcoming market, and being served as a fuel having lower emission characteristics and enhanced lubrication properties. It is a highly feasible and environment-friendly fuel. However, opportunities for the commercialization of these products have to be made easy. During experimentation, the physical characteristics for the B30 blend were significantly improved in comparison to jatropha biodiesel and mahua biodiesel. Chemical characteristics for the B30 blend were also affected which showed the possibility of usage under low climatic conditions with improved lubrication characteristics of the blends. The improvements observed in B30 blend with our experimentation conclude that the blending of two vegetable oils with mineral diesel can significantly improve the physio-chemical characteristics of the biodiesel.

References

1. Thapa S, Indrawan N, Bhoi PR (2018) An overview of fuel properties and prospects of Jatropha biodiesel as a fuel for engines. *Environ Technol Innovation* 9:210–219. <https://doi.org/10.1016/j.eti.2017.12.003>
2. Watkins RS, Lee AF, Wilson K (2004) Li-Cao catalyzed triglyceride transesterification for biodiesel applications. *Green Chem* 6(7):335–340. <https://doi.org/10.1039/b404883k>
3. Demirbas A (2005) Biodiesel production from vegetable oils via catalytic and non-catalytic supercritical methanol transesterification methods 31:466–487. <https://doi.org/10.1016/j.pecs.2005.09.001>
4. Ahmad AL, Yasin NHM, Derek CJC, Lim JK (2011) Microalgae as a sustainable energy source for biodiesel production: a review. *Renew Sustain Energy Rev* 15(1):584–593. <https://doi.org/10.1016/j.rser.2010.09.018>
5. Rahman KM, Mashud M, Galib A Al (2010) Biodiesel from jatropha oil as an alternative fuel for diesel engine. *Int J Mech Mechatron IJMME-IJENS* 10(3):1–6
6. Jongh A, Adriaans I (2007) Jatropha oil quality related to use in diesel engines and refining methods. Technical Note
7. Thirumarimurugan M, Sivakumar VM, Xavier AM, Prabhakaran D, Kannadasan T (2012) Preparation of biodiesel from sunflower oil by transesterification. *Int J Biosci Biochem Bioinf*. <https://doi.org/10.7763/IJBBB.2012.V2.151>
8. Mahmudul HM, Hagos FY, Mamat R, Adam AA, Ishak WFW, Alenezi R (2017) Production, characterization, and performance of biodiesel as an alternative fuel in diesel engines—a review. *Renew Sustain Energy Rev* 72(November 2016): 497–509. <https://doi.org/10.1016/j.rser.2017.01.001>
9. Gashaw A, Getachew T, Teshita A (2015) A review on biodiesel production as alternative fuel. *J For Prod Ind*
10. Openshaw K (2000) A review of Jatropha curcas : an oil plant of unfull@ led, 19. Retrieved from <https://www.sciencedirect.com/science/article/pii/S0961953400000192>
11. Kumar A, Tewari S (2015) Origin, distribution, ethnobotany, and pharmacology of jatropha curcas. *Res J Med Plants* 9:48–59

Slurry Pressure Drop Through Horizontal Mitre Pipe Bend Using CFD



Om Parkash, Arvind Kumar, and Basant Singh Sikarwar

Abstract In this paper, simulation of silica sand-water slurry is carried out through a horizontal mitre pipe bend of 0.050 m in diameter using ANSYS Fluent 16. The simulation of silica slurry was accompanied by using Eulerian two-phase model constrained with RNG K-epsilon turbulence model. The simulation was conducted using silica sand particulates of spherical size 448.5 μm for the volume fraction range 3.94–8.82%. The simulation of silica sand particulates was carried out with water properties available at different Prandtl numbers range, i.e. $Pr = 2.14\text{--}5.83$. The results of silica sand concentration contours and pressure drop were predicted at different mean flow velocity range, i.e. 1.78–4.5 ms^{-1} . It was found that the slurry pressure gradient escalates with increase in Prandtl number and mean flow velocity. Finally, the concentration contours of silica sand slurry for mean flow velocity 4.5 ms^{-1} at different angles i.e. $\theta = 0^\circ\text{--}90^\circ$ across the pipe bend are reported and discussed.

Keywords MITRE pipe bend • Silica sand contours • Pressure gradient

1 Introduction

Transferring of solids in the form of slurry through pipeline is generally practised by many industries across the world due to its numerous inborn advantages, such as endless distribution, flexible routing, comfort in self-regulation and lengthy range transportation capacity. Slurry pipelines are used for passage of different types of

O. Parkash (✉) · A. Kumar

JC Bose University of Science and Technology, YMCA, Faridabad 121006, India
e-mail: om.mech8@gmail.com

A. Kumar

e-mail: arvind_eem@yahoo.co.in

B. S. Sikarwar

Amity University Uttar Pradesh, Noida 201313, India
e-mail: bssikarwar@amity.edu

© The Author(s), under exclusive license to Springer Nature Singapore Pte Ltd. 2021

B. S. Sikarwar et al. (eds.), *Advances in Fluid and Thermal Engineering*,

Lecture Notes in Mechanical Engineering,

https://doi.org/10.1007/978-981-16-0159-0_32

materials such as coal ash, sand, zinc and iron tailing. The pressure drop across pipe bend usually incur relatively larger and thus liable to extreme erosion in comparison to straight pipeline. Kumar et al. [1] experimented and simulated the bend pressure drop of silica sand slurry and concluded that pressure drop is greater at the outer wall than the inner wall of the pipe bend with increase in velocity of flow. Singh et al. [2] experimentally analysed the rheological behaviour of coal water slurry flow and reported the variation of slurry pressure drop, pressure coefficient and settling velocity with and without additive. Singh et al. [3] carried out the experimental investigation by mixing the fly ash slurry to coarser silica sand slurry and reported the results of uniform mixing and reduction in sedimentation of particulates. Ahmed et al. [4, 5] simulated the glass beads slurry flow through horizontal pipeline and examined the various slurry flow characteristics such as pressure drop, concentration contour and velocity distribution. Bhusan Nayak and Chatterjee [6] analysed and presented the qualitative and quantitative effects of ash—water slurry flow through horizontal pipeline by using the mixture and Eulerian model. Parkash et al. [7] simulated the glass beads slurry flow through the straight pipeline at the Prandtl fluid and reported the slurry pressure drop. Parkash and Arora [8] numerically analysed the ash-water flow through straight pipeline and prophesied the pressure drop, velocity distribution, solid concentration and slip velocity at the pipe at the outlet of the pipeline. Verma et al. [9] in their study compared the slurry pressure drop through vertical and horizontal slurry pipeline. Consequently, from the literature review it is concluded that the availability of solid transport at different fluid property is still limited, and its experimental investigation to find out the various slurry flow characteristics is quite cumbersome and laborious. Conversely, the computational fluid technique has adequate competency to predict slow flow constraints at any cross section of the pipeline. In the present study, simulation of silica sand slurry is carried out at different Prandtl fluids. The outcome of the paper shows the variation of silica sand concentration and pressure drop across the pipe bend at different Prandtl fluids that play a vital role for the slurry pipeline engineer in the design of an efficient slurry pipeline system.

2 Mathematical Model

Eulerian two-phase model was implemented for simulation of silica sand slurry through pipe bend. The governing equations used for transportation of silica sand particulates are as described below.

Continuity Equation

$$\nabla \cdot (\alpha_t \rho_t \vec{v}_t) = 0 \quad (1)$$

where, t is either s or f .

Momentum Equations

For Fluids:

$$\begin{aligned} \nabla \cdot (\alpha_f \rho_f \vec{v}_f \vec{v}_f) = & -\alpha_f \nabla P + \nabla \cdot (\overline{\overline{\tau}_f} + \overline{\overline{\tau}_{t,f}}) + \alpha_f \rho_f \vec{g} + K_{sf} (\vec{v}_s - \vec{v}_f) + C_{vm} \alpha_s \rho_f (\vec{v}_s \cdot \nabla \vec{v}_s - \vec{v}_f \cdot \nabla \vec{v}_f) \\ & + C_L \alpha_s \rho_f (\vec{v}_f - \vec{v}_s) \times (\nabla \times \vec{v}_f) \end{aligned} \quad (2)$$

For Solids:

$$\begin{aligned} \nabla \cdot (\alpha_s \rho_s \vec{v}_s \vec{v}_s) = & -\alpha_s \nabla P - \nabla P_s + \nabla \cdot (\overline{\overline{\tau}_s} + \overline{\overline{\tau}_{t,f}}) + \alpha_s \rho_s \vec{g} + K_{fs} (\vec{v}_f - \vec{v}_s) + C_{vm} \alpha_s \rho_f (\vec{v}_f \cdot \nabla \vec{v}_f - \vec{v}_s \cdot \nabla \vec{v}_s) \\ & + C_L \alpha_s \rho_f (\vec{v}_s - \vec{v}_f) \times (\nabla \times \vec{v}_f) \end{aligned} \quad (3)$$

Here

$\tau_{t, f}$ is the Reynolds stress tensor and

τ_s and τ_f are viscous stress tensor for solid phase and fluid phase, respectively.

3 Computational Domain

3.1 Computational Mesh

The computational mesh of mitre pipe bend containing hexahedral cells is created in ANSYS 16 as shown in Fig. 1. The grid independent test is achieved through pipe bend geometry containing coarse, medium and fine cells and pipe bend geometry with 2.60 K is finalized for simulation of silica sand slurry.

3.2 Boundary Conditions

The pipe bend geometry comprises of three faces in the computational domain, viz. inlet, outlet and wall. The boundary condition of velocity inlet and pressure outlet is applied at specific velocity and volume fraction, though no slip condition is assumed at the wall. SIMPLE algorithm and second-order upwind scheme are used to solve the pressure and velocity field function of the computational domain (Table 1).

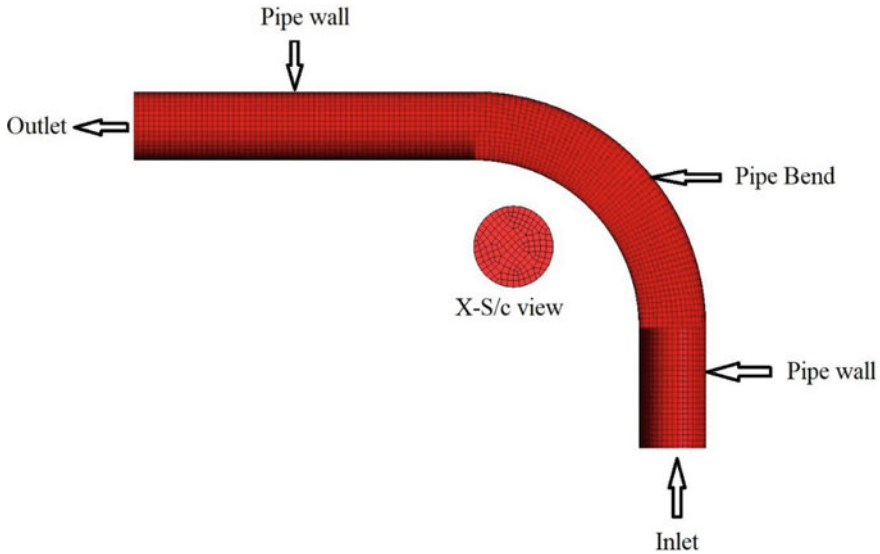


Fig. 1 Mesh geometry

Table 1 Properties of water at different Prandtl fluids

Prandtl number (Pr)	Density (kg/m ³)	Viscosity (kg/m-sec)
2.14	973	0.000343
3.42	987	0.000528
5.83	997	0.000855

4 Computational Results

4.1 Silica Sand Contours

Figure 2 depicts the silica sand contours across the horizontal pipe bend at $C_{vf} = 3.94\%$ and $V_{mf} = 4.5 \text{ ms}^{-1}$ for Prandtl number, $Pr = 2.14$. It is found that the at bend inlet, i.e. $\theta = 0^\circ$ the silica sand particulates are settled at the bottom of the pipeline. However, as the solid particulates enter in the pipe bend zone the particulates tend to deflect at the extrados of the pipe bend due to the effect of centrifugal force as displayed in the pipe bend cross section at $\theta = 15^\circ, 30^\circ$ and 45° . Moreover, as the particulates enter at the curvature angle ($\theta > 45^\circ$) the solid particulates deflect completely towards the extrados of the pipe bend as displayed in the pipe bend cross section at $\theta = 60^\circ, 75^\circ$ and 90° . Similar effects across the pipe bend can be seen from Figs. 3, 4, 5, 6 and 7. The Prandtl number also effects the distribution of solid particulates across the pipe bend, at low Prandtl number the viscosity of the fluid is low and thus causes the more suspension of the solid

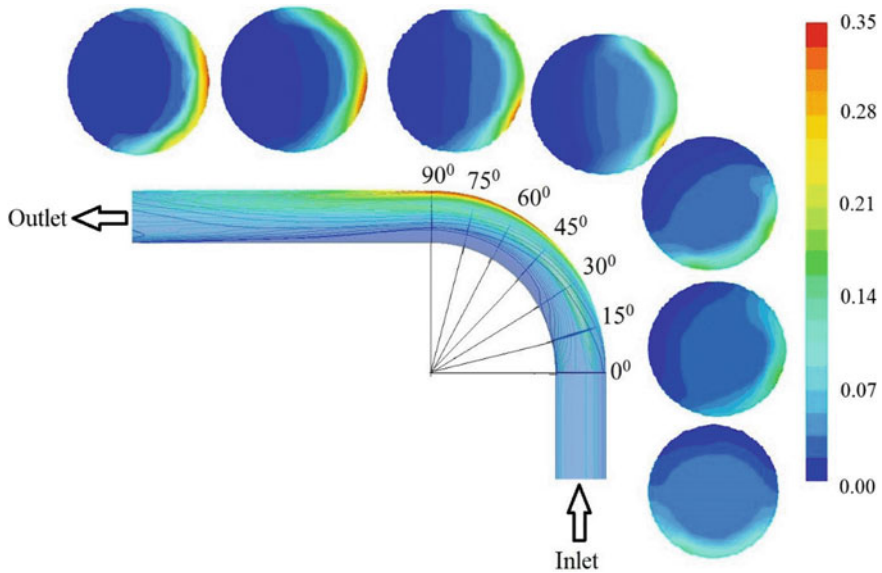


Fig. 2 Silica sand contours at $C_{vf} = 3.94\%$ and $V_{mf} = 4.5 \text{ ms}^{-1}$ at $Pr = 2.14$

particulates and plays a vital role in momentum exchange. However, as the Prandtl number increases, the viscosity of the carrier fluid carrying solid also increases and thus contributes to settling of solids in the pipe domain. The solid particulates at $\theta = 90^\circ$ as depicted in Fig. 2 show more spreading at the extrados of the pipe bend as compared to the solid particulates at $\theta = 90^\circ$ as depicted in Figs. 4 and 6. Similar effects can also be seen at other angles at Prandtl number 2.14, 3.42 and 5.83 as depicted in Figs. 3, 4, 5, 6 and 7.

4.2 Pressure Gradient

Pressure gradient is the imperative constraint for the design of slurry transportation system. The pressure drop at the transverse cross section of the pipe bend is prophesied for the silica sand range 3.94–8.82% and velocity range 1.78–4.56% at Prandtl number $Pr = 2.14, 3.42$ and 5.83. It is found that the pressure drop escalates with rise in velocity for chosen volume fraction of silica sand as depicted in Fig. 8a–c. Figure 9a and b depict the pressure drop variation with mean flow velocity at different Prandtl number and findings show that the pressure drop is higher at higher Prandtl number and decreases as the Prandtl number decreases. However, the pressure drop variation at higher velocity beyond 4 ms-1 is significant large than the lower velocity for the chosen volume fraction and Prandtl number.

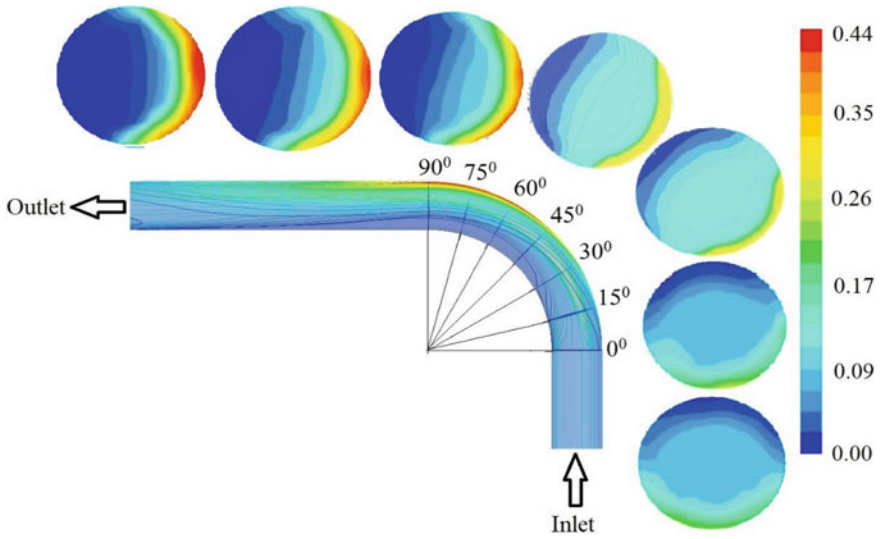


Fig. 3 Silica sand contours at $C_{vf} = 8.82\%$ and $V_{mf} = 4.5 \text{ ms}^{-1}$ at $Pr = 2.14$

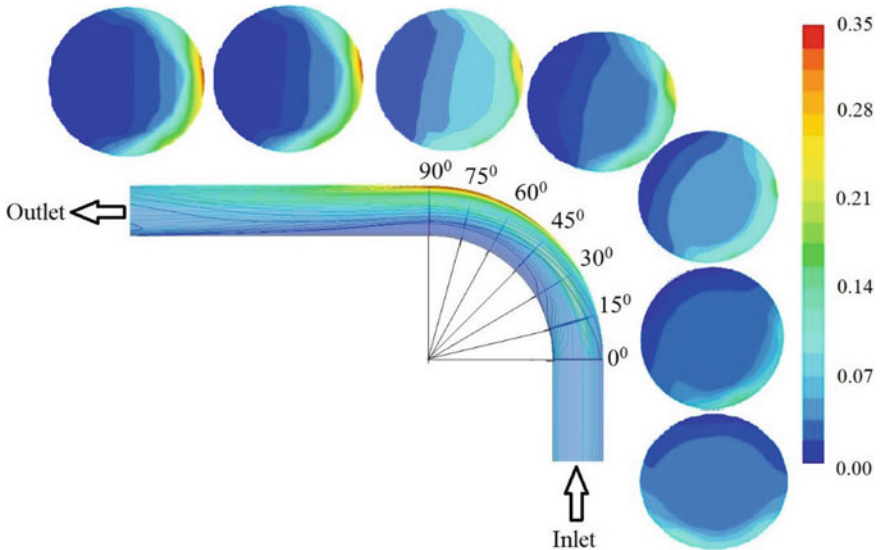


Fig. 4 Silica sand contours at $C_{vf} = 3.94\%$ and $V_{mf} = 4.5 \text{ ms}^{-1}$ at $Pr = 3.42$

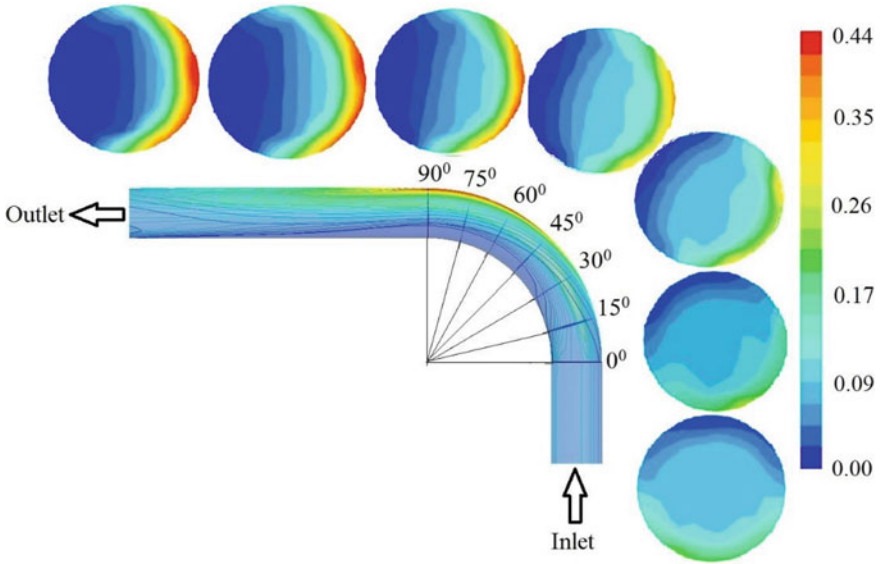


Fig. 5 Silica sand contours at $C_{vf} = 8.82\%$ and $V_{mf} = 4.5 \text{ ms}^{-1}$ at $Pr = 3.42$

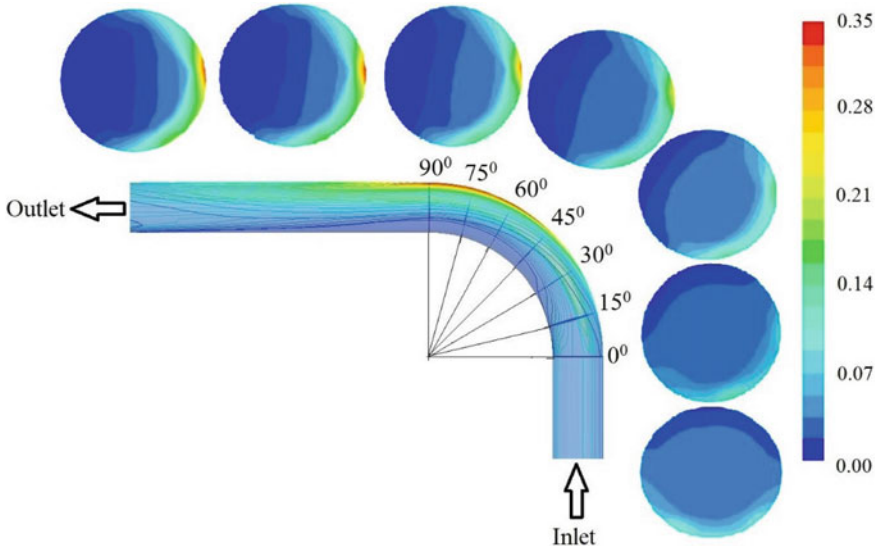


Fig. 6 Silica sand contours at $C_{vf} = 3.82\%$ and $V_{mf} = 4.5 \text{ ms}^{-1}$ at $Pr = 5.83$

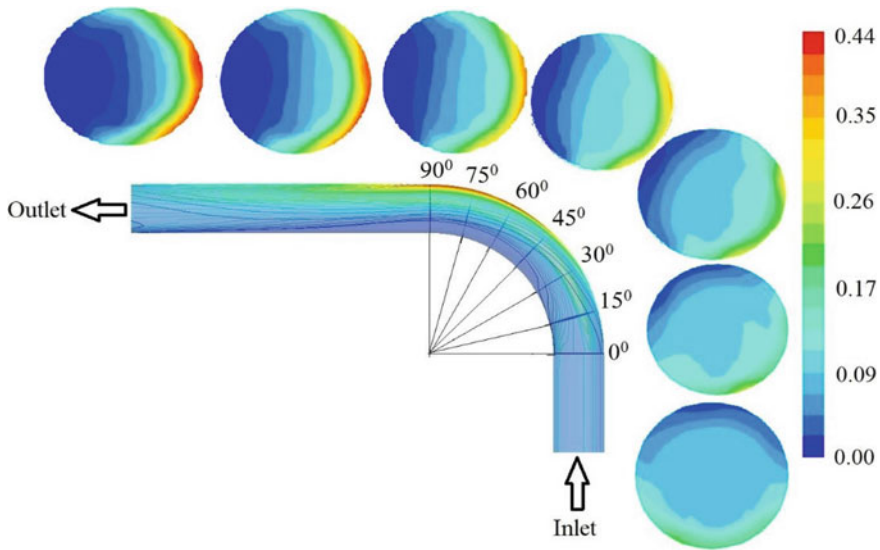


Fig. 7 Silica sand contours at $C_{vf} = 8.82\%$ and $V_{mf} = 4.5 \text{ ms}^{-1}$ at $Pr = 5.83$

5 Conclusions

The following remarks have been concluded for the transportation of silica sand slurry through mitre pipe bend:

1. It is found that Eulerian two-phase model with RNG $k - \varepsilon$ turbulence bound provides more spectacular and apposite results for the prognostication of pressure drop and particulates concentration across the mitre pipe bend.
2. The silica sand distribution at the extrados of the pipe bend is found more as compared to the inner wall of the pipe bend.
3. The pressure drop escalates with rise in velocity and silica sand concentration for different Prandtl number.
4. The pressure drop escalates with upturn in Prandtl number for chosen silica sand concentration.
5. The silica sand spreading and momentum exchange at lower Prandtl number is more at the extrados of the pipe bend as compared to higher Prandtl number.

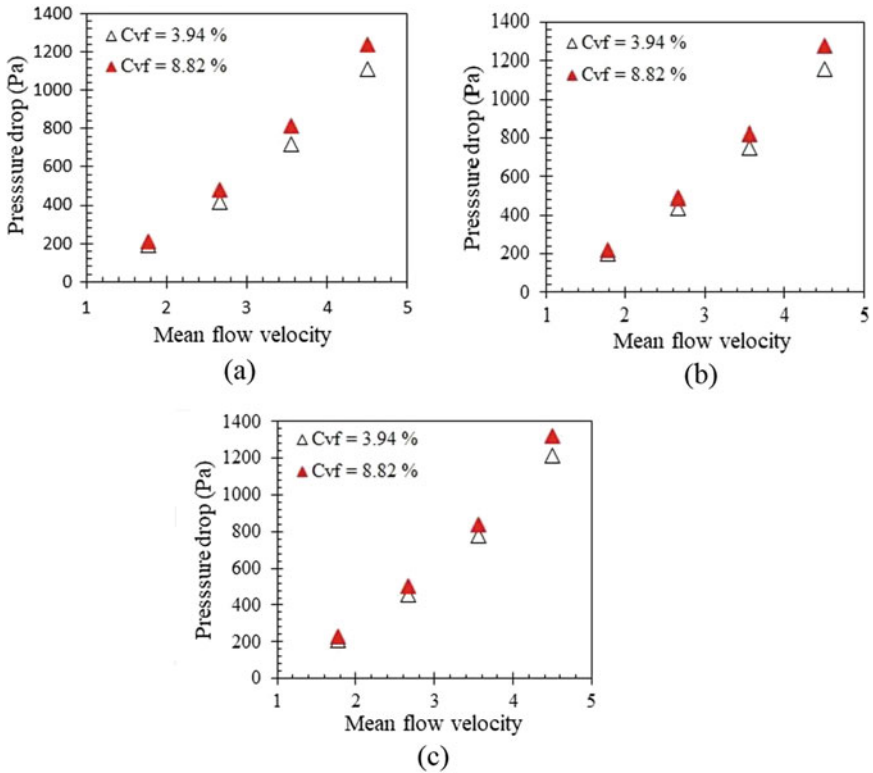


Fig. 8 Variation of pressure drop with mean flow velocity at a Pr = 2.14, b Pr = 3.42, and c Pr = 5.83

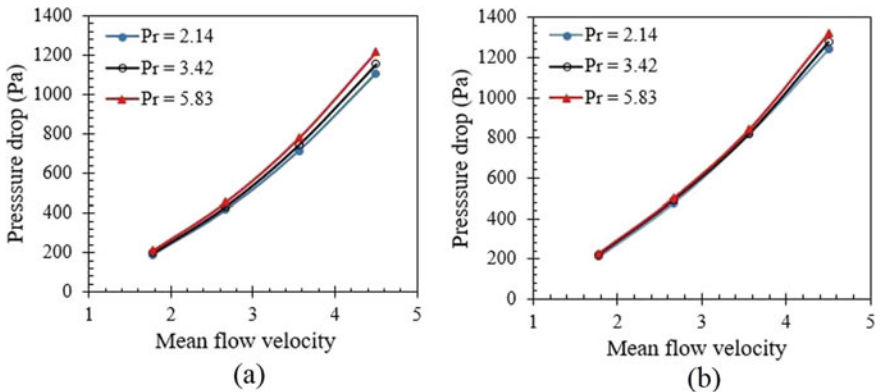


Fig. 9 Variation of pressure drop with mean flow velocity at a $C_{vf} = 3.94\%$, and b $C_{vf} = 8.82\%$

References

1. Kumar A, Kaushal DR, Kumar U (2008) Bend pressure drop experiments compared with FLUENT. *Proc Inst Civ Eng—Eng Comput Mech* 161(1):35–42
2. Singh JP, Kumar S, Mohapatra SK (2017) Head loss investigations inside 90° pipe bend for conveying of fine coal water slurry suspension. *Int J Coal Prep Utilization*
3. Singh KP, Kumar A, Kaushal DR (2018) Computation modelling for fine particle flow in horizontal slurry pipelines. *Res Rev J Phys* 8(1):1–6
4. Ahmed S, Arora R, Parkash O (2018) Prediction of flow parameters of glass beads-water slurry flow through horizontal pipeline using computational fluid dynamics. *Jordan J Mech Ind Eng* 12(3)
5. Ahmed SU, Arora R, Parkash O (2019) Flow characteristics of multiphase glass beads-water slurry through horizontal pipeline using computational fluid dynamics. *Int J Automot Mech Eng* 16(2):6605–6623
6. Bhusan Nayak B, Chatterjee D (2019) Assessment of mixture and eulerian multiphase models in predicting the thermo-fluidic transport characteristics for fly ash-water slurry flow in straight horizontal pipeline. *Heat Transf Eng* 40(8):679–692
7. Parkash O, Kumar A, Sikarwar BS (2019) CFD modeling of commercial slurry flow through horizontal pipeline. In: *Advances in interdisciplinary engineering*, pp 153–162. Springer, Singapore
8. Parkash O, Arora R (2020) Flow characterization of multi-phase particulate slurry in thermal power plants using computational fluid dynamics. *J Therm Eng* 6(1):187–203
9. Verma OP, Kumar A, Sikarwar BS (2020) Numerical simulation and comparative analysis of pressure drop estimation in horizontal and vertical slurry pipeline. *J Mech Eng Sci* 14(2):6610–6624

Development of Characteristic Equation for Evacuated Tubular Collector Under Constant Collection Temperature Mode of Operation



R. K. Mishra, Siddarth Gupta, Rajesh Tripathi, and Rajendra Prasad

Abstract Present paper reports the comprehensive study of evacuated tubular collector (ETC) for a fixed outlet temperature from the collector. The detailed numerical modeling has been done in terms of energetic and exergetic gains under constant collection temperature mode of operation. For getting higher outlet temperature, one have to decrease the rate of flow of water in the U-shaped copper tube inserted in the glass tube of the collector, but it has been noticed that mass flow rate gets saturated after a certain value of collection temperature, and there is no meaning of decreasing the mass flow rate after the saturated value for further increase of the outlet temperature. The characteristic equations similar to Hottel–Whiller–Bliss (HWB) have been developed for ETC with U-shaped copper pipe for getting constant outlet temperature. Values of gain and loss terms for constant collection temperatures are found to be 0.69 and 17.42, respectively.

Keywords Evacuated tubular collector · Solar energy · Exergy · Constant collection temperature

Nomenclature

A Area (m^2)
 C_f Specific heat of fluid (J/kgK)
 dx Elemental length (m)
 F' Flat plate collector efficiency factor

R. K. Mishra (✉) · R. Tripathi · R. Prasad
Department of Applied Science, Galgotias College of Engineering and Technology,
Greater Noida, India
e-mail: bhu.rajeev@gmail.com

R. Tripathi
e-mail: rajesh.tripathi@galgotiacollege.edu

R. Prasad
e-mail: drprnishad@gmail.com

S. Gupta
Hi-Tech Institute of Engineering and Technology, Ghaziabad, India
e-mail: 100siddgupta@gmail.com

h	Heat transfer coefficient, $\text{W/m}^2\text{K}$
L	Total length of the tube (m)
$I(t)$	Total solar radiation, (W/m^2)
\dot{m}_f	Mass flow rate of water in (kg/sec)
R	Outer radius of the glass tube (m)
r	Radius of U-shaped copper tube (m)
$U_{t,pa}$	Overall heat transfer coefficient from absorber plate to ambient through glass cover ($\text{W/m}^2\text{K}$)

Greek Letters

α	Absorptivity
τ	Transmittivity

Subscript

a	Ambient
c	Collector
f	Fluid
fi	Inlet fluid
g	Glass
p	Plate
fo	Outlet fluid

1 Introduction

Nowadays, the climate change and global warming because of the access use of conventional energy resources became the major concern for the researches. It causes the development of new alternative green sources of energy like solar, wind, biomass, geothermal, etc. [1–3]. Solar water heating system is unique type of energy conversion device used for domestic and industrial applications in which the sun's energy is transformed into thermal energy in the form of hot water [4–7]. The paramount component in these devices is the collector. It has been observed that the hot water yield and water temperature are affected by the collectors surface area and environmental conditions. Many researchers performed the study of flat plate collectors (FPC) and evacuated tubular collectors (ETC) for different configurations [8–12]. Nine test techniques in dynamic mode were suggested by Nayak and Amer [13] for flat plate collectors through theoretical and experimental results. The direct optical control method for flat plate collector in open loop was studied by Badescu [14, 15]. The author mentions different strategies for getting maximum energy in open loop operation of the conventional solar collector. Hobbi and Siddiqui [16]

considered the water heater using flat plate collector for optimizing the parameters like mass flow rate in force circulation mode of operation. A rigorous literature review has been discussed by Tiwari et al. [17] which includes the mathematical modeling, energy, exergy analysis, life cycle assessment of various solar systems. Detailed analysis of photovoltaic thermal solar water heater was performed by Mishra and Tiwari [18] in terms of energy and exergy. They developed characteristic equations for constant outlet temperature by varying the mass flow rate of water flowing inside the copper tubes of the collectors.

For water temperature 100 °C above the atmospheric temperature, flat plate collectors are commonly used [19]. Evacuated tubular collectors are more useful than FPCs because of their specific prosperities. The performance of both the collectors is greatly influenced by the solar radiation intensity, ambient temperature [20]. Various studies have been done to evaluate the thermal performance of FPCs and ETCs in different weathers conditions [21–29]. Diego et al. [22] examined the thermal behavior of FPC for a hot and sub-humid region in Mexico. Authors evaluated the thermal behaviour of the collector for thermo-siphon and forced mode of operations and revealed that the collector efficiency depends on the mass flow rate and fluid working temperature. Because of its shape and construction, the evacuated tubular collector (ETC) has some leading properties over the conventional flat plate collectors (FPC). The classification of varieties of ETCs was given by Mishra et al. [11]. The heating effect and sensitive parameters of a separate single-walled evacuated tube was analyzed by Badar et al. [30] by developing a systematic steady-state model. Kim and Seo [31] did the experimental study of evacuated tubular collector by considering for four absorbers of non-identical shape. The detailed theoretical investigation has been done by Zhao et al. [32] for a preliminary version of a single-walled ETC with looped heat pipe. Nkwetta et al. [33] investigated a single-walled evacuated tubular collector integrated with heat exchanger and an external/internal concentrator. They revealed that the outlet temperature was increased significantly. The Dewar-type evacuated tubes are very common in use in China nowadays for heating of water, and it has been reported that up to 95% of the market is of the same. The water flowing in the glass tube in which there is a direct contact of water with the absorber of the tube is very famous design and gives better results as compared with the Dewar tube due to its lower cost [34]. Xu et al. [35] also established the model for the study of heat performance of Dewar tube water heating system. They used air for the transfer of heat in dynamic outdoor conditions. Kim et al. [36] established one-dimensional mathematical model for Dewar tube water collector with a concentric fluid pipe placed in the tube by taking into account the heat flux between the inner and outer pipes. The outer side of the fluid pipe was filled with anti-freezing material. The thermal mass of the fluid is reported as a notable parameter in the daily performance of collectors connected as large arrays. The collectors consist of a single-walled tube in which heat pipes are used for heat extraction and the thermal mass was taken as about $1.01/\text{m}^2$. The thermal mass was mentioned as an important factor for the dynamic characterization of the collector [37].

For industrial uses, hot water at fix required temperature is having more importance as compared to water with changing outlet temperature at constant rate of flow. For high and constant outlet temperatures, some specific number of ETC needs to be connected in series and also the force mode of operation is required for getting fixed outlet temperature. To make this series connections and operation in force mode, U-shaped copper tube has been inserted in the evacuated glass tube. In present communication, an effort has been made to perform the comprehensive study of evacuated tube water collectors with U shape copper pipe for New Delhi, India, at constant outlet temperature.

2 System Description

Schematic diagram of the proposed system has been drawn in Fig. 1. It consists of a U-shaped copper tube inserted in the glass tube of ETC. The outer diameter of coaxial glass tube is 0.05 m and length is 1.25 m. The outer surface of the inner glass tube is coated with some selected metal having high value of absorption coefficient and heat transfer coefficient as shown in Fig. 2. The metal fin is fixed at inner surface of coaxial tube for fast heat transfer from inner tube to the working fluid (water) flowing through the tubes.

Radiant energy from Sun incident on the glass tube is first absorbed by the metallic fin, and the heat energy will be transferred to the water flowing in the U-shaped copper tube.

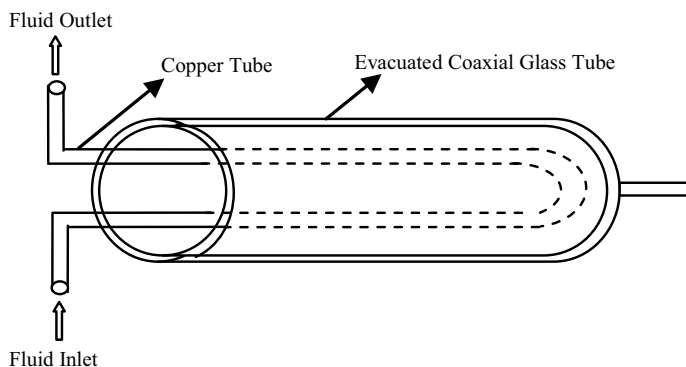
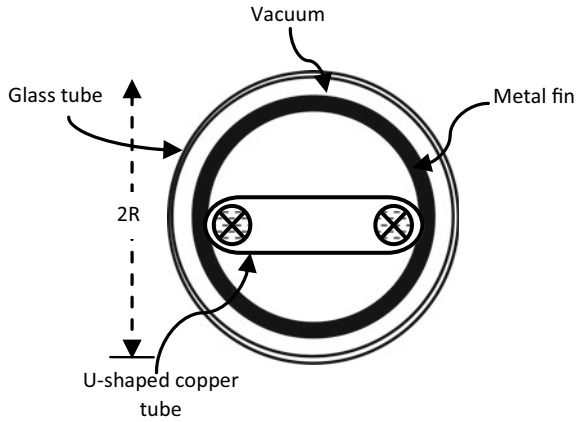


Fig. 1 Schematic diagram of the U-shaped ETC

Fig. 2 Cross-sectional view of the proposed evacuate tube collector



3 Mathematical Modeling

The energy balance equation can be given as:

$$\alpha\tau^2 I(t) 2Rdx = [F'h_{pf}(T_p - T_f) + U_{t,pa}(T_p - T_a)]2Rdx \tag{1}$$

and

$$\dot{m}_f C_f \frac{dT_f}{dx} dx = F'h_{pf}(T_p - T_f)2\pi rdx \tag{2}$$

From Eq. 1,

$$T_p = \frac{\alpha\tau^2 I(t) + F'h_{pf}T_f + U_{t,pa}T_a}{[F'h_{pf} + U_{t,pa}]} \tag{3}$$

From here,

$$T_p - T_f = \frac{\alpha\tau^2 I(t) - U_{t,pa}(T_f - T_a)}{[F'h_{pf} + U_{t,pa}]} \tag{4}$$

or,

$$h_{pf}(T_p - T_f) = \frac{h_{pf}}{(F'h_{pf} + U_{t,pa})} \alpha\tau^2 I(t) - \frac{U_{t,pa} \cdot h_{pf}}{(F'h_{pf} + U_{t,pa})} (T_f - T_a) \tag{5}$$

or,

$$F'h_{pf}(T_p - T_f) = PF_1\alpha\tau^2I(t) - U_L(T_f - T_a) \tag{6}$$

where $PF_1 = \frac{h_{pf}}{(F'h_{pf} + U_{i,pa})}$ and $U_L = \frac{U_{i,pa}h_{pf}}{(F'h_{pf} + U_{i,pa})}$

After substituting the values from Eq. 6 in Eq. 2, we have,

$$\dot{m}_f C_f \frac{dT_f}{dx} = 2\pi r [PF_1\alpha\tau^2I(t) - U_L(T_f - T_a)] \tag{7}$$

Integrating Eq. 4 under suitable boundary conditions:

at $x = 0$; $T_f = T_{fi}$ and at $x = L$; $T_f = T_{fo}1$

We have,

$$T_{fo}1 = \left[\frac{PF_1\alpha\tau^2I(t)}{U_L} + T_a \right] \left[1 - \exp\left(-\frac{2\pi rLU_L}{\dot{m}_f C_f}\right) \right] + T_{fi} \exp\left(-\frac{2\pi rLU_L}{\dot{m}_f C_f}\right) \tag{8}$$

$T_{fo}1$ is the outlet temperature from one (first) collector unit.

From Eq. 8,

$$T_{fo}1 = \frac{PF_1\alpha\tau^2I(t)}{\dot{m}_f C_f} \times \frac{\dot{m}_f C_f}{U_L} \left[1 - \exp\left(-\frac{2\pi rLU_L}{\dot{m}_f C_f}\right) \right] + \frac{T_a U_L}{\dot{m}_f C_f} \times \frac{\dot{m}_f C_f}{U_L} \left[1 - \exp\left(-\frac{2\pi rLU_L}{\dot{m}_f C_f}\right) \right] + T_{fi} \exp\left(-\frac{2\pi rLU_L}{\dot{m}_f C_f}\right) \tag{9}$$

Define;

$$\frac{\dot{m}_f C_f}{U_L A_R} \left[1 - \exp\left(-\frac{2\pi rLU_L}{\dot{m}_f C_f}\right) \right] \equiv F_R \tag{10}$$

Hence,

$$T_{fo}1 = PF_1\alpha\tau^2 A_R F_R \times \frac{I(t)}{\dot{m}_f C_f} + A_R F_R U_L \times \frac{T_a}{\dot{m}_f C_f} + \left(1 - \frac{A_R F_R U_L}{\dot{m}_f C_f} \right) T_{fi} \tag{11}$$

3.1 For Getting Fix Outlet Temperature

We have, as given by Eq. (11).

By using the Eq. (11) for the outlet temperature from first ETC and for constant outlet temperature ($T_{fo}1 = T_o = \text{constant}$), the equation for mass flow rate will be rewritten as, (12)

$$\dot{m}_f = \frac{A_c U_L}{C_f \left[\log \left\{ T_{fi} - \left(\frac{PF_1 \alpha \tau^2 I(t)}{U_L} + T_a \right) \right\} - \log \left\{ T_o - \left(\frac{PF_1 \alpha \tau^2 I(t)}{U_L} + T_a \right) \right\} \right]} \quad (12)$$

The rate of mass flow in the U-shaped tube can be optimized for a required value of outlet temperature for industrial use.

3.2 Rate of Thermal Energy Gain

The rate of thermal energy acquired through evacuated tubular collector can be given as

$$\dot{Q}_{u,\text{thermal}} = \dot{m}_f C_f (T_o - T_a) \quad (13)$$

3.3 Exergy Gain

Following Bejan [38] and Yunus and Micheal [39], the exergy drawn out by the water coming out from the ETC (\dot{E}_{ex}), in W is given by

$$\dot{E}_{ex} = \dot{m}_f c_f (T_{fo,1} - T_{fi}) - \dot{m}_f c_f (T_a + 273) \ln \frac{(T_{fo} + 273)}{(T_{fi} + 273)} \quad (14)$$

3.4 Instantaneous Thermal Efficiency

After calculating the value of thermal energy gain (\dot{Q}_u) using Eq. 13, instantaneous thermal efficiency of ETC may be evaluated by using,

$$\eta_i = \frac{\dot{Q}_u}{A_c \times I(t)} \quad (15)$$

4 Results and Discussion

4.1 Evolution of Characteristic Equation

Data of solar radiations and ambient temperatures for Delhi climatic conditions is taken from Indian Metrological Department (IMD), Pune, India. The change of sun

intensity and environmental air temperature during the sunshine hours for a clear day of June Month is plotted in Fig. 3. The system design specifications for proposed ETC are listed in Table 1. Instantaneous thermal efficiency (η_i) was evaluated by using Eq. 15. The graph showing the variation of η_i with $(T_{fi}-T_a)/I(t)$ is shown in Fig. 6. The characteristic equation for ETC under constant collection temperature mode has been developed with the help of Fig. 6 by using linear regression method. Obtained characteristic equations similar to standard Hottel–Whiller–Bliss (HWB) equation can be written as:

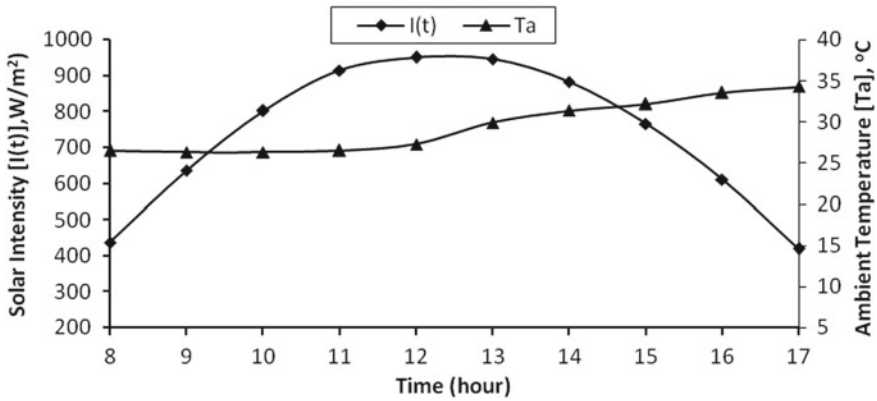


Fig. 3 Variation of sun intensity and air temperature for a clear day in the June month

Table 1 Design specifications of evacuated tubular collector (ETC)

Parameters	Values
r	0.0125 m
R	0.125 m
L	2.0 m
C_f	4190 J/kgK
F'	0.986
$h_{p,f}$	100 W/m ² °C
h_i	5.7 W/m ² °C
h_o	9.5
$PF1$	0.9789
L_g	0.0005 m
K_g	1.09 W/m °C
$U_{t p,a}$	3.5567 W/m ² °C
V_o	1.0 m/s
τ	0.95
α	0.80

$$\eta_{i,thermal} \text{ (in fraction)} = 0.699 - 17.42 \left[\frac{(T_{fi} - T_a)}{I(t)} \right] \tag{16}$$

After comparing above equation with the standard HWB equation [12], the values of gain and loss terms for constant collection temperature mode will be obtained as

Gain term $F_R(\alpha\tau) = 0.46$; Loss Term $F_R U_L = 4.2$.

Equation 11 is enumerated for the design specification given in Table 1 and climatic parameters in Fig. 3 to have various constant collection temperatures for various mass flow rates. The hourly variation of collection temperature with varying rate of mass flow in the tube for a clear day of June month is shown in Fig. 4. Figure shows that (i) for a given rate of mass flow, the collection temperature rises first due to increase in the value of sun intensity and (ii) the maximum outlet temperature decreases with rise of the mass flow rate as expected. From figure, we can tune (adjust) the rate of mass flow at a given time for a specific required value of the collection temperature.

The variation of rate of mass flow in the U-shaped copper tube for a fix value of outlet temperature for a clear day of June month is plotted in Fig. 5. Figure clearly shows that the rate of mass flow increases with the time due to increase of solar intensity and the highest value of mass flow rate decreases with the increase in the value of outlet temperature.

Figure 6 represents the characteristic curve of evacuated tubular collector under constant collection temperature mode of operation. Figure 7 shows the change of highest value of outlet temperature with the rate of mass flow for given clear day of June month. From figure, it is clear that as the constant collection temperature reduces the mass flow rate increases, but the rate of mass flow gets saturated at

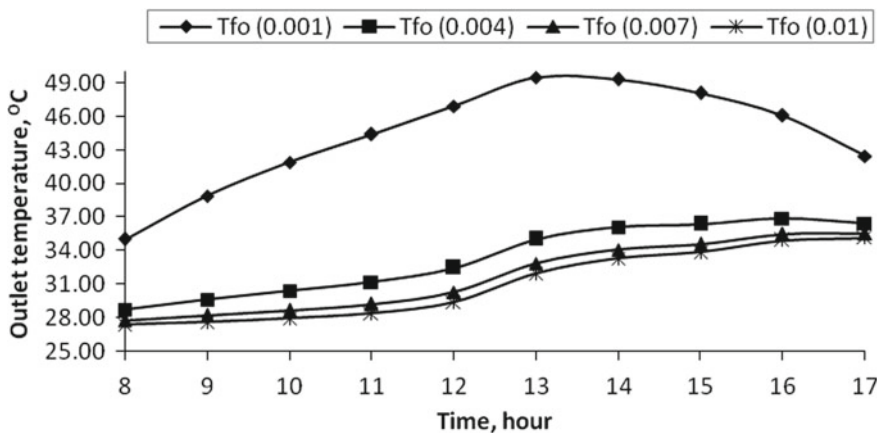


Fig. 4 Variation of collection temperature with various mass flow rates for a clear day of June month

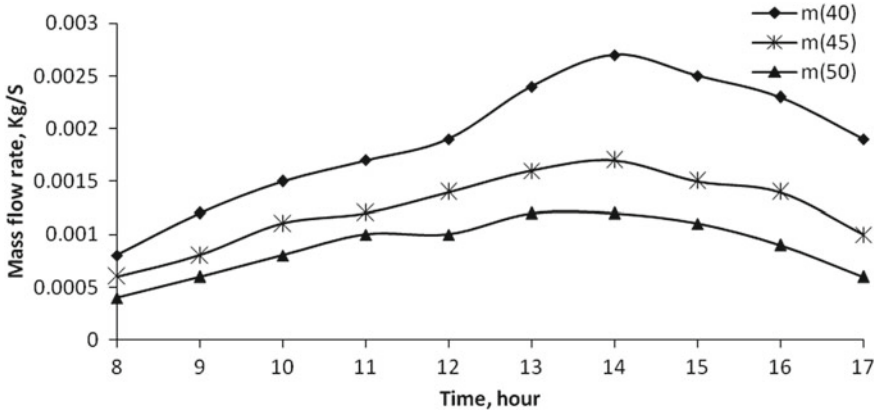


Fig. 5 Variation of mass flow rate for a constant collection temperature for a clear day of June month

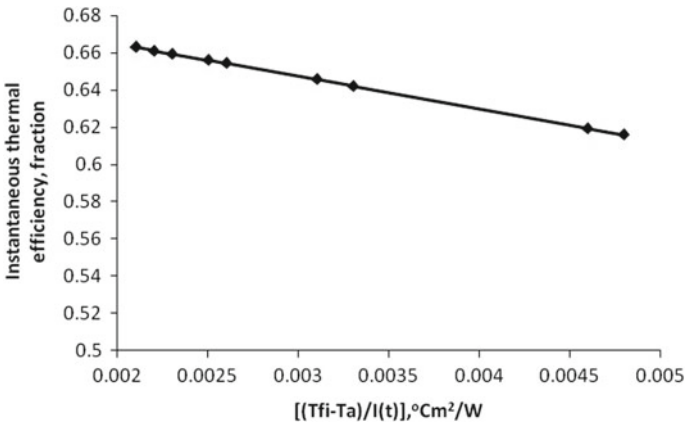


Fig. 6 Characteristic curve of evacuated tubular collector (ETC)

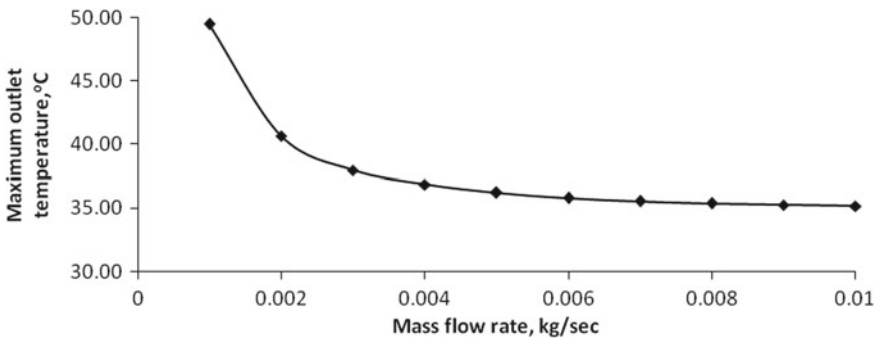


Fig. 7 Variation of maximum collection temperature with the mass flow rate for a typical day in the month of June

some value and there is no meaning of increase the mass flow rate after this saturated value.

5 Conclusion

Because of its unique design, evacuated tubular collectors (ETCs) are more useful as compared with conventional flat plate collectors (FPCs) particularly at elevated water temperatures. For industrial applications, hot water at fix required temperature is having more importance as compared to water with changing outlet temperature at constant rate of flow. Values of gain and loss terms for constant collection temperatures were found to be 0.69 and 17.42, respectively.

References

1. Solar Water Heating and Space Heating, Austin Energy Green Building Program, USA, 2003
2. Chow TT (2003) Performance analysis of photovoltaic-thermal collector by explicit dynamic model. *Sol Energy* 75:143–152
3. Tiwari GN, Mishra RK (2012) *Advanced renewable energy sources*. RSC Publishing, Cambridge, UK
4. Dubey S, Tiwari GN (2009) Analysis of PVT flat plate water collectors connected in series. *Sol Energy* 83:1485–1498
5. Prabhakant YN, Mishra RK, Tiwari GN (2011) Thermal modelling of hybrid photovoltaic thermal (HPVT) integrated biogas plants. *Appl Solar Energy* 47:304–311
6. Mekhilef S, Saidur R, Safari A (2011) A review on solar energy use in industries. *Renew Sustain Energy Rev* 15:1777–1790
7. Suman S, Khan MK, Pathak M (2015) Performance enhancement of solar collectors—a review. *Renew Sustain Energy Rev* 49:192–210
8. Shyam Tiwari GN, Fischer O, Mishra RK, Al-Helal IM (2016) Performance evaluation of N-photovoltaic thermal (PVT) water collectors partially covered by photovoltaic module connected in series: an experimental study. *Solar Energy* 137:302–313
9. Mishra RK, Tiwari GN (2011) Evaluation of an integrated photovoltaic thermal solar (IPVTS) water heating system for various configurations at constant collection temperature. In *WREC-2011*, pp 3749–3756. Linkoping University, Sweden
10. Mishra RK, Tiwari GN (2013) Energy matrices analyses of hybrid photovoltaic thermal (HPVT) water collector with different PV technology. *Solar Energy* 91:161–173
11. Mishra RK, Garg V, Tiwari GN (2015) Thermal modeling and development of characteristic equations of evacuated tubular collector (ETC). *Solar Energy* 116:165–176
12. Tiwari GN, Meraj M, Khan ME, Mishra RK, Garg V (2018) Improved hotel-whillier-bliss equation for N-photovoltaic thermal-compound parabolic concentrator (N-PVT-CPC) collector. *Solar Energy* 166:203–212
13. Nayak JK, Amer EH (2000) Experimental and theoretical evaluation of dynamic test procedures for solar flat plate collectors. *Sol Energy* 69:377–401
14. Badescu V (2005) Simulation analysis for the active solar heating system of a passive house. *Appl Therm Eng* 25:2754–2763
15. Badescu V (2008) Optimal control of flow in solar collector systems with fully mixed water storage tanks. *Energy Convers Manag* 49:169–184

16. Hobbi A, Siddiqui K (2009) Optimal design of a forced circulation solar water heating system for a residential unit in cold climate using TRNSYS. *Sol Energy* 83:700–714
17. Tiwari GN, Mishra RK, Solanki SC (2011) Photovoltaic modules and their applications: a review on thermal modeling. *Appl Energy* 88:2287–2304
18. Mishra RK, Tiwari GN (2013) Energy and exergy analysis of hybrid photovoltaic thermal water collector for constant collection temperature mode. *Sol Energy* 90:58–67
19. Duffie JA, Beckman WA (1991) *Solar engineering of thermal processes*, 2nd edn. Wiley-Interscience, New York
20. Rawlings R (2009) *Capturing solar energy* (CIBSE Knowledge Series)
21. Milani D, Abbas A (2016) Multiscale modeling and performance analysis of evacuated tube collectors for solar water heaters using diffuse flat reflector. *Renewable Energy* 86:360–374
22. Diego-Ayala U, Carrillo JG (2016) Evaluation of temperature and efficiency in relation to mass flow on a solar flat plate collector in Mexico. *Renewable Energy* 96:756–764
23. Ersöz MA (2016) Effects of different working fluid use on the energy and exergy performance for evacuated tube solar collector with thermosyphon heat pipe. *Renewable Energy* 96:244–256
24. Kalogirou SA, Karellas S, Badescu V, Braimakis K (2016) Exergy analysis on solar thermal systems: a better understanding of their sustainability. *Renewable Energy* 85:1328–1333
25. Colangelo G, Favale E, Miglietta P, Risi AD (2016) Innovation in flat solar thermal collectors: a review of the last ten years experimental results. *Renew Sustain Energy Rev* 57:1141–1159
26. Kalogirou SA, Karellas S, Braimakis K, Stanciu C, Badescu V (2016) Exergy analysis of solar thermal collectors and processes. *Prog Energy Combust Sci* 56:106–137
27. Sabiha MA, Saidur R, Mekhilef S, Mahian O (2015) Progress and latest developments of evacuated tube solar collectors. *Renew Sustain Energy Rev* 51:1038–1054
28. Mahian O, Kianifar A, Heris SZ, Wen D, Sahin AZ, Wongwises S (2017) Nanofluids effects on the evaporation rate in a solar still equipped with a heat exchanger. *Nano Energy* 36:134–155
29. Hamed M, Fellah A, Ben Brahim A (2014) Parametric sensitivity studies on the performance of a flat plate solar collector in transient behavior. *Energy Convers Manag* 78:938–947
30. Badar AW, Buchholz R, Ziegler F (2012) Single and two-phase flow modeling and analysis of a coaxial vacuum tube solar collector. *Sol Energy* 86:175–189
31. Kim Y, Seo T (2007) Thermal performance comparisons of the glass evacuated tube collectors with shapes of absorber tube. *Renewable Energy* 32:772–795
32. Zhao X, Wang Z, Tang Q (2010) Theoretical investigation of the performance of a novel loop heat pipe solar water heating system for use in Beijing, China. *Appl Therm Eng* 30:2526–2636
33. Nkwetta DN, Smyth M, Haghghi F, Zacharopoulos A (2013) Trevor hyde experimental performance evaluation and comparative analyses of heat pipe and direct flow augmented solar collectors. *Appl Therm Eng* 60:225–233
34. Tang R, Yang Y, Gao W (2011) Comparative studies on thermal performance of water-in-glass evacuated tube solar water heaters with different collector tilt-angles. *Sol Energy* 85:1381–1389
35. Xu L, Wang ZF, Yuan GF, Ruan Y (2012) A new dynamic test method for thermal performance of all-glass evacuated solar air collectors. *Sol Energy* 86:1222–1231
36. Kim JT, Ahn HT, Han H (2007) The performance simulation of all glass vacuum tubes with coaxial fluid conduit. *Int Commun Heat Mass Transfer* 34:587–597
37. Olivier G, Andre M, Bernard L, Olivier R (1986) The performance of solar heating, cooling and hot water systems using evacuated collectors: characterization of evacuated collectors, arrays and collection subsystems. IEA Report of Task VI 4–5:32–33
38. Bejan A (1978) General criterion for rating heat-exchanger performance. *Heat Mass Transfer* 21:655–658
39. Yunus CA, Micheal BA (2008) *Thermodynamic by engineering approach*, 5th ed. McGraw Hill

Simulation Studies on the Transition from Simple Expansion Chamber Muffler to Tapered Expansion Chamber Muffler



S. K. Vishwakarma and S. J. Pawar 

Abstract The pressure waves escape from the engine exhaust with a high velocity, producing an offensive exhaust noise. A properly designed exhaust silencer/muffler is helpful to reduce exhaust noise. In this paper, the effect of the shape variation in expansion chamber on the transmission loss of a reactive muffler (In line type) has been presented. The purpose of this paper is to evaluate the performance of the tapered expansion chamber muffler. The transfer matrix method is used for the evaluation of the transmission loss of the muffler. In addition, this paper discusses the shape variation from simple expansion chamber to tapered expansion chamber. The results revealed that as the area of tapered expansion chamber muffler approaches to the area of simple expansion chamber muffler, the transmission loss of both the mufflers become equal. Therefore, reactive muffler having combination of both designs can give the better performance.

Keywords Transfer matrix method · Tapered expansion chamber · Transmission loss

1 Introduction

Mufflers are the device used to suppress the noise originated from the IC engines, rotary fans, compressors, etc. Active and passive methods are the two methods for the suppression of noise. In the active method, a signal of the same frequency and opposite phase as of sound wave from the source is generated and by destructive interference the noise shall be suppressed. In the passive method, either geometrical modifications or sound-absorbing materials can be used for noise suppression.

S. K. Vishwakarma (✉) · S. J. Pawar
Motilal Nehru National Institute of Technology Allahabad, Prayagraj, UP 211004, India
e-mail: erskv1992@gmail.com

S. J. Pawar
e-mail: sjpawar@mnnit.ac.in

© The Author(s), under exclusive license to Springer Nature Singapore Pte Ltd. 2021
B. S. Sikarwar et al. (eds.), *Advances in Fluid and Thermal Engineering*,
Lecture Notes in Mechanical Engineering,
https://doi.org/10.1007/978-981-16-0159-0_34

389

The modeling of simple expansion chamber mufflers with the attention of the transmission line theory has been done. The equations for the pressure and acoustic particle velocity with the postulation of continuity of pressure and conservation of mass at area discontinuity have also been presented [1]. An analytical method for the investigation of a chamber having area discontinuities has been presented. The force oscillator method was employed for numerical analysis of the muffler [2]. The effect of the tailpipe length, impedance at the duct, and locations of measurement points on the performance parameters of muffler have been investigated. The transmission loss, insertion loss, and level difference for the muffler have been calculated and compared [3]. The sound propagation in a gradually varying circular cross-sectional duct has been analyzed. The varying cross section has been divided into a number of simple expansion chambers with a maximum area ratio of 1.05:1 [4]. The study of various methods for the calculation of the transmission loss has been presented. The transmission loss was used for evaluating the performance of mufflers. Methods used for calculation of the transmission loss were transfer matrix method, two load method, finite element method, numerical simulation, etc. [5]. A numerical method for higher-order modes of sound waves for a single expansion chamber has been presented with the medium as stationary. Results were compared with the result of the finite element method [6]. The effect of number of baffles and its position inside a gun silencer design have been presented using numerical, theoretical, and experimental studies [7].

The objective of this paper is to derive four pole parameters of tapered expansion chamber muffler and compute the transmission loss. This research paper contains following sections, viz. mathematical modeling, results and discussion, and conclusion.

2 Mathematical Modeling

Modeling of a traveling wave uses continuity condition and conservation of mass. The pressure for a 1D traveling wave is the superposition of incident wave and reflected wave. The pressure equation contains separate terms for the incident and reflected waves. Incident and reflected waves for inlet pipe, simple expansion chamber (length L), and outlet pipe have been shown in Fig. 1. It can be seen that there is no reflected wave in the outlet pipe. This is because of the assumption that the outlet pipe is infinitely long. The pressure equation for 1D traveling wave can be given by [3]:

$$P(x) = A * e^{-ikx} + B * e^{ikx} \quad (1)$$

where $k = \omega/c$ (ω is angular velocity and c is velocity of sound) is wave number, A and B are the coefficients for incident and reflected waves (Fig. 1), and $i = \sqrt{-1}$.

The particle velocity equation for a 1D traveling wave can be obtained by dividing the pressure with the impedance. The medium for the sound wave taken is

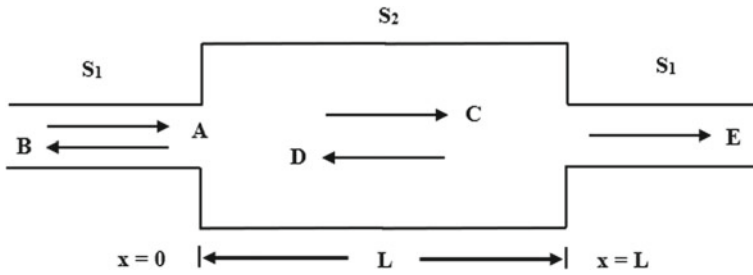


Fig. 1 Simple typical expansion chamber

air. The density (ρ) of air at 20 °C is 1.2 kg/m³. The particle velocity for the 1D traveling wave can be given by [3]:

$$V(x) = (A * e^{-ikx} - B * e^{ikx}) / (\rho * c) \tag{2}$$

By continuity, the pressure at the points just before the expansion and just after the expansion is equal. Similarly, the pressure at the points just before the contraction and just after the contraction is equal. By mass conservation, the mass of the particle is constant across all the junctions. Since the density of the medium is taken as constant, instead of mass one can equate the volume particle velocity at the junctions. With application of above conditions one can write:

$$A = C + D - B \tag{3}$$

$$C * e^{-ikL} + D * e^{ikL} + E * e^{-ikL} = 0 \tag{4}$$

$$A - B = (S_2/S_1) * (C - D) \tag{5}$$

$$(S_2/S_1) * (C * e^{-ikL} - D * e^{ikL} - E * e^{-ikL}) = 0 \tag{6}$$

Let, $(S_2/S_1) = m$

Above equations can be represented in the matrix form as:

$$\begin{bmatrix} -1 & 1 & 1 & 0 \\ 0 & \exp(-ikL) & \exp(ikL) & -\exp(-ikL) \\ 1 & m & -m & 0 \\ 0 & m * \exp(-ikL) & -m * \exp(ikL) & -\exp(-ikL) \end{bmatrix} \begin{bmatrix} B \\ C \\ D \\ E \end{bmatrix} = \begin{bmatrix} A \\ 0 \\ A \\ 0 \end{bmatrix} \tag{7}$$

Finally, the transmission loss can be obtained as [5]:

$$\text{Transmission loss} = 20 * \log_{10}(A/E) \tag{8}$$

2.1 Transfer Matrix for the Simple Expansion Chamber

Figure 2 shows the dimensions for the simple expansion chamber. The diameters for the inlet pipe, outlet pipe, and expansion chamber are 50 mm, 50 mm, and 150 mm, respectively. The length of the expansion chamber is 225 mm. The transfer matrix related the total sound pressure and volume velocity at two points in a mufflers. This method in acoustics domain is used when the complete system can be discretized and represented into a sequence of adjacent and interacting subsystems. Figure 3 shows the stations inside the expansion chamber upon which the acoustic variables are defined.

The sound pressure, P_i , and the volume velocity, V_i , on the inlet side of a muffler may be fully transferred to the outlet side (P_o, V_o) by using the transfer matrix, T , which consists of the four elements T_{11}, T_{12}, T_{21} , and T_{22} [5]. In the formulation, the mass velocity or volume velocity is used instead of acoustic particle velocity. The Y is characteristic impedance, defined as the ratio of acoustic pressure to the acoustic mass velocity.

$$\begin{bmatrix} P_i \\ V_i \end{bmatrix} = \begin{bmatrix} T_{11} & T_{12} \\ T_{21} & T_{22} \end{bmatrix} \begin{bmatrix} P_o \\ V_o \end{bmatrix} \tag{9}$$

$$Y = c/S \tag{10}$$

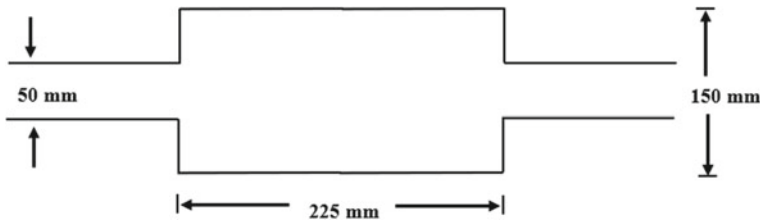


Fig. 2 Simple expansion chamber [6]

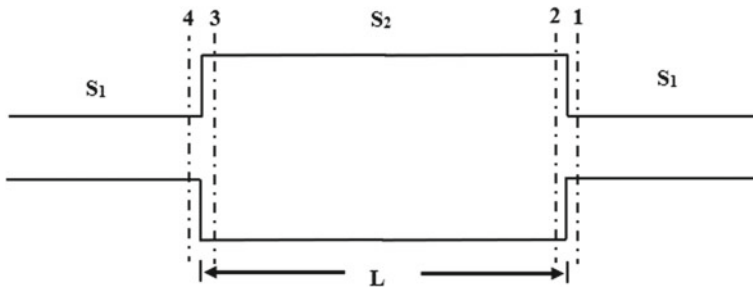


Fig. 3 Expansion chamber with stations

Relation among the variables of the station 1 and station 2 is as follows:

$$\begin{bmatrix} P_2 \\ V_2 \end{bmatrix} = \begin{bmatrix} 1 & 0 \\ 0 & 1 \end{bmatrix} \begin{bmatrix} P_1 \\ V_1 \end{bmatrix} \quad (11)$$

The same between station 3 and station 4 and station 2 and station 3 is as follows:

$$\begin{bmatrix} P_4 \\ V_4 \end{bmatrix} = \begin{bmatrix} 1 & 0 \\ 0 & 1 \end{bmatrix} \begin{bmatrix} P_3 \\ V_3 \end{bmatrix} \quad (12)$$

$$\begin{bmatrix} P_3 \\ V_3 \end{bmatrix} = \begin{bmatrix} T_{11} & T_{12} \\ T_{21} & T_{22} \end{bmatrix} \begin{bmatrix} P_2 \\ V_2 \end{bmatrix} \quad (13)$$

Using following boundary conditions:

$$T_{11} \text{ is } P_3 \text{ if } P_2 = 0 \text{ and } V_2 = 0 \quad (14)$$

$$T_{21} \text{ is } V_3 \text{ if } P_2 = 1 \text{ and } V_2 = 0 \quad (15)$$

$$T_{12} \text{ is } P_3 \text{ if } P_2 = 0 \text{ and } V_2 = 1 \quad (16)$$

$$T_{22} \text{ is } V_3 \text{ if } P_2 = 0 \text{ and } V_2 = 1 \quad (17)$$

The pressure equation and velocity equation for a traveling wave can be as follows [3]:

$$P(x) = A * e^{-ikx} + B * e^{ikx} \quad (18)$$

$$V(x) = (A * e^{-ikx} - B * e^{ikx})/Y \quad (19)$$

On applying the boundary conditions (Eqs. 14 and 15) in Eqs. 18 and 19, values of pressure and velocity at $x = -L$ can be as follows:

$$P(-L) = \cos(kL) = T_{11} \quad (20)$$

$$V(-L) = (i * \sin(kL))/Y = T_{21} \quad (21)$$

On applying the boundary conditions (Eqs. 16 and 17) in Eqs. 18 and 19, values of pressure and velocity at $x = -L$ can be as follows:

$$P(-L) = i * Y * \sin(kL) = T_{12} \quad (22)$$

$$V(-L) = \cos(kL) = T_{22} \quad (23)$$

As per Eq. 7, one can obtain:

$$\begin{bmatrix} P_4 \\ V_4 \end{bmatrix} = \begin{bmatrix} \cos(kL) & i * Y * \sin(kL) \\ i/Y * \sin(kL)/2 & \cos(kL) \end{bmatrix} \begin{bmatrix} P_1 \\ V_1 \end{bmatrix} \tag{24}$$

The transmission loss of simple expansion chamber can be obtained as [5]:

$$TL = 20 * \log \left\{ \left(\cos(kL) + (i * (Y_2/Y_1) * \sin(kL)/2) + \left(i * \left(\frac{Y_3}{Y_2} \right) * \frac{\sin(kL)}{2} \right) \right) \right\} \tag{25}$$

2.2 Transfer Matrix for Tapered Expansion Chamber

The smaller and larger diameters for the tapered expansion chamber (Fig. 4) are taken as 100 and 150 mm with the same length as of the simple expansion chamber. The variation of the area with the length of the expansion chamber is linear and can be given by:

$$S = \left(S_2 + \frac{(S_3 - S_2)}{L} * L(x) \right) \tag{26}$$

In Fig. 4, S_1 , S , and S_1 are the area of cross sections for the inlet pipe, tapered expansion chamber (length dependent), and outlet pipe, respectively. Let S_2 and S_3 are the areas of the circular cross section for 100 mm diameter and 150 mm diameters, respectively. The relation of the diameter of the inlet pipe to the minimum diameter of the expansion chamber to the maximum diameter of the expansion chamber is 1:2:3. The transfer matrix elements for the tapered expansion chamber are:

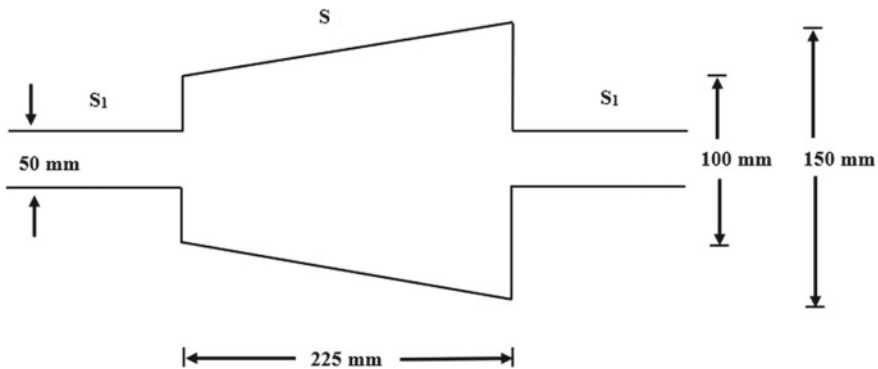


Fig. 4 Tapered expansion chamber

$$T_{11} = \cos(kL) \quad (27)$$

$$T_{12} = i * Y * \sin(kL) \quad (28)$$

$$T_{21} = (i/Y) * \sin(kL)/2 \quad (29)$$

$$T_{22} = \cos(kL) \quad (30)$$

The transmission loss of tapered expansion chamber can be given by Eq. 25.

3 Results and Discussion

The transmission losses of mufflers are used for the performance estimation of mufflers. Variations of the transmission loss with frequency, variations of Y with length of the expansion chamber, and variations of the transmission loss with impedance of the expansion chamber have been presented and discussed.

3.1 Comparison Between the Transmission Loss of Both Mufflers

The variation of the transmission loss with frequency for the simple expansion chamber and tapered expansion chamber has been shown in Fig. 5. The transmission loss for the simple expansion chamber having expansion area ratio 9 was calculated and validated with the work of Munjal [6]. After the validation of the model for the simple expansion chamber, the shape of expansion chamber was modified to the tapered expansion chamber and simulated. The range of frequency is taken from 0 to 3000 Hz. The Scilab (open-source software for numerical computation) has been used for the evaluation of the transmission loss of the different mufflers. From Fig. 5, it is clearly depicted that there is a constant trend in the transmission loss of a simple expansion chamber for the entire frequency range. This is due to the constant area of the expansion chamber for the whole length of the chamber.

Due to the constant area for the simple expansion chamber muffler, there is no impedance mismatch in the chamber and hence no reflection of waves. Impedance mismatch of waves can be increased by varying the area of the expansion chamber. The transmission loss of the tapered expansion chamber (solid (red) curve) shows some increase in the transmission loss in the chosen frequency range. This increment in transmission loss is because of the additional impedance mismatch of

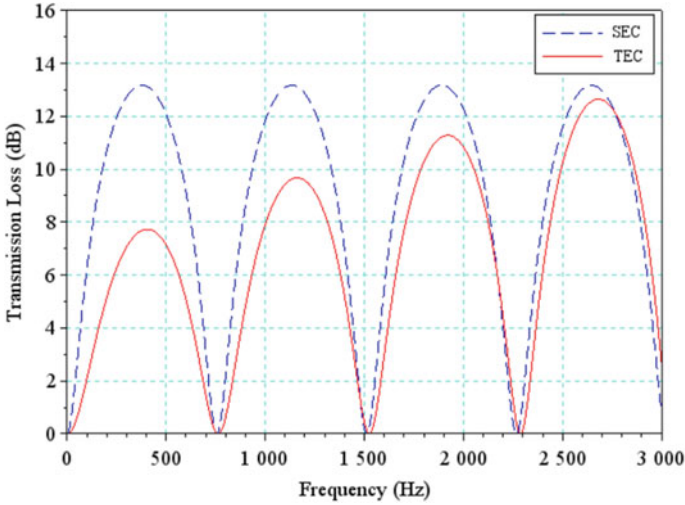


Fig. 5 Comparison of the transmission loss of simple and tapered expansion chambers

waves along the length of the chamber. This additional impedance mismatch is due to the variation in the area along the length of the chamber. As the area of the tapered chamber approaches the area of the expansion chamber, the transmission loss of both models becomes approximately the same.

3.2 Variation of the Characteristic Impedance (Y) with the Length of Muffler

The Y is a function of sound velocity and area of the expansion chamber as mentioned in Eq. 10. The variation of Y with the length of the simple expansion chamber muffler and the tapered expansion chamber muffler is shown in Fig. 6. As the area of the tapered expansion chamber is varying linearly with the length of the expansion chamber (Eq. 26), impedance also varies with the length of the expansion chamber. The Y for the simple expansion (dashed (blue) curve) chamber remains constant throughout the length. The Y for the tapered expansion chamber is varying from its maximum value to minimum value along the length of the muffler. The area is minimum at the entry and maximum at the exit of tapered expansion chamber. Therefore, the Y has its maximum value at the entry and minimum value at the exit of the tapered expansion chamber.

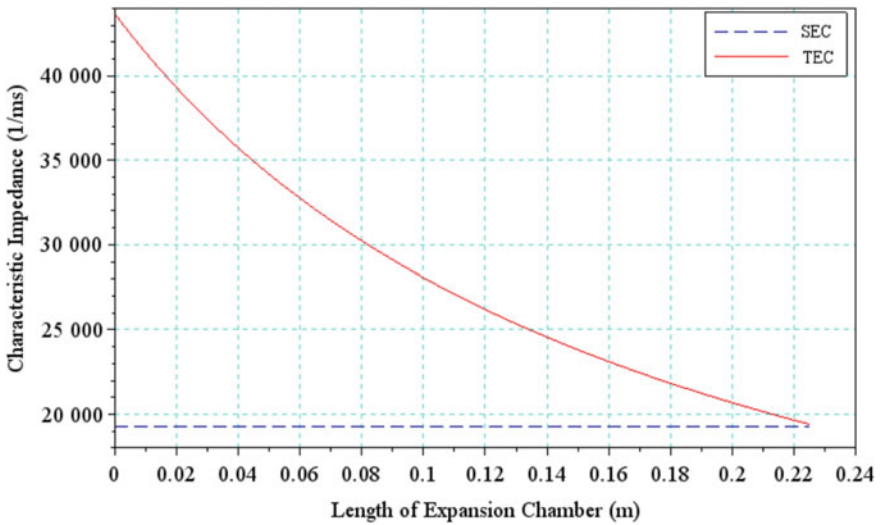


Fig. 6 Variation of characteristic impedance with length of expansion chamber

3.3 Variation of Transmission Loss with the Characteristic Impedance (Y)

Figure 7 shows the variation of the transmission loss with Y . The curve between transmission loss and Y also confirms the same behavior. When Y is at its lowest

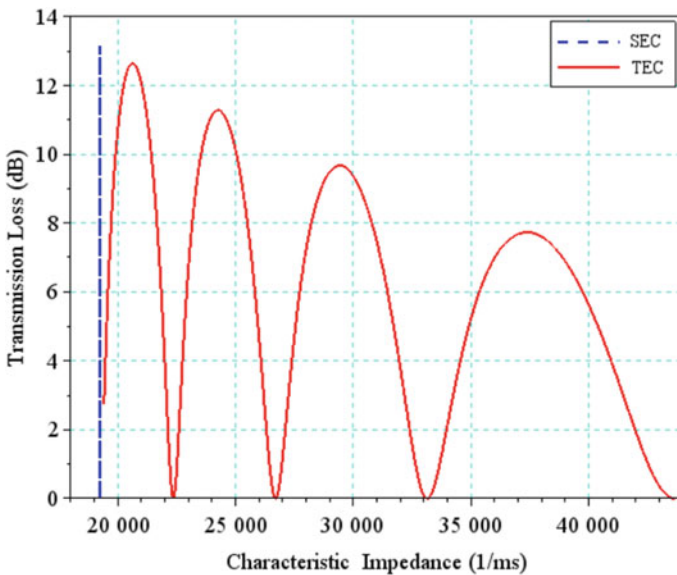


Fig. 7 Variation of transmission loss with characteristic impedance

value the transmission loss is maximum. The transmission loss decreases with the increase in the Y because of the less reflection of sound waves as compared to the right extreme of the expansion chamber.

4 Conclusion

The transfer matrix method has been used for the estimation of the transmission loss of mufflers. The area variation for the tapered expansion chamber was linear. The transmission losses for differently shaped expansion chamber were derived from the required boundary conditions. Through the comparison between the transmission losses of both the mufflers, it was found that there were more impedance mismatches along the length of the tapered expansion chamber. This was due to the area variation along the length of the expansion chamber. More impedance mismatch resulted in more reflection of sound waves inside the expansion chamber and hence transmission loss was showing an increase in its value. The characteristic impedance for simple expansion chamber was constant and hence the transmission loss was constant along the length of the muffler. From the analysis of the transmission loss and Y of the simple expansion chamber and tapered expansion chamber, it was found that tapered expansion chamber introduced additional impedance mismatches along the length and hence acted as a hindrance for the incident sound waves. Therefore, the tapered expansion chamber can be incorporated in the design of muffler according to the cost of the muffler, ease in the process of manufacturing the tapered section of the expansion chamber.

References

1. Davis DD, Stokes JM, Moorse SL (1954) Theoretical and experimental investigation of mufflers with components on engine muffler design. NACA Report, p 1192
2. Miles J (1944) The reflection of sound due to change in cross section of a circular tube. *J Acoust Soc Am* 16:14–19
3. Lee JK, Oh KS, Lee JW (2020) Methods for evaluating in-duct noise attenuation performance in a muffler design problem. *J Sound Vib* 464
4. Alfredson RJ (1972) The propagation of sound in a circular duct of continuously varying cross-sectional area. *J Sound Vib* 23(4):433–442
5. Gupta AK, Tiwari A (2015) Transfer matrix method for noise attenuation on single expansion chamber muffler having central inlet and central outlet with experimental techniques and FEA validation. *Int J Theor Appl Sci* 7(2):14–20
6. Munjal ML (1987) A simple numerical method for three-dimensional analysis of simple expansion chamber mufflers of rectangular as well as circular cross-section with a stationary medium. *J Sound Vib* 116(1):71–88
7. Arslan H, Ranjbar M, Secgin E, Celik V (2020) Theoretical and experimental investigation of acoustic performance of multi-chamber reactive silencers. *Appl Acoust* 157

Comparison of Supersonic Flow Regime for Two Different Symmetric Biconvex Circular-Arc Aerofoil



Rakesh Prasad, Sandeep Agarwal, Devendra Singh,
and Manipal Singh

Abstract Aerofoils NACA 2S-(50)(05)-(50)(05) and NACA 2S-(75)(05)-(75)(05), 2D symmetric biconvex circular arc are considered for analysis of supersonic regime. The work is aimed to determine the effect on force characteristics by shifting the location of maximum thickness toward the trailing edge. Fluent (Ansys V 12.0) tool is used for the study with the consideration of unsteady, viscous and laminar compressible flow model at three different angles of attack at $\alpha = 0^\circ, 10^\circ, 20^\circ$ in the Mach number range of (1.25–2.13) keeping Reynolds number fixed at 5×10^5 . It is found that there is a slight reduction of drag by shifting its location at $\alpha = 0^\circ$ and higher L/D ratio also achieved at higher Mach no. for $\alpha = 10^\circ$ and 20° because of a high intensity shock wave at beneath surface.

Keywords Viscous · Laminar · Compressible flow · Symmetric biconvex circular-arc aerofoil

1 Introduction

Interest in commercial supersonic aircraft has persisted for many decades, certainly since the celebrated breaking of the “sound barrier” at the end of 1947, after that, the importance of supersonic study offers attention to the researchers. The aerodynamic parameters are notably dependent on the design of the aerofoils, therefore great

R. Prasad (✉) · S. Agarwal
Hindustan College of Science and Technology, Mathura, India
e-mail: rprasadrose@gmail.com

S. Agarwal
e-mail: sandeep.agarwal@sgei.org

D. Singh
Sachdeva Institute of Technology, Mathura, India
e-mail: devendra.17@rediffmail.com

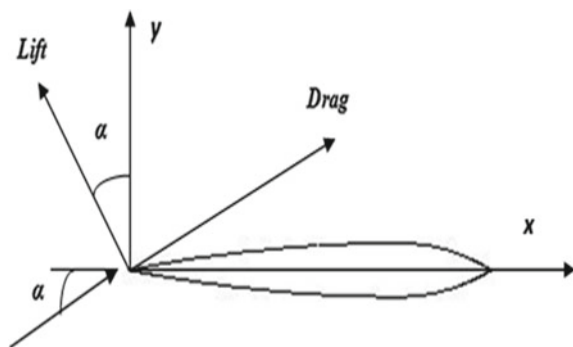
M. Singh
Shriram College of Engineering and Management, Palwal, India
e-mail: manipalsinghdhakrey@gmail.com

efforts are done by the researchers in order to minimize the drag co-efficient and enhance the lift-drag ratio. Although a large number of studies, both experimental and numerical have been done for biconvex circular-arc aerofoil at variable Mach no. during supersonic flow for the characterization of aerodynamic behavior, and only a few are available in the public domain. Lindsey et al. [1] investigated experimentally the flow and force characteristics of five supersonic aerofoils and, for comparison, two subsonic aerofoils at high subsonic speeds in the Mach number range 0.30–0.90 at angles of attack from 0° to 4° with Reynolds number ranged from 0.9×10^6 to 1.5×10^6 . Mayer [2] analyzed various forces of shock waves by using a semi-empirical method and compared the results with the experimental data. Eggers and Syvertson [3] investigated analytically steady inviscid flow about 10% thick biconvex circular-arc aerofoil at high supersonic speeds. The range of Mach number considered for this analysis was from 3.5 to 15, and the angle of attack was varied from 0° to 30° . Katzen et al. [4] studied various profiles for aerodynamics influence. Blunt-trailing-edge airfoils analysis had been done by Chapman [5]. Levy [6] performed an experimental study on steady and unsteady transonic flow on 14% thick symmetric biconvex aerofoil with a Mach number range of 0.81–0.85 at an angle of attack of 0° and a Reynolds number of 7×10^6 . Chen et al. [7] have done eddy simulation for a free-stream Mach number $M = 0.76$ and a Reynolds number $Re = 1.1 \times 10^7$. Akram [8] investigated numerically the flow dynamics of a biconvex circular-arc and new cusped leading-edge aerofoil by varying the Mach number from (0.5–2.13) at three different angles of attack keeping Reynolds number fixed at considering laminar, viscous, compressible model.

Since Akram [8] has been investigated the aerodynamics co-efficients and Spatio-temporal response of symmetric biconvex circular-arc aerofoil whose maximum thickness is at 50% from the leading edge, i.e., NACA 2S-(50)(05)-(50)(05); therefore, the aim of this work is to determine the effects on global flow parameters by shifting the location of maximum thickness hence, another symmetrical biconvex circular-arc aerofoil is considered whose location of maximum thickness is at 75% from the leading edge, i.e., NACA 2S-(75)(05)-(75)(05) keeping thickness to be constant.

Aerofoil coordinate generated by use Fortran and all the numerical investigations are carried out under the same condition only in supersonic regime, i.e., Mach number varies from (1.25–2.13). The geometry of symmetric biconvex circular-arc aerofoil NACA 2S-(75)(05)-(75)(05) shown in Fig. 1.

Fig. 1 Geometry of biconvex circular-arc aerofoil



Nomenclature

F_D	drag force
F_L	lift force
M	pitching moment about leading edge of aerofoil
C_D	drag co-efficient
C_L	lift co-efficient
C_M	moment co-efficient
C_P	pressure co-efficient \bar{k} thermal conductivity
C_v	specific heat at constant volume $\bar{\mu}$ viscosity
ϕ_F, ϕ_G	quantities in the flux vectors
\bar{x}, \bar{y}	cartesian spatial coordinate
\bar{Q}	conservative variables vectors
\bar{F}, \bar{G}	total flux vectors
\bar{p}	thermodynamic pressure
T	non-dimensional time ρ_∞ free stream density
T	non-dimensional temperature
\bar{t}	time
$\bar{\rho}$	density
\bar{T}	temperature
\bar{u}, \bar{v}	velocity components
\bar{E}	total specific energy
R	universal gas constant
A	reference area (1 m ²)
l	reference length (chord length)
p_∞	free stream pressure
u_∞	free stream velocity
α	angle of attack

2 Governing Equations and Boundary Conditions

The two-dimensional, unsteady, compressible Navier-Stokes equations are a set of four coupled, non-linear partial differential equations. The governing equations for unsteady, compressible gas dynamics in the framework is written in the most conservative form as,

$$\frac{\partial \bar{Q}}{\partial \bar{t}} + \frac{\partial \bar{F}}{\partial \bar{x}} + \frac{\partial \bar{G}}{\partial \bar{y}} = \bar{J}$$

$$\bar{Q} = \begin{Bmatrix} \bar{\rho} \\ \bar{\rho}\bar{u} \\ \bar{\rho}\bar{v} \\ \bar{\rho}\bar{E} \end{Bmatrix}, \bar{F} = \begin{Bmatrix} \bar{\rho}\bar{u}^2 + \bar{p} + \frac{2}{3}\bar{u}(\nabla \cdot \bar{U}) - 2\bar{u}\frac{\partial\bar{u}}{\partial\bar{x}} \\ \bar{\rho}\bar{u}\bar{v} - \bar{u}\left(\frac{\partial\bar{v}}{\partial\bar{x}} + \frac{\partial\bar{u}}{\partial\bar{y}}\right) \\ \bar{\rho}\bar{u}\bar{h}_T - \bar{k}\frac{\partial\bar{T}}{\partial\bar{x}} + \phi_F \end{Bmatrix}, \bar{G} = \begin{Bmatrix} \bar{\rho}\bar{v}^2 + \bar{p} + \frac{2}{3}\bar{v}(\nabla \cdot \bar{U}) - 2\bar{v}\frac{\partial\bar{v}}{\partial\bar{x}} \\ \bar{\rho}\bar{u}\bar{v} - \bar{u}\left(\frac{\partial\bar{v}}{\partial\bar{x}} + \frac{\partial\bar{u}}{\partial\bar{y}}\right) \\ \bar{\rho}\bar{v}\bar{h}_T - \bar{k}\frac{\partial\bar{T}}{\partial\bar{y}} + \phi_G \end{Bmatrix},$$

$$\bar{J} = \begin{Bmatrix} 0 \\ 0 \\ 0 \\ 0 \end{Bmatrix} \phi_F = \mu \left[\frac{2}{3}\bar{u}\left(\frac{\partial\bar{v}}{\partial\bar{y}} - \frac{2\partial\bar{u}}{\partial\bar{x}}\right) - \bar{v}\left(\frac{\partial\bar{v}}{\partial\bar{x}} + \frac{\partial\bar{u}}{\partial\bar{y}}\right) \right] \phi_G = \mu \left[\frac{2}{3}\bar{v}\left(\frac{\partial\bar{u}}{\partial\bar{x}} - \frac{2\partial\bar{v}}{\partial\bar{y}}\right) - \bar{u}\left(\frac{\partial\bar{v}}{\partial\bar{x}} + \frac{\partial\bar{u}}{\partial\bar{y}}\right) \right]$$

The gravity term is dropped as they are generally very weak in high-speed flows. The total specific energy and enthalpy are defined as, $\bar{E} = \bar{e} + \frac{\bar{U}\cdot\bar{U}}{2}$, $\bar{h}_T = \bar{E} + \frac{\bar{e}}{\rho}$.

The above system of equations is closed by bringing in the ideal gas assumption, $\bar{p} = \bar{\rho}R\bar{T}$, $\bar{e} = C_v\bar{T}$.

In order to determine the accurate solution of the governing equation of fluid flow, proper boundary conditions play a vital role. Therefore, these are the conditions that are implied for this investigation. The adiabatic condition of the wall and no-slip was assumed for aerofoil. Mathematically,

$$\bar{V} = (\text{Cos } \alpha\hat{i} + \text{Sin } \alpha\hat{j}), T = 1, \rho = 1$$

However, computations of external flow past an aerofoil have to be conducted on a finite domain. For this reason, artificial (far field) boundary conditions become necessary. The numeric computations of a circular boundary concentric with the aerofoil is used, which truncate the infinite domain and encase as shown in Fig. 2.

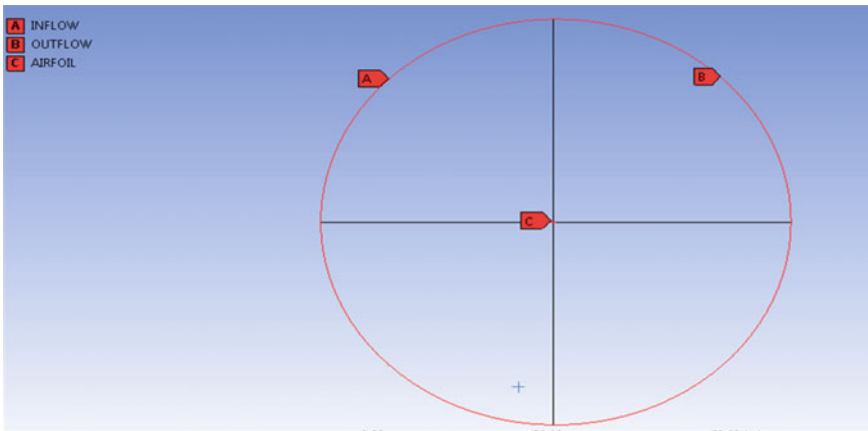


Fig. 2 Artificial boundaries around the aerofoil

Ansys Fluent is used as the CFD solver in which the circular domain is splits into two equal halves namely inflow and outflow and the boundary condition of far-field pressure are employed as per Akram [8].

3 Computational Details

In order to capture the flow physics accurately, near the aerofoil, various parameters are involved, these are: minimum grid size near the aerofoil, time step size, and scheme. ICEM CFD is used for generating multi-block structured mesh shown in Fig. 3 with the order of near the aerofoil, having 1,34,100 total number of nodes in the whole domain which is sufficient to perform calculation accurately in the optimum time step size of sec. For solving the numerical scheme, finite volume discretizing method is employed by using ANSYS Fluent commercial software. The study of an implicit formulation is density-based; second-order upwind scheme with the Roe's flux-difference splitting is applied to capture the discontinuity caused by the shock waves. Since the present work is for a comparative study between two symmetric biconvex circular-arc, therefore all the simulations for the aerofoil NACA 2S-(75)(05)-(75)(05) are performed under same consideration (regarding grid size, time step, and scheme)at which Akram [8] has already investigated. The non-dimensional aerodynamic co-efficients are defined as follows:

$$C_p = \frac{p - p_\infty}{\frac{1}{2}\rho_\infty u_\infty^2} \quad C_D = \frac{F_D}{\frac{1}{2}\rho_\infty u_\infty^2 A} \quad C_L = \frac{F_L}{\frac{1}{2}\rho_\infty u_\infty^2 A} \quad C_m = \frac{M}{\frac{1}{2}\rho_\infty u_\infty^2 AL}$$

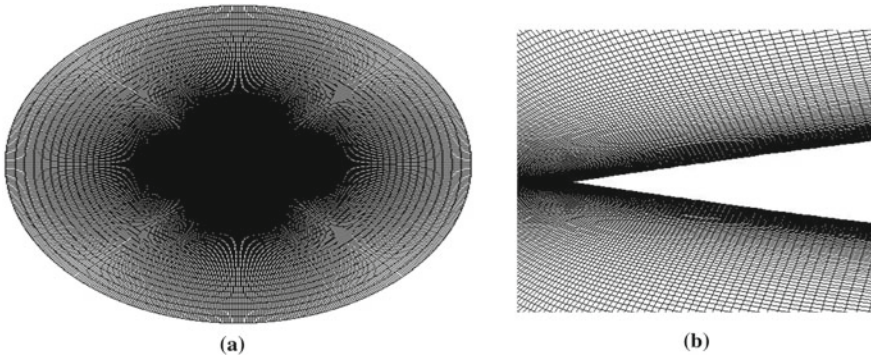


Fig. 3 **a** Structured mesh around the aerofoil, **b** Close up view of the grid generated around the aerofoil

4 Results and Discussion

In order to explain the flow dynamics, spatial flow patterns are presented by instantaneous streamlines and pressure contours. For visualizing the shock waves pattern, schlieren images are the appropriate way; therefore, these patterns are also generated. The pressure distribution over the surface of the aerofoil is demonstrated in the form of the co-efficient of pressure. The temporal dynamics are presented by the time histories of global flow parameters such as co-efficient of drag and co-efficient of lift. Figure 4 shows the instantaneous streamlines pattern for the flow past over the aerofoil NACA 2S-(75)(05)-(75)(05).

From the above contour plot, it is clearly visible that when the flow direction changes from ($\alpha = 0^\circ-20^\circ$) the flow separation shifted from trailing edge toward the leading edge of aerofoil. At $\alpha = 0^\circ$, lower drag has been achieved for the aerofoil NACA 2S-(75)(05)-(75)(05) as compared to NACA 2S-(50)(05)-(50)(05) because of smaller bow shock distance with respect to the aerofoil used by Akram [8], it is shown by pressure contour plots Fig. 5. At Mach = 1.25, the bow shock distance for the aerofoil NACA 2S-(75)(05)-(75)(05) is 0.024 m, whereas for the aerofoil NACA 2S-(50)(05)-(50)(05), it is about 0.058 m which causes a slight reduction of drag co-efficient. Furthermore, as Mach number increases, the distance between the shock wave and the leading edge of the aerofoil decreases result with the formation of weaker attached oblique shock wave for both the aerofoils as a result drag co-efficient decreases.

The surface distribution of co-efficient of pressure over the aerofoil NACA 2S-(75)(05)-(75)(05) and NACA 2S-(50)(05)-(50)(05)at $\alpha = 10^\circ$ for different super-sonic Mach numbers are shown in Fig. 6.

Figure 6 shows the variation of pressure co-efficient over the aerofoil; it is clearly depicted from the plot that as the Mach number increases for a fixed $\alpha = 10^\circ$, the pressure difference between the upper and lower surfaces of aerofoil decreases thereby, decreasing the lift co-efficient. From the above plots, we have seen that for the aerofoil NACA 2S-(75)(05)-(75)(05), the pressure co-efficient suddenly decreases at about $x/c = 0.75$ (which is the location of maximum thickness) due to the formation Prandtl Mayer expansion wave.

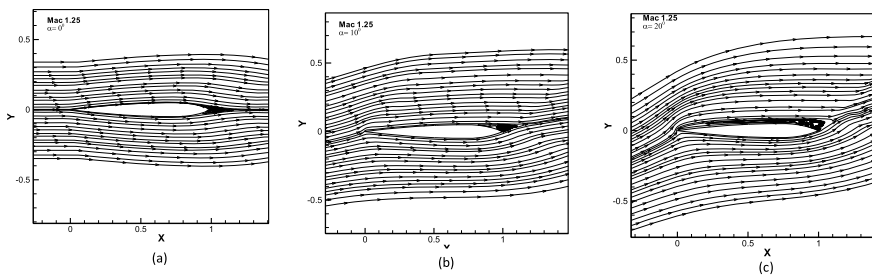


Fig. 4 Instantaneous streamlines at Mach = 1.25 for $\alpha = 0^\circ, 10^\circ, 20^\circ$

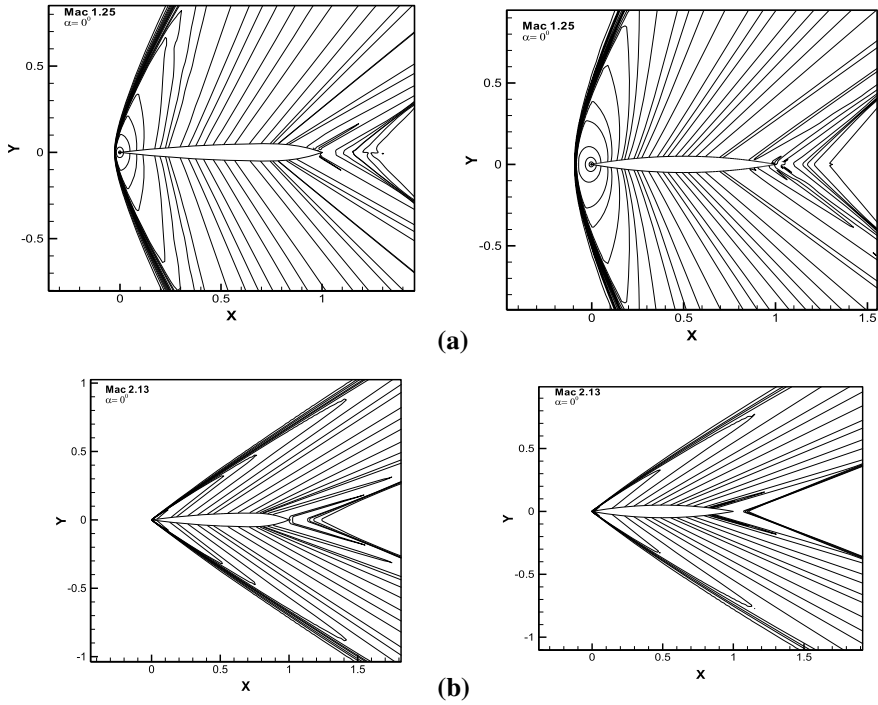


Fig. 5 **a** Instantaneous pressure plots at $\alpha = 0^\circ$ and Mach = 1.2, **b** instantaneous pressure plots at $\alpha = 0^\circ$ and Mach = 2.13

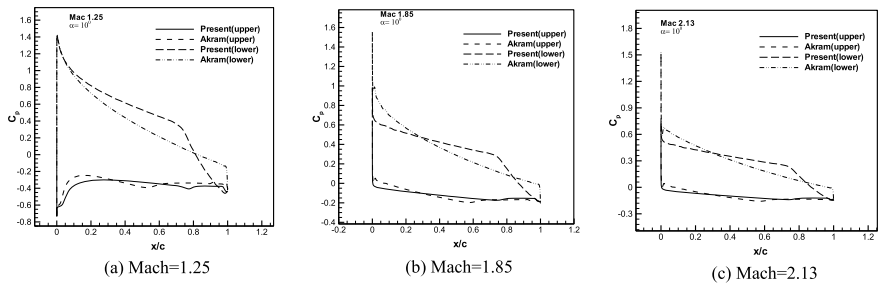


Fig. 6 Co-efficient of pressure plots at $\alpha = 10^\circ$, **a** Mach = 1.25, **b** Mach = 1.85, **c** Mach = 2.13

Lift-co-efficient for the present the aerofoil is slightly larger than Akram [8] because of larger difference of pressure between the upper and lower surface as shown in the above plots. In order to visualize the compressible flow, a Schlieren image plays a vital role, as we have seen from Fig. 7 which captures only the shock wave pattern. As the above plots showed that at Mach = 1.85 when the flow direction changes from ($\alpha = 0^\circ-20^\circ$), an oblique shock wave transforms into a bow

shock and as a result drag co-efficient increases. From Fig. 4c, the flow is completely separated from the upper surface of aerofoil but still lift co-efficient is achieved because of stronger bow impulsive wave is generated beneath of aerofoil as shown in Fig. 7c. Figures 8 and 9 show the time histories of the global flow parameters namely the co-efficient of drag and co-efficient of lift of NACA 2S-(75)(05)-(75)(05).

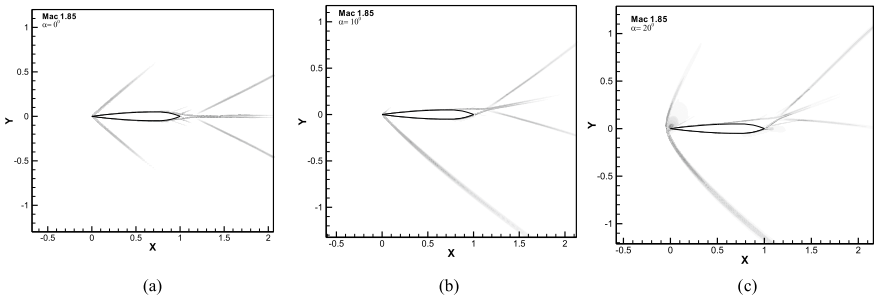


Fig. 7 Schlieren images for Mach = 1.85, a $\alpha = 0^\circ$, b $\alpha = 10^\circ$, c $\alpha = 20^\circ$

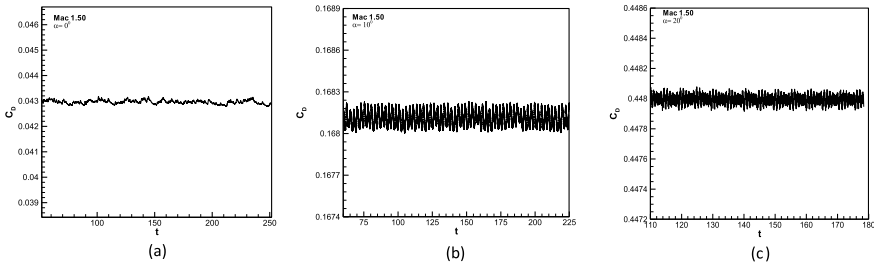


Fig. 8 Time histories of drag co-efficients for aerofoil at Mach = 1.50, a $\alpha = 0^\circ$, b $\alpha = 10^\circ$, c $\alpha = 20^\circ$

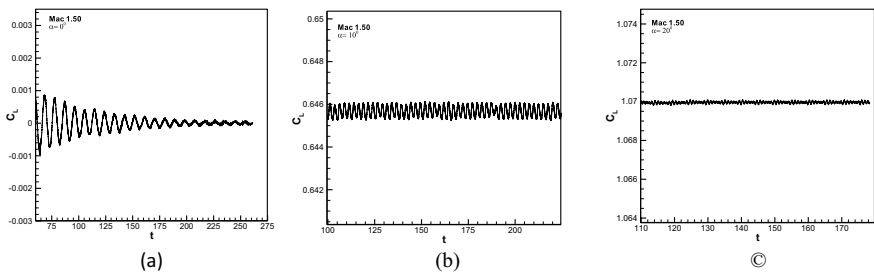


Fig. 9 Time histories of lift coefficients for aerofoil at Mach = 1.50, a $\alpha = 0^\circ$, b $\alpha = 10^\circ$, c $\alpha = 20^\circ$

Table 1 Comparison of aerodynamic parameters of NACA 2S-(75)(05)-(75)(05) with that of NACA 2S-(50)(05)-(50)(05) aerofoil

α	∞	Present				Akram [8]			
		C_D	C_L	$C_{M,LE}$	L/D	C_D	C_L	$C_{M,LE}$	L/D
0°	1.25	0.064	0.00	0.00	0.00	0.068	0.00	0.00	0.00
	1.50	0.042	0.00	0.00	0.00	0.050	0.00	0.00	0.00
	1.85	0.031	0.00	0.00	0.00	0.036	0.00	0.00	0.00
	2.13	0.026	0.00	0.00	0.00	0.029	0.00	0.00	0.00
10°	1.25	0.204	0.807	0.293	3.956	0.172	0.702	0.255	4.081
	1.50	0.169	0.649	0.248	3.845	0.153	0.585	0.221	3.823
	1.85	0.116	0.449	0.183	3.870	0.118	0.445	0.175	3.771
	2.13	0.095	0.365	0.149	3.842	0.096	0.362	0.144	3.770
20°	1.25	0.502	1.207	0.505	2.404	0.473	1.169	0.530	2.471
	1.50	0.450	1.076	0.446	2.391	0.431	1.061	0.466	2.461
	1.85	0.393	0.932	0.398	2.371	0.312	0.691	0.382	2.214
	2.13	0.336	0.800	0.348	2.380	0.311	0.687	0.334	2.209

In the above plot, the value of the co-efficient of drag increases due to the formation of bow shock at a higher angle of attack. There is no lift generation at an angle of attack of 0° because the pressure distribution is exactly the same on the upper and lower surfaces of the aerofoil due to its symmetry about the chord line. Figure 9 depicts that for the fixed Mach number 1.50 by varying the $\alpha = 0^\circ-20^\circ$, lift-co-efficient increases because at higher the angle of the attack bow shock is formed.

The comparative computational results of the present aerofoil NACA 2S-(75)(05)-(75)(05) as per Akram [8], i.e., with NACA 2S-(50)(05)-(50)(05) for drag, lift moment co-efficients and lift to drag ratio are shown in Table 1.

5 Conclusion

The symmetric biconvex circular-arc of an aerofoil NACA 2S-(75)(05)-(75)(05) is investigated numerically for supersonic aerodynamic characteristics. The numerical experiments solve the momentum and energy equation at $Re =$ and $Pr = 0.7$ for three different angle of attack at $\alpha = 0^\circ, 10^\circ, 20^\circ$ in the Mach number range of (1.25–2.13). All the investigation is performed with the same parameters with which the Akram [8] has done for another symmetric biconvex circular-arc aerofoil NACA 2S-(50)(05)-(50)(05) for the comparative study.

From the investigation, various important outcomes are drawn. It is found that at $\alpha = 0^\circ$ co-efficient of drag of the present aerofoil is smaller than the Akram [8] because of the small gap between a shock wave and the leading edge of aerofoil at lower Mach whereas for higher Mach weaker oblique attached shock waves are

formed. Since the aerofoil is symmetrical about the chord line, therefore, zero lift-co-efficient is achieved at $\alpha = 0^\circ$. At a higher angle of attack, lift co-efficient for the aerofoil NACA 2S-(75)(05)-(75)(05) is slightly larger than NACA 2S-(50)(05)-(50)(05) because of shifting the location of maximum thickness causes bow shock at large distance from the leading edge, whereas for the fixed angle of attack at higher Mach number large L/D ratio is achieved for the present aerofoil. In order to analyze the complete flow dynamics, further investigation is needed in the subsonic and transonic regime as well as the effect of Re to be investigated in detail.

References

1. Lindsey WF, Daley BN, Humphreys MD (1947) The flow and force characteristics of supersonic airfoils at high subsonic speeds. NACA TN 1211
2. Mayer JP (1949) Estimation of lift and drag of airfoils at near sonic speeds and in the presence of detached shock waves. NACA RM No. L8L07
3. Eggers AJ, Syvertson CA (1952) Inviscid flow about airfoils at high supersonic speeds. NACA TN 2646
4. Katzen ED, Kuehn DM, Hill WA (1957) Investigation of the effects of profile shape on the aerodynamic and structural characteristics of thin, two-dimensional airfoils at supersonic speeds. NACA TN 4039
5. Chapman DR (1955) Reduction of profile drag at supersonic velocities by the use of airfoil sections having a blunt trailing edge. NACA TN 3503
6. Levy LL Jr (1981) Predicted and experimental steady and unsteady transonic flows about a biconvex airfoil. NASA-TM- 81262
7. Chen L-W, Xu C-Y, Lu X-Y (2010) Numerical investigation of the compressible flow past an aerofoil. *J Fluid Mech* 643:97–126, Cambridge University Press 2009, <https://doi.org/10.1017/s0022112009991960>
8. Akram S (2013) The dynamics of flow past a new cusped leading edge airfoilin subsonic and supersonic flow regimes. M. Tech thesis, Aligarh Muslim University, Aligarh, India

Effects of Surface Geometries and Fin Modifications on the Thermal Performance of Solar Air Heaters: A Review



Rahul Khatri, Shyam Sunder Sharma, Shlok Goswami,
Shubham Sharma, and Mohd. Anas

Abstract Air heaters using solar energy are generally used for heating and drying applications, but lower heat transfer rates during the fluid passage result in low thermal performance. Surface geometry and fin modifications can result in higher thermal performance and lower heat losses. Studies suggested that artificial surface geometries (absorber plates with conical surfaces, ribbed surfaces) and fin modifications (wavy fins, inclined prismatic triangle fins) affect the heat transfer; as a result, both modifications are very effective for improving the performance of the system. These modifications along with the optimized working parameters can contribute a substantial development in the overall working of solar air heaters (SAH). This review presents effects of various types of surface geometries and fin modifications with specific working parameters and their potential effects on the performance of SAH.

Keywords SAH · Thermal performance · Surface geometry · Fin modifications

1 Introduction

Renewable energy is proved to be an alternate to the conservation of conventional sources of energy. Sun's radiations are available abundantly and free of cost which can be utilized in many industrial and domestic applications. Solar air heaters

R. Khatri (✉) · S. S. Sharma · S. Goswami · S. Sharma · Mohd. Anas
Manipal University Jaipur, Jaipur 303007, India
e-mail: rahul.khatri@jaipur.manipal.edu

S. S. Sharma
e-mail: shyamsunder.sharma@jaipur.manipal.edu

S. Goswami
e-mail: shlokgoswami13@gmail.com

S. Sharma
e-mail: sharma98shubham@gmail.com

Mohd. Anas
e-mail: mohdsaif96sdm@gmail.com

(SAH) use air to absorb and exchange heat; it has become very popular in winter prominent locations and proved to have high energy saving potential. They are commonly utilized for heating air and drying applications. It consists of a fluid channel with glazing surface and a collector plate confined in a frame which is completely insulated. It is economical, light weight and user friendly; however, its use is limited because of its low energy efficiency. This review provides a wide view on the modifications in SAH and performance parameters with their potential effect on the performance of SAH.

To enhance the performance, heat transfer between the air and the collector plate must be improved, while minimizing thermal losses. Turbulence in the flow can be increased using turbulators for creating higher contact between fluid and collector. Installing ribs, creating grooves and artificially roughened surfaces can also have positive effect on the performance of SAH. Efficiency increment of 9% was observed with ribs even at lower air flow rates (Figs. 1, 2) [1]. Figure 2 suggests that the convective heat transfer is higher in rough surfaces. This review assesses diverse types of modifications in solar air heaters such as absorber surface geometry modifications, fin modifications, flows of fluid and glazing modifications.

Various modifications were reviewed and presented by Arunkumar et al. [2]; suggesting the use of thermal energy storage and optimization of modifications parameters and shape was provided. Aravindh and Sreekumar [3] suggested that for better thermal performance optimized level of modifications should be established.

Modifications can be applied on absorber surface, fins, fluid flow, glazing surface and optimizing the air gap. Surface modifications improve the energy

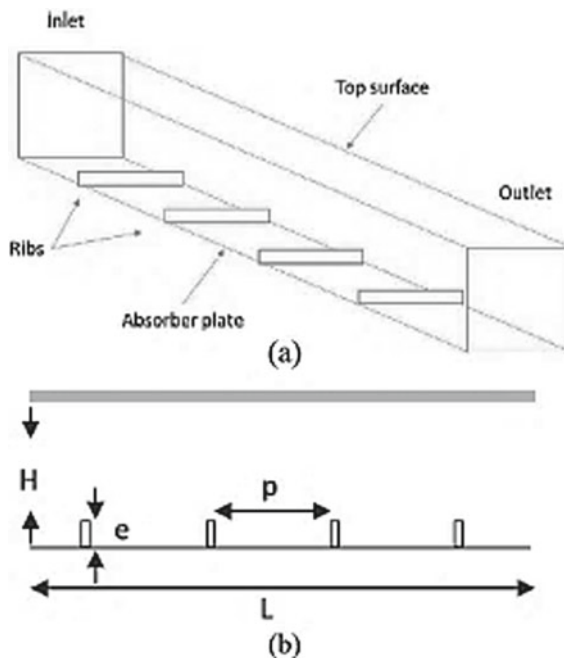
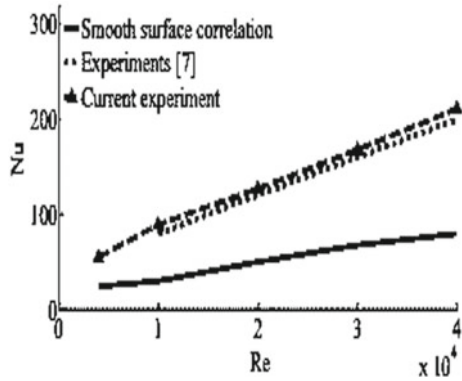


Fig. 1 SAH with turbulators [1]

Fig. 2 Nu variation with Re [1]



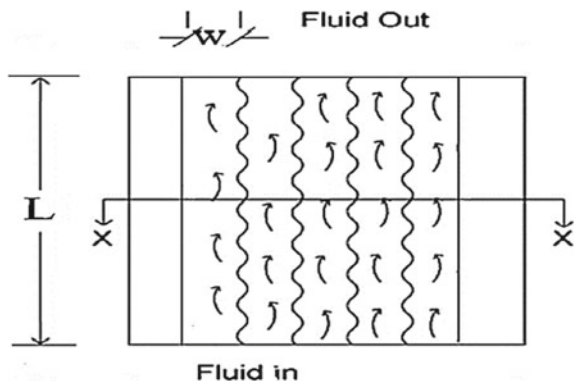
absorption, heat removal and thereby efficiency of the system, similarly the fin modifications tend to improve turbulence of the flow to increase heat transfer and thus contribute to higher performance.

2 Surface Geometry Modifications

Absorber surface has a high impact on the thermal performance of SAH. Its geometry and thermodynamic properties are always important for any thermal analysis. A wavy arrangement of fins in SAH (Fig. 3) was investigated [4] in which the maximum enhancement in thermo-hydraulic efficiency with minimum fin spacing was 36% and 18% approx. with lowest and highest fluid flow rates of 0.013 kg/s and 0.083 kg/s, respectively.

A mathematical investigation on herringbone framed corrugated fins attached on the absorber plate (Fig. 4) concluded that herringbone corrugated fins increases the area for transfer of heat and also extended the length of flow resulting in enhanced fluid mix and the collector efficiency increased by 18% when fluid flow was amplified from 0.016 to 0.033 kg/s [6].

Fig. 3 Air heater with wavy finned absorber [4]



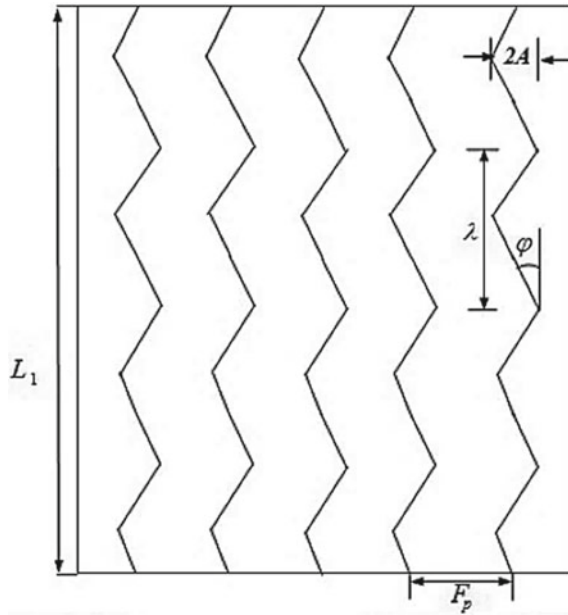


Fig. 4 Herringbone corrugated fins arrangement [6]

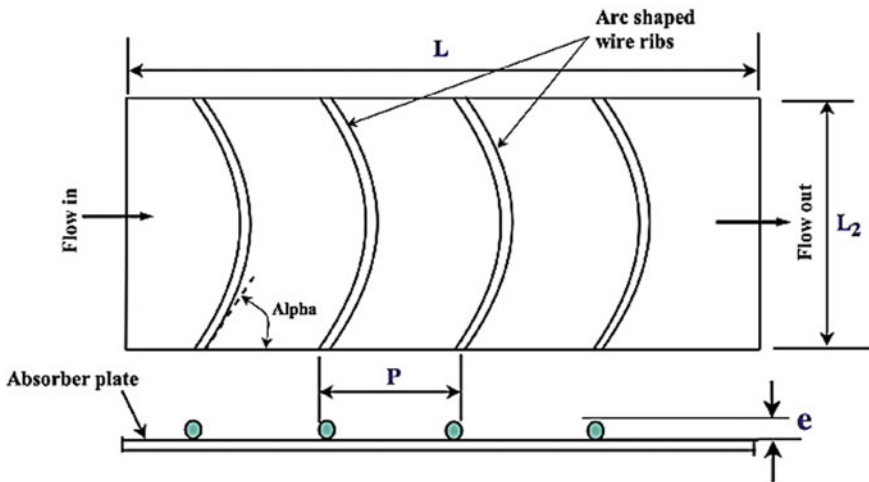


Fig. 5 Arc-shaped plate with wire rib roughness [7]

A solar air heater in which rib roughness created with arc-shaped circular wire on the back of the absorber (Fig. 5) was studied, and an effective increase in efficiency up to 15,000 Re and decrease with increase in further value Re were observed [7]. Energy analysis of SAH with trapezoidal corrugated plate (Fig. 6) along with gravel as

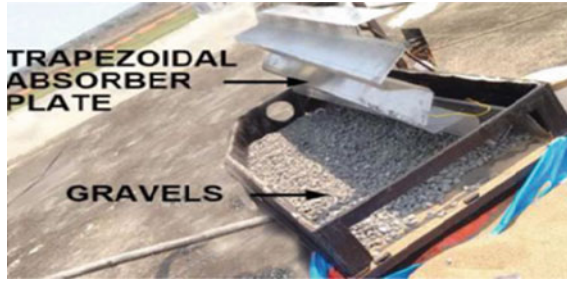


Fig. 6 Trapezoidal plate and gravels [5]

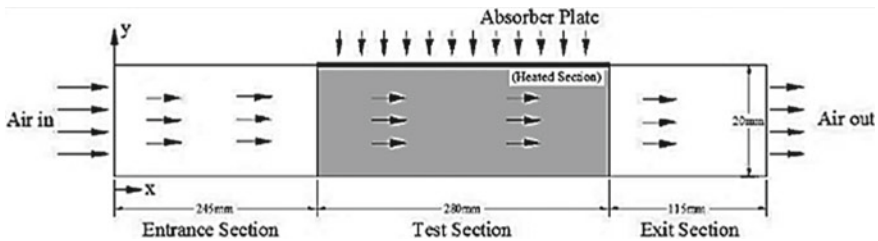


Fig. 7 Test section duct for solar air heater [8]

thermal energy storage medium was performed and concluded that the efficiency of trapezoidal corrugated absorber was enhanced by 36% compared with flat plate-based SAH [5]. An innovative solar air heating device with arched absorber (Figs. 7, 8) mounted with turbulators was evaluated and the system delivered significant enhancement in Nu at Re above 10,000, i.e. up to 80% enhancement for plane turbulators, 16% for triangular turbulators and nearly 55% for dimply turbulators [8].

V-corrugated absorber in rectangular duct-based SAH was experimentally evaluated, and the efficiency was increased when mass flow rate increases and decreases when temperature parameter, i.e. $(T_{out} - T_i)/I$ increases. The maximum enhancement was 1.35–1.56 times the smooth absorber plate. [9]. Conical-shaped-based absorber surface was (Fig. 10) compared with flat plate in single-pass conventional SAH, and an average percentage improvement in efficiency was recorded as 6, 9.8, and 10.6% with conical surface as compared with flat surface for flow rate of 0.04 kg/s, 0.08 kg/s and 0.1 kg/s, respectively, [10].

The thermal performance of repeated ribs on absorber surface (Figs. 1, 2) was studied, and the efficiency was improved with ribs; overall efficiency enhancement of more than 9% can be achieved at lower flow rates when a considerable temperature variation was desired [1]. Steady-state energy and exergy performance were investigated for different arrangements of fluid passage with different fin arrangements, i.e. single pass, double pass, finned plate, roughened plate, wire meshed, at various flow rates and solar radiations, and it was reported that the performance of wire meshed dual-pass SAH was best among various arrangements [11].

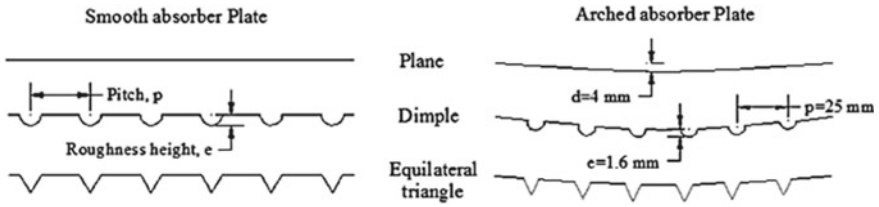


Fig. 8 Types of turbulators design [8]

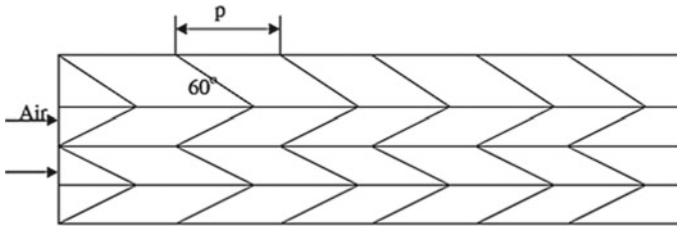


Fig. 9 W-shaped ribs [17]



Fig. 10 Absorber plate with conical surfaces [10]

Six different patterns of turbulators with six different configurations on the absorber surface were experimentally investigated in a single-pass SAH. The results suggested that 6 * 4 zigzag preparations of circular shaped turbulators demonstrates higher thermal performance in comparison to other investigated patterns and conventional arrangement [12].

Four different types of absorber surface, i.e. flat plate, V-shaped plate, wedge-shaped plate and wavy-shaped plate with two different materials of absorber plate (copper and aluminium), were compared for their energy performances, and the results suggested that the SAH with the copper plate has higher efficiency than aluminium plate as the heat capacity of aluminium is higher than copper. The wavy-shaped and V-shaped absorber plate achieved higher energy efficiencies [13].

Semi-ellipse type obstacles in SAH duct was investigated, and it was concluded that for staggered arrangement, the maximum improvement ratios of Nu and friction factor were 2.05 and 6.93, respectively, and for inline arrangement were 1.73 and 6.12, respectively, [14]. Similarly, performance of artificially roughened duct with multi-gap V-ribs was evaluated; the maximum improvement in Nu recorded was 3.34 times [15].

‘S’ shaped wire ribs arrangement was developed, and its influence on the transfer of heat and friction factor of SAH was considered; maximum improvement in Nu and friction factor was found to be nearly 4.6 and 2.7 times in comparison with smooth duct [16]. W-shaped rib roughened SAH was experimentally investigated (Fig. 9); the maximum improvement in Nu and friction factor when compared to smooth channel was found to be 2.36 and 2.01 times, respectively, [17]. An experimental study on multiple ribs having gap, for artificial roughness in absorber plate surface, established that the highest increment in transfer of heat and pumping power was nearly 5.8 and 4.9 times the smooth duct, and for Nu, the maximum increment was observed for Re value of 21,000 [18].

SAH duct with artificial roughness created from arc shape parallel wire was experimentally evaluated, and this geometry modification leads to the maximum improvement in Nu [19]. Experimental analysis on SAH duct having various arc ribs (Fig. 11) suggested that the thermal performance was maximum for roughness width (W/w) of 5 [20]. Effect of heat transfer for turbulent flow over a rectangular duct roughened by circular projections (Fig. 12) suggested that the heat transfer is 2.89 as compared with smooth duct [21].

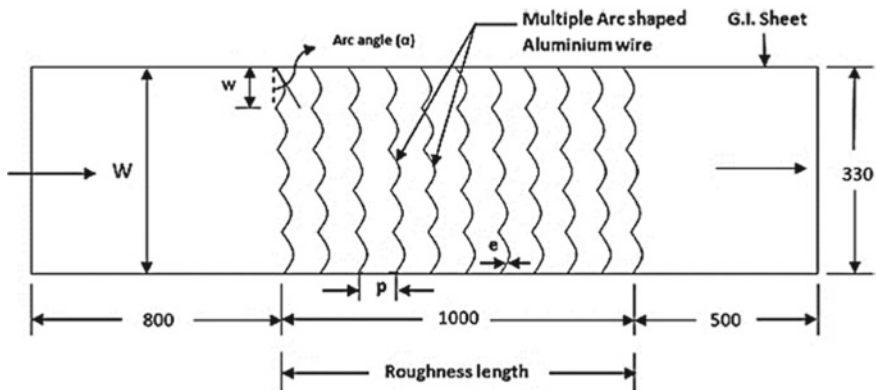


Fig. 11 Roughened absorber plate [20]

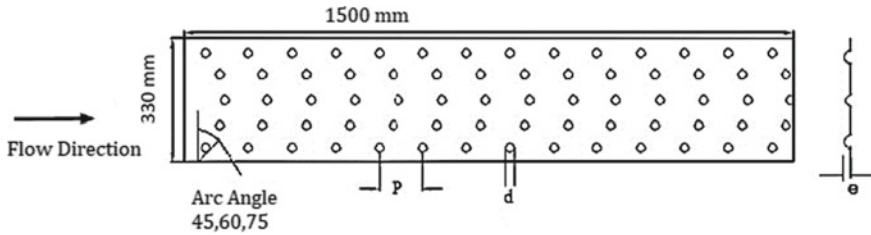


Fig. 12 Protruded roughened geometry in arc shape [21]

2.1 Fin Modifications

Fins are used to increase the contact area thus increasing the heat transfer rate in any fluid channel; in SAH, fin is added for having better heat transfer between fluid and plate by attaching them on absorber surface and also to increase the turbulence in the fluid flow pattern. Various modifications in fin development and arrangements in SAH have been presented in this section.

An absorber, with fins attached by baffles plate, was divided into two parts (Fig. 13) was used in a SAH, and the experimental results recommended that the baffled double-pass SAH improves the collector efficiency considerably due to greater turbulence and spreading the area for heat transfer [22]. Investigations on the hybrid PV and thermal double-pass SAH with vertical fins were carried out with various mass flow rate in the range of 0.03–0.15 kg/s; 20% increment in the

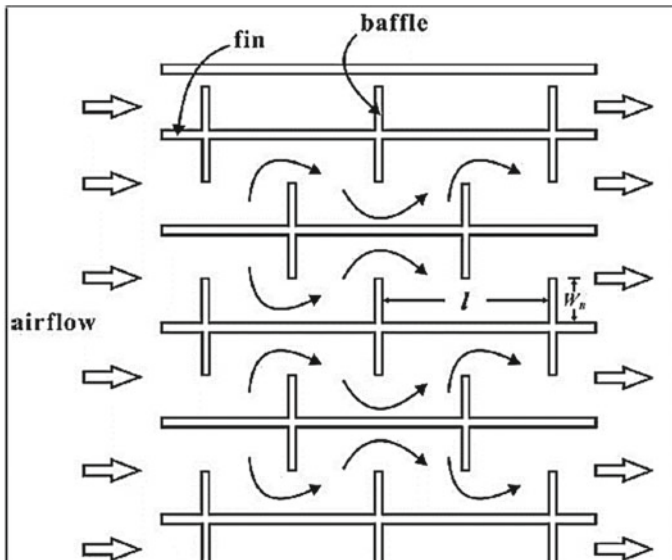


Fig. 13 Baffled solar air heater [22]

electrical efficiency was observed; also it was observed that the packing factor has a considerable effect on the overall efficiency of the collector [23]. An experimental analysis on solar still for increasing the heat transfer rate between saline water and absorber surface was carried out; three stills were designed, i.e. conventional type, finned still and corrugated still; the experimental results show that there is an increase of 40% and 21% in the production of distilled water using finned still and corrugated plate, respectively, [24].

A wavy fin in a single-pass flat plate SAH was mathematically studied for the effect of amplitude and wavelength, and it has been concluded that there is a direct relation between wavelength, amplitude and thermal efficiency of the SAH; maximum efficiency of nearly 78% was recorded with 2.5 cm increase in amplitude [25]. Experimental investigations on the influence of fin height have been carried out in a modified single-pass SAH having almost nineteen fins; experiments were carried out for various heights of fins; the highest efficiency obtained was 57% for a fin height of 8 cm and at a flow rate of 0.04 kg/s [26].

A solar cane air heater with rectangular fins was experimentally investigated, and the maximum improvement of 5% in efficiency was recorded due to the fins; the performance was found better with fins at lower air flow rates [27]. Different rib designs, i.e. multiple V-shaped, S-shaped, arc-shaped ribs were investigated for increasing the performance of the SAH; the ratio of Nu for multiple V-shaped ribs was maximum while the arcshaped ribs offer lowest frictional penalty [28].

Counterpoised rectangular fins on the absorber surface was numerically optimized for a solar air heater; convective heat transfer was maximized; and heat loss was minimized with high instantaneous thermal efficiency even at the lower flow rate was reported, results indicated that even at 100 m³/h of flow rate the instantaneous thermal efficiency exceeded 40%, where the solar irradiance was 600 W/m² [29]. An experimental set-up was developed for stimulating the convective heat transfer in solar air heating (Fig. 14), and it was reported that the inclination angle of the collector has a high impact on achieving the maximum efficiency, the conical pins used as turbulators also improved the convective heat transfer, the optimum inclination angle for Malaysian condition was found to be 45°, and 26.5% efficiency increment was achieved for absorber surface with 16 mm pin pitch when

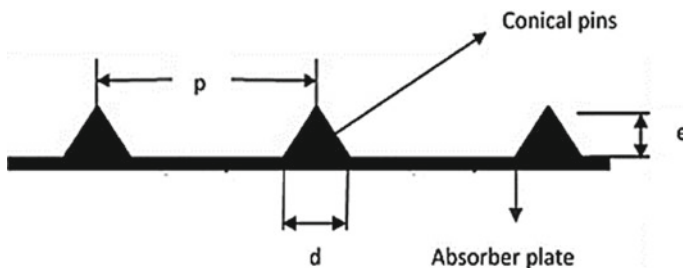


Fig. 14 Conical pin height (e), diameter (d), pitch (p) [30]

compared to flat smooth surface [30]. Multi V-shaped ribs were experimentally investigated, and it was reported that higher Nu and friction factor are achieved with multi V-shaped ribs having gap than that for continuous ribs [31].

2.2 Other Modifications in Solar Air Heaters

Other than the modification in absorber surface and fin arrangements, glazing modifications, entry and exit area modifications, absorber plate colour and optimization of working properties are presented in this section. Baffled glazed-bladed SAH was experimentally investigated which concluded that attaching baffles increases the area for heat transfer, which brought the thermal performance to 83.8%, while that of the conventional one is 32.12% at a fluid flow rate of 0.04 kg/s [32]. A review on the performance and comparison of packed bed double-pass SAH was (Fig. 15) proposed significant growth in the heat transfer with packed bed SAH while, the double-pass SAH performed better [33]. Thermal behaviour of perforated glazed SAH having various inner collector colours and a black coloured SAH was experimentally investigated; two perforated glazed SAHs having glazing with different inside bottom colours were compared with unglazed transpired SAH; the results showed that the dark coloured SAHs were having better efficiency than the light colour ones [34].

Experimental investigations in a single- and double-pass SAH with normal and quarter perforated cover were carried out; the SAH was tested with holes on one cover with centre-to-centre distance of 6 cm (20D) and 3 cm (10D) on the other

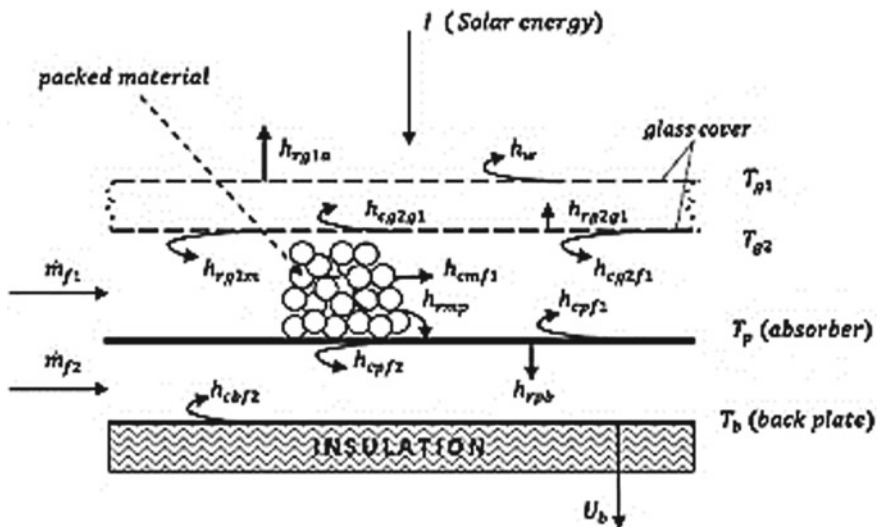


Fig. 15 Packed bed SAH [33]

cover, the SAH with quarter cover 10D performed better than the cover with lower number of holes [35]. Porous and non-porous passage in a SAH were studied for the effect of flow rate on fluid temperature, thermal efficiency and drop in pressure; with two wire matrix, WSM-I and WSM-II were analysed; the operations were carried out for Re between 194 and 591; the thermal efficiency increment for WSM-I was found to be 5–17%, and for WSM-II, it was 5–20% with flow rate ranging from 0.01 to 0.055 kg/s [36].

A single- and double-pass SAH were analyzed experimentally; fins were attached with wire mesh of steel as an absorber plate; the thermal efficiency of double pass was almost 10% higher for fluid flow rate of 0.038 kg/s [37]. An experimental analysis of a double-pass finned plate SAH and comparisons between double-pass finned and V-corrugated plate arrangements suggested that the maximum efficiency of the V-corrugated plate is 17.4% higher than finned plate SAH [38].

3 Conclusion

To increase the use of solar devices, their optimization is required so that they provide maximum output. Solar air heaters have a huge energy saving potential and thus can provide a clean and green environment. This review provides various modifications implemented on SAH to maximize its thermal performance in specific working conditions. The friction factor, Reynold's number and Nusselt number are the governing parameters for the heat transfer and pumping power requirements. From the review, it can be concluded that the important parameter affecting the thermal performance of SAH are:

- Flow rate of the working fluid
- Flow domain of the fluid passage
- Absorber plate material, colour and geometry
- Fin geometry and arrangement

Modifications in absorber plate surface geometry have a high impact on the performance; corrugated geometry, absorber plate colour, arched absorber plate, use of turbulators, etc. have proved to improve the thermal performance. Use of fins with its structural modifications (shape, size and arrangement) also has a considerable impact on the performance of solar air heaters. Wavy fins with optimized amplitude and frequency can provide an instantaneous efficiency of 78%. It can also be established that the working conditions of each modification should be optimized individually, as it has diverse impact based on the working conditions.

References

1. Ansari M, Bazargan M (2018) Optimization of flat plate solar air heaters with ribbed surfaces. *Appl Therm Eng* 136:356–363
2. Arunkumar H, Karanth KV, Kumar S (2020) Review on the design modifications of a solar air heater for improvement in the thermal performance. *Sustain Energy Technol Assessments* 39
3. Aravindha MA, Sreekumar A (2016) Efficiency enhancement in solar air heaters by modification of absorber plate—a review. *Int J Green Energy* 13(12):1209–1223
4. Priyam A, Chand P (2016) Thermal and thermohydraulic performance of wavy finned absorber solar air heater. *Sol Energy* 130:250–259
5. Lakshmi DVN, Layek A, Kumar M (2017) Performance analysis of trapezoidal corrugated solar air heater with sensible heat storage material. *Energy Procedia* 109:463–470
6. Kumar R, Chand P (2017) Performance enhancement of solar air heater using herringbone corrugated fins. *Energy* 127:271–279
7. Sahu MK, Prasad RK (2017) Thermohydraulic performance analysis of an arc shape wire roughened solar air heater. *Renewable Energy* 108:598–614
8. Singh S (2017) Performance evaluation of a novel solar air heater with arched absorber plate. *Renewable Energy* 114:879–886
9. Kumar PG, Panchabikesan K, Deeyoko LAJ, Ramalingam V (2018) Experimental investigation on heat transfer augmentation of solar air heater using shot blasted V-corrugated absorber plate. *Renewable Energy* 127:213–229
10. Abuşka M (2018) Energy and exergy analysis of solar air heater having new design absorber plate with conical surface. *Appl Therm Eng* 131:115–124
11. Velmurugan P, Kalaivanan R (2015) Energy and exergy analysis of solar air heaters with varied geometries. *Arab J Sci Eng* 40:1173–1186
12. Rajaseenivasan T, Srinivasan S, Sriithar K (2015) Comprehensive study on solar air heater with circular and V-type turbulators attached on absorber plate. *Energy* 88:863–873
13. Caglayan N, Ertekin C, Alta ZD (2015) Experimental investigation of various type absorber plates for solar air heaters. *J Agric Sci* 459–470
14. Alam T, Kim M-H (2016) Numerical study on thermal hydraulic performance improvement in solar air heater duct with semi ellipse shaped obstacles. *Energy* 112:588–598
15. Deo NS, Chander S, Saini J (2016) Performance analysis of solar air heater duct roughened with multigap V-down ribs combined with staggered ribs. *Renewable Energy* 484–500
16. Kumar K, Prajapati D, Samir S (2017) Heat transfer and friction factor correlations development for solar air heater duct artificially roughened with ‘S’ shape ribs. *Exp Therm Fluid Sci* 82:249–261
17. Lanjewar A, Bhagoria J, Sarviya R (2011) Heat transfer and friction in solar air heater duct with W-shaped rib roughness on absorber plate. *Energy* 36:4531–4541
18. Pandey N, Bajpai V, Varun (2016) Experimental investigation of heat transfer augmentation using multiple arcs with gap on absorber plate of solar air heater. *Sol Energy* 134:314–326
19. Saini S, Saini R (2008) Development of correlations for Nusselt number and friction factor for solar air heater with roughened duct having arc-shaped wire as artificial roughness. *Sol Energy* 82(12):1118–1130
20. Singh AP, Varun, Siddhartha (2014) Effect of artificial roughness on heat transfer and friction characteristics having multiple arc shaped roughness element on the absorber plate. *Sol Energy* 105:479–493
21. Yadav S, Kaushal M, Varun, Siddhartha (2013) Nusselt number and friction factor correlations for solar air heater duct having protrusions as roughness elements on absorber plate. *Exp Therm Fluid Sci* 44:34–41
22. Ho C, Yeh H, Cheng T, Chen T, Wang R (2009) The influences of recycle on performance of baffled double-pass flat-plate solar air heaters with internal fins attached. *Appl Energy* 86 (9):1470–1478

23. Kumar R, Rosen MA (2011) Performance evaluation of a double pass PV/T solar air heater with and without fins. *Appl Therm Eng* 31(8–9):1402–1410
24. Omara Z, Hamed MH, Kabeel A (2011) Performance of finned and corrugated absorbers solar stills under Egyptian conditions. *Desalination* 277(1–3):281–287
25. Priyam A, Chand P (2018) Effect of wavelength and amplitude on the performance of wavy finned absorber solar air heater. *Renewable Energy* 119:690–702
26. Kabeela A, Hamedb MH, Omara Z, Kandeal A (2018) Influence of fin height on the performance of a glazed and bladed entrance single-pass solar air heater. *Sol Energy* 162: 410–419
27. Murali G, Sundari A, Raviteja S, Chanukyachakravarthi S, Tejpraneeth M (2019) Experimental study of thermal performance of solar aluminium cane air heater with and without fins. *Mater Today Proc* 21(1):223–230
28. Singha I, Singh S (2018) A review of artificial roughness geometries employed in solar air heaters. *Renew Sustain Energy Rev* 92:405–425
29. Yang M, Yang X, Li X, Wang Z, Wang P (2014) Design and optimization of a solar air heater with offset strip fin absorber plate. *Appl Energy* 113:1349–1362
30. Gilani SE, Al-Kayiem HH, Woldemicheal DE, Gilani SI (2017) Performance enhancement of free convective solar air heater by pin protrusions on the absorber. *Sol Energy* 151:173–185
31. Kumar A, Saini R, Saini J (2013) Development of correlations for Nusselt number and friction factor for solar air heater with roughened duct having multi v-shaped with gap rib as artificial roughness. *Renewable Energy* 58:151–163
32. Kabeel A, Hamed M, Omara Z, Kandel A (2018) On the performance of a baffled glazed-bladed entrance solar air heater. *Appl Therm Eng* 139:367–375
33. Singh S, Dhiman P (2016) Thermal performance of double pass packed bed solar air heaters—a comprehensive review. *Renew Sustain Energy Rev* 53:1010–1031
34. Vaziri R, Ilkan M, Egelioglu F (2015) Experimental performance of perforated glazed solar air heaters and unglazed transpired solar air heater. *Sol Energy* 119:251–260
35. Nowzari R, Aldabbagh L, Egelioglu F (2014) Single and double pass solar air heaters with partially perforated cover and packed mesh. *Energy* 73:694–702
36. Rajarajeswari K, Alok P, Sreekumar A (2018) Simulation and experimental investigation of fluid flow in porous and nonporous solar air heaters. *Sol Energy* 171:258–270
37. Omojaro A, Aldabbagh L (2010) Experimental performance of single and double pass solar air heater with fins and steel wire mesh as absorber. *Appl Energy* 87(12):3759–3765
38. El-Sebaai A, Aboul-Enein S, Ramadan M, Shalaby S, Moharram BM (2011) Thermal performance investigation of double pass-finned plate solar air heater. *Appl Energy* 88 (5):1727–1739

Numerical Modelling and Simulation of Wind Turbine Blade Aerofoil for Performance Enhancement



Pankaj Negi, Tarun Kumar Dhiman, Gagan Bansal,
and Neeraj Panwar

Abstract Flow separation causes loss in performance of wind turbine blade. Investigation of S819 aerofoil through passive flow control technique is done using CFD code Fluent. In present work, numerical modelling and simulation of wind turbine blade aerofoil are performed. CFD simulation of S819 aerofoil is performed at various incident angles 0° – 30° . To control the flow separation over S819 aerofoil, a new technique with leading edge hole is provided. CFD investigation is done for both types of aerofoil using $k - \omega$ turbulent equation. Comparison is made between simple aerofoil and controlled aerofoil where results show delay in flow separation and improvement in lift force at different angle of attacks while reducing the drag force.

Keywords CFD · Drag and lift force · S819 aerofoil · Fluent · Horizontal axis wind turbine

Nomenclature

C_d	Coefficient of drag
C_l	Coefficient of lift
AOA	Angle of Attack
k	Turbulent kinetic energy
ω	Dissipation Rate

P. Negi (✉) · T. K. Dhiman · G. Bansal · N. Panwar
Graphic Era Hill University, Dehradun, Uttarakhand, India
e-mail: mechchaps@gmail.com

T. K. Dhiman
e-mail: tarunmechddn@gmail.com

G. Bansal
e-mail: gaganbansal12345@gmail.com

N. Panwar
e-mail: neeraj.pan28@gmail.com

1 Introduction

As wind energy is freely available in the environment. There is a need to develop such a mechanism which can capture maximum amount of energy from wind. In wind turbines, there is a problem known as stall means increment in drag and decrement in lift after some angle of attack. Flow is going to separate at higher angle of attacks in wind turbine aerofoil. This causes the decrement in lift while increasing the drag force.

To encounter such phenomena, we need to develop blade profile in a way that stall angle can be postponed. So that maximum performance could be achieved. The main objective of present work is to enhance the lift while reducing drag by implementing a controlled method. Flow separation of S819 aerofoil is investigated, and a better technique is provided to delay the stall.

In previous investigations, different controlling techniques are employed to control the flow separation like leading edge flap, vortex generator, etc. But limited research on medium size wind turbine aerofoil.

Present work is focused on numerical modelling and simulation of S819 aerofoil. CFD analysis of S819 aerofoil is done using Fluent. Using CFD simulation present work aims to analyse the flow field around blade aerofoil. Lift coefficient and drag coefficient are two important parameters for evaluation. The scope of flow separation control on an S819 aerofoil is to achieve more lift coefficient and less drag coefficient.

Hu et al. [1] horizontal wind turbine blade stall delay was investigated. Low Reynolds number flow was analysed around aerofoil for dynamic stall [2]. From investigation, it is observed that CFD simulation captures flow structure accurately [3]. Flow jet technique on low Reynolds number aerofoil was implemented, where momentum coefficient is around 5–13% [4]. S809 aerofoil under dynamic stall was analysed at different Reynolds numbers. Experimental study of NACA 2415 aerofoil was performed at low Reynolds number [5]. Result shows that stall angle varied with Reynolds number [6]. Experimental investigation shows that separation can be controlled by using synthetic jet actuator near the point of separation. Wind turbine blade profiles were investigated [7]. CFD investigation of different blade profile was performed using Reynolds average Navier stroke equation. NACA0012 aerofoil with wavy surfaces was investigated numerically [8]. Large eddy simulation performed for delaying the flow separation. To control the boundary layer separation, a constant suction technique was implemented [9]. An experimental result shows boundary layer reattachment. Numerical simulation [10] for flow and aerodynamic performance of the blades of G4-73No.8D of centrifugal fan was studied at different angles using CFD. Investigation of effect of pitch angle on the efficiency of wind turbine was performed [11] using $k - \omega$, SST turbulent model. A computed result shows that thrust decreases with increment in pitch angle for given wind velocity. Trailing edge flow control method [12] was implemented for NREL phase VI wind turbine blade. Computed result shows blade performance enhancement by 80%. S1210 hydrofoil was numerically investigated [13] and result

shows that after using vortex generator near trailing edge side stall angle delays from 10° to 12° . A new method is used for efficiency improvement and optimisation of Vertical axis wind turbine [14]. Experimental investigation of low Reynolds number aerofoil [15] with vortex generators was performed. NACA 0018 aerofoil was simulated using CFD code [16]. Numerical investigation of NACA S1210 hydrofoil was performed using tube slot [17]. Spalart-Allmaras model was used to simulate the flow and results show that optimum tube slot diameter is 9 mm for maximum performance.

In present work, aerodynamic performance of S819 aerofoil [18] is enhanced by doing computational fluid dynamics analysis.

2 Methodology

From top surface of the S819 aerofoil, a hole is provided from the forefront side of the aerofoil to control the flow, from which jet of air is passed from high pressure region to low pressure region. Due to which the upper layer of fluid will get some energy; hence, separation of flow will postponed.

Geometry generated for S819 aerofoil Fig. 1 using Fluent as CFD code. Figures 2 and 3 shows the design created for analysis having two different types of shapes, aerofoil S819 with leading edge hole and without hole. Hole in S819 aerofoil is created near the point of flow separation, 20% from the leading edge side. Sketch for S819 aerofoil is generated through java programme. This java programme was made using co-ordinates given for S819 aerofoil by [18] National renewable energy lab (NREL). Figure 4 shows a fluid domain was created around

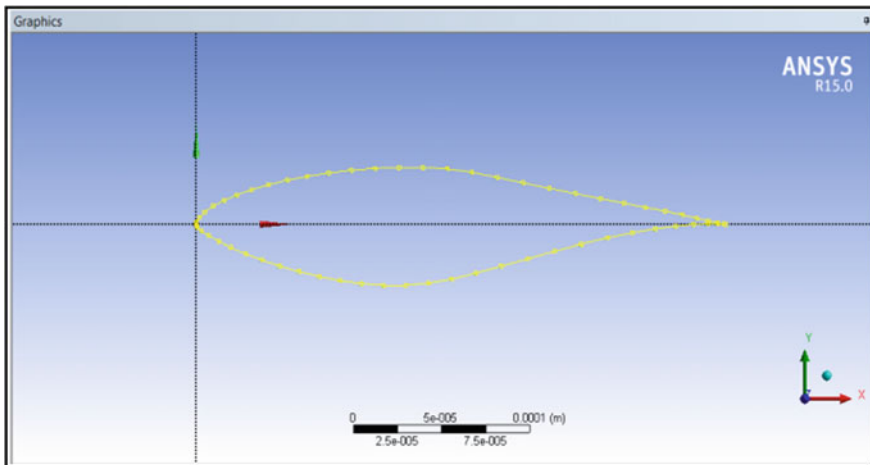


Fig. 1 S819 Aerofoil

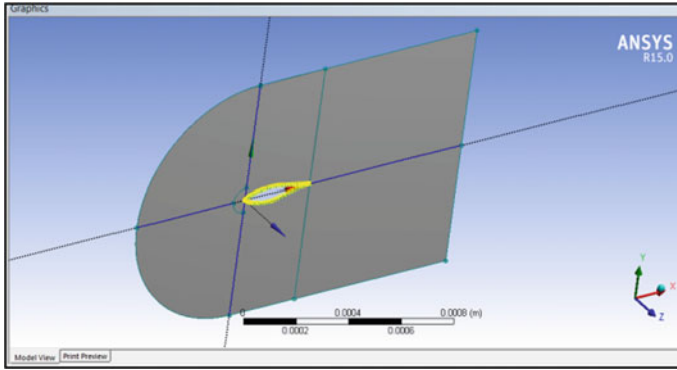


Fig. 2 S819 Aerofoil without hole

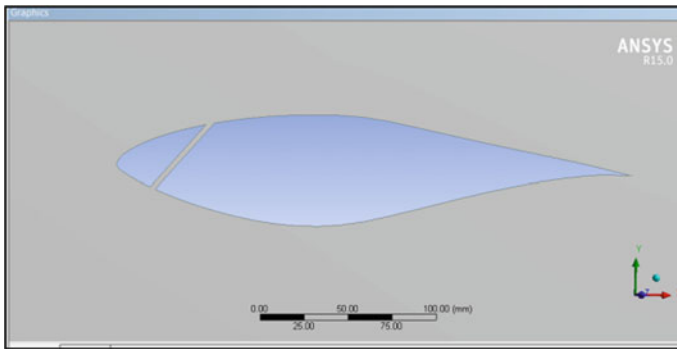


Fig. 3 S819 Aerofoil with leading edge hole

the aerofoil, length = 3000 mm, width = 2500 mm. Fluent is used as CFD code to simulate flow field around S819 aerofoil. The boundary conditions applied to the fluid domain. $K - \omega$ turbulent equation is used.

$K - \omega$ turbulence equation is used to solve the fluid domain. First variable shows the turbulence kinetic energy while the second relates the specific rate of dissipation. This turbulent model can easily capture the flow along boundary of the blade aerofoil. Following are the two variables:

K —Equation

$$\frac{\delta(\rho k)}{\delta t} + \frac{\delta(\rho u_j k)}{\delta x_j} = P - \beta^* \rho \omega k + \frac{\delta}{\delta x_j} \left[\left(\mu + \sigma_k \frac{\rho k}{\omega} \right) \frac{\delta k}{\delta x_j} \right] \quad (1)$$

ω —Equation

$$\frac{\delta(\rho \omega)}{\delta t} + \frac{\delta(\rho u_j \omega)}{\delta x_j} = \frac{\gamma \omega}{k} P - \beta \rho \omega^2 + \frac{\delta}{\delta x_j} \left[\left(\mu + \sigma_\omega \frac{\rho k}{\omega} \right) \frac{\delta \omega}{\delta x_j} \right] + \frac{\rho \sigma_d}{\omega} \frac{\delta k}{\delta x_j} \frac{\delta \omega}{\delta x_j} \quad (2)$$

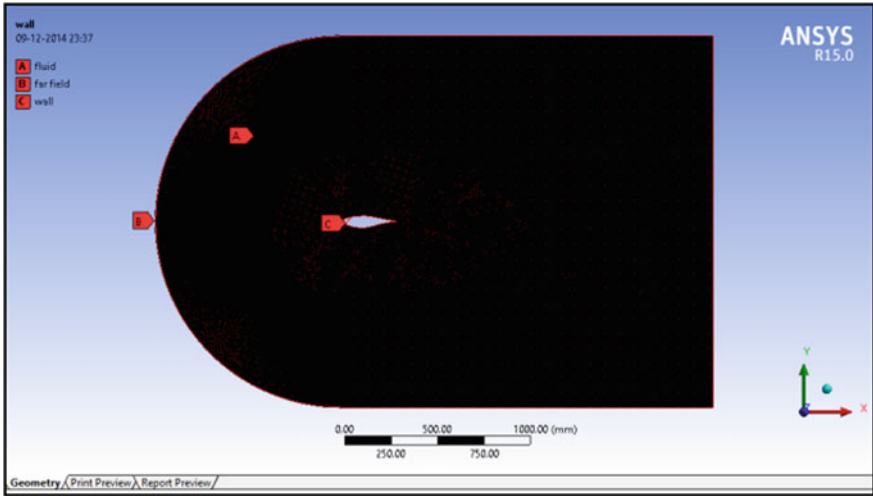


Fig. 4 Fluid domain for analysis

3 Mesh Details

Figure 5 shows the mesh structure for fluid domain. Meshing or discretization of fluid domain is done using Fluent. Following parameters was taken during meshing of fluid domain.

Quadrilateral mesh is generated to solve the fluid domain. Total 249703 elements were generated.

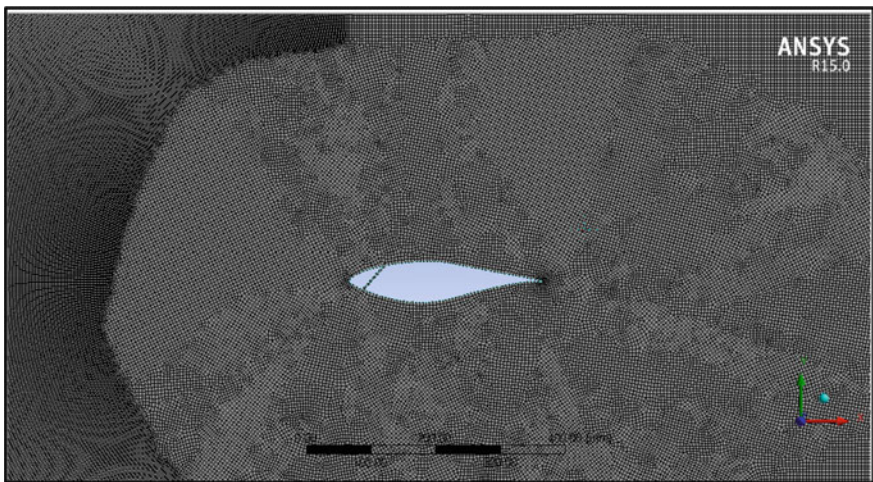


Fig. 5 Mesh structure of fluid domain

4 Analysis and Solution

CFD analysis of S819 aerofoil is performed using following boundary conditions and parameters.

Solver- density-based solver, equation used- $k - \omega$, SST, fluid-air, Mach no-0.7 (subsonic flow), angle of attack— 0° to 30° , parameters monitor-drag and lift coefficient.

5 Validation of Present Work

To check the validity of present numerical model, verification was made by solving the work of [9] numerically. The physical and geometrical assumptions are taken from [9]. Aerofoil S814 was designed and simulated using CFD code Fluent. The boundary conditions applied on computational domain for aerofoil S814.

Figures 6 and 7 shows comparison for aerofoil S814 for both numerical and experimental work. Drag and lift coefficient for both cases are compared at angle of attack from 0° to 21° . A result shows good agreement between experimental and numerical work. From this comparative study, it can be concluded that numerical investigation with proper boundary conditions can be used to simulate such a problem.

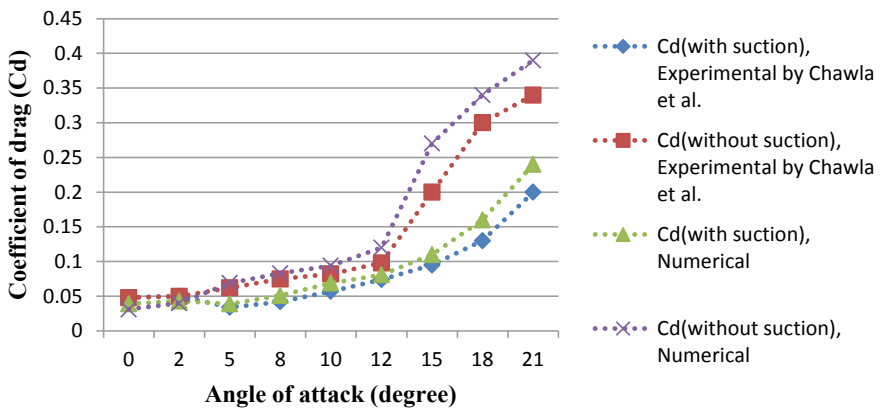


Fig. 6 Comparison in coefficient of drag between experimental and numerical work

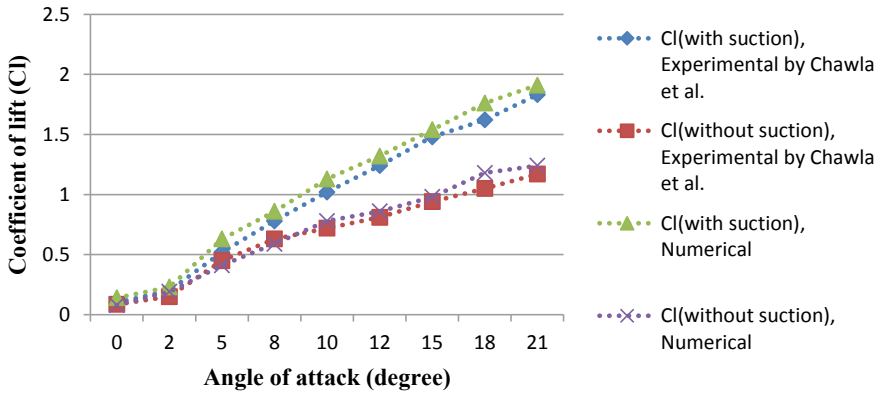


Fig. 7 Comparison in coefficient of lift between experimental and numerical work

6 Result and Discussion

Analysis has been carried out using CFD code Fluent by changing angle of attack on S819 airfoil with hole and without hole. By using leading edge hole, upper layer of boundary layer is going to energise and try to pull down flow separation towards trailing edge.

Results obtained from S819 aerofoil without hole is compared with S819 aerofoil having leading edge hole to see the changes in drag and lift and hence improvement in aerodynamic performance. The results obtained at 0°–30° of angle of attack (Figs. 8, 9, 10, 11, 12, 13).

Results shows prominent enhancement in lift in slotted aerofoil compare to simple aerofoil.

Following results are obtained from analysis:

1. Stall condition for aerofoil without hole occur at 15°.
2. Maximum lift for aerofoil without hole occurs at 15°.
3. S819 aerofoil with hole gives higher lift and lower drag then S819 aerofoil without hole.
4. Stall angle for S819 airfoil with hole is 28°, which shows improvement in lift force.

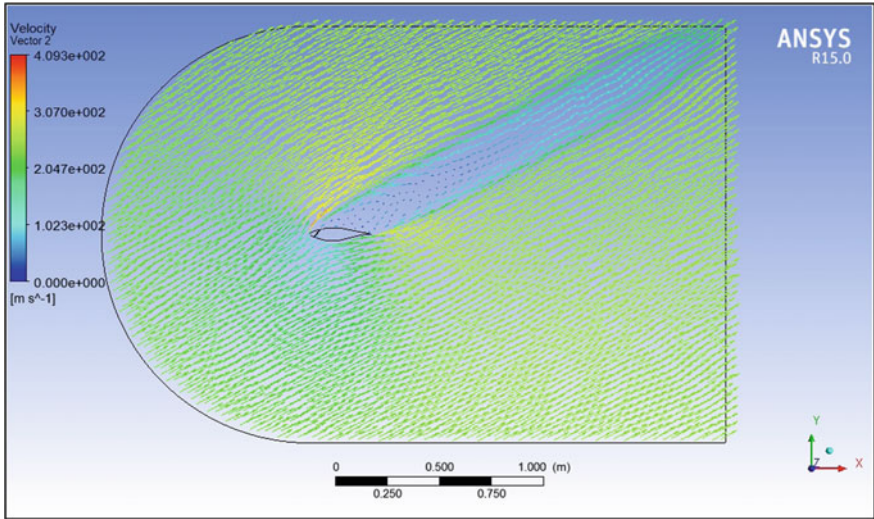


Fig. 8 Velocity vectors of S819 aerofoil with hole at AOA 30°

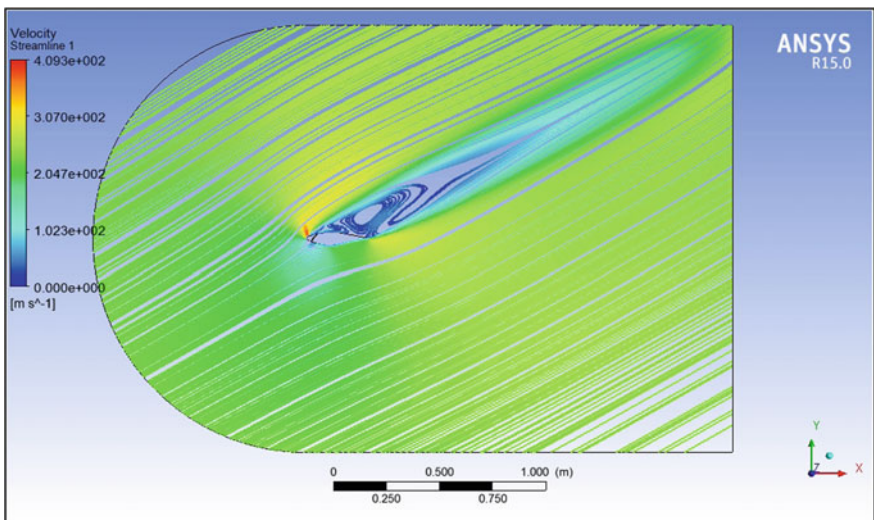


Fig. 9 Streamline of S819 aerofoil with hole at AOA 30°

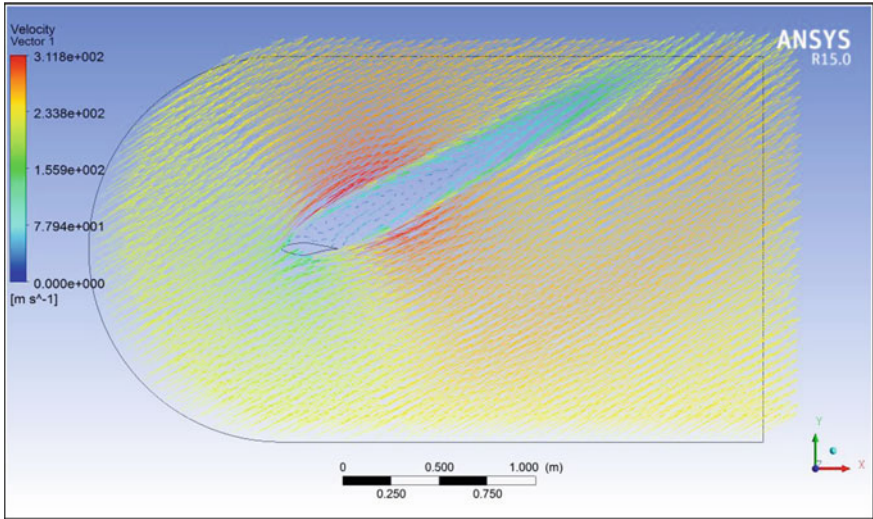


Fig. 10 Velocity vectors of S819 aerofoil without hole at AOA 30°

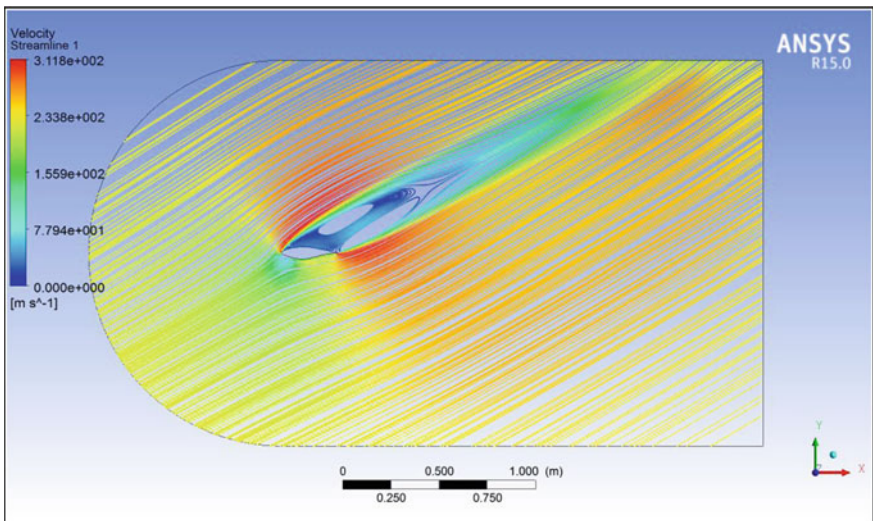


Fig. 11 Streamline of S819 aerofoil without hole at AOA 30°

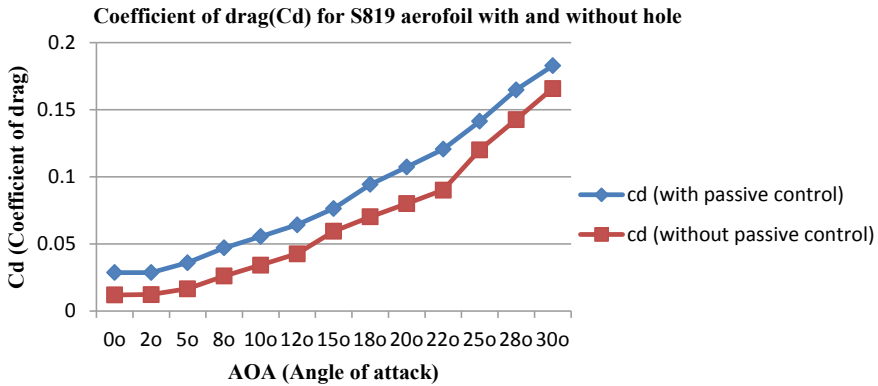


Fig. 12 Coefficient of drag for S819 aerofoil with and without hole

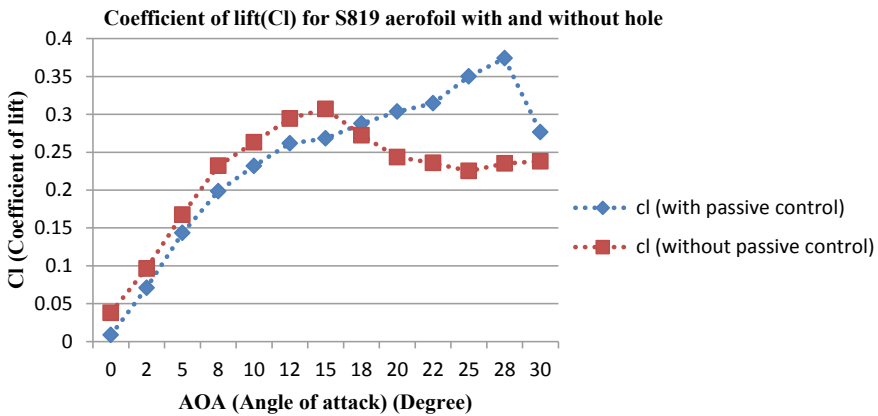


Fig. 13 Coefficient of lift for aerofoil with and without passive control

7 Conclusion

In present work, a medium size horizontal axis wind turbine blade having S819 aerofoil is designed and analysed at different angle of attack. A passive control method is used to control the flow separation over turbine blade aerofoil, which shows good improvement in aerodynamic performance of turbine blade.

After CFD simulation, computed results show increment in lift while decreasing drag force. Stall angle postponed up to 28° from 15°, which shows the effectiveness of this technique.

Analysis has been carried out in ANSYS Fluent by changing angle of attack from 0° to 30° on S819 aerofoil with slot and without slot. This technique used to delay the stall angle of blade aerofoil.

This passive control technique can be used to control the flow separation over different medium size wind turbine aerofoils and to capture maximum energy from wind. Because present work limited to medium size wind turbine, for other different sizes turbines in future this technique can be implemented in conjunction with active flow control technique to improve performance. For that further investigation is much needed in that direction.

Acknowledgements The authors are thankful to Management of Graphic Era Hill University, Dehradun for its necessary funding and support towards publication of this work.

References

1. Hu D, Hua Q, Du Z (2006) A study on stall delay for horizontal axis wind turbine. *Renewable Energy* 31:821–836
2. Wang S, Ingham DB, Ma L, Pourkashanian M, Tao M (2010) Numerical investigations on dynamic stall of low Reynolds number flow around oscillating airfoils. *Comput Fluids* 39:1529–1541
3. Mitsudharmadi H, Cui Y (2010) Implementation of co-flow jet concept on low Reynolds number aerofoil. In: *Proceedings of the 40th AIAA fluid dynamics conference, AIAA 2010-4717, Chicago, III, USA*
4. Gharali K, Johnson DA (2012) Numerical modeling of an S809 airfoil under dynamic stall, erosion and high reduced frequencies. *Appl Energy* 93:45–52
5. Serdar Genc M, Karasu I, Hakan Acikel H (2012) An experimental study on aerodynamics of NACA2415 aerofoil at low Re numbers. *Exp Therm Fluid Sci* 39:252–264
6. Wang J, Feng L, Xu C (2007) Experimental investigations on separation control and flow structure around a circular cylinder with synthetic jet. *Sci China E* 50(5):550–559
7. Sayed MA, Kandil HA, Shaltot A (2012) Aerodynamic analysis of different wind-turbine-blade profiles using finite-volume method. *Energy Convers Manag* 64:541–550
8. Lin YF, Lam K, Zou L, Liu Y (2013) Numerical study of flows past airfoils with wavy surfaces. *J Fluids Struct* 36:136–148
9. Chawla JS, Suryanarayanan S, Puranik B, Sheridan J, Falzon BG (2014) Efficiency improvement study for small wind turbines through flow control. *Sustain Energy Technol Assessments* 7:195–208
10. Rong R, Cui K, Li Z, Wu Z (2015) Numerical study of centrifugal fan with slots in blade surface. *Procedia Eng* 126:588–591
11. Sudhamshu AR, Pandey MC, Sunil N, Satish NS, Mugundhan V, Velamati RK (2016) Numerical study of effect of pitch angle on performance characteristics of a HAWT. *Eng Sci Technol Int J* 19:632–641
12. Chen H, Qin N (2017) Trailing-edge flow control for wind turbine performance and load control. *Renewable Energy* 105:419–435
13. Kundu P, Sarkar A, Nagarajan V (2019) Improvement of performance of S1210 hydrofoil with vortex generators and modified trailing edge. *Renewable Energy* 142:643e657
14. Elsakka MM, Ingham DB, Ma L, Pourkashanian M (2019) CFD analysis of the angle of attack for a vertical axis wind turbine blade. *Energy Convers Manag* 182:154–165
15. Delnero JS, Di Leo JM, Camocardi ME (2012) Experimental study of vortex generators effects on low Reynolds number airfoils in turbulent flow. *J Aerodyn* 2(1):50–66

16. Zhong J, Li J, Guo P, Wang Y (2019) Dynamic stall control on a vertical axis wind turbine aerofoil using leading-edge rod. *Energy* 174:246–260
17. Kundu P (2019) Hydrodynamic performance improvement on small horizontal axis current turbine blade using different tube slots configurations. *Appl Ocean Res* 91:101873
18. NREL (National renewable energy laboratory)

Hydrophobicity Enhancement of Mesh-like Surface for Moist Air Condensation



Punj Lata Singh and Basant Singh Sikarwar

Abstract Condensation on surfaces with low wettability is of great significance in microfluidics and the fabrication of nanostructures. In this work, condensation process of water vapor from moist air flowing on a mesh-like surface is investigated experimentally at controlled environment condition. In order to execute condensation, temperature difference is increased between the air dew point and Cu mesh surface temperature. The hydrophobicity on mesh-like surface is enhanced using chemical texturing. The static and dynamic surface properties are moderated on this fabricated mesh-like surface with contact angle hysteresis of 16° . Thus, this type of surface is suitable for improving the performances of condensation and to extend their practical applications worldwide.

Keywords Condensation · Wettability · Copper mesh · Moist air

1 Introduction

The condensation of vapor-to-liquid on a cold surface is a daily experience in industrial application, considerably an indispensable process in various arena of power generation, energy conversion, and harvesting water [1]. The enhancement in condensation is attributed by a wetting features of the surface and suitable temperature difference between the vapor and surface. Besides, the suitable temperature difference could maintain a stable condensation [2]. However, wettability is a fundamental property of a solid surface and is governed by their surface and free energy of surface. From past continuous progression, many natural materials such as lotus leaves, desert beetles, spider silks, fish scales, etc., performed excellent

P. L. Singh (✉) · B. S. Sikarwar

Department of Mechanical Engineering, Amity School of Engineering and Technology,
Amity University Uttar Pradesh (AUUP), Noida, India
e-mail: pksingh@amity.edu

B. S. Sikarwar

e-mail: bssikarwar@amity.edu

© The Author(s), under exclusive license to Springer Nature Singapore Pte Ltd. 2021

B. S. Sikarwar et al. (eds.), *Advances in Fluid and Thermal Engineering*,

Lecture Notes in Mechanical Engineering,

https://doi.org/10.1007/978-981-16-0159-0_38

surface wettability and entirely motivated to experiment on metallic surface [3]. Thereby, the hierarchical structures of metals with unique properties and limitations too when experimented and fabricated with synthetic processes have been developed to special wettability [4]. The condensing surface can be renovated to suitably engineered surface by texturing physically or chemically. The wettability feature on metallic surface also helps in preventing some metallic limitations such as anti-corrosion, friction reduction, liquid transportation [5].

According to literature, various modification on wettability on metal strategized a mesh-like surface to enhance the behavior of condensation pattern. So eventually, mesh-like surfaces appeared as an augmenting condensing surface to accelerate the moist air condensation due to proliferation of large contact area. From the past history, numerous modifications on mesh were acknowledged for generating economical condensation [6]. In a way, polypropylene meshes [7], white polyethylene UV stabilized insect mesh [8], a Hi-mesh surface (copper woven micro-mesh) [9, 10] reported for accelerating droplet and describing dynamic property of droplet shedding [11]. Besides all, a mesh from sintering method at constant temperature of 26 °C and relative humidity of 40–60% loomed to generated large scale micro-droplets [12]. The efforts to harvest water by consuming less power using solar system [13, 14] driven a porous metal—organic framework-based device to capture water vapor as low relative humidity 20% from the ambient air [15]. The phenomenal effect of the wettability established a hydrophobic or super-hydrophobic surface implements to an obstruction to fluid wetting and configures greater contact angle and less a hysteresis angle. Thus, condensation on hydrophobic mesh-like surface depicts high transport coefficient (mass and heat) favors an ideal reason to be preferred.

Therefore, this work aims at providing proficient concept of a self—sustained energy source with very limited resources to acknowledge the condensation on hydrophobic surface. A tubular copper mesh-like surface is considered as condensing surface in the presence of moist air at relative humidity above 80% under controlled environmental condition. However, tubular copper mesh is coated to obtain a low wettability surface for amplifying the condensation rate and droplet shedding under silylation of silica by sol-gel method. Thus, the coating facilitates the surface more volatile and more thermally stable which strengthened the durability of surface.

2 Materials and Methods

The fabrication of experimental setup begins with selection of material of condensing surface, i.e., the Cu tubes (99.9% purity) each of 40 mm length and 3 mm outer diameter. In order to achieve mesh-like surface, Cu tubes were kept to distance of 10 mm apart to one another both horizontally and vertically as shown in Fig. 1.

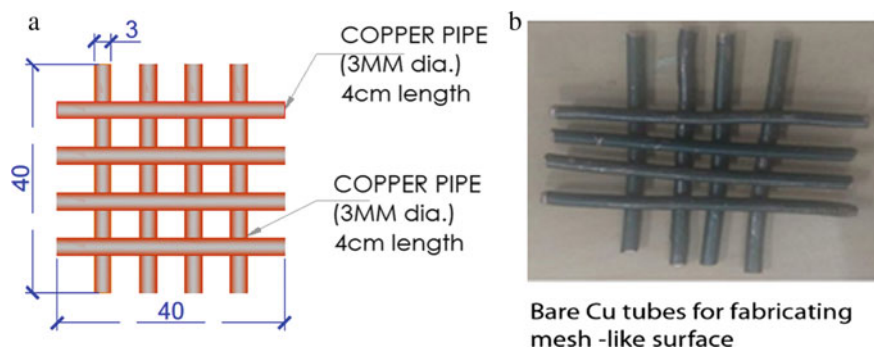


Fig. 1 a Schematic diagram of Cu mesh-like surface, b image of bare Cu tubes for fabricating Cu mesh-like surface

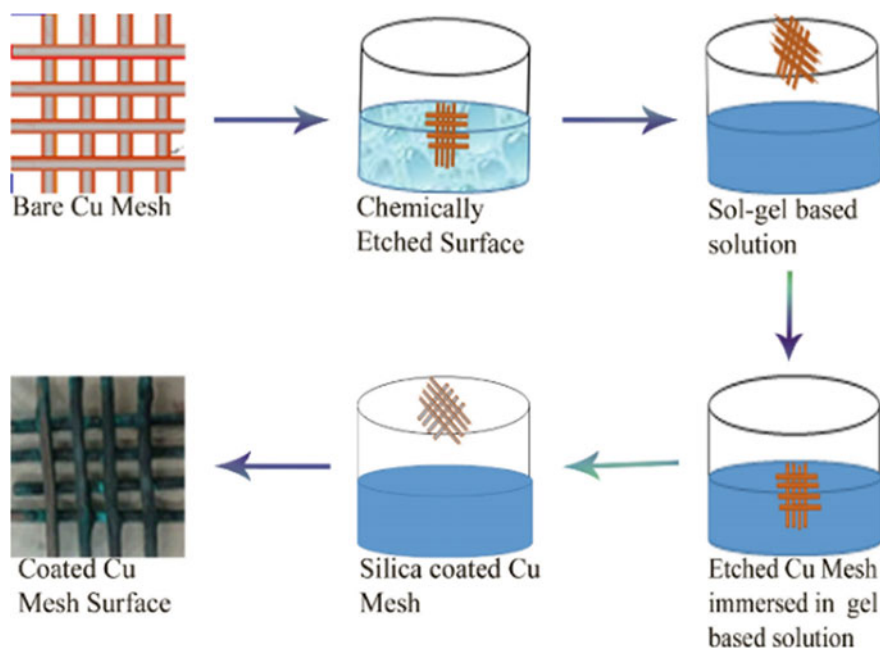


Fig. 2 Protocol for coating of Cu mesh-like surface

As of now, the Cu tubes were joined by brazing (mixture of propane and oxygen) to avoid the impact of weakness to the strength of joints. Thereby, the procedure to obtain the permanent layer is shown in Fig. 2.

Initially, the Cu mesh-like surface was cleaned with acetone and then etched in HCL solution for 30 s to remove the impurities and the oxide layer. After etching, the mesh surface was followed to dried for 30 min in vacuum desiccator.

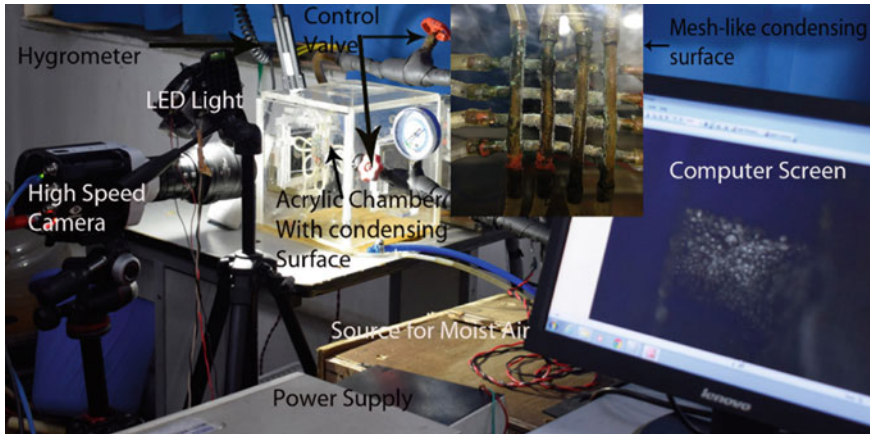


Fig. 3 Experimental setup of coated copper surface for moist air condensation [16]

Furthermore, the surface is again ultrasonically cleaned with acetone for 15 min to remove the roughness and dried up at room condition. To modify the wettability of surface, the mesh-like Cu surface was completely immersed in the chemically sol-gel-based solution of silicate solution for 4 days as reported in literature [16]. As a result, a uniform silicate coating of bluish color on mesh-like surface was achieved. Finally, the surface to uphold enduring layer was dried at 100 °C for 30 min at room temperature. Silylation method is preferred because it occurs through self-assembly process and forms proper symmetrical bonding on the treated metallic surfaces. It basically attaches to silylated hydroxyl groups which enhances the condensation rate.

Now, this prepared surface was placed in experimental setup for harvesting water from moist air via condensation as discussed in literature [17], as shown in Fig. 3.

After adequate process of condensation, the surface characteristics were performed by sessile method using the setup of goniometer [18] to measure static and dynamic contact angle as shown in Fig. 4.

The setup consists of an inbuilt capability of moving forward and reverse to an automated syringe pump with infusion and extraction capabilities. However, a configured and measured volume drop from the micro syringe pump was triggered on the surface of mesh like consecutively preserved on the stand of translation stages. These droplets are captured by high resolution camera in the presence of LED lights and thereby processed using Image J software for measuring the angle at liquid-vapor interface. Consequently, the chemically etched Cu mesh-like surface was carried successfully for condensation experiments followed to analyze surface morphology using sessile method under controlled condition.

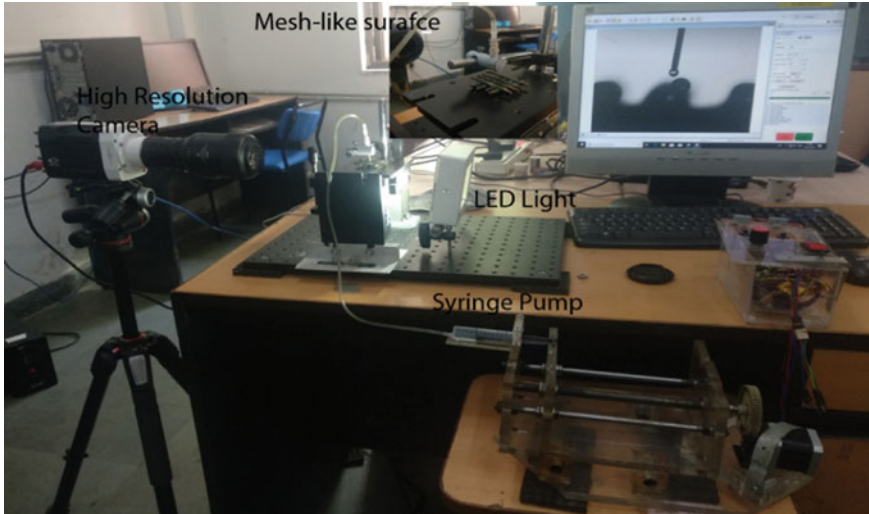


Fig. 4 Photograph of experimental setup for obtaining of static and dynamic contact angles

3 Result and Discussion

The engorgement of surface due to coating developed to a well-characterized hydrophobic surface resulted to a bouncing surface and high contact angles eventually profited to a loomed condensation rate. The condensation cyclic phenomenon at thermal equilibrium states was obtained in approx. 45 min as shown in Fig. 5 captured at different interval of time at relative humidity above 80%.

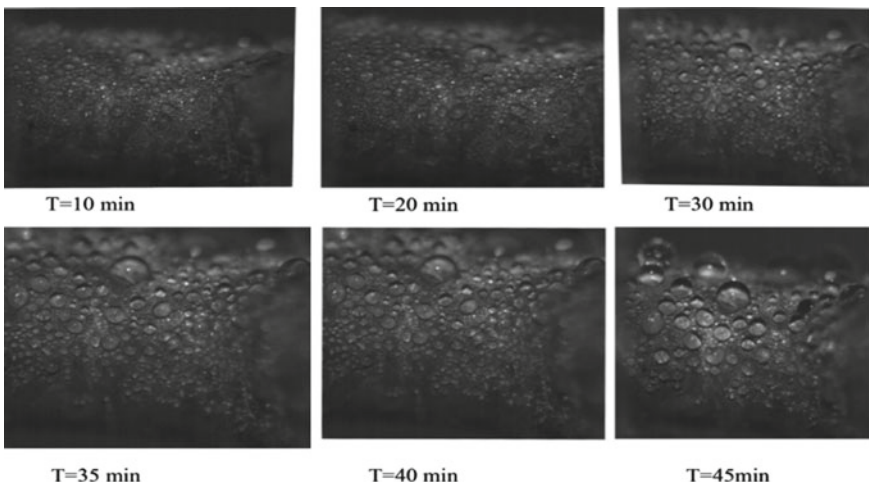


Fig. 5 Condensation of water vapor in presence of moist air on copper mesh-like surface for different time interval at relative humidity above 80%

Fig. 6 Static contact angle on consecutive tubes of copper mesh surface

- (i) $\theta = 133 \pm 4^\circ$
 (ii) $\theta = 126 \pm 5^\circ$
 (iii) $\theta = 135 \pm 5^\circ$
 (iv) $\theta = 141 \pm 4^\circ$

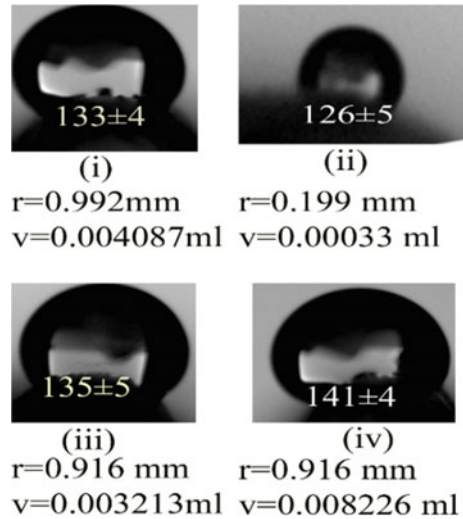


Figure 6 shows the static contact angle measurement using Image J, an image processing software of water droplet during experiment on goniometer for consecutive horizontal tubes on tubular copper mesh surface. During processing with the software, the diameter of the droplets was measured and volume were also calculated. The dynamic contact angles on the surface are shown in Fig. 7. The measured static advancing contact angle $\theta_A = 145^\circ$ and receding $\theta_R = 129^\circ$, thus the contact angle hysteresis (CAH) is allied with $\theta_A - \theta_R = \Delta\theta = 160^\circ$ on the micro-structured surfaces.

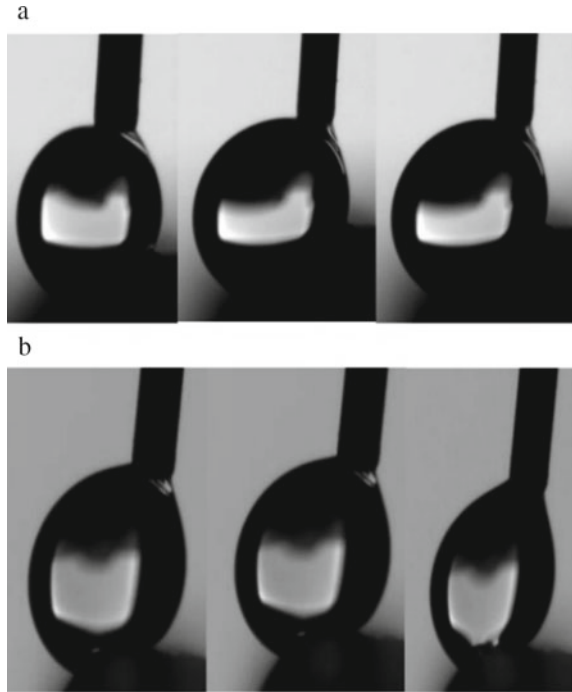
Thereby, the CAH ($\Delta\theta$) effects wettability of the surface and a low CAH procures a suitable and efficient condensing surface [19]. Significantly, lower CAH reduces the influence of the surface energy on the contact angle due to mesh-like structure of the surface.

4 Conclusion

The experimental study and investigating on condensation process of moist air around mesh-like surface have been carried out to present the effects of condensation rate due to heat and mass transfer coefficients. The conclusions obtained from the present study are listed briefly as follows:

1. A scalable, sustainable, low consuming energy dropwise condensation is achieved on silica gel-based coated mesh-like surface.

Fig. 7 Dynamic contact angles **a** advancing and **b** receding contact angles on surface



2. Surface texturing became a surface expansion technology extended to high transfer coefficient rates for nucleating and tailoring of drops.
3. A lower contact angle hysteresis (CAH) of 160 is achieved below 200 on tubular copper surface due to inherently limited restriction from surface energy.

The surface morphology considerably surface roughness can be experimentally carried in future to study the role of enhanced condensation rate. The effect of surface roughness can be concluded with respect to the static contact angle to support low wettability phenomenon.

Acknowledgements The author acknowledges the financial support from the Science and Engineering Research Board (SERB), India, established through an Act of Parliament: SERB Act 2008, Department of science & Technology (DST), India, Government of India (Project no: ECR/2016/000020) and also to Ms. Vishakha Bhagel, Research Scholar, Department of Amity School of Engineering and Technology, for support to operate Goniometer.

References

1. Khawaji AD, Kutubkhanah IK, Wie JM (2008) Advances in seawater desalination technologies. *Desalination* 221(1–3):47–69
2. Chen Kang H, Yu Wei L (2015) Enhancement or suppression of dehumidification process by surface treatments. *J Eng Technol Res* 7(5):59–65
3. Liu K, Yao X, Jiang L (2010) Recent developments in bio-inspired special wettability. *Chem Soc Rev* 39(8):3240–3255
4. Yao X, Song Y, Jiang L (2011) Applications of bio-inspired special wettable surfaces 719–734
5. Sun J, Wang HS (2016) On the early and developed stages of surface condensation : competition mechanism between interfacial and condensate bulk thermal resistances. *Nat Publ Gr* 1–12
6. Amirfazli A, Neumann AW (2004) Status of the three-phase line tension: a review. *Adv Colloid Interface Sci* 110(3):121–141
7. Fessehaye M, Abdul-Wahab SA, Savage MJ, Kohler T, Gherezghiher T, Humi H (2014) Fog-water collection for community use. *Renew Sustain Energy Rev* 29:52–62
8. Tu Y, Wang R, Zhang Y, Wang J (2018) Progress and expectation of atmospheric water harvesting. *Joule* 2(8):1452–1475
9. Wen R, Xu S, Zhao D, Yang L, Ma X, Liu W. Research article sustaining enhanced condensation on hierarchical mesh—covered surfaces
10. Wen R et al (2018) Sustaining enhanced condensation on hierarchical mesh-covered surfaces. *Natl Sci Rev* 5(6):878–887
11. Seo D, Lee J, Lee C, Nam Y (2016) The effects of surface wettability on the fog and dew moisture harvesting performance on tubular surfaces. *Sci Rep* 6(March):1–11
12. Xie J, Xu J, He X, Liu Q (2017) Large scale generation of micro-droplet array by vapor condensation on mesh screen piece. *Sci Rep* 7:1–13
13. Salek F, Moghaddam AN, Naserian MM (2018) Thermodynamic analysis and improvement of a novel solar driven atmospheric water generator. *Energy Convers Manag* 161 (January):104–111
14. Singh PL, Sikarwar BS (2020) Condensation of moist air on mesh-like surfaces. *Asian J Water Environ Pollut* 17(2):65–72
15. Kim H et al (2017) Water harvesting from air with metal-organic frameworks powered by natural sunlight. 8743(April):1–10
16. Sharma DK, Baghel V, Kumar R, Avasthi DK, Sikarwar BS (2019) Recent developments in fabrication of super-hydrophobic surfaces: a review. In: *Lecture notes in mechanical engineering*
17. Sikarwar BS, Singh PL, Muralidhar K, Khandekar S (2016) Atomistic modeling of dropwise condensation. *AIP Conf Proc* 1731:1–6
18. Baghel V, Singh B, Kumar D, Avasthi DK (2020) Materials today: proceedings a correlation of metallic surface roughness with its hydrophobicity for dropwise condensation. *Mater Today Proc* 21:1446–1452
19. Gao L, Mccarthy TJ (2006) Contact angle hysteresis explained 22:6234–6237

Studies on Flow Past Surface Cooled Circular Cylinder at Low Reynolds Number



Sujith Stephen and S. Ajith Kumar

Abstract A computational investigation on two-dimensional surface splitted (along x-axis through 0° and 180° and obtained top surface and bottom surface for the cylinder) circular cylinder has been conducted for various Richardson number ranges $-1 \leq Ri \leq 0$ and at Reynolds number 100. The negative value of Richardson number represents cooling effect on the surface of the cylinder. The cooling of surfaces of circular cylinder affects the vortex dynamics and causes variation in aerodynamic parameters and vortex shedding frequency. This work attempts to give a clear idea on changes in vortex dynamics due to cooling of top surface and bottom surface of the circular cylinder individually. Cooling effect on the surface created unstable density layers and caused asymmetry in vortex dynamics on both top half cooled and bottom half cooled cases. Cooling of top surface shown reduction in shedding frequency while cooling of bottom surface shown increase in shedding frequency, which is exactly opposite behavior. Cooling of top surface of the cylinder is an effective drag reduction method and also found reduction in shedding frequency.

Keywords Drag reduction · Cooled cylinder · Positive lift · Asymmetric vortex shedding

Nomenclature

C_L Coefficient of lift
 C_D Coefficient of drag
Re Reynolds number
Ri Richardson number
St Strouhal number
 C_p Coefficient of pressure

S. Stephen (✉) · S. Ajith Kumar
Department of Mechanical Engineering, Amrita Vishwa Vidyapeetham,
Amritapuri 690525, India
e-mail: sujith.stephen@outlook.com

S. Ajith Kumar
e-mail: ajithkumars@am.amrita.edu

1 Introduction

Fluid flow around bluff body has great scope in engineering and non-engineering applications. Circular cylinder is one of the most commonly studied bluff bodies with a great number of literatures [1]. Researchers noticed the formation and shedding of vortices for a range of Reynolds number. The studies were concentrating more on the vortex shedding and effect of vortex shedding in wake dynamics [2–4]. The heat transfer between fluid and cylinder surfaces adds more complexity to the wake dynamics as well as in the vortex shedding. The effect of buoyancy due to heat transfer creates these additional problems and understanding of complexity of physics due to heat transfer will aid the designers in the development of instruments to bluff body aerodynamics [5]. Moreover, this phenomenon also connected with other engineering applications, such as inshore structures, chimney structure, reactor rods, and cooling towers. Fluid flow, heat transfer, and flow-induced vibrations are linked and which should be carefully studies for engineering applications [6].

The flow over a static cylinder becomes time dependent above Reynolds number, $Re \approx 47$, and it is fundamental in fluid mechanics [7]. The dependency of fluid flow and aerodynamic coefficient with Re for flow past circular cylinder is reported in Roshko [2], Williamson 1996 [7], and Zdravkovich [8]. The Richardson number, Ri , has substantial influence in vortex shedding pattern as well as the frequency of shedding. This dependency is due to the variation of vortex shedding strength with Ri [9].

Ajith Kumar et al. [10] in their work studied on heated cylinder at low Reynolds number and found asymmetry in vortex shedding with negative lift with increase in Ri . Strouhal number and Nusselt number was found increasing with Richardson number due to increase in shedding frequency and heat transfer, respectively. They found out that the dissipation of vortex in the upside was faster compared to downside due to density stratification. Jain and Lohar [11] conducted vertical flow past heated circular cylinder for $Re = 100$ and 200 and found out increase in shedding frequency with heat input. The reason they pointed out is the dependency of vortex shedding strength with heat input. Lecordier et al. [12] conducted an experimental study on flow around heated circular cylinder with air and water as fluid mediums and found an opposite trend for air and water in wake dynamics. The trend of variation of dynamics viscosity of air and water is the reported reasons. Shi et al. [13] conducted a 2D numerical study on heated cylinder for Re up to 170 . They found that the heating effect can stabilize the flow past cylinder due to increase in kinematic viscosity of the air with rise in temperature. Also, they noted the reduction of coefficient of drag with heat input due to delayed flow separation.

Hatanaka and Kawahara [14] conducted a numerical study for vertically upward flow on both heated and cooled cylinders at $Re = 100$. Their major concentration was on vortex shedding trends in both cooled and heated cases. They found decrease in frequency of vortex shedding followed with a negative buoyancy force

for the cooled case. The reason for the reduction in shedding frequency was due to reduction in strength of vortices shed from cylinder with cooling. As reported, the negative buoyant force noticed for shed vortices is due to density increment. Chang and Sa [15] reported a reduction in movement of vortices in wake with cooling due to deceleration of wall boundary layer. Patnaik et al. [16] studied heated and cooled cases for $20 \leq Re \leq 40$. Their major concentration was on the twin counter rotation vortices (Föppl vortex) and its dynamics with heating and cooling of cylinder. They could see increase in coefficient of drag while cooling and the early flow separation found to be the reason.

We could see from the literature that heating will reduce the coefficient of drag and cooling does the inverse. However, despite all the studies, it is not clear that the effect of heating/cooling the top surface or bottom surface of the cylinder individually. The current study attempts to give an idea on effect of individual cooling of surfaces (top half and bottom half) in vortex dynamics, aerodynamic, and shedding parameters. To explore this objective, we have created a 2D rectangular flow domain with a circular cylinder. The overall 2D surface of the cylinder is splitted along the x-axis through 0° and 180° and obtained top surface and bottom surface for the cylinder. In this work, we are conducting a numerical study on surface cooled cylinder for five Richardson number, ranges $-1 \leq Ri \leq 0$. As a first step toward this complicated physics, we have chosen laminar flow at $Re = 100$.

2 Numerical Methodology

The conservation of mass, momentum, and energy equations are the governing equations for fluid flow are given in Eqs. (1)–(4)

$$\frac{\partial u}{\partial x} + \frac{\partial v}{\partial y} = 0 \tag{1}$$

$$\frac{\partial u}{\partial t} + u \frac{\partial u}{\partial x} + v \frac{\partial u}{\partial y} = -\frac{\partial p}{\partial x} + \frac{1}{Re} \left(\frac{\partial^2 u}{\partial x^2} + \frac{\partial^2 u}{\partial y^2} \right) \tag{2}$$

$$\frac{\partial v}{\partial t} + u \frac{\partial v}{\partial x} + v \frac{\partial v}{\partial y} = -\frac{\partial p}{\partial y} + \frac{1}{Re} \left(\frac{\partial^2 v}{\partial x^2} + \frac{\partial^2 v}{\partial y^2} \right) + Ri \cdot \Theta \tag{3}$$

$$\frac{\partial \Theta}{\partial t} + u \frac{\partial \Theta}{\partial x} + v \frac{\partial \Theta}{\partial y} = \frac{1}{Re \cdot Pr} \left(\frac{\partial^2 \Theta}{\partial x^2} + \frac{\partial^2 \Theta}{\partial y^2} \right) + Ri \cdot \Theta \tag{4}$$

The equations govern fluid flow for the two-dimensional flow that are discretized and solved using a commercial CFD tool, ANSYS 18.2. The PISO algorithm [17] is



Fig. 1 Schematic representation of problem with boundary conditions

adopted as pressure–velocity coupling, and the equations are solved using second-order upwind scheme. The PISO algorithm consists of one predictor step and two corrector steps. The convergence criteria are set to 10^{-06} .

Figure 1 represents computational domain with boundary conditions and the flow domain variables are non-dimensionalized with diameter of the circular cylinder. In the figure, the upper half and lower half of the cylinder are highlighted with different colors.

2.1 Grid-Independent Study

A grid-independent study is carried out to identify optimum grid size required to investigate this problem. ANSYS Workbench is used to create structured mesh for the domain.

Figure 2 manifests the quadrilateral mesh used for the numerical analysis. To get an accurate mesh near the surface of the cylinder, a square adapted quad meshing is

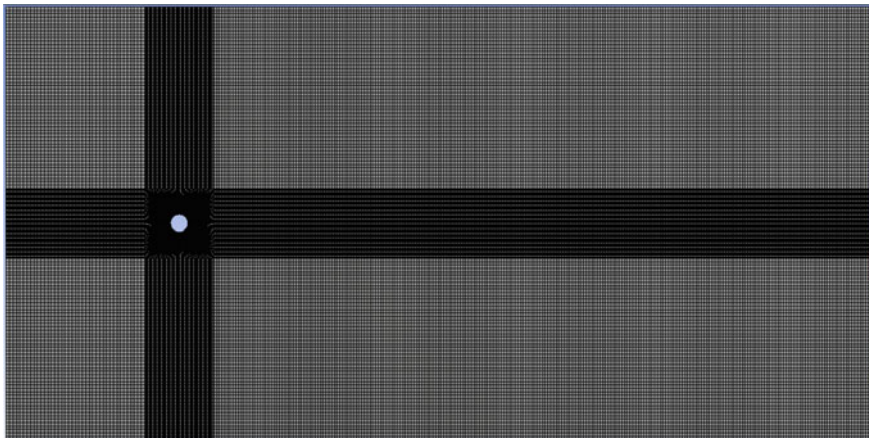


Fig. 2 Grid structure obtained after grid independence test

Table 1 Comparison of C_D values in the grid independence test

Grid size	Coefficient of drag (C_D)
38,904	1.500
56,026	1.404
65,721	1.407

done. Computations are done for three different grid structures and the C_D values are compared (Table 1). The percentage deviation for the calculated C_D values are noted and found a grid with 56,026 cells is optimum. The obtained optimum grid structure is used for the remaining studies presented in this work.2

2.2 Code Validation

The numerical algorithm used in this study is validated in advance for some standard problems such as flow over horizontal and vertical circular cylinder, flow past square and corner modified square cylinders, and flow over backward and forward facing steps. The algorithm in the present study is validated with flow around heated cylinder which is studied at $Re = 100$ and Ri ranges from 0 to 1. The coefficient of drag C_D and lift C_L and the Strouhal number (St) obtained from present study are compared with results available in some literature and are shown below (Table 2). The results obtained are matching very well with the literature.

Table 2 represents the comparison of present value of C_D and St at $Ri = 0$ and $Re = 100$ with Raghuvanshi and Mittal [18], Williamson [3], Wang and Russell [19], Calhoun [20] and Tritton [21] with maximum deviation less than 4.5%. That shows the results are in good agreement with the literature.

Table 3 shows the comparison of St in present study at $0 \leq Ri \leq 1$ and $Re = 100$ with Ajith Kumar et al. [10]. The maximum deviation is less than 2.5%, which shows a good agreement with the results in the literature and also shows the comparison of $|C_L|$ in present study at $0 \leq Ri \leq 1$ and $Re = 100$ with Ajith Kumar et al. [10]. The maximum deviation is less than 2%, which shows a fair agreement with the results in the literature.

The coefficient of drag (C_D) and lift (C_L) and the Strouhal number (St) obtained from present study are compared with results available in aforementioned literature and are shown a very good agreement with very low deviation. Thus, the validation of the numerical code has been done.

Table 2 Comparison of C_D and St with literature for $Ri = 0$ at $Re = 100$

Literature	C_D	St
Raghuvanshi and Mittal [18]	1.4	0.168
Williamson (Exp) [3]	–	0.164
Wang and Russell [19]	1.38	0.169
Calhoun [20]	1.33	0.175
Tritton [21]	1.45	–
Present study	1.404	0.167

Table 3 Comparison of C_L and St with Ajith et al. [10] for various Ri

Literature	Ajith Kumar et al. [10]		Present study	
	C_L	St	C_L	St
0	0	0.164	0	0.167
0.25	0.344	0.165	0.341	0.168
0.5	0.690	0.167	0.683	0.170
0.75	0.998	0.170	0.994	0.171
1.00	1.271	0.175	1.302	0.174

3 Results and Discussions

The present study is carried out for Richardson number $-1 \leq Ri \leq 0$ (specifically for $Ri = -1, -0.75, -0.5, -0.25, 0$) at Reynolds number $Re = 100$. The boundary conditions applied are velocity-inlet with non-dimensional velocity of 1 along X-direction and 0 on Y-direction with zero gauge pressure at the outlet. A non-dimensional temperature (θ) of -1 is kept on the top and bottom surfaces of the cylinder. The top and bottom walls of the domain are given as wall boundaries with adiabatic condition. Two studies have been conducted one with cooling of top half and other with cooling of bottom half of the cylinder.

The cylinder will produce an oscillating instantaneous lift above all values of $Re = 47$. If the cylinder is not having any heat transfer with fluid or the cylinder is non-rotating then net lift produced by a circular cylinder will be zero even though the instantaneous lift has oscillation. It can be seen from Fig. 3 that for $Ri = 0$, the average value of C_L is zero even though it is fluctuating with time. With decrease in Ri , the instantaneous value of C_L is shifting upward, which shows positive lift.

Figures 4 and 5 show the variation of C_P distribution on upper and lower halves of the cylinder for top surface and bottom surface cooled case at various Ri . From the plot, it is clear that the pressure difference is increasing for upper and lower

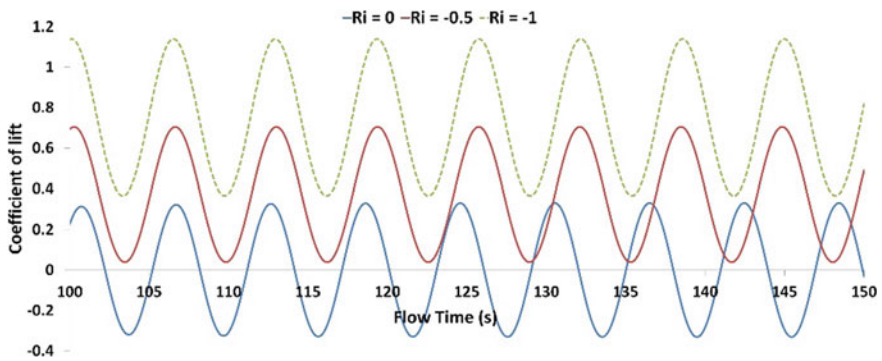


Fig. 3 Variation of C_L with flow time for various Ri at $Re = 100$. As Ri decreases, the time average of C_L is increasing due to positive lift with cooling

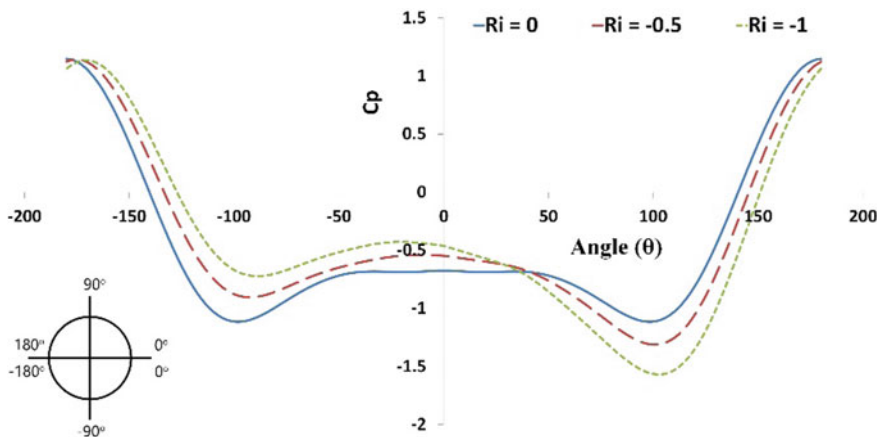


Fig. 4 Distribution of C_p on the cylinder for top surface cooled cases at various Ri

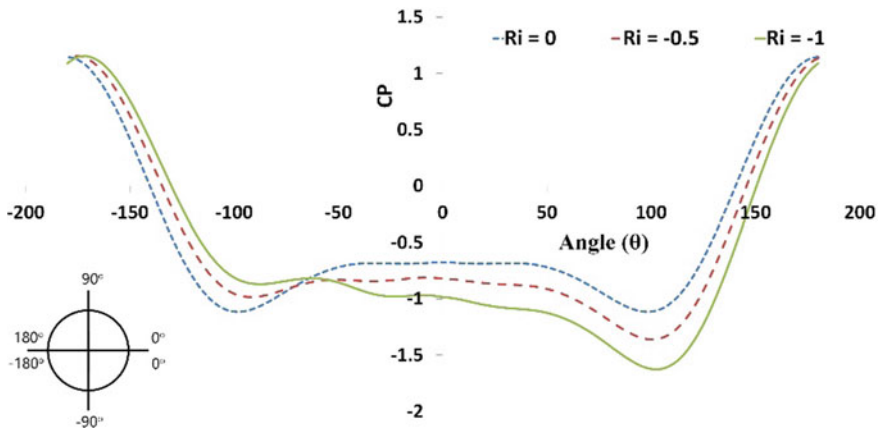


Fig. 5 Distribution of C_p on the cylinder for bottom surface cooled cases at various Ri

halves with negative Ri . The pressure variation causes an upward lift for the cylinder which is inversely proportional to Ri , and from Fig. 3 we can see the inverse proportionality of C_L with Ri for both the cases.

The pressure difference between upper and lower halves of the cylinder at $Ri = -1$ for both top surface cooled and bottom surface cooled cases has been observed from Fig. 6. The pressure difference is high for top surface cooled case compared to bottom surface cooled case, which causes a lower C_L for bottom surface cooled case compared to top surface cooled case and it is true for other values of Ri .

Figure 7 shows the variation of C_L at various values of Ri for top surface cooled and bottom surface cooled cases. From the figure, it can be seen that, more

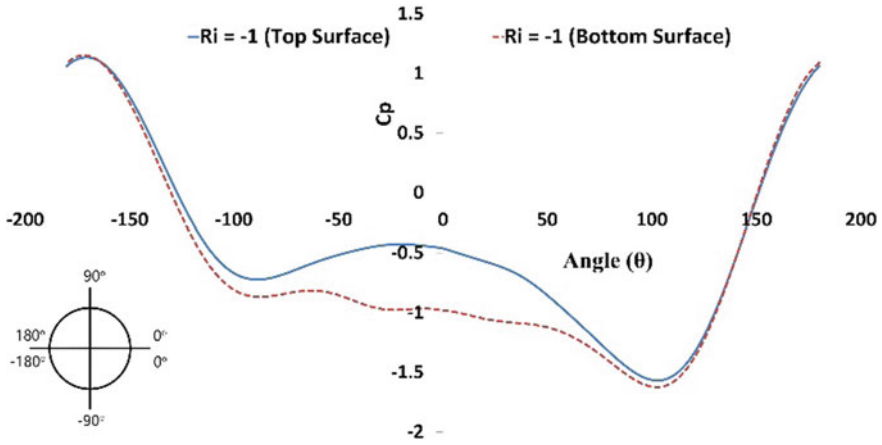


Fig. 6 Comparison of C_p distribution for top and bottom surface cooled cases at $Ri = -1$

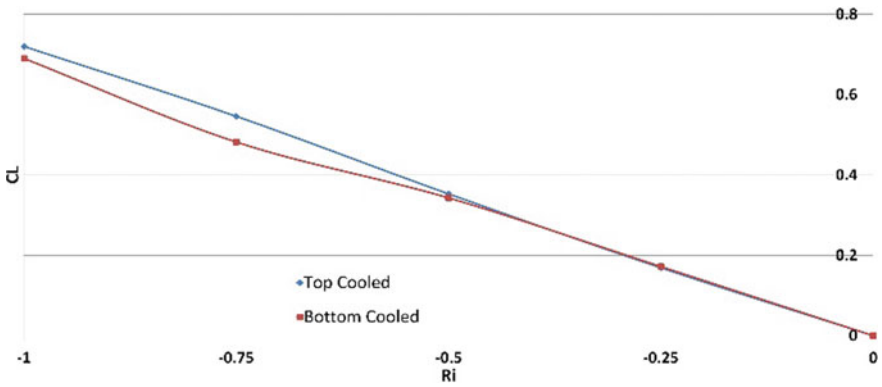


Fig. 7 Variation of C_L for different Ri at $Re = 100$ for top and bottom surfaces cooled cases

difference in C_L for both the cases are observed in higher negative value of Ri due to more variation in pressure difference between upper and lower halves.

While cooling the surfaces of the cylinder, the fluid passes over that surface will get cooled and it becomes denser and as a result of this increase in density, the fluid will move toward the direction of gravity. From Fig. 8, it can be observed that when there is no cooling, the shedding is symmetric about the horizontal axis of the flow. But when cooling is given on the surface of the cylinder, the vortex shedding became asymmetric for both top cooled case and bottom cooled case and it can be observed from Figs. 9 and 10 for $Ri = -1$ and it is true for other values as well.

When the top surface of the cylinder is cooled, the vortices shed from the top surface moved downward, which can be observed from Fig. 9 and caused reduction

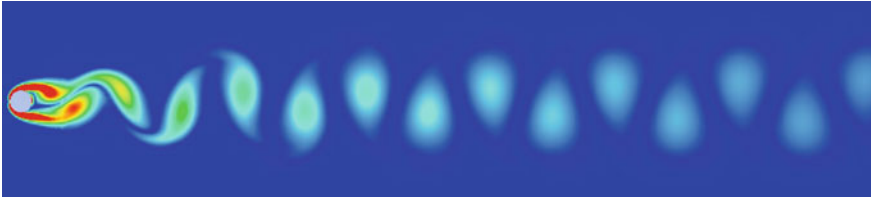


Fig. 8 Vortex structure at $Ri = 0$ and $Re = 100$. Shedding is symmetric to the horizontal axis



Fig. 9 Vortex structure at $Ri = -1$ on the top surface and $Re = 100$. Shedding is not symmetric to the horizontal axis due to cooling



Fig. 10 Vortex structure at $Ri = -1$ on the bottom surface and $Re = 100$. Shedding is not symmetric to the horizontal axis due to cooling

in wake width. Also, from Fig. 10, it can be seen that when the bottom surface is cooled, the vortices shed from the bottom surface moved downward toward gravity and caused widening of wake width. The reduction in wake width due to cooling top surface of the cylinder increased the pressure near the base point and from Fig. 4 it can be observed. This increment in pressure near the base point reduced the pressure difference between stagnation point and base point and caused reduction in C_D . Similarly, the widening of wake while cooling the bottom surface caused reduction of pressure in near the base point and it can be observed from Fig. 5. The reduction in pressure near base point increased the pressure difference between stagnation point and base point which caused increment in C_D .

Figure 11 shows the variation of C_D at various values of Ri for top surface cooled and bottom surface cooled cases. From the figure it can be seen that, more difference in C_D for both the cases are observed in higher negative value of Ri due to more variation in pressure difference between stagnation point and base point.

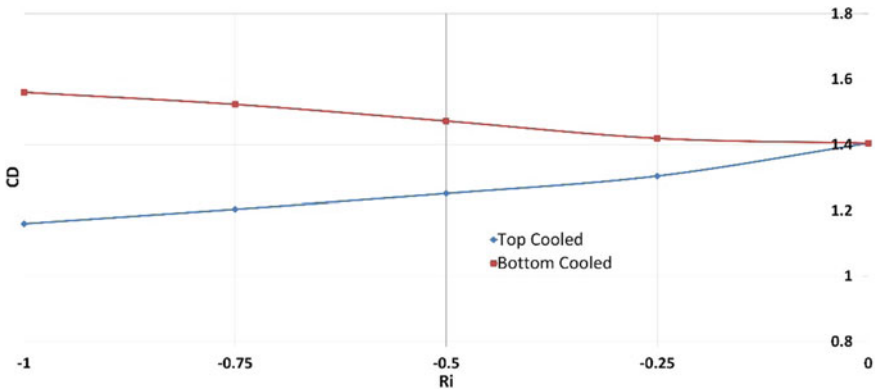


Fig. 11 Variation of C_D for various Ri at $Re = 100$ for top and bottom surface cooled cases

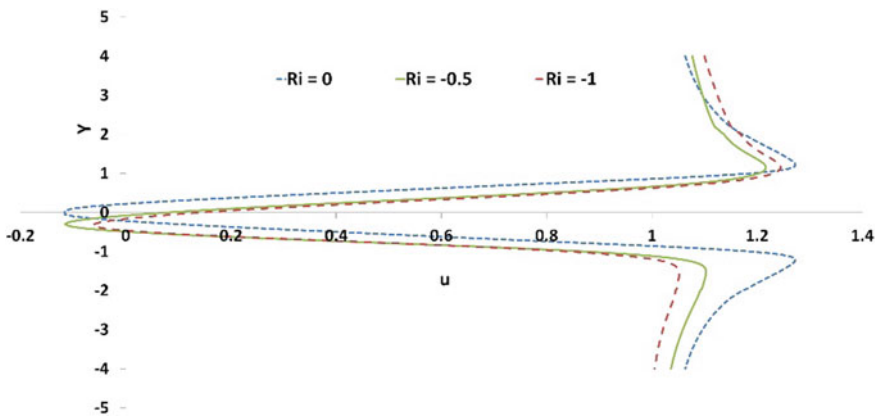


Fig. 12 Streamwise velocity profile at $X = 2$ for top surface cooled case at various Ri

From Fig. 12 it can be observed that, at non-cooled case ($Ri = 0$) the streamwise velocity profile at $X = 2$ is symmetric about the horizontal axis. When the cylinder surface is cooled, the profile became asymmetric about horizontal axis and which is due to the asymmetry in vortex shedding caused by the effect of negative buoyancy and is true for other values of Ri . The asymmetry in vortex shedding also can be observed from Figs. 9 and 10.

The vortex shedding frequency depends on Reynolds number (Re) and the Re at which shedding phenomenon starts is called as critical Reynolds number (Re_{cr}). For a flow past circular cylinder, $Re_{cr} = 47$ and the reason for the dependence of shedding frequency with Re is reported in [2–4, 8, 22], etc. Strouhal number (St) is a non-dimensional parameter, which represents the shedding frequency. For top surface cooled case, the fluid passes over the top surface that will move downward

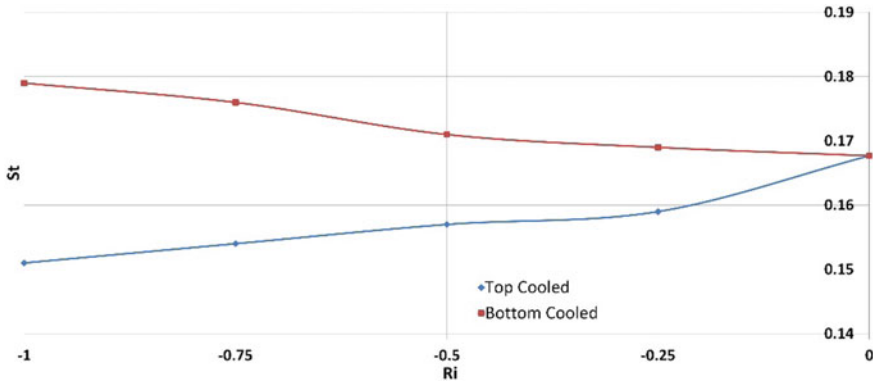


Fig. 13 Variation of St for different Ri at Re = 100 for top and bottom surface cooled cases

due to gravity and it will interfere with the vortices shedding from the bottom surface and slows down the shedding from the bottom half. This deceleration causes reduction in shedding frequency. For bottom surface cooled case, the fluid passes over the bottom surface that gets dissipated earlier than vortices from top surface due to unstable density stratification caused by cooling. This acceleration in shedding from the bottom half causes increment in shedding frequency.

Figure 13 shows the effect of cooling in vortex shedding frequency. It can be seen that when cooling the surfaces of the cylinders, top cooled and bottom cooled cases show exactly opposite trend in St.

4 Conclusion

A detailed numerical study is carried out to understand the effect of cooling of surfaces of circular cylinder at Re = 100. In this study, the variation of coefficient of drag, lift and Strouhal number with Richardson number ranges -1 to 0 are done. Major findings are,

- An asymmetry in vortex shedding found increasing with negative values of Ri toward the direction of gravity.
- Cooling the top surface of the cylinder reduced and wake width and caused reduction in pressure drag.
- The shedding frequency and C_D shown exactly opposite behavior for both top surface cooled and bottom surface cooled cases.
- The deceleration of vortices in top surface cooled case caused reduction in shedding frequency.
- The coefficient of the lift found increasing for both top surface and bottom surface cooled case in higher negative values of Ri due to variation in pressure distribution.

References

1. Berger E, Wille R (1972) Periodic flow phenomena. *Annu Rev Fluid Mech* 4(1):313–340
2. Roshko A (1993) Perspectives on bluff body aerodynamics. *J Wind Eng Ind Aerodyn* 49 (1):79–100
3. Williamson CHK (1996) Three-dimensional wake transition. *J Fluid Mech* 328:345–407
4. Williamson CHK, Roshko A (1990) Measurements of base pressure in the wake of a cylinder at low Reynolds numbers. *Zeitschrift fur Flugwissenschaften und Weltraumforschung* 14(1–2):38–46
5. Eckert E, Soehngen E (1952) Distribution of heat transfer coefficients around circular cylinders in crossflow at Reynolds numbers from 20 to 500. *Trans ASME* 74:343–347
6. Eaton B (1987) Analysis of laminar vortex shedding behind a circular cylinder by computer-aided flow visualization. *J Fluid Mech* 180:117–145
7. Williamson C (1996) Vortex dynamics in the cylinder wake. *Annu Rev Fluid Mech* 28:477–539
8. Zdravkovich M (1997) Flow around circular cylinders: fundamentals 1
9. Steenhoven A, Rindt C (2003) Flow transition behind a heated cylinder. *Int J Heat Fluid Flow* 24:322–333
10. Ajith Kumar S, Anil Lal S, Sameen A (2016) Flow past a moderately heated horizontal cylinder at low Reynolds number. *Proc Instit Mech Eng Part G J Aerosp Eng* 230(7):1224–1239
11. Jain P, Lohar B (1979) Unsteady mixed convection heat transfer from a horizontal circular cylinder. *J Heat Transf* 101
12. Lecordier J, Hamma L, Paranthoen P (1991) The control of vortex shedding behind heated circular cylinders at low Reynolds numbers. *Exp Fluids* 10:224–229
13. Shi J-M, Gerlach D, Breuer M, Biswas G, Durst F (2004) Heating effect on steady and unsteady horizontal laminar flow of air past a circular cylinder. *Phy Fluids* 16(12):4331–4345
14. Hatanaka K, Kawahara M (1992) A numerical study of vortex shedding around a heated/cooled circular cylinder by the three-step Taylor-Galerkin method. *Int J Numer Meth Fluids* 21(10):857–867
15. Chang K-S, Sa J-Y (1990) Effect of buoyancy on vortex shedding in the near wake of a circular cylinder. *J Fluid Mech* 220:253–266
16. Varaprasad Patnaik B, Aswatha Narayana P, Seetharamu K (1999) Numerical simulation of vortex shedding past a circular cylinder under the influence of buoyancy. *Int J Heat Mass Transf* 42:3495–3507
17. The computation of compressible and incompressible recirculating flows by a non-iterative implicit scheme. *J Computat Phy* 62(1):66–82
18. Mittal S, Raghuvanshi A (2001) Control of vortex shedding behind circular cylinder for flows at low Reynolds numbers. *Int J Numer Meth Fluids* 35(4):421–447
19. Russell D, Wang ZJ (2003) A cartesian grid method for modeling multiple moving objects in 2D incompressible viscous flow. *J Comp Phys* 191(1):177–205
20. Calhoun D (2002) A cartesian grid method for solving the two-dimensional stream function-vorticity equations in irregular regions. *J Computat Phys* 176(2):231–275
21. Tritton DJ (1959) Experiments on the flow past a circular cylinder at low Reynolds numbers. *J Fluid Mech* 6(4):547–567
22. Taneda S (1956) Experimental investigation of the wakes behind cylinders and plates at low Reynolds numbers. *J Phys Soc Japan* 11:302–307

Design and Thermal Analysis of Pipe Insulation



Shwetank Avikal, Reena Devi, Arjun Singh Bisht,
and K. C. Nithin Kumar

Abstract Water pipelines in hilly areas often burst during winter because the water in the pipes freezes due to low temperatures. During the expansion of freeze water, the pressure inside the pipe rises suddenly, and therefore, because of this sudden pressure rise, pipe ruptures. Protecting pipes from breakage, a concept of piping insulation is introduced. Pipe insulation is thermal or acoustic insulation which conserves thermal energy. Through pipe insulation, the freezing time of water standby in pipeline increases and therefore reduces the risk of immediate freezing of water up to a certain extent. For eradicating this problem, the local water supply regulatory body needs to use insulations in the pipeline. Thermal insulating materials are advanced materials that could be applied on pipe surfaces to reduce heat transfer and hence increasing insulating capability of a material. The present article proposes the method for eradicating water freezing and pipe bursting problems using thermal insulation which could reduce the heat transfer losses. Insulation capability of proposed insulating materials is analysed using ANSYS. Six different materials have been selected for thermal insulation coating. The results have been compared between all selected material, and a suitable material has been proposed for pipe insulation.

Keywords Pipe insulation · Thermal barrier coating · ANSYS · Finite element method · Heat loss reduction

S. Avikal (✉) · R. Devi · A. S. Bisht
Department of Mechanical Engineering, Graphic Era Hill University, Dehradun, India
e-mail: shwetank.avikal@gmail.com

R. Devi
e-mail: reenanegi4646@gmail.com

A. S. Bisht
e-mail: barjun32@gmail.com

K. C. Nithin Kumar
Department of Mechanical Engineering, Graphic Era Deemed to be University,
Dehradun, India
e-mail: kcnkumar@ymail.com

1 Introduction

When pipes are used for chilled water or are kept under critical conditions, the water inside the pipeline may freeze due to drop of ambient temperature. During expansion process, a high pressure arises inside the pipe and therefore its burst. In order to avoid such problems, thermal insulation systems are used. Thermal insulation has been used to restrict heat transfer rate from system to the surrounding and vice versa. It also dealt condensation and melting applications like providing comfort zone conditions, preservation of food items and medicines for many years. Change in climate, higher energy efficiency, utilization of available energy resources show the importance of thermal insulation, and therefore, it is widely accepted for many industrial applications. [1]. Large amount of energy can be saved in industrial and domestic use of water by using thermal insulation on the pipelines. It can reduce approximately 40–60% of the total cost [2]. That's why, it has become more important to insulate the pipelines with a less expensive material. Heat loss inside the material occurs due to conduction and convection phenomena from the system to the surrounding. Heat transfer primarily depends on thermal conductivity of the material. The material used in the thermal insulation must have lower heat transfer rate and higher stability. Thermal insulation materials may be natural substances or man-made [3]. Masatin et al. (2017) have conducted an experiment on 532 m long pipeline for calculating reduction in pipeline heat loss by implementing PUR prefabricated foam shell at the place of mineral wool. The onsite experiment was done in order to estimate pipeline heat loss reduction by changing old mineral wool insulation to prefabricated PUR foam shells. The results found that the reduction in the heat loss about 3.35 times as compared to the previous one [4]. The thickness of the insulation layer is also playing a key role in calculating the cost of insulation and minimizing the heat losses. The thickness of insulation increases, heat loss may decrease [5, 6].

A study has been carried out on multilayer walls considering the ambient conditions of turkey, using finite difference method and a MATLAB computer programme. Five different structural materials and two different insulation materials are used for analysis. The results are compared between insulated and un-insulated wall structure and obtained optimal thickness of insulation which varies between 228.2 cm. This data is useful for thermal design consideration like thermal comfort, etc. [1]. The main objective of this analysis was to investigate various insulating materials with similar properties, to analyze and find the best insulator that works better under the freezing conditions. Materials, which have a low thermal conductivity, determine a material's ability to resist the flow of heat. Therefore, the analysis was done to find a material of low thermal conductivity and that possess minimum heat loss from the pipes. This goal was achieved by conducting a critical review of the state-of-the art literature in this field and finding the top six materials that act as an insulator under low temperature conditions and by performing thermal analysis on pipe insulation with the help of a simulation software that predicts the performance of materials on the basis of temperature drops and thermal

conductivity operating below ambient temperature. The work has been done in the following steps:

Step I of this work was to study the different works of the engineers and researchers who have performed certain experiments and research on the thermal insulation for industrial and commercial purposes. It was found that the studies had been taken in account are related to the research and development of heat insulation materials under high temperature with low thermal conductivity. Our objective was to found an insulator which can withstand below ambient temperature with a very low thermal conductivity and minimum heat transfer losses.

Step II was the development of an experimental model as a solid surface like pipe and to perform thermal analysis showing water flow inside the pipe. The thermal insulation is modelled as solid material around a 3D pipe with defined thermal properties in fluent. A flow of hot water in a pipe was modelled using K-Epsilon turbulent model to calculate the total heat loss and the temperature difference between inlet and outlet section of the pipe. The whole procedure of analysis was done using finite element method.

Step III was to apply boundary conditions and certain thermal properties to get required output in respect of temperature drops for seven different materials with different thermal conductivities.

Step IV discusses the results, since a material that gives minimum temperature drop with low thermal conductivity is considered as the best insulator; therefore, at the end of the experiment, we find a material that can be applied with minimum thickness and satisfies the given conditions.

2 Insulation Materials and Properties

2.1 Insulation Materials

- (a) Calcium silicate: It is suitable to use in hot water pipe lines or in industrial process plant piping, fittings and vessels. It is also used in furnace insulation or in boiler insulation.
- (b) Rock mineral wool: Rock mineral wool in addition to good thermal insulation properties is used as a thermal insulation and fire protection of plant and in structures in the commercial and industrial sectors.
- (c) Cellulose/glass: This insulating material is obtained from fibre of the recycled newspaper obtained by hammer milling process. The obtained material is chemically treated for making it fire resistance.
- (d) Phenolic foam: It is rigid foam structure. It is one of the most efficient insulating materials. It is a mixture of resin, blowing agent and surfactants in the presence of acid catalyst.

- (e) Aerogel: It is a low density and low thermal conductivity ultra-light material. The structure of the aerogel is porous, and liquid component gel is replaced with gas.
- (f) Polyurethane foam: This insulating material is a type of thermosetting plastic, and it is composed of joining urethane links. It is used, where rigid thermal insulation is required.

2.2 *Material Properties*

- (a) Thermal conductivity: Thermal conductivity must be lower for insulation.
- (b) Thermal resistance (R): Thermal resistance should be high.
- (c) Specific heat capacity: Material should be high specific heat capacity.
- (d) Density: It increased the weight of insulation.
- (e) Thermal diffusivity: Lower thermal diffusivity is preferred for insulating material.

3 **Design and Analysis**

In this study, we have taken six best insulators with some required properties to find out the capability of thermal insulation. The modelling is done with Ansys 19.2 student version taking length of the pipe = 1 m, inside diameter (Di) = 50 mm, outside diameter (Do) = 60 mm and 10 mm coating of calcium silicate and 30 mm coating for all other materials. The model is meshed, and the number of nodes generated is 29,651, and elements are 54,362 for the model. After having meshed model, the boundary conditions are applied by taking surrounding temperature below 0 °C, since heat is dissipated through insulation by convection phenomena at outermost insulation surface. Therefore, surface heat transfer coefficient is chosen as per design material requirement. The following figure shows the performance of all the material. Figure 1 shows temperature distribution for calcium silicate, Fig. 2 for rock mineral wool, Fig. 3 for cellulose insulation, Fig. 4 for phenolic foam, Fig. 5 for polyurethane insulation and Fig. 6 for aerogel insulation.

Heat transfer is the movement of heat energy from an object of higher temperature to one of lower temperature. In heat loss, the object will have more temperature than its surroundings. Ansys CFD solutions can simulate heat forced and natural convection, diffusion and radiation, as well as heat conduction in solids. Computational fluid dynamics can be used to simulate the local surface heat transfer coefficient on the surfaces. Figure 7 shows velocity of fluid and total heat transfer loss for calcium silicate insulation, Fig. 8 shows for rock mineral wool insulation, Fig. 9 for cellulose insulation, Fig. 10 for phenolic foam insulation, Fig. 11 for polyurethane insulation, Fig. 12 for aerogel insulation.

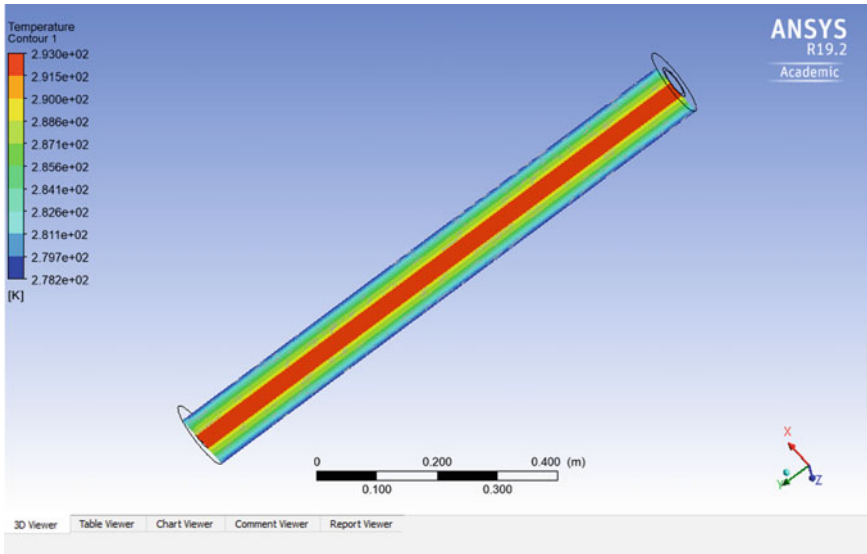


Fig. 1 Temperature distribution for calcium silicate

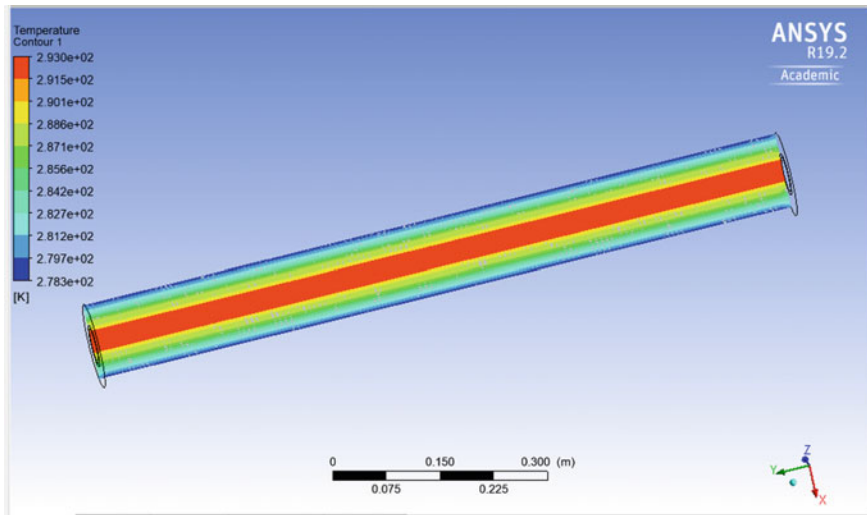


Fig. 2 Temperature distribution for rock mineral wool

The measured values for all the insulating material have been shown in Table 1, and heat transfer losses for all the insulating material have been shown in Table 2.

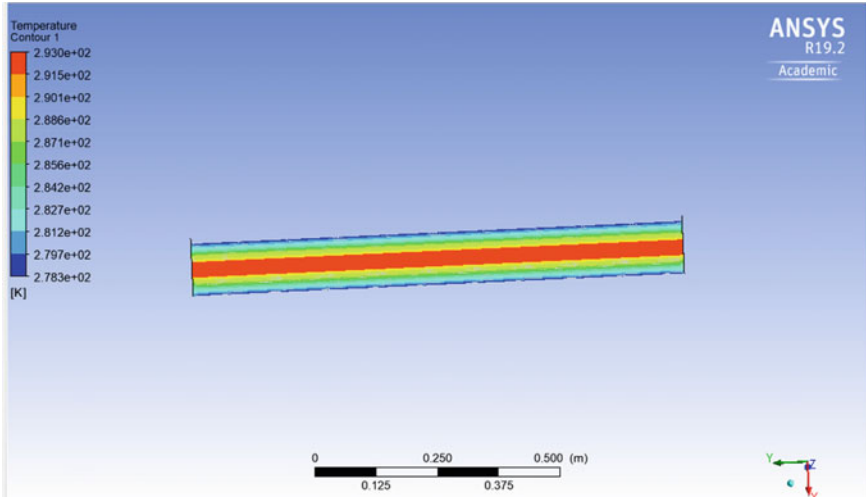


Fig. 3 Temperature distribution for cellulose insulation

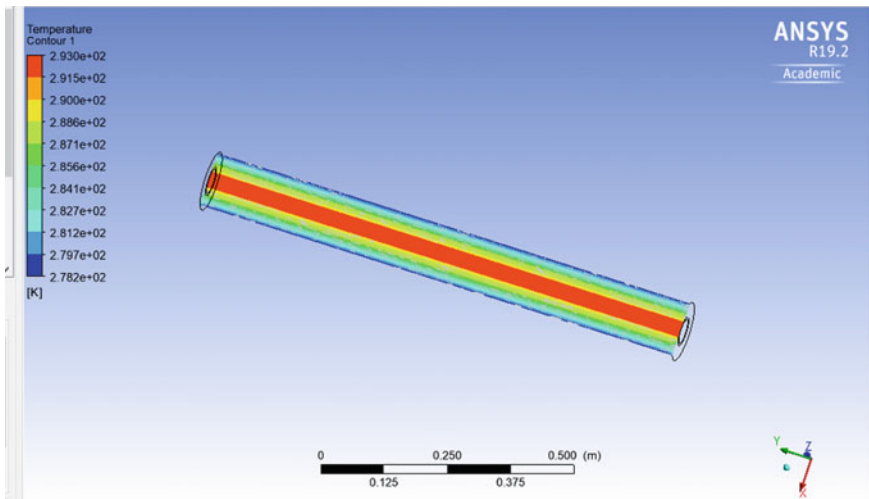


Fig. 4 Temperature distribution for phenolic foam

4 Results

In this experiment, we simulated the efficiency of some thermal insulating material to prevent significant heat loss in pipes. The thermal insulation is modelled as solid material around a 3D pipe with defined thermal properties in fluent. A flow of hot

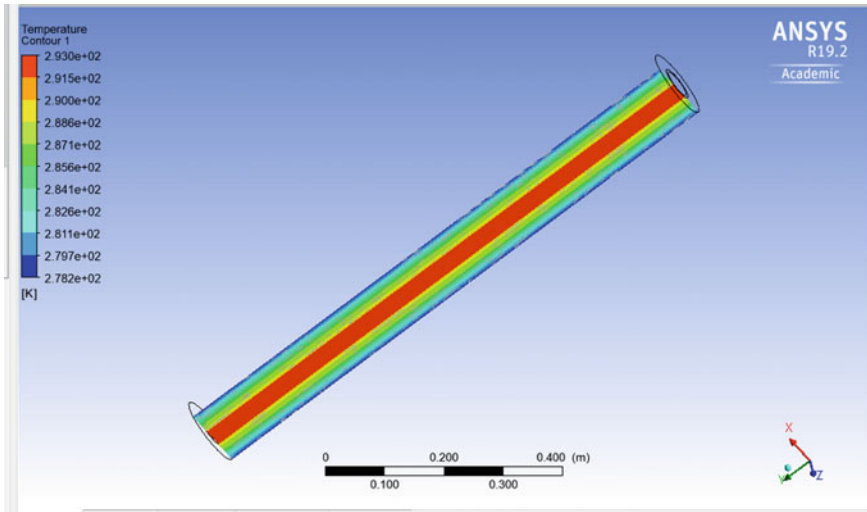


Fig. 5 Temperature distribution for polyurethane insulation

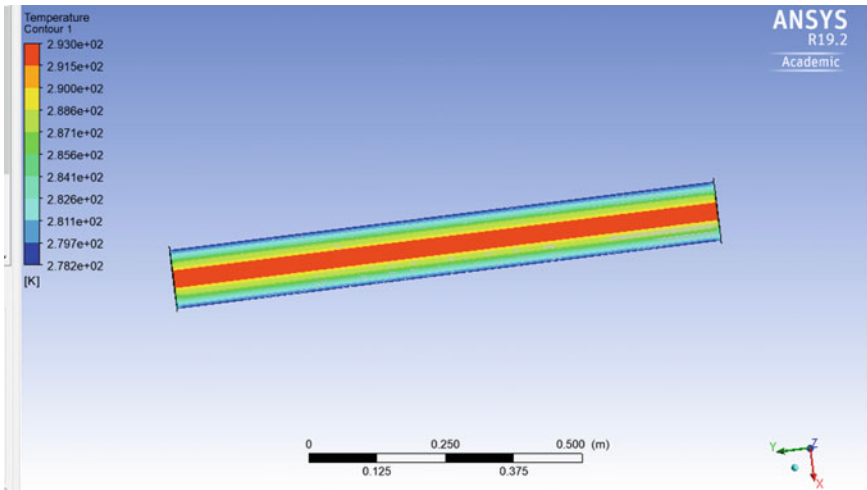


Fig. 6 Temperature distribution for aerogel insulation

water in a pipe was modelled using K-Epsilon turbulent model to calculate the total heat loss and the temperature difference between inlet and outlet section of the pipe.

Six different materials with defined properties were analysed to check which material is a best insulator that may solve the problem of water freezing due to heat loss. The values of energy loss are recorded in above table. It shows that aerogel is the best insulating material since it has minimum heat loss but then it does not

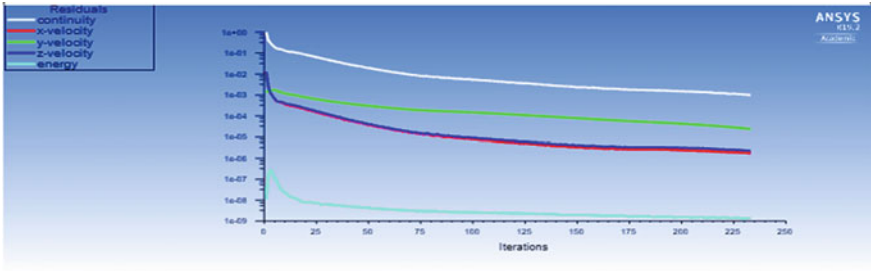


Fig. 7 Velocity of the fluid and total heat loss for calcium silicate

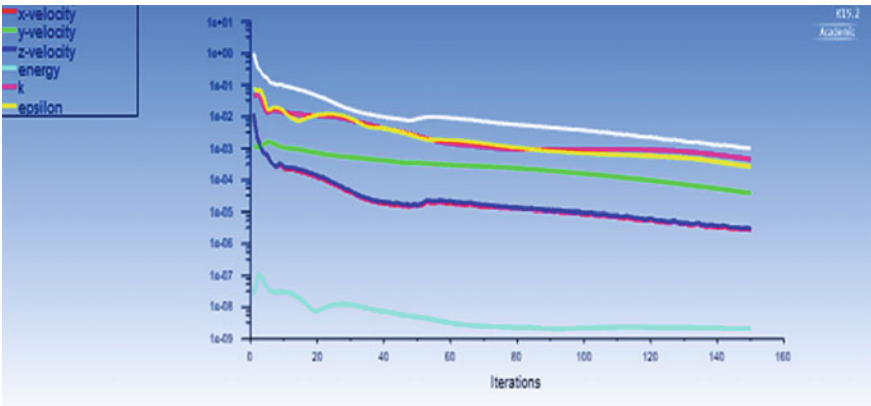


Fig. 8 Velocity of the fluid and total heat loss for rock mineral wool

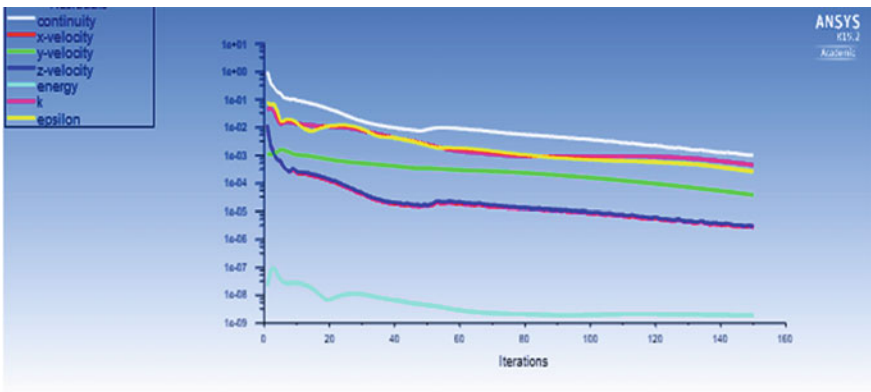


Fig. 9 Velocity of the fluid and total heat loss for cellulose

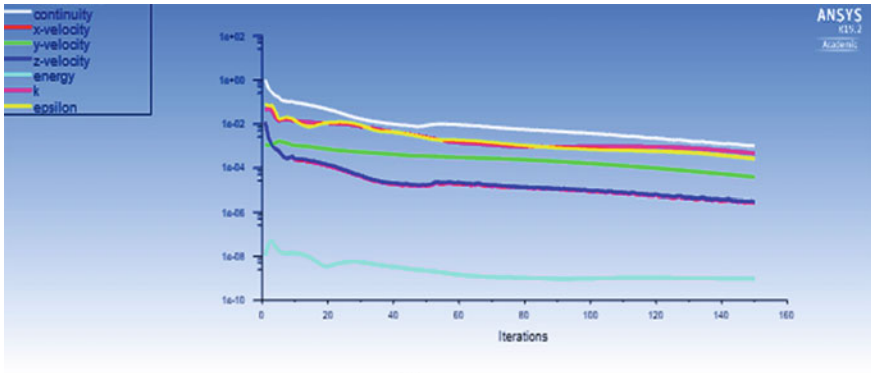


Fig. 10 Velocity of the fluid and total heat loss for phenolic foam

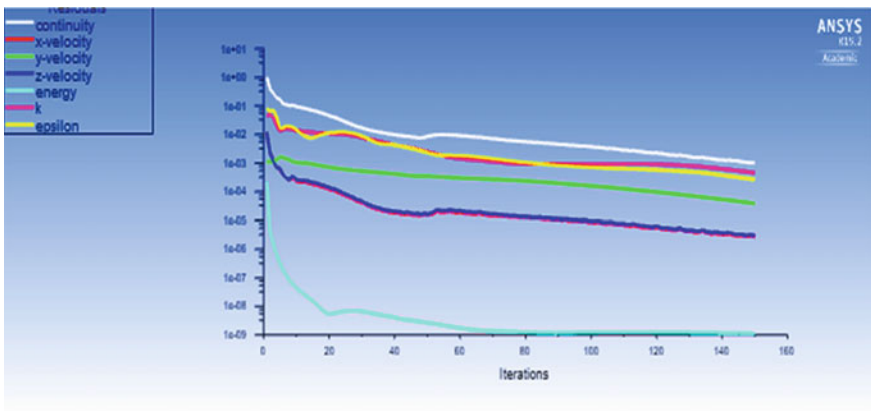


Fig. 11 Velocity of the fluid and total heat loss for polyurethane

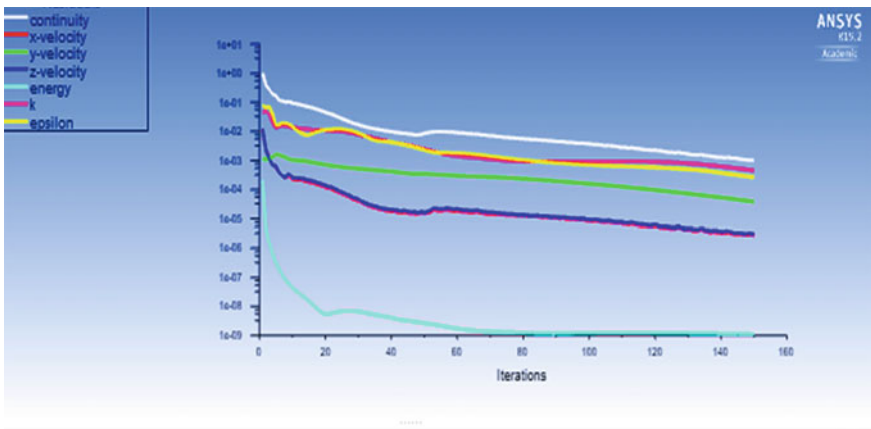


Fig. 12 Insulators and their respective measuring values

Table 1 Insulators and their respective measuring values

Sr. no.	Insulation material	Density (Kg/M ³)	Thermal conductivity (W/Mk)	Specific heat capacity (J/ Kg.K)	Ti (In °C)	To (In °C)
1.	Calcium silicate	250	0.014	1030	20	6.266
2.	Rock mineral wool	144	0.044	840	20	5.262
3.	Cellulose	65	0.04	2020	20	5.255
4.	Phenolic foam	35	0.02	1000	20	5.222
5.	Polyurethane	35	0.023	1450	20	5.181
6.	Aerogel	1.50	0.014	1000	20	5.184

Table 2 Heat transfer losses

Sr. no.	Insulation material	Heat transfer loss (Watt)
1.	Calcium silicate	1.868765
2.	Rock mineral wool	5.670153
3.	Cellulose	5.158158
4.	Phenolic foam	2.587796
5.	Polyurethane	2.983899
6.	Aerogel	1.816830

match other required conditions that are most needed for a good insulator. Therefore, with highest advantages and low thermal conductivity and minimum heat loss, calcium silicate gives the best result. Calcium silicate with a thickness of 10 mm layer when applied to the substrate gave the best results with minimum heat loss of 2.868765 W and low temperature drop of 13.734 °C.

5 Conclusion

Keeping water in the liquid form throughout a piping system is the major problem in some of the regions, where temperature falls even below the freezing point. Protecting pipes from bursting, insulation is provided. A good insulation provides low thermal conductivity which shows how well it can conduct heat through its mass, low density and higher mechanical strength. It also resists corrosion phenomena. Insulating material does not eliminate heat transfer but it reduces it flow up to certain required extent. Since calcium silicate has fulfilled all above properties with minimum heat loss, it is considered as a good thermal insulator. Also, the thickness of the insulation decides the performance of insulation. The thickness of insulation should select between optimum values which reduce cost of the

insulating material. Therefore, calcium silicate thermal insulation gives minimum energy loss and low temperature drop in 10 mm thickness and also prevents condensation on cold surfaces and so resulting corrosion.

References

1. Kaynakli O (2014) Economic thermal insulation thickness for pipes and ducts: a review study. *Renew Sustain Energy Rev* 30:184–194
2. Bloomquist RG (2001) Geothermal district energy system analysis, design and development. European summer school on geothermal energy applications, pp 213–253. University of Oradea, Romania
3. Sahu DK (2015) A review on thermal insulation and its optimum thickness to reduce heat loss. *Int J Innovative Res Sci Technol* 2(6):1–6
4. Wilkes K, Desjarlais A, Stovall T, McElroy D, Childs K, Miller W (2002) A pipe insulation test apparatus for use below room temperature. *Insul Mater Testing Appl* 4:241–256
5. Shanshan C (2013) Thermal performance of mechanical pipe insulation systems at below-ambient temperature. Oklahoma State University. https://shareok.org/bitstream/handle/11244/14750/CAI_okstate_0664D_13176.pdf
6. Masatin V (2017) Improvement of district heating network energy efficiency by pipe insulation renovation with PUR Foam Shells. *Energy Procedia* 113:265–269

Efficiency Analysis of Aerospike Nozzle by Comparison with a de-Level Nozzle Using Computational Fluid Dynamics



Clavin Wilton Sequeira and M. V. Sanjay

Abstract Nozzles are one of the most efficient ways of producing thrust. Most of the modern day launch vehicles use a conventional Converging-Diverging nozzle (CD nozzle). One of the critical drawbacks of using these nozzles is in their inability to provide the same efficiency under varying conditions of the course of the flight. CD nozzles when developed are designed to work at a certain range of altitudes, i.e. either at sea level or under near vacuum conditions. Hence, a sea level optimized nozzle can't provide the same efficiency at higher altitudes and vice versa. Thus, modern day rockets have multiple stages (usually 2), with the first stage having a sea level optimized nozzle which lifts the rocket from the launch pad and takes it to an altitude before being ejected along with first stage and the second stage having vacuum optimized nozzle which propels the payload in vacuum of space to a desired orbit. This results in higher operating costs for a single launch, makes the process of payload deployment more complicated. The problem of having to use multiple nozzles can be solved by using an altitude compensating nozzle, with aerospike nozzle being one of them. These nozzles under operation provide the same efficiency throughout the course of flight under varying ambient conditions. This makes possible the development of a single stage to orbit vehicle, SSTO having a single aerospike nozzle. An SSTO vehicle unlike modern rockets doesn't have components which require to be jettisoned during its flight and thus retains its expensive hardware even after being recovered. Hence, an SSTO vehicle results in less operating costs, having optimum payload capability. An SSTO having aerospike when developed properly is highly versatile in terms of thrust vectoring, and it has the potential of being completely reusable, by using a compact single structure similar to space shuttle and using aerodynamic re-entry. This paper analyses the performance of aerospike by comparison with CD nozzle using CFD (Computational Fluid Dynamics).

C. W. Sequeira · M. V. Sanjay (✉)

UG Scholar, Department of Aeronautical Engineering, Mangalore Institute of Technology and Engineering, Moodbidri, India
e-mail: jenusanjay@gmail.com

C. W. Sequeira

e-mail: clavinwiltonsequeira@gmail.com

Keywords Aerospike · CD nozzle · Altitude compensation · CFD · Performance · SSTO

1 Introduction

In order to further explore space and to expand humanities reach in the universe, researchers have been developing ways to propel launch vehicles into the orbit. There are hundreds of ways to send payloads of various sizes to the earth's orbit and also to other planets. One thing that they generally have in common is a nozzle. This paper focuses particularly on the comparison of a conventionally used (CD) nozzle and aerospike nozzle, thus enlightening their advantages and disadvantages.

1.1 Nozzle

In aerospace propulsion, just by burning the fuel, thrust or the required power to move the spacecraft can't be obtained. This is where nozzles come into picture. A nozzle is a device used to control the fluid flow characteristics by varying the cross-sectional area as it flows through it. In case of rocket nozzles, the fluids are the exhaust gases or the combustion products of the propellants. Nozzles when employed in rocket propulsion expand the flow along the length of the nozzle at supersonic and hypersonic velocities. The energy of high pressured hot gas flow coming out of the combustion chamber is converted into kinetic energy in order to attain the maximum thrust. There are various different types of nozzles being used with their geometry greatly depending on the altitude or the stage of the rocket at which they will be subjected to operation, i.e. a sea level optimized or a vacuum optimized nozzle. The size of the nozzles depends on the amount of impulse force (I_p) required.

1.2 CD Nozzle

A CD nozzle consists of a converging section till the throat area, further which the divergent section is present. In order to achieve flow in the nozzle, the back pressure P_a is reduced. The flow then accelerates in the converging section and decelerates through the diverging section and flows into the ambient as a subsonic exhaust jet. When the ratio of P^*/P_c , i.e. the ratio of pressure at the throat P^* to the pressure in the combustion chamber P_c becomes equal to 0.528 (for $\gamma = 1.4$), essentially indicating that the pressure of the fluid at the throat is nearly half of that combustion chamber as it is expanded by the convergent geometry. At this point flow, the flow

reaches Mach 1, at which it attains the choked condition. Mach 1 indicates that the speed of the fluid is same as the speed of sound of the ambient medium. Choked condition refers to the state after which the flow parameters remain constant in the converging section; at the same time, the flow expands in the diverging section till a normal shock is formed. An increase in the flow velocity can be obtained by further reducing the back pressure. The location of the normal shock wave in the nozzle is determined by the requirement that the increase of static pressure across the shock wave plus the remaining length in the diverging section of the nozzle should be enough for flow to have an exit pressure P_{exit} equal to the back pressure P_b . If P_b is lowered enough, then we can extend the supersonic region all the way down until the shock is sitting at the nozzle lip. However, the flow after the normal shock will be subsonic. In order to have a supersonic flow throughout the length of the diverging section of the nozzle, the pressure of the supersonic flow at the nozzle exit should be equal to the back pressure. This condition, as it is often desirable, is referred as the ‘design condition’.

Let us consider a CD Nozzle under operation in a Space Launch Vehicle (SLV). The thrust produced by CD nozzle is given by,

$$F = \dot{m} \cdot V_{\text{exit}} + (P_{\text{exit}} - P_a)A_{\text{exit}} \quad (1)$$

When the SLV is on the launch pad and the Nozzle is started up, the exit pressure is less than the ambient pressure ($P_{\text{exit}} < P_a$). This condition is referred to as over expanded flow (Fig. 2 case a). The normal shock at the exit of the nozzle splits into oblique shock wave also known as ‘Barrel Shock’ and forms a complex flow pattern after the interaction with the jet boundary which is also known as ‘Shock Reflection’ or ‘Shock Diamonds’. As the exhaust plume is ‘pinched’ by the greater ambient pressure, the efficiency is reduced. When the SLV reaches a certain altitude, the exit pressure becomes equal to the ambient pressure ($P_{\text{exit}} = P_a$). This condition is referred to as ‘Perfectly expanded flow’ also known as the design condition (Fig. 1 case b). As seen, the exhaust plume is perfectly straight; hence, at this stage, the nozzle is at its maximum efficiency. Along the course of flight when the SLV approaches higher altitudes or vacuum conditions, the exit pressure is greater than the ambient pressure ($P_{\text{exit}} > P_a$). This condition is referred to as under expanded flow (Fig. 1 case c). In this case, expansion waves are formed at the lip of the nozzle and the plume continues to expand past the nozzle exit reducing its efficiency. The flow past the nozzle expands as per the Prandtl Meyer expansion wave theory [1].

1.3 Altitude Compensation

From Sect. 1.2, we can analyse that in order to have maximum efficiency throughout the nozzle, the geometry of the nozzle should vary in order to compensate for the varying ambient conditions; however, a bell nozzle that

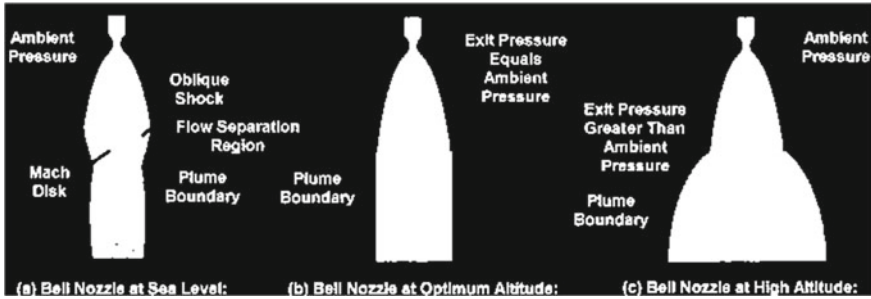


Fig. 1 Exhaust plume pattern at different altitudes of CD nozzle

continuously changes its geometry along the course of flight which is very much impractical with the available technology. Hence, while designing the nozzle a series of trade-offs has to be made while selecting the area ratio. The trade-offs depend on the application of the nozzle, i.e. which stage of the rocket will it be used. The RS-25 rocket engine used in the space shuttle was actually inefficient at sea level; it reached the design conditions later at higher altitudes. However, maximum efficiency can be maintained by using something known as ‘Altitude Compensating Nozzles’. This property of the nozzle to maintain a perfectly expanded exhaust with the variation of the ambient pressure makes it an altitude compensating nozzle. Altitude compensation is certainly a desirable property in any launch vehicle; this adaptive quality is a necessity in any Single Stage to Orbit (SSTO) vehicle, like the X-33. With the current technologies available, it is not possible to send reasonably sized payloads to orbit by using a single stage. Various efforts have been made in order to incorporate altitude compensating nozzles, such as the extendible geometry nozzles that ‘extend’ through flight, a dual-bell nozzle which allows the flow to expand along the length as per the back pressure and an expansion deflection nozzle (ED nozzle) which deflects the plume into the optimum expansion ratio. However, the ultimate strength of the aerospike nozzle is its altitude compensation capability.

1.4 Aerospike Nozzle

However, when we compare CD nozzle with an aerospike nozzle, the process of expansion is quite different. The aerospike nozzle comes with a unique set of combustion chambers or CD nozzles arranged in specific manner. Many types of aerospike engines are seen among them are the linear type, plug type [2], annular multi-thruster, etc. In a linear aerospike engine, the combustion chambers are arranged in a linear way upstream to the nozzle part. The hot gas flow is made to pass through a small CD nozzle next to the combustion chamber, where it attains supersonic speeds. Later, the flow allowed to expand along the wedge-shaped

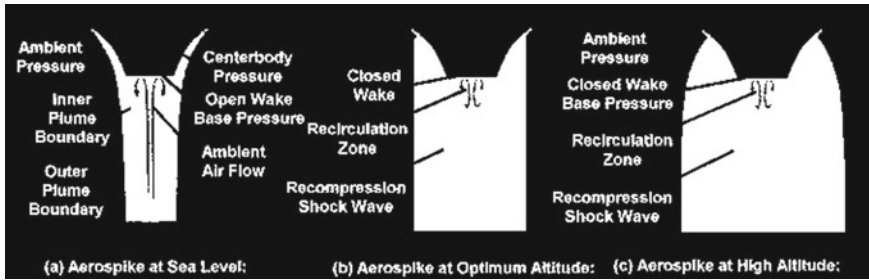


Fig. 2 Exhaust plume pattern at different altitudes of aerospike nozzle [3]

protrusion, the ‘spike’ by means of expansion waves. In case of a plug type [2], the central plug is surrounded annular type of combustion chamber through which the flow is expanded through a series of expansion waves/compression fans on the spike. For the analysis, we are considering an annular aerospike. The combustion process takes place in an enclosed chamber similarly as that of a conventional bell nozzle. Initially, there is a converging section, where the flow is accelerated to $M = 1$, in the throat section. Then, it is further accelerating in the diverging section, but this is where it varies from the bell nozzle. The bell nozzle has a continuous geometry of wall in the diverging section to direct the flow downwards, but in case of an aerospike nozzle, plug acts as an inner wall and the length of the outer wall is small compared to the spike. In an aerospike nozzle, the flows in directed downward as the ambient pressure pushes the flow on to the inner wall, i.e. the aerospike, where it expands. Initially, the flow has a curvature moving downwards, but it straightens out along with the geometry of the spike. As the ambient pressure reduces the same process would repeat but a greater expansion of the gases. Due to the aerospike geometry the exhaust would be relatively straight, unlike the bell nozzle, where in this condition, under expansion takes place. This property of the nozzle to maintain a perfectly expanded exhaust with the variation of the ambient pressure makes it an Altitude Compensating nozzle.

As shown in Fig. 2, though the CD nozzle in the aerospike is under expanded, the overall exhaust plume maintains the shape of a column, and hence, it attains maximum efficiency.

Thrust Characteristics of Aerospike nozzle

For an aerospike nozzle, the thrust characteristics can be studied from Fig. 3 [4]. The aerospike nozzle produces thrust in three distinct ways. Firstly, the converging-diverging annular thruster section (toroidal chamber), placed at the base of the nozzle, produce thrust as the fuel is combusted and exhausted. Let the thrust produced by this annular thruster be denoted by $F_{thruster}$. As the thruster is at an angle to the normal the cosine component ($\cos\theta$) comes into the picture, where θ is the angle between the axis of the thrust with respect to vertical

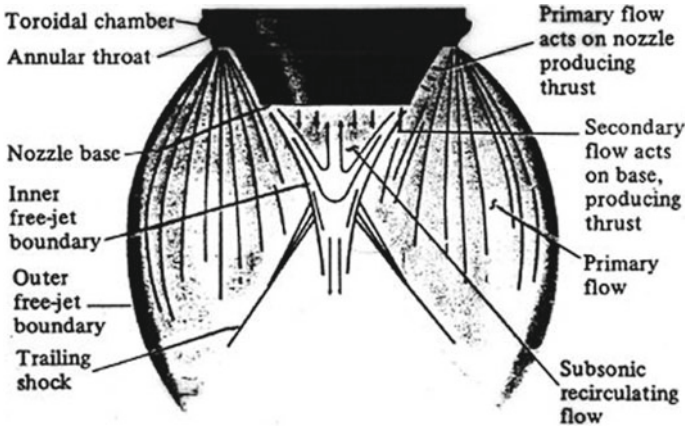


Fig. 3 Schematic of a truncated aerospike nozzle [4]

$$F_{\text{thrust}} = (\dot{m} \cdot V_{\text{exit}} + (P_{\text{exit}} - P_a)A_{\text{exit}}) \cdot \cos \theta \quad (2)$$

In Sect. 1.2, we have discussed how CD nozzles produce thrust, by expanding the gases in the diverging section and expelling them out ideally at supersonic velocities. Though we use the bell nozzle primarily for combustion, the exhaust gases from the nozzle lip are pressed against the centerbody of the aerospike by the ambient. As it presses against the centerbody, it exerts a force $F_{\text{centerbody}}$ onto it.

$$F_{\text{centerbody}} = \int A_{\text{centerbody}} \cdot (P_{\text{centerbody}} - P_a) \cdot dA \quad (3)$$

Finally, in Sect. 1.4, we have considered a truncated aerospike nozzle and as the inner plume boundary reaches the truncated corner along the centerbody, it re-circulates the flow on to the base of the aerospike. This happens so because of the low pressure wake region on the base; hence, the flow expands further circulating the flow. This re-circulated flow having low pressure presses against the base of the aerospike intern generating more thrust denoted by F_{base} .

$$F_{\text{base}} = (P_{\text{base}} - P_a) \cdot A_{\text{base}} \quad (4)$$

Addition of all these three force components gives us the total thrust generated by the aerospike nozzle given by F_{total} .

$$F_{\text{total}} = F_{\text{thrust}} + F_{\text{centerbody}} + F_{\text{base}} \quad (5)$$

2 Methodology

In the above context, we have analysed the flow theoretically. In order to prove it, we analyse the flow pattern of the CD nozzle and the aerospike nozzle at two different altitudes using computational fluid dynamics. The sea level and a height of 80 km from the ground are the two chosen altitudes. The reference static pressures are taken from the table provided by online source. The inlet of the nozzles in both the cases is taken as velocity inlets with the magnitude of velocity being supersonic. The far field boundary condition is given as the static pressure corresponding to the considered altitude. K-epsilon model of equation has been involved in solving this transient problem. The resultant contours are then compared, and its conclusions are outlined in the results. Analysis model—Ansys fluent 19.0.

3 Result and Discussion

3.1 CFD Analysis of CD Nozzle

Considering a sea level optimized De-Laval Nozzle, at the initial stages of flight the nozzle would work in the design condition, i.e. the flow would be perfectly expanded. At this stage the exit pressure is equal to the ambient pressure. ($P_{\text{exit}} = P_a$). This is the ideal operating condition for the nozzle as it is most efficient at this arrangement. As we move on to the later stages of the flight as the ambient conditions change the nozzle won't continue to be in the design condition. With the increase in the altitude, the ambient pressure decreases. At this point, the exit pressure P_a would be greater than the ambient pressure which results in an under expanded flow. ($P_{\text{exit}} > P_a$). This type of flow results in the reduced efficiency of the nozzle.

The simulation was carried out at sea level and at an altitude of 80 km. For both the cases, the chamber pressure was maintained constant. At sea level, the nozzle behaved as an under expanded nozzle. The flow contour is depicted in the Fig. 4a. At the altitude of 80 km above earth surface (Fig. 4b), the ambient pressure is very minimum (almost equal to vacuum). The exit pressure from the nozzle is greater than the ambient pressure, and hence, the hot gases tend to move sideways increasing the inefficiency of the nozzle.

3.2 CFD Analysis of Aerospike Nozzle

Considering an aerospike nozzle at sea level, at the initial stages of the flight the nozzle exhaust are perfectly expanded, and as it flows downstream, it is pushed against the aerospike plug by the ambient pressure p_a . At this point along with the

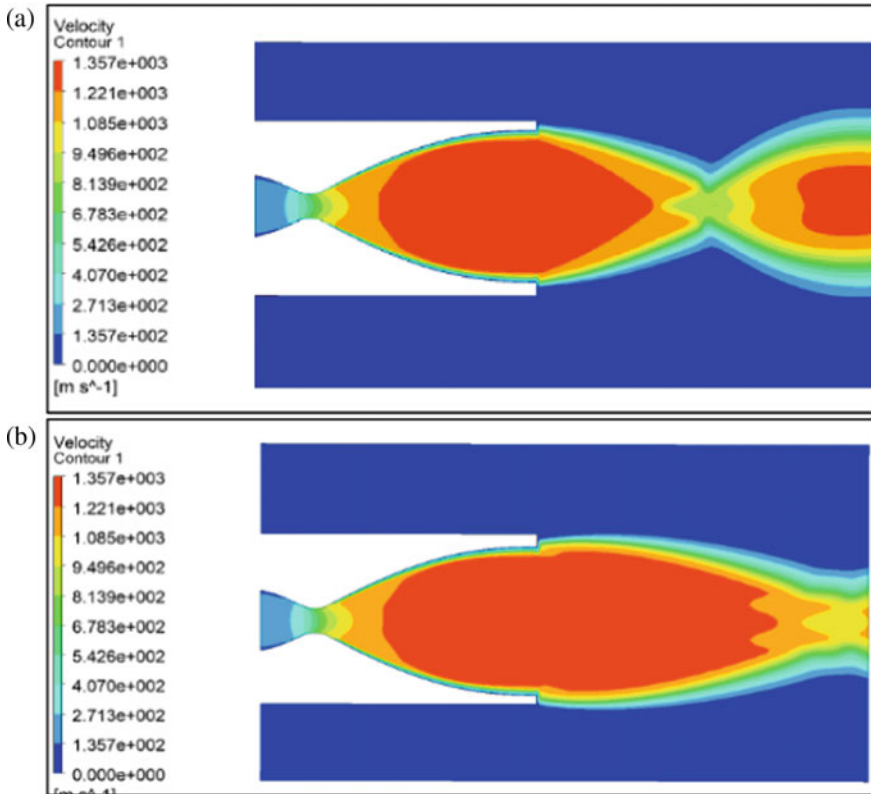


Fig. 4 **a** Flow contour at sea level, **b** flow contour at 80 km altitude

nozzle exhaust being perfectly expanded, the jet boundary of the flow downstream of the plug is perfectly expanded. This happens so because the geometry of the aerospike straightens out towards the end of the plug. As we move on to the higher altitudes in the later stages of the flight, though the nozzle exhaust is under expanded the shape of the exhaust along the length of the plug would be that of a perfectly expanded flow. This entirely depends on the profile of the aerospike. At the ambient conditions of vacuum, the shape of the exhaust is determined by the Prandtl Mayer expansion theory. Analysis is done at sea level and 80 km. At sea level, the ratio P_{exit}/P_a is less than one. The flow contour is depicted in the Fig. 5a. At the altitude of 80 km, the ratio P_{exit}/P_a is greater than 1; hence, the plume extends outwards expanding perfectly (Fig. 5b).

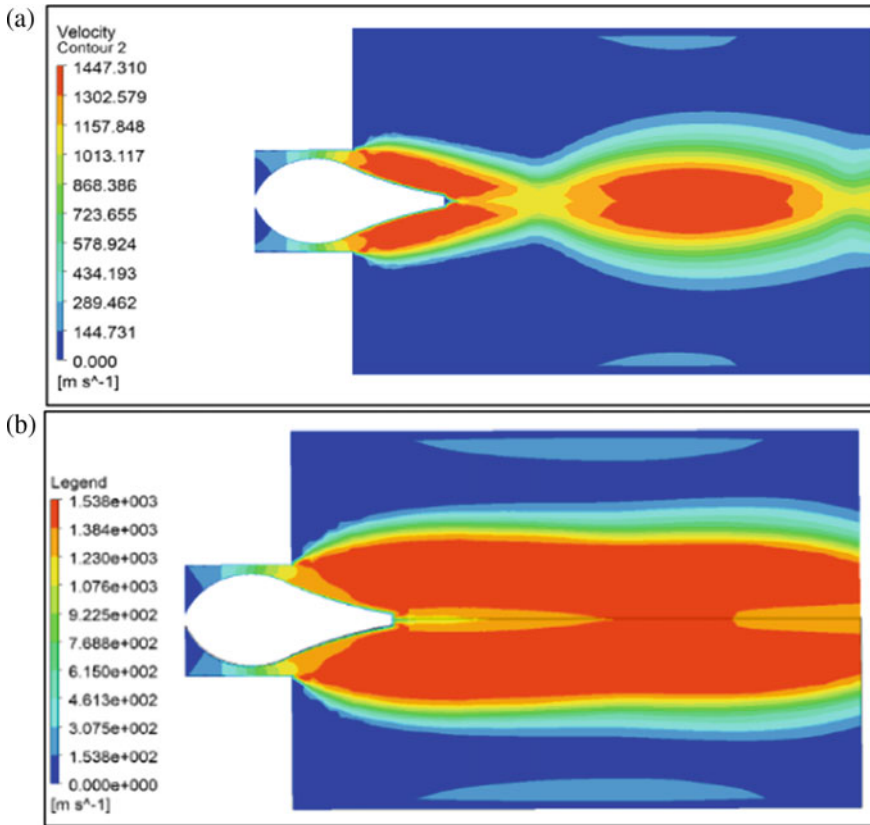


Fig. 5 a Flow contour at sea level altitude, b flow contour at 80 km altitude

4 Conclusion

It can be clearly inferred from the CFD result contours that the aerospike nozzle is able to produce a higher velocity of jet in comparison with CD nozzle with the similar boundary conditions. At sea level condition, this can be inferred as the presence of room in CD nozzle for the further expansion of hot gases. At the higher altitude, the excessive expansion is causing the inefficiency. The results give a clear picture about the inefficiency of the CD nozzle at a non-design altitude. Aerospike nozzle, not being a new concept can be a breakthrough in the field of aerospace industry. Altitude compensating, thrust vectoring, base bleed are some of the areas that make aerospike nozzle a perfect solution for future space exploration. As aerospike's size is small and efficiency of almost unity makes the dream of SSTO possible. Material limits and manufacturing complexions are on the downside of this nozzle. However, inventions of super alloys and ceramic composites have raised a new path for the development of aerospike nozzles.

References

1. Matyka M (2003) Prandtl-meyer expansion wave
2. Besnard E, Garvey J (2004) Aerospikes engines for Nanosat and small launch vehicles (NLV/SLV). In: A collection of technical papers—AIAA space 2004 conference and exposition 2. <https://doi.org/10.2514/6.2004-6005>
3. Muss JA, Nguyen TV, GenCorp Aerojet, Reske EJ, McDaniel DM (1992) Evaluation of altitude compensating nozzle concepts for RLV. NASA-MSFC AIAA 97-3222
4. Imran M (2016) Introduction to aerospikes and its aerodynamic features. Int J Sci Res Publ 6(5), ISSN 2250-3153

Vortex Formation in Liquid Columns During Draining: Influence of Drain Port Geometry



M. R. Harikrishnan, Mahadev Prabhu, and R. Ajith Kumar

Abstract Vortex air core formation has prime importance in the area of aerospace, metal casting and hydraulic engineering. Rotational and vibration disturbance will be imparted to draining fluid which is subjected to environmental disturbance. These disturbances trigger the formation of vortex air core in draining fluids. Thus, formed air core vortex can invite serious adverse effects in many engineering applications. Formation of such vortices in propellant tanks of spacecraft and rockets can choke the drain port and thus leads to underutilization of fuel. Feed pumps connected to the propellant tanks are more susceptible to cavitation under the ingestion of such air core vortex. Air core vortices also bring casting defects in casted metal products. Present study is conducted to investigate the influence of newly designed drain port geometries and their aspect ratios on vortex air core formation when a rotated liquid column is drained out from a cylindrical tank. For this, rectangular elliptical and crucifying cross sections were tested for various values of aspect ratios. All the drain ports are concentric to the tank base. Objective of the present study is to identify the geometry and its aspect ratio which gives least critical height and minimum draining time required to empty the tank which indicates vortex suppression. Effect of these geometries on vortexing phenomenon is not reported in the current literature, and hence, this is thought to be a novel investigation.

Keywords Vortexing · Critical height · Time of emptying

M. R. Harikrishnan (✉) · M. Prabhu · R. Ajith Kumar
Department of Mechanical Engineering, Amrita Vishwa Vidyapeetham, Amritapuri, India
e-mail: hmr.inde@gmail.com

M. Prabhu
e-mail: prabhumahadev1729@gmail.com

R. Ajith Kumar
e-mail: amritanjali.ajith@gmail.com

1 Introduction

Phenomenon of air core vortexing is observed when a liquid column is rotated and drained through a drain port located at the base of a cylindrical tank. Depending on the initial rotational speed, a kink or dip could form over the free surface which immediately penetrates vertically down through the liquid column to reach the drain port, called as air core vortex. The height of the free surface at which the air core passes through the drain port is termed as critical height (H_c) which serves as an important parameter in the analysis of the vortexing phenomenon. Time instance at which free surface attains the critical height is termed as critical time (T_c). Studies pertinent to air core vortex formation and its suppression are relevant in the field of aerospace propulsion, metal casting and hydraulic engineering. Vortex air cores are capable to trigger cavitation in feed pumps used in liquid propellant systems along with varying the discharge flow rate provided to rocket engines. Hence, investigation on air core suppression is inevitable in aerospace applications.

Lubin and Springer [1] experimentally investigated air core vortexing in draining of liquids from cylindrical tanks. They found that critical height (H_c) can be empirically related to fluid density ratio and fluid drain rate when two or more immiscible liquids were allowed to drain from their initial stationary state. Numerical study conducted by Sohn et al. [2] on air core vortexing in cylindrical tanks revealed that critical time (T_c) is a strong function of initial rotation imparted to the fluid, drain port size and tank size. They also proposed a correlation between various dimensionless parameters to characterize air core vortexing phenomenon. Experimental study conducted by Ajith Kumar et al. [3] revealed that critical height is greatly influenced by port diameter and distance of drain port from cylinder centre (eccentricity). Their study proposed that vortexing can be eliminated when port diameter equals to 0.3 times the tank diameter for liquid draining through concentric ports. Later, investigation by Ajith Kumar et al. [4] concluded that ratio between drain port diameter to tank diameter is strong function of port eccentricity. Experimental study performed by Ramamurthi and Tharakan [5] introduced the usage of stepped ports in controlling the air core vortices. Their results show that, compared to conventional circular ports, stepped ports are very effective in arresting the vortex formation. Mechanism of air core generation was described by Nazir and Sohn [6, 7]. They found that air core vortexing is significantly influenced by swirl and axial velocities. Their numerical and experimental investigation revealed that air core vortexing can be controlled by varying the initial height [6] and temperature [7] of the draining fluid. Usage of dish type suppressor to control air core vortexing was introduced by Gowda et al. [8]. They found that to suppress the air core, ratio of radius of curvature of dish to port diameter should be at least 1.5. Prabhu et al. [9] studied the phenomenon of air core vortexing during draining of liquids through two drain ports located equidistant from cylinder centre. They found that vortex air core can be fully suppressed when diameter of both ports are same. Prabhu et al. [10] have also studied the effect of polygonal ports on vortexing phenomenon and found that octagonal ports are highly efficient in controlling the air core vortices.

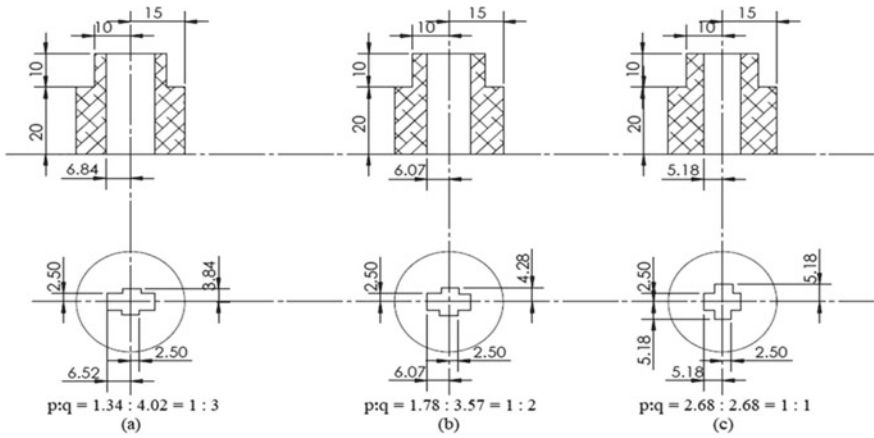


Fig. 1 Crucified cross-sectional drain port

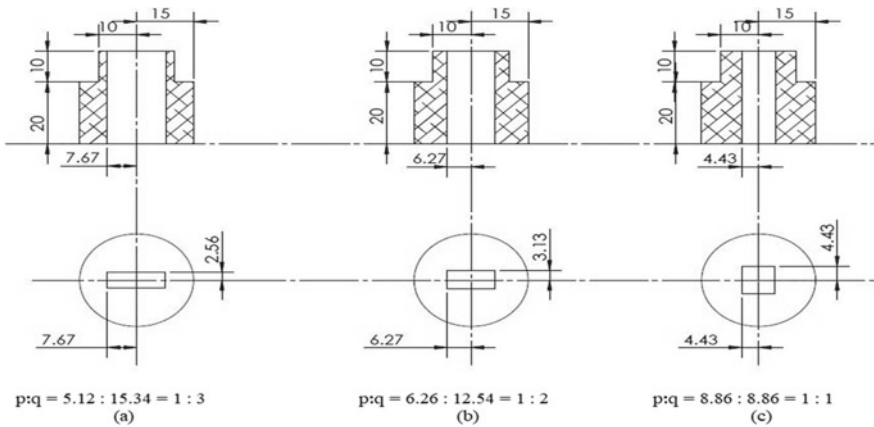


Fig. 2 Rectangular cross-sectional drain port

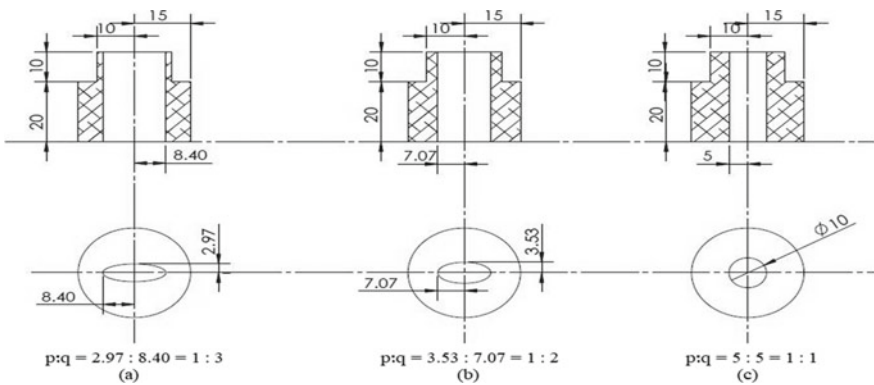


Fig. 3 Elliptical cross-sectional drain port

Literature reveals that shape of the drain ports has significant effect on air core vortexing. Hence, in this study, effect of drain port shapes and their aspect ratios (AR) on air core vortexing is studied under various values of initial liquid rotation. To conduct experiments on effect of drain port shapes on vortexing, authors have selected crucified, rectangular and elliptical cross sections as shown in Figs. 1, 2, 3. For each cross section, effect of its aspect ratio (ratio of major dimension to minor dimension) on vortexing phenomenon is also studied. To perform this study, for each cross-sectional shapes, aspect ratio was varied from 1:1 to 1:3. It should be noted that area of cross section for all the geometries is kept constant to ensure that the value of discharge flow rate is the same for all geometries selected for a given liquid column height. Objective of the present study is to find out the geometry and its aspect ratio that can give the least critical height and minimum time of liquid draining. Effect of these cross-sectional shapes on vortexing is not reported in any literature.

2 Experimental Set-up

Experimental set-up shown in Fig. 4 consists of a glass cylinder having 96 mm internal diameter and height 450 mm. Three different drain port geometries, each geometry with three aspect ratios, that is, nine different drain port adapters were made out of aluminium. In all these cases, the drain port area is kept constant at 78.54 mm^2 which is equal to the cross-sectional area of circle with a 10 mm diameter.

As mentioned earlier, the criterion of constant area is to maintain equal discharge flow rate for all the drain port geometries under identical conditions. This will result in an equal time of emptying for all geometries for a given value of initial height with no initial fluid rotation. Therefore, for all geometries, draining is expected to

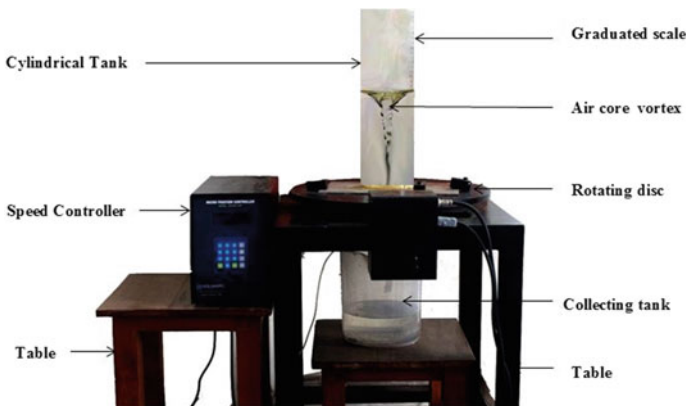


Fig. 4 Experimental set-up

occur in identical manner in the absence of air core. The glass tank was attached to an acrylic base plate which had the provision to insert drain port adapters of various cross sections and aspect ratios. The cylinder with acrylic base was mounted on a rotating disc. Water was filled into the cylinder to an initial height of 300 mm. An initial fluid rotation (N) in the range of 0 RPM to 240 RPM was provided for 4 min to the liquid column to ensure that fluid particles are imparted with uniform angular velocity. After 4 min, drain port stopper was removed, and draining of fluid was allowed. In the initial instances of draining, a dip formed on the free surface penetrates the liquid column and passes through the drain port. The free surface height of liquid when tip of vortex touched the drain port was measured using graduated scale attached to the cylinder. Thus, critical height was recorded. Time to empty the tank was measured using a stop watch. All experiments were repeated 10 times to check for repeatability of measurements. The measurement uncertainty in critical height and time of emptying were estimated to be 0.417384 mm and 0.152326 s, respectively.

3 Results and Discussion

The strength of air core vortex was quantified in terms of critical height (H_c), and it is non-dimensionalized with respect to initial height of the liquid column (H_i). Critical height will be negligibly small or it is practically nil when no rotation is imparted to the fluid column. As initial value of liquid rotation increases, vortexing phenomenon gets stronger. A strong vortexing indicates larger values of critical height, and this result in more blockage of the drain port area which in turn increases the time to empty the tank (T_d). Time of emptying is non-dimensionalized with respect to time of emptying without rotation. Non-dimensional time of emptying (T_d/T_o) was also analysed for various port geometries and aspect ratios.

To bring to light the effect of drain port geometry on vortexing phenomenon, for a typical aspect ratio ($AR = 1$), dimensionless critical height (H_c/H_i) and time of emptying are plotted against initial rotation and are shown in Figs. 5 and 6, respectively. It can be observed from Fig. 5 that critical height increases with initial rotation which complies with the results of Prabhu et al. [10]. For a specific value of initial rotation, it could be observed that critical height is not a function of geometry. Further, it is seen that for a specific value of initial rotation, crucified cross-sectional drain port is taking less time to empty the tank (Fig. 6). It means that crucified cross-sectional drain port is expected to give maximum rate of discharge for a given height of liquid column. That is, influence of geometry is reflected in the draining time but not in the critical height. These results indicate that critical height alone may not be sufficient to characterize vortex air core formation. Similar results are obtained for other aspect ratios also and hence, not presented here.

For various aspect ratios, variation in dimensionless critical height and time of emptying with initial rotation is shown in Figs. 7 and 8 respectively for typical crucified geometry. It is observed from Fig. 7 that for specific value of initial

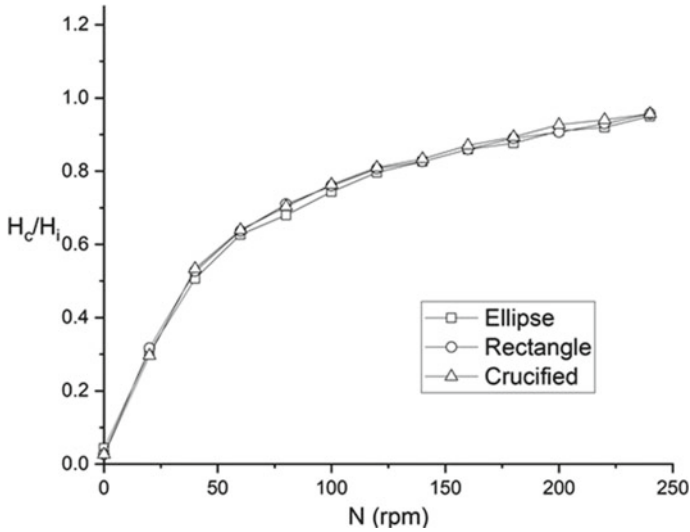


Fig. 5 Variation of H_c/H_i with N for $AR = 1$

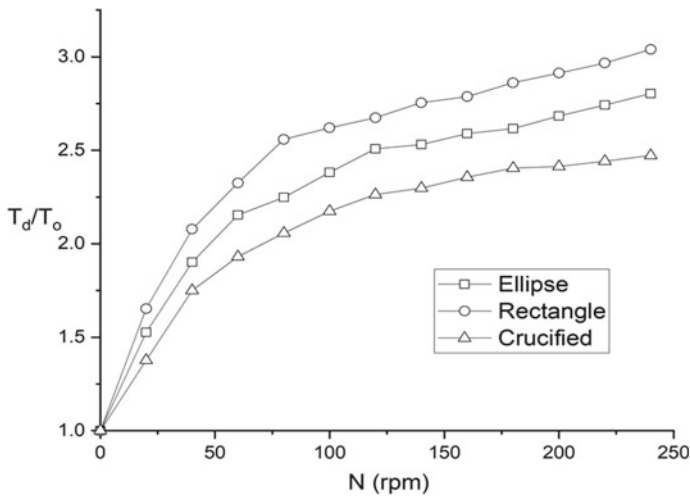


Fig. 6 Variation of T_d/T_o with N for $AR = 1$

rotation, critical height is invariant with respect to aspect ratio. It can also be inferred from Fig. 8 that time of emptying the tank is minimum for aspect ratio equals to 3. It means that crucified geometry with aspect ratio 3 is expected to give maximum rate of discharge for a given height of liquid column. Similar results are obtained for other drain port geometries and hence, not presented here.

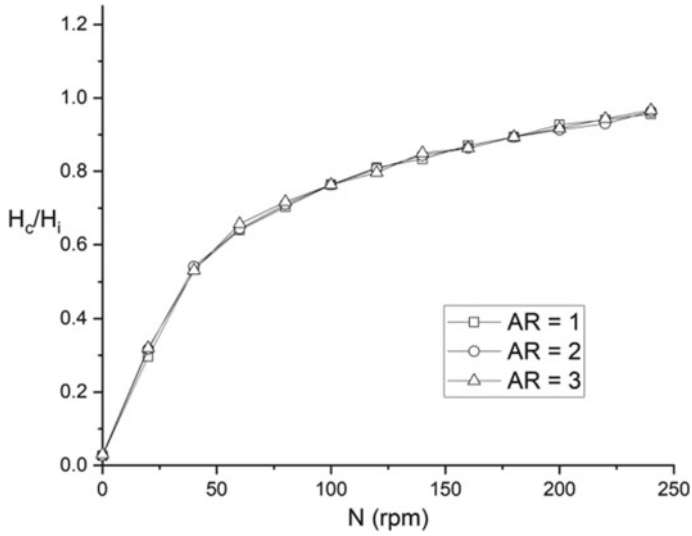


Fig. 7 Variation of H_c/H_i with N for crucified geometry

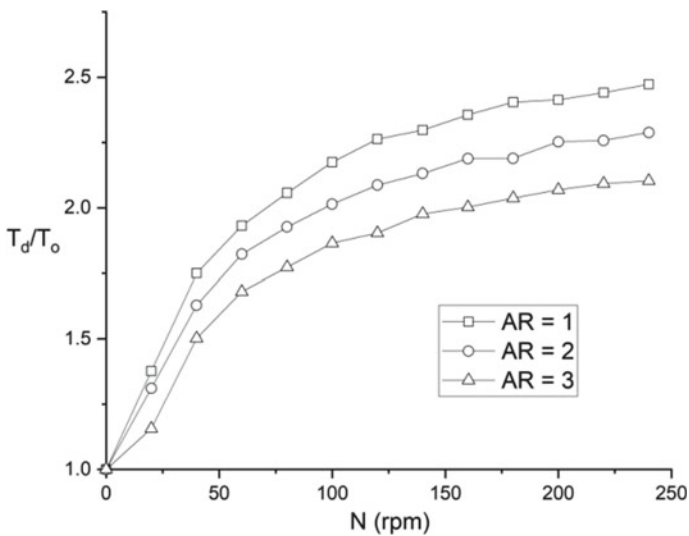


Fig. 8 Variation of T_d/T_o with N for crucified geometry

As authors have not conducted any numerical or Particle image Velocimetry (PIV) study, factors influencing the flow by changing the geometry of the drain port are not known yet. However, a tentative explanation could be provided as follows.

Gowda [11] has studied the effect of square and rectangular tanks on vortexing phenomenon. He found that, compared to circular tanks, square and rectangular tanks are efficient in suppressing air core vortex. He mentioned that exposure of draining fluid to four sharp corners and flow asymmetry dissipated rotational motion in the fluid and this created suppression of the vortex.

Ramamurthi and Tarakan [6] have used shaped discharge ports to suppress the vortexing. They found that stepped ports are efficient in arresting vortexing compared to bell mouth ports. They also found that conventional circular ports are very prone to vortexing. It should be noted that stepped ports have introduced sharp corners inside the drain port, and the port was asymmetric compared to conventional circular ports. This is the reason why stepped ports arrested vortexing very efficiently. Even though sharp corners were absent for bell mouth ports, they also introduced flow asymmetry in the flow field. This is the reason why performance of bell mouthed ports in suppressing the vortex was better compared to conventional circular drain ports.

Ramamurthi and Tarakan [6] showed that draining fluid can be exposed to flow asymmetry and sharp corners even by using drain ports. In the current study, for any specific drain port shape, it is found that vortexing is relatively suppressed at the highest value of aspect ratio tested ($AR = 3$). This is because as the aspect ratio increases, asymmetry of the drain port increases (Elliptical port with $AR = 1$ is a conventional circular port which is more prone to vortexing, and it is perfectly axisymmetric).

Regarding drain port shapes for a specific aspect ratio, it should be noted that elliptical drain ports are giving the highest value for time of emptying. This is because elliptical ports do not have any sharp corners. Rectangular ports are more efficient compared to elliptical ports because of the presence of sharp corners. Crucified shaped ports are the most efficient because they have more number of sharp corners (8 sharp corners) compared to rectangular ports. It was also mentioned by Prabhu et al. [10] that as the number of sharp corners of the drain port increases till 8, vortexing gets suppressed.

From the current results, it can be concluded that crucified geometry with aspect ratio 3 is the best drain port configuration with regard to vortexing phenomenon. As previously mentioned, it could also be concluded from the present study that critical height alone is not sufficient enough to characterize the phenomenon of vortex formation.

4 Conclusion

This study brings some important conclusions from the obtained results. It was found that drain port geometry need not necessarily influence the critical height of vortex formation. But effect of geometry is notably reflected in the liquid draining time. For a specific aspect ratio, crucified cross-sectional drain ports can deliver maximum discharge flow rate (minimum time of emptying). It was also found that

for specific drain port geometry, drain ports with aspect ratio equals to 3 can deliver the maximum discharge. Aspect ratio is found to have negligible influence on critical height but at the same time, it is found to have impact on the time of draining. Crucified cross-sectional drain port with aspect ratio 3 is found to be the drain port configuration to deliver maximum discharge flow rate and hence, thought to be the best among the geometries studied. It is also found from the present investigation that critical height alone is not sufficient to characterize the vortexing phenomenon.

The limitation of current investigation is that this work has not addressed the changes in flow field that occur due to changes in cross-sectional shape. These unknown changes in the flow field might have suppressed the vortexing phenomenon. A PIV analysis or a numerical study could be performed on draining of liquids through the novel cross-sectional shapes (discussed in the current study) to bring to light the changes in flow physics or flow structure in draining phenomenon. This is planned as a future study.

References

1. Lubin BT, Springer GS (1967) The formation of a dip on the surface of a liquid draining from a tank. *J Fluid Mech* 29(2):385–390
2. Sohn CH, Hyeon SJ, Park IS (2013) Numerical analysis of vortex core phenomenon during draining from cylinder tank for various initial swirling speeds and various tank and drain port sizes. *J Hydrodyn* 25(2):183–195
3. Ajith Kumar R, Joykutti J, Shaji RK, Srikrishnan AR (2016) Vortex suppression through drain port sizing. *ASCE J Aerosp Eng* 29(4):06016002
4. Ajith Kumar R, Nair RR, Prabhu M, Srikrishnan AR (2017) Vortex formation during draining from cylindrical tanks: effect of drain port eccentricity. *ASCE J Aerosp Eng* 30(5):06017001
5. Ramamurthi K, Tharakan J (1992) Shaped discharge ports for draining liquids. *J Spacecraft Rockets* 30(6):786–788
6. Nazir K, Sohn CH (2017) Study of air core phenomenon and influence of water height during liquid draining. *J Mech Sci Technol* 31(8):3831–3837
7. Nazir K, Sohn CH (2018) Effect of water temperature on air core generation and disappearance during draining. *J Mech Sci Technol* 32(2):703–708
8. Gowda BHL, Joshy PJ, Swarnamani S (1996) Device to suppress vortexing during draining from cylindrical tanks. *J Spacecraft Rockets* 33(4):598–600
9. Prabhu M, Ajith Kumar R, Gopikrishnan TH, Deshpande PJ, Anandhkrishnan U, Kiran AS, Govindu RP (2018) Rankine vortex formation during draining: a new twin port suppression strategy. *J Appl Fluid Mech* 13(1):147–160
10. Prabhu M, Ajith Kumar R, Nair RR, Anith TA (2019) Liquid draining through polygonal ports: an investigation on gas entraining vortices. *J Space Craft Rockets* 56(5):1651–1657
11. Gowda BHL (1996) Draining of liquids from tanks of square or rectangular cross sections. *J Spacecraft Rockets* 33(2):311–312

A Study for the Effect of Antioxidant EDA and Aluminium Hydroxide Additives to Mitigate CO and NO_x Emissions in Biodiesel–Diesel Blend Fuelled CI Engine



Ajai Prasad Nigam and Shailendra Sinha

Abstract This paper studies the effect of using *Jatropha* biodiesel–diesel blends as fuel in single cylinder CI engine on the most obnoxious CI engine exhaust emissions NO_x and carbon mono oxide (CO). Antioxidant ethylene diamine (EDA) and a novel additive aluminium hydroxide (Al(OH)₃) have been used as additives with fuel in different concentrations. Aluminium hydroxide is a new material, not yet referred in journals, which chemically decomposes into alumina and water at high temperature. The test results found were promising in reducing the NO_x and CO emissions. And aluminium hydroxide as expected has been proved to be an cost effective alternative to the alumina nanoparticles along with the advantages of water in mitigating emissions.

Keywords *Jatropha* • Ethylene Di-Amine • Aluminium Hydroxide • Alumina nano particles

Abbreviations

PPDA	p-Phenylenediamine
BHT	Butylated Hydroxy Toluene
EDA	Ethylene Di-Amine
PHC	Pyridoxine Hydro Chloride
AT	A-tocopherol acetate
LA	L-ascorbic acid
BSFC	Brake specific fuel consumption
DEA	Di-Ethyl Amine

A. P. Nigam (✉)

Department of Mechanical Engineering, Sri RamSwaroop Memorial Group of Professional Colleges, Lucknow, U.P, India
e-mail: ajai.nigam1@gmail.com

S. Sinha

Department of Mechanical Engineering, Institute of Engineering and Technology, Lucknow, U.P, India
e-mail: ssinhaet@gmail.com

TBHQ	Tert Butyl Hydro Quinone
WCO	Waste Cooking Oil
B20	20% Biodiesel and 80% Diesel Blend
JME	Jatropha Methyl Ester
B25EDA200A100	25% Biodiesel, 75% Diesel, 200 mg of EDA and 100 ppm of Al(OH) ₃

1 Introduction

The explosive population growth, rigorous lifestyles, adaptation of metropolitan culture by large populace, ever expanding businesses and rapid industrialization have resulted in increased energy consumption. The electricity generation, transportation sectors, agricultural sectors and industries, etc., are the main consumers of energy driven largely by diesel engines resulting in increased number of vehicles and stationary engines. Diesel engines play an indispensable part for these sectors throughout the world more so due to their high torque capability, durability, reliability, adaptability and economical fuel-efficiency [1]. These factors have increased the demand of diesel, a fossil fuel, being non-renewable energy resources obtained from the mortal remains of humans, animals, plants and micro-organisms beneath the earth after millions of years. Selective geographical concentration of fossil fuel and its fast depleting levels, subsequent rapid increase in diesel price throughout the world and thus forex crunch in oil importing countries have become the main cause of economic crisis.

The other deterring drawback of CI engines using diesel fuel is the obnoxious exhaust emissions like nitrogen oxides (NO_x), carbon dioxide (CO₂), carbon monoxide (CO), particulate matter (PM), soot, unburned hydrocarbons (HC), etc. These emissions are great threat to mankind, flora and fauna, the ozone layer and the environment. Nitrogen oxides (NO_x) and HC present in diesel exhaust is a chief cause of smog, acid rain and sick building syndrome [2]. Prolonged exposure to NO_x can cause fierce coughing, breathlessness, cyanosis, delayed chemical pneumonitis and pulmonary oedema. Smoke particulates are probable inducers of oxidative stress which is related with diseases such as Alzheimer's and Parkinson's that can impair cognitive function. Adverse effect on foetal development was stated when pregnant women are open to diesel fumes [3]. Therefore, the state enforcement authorities throughout the world are simultaneously mulling more rigorous emission norms.

The most promising and economical method scholars throughout the world researched to address diesel scarcity and exhaust emissions have been the modification of fuel. Through the last few decades, most focused alternative fuel has been the renewable biodiesel obtained by the trans-esterification of vegetable oils, animal fats and micro-algal oil in the presence of catalyst. The biodegradable

oxygenate biodiesels are mono-alkyl esters of long chain fatty acids with properties very similar to diesel, better lubricating property due to high viscosity with no sulphur content or polycyclic aromatics [1]. But the main hindrance to the use of biodiesel is the drastic increase in NO_x emission due to its high oxygen content. Cause of NO_x creation in CI engine is associated with three mechanisms viz. thermal, prompt and fuel. However, free radical formation with biodiesel as fuel is the main source for the higher NO_x emissions [4]. The CH radical produced from acetylene, the pre-combustion by-product of unsaturated constituents of biodiesel is probably liable for higher NO_x emissions [2]. More complete combustion and subsequent high temperature due to high oxygen content of biodiesel may also be partially responsible for increased NO_x , specifically at medium and high speeds [4, 5]. Mikulski M. et al. observed maximum NO_x increase of 22% with the exception with B50 mixture at 1500 RPM and under 50 Nm, 100 Nm and 150 Nm torque, respectively, where it is reduced. Decreases in CO and HC emissions are established in the literatures with oxygenates due to more complete combustion in the presence of excess oxygen [5]. However, comparative reduction in NO_x observed, while *Jatropha* biodiesel–diesel blend was used as fuel due to the complete combustion at high temperature in the presence of sufficient oxygen [6].

Combustion of hydrocarbon prompts the genre of free radicals at the flame front which accordingly quickens formation of NO_x . Amount of peroxy (HO_2) and hydrogen peroxide (H_2O_2) radicals produced during oxidation/ignition in the chamber and which are changed over to hydroxyl (OH) radicals through an endothermic reaction are highly active free radicals. Antioxidant flushes these free radicals resulting in diminished CO and HC oxidation and NO_x . The antioxidant present in the fuel likewise diminishes accessibility of oxygen, shoots up the aromatic content and C–C bonds which are fundamental drivers of smoke increment.

Spurt in CO and HC emissions detected when fuel comprising *jatropha* biodiesel mixed with antioxidant additives (either of PPDA, BHT, EDA, L-ascorbic acid and A-Tocopherol acetate) was utilized as fuel in DI diesel engine. L-ascorbic acid and EDA exhibited highest and lowest HC emission, respectively, while PPDA, BHT and EDA, A-tocopherol acetate exhibited highest and lowest CO emissions, respectively, at full load [2]. Comparative outcomes were found experimentally by utilizing PHC, DEA and TBHQ antioxidants with the blend of methyl ester of mango seed and diesel as fuel. PHC was found to have most noteworthy decreasing impact on CO and HC emissions, and also, it decreases over 20% NO_x for all loads [4]. A radical drop in NO_x emission was notified by the utilization of noval antioxidants Ethanox (1000 ppm) and BHT (500 ppm) with *Calophyllum Inophyllum* biodiesel (12.6% and 21% resp.) with the ensuing increment in CO, smoke and UHC emissions. When antioxidant (PPDA), (AT) and (LA) were used as additive with *Annona* biodiesel–diesel blend (A20) as fuel, NO_x emission increases with the increase of BMEP or load, but a steep decrease of it was observed with the increase of all the respective antioxidants from 50 to 250 mg. NO_x emission was then increased with the increase of antioxidant in excess of

250 mg indicating 250 mg of antioxidant as the most suitable quantity. PPDA and AT having nitrogen in their structure increase the NO_x emission, the effect, which overpowers reduction ability of antioxidants through reduction in free radicals when their quantity exceeds 250 mg. And when comparing the three antioxidants at 250 mg quantity, PPDA shows maximum decrease of NO_x followed by AT and LA. This is due to the higher tendency PPDA to flush hydroxyl free radicals by donating an electron or hydrogen atom to the radical [7].

Water had been also used as emulsion with diesel, diesel–biodiesel blend [8–13] or directly into intake air [14–16] to control emissions and more specifically NO_x , due to its high latent heat of vaporization which reduces in-cylinder temperature and also micro-explosion in water–oil emulsion resulted in better mixing of fuel with air and better combustion. But shortcomings found with water were its poor calorific value that resulted in inferior performance of engines.

Another fuel blend of Honge oil methyl ester, diesel (B20) mixed with alumina nanoparticles (20, 40 and 60 ppm, respectively) was tested in CI engine. Increase in NO_x emission was found with all fuel blends with nanoparticles due to high oxygen content, improved cetane number and subsequent improved combustion and heat removal rate. But there is extreme dip in CO emission by 47.43% followed by 37.72% and 27.84% reduction in HC and smoke due to the same reasons with B20 blend mixed with 40 ppm of nanoparticles, thereby improving BTE by 10.47% along with loss of 11.65% in BSFC [17].

Aluminium oxide nanoparticles are oxidizing catalyst with easy elevated temperature diffusivity and which diminishes ignition delay, fuel burning times and temperature of carbon activation. This also quickens propagation of flame with high energy release, propulsive performance and impulse of energy, thus supporting oxidation reaction [18, 19]. Nanoparticles have high surface to volume ratio effects in fine atomization and swift vaporization of extremely viscous biodiesel [20]. Alumina nanoparticles when used with biodiesel of poultry litter diesel blend reduce UHC and CO emission till 40 to 60% load with similar tendency for NO_x , while smoke opacity increases as later in the engine cycle alumina nanoparticles retard the combustion reaction thereby reducing heat release [20]. But with mahua biodiesel–diesel blend HC, CO and smoke emission decrease while NO_x rises with the increase of ppm level of nanoparticle in B20 [19]. Similar results of increased NO_x along with extreme dip in CO (47.43%) and HC (37.72 to 27.84%) emission were documented with blend of biodiesel of Honge oil–diesel with alumina nanoparticles [17]. When multi-walled nano tubes of carbon or nanoparticles of silver were blended with diesel–biodiesel and used as fuel in multi-cylinder CI engine, torque and force output incremented by 2%, while BSFC diminished by 7.08% in contrast with unadulterated diesel. In the same test, CO_2 and NO_x incremented by 17.03 and 25.32% individually, while CO and UHC exhaust diminished by 25.17 and 28.56% in that order [21]. Waste cooking oil (WCO) methyl ester blended with diesel (B5 and B10) and alumina nanoparticles (30, 60 and 90 ppm, respectively) when tested as fuel in single cylinder CI engine

drastically improves the performance parameters like reduction in SFC (14.66%) and rise in BTE, torque, power and EGT (10.63%, 5.36%, 5.36% and 5.80%, respectively). This fuel in turn escalates NO emission by 43.61% with fall in CO and UHC by 2.94% and 20.56%, respectively [22]. The reduction of CO and NO_x emissions (12% and 9%, respectively) with gloomier result for THC emission and improved BSFC (10% less) were witnessed with aluminium nanoparticles blended biodiesel and biodiesel–ethanol, respectively, fuel used in heavy duty diesel engine [23]. Carbon coated variant of this nanoparticle (30 ppm) in B10 and B10E4 lowers NO_x and CO emissions by 6% and 19%, respectively [24]. Other variants of nanoparticles like CeO₂, copper oxide (CuO) and TiO₂, etc., had been tested in the literatures with the use of biodiesel of different materials, diesel and their blends as fuel giving similar contrasting results. Procurement of nanoparticles is very difficult, and its complex production technique makes it an expensive prerogative. Also, in the developing country like India, the population density of latest sophisticated diesel engines is quite minimal and mostly limited to medium to big business houses, latest vehicles or government installations. Eying on the aforesaid constraints, this paper experimentally examines the effect of antioxidant EDA and aluminium hydroxide additives on jatropha biodiesel–diesel blend as fuel in a single cylinder CI engine.

2 Materials and Methods

2.1 Engine and Measuring Instrument

The experiments were accomplished on four-stroke, single cylinder, water cooled, diesel engine manufactured by Kirloskar Oil Engines Ltd. (Table 1) at engine lab, Institute of Engineering and Technology, Lucknow, India. Rope brake dynamometers coupled to engine have been used to measure engine power. AVL exhaust gases analyser and smoke metre manufactured by AVL India Pvt. Ltd. were used to measure the emissions of NO_x, CO and CO₂.

Table 1 Engine specification

Properties	Specification
Make	Kirloskar Oil Engines Ltd
Stroke	4 Stroke
Compression ratio	16.5:1
Fuel tank capacity	6.5 L
Cubic capacity	0.553 L
Cylinder bore × stroke	0.08 m × 0.110 m
Connecting rod length	0.022 m
Engine speed	1500 rpm

2.2 Fuel and Additives Used

Commercial diesel available in the local market has been used. Blends of diesel with biodiesel were formed using mechanical stirring process. Jatropha methyl ester (JME) procured from the Eco Green India Pvt. Ltd. India was used in the experiment. Antioxidant ethyl diamine (1,2-Diaminoethane) which is alkaline in nature (pH of 25% EDA in water is 11.9) readily dissolves aluminium hydroxide powder ($\text{Al}(\text{OH})_3$) additive as it is insoluble in water but soluble in strong acid and bases. A fixed measured quantity of 100 ppm of ($\text{Al}(\text{OH})_3$) mixed with 50 mg, 100 mg, 150 mg and 200 mg of EDA, respectively. Now, these four samples were mixed with different proportions by volume (10, 15, 22.5, 25 and 50% by volume) of biodiesel and diesel blends by mechanical stirring process (Table 2). Ethylene diamine (EDA) delays or impedes oxidative processes by donating an electron or hydrogen atom to a free radical derivative formed during combustion with one or more unpaired electrons, e.g. oxygen molecule, superoxide ion, nitric oxide and hydroxyl radical [2]. Aluminium hydroxide powder or granules ($\text{Al}(\text{OH})_3$) with density 2.42 g/cm^3 at 20°C (Table 3). It behaves as an ideal flame retardant, and at temperatures greater than 200°C , it decomposes through a strong endothermic reaction into alumina and three crystals water (Eq. 1), thus reducing in-cylinder temperature. This rate of decomposition is highest at 250°C .

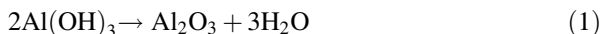


Table 2 Properties of diesel and biodiesel

Properties of diesel/biodiesel	Diesel	Jatropha biodiesel
Density 20°C , Kg/m^3	837	865
Cetane number	50	51
Kinematic viscosity at 40°C , mm^2/s	2.6	5.25
Flash point ($^\circ\text{C}$)	74	174
Cloud point ($^\circ\text{C}$)	5	13
Calorific value, MJ/Kg	42–46	39.1

Table 3 Properties of aluminium hydroxide

Properties	Aluminium hydroxide
Density g/cm^3	2.42 (at 20°C)
Melting point $^\circ\text{C}$	300
Solubility in water $\text{g}/100 \text{ mL}$	0.0001
Solubility product (Ksp)	3×10^{-34}
Acidity (pKa)	>7
Isoelectric point	7.7
Flash point	Non-flammable

Alumina is a hard, wear-resistant material with high thermal and chemical stability, thermal strength, creep resistance and dielectric properties and low thermal expansion coefficient. High purity alumina is usable in both oxidizing and reducing atmospheres to 1925 °C. Alumina apart from absorbing heat probably helps in appropriate mixing of air and fuel. Higher latent heat of vaporization of water moderates the adiabatic flame temperature, the factor responsible for the formation of thermal NO_x .

3 Results and Discussion

Different blends of Jatropha biodiesel and diesel used in this work along with EDA and aluminium hydroxide have been found to be stable for the study of emission characteristics. In this study, aluminium hydroxide has been used as a very inexpensive alternative of alumina nanoparticles with the added advantage of water in the air fuel mixture in the cylinder. Also, use of aluminium hydroxide does not require any specialized technique as it easily dissolves in the basic EDA.

3.1 NO_x Emission

NO_x emission level invariably increases at all concentrations of EDA in biodiesel–diesel blends from B10 to B25 (Fig. 1). The lowest NO_x level observed was 348 g/kW-hr with B25EDA200A100 which is less than that of diesel (386 g/kW-hr). This phenomenon is possibly due to dual action of EDA and $\text{Al}(\text{OH})_3$. Antioxidants decrease prompt NO_x formation by flushing highly reactive free radicals, with one or more unpaired electrons produced by the combustion of hydrocarbons which accelerates NO_x formation. $\text{Al}(\text{OH})_3$ at temperature exceeding 200 °C converts to alumina and crystal water through an endothermic reaction. This water having high heat capacity reduces the in-cylinder temperature, decreasing the formation of thermal NO_x . Also, alumina retards the combustion, thereby reducing heat release rate.

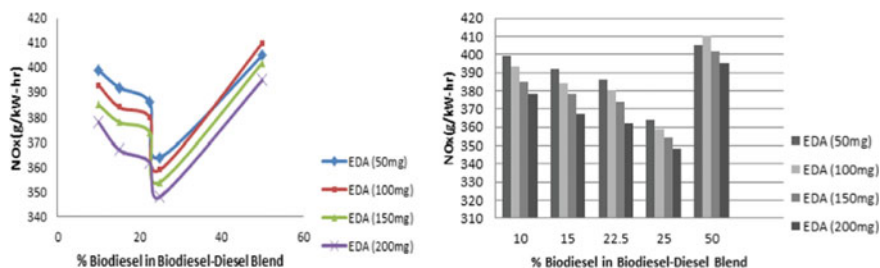


Fig. 1 NO_x emission in biodiesel–diesel fuelled engine with 100 ppm $\text{Al}(\text{OH})_3$ and EDA

It is also evident that at any concentration of biodiesel, NO_x level more or less continuously decreases with the increase in the concentration of EDA from 50 to 200 mg (Fig. 1) due to the enhanced effect of antioxidant in reducing the prompt NO_x with concentration. Also, concentration of biodiesel above B25 level, NO_x emission abruptly increases and becomes maximum at B50, as then inherent oxygen level in biodiesel extremely increases making a favourable condition for NO_x formation, and this effect surpasses mitigating effect of EDA and $\text{Al}(\text{OH})_3$.

3.2 CO Emission

Biodiesel having greater oxygen content in their structure renders greater availability of oxygen content during combustion in the cylinder when used as fuel. Thus, blends of biodiesel–diesel in any proportion give lower CO emission when used as fuel. As is evident from Fig. 2, CO level in the exhaust continuously decreases with the increase of biodiesel content in the blend across all concentrations of EDA. The biodiesel–diesel blends with 200 mg of EDA and 100 ppm of $\text{Al}(\text{OH})_3$ exhibited lowest CO emission with lowest value of it being 1.78 g/kW-hr. Also, with the increase of EDA content in the blended fuel, CO emission continuously decreases. The kinetics of CO formation reaction depends upon concentrations of OH and H radicals. The instantaneous hydroxyl concentration directly effects the rate of CO oxidation which subsequently depends upon the rate of consumption of OH radical. Antioxidants flush these hydroxyl free radicals, thus reducing the rate of formation of CO. Aluminium oxide nanoparticles act as oxidizing catalyst which reduces ignition delay, short fuel burning times [21, 22], accelerates propagation of flame and shortens temperature of carbon activation [21]. As such, availability of alumina (Al_2O_3) due to the presence of $\text{Al}(\text{OH})_3$ in the fuel further decreases CO emission. CO concentration in the exhaust depends upon its oxidation by the post-flame gases as they cool. Thus, as a step further availability of abundant oxygen induces the complete oxidation of CO, thus reducing its content in the exhaust.

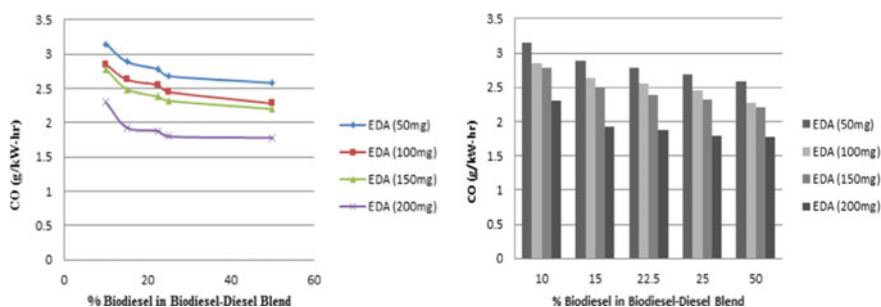


Fig. 2 CO emission in biodiesel–diesel fuelled engine with 100 ppm $\text{Al}(\text{OH})_3$ and EDA

4 Conclusion

Since long different blends of diesel and biodiesel, the oxygenated fuel, had been tested in diesel engines, by researchers, to address the high obnoxious exhaust emissions of such blends. This effectively has positive effect on CO emissions due to high cetane number and fuel bound oxygen content in oxygenated fuels. For the same reason, NO_x emission deteriorates. Researchers have also used antioxidants to the best benefit by positively effecting the CO and NO_x emissions. In the recent decade, there had been spurt in the use of metallic nanoparticles due to their favourable properties in reducing the emissions. Most studies have been performed using alumina nanoparticles. However, procuring and using nanoparticles are a difficult and expensive prerogative. In place of alumina nanoparticles, a very cheap alternative aluminium hydroxide has been used in this paper which chemically converts to alumina and crystalline water at high temperature in the engine cylinder. Thus, it gives the advantage of both alumina nanoparticles and water as well in fuel air mixture, having properties of reducing emissions, as had been already reported in the literatures. EDA has been used as antioxidant. NO_x was observed to be greatly reduced up to B25, where this reduction was even less than that of pure diesel. The reduction of CO has been observed across all the concentrations of EDA.

5 Future Scope

In this paper, the observed effect of EDA and aluminium oxide was limited to only emissions of CO and NO_x. A further extensive study is required for other components of the emissions too, apart from the performance parameters. Also, the effect of other oxygenated fuel ethanol can also be tested along with, to get the effect on emission and performance parameters.

References

1. Hosseini SH, Alisarai AT, Ghobadian B, Mayvan AA (2017) Performance and emission characteristics of a CI engine fuelled with carbon nano tubes and diesel-biodiesel blends. *Renewable Energy* 111:201–213
2. Varatharajan K, Cheralathan M, Velraj R (2011) Mitigation of NO_x emissions from a jatropa biodiesel fuelled DI diesel engine using antioxidant additives. *Fuel* 90:2721–2725
3. Kumar KS, Raj RTK (2013) Effect of fuel injection timing and elevated intake air temperature on the combustion and emission characteristics of duel fuel operated diesel engine. *Procedia Eng* 64:1191–1198
4. Velmurugan K, Sathiyagnanam AP (2016) Impact of antioxidants on NO_x emissions from a mango seed biodiesel powered DI diesel engine. *Alexandria Eng J* 55:715–722

5. Nguyen VH, Pham PX (2015) Biodiesels: oxidizing enhancers to improve CI engine performance and emission quality. *Fuel* 154:293–300
6. Jain S, Sharma MP (2010) Prospects of biodiesel from *Jatropha* in India: a review. *Renew Sustain Energy Rev* 14:763–771
7. Silambarasan R (2020) Effect of antioxidant additives on oxides of nitrogen (NO_x) emission reduction from *Annona* biodiesel operated diesel engine. *Renewable Energy*. <https://doi.org/10.1016/j.renene.2019.10.104>
8. Cheikh KR, Sary A, Khaled L, Abdelkrim L, Mohand T (2016) Experimental assessment of performance and emissions maps for biodiesel fueled compression ignition engine. *Appl Energy* 161:320–329
9. Raheman H, Kumari S (2014) Combustion characteristic and emissions of a compression ignition using emulsified *Jatropha* biodiesel blend. *Biosys Eng* 123:29–39
10. Qi DH, Chen V, Matthews RD, Bian YZ (2010) Combustion and emission characteristics of ethanol–biodiesel–water micro-emulsions used in a direct injection compression ignition engine. *Fuel* 89:958–964
11. Ogunkoya D, Li S, Rojas OJ, Fang T (2015) Performance, combustion, and emissions in a diesel engine operated with fuel-in-water emulsions based on lignin. *Appl Energy* 154:851–861
12. Fahd MEA, Wenming Y, Lee PS, Chou SK, Yap CR (2013) Experimental investigation of the performance and emission characteristics of direct injection diesel engine by water emulsion diesel under varying engine load condition. *Appl Energy* 102:1042–1049
13. Subramanian KA (2011) A comparison of water–diesel emulsion and timed injection of water into the intake manifold of a diesel engine for simultaneous control of NO and smoke emissions. *Energy Convers Manag* 52:849–857
14. Sahin Z, Tuti M, Durgun O (2014) Experimental investigation of the effects of water adding to the intake air on the engine performance and exhaust emissions in a DI automotive diesel engine. *Fuel* 14:884–895
15. Bhale PV, Deshpande NV, Thombre SB (2009) Improving the low temperature properties of biodiesel fuel. *Renewable Energy* 34:794–800
16. Tesfa B, Mishra R, Gu F, Ball AD (2012) Water injection effects on the performance and emission characteristics of a CI engine operating with biodiesel. *Renewable Energy* 37:333–344
17. Soudagar MEM, Nik-Nazri NG, Kalam MA, Badruddin IA, Banapurmath NR, Ali MAB, Kamangar S, Cho HM, Akram N (2020) An investigation on the influence of aluminium oxide nano-additive and honge oil methyl ester on engine performance, combustion and emission characteristics. *Renewable Energy* 146:2291–2307
18. Muthusamy S, Shanmuga SN, Ramasamy RK, Hussain STM (2017) Effect of aluminium oxide nanoparticles blended pongamia methyl ester on performance, combustion and emission characteristics of diesel engine. *Renewable Energy*. <https://doi.org/10.1016/j.renene.2017.10.002>
19. Aalam CS (2020) Investigation on the combustion and emission characteristics of CRDI diesel engine fuelled with nano Al_2O_3 and Fe_3O_4 particles blended biodiesel. *Mater Today Proc*. <https://doi.org/10.1016/j.matpr.2019.12.040>
20. Ramesh DK, Dhananjaya KJL, Hemanth KSG, Namith V, Parashuram BJ, Sharath S (2018) Study on effects of Alumina nano particles as additive with poultry litter biodiesel on performance, combustion and emission characteristic of diesel engine. *Mater Today Proc* 5:1114–1120
21. Ghanbari M, Najafi G, Ghobadian B, Yusaf T, Carlucci AP, Kiani MKD (2017) Performance and emission characteristics of a CI engine using nano particles additives in biodiesel–diesel blends and modeling with GP approach. *Fuel* 202:699–716
22. Hosseini HS, Alisaraei AT, Ghobadian B, Mayvan AA (2017) Effect of added alumina as nano-catalyst to diesel–biodiesel blends on performance and emission characteristics of CI engine. *Energy* 124:543–552

23. Wu Q, Xie X, Wang Y, Roskilly T (2017) Experimental investigations on diesel engine performance and emissions using biodiesel adding with carbon coated aluminum nano particles. *Energy Procedia* 142:3603–3608
24. Wu Q, Xie X, Wang Y, Roskilly T (2018) Effect of carbon coated aluminum nano particles as additive to biodiesel-diesel blends on performance and emission characteristics of diesel engine. *Appl Energy* 221:597–604

Thermal Performance Optimization of Heat Pipe Using Taguchi Method



Naveen Kumar Gupta

Abstract Heat pipes are very effective heat exchangers, used to enhance the heat transfer rate in limited temperature difference conditions. Heat pipes support in the effective operation of high heat flux generating equipment by diffusing the excess heat to the environment. Wire mesh heat pipe provides sufficient flexibility in terms of a wide range of applications. The thermal performance of heat pipe depends upon the various design and operating parameters. In the present paper, the Taguchi approach is used to obtain the most favorable combination of operating parameters like power input, orientation, charging %, and vacuum pressure. The levels of experiments have been considered after performing a sufficient number of pilot experiments.

Keywords Heat pipe · Thermal efficiency · Taguchi method · Thermal performance

1 Introduction

Heat pipes (HPs) are very efficient and effective heat exchangers. HP is used in limited temperature difference conditions. It works on the phase change phenomenon. Figure 1 shows the working principles of HP. HPs are closed hollow tubes charged with working fluid. Working fluid may be water, ethanol, propanol, or any other compatible fluid. Heat transfer takes place from one end to another end.

There are three sections like evaporator, adiabatic, and condenser of HP. The evaporator section is connected to the heat source, and the condenser section is connected to the cooling media. So, heat is absorbed from the evaporator section and diffuses into cooling media. The length of the adiabatic section depends upon the distance between the heat source and heat sink, so it will depend upon the application.

N. K. Gupta (✉)
GLA University, Mathura, India
e-mail: naveen.gupta@gla.ac.in

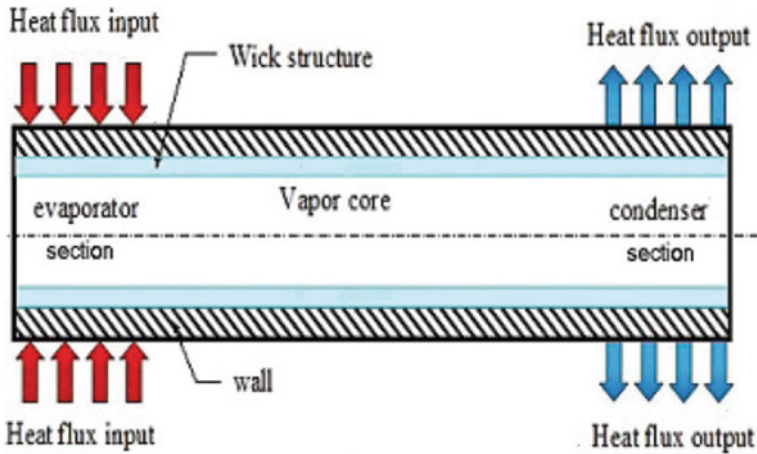


Fig. 1 Working principle of HP

Figure 1 shows that latent heat of vaporization is absorbed by the evaporator section and after absorbing it working fluid converted from the liquid phase to vapor phase. The amount of heat absorbed by the working fluid depends upon various factors like thermal conductivity (TC) of the material of HP, thermophysical properties, and volume of working fluid and heat loss to the environment. Now, vapors of working fluids move toward the condenser section, and after reaching the condenser section, vapors release the latent heat of condensation to the available cooling media and converted into the liquid phase. In HP envelope, wire mesh is used to produce capillary force. Capillary force is used to send the condensate from the condenser section to the evaporator section. In this way, the working fluid completes the cycle. So, heat can be absorbed from the evaporator section and released through the condenser section.

Nanofluids (NFs) are the new advancements in thermo-fluidics. Research on NFs was started in the year of 1995.

NFs are the colloidal mixture of nanoparticles in base fluids. The thermal conductivity of nanofluids (TCNFs) is higher as compared to base fluids [1]. Researchers used NFs as working fluids in HPs. Gupta et al. [2] published a review article on NFs application in HPs. Authors concluded that enhanced TCNFs are the main reason for the enhancement in TPHP. TC, specific heat, and viscosity are the main thermophysical properties of NFs which are responsible for the change in TPHP. Although NFs showed higher TPHP as compared to other base fluids, but in prolonged working conditions, thermophysical properties of NFs deteriorated with time. Therefore, stability issues of NFs are of great concern. Researchers noticed that NFs coating serves the solution of stability issues [3].

Many experimental studies like [4–7] showed that NFs are beneficial for HP applications because their applications enhanced TPHPs. Many researchers performed numerical studies to explore the main reasons to change in TPHPs. Many

research articles showing numerical and experimental studies to validate each other are available for ready reference. In the last 15 years, hundreds of research articles have been published on NFs application in HPs. Majority of research outcomes are in favor of NFs application in HPs. Very few research articles showed that NFs cause deterioration in TPHP also.

Research on optimizations of thermal performance of heat pipe (TPHP) using NFs is the new direction of research.

Researchers used RSM methodology to optimize the TPHP [5]. Researchers used Taguchi methodology to obtain the most favorable combination of operating parameters leading to optimum TPHP.

In present work, author used Taguchi methodology to find out the most suitable combination of operating parameters of NFs filled HP. The input operating parameters are evaporator power, the inclination of HP, the volume of NF, and concentration (volume %) of NF. Design parameters have remained constant. The factors and their levels are considered based on available literature and pilot experiments.

2 Method and Materials

The schematic of the experimental setup is shown in Fig. 3. The main components of the experimental setup are copper HP envelope, resistance heating element, data acquisition system, temperature controlling unit, orientation control unit, etc.

The selection of input and output parameters is shown in Fig. 2. All parameters related to design are constant. Evaporator power supply, NF charging %, HP orientation, and NF concentration are the parameters selected for the present experimental study.

All the experimental data are taken after achieving a steady state of experimental setup. Non-condensable gases are sucked through a vacuum pump. The orientation stand is used to give the desired inclination of HP. The entire unit is insulated with the help of glass wool. The air gap between the heating element and the evaporator surface is filled with the help of thermal paste. The temperature of the outer wall of

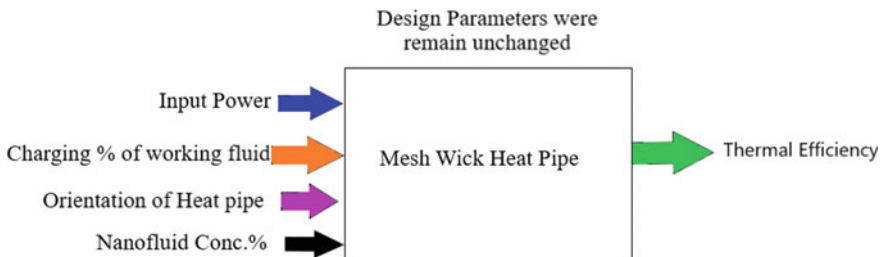


Fig. 2 Various operating parameters of heat pipe

insulation is recorded to monitor and control heat loss. HP envelope temperature is measured with the help of thermocouples. The main performance parameters of HP are wall temperature, overall conductivity, convective heat transfer coefficient, and thermal efficiency. In present work, thermal efficiency is the only performance parameter of HP. Performance index (thermal efficiency) of HP can be written as

$$\eta = \frac{MC(T_2 - T_1)}{VI} \quad (1)$$

To achieve the optimum value of thermal efficiency, the Taguchi method is used. The Taguchi method is an effective mathematical tool. The Taguchi method is used to identify the most suitable combination of operating parameters [10]. The predicted value of TEHP is validated by conducting five experiments at the selected values of operating parameters.

2.1 Level of Parameters

Pilot experiments were conducted to decide the different levels of operating parameters. In the present study, authors considered four factors with three levels of each for experimentation. The different levels of parameters are decided on the basis of the literature available (Table 1).

2.2 Selection of Orthogonal Array (OA)

Degree of freedom (DOF) is an important criterion to decide the orthogonal array (OA). It can be evaluated [8] as

Total DOF = (Number of levels - 1) * number of factors + 1 [Interaction effect is assumed to be zero].

$$DOF = (3 - 1) \times 4 + 1 = 9$$

OA is selected based on DOF. The order of OA is higher than DOF for effective results. But, a large number of experiments required more effort, time, and money.

Table 1 Levels of operating parameters

Factors	Evaporator power (watt)	HP inclination (°)	NF charging (%)	NF concentration (volume %)
Level	(A)	(B)	(C)	(D)
I	30	30	25	0.5
II	60	45	50	1.0
III	90	60	75	1.5

So, the selection of OA depends upon desired resolution and cost limitation [2]. In the present study, we will consider L27 OA for the optimization process.

2.3 Signal to Noise (S/N) Ratio and Confirmation of Experiments

For the calculation of S/N ratio, we will consider higher the better type of response which is given as

Higher is better [11]:

r

$$(S/N)_{HB} = -10 \log \left[\frac{1}{r} \sum_{i=1}^r [(1/y_i^2)] \right] \tag{2}$$

$i = 1$

$r =$ No. of experiment, $y_i =$ Value of i th experiment

j

$$X_{opt} = X + \sum_{i=1}^j (X_i - X) \tag{3}$$

$i = 1$

$j =$ Total number of control factors, $X =$ Mean of all experiments, $X_i =$ Average value for i th control factor in most favorable condition.

The confidence interval (CI) [4, 10, 11]

$$CI = [F_{\alpha}(1, f_e) V_e \{ (1/N) + 1/R \}]^{0.5} \tag{4}$$

$F_{\alpha}(1, f_e) = F$ ratio at a confidence level of $(1 - \alpha)$ against D.O.F. and error f_e

$V_e =$ Error variance, $N =$ Effective number of replication, $R =$ Size of sample,

$$N = N_t / [1 + (\text{Total D.O.F. associated in the estimation of } M_{opt})] \tag{5}$$

$N_t =$ Number of experimentation conducted.

3 Experimentation

The experimental setup is shown in Figs. 3 and 4. The outer diameter and thickness of thermosyphon are 20 and 1 mm, respectively.

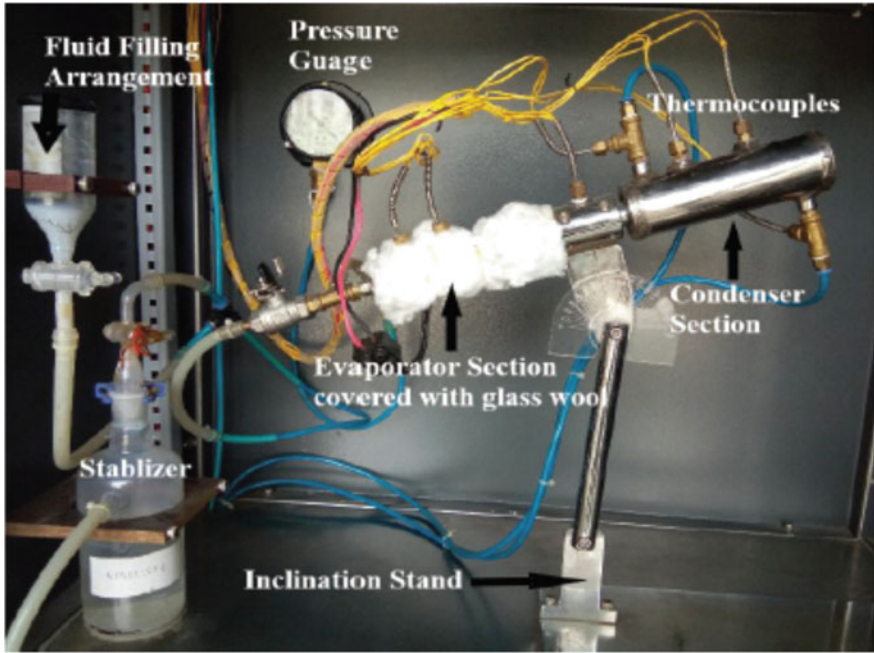


Fig. 3 Actual photograph of the experimental setup

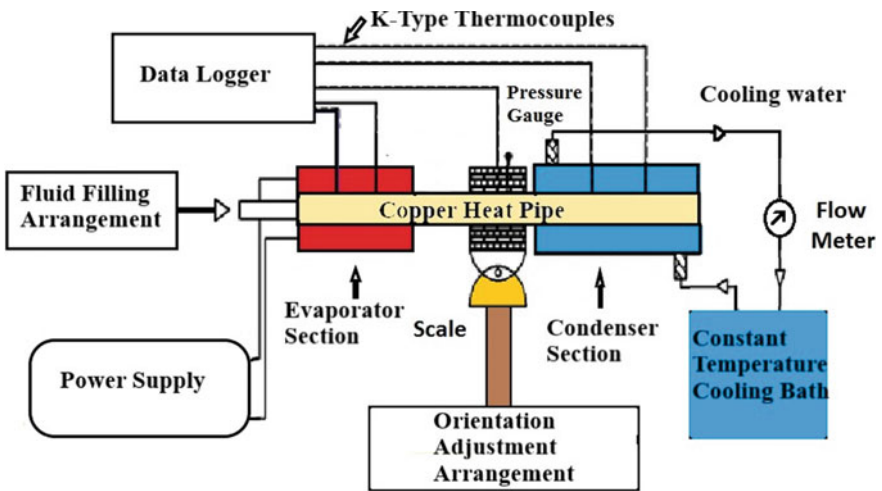


Fig. 4 Schematic of heat pipe experimental setup

Length of the evaporator, adiabatic, and condenser sections is 100, 100, and 150 mm, respectively.

Experiments performed according to the array L27. For every combination of parameters, three experiments have been done, and the average value has been taken.

3.1 Calculation for the Mean (S/N) Ratio

Signal to noise ratio is evaluated by considering the mean value of all S/N ratio for the corresponding level of the parameter. The S/N ratio for each parameter level is calculated by averaging the S/N ratios obtained when the parameter is maintained at that level [9]. Table 2 shows the experimental results. Thermal efficiency (TE) for each combination of operating combination is mentioned. Table 3 shows the S/N ratios for respective experiments. S/N ratios are calculated (using equation 2). Table 4 shows the S/N ratio based responses of each parameters.

Table 2 Experimental results

S. N.	A	B	C	D	TE %
1	30	30	25	0.5	58.52
2	30	30	50	1.0	59.40
3	30	30	75	1.5	61.20
4	30	45	25	1.0	62.50
5	30	45	50	1.5	64.25
6	30	45	75	0.5	66.45
7	30	60	25	1.5	64.60
8	30	60	50	0.5	66.85
9	30	60	75	1.0	66.25
10	60	30	25	1.0	66.50
11	60	30	50	1.5	65.45
12	60	30	75	.5	65.85
13	60	45	25	1.5	66.65
14	60	45	50	0.5	65.87
15	60	45	75	1.0	67.85
16	60	60	25	0.5	68.25
17	60	60	50	1.0	67.95
18	60	60	75	1.5	66.85
19	90	30	25	1.5	68.86
20	90	30	50	0.5	67.56
21	90	30	75	1.0	66.66
22	90	45	25	0.5	64.55
23	90	45	50	1.0	64.77
24	90	45	75	1.5	64.67
25	90	60	25	1.0	65.54
26	90	60	50	1.5	67.95
27	90	60	75	0.5	66.15

Table 3 Determination of S/N ratio

S. N.	A	B	C	D	S. N. Ratio (dB)
1	30	30	25	0.5	-7.3815
2	30	30	50	1.0	-7.2254
3	30	30	75	1.5	-6.9146
4	30	45	25	1.0	-6.6968
5	30	45	50	1.5	-6.4120
6	30	45	75	0.5	-5.9767
7	30	60	25	1.5	-6.2661
8	30	60	50	0.5	-5.9153
9	30	60	75	1.0	-5.8875
10	60	30	25	1.0	-5.5990
11	60	30	50	1.5	-6.2119
12	60	30	75	.5	-6.5095
13	60	45	25	1.5	-5.3960
14	60	45	50	0.5	-6.2464
15	60	45	75	1.0	-5.5739
16	60	60	25	0.5	-5.9640
17	60	60	50	1.0	-5.3789
18	60	60	75	1.5	-5.0953
19	90	30	25	1.5	-5.0635
20	90	30	50	0.5	-5.9775
21	90	30	75	1.0	-5.3944
22	90	45	25	0.5	-6.6241
23	90	45	50	1.0	-6.3491
24	90	45	75	1.5	-6.4250
25	90	60	25	1.0	-6.3478
26	90	60	50	1.5	-5.3789
27	90	60	75	0.5	-6.1030

Table 4 S/N ratio-based responses

Factors	Power (Watt)	Inclination angle (°)	Charging volume (%)	Pressure (Mpa)
Level	A	B	C	D
1	-6.2153	-6.8187	-6.9297	-6.7428
2	-6.6103	-6.2239	-6.5111	-5.1938 ^a
3	-6.1537 ^a	-6.0766 ^a	-5.2975 ^a	-5.2525
(Delta)	-0.4566	-0.7421	-1.6322	-1.549
Rank	1	2	4	3

“a” shows the maximum value

(a) For input power, S/N ratio for level 1 is evaluated as under:

$$N_{A1} = (N_1 + N_2 + \dots N_9)/9$$

The difference between Max. and Min depicts the wide range of changes in the S/N ratio among all the possible combinations. A higher value of difference represents the higher impact on the output of the system. Therefore, the rank of all operating parameters can be provided.

According to the value of delta, the rank of all operating parameters can be shown as

Power > Inclination angle > NF concentration % > NF charging

The most suitable combination of all operating parameters leads to the maximum value of TPHP with the least value of variance. Therefore, $A_3B_3C_3D_2$ is the combination for the optimum value of output.

3.2 Confirmation Test

Five confirmation experiments were conducted at the optimum setting of process parameters. The optimum thermal efficiency, at the most suitable combination of process parameter ($A_3B_3C_3D_2$), is obtained approximately 72.5%. The optimum thermal efficiency of HP using water was determined with the help of the Taguchi method, and it was 62.5% [8]. It means using nanofluid, 10% enhancement in TEHP is achieved. This value lies within the confidence interval (Eq. 4) of the predicted optimum thermal efficiency.

4 Conclusions

In the present investigation, TEHP is examined. The concluding remarks are as under

- Evaporator power supply (A) has a maximum impact on the TEHP. HP orientation (B) is the next most dominating operating input parameter. After that, nanofluid volume concentration (C) has the third rank. Nanofluid charging value has a fourth rank among all four parameters.
- The decreasing order of rank of all parameters is: Evaporator power supply > Orientation > Nanofluid concentration > Nanofluid charging %.

- ($A_3B_3C_3D_2$), i.e., 90 W power supply, 60° inclination angle, 75 ml of working fluid, and 1.0% (volume %) concentration of nanofluid is the best combination for the optimum thermal efficiency.
- The optimum value of thermal efficiency (72.5%) is obtained for 60 W power supply, 60° inclination angle, 75 ml of nanofluid, and 1.0% (volume %) concentration of nanofluid.

The present investigation concluded that thermal efficiency of heat pipe enhanced using nanofluid. Taguchi methodology is an effective tool to optimize the thermal efficiency of the heat pipe. The above results showed that the Taguchi method is very effective in case of thermal problems also. Therefore, more experimental studies are required to explore this method in other applications also.

References

1. Gupta NK, Ghosh SK (2019) Thermo physical properties of Nanofluids, 1–6. <https://doi.org/10.35940/ijitee.xxxxx.xxxxx>
2. Gupta NK, Tiwari AK, Ghosh SK (2018) Heat transfer mechanisms in heat pipes using nano fluids—a review. *Exp Therm Fluid Sci* 90:84–100. <https://doi.org/10.1016/j.expthermflusci.2017.08.013>
3. Gupta NK, Tiwari AK, Ghosh SK (2018) Experimental study of thermal performance of nanofluid-filled and nanoparticles-coated mesh wick heat pipes. *J Heat Transfer* 140:1–7. <https://doi.org/10.1115/1.4040146>
4. Gupta NK, Verma SK (2019) Effects of Ceo/H₂O nano fluid application on thermal performance of mesh wick heat pipe, 2188–2194
5. Gupta NK (n.d.) Parametric optimization of thermal performance of heat pipe using Taguchi method
6. Gupta NK, Verma SK, Kr P, Rathore S (2020) Effects of CuO/H₂O nanofluid application on thermal performance of mesh wick heat pipe. *Heat Transf Res*. <https://doi.org/10.1615/HeatTransRes.2020030772>
7. Gupta NK, Mishra S, Tiwari AK, Ghosh SK (2019) A review of thermo physical properties of nanofluids. *Mater Today Proc* 18:968–978. <https://doi.org/10.1016/j.matpr.2019.06.534>
8. Gupta NK (2020) Parametric optimization of thermal performance of heat pipe using taguchi method. *Test Eng Manag* 0193:12583–12588
9. Phadke MS (1989) *Quality engineering using robust design*. Prentice-Hall, Englewood Cliffs, NJ, 16
10. Roy RK (1990) *A primer on the Taguchi method*. Van Nostrand Reinhold, New York
11. Roy RK (2013) *Design of experiments using the Taguchi approach*. Wiley, United States. First Indian reprint

Effects of Hybrid Nanofluids on the Thermal Performance of Heat Pipe: An Experimental Investigation



Naveen Kumar Gupta

Abstract A heat pipe is an excellent heat transfer device, widely used in electronics cooling. Nanofluids have superior thermophysical properties. Researchers noticed that nanofluids are very effective working fluids as they enhanced the heat transfer characteristics of heat pipes (HPs). Mono nanofluids have their limitations regarding the applications in heat pipes. Therefore, the research community extends its work toward the application of hybrid nanofluids. In the present investigation, the authors used $\text{TiO}_2/\text{H}_2\text{O}$ and $(\text{TiO}_2 + \text{MWCNT})/\text{H}_2\text{O}$ as working fluid in the HP for a wide range of power input (50–100 watts). The authors noticed the significant enhancement in the performance of HP using hybrid nanofluids. The mechanisms/causes of enhancement in the TPHP have been identified.

Keywords Heat pipe • Thermal performance • Thermal conductivity • Thermal efficiency

Nomenclature

HP Heat Pipe
CHF Critical heat flux
HTC Heat transfer coefficient
TEHP Thermal efficiency of heat pipe
TPHP Thermal performance of heat pipe
TRHP Thermal resistance of heat pipe.

N. K. Gupta (✉)
Institute of Engineering and Technology, GLA University, Mathura 281406, India
e-mail: naveen.gupta@gla.ac.in

© The Author(s), under exclusive license to Springer Nature Singapore Pte Ltd. 2021
B. S. Sikarwar et al. (eds.), *Advances in Fluid and Thermal Engineering*,
Lecture Notes in Mechanical Engineering,
https://doi.org/10.1007/978-981-16-0159-0_45

1 Introduction

In the present era of science and technology, things are moving through various transformations. Speed and accuracy are the prime importance of various equipment. Every equipment is required to be changed in order to survive in the market. Advancement in equipment needs proper thermal management which further required the change in design and operating parameters. Forced convection enhanced the heat transfer by 10–15 times. Phase change phenomenon could further enhance the heat transfer rate of the process. Nanofluids (NFs) are the new options available for researchers working in thermal management research direction.

Choi et al. [1] proposed that NF is the new class of fluids, obtained by stirring nanoparticles in the base fluid-like water-ethanol, etc. Chandrasekar et al. [1] studied the thermophysical properties of NFs. Researchers studied the various mathematical models and produce the informative concluding remark. Authors suggest that interfacial layer contributes the enhancement in thermal conductivity (TC). Shape, size, and concentration are the other potential causes.

Murshid et al. [2] highlighted the various aspects of thermal conductivity of nanofluids (TCNFs). Authors concluded that there are various factors which decides the TCNFs. Material's type, nanoparticles shape size, concentrations, surface characteristics, and pH value are the dominating parameters, responsible for the change in thermophysical properties.

Gupta et al. [3] presented a review of the thermophysical properties of NFs. The authors concluded that NFs concentration and temperature show a significant change in TC, specific heat, and viscosity. In the last few years, many researchers [4–8] noticed the superiority of NFs. Researchers identified various reasons due to which NFs show enhanced thermophysical properties. Researchers presented various theoretical models after considering nano-level mechanics. Still, research work is going on, nanoparticles interaction with base fluid has many unfolded insights which need to be explored in future. Commercialization of NFs application in various application will take some more time. Researchers are trying to find out the solutions of various issue like high cost and stability of NFs, etc.

Heat pipe heat exchangers are very effective heat transfer elements. Heat pipes (HPs) are used to enhance the heat transfer rate in very compact devices. Due to rapid change in density of electronics components, enormous heat is produced. For safe, effective, and efficient working of electronics components, proper thermal management is required. HP were used in electronics cooling application for a long time. Researches used NFs as working fluid in HPs and noticed positive results. Gupta et al. [9] presented an experimental investigation and figure out the most suitable combinations of various input parameters like power supply, inclination angle, and volume of working fluid. The authors used NF as a working fluid in HPs and noticed a significant enhancement in thermal performance [10]. So experimental studies conclude that majority of the NFs enhanced the TPHP. Numerical investigations [11–13] also confirmed the enhancement in the TPHP. All the experimental and numerical data were in good agreement. The main cause of the

change in TPHP is the enhanced TCNF as compared to the base fluid. Researchers are trying to increase the TC of mono NF by further dispersing the highly conductive nanoparticles like CNT and graphene, etc. Hybrid NFs are the new research direction. Limited work is available on the application of hybrid NFs. Mono NF have many limitations regarding compatibility with system, stability, availability, and cost, etc. Therefore, hybrid nanofluid may be design as per the suitability and availability of NFs.

In the present experimental study, the authors made an attempt to study the effects of hybrid NF application on thermal performance of mesh wick HPs.

2 Experimentation

2.1 Preparation of Nanofluid

TiO₂/D.I. water NF is very compatible with copper HP. In literature many research articles on TiO₂/D.I water applications in HP are available. TiO₂ nanoparticles were procured from Reinste nano ventures (India). According to the information given by the supplier size of TiO₂ nanoparticles was 30–40 nm. The required quantity of nanoparticles was stirred in D.I. water with the help of an ultra sonicator. The sonication process was carried out for 8 h. NF of wt% 0.5, 1.0, 1.5, 2.0, and 2.5 has been prepared. Hybrid NF has been prepared by mixing 20% by weight functionalized MWCNT and 80% by weight TiO₂ nanoparticles, and then sonication had been done. The stability of NFs was ensured by the sedimentation technique. Samples of various concentrations were observed for 10 days. It was noticed that no sedimentation was observed.

The TC of mono and hybrid NFs were measured by a KD2 pro thermal analyzer (Decagon Devices, Inc; USA). The increase in TC for 0.5, 1.0, 1.5, 2.0 and 2.5 vol. % of TiO₂/Water NFs samples are 4.6, 5.4, 8.3, 10.3, and 12.5%, respectively. Brookfield viscometer was used to measure the viscosity of NFs. The increase in dynamic viscosity for TiO₂/Water NFs samples was 3.2, 4.9, 5.2, 5.2, and 6.5%, respectively. The dynamic viscosity of NFs decreased with the increase in temperature. The enhancement in TC and dynamic viscosity of (TiO₂ + MWCNT)/H₂O hybrid NF (1.5 vol.%) is 13.8 and 6.5%

2.2 Experimental Setup

HP experimental setup is designed and fabricated for conducting the experiments. Figure 1 shows the schematic view of the experimental setup. There are three sections of HP like evaporator, adiabatic, and condenser section. Heat is supplied with the help of an electric heater. To reduce the heat loss, the evaporator section

was covered by glass wool. K-type thermocouples were soldered an outer as well as the inner surface of HP. The temperatures were recorded by the data logger. A pressure gauge was attached at the inner side of the adiabatic section. To provide an efficient cooling at the condenser section, a water jacket is provided. The temperature of cooling water was maintained by a constant cooling bath. An orientation stand was used to provide the proper inclination angle. In the present study, all experiments were performed in a horizontal condition. A vacuum pump was used to evacuate the HP. The noncondensable gases were removed before filling the working fluid.

2.3 Uncertainty Analysis

Moffat et al. [14] described the method to evaluate the uncertainties associated with experimentation work. Uncertainty analysis is an inevitable part of the experimental study. Thermocouples, pressure gauge, and flow meter have uncertainty in measurement. The uncertainties in the measurement of heat input, heat flux, heat transfer coefficient, and thermal resistance are calculated as [15].

$$\frac{\Delta Q}{Q} = \left[\left(\frac{\Delta V}{V} \right)^2 + \left(\frac{\Delta I}{I} \right)^2 \right]^{1/2} \quad (1)$$

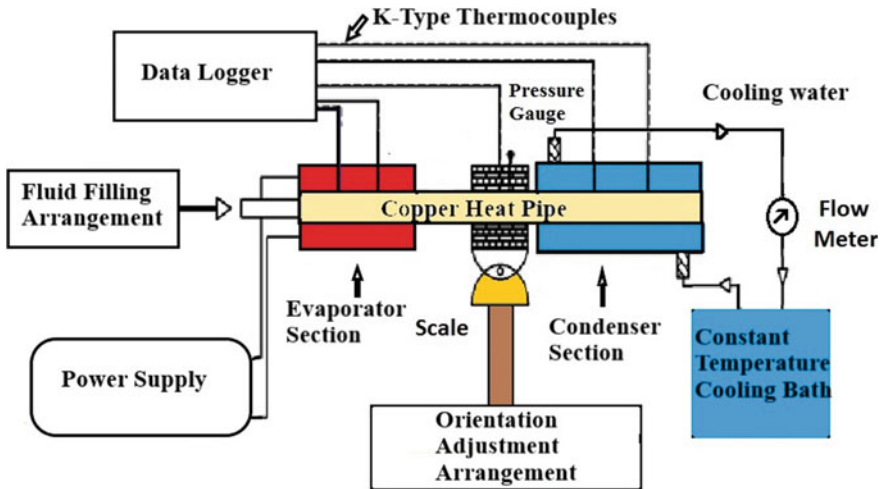


Fig. 1 Schematic view of HP experimental setup

$$\frac{\Delta h}{h} = \left[\left(\frac{\Delta q}{q} \right)^2 + \left(\frac{\Delta(\Delta T)}{\Delta T} \right)^2 \right]^{1/2} \quad (2)$$

$$\frac{\Delta R}{R} = \left[\left(\frac{\Delta Q}{Q} \right)^2 + \left(\frac{\Delta(\Delta T)}{\Delta T} \right)^2 \right]^{1/2} \quad (3)$$

The uncertainty in the heating area was 2.5%. The uncertainties in the heat loss and wall superheat were less than 4.5 and 3.8%. The maximum uncertainty in heat input, heat flux, heat transfer coefficient (HTC), and thermal resistance (TR) is 5.9, 4.1, 8.6, and 5.9%.

2.4 Data Reduction

The various performance parameters were calculated by using the following relations.

$$\text{TRHP} = (\text{Evaporator temperature} - \text{Condenser temperature}) / \text{Heat supplied} \quad (4)$$

Effective thermal conductivity (ETC)

$$K_E = \frac{(\text{Heat supplied } (Q) * \text{Effective length of HP } (L_E))}{((\text{Evaporator temperature} - \text{Condenser temperature}) * A)} \quad (5)$$

$$\text{Convective heat transfer coefficient} = \frac{\text{Heat supplied } (Q)}{((\text{Evaporator temperature} - \text{Condenser temperature}) * A)} \quad (6)$$

Performance Index (Thermal Efficiency) of HP is the rate of heat transfer diffused into cooling water to the heat intake at the evaporator section.

$$\text{Performance Index } (\eta) = \frac{mc(T_2 - T_1)}{Q} \quad (7)$$

m = Flow rate (kg/sec) of cooling water, c = Specific heat of cooling water, T_2 = cooling water exit temperature, T_1 = cooling water entry temperature, Q = Supplied heat.

2.5 Results and Discussion

The HP is evacuated before filling the working fluid. Vacuum pressure is maintained to remove the noncondensing gases and to reduce the saturation temperature of the working fluid. In the present investigation, 10–15 kPa pressure is maintained inside the HP. Working fluid is filled with the help of filling arrangement. Cooling water is allowed to flow in a water jacket. The temperature of cooling water was maintained at 15 °C. The heat was supplied at evaporator section.

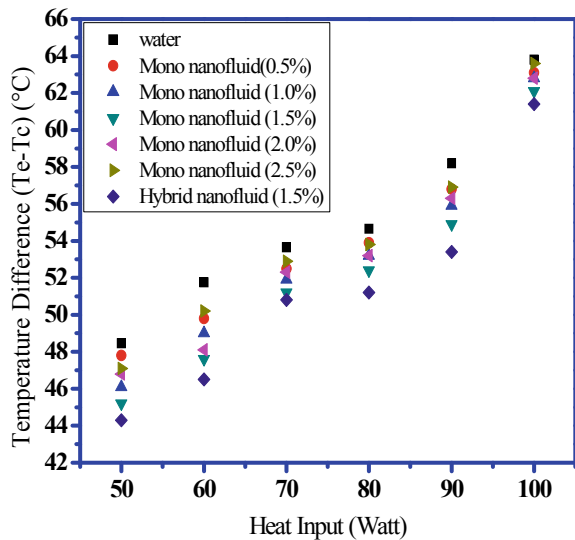
Steady-state was achieved after 30 min. Power was gradually increased in small steps of 10 watts. HP wall temperature is an important and foremost output parameter. Reduction in wall temperature shows the enhancement in TPHP.

Figure 2 shows the variation in temperature difference of the evaporator and condenser section. Figure 2 shows that wall temperature difference increases with the increase in the power supply. An increase in power supply causes more heat transfer in all three directions. Heat transfers through conduction, convection, and radiation modes increased. Heat losses through HP are also increased. Figure 2 shows that HP using D.I. water has the highest wall temperature difference. HP using hybrid NF (1.5%) shows the lowest temperature difference.

Other mono and hybrid NF show better performance as compared to D.I. water.

Figure 3 shows the variation in thermal resistance (TR) with the increase in power. Figure 3 shows that TR decreases with an increase in power. HP with D.I water shows the highest TR while 1.5% of hybrid NF shows the minimum TR. An increase in power supply enhanced the vaporization rate and pressure difference

Fig. 2 Variation in surface temperature difference with heat input



between the evaporator and condenser section. The TCNF is also increased which further increased the heat transmission rate. The suspended nanoparticles were energized and their Brownian motion was increased. A solid-liquid interface the bubble formation is the main cause of TRHP. The increased Brownian motion causes the enhanced puncture rate of bubbles. Therefore, the TRHP decreases with an increase in power. Hybrid NF shows better performance as compared to mono NF. There may be so many reasons for the difference in the performance of mono and hybrid NF. The hybrid NF has a higher TC as compared to mono NF. MWCNT nanoparticles have very high TC as compared to TiO_2 nanoparticles. In the case of hybrid NF, MWCNT were also deposited at HP and mesh surfaces. Deposited MWCNT layer enhanced the TC as compared to all other cases.

Figure 6 shows the variation in the TEHP with the increase in power. Thermal efficiency increases with an increase in power. It can be observed from Figs. 3, 4, 5 and 6 that increase in power input decreases the TR, increase the TC, increases the convective HTC, and finally increases the TEHP.

All NFs were used as working fluids. Applications of NFs show the enhancement in TEHP as compared to D.I. water. Among all mono NFs, TiO_2/H_2O NF of 1.5 vol.% shows higher thermal characteristics. $(TiO_2 + MWCNT)/H_2O$ hybrid NF shows maximum enhancement in all TPHP. NFs have superior TC as compared to D.I. water. Hybrid NFs have higher TC as compared to D.I. water and NF. The enhancement in thermophysical properties of NFs and hybrid NFs depend upon the type of material, nanoparticle shape, size, concentration, etc [16, 17].

Fig. 3 Variation in TRHP with heat input

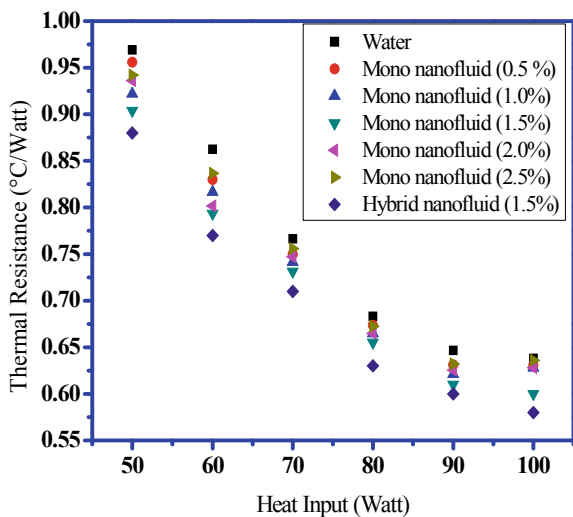


Fig. 4 Variation in effective TCHP with heat input

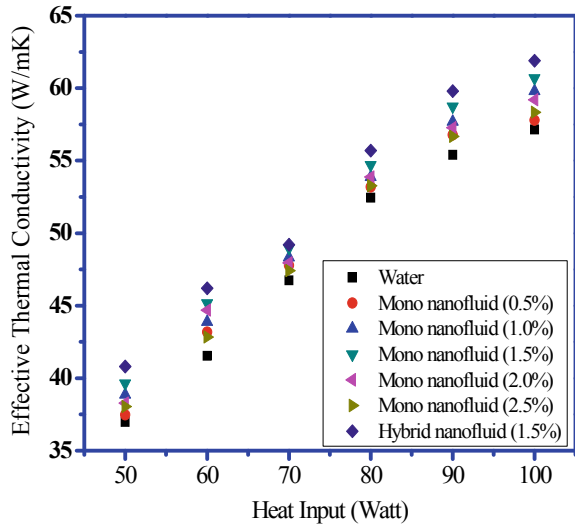
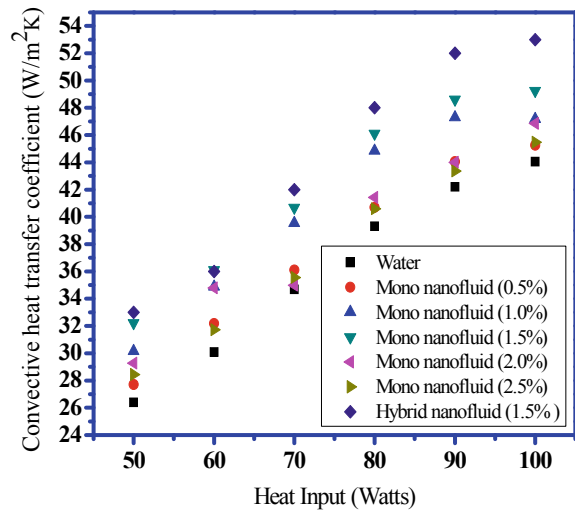


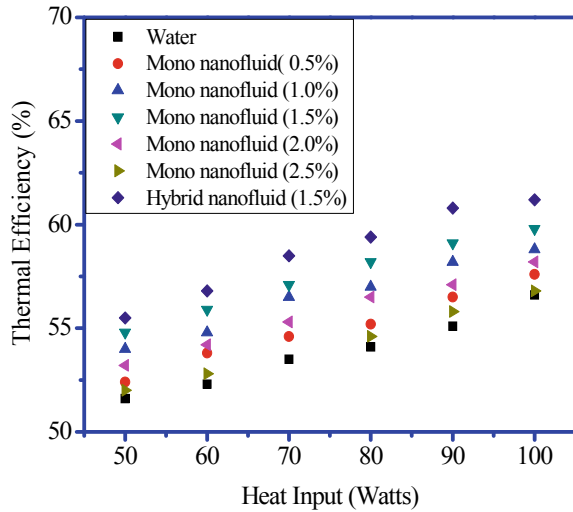
Fig. 5 Variation in convective HTC of HP with heat input



3 Conclusions

Nanofluids showed higher thermal as compared to D.I. water. Thermal performance of heat pipe using 1.5 vol.% of $\text{TiO}_2/\text{H}_2\text{O}$ nanofluid was higher as compared to other concentrations of the same nanofluid. $\text{TiO}_2/\text{H}_2\text{O}$ mono nanofluid and $(\text{TiO}_2 + \text{MWCNT})/\text{H}_2\text{O}$ hybrid nanofluid showed their potential as effective working fluids. $(\text{TiO}_2 + \text{MWCNT})/\text{H}_2\text{O}$ hybrid nanofluid showed superior thermal performance as compared to others. 1.5% $(\text{TiO}_2 + \text{MWCNT})/\text{H}_2\text{O}$ hybrid nanofluid

Fig. 6 Variation in the TEHP with heat input



showed the highest thermal performance among all the available concentrations of nanofluids. Enhanced thermal conductivity of nanofluid, the Brownian motion of nanoparticles, and wettability of liquid-solid surface increase with the temperature. Therefore, the thermal performance of heat pipe increased as the input power increased. Many other hidden causes are still to be explored.

References

1. Chandrasekar M, Suresh S, Chandra Bose A (2010) Experimental investigations and theoretical determination of thermal conductivity and viscosity of $\text{Al}_2\text{O}_3/\text{water}$ nanofluid. *Exp Therm Fluid Sci* 34:210–216. <https://doi.org/10.1016/j.expthermflusci.2009.10.022>
2. Murshed SMS, Leong KC, Yang C (2005) Enhanced thermal conductivity of TiO_2 —water based nanofluids. *Int J Therm Sci* 44:367–373. <https://doi.org/10.1016/j.ijthermalsci.2004.12.005>
3. Gupta NK, Mishra S, Tiwari AK, Ghosh SK (2019) A review of thermo physical properties of nanofluids. *Mater Today Proc* 18:968–978. <https://doi.org/10.1016/j.matpr.2019.06.534>
4. Gupta NK, Tiwari AK, Ghosh SK (2018) Heat transfer mechanisms in heat pipes using nanofluids—a review. *Exp Therm Fluid Sci*. <https://doi.org/10.1016/j.expthermflusci.2017.08.013>
5. Daungthongsuk W, Wongwises S (2007) A critical review of convective heat transfer of nanofluids, 11:797–817. <https://doi.org/10.1016/j.rser.2005.06.005>
6. Lomascolo M, Colangelo G, Milanese M, De Risi A (2015) Review of heat transfer in nano fluids: conductive, convective and radiative experimental results. *Renew Sustain Energy Rev* 43:1182–1198. <https://doi.org/10.1016/j.rser.2014.11.086>
7. Kakaç S, Pramuanjaroenkij A (2009) Review of convective heat transfer enhancement with nanofluids. *Int J Heat Mass Transf* 52:3187–3196. <https://doi.org/10.1016/j.ijheatmasstransfer.2009.02.006>

8. Murshed SMS, De Castro CAN, Lourenc MJV, Lopes MLM, Santos FJV (2011) A review of boiling and convective heat transfer with nanofluids. *Renew Sustain Energy Rev* 15:2342–2354. <https://doi.org/10.1016/j.rser.2011.02.016>
9. Gupta NK, Tiwari AK, Ghosh SK (2018) Experimental investigation of the thermal performance of mesh wick heat pipe. *Heat Transf Res* 49:1793–1811
10. Gupta NK, Tiwari AK, Ghosh SK (2018) Experimental study of thermal performance of nanofluid-filled and nanoparticles-coated mesh wick heat pipes. *J Heat Transfer* 140:1–7. <https://doi.org/10.1115/1.4040146>
11. Gupta NK, Barua A, Mishra S, Singh SK, Tiwari AK, Ghosh SK (2019) Numerical study of CeO₂/H₂O nanofluid application on thermal performance of heat pipe. *Mater Today Proc* 18:1006–1016. <https://doi.org/10.1016/j.matpr.2019.06.541>
12. Solomon AB, Ramachandran K, Asirvatham LG, Pillai BC (2014) Numerical analysis of a screen mesh wick heat pipe with Cu/water nanofluid. *Int J Heat Mass Transf* 75:523–533. <https://doi.org/10.1016/j.ijheatmasstransfer.2014.04.007>
13. Humnic G, Humnic A (2013) Numerical study on heat transfer characteristics of thermosyphon heat pipes using nanofluids. *Energy Convers Manag* 76:393–399. <https://doi.org/10.1016/j.enconman.2013.07.026>
14. Moffat RJ (1988) Describing the uncertainties in experimental results. *Exp Therm Fluid Sci* 1:3–17. [https://doi.org/10.1016/0894-1777\(88\)90043-X](https://doi.org/10.1016/0894-1777(88)90043-X)
15. Wang P-Y, Chen X-J, Liu Z-H, Liu Y-P (2012) Application of nanofluid in an inclined mesh wick heat pipes. *Thermochim Acta* 539:100–108. <https://doi.org/10.1016/j.tca.2012.04.011>
16. Gupta NK, Tiwari AK, Verma SK, Kr P, Rathore S, Ghosh SK (2019) A comparative study of thermal performance of a heat pipe using water and nanofluid, and a nanoparticle coated wick heat pipe using water, 50:1767–1779
17. Gupta NK, Verma SK, Rathore PKS, Sharma A (2020) Effects of CuO/H₂O nanofluid application on thermal performance of mesh wick heat pipe. *Heat Transfer Res* 51(9):837–850

Energy Saving Technique for Separation of a Fuel Additive



Asma Iqbal and Syed Akhlaq Ahmad

Abstract The identification of a suitable diesel fuel additive is highly crucial for both the performance of the system as well as its efficiency. This case study deals with the exploration of an efficient fuel additive in diesel engines, with reduced emissions and high energy efficiency. Methylal exhibits unique characteristics and is regarded as a favorable fuel additive for reciprocating combustion engines. But its existence as an azeotropic mixture with methanol is the main bottleneck which inhibits to utilize its potential as a feasible fuel additive in diesel engines. The present study is focussed on an economic separation technique of extractive distillation which has a potential to separate methanol from methylal. This separation technique using water as an entrainer has been explored first time in open literature. In addition to extractive distillation technique, a comparative analysis of different separation techniques has also been done. This analysis has been carried out using a commercial simulation software package of Aspen Plus V8.8. The results show that water is an effective entrainer for the separation of methylal-methanol azeotropic mixture as it has resulted in 69.41% savings in comparison to extractive distillation using DMF as an entrainer, 65.33% savings in comparison to divided wall column, and 52.72% savings in comparison to pressure swing distillation technique.

Keywords Diesel fuel • Additive • Aspen plus • Methylal • Methanol

Nomenclature

DMF	Dimethyl Formamide
EG	Ethylene Glycol
IE	Ionic entrainers
P	Pressure

A. Iqbal (✉) · S. A. Ahmad
Department of Chemical Engineering, Aligarh Muslim University, Aligarh, India
e-mail: asmajawahira@gmail.com

S. A. Ahmad
e-mail: sa.ahmad.ke@amu.ac.in

PSD	Pressure Swing Distillation
DWC	Divided wall Column
TAC	Total Annual Cost
Di	Internal diameter
QR	Reboiler duty
RR	Reflux Ratio
METHY	Methylal
METH	Methanol

1 Introduction

High emissions from engines are one of the major concerns which the country is facing nowadays. To overcome this global issue, either there should be changes in engine design or researchers should explore fuel additives which can lower the emissions. But changing the engine design is a challenging task and requires expert engineering rationale. The suitable option is to search alternative fuels or fuel additives which can reduce emissions. Methylal is found to exhibit unique fuel characteristics with low auto-ignition temperature, burns soot free, low toxicity, and, is completely miscible in middle distillate fuels. Besides, its cetane number is very high which is compatible with diesel engines, therefore, can be easily used as a diesel fuel additive. The blends of methylal and diesel not only reduce the smoke in diesel engines but also enhance the combustion efficiencies and lubrication properties of engine [1–3]. The major drawback is that methylal forms a minimum boiling azeotrope with methanol which reduces its energy efficiency of being used as a fuel additive. The only solution to tackle this problem is to separate the two components of this azeotropic mixture so that methylal can be effectively used in diesel engines. Hence, the objective now is to explore a suitable separation technique which can separate the azeotropic mixture of methylal and methanol. Looking at the separation techniques, many techniques have been invented and utilized in past starting from affinity separations, to membrane separations, to adsorption, etc., where we have seen that distillation has achieved maximum technical as well as utilization maturity [4].

Distillation is a separation technique which is widely used in chemical and petrochemical industries to separate impurities, and other by-products from various processes. It is a highly competitive and challenging process which is currently on high demand in industries. It has been observed that there is a tremendous rise in the applications of distillation-based separation techniques because of the advantages of distillation processes. The separation of methylal-methanol has also been reported in literature using various separation techniques. For example, the separation using membrane separation techniques like pervaporation, membrane distillation, etc. has been investigated [5] but due to the technical disadvantage of membranes like poor permeating flows, membrane wear and tear issues, etc., some other separation techniques have been investigated. A technique of reactive separation has been

explored by a group of researchers for the separation of this azeotropic mixture but the results show that the purity of methylal is less than 99% [6]. Pressure swing distillation has been also reported for methylal-methanol azeotropic mixture but the technique involves complexities in maintaining the high pressure in the column and also leads to high capital cost [7]. Another method of divided wall column (DWC) has been reported in literature which utilizes only single column for the separation purposes. A technical disadvantage associated with the DWC is the internal interactions involved within it. Moreover, the control of DWC is highly complex and requires high maintenance online composition controllers to maintain the product purity [8].

Extractive distillation is known to be a simple and widely used separation process used for the separation of azeotropic mixtures [9]. Because of the numerous advantages of extractive distillation process like, less complexity involved, low maintenance cost, no internal interactions, etc., the mixture of methylal-methanol can be separated using extractive distillation process. This process uses an external agent, known as solvent for the separation of complex azeotropic mixtures. The solvent alters the relative volatility of the mixture to be separated which helps in breaking the azeotrope formed between the different components of the mixture. This process has huge economic benefits in comparison to other separation techniques (azeotropic distillation, pressure swing distillation, divided wall column, membrane separation, etc.) provided an appropriate entrainer is selected. The selection of entrainer plays a crucial role in determining the feasibility and economy of the entire process. For the separation of methylal-methanol azeotropic mixtures, various entrainers have been recommended. Many researchers have evaluated Dimethyl sulfoxide (DMSO), Dimethyl formamide (DMF), Ethylene glycol (EG), and ionic entrainers [10]. But all of these entrainers have negative impact on environment. To overcome the environmental impact of entrainers, a new entrainer with zero environmental impact has been explored in this study. Water is used as an entrainer for separating methylal-methanol which has not been previously reported in open literature.

This work is primarily focused on steady-state design of extractive distillation process for separating methylal-methanol using water as an entrainer. The distillation columns are simulated using simulation software of Aspen Plus V8.8. The steady-state design is followed by the economic analysis of this technique with the existing techniques already published in literature. The comparison is based on the different operating and design parameters to evaluate total annual cost (TAC) of all schemes of separation for methylal-methanol.

2 Steady-State Design of Extractive Distillation Process

The steady-state process design of extractive distillation is initiated by selecting an appropriate thermodynamic model. Here, in this process example, the thermodynamic property package used is NRTL [11]. The binary interaction parameters for the model are obtained from Aspen Plus. The model selection is done on the basis

of comparing the available experimental data [12] with the simulated data generated from Aspen Plus. NRTL model is used for liquid phase calculations and SRK calculates vapor phase fugacity coefficients that predict the vapor-liquid equilibrium (VLE) correctly.

The minimum boiling azeotrope of methylal and methanol at 94.06 wt% methylal at atmospheric pressure has been separated using extractive distillation scheme with water as an entrainer. A two-column distillation scheme operating at atmospheric pressures have been used for the separation of methylal-methanol. The feed mixture consists of an equimolar solution of methylal and methanol at a flow rate of 100 kmol/h at atmospheric pressure. The number of stages in both distillation columns has been taken to be equal to 20. The number of stages in two columns is set by performing the DSTWU analysis in Aspen Plus which provides the minimum number of trays. The number of trays calculated from DSTWU analysis is multiplied by a factor of 2 or 3 as per the rule of thumb to get the exact number of trays to be taken in a RadFrac column [13]. The stages are numbered from top to bottom of the column using the Aspen notation of considering condenser being stage 1 and reboiler being stage 20 [14]. Both columns are operated at 1 atm pressure with a column pressure drop of 0.2 atm. After fixing the number of trays in both columns, the feed stage location and entrainer stage location are evaluated by using the sensitivity analysis tool of Aspen Plus which estimates the feed stage tray at stage 19 and entrainer stage location at stage 12. The operating parameters in both columns are distillate rate and Reflux ratio (RR). The design spec/vary tool of Aspen Plus is used to fix the product purities of both products. The steady-state design flow sheet schematic is shown in Fig. 1. From Fig. 1, we observe that pure methylal is obtained from the top of column 1 while the bottom of

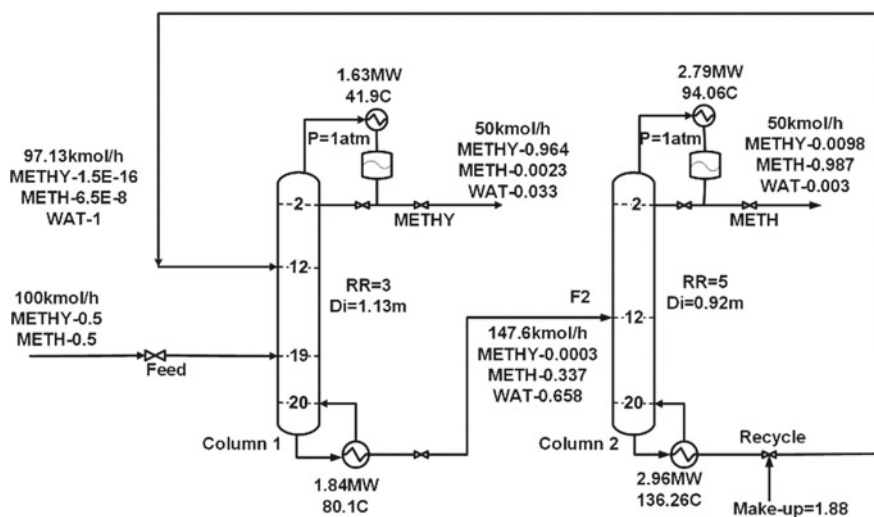


Fig. 1 Steady-state design flowsheet of extractive distillation process

column 1 which is an azeotropic mixture of methylal and methanol is sent to column 2 at stage no 12. From the top of column 2, pure methanol is recovered and the bottom of column 2 is recycled back to column 1 at stage no. 12.

3 Results and Discussions

A thorough comparison of extractive distillation method with the alternative separation methods reported in open literature has been made. Table 1 provides the details about the comparison drawn between extractive distillation technique using water as an entrainer (present work) and extractive distillation using DMF, EG, ionic entrainers, divided wall column (DWC), and pressure swing distillation (PSD) [7, 8, 11, 15, 16]. The cost correlations used in this study are same as that used in reported literature [17] to maintain consistency. From the table of comparison (Table 1), we have observed that the entrainers reported in literature have resulted in very high total annual costs (TAC) besides causing environmental concerns. The number of stages used in column 1 and column 2 are also higher than those used in the present work. The purity of methylal in our study is slightly less than the reported one but the recovery is 100% for both products. The results reported in published work has less methanol purity in comparison to the purity attained by using water as an entrainer.

From the results tabulated below, it can be observed that the proposed design of extractive distillation technique has successfully as well as economically separated methylal from methanol. These results also refer to the fact that the suggested scheme of separation has proved to be environment friendly as water has been used as an entrainer in comparison to other techniques reported in literature. This is because of the fact that the water has been found to be having a very high selectivity. Further, water is relatively an inexpensive solvent with low toxicity and low thermal and chemical degradation characteristics.

4 Conclusions


A comparison between proposed technique of extractive distillation using water as an entrainer and the existing alternative techniques of separation reported in literature (extractive distillation using DMF, EG, ionic entrainers, and PSD scheme) has been addressed in this case study. The proposed technique has economic benefits over all other reported schemes in literature. It has been assessed that the current scheme results in 69.41% savings in TAC in comparison to extractive distillation using DMF as an entrainer, 65.33% savings in TAC in comparison to DWC, 52.72% using PSD scheme. The proposed scheme is thought to be environmental friendly also as water is used as an entrainer.

References

1. Process for purification of methylal (1995)
2. Li S (2005) Study on the preparation of methylal by slurry catalytic distillation process
3. Process for producing methylal (1999)
4. Keller GE (1987) Separations: new directions for an old field
5. Carretier E, Moulin P, Beaujean M, Charbit F (2003) Purification and dehydration of methylal by pervaporation. *J Memb Sci* 217:159–171. [https://doi.org/10.1016/S0376-7388\(03\)00125-X](https://doi.org/10.1016/S0376-7388(03)00125-X)
6. Liu H, Gao H, Ma Y, Gao Z, Eli W (2012) Synthesis of high-purity methylal via extractive catalytic distillation. *Chem Eng Technol* 35:841–846. <https://doi.org/10.1002/ceat.201100446>
7. Yu B, Wang Q, Xu C (2011) Design and control of distillation system for methylal/methanol separation. Part 2 : pressure swing distillation with full heat integration, 1293–1310
8. Xia M, Yu B, Wang Q, Jiao H, Xu C (2012) Design and control of extractive dividing-wall column for separating methylal-methanol mixture. *Ind Eng Chem Res* 51:16016–16033. <https://doi.org/10.1021/ie3015395>
9. Seader JD, Henley EJ, Roper DK (2011) Separation process principles. <https://doi.org/10.5860/CHOICE.36-5112>
10. Process for the recovery of pure methylal from methanol-methylal mixtures (1982)
11. Wang Q, Yu B, Xu C (2012) Design and control of distillation system for methylal/methanol separation. Part 1 : extractive distillation using DMF as an entrainer, 1281–1292
12. Liley PE, Buck E, Ch MSE (1999) Physical and chemical data*. *Perry's Chem Eng Handb*, 2–86
13. Fisher WR, Doherty MF, Douglas JM (1985) Effect of overdesign on the operability of distillation columns. *Ind Eng Chem Process Des Dev* 24:593–598. <https://doi.org/10.1021/i200030a013>
14. Li R, Ye Q, Suo X, Dai X, Yu H (2016) Heat-integrated pressure-swing distillation process for separation of a maximum-boiling azeotrope ethylenediamine/water. *Chem Eng Res Des* 105:1–15. <https://doi.org/10.1016/j.cherd.2015.10.038>
15. Dong Y, Dai C, Lei Z (2018) Extractive distillation of methylal/methanol mixture using ethylene glycol as entrainer. *Fluid Phase Equilib* 462:172–180. <https://doi.org/10.1016/j.fluid.2018.01.038>
16. Dong Y, Dai C, Lei Z (2018) Extractive distillation of methylal/methanol mixture using the mixture of dimethylformamide (DMF) and ionic liquid as entrainers. *Fuel* 216:503–512. <https://doi.org/10.1016/j.fuel.2017.12.043>
17. Douglas JM (1988) Conceptual design of chemical processes. McGraw-Hill. <https://doi.org/10.1002/jctb.280460308>

Opportunities and Issues with Clean Renewable Energy Development in India: A Review



Prakarti Sharma, Anbesh Jamwal , Nidhi Sharma, and Rajeev Agrawal

Abstract India's energy requirement is growing up with its economic growth. The increase in energy consumption is a sign of increasing prosperity of a nation. The large requirement of energy is fulfilled by non-renewable source of energy, which is a fast depleting source and causes heavy pollution in the environment. With the rising concern for the environment because of the change in climate conditions have forced developing nations to opt for alternate source of energy other than non-renewable sources. The best alternate is provided by the clean and renewable sources of energy such as solar, wind, biomass, small hydropower and waste to wealth. Because of the favourable environment condition, India has the great potential for clean and renewable sources of energy. India's geographical condition gives it a leverage in the generation of wind, solar and biomass energy, and with the increasing urbanisation and industrialization, rise in solid waste gives it a great potential for the generation of energy from waste. This paper discusses over the different sources of clean and renewable energy available in India and the potential of these sources to fulfil the energy need of the nation in future for a sustainable economic growth. The different policies and programmes that are adopted by the government for the promotion of clean and renewable source of energy and the various obstacles that are faced for the further growth of this sector.

P. Sharma · N. Sharma
Department of Humanities and Social Sciences, Malaviya National Institute
of Technology, J.L.N. Marg, Jaipur, Rajasthan 302017, India
e-mail: 2019rhs9112@mnit.ac.in

N. Sharma
e-mail: nidhis.hum@mnit.ac.in

A. Jamwal (✉) · R. Agrawal
Department of Mechanical Engineering, Malaviya National Institute of Technology,
J.L.N. Marg, Jaipur, Rajasthan 302017, India
e-mail: anveshjamwal73@gmail.com

R. Agrawal
e-mail: rajeevag1@gmail.com

Keywords Renewable energy · Solar energy · Biomass energy · Wind energy · Waste to energy · India

1 Introduction

Recent developmental activities have caused the risk of global warming resulting into the climate change of the planet. The rise of greenhouse effect has affected the temperature of earth leading to extreme weather conditions. There is an average increase in the temperature of 0.9 °C over the last century. As per an estimate, around 65% of total greenhouse gas emission comes from energy production contributing to climate change activities [1].

There are renewable and non-renewable sources of energy. Renewables are the ones, which are replenished and will never deplete in the environment, and non-renewables are the ones, which are non-replenished and exist in limited capacity. Fossil fuels are the most prevalent and non-renewable sources of energy, which include oil, coal and natural gases [2]. These resources are depleting very fast, and we have the responsibility to protect them for the future developmental activities [3]. These sources of energy emanate greenhouse gases, e.g. methane, carbon dioxide, etc., into the environment. As per an estimate, around 65% of total greenhouse gas emission comes from energy production contributing to climate change activities. The renewable sources which include solar, wind, hydro, biomass and waste are rather new and clean sources of energy. The conventional sources of energy like oil and coal are limited in supply and are one of the reasons for global warming which is causing many adverse effects on the planet. The rising demand for energy consumption can be met with the non-renewable sources of energy. These resources preserve the limited non-renewable sources of energy, are relatively environmental friendly and help in the reduction of greenhouse gas emission. The rise in the use of renewable sources from 13% in 2014 to 20% in 2018 shows great potential in this sector though non-renewable sources of energy continue to dominate by fulfilling the 80% of energy requirements [4].

In 2015, all member states of United Nations have adopted sustainable development goals (SDG's) where clean and affordable energy has been taken as one of the goals out of 17 goals. These goals are scheduled to be achieved by 2030. The decade of 2014–2024 has been declared as the decade of sustainable energy for all by the United Nations. Various international level organizations such as International Solar Energy Society, Renewable Energy and Energy Efficiency Partnership (REEP), World Wind Energy Association (WWEA), International Renewable Energy Alliance (IREA) are working towards the aim of producing renewable and affordable energy [5]. Many public–private partnerships are also taking initiatives in this direction providing greater investment opportunities in the renewable energy field [6].

India has witnessed a rapid growth in its energy demand in the last 25 years because of growing population and rising developmental activities. The energy

production has increased by 5.6%, whereas consumption has increased by 7.3% in the last decade from 2008 to 2018. The energy consumption in India is largest in industrial sector with 60% share followed by transport sector, services sector and agriculture sector. India’s growth in energy consumption is expected to be the highest among major economies. Non-renewable resources fulfil a largest share of energy demand with 58% by coal, 27% by oil and around 7% by natural gas. The renewable sources account for less than 10% of energy supply. Even with the large increase in energy production and consumption, 300 million people have no access to electricity, and around 750 million are not having access to clean cooking fuels. However, India aims to achieve its target of removing energy poverty in a sustainable manner [7].

There is a high potential for renewable energy generation in India from wind, solar, hydro and biomass sources. Solar energy with 68% accounts the highest potential for renewable energy followed by 28% of wind energy and rest by other sources. The potential capacity for renewable resources on account of solar power is highest in Rajasthan followed by Gujarat and Maharashtra. Figure 1 shows the installed generating capacity of electricity by renewable sources of energy from 2009 to 2018.

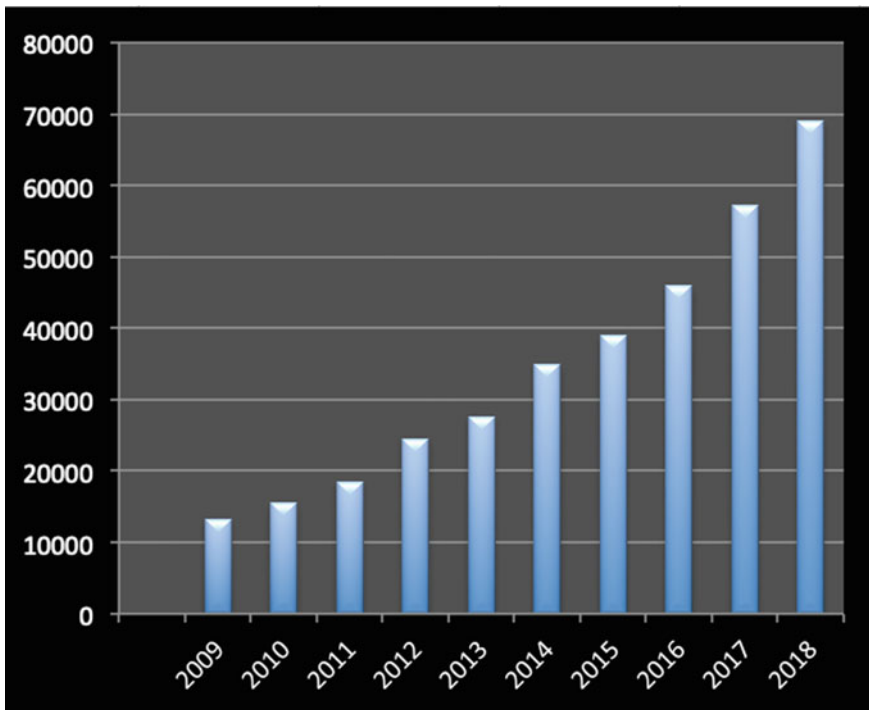


Fig. 1 Installed generating capacity of electricity by renewable sources of energy in utilities (in MW)

Ministry of New and Renewable Energy is the nodal ministry for all the matters related to the new and renewable energy. In December 2015, United Nations Framework Convention on Climate Change (UNFCCC) Conference of Parties (COP21) in Paris, India, announced its Intended Nationally Determined Contribution (INDC). Under its INDC, India announced its plan to set up the 175 GW of renewable energy capacity by 2022. Out of 175 GW, 100 GW from solar capacity, 60 GW from wind, 10 GW from biomass and 5 GW from small hydro-power have been planned. India has also initiated International Solar Alliance (ISA) with 121 countries, which are rich in sunlight also known as sunshine counties [8]. The sole aim of this alliance is to efficiently exploit solar energy and reduce the use of fossil fuels in energy generation.

Though India has set up ambitious targets in terms of renewable energy, achieving of these targets seem to be very difficult. India has targeted to set up 100 GW of solar capacity by 2022, but so far, it has been able to install just 29 GW of capacity by 2018. Domestic and foreign investors are shying away from taking investment in this sector because of many policy hurdles. These policy hurdles are tariff issues, newly introduced GST system, problem in land acquisition, failure of interstate transmission system bids and liquidity crunch into the system. Moreover, abrupt policy changes by the state governments with the change in the governments shake confidence of the investors, making this sector less lucrative for investment. With the continuation of current trend, the goal of India's renewable energy targets of installing 40% of installed capacity by 2030 seems difficult to achieve. India being the third largest emitter of greenhouse gas after US and china needs to focus on its renewable energy generation to avoid the climate change. These ambitious targets can be materialized with the commitment to overcome the various challenges faced by the sector [9]. The present study highlights the various sources of renewable and clean energy in India such as wind, solar, biomass, small hydro-power and waste to wealth. Present status, related policy design, challenges faced by the renewable energy sector in India and the future potential of these resources have been discussed.

2 Renewable Energy in India

India is one of the fastest growing economies in the world with its ambitious target to become \$5 trillion economy by 2025. India is also the third largest emitter of carbon dioxide in the world. Although India has plans to reduce its greenhouse gas emission by 30–35% by 2030 from its 2005 level of emission. To achieve the targets of sustainability, India has started focusing over its renewable sources of energy and plans to achieve 40% of its energy requirement from renewable sources of energy by 2030 [10]. The renewable sources of energy in India are solar, wind, biomass and hydropower plans and waste to wealth. The associated benefits with the renewable energy sources are as follows: (1) reduction in pollution as electricity generation from the burning of fossil fuel causes greenhouse gas emission

(2) reduction in import bills as India is heavily dependent on the import of fossil fuels because of unfavourable geography (3) a reduction in the uncertainty of electricity prices. India has the high potential for renewable sources of energy. The total potential of renewable energy in India is around 1000 GW. The potential for solar energy is around 68%, wind is 28%, and rest 4% is for small hydro plants, biomass and from waste to energy sources. The total installed capacity of renewable energy in India is 83 GW by September 2019, which is 23% of total installed capacity. And India plans to fulfil 40% of its energy requirement from the renewable sources by 2030 [11].

India has shown a clean energy transition in the last five years and has made many sustainable decisions where environmental, social and economical factors are taken into consideration [12]. It has become an attractive market for the renewable energy. More than \$40US has been invested in India in the renewable energy sector since 2014. Interstate distribution of wind power has been started from August 2018. Solar sector has received a total investment of around \$9US billion in the financial year of 2018. There are various initiatives taken by the government of India to promote green energy. The government has drafted a hydropower policy for 2018–2028. Custom and excise duty benefits have been provided to the solar rooftop sector. Indian railway is planning to reduce its emission by 34% by 2030. India has set out an ambitious target to produce 175 GW of green energy by 2022. And recently in New York summit, prime minister of India has upgraded this target to 430 GW, which is more than double of the previously set target. After four years of rapid growth, India is seeing a slowdown in its renewable energy sector. Though the economy is seeing a slowdown in every sector, but in renewable energy sector, the reasons are very different. The policy sluggishness and delay in payments by the power distribution companies have lowered down the pace of investment in the sector so is the growth of this sector [13]. The allocated capacity in this sector in 2019 was 19,775 MW, but the commissioned capacity was just 6882 MW. Total number of projects that were delayed in 2019 are of the capacity of 19.6 GW that have either been cancelled or unsubscribed or undersubscribed showing the sluggishness in this sector.

2.1 Solar Energy in India

There are two routes for the conversion of solar radiation into heat and electricity, one is the solar thermal and solar photovoltaic. In solar thermal power generation system, sunlight is collected and concentrated to produce the heat for the generation of electricity. The reflectors in the power system capture the sunlight onto a receiver. Further steam is produced in the receiver with the help of heat transfer fluid and then in a turbine that steam is converted into mechanical energy. Under solar photovoltaic system, solar cells are used for the conversion of energy into a flow of electrons by the photovoltaic effect. Solar cells produce direct electricity from the sunlight [14].

India's landmass falls in the 8 and 37.6 degrees north latitude in the tropical region blessing it with the abundant of sunshine. Under the national solar mission started in 2010, India had set the target of producing 20 GW of solar energy by 2022, which was revised by the present government to 100 GW. Out of this, 40 GW comprise rooftop projects, and 60 GW is for large- and medium-scale grid power plants. Investment required for the 100 GW of solar energy would be Rs. 600,000 cr. To promote the growth of this sector, government is also providing a capital subsidy of Rs. 15,000 cr. This subsidy will be given for the rooftop projects in various cities and towns of India, whereas viability gap funding projects will be provided by the solar energy corporation of India, which is a public sector unit for solar energy. Government has also launched various programs under its national solar mission such as solar park scheme, Pradhan Mantri—Kisan Urja Suraksha Evam Utthaan Mahabhiyaan (KUSUM), off grid solar PV scheme, etc. As a result of these initiatives, 42 solar parks with the generation capacity of around 23,500 MW have been approved in 17 states up to March 2019. The largest solar park in the world is under installation in Pavagada taluk of Tumkur District of Karnataka. According to central electricity authority, the rise in solar capacity, which is around 12 times, is the highest in the last 5 years, has reached to 31 GW. Though there are some dark trends in the growth story of this sector, which are likely to be the hurdles for the achievement of ambitious target of 100 GW of solar energy by 2022. With the continuation of the current scenario, the likely capacity for solar energy seems to be the 58 GW by 2022 [15]. The outstanding dues of distribution companies making them to fail in their payments, cancellation of the bids by the central and state agencies and delayed compensation for goods and service tax on imported cells are setting a bad precedent for industry growth [16].

2.2 Wind Energy in India

Wind turbines having propellers are used to capture kinetic energy in the wind to generate electricity out of wind. When wind blows, it moves the blades of turbines, which captures the kinetic energy. For the distribution of wind energy, transformers are used for the transfer of electricity along the long routes. National Institute of Wind Energy was set in 1998 in Chennai as an autonomous institute under the auspices of Ministry of New and Renewable Energy for the research and development for the utilization of wind energy.

India has the great potential in the wind energy sector. India's wind power potential has been estimated at around 102,780 MW, and the potential states are Rajasthan, Gujarat, Karnataka, Tamil Nadu and Maharashtra. India has plans to achieve the 60 GW of wind energy by 2022 out of 175 GW of renewable energy targets [17]. It is the fourth largest wind market and also having the fourth largest installed capacity in the world. Wind energy is having the largest share of installed capacity out of total capacity of renewable energy. The output of wind energy depends on wind speed, its density among many factors. NIWE has set up 850

monitoring stations in different states after drawing wind energy map at different heights. Recently, government is taking various initiatives for the promotion of wind energy by introducing various programmers. A National Wind and Solar Hybrid Policy was introduced in 2016 by the ministry under which a financial aid of Rs. 100,000 per KW will be given to the small wind turbine and solar panels for their installation [18]. A wind bidding scheme where 1 GW of wind projects connected with central transmission unit was to be set up by the government. Repowering of wind projects where the Indian Renewable Energy Development Agency Ltd. will provide the financial support for the repowering of wind projects. For the utilization of offshore wind energy, NIWE has been declared as the nodal agency for carrying out the assessment in the coastal areas. Recently, the government has removed the interstate transmission charges on wind energy [19].

There are many hurdles in the sustained growth of wind energy in India. Some of the hurdles are lack of refined indigenous technology in wind turbines, environmental problems such as noise pollution and risk to the life of birds passing through the wind parks. Also, acquiring of land for wind farm is also a major problem in India where people are emotionally linked to their land. Further, the frequent policy changes by the state governments dissuade the investors to take investment in this sector [20].

2.3 Biomass Energy in India

Biomass energy is produced out of plant and animal waste. All the organic material comes under the ambit of biomass. There are two ways to produce energy from biomass, one is from directly burning of biomass and use of steam turbines to produce electricity. Another way is through the gasification where a synthesis gas ($\text{CO} + \text{H}_2$) and CH_4 is being produced in a digestion tank, which is then used for electricity generation. The generation of electricity by biomass is one of the clean and renewable source of energy. India given its geographical position in a tropical region receives good amount of rain and sunshine and a large agriculture area with residue and provides conducive environment for the biomass energy. Biomass power projects have the twin benefits attached to it, one is that it helps to reduce greenhouse gas, and another one is that it helps to solve the waste management problem of India. More than 30% of India's primary energy comes from the biomass. The current share of biomass in total renewable energy is around 12.5% [21]. The energy potential from biomass is around 19 GW in India. Though India has set the target to achieve 10 GW of its renewable energy from biomass. States like Punjab, Maharashtra, Uttar Pradesh and Bihar are having the great potential for biomass energy. Although India uses just 30–32 million tons of its biomass for electricity generation [22].

Even after being a reliable source of energy, the generation of electricity from biomass faces many challenges. Some of the major challenges faced by this are lack of a proper supply chain of biomass as agriculture residue is not available throughout the year, lack of information among the masses, absence of an organized market for biomass, lack of infrastructure such as transportation and storage and lack of investment in this sector.

Government is providing Central Financial Assistance to the biomass power projects through a competitive and transparent process based on the potential of the project. Indian Renewable Energy Development Agency is providing loans for setting up of biomass power projects. Apart from that, various tax benefits have also been provided to the biomass plants [23].

2.4 Small Hydropower

Energy generation from falling water by converting the kinetic energy into mechanical energy is called hydropower. India is the seventh largest producer of hydropower in the world. Large hydropower plants with the capacity of 25 MW and above come under the ambit of ministry of power, while power plants with less than 25 MW capacity come under the ambit of Ministry of New and Renewable Energy [24]. Small hydropower projects are most cost intensive and environment friendly. India is having the potential of 20 GW of power generation from small hydropower plants. Much of the potential lies in the Himalayan states because of the availability of river base. MNRE has recognized 6473 MW potential sites for the small hydro projects and has created a database of this. Central financial assistance of MNRE provides financial assistance for the setting of new small hydro plants, for renovation of existence plants in government sector and for the research and development in this sector [25, 26].

2.5 Waste to Energy

Generation of electricity from non-biodegradable material through incineration is called energy from waste material. With the increase in urbanization and industrialization, there is a rise in the solid waste. With the increase in consumption and urbanization, the potential for waste to energy has reached to around 5400 MW. With the increase in potentiality, around 91 plants have been set up so far for power generation. MNRE provides financial support in the form of interest subsidy and various custom duty concessions for the promotion of waste to energy projects. Even after providing incentives, the cost of setting up waste to energy plant and electricity generation is relatively higher making it a non-feasible option [27]. Furthermore, there are also air emissions of some toxic gases during incineration process of solid waste causing health problems [28].

3 Future Potential

There is a tremendous growth in the area of renewable energy in the last five years. India has the huge potential in this sector. The estimated potential from the renewable sources of energy is expected to be 890 GW, out of this 890 GW, solar accounts 730 GW, wind—105 GW, bio-energy—30 GW and small hydro—25 GW. Wind power accounts the largest share of installed capacity, and solar power is having the highest potential in this sector [29]. The other sources of energy such as biomass, small hydro and waste to wealth are having a small share but a significant contribution for this sector's growth [30]. The government of India is playing a proactive role for the development of renewable energy by providing financial aid through interest subsidy, viability gap funding and easier loans for installing plants and favouring foreign direct investment by allowing 100% FDI through automatic route in the sector. Though there are many hurdles in this sector such as lack of infrastructure, research and development, and a disparate policy design. If these challenges are focused upon, it can help for a higher economic growth and a better standard of living for the energy deprived population. By focusing over its renewable energy, potential India can reduce its dependence on fossil fuel and can fulfil its commitment to reduce the greenhouse gas emission under the Paris agreement. Renewable energy has the potential to solve the job crisis of India by providing employment opportunities to the unemployed youth and can help to achieve the ambitious target of 50% renewable energy by 2040. To achieve this, there is an urgent need for India to tap its untapped resources of renewable energy for achieving its target. Further, this study can be extended by finding challenges to renewable energy in different industries sectors of India and assessment of their challenges with MCDM techniques such as AHP, VIKOR, ISM, TISM, TOPSIS method [31–35].

4 Conclusion

India is one of the fastest growing economies in the world with rising demand for energy consumption. Energy consumption of a nation is associated with its human development and well-being of the people. India fulfils 80% of its energy needs from fossil fuels, a non-renewable source of energy, which is a fast depleting and polluting source of energy. Energy generation from fossil fuels pollutes the environment by releasing many greenhouse gases. Rising temperature of the earth because of greenhouse gas effect has changed the climatic conditions on planet affecting the life on planet adversely. India depends heavily on the import of fossil fuels because of non-favourable natural conditions. Renewable source of energy is the only option, which can help to achieve its goal of clean energy to all. It can help to reduce the environment pollution for a sustainable growth, can provide energy security to the nation, save money and has the potential to provide employment and

job opportunities to the unemployed youth of the nation. There is an urgent need to focus over the renewable source of energy by a well-organized policy design, favourable infrastructure, easy taxation policy, research and innovation and public awareness for the promotion of renewable source of energy. This can help to achieve the economic growth without compromising environmental integrity.

References

1. Sohag MAZ, Kumari P, Agrawal R, Gupta S, Jamwal A (2020) Renewable energy in Bangladesh: current status and future potentials. In: Proceedings of international conference in mechanical and energy technology. Springer, Singapore, pp 353–363
2. Kumar A, Kumar K, Kaushik N, Sharma S, Mishra S (2010) Renewable energy in India: current status and future potentials. *Renew Sustain Energy Rev* 14(8):2434–2442
3. Boral S, Howard I, Chaturvedi SK, McKee K, Naikan VNA (2020) A novel hybrid multi-criteria group decision making approach for failure mode and effect analysis: an essential requirement for sustainable manufacturing. *Sustain Prod Consum* 21:14–32
4. Khare V, Nema S, Baredar P (2013) Status of solar wind renewable energy in India. *Renew Sustain Energy Rev* 27:1–10
5. Sen R, Bhattacharyya SC (2014) Off-grid electricity generation with renewable energy technologies in India: an application of HOMER. *Renew Energy* 62:388–398
6. Pillai IR, Banerjee R (2009) Renewable energy in India: status and potential. *Energy* 34(8):970–980
7. Luthra S, Kumar S, Garg D, Haleem A (2015) Barriers to renewable/sustainable energy technologies adoption: Indian perspective. *Renew Sustain Energy Rev* 41:762–776
8. Bhattacharyya SC, Jana C (2009) Renewable energy in India: historical developments and prospects. *Energy* 34(8):981–991
9. Puhan S, Vedaraman N, Rambrahamam BV, Nagarajan G (2005) Mahua (*Madhuca indica*) seed oil: a source of renewable energy in India
10. Jamwal A, Agrawal R, Sharma M, Kumar V (2021) Review on multi-criteria decision analysis in sustainable manufacturing decision making. *Int J Sustain Eng* 1–24
11. Boral S, Chaturvedi SK, Naikan VNA, Howard IM (2019) A hybrid AI-based conceptual decision-making model for sustainable maintenance strategy selection. In: Advanced multi-criteria decision making for addressing complex sustainability issues. IGI Global, pp 63–93
12. Hiremath RB, Kumar B, Balachandra P, Ravindranath NH, Raghunandan BN (2009) Decentralised renewable energy: scope, relevance and applications in the Indian context. *Energy Sustain Dev* 13(1):4–10
13. Sirajudeen M, Ashraf P (2020) How to strengthen indian economy, opportunities and challenges. *Our Heritage* 68(17):253–258
14. Bhide A, Monroy CR (2011) Energy poverty: a special focus on energy poverty in India and renewable energy technologies. *Renew Sustain Energy Rev* 15(2):1057–1066
15. Sahoo SK (2016) Renewable and sustainable energy reviews solar photovoltaic energy progress in India: a review. *Renew Sustain Energy Rev* 59:927–939
16. Panwar NL, Kaushik SC, Kothari S (2011) Role of renewable energy sources in environmental protection: a review. *Renew Sustain Energy Rev* 15(3):1513–1524
17. Ghosh D, Shukla PR, Garg A, Ramana PV (2002) Renewable energy technologies for the Indian power sector: mitigation potential and operational strategies. *Renew Sustain Energy Rev* 6(6):481–512
18. Suganthi L, Williams A (2000) Renewable energy in India—a modelling study for 2020–2021. *Energy Policy* 28(15):1095–1109

19. Kanase-Patil AB, Saini RP, Sharma MP (2011) Sizing of integrated renewable energy system based on load profiles and reliability index for the state of Uttarakhand in India. *Renew Energy* 36(11):2809–2821
20. Purohit P (2007) Financial evaluation of renewable energy technologies for irrigation water pumping in India. *Energy Policy* 35(6):3134–3144
21. Purohit P, Kumar A, Rana S, Kandpal TC (2002) Using renewable energy technologies for domestic cooking in India: a methodology for potential estimation. *Renew Energy* 26(2):235–246
22. Ramachandra TV, Shruthi BV (2007) Spatial mapping of renewable energy potential. *Renew Sustain Energy Rev* 11(7):1460–1480
23. Mallon K (ed) (2006) *Renewable energy policy and politics: a handbook for decision-making*. Earthscan
24. Hammar L, Ehnberg J, Mavume A, Cuamba BC, Molander S (2012) Renewable ocean energy in the Western Indian Ocean. *Renew Sustain Energy Rev* 16(7):4938–4950
25. Pohekar SD, Kumar D, Ramachandran M (2005) Dissemination of cooking energy alternatives in India—a review. *Renew Sustain Energy Rev* 9(4):379–393
26. Mishra MK, Khare N, Agrawal AB (2015) Small hydro power in India: current status and future perspectives. *Renew Sustain Energy Rev* 51:101–115
27. Chauhan A, Saini RP (2015) Renewable energy based off-grid rural electrification in Uttarakhand state of India: technology options, modelling method, barriers and recommendations. *Renew Sustain Energy Rev* 51:662–681
28. Boudri JC, Hordijk L, Kroeze C, Amann M, Cofala J, Bertok I, Panwar TS (2002) The potential contribution of renewable energy in air pollution abatement in China and India. *Energy Policy* 30(5):409–424
29. Kumar A, Kandpal TC (2007) Renewable energy technologies for irrigation water pumping in India: a preliminary attempt towards potential estimation. *Energy* 32(5):861–870
30. Wilkins G (2010) *Technology transfer for renewable energy*. Routledge
31. Singh PL, Sindhvani R, Dua NK, Jamwal A, Aggarwal A, Iqbal A, Gautam N (2019) Evaluation of common barriers to the combined lean-green-agile manufacturing system by two-way assessment method. In: *Advances in industrial and production engineering*. Springer, Singapore, pp 653–672
32. Jamwal A, Aggarwal A, Gupta S, Sharma P (2019) A study on the barriers to lean manufacturing implementation for small-scale industries in Himachal region (India). *Int J Intell Enterprise* 6(2–4):393–407
33. Gautam N, Ojha MK, Swain P, Aggarwal A, Jamwal A (2019) Informal investigation of fourth-party and third-party logistics service providers in terms of Indian context: an AHP approach. In: *Advances in industrial and production engineering*. Springer, Singapore, pp 405–413
34. Sharm P, Jamwal A, Aggarwal A, Bhardwaj S, Sood R (2018) Major challenges in adoption of RFID for Indian SME's. *Int Res J Eng Technol* 5:2247–2255
35. Jamwal A, Agrawal R, Gupta S, Dangayach GS, Sharma M, Sohag MAZ (2020) Modelling of sustainable manufacturing barriers in pharmaceutical industries of Himachal Pradesh: an ISM-fuzzy approach. In: *Proceedings of International Conference in Mechanical and Energy Technology*. Springer, Singapore, pp 157–167

A Review on Scramjet Engine



Riyan Cyriac Jose, Rhitik Raj, Yogesh Dewang, and Vipin Sharma

Abstract Combustion occurs at supersonic speeds in a scramjet engine. Lower air residence time is the factor affecting proper fuel–air mixing, flame propagation and cooling of engine components. This current study includes systematic review of fuel–air mixing inside the combustor through various design changes and augmentations and strides to present at the future scope of this technology. Methods of sufficient and rapid fuel–air mixing used are also studied. Various methods of augmentation applied to the geometry of combustion chamber are presented which are developed for greater fuel–air mixing. Enhanced mixing time in real-time situations is studied by hypothesis of the fluid flow inside the combustion chamber using CFD analysis for air speeds higher than Mach 1.6. Fuel injectors placed in upstream, studied through CFD analysis, have also been included in this review. Recent development in fuel injector is studied too. Single and multiple fuel injectors are used to compare the mixing efficiency with variation in Mach speeds and inlet angle of air inside the combustor. Liquid and gaseous fuels are considered for better fuel–air mixture, and their secondary function as a cooling system is assessed.

Keywords Fuel air mixing · Fuel injectors · Combustor geometry · Fluid flow analysis

R. C. Jose (✉) · R. Raj · Y. Dewang
Lakshmi Narain College of Technology, Bhopal, MP 462022, India
e-mail: joseriyanryciac@gmail.com

R. Raj
e-mail: rhitikraj0035.rr@gmail.com

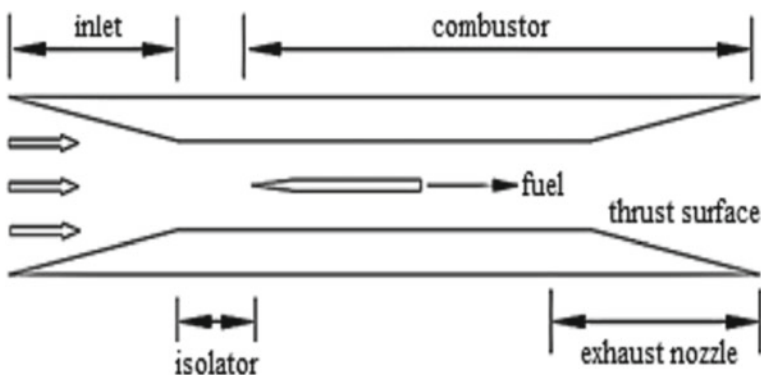
Y. Dewang
e-mail: dewang.yogesh3@gmail.com

V. Sharma
Sagar Institute of Research Technology, Bhopal, MP 462041, India
e-mail: vipinsati@gmail.com

1 Introduction

Scramjet engine stands for supersonic combustion ramjet engine. It is a great discovery which spanned over six decades. It finds its use in aeronautical and space research. The scramjet engine has the potential to make flight time short and less expensive. It was first proposed by René Lorin as a ramjet engine in 1913 [1]. The supersonic combustion ramjet engine has a very simple construction, relative to any air breathing jet propulsion system, as it has no moving parts. The engine consists of an inlet, isolator, fuel injector, combustion chamber and an exhaust nozzle (see Fig. 1). The inlet functions as a compressor and its geometry is designed with shock layer characteristics induced by the type of compression used. The inlet can be used to increase or decrease pressure with slight changes in geometry because at speeds above Mach 2, physical compressor is insignificant. The isolator separates inlet from combustion chamber and is used as supersonic diffuser capable of creating compound shockwave. It is used to prevent back pressure, developing in the combustion chamber, from disturbing inlet supersonic stream.

The powerhouse of a scramjet engine is the combustion chamber along with fuel injector and accompanying system. It is designed to sustain combustion at higher air speeds, which is rather a complicated task. The airflow inside the combustion chamber is required to be turbulent for maximum efficiency and is achieved by ramps and flame holding cavities along the path. The exhaust nozzle is utilized to increase the thrust which is generated during the combustion process. It is achieved by expansion through exhaust nozzle at the end of the thermodynamics cycle [3]. Scramjet engines are also known as aero-thermodynamic duct and work on thermodynamics cycle known as Brayton cycle or Joules cycle. Unlike ramjet, the air speed is always supersonic in scramjet engine, hence the name. These engines are



Source: Engineering Department, ANU

Fig. 1 Schematic of scramjet engine [2]

used in prototype space exploration vehicles, to launch it in much easier manner. They find their application in ICBM (Inter-Continental Ballistic Missile) as well. Utilizing the latest technological advancement would prove essential for research and scientific study. Understanding the scope of this propulsion system brings to light the technological hindrances and difficulties experienced during the operation cycle.

The factor that inhibits the proper operation of engine cycle is the lower air residence time inside the combustion chamber due to high speed airflow through the engine body. Less time for air to pass through chamber would lead to decrease in the rate of combustion, resulting in ineffective combustion. Adding mechanisms to increase the time for residence for the air, leads to loss in efficiency by increasing weight. With lower air residence time, comes the problem of flame stability. Combustion of fuel and sustaining the flame is primary concern in high functioning and high requirement scramjet engine. The flame holder augmentations are used for reducing the ignition delay and provide a constant parametric condition for combustion [4]. Increased flight duration at a higher working temperature, accompanied by heating due to friction at high speed, all make the scramjet engine body hot. Such high temperatures can lead to the weakening of the body structure due to stress generated by rapid cooling and heating, causing fatigue failure. These problems are acknowledged by the recent research in the above-concerned fields. The objective of the present study is to critically review the recent advancement carried in the domain of scramjet engines.

2 Various Aspects of Scramjet Engine

In the current work, the challenges to develop a rather simple working engine and the possible countermeasures have been accumulated. This work presents the cumulative approach to the development and research done in the regards of:

- Fuel Injection System
- Fuel–Air Mixture
- Cooling of Engine Body.

Information is collected, and a conclusion is made on the basis of previous work done.

With reference to simulation and analysis done in the last 10 years in the field of scramjet engine, especially briefing on the developments done in past couple of years is addressed. The assessment is based on interpretation of data and strives to present a simple and clear picture of the scramjet propulsion system with its important challenges, which if solved would prove to be a great leap in mankind's space ventures and for revolutionizing transport.

2.1 Fuel–Air Injection System

The subsystem responsible for fuel introduction is crucial for combustion process. The method of injection, the angle of penetration and placement of injectors are vital considerations to be taken up while designing a scramjet engine. Various strategies employed by previous researchers for fuel injection systems are given in Table 1 which clearly illustrates the type of injection systems and its related methodologies. It is gathered that major fuel injection strategies were cavity, struts and wall injector while on the other hand plasma assisted combustion is found to be relatively newer technique.

2.2 Fuel–Air Mixing Inside Combustor

The first challenge is mixing of fuel and air inside the combustor. This problem arises due to the short air residence time in the scramjet engine combustion chamber. The air residence time is of the order of 10^{-3} seconds. Time taken for the chemical reaction for the combustion should be less than the air residence time. In a study by Qui et al. [13], characteristics of air residences time were studied at flow velocity of Mach 6.5 with strut injectors, relying on recirculation of air to reduce the flow speed and increasing the time for combustion to take place. Flame oscillations were observed at the beginning, but soon were diffused into the surrounding as the flame propagated because of recirculation zone. This recirculation phenomenon was first observed in the cavity-based flame holder introduced by CIAM-NASA in the scramjet body [14]. The recirculation of inlet air to increase the air residence time that depends upon the internal geometry of the combustion chamber is relatively easy to achieve.

The second challenge is mixing rate. Mixing rate is the influencing factor in determining the mixing efficiency of fuel in the combustion chamber at a given time. Penetration is the injection of the fuel into the flow of air. Penetration should be high for the fuel injectors, to greatly increase the maximum efficiency. Penetration can be assessed by the free stream to jet momentum flux ratio of the fuel flow into the cross-flow [15, 16]. Proper fuel–air mixing is vital for scramjet engine. Detailed and concise culmination of different mixing strategies presented herein helps in understanding the depth of this underlying concept.

All the different well-studied strategies of fuel–air mixing, including the ones mentioned in the previous table, can be cumulated as described below:

- Struts [17–22], Ramps [23–25], Chevron [26] produce stream-wise vorticity;
- Vanes induce swirl;
- Transverse injection [27–30] brings curvature to the flow;
- A cavity [4, 31–34] creates acoustic excitation;
- Pulsed jet [35], piezoelectric actuators employ forced excitation at large scale;
- Wavy wall creates spatial excitation;

Table 1 List of Different Injection System

Method of fuel injection	Author	Methodology
Plasma Assisted Fuel Injector	Macheret et al. [5]	A scheme is proposed where the plasma is used for breaking down fuel faster thereby decreasing the ignition delay, by generating radicals exhibiting uniform ignition. It also suggests an electron beam-based multipoint fuel injection system
Strut + Wall Fuel Injector	Choubey et al. [6]	Studied the effect of different strut and wall combinations for hydrogen-based scramjet engine by employing 2-D RANS and K-ε turbulence model. The results show two strut + wall 1 + wall 2 proved to be better at fuel–air mixing when compared to two strut + wall 1, two strut + wall 1 + wall 2 + wall 3, two strut + wall 1 + wall 2 + wall 3 + wall 4 and single strut
	Zhang et al. [7]	Flame interaction characteristic in strut + wall injection is experimentally investigated the kerosene-based flush wall scramjet engine at Mach 2. Flame behaviour without wall injection, with wall injection and combustion efficiency with different location is documented
Cavity Fuel Injector	Kang et al. [8]	Interchangeable plates for fuel injector that are no cavity, plain cavity and zigzag cavity were used at flow field condition of Mach 2.5
	Huang et al. [9]	Numerical simulation with RANS equations was applied. Speed painted is 2 Mach with total pressure and temperature as 237 kP and 288 K, respectively
Strut Injector	Roga [2, 10]	CFD analysis of diamond-shaped strut injector was done at Mach 4.5. The combustion efficiency was found to be 87.2% with maximum temperature and pressure as 3517 K and 1.487 MPa And an alternating wedge strut injector with Mach 6.5 was assessed with the same method
	Manna et al. [11]	Computational flow was analysed considering two different types of strut injectors, namely diamond strut with five faces and swept back strut. Three-dimensional Navier–Stokes equations and single K-ε turbulence model were solved
Rear Wall Expansion Cavity fuel injector	Cai et al. [12]	Analysis of hydrogen-based scramjet engine in rear wall expansion with conditions of 2.52 Mach 1486 K and 1.6 MPa was maintained

These fore-mentioned techniques and devices are method of mixing fuel and air effectively.

Flame Holder Cavity. Out of the strategies mentioned earlier, flame holder cavity is the best suggested and organized system for combustion because almost all other methods depend on the creation of vortices which helps in mixing but is stretched

throughout the area which causes inefficient combustion process. Cavity flame holder is effective in maintaining the flame and parametric conditions for combustion inside the scramjet engine. The recirculation of the inlet air in the cavity provides sufficient time for the fuel and air to mix properly and give an efficient combustion. In a cavity flame holder, the flame stability is directly determined by the shear layer boundary separating supersonic air flow and subsonic recirculation zone. The shear layer tends to move back and forth depending upon the geometric parameter of the cavity, which in-turn lead to pressure variation inside the recirculation zone and can be referred to as oscillations. These oscillations directly affect the flame base, which begins oscillating as well. These oscillations at the base grow into unstable flame which can be blown out due to failure in maintaining auto-ignition conditions [36].

Therefore, the two aspects to be taken into consideration [4] while discussing cavity flame holder are

1. Shape/Geometry Cavity
2. Injector Placement.

Shape/geometry. The cavity shape and geometry are decided taking into account the following [34].

- Type of flow inside the cavity namely “open” and “closed” helps in determining the length (L) of the cavity.
- Residence of time of air helps in deciding the depth (D) of the cavity.
- Oscillations inside the cavity affected by the shear layer and described as “stable” and “unstable”, are used to determine the extent of mixing of fuel and air.

For a $L/D < 7$, open cavity, stable system with fuel injection over or inside the cavity that can have longer air residence time is the idea of a suitable geometry of the cavity according to Ben-Yakar et al. [34]. Li et al. [37] realized experimentally that flame propagation reaches the upstream of the cavity leading edge with an increment in length-to-depth ratios which consequently results in mode transitions. It was concluded that the greater the L/D ratio, more will be flame propagation to the upstream direction to the leading edge. Decreasing the length (L) of the cavity resulted in reduced flame oscillation. Li et al. [37] discussed that the experimental configuration having greater L/D ratio with the injector orifice near to the leading edge was the better choice in their case study, but with increase in L/D ratio, the flame oscillations are higher because greater the length (L), longer will be the shear layer leading to greater oscillating flame base.

Injector Placement. The positioning of injectors has substantial effects on the mixing efficiencies. The few recent developments of last couple of years have been mentioned. In an experimental set-up by Song et al. [38], the fuel injector was placed 10 mm upstream from the cavity leading edge with single and multiple orifice injection cases. It was concluded that having multiple injectors upstream the

leading edge is better because more fuel gets into the cavity and the distribution of fuel in the air is much more spread out and uniform in the inlet air flow. The placement of the multiple injectors helps to have a stable flame as compared to the single orifice injection because the flame oscillations between leading and trailing edge of the cavity for a single orifice injector were more unstable. An et al. [39] incorporated laser to ignite the fuel–air mixture for a set-up similar to that described just before. In the study, a comparison is done between single laser ignition and dual laser ignition. The first of the dual laser was placed 3 mm downstream from the leading edge of the cavity, and the second was 7 mm downstream from the leading edge. After experimentation with the model, a result was obtained where the dual laser ignition was not better than the single ignition because of the second laser placement which had a longer distance from the leading edge, and hence, there were significant losses in time of ignition, heat and speed of the flow; but the stabilization of the flame was similar in both cases. Jeong et al. [40] studied the effects of injector placement in the cavity at three different positions, using angled injector with 15° injection inclination to the horizontal 20 mm upstream the leading edge, upstream injector placed on cavity rear wall and parallel injection at the leading step of the cavity. It was concluded that the angled injection had the best penetration and upstream injection gave rise to increased diffusion and better ignition. The study considered different equivalence ratio of the fuel and air and stated that higher the equivalence ratio the more effective the combustion is.

2.3 Cooling of Scramjet Engine

Increasing the Mach number would also increase the heating due to aero-thermodynamics. This poses another challenge to the supersonic vehicle. If this is overlooked, it could result in severe structural and cooling problem for the supersonic vehicle and the engine body [41]. To increase the duration of flight and to push the operating speed above Mach 5, proper and efficient cooling is required. Various methods and concepts have been developed, which suggest using the onboard fuel as a coolant, circulating throughout the body, acting as a heat absorber [42]. One of the methods suggest that thin film cooling facilitated by the fuel injectors which would be injected parallel to the surface and prevent the engine structure for heating [43].

Another research focuses on using material of composite nature with better heat releasing capabilities. The availability of composite material and technology helps in effectively removing heat generated due to thermo fluid interactions and has an edge over metal and ceramics. Three different material composites are studied are polymer matrix composite, metallic matrix composite and ceramic matrix composite; of which polymer matrix composite is better because of better heat dissipation and better strength to weight ratio [44].

3 Conclusions and Remarks

In the wake of the recent developments in the scramjet propulsion system, many opportunities have come up in the field of research and development. Different aspects of the scramjet engine and supersonic propulsion have been explored, and new avenues have opened up. This present study is focused to critically review the recent technological changes and development in the field of fuel injection system, fuel–air mixing, especially concerning cavity flame holder, and cooling practices in hope to provide better and simpler understanding of the recent development to other researchers. It can be concluded that higher air residence time gives increased power output for the same amount of fuel used, when compared to shorter air residence time. The cavity combustor in a scramjet engine is one of the reliable forms of strategy that significantly increases the air residence time by recirculation of air in the cavity. The step of the leading edge of the cavity causes shear layer to propagate in downstream direction. The shear layer causes separation of combustor into supersonic flow field and subsonic recirculation zones. Since standard air residence time is 1 ms for Mach 2 and above, the subsonic velocity in cavity provides enough time gaps to chemical reactions for combustion, to sustain and propagate ignition. This set-up is affected by following aspects:

- Fuel Injection

Positioning fuel injectors highly influences the mixing rate, penetration and flame stability. Using along-side different the fuel injectors, different strategies like struts and plasma-assisted combustion open the avenue to explore more in this particular field. The number of injectors and how far in the upstream they are placed affect the mixing and penetration of fuel in air.

- Fuel–Air Mixing

The geometry of the cavity is responsible for fuel–air mixing inside the cavity. The length of the cavity determines the type of the flow which depends on shear layer. The longer the cavity more will be the frequent pressure difference caused by shear layer giving rise to oscillation of flame base in the cavity. The depth of the cavity determines the amount of air residence time. The deeper the cavity the more will be the air residence due to the greater quantity to hold air.

The aero-thermodynamics, which comes into play with increasing speeds, is also a concern for the real-world long flight durations. This would lead to structural and cooling problems, which may affect the vehicle in mid-flight and prove to be fatal, so various methods of film cooling, fuel circulation and using composite materials have been proven efficient in cooling the vehicle during supersonic regime. Since our ultimate aim is to move faster, cooling the scramjet would be increasingly necessary.

References

1. Curran ET (2001) Scramjet engines: the first forty years. *J Propul Power* 17(6):1138–1148
2. Roga S (2019) CFD analysis of scramjet engine combustion chamber with diamond-shaped strut injector at Flight Mach 4.5. *J Phys Conf* 1276(1):012041
3. Seleznev RK, Surzhikov ST, Shang JS (2019) A review of the scramjet experimental data base. *Prog Aerosp Sci* 106:43–70
4. Choubey G, Yuvarajan D, Wei H, Kulmani M, Manvendra T, Pandey KM (2019) Recent advances in cavity-based scramjet engine—a brief review. *Int J Hydrog Energ* 44(26):13895–13909
5. Macheret SO, Shneider MN, Miles RB (2019) Plasma-assisted fuel atomization and multipoint ignition for scramjet engines. *J Propul Power*, 1–5
6. Choubey G, Pandey KM (2017) Effect of different strut + wall injection techniques on the performance of two-strut scramjet combustor. *Int J Hydrog Energ* 42(18):13259–13275
7. Zhang J, Chang J, Tian H, Li J, Bao W (2019) Flame interaction characteristics in scramjet combustor equipped with strut/wall combined fuel injectors. *Combust Sci Technol*, 1–24
8. Kang SH, Lee YG, Yang SS, Choi B (2012) Effects of flameholder configurations on combustion in scramjet engines. *J Propul Power* 28(4):739–746
9. Huang W, Wang ZG, Yan L, Liu WD (2012) Numerical validation and parametric investigation on the cold flow field of a typical cavity-based scramjet combustor. *Acta Astronaut* 80:132–140
10. Roga S (2019) CFD analysis of scramjet engine combustion chamber with alternating wedge-shaped strut injector at Flight Mach 6.5. *J Phys* 1276(1):012038
11. Manna P, Behera R, Debasis C (2008) Liquid-fueled strut-based scramjet combustor design: a computational fluid dynamics approach. *J Propul Power* 24(2):274–281
12. Cai Z, Zhu X, Sun M, Wang Z (2017) Experiments on flame stabilization in a scramjet combustor with a rear-wall-expansion cavity. *Int J Hydrog Energ* 42(43):26752–26761
13. Qui H, Zhang J, Sun X, Chang J, Bao W, Zhang S (2020) Flowing residence characteristics in a dual-mode scramjet combustor equipped with strut flame holder. *Aerosp Sci Technol* 99:105718
14. National Aeronautics and Space Administration. <https://ntrs.nasa.gov/archive/nasa/casi.ntrs.nasa.gov/19980137604.pdf>. Accessed 2020/05/28
15. Holdeman JD (1993) Mixing of multiple jets with confined subsonic crossflow. *Prog Energy Combust Sci* 19(1):31–70
16. Lee SH (2006) Characteristics of dual transverse injection in scramjet combustor, part 1: mixing. *J Propul Power* 22(5):1012–1019
17. Gerlinger P, Peter S, Markus K, Fernando S, Manfred A (2008) Numerical investigation of mixing and combustion enhancement in supersonic combustors by strut induced streamwise vorticity. *Aerosp Sci Technol* 12(2):159–168
18. Huang ZW, He GW, Shuai W, Fei Q, Wei XG, Lei S (2017) Simulations of combustion oscillation and flame dynamics in a strut-based supersonic combustor. *Int J Hydrog Energ* 42(12):8278–8287
19. Kummitha OR, Lakka S, Pandey KM (2017) Numerical analysis of scramjet combustor with innovative strut and fuel injection techniques. *Int J Hydrog Energ* 42(15):10524–10535
20. Pandey KM, Roga S, Gautam C (2015) Computational analysis of hypersonic combustor using strut injector at Flight Mach 7. *Combust Sci Technol* 187(9):1392–1407
21. Soni RK, De A (2017) Investigation of strut-ramp injector in a scramjet combustor: effect of strut geometry, fuel and jet diameter on mixing characteristics. *J Mech Sci Technol* 31(3):1169–1179
22. Soni RK, De A (2018) Role of jet spacing and strut geometry on the formation of large scale structures and mixing characteristics. *Phys Fluids* 30(5)
23. Salam TM, Tiwari SN, Mohieldin TO (2003) Effects of ramp side angle in supersonic mixing. *AIAA J* 41(6):1199–1201

24. Dong X, Yaohui C, Gang D, Yixin L (2017) Study on wake structure characteristics of a slotted micro-ramp with large-eddy simulation. *Fluid Dyn Res* 49(3)
25. Parent B, Sislian JP, Jurgen S (2002) Numerical investigation of the turbulent mixing performance of a cantilevered ramp injector. *AIAA J* 40(8):1559–1566
26. Hariharan AR, Babu V (2014) Transverse injection into a supersonic cross flow through a circular injector with chevrons. *J Fluids Eng* 136(2)
27. Huang W, Li MH, Yan L (2016) Mixing augmentation mechanism induced by the pseudo shock wave in transverse gaseous injection flow fields. *Int J Hydrog Energ* 41(25):10961–10968
28. Huang W, Wang ZG, Wu JP, Li SB (2013) Numerical prediction on the interaction between the incident shock wave and the transverse slot injection in supersonic flows. *Aerosp Sci Technol* 28(1):91–99
29. Huang W (2016) Transverse jet in supersonic crossflows. *Aerosp Sci Technol* 50:183–195
30. Pudsey AS, Boyce RR, Wheatley V (2013) Influence of common modeling choices for high-speed transverse jet-interaction simulations. *J Propul Power* 29(5):1076–1086
31. Bao H, Zhou H, Pan Y (2015) Effect of cavity configuration on kerosene spark ignition in a scramjet combustor at Ma 4.5 flight condition. *Acta Astronaut* 117:368–375
32. Huang W, Luo SB, Liu J, Wang ZW (2010) Effect of cavity flame holder configuration on combustion flow field performance of integrated hypersonic vehicle. *Sci China Technol Sci* 53(10):2725–2733
33. Wang H, Wang Z, Sun M, Wu H (2013) Combustion modes of hydrogen jet combustion in a cavity-based supersonic combustor. *Int J Hydrog Energ* 38(27):12078–12089
34. Yakar AB, Hanson RK (2001) Cavity flame-holders for ignition and flame stabilization in scramjets: an overview. *J Propul Power* 17(4):869–877
35. Haitao S, Wang G, Luo X, Yang J, Lu XY (2016) Large-eddy simulation of a pulsed jet into a supersonic crossflow. *Comput Fluids* 140:320–333
36. Barnes FW, Segal C (2015) Cavity-based flameholding for chemically-reacting supersonic flows. *Prog Aerosp Sci* 76:24–41
37. Fan L, Sun M, Cai Z, Sun Y, Li F, Zhang J, Zhu J (2020) Experimental study of flame stabilization in a single-side expansion scramjet combustor with different cavity length-to-depth ratios. *Acta Astronaut* 173:1–8
38. Song X, Wang H, Sun M, Cai Z, Liu C, Yu J (2019) Mixing and combustion characteristics in a cavity-based supersonic combustor with different injection schemes. *Acta Astronaut* 159:584–592
39. An B, Wang Z, Yang L, Li X, Liu C (2018) The ignition characteristics of the close dual-point laser ignition in a cavity based scramjet combustor. *Exp Ther Flu Sci* 101:136–140
40. Jeong E, O’Byrne S, Jeung I, Houwing AFP (2020) The effect of fuel injection location on supersonic hydrogen combustion in a cavity-based model scramjet combustor. *Energies* 13:193
41. Pish F, Moradi R, Edalatpour A, Gerdroodbary MB (2019) The effect of coolant injection from the tip of spike on aerodynamic heating of nose cone at supersonic flow. *Acta Astronaut* 154:2–60
42. Bao W, Qin J, Zhou WX, Yu DR (2010) Effect of cooling channel geometry on re-cooled cycle performance for hydrogen fueled scramjet. *Int J Hydrog Energ* 35(13):7002–7011
43. Zheng K, Wei T, Qin J, Zhang S, Hu H (2019) Effect of film cooling injection on aerodynamic performances of scramjet isolator. *Aerosp Sci Technol* 94:105383
44. Choubey G, Suneetha L, Pandey KM (2018) Composite materials used in Scramjet-a review. *Mater Today Proc* 5(1):1321–1326

Numerical Simulation of Ribbed Solar Air Heater



Anil Singh Yadav and Sanjay Kr Sharma

Abstract A numerical simulation of a solar air heater (SAH) with transverse equilateral triangular ribbed surface is carried out. The rib-pitch (P) and rib-height (e) ratio P/e 14.29, rib height and hydraulic diameter (D) of the duct ratio (e/D) are 0.021 to 0.042 and Reynolds number (Re) is 3800–18,000. The thermal and flow properties are investigated through ANSYS FLUENT 12.1. The SIMPLE algorithm is used for coupling pressure and velocity. Second-order upwind scheme for discretization of the equations and renormalization-group (RNG) k - ϵ model is used for simulation. An optimum thermal enhancement factor (TEF) obtained is 1.99.

Keywords CFD • RNG k - ϵ mode • SAH

1 Introduction

Solar air heaters (SAHs) have poor performance due low convective heat transfer coefficient (h) of air [1, 2]. However, h can be increased by creating turbulence near to the ribbed surface. This enhancement also results in higher frictional losses due to pressure drop. Numerous artificially roughened SAHs have been developed and tested for thermal-hydraulic performance with different shapes, sizes and orientations. To minimize the friction losses, the turbulence is created near the surface. The effects of different ribs on the SAHs have been widely reported in the literatures [3, 4]. The few literature reviews using CFD approach can be seen in [5–7].

This study investigates the effect of equilateral triangular transverse ribs on TEF characteristics in a SAH using CFD.

A. S. Yadav

Mechanical Engineering Department, Lakshmi Narain College of Technology,
Bhopal, MP 462022, India

S. K. Sharma (✉)

Mechanical Engineering Department, Amity University Chhattisgarh, Raipur 493225, India
e-mail: sksharma@rpr.amity.edu

© The Author(s), under exclusive license to Springer Nature Singapore Pte Ltd. 2021

549

B. S. Sikarwar et al. (eds.), *Advances in Fluid and Thermal Engineering*,

Lecture Notes in Mechanical Engineering,

https://doi.org/10.1007/978-981-16-0159-0_49

2 CFD Simulation

A 2D CFD investigation methodology of SAH is done with ANSYS FLUENT is discussed below in the subsections.

2.1 Geometry and Mesh

The geometry is created in ANSYS DESIGN MODELER (Fig. 1), consisting of entry section ($L_1 = 225$ mm), test section ($L_2 = 115$ mm) and outlet section ($L_3 = 121$ mm). The flow is internal, and the cross section area with width and height ($W \times H$) is 100×20 mm². Table 1 presents different rib arrangements and some parameters. Aluminum sheet is taken as absorber plate material of 0.5 mm thickness. The ribs are attached at the underside of the absorber plate. The geometrical parameter range ' e ' = 0.7 – 1.4 mm. Heat flux of 1000 w/m² is considered uniformly on the absorber plate. The different rib arrangement is shown in Fig. 2. Non-uniform grids are used with ICEM CFD for the 2D simulation for solving the governing equations for mass, momentum and energy. The quad cells of 239,662 with size of 0.2 mm are used for simulation after grid independence test.

2.2 Equation

Average Nusselt number is computed by:

$$Nu_t = hD/k \quad (1)$$

The average friction factor is computed by:

$$f_r = \frac{(\Delta P/l)D}{2\rho v^2} \quad (2)$$

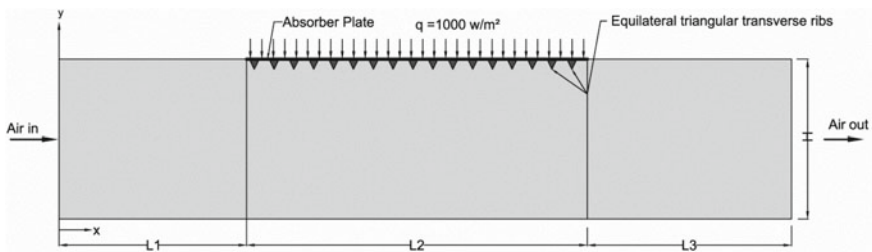


Fig. 1 2D computational domain

Table 1 Different rib arrangements

Rib arrangement	Height, e (mm)	Pitch, P (mm)	Hydraulic Diameter, D (mm)	P/e	e/D
1	0.7	10	33.33	14.29	0.021
2	1	14.29			0.03
3	1.4	20			0.042

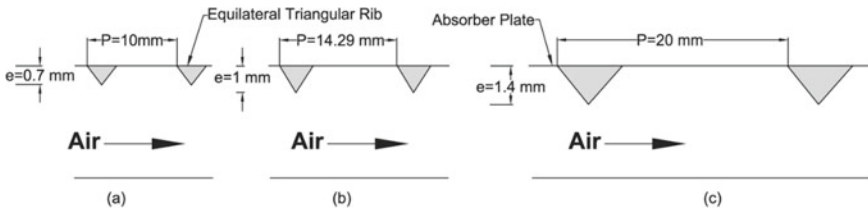


Fig. 2 Rib arrangement

where ΔP is pressure drop across the duct.

$$\text{Thermal Enhancement Factor} = \frac{(Nu_r/Nu_s)}{(f_r/f_s)^{1/3}} \tag{3}$$

Nusselt number (Nu_s) for smooth duct is obtained by Dittus–Boelter equation [8].

$$Nu_s = 0.023 Re^{0.8} Pr^{0.4} \tag{4}$$

Friction factor (f_s) for smooth duct is obtained by Blasius equation [9].

$$f_s = 0.0791 Re^{-0.25} \tag{5}$$

2.3 Simulation Conditions

A uniform air velocity, initial inlet temperature of 300 K and flux of 1000 W/m² are applied on absorber plate, and outlet condition is atmospheric pressure. The thermal and physical properties of working fluid and ribbed plate are taken from the database of ANSYS FLUENT.

2.4 Solution Method

The detailed information of the simulation can be referred in [7]. The similar algorithm, scheme and turbulence model are used here also with convergence criteria of 0.001.

3 Result and Discussion

Figure 3 shows enhancement of Nusselt number (Nu_r) for artificially roughened SAH over smooth SAH (Nu_0) at different Re , e/D and P/e . The values of Nu_r increase with increasing Re in all cases. The rib roughened SAH yields higher Nu_r over the smooth SAH. The high turbulence created in between the equilateral triangular ribs increases heat transfer from the surface. The Nu_r increases as there is increment in e/D for constant P/e .

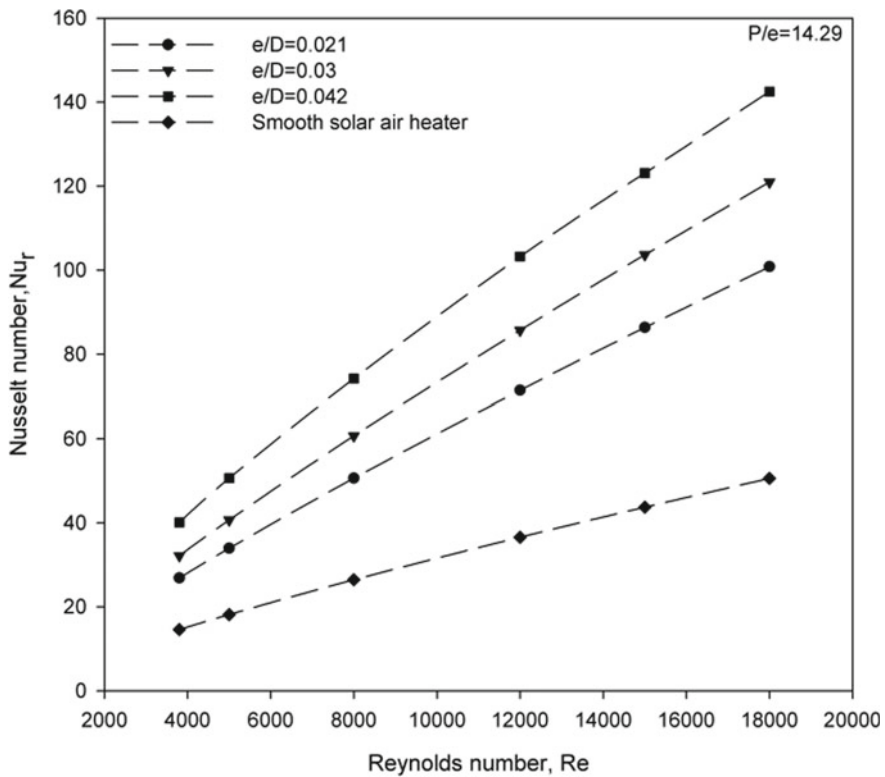


Fig. 3 Nu versus Re

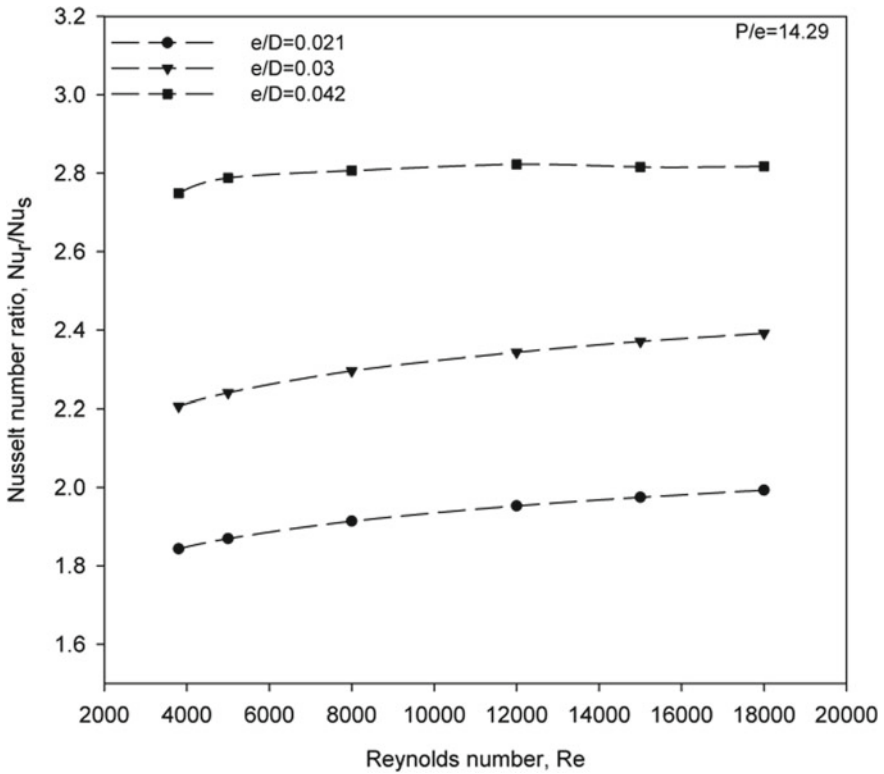
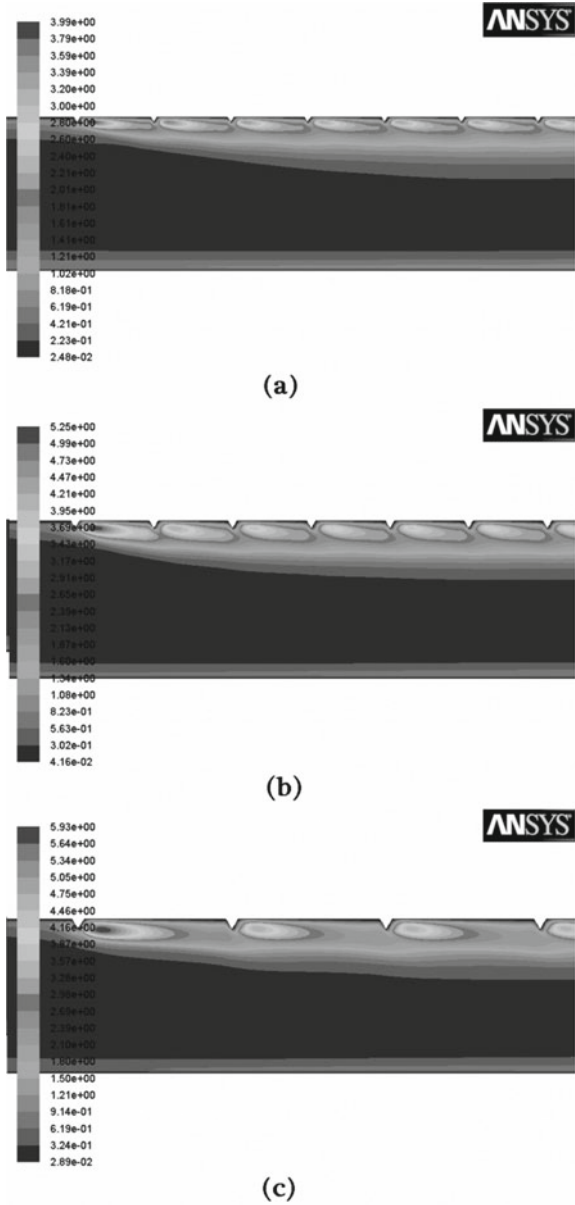


Fig. 4 Nu_r/Nu_0 versus Re

Figure 4 illustrates the effect of rib on Nusselt number ratio (Nu_r/Nu_0) as a function of e/D for constant P/e . This type of rib enhances the heat transfer significantly. The Nu_r/Nu_0 enhancement achieved varies from 1.84 to 2.82 for the selected parameters. The highest value of Nu_r is found to be 2.82 over the smooth duct at e/D of 0.042 and Re of 12,000. It is the established fact that turbulence kinetic energy (TKE) and dissipation rate (TDR) increase with the increasing Re , which results in higher turbulence intensity leading to increased Nu_r . The TKE contours give an insight of its effect for causing heat transfer enhancement. Figure 5 shows TKE contours for various e/D values and constant Re and P/e of 15,000 and 14.29, respectively. The maximum TKE value is found to be near heated wall at top surface of rib in the downstream direction. As it moves forward from the wall, its effect goes on decreasing.

Turbulence intensity also gives an insight of the reasons for the heat transfer increment in such ribbed surfaces. The values of the turbulence intensity show similar pattern as that TKE. Gradually with the increase in Re , the ribs start protruding beyond the laminar sub-layer or it can be said that the layer thickness starts decreasing with increase in the velocity of the flowing fluid.

Fig. 5 TKE contours for $Re = 15,000$ and $P/e = 14.29$ at **a** $e/D = 0.021$, **b** $e/D = 0.03$ and **c** $e/D = 0.041$



Additionally, the vortices originating from the ribbed surface also contribute toward the localized heat transfer.

3.1 Flow Friction

Frictional losses occur due to rib attachment on the absorber plate which causes pressure drop. Figure 6 shows the effect on friction factor (f) for ribbed SAH and smooth SAH with Re and e/D for different P/e values. The f_r decreases with increase in Re as the viscous sub-layer suppresses with increase in velocity of the working fluid. The ribbed SAH shows higher f values over the smooth SAH. Also, the increase in f_r is observed with the increase in e/D for constant P/e due to higher protrusion of ribs outside the laminar sub-layer. Figure 7 depicts the effect on the absorber plate for friction factor ratio (f_r/f_o) for the values of e/D and constant P/e . The f_r/f_o enhances substantially due to insertion of ribs on the absorber plate.

The f_r/f_o achieved varies from 2.38 to 3.02 for the considered parameters. The increase in f_r/f_o shows the same trend as that of f_r with increase or decrease of e/D for considered parameters and shows reverse trend with an increase of Re . The highest numerical value of f_r obtained is 3.02 times that of smooth duct (f_o) at e/D of 0.042 and Re of 3800.

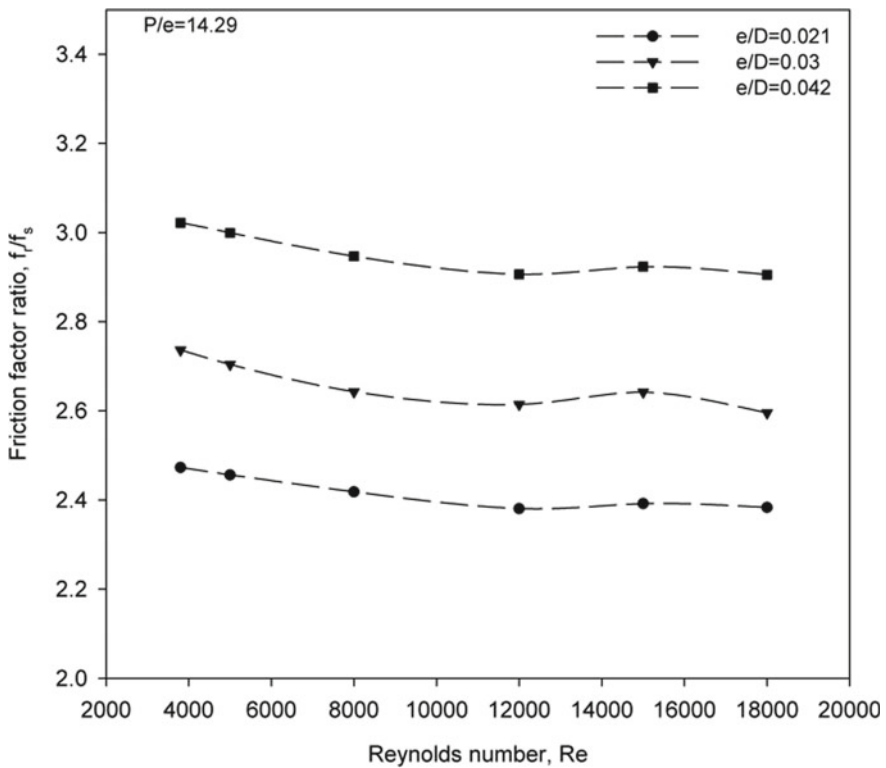


Fig. 6 f_r versus Re

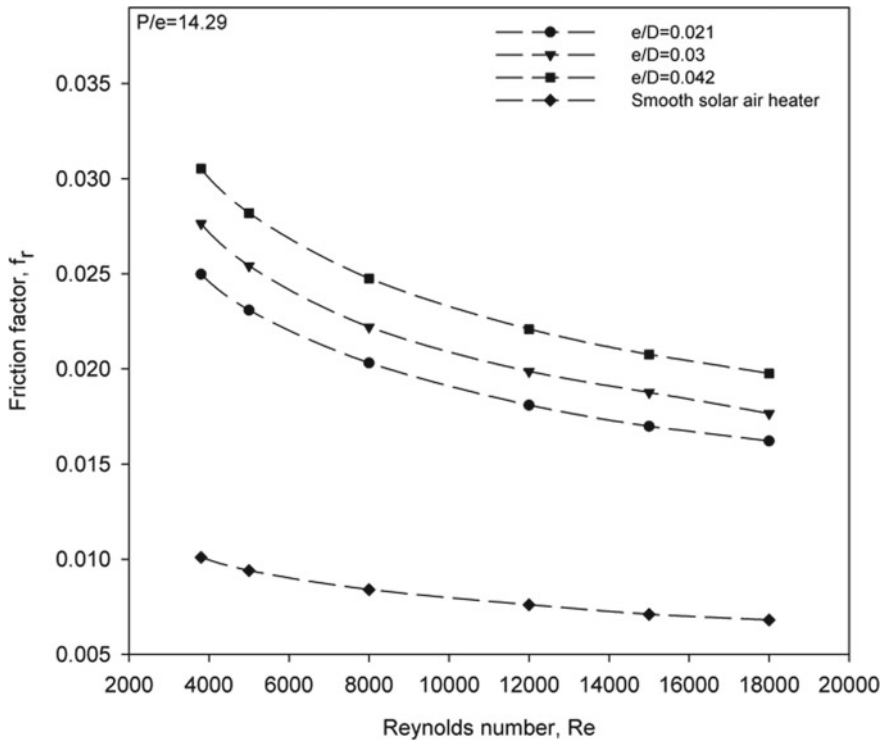


Fig. 7 f_r/f_o versus Re

The vortices shedding at the top of the rib causes an additional loss of energy resulting, so f_r further increases. From the observations, it is evident that the f decreases with increase in Re due to viscous sub-layer suppression. The drop in pressure is quite high due to the presence of ribs on the surface for all value of Re ($3800 < Re < 18,000$).

3.2 Thermal Enhancement Factor

The value of Nu_r/Nu_o reported in Fig. 4 can determine whether or not a given ribbed surface is potentially advantage over the smooth one or not, for the same pumping power and is given in the form of thermal enhancement factor $\{(Nu_r/Nu_o)/(f_r/f_o)\}^{1/3}$ [10]. Figure 8 shows the variation of $\{(Nu_r/Nu_o)/(f_r/f_o)\}^{1/3}$ for Re at different e/D and constant P/e of 14.29. It is seen that the $\{(Nu_r/Nu_o)/(f_r/f_o)\}^{1/3}$ values are above unity for all the cases. The $\{(Nu_r/Nu_o)/(f_r/f_o)\}^{1/3}$ initially increases then decreases after reaching peak value with the increase in Re . The $\{(Nu_r/Nu_o)/(f_r/f_o)\}^{1/3}$ values range from 1.37 to 1.99 for the present study. It is seen that the $\{(Nu_r/Nu_o)/(f_r/f_o)\}^{1/3}$ of $e/$

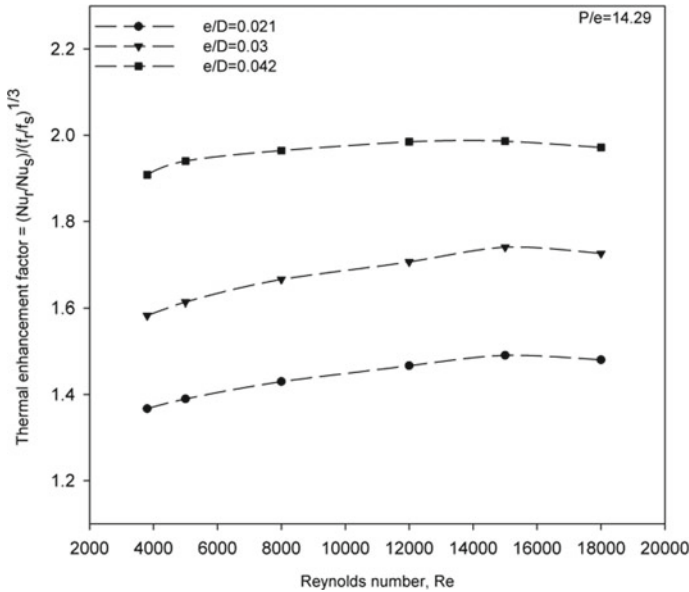


Fig. 8 THF with Re

$D = 0.042$ is found to be the best and is about 1.99 at a Reynolds number of 12,000. Trends in Nu , f and $\{(Nu_r/Nu_0)/(f_r/f_0)\}^{1/3}$ follow the same pattern as trends in experimental results of Ahn [11] and Wang and Sunden [12].

4 Conclusions


1. The rib parameters like e and P strongly affect the flow. The equilateral triangular sectioned ribs enhance the heat transfer.
2. The better heat transfer results are obtained when thermal enhancement factor, i.e., $\{(Nu_r/Nu_0)/(f_r/f_0)\}^{1/3}$ is high, i.e., Nu_r/Nu_0 should be high at minimum f_r/f_0 penalty.
3. The maximum Nu_r/Nu_0 is found to be 2.82 corresponding to e/D of 0.042 at a Re of 12,000.
4. The maximum f_r/f_0 is found to be 3.02 corresponding to e/D of 0.042 at a Re of 3800.
5. The equilateral triangular ribs in SAHs with $e/D = 0.042$ result in better $\{(Nu_r/Nu_0)/(f_r/f_0)\}^{1/3}$ of 1.99 at Re of 12,000 and can be used for as rib on the surface.

References

1. Duffie JA, Beckman WA (1980) *Solar engineering of thermal processes*. Wiley, New York
2. Yadav AS, Bhagoria JL (2013) Renewable energy sources—an application guide. *Int J Energy Sci* 3(2):70–90
3. Hans VS, Saini RP, Saini JS (2009) Performance of artificially roughened solar air heaters—a review. *Renew Sustain Energy Rev* 13(8):1854–1869
4. Bhushan B, Singh R (2010) A review on methodology of artificial roughness used in duct of solar air heaters. *Energy* 35(1):202–212
5. Kumar A, Saini RP, Saini JS (2012) Heat and fluid flow characteristics of roughened solar air heater ducts—a review. *Renew Energy* 47:77–94
6. Sharma SK, Kalamkar VR (2016) Computational fluid dynamics approach in thermo-hydraulic analysis of flow in ducts with rib roughened walls—a review. *Renew Sustain Energy Rev* 55:756–788
7. Yadav AS, Bhagoria JL (2013) Heat transfer and fluid flow analysis of solar air heater: a review of CFD approach. *Renew Sustain Energy Rev* 23:60–79
8. Webb RL, Eckert ERG (1972) Application of rough surface to heat exchanger design. *Int J Heat Mass Transf* 15(9):1647–1658
9. McAdams WH (1942) *Heat transmission*. McGraw-Hill, New York
10. Fox W, Pritchard P, McDonald A (2010) *Introduction to fluid mechanics*. Wiley, New York, p 754
11. Ahn SW (2001) The effects of roughness types on friction factors and heat transfer in roughened rectangular duct. *Int Commun Heat Mass Transfer* 28(7):933–942
12. Wang L, Sunden B (2007) Experimental investigation of local heat transfer in a square duct with various-shaped ribs. *Heat Mass Transf* 43:759–766

The Coatings Developed by Thermal Spraying Technique for Hydroturbine Applications—A Brief Review



Purusharth Bhati , Vishal Shrama , Raghav Jha ,
Sujeet Gupta , Mohit Vishnoi , and T. G. Mamatha 

Abstract In hydropower plants, water is used for the generation of power by the help of turbines due to which the erosion in runner and other components often lead to the losses in power generation and efficiency. Due to these conditions, sometimes turbines is shut down for repair work, replacement of runner, or other components. There are the various reasons for this failure mechanism such as silt erosion, cavitation erosion, and surface fatigue of underwater parts of the turbine and sometimes this leads to the mechanical vibration in the components. These problems can be eliminated by understanding the various causes of erosion and the methods of preventions. High-velocity oxy-fuel technique is most widely used among all of the thermal spray coatings methods. We will have studied the coatings of tungsten carbide, NiCoCrAlY, and chromium carbide by the HVOF spray process in our present work.

Keywords Hydroturbines · Surface coating materials · Coating methods · HVOF

P. Bhati · V. Shrama · R. Jha · S. Gupta · M. Vishnoi (✉) · T. G. Mamatha
Department of Mechanical Engineering, J S S Academy of Technical Education,
Noida 201301, India
e-mail: vishnoi.mohit06@gmail.com

P. Bhati
e-mail: dpsvn.puru09120@gmail.com

V. Shrama
e-mail: sharmavishal081998@gmail.com

R. Jha
e-mail: raghav2852@gmail.com

S. Gupta
e-mail: sujeet.bapu1996@gmail.com

T. G. Mamatha
e-mail: mamathatg@jssaten.ac.in

1 Introduction

As we know that there are the various types of techniques which are available in the market for the purpose of applying the thin-film coating on the different substrate materials in order to improve the outer surface properties such as wear resistance, electrical resistance, oxidation resistance, corrosion resistance or protection against the thermal disordering of the surface. We have seen that there are the different ways available in the thermal spraying processes technique which could be useful for the coating on any type of substrate material and we have selected HVOF process for the coating in order to produce a wear and corrosion resisting surface. In this coating technique, there is very fine material depositing (either metallic or non-metallic) on the molten and semi-molten surface of the substrate material and there is a very fine-powered form, molten material or ceramic-rod type of coating material is used in the coating. Also, there are some more traditional techniques of thermal spraying process that are available such as arc spraying or plasma spraying which could also be used but the main advantage of the HVOF is that it produces lower level of porosity by creating a cermets-based coating on the surface [1]. By making the different compositions in Co, Ni, or Cr which are the main metallic alloy matrix of the coating powders, we could make different combinations of tungsten carbide or NiCoCrAlY or chromium carbide and the two most common carbide coatings WC-Co and $\text{Cr}_3\text{C}_2\text{NiCr}$ [2]. The purpose of coating for the industry conditions is to protect the material against the wear and the corrosion, with the help of ductile metal binder and commonly cobalt or nickel are used in coating material composition. There are the various engineering applications for which this coating technique is used such as in coating on the valves, gears, pistons, rods, and the various machine parts for providing wear resistance and better hardness [3]. It is also used as an alternative technique for hardening the chromium plating [4]. To investigate and compare the sliding wear performance of tungsten carbide and chromium carbide, coating is done in the present studies by using the various compositions of coating materials which are applied by the HVOF process.

2 Theoretical Investigations

There are the various important characteristics of the martensitic stainless steel such as good weldability, high fracture toughness, corrosion resistance that is why it is used in the manufacturing of the different components of the hydroelectric plants such as turbines, valves, and injectors [5]. Instead of having these characteristics in the steel, it also subjected to surface damages in hydropower plants which may result in lowering down the efficiency of the turbines. As we are going to compare HVOF coating with the plasma nitriding, we will found the coating of NiCoCrAlY by HVOF process produces better erosion resistance when impinged at all angles of spraying. All these things contributed toward the result that the transformability and

hardness enhancing quality of the martensitic stainless steel that is why this steel is far better than any other types of steel. The results of the SEM examinations have founded out that the main reason of the material removal in hardened steel is the plastic deformations of the upper surface of the substrate material [6].

There different are the compositions of the various coating materials which are prepared for the testing of enhancement in the hardness of the steel substrate materials. Some of the studies have founded out that when coating mixture of the $\text{Cr}_3\text{C}_2\text{-NiCr}$ is done by HVOF thermal spray process on the steel substrate gives very much improvements in the hardness when analyzed by the cavitation silt erosion (CSE) [7].

2.1 Sample Preparation

The art of the sample preparation is done for the selection of the substrate material, so that the suitable coating compound is further selected. When the idea is to increase the hardness of the substrate, then the thermal spray coating is best method technique to do so [8].

2.2 Surface Roughness Measurement

After the deposition of the coating on the substrate material, there is the need of the measurement of the depth or the thickness of the coating compound on the surface so that the roughness obtained after coating would be measured for the final surface treatment [8].

2.3 Microstructural Analysis

There are not always the perfect coating occurs but sometimes there are the chances of generation of pores on the outer surface of the material which would weaken the material and melt down polymer during molding. This is the main reason of why the microstructural analysis is necessary for finding out the homogeneity and porosity of the coating.

2.4 Bond Strength

The criteria for finding out the bonding strength between the substrate material and the coating depend on the ranges of the temperatures and rates at which the heating

is produced during the coating. It has been seen that if the bond strength is better than there are more number of chances of survival of the material's surface without producing any types of visible signs coating deformations [8].

3 Experimental Studies

Here are some experimental data that are carried out to examine the metallurgical, topological, and wear properties of HVOF coating of nickel cobalt chromium aluminum alloy, tungsten carbide, and chromium carbide [9], and some of the researcher's studies are shown in Table 1.

3.1 Coating Selection

After being studying numerous research papers related to the properties enhancement of the steel substrate by the help of thermal spraying coating techniques, we have founded out that every different composition of coating materials have its own characteristic and advantages which may according to the application of use and methods used in applying it on the substrate surface [26]. We have selected out composition of three different powders, i.e., nickel cobalt chromium aluminum alloy, tungsten carbide, and chromium carbide powder for our work and the selected substrate material is 304 ASS because it has better corrosion and wear resistance as compared to other steels. There are also some of the other important factors which should be considered as they may effect in overall coating which are as material cost, finishing requirements, deposition rate, outer geometry, availability of equipments, etc.

All the analysis is done by considering each and every factor that may affect our coating analysis and we have founded out that the cost and technical consideration are the two important criterions for the proper coating systems. These can be done by understanding out the wear mechanism and environmental factors that are exposed in various cases studies in numerous research papers.

3.2 Properties Considered in Selecting Materials for Coating

There are the various parameters of the selecting out the suitable materials by analyzing the function, objectives and the services conditions in the turbines would be operating [26]. Here are some of the ways of selecting out it and these should be considered seriously:-

Table 1 Recent studies by different researchers

Reference/author/paper year	Size of coating powder (µm)	Coating powder composition	Parent material composition	Test performed	Coating thickness (µm)	Process parameter of HVOF	Result or conclusion	Microhardness (HV)/porosity (%)/surface Roughness (µm)
[3]/Bano et al./(2019)	16	46.1 SiO ₂ , 26.9 CaO, 24.4 Na, 2 O, and 2.6 P, 2 O 5—All In mol%	45S5 stainless steel	1. Simulated body fluid test (SBF), 2. X-ray diffraction (XRD), 3. Raman spectroscopy	6–25	Hydrogen flow rate equals to 180 SLPM Torch passes was 20 Flame heat power (kW) was 25	Development of bioactive coating to reduce wear rate	HV (253 ± 2) Porosity (6 ± 2) SR (2 ± 0.1)
[5]/Warda et al./(2019)	–	Al ₂ O ₃ -30(Ni ₂ OAl)	AISI 304 and aluminum alloy (30*29*5)mm ³	1. X-ray diffraction (XRD) analysis	–	Powder feed rate (g/min) was 26 Spray distance (mm) was 150	High hardness and wear protection	HV (250 ± 2) Porosity (7.2 ± 0.67)
[10]/Sharma et al./(2019)	45–10	Ni-20TiO ₂ -20Al ₂ O ₃	CA6NM steel (20* 20* 5) mm ³	1. Surface scale morphology 2. Energy-dispersive spectroscopy (EDS) analysis	300–400	High gas velocities cause particle Velocities of around 400_800 m/s (1320_2600 ft/s)	Higher bond strength and lesser porosity	HV (605 ± 37) Porosity (0.8 ± 2) SR (6.61 ± 0.4)
[11]/Kiragi et al./(2018)	105–150	WC-Co-Cr	AA1050 (25*25*25) mm ³	1. Scanning electron microscopy (SEM), 2. Fatigue test	170	Erodent feed rate: 30 m/s Impingement angle was 30° Erodent size was 225 µ	Minimization in erosive wear	HV (200 ± 4) Porosity (0.75)
[12]/Kumar et al./(2018)	5–10	86-88% WC 6-13% Co 1.5-8% Cr	WC-Cr ₃ -C ₂	1. Erosion, 2. Wear	1–10	Coating oxide content of 0.16, 0.94 and 1.8 wt.% for LPPS, HVOF and APS, respectively	Slurry erosion resistance and abrasive wear decreased	HV (585 ± 33) Porosity (0.6 ± 1.7)

(continued)

Table 1 (continued)

Reference/author/paper year	Size of coating powder (μm)	Coating powder composition	Parent material composition	Test performed	Coating thickness (μm)	Process parameter of HVOF	Result or conclusion	Microhardness (HV)/porosity (%)/surface Roughness (μm)
[13]/Currat et al./(2017)	–	13% Cr–4% Ni	S41500 steel plate (6.75*6.5*1.25) mm ³	1. Hardness test 2. Fatigue testing	20–25	Rearward tilting angle was 4° Velocity was 4.5 mm/s Frequency was 36 Hz Force was 105 N	Average hardness is improved	HV (250 \pm 7) Porosity (11 \pm 6.7)
[14]/Mohan et al./(2017)	300	Ti–Mo–Zr–Fe	Stainless steel (3.1*1.4*8) mm ³	1. Scanning electron microscopy (SEM)	100	TMP is done at 950 and 1050 °C using strain rates of 0.001/s and 10/s	Increases in the bending strength	HV (277 \pm 15) Porosity (16.65 \pm 5.57) SR (5.1 \pm 0.5)
[9]/Martín et al./(2017)	20–60	Cr ₂ O ₃ –25% NiCr	Fe-based superalloy A-286 (20*10*6) mm ³	1. Scanning electron microscopy (SEM), 2. Microscopy (SEM), 3. Energy-dispersive spectroscopy (EDS) 4. X-ray Diffraction (XRD)	100–200	Ar gas atomization at a dynamic pressure of 7 MPa after heating to 1823 °K	Corrosion resistance and wear resistance	HV (300 \pm 4) Porosity (14 \pm 3)
[15]/Sames et al./(2016)	100	Fe–Si–Mn–Cr	AISI 316 L (100*20*35) mm ³	1. Optical microscopy (OM), 2. Scanning electron microscopy (SEM), 3. Energy-dispersive spectroscopy (EDS)	30	Comp. air pressure 3 bar Flame condition neutral	Increase in strength, Nanostructure improvement	HV (325 \pm 4) Porosity (16 \pm 3) SR (6.2 \pm 0.7)

(continued)

Table 1 (continued)

Reference/ author/paper year	Size of coating powder (μm)	Coating powder composition	Parent material composition	Test performed	Coating thickness (μm)	Process parameter of HVOF	Result or conclusion	Microhardness (HV)/porosity (%)/surface Roughness (μm)
[16]/Bourell et al./(2016)	90	1.4404 Fe ₉₀ -Mn-Ni	Stainless steel 1.4404 (80*30*50) mm ³	1. Scanning electron 2. Microscopy (SEM), 3. Energy-dispersive 4. Spectroscopy (EDS), 5. Disseminated intravascular coagulation (DIC)	50	Solution annealed 980 °C and water quenched	Bonding quality, Surface structure improved	HV (275 ± 8) Porosity (18 ± 6)
[17]/ Arabnejad et al./(2015)	200– 250	10TiO ₂ -Cr ₂ O ₃	CA6NM steel (20 *20*6) mm ³	1. Scanning electron microscopy (SEM)	200–300	Initial 2 h/1080 °C heat treatment coatings are deposited on relatively thin (50–100 μm)	Higher microhardness, better surface finish and lower porosity than Cr ₂ O ₃ coating	HV (259 ± 606) SR (2.91 ± 2.73)
[18]/Syam et al./(2015)	30–40	Fe-C-15.53Cr- 5.15Ni-1.06Si- 0.82Mn	I6Cr5Ni Martensitic stainless steels	1. X-ray diffraction (XRD)	300–350	Temperatures above 1200 ° C Spray distance (mm) 50	Higher tensile toughness and hardness	HV (335 ± 40) Porosity (24 ± 5)
[19]/ Senapati et al./(2015)	150	NiCrBSi	SS304 stainless steel (50*75*80) mm ³	1. Friction stir method (FSP) 2. Rotating disk apparatus (RDA)	20	In vacuum, 1248 °K, 4 h, cooling in a stream of argon of up to 1137 °K for 10 min	Hardness Increased, Erosion is minimized	HV (300 ± 5) SR (4.2 ± 0.2) Porosity (6.1 ± 0.8)
[20]/ Karaoglanli et al./(2014)	55	NiCoCrAlY	AISI 304 stainless steel (200*3*30) mm ³	1. Scanning electron microscopy (SEM), 2. X-ray diffraction (XRD)	64	Cylindrical shape having diameter up to 1–1.2 mm and length from 35 to 45 mm	Microhardness and bending strength improved	HV (275 ± 5) SR (6.2 ± 0.2) Porosity (2.1 ± 0.3)

(continued)

Table 1 (continued)

Reference/author/paper year	Size of coating powder (μm)	Coating powder composition	Parent material composition	Test performed	Coating thickness (μm)	Process parameter of HVOF	Result or conclusion	Microhardness (HV)/porosity (%)/surface Roughness (μm)
[21]/Zhao et al./(2012)	–	MnCr:AlY	In718 stainless steel (5*30*50) mm ³	1. Thermal test	150	Pressure of oxygen equals to 10.3 bars Flow rate of propylene equals to 89 SLPM	Reduction in slurry wear erosion	HV (497 \pm 788) SR (5.72 \pm 1) Porosity (6.32)
[22]/Goyal et al./(2012)	150	WC–Co–Cr	AA5083 (39*20*35) mm ³	1. Scanning electron microscopy (SEM)	150	Particle size equals to 250 μ Velocity equals to 25 m/sec	Corrosion resistance	HV (253 \pm 4) SR (2.91) Porosity (3.1)
[8]/Norouzi et al./(2012)	130	Wt–Cr–Ni	SS306 (90*80*10) mm ³	1. Scanning electron microscopy (SEM), 2. Energy-dispersive spectroscopy (EDS), 3. Pinon disk, 4. Thermal conductivity	130	Specimens in the range of 3–5 mg-cm-2 at 250 °C	Thermal conductivity, better wear resistance occurs	HV (320 \pm 5) SR (3.2 \pm 0.2) Porosity (4.1 \pm 2.3)
[23]/Ialali et al./(2012)	125	Cr ₂ O ₃ –NiCr	SS304 (100*5*50) mm ³	1. Scanning electron microscopy (SEM), 2. Image analyzer, 3. X-ray diffraction (XRD)	150	Fuel kerosene Kerosene flow rate 0.00038–0.00039 m ³ /min Oxygen flow rate 0.85–0.9 m ³ /min Stand-off distance 330 mm Powder flow rate 70 g/min	Lower porosity and surface roughness is lower	HV (323 \pm 26) SR (2.6 \pm 1.2) Porosity (4.2 \pm 5.6)

(continued)

Table 1 (continued)

Reference/ author/paper year	Size of coating powder (μm)	Coating powder composition	Parent material composition	Test performed	Coating thickness (μm)	Process parameter of HVOF	Result or conclusion	Microhardness (HV)/porosity (%)/surface Roughness (μm)
[24]/Mateen et al./(2011)	2–20	WC-17 wt%Co	Stainless steel (9*7*5) mm ³	1. Scanning electron microscopy (SEM)	45	Powder is accelerated at a high velocity (600–1200 m/ s)	Near-nanostructured coating appeared to be denser and free of micro-voids or Porosity	HV (523 \pm 26) SR (3.64 \pm 5) Porosity (4.99 \pm 0.56)
[25]/ Rajasekaran et al./(2010)	–	X190CrVMo20-4	Stainless steel (20*10*10) mm ³	1. Scanning electron microscopy (SEM)	200	Thick (In millimeters) cold Work tool steel coatings can be processed using HVOF	Thicker cold work tool steel coatings can be developed	HV (423 \pm 25) Porosity (5.3 \pm 0.5)

- **Temperature**

The material should have high temperature bearing capacity at the time of coating which is done on the substrate material by the help of thermal spraying technique.

- **Thermal Conductivity**

There should be the low thermal conductivity of the selected material so that the heat transfer to the underneath of the surface would be minimum.

- **Thermal Expansion**

Both the metallic substrate and the coating material should have closely matched thermal expansion so that there would be minimum potential stresses.

- **Porosity**

For the minimum thermal conduction between the coating and the substrate material, the selected material should be having grain and pores on the outer surface.

- **Adhesivity**

There should be the rigid bonding between the coating material and the substrate material so that it would prevent the spalling of the coating from the surface. This adhesivity prevents the material's coating from the sudden impacting of the high flowing water on the surfaces of the blades.

- **Density**

In order to reduce the weight of the coating on the surface, there should be minimum density of the coating material.

4 Case Studies

Arai et al. [1] reported a field study carried out by China North West Electric Power by mounting coated specimens in different places in Kaplan and Francis turbines and left during the flood season. Coated region had reduced the worn out thickness between 5 and 43 mm, whereas the surrounding uncoated metal had been worn down by between 1 and 10 mm. The research program concluded that minimum loss of efficiency can only be reached by a combination of design optimization, based on erosion prediction and protection of surfaces with wears reducing coatings.

Hawley et al. [26] examine the nature of sediment impact of Modi River on turbine specimen using rotating disk. Impact on turbine material test specimen by sediment of Modi River were analyzed in two different ways, firstly impact on four

turbine material specimen of same type, weight, and material by same sand sample and another impact on four turbine material by different three sand samples of eight different locations of Modi River. The result from above experiment has shown that the first location sediment has high eroding property. It has high impact value with weight loss of 7.764 mg on first rotating disk with sand sample of location 1 and least 3.5 mg on third rotating disk by same location sediment but by sand sample 3. The average impact is highest by sediment of location 1 with weight loss of 5.929 mg and least by sand samples of location 8 with weight loss of 4.008 mg. It is evident from the above result that the sediment particles of Modi River have more or less same eroding properties at upstream and downstream. According to above result, they have concluded that the sediments in course of rolling down from

Table 2 Comparative advantages and disadvantages of different types of carbides coating [11, 24]

S. no.	Material	Advantage	Disadvantage
1	Tungsten carbide/cobalt	<ol style="list-style-type: none"> 1. High bond strength 2. Low residual stresses 3. Low porosity (typically lesser than 0.5%) 4. High wear resistance 	<ol style="list-style-type: none"> 1. The coating equipments are quite affordable 2. The process is not well-suited for coating larger objects
2	Titanium nitride (TiN)	<ol style="list-style-type: none"> 1. High hardness and adhesion 2. Good ductility 3. Excellent lubricity 4. High chemical stability 5. Tough resistance to wear, corrosion, and temperature 	<ol style="list-style-type: none"> 1. Films generates were of inferior quality 2. Hardness was lower
3	Titanium aluminum nitride (TiAlN)	<ol style="list-style-type: none"> 1. TiAlN forms a robust bronze outer layer that coats the tool with an exceptionally hard and durable material 2. It retains its hardness even at higher temperatures 3. TiAlN sticks to its target surface through a strong molecular bond which actually forces it to connect right to the substrate metal 	<ol style="list-style-type: none"> 1. Max. temperature only up to 800 °C 2. Mostly applicable on hard materials only
4	Chrome nitride (CrN)	<ol style="list-style-type: none"> 1. Higher temperature resistance than TiN 2. Uniform coating with no build-up on edges 3. Conductive—does not oxidize 4. Environmentally friendly process 5. Extremely strong adhesion—molecular bond to substrate metal 	<ol style="list-style-type: none"> 1. Chrome-lined barrels still need outer surface protection
5	Titanium carbo-nitride (TiCN)	<ol style="list-style-type: none"> 1. High hardness and corrosion resistance 2. Low residual stress 3. Good abrasive wear 4. High reliability in dry operations 5. Uniform under conditions of high load 	<ol style="list-style-type: none"> 1. Max. temperature only up to 398 °C 2. Max. process temperature only up to 448 °C

upstream to downstream its shape and size changes and have less eroding property than one found in upstream of the river.

HVOF cermet's coatings of hard carbide phase tungsten carbide (WC) embedded in ductile matrix; typically coating system consisting of WC-Co, WC-Co-Cr, WC-Ni-Cr, and FeCrAlY-Cr₃C₂ are being used in different industries. The most satisfactory results have been obtained with the powder having carbide content of more than 80% (Table 2).

5 Application

5.1 Turbine Applications

As we have studied that the coating on the turbine runner blades is the most appropriate technique to use the blades again without the replacement. Nowadays, the cost in repairing and the efficiency of the turbine running is the main factor which effects the power generation of the power plant. So people are engaged in developing the never techniques to make the process of turbine repairing more reliable and compatible in every aspects of changes.

5.2 Steel

Typical applications for tungsten carbide-based spray powders include rolls for galvanizing lines in the steel industry. Cermets for coatings on furnace rolls are part of our specialty portfolio as well.

5.3 Oil and Gas

Nickel cobolt chromium aluminum alloy or tungsten carbides powders are highly used in the oil and gas industry because of high standards in wear, erosion, abrasion, and corrosion resistance are the main reasons. Our tungsten carbide products make it possible for applications such as mud pump rotors, ball and gate valves, plungers, and piston rods.

5.4 Pulp and Paper/Printing

Wear resistance is required across the entire range of pulp and paper production. Corrosion makes this production process particularly difficult. Therefore, powders offer ceramic or carbide powders for wear-resistant paper roll coatings [6]. Laser engravable Cr_2O_3 coatings for printing rolls meet all coating layer requirements of this industry.

5.5 Automotive

The development of the automotive industries is making the life easier and reliable, which also results in the growing demand for safe, reliable, and fuel saving vehicles, the automotive industry develops and uses new processes and materials. Also, there are different thermal spray powders can help to reduce friction between piston rings and cylinder bores. T-800 for EGR valves, Mo and NiSF powders are the excellent examples for the piston rings.

6 Result and Discussions

6.1 Mechanical Characterization

Vuoristo et al. [27] the solution was a WC-CoCr coating with thickness of 0.4–0.5 μm thick, in-sprayed condition. Hardness was recorded as 1171 with coating of WC-12% Co.

Stokes et al. [28] hammer peening increases surface hardness of the E309L to level similar to hardness in HAZ. This high level in HAZ is likely due to presence of untempered martensitic. This study induces fatigue failure in the weld material but subsequent testing will occur to determine whether or not the HAZ is weak in fatigue than filler metal.

Rastegar et al. [29] a series of high velocity oxy fuel coating developed are considered to be an excellent replacement of chrome plating. Highly dense chrome-carbide-based HVOF cermet coating was developed and shown to have reasonable crack resistance during service. The ring wear was determined to be six times lower than current chrome. In contrast, liner wear was found to be equivalent to three times higher than chrome under abuse condition.

6.2 Morphology Characterization (SEM and XRD/EDS/XPS)

Goyal et al. [22] the HVOF thermal spraying technique has been used to deposit Cr_2O_3 and $10\text{TiO}_2\text{-Cr}_2\text{O}_3$ coatings on CA6NM steel, resulting in 250 mm thick layer. Porosity of Cr_2O_3 was observed 3.1% and reduced to 2.7% with addition of 10 wt% TiO_2 .

Mann et al. [6] Laser-hardened 12Cr steel has shown excellent performance. This is due to the retention of higher austenitic phase and complete dissolution of carbide. The austenitic phase has an excellent characteristic of absorbing water impact shocks. Later on, it is converted into martensitic phase. Conversion of austenitic phase into martensitic phase has induced compressive stresses on the surface, which are beneficial to overcome impingement erosion.

6.3 Tribological Behavior

Kiragi et al. [11] the erosion mechanism was witnessed from SEM observation reveal mixed ploughing and microcutting, platelet mechanisms were dominant at low operating velocity for both the alloys. However, at high velocity, detachment of peaks and valleys, cracks, abrasion grooves and formation of crater were evident for high operating velocity.

7 Conclusion

Silt erosion in hydroturbines cannot be avoided completely, but excellent materials and surface coating can be used to increase the life of the runner and other underwater parts, which can save the down time, maintenance cost and shall not reduce the power generation capacity of the hydropower plant. Many investigators have studied the erosion behavior of different hydroturbine materials, hard surface coating materials through experimental and analytical studies. Few case studies are also reported in the literature. Some of the investigators have reported that in spite of design changes in the turbine components and providing different materials and coatings to the turbine blades, the improvement in most cases are not quite significant. Hence, further experimental studies are required for studying the effect of hydroabrasive erosion in different base materials and hard surface coatings taking into consideration shape of hydroturbine components and parameters related to silt erosion and operating conditions of hydropower plants.

References

1. Arai T (1995) Coating greatly expands tool life. *Am Mach (USA)* 139(11):37–39
2. Fedrizzi L, Rossi S, Cristel R, Bonora PL (2004) Corrosion and wear behaviour of HVOF cermet coatings used to replace hard chromium. *Electrochim Acta* 49(17–18):2803–2814
3. Bano S, Ahmed I, Grant DM, Nommeots-Nomm A, Hussain T (2019) Effect of processing on microstructure, mechanical properties and dissolution behaviour in SBF of Bioglass (45S5) coatings deposited by Suspension High Velocity Oxy Fuel (SHVOF) thermal spray. *Surf Coat Technol* 372:229–238
4. Barbezat G, Herber R (2001) Breakthrough in improving car engine performance through coatings. *Surface World* 8(8):30
5. Abu-warda N, López AJ, López MD, Utrilla MV (2019) High temperature corrosion and wear behavior of HVOF-sprayed coating of Al₂O₃-NiAl on AISI 304 stainless steel. *Surf Coat Technol* 359:35–46
6. Mann BS, Arya V (2001) Abrasive and erosive wear characteristics of plasma nitriding and HVOF coatings: their application in hydro turbines. *Wear* 249(5–6):354–360
7. Wright PK, Evans AG (1999) Current opinion solid state mater. *Sci* 4:255
8. Jalali Azizpour M, Norouzi S, Mohammadi Majd H, Talebi H, Ghamari A (2010) World academy of science, engineering and technology, Application of HVOF in high speed compressor shaft, 360–362
9. Martín Ó, De Tiedra P, San-Juan M (2017) Combined effect of resistance spot welding and precipitation hardening on tensile shear load bearing capacity of A286 superalloy. *Mater Sci Eng A* 688:309–314
10. Sharma V, Kaur M, Bhandari S (2019) Slurry jet erosion performance of high-velocity flame-sprayed nano mixed Ni-40Al₂O₃ coating in aggressive environment. *Proc Inst Mech Eng J* 233(7):1090–1106
11. Kiragi VR, Patnaik A, Singh T, Fekete G (2019) Parametric optimization of erosive wear response of TiAlN-coated aluminium alloy using Taguchi method. *J Mater Eng Perform* 28(2):838–851
12. Kumar H, Chittosiya C, Shukla VN (2018) HVOF sprayed WC based cermet coating for mitigation of cavitation, erosion & abrasion in hydro turbine blade. *Mater Today Proc* 5(2):6413–6420
13. Curtat JL, Lanteigne J, Champliand H, Liu Z, Lévesque JB (2017) Influence of hammer peening on fatigue life of E309L steel used for 13% Cr-4% Ni blade runner repairs. *Int J Fatigue* 100:68–77
14. Mohan P, Elshalakany AB, Osman TA, Amigo V, Mohamed A (2017) Effect of Fe content, sintering temperature and powder processing on the microstructure, fracture and mechanical behaviours of Ti-Mo-Zr-Fe alloys. *J Alloy Compd* 729:1215–1225
15. Sames WJ, List FA, Pannala S, Dehoff RR, Babu SS (2016) The metallurgy and processing science of metal additive manufacturing. *Int Mater Rev* 61(5):315–360
16. Bourell DL (2016) Perspectives on additive manufacturing. *Annu Rev Mater Res* 46:1–18
17. Arabnejad H, Mansouri A, Shirazi SA, McLaury BS (2015) Development of mechanistic erosion equation for solid particles. *Wear* 332:1044–1050
18. Syamsundar C, Chatterjee D, Kamaraj M (2015) Experimental characterization of silt erosion of 16Cr–5Ni steels and prediction using artificial neural network. *Trans Indian Inst Met* 68(4):587–599
19. Padhy M, Senapati P (2015) Turbine blade materials used for the power plants exposed to high silt erosion—a review. In: ICHPSD
20. Karaoglanli AC, Caliskan H, Gok MS, Erdogan A, Turk A (2014) A comparative study of the microabrasion wear behavior of CoNiCrAlY coatings fabricated by APS, HVOF, and CGDS techniques. *Tribol Trans* 57(1):11–17

21. Zhao Y, Shinmi A, Zhao X, Withers PJ, Van Boxel S, Markocsan N, ... Xiao P (2012) Investigation of interfacial properties of atmospheric plasma sprayed thermal barrier coatings with four-point bending and computed tomography technique. *Surf Coat Technol* 206 (23):4922–4929
22. Goyal DK, Singh H, Kumar H, Sahni V (2012) Slurry erosion behaviour of HVOF sprayed WC–10Co–4Cr and Al₂O₃ + 13TiO₂ coatings on a turbine steel. *Wear* 289:46–57
23. Jalali Azizpour M, Sajedipour D, Moh. Majd H, Birgani MRT, Rabiae M (2012) World academy of science, engineering and technology. Impact temperature in splat and splat substrate Interface in HVOF thermal spraying, 576–578
24. Mateen A, Saha GC, Khan TI, Khalid FA (2011) Tribological behaviour of HVOF sprayed near-nanostructured and microstructured WC-17wt.% Co coatings. *Surf Coat Technol* 206 (6):1077–1084
25. Rajasekaran B, Mauer G, Vaßen R, Röttger A, Weber S, Theisen W (2010) Thick tool steel coatings using HVOF spraying for wear resistance applications. *Surf Coat Technol* 205 (7):2449–2454
26. Hawley D (2006) A promising new tool for thermal spraying. *Weld Cutting* 5(1):38–43
27. Petri MJ, Vuoristo PM (2007) High velocity sprays boost hard metal industrial coatings. *Met Powder Rep* 62(3):22–29
28. Stokes J, Looney L (2001) HVOF system definition to maximise the thickness of formed components. *Surf Coat Technol* 148(1):18–24
29. Rastegar F, Richardson DE (1997) Alternative to chrome: HVOF cermet coatings for high horse power diesel engines. *Surf Coat Technol* 90(1–2):156–163

Study on Tribological Behavior of HVOF Developed Coatings Especially for Hydroturbine Runner Application— A Concise Review



Adheesh Tripathi , Aman Pandey , Aakash Rathore ,
Abhishek Singh , and Mohit Vishnoi 

Abstract This paper presents the study of different investigations on the wear behavior of coating materials like tungsten carbide with traces of cobalt, nickel and rare earth elements. The main objective of this paper is to study the effect of different parameters of a coating such as impingement velocity, particle size and angle of impingement. Hydro turbine runners made up of different steel grades were coated with different thermal spraying techniques such as High Velocity Oxy-Fuel (HVOF). The life of a hydro turbine runner mainly depends on the method and the material of the coating. The paper discusses different environmental conditions respective to the effective working of coating materials.

Keywords Tribological · Corrosion · Erosion · Abrasion · Hydroturbine runner · HVOF coating

A. Tripathi · A. Pandey · A. Rathore · A. Singh · M. Vishnoi (✉)
Department of Mechanical Engineering, J S S Academy of Technical Education,
Noida 201301, India
e-mail: vishnoi.mohit06@gmail.com

A. Tripathi
e-mail: adheeshtripathi97@gmail.com

A. Pandey
e-mail: amanpandey1307@gmail.com

A. Rathore
e-mail: aakash02rathore@gmail.com

A. Singh
e-mail: singh1abhi2@gmail.com

1 Introduction

Apparently, hydropower is the world's largest renewable power source, and in many areas the capacity remains untapped. This resource may be used on an ongoing basis to address world electricity requirements.

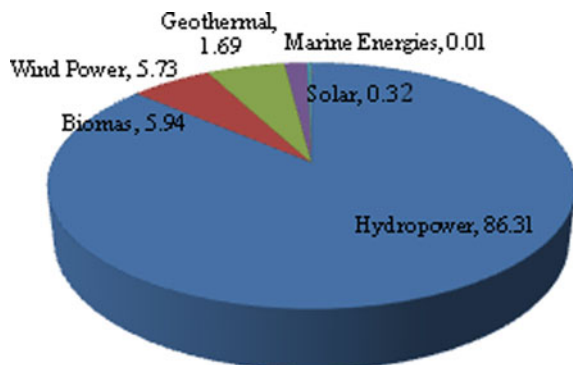
Most of the renewable energy is produced by hydropower plants. They generate 86.31% of renewable energy. According to Lejeune et al. [1], the renewable energy sources used since 2008 are shown in Fig. 1.

Given pie chart values reflect the significance of hydropower growth which qualifies importance of other alternatives, for instance, biomass, wind, geothermal, solar, and marine energy. However, there are some obstacles such as building, operational, and maintenance problems that may attenuate the plant's potential to harness electricity. Such hindrance is the hydroturbine failure where corrosion, erosion, and abrasion, or combinations of these processes, are the main cause of material degradation. India is more susceptible to such failures due to the presence of silt in river water during season of monsoon. Consequently hydroelectric project sites in the Himalayan range and India's north-eastern states witness severe erosion. Unsettled particles of silt after bypassing tank strikes turbine runner and other underwater components repercussions of which are eroded turbine blades and rest underwater parts in proximity [2]. The silt consists mainly of quartz with a Mohr hardness scale of 7 [3–7].

Due to its high temperature working range of 2500–3200 °C and strong mechanical properties such as hardness and durability and improved binding ability, high-velocity oxy-fuel thermal spraying method has been found prevalent for coating substrate materials such as stainless steel and aluminum [8, 9].

Being lighter in weight and cost effective, aluminum makes it a suitable material for industrial use. However, due to some of its poor mechanical properties, pure aluminum cannot be used for direct use, so it is either coated or alloyed with different elements to improve its longevity and reliability. WC–Co, CrC, CrN, and TiAlN coatings have been used in various methods for substratum metal coating, and they all have different properties and have varying effects on the surface of the

Fig. 1 World's Renewable Energy Harnessed as of 2008, [1]



substratum. To strengthen the resistive properties of the film, rare-earth metals and their oxides were alloyed with the coating film. Adding Zr–Y to the TiAl coating increases oxidation resistance 8 times greater than that of TiAl alone and 3 times greater than that of Zr alone [10].

High-speed impingement of water has to be sustained by hydroelectric power plants; hence, they should have excellent corrosion and wear resistance properties in addition to low density to improve their working efficiency [3]. Turbine production decreases with erosive wear and leads to the final breakdown of the turbine. The blades are therefore coated with materials that reduce the wear rate and increase the surface's tribological properties.

Case studies show how various issues and situations have occurred in which the hydropower projects have encountered difficulties due to erosion and wear of blade material. This mainly resulted from silt erosion and made the plant with tremendous loss and reduced production. The silt content of water at the Salal hydropower station indicated 75–98% quartz hardness of 7–8 on Mohr's scale. Guide vanes made from 13Cr4Ni stainless steel lost approximately 10–15% of the build weight after being in service for 4000 h [12].

2 Causes and Failure of Turbine

Hydroelectric power plant components must withstand high-speed impingement of water; therefore, they should have excellent corrosion and wear resistance properties besides low density. Mixed plowing and cutting, platelet formation, abrasion grooves, and cracks are the primary mechanisms which cause loss of coating. Responsible control parameters are velocity of impact, angle of impingement, rate of feed for eroding, and eroding scale. In addition to these coating thicknesses, binding strength, hardness with reduced porosity, and defects are essential features needed for better coating performance in erosive setting. While erosion results in the gradual removal of material, continuous removal of equipment can prove fatal [12]. Repetitive deformation and cutting behavior engender erosive wear. Another form of abrasive wear is sand erosion. As a result, oxide layer on the flow guiding surfaces is impaired which partially renders the surfaces rough which can precipitate cavitation erosion. Turbine output decreases with erosive wear and contributes to final turbine breakdown [11]. The brittle coating mode tends to increase and hit zenith at 90° while the ductile mode takes place at much lower angles of impingement.

Considering the velocity of the impingement particles, the shielding effect displayed by the rebounding particles will be very profound as opposed to the high-velocity state as carrier fluid is gas, essentially air. Hence, the erosion rate will decrease with an increase in concentration at low velocity. However, at high speeds, the rate of erosion with concentration may increase due to reduced shielding effect [13]. Increased vibration, alteration in blade profile, fatigue damage, lack of efficient operation, and failure in system in the hydroturbines are the corollaries of

erosion [14]. Driver, bins, nozzles, spear suffer drastic damage by slurry erosion in case of impulse turbine and impeller blades, guidance vanes and complex seal in reaction turbines [15]. Plastic deformation and chip deformation are consequences of the effect of small particles and/or low velocities while flaking results in larger particles and/or high velocity effects [16]. Metallic chromium coatings containing up to 10–15% of nitrogen can have usefully high levels of “ceramic” hardness (i.e., 15 GPa or more), while maintaining the metal’s elastic properties [17].

3 Turbine Materials

Full replacement of mechanical elements due to output losses and maintenance shutdowns are supplanted by surface coating in most components. In the automobile, power generation and oil extraction industries, AISI 4140 steel is universally accepted [18].

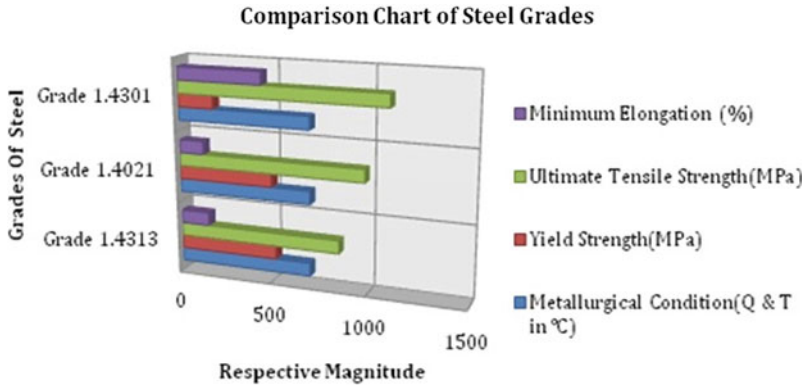
Generally, turbines are made with aluminum and steel but hydroturbine runners are commonly made of stainless steel alloys. Owners’ requirements for new and replacement runners are often unclear about the form of “stainless steel” or the production process to open the market to the most innovative and least expensive bids. There are several types of stainless steel alloys in the market. The styles—known as “martensitic” and “austenitic” or even “duplex”—were used to manufacture runners, and the latter were also used on carbon steel runners as corrosion- and cavitation-resistant overlays. Stainless steel relies for its corrosion resistance on a thin passive film. The film naturally forms on air-exposed clean surfaces and is rich in oxides of chrome. To impair atmospheric corrosion resistance to moderate amount, steel must have minimum 10.5% chromium, but for pragmatic applications 12% chromium is required. Increasing the chromium content to 17–20% makes it more robust and hence the aqueous corrosion is attenuated significantly [19].

Corrosion resistance is of paramount importance in parts of hydroturbines in which contact of water is mainly with dynamic parts.

Good resilience to cavitation erosion is of supreme importance in high speeds of impulse turbines and high flow rates of Kaplan and Francis turbine. Large-scale turbines employ use of grades 1.4418 and 1.4313 [20].

As far as aluminum is considered, pure aluminum is not suitable for construction as its tensile strength and hardness are low. But its special feature is its low density and its ability to form oxides further impedes oxidation. New formation of alumina starts simultaneously in case of impairment of this layer. Hence, to bolster its mechanical properties such as hardness, toughness, wear resistance, etc., it must be coated with a suitable composition.

To engage aluminum in applications requiring high hardness and wear resistance, arduous efforts are being made. With addition of elements such as Ti, B, Cu, Fe, Si, toughness is improved to large extent. Fine-grained structure is the prime reason of augmentation in toughness. By adding traces of Ti, B, Cu, Si, Fe, enhanced toughness can be achieved [21] (Fig. 2).



Grades	Corrosion Resistance	Main Application
1.4313 ACI CA6NM	Cavitation Damage Resistant	Runners and Guide Vanes
1.4021 AISI 420	Wear Resistant	Nozzles and Wear Rings
1.4313 AISI 304 ACI CF3	Good Corrosion Resistant	Housing and Casings

Fig. 2 ISSF stainless steels in microhydroturbines [20]

Grades	Corrosion resistance	Main application
1.4313 ACI CA6NM	Cavitation damage resistant	Runners and guide vanes
1.4021 AISI 420	Wear resistant	Nozzles and wear rings
1.4313 AISI 304 ACI CF3	Good corrosion resistant	Housing and casings

4 Coating Materials

Over the past 100 years, chromium-based and tungsten carbide-based coatings have attracted the attention of thermal spraying researchers. The inventor of thermal spraying, Max Ulrich Schoop, made the first attempts using a simple technique of flame spraying technique [22]. During this time, the performance of carbide coatings is improved.

Tungsten carbide coatings provide a wide range of industrial applications in order to protect mechanical parts from sliding and abrasive damage at different temperatures. The decomposition of WC-Co powder precipitates multiphase microstructures of sprayed WC-Co coatings. The breakdown of carbide in the molten matrix which is followed by subsequent decarburization is directly influenced by the degree of decomposition; temperature, carbide grain size, and time (or velocity) are the influencing factors and insinuate to alter wear characteristics as

well. The dimensions and volume of feedstock and matrix composition of the WC material are primary factor in determining properties of WC–Co–Cr coatings [23]. Figure 3 gives both candidate materials and advanced coatings corrosion check data.

The effects of corrosion indicated in Fig. 3 show that HVOF WC10Co4Cr (58 times better than steel X20Cr13) is the best erosion-resistant material for this application, followed by TiAlN PVD (25 times better than steel X20Cr13) and Armcore “M”.

HVOF-coated (both grades) Stellite is around 2–2.5 times stronger than stainless steels. Stellite welded grades are around 1.5–1.6 times higher than the X20Cr13 material.

The advanced TiAlN PVD coating performed very well, but the HVOF WC10Co4Cr coating is no better than stainless steel.

The WC10Co4Cr and Armcore “M” HVOF coatings were solid, free of any cracks, but there were a few surface cracks in the Stellite 6 and 12 HVOF coatings that were subsequently eliminated by modifying some of the parameters.

The lower thermal expansion of these materials would have caused these cracks, close to carbide and Armcore “M” coatings. Precautions to reduce or increase some cracks are obligatory for deposition of Stellite 6 and 12 HVOF [24].

In hydroturbines, for turbine runner and slurry pumps 13Cr-4Ni steel is mostly employed. Despite their excellent mechanical properties, they are susceptible to erosive wear.

WC has melting point of 2800 °C. It is pertinent for applications involving temperature less than 500 °C. At high temperature, it is vulnerable to oxidation. WC–Co is used to increase wear resistant in aeronautical applications. Carbon-based coating is used in abrasive, erosive, and oxidizing environment. CrC can be used for higher temperature applications (540–815 °C) [9]. It can resist oxidation up to 850 °C [25].

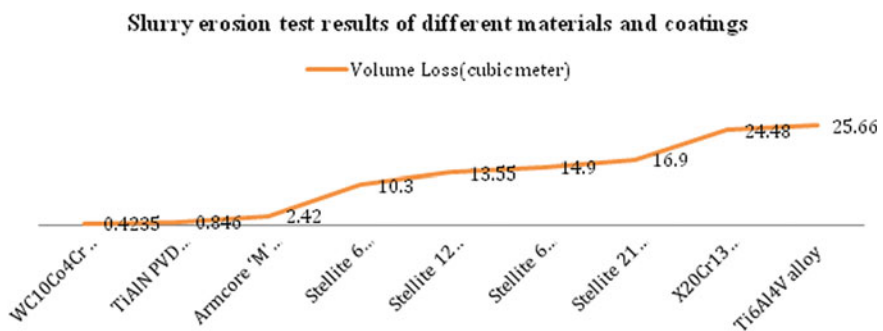


Fig. 3 Test conditions: Eroding form, mineral sand of 1100 HV hardness; eroding thickness, –40 to +80 mesh; silt concentration, 25.000 ppm; water velocity, 18.2 m/s; indentation angle, 60°; water temperature, 28 °C; chamber pressure, atmospheric; experimental error, ±3.0%; specimen size, 50 mm approx. 50 mm approx. 6 mm thick; test period, half an hour [24]

CrN is high in hardness, wear resistance, chemically inert, and ideal for corrosion testing. Cr has friction coefficient 1.5 times less than that of AISI 304. Stainless steel specimen coated with CrN showed improved corrosion resistance as high as 4000 times as substrate material. TiAlN is an ultra-hard coating which can brook temperature up to 800 °C. As a consequence of its low thermal conductivity, it protects the tool against damage due to high temperatures [26]. Reduced friction coefficient results in high hardness and wear resistant [27]. Nb and Ta can also be incorporated to enhance oxidation resistance above 800 °C [28].

Having exceptional oxidation resistance, microstructural stability at high temperature up to 850 °C [28], Gamma TiAl is considered for high temperature applications (600–850 °C) [29]. At temperature higher than 850 °C, it is vulnerable to oxidation. To increase its oxidation at such higher temperatures, Cr is incorporated into TiAl. Oxidation is precipitated due to intermixed scales of TiO₂ and Al₂O₃ which are protective only till 800–850 °C. TiO₂ acts as transport path resulting in interstitial O₂/N₂ dissolution at high temperature which degrades mechanical properties. Cr forms laves phase Ti(CrAl)₂ which produces continuous scales Al₂O₃, thus increases its oxidation resistance [29].

The E-C 29123 coating applied by oxy-fuel powder (OFP) process onto AISI 304 stainless steel mostly enhanced the slurry erosion resistance of the studied materials. Ambivalent properties of hard, wear-resistant particles, and a ductile metallic matrix are responsible for enhanced resilience against slurry erosion [30].

Single layer structures are superseded by multilayer coatings and super-lattices for being better alternatives [31].

Apart from layering, with respect to the coating materials, many properties like high hardness, low coefficient of friction, high stability, high insulation, good wear properties, and transparency are traits of alumina (Al₂O₃) and titania (TiO₂) [14]. Furthermore, composite coatings encapsulating hard reinforcing phase embedded in a tougher matrix material could acquire disparate properties [32].

Wear and oxidation resistance of the cermet were significantly enhanced by including Cr in the coating matrix [33]. The wear of ceramic combinations is generally one or two order times less than other materials [34].

5 Thermal Spray Techniques (Preference of HVOF Over Others)

The method of high-velocity oxy-fuel (HVOF) belongs to a family of thermal spraying technologies is used to boost the surface properties of the base materials. Compared with plasma spray coatings, HVOF coatings have comparatively less porosity. In the corrosion resistance of thermal spray coatings surface porosities play pivotal role, there is extensive study of HVOF coatings for their corrosion-resistant properties. The composition of HVOF coatings, by comparison, is almost identical to that of spraying powder. Marine, aircraft, automotive, and

other industries inculcate copious applications of HVOF sprayed coatings. The Amoco Oil Company regularly uses the HVOF process by applying coatings AISI 316 L and Hastalloy C-276 [35] to recover a wide variety of petrochemical plant components such as storage tanks, heat exchangers, tube end fittings, and valves that are subject to extreme erosive, rust and corrosive conditions.

HVOF thermal spraying is a process by which the powder material is melted and moved at high speed to a substrate, using oxygen and fuel gas mixtures. Propylene, propane, hydrogen, acetylene, ammonia, ethylene, SPRAL 29 kerosene, MAPP (methylene-propadien-stabilized gas), LPG, etc., are used for combustion.

The HVOF system consists of a spray gun, an air and gas supply unit, a powder feed unit, and a flow meter unit. The feed unit for the powder consists of a hopper assembly, air vibrator, feed rate meter, and control cabinet. The desired powder is fed to the gun through a carrier gas from the powder feed unit, where combustion occurs. Using the powder feed rate meter, the amount of powder necessary for deposition can be controlled. Depending upon the melting temperature and feed rate of the fuel, the powder fuel is molten after it reaches the flame in the combustion zone.

For the HVOF cycle, the flame temperature is about 3000 °C. The gun nozzle ejects the molten or semi-molten particles onto the substrate at supersonic velocities, where the substance is deposited. Speeds of 300–800 m/s are reached by particles usually in the range of 10–63 at the substrate to be coated [35].

The technique can create dense coatings with negligible degradation and oxidation of metallic materials because of the short dwelling time. HVOF has a lower temperature than plasma spray process [8, 9]. A high HVOF ability provides high strength coating, durability, wear resistance, lower porosity, and lower binding capacity defects. The production of HVOF spraying increased the use of hard metals as coating dramatically, creating very dense and highly adherent coating with low residual tensile stress [12]. Grit blasting is used before deposition to improve improved binding capability between the coatings and the target material. By increasing the roughness of individual location, it provides better binding capacity to coat on substratum. Coating properties are also produced with negligible porosity [12] (Table 1).

6 Behavior of Rare-Earth Metals in HVOF Coating

While using the optimized thermal spray process, adding Zr–Y to TiAl coating improves 8 times oxidation resistance than TiAl alone and 3 times better than Zr alone [10]. Zr and Y combine faster with O₂ hindering it to disseminate into layers to fully oxidize Ti atoms. Outer layer consists of ZrO₂, Y₂O₃ while inner layer consists of Al₂O₃, Ti₄O₇ thus more protective than TiAl alone.

Table 1 Compares properties of different thermal spraying process for WC-Co coating [35]

Deposition technique	Heat source	Propellant	Typical temperature (°C)	Typical particle velocity (ms^{-1})	Average spray rate (kg hr^{-1})	Coating porosity (% by volume)	Relative bond strength
Flame spraying	Oxyacetylene/ Oxyhydrogen	Air	3000	30–120	2–6	10–20	Fair
Plasma Spraying	Plasma Arc	Inert Gas	16,000	120–600	4–9	2–5	Very Good to excellent
Low-pressure plasma spraying	Plasma arc	Inert gas	16,000	Up to 900	–	<5	Excellent
Detonation gun spraying	Oxygen/acetylene/ nitrogen gas detonation	Detonation shock waves	4500	800	0.5	0.1–1	Excellent
High-velocity oxy-fuel (HVOF)	Fuel gases	Combustion jet	3000	800	2–4	0.1–2	Excellent

La, Y, Ce can be used to reduce oxidation rate and improving corrosion rate. Incorporating Y to coating material bolstered non-oxidizing ability of alloy powders hence reduces oxygen content. Carbide is formed uniformly due to addition of Mo which bolsters mechanical properties such as shock property. Nb strongly forms carbide and effectively refines grains which ultimately enhance mechanical properties. With addition of rare-earth elements, uniform structure with high density coating is deposited [36].

7 HVOF in Hydroturbines

At the end of the 1980s, METCO launched the new Diamond Jet TM high-speed fuel oxygen spray (HVOF) package. This new technology was apt for the laboratory and as well as for mundane. The earliest attempts at the front sleeve were very successful and the number of components to which tungsten carbide (WC-Co-Cr) materials were applied inflated rapidly. This latest HVOF covering surpassed the highest standards for the length of the part achieved.

Although turbine steel material erosion (1.4313) was reduced by a factor of 50, the transformation from the very thick layers typical then (e.g., 10 mm thick wire combustion-sprayed Metcoloy 2) to the thinner, but still more erosion-resistant, HVOF-sprayed carbide coatings was initiated. Figure 4 demonstrates a comparison of the wear properties of various surface coatings with HVOF technique. The dominant position of the HVOF process is evident with WC-Co-Cr as the coating material [37].

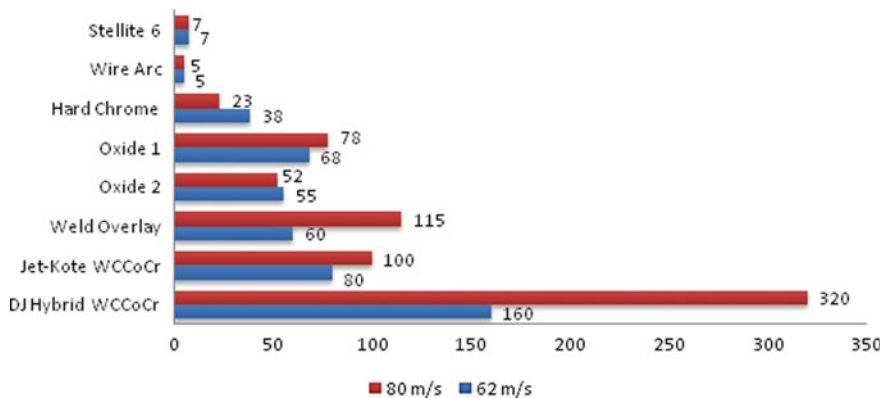


Fig. 4 Resistance to corrosion of the different materials and surface systems after HVOF spraying method [37]

8 Recent Advancement in HVOF Coating

Lots of researches are going on in the field of HVOF coating because it has a great advantage over other methods of thermal spray coating. According to the literature survey, after coating on the metal or alloy sheet, the authors found that HVOF coating induces uniform coating thickness and high hardness. For this, they conducted an experimental research on the effect of different parameters on the coating.

The HVOF coating was applied to aeronautical purposes on the AISI 4340 steel plate. The sheet had hard chromium coated. This study's main objective was to equate HVOF's coating with other methods. It was noticed after that HVOF provides high hardness and lower percentage porosity. In accordance with the works of different researches, the repercussions of surface modification on heat cycling life barrier coating with HVOF, Ni-Cr-Al-Y bond coat was explored with the experiment on other methods of surface alteration such as grit blowing, shot peening, etc. It was found that bond coat has high strength and low hardness [38].

Cinca Nuria described the wear and corrosion of the TiC metal coating matrix. Developments in the various spraying technologies such as plasma and high-velocity oxy-fuel have been made to obtain TiC-stainless steel or NiTi matrix coatings. SHS engineering has acquired the starting feedstock powders. The fraction of particles between 20 and 63 μm was selected for thermal spray after crushing and sieving. XRD and SEM-EDS have identified the coatings obtained for surface and cross-sectional inspection. Coatings and electrochemical corrosion testing are performed for adhesion wear (ball on disk and rubber surface tests) [39].

The coating properties such as stiffness, crystalline form, strength of fracture, thickness per pass, and resistance to abrasive wear were investigated. Fatigue strength was found to be better compared to other approaches. Ragupathy et al. established an empirical relationship between WC10Co-4Cr HVOF sprays coatings to predict hardness in which he clarified the result on the toughness of the coatings, and the author used the four parameters as oxygen flow rate, powder feed speed, LPG flow rate, standoff range, etc., to define the relationship [40] (Table 2).

9 Case Studies

The obstacle posed by silt erosion is more idiosyncratic to Indian conditions, and therefore more data generation efforts are needed.

Studies have disclosed that,

1. There was abstemious abrasion for all particles below 0.05 mm and increased for greater diameters.
2. Operating head product H and harmful sediment content ($d > 0.05$ mm) must be less than 7 to hold erosion at its nadir.

Table 2 Various studies on HVOF by different researchers (2019–2020)

Reference/ author/paper year	Size of coating powder (μm)	Coating powder composition	Parent material	Test performed	Coating thickness (μm)	Process parameter	Conclusions	Microhardness (HV)/ porosity (%) / surface roughness (μm)
[41] Thermsuk et al. (2019)	–	WC-12Co	SUS400	Central composite design (CCD)	322.0816	1. Oxygen flow rate (280 L/min) 2. Propane flow rate (19 L/min) 3. Powder feed rate (107 g/min) 4. Spraying distance (260 mm)	Increased harness, reduced porosity, reduced surface roughness	Hardness: (1288.6306 HV) Porosity: (0.0721% vol) Surface roughness: (6.5551 μm)
[42] Liu et al. (2019)	15–45	WC-12Co WC-17Co	ICH18Ni9Ti	1. Scanning electron microscope (SEM) 2. Laser scanning confocal microscopy 3. X-ray diffraction (XRD) 4. Vickers hardness tester 5. Cavitation Erosion Test	232 \pm 9 μm 221 \pm 6 μm	1. Oxygen flow rate (950 L/min) 2. Kerosene flow rate (22 L/min) 3. Powder feed rate (100 g/min) 4. Spray distance (420 mm)	Increased cohesion, reduced porosity, surface roughness, improved fracture toughness and resistance, [reduced hardness due to increase in Co	Hardness: (1181 HV and 1121 HV) Porosity: (0.84%) Surface roughness: (2.47 μm)
[43] Zouari et al. (2019)	NiCrBSi 25 microns 316L SS 17 microns	NiCrBSi 316L SS	Brass (Cu/Zn ₄₀ /Pb ₂) substrates	1. Scanning electron microscope (SEM) 2. 3D profilometer 3. Salt fog test 4. X-ray spectroscopy (EDS) 5. Tensile test	195 \pm 12.5 μm 158.5 \pm 24 μm	1. Pressure (4 bar) 2. Oxygen flow rate (180 NL/min) 3. Methane flow rate (180 NL/min) 4. Nitrogen flow rate (carrier for feedstock powder, 40 NL/min) 5. Spraying distance (280 mm)	More defects such as micropores, un-melted particles and oxides on the 316L SS coating, compared to the NiCrBSi coating, 316L SS coatings presented a lower microhardness and higher adhesion strength than the NiCrBSi coatings despite their lower corrosion resistance, increased bond strength	Hardness (643.14 \pm 29 HV to 469.13 \pm 23 HV) Porosity (0.24 \pm 0.2% to 0.22 \pm 0.2%) Surface roughness (6.92 \pm 1.2 μm to 7.10 \pm 1.6 μm)

(continued)

Table 2 (continued)

Reference/ author/paper year	Size of coating powder (μm)	Coating powder composition	Parent material	Test performed	Coating thickness (μm)	Process parameter	Conclusions	Microhardness (HV)/ porosity (%) / surface roughness (μm)
[44]/Zhang et al./2019)	5.6 ± 15.6	TiO ₂ nanopowder (Aeroxide P25)	SS304 (25 mm × 25 mm × 1.5 mm)	Scanning electron microscopy (SEM), X-ray diffraction (XRD) Nano-indentation	5.6 ± 15.6	UTP Top Gun torch with a 22 mm long combustion chamber and a 135 mm long expansion nozzle mounted on an OTC AII-Y20 robot At 55 °C	Increase in overall hardness, wear resistance not rational to the hardness	HV: (2.1 ± 7.8) SR: (0.53 ± 1.18)
[45]/ Kiiakoski et al./2019	(5–10)	Cr ₂ O ₃ powders with TiO ₂	Steel	Scanning electron microscopy (SEM)	(5–10)	Suspension feed rate of up to 53 g/ min at 250 °C and at load 300 gm	Hardness was lower and the roughness higher Cavitation erosion tests were performed with an ultrasonic transducer	HV (1350–1400)
[46]/Inam et al./2020	200	Nichrome wires having 80% Ni and 20% Cr	304L (305±305±3) mm ³	1. Scanning electron microscopy (SEM), 2. Light optical micrographs	200	Coatings were deposited by placing coating gun at an angle of 90° through 4–6 numbers of passes	Increase in porosity, less surface roughness, increase in hardness	SR (13.51) HV (46.3)
[47]/ Eishakany et al./2019	(55 ± 17) And (64 ± 20)	NiCoCrAlY (Ni 23Co 17Cr 12Al 0.5Y wt %) And CoNiCrAlY (Co 32Ni 21Cr 8Al 0.5Y wt%)	SS304 (200 mm × 30 mm × 3 mm)	Scanning electron microscopy (SEM), X-ray diffraction (XRD)	(388 ± 21.87) (HVOF)	Coatings were deposited by a spray gun CDS-80,000 with particles velocity at around 300 m/s and a peak temperature of 3200 °C	Increase in hardness, bending strength coating was poor	SR (5.1 ± 0.5)
[48]/Pulsford et al./2020)	45/5	NiCrFeSiB	WC-Co	Scanning electron microscopy (SEM), X-Ray diffraction(XRD)	NiSF_HF = 518 ± 11 NiSF_LF = 576 ± 8	Gas flow rate	Improved sliding wear resistance	HV (14,293 + 1,393) Porosity: NiSF_HF = 0.3 ± 0.1 NiSF_LF = 1.3 ± 0.2

(continued)

Table 2 (continued)

Reference/ author/paper year	Size of coating powder (μm)	Coating powder composition	Parent material	Test performed	Coating thickness (μm)	Process parameter	Conclusions	Microhardness (HV)/ porosity (%) / surface roughness (μm)
[49]/ Pulsforda et al./2019	D90(18-24) D10(5-8)	WC-10Co-4Cr	416 stainless steel ($0.38.1 \times 6 \text{ mm}^2$)	Scanning electron microscopy (SEM), X-ray diffraction (XRD)	ID70(224 \pm 7) ID90(214 \pm 7) ID110(129 \pm 4)	Internal diameter of pipes	Low specific wear rate	Vickers microhardness: ID70(1201 \pm 106) ID90(1319 \pm 40) ID110(1310 \pm 52)
[50]/ Amousoliani et al./2020	35 \pm 10	WC-12Co	ST-37 carbon steel ($0.50 \times 5 \text{ mm}^2$)	Scanning electron microscopy (SEM), X-ray diffraction (XRD)	583 \pm 10	Spraying distance, oxygen liquid fuel, powder feed rate	Enhanced corrosion and wear resistance	HV (1.2590 \pm 150) Porosity (1.3) SR (5 \pm 0.5)
[51]/Sharma et al./2019	–	WC-10Co-4Cr	CF8M	1. Scanning electron microscopy (SEM), 2. X-ray diffraction (XRD) 3. Optical microscopy	200	Multidimensional, nano-structured coating	Increased resistance against wet abrasive impingement	HV (1120) Porosity (1.7)
[52]/ Tillmann et al./2019	–15 + 5 μm	WC-CoC 86- 10-4	C45 steel (70 \times 50 \times 10 mm) (1.0503; 258 \pm 4 HV0.3)	1. Scanning electron microscopy (SEM) 2. Vicker hardness test	–	Spray angle [90°] Gun velocity [30.00 mm/s] Backside cooling pressure [30 psi] Powder carrier gas flow [10 l/min]	Low porosity (0.9%) and reduced (Rz 13.8 μm) were achieved. Furthermore the MH and DE were significantly lower than predicted	HV (1030,33) SR (13.8) Porosity (0.9)

(continued)

Table 2 (continued)

Reference/ author/paper year	Size of coating powder (μm)	Coating powder composition	Parent material	Test performed	Coating thickness (μm)	Process parameter	Conclusions	Microhardness (HV)/ porosity (%) / surface roughness (μm)
[53] Mätkäinen et al./2020	-38 + 10 or -45 + 15	Cr ₃ C ₂ - 50NiCrMoNb	low carbon steel substrates (S235) (200 × 50*5 mm)	1. Scanning electron microscopy (SEM)	-	Oxygen—240 slpm Air 383 slpm Spray distance 230 mm Surface speed 0.8 m/s Spray pass spacing 5.4 mm Powder feed rate 130-200 g/min 60 g/min	The abrasion and dry particle erosion resistance of the coatings increases	Microhardness (806) Porosity (0.8) Fracture toughness (4.9 MPa.m ^{1/2})
[54] Praveen/ 2020	12	NiCrSiB + 1.4 wt% nano-Al ₂ O ₃	AISI 304 stainless steel (25 × 25 × 6 mm)	1. Scanning electron microscopy (SEM) 2. X-ray diffraction	250 ± 30 μm	Temperature (450 ° C) Feed rate (5 g min ⁻¹) Velocity (40 m s ⁻¹)	A lamellar structure of deformed dark Al ₂ O ₃ reinforcing phase with grey Ni phase is formed	Porosity (%) 1.8 ± 0.65 Surface roughness (μm) 8.5 ± 1.5 Microhardness (HV0.3) 748 ± 80

In another case study of the Salal hydropower station, water silt content suggested the existence on Mohr’s scale of 75–98% hardness quartz 7–8. The loss was around 10–15% of design weight after 4000 h of service guide vanes made of stainless steel 13Cr4Ni.

Traditional design requirements for 0.2 mm sediment trapping have proved to be useless in the service of river power plants in steep sediment-filled rivers. Projects have usually been abandoned due to significant silt erosion. A profound dependence has been identified between the sediment load to which the turbine was susceptible and the corresponding decrease in output. Output loss after extrapolation was 4% at the maximum output and 8% at 25% load.

WC thermal spray coating was applied on site at Svartisen hydroelectric plant (Norway) and was chosen as a refurbishment process and to increase turbine life to 16 years. The results continued to meet their standards in a survey that was conducted two years later.

For Tiloth Hydropower Station on Bhagirathi River, on Mohr’s scale, the source of corrosion was mainly silt particles with hardness 7. In rainy season, their concentration increased to 4000 ppm [11] (Fig. 5).

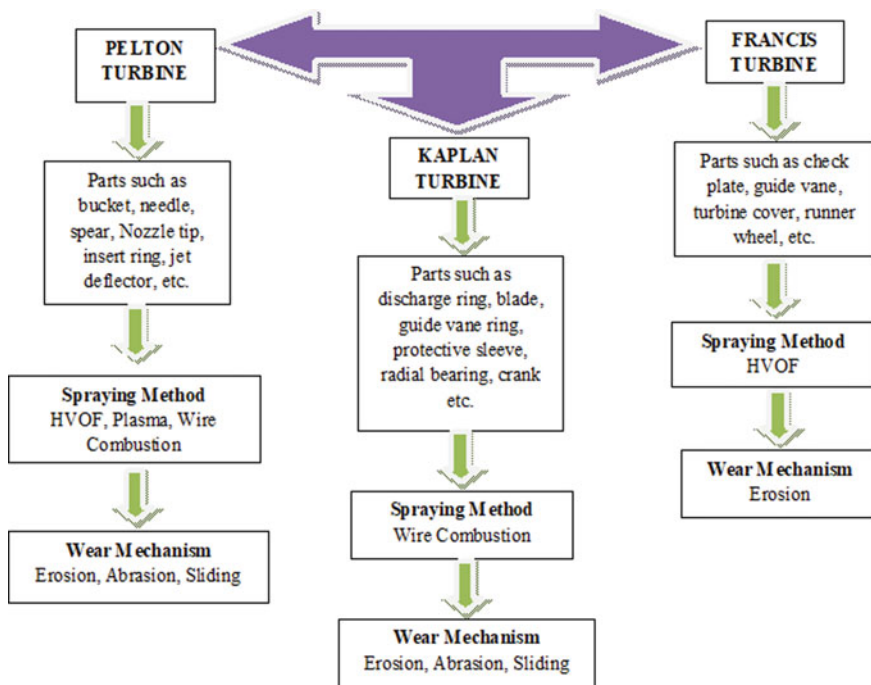


Fig. 5 Shows an overview of commonly used coating systems for different types of hydroturbines

10 Discussion and Conclusion

The inference which has been drawn from each and every aspect of this paper regarding the thermal spray method, substrate selection, coating material and parameters, alloying elements which increase the resistance properties of the substrate surface, and working parameters that have been practically found out to be responsible for the erosion of blades are listed below:

1. High-velocity oxy-fuel thermal spray technique has been found to be the most prevalent and effective method among others. It is best suited for hydroturbines runner. HVOF coating provides high hardness and volume fraction percentage porosity level can be achieved up to 1%. HVOF coatings have uniform coating thickness and have continuous layer of coating. Due to short dwell time, it is able to produce dense coatings with meager degradation and oxidation of metallic materials.
2. High proficiency of HVOF produces coating with high hardness, toughness, wear resistant, less porosity, and less defects with better binding ability. With the help of HVOF coating, the cost of replacement can be reduced approximately 50% and the lifetime of a hydroturbine increases.
3. Pure aluminum cannot be used due to its low density and oxide formation. To increase its hardness and toughness, elements such as Ti, B, Cu, Si, Fe are added making fine grain structure.
4. CrN is high in hardness and wear resistance, chemically inert, and ideal for testing corrosion. Since the TiAlN's low thermal conductivity it protects the instrument from damage due to high temperatures.
5. Adding Zr-Y to TiAl coating improves 8 times oxidation resistance than TiAl alone and 3 times better than Zr alone. La, Y, Ce can be used to reduce oxidation rate and improving corrosion rate. Nb strongly forms carbide and effectively refines grains which ultimately enhance mechanical properties.
6. In application as in hydropower turbine, the primary mechanisms causing loss of coating are mixed plowing and cutting, formation of platelets, abrasion grooves, and cracks. The efficiency of turbine decreases with erosive wear and leads to final break down of turbine. Impact velocity has the highest contribution in detaching coating from substrate followed by impingement angle, erodent size, and erodent feed rate.

11 Limitations of the Study

1. The review presented here has a scope limited to the information regarding the prerequisites of thermal spray process and its influencing parameters on the material structural as well as tribological properties only.

2. The paper also introduces use of rare-earth materials that have been an active participant of recent advancements. The study is restricted too few researches as the optimal utilization of these materials is still under observation and analysis.
3. Though use of their adequate quantities reveals that these metals can be a critical part of coating material composition, the further establishments are still under consideration.
4. Environmental factors are also an independent part of the research, and their proper optimization for further research is required.

12 Future Scope

This review paper has been devised to incorporate all the essential features of the high-velocity oxy-fuel (HVOF) technique and the different ways of implementing it on the hydroturbine material. Each section deals with the recent or important researches that have been made under the respective topic. One of the most important parts of this review is the inclusion of rare-earth metal in the coating powder on which very less investigations have been made, comparatively. The paper focuses on the demand of new material compositions affecting the tribological behavior of the coated metal and hence provides sustainability to the working departments. Thus, a better opportunity awaits in the field of hydromachines for their sustainable working with use of new and less used materials. Different case studies presented in the paper reveal that how important preservation of material becomes for the industry and their growth and therefore further researches in the same is advisable.

References

1. Lejeune A, Hui SL (2012) Hydropower: a multi benefit solution for renewable energy. In: Comprehensive renewable energy, vol 6, pp 15–47
2. Senapati P, Padhy M, Sahu T (2017) Coating materials and methodologies for the protection of hydro turbine runner. *Int J Mech Eng Technol* 8(7):524–536
3. Khera DV, Chadhawork RS (2001) Silt erosion, trouble for turbines. *Int Water Power Dam Constr* 53:22–23
4. Tong D (1981) Cavitation and wear on hydraulic machines. *Int Water Power Dam Constr*
5. Pande VK (1987) Criteria for developing silt erosion model test Facility. In: Conference of CBIP
6. Singh SC (1990) Operational problems and development of a new runner for silty Water. *Int Water Power Dam Constr*
7. Padhy MK, Saini RP (2009) Effect of size and concentration of silt particles on erosion of Pelton turbine buckets. *Energy* 34:1477–1483
8. Amin S, Panchal H (2016) A review on thermal spray coating process. *Int J Curr Trends Eng Res (IJCTER)* 2(4):556–563

9. Vuoristo PMJ (2007) Hard velocity sprays boost hardmetal industrial coatings. In: Metal powder report, vol 62, no 3. Elsevier, Netherlands, pp 22–26, 28–29
10. Ding F, Zhang P, Wei D, Chen X, Wang S, Wang Z, Zhu Y (2018) Isothermal Oxidation Behavior of Zr-Y coating on α -TiAl by double glow plasma surface metal alloying technique. Coatings, MDPI
11. Padhy MK, Saini RP (2008) A review on silt erosion in hydro turbines. Renew Sustain Energy Rev 12:1974–1987
12. Kiragi VR, Patnaik A, Singh T, Fekete G (2018) Parametric optimization of erosive wear response of TiAlN-coated aluminium alloy using Taguchi method. J Mater Eng Perform
13. Grewal HS, Agrawal A, Singh H (2013) Slurry erosion mechanism of hydroturbine steel: Effect of operating parameters. Tribol Lett 52(2):287–303
14. Sharma V, Kaur M, Bhandari S (2019) Development and characterization of high-velocity flame sprayed Ni/TiO₂/Al₂O₃ coatings on hydro turbine steel. J Therm Spray Technol, 1–23
15. Kumar R, Bhandari S, Goyal A (2018) Synergistic effect of Al₂O₃/TiO₂ reinforcements on slurry erosion performance of nickel-based composite coatings. Proc Inst Mech Eng J 232 (8):974–986
16. Beste U, Hammerström L, Engqvist H, Rimlinger S, Jacobson S (2001) Particle erosion of cemented carbides with low Co content. Wear 250(1–12):809–817
17. Leyland A, Matthews A (2000) On the significance of the H/E ratio in wear control: a nanocomposite coating approach to optimised tribological behaviour. Wear 246(1–2):1–11
18. Krelling AP, Souza MMD, Costa CED, Milan JCG (2018) HVOF-sprayed coating over AISI 4140 steel for hard chromium replacement. Mater Res 21(4)
19. Spicher T (2013) Choosing the right material for turbine runners. Hydro Rev, 86–93
20. ISSF Stainless Steels in Micro Hydro Turbines. http://www.worldstainless.org/Files/issf/nonimagefiles/PDF/ISSF_Stainless_Steel_in_Micro_Hydro_Turbines.pdf
21. Lugscheider E, Kramer G, Barimani C, Zimmermann H (1995) PVD coatings on aluminium substrates. In: Surface and coatings technology, vol 74–75. Elsevier, Netherlands, pp 497–502
22. Schoop MU (1942) Über die Herstellung von Überzügen aus Wolfram, bzw. Wolfram-Karbidmittels der “Schoop-Pistole”, Korr. Metallschutz, 18(7):243–244
23. Strachowiak B, Stachowiak W (2010) Int J Refract Met Hard Mater 28:95–105
24. Mann BS, Arya V, Maiti AK, Rao MUB, Joshi P (2006) Corrosion and erosion performance of HVOF/TiAlN PVD coatings and candidate materials for high pressure gate valve application. Wear 260(1–2):75–82
25. Sidhu HS, Sidhu BS, Prakash S (2006) Mechanical and microstructural properties of HVOF sprayed WC–Co and Cr₃C₂–NiCr coatings on the boiler tube steels using LPG as the fuel gas. J Mater Process Technol 171:77–82
26. Jagielski J, Khanna AS, Kucinski J, Mishra DS, Racolta P, Sioshansi P, Tobin E, Thereska J, Uglov V, Vilaithong T, Viviente J, Yang S-Z, Zalar A (2000) Effect of chromium nitride coating on the corrosion and wear resistance of stainless steel. Appl Surf Sci 156:47–64
27. Jin X, Wang B, Xue W, Du J, Wu X, Wu J (2013) Characterization of wear-resistant coatings on 304 stainless steel fabricated by cathodic plasma electrolytic oxidation. In: Surface and coatings technology, vol 236, pp 22–28
28. Sienkiewicz J, Kuroda S, Murakami H, Araki H, Gizynski M, Kurzydowski KJ (2019) Microstructure and oxidation performance of TiAl-(Cr, Nb, Ta) coatings fabricated by warm spray and high-velocity oxy-fuel spraying. J Therm Spray Tech 28:563–579
29. Brady MP, Brindley WJ, Smialek JL, Locci IE (1996) The oxidation and protection of gamma titanium aluminides. JOM 48(11):46–50
30. Santa JF, Baena JC, Toro A (2007) Slurry erosion of thermal spray coatings and stainless steels for hydraulic machinery. Wear 263(1–6):258–264
31. Rizzo A, Mirengi L, Massaro M, Galietti U, Capodiecchi L, Terzi R, ... Valerini D (2013) Improved properties of TiAlN coatings through the multilayer structure. In: Surface and coatings technology, vol 235, pp 475–483

32. Grewal HS, Singh H, Agrawal A (2013) Microstructural and mechanical characterization of thermal sprayed nickel–alumina composite coatings. In: *Surface and coatings technology*, vol 216, pp 78–92
33. Maiti AK, Mukhopadhyay N, Raman R (2007) Effect of adding WC powder to the feedstock of WC–Co–Cr based HVOF coating and its impact on erosion and abrasion resistance. In: *Surface and coatings technology*, vol 201, no 18, pp 7781–7788
34. Abudaia FB, Bull SJ, Oila A (2012) Surface wear resistance of 304 austenitic stainless steels modified by colossal carbon supersaturation and TiN coating. *J Mater Sci Eng B* 2(2):103–111
35. Sidhu TS, Prakash S, Agrawal RD (2005) State of the art of HVOF coating investigations—a review. *Marine Technol Soc J* 39(2):53–64
36. Hou S, Hu C (2017) Effects of rare earth elements on properties of Ni-base superalloy powders and coatings. *Coatings*, MDPI
37. Höhle H-M, Montia C (2011) Nestler Sulzer Technical Review 3
38. Gupta G, Acharya G, Verma A (2015) A review of HVOF thermal spray coating technique on metal plate. *Int J Technol Res Eng* 3(2)
39. CINCA NURIA (2010) Comparison of mechanical and tribological properties of TiC–NiTi and TiCTiB2–NiTi coating. In: *Physics procedia*, vol 10. Elsevier, Netherlands, pp 65–68
40. Murugan K, Ragupathy A, Balasubramanian V, Sridhar K (2014) Developing empirical relationship to predict hardness in WC–10Co–4Cr HVOF sprayed coatings. *Proc Mater Sci* 5:918–927
41. Thermsuk S, Surin P (2019) Optimization parameters of WC–12Co HVOF sprayed coatings on SUS 400 stainless steel. *Proc Manuf* 30:506–513
42. Liu J, Bai X, Chen T, Yuan C (2019) Effects of cobalt content on the microstructure, mechanical properties and cavitation erosion resistance of HVOF sprayed coatings. *Coatings* 9(9):534
43. Zouari S, Ghorbel H, Danlos Y, Liao H, Elleuch R (2019) Comparative study of HVOF-sprayed NiCrBSi alloy and 316L stainless steel coatings on a brass substrate. *J Therm Spray Technol* 28(6):1284–1294
44. Zhang F, Wang S, Robinson BW, Lovelock HL, Wood RJ (2019) Structure-property relationships in suspension HVOF nano-TiO₂ coatings. *Coatings* 9(8):504
45. Kiilakoski J, Trache R, Björklund S, Joshi S, Vuoristo P (2019) Process parameter impact on suspension-HVOF-sprayed Cr₂O₃ coatings. *J Therm Spray Technol* 28(8):1933–1944
46. Inam A, Raza MA, Hafeez MA, Shah SB, Ishtiaq M, Hassan MH, ... Maqbool A (2020) Effect of voltage and spray-off distance of electric-arc spray technique on surface properties of nickel–chrome (Ni–Cr) coating developed on 304L stainless steel. *Mater Res Express* 7(1):016525
47. Elshalakany AB, Osman TA, Hoziefa W, Escuder AV, Amigó V (2019) Comparative study between high-velocity oxygen fuel and flame spraying using MCrAlY coats on a 304 stainless steel substrate. *J Mater Res Technol* 8(5):4253–4263
48. Pulsford J, Venturi F, Kamnis S, Hussain T (2020) Sliding wear behaviour of WC–Co reinforced NiCrFeSiB HVOAF thermal spray coatings against WC–Co and Al₂O₃ counterbodies. In: *Surface and coatings technology*, vol 386, p 125468
49. Pulsford J, Venturi F, Pala Z, Kamnis S, Hussain T (2019) Application of HVOF WC–Co–Cr coatings on the internal surface of small cylinders: effect of internal diameter on the wear resistance. *Wear* 432:202965
50. Amousoltani N, Salimijazi H, Golozar M (2019) Study of alumina sealing of HVOF thermally sprayed WC–Co coatings by sol-gel method. *Mater Res Express* 7(1):016410
51. Sharma V, Kaur M, Bhandari S (2019) Micro and nano ceramic-metal composite coatings by thermal spray process to control slurry erosion in hydroturbine steel: an overview. *Eng Res Express* 1(1):012001
52. Tillmann W, Schaak C, Hagen L, Dildrop M (2019) Investigation of HVOF-ID spraying with WC–CoCr–15 + 5 µm feedstock powder. In: *IOP conference series: materials science and engineering*, vol 480, no 1. IOP Publishing, p 012008

53. Matikainen V, Koivuluoto H, Vuoristo P (2020) A study of Cr₃C₂-based HVOF-and HVAF-sprayed coatings: abrasion, dry particle erosion and cavitation erosion resistance. *Wear*, 203188
54. Praveen AS, Arjunan A (2019) Effect of nano-Al₂O₃ addition on the microstructure and erosion wear of HVOF sprayed NiCrSiB coatings. *Mater Res Express* 7(1):015006

Emission Characteristics of Renewable Diesel and Its Comparison with the Diesel Fuel on Single-Cylinder Diesel Engine



Rashi Koul , Naveen Kumar , and R. C. Singh

Abstract The world is already facing environmental degradation, extinction of fossil fuels, global warming, and many health hazards due to the mentioned reasons. Researchers are finding ways in which the exhaust emissions coming out from diesel (D100) can be reduced, and the environment can be made pollutant free. It is imperative and the need of an hour to switch from fossil fuels and biodiesels to more reliable and sustainable alternate fuels. Hydroprocessing is the process in which the vegetable oil, animal fats, algae, etc., is converted to the transportation fuels in the presence of hydrogen and catalyst at a high temperature and high pressure. The product formed is called renewable diesel (RD), hydroprocessed fuel (HD), or green diesel (GD), etc. This process is very popular in developed countries, and many airlines have tested such fuels (in the blended form) on their commercial flights. In this work, the main focus is kept on the RD's exhaust emissions like particulate matter (PM), hydrocarbons (HC) and NO_x. It is compared to the D100 and a blend RD50D50 (50% v/v of RD and D100). There was approximately 30–40% reduction in PM and 40–60% reduction in NO_x by adding RD into D100. However, for 100% load on an engine, HC emission was more in RD than in D100.

Keywords Renewable diesel · Hydroprocessing · Exhaust emissions · Particulate matter · NO_x emissions · Hydrocarbon emissions

R. Koul (✉)

Department of Mechanical Engineering, Amity University Gurgaon, Gurgaon, Haryana, India
e-mail: rashikoul@gmail.com

R. Koul · N. Kumar

Centre for Advanced Studies and Research in Automotive Engineering,
Delhi Technological University, Delhi, India
e-mail: naveenkumardce@gmail.com

R. C. Singh

Department of Mechanical Engineering, Delhi Technological University, Delhi, India
e-mail: rcsingh@dce.ac.in

1 Introduction

Due to the greenhouse gas emissions (GHG), environmental degradation, increasing level of pollution, many researchers, academicians, and industrialists are finding ways to curb the problem to a maximum extent. The conventional fuel is a problem as it releases more carbon and will be present in the earth's ecosystem for a long period of time. It also leads to the fact, more burning of such fuel leads to more release of carbon-dioxide, hence increasing the earth's temperature and affecting the ecosystem completely. The world has also seen an energy crisis in the past ten years very severely, where fossil fuels are getting exhausted [1, 2]. The main focus is kept on finding certain alternatives to fossil fuels and biodiesel. It is advised to find alternatives to diesel fuel and biodiesel which is more reliable, sustainable, and majorly environment friendly. In many countries, biodiesel is already in use in certain percentages with diesel fuel [3]. It has helped in overcoming the pollution and depletion of fossil fuel to some extent. Biodiesel can reduce carbon-dioxide by about 78% in comparison with conventional fuel [4]. Various researchers have studied the performance of RD and its blends wherein it is clearly concluded that at 100% load the BD shows the maximum power loss in comparison with the RD [5, 6]. This is due to the better atomization in RD and its blends than BD [5]. Due to high cetane index in RD and its blends, the ignition delay is reduced in comparison with BD and its blends. The advantage of using RD is that it can be used as it is without doing any modifications in the CI engines. Due to high calorific Value (CV) of RD, its thermal efficiency is more than the BD [7]. The various studies show that there is an improvement in various emission gases like carbon-monoxide (CO), particulate matter (PM), unburnt hydrocarbons (UBHC) by 45.6%, 63.7%, and 45.2%, respectively [8, 9]. However, due to its certain limitations, the automobile industry cannot completely rely on it. It is because of the reasons like low cetane index, less calorific value, low cold flow properties, corrosivity as is shown in Table 1 [5]. Apart from using the biodiesel and exhaustive research is already done on it, it is time to give attention to the hydroprocessing of various vegetable oil. Hydroprocessing is a method in which the vegetable oil is reacted at an elevated temperature and pressure in the presence of a catalyst to give straight-chain hydrocarbons called renewable diesel (RD). Other than hydroprocessing, cracking or pyrolysis can also be used to produce diesel-like fuel called RD [10]. The molecular structure of these hydrocarbons is similar to fossil fuel [5, 7, 11, 12]. The feedstock used for the production of biodiesel, and renewable diesel is same. These sources since are based on the photosynthesis process will reduce the carbon footprint and help in mitigating global warming [13]. It is very advantageous for the world in terms of environmental cleanliness, finances, economy, and the people using RD as it is biodegradable and sustainable. The liquid and gaseous fuels produced from agricultural wastes, municipal wastes, forests, and biomass are called bio-oils which can be used in the production of RD. RD also has the advantage of reducing the emissions from 20 to 60% [13]. Cracking was a process that was used in 1930 in China in World War II for replacing fossil fuel in case of

Table 1 Physical-chemical properties of BD, D100, and RD

Properties	Biodiesel	Diesel	Renewable diesel
Heating value (MJ/kg)	37	45.58	46.83
Viscosity (mm ² /sec at 40 °C) [20]	4.6	3.6	3–4
Density (kg/m ³)	883	835	819
Cloud point (°C) [1]	–5	–5	–5 to –30
Stability [1, 21]	Marginal	Good	Good
Sulfur content (ppm)	<10	<10	<1
Cetane number [20]	50–65	53	80–90
Oxygen content (%)	11	0	0
% NOx emissions [1]	+10		0 to –10
Fire point [7, 22]	182	66	76
Flash point (°C) [5, 23]	165	58	68

an emergency [10, 14]. Few papers were also written during that period on the cracking of oil produced from cottonseed, fish, and palm oil at high temperature by adding hydrogen [15–17]. Economically, for the production of RD, no separate setup is required as the feedstock can be processed in the diesel production unit. At the same time, the cost of acquiring the feedstock for BD and RD is also same as both can be produced from the same raw material. The disadvantage in case of the BD is its by-product glycerol. The market of glycerol in current situation is huge which can affect the economics of the BD in terms of its production. The RD post-production process involves less investment in terms of pipeline infrastructure due to its similar molecular structure of D100 [10, 18]. As per the ‘govermet Fleet’, the pricing of the RD can depend upon the location. In the year 2019, its price was 42 rs per liter [19].

Hydro-processing is used in various industries to convert the larger molecules to smaller HC chains, removes the impurities like sulfur, nitrogen, and some other metals. The catalyst commonly used are Ni–Mo/Al₂O₃, Co–Mo/Al₂O₃ [24–29], and Ni–W/SiO₂–Al₂O₃ [24, 26]. Some noble metals are also used as catalyst like Rh/Al₂O₃ [30, 31], Pd/C, Pt/C, Pd/SiO₂, and Pd/NiO₂ [23, 32–34]. The fuels produced from this process have viscosity, calorific value (CV), cetane index, atomization, and lubricity similar to that of conventional fuel [5]. RD is a straight-chain HC compound or fatty acid triglycerides from the plant oil taken. The present study compares the emission characteristics of the diesel (D100), RD, and the blends of D100 and RD.

2 Renewable Diesel (RD)

In the high-pressure stirred reactor, the jatropha oil (JO) is mixed with the hydrogen at high pressure and high temperature in the presence of the catalyst ruthenium (Ru). The reactor is set for the time reaction up to 4 h at a temperature of 320 °C and 50 bar pressure. The product produced was named as renewable diesel, RD. The RD was mixed with neat diesel at various percentages vol/vol, and samples were created for the testing purpose. RD50D50 contained 50% by volume diesel and 50% by volume RD, neat renewable diesel was named as RD, and neat diesel was named as D100.

3 Experimental Setup

The samples were tested on the setup which consisted of single-cylinder, four-stroke, common rail diesel injection (CRDI), and variable compression ratio (VCR) engine connected to eddy current dynamometer. It has other necessary instruments for combustion pressure, crank-angle, airflow, fuel flow, temperatures, and load measurements [7]. The results received are signaled and interfaced to the computer through a high-speed data acquisition device. Emission characteristics and exhaust gases were analyzed by connecting AVL gas analyzer to the exhaust pipe.

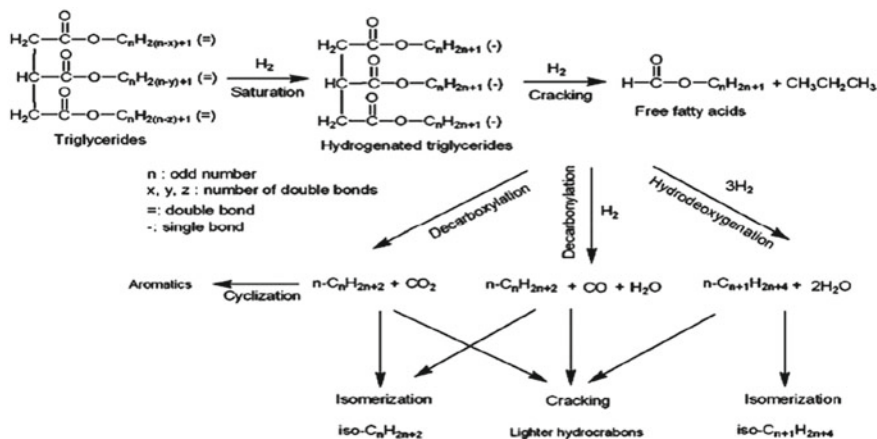


Fig. 1 Chemical reaction for the production of renewable diesel [5, 7, 35, 36]

4 Results and Discussions

4.1 Exhaust Emissions

During the combustion process, exhaust gases come out from the muffler of the diesel engine. These exhaust emissions can be in the form of gases, liquids, and solid particles [37]. When these pollutants are high in percentage than the acceptable standards, then they cause a serious problem for the environment. Many alternative fuels are being explored nowadays to reduce the harmful impact of these exhaust gas emissions. Many researchers have demonstrated that diesel engine, in particular, is accountable for NO_x and PM release in the environment [9, 37].

The exhaust gases include CO, UBHC, NO, PM, sulfur compounds, aldehydes, cyanide, ammonia, pyrene, fluorene, etc. [30]. These diesel emissions are one of the main reasons for the increase in GHG, hence leading to an increase in the earth's temperature by 2–5 °C over the past decade.

The maximum percentage of NO produced is within the range of 70–90%. NO_x usually consists of NO and NO₂ gases. More percentage of NO₂ leads to more pollutants in the atmosphere. DeNO_x systems reduce the NO_x soot particles. As per the vehicle standard acts, a limit of 30% of NO_x emission is acceptable. The release of NO depends upon the combustion chamber temperature. With the help of a gas analyser, NO was found in the present study. As is seen in Fig. 2, NO variation has been analyzed at 50, 75, and 100% load for each of D100, RD, and a blend of RD50D50. It is observed that maximum NO emission is produced by D100 at all the loads. At 100% load maximum NO is produced all the fuels, however, maximum by D100. The RD50D50 values lie between the RD and D100. This indicates by adding a certain percentage of RD into D100, and the NO emissions can be reduced. NO is less in RD due to less exhaust temperature. It is also seen in Fig. 2, that with the rise in the load, NO release rises. This is due to the increased exhaust temperature. The results for NO emission are in synchronization with Murtonen et al. [38].

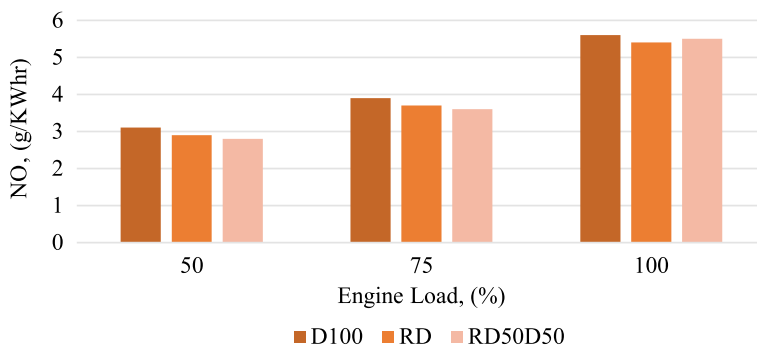


Fig. 2 Effect of D100, RD, and RD50D50 on the emission of NO

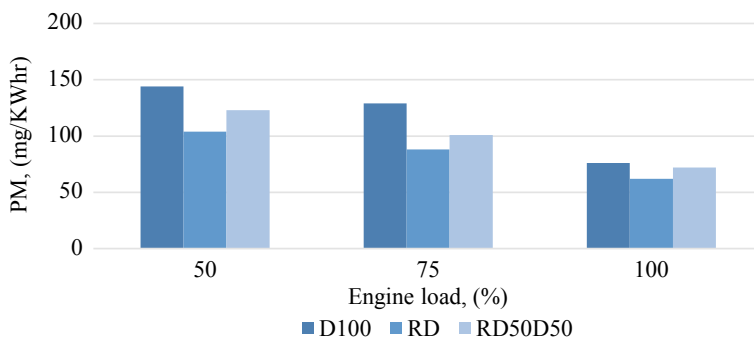


Fig. 3 Effect of D100, RD, and RD50D50 on the emission of PM

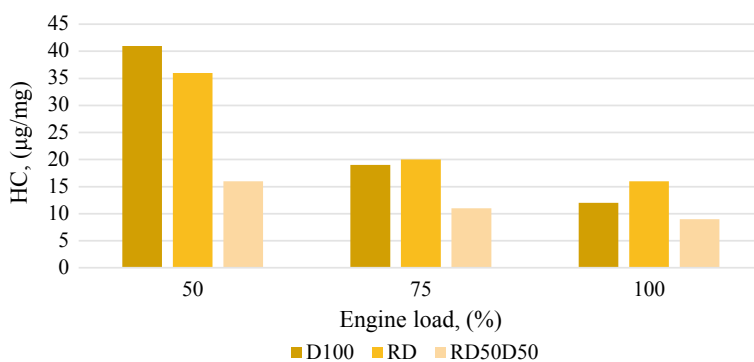


Fig. 4 Effect of D100, RD, and RD50D50 on the emission of HC

Figure 3 shows the PM emissions from the D100, RD, and RD50D50. The highest particulate matter can be seen in D100 at 50% load in comparison with RD and RD50D50. The PM emissions can be seen getting reduced with the rise in the engine load. It is due to the fact of the level of unsaturation content present. The PM emissions from the blend are in between the D100 and RD. Thus, indicating that the addition of RD to D100 is advantageous in reducing the percentage of PM emissions. On average, a reduction of 30–40% can be observed. The same results were observed by Murtonen et al. and Knothe [10, 38]. A similar trend was observed in the HC emissions in Fig. 4 for the load at 50%. This trend can be due to the reason of the strong straight hydrocarbon chain and less of aromatic components. However, it is analyzed that by increasing the load, HC% emission was accounted to be more for RD than D100. Also, it was observed that RD50D50 emitted less HC than the RD.

5 Conclusion

The emission tests performed on the single-cylinder diesel engine were concluded as follows:

1. The cold flow properties of RD were better than BD and D100, thus making it more compatible to be used in the winter region.
2. With the use of the RD in D100 making a blend of 50% v/v, reduction in NO was accounted for 30–45% and RD versus D100 was about 40–60%.
3. A reduction of about 30–40% was observed in PM by using RD in comparison with D100.
4. For HC, the trend was different than PM and NO. There was an increase in HC emissions for RD than D100 for 100% load on an engine.
5. The percentage reduction in the NO_x of RD50D50 is approx. ranges in between 2.8 and 10% for the varying load from 50 to 100%, respectively. Similarly, the reduction in NO is less when compared to the RD than D100 which lies between 2.7 and 3.4%.
6. RD is a potential fuel to be used for reducing the emissions.

References

1. Othman MF, Adam A, Najafi G, Mamat R (2017) Green fuel as alternative fuel for diesel engine: a review. *Renew Sustain Energy Rev.* <https://doi.org/10.1016/j.rser.2017.05.140>
2. Li T, Liu Z, Zhang H, Jiang Q (2013) Environmental emissions and energy consumptions assessment of a diesel engine from the life cycle perspective, 53
3. Koul R (2015) Performance characteristics of a single cylinder diesel engine fuelled with 1-octanol diesel blends 5:302–306
4. Go–DOE (2016) Biodiesel handling and use guide
5. Koul R, Kumar N, Singh RC (2019) Environmental effects a review on the production and physicochemical properties of renewable diesel and its comparison with biodiesel, 7036. <https://doi.org/10.1080/15567036.2019.1646355>
6. Sonthalia A (2019) Comparison of fuel characteristics of hydrotreated waste cooking oil with its biodiesel and fossil diesel
7. Bezergianni, S., & Dimitriadis, A. (2013). Comparison between different types of renewable diesel. *Renewable and Sustainable Energy Reviews*, 21, 110–116.
8. Dunn RO, Shockley MW, Bagby MO (1996) Improving the low-temperature properties of alternative diesel fuels: vegetable oil-derived methyl esters. *JAOCS, J Am Oil Chem Soc* 73:1719–1728. <https://doi.org/10.1007/BF02517978>
9. Srivastava A, Prasad R (2000) Triglycerides-based diesel fuels. *Renew Sustain Energy Rev* 4:111–133. [https://doi.org/10.1016/S1364-0321\(99\)00013-1](https://doi.org/10.1016/S1364-0321(99)00013-1)
10. Knothe G (2010) Biodiesel and renewable diesel: a comparison. *Prog Energy Combust Sci.* <https://doi.org/10.1016/j.peccs.2009.11.004>
11. Bezergianni S, Kalogianni A (2009) Hydrocracking of used cooking oil for biofuels production. *Bioresour Technol* 100:3927–3932. <https://doi.org/10.1016/j.biortech.2009.03.039>

12. Singh D, Subramanian KA, Garg M (2017) Comprehensive review of combustion, performance and emissions characteristics of a compression ignition engine fueled with hydroprocessed renewable diesel. *Renew Sustain Energy Rev.* <https://doi.org/10.1016/j.rser.2017.06.104>
13. Kiatkittipong W, Phimsen S, Kiatkittipong K, Wongsakulphasatch S (2013) Diesel-like hydrocarbon production from hydroprocessing of relevant refining palm oil. *Fuel Process Technol* 116:16–26. <https://doi.org/10.1016/j.fuproc.2013.04.018>
14. China's Motor Fuels from Tung Oil (1947)
15. Cottonseed H, Pressure RH (1961) Hydrogenating cottonseed relatively high pressure 53:375–380
16. Egloff G, Morrell JC (n.d.) The cracking of cottonseed oil
17. Egloff G, Morrell JC (n.d.) The cracking of fish oil 24:3–4
18. Balat M (2011) Potential alternatives to edible oils for biodiesel production—a review of current work. *Energy Convers Manag* 52:1479–1492. <https://doi.org/10.1016/j.enconman.2010.10.011>
19. Fleet G (2020) Is renewable diesel still a 'Miracle Fuel'?, 1–13
20. Napolitano P, Guido C, Beatrice C, Pellegrini L (2018) Impact of hydrocracked diesel fuel and hydrotreated vegetable oil blends on the fuel consumption of automotive diesel engines. *Fuel.* <https://doi.org/10.1016/j.fuel.2018.02.097>
21. Knothe G (2007) Some aspects of biodiesel oxidative stability 88:669–677. <https://doi.org/10.1016/j.fuproc.2007.01.005>
22. Phoon LY, Hashim H, Mat R, Mustaffa AA (2016) Flash point prediction of tailor-made green diesel blends containing B5 palm oil biodiesel and alcohol. *Fuel* 175:287–293. <https://doi.org/10.1016/j.fuel.2016.02.027>
23. Bezergianni S (2013) Catalytic hydroprocessing of liquid biomass for biofuels production. *Liq Gaseous Solid Biofuels Convers Tech*, 299–326. <https://doi.org/10.5772/52649>
24. Kordulis C, Bourikas K, Gousi M, Kordouli E, Lycourghiotis A (2016) Development of nickel based catalysts for the transformation of natural triglycerides and related compounds into green diesel: a critical review. *Appl Catal B Environ.* <https://doi.org/10.1016/j.apcatb.2015.07.042>
25. Plazas-González M, Guerrero-Fajardo CA, Sodr e JR (2018) Modelling and simulation of hydrotreating of palm oil components to obtain green diesel. *J Clean Prod.* <https://doi.org/10.1016/j.jclepro.2018.02.275>
26. Kordulis C, Bourikas K, Gousi M, Kordouli E, Lycourghiotis A (2016) Development of nickel based catalysts for the transformation of natural triglycerides and related compounds into green diesel: a critical review. *Appl Catal B Environ* 181:156–196. <https://doi.org/10.1016/j.apcatb.2015.07.042>
27. Orozco LM, Echeverri DA, S anchez L, Rios LA (2017) Second-generation green diesel from castor oil: development of a new and efficient continuous-production process. *Chem Eng J.* <https://doi.org/10.1016/j.cej.2017.04.027>
28. Patel M, Kumar A (2016) Production of renewable diesel through the hydroprocessing of lignocellulosic biomass-derived bio-oil: a review. *Renew Sustain Energy Rev.* <https://doi.org/10.1016/j.rser.2015.12.146>
29. Afshar Taromi A, Kaliaguine S (2018) Green diesel production via continuous hydrotreatment of triglycerides over mesostructured Γ -alumina supported NiMo/CoMo catalysts. *Fuel Process Technol.* <https://doi.org/10.1016/j.fuproc.2017.10.024>
30. Sn are M, Kubic I, Murzin DY, A F-T (2006) Heterogeneous catalytic deoxygenation of stearic acid for production of biodiesel, 5708–5715
31. Liu Y, Sotelo-Boy as R, Murata K, Minowa T, Sakanishi K (2012) Production of bio-hydrogenated diesel by hydrotreatment of high-acid-value waste cooking oil over ruthenium catalyst supported on Al-polyoxocation-pillared montmorillonite. *Catalysts* 2:171–190. <https://doi.org/10.3390/catal2010171>

32. Viêgas CV, Hachemi I, Freitas SP, Mäki-Arvela P, Aho A, Hemming J et al (2015) A route to produce renewable diesel from algae: synthesis and characterization of biodiesel via in situ transesterification of *Chlorella* alga and its catalytic deoxygenation to renewable diesel. *Fuel* 155:144–154. <https://doi.org/10.1016/j.fuel.2015.03.064>
33. Al-Muhtaseb AH, Jamil F, Al-Haj L, Al-Hinai MA, Baawain M, Myint MTZ et al (2016) Efficient utilization of waste date pits for the synthesis of green diesel and jet fuel fractions. *Energy Convers Manag.* <https://doi.org/10.1016/j.enconman.2016.09.004>
34. Sari E, Kim M, Salley SO, Ng KYS (2013) A highly active nanocomposite silica-carbon supported palladium catalyst for decarboxylation of free fatty acids for green diesel production: correlation of activity and catalyst properties. *Appl Catal A Gen.* <https://doi.org/10.1016/j.apcata.2013.07.053>
35. Kim SK, Brand S, Lee HS, Kim Y, Kim J (2013) Production of renewable diesel by hydrotreatment of soybean oil: effect of reaction parameters. *Chem Eng J* 228:114–123. <https://doi.org/10.1016/j.cej.2013.04.095>
36. Veriansyah B, Han JY, Kim SK, Hong SA, Kim YJ, Lim JS, Shu YW, Oh SG, Kim J (2012) Production of renewable diesel by hydroprocessing of soybean oil: Effect of catalysts. *Fuel* 94:578–585. <https://doi.org/10.1016/j.fuel.2011.10.057>
37. Mollenhauer, K, Tschöke H (eds) (2010) Handbook of diesel engines. In: Handbook o. Springer, Berlin
38. Murtonen T, Aakko-Saksa P, Koponen P, Lehto K, Sarjovaara T, Happonen M et al (2012) Emission reduction potential with paraffinic renewable diesel by optimizing engine settings or using oxygenate. <https://doi.org/10.4271/2012-01-1590>

Effect of Tyre Inflation Pressure on Fuel Consumption and Vehicle Handling Performance



Nigatu Belayneh, Ramesh Babu Nallamothe,
Anantha Kamal Nallamothe, and Seshu Kishan Nallamothe

Abstract The inflation pressure of tyres has great influence on power loss due to rolling resistance. This paper describes the effect of inflation pressure of tyre on fuel consumption and vehicle handling performance of bus. This work was done based on the specifications and study done on Anbessa city bus. Initially, three vehicle tyre models are built in different range of inflation pressure in CATIA. The models were analysed for aerodynamic drag and lift forces using Phoenix software. The specifications of the tyre P295/80R225 which is used in Anbessa city bus were taken for building models. The load on the tyres, rolling resistance variations and the rotational aerodynamic effect of tyre were used as inputs among other parameters to analyse the fuel consumption. From the analysis, it is found that in case of model 3, which is under inflation, the fuel consumption is about 11.05% more than model 1 with recommended inflation pressure with speed of 60 km/hr.

Keywords Rolling resistance · Mathematical model · Aerodynamic drag · CFD · Lift force · Fuel consumption · Vehicle handling

N. Belayneh

Technology and Innovation Institution, Addis Ababa, Ethiopia
e-mail: niga87379@gmail.com; nigatu.belayneh@techin.gov.et

R. B. Nallamothe (✉)

Mechanical Systems and Vehicle Engineering Department, Adama Science and Technology University, Adama, Ethiopia
e-mail: rbnallamothe@gmail.com; ramesh.babu@astu.edu.et

A. K. Nallamothe · S. K. Nallamothe

School of Industrial and Information Engineering, Politecnico Di Milano, Milan, Italy
e-mail: ananthakamal@gmail.com

S. K. Nallamothe

e-mail: seshukishan1997@gmail.com

1 Introduction

The tyre inflation pressure plays an important role on the performance and fuel economy of the vehicle. Tyres are required to produce the forces necessary to control the vehicle [1–3]. Tyre is the only means of contact between the road and the vehicle, but they are at the heart of vehicle handling and performance [4–6]. The tyre inflation pressure plays an important role in the vehicle's fuel consumption. The results of a survey released by the US Department of Transportation's NHTSA (National Highway Traffic Safety Administration) in 2001 showed that a decrease of 0.55 bar, from the recommended inflation pressure, resulted in the reduction of fuel efficiency by 3.3%, in miles per gallon [7–9]. This report emphasized on the losses from the tyres and the effect on the overall fuel consumption of the vehicle [10, 11].

The relationship between tyre pressure, rolling resistance and fuel economy is complex and dynamic and is dependent on several other factors, including vehicle type and load, road and environmental conditions [3].

In this paper, the effect of tyre inflation pressure on the fuel consumption is analysed and investigated. The tyre models, tyre pressure, and fuel consumption survey were done on the Addis Ababa city bus. The overall analysis was done by applying the loads of Addis Ababa city bus specifications (Table 1) by applying different inflation pressure in each tyre model. The Horizen Addis tyre manufacturing company made 295/80R22.5 size number tyre was selected for the experimentation. The three tyre model geometries were analysed. Tyre model geometry was created based on the tyres used mostly on Anbessa city bus in Addis Ababa. The load-carrying capacity of the tyre is equally assumed for each model. The three vehicle tyre models were built in different range of inflation pressure using CATIA V5R20. The aerodynamic drag of rotating tyre was analysed using on PHOENIX VR 215 software. Table 2 gives the model of tyres in different inflation pressure, and Fig. 1 shows the 3D view of three models. The different tyre inflation pressure, load on the tyres and the rotational aerodynamic effect of tyre were considered as model inputs with the output of fuel consumption in litres per 60 km.

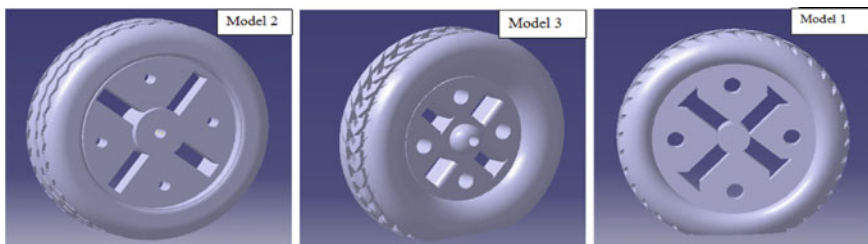


Fig. 1 3D view of different models

Table 1 Vehicle specifications

Vehicle dimension		Quality parameters (kg)	kg
Length	11,890 mm	Curb weight	11,300
Width	2550 mm	Front axle	5700
Height	3400 mm	Rear axle	5600
Wheelbase	6400 mm		
Ground clearance	210–231 mm		
Gross weight	18,500 kg		
Front track	1880 mm		
Rear track	3380 mm		

Table 2 Model of tyres in different inflation pressure

Model no.	Specification
Model 1 A 295/80R22.5 size number	At normal inflation or recommended
Model 2 A 295/80R22.5 size number	High inflation condition
Model 3 A 295/80R22.5 size number	Under inflation condition

1.1 Measurement of Tyre Pressure and Fuel Consumption on Addis Ababa City Bus

The focus area of this research is to determine the effects of tyres inflation pressure in order to improve fuel economy, vehicle safety and performance. Studying the different parts of a tyre is necessary to see how they influence fuel economy related with rolling resistance and vehicle ride and safety [4, 5].

From the experimental approach, it was found that the fuel consumption is more as the tyre pressure is below or above the recommended tyre pressure. In other words, more fuel is needed for the same amount of distance to be covered with the variation of tyre pressure from the recommended value. The fuel consumption analysis of tyre for different range of inflation pressure was done by relating the rolling resistance phenomena on each tyre model. In each day, the selected bus tyre pressure, odometer reading and the fuel reading were recorded for each analysis which are tabulated in Table 3. Records were taken from the bus.

2 Methodology

In this part, it is described how the research is conducted and the sampling technique used to analyse the influence of tyre inflation pressure on the fuel consumption and vehicle handling performance and also presented the methodology and tools and software used to build models of tyre.

Table 3 Reading of tyre pressure, taken kilometre and fuel consumed

Day	Odometer reading (km)		Fuel left out of 40 litres	Tyre pressure measured (MPa)			
	2:30 AM LT	11: 30 PM LT		Front right	Front left	Rear right avg	Rear left avg
1	18,004	18,122	6.1733	0.812	0.806	0.751	0.749
2	18,973	19,096	3.1	0.825	0.829	0.801	0.793
3	19,941	20,063	4.01	0.791	0.819	0.761	0.795
4	20,903	21,031	3.3	0.783	0.791	0.810	0.788
5	21,872	21,995	2.485	0.831	0.810	0.792	0.81
6	23,205	23,326	-0.33	0.71	0.73	0.751	0.76

A survey of vehicles was conducted in Anbessa city bus. The survey was based on field data on vehicles in Addis Ababa. The survey was based on field data on bus by considering its tyre inflation pressure range and fuel consumption on road. Three vehicle tyre models are built in different range of inflation pressure using CATIA. The aerodynamic drag of rotating tyre was analysed using on PHOENIX VR 215 software. The effect of tyre inflation pressure on fuel consumption and handling performance were analysed.

2.1 Geometry

Because tyres must carry heavy loads, steel and fabric cords are used in their construction to reinforce the rubber compound and provide strength. The most common materials suitable for the tyre application are cotton, rayon, polyester, steel, fiberglass and aramid. There are two major ingredients in a rubber compound: the rubber and the filler. They are combined in such a way to achieve different objectives.

Theoretically, a tyre model should consider the following:

- All tyres used were from the same manufacturer; Horizon Addis Tyre Manufacturing.
- A 295/80R22.5 size number tyre was maintained throughout the experimentation.
- Tyre widths were matched as closely as possible; however, not all tyres were available in the same width; hence, there was some slight variation.
- The composite structure (rubber and reinforcement) and the significant anisotropy caused by great differences in stiffness between rubber and reinforcement.

The weight percentage of the components of a tyre is:

- Reinforcements: steel, rayon, nylon, 16%
- Rubber: natural/synthetic, 38%
- Compounds: carbon, silica, chalk, 30%
- Softener: oil, resin, 10%
- Vulcanization: sulphur, zinc oxide, 4%.

2.1.1 Material Properties: Rubber

- Density = 2.33 kg/m^3
- Young's modulus = $50,000 \text{ N/mm}^2$
- Poisson's ratio = 0.49.

2.2 Operating Range

Initial boundary conditions

- Velocity condition of Anbessa city bus is up to 120 km/hr.
- The bus cover 150 km on half day (12 h).
- On a dry surface.
- No slip condition at the surface of the model tyre.
- Moving boundary condition on the ground surface of road.

Three tyre model geometries were analysed. Tyre model geometry was created based on the tyres used mostly on Anbessa city bus in Addis Ababa. Its tread structure, inflation pressure and overall dimension are from HORIZON ADDIS TYRE manufacturing. But in the analysis, the load-carrying capacity of the tyre is equally used in each model. The models are different size number. The tyre models are created by CATIA V5R20.

3 Result and Discussions

3.1 Tyre Rolling Resistance Coefficient on Each Tyre Model

For each tyre inflation pressure, tyre rolling resistance coefficient was calculated. Figure 2 shows the variation of tyre rolling resistance coefficient at different tyre inflation pressure of Anbessa city bus.

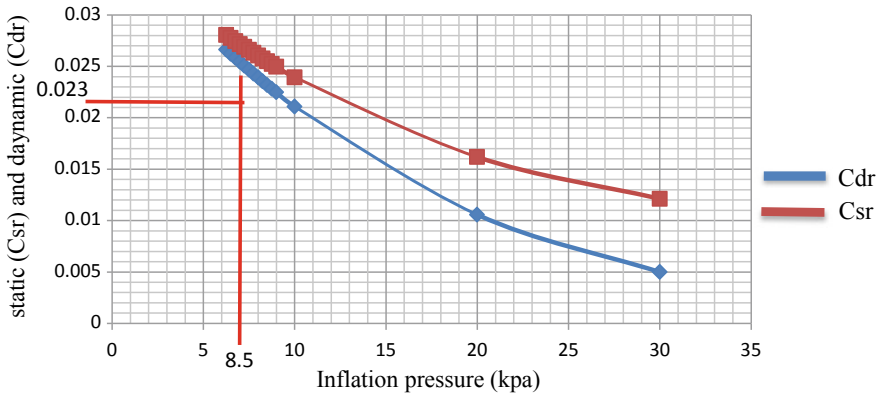


Fig. 2 Tyre static and dynamic coefficients versus inflation pressure

The regression analysis resulted in some very accurate expressions for $C_{sr||}$ and $C_{dr||}$ as a function. These expressions were used to establish the baseline reference $C_{sr||}$ and $C_{dr||}$.

$$(C_{sr})_{Ref} = -0.0000001687P_i^3 + 0.0000255349P_i^2 - 0.0012944847P_i + 0.0305104628 \tag{1}$$

$$(C_{dr})_{Ref} = -0.0000002636P_i^3 + 0.0000404822P_i^2 - 0.0020812137P_i + 0.0381150798 \tag{2}$$

where C_{dr} and C_{sr} are the dynamic and static rolling resistance coefficients [3].

The graph gives the static and dynamic rolling resistance coefficients of tyre models with different inflation pressure (model 1 is 0.83 MPa, model 2 is 0.90 MPa, and model 3 is 0.70 MPa). It can be seen from Fig. 2 that the estimated static and dynamic tyre rolling resistance coefficient decreased while increasing the tyre inflation pressure and vice versa. As the tyre inflation pressure increase, the surface contact will decrease, so the dynamic rolling resistance decreases. The static rolling coefficient is higher on the under inflation pressure than the over inflation pressure because there is an increase in the surface area. In model 3 (under inflation pressure), the static coefficient becomes higher as compared to model 1 and model 2.

3.2 Effect of Inflation Pressure and Load on the Rolling Friction Coefficient

The rolling friction coefficient was calculated by considering the load on the bus at different tyre inflation pressure. The calculation was done for all three models with a gross load of bus is 46,250 N and forward speed of 60 km/hr. Variation of tyre

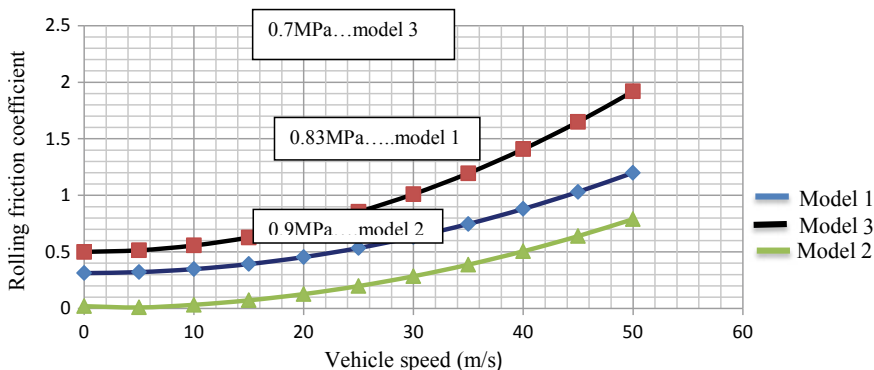


Fig. 3 Variation of rolling friction coefficient with the vehicle speed

rolling friction resistance of Anbessa city bus with vehicle speed for all three models is shown in Fig. 3.

As shown in Fig. 3, the rolling friction coefficient has reduced as the tyre inflation pressure increased in all the models. It can be seen from the plot that the rolling friction coefficient in model 3 increased by 24.8% as compared to model 1, whereas the rolling friction coefficient in model 2 (over inflation) reversely decreased by 72.5% from model 1. According to literatures [3], a 10% reduction in rolling friction coefficient can bring about 2% reductions in the fuel consumption.

3.3 Overall Contribution of Tyre Inflation Pressure on the Fuel Consumption of Anbessa City Bus

This section describes the power used by the bus within different tyre inflation pressure model. The overall fuel consumption of the bus in each model at various speeds was calculated. The results are given in Table 4. The power used in each model is shown in Fig. 4.

Table 4 Power used in each model [6]

Bus speed (m/s)	Power used on the model $P_{used} = (\mu_r \times (F_z + F_L) \times V_{bus})$ (kW) [6]		
	Model 1	Model 2	Model 3
10	414.541	5,176,908	436.083
15	662.402	168.031	737.449
16.67	751.22	226.41	853.408
20	958.969	392.748	1138.804
25	1320.479	762.070	1673.477

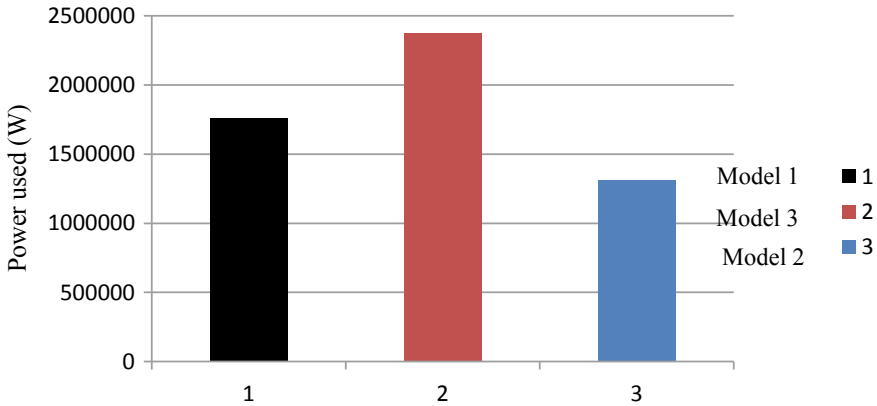


Fig. 4 Power used in each model at a speed of 60 km/hr

3.3.1 Fuel Used by Each Model

According to the Willans relationship of power consumed on the bus and required power from the specification, we can analyse the exact fuel consumption of the bus in field. By adjusting the bus at a constant 60 km/h, the engine speed is 1900 rpm (in fifth gear) using equation below.

$$P_{\text{consumed}} = 2.23 \times P_{\text{required}} + 6.82 \times N_{\text{rpm}}$$

The bus data from specification	
Gross weight	18,500 kg
Fuel consumption	25L/100 km (full load, on flat good road)
Engine rated power	199 kW/1900 rpm

In addition to theoretical analysis, the performance of the vehicle on real road conditions of Addis Ababa is also considered in this work. The fuel consumption of the selected vehicle with varying inflation pressure of the tyre was measured. The bus can travel on an asphalt road at a constant 60 km/h, i.e., 16.67 m/s. There are about 18975.752 N (assume that the coefficient of rolling resistance for all tyres on the vehicle is uniform 0.45 when doing model 1) of resistive forces being exerted on the bus in case of model 1. Different resistive force developed in each tyre inflation pressure ranges, or in each model, this varied condition of resistive force and tyre pressure are a significant effect in real analysis.

The power required for the bus is by the real bus speed, and total resistive force of model 1 is 751.22 kW. At 60 km/h, the bus therefore consumes 751.22 kW in one hour.

The bus engine energy value is 199 kW/litre. When assuming model 1 for the bus with 100% engine efficiency, we would only need $\frac{751,220 \text{ W}}{199,000 \text{ W}} = 3.77$ litre of fuel for 60 km. Realistically, for a 199 kW per litre rated engine power, consumption is around 17–20 litres per 60 km/hr.

We have: the bus consumed power is as follows

$$P_{\text{consumed}} = 2.23 * 751.22 \text{ kW} + 6.82 * 1900 \text{ rpm} = 1688.18 \text{ kW}$$

The efficiency of the engine using equation

$$\eta = \frac{P_{\text{required}}}{P_{\text{consumed}}} = \frac{751,220 \text{ W}}{1,688,178.6} = 0.44$$

The fuel consumed within given speed means at 60 km/hr is 1688.18 kW in hour, but the engine rated power is 199 kW/litre. Then, by dividing the power required during real motion to the rated.

$$\text{Fuel consumption} = \frac{1688.18 \text{ kW}}{199 \text{ kW}} = 8.4 \text{ in } 60 \text{ km}$$

3.4 Fuel Used by Each Model

The CFD result on fuel consumed by the bus to cover the distance of 60 km/hr on different model is described here. Figure 5 and Table 5 depict the fuel consumption in each model at 60 km/hr and at different speed, respectively. The model 3, as bus is under inflated pressure, consumes 0.378 litre of fuel per km at a speed of 60 km/hr which is 11.05% more compared to model 1. However, it is observed from the plot, and the model 3 consumes 29.24% fuel as compared to model 2 which is over

Fig. 5 Fuel consumption in each model with speed of 60 km/hr

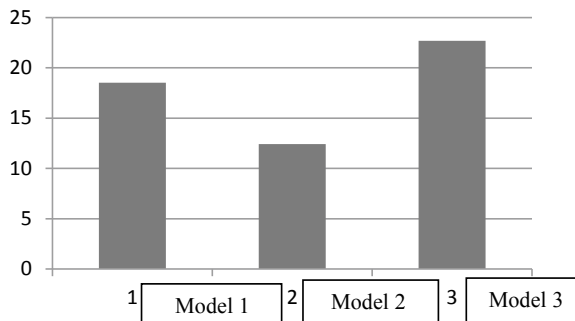


Table 5 Fuel consumption in litre per km at different speed

Speed of bus (km/h)	Fuel consumption (when bus travelled distance is 60 km)		
	Model 1	Model 2	Model 3
10	16.343	11.48	19.64
15	17.983	12.18	21.93
16.67	18.53	12.42	22.7
20	19.622	12.89	24.2

inflation pressure. It is also observed that the fuel consumption decreases by 9.74% when the tyre pressure was increased from the recommended pressure of 0.83–0.9 Mpa, at given speed and distance.

4 Conclusion

In this article, the effect of inflation pressure of tyre on fuel consumption and vehicle handling performance of bus has been studied. For this purpose, three models were built in different range of tyre inflation pressure based on the specifications of Anbessa City bus of Addis Ababa. The outcomes of the analysis are as follow.

- The estimated static and dynamic tyre rolling resistance coefficient decreased while increasing the tyre inflation pressure and vice versa. As the tyre inflation pressure increases, the surface contact will decrease, so the dynamic rolling resistance decreases.
- The rolling friction coefficient has reduced as the tyre inflation pressure increased. In model 3 (under inflation pressure), the static coefficient becomes higher as compared to model 1 and model 2.
- The model 3, as bus is under inflated pressure, consumes 0.378 litre of fuel per km at a speed of 60 km/hr which is 11.05% more compared to model 1 which is at recommended inflation pressure. However, the model 3 consumes 29.24% fuel as compared to model 2 which is over inflation pressure.

References

1. Ramesh G (2015) FE analysis of effect of tyre overload and inflation pressure on rolling loss in cars. *J Eng Res Appl* 5(8):01–08. ISSN 2248-9622
2. Göteborg (2013) Influence of tyre inflation pressure on fuel consumption, vehicle handling and ride quality modeling and simulation. Alexander Varghese Chalmers University of Technology, Sweden

3. Alhassan T (2011) The effect of tyre pressure on vehicle performance Mechanical Engineering. B.Sc. Honors, September
4. Global.yokohamatire.net (2014) Rolling resistance and fuel consumption (tire care & safety). The Yokohama Rubber Co., Ltd. Accessed 6 June
5. Yesfalign Demissie N, Babu R (2017) Aerodynamic drag reduction on locally built bus body using computational fluid dynamics (CFD): a case study at bishoftu automotive industry. *Int J Eng Res Technol (IJERT)* 6(11):276–283
6. Jazar RN. *Vehicle dynamics: theory and applications*. Dept. of Mechanical Engineering Manhattan College Riverdale, NY 10471
7. Venkataraman P (2007) Effect of nitrogen filling on tire rolling resistance and vehicle fuel economy. Clemson University 12
8. Committee for the National Tire Efficiency Study Transportation Research Board (2006) *Tires and passenger vehicle fuel economy, informing consumers, improving performance national research council of the national academies*. Washington, DC
9. MyTechZone (2015) Estimation of rolling resistance coefficient. My Tech Zone
10. Ashagrie G, Nallamotheu RB, Nallamotheu SK, Nallamotheu AK (2017) A study on driving stability of bus using computational fluid dynamics (CFD). *Int J Res Appl Sci Eng Technol* 5 (11)
11. Molla KY, Ho K-C, Ramesh Babu N (2017) Aerodynamic design of the Ethiopian train for energy economy under cross wind conditions, vol 10, pp 342–344. KSR2017A142. The Korean Society for Railway

CFD Analysis on Aerodynamic Drag Reduction of Pickup Vehicles Using Rear Spoiler



Engidayehu Wotango, Ramesh Babu Nallamothe, Surafel Kebede, Natnael Bekele, Anantha Kamal Nallamothe, and Seshu Kishan Nallamothe

Abstract Global warming and environmental pollution have recently been threatening factors for our survival. The prime concern of automotive industry is to reduce the fuel consumption of the vehicle for the sake of saving energy, thereby conserving the environment. Improving the performance of the engine, reducing the mass of the vehicle and reducing the resistance of aerodynamic drag are some of the recent options used for improving fuel economy. A large chunk of the fuel used is employed in overcoming the aerodynamic drag at highway speeds and therefore if reduced could produce a large reduction in the total fuel consumption and minimize the negative environmental effects. In this work, air flow over a pickup vehicle with spoiler attached on the rear end of the vehicle roof at different inclination angles and spoiler length using computational fluid dynamics (CFD) with the objective of reducing the aerodynamic drag was studied. All numerical simulations were performed using commercial CFD software Fluent and realizable k-epsilon turbulence modeling at different vehicle speeds. A 1/12 scaled down generic pickup model with extended cab modeled with SolidWorks was used as the baseline model. Improvement in drag coefficient was obtained in models with spoiler when com-

E. Wotango

Mechanical Engineering Department, Bule Hora University, Bule Hora, Ethiopia
e-mail: engidawotango@gmail.com

R. B. Nallamothe (✉) · S. Kebede · N. Bekele

Mechanical Systems and Vehicle Engineering Department, Adama Science and Technology University, Adama, Ethiopia
e-mail: rbnallamothe@gmail.com

S. Kebede

e-mail: suraprincekb@gmail.com

N. Bekele

e-mail: natnaelbekele4@gmail.com

A. K. Nallamothe · S. K. Nallamothe

School of Industrial and Information Engineering, Politecnico Di Milano, Milan, Italy
e-mail: ananthakamal@gmail.com

S. K. Nallamothe

e-mail: seshukishan1997@gmail.com

© The Author(s), under exclusive license to Springer Nature Singapore Pte Ltd. 2021

B. S. Sikarwar et al. (eds.), *Advances in Fluid and Thermal Engineering*,

Lecture Notes in Mechanical Engineering,

https://doi.org/10.1007/978-981-16-0159-0_54

pared to the baseline model without any add-on device. A drag reduction of 6.50, 6.12 and 0.493% was achieved on model one, model three and model two, respectively, when compared to the baseline model. The decrease in the amount of drag was attributed to the decrease in wake region and swirling air inside the bed box of the pickup vehicle. Because of the reduction in drag, a maximum of 3.90% reduction in fuel consumption was achieved. Overall aerodynamic drag reduction of pickup vehicle using spoiler as an add-on device which leads to better fuel economy was shown here.

Keywords Drag · Fuel consumption · Global warming · Spoiler

1 Introduction

Since the inception of the modern motor vehicle the in early 1900s, vehicle manufacturers have shown much interest in producing stylish cars with little or no interest in reducing aerodynamic resistance by producing a streamlined vehicle body shape. The oil crisis due to Middle East oil embargo in the 1970s compelled vehicle manufacturers to bring sound aerodynamic design to the forefront for practical and scientific uses rather than for aesthetic purposes as in the previous decades. In addition to the economic benefit, fuel consumption reduction also helps in avoiding environmental upside. The environmental upside has revealed itself currently through El Nino which caused devastating drought especially in Eastern Africa. So, tackling this upside means reducing the amount of fuel consumption which will come into effect by decreasing aerodynamic drag [1].

At vehicle speeds of above 70 km/h, the resistance to forward motion of the vehicle due to aerodynamic drag exceeds 50% of the total resistance. For vehicle speeds more than 100 km/h, aerodynamic resistance is the most responsible factor which is responsible for resistance to forward motion. Recognizing the importance of aerodynamic resistance, automobile engineers and scientists exert maximum effort in finding the ways to reduce it [1]. Add-on devices are being used as a mechanism to reduce aerodynamic resistance. Various studies are generally being done using computer simulation approaches on scale modeling.

Around 7% of fuel cost can be saved by installing a sloping front roof on a lorry [2]. Any small change either in design or shape of the vehicle can cause a change in aerodynamic resistance. Greater savings can be realized from better aerodynamic styling in the vehicles traveling longer distances at higher speeds. Irrespective of the vehicle types, in long-distance journeys, around 26% of total fuel consumed is used in overcoming the resistance caused in pushing the vehicle through the air. Approximately, 60% of fuel used in overcoming drag in loaded vehicles moving with cruising speeds and empty vehicles it amounts to 70%.

The aerodynamic characteristics of the vehicle greatly influence the safety, handling, comfort and the performance of the vehicle. In achieving greater stability and greater reduction of the aerodynamic drag, various types of add-ons like air

dams, lower front and rear bumpers, rear spoilers and many more aid to direct and control flow of air in a favorable. Especially in a passenger car, add-on like rear spoiler is used to decrease the overall drag and at the same time increase downward force of a vehicle. Rear spoiler spoils the unfavorable airflow over the body of the car in achieving the aerodynamic drag. After body shape of the vehicle like square back, fast back, hash back and notch back, determine the fixing location of the rear spoiler on rear portion of the vehicle. The use of rear spoiler can contribute to the reduction of drag. Fuel can be saved due to the reduction of drag. Also, spoiler helps in controlling the stability of the vehicle in cornering.

Swirling motion of air inside the bed box of pickup vehicles in addition to the wide wake region subjects pickup vehicles to high amount of drag. At higher speed of the vehicle major portion of the resistance to forward motion of the vehicle is caused by the aerodynamic drag. With increased resistance to motion the vehicle must produce additional power by utilizing more fuel to overcome the drag. Besides, there will be more emission from more fuel supply which has its own adverse environmental impact, again affecting the economy of our nation by a devastating drought and/or climate change.

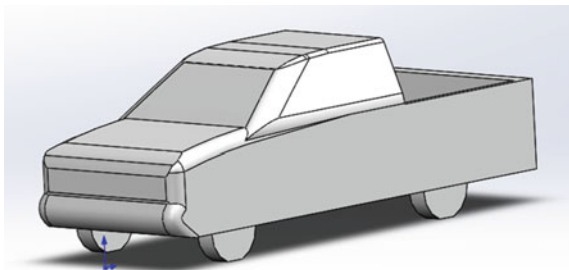
2 Methodology

Extended cab Toyota pickup vehicle model was used for the present work. The model represents a 1:12 scale of the full-scale pickup vehicle. In general, 1:12 scale model is used for wind tunnel test. The model was designed using SolidWorks with a smooth underbody, enclosed wheel wells, with no side view mirrors and without openings for cooling airflow. The model used has been modified to resemble the generic pickup vehicle in [3].

The width of the model is 0.152 m, the length of the model is 0.432 m, and the height is 0.1488 m. A coordinate system in the symmetry plane is attached to the front tip of the vehicle (Fig. 1).

In this study, one drag reducing device (a rear spoiler) with different arrangements is employed, and each arrangement is simulated using Ansys Fluent, and their values are compared with each other and to the baseline.

Fig. 1 1/12 scaled down pickup vehicle



The spoiler airfoil shape was selected from NACA catalog. NACA6409 airfoil was selected, and the coordinates are imported to SolidWorks for modeling. Then, to increase its length, rectangular feature was added and was connected with the baseline vehicle. The arrangements are such that for model one, the spoiler with 21 mm slant length is attached to the rear end of the cab at an angle of zero-degree inclination. In the second model, the spoiler with 21 mm slant height is inclined upward at 12° . Only the slant length of the spoiler is reduced to 11 mm keeping the inclination angle at zero degree in the third model.

After the vehicle model was uploaded to Ansys, an enclosure was generated surrounding it. For experimental study, the enclosure was designed based on recommendation from Fluent for accurate results [5–8]. The upstream dimension for wind tunnel enclosure was 1701 mm, downstream 2268 mm, width and height were 1296 mm. To help with the control of the volume mesh near the car, an inner box was generated having an upstream length of 216 mm, downstream 648 mm, width 292 mm and height 365 mm. Tetrahedral and triangular mesh types were developed in this study. Just off the vehicle surface with exception of underbody and wheels, cells of prismatic layers were developed. For best meshing, the inner box body sizing was 10 mm element length and face sizing of 10 mm was used on the vehicle. The advanced size function is proximity and curvature, used for the progression from minimum size elements, near and around the curvature of the vehicle to maximum size elements far away from the vehicle toward the walls of the wind tunnel box. High smoothing which increases the number of smoothing iterations and improving element quality by moving nodes and elements in the vicinity was used. The car and the road were included in the program-controlled inflation.

In this work, commercial CFD software Fluent was used for analysis. Three-dimensional RANS equation was solved using realizable $k-\varepsilon$ turbulence model with non-equilibrium wall function. For all the models, the turbulence model was employed in the Fluent simulations. The simulations were run with a velocity of 80, 100 and 120 kmph. In the simulation, the air flew from the velocity inlet toward the pressure outlet with a selected amount of velocity. 1% reduction was achieved in turbulence intensity for the velocity at inlet. The flow Courant number was set to 50, while both the explicit relaxation factors for momentum and pressure were 0.25, while employing a coupled scheme. The turbulent viscosity relaxation factor was set to 0.8 during the first upwind and changed to 0.95 for the second upwind. To ensure numerical stability, the numerical computation was first started with the first-order scheme. For better numerical accuracy, after one hundred iterations, the numerical scheme was switched to the second-order scheme. This scheme was continued for another 500 iterations. Most of the scaled residuals and the global aerodynamic quantities such as the drag coefficient and the lift coefficient converged to $1e-3$ long way before the 600th iteration. Once convergence was reached, the solution could be analyzed to determine the effectiveness of the spoilers. Non-slip wall boundary condition is set on the vehicle surface. Inviscid wall boundary conditions are set on the rest of the wind tunnel surfaces.

3 Result and Discussions

Results of flow over the pickup vehicle and flow structures in terms of streamlines, pressure contour and velocity profiles in the wake region are compared with the CFD analysis of similar model by Yang and Khalighi [3]. Also, the surface pressure distribution along the symmetry plane is compared to that of Pramod et al. [4] which yielded the same distribution (Fig. 2).

Comparisons of streamlines were made between the analysis of present study and Yang and Khalighi [3] as shown in Figs. 3, 4, 5 and 6. It can be seen that the present study has shown accurately similar flow structures as that of Yang and Khalighi [3]. So, the present CFD simulation is validated against the CFD simulation of the same pickup truck by Yang and Khalighi [3] and with that of Pramod et al. [4].

Figure 5 above shows a pickup vehicle with no spoiler. Swirling motion of air inside the bed box of the vehicle in addition to the wide wake region subjects the baseline vehicles to high amount of drag. The flow around the pickup vehicle and the change in aerodynamic drag coefficient were investigated by carrying CFD simulation on all four models. The results of the simulation are analyzed as follows.

Fig. 2 Surface pressure distribution along symmetry plane of baseline model

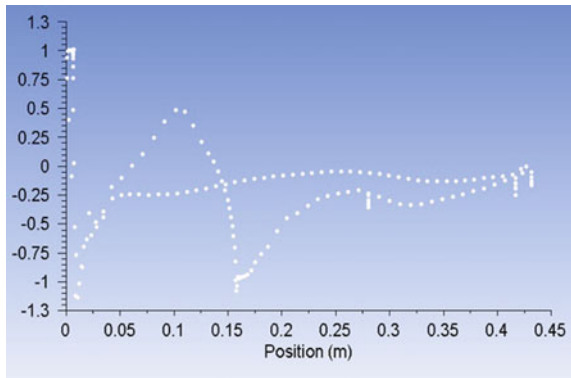


Fig. 3 Streamline on symmetry plane (Validation) [3]

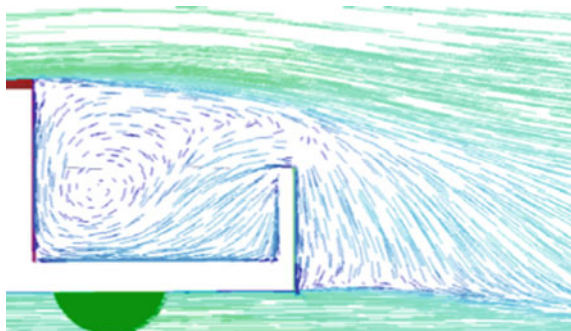


Fig. 4 Streamline on symmetry plane

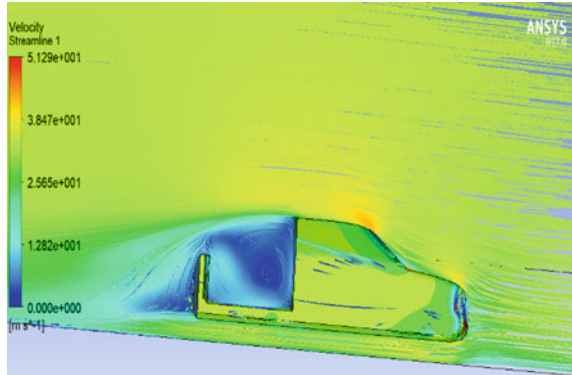


Fig. 5 Pressure distribution

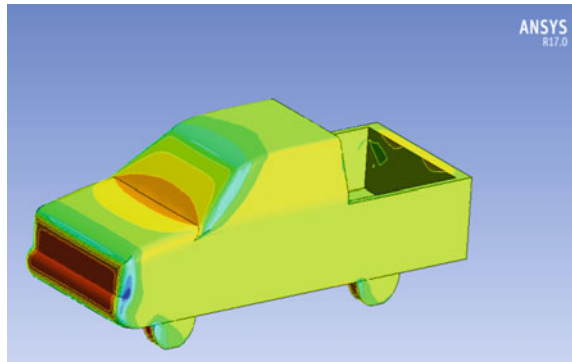


Fig. 6 Pressure distribution (Validation) [3]

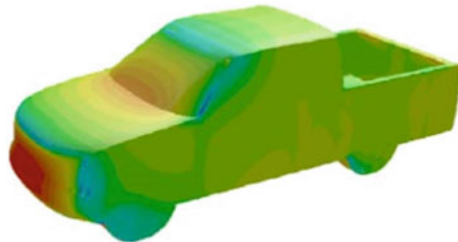


Fig. 7 Velocity contour of baseline model at 120 kmph

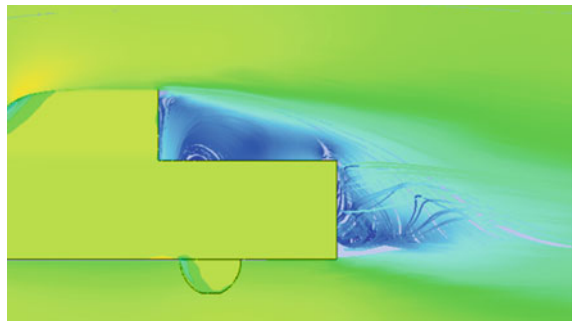


Fig. 8 Velocity contour of model I at 120 kmph

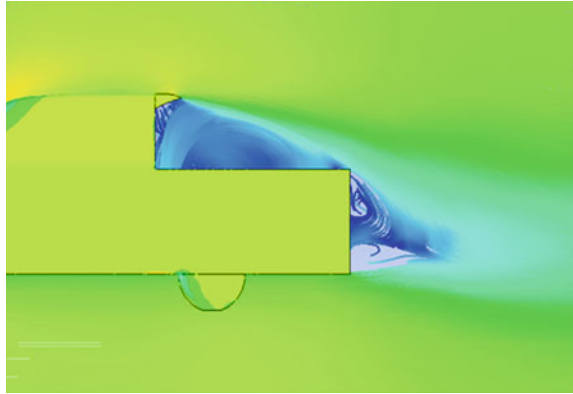


Fig. 9 Velocity contour of model II at 120 kmph

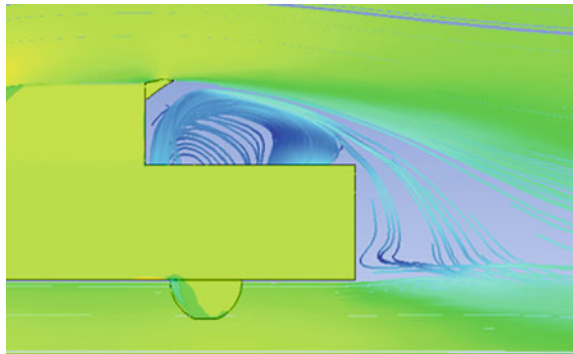
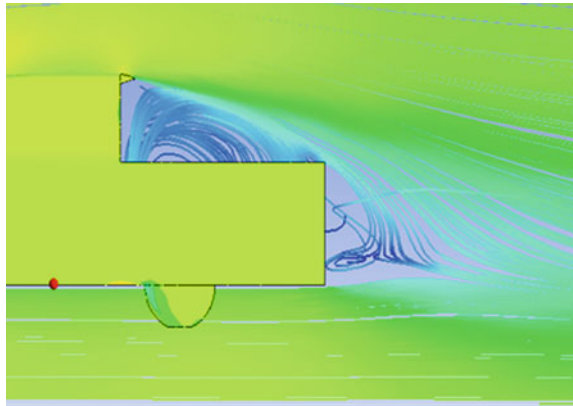


Fig. 10 Velocity contour of model III at 120 kmph



Figures 7, 8, 9 and 10 show the amount of the velocity streamline on the symmetry plane for different spoiler arrangements at speed of 33.33 m/s. As shown in Fig. 9, the height and length of wake region are bigger than the rest of the models, even it is bigger than the baseline model. The reason can be attributed to

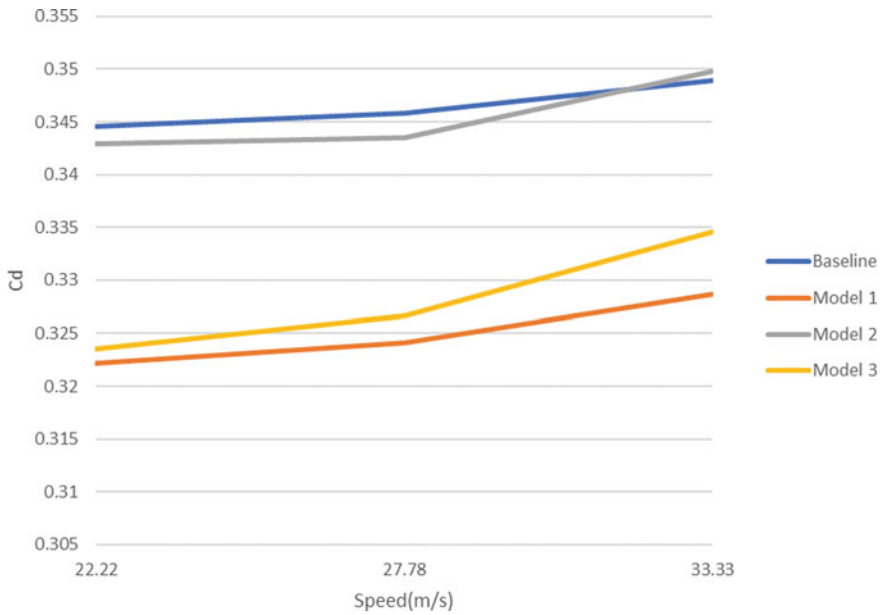


Fig. 11 Drag coefficient of all models at different speeds

that the spoiler is exposed to the flowing air over the vehicle which will increase the drag area. Since the air is flowing against the spoiler, the flow separation will be early because of the disturbed streamline air flow. The velocity contours show that by attaching spoiler, the flow separation can be delayed and the amount of swirling air inside the bed box of the pickup vehicles can be decreased. This will minimize the aerodynamic drag coefficient by reducing the wake region.

The aerodynamic drag coefficient for each model is plotted in Fig. 11. The drag coefficient of all models increases as their speed increases. However, the slope is different for each model. The graph shows that the drag rises quickly at higher speeds. The quick rise in the slope is higher for model three than the other three models. Model two has low drag than baseline model, but as the speed approaches 120 kmph, the drag coefficient of model two starts to rise above the baseline model. At low speed, model two has the lowest drag amount, and the baseline model has the highest drag coefficient, and at speed about 120 kmph, model one has still the lowest amount of drag, whereas model two has the highest drag. So, because of the reduced drag coefficient at both low- and high-speed models, one saves more fuel and has less environmental effect because of its reduced fuel consumption and reduced emission.

Table 1 summarizes the drag coefficient for the studied configuration along with the percentage difference from the baseline case. Compared to the baseline model, the entire studied configuration reduces the drag which is represented as drag coefficient. At 80 kmph, model one has the maximum improvement in drag

Table 1 Comparison of drag coefficients

Speed (m/s)	Models						
	Baseline Cd	Model 1 Cd	% diff. from Baseline	Model 2 Cd	% diff. from Baseline	Model 3 Cd	% diff. from Baseline
22.22	0.3446	0.3222	-6.500290	0.3429	-0.493325	0.3235	-6.123047
27.78	0.3458	0.3241	-6.275303	0.3435	-0.665124	0.3266	-5.552342
33.33	0.3489	0.3287	-5.789624	0.3498	0.257953	0.3346	-4.098596

reduction of 6.50% followed by model three with a drag reduction improvement of 6.12%. The least improvement in drag reduction is achieved by model two which is 0.493%.

At 100 kmph, model one has the best drag reduction of 6.27% and model three has 5.55% drag reduction from the baseline model which is better than that of model two which has only 0.66% reduction.

At speed of 120 kmph, model one still has the maximum improvement in drag reduction by 5.78% followed by model three with a drag reduction improvement of 4.09%. At this speed, the drag coefficient of model two has reached a point where it exceeds the drag coefficient of baseline model. So, driving model two at speed near and above 120 kmph will increase the drag coefficient more than the baseline model.

Table 2, we can see that maximum fuel amount of 3.90% can be reduced in model one traveling at 80 kmph. Model one reduces 3.76 and 3.47% of fuel when compared to baseline model at speed of 100 and 120 kmph, respectively. The other high reduction is from model three with 3.67, 3.33 and 2.45% at speed of 80, 100 and 120 kmph, respectively. Model two has the least fuel reduction with 0.29% at 80 kmph and 0.39% at 100 kmph. But, when model two travels at speed approaching 120 kmph, instead of reducing it consumes more amount of fuel than the baseline model.

Table 2 Fuel consumption reduction

Model	Speed (m/s)	% diff. from Baseline	Percent of Fuel Saving
Baseline	22.22		
	27.78		
	33.33		
Model One	22.22	-6.500290192	3.900174115
	27.78	-6.275303644	3.765182186
	33.33	-5.789624534	3.473774721
Model Two	22.22	-0.493325595	0.295995357
	27.78	-0.665124349	0.39907461
	33.33	0.257953568	-0.154772141
Model Three	22.22	-6.123041207	3.673824724
	27.78	-5.552342394	3.331405437
	33.33	-4.098595586	2.459157352

4 Conclusions

After the analysis on all models, the spoiler minimized the amount of swirling air in the bed of the vehicle and hence reduced the amount of drag coefficient compared to baseline model. The highest improvement of aerodynamic coefficient (Cd) of 6.50% was achieved for model one. The reduction in the amount of drag coefficient has helped models one, two and three, especially model one to reduce total fuel consumption by 3.90%. On all model, the amount of drag has increased with increasing speed. So, with respect to the length of the spoiler, it can be seen that the model with long spoiler has better drag reduction than the model with short spoiler. Therefore, it is possible to say that increasing the length of the spoiler to 21 mm has reduced the amount of drag coefficient, whereas inclining the spoiler to 12° has increased the drag more than the model without spoiler at higher speeds.

Acknowledgements We would like to thank God for all His blessings and provisions in our life. We would also like to thank N. Ramesh Babu (Ph.D.) for his immense contribution.

References

1. Alam F et al (2010) Effects of vehicle add-ons on aerodynamic performance. In: Proceedings of the 13th Asian congress of fluid mechanics, pp 186–189
2. Diehl A et al (2002) Reducing drag forces in future vehicles. University of Technology, Chalmers
3. Yang Z, Khalighi B (2005) CFD simulations for flow over pickup trucks. General Motors Corporation, Society of Automotive Engineers. 2005-01-0547
4. Krishnani P et al (2009) CFD analysis of drag reduction using external devices on pickup trucks. In: Proceedings of the 2010 ASME international mechanical engineering congress & exposition, pp 1–11. IMECE2010-39732
5. Lanfrit M (2005) Best practice guidelines for handling automotive external aerodynamics with FLUENT. Fluent Deutschland GmbH Birkenweg, 14a. 64295 Darmstadt/Germany
6. Demissie Y, Babu NR (2017) Aerodynamic drag reduction on locally built bus body using computational fluid dynamics (CFD): a case study at bishoftu automotive industry. *Int J Eng Res Technol (IJERT)* 6(11):276–283
7. Ashagrie G, Nallamotheu RB, Nallamotheu SK, Nallamotheu AK (2017) A study on driving stability of bus using computational fluid dynamics (CFD). *Int J Res Appl Sci Eng Technol.* 5 (11)
8. Molla KY, Ho K-C, Babu NR (2017) Aerodynamic design of the Ethiopian train for energy economy under cross wind conditions. *The Korean Society for Railway.* 2017.10, 342–344. KSR2017A142

Simulation of Performance and Emission of SI Engine Fuelled with Ethanol–Gasoline Blend (E15)



Tamiru Tesfaye Gemechu and Ramesh Babu Nallamothu

Abstract Conducting experiments to establish the suitability of biofuels to IC engines is time-consuming and expensive. In this study, the emission and performance of SI engine fueled with a gasoline–ethanol blend (E15) was simulated using a computer program developed with C++. Parameters analyzed included brake power, brake torque, thermal efficiency, bmep, combustion efficiency, bsfc and emissions. From the analysis, it was found that the bp and brake torque for E15 are increased by 1.6% compared to E0. The fuel consumption decreased by 2.4, 4.35 and 3.15% at a lower speed, maximum bp and maximum speed, respectively, for E15 compared to E0. The bp, brake torque, combustion efficiency, thermal efficiency, and bmep are higher for E15 than E0. In the experimental investigation, the bp and brake torque for E15 were increased by 2.96 and 1.6%, respectively. The fuel consumption for E15 is lower by 1.3% than E0 at a lower speed of 2308 rpm, higher for E15 by 1.7% than E0 at maximum brake power (2950 rpm), and higher for E15 by 2.5% than E0 at maximum speed (3440 rpm). The deviation between the simulated result and the experimental result was less than 5% for all parameters.

Keywords Alternative fuels · Thermodynamic analysis · SI engine

T. T. Gemechu

Department of Agricultural Engineering, Haramaya Institute of Technology,
Haramaya University, Dire Dawa, Ethiopia
e-mail: tamiru787@gmail.com

R. B. Nallamothu (✉)

Mechanical Systems and Vehicle Engineering Department, School of Mechanical Chemical and Materials Engineering, Adama Science and Technology University, Adama, Ethiopia
e-mail: rbnallamothu@gmail.com

1 Introduction

The prices of petroleum products are generally on an increasing trend and consequently affecting the cost of living in general. This continuous increase has resulted in the prices of some products tripling in the last decade. The infrastructure necessary for the distribution of petroleum products is not well developed in some regions of developing countries, due to which these products are not readily available and are very expensive. The usage of petroleum fuels causes dangerous environmental pollution. Also, there exists an emission of GHGs which are responsible for global warming. There is a need to reduce over-dependence on petroleum products for the sake of reducing harmful emissions and their ill effect on human health and the environment. Ethanol–gasoline blend with percentage volume of ethanol up to 15% can be used in unmodified SI engines. The presence of oxygen and high ON were significant features of usage ethanol–gasoline blends [1].

The fuel consumption and SFC showed a marginal decrease with the usage of ethanol–gasoline blends [2]. Leaner and better combustion is possible with the usage of ethanol–gasoline blends. It was demonstrated that the addition of ethanol up to 5–15% to gasoline blends caused an increase in the engine bp, torque and volumetric efficiency, brake thermal efficiency, and decreases the bsfc [3–5].

The emission characteristics improved as the percentage of ethanol increases in gasoline. The HC and CO emission values observed to be reduced with an increase in ethanol percentage in the blend. The efficiencies increase with the increase in the percentage of ethanol. For all measured parameters, E5 and E10 gave the best result at a constant speed of 2000 rpm; thus, ethanol can be comfortably used as an additive for gasoline. Brake thermal efficiency observed to be increasing as the volume percentage of ethanol fuel is increased in the mixture [6]. HC, CO, and NO_x emissions decreased with ethanol blends due to leaner air–fuel mixtures. Catalytic converter showed a reduction in all three emissions. The reduction percentage increased with ethanol percentage in a blend. A small increment in NO_x emissions was noticed with catalytic converter [7].

Ethiopia is one of the countries which totally import petroleum from other country, and the high demand for energy is observing from day today. As a result, the country's economy highly depends on the fuel price and vulnerable to it which shocked by its fluctuation. Due to this, the government formulated a policy to blend locally produced biofuel with petrol, and several researchers recommend this blended fuel to minimize the emissions of GHG and also to save hard currency [8, 9].

Since 2009, Nile petrol, a company belonging to Sudan, is a sole agent in Ethiopia and was carrying out the process of blending ethanol 5% with gasoline (E5) and providing for the local market. But now Oil Libya is awarded the task of blending the 10% ethanol–benzene blend by the Ministry of Water, Irrigation, and Electricity (MoWIE) (<https://www.ezega.com>). Many researchers concluded that using E15 (15% ethanol and 85% gasoline) is possible without engine modification. Previously, the research methods used for evaluation of the performance of the engine were very time-consuming and were requiring the service of a professional

in the area. Despite the fact that a number of studies have been done in this area in other countries, there is no basis for applying the results to practical operations. If a thermodynamic analysis of blend fuel is done using a computer program, one can determine the engine performance and emissions rapidly and easily for every blend product.

The objectives of this work are: (i) to develop a computer program (written in C++ language) that can predict the engine performance and emissions for every amount of blend proportion; (ii) to carry out experiments in order to validate the predicted data based on some engine performance parameters such as brake power, brake thermal efficiency, torque, volumetric efficiency, bmep and bsfc on different proportions of blend; and (iii) to determine the amount of emission for all selected blend proportions by including combustion products like CO₂, H₂O, O₂, N₂, HC, CO.

2 Materials and Methods

2.1 System Simulation

A C++ code was developed for theoretical thermodynamic analysis of a selected engine for its performance. The developed code was validated by the experimental data obtained by conducting experiments on the engine.

2.2 Experimental Site

The experimental analysis was conducted at Dilla University at a city called Dilla, which is located on the main road from Addis Ababa to Nairobi. It is the administrative center of SNNPR. The longitude and latitude of Dilla are 6°24'30"N 38°18'30"E with an elevation of 1570 m above sea level.

2.3 Specifications of Equipment

The specifications of the selected SI engine are given in Tables 1, 2, 3 and 4 show the details of exhaust gas analyzer used in this experiment. Physical and chemical characteristics of both pure gasoline and blends of gasoline and ethanol were measured. The SI engine test stand and exhaust gas analyzer are shown in Figs. 1 and 2, respectively.

Table 1 Engine specifications

Engine specification	
Engine type:	Air-cooled 1-cylinder, 4-stroke petrol engine
Dimensions:	L × W × H: 500 × 345 × 410 mm
Weight: approx.	34 kg
Compression:	8.5:1
Bore:	89 mm
Stroke:	63 mm
Connecting rod length:	110 mm
Crank throw:	31.5 mm
Max. power:	8.2 kW
Max. speed:	3600 rpm
Max. torque:	24.6 Nm at 2200 rpm
Oil capacity:	1.4 L
Ignition:	Magneto ignition
Sound level	96 dB(A)
Intake valve open bTDC	15°
Intake valve close aBDC	50°
Start of combustion bTDC	15°
Duration of combustion	55°
Exhaust valve open bBDC	50°
Exhaust valve close aTDC	15°

Table 2 Environmental requirements for exhaust gas analyzer

Environment parameters	Requirements
Ambient temperature	5...45 °C
Ambient air pressure	860...1060 hPa
Max. temperature/humidity ratio	35/95

2.4 Collection of Required Data

With the aid of the equipment described above, the following engine performance parameters were determined and recorded: torque, bhp, mep, SFC. Others include temperature, pressure, volume at each revolution of crank angle, amount of exhaust gases such as CO₂, CO, and HC. This data was used to validate the results predicted by the computer simulation.

Table 3 Technical data of exhaust gas analyzer

Gas concentration resolution	4 digits
Device status	Errors will be displayed
Warming-up time	30 s
Automatic zero-point check	Every 60 min, 3.2 °C temperature change or negative measuring values
Zero gas	Fresh air, free of HC, CO and CO ₂
Response time	IR-Components: T95 < 15 s O ₂ : T95 < 60 s @ Flow rate >90 dm ³ /h
Position of use	Horizontal, required because of the operation of the condensate separator; Slope <8°
Dimensions	Width 258 mm, depth 330 mm, height 203 mm (including foots + printer)
Mass	ca. 6.5 kg
Degree of protection	IP 20

Table 4 Functional requirements of exhaust gas analyzer

Measuring components and ranges	CO 0–10.00% vol, CO ₂ 0–20.00% vol, HC 0–2500 ppm vol (C ₆ H ₁₄), O ₂ 0–22.00% vol, NO 0–5000 ppm vol (available as an option) NO _x 0–5000 ppm vol (available as an option)
Measuring components absolute tolerances	CO ± 0.03% vol, CO ₂ ± 0.5% vol HC ± 10 ppm vol (C ₆ H ₁₄), O ₂ ± 0.1% vol NO ± 2 ppm vol (available as an option) NO _x ±25 ppm vol (available as an option)
Measuring components relative tolerances	± 5%

3 Result and Discussion

The results of the simulation process using the computer program (written in C++) and the data obtained from actual experiments are presented and discussed in this section. The parameters include brake horsepower, brake torque, brake-specific fuel consumption, and exhaust gas emissions. The simulated results and experimental results were also compared.

3.1 Temperature, Pressure, and Volume

The temperature–crank angle plot, pressure–crank angle plot, and pressure–volume plot, as predicted by the computer simulation (C++ program), are shown in Figs. 3,



Fig. 1 Experimental setup

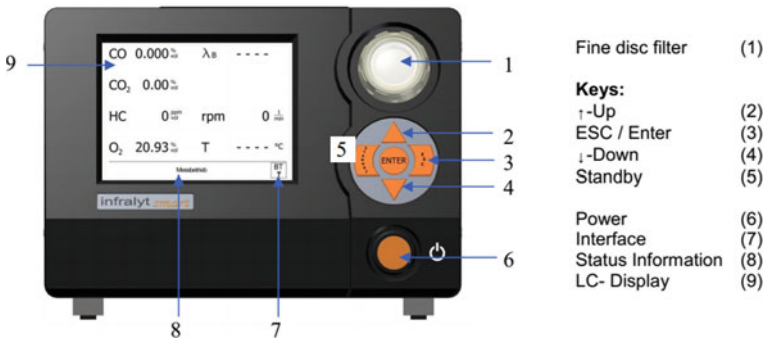


Fig. 2 Infracal smart exhaust gas analyzer

4, and 5, respectively. Temperature, pressure, and volume curve are analyzed for each revolution of crank angle. The curves show intake, compression, expansion, and exhaust stroke, and the maximum temperature and pressure predicted at end compression stroke of all blend proportions are as shown in Figs. 3 and 4, respectively. As the amount of blend proportion increases from E0-E15, the recorded temperature and pressure also increased.

Fig. 3 Maximum temperature versus engine crank angle

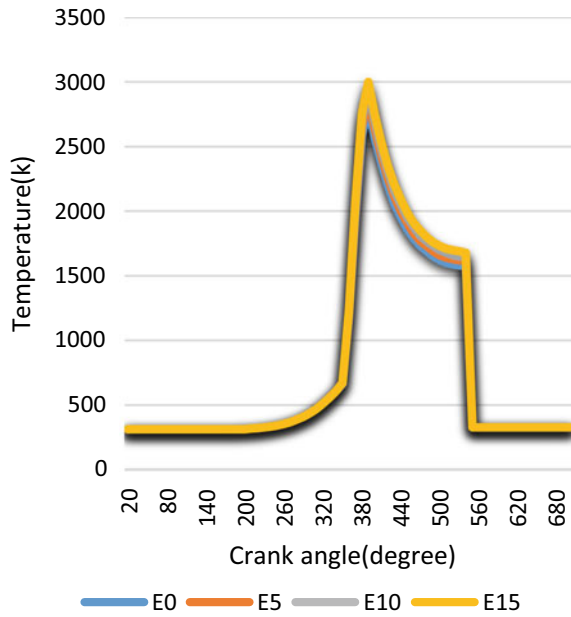
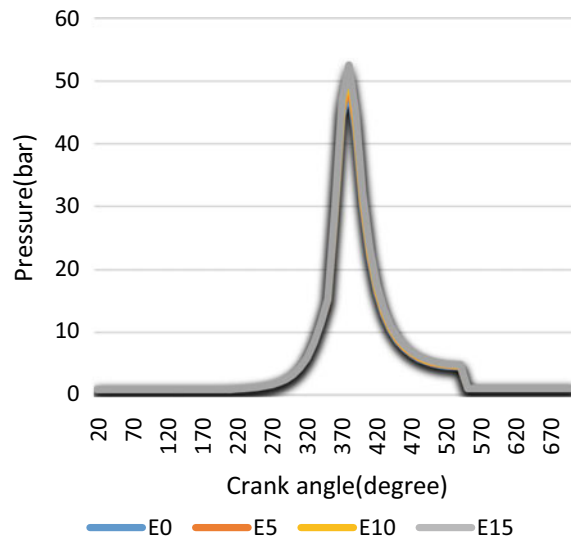


Fig. 4 Maximum pressure versus engine crank angle



The P-V diagram shown in Fig. 5 and which has a significant role in engine design can almost represent actual engine cycle, but the thermodynamic analysis of both intake and exhaust strokes is ideal.

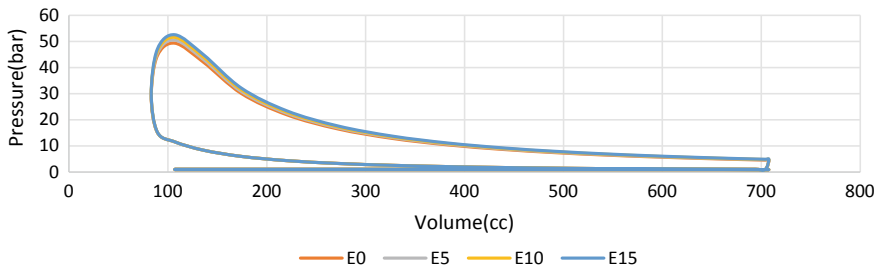


Fig. 5 Pressure versus volume diagram

3.2 Engine Performance Parameters

The simulated result and experimental result obtained for break power are as presented in Figs. 6 and 7, respectively. Brake power increased with increasing engine speed from 0 to 3000 rpm after which it decreased with further increase in engine speed for all levels of blend proportion for both simulated and experimental results. Also, brake power increased with an increasing blend from E0 to E15 for both simulated and experimental results. Brake torque increased with an increasing engine speed from 0 to 1500 rpm after which it decreased with further increase in engine speed (Figs. 8 and 9). In the same development, brake torque increased with an increasing blend from E0 to E15 for both simulated and experimental results. Brake-specific fuel consumption decreased with increasing engine speed from 0 to 2000 rpm after which it increased with further increase in engine speed for both simulated and experimental results (Figs. 10 and 11).

Fig. 6 Brake power versus engine speed from computer C++ program for E0–E15

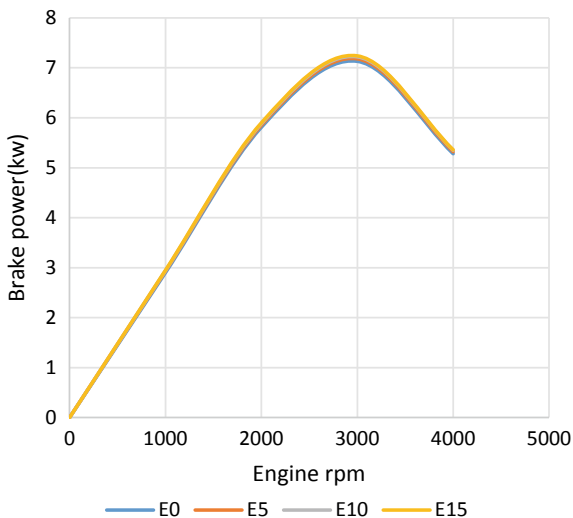


Fig. 7 Brake power versus engine speed for experimental investigation for E0 and E15

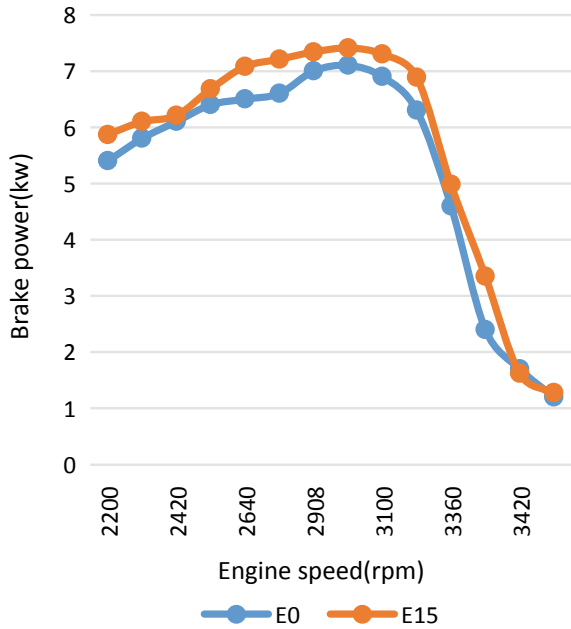


Fig. 8 Brake torque versus engine speed from computer C++ program for E0–E15

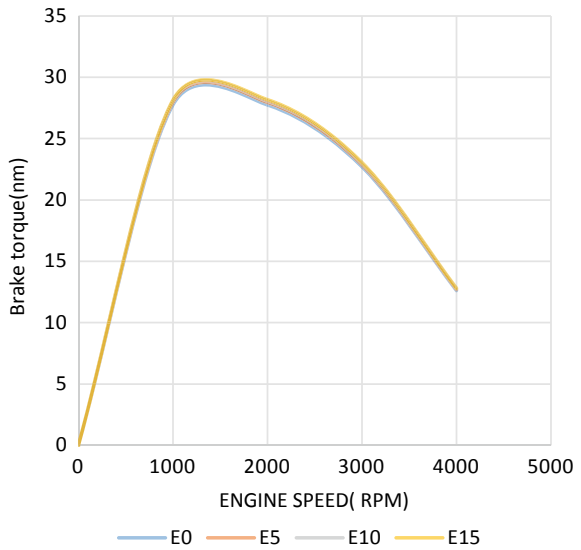


Fig. 9 Brake torque versus engine speed for experimental investigation for E0 and E15

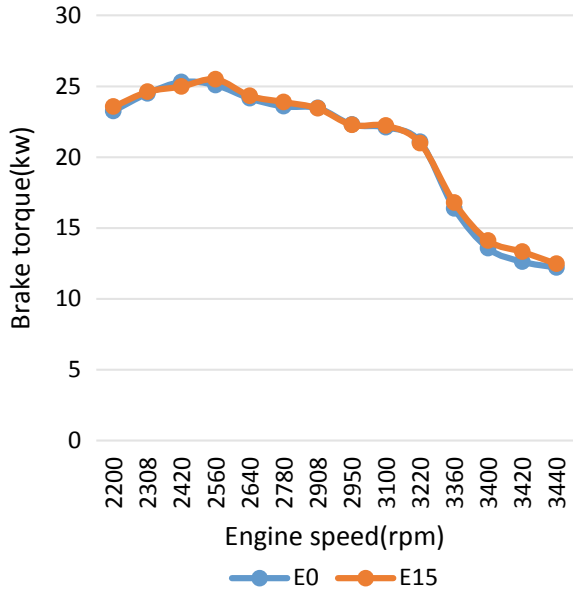


Fig. 10 Brake-specific fuel consumption versus engine speed from computer C++ program for E0-E15

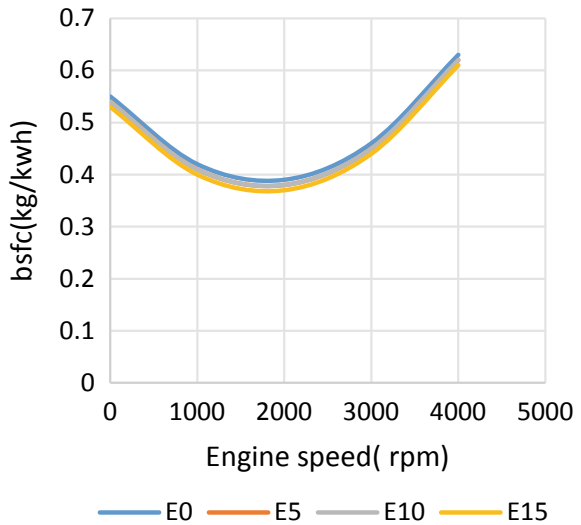
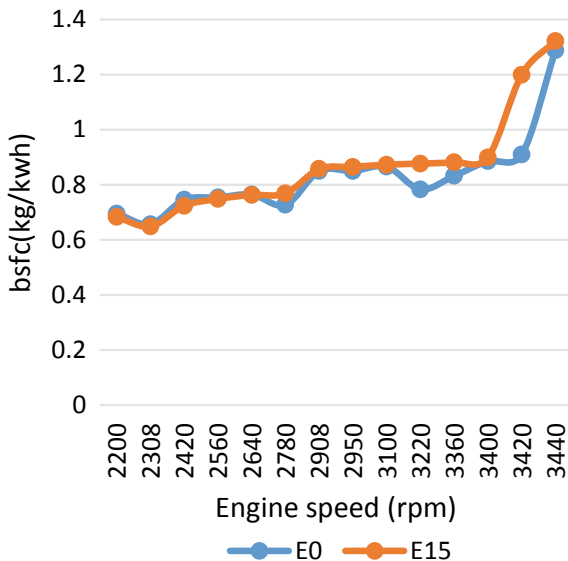


Fig. 11 Brake-specific fuel consumption versus engine speed for experimental investigation for E0 and E15



3.3 Emission Analysis

The emission amounts of CO₂ and CO were simulated for a selected engine speed as shown in Figs. 12 and 14, respectively. As shown in the figures, as the amount of blend proportion increased, the emission of both CO₂ and CO decreased up to E50, but this one focused only on E15 which was experimentally investigated. As shown, in Figs. 13 and 15, the amount of emission of both CO₂ and CO for E15 is less than E0 for almost all recorded engine speeds.

Fig. 12 CO₂ emission versus blend proportion from computer C++ program for E0–E15 for a selected speed

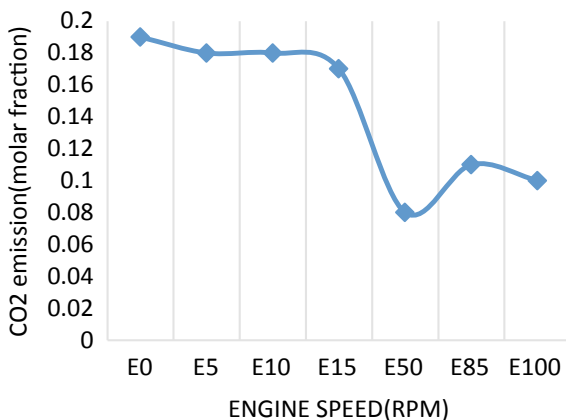


Fig. 13 CO₂ emission versus blend proportion for experimental investigation for E0 and E15

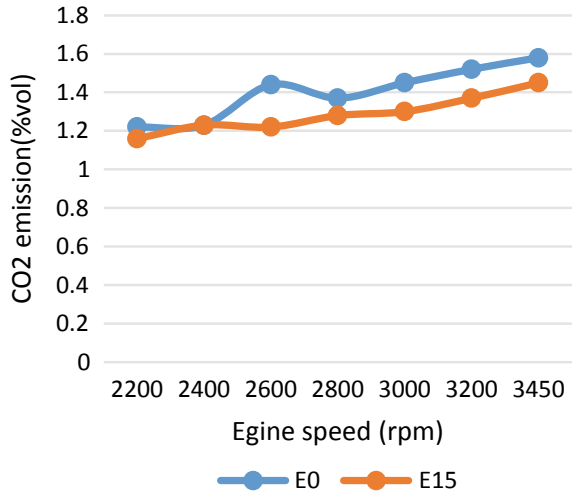


Fig. 14 CO versus blend proportion from computer C++ program for E0–E15 for a selected speed

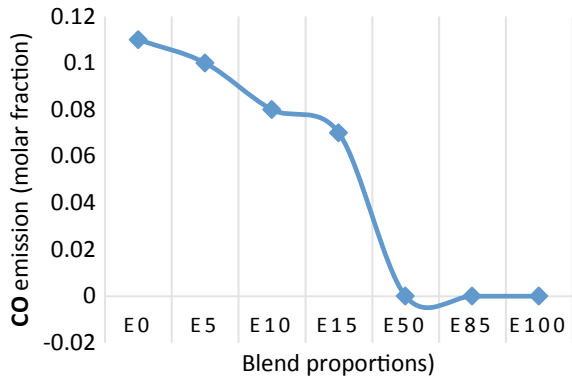
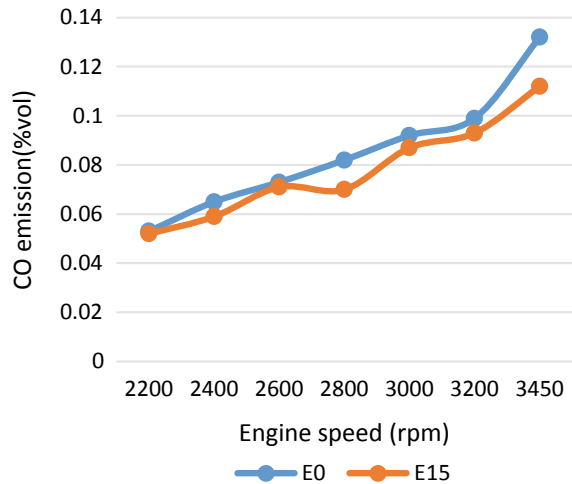


Fig. 15 CO versus blend proportion for experimental investigation for E0 and E15



4 Conclusion

In this work, the thermodynamic analysis of actual engine cycle with ethanol-gasoline blend fuel (E15) was carried out using mathematical model. Based on the model, the computer C++ program was developed to predict the engine performance parameters such as brake power, brake torque, bsfc, and exhaust gas emission. This program is versatile that can be functional for every type of engine and any type of blend proportions. The brake power and brake torque are higher while specific fuel consumption is lower for E15 than E0, and the brake-specific fuel consumption is lower for E15 than E0. Therefore, the brake power torque for E15 is increased by 1.6% from E0. But the fuel consumption decreased by 2.4, 4.35 and 3.15% at a lower speed, maximum power and maximum speed, respectively, for E15 than E0. The emission value which gained by computer C++ program and experimental investigation was almost similar. According to experimental investigation, the emission of CO, CO₂, HC and O₂ is lower for E15 than E0. The emission of CO, CO₂, HC increases with the increase of engine speed, and O₂ emission decreases. The deviation between result of developed computer C++ program and experimental investigation was less than 5% for all analyzed engine parameters.




References

1. Pandey V, Gupta VK (2016) Experimental analysis of performance characteristics of an SI engine on ethanol-gasoline blended fuel. *Int J Eng Develop Res* 4(3). ISSN 232
2. Mostafa Ahmed A, Youssef I, Mourad M (2017) The influence of ethanol-gasoline blends on performance characteristics of engine generator set. *Am J Eng Res (AJER)*, 6(9). p-ISSN 2320-0936
3. Nallamothe RB, Fekadu G, Appa Rao BV (2013) Comparative performance evaluation of gasoline and its blends with ethanol in gasoline engine. *Global J Biol Agric Health Sci*. ISSN 2319-5584
4. Yusaf T, Najafi G, Buttsworth D (2014) Theoretical and experimental investigation of SI engine performance and exhaust emissions using ethanol-gasoline bend. <http://www.researchgate>
5. Nallamothe RB, Kamal NA, Kishan NS, Niranjana Kumar IN, Appa Rao BV (2020) Effect of multiple injection strategy on combustion of cotton seed oil biodiesel in CRDI diesel engine. In: *Recent trends in mechanical engineering*. Springer Nature Singapore Pvt Ltd., pp 107–119. https://link.springer.com/chapter/10.1007/978-981-15-1124-0_9
6. Saikrishnan V, Karthikeyan A, Jayaprabakar J (2018) Analysis of ethanol blends on spark ignition engines. *Int J Ambient Energy* 39(2):103107. <https://doi.org/10.1080/01430750.2016.1269678>
7. Samuel Raja A, Valan Arasu A, Sornakumar T (2015) Effect of gasoline ethanol blends on performance and emission characteristics of a single cylinder air cooled motor bike si engine. *J Eng Sci Technol* 10(12):1540–1552

8. Teka M (2007) Biofuel strategy of Ethiopia. East African Power Industry Convention, Addis Ababa
9. Babazadeh Shayan S, Seyedpour M, Ommi F, Moosavy SH, Alizadeh M (2011) Impact of methanol-gasoline fuel blends on the performance and exhaust emissions of a SI engine. *Int J Automot Eng* 1(3)

CFD Studies on the Modified Laparoscopic Instrument Used in Minimally Invasive Surgeries



Md. Abdul Raheem Junaidi , Gourabh Pandey, K. Ram Chandra Murthy , and Y. V. Daseswara Rao 

Abstract Laparoscopic surgery has gained importance over the open-cut surgery in the recent decades. However, multiple insertions are still needed while performing laparoscopic surgery for suction and irrigation which in turn might lead to post-surgical pain and scars over the abdominal region. Our aim is to reduce the number of instruments by creating a modified one which will work both as a flow tube (for suctioning and irrigating purposes) and as a laparoscopic dissector accordingly as per the need of a surgeon. This reduces the time spent in swapping them, thereby contributing to the reduction in surgeon's effort and time. This paper is based on CFD studies done on the modified laparoscopic instrument which is designed to work both as a suction–irrigation device and as a surgical forceps. Five different pressure differences have been used to study the performance of the new design in terms of the resulting mass flow rate in both suction and irrigation modes.

Keywords Computational fluid dynamics · Suction · Irrigation · Laparoscopic instruments · Forceps

1 Introduction

Laparoscopy is a surgical diagnostic method used to examine the organs within the abdomen. Laparoscopy uses an instrument called a laparoscope, which allows doctors to visually inspect inside the human body in real time, without open

Md.A. R. Junaidi (✉) · G. Pandey · K. Ram Chandra Murthy · Y. V. Daseswara Rao
Department of Mechanical Engineering, BITS Pilani, Hyderabad Campus, Hyderabad,
Telangana, India
e-mail: raheem.junaidi@gmail.com

G. Pandey
e-mail: f20170413@hyderabad.bits-pilani.ac.in

K. Ram Chandra Murthy
e-mail: rcmurthy@hyderabad.bits-pilani.ac.in

Y. V. Daseswara Rao
e-mail: yvdrao@hyderabad.bits-pilani.ac.in

surgery. During laparoscopic surgery, endoscopic instruments are passed through small incisions on the abdominal wall to reach the surgical site within the abdominal cavity of the patient [1]. Using this procedure, doctors can also obtain biopsy samples. It is generally performed when non-invasive methods cannot help with diagnosis.

The development of minimally invasive surgery over the past two decades had a great impact on surgical practice [2]. Laparoscopic surgeries are performed through one or multiple small incisions. Mechanical advances have continuously delivered us with smaller laparoscopic instruments and higher-quality imaging that permits laparoscopic surgeons to perform dissections precisely with least possible bleeding through maximal dissection planes, even those that are exceptionally vascular [3]. Many imaging techniques have been developed such as ultrasound (uses high-frequency sound waves), CT scan (uses a series of special X-rays) and MRI scan (uses magnets and radio waves) [4]. Many major advancements have been made in the field of robot-assisted surgeries to ensure removal of any human error in some of the most complex surgeries [5]. Government of India is keen on fostering biotech innovation to commercialize the growth in industries and advances in the field of medicine [6].

For any laparoscopic surgeries, since the incisions are small, it requires high-precision dissectors and demands highly skilled surgeons. Different types of surgeries demand different laparoscopic surgical instruments. In abdominal laparoscopic surgeries, it is very important to have incisions for suction and irrigation. During the surgery, irrigation operation is done to wash the abdominal cavity during the surgery to remove infection, blood, bile, pus and other body fluids [7]. Suction operation is then used to remove the bleeding that could possibly occur at the site of surgery. In a similar manner, suction irrigation cannula is one such instrument which is used for both suction and irrigation operations. The most commonly used suction–irrigation (S–I) device is basically of 5 mm diameter with a length of 330 mm [8].

Out of all different types of laparoscopic dissectors, Maryland forceps, an often used laparoscopic instrument, has been considered in this work. It requires an incision of 10 mm diameter and can go up to the depth of 200 mm. We have designed the modified forceps such that the flow tube is merged with the laparoscopic dissector. This enables the modified instrument to transform into a suction–irrigation device or into forceps on demand. Flow inside the flow tube has been simulated using ANSYS Fluent for five different pressure differences by considering 10 mm Hg as the average pressure inside the abdominal cavity for both suction and irrigation [9, 10]. Simulations are done using water as the fluid for suction and irrigation.

In this analysis, a modified design of Maryland forceps is used that incorporates the functions of a forceps, suction–irrigation and cauterization in order to reduce the repeated insertions and removal of different devices like suction–irrigation device and Maryland forceps. In contrast to the conventional procedures, this design requires only one instrument to play a role as both suction–irrigation device and as a forceps. This minimizes the operation time by reducing the number of instruments used and time spent in swapping them, thereby contributing to the reduction in surgeon's effort and time.

2 Geometry

The geometry of the modified design used for CFD analysis and its bounding surfaces are shown in Fig. 1. The flow tube is designed along the axis of laparoscopic dissector with a protrusion angle of 30° and a diameter of 7 mm at the proximal end. A slider mechanism helps it to transform into a suction–irrigation pipe or into forceps in real time.

3 Mesh

Meshing is done using a 3D tetrahedral mesh over the entire geometrical domain. A boundary layer is created along the fluid–surface interface with seven layers and a growth rate of 1.2. Grid independence study has also been carried out to ensure the invariance of results. The final mesh used for simulations consists of 77,144 nodes and 244,717 elements.

Suction pressure (25 mm of Hg)	Nodes	Elements	Mass flow rate (g/s)	% error
Coarse	45,276	115,761	48.058	0.087
Intermediate	77,144	244,717	48.1	0
Fine	143,729	598,905	47.8	0.624

As seen from the table above, mass flow rate in the modified instrument and the S–I device resulting from the coarse, medium and fine meshes resembles each other closely. Therefore, an intermediate mesh of 77,144 nodes and 244,717 elements is used for further analysis of the modified instrument. Similarly, mesh independent study for the S–I device gives the desired mesh for 171,051 nodes and 165,600 elements.

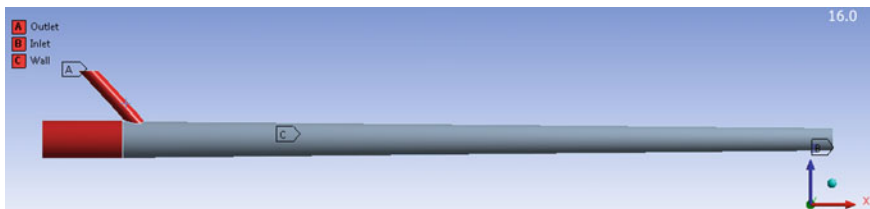


Fig. 1 Geometry of the modified design used for CFD analysis

4 Simulation Setup

The flow simulation is carried out using ANSYS Fluent and is assumed to be steady with no heat transfer. RNG $k-\epsilon$ model (2 equation) turbulence model [11] with default model constants is used with enhanced wall treatment. Pressure boundary conditions with 10 mm Hg at the inlet and five different pressure values at the outlet are used as shown in Table 1. The wall surface is modeled as a no-slip stationary wall.

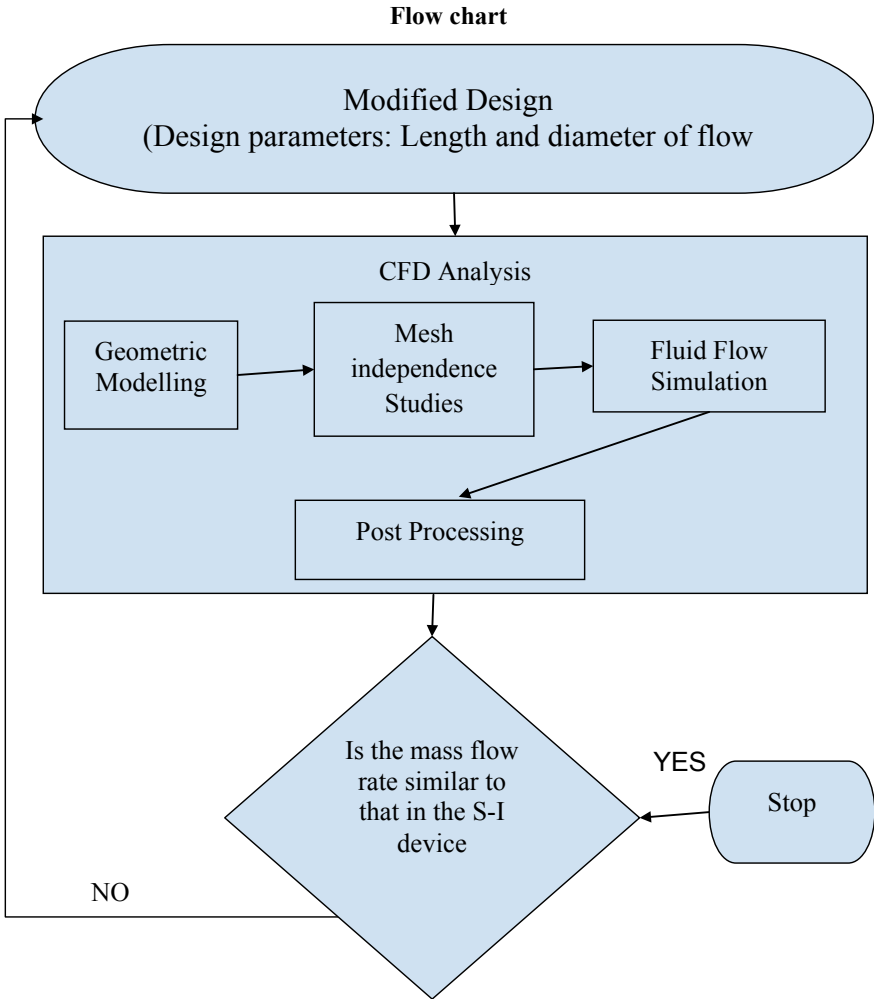


Table 1 Pressure boundary conditions (values shown in mm Hg)

S. No	Pressure difference	Suction mode		Irrigation mode	
		Inlet	Outlet	Inlet	Outlet
1	5	10	5	15	10
2	10	10	0	20	10
3	15	10	-5	25	10
4	20	10	-10	30	10
5	25	10	-15	35	10

5 Results

The contour plots shown in Figs. 2, 3, 4, and 5 are for the suction case with 25 mm Hg pressure drop, i.e., 10 mm Hg (1333 Pa) at the inlet and -15 mm Hg (-2000 Pa) at the outlet.

The pressure contours show that the regions of larger pressure drop are at the jaws and protrusion as the geometry is less streamlined. Correspondingly, the flow velocity also peaks at these locations above the mean value.

The magnitude of turbulence is illustrated in the turbulence eddy dissipation rate and kinetic energy contours. It can be again observed that the magnitude of turbulence kinetic energy is larger primarily near the protrusion and next at the jaws. The geometric irregularities at these locations are large which result in large turbulence and hence a large pressure drop as explained in the preceding paragraph.

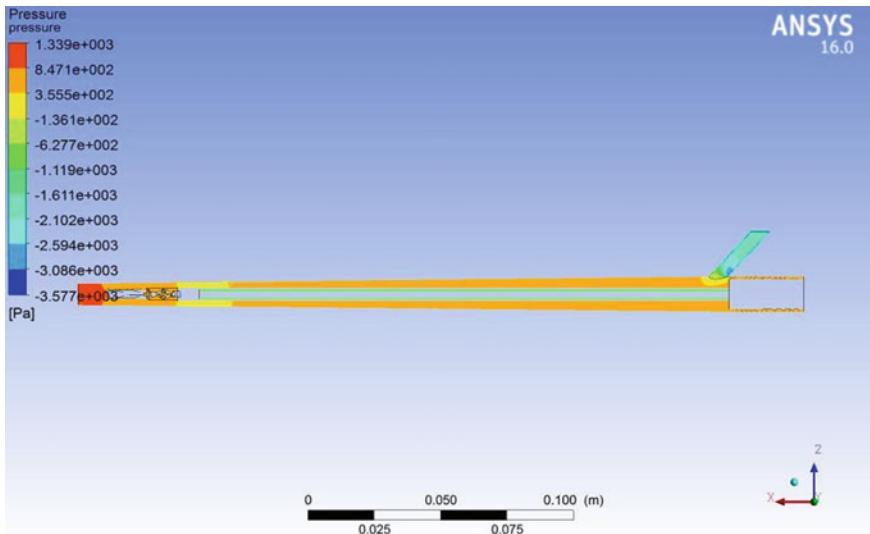


Fig. 2 Pressure distribution contours

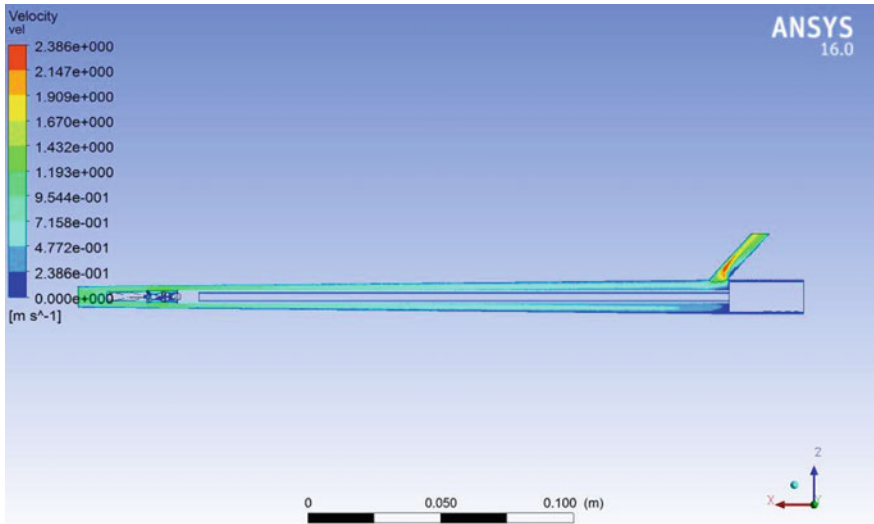


Fig. 3 Velocity contours

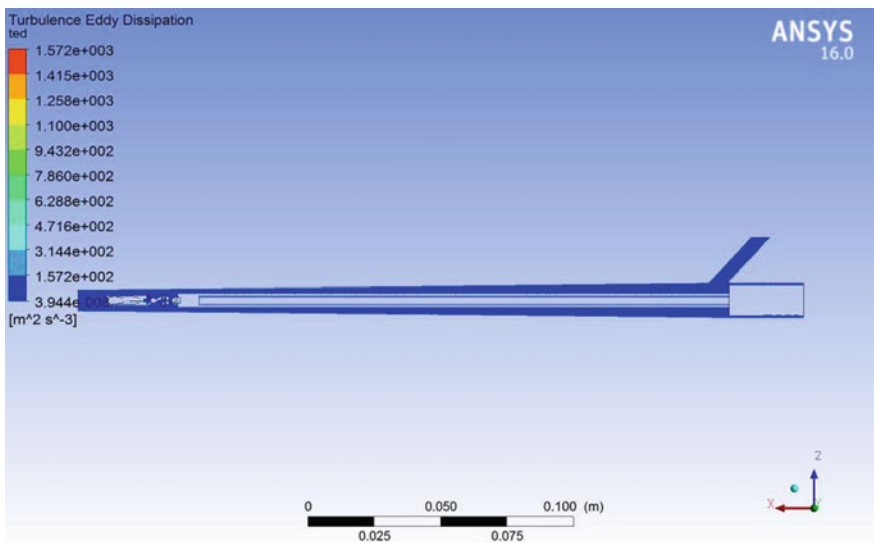


Fig. 4 Turbulence eddy dissipation contours

The mass flow rates of water found from the simulations for the S-I device (modeled as a simple pipe) and the modified laparoscopic device are shown in Table 2 in both suction and irrigation modes of operation. The same is shown

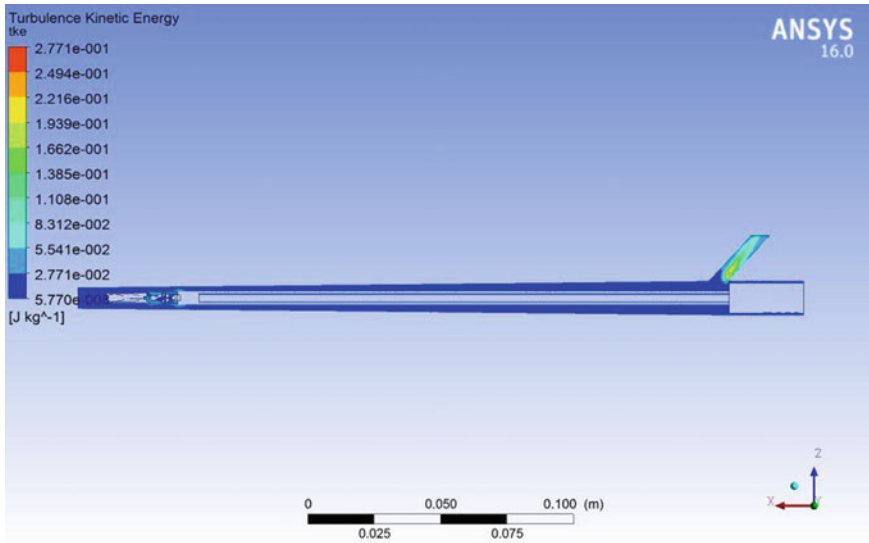


Fig. 5 Turbulent kinetic energy contours

Table 2 Mass flow rate (in g/s)

S. No.	Pressure difference (mm of Hg)	S-I device in suction and irrigation modes	Modified laparoscopic instrument	
			Suction mode	Irrigation mode
1	5	6.4	18.8	20.1
2	10	9.9	28.6	30.6
3	15	12.9	36.2	38.7
4	20	15.5	42.5	45.4
5	25	17.9	48.1	51.2

graphically in Fig. 6 where we see that the mass flow rate delivered by the modified instrument is more than that of the S-I device. Therefore, the proposed instrument caters to the mass flow rate delivered by the S-I device currently in use.

6 Conclusion

In our work, a modified laparoscopic instrument is proposed to ensure a reduced number of incisions over the abdominal region. This design requires only one incision to play a role as both suction-irrigation device and as a forceps thus reducing the risk of postoperative [12, 13] injuries which can happen due to

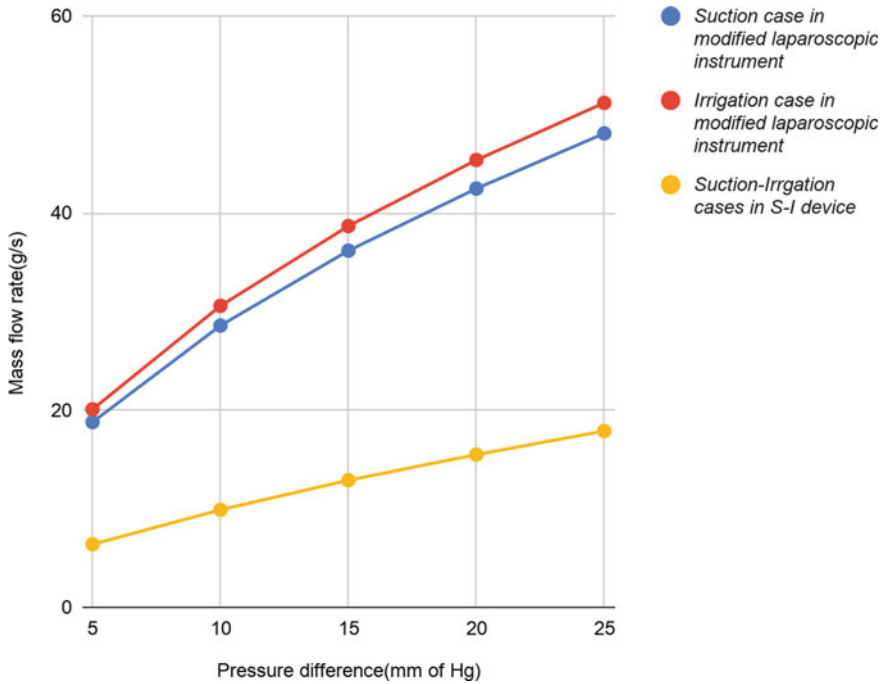


Fig. 6 Mass flow rate comparison

multiple incisions. The flow is simulated using water from which we can conclude the following.

- For the S–I device, the suction and irrigation mass flow rates are the same as the device is symmetric from both ends. In the modified instrument, the suction and irrigation mass flow rates are slightly different as the flow from both the ends is not symmetric.
- The mass flow rate provided by the new design is larger than the suction irrigation device that is already under use by the surgeons and hence meets the requirements from the flow perspective.
- Fabrication of the prototype of the new design is in progress which will be used for experimental validation of the above results.

The proposed design can be further optimized to meet the requirements of surgeons for onsite applications. This modified design has potential applications in laparoscopic surgeries like splenectomy, myomectomy, hysterectomy, appendectomy, diagnostic laparoscopy, nephrectomy, cholecystectomy, etc. Most of these procedures consume a significant amount of time which can be reduced with the proposed forceps design.

Acknowledgements Inputs on the medical front by Dr. Niranjan, Founder and CEO of Pinoty and Caremotto, are acknowledged. The contributions to this work by Anirudh and Harsha, students of BITS PILANI, Hyderabad Campus, are duly acknowledged. The authors also are grateful to the Department of Mechanical Engineering, BITS PILANI, Hyderabad Campus, for providing the computational resources.

References

1. Md. Abdul Raheem Junaidi, Harsha Sista, Ram Chandra Murthy Kalluri, YV Daseswara Rao, (2020) Laparoscopic surgical device, IN Patent Application: 202011034072.
2. Lai EC, Yang GP, Tang CN (2013) Robot-assisted laparoscopic liver resection for hepatocellular carcinoma: short-term outcome. *Am J Surg* 205(6):697–702 (Jun 1)
3. Guo S, Cui J, Xiao N, Bao X (2018) Simulation analysis of catheter bending in vascular intervention robot based on ANSYS. In: 2018 IEEE international conference on mechatronics and automation (ICMA), pp 585–590
4. Healthline homepage. <https://www.healthline.com/health/laparoscopy>. Last accessed 30 Mar 2020
5. Mocan B, Bintintan VV, Brad S, Ciuce C, Mocan M, Murar M (2016) Development of a robotic driven handheld laparoscopic instrument for non-invasive intraoperative detection of small endoluminal digestive tumors. In: *New trends in medical and service robots*. Springer, Cham, pp 197–210
6. Gupta S, Vashisht S (2019) A canvass on innovation and commercialization in biotechnology industry. *Amity J Comput Sci (AJCS)* 3(2):16–18
7. Elprama SA, Kilpi K, Duysburgh P, Jacobs A, Vermeulen L, Van Looy J (2013) Identifying barriers in telesurgery by studying current team practices in robot-assisted surgery. In: 2013 7th international conference on pervasive computing technologies for healthcare and workshops, May 5. IEEE, pp 224–231
8. Abdul Raheem Junaidi, Aakrit Patel, Ram Chandra Murthy, Y.V.Daseswara Rao (2021) Advances in laparoscopic surgeries and CFD perspective of suction-irrigation devices, AIP Conference Proceedings 2317, 030025. <https://doi.org/10.1063/5.0036257>
9. Md. Abdul Raheem Junaidi, Harsha Sista, Ram Chandra Murthy Kalluri, YV Daseswara Rao, (2020) Laparoscopic Surgical Device, IN Design Patent Application: 334185-001
10. Sandhu T, Yamada S, Ariyakachon V, Chakrabandhu T, Chongruksut W, Ko-Iam W (2008) Low-pressure pneumoperitoneum versus standard pneumoperitoneum in laparoscopic cholecystectomy, a prospective randomized clinical trial. *Surg Endosc* 23(5)
11. Wain RA, Whitty JP, Dalal MD, Holmes MC, Ahmed W (2014) Blood flow through sutured and coupled microvascular anastomoses: a comparative computational study. *J Plast Reconstr Aesthet Surg* 67(7):951–959 (Jul 1)
12. Kazemier G, De Zeeuw GR, Lange JF, Hop WC, Bonjer HJ (1997) Laparoscopic vs open appendectomy. *Surg Endosc* 11(4):336–40 (Apr 1)
13. Junaidi M, Kalluri R, Rao Y, Gokhale A, Patel A (2020) Design and fluid flow simulation of modified laparoscopic forceps. *Computer methods in biomechanics and biomedical engineering*, 1–20. <https://doi.org/10.1080/10255842.2020.1855331>

Study of Existing Systems to Control Inside Temperature of Car Compartment and Factors Influencing the Rise of Temperature Within the Car Compartment—A Review



Alok Bharti, P. Mathiyalagan, and Pawan Kumar Singh Nain

Abstract This paper presents the review of the influencing factors which led to the ascendancy in temperature of the car cabin and the effects of the subsisting ventilation system and solar reflective cover on cabin temperature when a vehicle is parked without shade during the daytime on a hot day. The commercially available ventilation system is not able to do the required cooling, and also it was unable to provide the same cooling throughout the car cabin. The solar reflective cover is an effective system, but it is very time-taking system because we need to cover the car to reflect back the sunlight. So this paper gives the idea about the how much existing system work and able to decrease the temperature.

Keywords Solar ventilation system • Solar reflective cover • Thermoelectric • Cooling

1 Introduction

During summer, the temperature in many countries mainly in gulf countries reaches up to 55 °C. But now in India also mercury is touching 50 °C mark in some parts of the country. According to the reports, around one billion units of cars travel the street and road in the world. But due to lack of shaded covered parking space most of the time, many cars are directly parked under direct sunlight. Due to parking in an open area without shade, the car compartment temperature ascends basically due

A. Bharti (✉) · P. Mathiyalagan · P. K. S. Nain
Galgotias University, Greater Noida, UP, India
e-mail: bhartialok1996@gmail.com

P. Mathiyalagan
e-mail: p.mathiyalagan@galgotiasuniversity.edu.in

P. K. S. Nain
e-mail: pawan.kumar@galgotiasuniversity.edu.in

to convection, conduction and sun rays [1, 2]. Because of ascending in the temperature of the car compartment, passengers feel very uncomfortable and also it reduces the quality of rubber, seat, plastic, etc. However, study [1] shows that some people use to cover their car and some use to leave a small gap in the car window, but these types of measures were very less effective in improving the situation. It also increases the chances of theft. Hence, it is very much important to have a good oxygenating system to decrease the temperature of the parked car compartment. Researchers had developed various systems to manage the compartment temperature of the vehicle either via solar reflective cover or solar-based oxygenating system. This paper deals with the investigation of the already developed systems.

2 Background

On a hot day, when a vehicle is parked without shade, the temperature of the car compartment will ascend, sometimes it becomes life-threatening for the children and pet and also creates lots of thermal discomfort for the travelers. To overcome this issue, systems like the solar car ventilation system and solar reflective cover had been developed. The solar ventilation system is not able to meet the cooling required and also it is unable to provide the same temperature throughout the cabin. The solar reflective cover has a drawback that it requires a lot of time to cover the car by solar reflector. Instead of these systems, we can use automatic solar-powered thermoelectric cooling so that we can manage the temperature of the car compartment.

3 Recent Researches to Avoid Heating of Car Cabin

In this paper, researchers did an experiment that was performed on a car that was parked in a certain direction and location. The researchers did an experiment by parking a car without shade for a long time on a hot day in Muscat. The study showed that with the ventilation device, the time taken to lessen the temperature also becomes less. With advanced ventilation device, the internal temperature of the car cabin reached to the desired degree in lesser than the half of the time in comparison to the ones values tested without ventilation gadget. The developed ventilation system increases the total average of the car due to a decrease in fuel consumption for cooling purpose. However, the decrease in temperature was not the same throughout the car (Figs. 1 and 2). The temperature drop on the rear end (Fig. 3) of the auto was maximum than in the center (Fig. 2) and in the front (Fig. 1). On the front end, very minimal temperature drop was observed in contrast to two other ends of the auto. It became cited that the car cabin with a ventilation device was around 10 °C cooler than a car without a ventilation device [3].

Fig. 1 AC test reading at 12 noon at front zone of the car

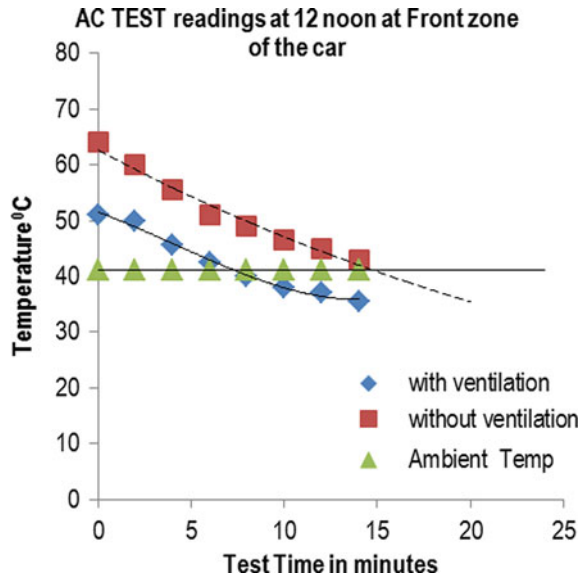
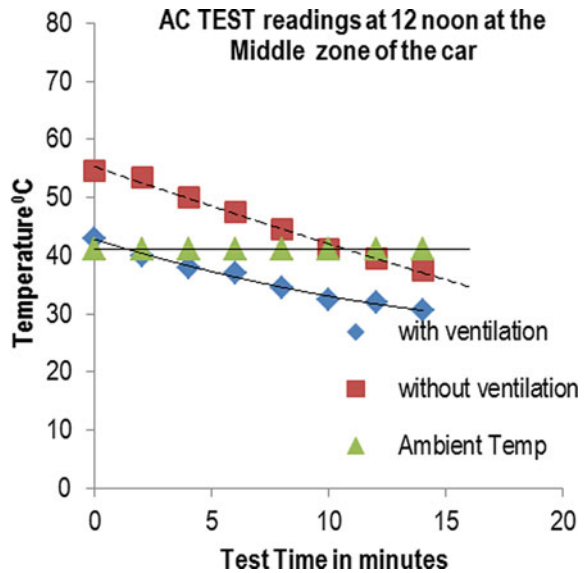
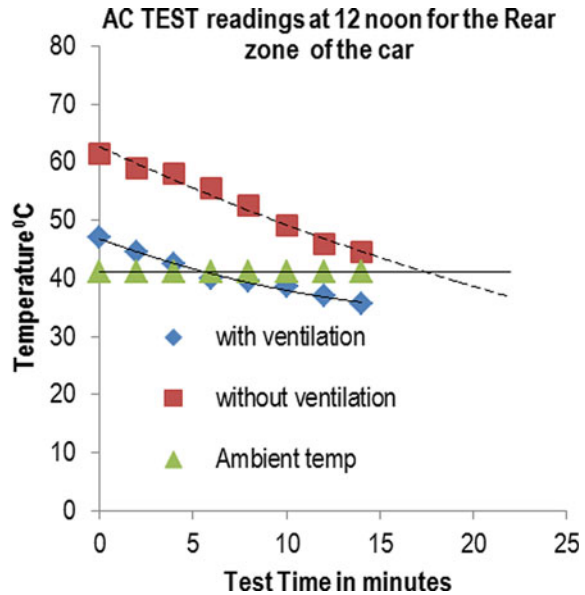


Fig. 2 AC test reading at 12 noon at front middle zone of the car



In this paper, researchers did a test that was implemented on a car to assess the effect of solar reflective cover on vehicle compartment temperature. This test was performed in UKM, Bangi city, Malaysia, where the ambient temperature was 33 °C with partly cloudy day. There were four cases considered in this experiment: first case: car with and without SRC (at different measurement time) the investigation showed (Fig. 4) that 39.6 °C temperature was observed within the car compartment

Fig. 3 AC test reading at 12 noon for the rear zone of the car



with SRC which was lower than the car without SRC nearly by 19 °C; second case: Usage of two similar cars concurrently (SRC as opposed to baseline) investigation showed (Fig. 5) that when two identical cars were exposed under the direct sunlight for 75 min, the temperature within the car compartment increases rapidly for initial 15 min and then in next 60 min, it touches the temperature value of 55.4 °C. The result of this experiment showed that there was approximately 13.4 °C temperature distinction between SRC and baseline; third case: Usage of two similar cars concurrently (solar reflective film (SRF) as opposed to baseline) investigation showed (Fig. 6) that in the beginning the temperature inside a car with SRF was more in comparison to the baseline and after 18 min the temperature inside a car with SRF and with baseline become almost same. The result of the experiment showed that the SRF was not able to decrease temperature up to the expectation and the difference between SRF and baseline was not that significant. Fourth case: Usage of two similar cars concurrently (SRF vs. SRC) it was observed (Fig. 7) that the compartment temperature of the car rises rapidly with SRC for first the 7 min and then continues to reach the maximum value of 45.9 °C. In-car cabin with SRF, the temperature increases rapidly for 14 min and then continues to ascend till it reaches the maximum value of 60.1 °C. Overall investigation showed that SRC is cooler than SRF by approximately 14 °C [4].

In this paper, researchers demonstrated that when the car is parked below the direct sunlight, the temperature within the car compartment can be greater than 20 °C in comparison to the ambient temperature. During summers, the temperature within the vehicle compartment can be more than 70 °C when the vehicle is standing below direct sunlight with close windows. Basically due to the close windows of cars, the

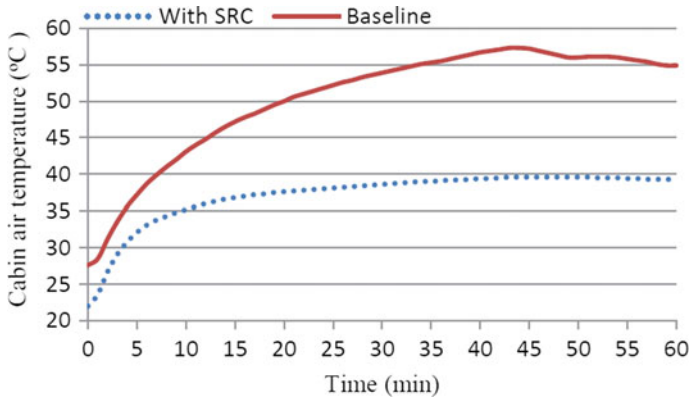


Fig. 4 Comparison of cabin soaks air temperature at breath level (SRC vs. baseline) using one car with measurements at different time

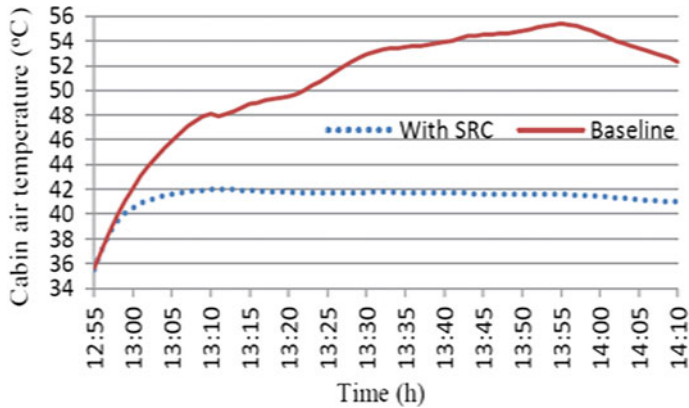


Fig. 5 Comparison of cabin soaks air temperature at breath level (SRC vs. baseline) using two identical cars concurrently

greenhouse effect came into the picture and due to this temperature rise sharply inside the cabin. This much rise in temperature within the car compartment can be life-threatening for children left unattended inside the car. The overall rise in temperature within the car compartment depends upon the weather condition and season. In summers with clear days, the temperature within the car compartment ascends with an average value of 68 and 61 °C in the spring season. Cloudy days were recorded nearly 10 °C cooler than clear days in both summer and spring. According to the investigation, it was found that even during cloudy days the temperature rise in the car cabin can be life-threatening. This paper also showed that the rise in temperature also depends upon the color of the car. It was observed that the rise in temperature within the dark color cars was more than light color cars by nearly 5%. This research paper

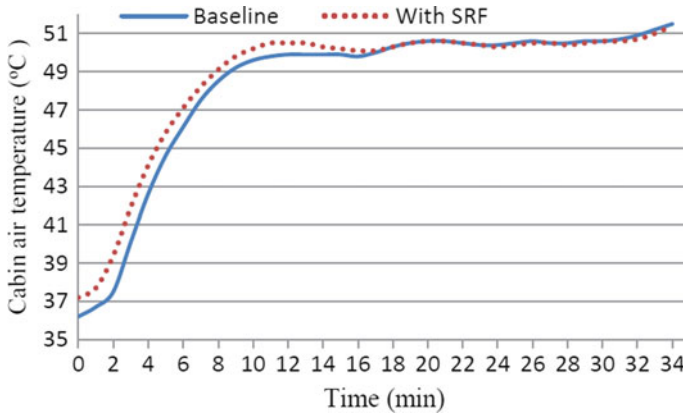


Fig. 6 Comparison of cabin soaks air temperature at breath level (SRF vs. baseline) using two identical cars concurrently

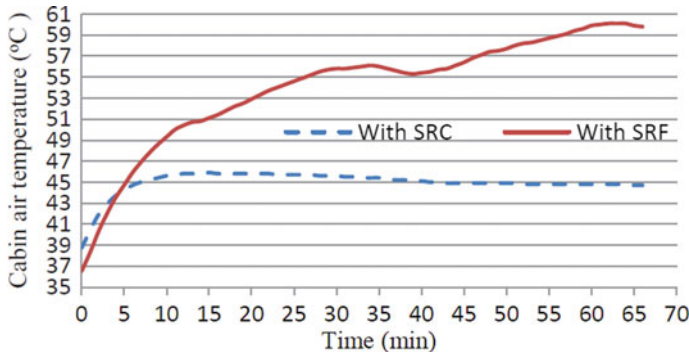


Fig. 7 Comparison of cabin soaks air temperature at breath level (SRC vs. SRF) using two identical cars concurrently

also concluded that the rise in temperature above 65 °C is not suitable for children and pets. This research paper also advises some prevention method like solar wall exhaust to extract heat from the cabin, steering cover, etc. [5] (Fig. 8).

In this paper, a cooling system was developed using thermoelectric device for the car seat and practical application was done for testing. The developed cooling system consists of a heat sink and a fan to increase the effect of cooling. To control the temperature, researcher had presented a mathematical model for the car seat and sliding mode control algorithm was developed. Here PIC16F873 was applied as one chip microprocessor. The developed system was tested on the car seat when the ambient temperature was 28 °C and thermoelectric was set to 10 °C for cooling. The result was encouraging as the temperature of the seat drop down to the required within one hour [6].

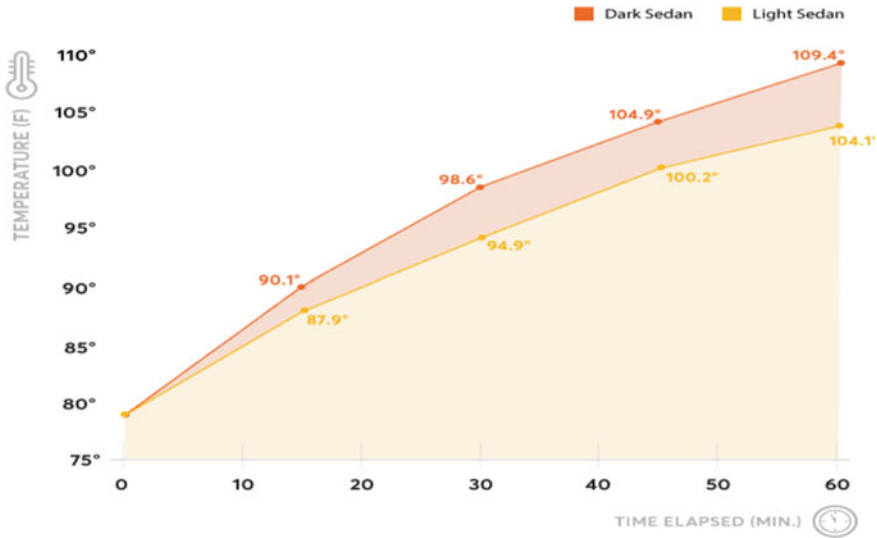


Fig. 8 Vehicle temperature rise in one hour

In this paper, researcher used the thermoelectric device to control the compartment temperature of a car. The thermoelectric device was composed of four heat sink and six TECs. The arrangement of heat sink and TECs was done in such a way that maximum amount of heat can be removed. The developed cooling system was applied showed a good result when outside temperature was 32 °C, TECs decrease the temperature by 4 °C inside the car compartment. But in the afternoon, when the temperature was 43 °C result was not satisfying because the decrease in temperature was very less, i.e., around 1 °C. Again during night when ambient temperature was 28 °C, the temperature decreases to 25 °C in 20 min which was encouraging result [7].

4 Conclusion

The above paper gives us an idea that the temperature of the car compartment increases by 31 °F when the ambient temperature was 78 °F. Above we also studied the use of solar ventilation systems and the effect of solar reflective cover. Solar ventilation system is efficient to use, but it does not provide the same cooling throughout the car cabin; hence, it has also become time-taking system. The major drawback of solar reflective cover is that every time it is not possible to cover the car because this will take a lot of time. Also we saw that TEC system was applied for cooling the car compartment, but it was not giving encouraging result above 40 °C ambient temperature and also it was using energy from car battery which can decrease the efficiency of the car. Hence, we can use automatic sun-powered

thermoelectric cooling device to manage the temperature within the car cabin when car is parked below the sunlight because it will be time saving and can provide the same cooling throughout the cab cabin.

References

1. Almanjahie I (2008) Temperature variations in a parked car. *Forensic Sci Int* 207:205–211 (2011). <https://doi.org/10.1016/j.forsciint.2010.10.009>
2. Jaiswal GK, Gandhi M. Design of a smart automotive ventilation system for a parked car. *Int J Theor Appl Res Mech Eng* 1(1):83–88
3. Sudhir CV, Jalal Marhoon Al Dhali. Effect of solar ventilation on air conditioning system performance of the car parked under sunlight. *ARPN J Eng Appl Sci*. ISSN 1819-6608
4. Lahimer AA, Alghoul MA, Sopian K, Khrit NG (2017) The effect of solar reflective cover on soak air temperature and thermal comfort of car parked under the sun. *E3S Web of Conferences* 23:08003. <https://doi.org/10.1051/e3sconf/20172308003>
5. Hingane AK (2018) Temperature variation in parked vehicle during summer and its threats and prevention. *Int Res J Eng Technol* e-ISSN: 2395-0056, p-ISSN: 2395-0072
6. Choi H-S, Yun S, Whang K-I (2007) Development of a temperature-controlled car-seat system utilizing thermoelectric device. *Appl Therm Eng* 27:2841–2849
7. Raut MS, Walke DV (2012) Thermoelectric air cooling for cars. *Int J Eng Sci Technol (IJEST)* 4(5):2381–2394
8. McLaren C, Null J, Quinn J (2005) Heat stress from enclosed vehicles: moderate ambient temperatures cause significant temperature rise in enclosed vehicles. *Pediatrics* 116(1):109–112

Air-Conditioning System in Surgical and Critical Care: A Review



Triyank Mishra, Ravneet Singh, Vikas Giri, Joydeep Chakraborty,
and Sorabh

Abstract Air-conditioning systems in operating theaters must be carefully designed so as to meet the standards set by NABH (National Accreditation Board for Hospitals & Healthcare Providers) and other govt. medical agencies. There are several factors to be taken into consideration for avoiding the life-threatening problems such as hypothermia and anaesthetic gas pollution. Comfort conditions can be achieved by air movement which gets from the air-conditioning system. This paper summarizes the relevant use of air-conditioning systems in operation theatre for achieving a healthy environment and assuring the comfort of the patient and surgical team.

Keywords Air conditioning system · Surgical and critical care

1 Introduction

An air-conditioning system and handling units through which air passes and undergoes different processes to deliver air with specific conditions such as temperature, dust, and air quality and bacteria in the air which is present in the operation theater. It has certain components of different arrangements according to the application in hand. But generally, it serves one zone with single or multiple spaces.

T. Mishra (✉) · R. Singh · V. Giri · J. Chakraborty · Sorabh
Department of Mechanical Engineering, MRIIRS, Faridabad, India
e-mail: mishratriyank2000@gmail.com

R. Singh
e-mail: 9ravneetsingh@gmail.com

V. Giri
e-mail: Vikasgiri817@gmail.com

J. Chakraborty
e-mail: joydeep.fet@mriu.edu.in

Sorabh
e-mail: sorabh012@gmail.com

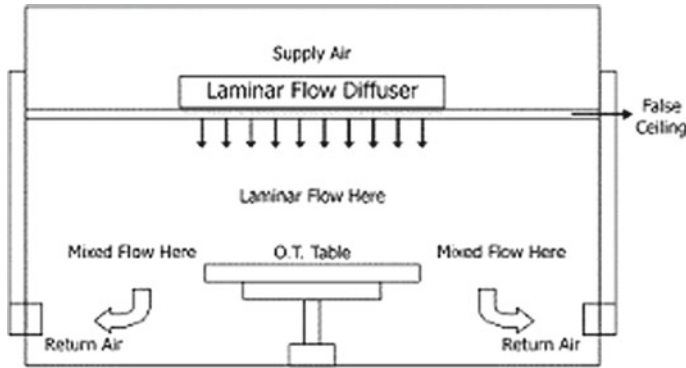


Fig. 1 An illustration of laminar flow in operation theater

The outer casing may be made of heavy gauge pre-galvanized sheet steel, folded to form study side, top, and bottom panels and a self-supporting structure. The supply air ducts may be either directly connected to the unit or may be connected to the unit using a flexible adapter piece, to reduce vibration transmission from the air-conditioning system to the air duct. For medical purpose, air-conditioning system in hospital operation theater provides indoor thermal comfort as well as suitable air quality (Fig. 1).

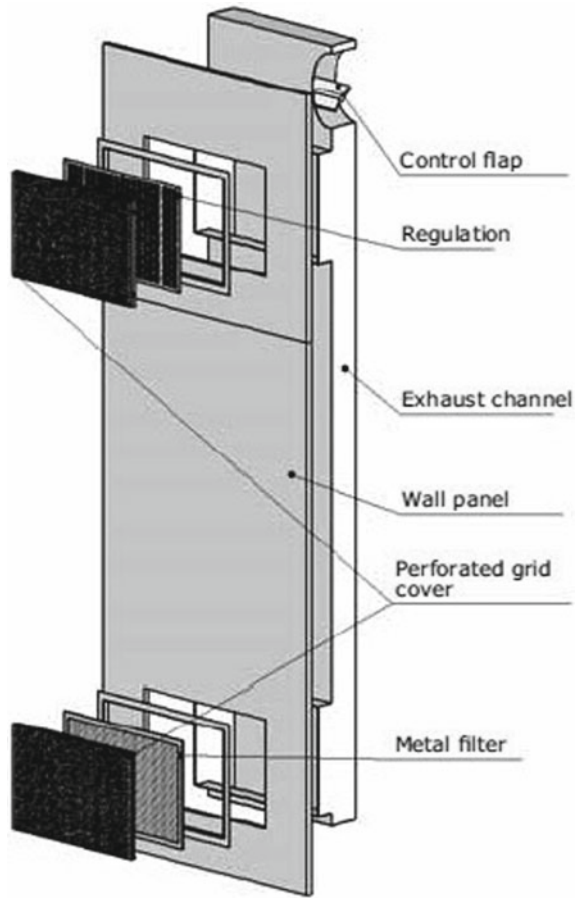
2 Laminar Flow

It was found in the study of laminar flow in operation theater that it reduces the infective bacteria to a large extent. However, APH (air changes per hour) for laminar flow in OT is to be increased about twelve to twenty times the earlier values of 15–25 [1]. Laminar flow systems may be used for a horizontal or vertical system where high-level equipment is installed on one part of the OT and later incorporates air-to-ground filters to each operating range.

3 Air-Conditioning Exhaust Channels

The purpose of AC exhaust channel is to provide a passage for the exhaust air that is coming out from the room. The ideal location of these channels is in partition wall. Control flaps are integrated with these in order to control all exhaust channels. As depicted in Fig. 2, AC exhaust channels are also provided with perforated air-conditioning grids [2–5].

Fig. 2 A typical air-conditioning exhaust channel



4 Ventilation

During an operation the used anesthetic gases, odor released may cause discomfort to the occupants which is removed by ventilation. It also brings the dust concentration apart from reducing bacteria, viruses at acceptable levels which helps in satisfying the indoor air quality as per mandatory health guidelines [6] (Fig. 3).

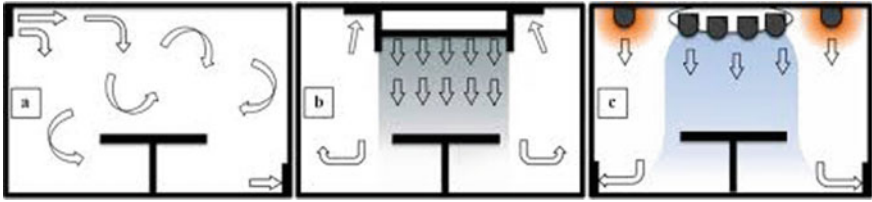


Fig. 3 Ventilation system for OT [6]

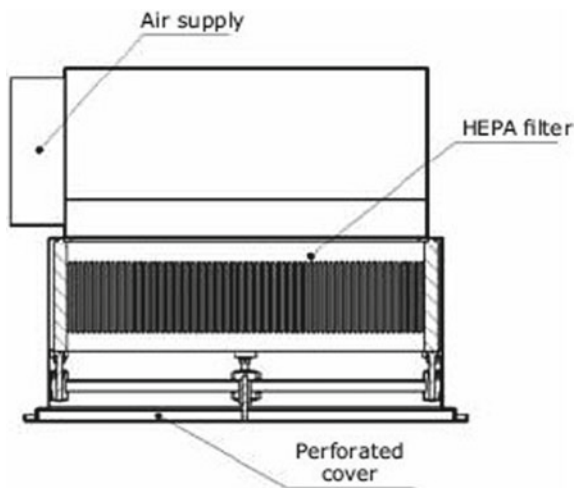
5 Air Supply Outlet

The sterilization and preparation rooms of patients have arrangement of AC supply outlet. It can be provided in OT also in case of air exchange quality is not critical. These are provided with HEPA filters, which ensure better filtration [3, 4, 7] (Fig. 4).

6 Surgery and Critical Care

The most venerable part is surgery and critical care which needs a careful design to prevent airborne organisms. The studies found that air delivery from the roof, through the inward movement to the many vents located on the opposite walls, is the most effective air flow path to prevent contamination inside the room. As compared to the adjoining room, there should be good air pressure with 15% excess supply [8].

Fig. 4 Air supply outlet



7 Obstetrical Area

In this area too, positive pressure or at least equal to the other area should be applied.

8 Delivery Rooms

The design of delivery rooms should be such that it should meet requirement of OT.

9 Recovery Rooms

The recommended temperature and humidity for recovery rooms are 24 °C and 45–55%, respectively [3].

10 Nursery Suites

For newborn babies, positive pressure is recommended in nursery suites which also to be maintained at constant temperature and humidity [5].

11 Healthcare Facilities [9]

Healthcare facilities should not be in the vicinity of nursery; otherwise, influx of exhaust air from these may affect infants.

12 Emergency Rooms

The most contaminated area of hospital is emergency rooms where temperature and humidity should be within the normal comfort range.

13 Anesthesia Storage Room

Mechanical ventilation should be preferred over others in anesthesia storage room.

14 Nursing

When centralized system is used to condition the patient, then standard air filtration and air change rates should be followed to reduce cross-infection. But for the patient who is both immune suppressed and contagious should be provided with isolation rooms within the unit (Table 1).

15 Fan Motor

Standard fans are forward-curved selected for optimum outlet velocities and low sound levels. They may be supplied with a flexible connection between the fan discharge outlet and the unit casing. This will minimize the vibration, and accordingly, the sound level and completely isolate the fan motor assembly from the rest of the unit structure.

Fan selection depends on the application in hand, the amount of air needed, and noise level limitations [10, 11].

Options:

- Inlet guide vanes for backward curves fans and airfoil fans to control air flow rate.
- Belt guard.
- Wire mesh on the fan inlet (Table 2).

16 Infectious Isolation Unit

In this case, switchable isolation rooms can function with either positive or negative pressure. The major issues with this approach are difficult in maintenance of mechanical dampers and controls.

17 Air Changes Per Hour [5]

On the base of location and required load, APH should be 20. There should be at least four air changes of fresh air components out of total minimum of 20 air changes. The air supply is done through high-efficiency particulate air (HEPA) filters located in the ceiling.

Table 1 Approved standard for air-conditioning of the hospital area [3]

Function of space	Pressure relationship to adjacent areas (n)	Minimum outdoor ach	Minimum total ach	All room air exhausted directly to outdoor (j)	Air recirculated by means of room units (a)	Design relative humidity (k), %	Design temperature (l), °F/°C
Continued care nursery	NR	2	6	NR	No	30-60	72-78/22-26
Labor/delivery/recovery (LDR) (s)	NR	2	6	NR	NR	Max 60	70-75/21-24
Labor/delivery/recovery/postpartum (LDRP) (s)	NR	2	6	NR	NR	Max 60	70-75/21-24
Newborn nursery suite	NR	2	6	NR	No	30-60	72-78/22-26
Nourishment area or room	NR	NR	2	NR	NR	NR	NR
Patient corridor	NR	NR	2	NR	NR	NR	NR
Patient room	NR	2	4 (Y)	NR	NR	Max 60	70-75/21-24
PE anteroom (t)	(e)	NR	10	NR	No	NR	NR
Protective environment room (t)	Positive	2	12	NR	No	Max 60	70-75/21-24
Toilet room	Negative	NR	10	Yes	No	NR	NR
Function space	Pressure relationship to adjacent areas	Minimum outdoor air per hour	Minimum air changes of outdoor air per hour	Minimum total air changes per hour	All air exhausted directly to outdoors	Air recirculated within room units	
Surgery and critical care							
Operating room (all outdoor air system)	P		15		Yes	No	No
(recirculating air system)	P		5		Optional	No	No
Delivery room (all outdoor air system)	P		15		Optional	No	No

(continued)

Table 1 (continued)

Function space	Pressure relationship to adjacent areas	Minimum air changes of outdoor air per hour	Minimum total air changes per hour	All air exhausted directly to outdoors	Air recirculated within room units
(recirculating air system)	P	5	25	Optional	No
Recovery room	E	2	6	Optional	No
Nursery suite	P	5	12	Optional	No
Trauma room	P	5	12	Optional	No
Anesthesia storage (see code requirements)	±	Optional	8	Yes	No
Nursing					
Patient room	±	2	4	Optional	Optional
Toilet room	N	Optional	10	Yes	No
Intensive care	P	2	6	Optional	No
Protective isolation	P	2	15	Yes	Optional
Infectious isolation	±	2	6	Yes	No
Isolation alcove or anteroom	±	2	10	Yes	No
Labor delivery/recovery/postpartum (LDRP)	E	2	4	Optional	Optional
Patient corridor	E	2	4	Optional	Optional
Ancillary					
Radiology X-ray (surgery and critical care)	P	3	15	Optional	No
X-ray (diagnostic and treatment)	±	2	6	Optional	Optional
Darkroom	N	2	10	Yes	No
Laboratory, general	N	2	6	Yes	No
Laboratory, bacteriology	N		6	Yes	No

(continued)

Table 1 (continued)


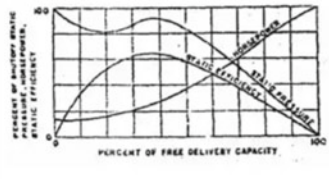


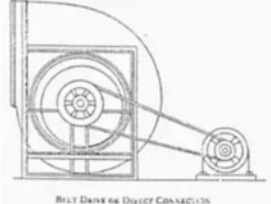

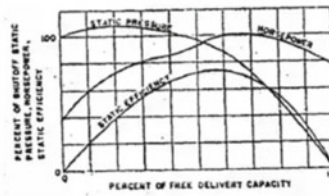

Function space	Pressure relationship to adjacent areas	Minimum air changes of outdoor air per hour	Minimum total air changes per hour	All air exhausted directly to outdoors	Air recirculated within room units
Laboratory, biochemistry	P		6	Optional	No
Laboratory, cytology	N	2	6	Yes	No
Laboratory, glass swashing	N	Optional	10	Yes	Optional
Laboratory, histology	N	2	6	Yes	No
Laboratory, nuclear medicine	N	2	6	Yes	No
Laboratory, pathology	N	2	6	Yes	No
Laboratory, serology	P	2	6	Optional	No
Laboratory, sterilizing	N	Optional	10	Yes	No
Laboratory, media transfer	P	2	4	Optional	No
Autopsy	N	2	12	Yes	No
Nonrefrigerated body-holding room	N	Optional	10	Yes	No
Pharmacy	P	2	4	Optional	Optional
Administration					
Admitting and waiting Room;	N	2	6	Yes	Optional
Diagnostic and treatment					
Bronchoscopy, sputum collection, ana pentamidine administration	N	2	10	Yes	Optional
Examination room	±	2	6	Optional	Optional
Medication room	P	2	4	Optional	Optional
Treatment room	±	2	6	Optional	Optional
Physical therapy and hydrotherapy	N	2	6	Optional	Optional
Soiled workroom or soiled holding	N	2	10	Yes	No
Clean workroom or clean holding	P	2	4	Optional	Optional

(continued)

Table 1 (continued)

Function space	Pressure relationship to adjacent areas	Minimum air changes of outdoor air per hour	Minimum total air changes per hour	All air exhausted directly to outdoors	Air recirculated within room units
Sterilizing and supply					
Sterilizer equipment room	N	Optional	10	Yes	No
Soiled Or decontamination room	N	2	6	Yes	No
Clean workroom and sterile storage	P	2	4	Optional	Optional
Equipment storage	±	2 (Optional)	2	Optional	Optional
Service					
Food preparation center	±	2	10	Yes	No
Warewashing	N	Optional	10	Yes	No
Dietary day storage	±	Optional	2	Optional	No
Laundry, general	N	2	10	Yes	No
Soiled linen sorting and storage	N	Optional	10	Yes	No
Clean linen storage	P	2 (Optional)	2	Optional	Optional
Linen and trash chute room	N	Optional	10	Yes	No
Bedpan room	N	Optional	10	Yes	No
Bathroom	N	Optional	10	Optional	No
Janitor's closet	N	Optional	10	Optional	No

Table 2 Fan type for various applications [6]

Fan type	Curves & Layout	Description
<p>1. Forward curved fan</p>  <p style="text-align: center;">FORWARD-CURVED</p>		<ul style="list-style-type: none"> • Runs at a relatively low speed compared to other types for the same capacity. • Smaller fan for a given duty, excellent-for fan coil units. 
<p>2. Radial fan</p>  <p style="text-align: center;">RADIAL</p>	 <p style="text-align: center;">BELT DRIVE OR DIRECT CONNECTION</p>	<ul style="list-style-type: none"> • Self cleaning. • Can be designed for high structural strength to achieve high speed and pressures
<p>3. Backward curved fan</p>  <p style="text-align: center;">BACKWARD CURVED</p>		<ul style="list-style-type: none"> • More efficient • Power curve has a flat peak so that the motor may be sized to cover the complete range of operation from 0% to 100% air flow for a single speed, non-overloading. • Pressure curve is generally steeper than that of the forward curved fan. This results in a smaller change in air volume for any variation in system pressure for selections at comparable percentages of free delivery. • Point of maximum efficiency is to the right of the pressure peak, allowing efficient fan selection with a built in pressure reserve. • Quieter than other types. 

18 Design Consideration [8]

External AHU emissions should not be near the source of pollution, e.g., DG demolition, parking lot. All the requirements described for the new design and type A and type B OTs over the course of the changes in air, particle counts, positive pressure, and temperature, humidity, and air velocity will be required for such OTs for the old construction/HCOs.

19 Maintenance of System

The periodical system check is required which includes the following:

1. Temperature and humidity
2. Air particulate count
3. APH calculation
4. Air speed at filter outlet.
5. Pressure differential levels of the OT concerning adjoining area.
6. Validation of HEPA filters.

20 Conclusion

Unlike the normal air-conditioning for comfort and other applications, it is quite obvious from literature in this paper that hospital air-conditioning is completely different and involves the extreme precautions to be followed. This paper provided a brief understanding of the existing practices of air-conditioning as per set standards by ASHRAE, NABH. Each part of hospital premises which includes critical care needs a different type of standard to be followed concerning various parameters, e.g., indoor air quality, duct design, fan type, pressure, temperature, and humidity.

References

1. Lindsay W, Bigsby E, Bannister G (2011) Prevention of infection in orthopaedic joint replacement. *J Perioper Pract* 21(6):206–209
2. Ramachandran M, Eastwood D, Singh D, Skinner J (2007) *Basic orthopaedic sciences: the Stanmore guide*. Hodder Arnold, London
3. *HVAC Design manual for hospitals and clinics* 2nd ed, ASHRAE 2016
4. *CPWD design guidelines HVAC guide 2017* ministry of public works New Delhi 2017
5. *NABH guidelines for air conditioning in operations theatre* 2015
6. *ASHRAE standards ventilation for indoor air quality* 2013
7. *SMACNA. 1995. HVAC duct construction standard—metal and flexible*
8. Memarazadeh I, Manning A (2002) Comparison of operating room ventilation system in the protection of surgical site
9. *CEN ventilation for buildings test producer and measuring method for handling over installed ventilation and air conditioning systems*
10. *Sheet metal and air conditioning contractors national association*, 2nd ed, Chantilly, VA
11. *SMACNA (1998) Seismic restraint manual: guidelines for mechanical systems*, 2nd ed. Air Conditioning

Static Analysis of Euler–Bernoulli Beam by Using Bond Graph



Anandit Wadhwa, Bhuwandeep, Harsh Vishwakarma, Jatin Mahato,
and Anuj Kumar Jain

Abstract The matter for discussion in this paper is the detection of cracks in simply supported beams based on different static crack detection techniques used by many researchers for their defective structures. Finite element method analysis, experimental analysis, mathematical analysis and bond graphs are used in the above techniques. Detection of crack much before it causes any failure could prove life saver. Due to cracks, the stiffness of beam reduces and changes its natural frequency; these changes are the carriers of crack depth and its location as well. Artificial intelligence is also finding place in the detection of beam cracks by taking references from these analysis. This paper aims to works on cracked beam analysis and detection of cracks.

Keywords Multi-cracked rotor · Euler–Bernoulli beam · Bond graph

Nomenclature

V	Shear force
x	Distance from support
Δx	Length of small element
M	Bending moment
E	Modulus of elasticity of beam

A. Wadhwa · Bhuwandeep · H. Vishwakarma · J. Mahato (✉) · A. K. Jain
ABES Engineering College, Ghaziabad, UP 201001, India
e-mail: jatin.16bme2008@abes.ac.in

A. Wadhwa
e-mail: anandit.16bme1060@abes.ac.in

Bhuwandeep
e-mail: bhuwandeep.16bme1005@abes.ac.in

H. Vishwakarma
e-mail: harsh.16bme1056@abes.ac.in

A. K. Jain
e-mail: anuj.jain@abes.ac.in

MOI	Moment inertia of beam
ΔM	Change in bending moment
ρ	Density of material of beam
A	Cross-sectional area of beam
y	Deflection of beam at any distance x
\ddot{y}	Double differentiation of deflection with respect to x
I	Inertance
C	Capacitance
Sf	Source of flow
Se	Source of effort
TF	Transformer
1, 0	Junction

1 Introduction

Different machines, for example, steam and gas turbines, generators, rapid blowers, siphons and so forth, have overwhelming segments joined in them. Such machines are differently utilized in fields, for example, power age, vehicle, airplane and so forth and have a rotor shaft as one of its significant segments. One of the greatest reasons for the cataclysmic disappointment in such turning shafts are because of fatigue. Cracks initiate and propagate because of high stress intensity happening because of thermal shocks and stresses. Cracked rotors have consequently drawn the consideration of analysts in the course of recent decades as they might be a wellspring of human injury, extraordinary monetary and gear misfortunes.

The investigation of cracked shaft by the Euler–Bernoulli beam method is talked about which can help in assurance of cracks in the shafts. The differential condition of beams under static condition is especially useful. Numerical examination and computational investigation is utilized for recognition of numerous cracked areas and their intensities in the Euler–Bernoulli beam. Right now examination of multi-cracked Euler–Bernoulli beam is finished by stacking it with static load. There are many research papers distributed seeing crack modelling as it assumes a significant job in crack detection. Research papers [1–4] have been published over the most recent 50 years to recognize the cracks and its effects. Numerous analysts are as yet chipping away at their papers [5, 6] to contemplate the cracked rotor system. The studies and investigations of such cracks are in papers [7, 8] for beam structures and [9] for rotors. Kumar and Rastogi [10] additionally gave a nitty gritty examination with respect to the equivalent. The modelling of crack is complex because of physical discontinuity at the crack location, large stress concentration close to the crack tip and at the cracked section. The crack prompts significant localization of distortion which prompts increment in flexibility, decline in stiffness and change in damping. It is hard to propose a model to mirror the adjustment in stress. Wu and Meagher [11] as of late built up a model thinking about lateral/

torsional coupling utilizing Lagrange's condition. Variety of amplitude because of asymmetries was anyway disregarded in their model. A few research papers were published by Vujanovic [12, 13] and Djukic [14, 15] building up the association between symmetries conservation laws. Unmistakable commitment was finished by Noether's theorem [16] in inferring invariance properties. Subsequently, constant motion was gotten by investigating of symmetric properties of the dynamical system. The crack might be considered as breathing. If there should arise an occurrence of open crack, the crack remains open during the whole pattern of vibration, while in breathing crack, crack remains open just during part of the stress cycle. The greater part of the cracks that create in the beam is viewed as breathing as they are exposed to fatigue loading. There are many research papers that are published with respect to the breathing of crack. Vibrations because of rotation will have most extreme speed close to the critical speed. The breathing crack conduct can be modelled or examined by growing the stiffness of the crack. Mukherjee [17] later gave a novel proposal of virtual time like variable called 'umbra-time' to defeat the restrictions of Lagrange's condition.

Anuj K. Jain et al. [18, 19] gave the effect of asymmetric stiffness on parametric in stabilities of multi-cracked rotor using the Lagrangian formulation and modelling technique used for this type of system is bond graph. The Lagrangian formulation was useful in finding the effect of stiffness on amplitude and frequencies. The dynamic behaviour of the multi cracked shaft which is analysed experimentally and analytically by the taking record of crack depth, crack location and shaft rotational speed. This paper also uses Lagrangian formulation. In this paper, natural frequencies are obtained and also include dynamic behaviour of crack due to breathing phenomenon by the help of OROS. As a case study, one-dimensional rotor shaft with internal and outside damping in conjunction with transverse crack in middle span was discussed. The rotor is symmetrical, that is to be moved by way of a consistent velocity supply via a dissipative coupling given by Kumar [20].

2 Methodology

When a crack is developed at the surface of a rotating shaft, the crack fully opens and fully closes as it reaches its lowest and highest points, respectively. This phenomenon of opening and closing of crack is called breathing.

In Euler–Bernoulli beam model, we do not consider the shear when a crack is developed at the surface of a rotating shaft, the crack fully opens and fully closes as it reaches its lowest and highest points, respectively. This phenomenon of opening and closing of crack is called breathing—deformation and rotational inertia of the beam. We continue with governing conditions in difference form since modelling of distributed parameter systems essentially start with finite approximations and in this manner, space reticulation. This is just pertinent if there should be an occurrence of small deviations.

An Euler–Bernoulli beam element with density ρ , cross-sectional area A and flexural rigidity EI is shown in the figure. For sufficiently small length Δx , ignoring the influence of second and higher powers of Δx .

$$V(x + \Delta x) - V(x) = \rho A \Delta x \ddot{y}(x, t)$$

$$\Psi = \frac{\Delta y(x, y)}{\Delta x}$$

$$M(x) = EI \frac{\Delta \Psi}{\Delta x} \text{ and}$$

$$V(x) = \frac{\Delta M}{\Delta x}$$

where V is the shear force and M is the bending moment.

The differential equation [21] for the transverse vibration is

$$\rho A \ddot{y}(x, t) + EI \frac{\partial^4}{\Delta x^4} y(x, t) = 0$$

A bond graph technique is a technique which represents a physical dynamic system in graphical form [21]. It allows the conversion of the system into a state-space representation. The bond graph is composed of the “bonds” which link together “single port”, “double port” and “multi-port” element. Each bond represents the instantaneous flow of energy (dE/dt) or power. The flow in each bond is denoted by a pair of variables called power variables, whose product is the instantaneous power of the bond. The power variables are broken into two parts: flow and effort. By the using of bond graph, we are doing simulation. It is a unified approach. We can simulate different energy domain at one plate form so we are using this approach here. Because in dynamics analysis, electric motor is also used. So we can simulate electrical system as well as mechanical system at one platform. That is not possible in any other tool. In other software tool, we can simulate only one domain at a time.

3 Experimental Study

3.1 Experimental Setup

The schematic chart for stiffness measurements is appeared in Fig. 6 and experimental study was additionally led to dissect the multi crack system. The test rig which is likewise appeared in the figure was utilized for experimentation and analysis. In the testing arrangement, a rotor shaft is upheld between a couple of support. The cross section of shaft utilized is circular having a diameter of 20 mm. Schematic diagram of experiment is shown in Fig. 1, and the actual setup is shown in Fig. 2.

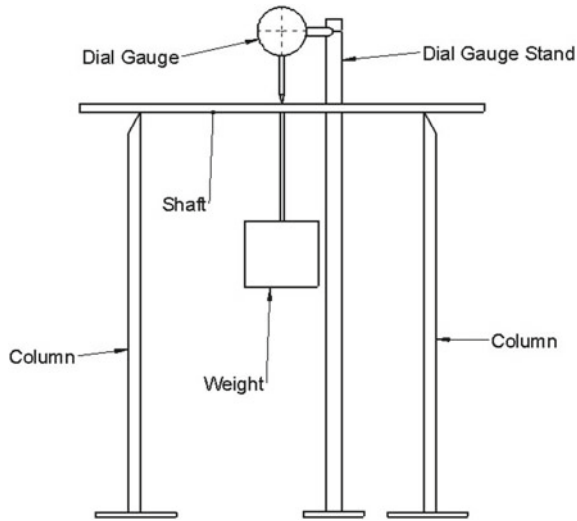


Fig. 1 Schematic diagram of experimental setup for stiffness measurement



Fig. 2 Original experimental setup

3.2 Test Specimen

The shaft used in the practical analysis is made of aluminium and is tested by applying load on the mid-distance of the shaft as shown in Figs. 3, 4 and 5. The test is performed on three shafts one with no crack, second with crack at the mid-distance of support span and third one with two cracks one at the mid-distance and other one from one-fourth distance of support span from one support. The shaft is rotated 45° after each observation at one crack depth and after each complete 360° rotation the depth of crack is increased and observation is taken. In first shaft, there is no crack so observation is taken by only rotating it 360°; in second shaft, crack is varied from 1 to 7 mm having difference of 2 mm at each variation; and in the third shaft, the crack at middle is varied from 1 to 7 mm and for crack at one-fourth distance is varied from 1 to 5 mm having difference of 2 mm at each variation.

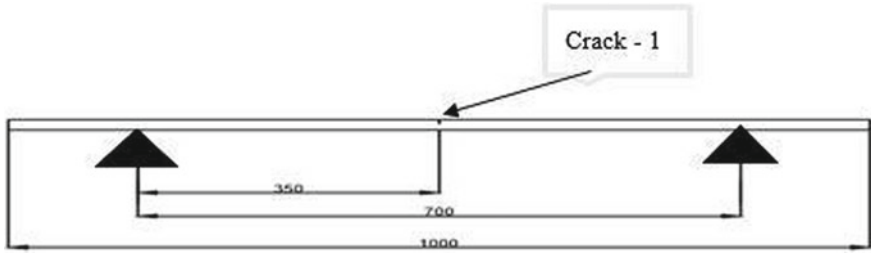


Fig. 3 Schematic diagram of single crack test specimen

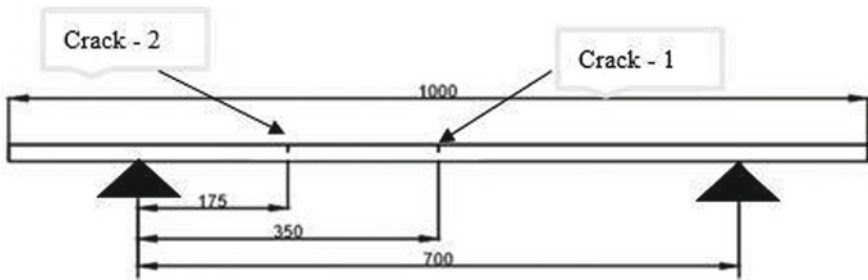


Fig. 4 Schematic diagram of multi crack test specimen

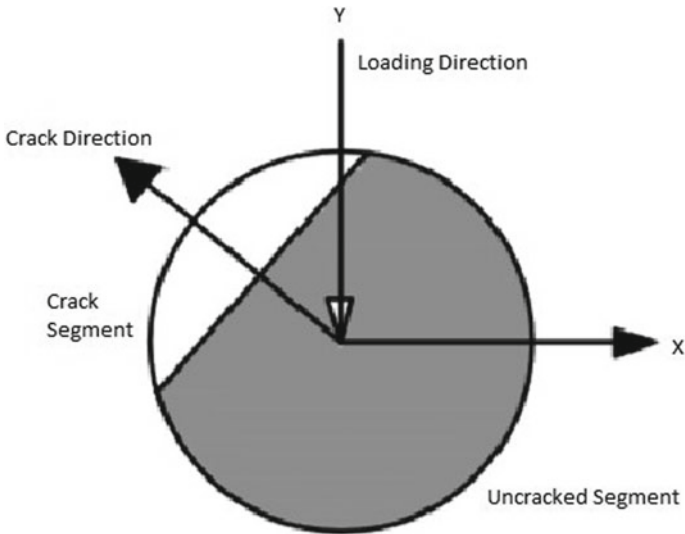


Fig. 5 Cross-sectional view of rotating angle between crack and loading

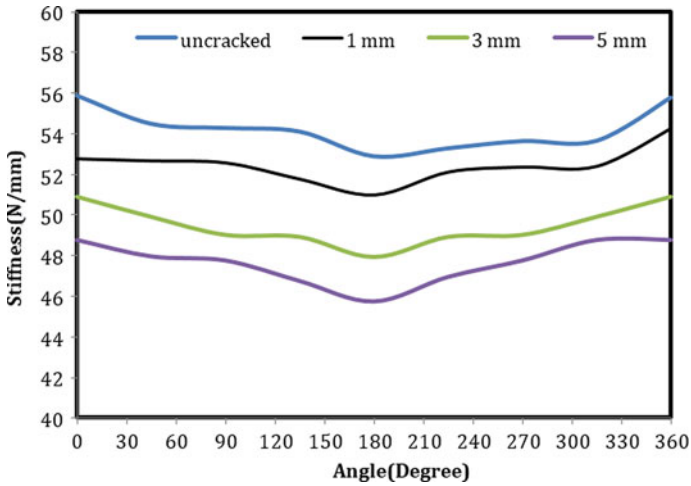


Fig. 6 Variation of stiffness at different angle

Table 1 Details of test specimen

Shaft specification	Details
Shaft material	Aluminium
Effective length (support to support)	700 mm
Overhang (each side)	150 mm
Diameter of shaft	20 mm
Weight of shaft	0.593 kg
Density	2700 kg/m ³
Ixx and Iyy	7854 mm ⁴
Stiffness	52 N/mm

Figure 6 shows the variation of stiffness when it is rotated by 360°. This variation is for all the four cracks that were tested on transverse load. In the four readings, first is un-cracked, second is crack with 1 mm depth, third is crack with 3 mm depth, and fourth is crack with 5 mm depth (Table 1).

3.3 Experimental Procedure

Right now most significant undertaking is producing the artificial transverse crack at the correct distance from the support. The instrument used to make is jewel saw as the assignment is to make a crack that looks like most to the real crack and the more the artificial crack is fine, the better outcomes will be seen during the loading. The loads applied fluctuates from 6 to 20 kg having 0.5 kg as the contrast between

two successive loads applied and shaft is rotated 360° taking observations at each 45° . The testing can be partitioned following sections.

Firstly, a shaft is loaded with no crack to see that in what manner will the crack acts when it is loaded with some weight. After stacking the shaft without crack, now a crack is produced at the mid-separation of the shaft which has starting depth 1 mm which is expanded to 3 mm then 5 mm then 7 mm observation. The readings are taken after each increase in depth of crack. Finally, on another shaft a 5-mm depth crack is created and an another crack is produced at a same shaft at one-fourth distance from the support, at first this crack is of 1 mm after that it is expanded to 3 mm then 5 mm then 7 mm and readings are taken after each expansion in the depth of split.

In the wake of taking the observation, the stiffness of shaft is determined at the each reading by the equation $K = F/y$ where F is the load applied on the shaft, y is the transverse displacement of the shaft, and K is the stiffness of shaft. With these stiffness values, a graph is plotted among stiffness and angle at which that specific stiffness value is determined.

4 Result and Discussion

Experimental results are shown in Figs. 6 and 7; Fig. 6 shows the variation of stiffness with the angle rotated; and Fig. 7 shows the angular positions of the crack during one rotation of the shaft. The variation of stiffness with the angle rotated is in the shape of broad V from which we can easily observe that the stiffness first decreases from angle of 0° to 180° reaching a minimum value and after that again

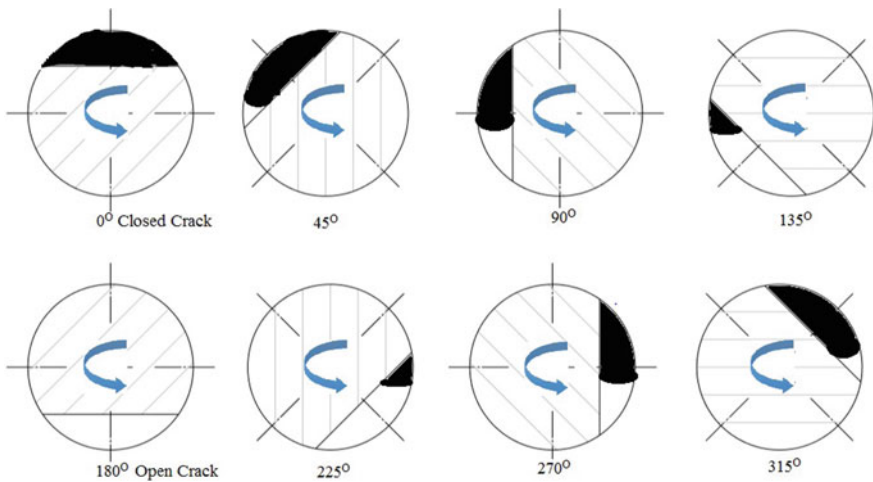


Fig. 7 Some of the angular positions of the crack during one rotation of the shaft

increases from 180° to 360° reaching a final value that is nearly equal to value from which we have started the rotation that is 0° . This decrease and the increase of stiffness is due to opening and closing of shaft that causes the moment of inertia of the shaft of decrease and increase, respectively.

When the crack opens, i.e. when crack rotates from 0° to 180° , the moment of inertia of shaft decreases due to which the stiffness of shaft decreases as the stiffness is directly proportional to the moment of inertia and when the crack closes, i.e. when crack rotates from 180° to 360° , then the moment of inertia increases due to which the stiffness increases. As the crack opens and closes gradually so there is a gradual variation of stiffness and not the sudden increase.

5 Conclusion

Static analysis of Euler–Bernoulli shaft has been effectively done and approved by the assistance of bond graph made for a same arrangement of shaft and cracks. Following ends can be made:

1. Variation in stiffness is obviously seen to increment with the expansion in crack depth. The stiffness diminishes as the crack depth increments.
2. After the making of second crack, stiffness still diminishes but the impact of second crack is not much as in the past. Stress concentration at centre crack is likewise influenced.
3. More the depth of shaft, the more shaft will get affected.
4. Crack at the mid-separation of shaft has the optimum effect on stiffness of the shaft, through advancement of crack at some other situation of shaft.
5. It can be plainly seen that natural frequencies diminishes with decrease in stiffness and can likewise cause resonance at much low excitation.

References

1. Dimarogonas AD (1970) Dynamic response of cracked rotors, technical information series. General Electric, Schenectady, New York
2. Pafelias T (1974) Dynamic behavior of a cracked rotor, technical information series, No. DF-74-LS-79. General Electric, Schenectady, New York
3. Kirmsner PG (1944) The effect of discontinuities on the natural frequency of beams. Proc ASTM 44:897–904
4. Thomson WJ (1949) Vibration of slender bars with discontinuities in stiffness. J Appl Mech 17:203–207
5. Dimarogonas AD, Paipetis SA (1983) Analytical methods in rotor dynamics. Applied Science Publishers, London, pp 144–193
6. Wauer J (1990) Dynamics of cracked rotors: literature survey. Appl Mech Rev 43:13–17
7. Gasch R (1993) A survey of the dynamic behavior of a simple rotating shaft with a transverse crack. J Sound Vib 160:313–332

8. Dimarogonas AD (1996) Vibration of cracked structures: a state of the art review. *Eng Fract Mech* 55:831–857
9. Ichimonji M, Watanabe S (1988) The dynamics of a rotor system with a shaft having a slant crack (a qualitative analysis using a simple rotor model). *J Soc Mech Eng Int J Ser III* 31 (4):712–718
10. Ichimonji M, Kazao Y, Watanabe S, Nonaka S (1994) The dynamics of a rotor system with a slant crack under torsional vibration. In: *Nonlinear and stochastic dynamics ASME, AMD-192/DE-78, International Mechanical Engineering Congress and Exposition, Chicago, IL*, pp 81–90
11. Papadopoulos CA, Dimarogonas AD (1987) Coupled longitudinal and bending vibrations of a rotating shaft with an open crack. *J Sound Vibr* 117:81–93
12. Qian G-L, Gu SN, Jiang JS (1990) The dynamic behavior and crack detection of a beam with a crack. *J Sound Vibr* 138:233–243
13. Sekhar AS, Prabhu BS (1994) Vibration and stress fluctuations in cracked shafts. *J Sound Vibr* 169:655–667
14. Nelson HD, McVaugh JM (1976) The dynamics of rotor-bearing systems using finite elements. *Trans ASME J Eng Ind* 98(2):593–600
15. Ozguven HN, Ozkan ZL (1984) Whirl speeds and unbalance response of multi-bearing rotor using finite elements. *Trans ASME J Vibr Acous Stress Reliab Des* 106:72–79
16. Rao SS (1980) *The finite element method in engineering*. Pergamon Press, Oxford
17. Papadopoulos CA, Dimarogonas AD (1988) Stability of cracked rotors in the coupled vibration mode. *Trans ASME J Vibr Acous Stress Reliab Des* 110:356–359
18. Jain AK, Rastogi V, Agrawal AK (2016) Experimental investigation of vibration analysis of multi-crack rotor shaft. In: *International conference on vibration problems*, vol 144, pp 1451–1458
19. Jain AK, Rastogi V, Agrawal AK (2018) A novel approach to study effects of asymmetric stiffness on parametric instabilities of multi-rotor-system. *J Sound Vibr* 413:159–172
20. Kumar C (2013) *Investigation of Dynamics of cracked rotor through Extended Lagrangian Mechanics*, Ph.D Thesis, SLIET, Longowal
21. Mukherjee A (2006) *Bond graph in modeling simulation and fault identification*, IK International Publishing House
22. Sekhar AS, Prabhu BS (1994) Transient analysis of a cracked rotor passing through critical speed. *J Sound Vibr* 173:415–421

Design Optimization and Computational Analysis of Heat Transfer Through IC Engine Fins



Ashish Kumar, Amit Kumar Gupta, Banti, and Samsher

Abstract The extended surface is provided in the engines to dissipate the heat generated from the engine called fins. The engine is an essential part of automobiles, which is subjected to high temperature and high thermal stresses. Automobile industries work to increase the heat dissipation rate by which engine efficiency and life both can be enhanced. The main aim of this research is to analyse and compare the thermal properties of the engine like total heat flux and temperature gradient of fins by varying geometries, the shape of fins, material, and thickness of fins. The rate of heat transfer analysis for thermal properties has been done on circular and longitudinal fins of different materials like aluminium, magnesium (AZ31B), and cast iron with varying fin thickness. Presently, the material of circular fins which has been taken into consideration is aluminium alloy 6061 which has a thermal conductivity of 237 W/mK, grey cast iron having a thermal conductivity of 52 W/mK, and magnesium alloy AZ31B which has higher thermal conductivity from other material with 96 W/mK. From results, it has been shown that heat dissipation is best in aluminium alloy 6061 with circular geometry, 1.5 mm thickness. The cylinder engine block with circular fins is modelled in Solidworks, and all the analysis work is done with the help of Ansys Workbench 2016 Simulation software.

Keywords IC engine · Fins · Heat flux · Ansys16.0 · Fin thickness · Temperature gradient

A. Kumar (✉) · A. K. Gupta · Banti · Samsher
Delhi Technological University, Delhi, India
e-mail: askr10311@gmail.com

A. K. Gupta
e-mail: amitmech159@gmail.com

Banti
e-mail: bantisingh55596@gmail.com

Samsher
e-mail: samsher@dce.ac.in

Nomenclature

q	Heat flux (W/m^2)
h	Heat transfer coefficient of air ($\text{W}/(\text{m}^2\text{K})$)
k	Thermal conductivity of the material ($\text{W m}^{-1} \text{K}^{-1}$)
θ°	Difference b/w base and ambient temperature
θ	Temp difference at a distance x from the base of the fin
A	Area of cross section of fin (m^2)
P	Perimeter of fin (m)
L	Length of fin (m)
X	Distance along the length of the fin where we have to find temperature (m)
t	Thickness of the fin (m)
r	Inside radius of fin (m)
R	Outside radius of the fin (m)

1 Introduction

In internal combustion (IC) engine, the combustion of the air-fuel mixture takes place, which develops a lot of heat energy. The temperature of gases inside the cylinder of the IC engine is around 2000–2400 °C. There is a need for cooling in IC engine to save it from overheating as overheating can cause engine seizure. Fins are extended surfaces from the body that is used to increase the rate of cooling through convection. Fins are used to increase the heat transfer and to reduce the adverse effects which can occur due to overheating of the engine. Generally, the overall size of the system comes as a constraint to the heat transfer through fins. Considering the overall size of the system as a constant term, the other parameters such as materials, fin thickness, and geometry of fin can still be changed to increase the heat transfer through fins.

In this paper, attempt is made to enhance the rate of heat transfer through fins by changing the geometrical parameters and materials. Solidworks 17 is used to develop the CAD design of the different models by changing the thickness and geometry of the fins. The material selection of the fins is also taken under consideration to increase the overall heat transfer through fins in IC engine. Each model is carried through steady-state thermal analysis in Ansys16.0 FEA software.

2 Literature Review

K. M. Sagesh et al. [1] proposed that the increment in the surface area leads to an increase in heat loss by the body, and this can also be achieved by creating holes of different sizes on the surface of an extended surface, i.e., fins. Overall temperate of

the body lower with decreasing the diameter of holes created on fins surfaces. The result was verified by performing a CFD analysis of the rectangular fin of aluminium alloy 60,603 on the steady and transient states both Vigesh et al. [2] experimented for enhancing the heat transfer in the engine, in which flat-structured fin has been changed with sinusoidal structured fin and found a significant improvement in the heat transfer rate in the engine. Also, the possibility of faster as well as uniform cooling in this type of structure.

Satish et al. [3] replaced older material with different aluminium alloys like aluminium alloys 6061, aluminium alloys C443 and aluminium alloys 2014 and done the thermal analysis of the fin body by varying slot sizes, geometries, and material. The weight of fins reduces by producing slotting, thus increment in heat transfer is observed.

Hardik et al. [4] investigated that the heat transfer coefficient is affected by fin geometry and cross-sectional area. And also, the author found that thicker fins give better efficiency in the high-speed vehicle; the increased fin thickness resulted in swirl being created, which helped in increasing the heat transfer. In a high-speed vehicle, greater the number of fins with less thickness is preferred because it helps to induce more considerable turbulence and results in a higher heat transfer rate. And Hardik et al. [4] also found that heat transfer depends on stream velocities, and it is necessary to maintain fluid velocity around the fins. And heat transfer coefficient depends upon space, flow condition, and time, these changes lead to an increase in the heat transfer coefficient and efficiency too.

Satish Kumar et al. [5] done an analytical analysis in which he designed a 100cc engine and replaced the old material with AL 6061, A2014, C443 of different geometries that are curved, circular, and angular instead of being rectangular fins. The observation from their research work is, as compared with AL Alloy 204, Al alloy 2014 has a 17% higher temperature distribution due to its higher thermal conductivity and of its material composition. It is also observed that linear distribution of temperature is shown by all material along the length of the fin, and the increment of efficiency is enhanced in circular fins by reducing the weight of the engine. And also, observed that the engine with curved fins shows better efficiency due to its less weight.

3 Problem Definition

At present, the cylinder block that we are using here having a capacity of 150cc engine or more is made up of cast iron that possesses excellent thermal properties though cast iron provides considerable cooling effects in comparison with any other materials and the usage of this leads to an increment in weight of the assembly. Our project focusses on making a model that is lightweight by changing the material and modifying the geometries by changing the fins thickness and orientation so that it extracts maximum heat from the engine. The main objective is to study the present model and to change its geometry and vary its thickness to observe the heat flux and

temp gradient. To replace the material of the block from cast iron to aluminium, magnesium and to observe the cooling effect by making variations in the thickness of all the three materials for different geometries. The CAD design of all the geometries is made by solid works and steady-state thermal analysis using Ansys to determine the optimum design from all the models which extract max heat from the engine or which provide the maximum cooling effect.

3.1 Methodology and Fin Parameters

Various materials and their properties which could be used for the given project were thoroughly studied, and accordingly, materials were selected. Design of fins, their configurations, and geometries have been done using solid works. Ansys was being used for thermal or steady-state analysis to examine the heat flux and temperature gradients. To calculate the analytical results, steady-state Fourier's equations and Bessel's functions were used [2]. Fins parameters (geometry, thickness, and material) were considered to observe the change in the amount of heat extracted by different fin models and temperature gradient along the length of the fins. Two geometries that are longitudinal and circular fins were considered, and corresponding data were duly recorded in order to get maximum cooling effect thickness of fins varied from 3 to 1.5 mm with an interval of 0.5 mm. Aluminium and magnesium materials other than cast iron were selected because of high thermal conductivity and lightweight.

3.2 Material Properties

The material properties play a very vital role in the heat transfer rate. The different materials are taken under consideration to achieve the maximum heat transfer in the engine block. The availability of all the material under consideration is also good. The mechanical properties of the material are shown in Tables 1, 2, and 3.

Table 1 Material properties of Mg (AZ31B) alloy

Density (kg/m^3)	1770
Young's modulus (Pa)	4.48e+10
Poisson's ratio	0.35
Bulk modulus (Pa)	4.97e+10
Shear modulus (Pa)	1.659e+10
Isotropic thermal conductivity ($\text{Wm}^{-1} \text{K}^{-1}$)	96

Table 2 Material properties of Al alloy

Density (kg/m ³)	2770
Young's modulus (Pa)	7.1e+10
Poisson's ratio	0.33
Bulk modulus (Pa)	6.96e+10
Shear modulus (Pa)	2.669e+10
Isotropic thermal conductivity (Wm ⁻¹ K ⁻¹)	237

Table 3 Material properties of cast iron

Density (kg/m ³)	7200
Young's modulus (Pa)	1.1e+11
Poisson's ratio	0.28
Bulk modulus (Pa)	8.3e+10
Shear modulus (Pa)	4.29e+10
Isotropic thermal conductivity (Wm ⁻¹ K ⁻¹)	53.3

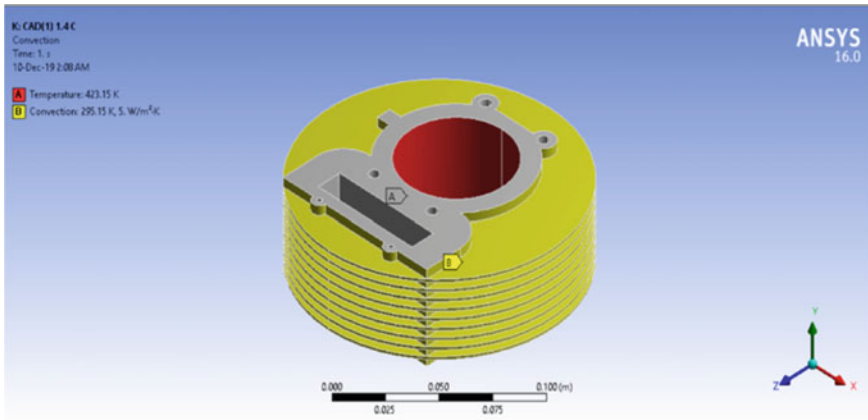


Fig. 1 Boundary condition of circular geometry

3.3 Boundary Conditions

The inner surface of the engine cylinder is at temperature 423.15 K for both the geometries (Figs. 1 and 2). The selected extended surface in the geometry is the convective area of the model. The ambient temperature is taken at 35 °C. The mode of heat transfer is selected as convection only.

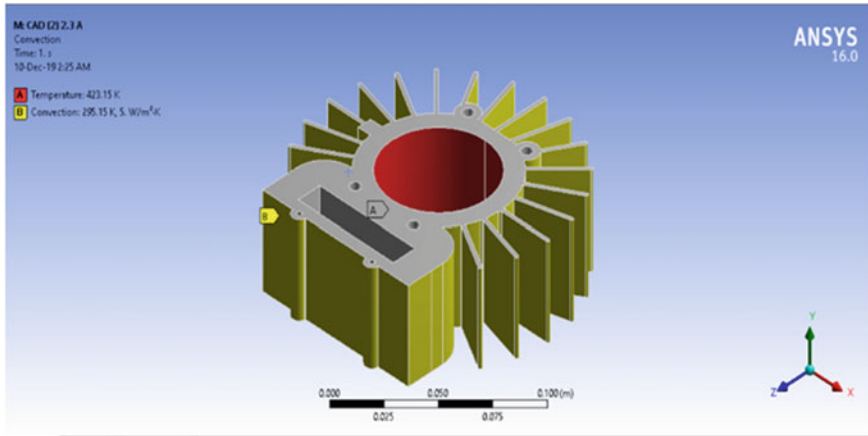


Fig. 2 Boundary condition of longitudinal geometry

3.4 Governing Equations

To calculate the amount of heat flux extracted by both the fins and to observe the temp gradient along the length of fins in case of longitudinal fins and along with the radial directions in case of circular fins Fourier equation and Bessel equation were used respectively [6]. Steady-state heat conduction equations, material properties independent of temperature, the thickness of fins negligible as compared to the length of fins, uniform cross-sectional area, etc. The following assumptions were made while calculation the heat flux from the fins. It was assumed that for longitudinal fins at the end, convection had occurred and for circular fins end of fins was perfectly insulated [7]. To determine the heat flux extracted by longitudinal fins, the governing equation used was based on Fourier’s law steady-state 1D heat conduction equation, i.e.,

$$q = \frac{mk\theta^{\circ} \left(\tanh \tanh ml + \frac{h}{mk} \right)}{1 + (h/mk) \tanh \tanh ml} \tag{1}$$

$$m = \sqrt{\left(\frac{hP}{KA} \right)} \tag{2}$$

The temperature variation along the length of the fin can be calculated as:

$$\theta = \theta^{\circ} \frac{\cosh \cosh m(l-x) + (h/mk) \sinh \sinh m(l-x)}{\cosh \cosh ml + (h/mk) \sinh \sinh ml} \tag{3}$$

To determine the amount of heat flux extracted by circular fins, following modified Bessel's equation was used.

$$q = 2\pi k r t m \theta^{\circ} \frac{K_1(mr) \times I_1(mR) - I_1(mr) \times K_1(mR)}{I^{\circ}(mr) \times K_1(mR) + I_1(mR) \times K^{\circ}(mr)} \quad (4)$$

$$m = 2h/Kt \quad (5)$$

K° , I° , K_1 , I_1 were modified zero-order and first-order Bessel function of a first and second kind, respectively. Corresponding temperature variation in the radial direction can be calculated as [8]:

$$\theta = \theta^{\circ} \frac{I^{\circ}(mr) * K_1(mR) + K^{\circ}(mr) * I_1(mR)}{I^{\circ}(mr) * K_1(mR) + I_1(mR) * K^{\circ}(mr)} \quad (6)$$

3.5 2D Layout of Models

See Fig. 3.

4 Design Modelling and Analysis of Fins

The engine cylinder with fin geometry was modelled in Solidworks 17. The dimensions of the geometries were taken from the commercially available engine datasheet. Models with different fin geometries were designed using Solidworks software (Fig. 4).

4.1 Thermal Analysis of Circular Fin Geometry

Analysis of circular fin geometry was carried out in Ansys Workbench. The CAD model was developed using Solidworks and then imported to Ansys Workbench for the thermal analysis. Meshing was also performed in the Ansys. The materials are aluminium, cast iron, and magnesium (AZ31B). The total mesh elements are 43,3391, and the average element quality is 0.8432 (Fig. 5).

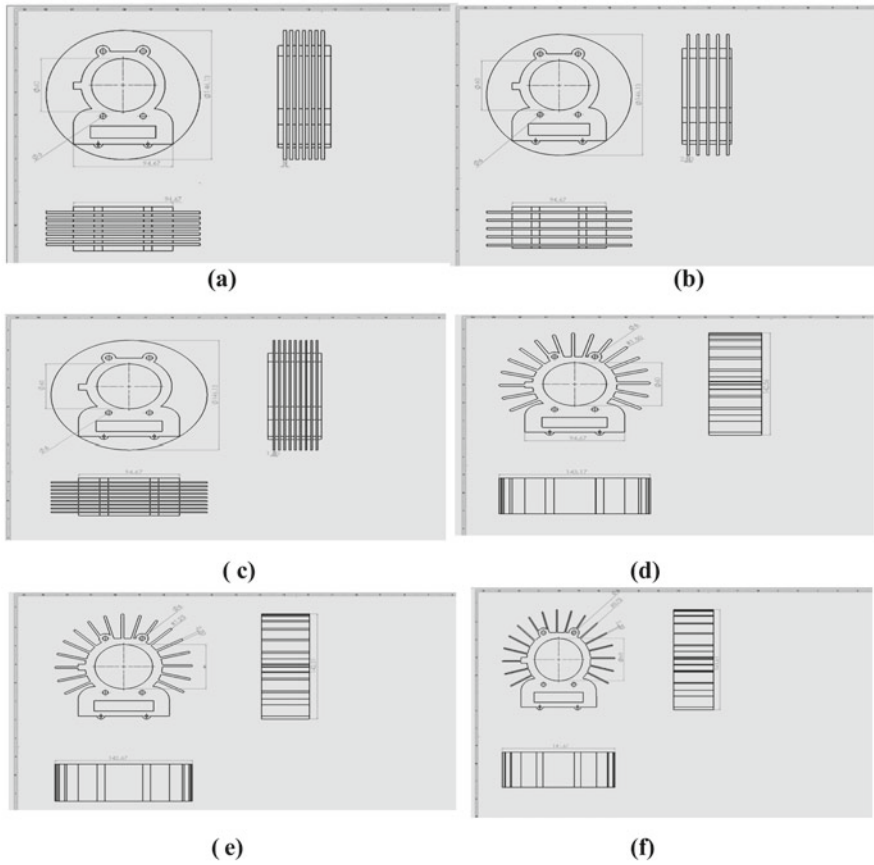


Fig. 3 2D layout of fin geometry. **a** Engine cylinder with circular fin (thickness 3 mm). **b** Engine cylinder with circular fin (thickness 2.5 mm). **c** Engine cylinder with circular fin (thickness 1.5 mm). **d** Engine cylinder with longitudinal fin (thickness 3 mm). **e** Engine cylinder with longitudinal fin (thickness 2.5 mm). **f** Engine cylinder with longitudinal fin (thickness 1.5 mm)

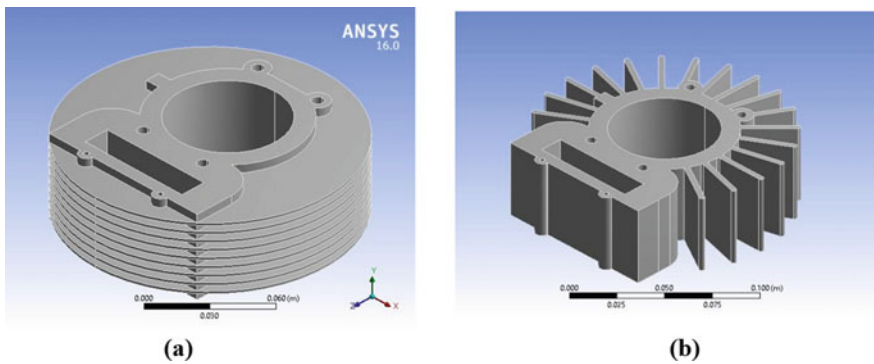


Fig. 4 CAD model of geometries. **a** Cylinder with circular fin geometry. **b** Cylinder with longitudinal fin geometry

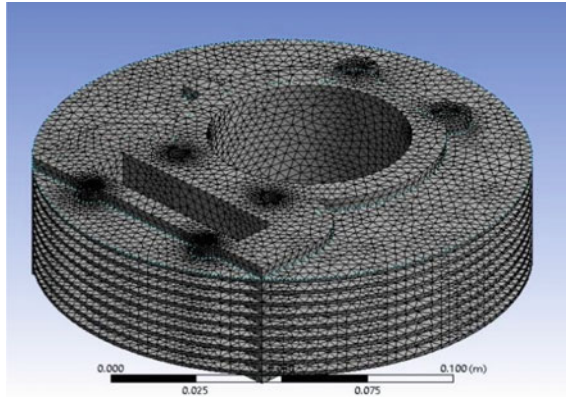


Fig. 5 Mesh of circular fin geometry

Table 4 Comparison of the different combinations in circular geometry

Circular fin geometry		Heat flux (W/m ²)	Temp. at the tip (°C)	Weight (kg)
1 Aluminium				
1.1	Fin thickness (3 mm)	18,016	145.97	1.12
1.2	Fin thickness (2.5 mm)	19,833	146.42	0.92
1.3	Fin thickness (1.5 mm)	32,158	144.52	0.95
2 Magnesium				
2.1	Fin thickness (3 mm)	17,798	142.9	0.71
2.2	Fin thickness (2.5 mm)	19,607	143.77	0.59
2.3	Fin thickness (1.5 mm)	31,594	140.56	0.60
3 Cast iron				
3.1	Fin thickness (3 mm)	17,394	137.54	2.92
3.2	Fin thickness (2.5 mm)	19,185	138.86	2.41
3.3	Fin thickness (1.5 mm)	30,561	133.4	2.47

4.2 Results of Circular Fin Geometry

The maximum heat flux from all the combinations of materials and fin thickness for the circular fin geometry is 32,158 W/m². The best combination from all the models in circular fin geometry is of aluminium material with a fin thickness of 1.5 mm.

The total weight of the geometry model 1.3 is 0.95 kg, which makes a very significant weight reduction of 42% compared with commercially available fins (Table 4 and Fig. 6).

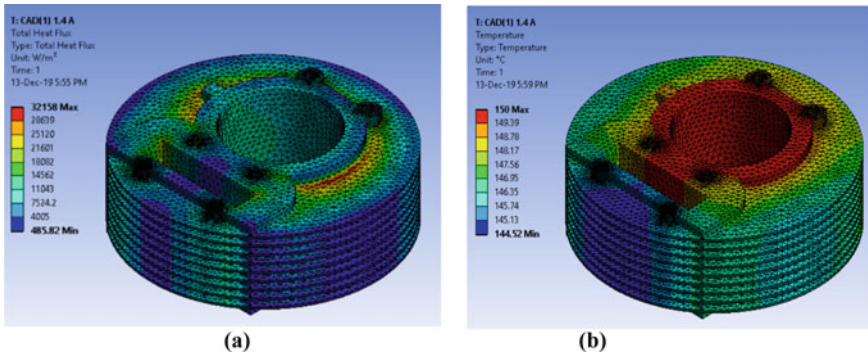


Fig. 6 a Maximum total heat flux of circular fin geometry model 1.3. b Temperature variation along the fin of circular fin model 1.3

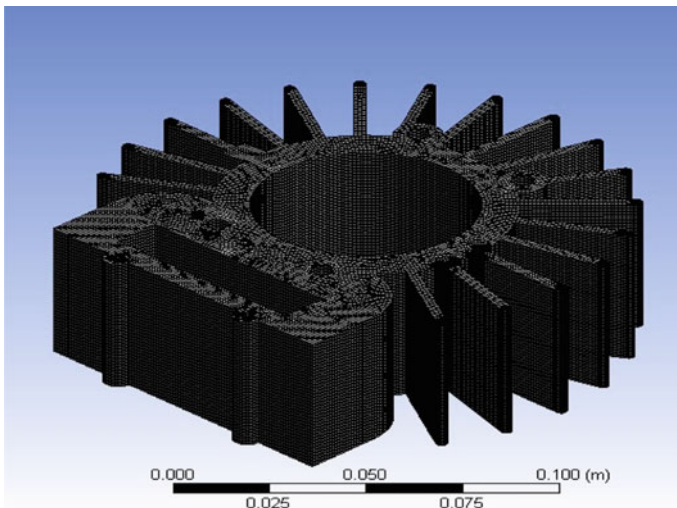


Fig. 7 Mesh of longitudinal fin geometry

4.3 Thermal Analysis of Longitudinal Fin Geometry

Analysis of longitudinal fin geometry was carried out in Ansys Workbench. The CAD model was developed using Solidworks and then imported to Ansys Workbench for the thermal analysis. Meshing operation was processed in the Ansys. The materials are aluminium, cast iron, and magnesium (AZ31B). The total mesh elements are 585,504, and the average element quality of the mesh is 0.8778 (Fig. 7).

4.4 Results of Longitudinal Fin Geometry

The maximum heat flux from all the combinations of materials and fin thickness for the longitudinal fin geometry is 30,116 W/m². The best combination of all the models in longitudinal fin geometry is of aluminium material with a fin thickness of 1.5 mm. The total weight of the geometry model 1.3 is 0.74 kg, which makes a very significant weight reduction of 46% compared with commercially available fins (Table 5 and Fig. 8).

Table 5 Comparison of the different combinations in longitudinal geometry

Longitudinal fin geometry		Heat flux (W/m ²)	Temp. at the tip	Weight (kg)
1 Aluminium				
1.1	Fin thickness (3 mm)	18,486	148.1	0.85
1.2	Fin thickness (2.5 mm)	20,835	147.84	0.81
1.3	Fin thickness (1.5 mm)	30,116	146.93	0.74
2 Magnesium				
2.1	Fin thickness (3 mm)	18,354	146.66	0.54
2.2	Fin thickness (2.5 mm)	20,636	146.22	0.52
2.3	Fin thickness (1.5 mm)	29,747	144.65	0.50
3 Cast iron				
3.1	Fin thickness (3 mm)	18,060	143.95	2.21
3.2	Fin thickness (2.5 mm)	20,290	142.25	2.11
3.3	Fin thickness (1.5 mm)	29,047	140.4	1.92

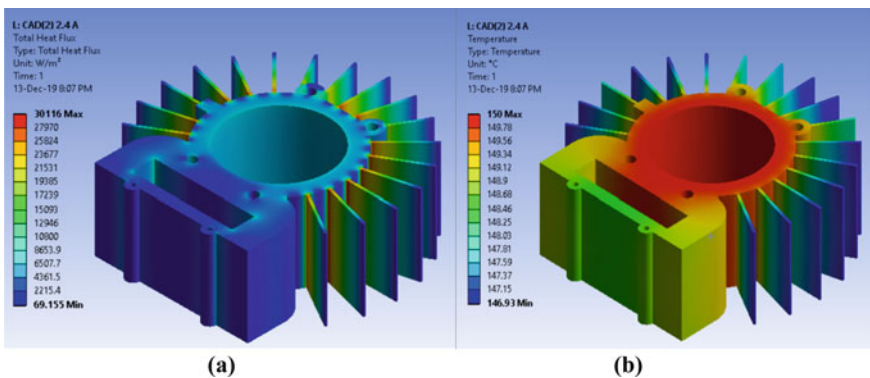


Fig. 8 **a** Maximum total heat flux of longitudinal fin geometry model 1.3. **b** Temperature variation along the fin of longitudinal fin model 1.3

5 Conclusion

In this paper, steady-state thermal analysis is carried out on 150 cc engine cylinder block fins by varying the geometry, thickness, and material of the fins. The maximum total heat flux of circular geometry fin is with thickness 1.5 mm, and the material of aluminium fin is 32,158 W/m². The maximum total heat flux of longitudinal geometry fin is 1.5 mm, and the material of aluminium is 30,116 W/m². Circular geometry of material aluminium with 1.5 mm thickness shows the best results as compared to other models. This research shows the maximum convection rate of heat transfer can be achieved by using the circular fin geometry under the steady-state analysis. However, further research shall work on determining the convection rate considering the forced convection due to the air in the environment.

The advantages of using the modified model of the geometries are:

- A weight reduction of 42% can be achieved using aluminium instead of cast iron as fin material.
- Improving the fin parameter helps us to increase the total heat transfer through the engine cylinder.

References

1. Sajesh KM, Soni N, Kosti S (2016) Design modification and heat transfer analysis of air cooled rectangular fin engine. *Int J Recent Sci Res* 7(3):9653–9656, March
2. Vignesh P, Selva Muthu Kumar P (2014) Design, modification, and analysis of two wheeler cooling sinusoidal wavy fins. *Int J Eng Res Technol (IJERT)* 3(11). ISSN: 2278-0181, Nov
3. Sathishkumar A, Kathirkaman MD, Ponsankar S, Balasuthagar C (2016) Design and thermal analysis on engine cylinder fins by modifying its material and geometry. *J Chem Pharm Sci.* ISSN: 0974-2115
4. Rathod HD, Modi AJ, Rathod PP (2013) Effect of different variables on heat transfer rate of four-stroke SI engine fins—review study. *Int J Mech Eng Technol* 4(2):328–333
5. Sathishkumar K, Vignesh K, Ugesh N, Sanjeevaprath PB, Balamurugan S (2017) Computational analysis of heat transfer through fins with different types of notches. *Int J Adv Eng Res Sci* 4(2). ISSN: 2349-6495(P)| 2456-1908(O), Feb
6. Yoshida M, Ishihara S, Nakashima K, Yamamoto M (2005) Development of air-cooled cylinder by utilizing natural convection. In: *SAE Technical Papers*
7. Natrayan L, Selvaraj G, Alagirisamy N, Santhosh M (2016) Thermal analysis of engine fins with different geometries. *Int J Innov Res Sci Eng Technol* (May):6900–6906
8. Chandanshive A, Pise SM (2019) Thermal analysis and optimization of two-wheeler engine cylinder fins. *Int Res J Eng Technol* 6(5):6253–6260, May

Energy Utilization Reduction of Domestic Refrigerator Using Phase Change Materials



Anand Pavithran, Meeta Sharma , and Anoop Kumar Shukla 

Abstract Domestic refrigerators being a household appliance utilizes a tremendous amount of energy. To enhance the performance of refrigerators, many approaches have been introduced. Among them, phase change material (PCM) is a novel approach, which seeks the attention of researchers for improving the energy efficiency and performance of the system. A PCM is a substance that can store or discharge a large amount of heat energy by changing its phase. Hence, the integration of PCM in refrigerator improves its performance and can decrease energy utilization by keeping up a steady temperature inside the system during its compressor off time. The current work is focusing upon PCM incorporation in refrigeration system for reducing the energy utilization. The objective of the work is to study various methodologies adopted for the PCM incorporation and to study various factors influencing the performance of PCM incorporated refrigerator. Moreover, the properties improvements of PCM using nano-materials are also discussed.

Keywords PCM: Phase change material · VCR: Vapour compression refrigerator · TES: Thermal energy storage · COP: Coefficient of performance · LHS: Latent heat storage · PCT: Phase change temperature · CFD: Computational fluid dynamics

A. Pavithran (✉) · M. Sharma · A. K. Shukla
Amity University Uttar Pradesh, Noida, UP, India
e-mail: anandpavithranov@gmail.com

M. Sharma
e-mail: msharma15@amity.edu

A. K. Shukla
e-mail: shukla.anoo-phbti@gmail.com

1 Introduction

In these days, every family utilizes at least one refrigerator framework for food preservation. Due to the wide usage and continuous operation of domestic refrigerators, these systems demand a large amount of electric energy. The survey conducted by the Indian Brand Equity Foundation (IBEF) [1] shows that the refrigerator consumes about one-fourth of the total energy consumption in the domestic sector. Thus, even a little improvement in these types of equipment brings a colossal measure of energy conservation. As mentioned by Cheng et al. [2], numerous methodologies were adopted for reducing the electric power utilization of refrigerator units. Improving the thermal insulation of refrigerator is one of the methods used for reducing the energy utilization. Insulation reduces the heat interaction between the system and atmosphere. Insulation can be improved by using polyurethane material instead of polystyrene as body material or by vacuum insulation technique. The use of high energy-efficient compressor is another method. Variable speed compressors are the best option for this method. The motor speed of these compressors adjusts according to the thermal load of the system which results in energy saving. Next method for reducing the energy consumption is improving the heat transfer performance of the condenser and evaporator. By increasing the heat transfer area and heat transfer coefficient, we can improve the heat transfer performance of these components.

For reducing the energy utilization by refrigerators, the PCM integration with refrigerator is an innovative approach. A phase change material (PCM) is a heat energy stockpiling unit that changes the phase at a specific temperature. During its phase transition, the material stores or releases a large amount of heat energy, which depends upon the latent heat value of materials, so it is called as latent heat storage system (LHS) [3]. As mentioned by Azzouz et al. [4], the cold stored in the PCM can be utilized to balance out the temperature inside the refrigerator compartments during compressor off time of the refrigerator and this procedure improves the energy efficiency of the system.

Current work is focusing on the PCM integration in domestic refrigeration frameworks; the objectives of this study includes review and evaluation of various works conducted by the researchers on the PCM-integrated refrigerator systems and identify factors affecting on the performance of the system. Moreover, identification of limitations and challenges associated with the PCM-integrated refrigerators are also included.

2 Working Method

In the vapour compression refrigeration (VCR) system, the compressor works in on-off mode. While the compressor is in on-mode, refrigerant moving through evaporator coil absorbs heat from the refrigerator cabinet and after achieving a

predefined temperature inside the refrigerator the compressor turns off automatically. During the off-time period, the temperature inside the refrigerator increases due to the heat transfer from the ambient to the system and by the heat released by the stored food materials. When the temperature reaches the upper limit set by the manufacturer, the compressor also turns on automatically and starts to pump the refrigerant through the evaporator. As mentioned by Cerri et al. [5], phase change material (PCM) could be a decent alternative for reducing the temperature variance inside the fridge during compressor off mode. Azzouz et al. [4] mention that, when PCM is integrated with refrigerator, it will take most of the heat released by the stored food and heat gain to the system from the atmosphere during compressor off mode and keeps up a steady temperature until the melting procedure of PCM is finished. Along these lines for a specific period (until the PCM melts), the desired temperature inside the unit will maintain during the off-time period of the compressor. This strategy expands the compressor off-time period. On the other hand, the PCM integration requires more compressor on time for charging the PCM but by comparing the total cyclic on- and off-time period of the compressor, the total cyclic off period is very long and it helps to reduce the energy consumption rate. A schematic representation of PCM-integrated refrigerator by Berdja et al. [6] is shown in Fig. 1.

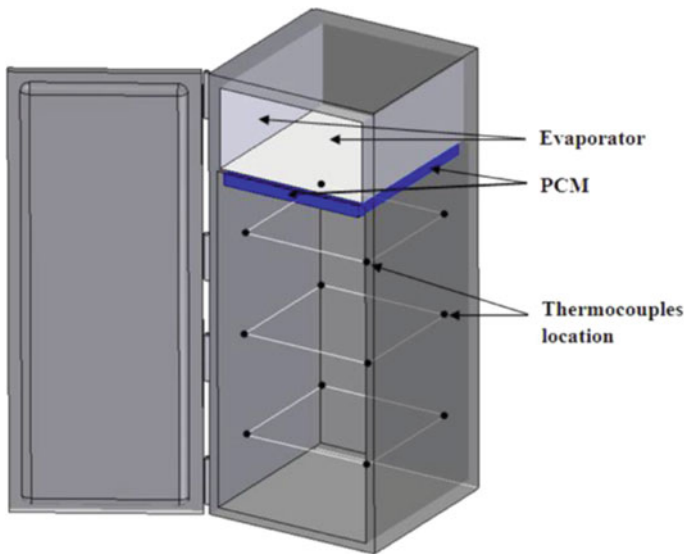


Fig. 1 PCM-integrated refrigerator [6]

3 PCM Integration on the Refrigerator

The works related to PCM integration on refrigerator can be categorized as—PCM integration at evaporator and refrigerator cabin (i.e. at low-temperature side) and PCM at condenser (i.e. at high-temperature side)

3.1 PCM at Evaporator and Refrigerator Cabins (Low-Temperature Side)

The integration of PCM slab on the evaporator affects into two sorts of heat transmission mechanisms to take place, conduction from the evaporator to PCM and convection heat transfer from PCM to air [7]. Due to the high latent heat and smaller conductivity values of PCMs, the compressor has to work for a longer period to solidify the PCM (charging the PCM). This will cause to longer compressor on time in every cycle to charge PCM. During compressor off time, the charged PCM maintains the temperature within the cabin by way of absorbing the heat gain to the system from the atmosphere and the released heat from the stored food. That is for a sure length, till the PCM melts completely the temperature inside the unit will be maintained and this method results longer compressor off time duration. The principal points of interest of longer compressor off time are: lower electric power utilization, better nourishment quality and forestalling the damaging impact of regular compressor start and stop, as referenced by Elarem et al. [8].

Cerri et al. [5] simulated PCM-integrated refrigerator unit and analysed the effect of PCM incorporation, the outcome turned into 12% improvement in the coefficient of performance.

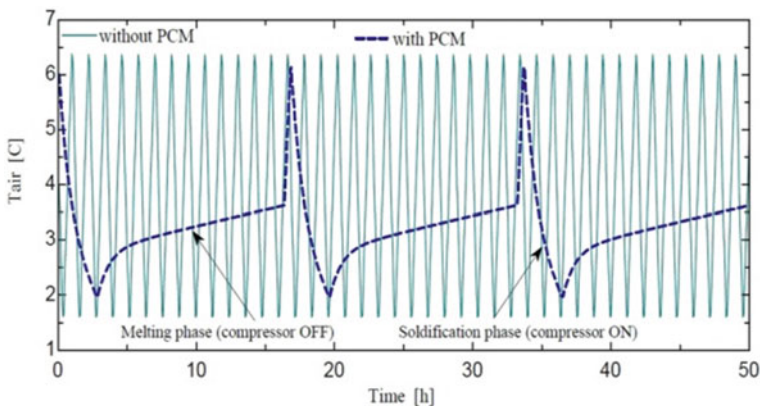


Fig. 2 Air temperature inside the refrigerator unit with and without PCM [9]

Azzouz et al. [4, 9] conducted a series of experimental and numerical studies on a PCM integrated refrigerator. These studies analysed the effect of different PCMs (water and some eutectic solutions) and different orientations of PCM at the low-temperature side of the refrigerator unit. These works concluded that the PCM-integrated refrigerator enhances the COP up to 72%. A simplified dynamic mathematical model also has been developed by the author, for predicting the energy impact, the work estimated 35% reduction in compressor working time. The temperature of air inside the refrigerator versus time graph obtained from the experimental study [9] is shown in Fig. 2. By analysing the results, it is noted that, with the use of PCM the rise in air temperature inside the refrigerator unit is in slow manner as compared with the system without PCM incorporation during compressor off time and this results longer compressor off time duration.

Marques et al. [10] designed a novel refrigerator with the PCM units and investigated the performance improvement of the refrigerator experimentally and numerically using different PCMs (water and some eutectic solution). The outcomes demonstrated that the integration of a 5-mm PCM slab results to maintaining the temperature inside the refrigerator for around 3–5 h and presumed that eutectic PCM is far superior to water. Marques et al. [11] also conducted a CFD simulation to determine the effect of different orientations of PCM slab on the refrigerating system and the work concluded that the configuration of combined horizontal and vertical PCM slabs on the refrigerator system is more suitable than a simple horizontal or vertical configurations of PCM.

Khan et al. [12, 13] conducted many studies on PCM incorporation on refrigerators to enhance the system performance by utilizing water and eutectic solutions as PCM. The PCM placed behind the evaporator compartment. Depending on the PCM type and heat load, the COP improved around 20–27%. The studies also noticed that an increase (approximately 40%) in the amount of PCM results around 6% increment in the COP. Through experimental investigation Khan et al. noted that, the usage of eutectic solution as PCM increases the COP of refrigerator more than that of water as PCM.

Gin et al. [14] researched about the performance enhancement of a refrigerator using PCM, when PCM modules were set against the internal areas of the system, the energy utilization was diminished by 8% during a defrost cycle and 7% while considering the door openings.

Geethanjali et al. [15] examined the improvement in the performance of the domestic refrigerating unit by utilizing PCM with nanoparticles. Researchers mixed the PCM with copper oxide (CuO) nanofluid. It has been observed that the nanoparticle increases the thermal conductivity of the PCM solution. The increase in thermal conductivity results reduction in the charging time of PCM and which directly reduces the energy consumption by the compressor. The experimental result confirmed that the integration of PCM with refrigerator unit reduces the power consumption.

Toledo et al. [16] conducted a study with two eutectic PCMs, PLUS-ICE E-10 and ammonium chloride aqueous solution were taken. The outcomes shows that, the energy utilization decreased up to 5.81% when the evaporator altered with

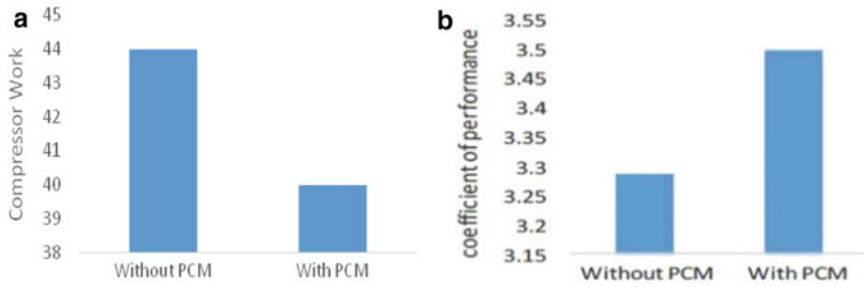


Fig. 3 Results obtained by Reddy et al. [17] shown as **a** Compressor work with and without PCM and **b** Coefficient of performance with and without PCM

PCM. The compressor working time was also decreased 3.71% and 9% for PLUSE ICE and ammonium chloride aqueous solution respectively. The researcher additionally observed that the first compressor cycle was extremely long for charging PCM compared with the conventional system.

Elarem et al. [8] integrated an array of 12 copper tubes containing PLUS-ICE as PCM with the evaporator. The exploratory outcomes indicate that power consumption is reduced by 12%, and the COP is expanded by 8% compared to conventional VCR. Elarem et al. also investigated the effect of four different configurations of PCM integration with the help of CFD simulation software and this work concluded that, the coverage area of PCM more than 75% did not lead to any significant improvement for the system.

Reddy et al. [17] experimentally investigated the performance improvement of the refrigerating unit, by covering the evaporator with a metallic box filled with eutectic solution of $KCl + H_2O$ as PCM. The results showed that 9% improvement in COP and the compressor work reduced from 44 to 40 kJ/kg. The graphical representation of results obtained by this study is shown in Fig. 3 (Table 1).

3.2 PCM at Condenser (i.e. High-Temperature Side)

A condenser is a device that is used to condensate the vapour refrigerant. When the hot vapour refrigerant passes through the condenser it rejects the heat to the atmosphere and changes its phase from gaseous state to liquid state. The studies explained that higher heat rejection during the condensation process increases the performance of the system. The objective of integration of PCM with the condenser is to reduce the condensation temperature, and also used for de-superheating and sub-cooling the refrigerant [18]. Unlike wide investigative studies in PCM integration on the low-temperature side of the refrigerator, the integration of PCM at the high-temperature side did not get much consideration because of undesirable outcomes of such configuration [20].

Table 1 Summary of various research works on PCM-integrated refrigerator

Researchers	PCM used	Area of application	Remarks
Azzouz et al. [4, 9]	Water eutectic solution	Evaporator and refrigerator cabin	COP and energy efficiency improved
Rahman et al. [27]	Water	Evaporator	Energy efficiency increases
A.C Marques et al. [10, 11]	Water eutectic solution	Evaporator and components	Combined horizontal and vertical combination of PCM is more stable
Khan et al. [12, 13]	Water eutectic solution (NaCl + H ₂ O)	Evaporator	Increasing the quantity of PCM also increases the performance
Gin et al. [14]	Eutectic solution	Internal walls	Energy consumption reduced
Ahamed et al. [28]	Eutectic solution (ethylene glycol + H ₂ O)	Evaporator	Maintain a constant temperature inside refrigerator cabin up to 8 h
Geethanjali et al. [15]	Eutectic solution + Nano fluid	Evaporator	Addition of nanofluid increases the heat transfer coefficient
Cofre–Toledo et al. [16]	PLUS-ICE (E-10) Eutectic solution (NH ₄ Cl + H ₂ O)	Evaporator	Performance improved
Elarem et al. [8]	Plus-ICE	Evaporator and internal walls	COP improved. PCM coverage of more than 75% does not lead to any significant improvement
Reddy et al. [17]	Eutectic solution (KCl + H ₂ O)	Evaporator sidewalls	Compressor work reduced. COP improved 10%
Sonnenrein et al. [18]	Paraffin	Condenser	Power consumption and condensation temperatures are reduced
Arjaria et al. [19]	Paraffin wax ethylene glycol lauric acid	Condenser	Performance improved. Ethylene glycol as PCM showed better result

Sonnenrein et al. [18] conducted many research and studies to reduce the power consumption by the refrigerator units. The researcher conducted a series of experiments with incorporating different PCMs (water, paraffin, or copolymer compound) at the condenser side. This study found out that the application of phase change materials (PCM) decreases the condensation temperature which helps to reduce the compressor work and prompts a significant decrease in power consumption.

Arjaria et al. [19] conducted CFD simulation studies to analyse the enhancement in system performance by integrating PCM at condenser side. Different phase

change materials like paraffin wax, ethylene glycol and lauric acid are taken for the simulation study. This work noted that the condenser wrapped with ethylene glycol as the PCM showed the best results as compared to other two PCM materials (paraffin wax and lauric acid).

Wang et al. [20, 21] led to a progression of trials utilizing PCMs in different areas of a refrigerator. PCM-A was introduced between the condenser and compressor, PCM-B was situated between the expansion valve and condenser, while PCM-C in the middle of the compressor and evaporator. The researchers observed that the addition of PCM-A and PCM-B with the refrigerator increases the COP by de-superheating and sub-cooling effects, respectively. Wang et al. denoted that there is not much improvement in the system performance for the incorporation of PCM-C.

4 Factors Effecting the PCM-Integrated Refrigerator

The observation through the literature review upon the PCM integration on the refrigerator, the various factors and parameters which affect the refrigeration system are summarised in this section.

4.1 Effect of PCT

Phase change temperature (PCT) is the most vital feature for choosing a PCM. While integrate PCM with the refrigerator unit, the PCT should match with the operational temperature of the system. Studies show that the PCT is directly effects on the compressor off-time duration. Khan et al. [13] stated that the integration of PCM having high PCT leads to an increase in the compressor off-time duration but it reduces the quality of stored food because high PCT maintains the temperature inside the system at some higher temperature than usual. In the case of low PCT, it maintains a low temperature inside the system but it causes to reduce the COP.

4.2 Effect of Amount/Quantity of PCM

The amount of PCM influences the performance of the refrigerator units. Berdja et al. [6] carried out some theoretical and experimental investigation on the thickness impact of PCM on the refrigerator performance. The outcomes show that the addition of PCM layer produces an improvement in COP and a decrease in energy utilization, yet it would decrease the heat transfer that happens between the evaporator unit and the air inside the system. Studies by Khan et al. [13] detailed that the PCM thickness significantly influences the performance of the refrigeration

framework, an increase (approximately 40%) in the amount of PCM brought about a 6% increment in the COP. Mastani et al. [22] mention that the thicker PCM is costly and requires more compressor work for charging the PCM. As mentioned by Onyejekwe et al. [23] while selecting the thickness of PCM, the thermal load acting on the system should be a considerable factor. The minimum quantity of PCM required according to the thermal load can be calculated by considering the steady-state energy equation.

Energy stored in the PCM is equal = Heat gain to the compartment

$$\rho Vh = \text{toff} * (UA)\text{cold}(T_{\text{amb}} - T_{\text{cold}})$$

where E = Energy stored in the PCM, ρ = Density of PCM, h = Latent heat value of PCM, V = Volume of PCM, Q = total heat gain, toff = Compressor off-time period, U = Overall heat transfer coefficient, A = Area of PCM, T_{amb} = Ambient temperature, T_{cold} = Average temperature inside the refrigerator. Minimum volume required for PCM according to the thermal load is,

$$V = \frac{\text{toff} * (UA)\text{cold}(T_{\text{amb}} - T_{\text{cold}})}{\rho h}$$

4.3 Effect of Thermal Load

Studies conducted by Borges et al. [24] mention that the heat load resulting from frequent door openings increases the thermal load within the cabin. The thermal load and energy efficiency rate of the refrigerator is inversely proportional; i.e., an increase in thermal load results to decrease in the energy efficiency and performance of the system. As noticed by Azzouz et al. [9], the high thermal load influences both charging and discharging lengths of the PCM. So while choosing the PCM, one should consider the thermal load acting on the system. As mentioned by A. C. Marques et al. [11] for high thermal loads water is the best option because of its high latent heat storage capacity and for low thermal loads eutectic PCMs are much suitable.

4.4 Effect of PCM Position, Orientation and Percentage Coverage

The effects of PCM position, orientation and percentage of PCM coverage on refrigeration were analysed by many researchers. Marques et al. [11] carried out CFD simulation for analysing the effect of different orientations of PCM (horizontal, vertical and combined horizontal and vertical orientation) on refrigerator

system. The study concluded that the horizontal configuration of PCM is better than the vertical configuration and comparing the horizontal and vertical configuration with combined one, the combined configuration shows more predominate temperature maintenance.

As mentioned by Elarem et al. [8] in addition to the types of PCM orientation, the percentage of PCM coverage also affects the performance of the refrigerator. Elarem et al. studied four different percentage PCM coverage cases (Case-1 with 10%, Case-2 with 50%, Case-3 with 75%, Case-4 with 90%). It has been observed that, to decrease the compartment temperature Case-1 required more time compared with Case-2, Case-3 and Case-4. The computational results indicate that, more percentage increase in PCM stabilizes and homogenizes the temperature inside the refrigerator faster. However, beyond 75% of PCM coverage on the refrigerator compartments does not prompt any significant improvement. In fact, the combination of vertical and horizontal configurations with 75% of area cover of PCM is considered as the best.

4.5 Effect of Ambient Temperature

As mentioned by Marques et al. [11], the phase change material melts fast at higher ambient temperature, which reduces the compressor off-time duration and performance of the refrigerator. Higher ambient temperature also increases the condensation temperature for the refrigerator which results in to decrease the COP of the system.

5 Limitation and Challenges

For improving the refrigerator system performance, the PCM integration is the best option. However, there are some limitations and challenges. One of the main limitations of PCM is its low thermal conductivity. Recent studies showed that this limitation can be overcome by adding the nanoparticles like TiO_2 , Al_2O_3 , Fe_3O_4 , CuO , etc. with PCM [15, 25]. There are many challenges associated with PCM-integrated refrigerators. The material selection for the PCM container is one of them. Most of the PCM materials are corrosive so the PCM container should have anti-corrosive properties. To overcome this problem aluminium, copper and stainless steel materials can be selected as container material but the carbon steel must be avoided due to its high corrosion rate [26]. Maintaining the correct proportion of the thickness of PCM material in the refrigerator is another challenge. It is noticed that higher thickness improves the COP but it acts as an additional thermal load and it may reduce the compressor efficiency [9].

6 Conclusion

A review upon the PCM integration in domestic refrigeration system has been carried out and the major observations are:

- The latent heat storage technique is a promising one.
- The PCM integration in the refrigerator enhances performance and reduces the consumption of electric power.
- Most of the studies were focused on the application of PCM in the low-temperature side. The application of PCM at the high-temperature side proves less promising because of its undesirable effects on the system.

References

1. IBEF presentation, Indian Consumer Durables Industry Analysis. <https://www.ibef.org/industry/consumer-durables-presentation>
2. Cheng WL, Mei BJ, Liu YN, Huang YH, Yuan XD (2011) A novel household refrigerator with shape-stabilized PCM (Phase Change Material) heat storage condensers: an experimental investigation. *Energy* 36(10):5797–5804
3. Riffat SB, Ma X (2003) Thermoelectrics: a review of present and potential applications. *Appl Therm Eng* 23(8):913–935
4. Azzouz K, Leducq D, Gobin D (2008) Performance enhancement of a household refrigerator by addition of latent heat storage. *Int J Refrig* 31(5):892–901
5. Cerri G, Palmieri A, Monticelli E, Pezzoli D (2003) Identification of domestic refrigerator models including cool storage. In: International congress of refrigeration, Washington, DC, August
6. Berdja M, Hamid A, Sari O (2019) Characteristics and thickness effect of phase change material and frost on heat transfer and thermal performance of conventional refrigerator: theoretical and experimental investigation. *Int J Refrig* 97:108–123
7. Du K, Calautit J, Wang Z, Wu Y, Liu H (2018) A review of the applications of phase change materials in cooling, heating and power generation in different temperature ranges. *Appl Energy* 220:242–273
8. Elarem R, Mellouli S, Abhilash E, Jemni A (2017) Performance analysis of a household refrigerator integrating a PCM heat exchanger. *Appl Therm Eng* 125:1320–1333
9. Azzouz K, Leducq D, Guilpart J, Gobin D (2005) Improving the energy efficiency of a vapor compression system using a phase change material
10. Marques AC, Davies GF, Maidment GG, Evans JA, Wood ID (2014) Novel design and performance enhancement of domestic refrigerators with thermal storage. *Appl Therm Eng* 63(2):511–519
11. Marques AC, Davies GF, Evans JA, Maidment GG, Wood ID (2013) Theoretical modelling and experimental investigation of a thermal energy storage refrigerator. *Energy* 55:457–465
12. Khan MIH, Afroz HM (2013) Effect of phase change material on performance of a household refrigerator. *Asian J Appl Sci* 6(2):56–67
13. Khan MIH, Afroz HM (2011) An experimental investigation of the effects of Phase Change Material on Coefficient of performance (COP) of a household refrigerator. In: Proceedings of the international conference on mechanical engineering and renewable energy
14. Gin B, Farid MM, Bansal PK (2010) Effect of door opening and defrost cycle on a freezer with phase change panels. *Energy Convers Manag* 51(12):2698–2706

15. Geethanjali S, Durga Prasad B (2017) Performance enhancement of domestic refrigerator using phase change materials mixed with nano fluid. *IJTIMES* 3(9)
16. Cofre-Toledo J, Vasco DA, Isaza-Roldan CA, Tangarife JA (2018) Evaluation of an integrated household refrigerator evaporator with two eutectic phase-change materials. *Int J Refrig* 93:29–37
17. Reddy MS, Venkatesh G, Reddy KJ, Suresh B () Performance improvement of a domestic refrigerator by using phase change material. *IJARSE*. ISSN: 2319-8354
18. Sonnenrein G, Elsner A, Baumhögger E, Morbach A, Fieback K, Vrabec J (2015) Reducing the power consumption of household refrigerators through the integration of latent heat storage elements in wire-and-tube condensers. *Int J Refrig* 51:154–160
19. Arjaria S, Varghese L Analysis of PCM material in heat transfer system
20. Wang F, Maidment G, Missenden J, Tozer R (2007) The novel use of phase change materials in refrigeration plant. Part 1: Experimental investigation. *Appl Therm Eng* 27(17–18):2893–2901
21. Wang F, Maidment G, Missenden J, Tozer R (2007) The novel use of phase change materials in refrigeration plant. Part 2: Dynamic simulation model for the combined system. *Appl Therm Eng* 27(17–18):2902–2910
22. Joybari MM, Haghighat F, Moffat J, Sra P (2015) Heat and cold storage using phase change materials in domestic refrigeration systems: the state-of-the-art review. *Energy Build* 106:111–124
23. Onyejekwe DC (1989) Cold storage using eutectic mixture of NaCl/H₂O: an application to photovoltaic compressor vapour freezers. *Solar Wind Technol* 6(1):11–18
24. Borges BN, Melo C, Hermes CJ (2014) Prediction of evaporator frosting in household refrigerators subjected to periodic door opening
25. He Q, Wang S, Tong M, Liu Y (2012) Experimental study on thermophysical properties of nanofluids as phase-change material (PCM) in low temperature cool storage. *Energy Convers Manag* 64:199–205
26. Tikudave VK, Hole JA (2018) A review of a latent heat storage through PCMs with VCC system integrations for domestic refrigerator 3(1)
27. Rahman R, Hossain MA, Das SK, Hasan A (2014) Performance improvement of a domestic refrigerator by using PCM (phase change material). *Global J Res Eng*
28. Ahamed MM, Kannakumar J, Reddy PM (2013) Experimental investigation on the performance analysis of cold storage plant using with and without phase change material (PCM). *Int J Sci Eng Res (IJSER)* 1(4)

Flutter and Modal Analysis of Gas Turbine Compressor Blades



Priya Singh, V. K. Chawla, and N. R. Chauhan

Abstract This study aims to analyze the fluttering in the gas turbine compressor blade and the aerodynamic damping effects on the gas compressor blades by analyzing the damping coefficient sign in the model. The flutter in aerodynamic profiles is referred to as the self-excited vibration in air-foils due to unsteady pressure oscillations in the air flow field. The modal analysis of the gas compressor blade of aluminum alloy is carried out at modes 1, 2, and 3 in which the natural and modal frequency of blade is tested by using the ANSYS 17 platform. The various cases are studied for the different number of blades of gas turbine compressor to analyze the effect of fluttering on the blades.

Keywords Fluttering · Damping · Aerodynamic coefficient · Nodal diameter

1 Introduction

The flutter can be defined as the self-excited unstable vibration of an aerodynamic structure caused by the effect of pressure fields generated due to its motion. This study aims to carry out a flutter analysis by simulation on the Ansys CFX application to calculate the fluttering effect on the blade surface produced by the unsteady pressure distributions and aerodynamic damping coefficient. The value of the aerodynamic damping coefficient defines the stable and unstable modes of compressor blade made up of aluminum alloy. The blade vibration is observed to be damped when the aero-damping coefficient is positive, and flutter occurred when it is negative [1]. The analysis of the model can be delineated from the following steps:

P. Singh (✉) · V. K. Chawla · N. R. Chauhan
Department of MAE, Indira Gandhi Delhi Technical University for Women, Delhi, India
e-mail: priya.singh300994@gmail.com

V. K. Chawla
e-mail: vivekchawla@igdtuw.ac.in

© The Author(s), under exclusive license to Springer Nature Singapore Pte Ltd. 2021
B. S. Sikarwar et al. (eds.), *Advances in Fluid and Thermal Engineering*,
Lecture Notes in Mechanical Engineering,
https://doi.org/10.1007/978-981-16-0159-0_62

707

- An aerodynamic structure moves in space due to some internal excitement.
- The structure interacts with the surrounding fluid and generates pressure waves in the fluid.
- The generated pressure waves exert a force on the structure.
- In case, the effect of this aerodynamic-structural interaction results in amplification of a vibration, the condition is considered to be having a flutter effect.

The onset and growth of flutter are governed by the aerodynamic-structural interaction, which can be quantified in the form of aerodynamic damping coefficient of the system [1]. Damping can generally be classified as structural damping and aerodynamic damping for a system. The onset of flutter is in general governed by the aerodynamic damping while the subsequent growth is governed by the combined effect of aerodynamic and structural damping. The significance of the critical damping factor is found in the fact that this coefficient is an indicator of the effect of aerodynamic damping on the blades. The positive damping condition signifies that it is dissipating the energy from the system and will not cause any kind of instability on the system. However, if the value of damping is negative, the aerodynamics will add some energy to the vibrating structure that will cause a fluttering effect within the system. The effect of aerodynamic damping on a blade profile is determined through the sign of aerodynamic damping coefficient.

For the proposed case, the work is done toward finding out the onset of flutter, which leads to an eigenvalue problem to find out the complex natural frequency of the system. In this value, the imaginary part of the frequency is a measure of critical damping ratio for the system. And from this, the nature of stability in the system can be predicted. Additionally, to quantify the stability or instability the value of the logarithmic decrement for the system is also calculated. The nodal diameter is also one of the significant parameters for the analysis of the fluttering effect. For instance, in this paper, an 80-bladed rotor is considered under different mode shapes each having different nodal diameters value, i.e., diameters joining the zero displacement blades at a time. These nodal diameters are rotating with time, and in detail, the value of aerodynamic damping is different for each case of nodal diameters. This is considered in the analysis and is adopted as the base for defining the stable modes.

1.1 Part-1(Modal Analysis of the Blade)

For the first part, the blade model with tetrahedral mesh elements was analyzed with ANSYS.

Some of the major steps involved in the analysis are listed below:

1. Fixing the nodes at the blade base, i.e., defining structural constraint with displacement attribute as zero.

2. Inserting material properties, i.e., Young’s modulus of elasticity, isotropic material behavior, the mass density of the material, and Poisson’s ratio corresponding to aluminum.
3. The blade was subjected to a rotational speed of 2800 rpm.
4. Prestress on.
5. External forces were assumed to be zero, in command to obtain modal shapes and natural frequencies.

The solution to the stress analysis problem was obtained in the form of the first three modes of the blade. Each mode was analyzed to provide the corresponding natural frequency and modal shape for respective modes was generated in the displacement domain.

Following are the key observations of Fig. 1:

1. The trailing edge tip of the blade undergoes max. displacement, which is to be expected because of the low stiffness of the nodes due to the distance of the tip from the blade root as well as comparatively less thickness as opposed to the leading edge.
2. The deformation occurs along the edges of the blade.
3. Displacement is approximately linear to the distance of a node from the blade hub in the radial direction.

The deformed shape can be compared approximately to that of a cantilever beam undergoing deformation due to tip load. Hence, the first mode can be appropriately designated as the first bending mode or chordwise bending mode for the blade.

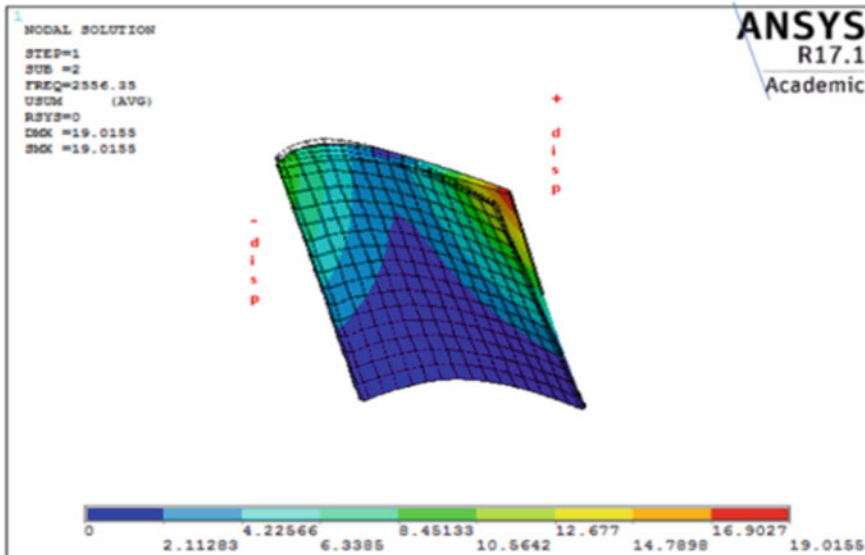


Fig. 1 Mode 1

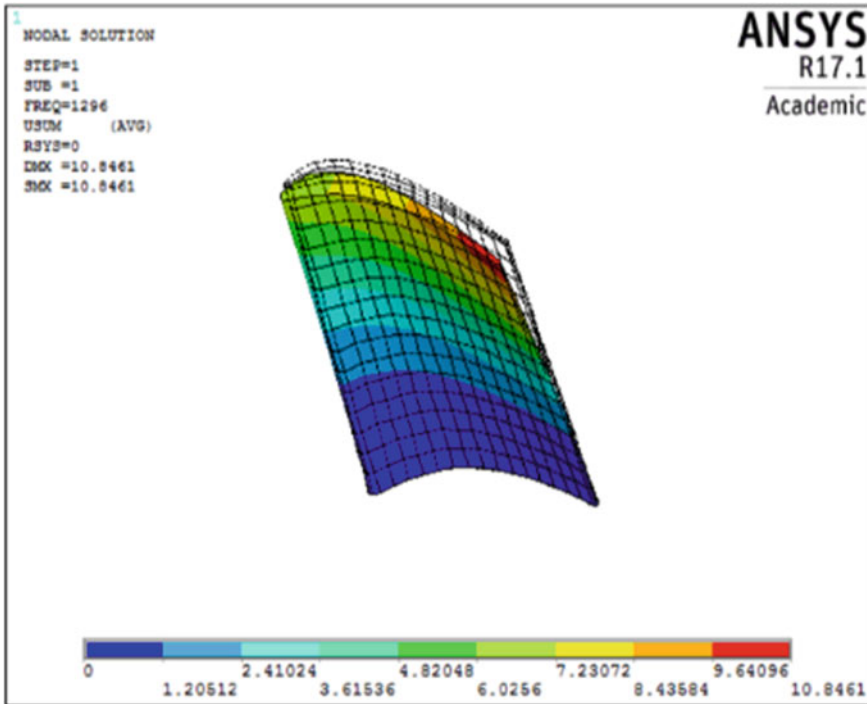


Fig. 2 Mode 2

Following are the key observations of Fig. 2:

1. The trailing edge tip of the blade undergoes maximum displacement.
2. The displacement of the trailing edge and the leading edge are in opposite orientations.
3. Displacement is approximately linear to the distance of a node from the blade hub in the radial direction but at the same time, the displacement vector has opposite directions nodes on either side of the central radial line of the blade.

The deformed shape can be compared approximately to the rotational deformation of beam geometry under the effect of pure torque applied to its tip. Hence, the second mode is appropriately designated as the first torsional mode for the blade (Fig. 3).

Following are the key observations of Fig. 4:

1. The leading edge tip of the blade undergoes maximum displacement.
2. The deformation is seen as bending along the edges of the blade.
3. Displacement is approximately linear to the distance of a node from the blade hub in the radial direction.

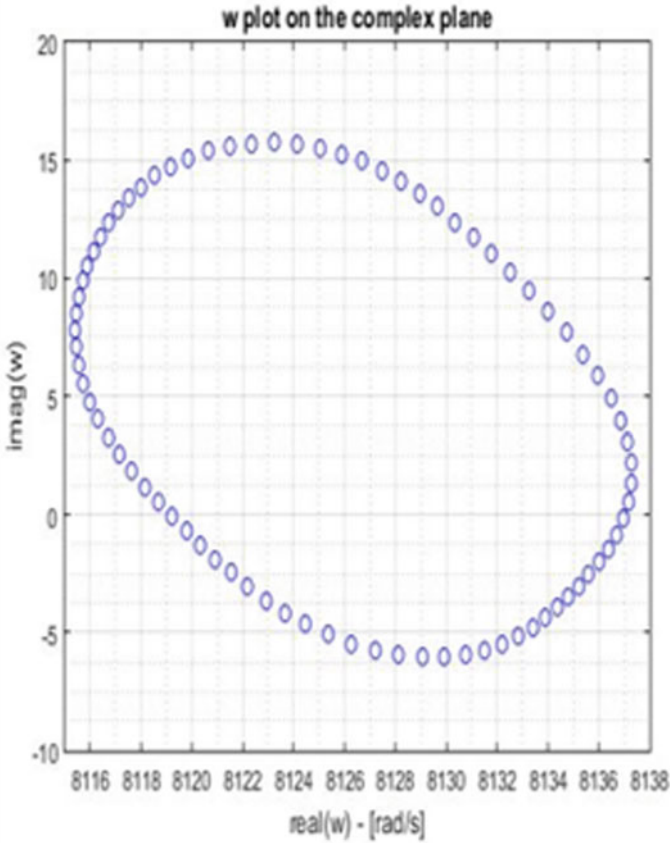


Fig. 3 W plot on the complex plane

- 4. In this mode in addition to bending of the chords, the blade edges also displace from their original position and dominate the shape of this mode.

2 Methodology

2.1 Part-2 (For Flutter Analysis)

To start the process, we begin with the general equation of motion system defined as:

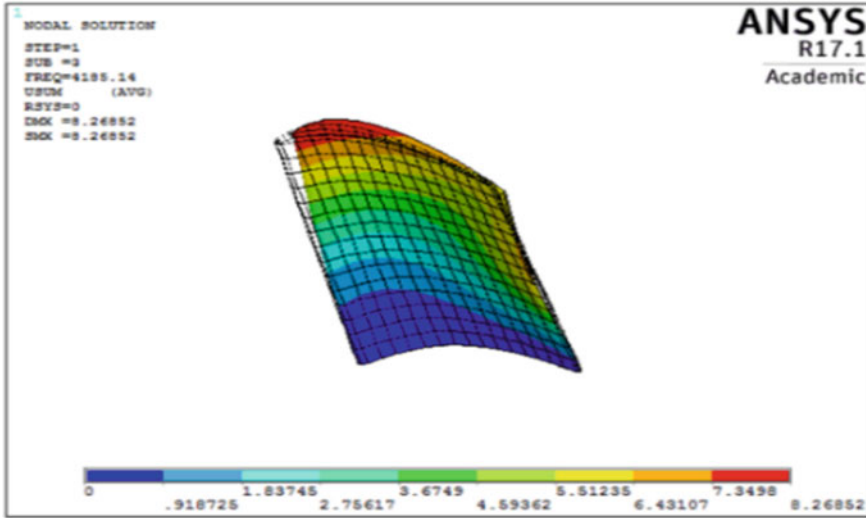


Fig. 4 Mode 3

$$M\ddot{x} + C\dot{x} + Kx = F_{st} + F_{aero} \tag{1}$$

Here,

- M Mass matrix
- C Damping coefficient matrix
- K Stiffness matrix
- F_{st} Structural forces on the system
- F_{aero} Aero dynamic forces on the system
- x Time-domain response of the system

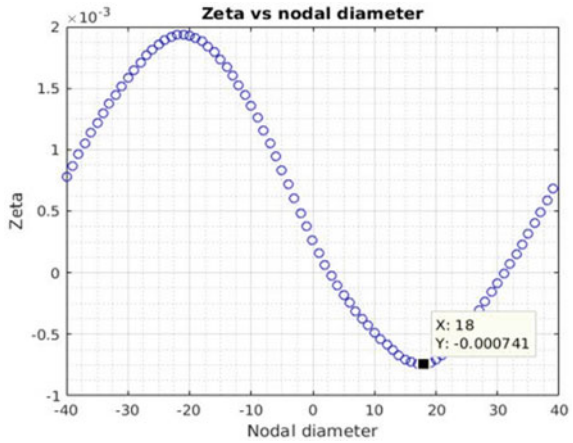
For performing flutter analysis, the F_{st} is assumed to be zero and a force response analysis is being done concerning the aerodynamic force only. To obtain decoupled equations for the system, use the property of orthogonality of mode shapes and the fact that mode shapes are the natural coordinates for a system. To exploit this property, choose to transform out a solution to the natural coordinates. Thus can assume the solution x to have the following form

$$x = Z_i V_i \tag{2}$$

Here,

- Z_i Modal coordinates
- V_i Modal vectors

Fig. 5 Zeta vs nodal diameter



Introducing this solution in our equation and pre-multiplying the resulting equation with the transpose of the modal vector, we can write

$$[\omega_1^2 V^T M V - \omega V^T C V + V^T K V] Z_i = V^T F_{aero} \tag{3}$$

Here, $[V^T F_{aero}]$ is now an abstract force vector of the original force vector. Additionally, this can club the damping and the inertial forces by introducing the concept of complex response frequency. To include the phase difference between these two forces, one can introduce the concept of complex numbers. Observing the fact that the imaginary and real part of a complex number has a phase difference of 90 degree, which is also the phase difference between inertial force and stiffness force in the system, and dividing throughout by modal mass, one can write the system equation in the formula of complex frequency as:

$$[-\omega^2 + \omega_0^2] I z = V^T F \tag{4}$$

Here,

$$\omega = \omega_n(1 + \zeta) \tag{5}$$

Next, move the attention to the right-hand side of Eq. (4). This nodal force is transformed using the most important assumption of flutter analysis. The aerodynamic force is assumed to be linearly proportional to the respective blade displacements. This property has been tested by many researchers and found to be true. Using this assumption of linearity, one can write

$$F_{aero} = b \times Z_i \tag{6}$$

Here, b is the constant of proportionality

Using this, we transform our nodal force in the following form:

$$V^T F = CZ \quad (7)$$

Here, C is the aerodynamic influence matrix which is diagonally symmetrical for systems exhibiting linear behavior as in the present case.

Therefore

$$[(\omega_0^2 I - C) - \omega^2 I]z = 0 \quad (8)$$

$$[E - \lambda I]x = 0 \quad (9)$$

$\omega = \sqrt{(\lambda)}$ is the aeroelastic eigenvalue which is to be obtained as the solution of the above eigenvalue problem.

$$\omega = \omega_n(1 + i)\zeta \quad (10)$$

For flutter analysis, if $\zeta < 0$, the system is unstable and the aerodynamic structure experiences onset of flutter. For the present analysis, we compute using only the aerodynamic force and hence the value of ζ obtained in the value of aerodynamic damping coefficient. However, the other part of damping is offered by the structural damping. However, if the structural damping is large enough to overcome the effect of aerodynamic damping, it is possible to have a flutter free system.

3 Calculations

The above-decoupled frequency domain eigenvalue problem forms the basis of our flutter analysis. To proceed, it becomes instrumental to determine the stiffness coefficient matrix. The influence coefficients for various blade pairs can be obtained by using the linearity assumption of the forces through displacement. For obtaining the modal forces, the AETR was used and a blade was vibrated at an amplitude of 0.5 mm. Henceforth, we can obtain the influence coefficients as follows:

$$V^T F_{\text{aero}} = Cz \quad (11)$$

$$C = V^T F_{\text{aero}}/z \quad (12)$$

i.e., Influence coefficient = Modal force/modal displacement

The modal displacement is calculated using the normalized modal vector obtained from our modal analysis in ANSYS and using a multiplication factor such

that the maximum modal vector is equal to 0.5 mm. Designed for the first mode, the modal vector has a maximum displacement of 10.8461. The corresponding scalar multiplier is found to be

$$a = 0.5 \times 10e^{(-3)}/10.8461 \tag{13}$$

$$a = 4.60995 \times 10e^{(-5)} \tag{14}$$

Hence,

$$C_0 = (12.835273 - i3.521036) / 5 = 278425.308970600 - 76379.0171192000i$$

All other coefficients are calculated similarly. These are the stiffness influence coefficients in the condition that the blade 0 is vibrating and the effect is observed at adjacent blades. However, for our analysis, we are required to find out the effect on blade 0 due to the motion of other blades. It will be equivalent to the condition in which we vibrate blade 0 and look at its effect on blade 1, similarly. Following this logic, a stiffness influence matrix was constructed as follows:

$$\begin{matrix}
 C_0 & C-1 & C-2 & C-3 & C-4 & C-5 & 0 & 0 & - & - & - & 0 & 0 & C_5 & C_4 & C_3 & C_2 & C_1 \\
 C_1 & C_0 & C-1 & C-2 & C-3 & C-4 & C-5 & 0 & 0 & - & - & - & 0 & 0 & C_5 & C_4 & C_3 & C_2 \\
 \vdots & & & & & & & & & & & & & & & & & \\
 C-1 & C-2 & C-3 & C-4 & C-5 & 0 & 0 & - & - & 0 & 0 & C_5 & C_4 & C_3 & C_2 & C_1 & C_0
 \end{matrix}$$

Using the above matrix, we solve the eigenvalue problem for three different cases, altering the number of adjacent blades, the aerodynamic pressure created by which is assumed to be affecting blade 0. The variation in the results of these cases arises from the difference in the aerodynamic influence coefficient matrix. For the first take 0 affecting blades only, i.e., C0 is considered and all the other elements of the matrix are equated to zero, i.e., C1 = C2 = C3 = C4 = C5 = C-1 = C-2 = C-3 = C-4 = C-5 = 0.

For considering the effect of three blades, we take into account the effects of C0, C1, and C-1. Correspondingly: C2 = C3 = C4 = C5 = C-2 = C-3 = C-4 = C-5 = 0.

And for considering the effect of five blades we use the matrix with succeeding modification: C3 = C4 = C5 = C-3 = C-4 = C-5 = 0.

4 Results

4.1 Case 1—Effect of 11 Blades

For flutter analysis, we are interested in the values of (ω) obtained from the eigenvalue problem. For case 1, it is assumed that 10 adjacent blades, i.e., -5 to -1

and 1 to 5 and the blade 0 itself have aerodynamic pressures that affect blade 0 in time. This problem is treated as an eigenvalue problem whose K matrix is given by the matrix developed in the previous section. The solution for the eigenvalue problem generates eigenvalues which are the values for ω^2 and eigenvectors, which define mode shapes for the bladed rotor. The eigenvalues can be used to calculate the natural frequencies of various modes as follows

$$\omega = \sqrt{(\lambda)} \tag{15}$$

ω being a complex entity can be plotted on the real-imaginary plane. Figure 3 shows a graph of ω for the case. To predict the stability of the system, we are required to compute the values of aerodynamic damping coefficient ζ . The aerodynamic damping ζ can be calculated using the following relation as in Eq. 10.

$$\omega = \omega (1 + i\zeta) \tag{16}$$

$$Z = \text{Imaginary}(\omega) / \text{Real}(\omega) \tag{17}$$

The next step is to calculate the nodal diameters for corresponding values of ζ . This is done by recognizing that the IBPA is related to nodal diameters as follows:

$$\text{BPA} = 2 \times \pi \times (\text{nodal diameter} / \text{no. of blades}) \tag{18}$$

The inter blade phase angle can be calculated using its basic definition as IBPA is the phase difference between the motion of adjacent blades. For a particular mode of vibration, this IBPS is a constant value owing to the symmetry of the system.

$$\text{IBPA} = \text{Phase blade (i)} - \text{Phase blade (i - 1)} \tag{19}$$

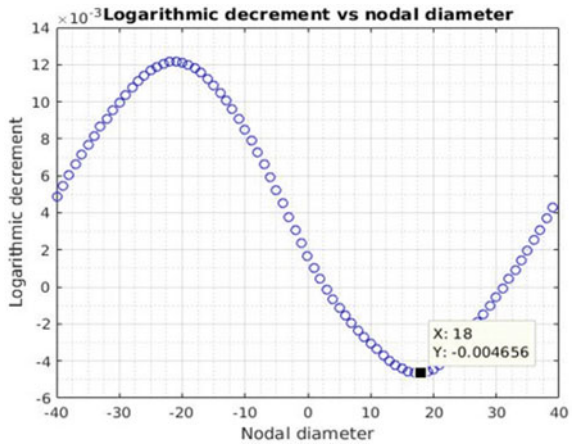
Using the above two formulations, we can calculate nodal diameters corresponding to eigenvalues and corresponding ζ values. A plot of ζ versus nodal diameters can then be obtained and has the following shape in Fig. 5. As can be seen from the “ ζ —nodal diameter” plot, the maximum negative value of ζ is found for a nodal diameter of +18 and this is the least stable mode for our rotor (Fig. 6).

The positive value of nodal diameter indicates that the wave is traveling in the same direction that of rotor rotation. To further obtain a quantitative estimate of the instability of the system, we as resort calculating the logarithmic decrement for various modes, which can be found using the corresponding values of ζ as per the following formulation.

$$\text{Logarithmic decrement} = 2 \times \pi \times \zeta / \text{sqrt}(1 - \zeta^2) \tag{20}$$

As can be seen from the chart, the logarithmic decrement for nodal diameters from 3 to 31 has a negative value. This indicates that the consecutive peaks of an amplitude-time plot for these cases increase in magnitude as we move from peaks

Fig. 6 Logarithmic decrement vs nodal diameter



on the left-hand side to those on the right-hand side on the time axis. From this, we can infer that for these nodal diameters the vibration amplitude increases with time. This directly indicates an unstable system that is gaining energy with time and the highest rate of increase can be found for the previously deduced least stable mode, i.e., nodal diameter 18. This value turns out to be -0.004656 .

4.2 Case 2—Effect of 1 Blade

As can be deduced from case 2 in Fig. 7 in which the adjacent blade effect is neglected as the imaginary part of ω is positive, it cannot have a flutter. Hence, it can be inferred that flutter occurs only due to the effect of aerodynamic pressures created by adjacent blades.

Fig. 7 Zeta vs nodal diameter

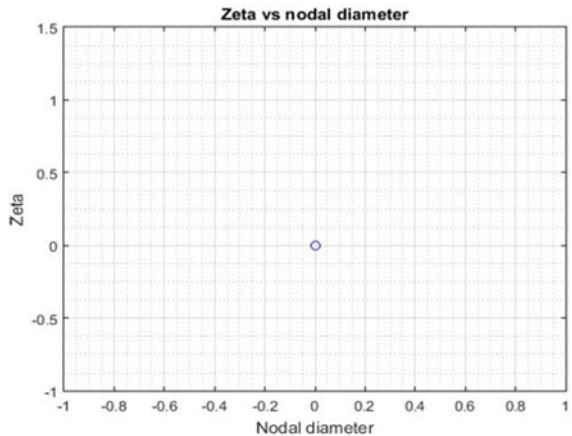
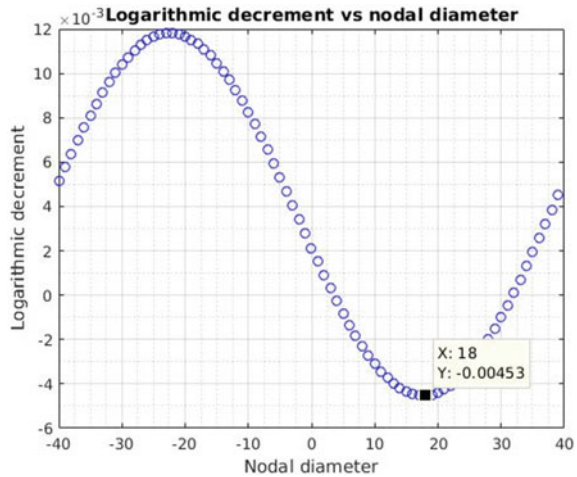


Fig. 8 Logarithmic decrement vs nodal diameter



4.3 Case 3—Effect of Three Blades

As can be seen from the chart in Fig. 8, the logarithmic decrement for nodal diameters from 3 to 31 has a negative value similarly as in case 1. From this, we can infer that for these nodal diameters the vibration amplitude increases with time. This directly indicates an unstable system that is gaining energy with time and the highest rate of increase can be found for the previously deduced least stable mode, i.e., nodal diameter 18. This value turns out to be -0.00453 .

5 Conclusion

The strongest effect for blade flutter is experienced due to the immediately adjacent blades, i.e., blade 1. One such change can be seen as a shift in the least stable mode from 18ND in the case of 11 blades and 3 blades to that of 16ND in the case of 5 blades. However, the expected quantitative value of the change is quite small. The blades further away from blade 0 have a smaller effect and hence subsequent addition of influence coefficients although change the system stability, but by a very small factor. Additionally, we can infer from the near similar shape of ζ -nodal diameter curve and logarithmic decrement versus nodal diameter curve that numerical value of aerodynamic damping is very low, which leads to the following approximation to hold good logarithmic decrement equal to $2 \times \pi \times \zeta$. However, even small values of negative damping are sufficient to induce instability in the system, as this damping accrue over time and adds enough energy to the system to create a flutter.

References

1. Kielb, R., Barter, J., Chernysheva, O., & Fransson, T. (2006). Flutter design of lowpressure turbine blades with cyclic symmetric modes. *unsteady aerodynamics, aeroacoustics and aeroelasticity of turbomachines*, 41–52
2. Conner MD, Tang DM, Dowell EH, Virgin LN (1997) Nonlinear behaviour of a typical air foil section with control surface freeplay: a numerical and experimental study. *J Fluids Struct* 11(1):89–109
3. Panovsky J, Kielb RE (1998). A design method to prevent low pressure turbine blade flutter. In: *Proceedings of the manufacturing materials and metallurgy; ceramics; structures and dynamics; controls, diagnostics and instrumentation; education*, vol 5
4. Lee BHK, Liu L, Chung KW (2005) Airfoil motion in subsonic flow with strong cubic nonlinear restoring forces. *J Sound Vib* 281(3–5):699–717
5. Chung KW, Chan CL, Lee BHK (2007) Bifurcation analysis of a two-degree-of-freedom aeroelastic system with freeplay structural nonlinearity by a perturbation-incremental method. *J Sound Vib* 299(3):520–539
6. Shams S, Sadr Lahidjani MH, Haddadpour H (2008) Nonlinear aeroelastic response of slender wings based on Wagner function. *Thin-Walled Struct* 46(11):1192–1203
7. Vedenev V, Kolotnikov M, Makarov P (2013) Numerical analysis of compressor blade flutter in modern gas turbine engines, etc. 10. In: *Proceedings of 10th European Conference on Turbomachinery Fluid Dynamics and Thermodynamics*, Lappeenranta, Finland
8. Corral R, Beloki J, Calza P, Elliott R (2018) Flutter generation and control using mistuning in a turbine rotating rig. *AIAA J* 1–14
9. Frey C, Ashcroft G, Kersken H-P, Schluß D (2019) Flutter analysis of a transonic steam turbine blade with frequency and time-domain solvers. *Int J Turbomac Propul and Power* 4 (2):15
10. Corral R, Greco M, Vega A (2019) Tip-shroud labyrinth seal effect on the flutter stability of turbine rotor blades. *ASME J Turbomach* 141(10): 101006. Oct

Biomass Thermochemical Processing in Fixed Bed Downdraft Gasifier: A Review



Praveen Kumar

Abstract The co-current gasification technology has increased interest among investigator worldwide because of their ability to generate small-scale mechanical and electrical energies from biomass waste affordably. In this paper, characterisation of biomass suitable for gasifier and development of gasifier like in downdraft gasification systems, including the influence of various parameters such as turn-down ratio, moisture content, superficial velocity, gasification media, etc. on gasifier efficiency are reviewed.

Keywords Biomass · Producer gas · Virgin biomass · Downdraft gasifier

1 Introduction

Biomasses are seen as an alternative fuel and environment-friendly fuel. Gasification of biomass generated oil and gas may be used as petroleum or natural gas substitutes. Biomass has different behaviour due to its composition such as carbon, hydrogen, oxygen, nitrogen and sulphur. Biomass consumption is an essential energy source in the world, in particular in remote areas where fossil fuels are not available. Biomass gasification is a thermochemical conversion process in which raw biomass or agriculture residue converts into syngas or producer gas. The gasifier has five-zone as follow: (1) preheating zone, (2) drying zone, (3) pyrolysis zone, (4) oxidation zone and (5) reduction zone. During the gasification process, the biomass is partially oxidised in the gasification medium at a temperature of between 800 and 900 °C. The gas produced is more convenient and flexible to use than the original biomass, and it is sustainable and reliable. The gas produced from gasifier may be used for gas engines, gas turbines, and chemical feedstock for producing liquid fuels. The gasification method is a transformation of biomass into a mixture of combustible gas. Combustion is an oxidation process, which is completed

P. Kumar (✉)
Indian Institute of Technology, Delhi, India
e-mail: praveen.dimenssion@gmail.com

significantly in one step. In contrast, in two steps, gasification transforms the intrinsic chemical energy of the carbon in biomass into syn or producer gas. Two fundamental steps are which differentiates primary combustion from the gasification process. Two basic steps of combustion

Stage 1 Partial oxidation, $C + \frac{1}{2}O_2 \leftrightarrow CO$ $dH = -268$ MJ/kg mole

Complete oxidation, $C + O_2 \leftrightarrow CO_2$ $dH = -406$ MJ/kg mole

The heat of reaction: Positive (endothermic reaction), Negative (exothermic reaction)

Water-gas reaction, $C + H_2O \leftrightarrow CO + H_2$ $dH = +118$ MJ/kg mole

Maximum energy/Greatest (E) released is derived from the complete combustion of carbon

Stage 2 Water-gas shift reaction, $CO + H_2O \leftrightarrow CO_2 + H_2$ $dH = -42$ MJ/kg mole

Methane formation $CO + 3H_2 \leftrightarrow CH_4 + H_2O$ $dH = -88$ MJ/kg mole

\leftrightarrow Sign reaction means in equilibrium can proceed in either direction depending on temperature, pressure, and concentration of reacting species. The consequence of this reaction is gaseous product gas, a combination of $CO + CO_2 + CH_4 + H_2 + H_2O$ (steam). Some developments in the gasifier, such as hopper system, grate design, and air feeding system improve the performance of gasifier stated by numerous investigators [1–7]. The current paper is literature survey on design, modification, and performance parameter (turndown ratio, moisture content, superficial velocity, gasification media, etc.) of the Imbert downdraft gasifier using low-density and high-density fuels.

2 Characterisation of Biomass

Biomass is categorised into two types: one is virgin biomass (obtained from plant and animals) and other waste or derived biomass comes from different products extracted from biomass [8]. Virgin and waste biomass have appeared in Table 1. In any biomass, carbon (C), hydrogen (H), nitrogen (N), and oxygen (O) are a vital constituent. The ultimate analysis can classify the fraction of the elements. The ultimate and proximate analyses of different feedstocks of biomass mentioned are listed in Table 2.

Table 1 Different types of biomass

Type of biomass	Biomass	Example
Virgin	Terrestrial biomass	Forest biomass, grasses, cultivated crops
	Aquatic biomass	Algae, water plant
	Municipal waste	Municipal solid waste, sewage, landfill gas
Waste	Agricultural waste	Livestock and manures, agricultural residue
	Forestry residues	Bark, leaves, floor residues
	Industrial wastes	Black liquor, demolition wood, waste oil or fat

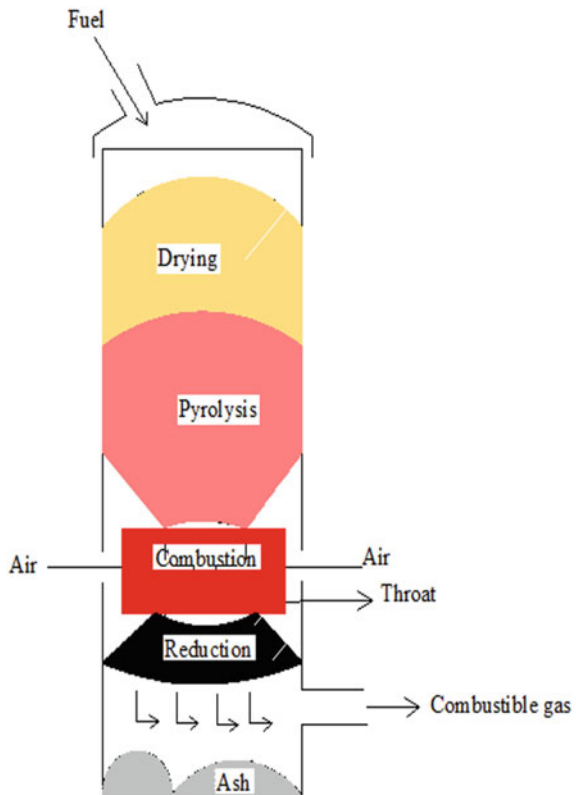
Table 2 Ultimate and proximate analysis of different biomass (in weight %)

Biomass	C	H	N	O	Moisture	Volatile matter	Ash	Fixed carbon
Bagasse	18.3	41.3	22.6	17.8	10	84.2	2.9	15.8
Corn cob	16.6	40.3	28.6	14.5	10.2	80.1	6.8	19.8
Groundnut shell	30.2	35.7	18.7	15.4	11.12	5.13	2.89	20.86
Saccharum benalense	41.2	4.2	0.9	53.7	8.46	74.18	1.1	11.3

3 Process and Design in Downdraft Gasifiers

For downdraft gasifiers, there are primarily two designs first one is Imbert or Throated gasifier in which top is closed in the gasifier and second is named stratified or Throatless which was open the centre of the gasifier. The process of downdraft gasifier is shown in Fig. 1.

Fig. 1 Imbert downdraft gasifier



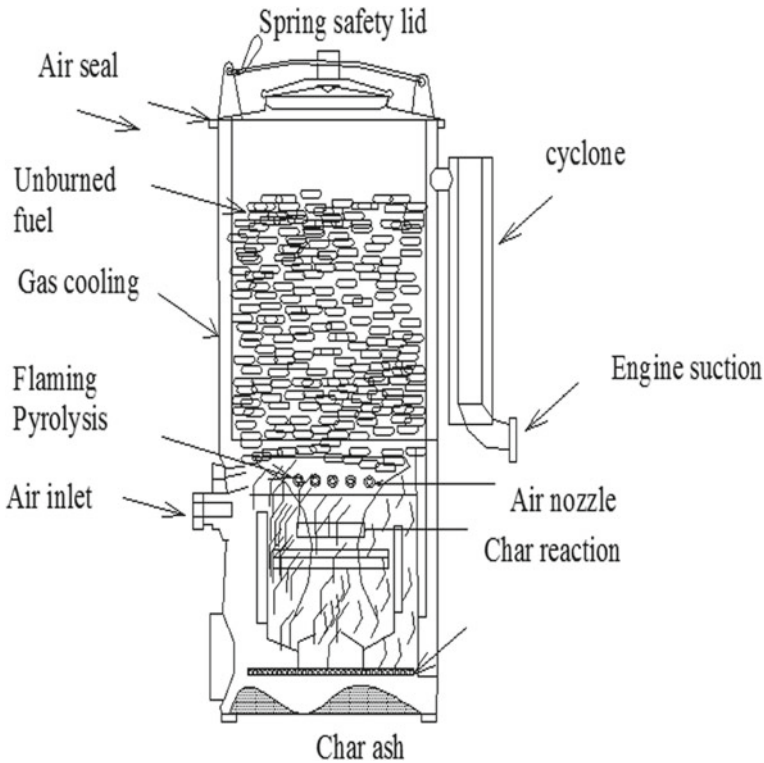


Fig. 2 Imbert downdraft gasifier design

3.1 Imbert Downdraft Gasifiers

These gasifiers are suitable for handling ash and moisture content of biomass fuel which is less than 5 and 20%, respectively [9, 10]. The Imbert gasifier is shown in Fig. 2. This gasifier provides continuous streaming of gases and solids through a downward stacked bed that assisted over a constriction or throat. In the Imbert process, the downstream gasifier forms the maximum gas mixing at high temperatures, allows tar cracking below the gasifier's throat position, burning tar along with biomass produces CO and H₂ and decreases resin production.

This kind of gasifier is best suited for woody biomass of similar shape and size or standardisation because it flows very nicely in the restricted core. The gas produces Imbert gasifier with a lower tar and gas temperature about 700 °C. Imbert downdraft gasifiers' drawbacks are particle size restriction and a power of up to 500 kW.

3.2 *Design Improvements in Imbert Downdraft Gasifiers*

The maximum hearth load for an Imbert downdraft gasifier is $0.9 \text{ m}^3/\text{cm}^2\text{h}$ which has been calculated by experimental studies. Such adjustment was made for low and medium density biomass such as forest waste, energy crops, agriculture residues, waste and residues of various industry, residues of livestock, solid municipal waste, and landfill waste [11–15]. The biomass was lower in density and higher in ash relative to coal that was densified into briquettes. In the gasifier, two conical hoppers provided space to spread the fuel briquettes when heating up to prevent the problem of bridging in the pyrolysis region. For the continuous movement or flow of biomass, a hopper is installed at the top level of Imbert gasifier [16]. These change in gasification for prevention of the bridging and channelling of loose biomass waste in the gasification process. Other investigator stated that in the gasifier the air is supplied in the first stage via a vertical pipe and in the secondary and tertiary air fed in the gasifier with nine air nozzles around the gasifier [1, 17–20]. The biomass filled in the hopper may also be distributed through conveyors, which helps to maintain a constant flow in the co-current reactor [21], so that man loading time can be minimised [22, 23]. For the above purposes, a pneumatic conveyor type [22, 24] and a conveyor belt [2, 25] may be used. Based on the size of the biomass, the feed system is chosen [3, 4] for the gasifier. The installing rotating grate inside it broke the agglomeration of slag in the gasifier. A rotating grate breaks the slag flakes before their agglomeration inside the gasifier. Also, the gap between the choke plate and the grate was raised to raise the thickness of the reduction zone to improve the distribution of the slag in the char bed. Recent technological developments in gasifier several forms of the grate are shaking [3, 5, 24], vibrating [6], revolving [7], and reciprocal grates [26]. Such technologies are designed to prevent bridging and channelling of loose biomass in gasification operation. A cyclone in the gasification used for extraction of coarse dust and for removal of fine material the glass fibre-fabric was used. The life and costs of downdraft gasifiers made from ceramic material are higher austenitic steel made gasifier under 500 kW. Due to high-temperature oxidation and corrosion, the steel gasifier failed in the throat and air nozzle area in 1500 h of operation while the ceramic material (made of aluminium (50–70%), kaolin (16–20%), feldspar (10–15%) and talc (3–7%)) mixture filled gasifier may resist thermal shock for a long time of period.

3.3 *Turndown Ratio*

For sizing, the gasifier turndown ratio is the critical parameter, i.e. the ratio of the highest effective gas generation rate to the lowest possible rate. In World War II, the turndown ratio of gasifier range is three for Imbert type gasifiers with uninsulated V-hearth, and highly insulated V-hearth gasifiers are 18. For automobile operation,

turndown ratio should be at least 8:1. A low specific hearth load generates more tar formation problem. High turndown ratio is not essential for irrigation pump and power generation. On using high volatile biomass, Imbert gasifier produces low tar syngas.

3.4 Gasification Variable

Gasifier efficiency is measured by the following variables, such as equivalence ratio (ER) [7, 27], cold gas output (CGE) [23] and the carbon conversion rate (CCR) [28].

$$ER = \frac{(\text{Airflow rate/Biomass consumption rate})_{\text{Actual}}}{(\text{Airflow rate/Biomass consumption rate})_{\text{stoichiometric}}} \quad (1)$$

$$GPR = \frac{\text{Gas Volume per Hour}}{\text{The weight of Biomass consumption per hour}} \quad (2)$$

$$CGE = \frac{(\text{Calorific value}) \times (\text{Gas Production Rate})}{(\text{Lower Heating Value of the biomass})} \quad (3)$$

$$CCR = \frac{12(\text{CO}\% + \text{CO}_2\% + \text{CH}_4\%)}{22.4 \times (298/273) \times C\%} \times GPR \quad (4)$$

3.5 Moisture Content

Moisture content is the key characteristics of biomass for the estimation of the thermal energy importance of biomass. The moisture found in the biomass in two ways is the first natural, or free moisture, i.e. beyond the membrane of the cells. Within the cell wall, the second moisture content is known as equilibrium or endogenous moisture content. When the membrane is saturated, the biomass is said to have good moisture content. It depends on relative humidity and air temperature. Higher moisture content may be used in updraft gasifiers, but a dry-based upper limit of 45% is sufficient for downdraft reactors.

3.6 Superficial Velocity

The average of the output rate of syngas at standard circumstances and the narrowest cross-sectional gasifier area are defined as superficial velocity. Superficial velocity does not depend on the measurements of the reactors allowing the gasifier

to be compared explicitly with specific output capacity. Yamazaki et al. [29] analyse an effective gasifier process when the quantity of tar in the syngas is small, and the result for 0.4 Nm/s superficial velocity was a more excellent performance. The syngas composition fulfilled the process of an engine within the range of 0.4–0.6 m/s superficial velocity, yield less tar [30].

3.7 Operating Temperature for Tar Removal

Researchers undertook an extensive investigation into the influence of temperature on tar production in the process of biomass gasification [31]. Although this has demonstrated the benefit of higher temperatures for biomass gasification [32–35], Mahishi and Goswami investigate that H₂ increased gradually as an increase of temperature at a certain point after the highest temperature achieving than it decreased slowly in the chemical equilibrium [36]. The quantity of tar production during gasification is not affected by temperature but constituent present in the tar influence by chemical reaction [37].

3.8 Gasifying Agents

Several researchers have stated that thermochemical gasification occurs under various conditions, such as air, steam, O₂ and CO₂. The gasifier media is a significant factor for evaluating the calorific value of gas produced in the gasifier, when the air used as gasification media low heating value producer gas obtained due to the solubility of the nitrogen compound in the air [38, 39]. If one uses a mixture of oxygen and steam or only steam, a producer gas with medium calorific value is obtained [40]. Higher hydrogen obtained when steam and air used in gasifier in comparison with air alone. It helps to reduce the energy needed for the process usually given by burning of a segment of biomass.

4 Future Improvement

The downstream gasifier is usually designed for a particular feedstock. It makes the gasifier only suitable for the designed feedstock of biomass. The same gasifier may be operated pellet based feedstock, but dissimilarities in operating parameter such as air-fuel ratio, the temperature of producer gas, quality of gas occur. Using pelletized feedstock requires the pelletizing fuel process, which requires more additional cost.

5 Conclusions

The downstream gasifier is effective for thermal and electrical applications due to simple adjustment and fabrication. The quality of the producer gas and the performance of the gasification process are affected by some important parameters (turndown ratio, moisture content, superficial velocity, residence time, gasification media, etc.) in the downstream gasifiers. The proper modification and operation increase the performance of downdraft gasifier.

References

1. Guo F, Dong Y, Dong L, Guo C (2014) Effect of design and operating parameters on the gasification process of biomass in a downdraft fixed bed: an experimental study. *Int J Hydrogen Energy* 39(11):5625–5633
2. Erol M, Haykiri-Acma H, Küçükbayrak S (2010) Calorific value estimation of biomass from their proximate analyses data. *Renewable Energy* 35(1):170–173
3. Sharma S, Sheth PN (2016) Air–steam biomass gasification: experiments, modeling and simulation. *Energy Convers Manag* 110:307–318
4. Prasad L, Subbarao PMV, Subrahmanyam JP (2014) Pyrolysis and gasification characteristics of Pongamia residue (de-oiled cake) using thermogravimetry and downdraft gasifier. *Appl Therm Eng* 63(1):379–386
5. Sharma AK (2009) Experimental study on 75 kWth downdrafts (biomass) gasifier system. *Renewable Energy* 34(7):1726–1733
6. Galindo AL, Lora ES, Andrade RV, Giraldo SY, Jaén RL, Cobas VM (2014) Biomass gasification in a downdraft gasifier with a two-stage air supply: effect of operating conditions on gas quality. *Biomass Bioenergy* 61:236–244
7. Gai C, Dong Y (2012) Experimental study on non-woody biomass gasification in a downdraft gasifier. *Int J Hydrogen Energy* 37(6):4935–4944
8. De Lasa H, Saldaña E, Mazumder J, Lucky R (2011) Catalytic steam gasification of bio-mass: catalysts, thermodynamics and kinetics. *Chem Rev* 111(9):5404–5433
9. Basu P (2010) Biomass gasification and pyrolysis: practical design and theory. Academic Press
10. Pathak BS, Patel SR, Bhave AG, Bhoi PR, Sharma AM, Shah NP (2008) Performance evaluation of an agricultural residue-based modular throat-type down-draft gasifier for thermal application. *Biomass Bioenergy* 32(1):72–77
11. Ladanai S, Vinterbäck J (2009) Global potential of sustainable biomass for energy report 013. SLU, Institutionen för energi och teknik, Swedish University of Agricultural Sciences, Uppsala
12. Kontor S (2013) Potential of biomass gasification and combustion technology for small-and medium-scale applications in Ghana
13. Balat M, Ayar G (2005) Biomass energy in the world, use of biomass and potential trends. *Energy Sources* 27(10):931–940
14. Simbolotti G (2007) Biomass for power generation and CHP. IEA energy Technology Essentials
15. Chowdhury N (2014) Advances in trends in woody biomass gasification. *Energy engineering and management, Tecnico Lisboa*
16. Fan S, Xu LH, Kang TJ, Kim HT (2017) Application of eggshell as catalyst for low rank coal gasification: experimental and kinetic studies. *J Energy Inst* 90(5):696–703

17. Striūgas N, Zakarauskas K, Džiugys A, Navakas R, Paulauskas R (2014) An evaluation of performance of automatically operated multi-fuel downdraft gasifier for energy production. *Appl Therm Eng* 73(1):1151–1159
18. Mahapatra S, Dasappa S (2014) Influence of surface area to volume ratio of fuel particles on gasification process in a fixed bed. *Energy Sustain Dev* 19:122–129
19. Bhattacharya SC, Pham HL (2001) A study on a multi-stage hybrid gasifier-engine system. *Biomass Bioenerg* 21(6):445–460
20. Kallis KX, Susini GAP, Oakey JE (2013) A comparison between Miscanthus and bioethanol waste pellets and their performance in a downdraft gasifier. *Appl Energy* 101:333–340
21. Simone M, Barontini F, Nicoletta C, Tognotti L (2012) Gasification of pelletized biomass in a pilot scale downdraft gasifier. *Biores Technol* 116:403–412
22. Asadullah M (2014) Barriers of commercial power generation using biomass gasification gas: a review. *Renew Sustain Energy Rev* 29:201–215
23. Sheth PN, Babu BV (2009) Experimental studies on producer gas generation from wood waste in a downdraft biomass gasifier. *Biores Technol* 100(12):3127–3133
24. Jia J, Xu L, Abudula A, Sun B (2018) Effects of operating parameters on performance of a downdraft gasifier in steady and transient state. *Energy Convers Manag* 155:138–146
25. Lv P, Yuan Z, Ma L, Wu C, Chen Y, Zhu J (2007) Hydrogen-rich gas production from biomass air and oxygen/steam gasification in a downdraft gasifier. *Renewable Energy* 32(13):2173–2185
26. Ma Z, Zhang Y, Zhang Q, Qu Y, Zhou J, Qin H (2012) Design and experimental investigation of a 190 kWe biomass fixed bed gasification and polygeneration pilot plant using a double air stage downdraft approach. *Energy* 46(1):140–147
27. Martínez JD, Mahkamov K, Andrade RV, Lora EES (2012) Syngas production in downdraft biomass gasifiers and its application using internal combustion engines. *Renewable Energy* 38(1):1–9
28. Karmakar MK, Mandal J, Haldar S, Chatterjee PK (2013) Investigation of fuel gas generation in a pilot scale fluidised bed autothermal gasifier using rice husk. *Fuel* 111:584–591
29. Yamazaki T, Kozu H, Yamagata S, Muraio N, Ohta S, Shiya S, Ohba T (2005) Effect of superficial velocity on tar from downdraft gasification of biomass. *Energy Fuels* 19(3):1186–1191
30. Tinaut FV, Melgar A, Perez JF, Horrillo A (2008) Effect of biomass particle size and air superficial velocity on the gasification process in a downdraft fixed bed gasifier: an experimental and modelling study. *Fuel Process Technol* 89(11):1076–1089
31. Skoulou V, Swiderski A, Yang W, Zabaniotou A (2009) Process characteristics and products of olive kernel high temperature steam gasification (HTSG). *Biores Technol* 100(8):2444–2451
32. Hanping C, Bin L, Haiping Y, Guolai Y, Shihong Z (2008) Experimental investigation of biomass gasification in a fluidised bed reactor. *Energy Fuels* 22(5):3493–3498
33. Luo S, Xiao B, Hu Z, Liu S, Guo X, He M (2009) Hydrogen-rich gas from catalytic steam gasification of biomass in a fixed bed reactor: influence of temperature and steam on gasification performance. *Int J Hydrogen Energy* 34(5):2191–2194
34. Gao N, Li A, Quan C (2009) A novel reforming method for hydrogen production from biomass steam gasification. *Biores Technol* 100(18):4271–4277
35. Salaiques E, Serrano B, de Lasa H (2010) Biomass catalytic steam gasification thermodynamics analysis and reaction experiments in a CREC riser simulator. *Ind Eng Chem Res* 49(15):6834–6844
36. Mahishi MR, Goswami DY (2007) Thermodynamic optimisation of biomass gasifier for hydrogen production. *Int J Hydrogen Energy* 32(16):3831–3840
37. Wolfesberger U, Aigner I, Hofbauer H (2009) Tar content and composition in producer gas of fluidised bed gasification of wood—influence of temperature and pressure. *Environ Prog Sustain Energy: Official Publ Am Inst Chem Eng* 28(3):372–379

38. Fagbemi L, Khezami L, Capart R (2001) Pyrolysis products from different biomasses: application to the thermal cracking of tar. *Appl Energy* 69(4):293–306
39. Mathieu P, Dubuisson R (2002) Performance analysis of a biomass gasifier. *Energy Convers Manag* 43(9–12):1291–1299
40. Zhang R, Brown RC, Suby A, Cummer K (2004) Catalytic destruction of tar in biomass-derived producer gas. *Energy Convers Manag* 45(7–8):995–1014

Utilization of Nanofluids as Coolant— A Review



Aashray Sharma, Preeti Joshi, and Jaspreet Hira

Abstract Fuel efficiency and performance of the vehicle are the main priorities of the customer. The engine capacities have gone up resulting in greater requirement of efficient cooling. Modifying radiator is one of the options, but it comes with increased weight and size, thus compromising the efficiency due to this unwanted addition. A better alternative is to use better coolants inside the radiator. One such possibility exists in the nanofluids. It is observed that even small volumetric concentration of nanoparticle enhances the heat transfer coefficient of base fluids to greater extent. Even a small addition of 0.4 vol% CuO nanoparticles enhances the thermal conductivity of water by 8%. The viscosity is also increased up to 90% based on volumetric concentration. The fluids with vol. conc. less than 13% behave as Newtonian fluids. Shape and size of nanoparticles also play an important role in determining the viscosity and thermal conductivity of nanofluid. Various models related to viscosity and thermal conductivity have been studied. A comparison of various models has been made, and their overall impact on nanofluid has been studied.

Keywords Nanofluid · Heat transfer coefficient · Viscosity · Thermal conductivity

1 Introduction

Heat dispersal system in an automobile is one of the most important components for maintenance of engine temperature for its optimal performance. This system in vehicles comprises radiator where excess heat is removed by pumping and circulating

A. Sharma · P. Joshi (✉) · J. Hira
Amity School of Engineering and Technology, Amity University, Noida, India
e-mail: pjoshi5@amity.edu

A. Sharma
e-mail: aashray119@gmail.com

J. Hira
e-mail: jhira@amity.edu

the coolant in cooling channels or around the various components in close contact. Water, mineral oils and ethylene glycol are being used as coolants, but owing to their poor thermal conductivity, the performance enhancement and compactness are restricted in the cooling systems. The scope of improving fins and micro-channels for increasing the cooling rates has already reached the limits. Further, with the rising demand of latest technology applied vehicles to be lightweight with compact radiator, the need to develop more effective coolants has emerged. Water cooling is very cheap and safe, but its main drawback is poor heat exchange property. Since the conductivity of metals as well as their oxides is more, fluids containing their suspensions were expected to possess high thermal conductivities and utilization of millimeter or micrometer scale particles started over hundred years ago [1–3]. In a quest for developing better coolants, nanofluids obtained by suspending smaller than 100 nm solid “nanoparticles” in “base fluids”, emerged as a new category of coolants due to their great performance. Choi and Eastman [4] were probably the first to develop this fluid termed as nanofluid as their theoretical results indicated better thermal conductivity by using suspension of copper nanoparticles in water.

Due to smaller size of the nanoparticles, there is a greater flexibility which leads to more heat transfer and dispersion of heat rapidly [5], thus increasing the thermal conductivity of the nanofluids as the temperature rises [6]. Owing to lower size, the odds of settling down of nanoparticles are fewer giving stability to the nanofluids [7, 8] and make them superlative for micro-channeled systems to lever greater heat loads with lesser chances of clogging. Further, the chances of erosion in components of cooling systems are very less due to the smaller-sized particles, and compact and lighter heat exchangers can be prepared and used for cost cutting [9]. Pumping power can be reduced substantially with the use of lower volume fraction of nanoparticles in nanofluids owing to their very high thermal conductivity [4] unless the fluid viscosity increases.

Nanoparticles of metals, ceramics, carbon nanotubes, etc., are used for making nanofluids by making their suspensions in base fluids like water, ethylene glycol and water–ethylene glycol combinations [10, 11]. Most common nanofluids are TiO_2 in H_2O , CuO in H_2O , Al_2O_3 in H_2O and ZnO in ethylene glycol. The pertinent literature on various aspects of nanofluids has been reviewed in the following sections.

Masuda et al. [12] observed that addition of 4.3% nano Al_2O_3 by volume in water elevated the thermal conductivity by 30%. Lee et al. [7] on the other hand observed no significant increase in the thermal conductivity on dispersing 4.3% Al_2O_3 nanoparticles by volume in water, probably due to larger-sized nanoparticles (33 nm) in comparison with 13 nm-sized particles used by Masuda et al. [12]. Better thermophysical properties of nanofluids have been demonstrated by many workers including Choi et al. [13]. Godson et al. [14] also detected that nanofluids upgraded the thermophysical properties viz. thermal conductivity and thickness contrast in comparison with water and ethylene glycol. Numerical reviews have been conducted on laminar warmth exchange utilizing CuO and Al_2O_3 -ethylene glycol and H_2O inside a level container of an auto radiator [15, 16] and water and water–ethylene glycol-blend in meso-channeled heat exchanger [17, 18].

2 Salient Findings

The first major publication in this area involved nanofluids with volume fractions of only 1–5% Al_2O_3 and CuO reporting very high conductivity enhancement [19] of the magnitude of 20% with 4.0% volumetric fraction of copper oxide nano powder in EG as base fluid. This enhancement was, however, just 12% with 3.5 vol% of CuO and 10% with 4 vol% Al_2O_3 when water was the base fluid [7]. Likewise, other studies suggested 30–60% increase in thermal conductivities under varying volume fractions of Al_2O_3 in deionised water and temperatures of base fluids [20]. Xie et al. [21] observed that if thermal conductivity of the base fluid increases the thermal conductivity ratios decrease. Sundar et al. [22] observed a higher conductivity of CuO nanofluid (15.6–24.56% enhancement) as compared to Al_2O_3 nanofluid (9.8–17.89% enhancement) and evolved new correlation for its estimation.

Metal nanoparticles-based nanofluids proved better as compared to oxide nanoparticles-based fluids [23]. Xuan and Li [8] used 5% volume conc. of copper nanoparticles of about 100 nm size in transformer oil for the first time to prepare metallic nanofluid and observed about 55% increase in heat conductivity, whereas rise of 40% in conductivity of heat was observed by using only 0.3 vol% of fine copper nanoparticles (10 nm) suspended in EG [23]. Patel et al. [24] were the first to report a substantial enhancement in thermal conductivity in gold and silver-based nanofluids in pure water and toluene as base at extremely small concentrations. Hong et al. [25] studied the effect on conductivity due to of particle size in nanofluid. Alloying of metals produces new material which possesses better results in comparison with their parent metals [26] and exhibits higher catalytic activity than their metallic counterparts [27, 28].

Viscosity Nanofluids having less than 13% volume fraction of particles behave as Newtonian fluids [29]. Mostly, viscosity increases as nanoparticles are mixed in base fluid. Masuda et al. [12] observed 60% enhancement in the base fluid viscosity with the addition of 5% volume fraction of nanoparticles, whereas Murshed et al. and Wang et al. [30, 31] reported an augmentation in viscosity up to 80%. Motta [32] noticed that larger-sized (20–30 nm) alumina nanoparticles had comparatively less effect on enhancing the viscosity (55%) than smaller (15 nm) alumina nanoparticles (up to 90%) at same volumetric concentration of 1%. Some models for evaluating viscosity of nanofluids are summarized in Table 1.

Temperature of nanofluids also has effect on the dynamic viscosity as Mena et al. [29] and Nguyen et al. [35] reported upsurges in viscosity for lower temperatures and greater strengths of nanoparticles. Timofeeva et al. [41] studied the effect of shapes of the nanoparticles. Cylindrical nanoparticles created more viscosity than spherical nanoparticles at same concentrations in the nanofluids.

Thermal Conductivity The primary characteristic for examining heat transfer performance of a nanofluid is thermal conductivity [42]. Moosavi et al. [43] measured thermal conductivity, consistency and surface pressure of nano ZnO in

Table 1 Summary of models for viscosity correlations

Correlation	Authors and remarks
$\eta = 1 + 2.5\phi + (2.5\phi)^2 + (2.5\phi)^3 + (2.5\phi)^4 + (2.5\phi)^5 + \dots$	Cheng and Law [33], for two phase flow particles >100 nm
$\eta = \frac{1+0.5k\phi-\phi}{(1-k\phi)^2(1-\phi)}$	Toda and Furuse [34], concentrated dispersion
$\eta = \eta_f(1.1250 - 0.0007\tau)$	Ngyuen et al. [35], concentration 1–4%
$\eta = \eta_f \left(1 - \frac{\phi}{\phi_m} \left(\frac{d_p}{\lambda} \right) 1.2 \right) [\eta] \phi_m$	Chen et al. [36], considering aggregates
$\log \eta = Ae^{-B\tau}$	Namburu et al. [37], $A = 1.8375(\phi)^2 - 29.643(\phi) + 165.56, B = 4 \times 10^{-6}(\phi)^2 - 0.001(\phi) + 0.0186$
$\eta = \eta_f + \frac{\rho_p V_{fd}^2}{72cI}$	Masoumi and Behzadmeh [38], temperature consideration for density of base fluid
$\eta = \eta_f \left(1 + 2.5 \left(\frac{d_p + \tau + h}{d_p} \right)^2 \phi \right)$	Yang et al. [39], salvation effect

Adapted from Saxena and Raj (2017) [40]

ethylene glycol and glycerol base fluid, observed that the upgraded thermal conductivity proportion declines with expanding thermal conductivity of base fluid. Choi et al. [44] reported intensification of heat transfer coefficient occurred mainly due to increments in thermal conductivity of nanofluids and invited the interest of many workers [45]. Thermal conductivity of the dispersed phase is generally double as compared to the base fluid. The enhancement in thermal conductivity of the nanofluid has been found to be proportional to the thermal conductivity of the nanoparticles, thereby metallic nanofluids having as higher thermal conductivity [30, 46, 47] than ceramic nanofluids [6, 30, 46, 48].

Increasing the vol. conc. of nanoparticles boosts the thermal conductivity [6, 7, 30, 48]. However, Beck et al. [49] and Feng et al. [50] observed lower thermal conductivity with reduction in particles size, particularly in case of nanoparticles <50 nm size. Some workers have reported thermal conductivity enhancement with temperature [6, 51, 52], while others did not observe any effect [53]. However, Masuda et al. [12] reported reduction.

Nanofluids have either cylindrical or spherical nanoparticles, and their shapes play part in thermal conductivity improvement as nanofluids with spherical shape nanoparticles show lesser increment in thermal conductivity than nanofluids containing cylindrical shaped (nano-bar or tube) nanoparticles Murshed et al. [54].

On the basis of studies conducted on seven distinct nanofluids by thirty-four independent research groups, it was confirmed that the thermal conductivity enhancement in nanofluids increases linearly with concentration and aspect ratio of nanoparticles but is inversely affected by the thermal conductivity of the base fluid [55].

Greater thermal conductivities of carbon-based nanostructures (fullerenes, single-walled, double-walled, multi-walled nanotubes and ultra-scattered jewels) made them alluring contender for their use in nanofluids. Thermal conductivity values for single-walled, double-walled, multi-walled nanotubes are 6000, 3986 and 3000 W m⁻¹ K⁻¹, respectively [56, 57]. Choi et al. [4] reported phenomenal increase of 160% in thermal conductivity with CNT nanofluids having 1% volume MWNTs dispersed in engine oil. Biercuk et al. [58] also reported similar enhancement with polymer nanotubes.

Numerous mathematical models have been framed to forecast the thermal conductivity of heterogeneous materials. Some of these are given in Table 2.

Table 2 Mathematical models to forecast the thermal conductivity of heterogeneous materials

Model	Authors and remarks
$k_{nf} = \frac{\alpha + 2 + 2(\alpha - 1)\phi}{\alpha + 2 - 2(\alpha - 1)\phi} k_{bf}$	Maxwell’s model [1] , $\alpha = \frac{k_{np}}{k_{bf}}$
$k_{nf} = \frac{\alpha + (n - 1) + (n - 1)(\alpha - 1)\phi}{\alpha + (n - 1) - (\alpha - 1)\phi} k_{bf}$	Hamilton and Crosser [59] where $n = 3/\psi$
$k_{nf} = \frac{\alpha + 2 + 2(\alpha - 1)\phi + 2\alpha(1 - \phi)\frac{R_{bd}k_{bf}}{r_{np}}}{\alpha + 2 - (\alpha - 1)\phi + \alpha(2 + \phi)\frac{R_{bd}k_{bf}}{r_{np}}} k_{bf}$	Nan et al. [60], R_{bd} is thermal resistance between dispersed and continuous phases, and r_{np} is the nanoparticle radius

Table 3 Effects of nanofluids on thermal conductivity enhancement

Nanoparticles	Volume fraction of particles	Heat transfer enhancement	References
Al ₂ O ₃ /H ₂ O	4.3%	32.4%	Masuda et al. [12]
Cu/EG	0.3% (10 nm)	40%	Eastman et al. [23]
CuO/H ₂ O	0.40%	8%	Naraki et al. [65]
Cu/EG	2%	3.8%	Leong et al. [66]
Al ₂ O ₃ /H ₂ O	6.8%	40%	Nguyen et al. [67]
Al ₂ O ₃ /EG, CuO/EG, Al ₂ O ₃ /H ₂ O, CuO/H ₂ O	10% (25–65 °C)	Increased with temp. and conc.	Vajjha et al. [68]
MWCNTs/engine oil	4%	150%	Choi et al. [69]
Fe ₂ O ₃ -CuO/H ₂ O	0.5–1.5%	21% at 1.5%	Gaidhande et al. [70]
Graphene oxide/H ₂ O-EG	0.01–0.1%wt. conc.	13.0% at 0.1 wt%	Sajjad et al. [71]
TiO ₂ -CNT/H ₂ O	0.1–0.2% wt. conc.	38% at 0.2 wt%	Megatiff et al. [72]

Adapted from Singh et al. 2019 [73]

There are few more models developed by various researchers to predict thermal conductivity of nanofluids such as Davis model [61], Jang and Choi model [62] and Prasher et al. [63] model. Recently, Moreira et al. [9] and Ali et al. [64] have excellently reviewed the work done by various workers on thermal conductivity enhancements for nanofluids and the predictive models.

Thermal conductivity enhancements of various nanofluids observed by various workers are given in Table 3.

3 Conclusion

Conductivity and viscosity are directly proportional to concentration of particles. Thermal conductivity enhancement of nanofluid is directly proportional to nanoparticles conductivity and is inversely to the thermal conductivity of the base fluid. Size of the nanoparticles affects the conductivity and viscosity to great extent. Smaller size <50 nm decreases thermal conductivity, and also, sizes lower than 20 nm increase the viscosity. Thermal conductivity and viscosity are shape dependent. Nanofluids with cylindrical nanoparticles create more viscosity than fluids with spherical nanoparticles at same concentrations, and also, fluid with

cylindrical nanoparticles shows greater enhancement in thermal conductivity as compared to fluid with spherical nanoparticles at same concentrations. An optimum balance of these two properties is to be maintained to use nanofluid in car radiator so as to decrease the pumping power and maintain optimum engine temperature.

References

1. Maxwell JC (1904) A treatise on electricity and magnetism. Oxford University Press, Cambridge, UK
2. Batchelor GK (1977) The effect of Brownian motion on the bulk stress in a suspension of spherical particles. *J Fluid Mech* 83(1):97–117
3. Gupte et al (1995) Role of micro-convection due to non-affine motion of particles in a mono-disperse suspension. *Int J Heat Mass Transf* 38(16):2945–2958
4. Choi et al (1995) Enhancing thermal conductivity of fluids with nanoparticles. No. ANL/MSD/CP-84938; CONF-951135-29. Argonne National Lab, IL, US
5. Das SK, Choi SUS, Patel HE (2006) Heat transfer in nanofluids—a review. *Heat Transf Eng* 27(10): 3–19
6. Das SK et al (2003) Temperature dependence of thermal conductivity enhancement for nanofluids. *J Heat Transf* 125(4): 567–574
7. Lee et al (1999) Measuring thermal conductivity of fluids containing oxide nanoparticles. *J Heat Transf* 121:280–289
8. Xuan Y, Li Q (2000) Heat transfer enhancement of nanofluids. *Int J Heat Fluid Flow* 21(1):58–64
9. Moreira et al (2018) Nanofluids for heat transfer applications: a review. *J Braz Soc Mech Sci Eng* 40(6):303
10. Choi SUS, Singer DA, Wang HP (1995) Developments and applications of non-Newtonian flows. *ASME Fed* 66:99–105
11. Li et al (2010) Experimental studies of natural convection heat transfer of $\text{Al}_2\text{O}_3/\text{DI}$ water nanoparticle suspensions (nanofluids). *Adv Mech Eng* 2:742739
12. Masuda et al (1993) Alteration of thermal conductivity and viscosity of liquid by dispersing ultra-fine particles (dispersion of $\gamma\text{-Al}_2\text{O}_3$, SiO_2 and TiO_2 ultra-fine particles)
13. Choi et al (2002) Nanofluids for vehicle thermal management. *SAE Trans* 38–43
14. Godson Lazarus et al (2010) Enhancement of heat transfer using nanofluids—an overview. *Renew Sustain Energy Rev* 14(2):629–641
15. Vajjha RS, Das DK (2009) Experimental determination of thermal conductivity of three nanofluids and development of new correlations. *Int J Heat Mass Transf* 52(21-22):4675–4682
16. Hussein et al (2014) Study of forced convection nanofluid heat transfer in the automotive cooling system. *Case Stud Therm Eng* 2:50–61
17. Dehghandokht et al (2011) Flow and heat transfer characteristics of water and ethylene glycol-water in a multi-port serpentine meso-channel heat exchanger. *Int J Therm Sci* 50(8):1615–1627
18. Hussein et al (2014) Heat transfer enhancement using nanofluids in an automotive cooling system. *Int Commun Heat Mass Transf* 53:195–202
19. Eastman JA et al (1996) Enhanced thermal conductivity through the development of nanofluids. *MRS online proceedings library archive* 457
20. Jung J-Y et al (2011) Thermal conductivity measurement and characterization of binary nanofluids. *Int J Heat Mass Transf* 54(9-10):1728–1733
21. Xie H et al (2002) Dependence of the thermal conductivity of nanoparticle-fluid mixture on the base fluid. *J Mater Sci Lett* 21(19):1469–1471

22. Sundar LS et al (2013) Experimental thermal conductivity of ethylene glycol and water mixture based low volume concentration of Al_2O_3 and CuO nanofluids. *Int Commun Heat Mass Transf* 41:41–46
23. Eastman et al (2001) Anomalously increased effective thermal conductivities of ethylene glycol-based nanofluids containing copper nanoparticles. *Appl Phys Lett* 78(6):718–720
24. Patel HE et al (2003) Thermal conductivities of naked and monolayer protected metal nanoparticle based nanofluids: manifestation of anomalous enhancement and chemical effects. *Appl Phys Lett* 83(14):2931–2933
25. Hong TK, Yang HS, Choi CJ (2005) Study of the enhanced thermal conductivity of Fe nanofluids. *J Appl Phys* 97(6):064311
26. Maiga SEB et al (2005) Heat transfer enhancement by using nanofluids in forced convection flows. *Int J Heat Fluid Flow* 26(4):530–546
27. Zheng B et al (2015) Fast microwave-assisted synthesis of AuAg bimetallic nanoclusters with strong yellow emission and their response to mercury (II) ions. *Sens Actuators B: Chem* 221:386–392
28. Menezes WG et al (2012) Synthesis of stable AuAg bimetallic nanoparticles encapsulated by diblock copolymer micelles. *Nanoscale* 4(5):1658–1664
29. Mena JB, Moraes AAU, Benito YR, Ribatski G, Parise JAR (2013) Extrapolation of Al_2O_3 -water nanofluid viscosity for temperatures and volume concentrations beyond the range of validity of existing correlations. *Appl Therm Eng* 51:1092–1097
30. Murshed SMS, Leong KC, Yang C (2008) Investigations of thermal conductivity and viscosity of nanofluids. *Int J Therm Sci* 47(5):560–568
31. Wang X, Xu X, Choi SUS (1999) Thermal conductivity of nanoparticle-fluid mixture. *J Thermophys Heat Transfer* 13(4):474–480
32. Motta FDC (2012) Caracterização da condutividade térmica, viscosidade dinâmica e ângulo de contato para nanofluidos baseados em partículas de alumina-gama em água. Diss. Universidade de São Paulo
33. Cheng N-S, Law AW-K (2003) Exponential formula for computing effective viscosity. *Powder Technol* 129(1-3):156–160
34. Toda K, Hisamoto F (2006) Extension of Einstein's viscosity equation to that for concentrated dispersions of solutes and particles. *J Biosci Bioengg* 102(6):524–528
35. Nguyen et al (2008) Viscosity data for Al_2O_3 -water nanofluid-hysteresis: is heat transfer enhancement using nanofluids reliable? *Int J Therm Sci* 47(2):103–111
36. Chen Ha et al (2007) Rheological behaviour of ethylene glycol based titania nanofluids. *Chem Phys Letters* 444(4-6):333–337
37. Namburu PK et al (2007) Viscosity of copper oxide nanoparticles dispersed in ethylene glycol and water mixture. *Exp Therm Fluid Sci* 32(2):397–402
38. Masoumi N, Sohrabi N, Behzadmehr A (2009) A new model for calculating the effective viscosity of nanofluids. *J Phys D: Appl Phys* 42(5):055501
39. Yang L et al (2012) Viscosity-prediction models of ammonia water nanofluids based on various dispersion types. *Powder Technol* 215:210–218
40. Saxena G, Raj J (2017) A critical review on applications of nano-fluid as coolant. *Int J Eng Manag Res* 7(1):304–311
41. Timofeeva EV, Routbort JL, Singh D (2009) Particle shape effects on thermophysical properties of alumina nanofluids. *J Appl Phys* 106(1):014304
42. Kleinstreuer C, Feng Yu (2011) Experimental & theoretical studies of nanofluid thermal conductivity enhancement: a review. *Nanoscale Res Lett* 6(1):229
43. Moosavi et al. Fabrication, characterization, and measurement of some physicochemical properties of ZnO nanofluids. *Int J Heat Fluid Flow* 31(4):599–605
44. Choi SUS et al (2001) Anomalous thermal conductivity enhancement in nanotube suspensions. *Appl Phys Lett* 79(14):2252–2254
45. Lomascolo et al (2015) Review of heat transfer in nanofluids: conductive, convective and radiative experimental results. *Renew Sustain Energy Rev* 43:1182–1198

46. Zhu D et al (2009) Dispersion behavior and thermal conductivity characteristics of Al_2O_3 - H_2O nanofluids. *Curr Appl Phys* 9(1):131–139
47. Colangelo et al (2012) Results of experimental investigations on the heat conductivity of nanofluids based on diathermic oil for high temperature applications. *Appl Energy* 97:828–833
48. Xie H et al (2002) Thermal conductivity of suspensions containing nanosized SiC particles. *Int J Thermophys* 23(2):571–580
49. Beck MP et al (2009) The effect of particle size on the thermal conductivity of alumina nanofluids. *J Nanopart Res* 11(5):1129–1136
50. Feng et al (2007) The effective thermal conductivity of nanofluids based on the nanolayer and the aggregation of nanoparticles. *J Phys D: Appl Phys* 40(10):3164
51. Oliveira LR et al (2017) Thermophysical properties of TiO_2 -PVA/water nanofluids. *Int J Heat Mass Transf* 115:795–808
52. Yiamsawasd T et al (2012) Measurement of the thermal conductivity of titania and alumina nanofluids. *Thermochim Acta* 545:48–56
53. Turgut A et al (2009) Thermal conductivity and viscosity measurements of water-based TiO_2 nanofluids. *Int J Thermophys* 30:1213–1226
54. Murshed SMS, Leong KC, Yang C (2005) Enhanced thermal conductivity of TiO_2 -water based nanofluids. *Int J Therm Sci* 44(4):367–373
55. Buongiorno J, Venerus DC, Prabhat N et al (2009) A benchmark study on the thermal conductivity of nanofluids. *J Appl Phys* 106:094312
56. Kim J et al (2006) The effect of nano-particles on the bubble absorption performance in a binary nanofluid. *Int J Refrig* 29(1):2–29
57. Kim J et al (2007) Absorption performance enhancement by nano-particles and chemical surfactants in binary nanofluids. *Int J Refrig* 30(1):50–57
58. Biercuk MJ et al (2002) Carbon nanotube composites for thermal management. *Appl Phys Lett* 80(15):2767–2769
59. Hamilton RL, Crosser OK (1962) Thermal conductivity of heterogeneous two-component systems. *Indus Eng Chem Fundam* 1(3):187–191
60. Nan C-W et al (1997) Effective thermal conductivity of particulate composites with interfacial thermal resistance. *J Appl Phys* 81(10):6692–6699
61. Davis RH (1986) The effective thermal conductivity of a composite material with spherical inclusions. *Int J Thermophys* 7(3):609–620
62. Jang SP, Choi SUS (2004) Role of Brownian motion in the enhanced thermal conductivity of nanofluids. *Appl Phys Lett* 84(21):4316–4318
63. Prasher R et al (2006) Brownian-motion-based convective-conductive model for the effective thermal conductivity of nanofluids. *J Heat Trans* 128:588–595
64. Ali et al (2014) The effect of nanofluid concentration on the cooling system of vehicles radiator. *Adv Mech Eng* 6:962510
65. Naraki M et al (2013) Parametric study of overall heat transfer coefficient of CuO /water nanofluids in a car radiator. *Int J Therm Sci* 66:82–90
66. Leong KY et al (2010) Performance investigation of an automotive car radiator operated with nanofluid-based coolants (nanofluid as a coolant in a radiator). *Appl Therm Eng* 30(17-18):2685–2692
67. Nguyen CT et al (2007) Heat transfer enhancement using Al_2O_3 -water nanofluid for an electronic liquid cooling system. *Appl Therm Eng* 27(8-9):1501–1506
68. Vajjha RS, Das DK (2012) A review and analysis on influence of temperature and concentration of nanofluids on thermophysical properties, heat transfer and pumping power. *Int J Heat Mass Transf* 55(15-16):4063–4078

69. Choi SUS, Zhang ZG, Keblinski P, Nalwa HS (2004) Encyclopedia of nanoscience and nanotechnology, vol 6. American Scientific Publishers, pp 757–773
70. Gaidhane T, Bhosale S (2016) CFD analysis and experimental investigation of percentage heat transfer enhancement of CFHX with hybrid nano fluid as a coolant. *Int J Sci Res Develop* 4(6):918–922
71. Sajjad M et al (2018) Numerical investigation of laminar convective heat transfer of graphene oxide/ethylene glycol-water nanofluids in a horizontal tube. *Eng Sci Technol Int J* 21(4):727–735
72. Megatiff L et al (2016) Investigation of laminar convective heat transfer of a novel TiO₂–carbon nanotube hybrid water-based nanofluid. *Exp Heat Transf* 29(1):124–138
73. Singh J et al (2019) Heat transfer using nanofluid. *Int J Eng Adv Technol (IJEAT)* 9(2):3205–3211

Biodiesel in India—A Review



Sanjay Mohite and P. K. Rohtagi

Abstract This article provides the information of biodiesel development in India. It reviews the advantages and limitations of biodiesel, comparative analysis of diesel and biodiesel, economic analysis, and the comparative analysis of the findings and results of various authors. Standard energy audit methods and biofuel performance certification methods are found as future challenge and scope for biodiesel.

Keywords Fossil fuels · Biodiesel · Diesel engines · Energy audit · Biofuel performance certification

1 Introduction

Biodiesel is simply an alkyl esters of lengthy chain fatty acids obtained from renewable sources. It is an oxygen added fuel obtained from natural biological sources. It could be used in diesel engines with no engine modifications [1]. Biodiesel is highly biodegradable and has reduced levels of toxicity. It can be used in diesel engines instead of diesel fuel without any major modification of engines. Biodiesel emits a very less amount of harmful emissions like carbon monoxide, particulate matters, smoke, and hydrocarbon emission. Biodiesel does not emit sulphur and net carbon dioxide [2, 3].

Harmful emissions are reduced by biodiesel. Biodiesel is produced with an ease. Biodiesel is found to have superior lubricating properties, superior cetane number, higher density, and lower sulphur emissions. In the world, biodiesel production has found to reach about 2.2 billion gallons. Biodiesel is being manufactured with the

S. Mohite (✉)

Brahma Valley College of Engineering and Research Institute, Nashik, India

e-mail: smohite001@yahoo.com

P. K. Rohtagi

Amity University, Noida, India

e-mail: pkrohtagi@amity.edu

© The Author(s), under exclusive license to Springer Nature Singapore Pte Ltd. 2021

B. S. Sikarwar et al. (eds.), *Advances in Fluid and Thermal Engineering*,

Lecture Notes in Mechanical Engineering,

https://doi.org/10.1007/978-981-16-0159-0_65

help of more than 350 numbers of oil bearing crops [4, 5]. Biodiesel has a viscosity as compared to that of diesel. These vegetable oil esters are found to have 10% more oxygen by weight causing better combustion. Biodiesel is found to have higher flash point and cetane number. The value of biodiesel's cetane number is 50. It has about 10% low calorific value as compared to that of diesel [6].

2 Advantages and Limitations of Biodiesel

Biodiesel has certain advantages over diesel as follows:

1. Higher cetane number, absence of aromatics and sulphur are advantages of biodiesel, and biodiesel also has about 10% more oxygen than diesel.
2. It is renewable feedstocks containing tri glyceride and can be converted by transesterification to biodiesel.
3. In India, biodiesel could be considered as supplementary fuels to diesel. Biodiesel is also helpful to generate employments for rural people through plantation for vegetable oils. The biodiesel blends are helpful to solve the problem of Indian diesel which has generally lower flash point about 35 °C as compared to world average of 52 °C [7].
4. It is neither toxic nor polluting in comparison with diesel. This is sustainable, in terms of life cycle analysis [8].

Limitations of biodiesel are as follows:

1. In India, existing agricultural land cannot be used for the cultivation of vegetable oils, which is used for biodiesel production. India has more than 100 Mha of waste and degraded land which could be utilized for the cultivation of non-edible vegetables [7].
2. Production price of biodiesel is higher in comparison with diesel, which is the main barrier to commercialize it [8].
3. Biodiesel feedstocks of first generation are used for food and it cannot be used as fuel in India as it could generate food shortage problem [8].
4. The use of fit for growing crops lands for fuel can create ecological problems.
5. Cost of biodiesel raw material obtained from vegetable oils carries 70–95% cost of biodiesel. The low price of biodiesel can be achieved when proper feedstock is selected [8].
6. Availability of biodiesel feedstocks depends on geographical location, regional climate, and soil conditions [8].
7. The limitations for commercialization of biodiesel are its high raw material price and also alteration technology to decrease viscosity. The option of raw material and biodiesel production should depend on its techno-economic concept [8].

3 Biodiesel Development in India

India is principally an agricultural nation and requires main awareness to fulfil energy burden of a cultivator. The rise in role of diesel fuel in farming and transport sectors has caused shortages of diesel fuel. Complete replacement of oil imports is found to be the toughest challenge in the transportation and agricultural sectors in India. 17% of world population is found to be accounted in India and only 0.8% of the world's oil and natural gas resources are found to be contributed in India. Oil demand in India is 114 million tons per year and 25% of the demand is produced in India. Oil and natural gas are being imported with a cost of INR 2000 billion in India. India has about 60 million hectares of wasteland out of which energy plants such as *Jatropha* can be grown on 30 million hectares. It is reported that 2 tons of biodiesel would produce in one acre of land which costs INR 20 per litre [9]. India use to import 70% of the total petroleum fuel required, costing about INR 80,000 crore every year. INR 4000 crore can be saved by blending 5% biofuel to diesel fuel in India every year [10]. The growth rate of energy demand is 4.8% per year in India [11]. India ranks as sixth in demand of total energy. Crude oil imports in India were found to increase steadily. In 2015, the need for transport fuels was 124 billion litres and would liable to attain 202 billion litres in 2024 [12]. Energy consumption in the world was 1.58×10^{14} kWh in 2012. India imported 189.238 MMT (Million Metric Tons) crude oil in the year 2013–2014 which was increased by 2.4% as compared to that of year 2012–2013 [13]. In 2013, entirety oil utilization was found to be 3509 thousand barrels in a day and total oil supply was found to be 982.2 thousand barrels in a day. Therefore, 28% of oil consumption was fulfilled by indigenous production. Consequently, the oil bring in expenses in India has found to rise almost threefold ever since financial year 2004–2005. Oil import expenses were found to be USD 87.1 billion in financial year 2009–2010 and it was risen to USD 167.6 billion in financial year 2013–2014. India is likely to turn out to be the fourth chief net oil importer in the globe up to 2025. Rise in price and supply problems may cause problems in Indian economy [14].

Transport sector, agricultural, and industrial sectors depend on supply of fuel causing rise in crude oil prices sharply. The crude oil prices have witnessed a steep hike from just around \$20/barrel to around \$140/barrel and then again back to around \$60 in 1999–2014 [15]. 184.68 MT (Metric Tons) of crude oil was consumed in fiscal year 2007–2008 out of which 80% of this crude oil was imported in India. World crude oil production of 1% is produced but its consumption is 3.1% of overall globe utilization in India. In 1971, 63% of crude oil was imported, whereas it was 80% in fiscal year 2007–2008. 9.3% of total oil seed of the world was produced in India. India is the fourth-largest country to produce edible oil. But still, 46% of edible oil was imported in India. 1 million tons of non-edible oils may be produced in India [16].

In 2020, India is expected to be the third major user of fuel in transportation subsequent to USA and China with yearly fuel utilization increase rate of 6.8% [3, 17]. India would have 500 million vehicles in subsequently two decades, as

compared to 150 million vehicles presently. It will raise India's dependency for import of fuel. It also increases greenhouse gas (GHG) emissions [18]. In India, consumption of diesel, as compared to petrol, is more than five times. There is a large utilization of diesel fuel in transport, commercial, agriculture, and industrial sectors and if a small fraction of diesel is replaced by biodiesel, it will have a considerable strength on economic system and the atmosphere [19].

The developing countries could not use edible oils as fuel. Therefore, in-edible vegetable oils would be preferred for production of biodiesel. In-edible oilseed crops comprise of Karanja, Mahua, Camelina, Jatropha, Cotton seed, Neem, Cumaru, Jojoba, Moringa, Tobacco seed, Passion seed, Rubber seed tree, Tall, Salmon oil, Coffee Ground, Terminalia bellirica, Croton megalocarpus, Nagchampa, Aleurites moluccana, Pachira glabra [2]. Developing countries such as India can produce renewable energy from non-edible oils such as Karanja, Jatropha, and Linseed oil economically [20]. The forest of India has a wide range of non-edible plants. The Indian economy can be improved by using these non-edible oils such as Neem, Karanja, Kusum, Ratanjyot, Tumba, Pilu, Sal, Mahua, Phulware, Simarouba, Jojoba, Chullu, and Kokum. Out of the above-mentioned non-edible plants, Karanja is easily available and may be cultivated easily in many parts of India (Table 1). Biodiesel and ethanol are renewable biofuels and more attention is given to the feasibility of these fuels in India due to energy self-sufficiency, environmental concerns, and increase in the rural economy. Indian diesel has 17 °C lower flash point as compared to that of diesel which has flash point of 52 °C in the world and also content higher sulphur and it could be blended with biodiesel to improve these parameters [5]. Biodiesel shall be produced from in-edible oil seeds which shall be cultivated from waste, degraded, and marginal lands. Biodiesel would produce from indigenous feedstocks [11]. Biofuel policy of India is found to be limited to Jatropha-based biodiesel. In 2017, the requirement of biodiesel would increase to 16.72 million tons and it would promote 20% biodiesel blends [21].

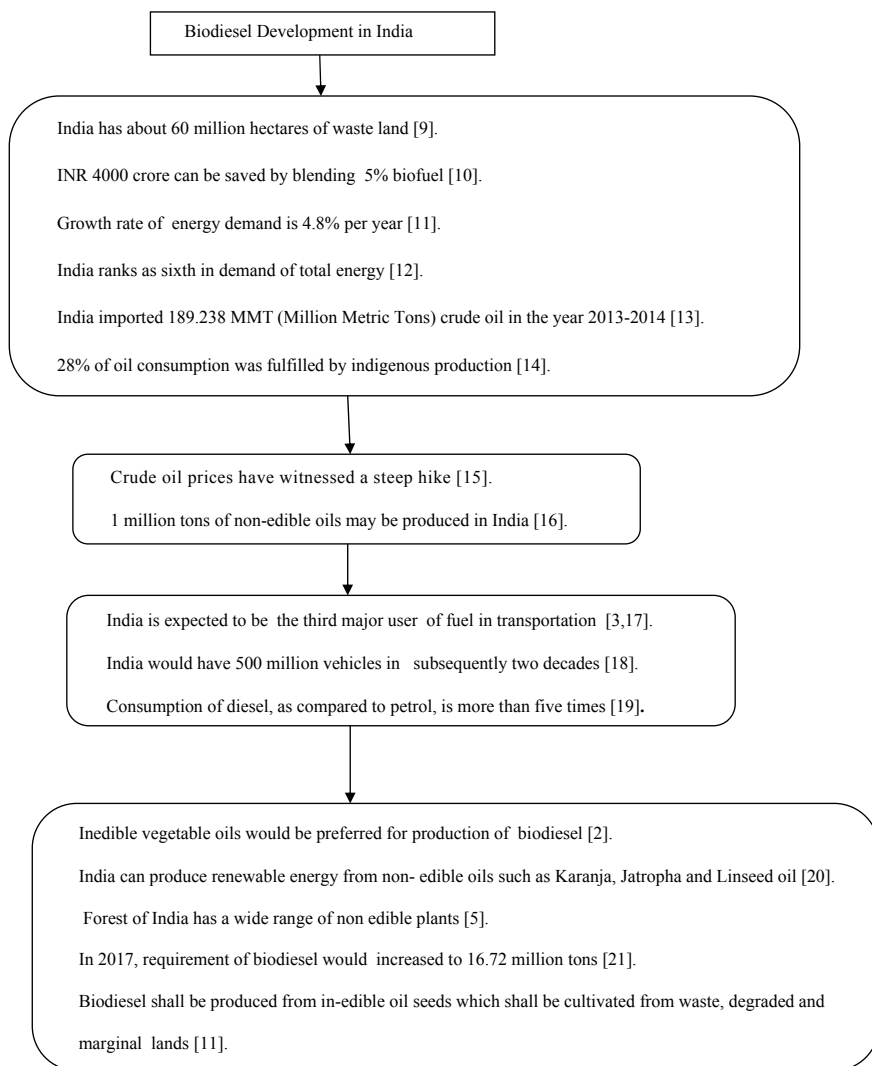
4 Comparative Analysis of Diesel and Biodiesel Properties

The comparative property of diesel and biodiesel is listed in Table 2 [22].

5 Economic Analysis

It was a good option to select suitable algae species with maximum lipid productivity to produce biodiesel economically. Feedstock price covers 80% total biodiesel production price. The cost of waste cooking oil was found to be 2.5–3.5 times lesser than cost of vegetable oils. The cost of process is influenced by molar ratio of oil/alcohol and catalyst percentage [23, 24]. The total production cost was

Table 1 Biodiesel development in India



affected by production cost. Eggshell, biochar from coconut shells could be used as catalyst as low-cost materials. Heterogeneous catalyst such as biomass waste derived could be a suitable option to decrease price of production of biodiesel [25]. Cost of biodiesel production was evaluated from different sources by several studies. It was estimated that 0.82 USD/litre was price of biodiesel from palm oil containing highest price of feedstock as 0.73 USD. It was estimated that the lowest production cost with the use of tallow fat was 0.6 USD/litre which includes the

Table 2 Comparative property of diesel and biodiesel

S. No.	Name of property	ASTM D6751 biodiesel standards	Diesel
1	Density kg/m ³	880	850
2	Viscosity cSt	1.9–6.0	2.8
3	Heating value MJ/kg	–	43.7
4	Pour point in °C	–15 to 10	–15
5	Flash point in °C	130 min.	76
6	Cloud point in °C	–3 to –12	–10

feedstock cost of 0.4 USD [26]. In 2011, 0.7 USD/litre was the estimated cost of biodiesel production from palm oil [27]. The cost of algae biodiesel was found to be in the range of 0.53–0.85 USD per litre according to cost analysis of U.S. National Renewable Energy Laboratory. In addition, 0.42–0.97 USD per litre was found to be the final cost of biodiesel as calculated by different sectors [28]. It was estimated that there were not much difference in the price of biodiesel production since last decade [23]. In case of biodiesel production from non-vegetable oils, the high cost of labour from harvesting was an important issue such as in Malaysia and Brazil [29]. Various parameters such as raw material and cost of by-product, operation cost, plant capacity, and location were found to be dependent on production cost of biodiesel from seed oil. The required cost of biodiesel production for castor would be 9% lower than that of diesel including tax. Therefore, it would be well proposed as a lower price vegetable to produce biodiesel [30]. The price of biodiesel production could be decreased by 60–70% with use of waste cooking oil [31].

6 Comparative Study of Diesel with Biodiesel in Terms of Performance and Emissions Characteristics

The comparative study of diesel with biodiesel is given in Table 3 [8].

Table 3 Comparative study of diesel with biodiesel in terms of performance and emissions characteristics

S. No.	Effect of performance and emissions characteristics	Fuel used	
		Diesel	Biodiesel blends
1	BTE (Brake Thermal Efficiency)	Increase	Decrease
2	BSFC (Brake-Specific Fuel Consumption)	Decrease	Increase
3	BSEC (Brake-Specific Energy Consumption)	Decrease	Increase
4	EGT (Exhaust Gas Temperature)	Decrease	Increase
5	ME (Mechanical Efficiency)	Decrease	Increase
6	VE (Volumetric Efficiency)	Decrease	Increase
7	SO (Smoke Opacity)	Increase	Decrease

7 Energy Audit and Biofuel Certification

Energy audits were used in plants, equipments, and buildings [32]. Energy audit method was also found to develop for fishing vessels [33]. Vehicle's energy audit is a way to assess use of energy efficiently. Its purpose is to examine different areas to save fuel [34]. An energy audit is used to locate use of energy in a plant, process, structure, and system and also studies the energy conservation. If energy consumption is found out, then it is easier to reduce energy consumption with proper management [35].

Biofuel sustainability's assessment is necessary for, analysis of various factors for consideration of their multidimensional impacts. Fulfilment of one specific objective of biofuel does not mean its sustainability [36]. A programme of biodiesel development is required for its awareness. It analyse the actions which should be taken for improvements in outputs and minimize risks in analysis of biofuel [37]. The certification is recognized as an efficient tool for evaluation of energy performance [38].

8 Findings and Results of Authors

It is found that various experiments have been performed on performance and emission characteristics of biodiesel engines. There are wide range of lands available in India to cultivate in-edible plants and to produce biodiesel. Standard energy audit method is required to be implemented for biodiesel engine which could appraise the viability of biodiesel as fuel. It is also established that a performance certification is obligatory in biodiesel trade to endorse biodiesel to utilize in diesel engine. The new findings and results are listed in Table 4.

Table 4 Findings and results of authors

Thiruvengadam et al. [39]	The efficiency, the losses of energy, and the prospects for improvement in 12.8 litre heavy duty and 6.7 litre medium duty diesel engine have been analysed in the experimental work. In this experimental work, two baseline diesel engines were tested and analysed in the laboratory. The abilities of emerging technologies to reduce consumption of fuel with focus on each loss mechanism were found out with the application of energy audit and technology forecasting. Improvements in fuel consumption were investigated with improvement in the heavy duty diesel engine in this research work with the help of future technology
Mohite et al. [40]	Performance and smoke emission characteristics of diesel engine fuelled with Karanja biodiesel blends was conducted at constant speed. BTE of Karanja biodiesel blend was comparable with diesel. Increase in BSFC of Karanja biodiesel blends were found as compared to diesel. Exhaust gas temperature of Karanja biodiesel blends was increased. Mechanical efficiencies were also found to be increased to some extent as compared to diesel. Smoke opacity of Karanja biodiesel blends were found to be reduced

(continued)

Table 4 (continued)

Mohite et al. [41]	Experimental studies were carried out to evaluate performance characteristics and smoke with 10, 20, and 30% blend in diesel at brake power of 0.5–3.5 kW at a 1500 rpm speed. BTE, BSEC, EGT, ME, VE, air fuel ratio, and SO of biodiesel blended fuel were investigated. It was found suitably. B20 blend was investigated to be more useful among all tested fuels with respect to BTE
Mohite et al. [8]	Biodiesel would be prepared with Karanja and Linseed oils mixture with alkaline transesterification process. Blends of biodiesel with 10, 20, and 30% were mixed with diesel to check BTE, BSFC, BSEC, EGT, ME, VE, air fuel ratio, and SO found satisfactorily. BTE of B10 was measured as 28.76% at a load of 3.5 kW. Smoke opacity of all biodiesel blends was also found to be reduced. It was shown that biodiesel prepared with Karanja and Linseed oils mixture could be utilized in diesel engines with no engine modification and B10 was investigated as the best possible biodiesel blend
Mohite et al. [22]	Biodiesel blends, obtained by mixing Karanja and linseed oil, of 10, 20, and 30% were mixed with diesel at 1500 rpm to measure BTE, BSEC, HC emissions, CO emissions, NOx emissions, and smoke opacity. B30 was found to emit lowest HC emissions and lowest CO emissions and diesel delivered the lowest NOx emissions at all loads. Reduction up to 37.32% was found in smoke opacity of biodiesel blends. It was revealed that 10% biodiesel blend could be effectively used in an unmodified diesel engine
Mohite et al. [42]	It was mentioned that in-edible oil would be one of the best source as fuel. India has wide range to cultivate in-edible plants and to produce biodiesel. Wild Apricot, Cottonseed, Linseed, Thumba, Algae, and Mahua were reviewed to discover its utility as possible assets for biodiesel and found suitable for it
Mohite et al. [43]	There would be a need to find out non-edible oils which can be easily produced in India. Wild Apricot, Linseed, Thumba, Algae, Mahua, and Cottonseed would be utilized as probable resources to produce biodiesel. Densities, Viscosities, and Calorific values of these biodiesel were compared and found comparable to that of diesel. Brake thermal efficiency, brake-specific fuel consumption, and smoke emissions of biodiesel were reviewed in different diesel engines. BTE and BSFC were found to be similar to diesel. Smoke emission of these biodiesel was found to be lower than that of diesel
Mohite and Maji [44]	There would a large span to implement regular energy audit in biodiesel engines. Its purpose was to find out a standard energy audit method for diesel engine which could appraise the viability of biodiesel as a fuel
Mohite and Maji [45]	Performance certification's capacity was reviewed. It was documented as an useful appraisal tactic and tool to supervise biofuel utilization and get better performance analytically. It was established that a performance certification was obligatory in biodiesel trade to endorse biodiesel to utilize in diesel engine. Some of the characteristics of engine were preferred as key parameters to work out biodiesel engine with energy audit in prime stage

9 Conclusion

In this review paper, biodiesel is defined with its main properties. Biodiesel development in India has been explained. Advantages of biodiesel are also explained. The comparative analysis of diesel and biodiesel properties, advantages and limitations of biodiesel, comparative study of diesel and biodiesel for various characteristics, advantages of biodiesel in India, economic analysis, and the findings and results of authors are explained.

There are future challenge and scope for biodiesel which are listed below:

1. Different types of non-edible oils shall be analysed to find out its feasibility as fuel with the help of standardize energy audit [42].
2. Biofuel performance certification method shall be find out to verify biodiesel to utilize in diesel engine [44, 45].

References

1. Ramadhas AS, Jayaraj S, Muraleedharan C (2005) Biodiesel production from high FFA rubber seed oil. *Fuel* 84:335–340
2. Atabani AE, Silitonga AS, Badruddin IA, Mahlia TMI, Masjuki HH, Mekhilef S (2012) A comprehensive review on biodiesel as an alternative energy resource and its characteristics. *Renew Sustain Energy Rev* 16:2070–2093
3. Pal A, Kachhwaha SS, Maji S, Babu MKG (2010) Thumba (*Citrullus colocynthis*) seed oil: a sustainable source of renewable energy for biodiesel production. *J Sci Ind Res* 69(5):384–389
4. Chhetri AB, Islam MR (2008) Towards producing a truly green biodiesel. *Energy Sources Part A* 30:754–764
5. Subramanian KA, Singhal SK, Saxena M, Singhal S (2005) Utilization of liquid biofuels in automotive diesel engines: an Indian perspective. *Biomass Bioenergy* 29:65–72
6. Shrivatava A, Prasad R (2000) Triglycerides-based diesel fuels. *Renew Sustain Energy Rev* 4:111–133
7. Mohite S, Kumar S, Maji S, Pal A (2014) Use of karanja oil for biodiesel production. *Int J Eng Res Appl* 4(7):286–289
8. Mohite S, Kumar S, Maji S (2016) Performance characteristics of mix oil biodiesel blends with smoke emissions. *Int J Renew Energy Develop* 5(2):163–170
9. Banapurmath NR, Tewari PG, Kumar VV (2009) Combustion and emission characteristics of a direct injection CI engine when operated on marotti oil methyl ester and blends of marotti oil methyl ester and diesel. *Int J Sustain Eng* 2(3):192–200
10. Misra RD, Murthy MS (2010) Straight vegetable oils usage in a compression ignition engine—a review. *Renew Sustain Energy Rev* 14:3005–3013
11. Agoramoorthy G, Minna JH, Chaudhary S, Shieh PC (2009) Can biofuel crops alleviate tribal poverty in India's drylands? *Appl Energy* 86(1):S118–S124
12. Verma P, Sharma MP (2016) Review of process parameters for biodiesel production from different feedstocks. *Renew Sustain Energy Rev* 62:1063–1071
13. Panigrahi N, Mohanty MK, Mishra SR, Mohanty RC (2016) Energy and exergy analysis of a diesel engine fuelled with diesel and simarouba biodiesel blends. *J Inst Eng (India): Series C* 99(1):9–17

14. Goswami K, Hazarika A (2016) Supply chain network of jatropha based biodiesel industry in north east India. *Sustain Prod Consumption* 6:38–50
15. Saluja RK, Kumar V, Sham R (2016) Stability of biodiesel—a review. *Renew Sustain Energy Rev* 62:866–881
16. Jain S, Sharma MP (2010) Prospects of biodiesel from jatropha in India: a review. *Renew Sustain Energy Rev* 14(2):763–771
17. Rarnesh D, Sampathrajan A (2008) Investigations on performance and emission characteristics of diesel engine with jatropha biodiesel and its blends. *Agric Eng Int: CIGR Ejournal X: EE* 07 013
18. Ajayebi A, Gnansounou E, Raman JK (2013) Comparative life cycle assessment of biodiesel from algae and jatropha: a case study of India. *Bioresour Technol* 150:429–437
19. Barnwal BK, Sharma MP (2005) Prospects of biodiesel production from vegetable oils in India. *Renew Sustain Energy Rev* 9(4):363–378
20. Dixit S, Kanakraj SA, Rehman A (2012) Linseed Oil as a potential resource for biodiesel: a review. *Renew Sustain Energy Rev* 16:4415–4421
21. Planning Commission of India (2003) Report of the committee on development of biofuel, Government of India. http://planningcommission.nic.in/reports/genrep/cmtt_bio.pdf. Last accessed 5 Aug 2009
22. Mohite S, Kumar S, Maji S (2016) Investigations on performance and emission characteristics of mix oil biodiesel blends. *Iran J Energy Environ* 7(3):255–261
23. Shahabaldin R, Oryani B, Park J, Hashemi B, Yadav KK, Kwon EE, Hur J, Cho J (2019) Review on transesterification of non-edible sources for biodiesel production with a focus on economic aspects, fuel properties and by-product applications. *Energy Convers Manag* 201:112–155
24. Hussain MN, Samad TA, Janajreh I (2016) Economic feasibility of biodiesel production from waste cooking oil in the UAE. *Sustain Cities Soc* 26:217–226
25. Tang ZE, Lim S, Pang YL, Ong HC, Lee KT (2018) Synthesis of biomass as heterogeneous catalyst for application in biodiesel production: state of the art and fundamental review. *Renew Sustain Energy Rev* 92:235–253
26. Demirbas A (2009) Political, economic and environmental impacts of biofuels: a review. *Appl Energy* 86:S108–S117
27. Yusuf N, Kamarudin SK, Yaakub Z (2011) Overview on the current trends in biodiesel production. *Energy Convers Manag* 52(7):2741–2751
28. Nagarajan S, Chou SK, Cao S, Wu C, Zhou Z (2013) An updated comprehensive techno economic analysis of algae biodiesel. *Biores Technol* 145:150–156
29. Lim BY, Shamsudin R, Baharudin BTHT, Yunus R (2015) A review of processing and machinery for jatropha curcas L. fruits and seeds in biodiesel production: harvesting, shelling, pretreatment and storage. *Renew Sustain Energy Rev* 52:991–1002
30. Rahimi V, Shafiei M (2019) Techno-economic assessment of a biorefinery based on low impact energy crops: a step towards commercial production of biodiesel, biogas and heat. *Energy Convers Manag* 183:698–707
31. Joshi S, Hadiya P, Shah M, Sircar A (2019) Techno-economical and experimental analysis of biodiesel production from used cooking oil. *Biophys Econ Resour Qual* 4(1):1–6
32. Thumann A, Younger W (2010) *Handbook of energy audit*, 7th edn. The Fairmont Press, Lilburn
33. Thomas G, O'Doherty D, Sterling D, Chin C (2010) Energy audit of fishing vessels. *Proc Inst Mech Eng Part M: J Eng Maritime Environ* 224(2):87–101
34. Erkut E, Maclean D (1992) Alberta's energy efficiency branch conducts transportation audits. *Interfaces* 22(3):15–21
35. Parker SA (2015) Ideas that works! the midnight audit. *Strategic Planning Energy Environ* 35 (1):7–9
36. Gino B, Delrue F, Legrand J, Pruvosta J, Vallée T (2017) The challenge of measuring biofuel sustainability: a stakeholder-driven approach applied to the French case. *Renew Sustain Energy Rev* 69:933–947

37. Goetza A, Searchinger T, Beringer T, German L, McKay B, Oliveira GLT, Hunsberger C (2018) Reply to commentary on the special issue scaling up biofuels? a critical look at expectations, performance and governance. *Energy Policy* 118:658–665
38. Cai W, Liu C, Lai KH, Li L, Cunha J, Huf L (2019) Energy performance certification in mechanical manufacturing industry: a review and analysis. *Energy Convers Manag* 186: 415–432
39. Thiruvengadam A, Pradhan S, Thiruvengadam P, Besch M, Carder D (2014) Heavy duty vehicle diesel engine efficiency evaluation and energy audit. Center for Alternative Fuels, Engines, and Emissions, West Virginia University, Morgantown, WV, Final report on Oct, 2014 published by Oscar Delgado, the International Council on Clean Transportation, Washington DC
40. Mohite S, Kumar S, Maji S, Pal A (2015) Experimental investigations of performance and smoke emission of Karanja biodiesel blends and diesel in a diesel engine. In: *International Seminar on Renewable Energy and Sustainable Development*, vol 2, pp 32–35. Weentech Proceedings in Energy, published by World Energy & Environment Technology, 15–17 June 2015, Royal University of Bhutan (RUB) Bhutan
41. Mohite S, Kumar S, Maji S (2016) Experimental studies on the use of Karanja biodiesel as blend in a compression ignition engine. *Int J Renew Energy Res* 6(2):355–360
42. Mohite S, Kumar S, Maji S, Pal A (2016) Biodiesel feedstock in India: a review. In: *International Conference on Recent Advances in Mechanical Engineering (RAME-2016)*, pp 45–52, 14–15 Oct 2016 at Delhi Technological University. Enriched Publications, New Delhi
43. Mohite S, Kumar S, Maji S, Pal A (2016) A feasibility study of potential biodiesel feedstock in Indian sub-continent. In: *International Conference on Recent Advances in Mechanical Engineering (RAME-2016)*, pp 631–640, 14–15 Oct, 2016 at Delhi Technological University. Enriched Publications, New Delhi
44. Mohite S, Maji S (2020) Importance of energy audit in diesel engine fuelled with biodiesel blends: review and analysis. *Eur J Sustain Develop Res* 4(2):em0118
45. Mohite S, Maji S (2020) Biofuel certification performance: a review and analysis. *Eur J Sustain Develop Res* 4(3):em0124

Numerical Analysis of Turbulent Heat Exchanger Tube Using Novel Para-Winglet Tape



R. Thejaraju, K. B. Girisha, S. H. Manjunath, and B. S. Dayananda

Abstract From the last decade, passive enhancement techniques in heat exchanger have proved to be one of the promising techniques in heat transfer enhancement. The current study involves para-winglet tape which is examined numerically with three sets of slant angle namely 10° , 15° , and 20° with a constant pitch of 30 mm in the forward and backward arrangements for Reynolds number 6000 to 30,000. The inclusion of para-winglet tape in the tube has intensified the turbulent kinetic energy and has resulted in recirculation in-between the inserts. Both the arrangements of the para-winglet tape have proved their worthiness over the plain tube. The Nusselt number and friction factor increase with the increase in the Reynolds number over the plain tube. Maximum, Nusselt number, and friction factor were obtained for 20° slant angle in forward arrangement. Nusselt number and friction factor increased from 3.2 to 2.99 times and 9.95 to 9.61 times, respectively, when compared with plain tube. A maximum value of 1.63 thermal performance index was obtained at 15° slant angle for forward arrangement and 1.62 thermal performance index was obtained at 20° slant angle for backward arrangement.

Keywords Passive enhancement · Para-winglet tape · Nusselt number · Thermal performance index

R. Thejaraju (✉)

VTU, Department of Mechanical Engineering, Belgaum, India

e-mail: thejaraju.r@gmail.com

K. B. Girisha · S. H. Manjunath

Department of Mechanical Engineering, BGSIT-Adichunchanagiri University, BG Nagara 571448, India

e-mail: girish.kn03@gmail.com

S. H. Manjunath

e-mail: sh_manjunath@rediffmail.com

B. S. Dayananda

Department of Mechanical and Manufacturing Engineering, MS Ramaiah University of Applied Sciences, Bangalore, Karnataka 560054, India

e-mail: bannurdaya@gmail.com

© The Author(s), under exclusive license to Springer Nature Singapore Pte Ltd. 2021

B. S. Sikarwar et al. (eds.), *Advances in Fluid and Thermal Engineering*,

Lecture Notes in Mechanical Engineering,

https://doi.org/10.1007/978-981-16-0159-0_66

1 Introduction

Heat transfer in tubes is basically applied in refrigerators, boilers, condensers, regenerators, recuperators, reheaters, air heaters, and so on. Enhancement techniques in tubes have proven to optimize the rate of heat transfer with compensation of pumping pressure. The enhancement techniques are broadly classified into (a) passive techniques-no external aid and (b) active technique-requires external aid. Some of the important techniques which are proven to be very promising in recent years are as discussed below.

2 Literature

The application of vortex generator inserts by Prashant [1] saw an increase of the Nusselt number from 1.3 to 5.0 for the various angles of attack and diameter ratio. Vortex generator inserts by Alibadi [2] proved to have the maximum performance criterion of 1.41 at Re 8715. The thermal performance factor of delta winglets was examined by Skullong [3] between Reynolds numbers ranging from 4100 to 25,400. An increment of 1.22–1.55 was obtained for a pitch ratio of 1.0 and angle of attack 45°. The curved delta wing was examined for the laminar zone by Deshmukh [4]. Longitudinal vortex generator [5] was experimented for the Reynolds number varying from 4200 to 25,500 and saw a maximum enhancement factor of 1.49. Skullong [6] perforated-cross tape delta-winglet pairs assured an enhancement factor of 1.9 for a blockage ratio of 0.15 and pitch ratio 1.0. A thermal enhancement factor of 1.65 was achieved by investigating perforated vortex generators developed Sunil [7]. Multiple twisted tapes by Piriayarungrod [8] resulted in a maximum performance index of 1.2 with a number of twist 6 and twist ratio 2.5.

A new set of longitudinal vortex generators was experimented by Wang [9] for the laminar zone and resulted in an overall thermo-hydraulic performance index of 2.55–7.1. The numerical investigation by Nakhchi on rectangular-cut twisted tape [10] and V-cut twisted tape inserts [11] resulted in an enhancement factor of 1.64 and 1.83. Skullong [12] proved that Diamond-shaped Baffle Inserts can optimize the tube heat exchanging from 1.25 to 1.55 at a baffle ratio of 1.0 over the plain tube. Delta-winglet vortex generator pairs by Islam [13] were introduced to examine the performance over the plain tube and resulted in a maximum enhancement of 1.44 over the plain tube.

Some of the recent findings on optimizing the heat transfer in the heat exchange tube are as follows: perforated triple twisted tape by Muhammad [14] saw an enhancement of 1.5 over a porosity of 4.6%. On the laminar zone, twisted conical strip inserts were investigated by Mehdi [15] and the highest performance factor was obtained at Reynolds number 460 and was equal to 1.3. Skullong [16]

proposed a new thermal performance factor to overcome the difficulties in the current performance factor for a V-shaped winglet vortex generator and obtained a value of 1.82–2.0 for V-shaped rectangular-winglets. Multiple rectangular winglet vortex generators were investigated between Reynolds numbers 5000 to 20,000 and obtained a maximum enhancement of 1.27 for Reynolds number 6135. A compound twisted tape and twisted tube were investigated by Aliabadi [17] for the laminar zone, which resulted in the optimization of 3.21. From the above literature survey, it shows that there is always scope for the new design for better optimization and ease of manufacturing.

So, the present study involves the prediction of the heat transfer characteristics and flow behavior of the para-winglet tape (PWT) in the turbulent flow zone. The effect of pressure drops, flow friction, heat transfer coefficient, and Nusselt number is investigated concerning the Reynolds number varying from 6000 to 30,000. The PWT is examined numerically with three sets of slant angle, namely 10°, 15°, and 20° with a constant pitch of 30 mm in the forward and backward arrangements.

3 Physical Model

The arrangement of PWT in the flow domain of the heat exchanger tube is as shown in Fig. 1. The PWT is arranged in the forward and backward directions to understand their flow behavior. The geometric characteristics of the domain comprise the diameter of the tube ($b = 18.5$ mm), the thickness of the tape ($e = 0.8$ mm), a width of the tape ($y = 16.5$ mm), pitch distance ($w = 30$ mm), length of the test tube ($c = 1500$ mm), and slant angles 10°, 15°, and 20°. The numerical domain is extended to a distance of ten times the diameter of the tube at the inlet and outlet for fully developed flow conditions. The numerical study on the PWT is carried out with a constant pitch for the forward and backward arrangements.

The type of fluid used for the analysis is air, and the properties are maintained to be constant for simplicity. There is no heat exchange between the environment and the tube. Inlet is maintained with the velocity boundary at 300 K. Outlet has a pressure boundary condition with zero-gauge pressure, walls are maintained in the no-slip condition with adiabatic, and the heat is supplied to surface with a constant heat of 100 W. The inlet conditions are varied between Reynolds numbers 6000–30,000 to understand the turbulent behavior of the PWT. The effect of gravity was neglected and a steady incompressible turbulent heat transfer flow analysis for a three-dimensional heat exchanger tube was carried out using the Starccm+ 13.06 CFD software.

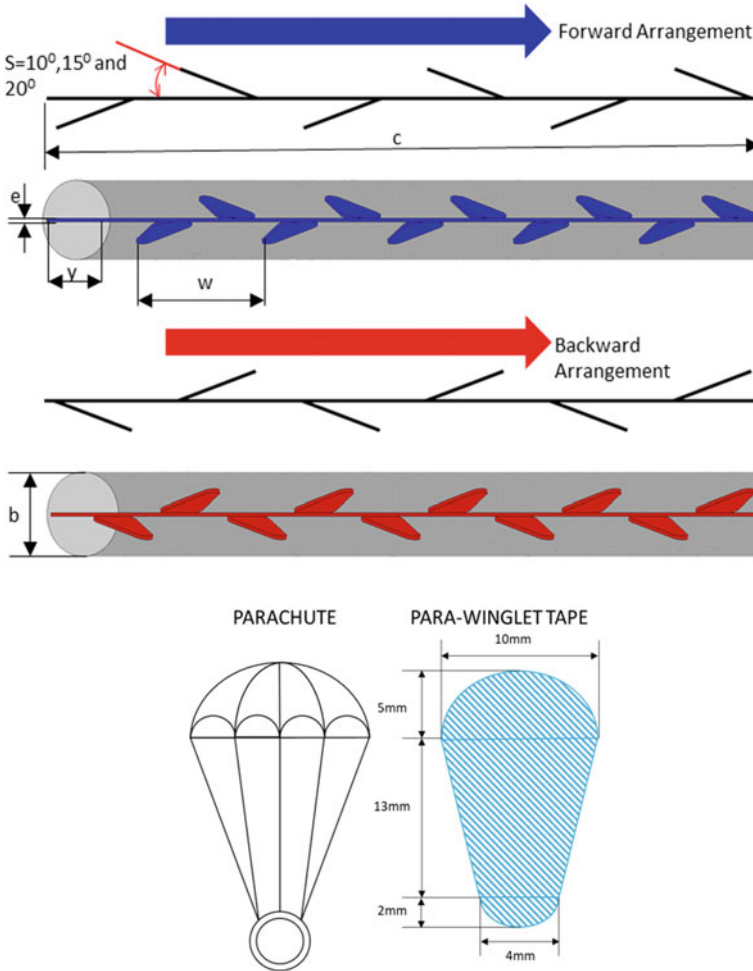


Fig. 1 Geometric details of heat exchanger tube equipped with PWT

4 Numerical Method and Technique

Governing Equation and Turbulent Model CFD technique was used to model the present fluid domain. The technique incorporates mainly three important governing equation continuity equation, momentum equation, and energy equation, where the continuity equation describes the conservation mass, the momentum equation describes the conservation of forces, and the energy equation describes the conservation of energy (temperature). The governing equations are as follows:

Continuity Equation:

$$\frac{\partial}{\partial x_i}(\rho u_i) = 0 \tag{1}$$

Momentum Equation:

$$\frac{\partial}{\partial x_i}(\rho u_i u_k) = \frac{\partial}{\partial x_i} \left(\mu_f \frac{\partial u_k}{\partial x_i} \right) - \frac{\partial p}{\partial x_k} \tag{2}$$

Energy Equation:

$$\frac{\partial}{\partial x_i}(\rho u_i T) = \frac{\partial}{\partial x_i} \left(\frac{\Gamma}{C_p} \frac{\partial T}{\partial x_i} \right) \tag{3}$$

where ρ is the density of the fluid, u is the mean component velocity, p is the pressure, μ_f is the dynamic viscosity of the fluid, C_p is the specific heat, Γ is the thermal conductivity of the fluid, and T is the temperature. The subscripts i and k indicate that the direction is toward i and k .

The models applied in STAR-CCM+ to solve the fluid domain are RANS models with realizable k-epsilon two-layer, segregated flow with exact wall distance and segregated fluid temperature on energy. The transport equation for kinetic energy (k) and dissipation (ϵ) is as shown below:

$$\frac{\partial}{\partial x_i}(\rho u_i k) = \frac{\partial}{\partial x_j} \left\{ \left[\frac{\mu_t}{\sigma_k} + \mu \right] \frac{\partial k}{\partial x_j} \right\} + G_k - \rho \epsilon \tag{4}$$

$$\frac{\partial}{\partial x_i}(\rho u_i \epsilon) = \frac{\partial}{\partial x_i} \left\{ \left[\frac{\mu_t}{\sigma_\epsilon} + \mu \right] \frac{\partial \epsilon}{\partial x_i} \right\} + \frac{\epsilon}{k} [C_{1\epsilon} G_k - \rho C_{2\epsilon} \epsilon] \tag{5}$$

Important Definition The following equations are used to determine the Reynolds number (Re), Nusselt number (Nu), friction factor (f), and thermal performance index [18] (TPI).

$$Re = \frac{\rho u b}{\mu} \tag{6}$$

$$Nu = \frac{h b}{k} \tag{7}$$

$$f = \frac{2b \Delta p}{c \rho u^2} \tag{8}$$

$$\text{TPI} = \frac{Nu_p/Nu_s}{(f_p/f_s)^{1/3}} \quad (9)$$

TPI determines the overall performance of utilizing the para-winglet tape over the smooth pipe. It indicates the ratio of Nusselt number over the ratio of friction factor to the power one-third as shown in Eq. (9). The parameter Nu_p and f_p indicates the Nusselt number and friction factor of the PWT post-analysis. Similarly, Nu_s and f_s are the parameters for a smooth pipe without PWT.

Numerical Method The steady-state segregated flow solver has been selected to solve the turbulent flow heat transfer using the RANS model for turbulence. The wall was treated with two-layer All $y+$ wall treatment with exact wall distance models used with realizable K-epsilon. Segregated fluid temperature models have been selected on the energy front. The convergence criteria have been set to 10^{-6} for momentum, continuity, turbulence, and 10^{-9} for energy. Default convection second-order scheme is used for discretization in the turbulence, momentum, continuity, and energy.

A three-dimensional unstructured tetrahedron mesh has been developed to solve the domain with a $y+$ value equal to unity. A boundary layer meshing technique was adopted near walls to solve the velocity and temperature. Figure 2 shows the meshing details fluid domain the PWT.

Grid Dependency Check In any numerical analysis, the grid dependence check is very important to finalize the number of grids for the simulation. For the current study, five different sets of grids were generated for a 20° slant angle and Reynolds number 12,000. The fluid domain was generated with an unstructured grid of 789190, 1258700, 2634732, 3645127, and 7751839 sets. The percentage deviation in the Nusselt number and friction factor from the different sets of grids are as shown in Table 1. The percentage deviation for 7751839 grids was found to be less than 1% and the same was followed for the remaining cases.

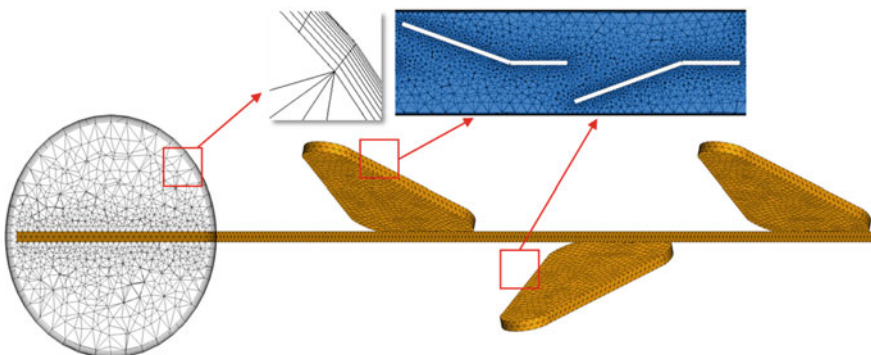


Fig. 2 Grid generation of heat exchanger tube with PWT

Table 1 Grid dependency check

Cell numbers	Nu	Percentage of deviation	f	Percentage of deviation
7,89,190	101.32	–	0.168	–
12,58,700	111.89	9.45	0.196	14.29
26,34,732	119.57	6.42	0.208	5.77
36,45,127	122.2	2.15	0.2175	4.37
77,51,839	123.07	0.71	0.219	0.68

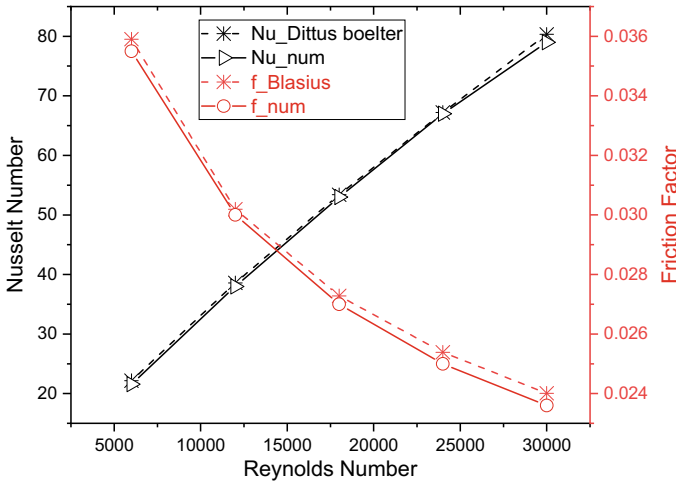


Fig. 3 Comparison between numerical and analytical results of a plain tube

In most of the research, Dittus-Boelter and Blasius correlations are employed to find the analytical values of the plain tube. Figure 3 conveys the approximation Nusselt number and friction factor between the analytical and numerical simulation.

$$Nu_D = 0.023Re_D^{\frac{4}{5}}Pr^{0.3} \tag{10}$$

$$f = 0.316Re^{-\frac{1}{4}} \tag{11}$$

5 Results and Discussion

Figure 4 shows the streamlines for 15° slant angle with forward and backward arrangements at Re12000. In the forward arrangement, the flow tries to move from upstream to the downstream, center region to walls and vice versa. In the backward

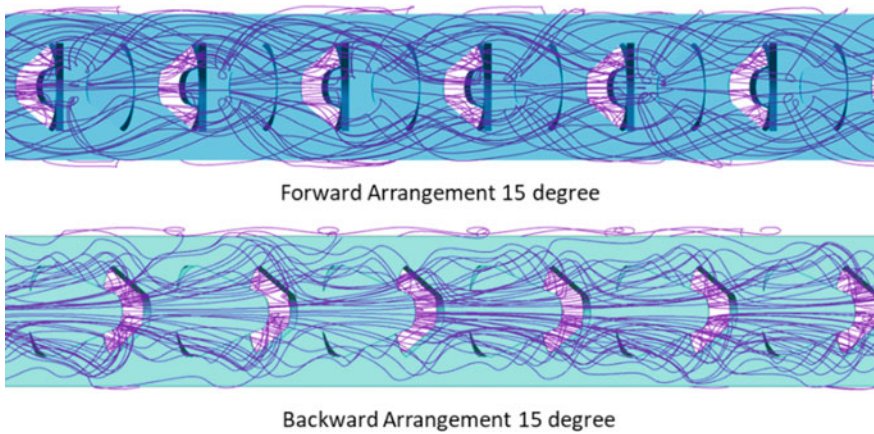


Fig. 4 Streamlines of PWT at 15° inclination for Re_{12000} with forward and backward arrangement of PWT

arrangement, the major portion of the flow moves in the central region. The flow moves toward the wall at the end of the insert with some portion entering the downstream. The forward arrangement shows a better distribution in the center and the wall region than backward arrangement.

The axial velocity in the tube at different cross sections is as shown Fig. 5. The velocity has been shown to increase with the inclusion of the insert in the tube. The maximum velocity near the wall or away from the center will promote the boundary layer mixing and increase the rate of heat transfer near the wall. The inserts in forward direction create a zig-zag pattern of increase in velocity, which is absent in another case. Higher velocity can be seen in the forward arrangement than the backward arrangement over the plain tube. So, both the arrangement can increase overall optimization of heat transfer, but the maximum will be toward the forward arrangement.

The temperature changes in cross sections are as shown in Fig. 6. The temperature distribution on both the case was seen to be almost similar but a let increase in the forward arrangement sections. The maximum temperature is seen on the walls in the backward arrangement and a distributed temperature is seen in the forward arrangement, which proves that forward arrangement is better than backward.

The recirculation in the forward and backward arrangement is as shown in Fig. 7. The recirculation in the forward arrangement was shown to be very much intense in all the four directions which are created as a four-quadrant. The turbulent kinetic energy (TKE) is high near the insert and shifts up and down concerning the insert opening in the forward arrangement. In the backward direction, the circulation swifts to the opposite direction of the insert opening by creating the swirl with less intensity compared to forward.

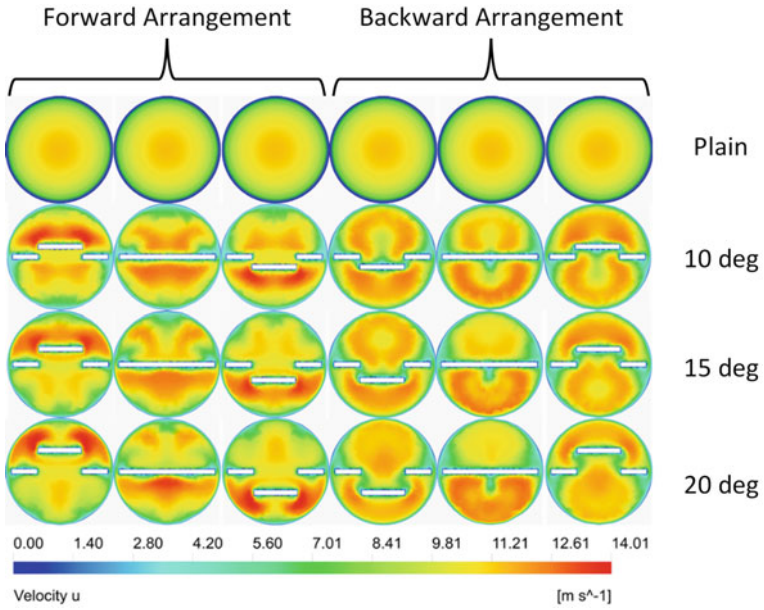


Fig. 5 Axial velocity at $x = 0.37$ m, $x = 0.745$ m and 1.12 m

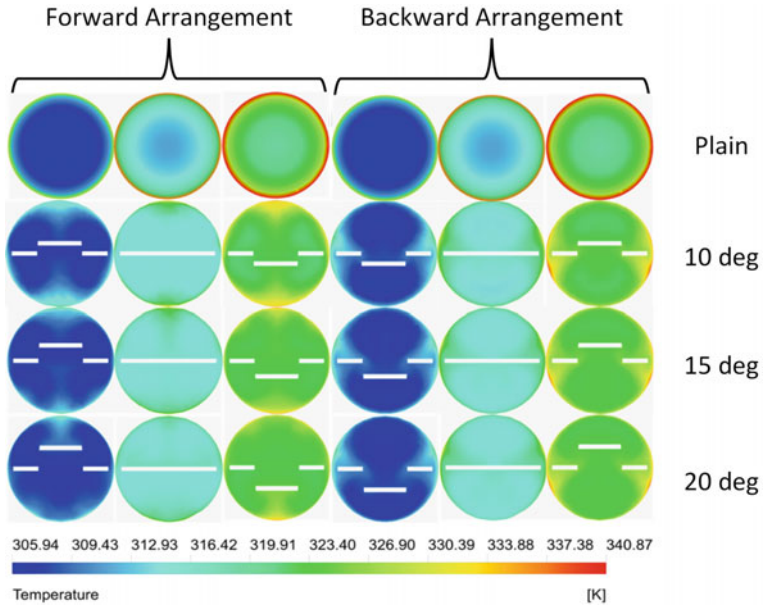


Fig. 6 Temperature at $x = 0.37$ m, $x = 0.745$ m, and 1.12 m

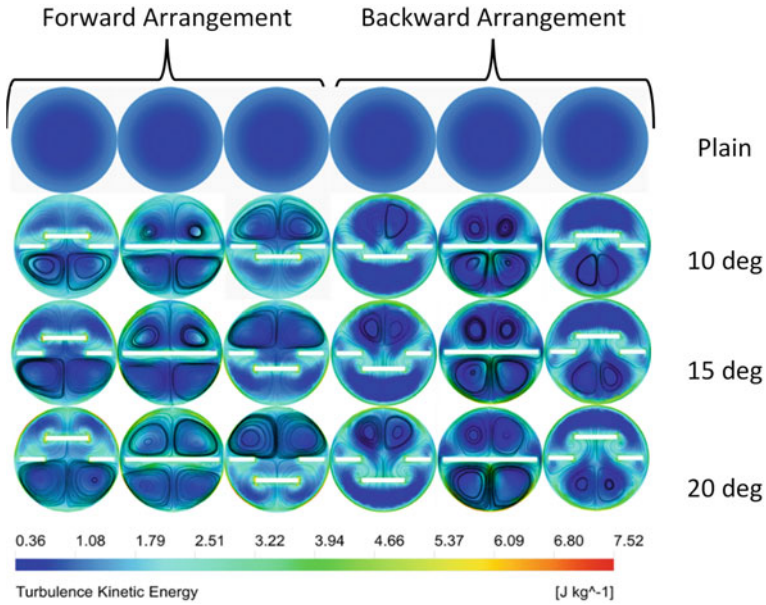
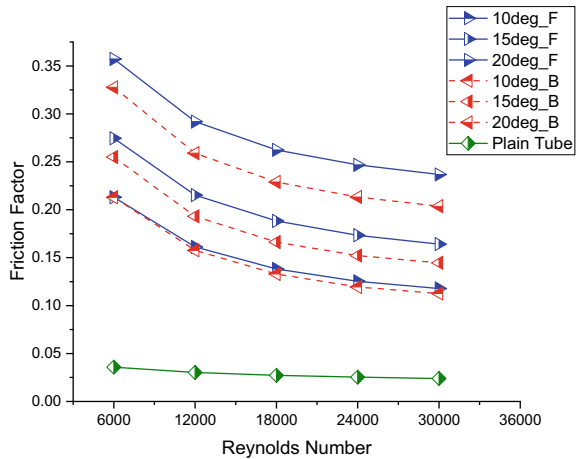


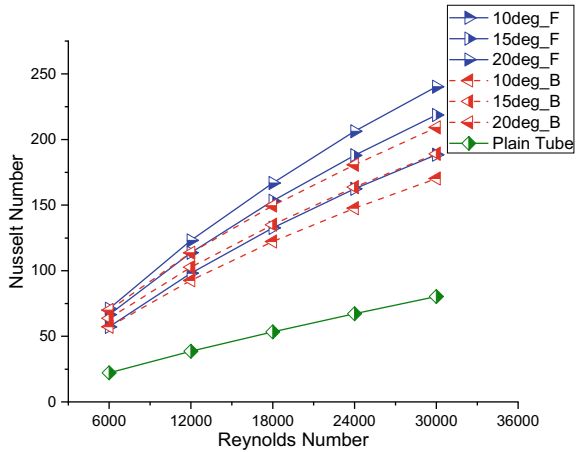
Fig. 7 Turbulent kinetic energy and streamlines at $x = 0.37$ m, $x = 0.745$ m, and 1.12 m

Fig. 8 Friction factor versus Reynolds number for forward and backward arrangements of para inserts at a various slant angle



From Fig. 8, friction factor follows the trend of decrease in the value with the increase in the Reynolds number. The friction factor for a forward and backward arrangements of para inserts at 20° slant angle increase from 9.95 to 9.61 times and 9.12 to 8.38 times concerning plain tube. At 15° slant angle, it varies from 7.64 to 6.82 times and 7.1 to 5.99 times concerning plain tube for forward and backward arrangements. Similarly, for 10° slant angle, the variation is from 5.93 to 4.91 times

Fig. 9 Nusselt number versus Reynolds number for forward and backward arrangements at a various slant angle



and 5.93 to 4.68 times for plain tube. Overall, with the increase in the friction factor the pumping energy also increases with the presence of the PWT.

From Fig. 9, Nusselt number follows the trend of increase in the value with the increase in the Reynolds number. The Nusselt number for forward and backward arrangements of PWT at 20° slant angle increase from 3.2 to 2.99 times and 3.16 to 2.6 times for plain tube. At 15° slant angle, it varies from 3 to 2.72 times and 2.87 to 2.35 times concerning plain tube for forward and backward arrangements. Similarly, for 10° slant angle, the variation is from 2.57 to 2.34 times and 2.58 to 2.11 times concerning plain tube. Overall, with the increase in the Nusselt number, the rate of heat transfer between the flowing fluids will increase in the presence of the PWT.

The thermal performance index (TPI) in Fig. 10 shows the percentage of increase in the rate of heat transfer between the two fluids for the pressure drop

Fig. 10 Thermal performance index (TPI) versus Reynolds number for forward and backward arrangements at a various slant angle

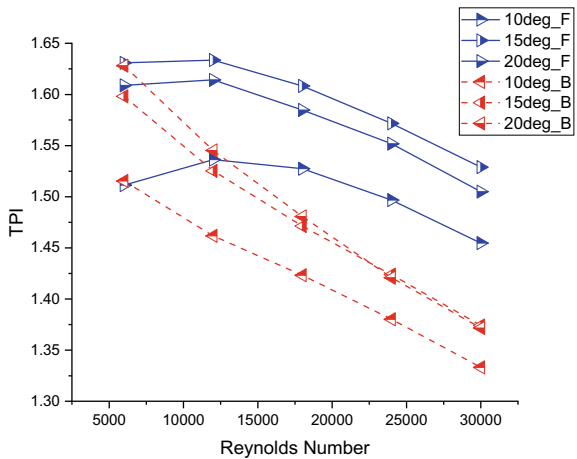
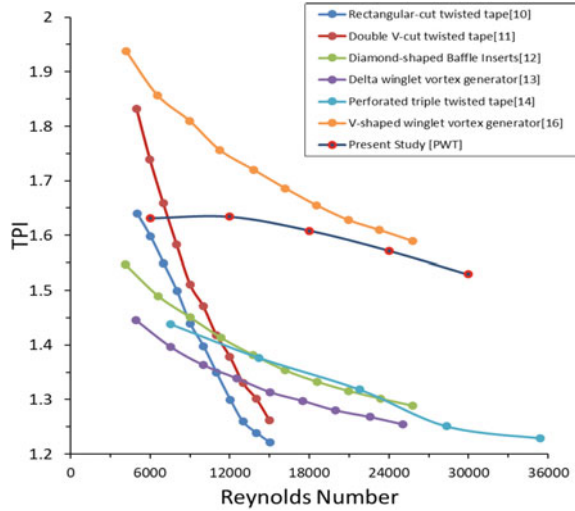


Fig. 11 Comparison of thermal performance index (TPI) with other numerical studies



developed by the presence of the PWT. The maximum performance of the inserts for the forward arrangement is achieved at $Re12000$ varying from 1.63 to 1.53. Similarly, for backward arrangement, it is achieved at $Re6000$ varying from 1.62 to 1.51. At 20° , 15° , and 10° slant angles to the forward direction, the TPI obtained is 1.61 to 1.5, 1.63 to 1.52, and 1.53 to 1.45. Similarly, in the backward direction the TPI was 1.62 to 1.37, 1.59 to 1.37, and 1.51 to 1.33. Overall, the insert with forward direction proves to be offering better optimization at a larger Reynolds number when compared to the backward direction.

The comparison graph in Fig. 11 shows the variation of the respective turbulators of the past studies, namely rectangular-cut twisted tape [10], double V-cut twisted tape [11], diamond-shaped baffle inserts [12], delta-winglet vortex generator [13], perforated triple twisted tape [14], and V-shaped winglet [16]. The PWT has the same trend for other inserts and has a better TPI compared with recently developed ones.

6 Conclusion

Six cases of PWT were investigated in the forward and backward arrangements with a slant angle of 10° , 15° , and 20° against the plain tube. All the inserts as above-mentioned were investigated in the Reynolds number varying from 6000 to 30,000. Following are some of the conclusions which can be drawn through the above investigation:

- The inclusion of PWT in the tube has intensified the turbulent kinetic energy and has resulted in recirculation in-between the inserts.

- Both the arrangements of the PWT have proved their worthiness over the plain tube. The Nusselt number and friction factor increase with the increase in the Reynolds number over the plain tube.
- Maximum, Nusselt number and friction factor were obtained for 20° forward arrangement varying from 3.2 to 2.99 times and 9.95 to 9.61 times.
- A maximum value of 1.63 TPI was obtained at 15° slant angle for forward arrangement and 1.62 TPI was obtained at 20° slant angle for backward arrangement.

The current research presented above deals only with numerical investigation of para-winglet inserts. So, in future the para-winglet inserts are required to be investigated practically for its performance. Right now only turbulent zone of Re varying from 6000 to 30000 is verified. But, in the near future, it is also required to foreseen on the lamina side of the para-winglet insert performance.

References

1. Deshmukh PW, Vedula RP (2014) Heat transfer and friction factor characteristics of turbulent flow through a circular tube fitted with vortex generator inserts. *Int J Heat Mass Transf* 79:551–560
2. Khoshvaght-Aliabadi M, Sartipzadeh O, Alizadeh A (2015) An experimental study on vortex-generator insert with different arrangements of delta-winglets. *Energy* 82:629–639
3. Koolnapadol N, Sripattanapipat S, Skullong S (2016) Effect of pitch spacing of delta-winglets on thermal characteristics in a heat exchanger tube. *J Res Appl Mech Eng* 4(2):166–174
4. Deshmukh PW, Prabhu SV, Vedula RP (2016) Heat transfer enhancement for laminar flow in tubes using curved delta wing vortex generator inserts. *Appl Therm Eng* 106:1415–1426
5. Skullong S, Promvongse P, Jayranaiwachira N, Thianpong C (2016) Experimental and numerical heat transfer investigation in a tubular heat exchanger with delta-wing tape inserts. *Chem Eng Process-Process Intensif* 109:164–177
6. Skullong S, Promvongse P, Thianpong C, Jayranaiwachira N (2017) Thermal behaviors in a round tube equipped with quadruple perforated-delta-winglet pairs. *Appl Therm Eng* 115:229–243
7. Chamoli S, Lu R, Yu P (2017) Thermal characteristic of a turbulent flow through a circular tube fitted with perforated vortex generator inserts. *Appl Therm Eng* 121:1117–1134
8. Piriyarungrod N, Kumar M, Thianpong C, Pimsam M, Chuwattanakul V, Eiamsa-ard S (2018) Intensification of thermo-hydraulic performance in heat exchanger tube inserted with multiple twisted-tapes. *Appl Therm Eng* 136:516–530
9. Wang Y, Liu P, Shan F, Liu Z, Liu W (2019) Effect of longitudinal vortex generator on the heat transfer enhancement of a circular tube. *Appl Therm Eng* 148:1018–1028
10. Nakhchi ME, Esfahani JA (2019) Numerical investigation of rectangular-cut twisted tape insert on performance improvement of heat exchangers. *Int J Therm Sci* 138:75–83, Dec 2018
11. Nakhchi ME, Esfahani JA (2019) Performance intensification of turbulent flow through heat exchanger tube using double V-cut twisted tape inserts. *Chem Eng Process-Process Intensif* 141:107533
12. Khanoknaiyakarn C, Sripattanapipat S, Promvongse P, Skullong S (2019) Heat transfer augmentation in round tube with diamond-shaped baffle inserts. *IOP Conf Ser Mater Sci Eng* 501(1):0–7

13. Zhai C, Islam MD, Simmons R, Barsoum I (2019) Heat transfer augmentation in a circular tube with delta winglet vortex generator pairs. *Int J Therm Sci* 140:480–490, Aug 2018
14. Bhuiya MMK, Roshid MM, Talukder MMM, Rasul MG, Das P (2020) Influence of perforated triple twisted tape on thermal performance characteristics of a tube heat exchanger. *Appl Therm Eng* 167:114769
15. Bahiraei M, Gharagozloo K, Moayedi H (2020) Experimental study on effect of employing twisted conical strip inserts on thermohydraulic performance considering geometrical parameters. *Int J Therm Sci* 149:106178, Nov 2019
16. Promvongse P, Skullong S (2020) Thermo-hydraulic performance in heat exchanger tube with V-shaped winglet vortex generator. *Appl Therm Eng* 164:114424, Apr 2019
17. Khoshvaght-Aliabadi M, Feizabadi A (2020) Performance intensification of tubular heat exchangers using compound twisted-tape and twisted-tube. *Chem Eng Process-Process Intensif* 148:107799
18. Webb RL (1981) Performance evaluation criteria for use of enhanced heat transfer surfaces in heat exchanger design. *Int J Heat Mass Transf* 24(4):715–726

Identification of Gas-Liquid Two-Phase Flow Patterns Using Various Experimental Techniques: A Review



Dhiren Makwana  and Jignesh Thaker 

Abstract The present article covers various aspects of different experimental techniques utilized for identifying the gas-liquid two-phase flow patterns in horizontal pipe. Description of commonly observed gas-liquid two-phase flow patterns is reported in the beginning of the present paper. Utilized experimental techniques for determination of two-phase flow patterns are reviewed in detail. These include optical visual observation technique using high-speed photography system, impedance wire-mesh technique using capacitance probe or conductance probe, pressure fluctuations technique using pressure transmitters or sensors, and photon attenuation (X-ray or γ -ray or neutron beams) or tomographic visualization technique. Detailed descriptions of these techniques along with their utilization by various researchers have been reported in the present review. An attempt has been made through this review article to assist the young researchers who are looking for experimental techniques for determining the two-phase flow patterns precisely and accurately as per their requirements.

Keywords Two-phase flow • Optical visual observation technique • Impedance wire-mesh technique • Pressure fluctuations technique • Photon attenuation technique

1 Introduction

Two-phase gas-liquid flows are commonly observed in different applications such as petroleum, chemical, aerospace, mechanical, biological, bio-medical, and nuclear industries. The complexity in gas-liquid flow is associated with the interfacial interaction which leads to different geometric configurations of the flow structure.

D. Makwana (✉)

Gujarat Technological University, Ahmedabad, Gujarat, India
e-mail: dhirenphd201819@gmail.com

J. Thaker

Adani Institute of Infrastructure Engineering, Ahmedabad, Gujarat, India

These geometric shapes which are commonly referred as two-phase flow patterns or flow regimes that arise due to various operating parameters such as pressure, temperature, pipe orientation, mass velocity, and fluid properties in two-phase flow systems. Distinguishable of these two-phase flow patterns is available in literature [1, 2]. These are mainly classified into three basic patterns, namely separated flow patterns, intermittent flow patterns, and dispersed flow patterns. Sketches of different flow patterns for gas-liquid two-phase flow in horizontal pipe are presented in Fig. 1.

Two-phase flow patterns, separated by an uninterrupted interface, are called separated flow patterns. These may include stratified, wavy-stratified, annular, and wavy kind of flow patterns. At moderately low gas and liquid flow rates, the gas remains to the upper and the liquid to the bottom of the pipe (due to buoyancy effect) and these phases are separated by an undisturbed horizontal interface. Such flow pattern is referred as stratified flow pattern because the liquid and gas flow in stratified manner for horizontal orientation as shown in Fig. 1a. With increase in small amount of gas flow rate, irregular waves are formed on the interface (see Fig. 1b). This flow pattern is referred as stratified-wavy flow pattern. Still, with further increase in gas flow rate, continuous waves with similar amplitude are formed as shown in Fig. 1c, known as wavy flow pattern. The amplitude of waves depends on the relative flow rates of the two phases. However, wave crest does not reach at the top of the pipe in wavy flow pattern. The wave climbs up on the sides of the pipe and leaves thin films of the liquid on the wall after the passageway of the wave.

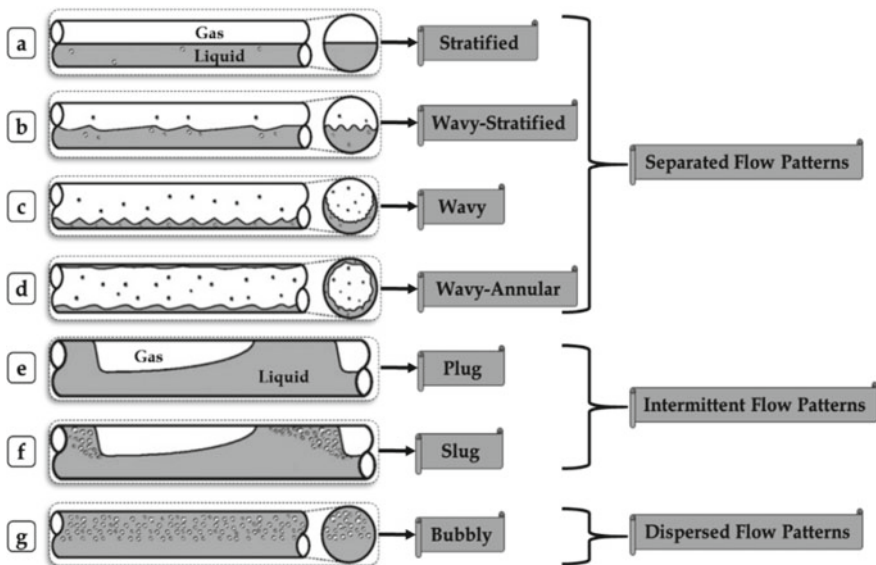


Fig. 1 Different flow patterns for gas-liquid two-phase flow in a horizontal pipe

At further higher liquid flow rates, these interfacial waves can elevate to the highest level of pipe and form fluid (liquid) blockages. This creates intermittent flow pattern, and it is characterized by irregular (intermittent) appearance of liquid pocket possessing the whole area of the pipe. These liquid pockets are separated from each other by an elongated long bubble passing through the top of a fluid (liquid) layer (due to buoyancy effect). Intermittent flow pattern can be classified into two sub-patterns, namely plug flow and slug flow. At the point when the liquid pocket (plug) is observed free from gas bubbles, the pattern is called as plug flow (see Fig. 1e). Plug flow commonly observes at extremely low gas velocities, and it comprises of liquid plug and elongated gas bubble. Slug flow is characterized as non-appearance of aeration (bubbles) inside the liquid slugs separated from each other by elongated bubbles as shown in Fig. 1f and it is generally found at higher gas flow rates.

At very high gas flow rate, the liquid develops a constant annular film around the diameter (perimeter) of the pipe and gas flows through the center of the pipe. This pattern is referred as annular flow pattern. Because of gravity, the liquid film at the base of the pipe observes to be much thicker than the film at the top. In some cases, interface between the liquid annulus and gas core is disturbed by small-amplitude waves. Droplet can be observed and dissipated in the gas core. Such pattern is called as wavy-annular flow pattern (see Fig. 1d). At high liquid flow rate and for low gas flow rate, small gas bubbles are scattered all through the continuous liquid phase (bubbly flow or additionally called dispersed flow). These air pockets (bubbles) accumulate in the upper level of the pipe due to buoyancy effect (see Fig. 1g).

For better understanding and explaining the rigorous dynamics of mentioned two-phase flow patterns, it is necessary to distinguish these flow patterns accurately. The aim of the present paper is to accumulate the database/study of various researchers who have classified or identified two-phase flow patterns by adopting different experimental approaches or techniques in horizontal pipe. This review can significantly assist young researchers for implementing the right experimental approach/technique for determining the two-phase flow patterns precisely as per their requirements.

2 Techniques Adopted for Identifying the Intermittent Flow

One of the simplest methods or approaches to identify two-phase flow patterns is by observing the gas-liquid two-phase flow through transparent pipe. Such experimental approach is called as an optical visual observation technique. This technique is widely used for visualizing the flow at low fluid velocities, but it is quite complex to observe the flow behavior at higher velocity. Photographs captured with a high-speed flash/frame can help to overcome this issue at higher fluid velocities.

Since industrial pipelines are non-transparent in nature, many other techniques have been used by various researchers to identify the flow patterns. These techniques or approaches are:

- Impedance wire-mesh technique using capacitance or conductance probe;
- Pressure fluctuations technique;
- Photon attenuation (X-ray or γ -ray or neutron beams) or tomographic visualization technique and ultrasonic echoes reflection technique.

Detailed descriptions of each of the above-mentioned techniques are presented in following sub-sections.

2.1 Optical Visual Observation Technique

Optical visual observation technique is widely used by researchers for identifying the two-phase flow patterns due to its non-intrusive type, means it cannot disturb the fluid flow. In this technique, normal, digital, and high-speed camera have been used by numerous researchers for capturing the images of two-phase flow patterns. These captured images at high frame rate are analyzed in detail for better understanding of dynamics of each pattern of two-phase flow. Literatures on optical visual observation technique for identifying two-phase flow patterns reported by various researchers are tabulated in Table 1. The details on author name, internal diameter (ID) of test section, and test fluid used in their experimental investigations and their main research content are highlighted in Table 1.

2.2 Impedance Wire-Mesh or Wire-Sensor Technique

Many of the researchers have used impedance wire-mesh procedure (electrical tomography) to recognize the two-phase flow patterns. This method is intrusive in nature, implies wire probe/wire-mesh sensor needs to be kept inside the fluid flow. The field of electrical tomography can be divided into two types, either conductance or capacitance, in light of the strategy by which the electrical field is created. The decision essentially depends on electrical properties of fluids, regardless of whether they may conduct or not.

Conductance Tomography Multiple conductance probes (flush mounted) are used in conductance tomography. These probes are evenly distributed to the entire cross section of the pipe. Two different methodologies can be used for measurement: first, by maintaining the constant potential difference between the electrodes and measuring the current across the electrodes; and second by measuring the potential difference at the electrodes while keeping constant current. Necessary condition for conductance tomography is required to have direct electric contact of

Table 1 Literature on optical visual observation technique for identifying two-phase flow patterns reported by various researchers

Author	Test fluids and test section ID	Main research content
Govier and Omer [7]	Air-water, 26 mm	Flow visualization study was performed in transparent cellulose acetate butyrate pipe and new data were obtained
Lin and Hanratty [8]	Air-water, 25.4 mm and 95.3 mm	Experimental investigations have been carried out and visualized the flow patterns in Plexiglas section and also the effect of tube diameter on flow pattern was analyzed
Ghajar and Tang [1]	Air-water, 25.4 mm	Flow visualization study was performed in polycarbonate test section using Nikon camera and flow pattern plot for two-phase horizontal and inclined (2, 5, 7) flows were taken
Vaze and Banerjee [2]	Air-water, 25.4 mm	Two-phase flow patterns were captured for various inlet flow conditions of air and water phases and flow pattern map has been made. Stratified to slug flow transition has been captured using flow visualization
Thaker and Banerjee [9]	Air-water, 25.4 mm	Intermittent/discontinuous-type two-phase flow sub-patterns were captured using high-speed photography (FASTCAM made Photron Camera) and their detailed dynamics have been reported. These dynamics have been correlated with severe erosion-corrosion problems
Akhlaghi et al. [10]	Air-water, 44 mm	Intermittent flow and its characteristics investigated by combining the experimental visualization and numerical investigation studies
Deendarlianto et al. [11]	Air-water, 26 mm	The hydrodynamic behavior on transition to slug flow of air-water two-phase flow in horizontal pipes

sensing electrodes with conducting fluid for getting tomographic imaging for flow patterns. But in case of plug and slug flow, it cannot be performed with flush-mounted method due to intermittent appearance of gas and liquid phases. In order to address this challenge, Reinecke et al. [3] suggested an extension of the conductance approach (as shown in Fig. 2) that used wire-mesh electrodes. The arrangement consists of 29 wires of 0.1 mm diameter in three planes. These planes are set at 3 mm apart, and the angle formed between wires of two successive planes is 60°.

Involved impedance with all pairs of neighboring wires in the same plane is measured so as to obtain the projection of the conductivity allocation in the direction of the wires. The impedance measurement is performed with the sampling of each pair of electrodes with a frequency of 1000 Hz. Due to this process, three independent projections have been formed. These projections are transformed into the conductivity distribution and further utilized as void fraction distribution.

The limitation of the approach mentioned by Reinecke et al. [3] was reconstruction step of the image as it cannot be determined the equations in terms of time

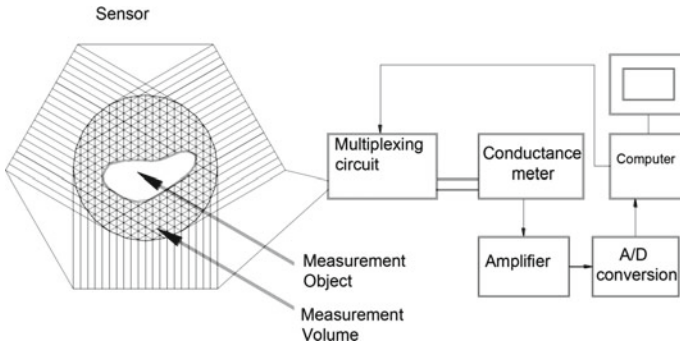


Fig. 2 Schematic diagram for wire-mesh tomographic measurement technique [3]

overhead as reported by Prasser et al. [4]. In addition, Prasser et al. [4] proposed a novel wire sensor for tomographic imaging which cannot time consuming and does not require the image reconstruction procedure. The schematic representation of the sensor is shown in Fig. 3. The arrangement consists of sixteen electrode wires of 0.12 mm diameter in each plane. The two electrode planes are 1.5 mm apart one for receiving and other for transmitting signals. A grid of 16×16 measurement points was equally distributed in the cross section of the pipe. The transmitter electrodes are activated by a multiplex circuit in consecutive order in each measurement cycle.

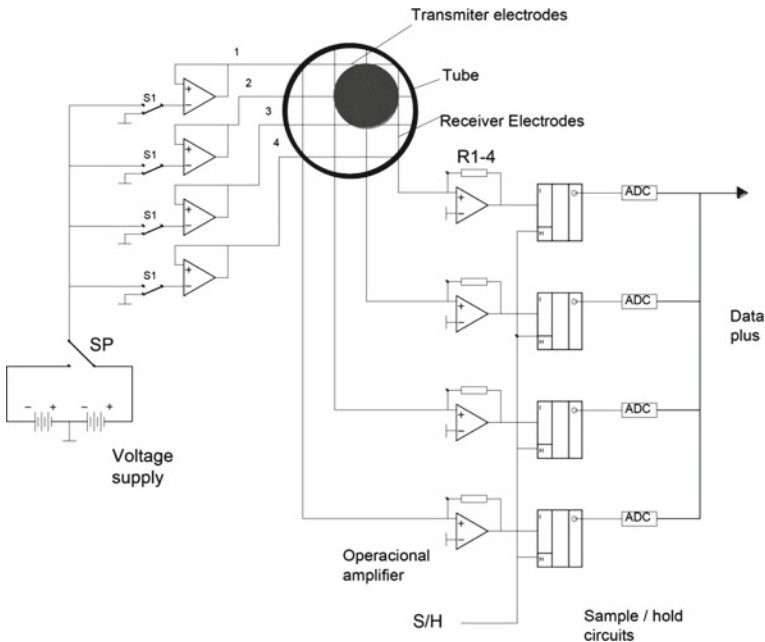


Fig. 3 Schematic representation of two-plane electrode-mesh device [4]

Table 2 Literature on impedance wire-mesh technique using capacitance or conductance probe for identifying two-phase flow patterns reported by various researchers

Author	Test fluids	Test section ID (mm)	Measurement technique
Hoogendoorn [12]	Water and air	50, 91	Capacitance tomography
Barnea et al. [13]	Water and air	25	Conductance tomography
Andritsos et al. [14]	Water and air	25.2, 95.3	Conductance tomography
Dykhno et al. [15]	Water and air	95.3	Conductance tomography
Ko et al. [16]	Water and air	40	Ring-type impedance sensor
Vieira et al. [17]	Water and air	76	Conductance tomography
Arunkumar et al. [18]	Oil-air	4.7	Capacitance tomography

Capacitance Tomography In this technique, the sensing electrodes are not electrical connected with fluid but the electrodes are located at outer periphery of the pipe wall. The permittivity, the dielectric property of each phase available in system is the imaging parameter. Reconstruction of the image depends upon the permittivity partition obtained from the measurement of the electrical capacitance which has been taken among all possible pairs of electrodes. The literature on impedance wire-mesh technique using capacitance or conductance probe for identifying two-phase flow patterns reported by various researchers is summarized in Table 2.

2.3 Pressure Fluctuation Technique

Many of the researchers have used pressure fluctuation method to identify the two-phase flow patterns, but, they must have to validate their results with flow visualization results of earlier researchers or their own results. This technique is intrusive type, means pressure probe/sensor has been placed inside the fluid flow. In this technique, instantaneous pressure signals are recorded for various inlet flow conditions and then identified the behavior of the signals respective to the flow pattern. Thus, it can be determined different flow patterns based on their variation in pressure signal analysis. Hubbard and Dukler [5] were the first who detect pressure changes and distinguish two-phase flow patterns. They proposed an approach to distinguish the flow patterns from the spectral dispersion of the wall pressure variations. These pressure signals have been measured on horizontal air-water flow facility.

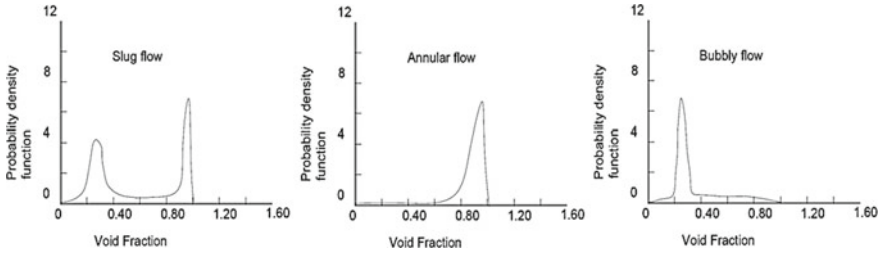


Fig. 4 X-ray absorption PDF of void fraction [6]

2.4 Photon Attenuation Technique

Photon attenuation method is widely known for medicine and non-destructive testing. This approach is applied for multi-phase flow due to their non-intrusive nature. Images made by utilizing the present approach are reproduced from a set of integral measurements. The photon attenuation procedure depends on the absorption of X-beams or γ -beams or neutron beams by the liquid phase and its interrelation to the void fraction. The beams can either come along a single beam as utilized by Jones and Zuber [6] or variety of numerous beams passing over the flow path. It was a critical work utilizing X-ray absorption, which featured the convenience of numerical investigation methods for flow pattern identification. For identifying the two-phase flow patterns, they have used probability density functions of the void fraction variations as shown in Fig. 4.

3 Summary and Conclusions

In summary, presented review relates with three experimental techniques adopted for identifying the two-phase flow patterns and it suggests that optical visual observation technique (using high-speed camera) is frequently employed as diagnostic tool for lab-scale model due to its availability, non-intrusiveness, easier and safer operational functionality, and moderate cost. Such techniques provide only qualitative information and require transparent test section facility. From industrial perspective (especially for non-transparent piping system), impedance wire-mesh (using conduction or capacitance probe) technique is more convenient due to its higher sensitivity and it is widely used for the measurement of void fraction or shape/location of the interface in two-phase pipe flow. Such techniques have one major limitation in terms of their intrusive nature as they disturb the flow behavior (especially at the interface). Precise measurement of quantitative parameters (such as liquid height) is thus challenging due to intrusive nature of these probes. Pressure fluctuations technique is not a very reliable technique because many times different flow patterns at different inlet flow conditions produce nearly similar spectral



distribution of wall pressure fluctuations. This can create difficulty while identifying the flow patterns based on the pressure signals. In photon attenuation technique, imaging modalities (X-ray, γ -ray, MRI, etc.) are too slow and they do not achieve sufficient spatial resolution compared to impedance and optical measurement techniques.

References

1. Ghajar AJ, Tang CC (2007) Heat transfer measurement, flow pattern maps and flow visualization for non-boiling two-phase flow in horizontal and slightly inclined pipe. *Heat Transfer Eng* 28(6):525–540
2. Vaze MJ, Banerjee J (2011) Experimental visualisation of two-phase flow patterns and transition from stratified to slug flow. *IMEchE, Part C J Mech Eng Sci* 225:382–389
3. Reinecke N, Petrisch G, Boddem M, Mewes D (1998) Tomographic imaging of the phase distribution in a two-phase slug flow. *Int J Multiphase Flow* 24(4):617–637
4. Prasser HM, Bottger A, Zschau J (1998) A new electrode-mesh tomography for gas liquid flows. *Flow Meas Instru* 9(2):111–119
5. Hubbard MG, Dukler AE (1996) The characterization of flow regimes for horizontal two-phase flow I: statistical analysis of wall pressure fluctuations. In: *Proceedings of the heat transfer and fluid mechanics institute*. Stanford University Press, pp 385–400
6. Jones OC Jr, Zuber N (1975) The interrelation between void fraction fluctuations and flow pattern in two-phase flow. *Int J Multiphase Flow* 2:273–306
7. Govier GW, Omer MM (1962) The horizontal pipe line flow of air-water mixtures. *Can J Chem Eng* 40:93–104
8. Lin PY, Hanratty TJ (1987) Effect of pipe diameter on flow patterns for air-water flow in horizontal pipes. *Int J Multiphase Flow* 13(4):549–563
9. Thaker J, Banerjee J (2016) Influence of intermittent flow sub-patterns on erosion-corrosion in horizontal pipe. *J Petrol Sci Eng* 145:298–320
10. Akhlaghi M, Taherkhani M, Nouri NM (2020) Study of intermittent flow characteristics experimentally and numerically in a horizontal pipeline. *J Natural Gas Sci Eng* 79:103326
11. Deendarlianto O, Rahmandhika A, Widyatama A, Dinaryanto O, Widyaparaga A (2019) Indarto: experimental study on the hydrodynamic behavior of gas-liquid air-water two-phase flow near the transition to slug flow in horizontal pipes. *Int J Heat Mass Transf* 130:187–203
12. Hoogendoorn CJ (1957) Gas-liquid flow in horizontal pipes. *Chem Eng Sci* 9:205–217
13. Barnea D, Shoham O, Taitel Y, Dukler A (1980) Flow patterns transition for gas liquid flow in horizontal-inclined pipes. *Int J Multiphase Flow* 6:217–225
14. Andritsos N, Williams L, Hanratty TJ (1989) Effect of liquid viscosity on the stratified-slug transition in pipe flow. *Int J Multiphase Flow* 15:877–892
15. Dykhno LA, Williams LR, Hanratty TJ (1994) Maps of mean gas velocity for stratified flow with or without atomization. *Int J Multiphase Flow* 20:691–702
16. Ko MS, Lee SY, Lee BA, Yun BJ, Kim KY, Kim S (2013) An electrical impedance sensor for water level measurements in air-water two-phase stratified flows. *Meas Sci Technol* 24:95301–95311
17. Vieira RE, Kesana N, Torres C, Mclaury BS, Shirazi SA, Schleicher E, Hampel U (2014) Experimental investigation of horizontal gas-liquid stratified and annular flow using wire-mesh sensor. *J Fluids Eng* 136:121301–121315
18. Arunkumar S, Adhavan J, Venkatesan M, Balakrishnan AR (2015) Characterization of gas-liquid two phase flows using dielectric sensors. *Flow Meas Instru* 45:274–279

Fuzzy Grey Relational-Based Risk Analysis of Steam Generating Unit



Priyank Srivastava Srivastava , Yash Sharma, Prikshit Rana, Rohit Gupta, Melfi Alrasheedi , and Naveen Kumar

Abstract The objective of this article is to identify the proactive and reactive risk identification and analysis of steam generating unit (SGU) in sugar plant. The expert discussion and fish-bone diagram were used for identification and presentation of operational risk, and in the second phase, fuzzy multi-attribute decision-making method (MADM) and failure mode and effect analysis (FMEA) were used to carry out the risk analysis. The conventional FMEA is susceptible to uncertainties. This uncertainty lies in the perfectly white and perfectly black area. This region of confusion is also called grey area. The limitation of conventional FMEA was removed by the application of fuzzy-based grey relational approach for prioritizing cause of failure. The results of the analysis were shared with maintenance engineer and system analyst. The output of the analysis will assist maintenance engineer for better understanding of risk in SGU and thereby planning its proper maintenance.

Keywords Risk analysis · FMEA · Fuzzy grey relational analysis

P. S. Srivastava (✉) · Y. Sharma · P. Rana · R. Gupta · N. Kumar
Amity University, Noida, India
e-mail: psrivastava5@amity.edu

Y. Sharma
e-mail: ys83836@gmail.com

P. Rana
e-mail: ranaprikshit97@gmail.com

R. Gupta
e-mail: rohitsinghal278@gmail.com

N. Kumar
e-mail: nkumar12@amity.edu

M. Alrasheedi
King Faisal University, Hofuf, Saudi Arabia
e-mail: malrasheedy@kfu.edu.sa

1 Introduction

Risk is present almost in every industry. Identification of risk and its mitigation is a very important task, to make sure that the industry should work for a long time without breakdown. Risk can be defined as a threat to the health of a worker, occurred due to internal or external factors and should be kept in check to avoid huge loss. Risk can be determined as the danger or loss to any organization or an industry either financially or as danger to human life [1]. Risk present in an industry can be classified as internal as well as external. The internal risk can occur due to the human, breakdown of line, and physical damage to any part and machinery of the industry. External risk can occur due to the change in government policies, natural disaster, etc. There are many factors that can lead to the risk in an industry. Financial risk can also take place in the industry. Risk management of a process industry like sugar processing industry is important because it is contributing towards the GDP or economy of the country directly or indirectly [2, 3]. There are several accidents that had taken place in the past which could have been controlled or the damage due to them could be minimized if the proper risk management has been done. For example, the Bhopal gas tragedy that took place in the year 1984 was one of the massive incidents in industrial disaster. The proper maintenance process was not taken at that time and around 8000 people were killed in the same week of the incident and other 8000 died in the whole month. In such big industry, small negligence can lead to a huge loss to human life working at that place. In the city of Texas, another incident took place which is the blast in the oil refinery. Oil refinery is a place where a little negligence can lead to a huge massacre. In that blast, around 20 workers lost their lives and around 200 people were heavily injured. Risk management is necessary whether it is oil industry or chemical industry. The accidents could have been avoided or impact could have been less, if proper risk analysis was done. Risk analysis is required for identifying failure cause, prioritize it, proper maintenance planning and emergency planning for saving asset, i.e. men and machine. There has been lots of research using MADM for risk analysis [4–10]. The present article expounds the application of fuzzy-based grey relational analysis for prioritizing failure cause of steam generating unit in sugar plant located in northern region of India. The rest of the paper is organized as Sect. 2: reviews the literature related to risk identification and analysis, Sect. 3: presents the research methodology, Sect. 4: discusses the case study, Sect. 5: discusses result, and Sect. 6: gives conclusion and future course of action.

2 Literature Review

This section presents comprehensive literature review of the tool used for risk analysis, methods used for risk analysis and techniques of removing uncertainty from analysis. For extracting the relevant literature, search engines of Scopus and

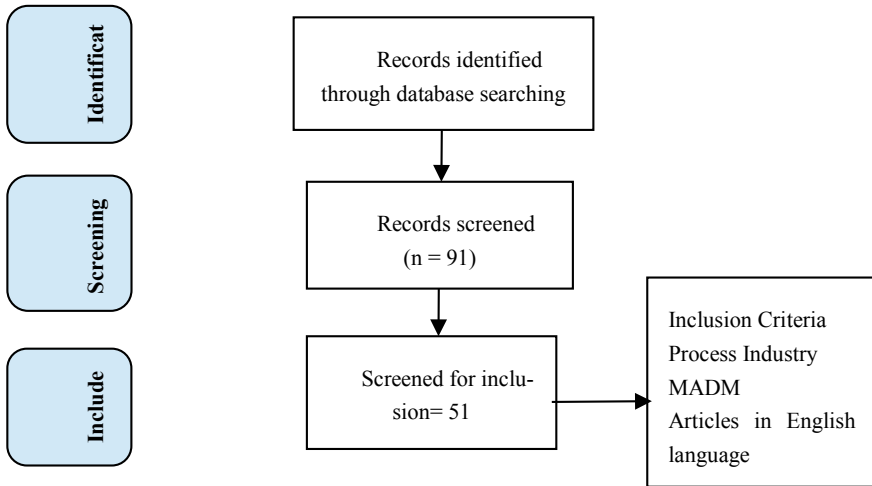


Fig. 1 Flow of literature review

Web of Sciences were used. The extraction was done using protocol. The PRISMA flowchart [11] (refer Fig. 1) was used for literature review.

The keywords are “Risk Analysis AND Process Study”; “Risk Analysis AND MADM”.

The literature review was divided into sections as follow.

2.1 Risk Identification

Identification of risk is one of the initial and important steps in risk analysis process. It is done with consultations of experts, checking the logbooks of the failure data and literature. Once risk is identified then for proper understanding, the findings are shown diagrammatically showing each subsystem and associated causes of failure. Some of the techniques used for risk identification are fish-bone diagram [12, 13], fault tree analysis (FTA) [14, 15], bow tie [16], etc.

2.2 Risk Analysis MADM Techniques

The failure mode and effect analysis (FMEA) is used for risk analysis. The risk analysis is based on risk priority number (RPN). The RPN is product of occurrence (Oc), severity (Sr) and probability of non-detection (Dn). Table 1 shows the rating of Oc, Sr and Dn, respectively.

Table 1 Rating of Oc, Sr and D_n

Rating	Meaning	Severity	Occurrence	Not detection
1	Almost none	No breakdown of any component	Failure is very unlikely to happen	Detected 9/10 times
2, 3	Low	Minor breakdown of component which can be fixed with some adjustment	These failures are relatively rare	Detected 7/10 times
4, 5, 6	Medium	Breakdown of any component which can be replaced without any harm for the whole machine	Occasional	Detected 5/10 times
7, 8	High	Permanent damage of component and harmful for machine not for people	More frequent failures	Detected 2/10 times
9, 10	Very high	Hazardous/permanent damage of the component which may cause harm the people	These are common failures	Detected 0/10 times

This approach was developed by NASA for APPOLLO mission. This technique has been used extensively for risk analysis in varied area of application [17–21]. There has been the application of MADM approach for evaluating RPN [22, 23]. However, the conventional FMEA approach is susceptible to errors due to uncertainty issues. There have been studies of removing these errors using fuzzy-integrated approach [24–26].

2.3 Integrated Approach

In recent years, there has been the trend of integrating MADM approach for risk analysis. In most of the MADM approach, weights of expert’s judgement (refer Table 2), attributes, variables in RPN calculation, etc. are either calculated or taken from some reference study.

Table 2 Linguistic variables and crisp scores for TFN

Linguistic variable	Symbol	Crisp score
Almost none	AN	0.9983
Low	L	2.515
Medium	M	5.015
High	H	7.515
Very high	VH	9.324

In the articles addressing MADM approach, the above-mentioned weights are calculated using one type of MADM approach and prioritization is done using another MADM approach [27–29].

2.4 Objective

From the above literature reviewed, the following objectives have been defined:

- (a) To assess the causes of failure and its effect in the system and subsystems.
- (b) To perform risk analysis using fuzzy-integrated FMEA and MADM techniques and validate the result.
- (c) To prioritize the various causes of risk and failures with the help of risk analysis.

3 Research Methodology

The research methodology of the research work is as follow (refer Fig. 2):

- (a) Risk identification: The risk identification is done using expert judgements regarding the subsystems, literature and records in logbooks.

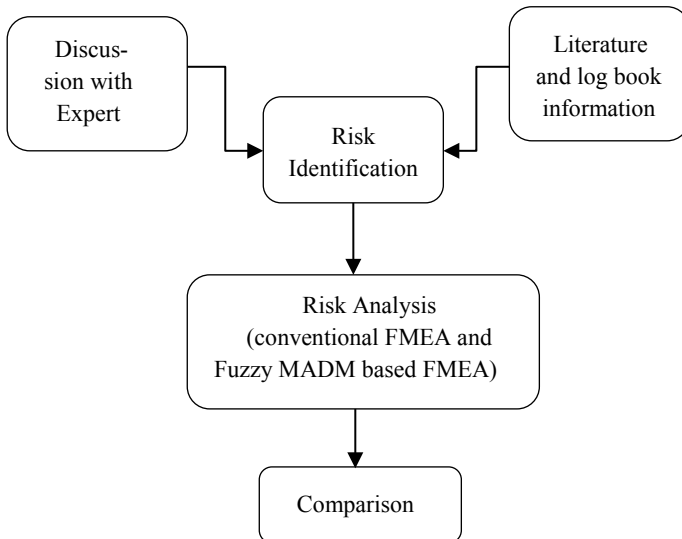


Fig. 2 Research methodology

- (b) Risk analysis: The risk analysis is performed using conventional FMEA and fuzzy MADM-based FMEA.
- (c) The results from both methods will be compared for comprehensive analysis of results.

4 Case Study

This case study was done for SGU of a sugar mill located in northern part of India. It is having capacity of 2500 TCD with a generation of 2 MW electricity. From the experts, the FMEA table was constructed and conventional RPN [12] was calculated using Tables 1 and 2 respectively (refer Table 3).

As the conventional FMEA is susceptible to uncertainty error, therefore fuzzy grey relational analysis was done to evaluate grey RPN [30] [1]. The equal weights of O_c , S_r and D_n were considered for analysis (Table 4).

Table 3 FMEA sheet and RPN

Components	Potential effect of failure	Potential cause of failure	O	S	D	RPN
Furnace	Boiler thermal efficiency loss	Coal quality (CF1)	4	5	6	120
		Slag formation (CF2)	5	4	6	120
Coal burner	Deregulated combustion	Improper cleaning (CF3)	6	6	3	108
		Wear and tear (CF4)	7	4	5	140
Water tubes	Loss of steam and hot water flow	Tube puncture or failure (CF5)	2	8	5	80
Super heater	Operational efficiency loss	External and internal tube surface damage (CF6)	4	8	4	128
Re-heater	Tube failure	Decrease in the thickness (CF7)	5	8	5	200
		Tube fissures (CF8)	5	7	5	175
Economizer	Operational efficiency loss	Shoot presence in cast iron pipes (CF9)	4	7	5	140
Safety valve	Steam pressure loss	Valve tear (CF10)	6	6	5	180
		Improper cleaning (CF11)	5	5	6	150
I D/FD fan	Operational loss	Improper lubrication (CF12)	5	5	5	125
Pump	Operational loss	Improper lubrication (CF13)	2	8	3	48
I D fan motor	Operational loss	Overheating (CF14)	2	5	5	50
Hydraulic coupling	Operational loss	Rubber hose failure (CF15)	6	6	6	216

Table 4 Grey relational RPN

Potential cause of failure	GR(O)	GR(S)	GR(D)	Weighted OSD
Coal quality (CF1)	0.715019	0.715019	0.715018524	0.707868339
Slag formation (CF2)	0.715019	0.715019	0.715018524	0.707868339
Improper cleaning (CF3)	0.715019	0.715019	1	0.801912226
Wear and tear (CF4)	0.556443	0.715019	0.715018524	0.655538307
Tube puncture or failure (CF5)	1	0.556443	0.715018524	0.749582194
External and internal tube surface damage (CF6)	0.715019	0.556443	0.715018524	0.655538307
Decrease in the thickness (CF7)	0.715019	0.556443	0.715018524	0.655538307
Tube fissures (CF8)	0.715019	0.556443	0.715018524	0.655538307
Shoot presence in cast iron pipes (CF9)	0.715019	0.556443	0.715018524	0.655538307
Valve tear (CF10)	0.715019	0.715019	0.715018524	0.707868339
Improper cleaning (CF11)	0.715019	0.715019	0.715018524	0.707868339
Improper lubrication (CF12)	0.715019	0.715019	0.715018524	0.707868339
Improper lubrication (CF13)	1	0.556443	1	0.843626081
Overheating (CF14)	1	0.715019	0.715018524	0.801912226
Rubber hose failure (CF15)	0.715019	0.715019	0.715018524	0.707868339

Table 5 Comparative table

Potential cause of failure	Conventional RPN	Ranking	Grey RPN	Ranking
(CF1)	120	10	0.707868339	4
(CF2)	120	10	0.707868339	4
(CF3)	108	11	0.801912226	2
(CF4)	140	7	0.655538307	5
(CF5)	80	12	0.749582194	3
(CF6)	128	8	0.655538307	5
(CF7)	200	2	0.655538307	5
(CF8)	175	4	0.655538307	5
(CF9)	140	6	0.655538307	5
(CF10)	180	3	0.707868339	4
(CF11)	150	5	0.707868339	4
(CF12)	125	9	0.707868339	4
(CF13)	48	13	0.843626081	1
(CF14)	50	14	0.801912226	2
(CF15)	216	1	0.579073783	5

5 Result and Discussion

The comparative table has been shown in Table 5. It is quite evident that there is some agreement in the ranking done by both the methods. From Table 2, it is clear that for different rating two RPNs are same. Also, for same linguistic variables, RPN is different. It can lead to confusion in the minds of system analyst and maintenance engineer.

6 Conclusion

The article expounds the use of fuzzy grey relational approach for assessing failure cause of SGU in sugar mill. The uncertainty issue in conventional approach was removed by the use fuzzy MADM approach. This case study will help the maintenance engineer and system analyst to plan for effective maintenance policy. The error in logbooks is one of the limitations. In future course of action, risk mitigation can be planned for the risk identified. Other fuzzy MADM approaches can be used to evaluate RPN and comparison of the results can be done.

References

1. Panchal D, Srivastava P (2019) Qualitative analysis of CNG dispensing system using fuzzy FMEA–GRA integrated approach. *Int J Syst Assur Eng Manag* 10(1):44–56 Feb
2. Srivastava P, Khanduja D, Ganesan S (2019) Fuzzy methodology application for risk analysis of mechanical system in process industry. *Int J Syst Assur Eng Manag* 11(2):297–312
3. <http://agriexchange.apeda.gov.in/MarketReport/Reports>
4. Panchal D, Mangla SK, Tyagi M, Ram M (2018) Risk analysis for clean and sustainable production in a urea fertilizer industry. *Int J Qual Reliab Manag* 35(7):1459–1476
5. Panchal D, Kumar D (2016) Integrated framework for behaviour analysis in a process plant. *J Loss Prev Process Ind* 40:147–161
6. Panchal D, Kumar D (2017) Risk analysis of compressor house unit in thermal power plant using integrated fuzzy FMEA and GRA approach. *Int J Indus Syst Eng* 25(2):228–250
7. Aghaie A (2004) Evaluating ISO 9001: 2000 implementation using Fault Tree Analysis (FTA). *Total Qual Manag Bus Excellence* 15(7):971–983 Sep
8. Chanamool N, Naenna T (2016) Fuzzy FMEA application to improve decision-making process in an emergency department. *Appl Soft Comput J* 43:441–453
9. Kutlu AC, Ekmekçioğlu M (2012) Fuzzy failure modes and effects analysis by using fuzzy TOPSIS-based fuzzy AHP. *Expert Syst Appl* 39(1):61–67
10. Chang C-L, Wei C-C, Lee Y-H (1999) Failure mode and effects analysis using fuzzy method and grey theory. *Kybernetes* 28:1072–1080
11. Moher D, Liberati A, Tetzlaff J, Altman DG, Antes G (2009) Preferred reporting items for systematic reviews and meta-analyses: the PRISMA statement. *J Chin Integr Med* 7 (9):889–896

12. Agarwal M, Narayanan GAS, Srivastava P (2018) Risk prioritization in a gas power plant using fuzzy inference system. In: 2018 8th international conference on cloud computing, data science and engineering (confluence), pp 753–757
13. Srivastava P, Agarwal M, Narayanan A, Tandon M, Tulsian M (2019) Mitigation of risk in CNG station using fuzzy-integrated technique, pp 535–542
14. Song Y-H, Yu H-Q, Lv W (2018) Risk analysis of dairy safety incidents in China. *Food Control* 92:63–71 Oct
15. Aneziris ON, Papazoglou IA, Konstantinidou M, Nivolianitou Z (2014) Integrated risk assessment for LNG terminals. *J Loss Prev Process Indus* 28:23–35, Apr
16. Khakzad N, Khan F, Amyotte P (2013) Quantitative risk analysis of offshore drilling operations: a Bayesian approach. *Saf Sci* 57:108–117 Aug
17. Panchal D, Jamwal U, Srivastava P, Kamboj K, Sharma R (2018) Fuzzy methodology application for failure analysis of transmission system. *Int J Math Oper Res* 12(2):220–237
18. Basheer A, Tauseef SM, Abbasi T, Abbasi SA (2019) Methodologies for assessing risks of accidents in chemical process industries. *J Fail Anal Prev* 19(3):623–648 Jun
19. Takalo SK, Sadr Abadi ARN, Vesal SM, Mirzaei A, Nawaser K (2013) Fuzzy failure analysis: a new approach to service quality analysis in higher education institutions (Case study: Vali-e-asr University of Rafsanjan-Iran). *Int Educ Stud* 6(9):93–106
20. Parameshwaran R, Srinivasan PSS, Punniyamoorthy M (2010) An integrated approach for performance enhancement in automobile repair shops. *Int J Bus Excellence* 3(1):77–104
21. Wang H-S, Ho L-H (2012) Application of service blueprint and FMEA in security management. *Int J Innov Comput Inf Control* 8(10 B):7467–7485
22. Ilangkumaran M, Shanmugam P, Sakthivel G, Visagavel K (2014) Failure mode and effect analysis using fuzzy analytic hierarchy process. *Int J Productivity Qual Manag* 14(3):296–313
23. Fouladgar MM, Yazdani-Chamzini A, Zavadskas EK (2012) Risk evaluation of tunneling projects. *Arch Civil Mech Eng* 12(1):1–12 Mar
24. Srivastava P, Khanduja D, Ganesan S (2019) Fuzzy methodology application for risk analysis of mechanical system in process industry. *Int J Syst Assurance Eng Manag* 11(2):297–312 Sep
25. Al-Humaidi HM, Tan FH (2012) Using fuzzy failure mode effect analysis to model cave-in accidents. *J Perform Constructed Facil* 26(5):702–719
26. Liao R, Zhang Y, Yang L, Zheng H, She X (2014) A cloud and evidential reasoning integrated model for insulation condition assessment of high voltage transformers. *Int Trans Electr Energy Syst* 24(7):913–926 Jul
27. Selvan TA, Jegadheesan C, Ashoka Varthanan P, Senthilkumar KM (2013) A novel FMEA approach for ranking mould designs in foundries. *Life Sci J* 10(2):51–60
28. Cebi S (2011) Developing a fuzzy based decision making model for risk analysis in construction project. *J Multiple-Valued Logic Soft Comput* 17(4):387–405
29. Li Y-L, Yang Q, Chin K-S (2019) A decision support model for risk management of hazardous materials road transportation based on quality function deployment. *Transp Res Part D: Transport Environ* 74:154–173
30. Panchal D, Jamwal U, Srivastava P, Kamboj K, Sharma R (2018) Fuzzy methodology application for failure analysis of transmission system. *Int J Math Oper Res* 12(2):220–237

Development and Testing of Binary Organic Eutectic Mixture for Thermal Energy Storage



Alok Kumar Ansu, Pooja Singh, and Ravi Kumar Sharma

Abstract The most efficient way to store thermal energy is the latent heat energy storage method because of its high energy storage density and almost constant freezing/melting temperature. The present study deals with the preparation and development of eutectic mixture phase change materials (PCMs). The mixture consists of polyethylene glycol (PEG) and myristic acid (MA) and is prepared in different mass fractions. The thermal properties such as melting point and latent heat were measured by differential scanning calorimetry (DSC) technique, and the changes in the chemical/functional group of the mixture were analysed by Fourier transform and infrared spectroscopy (FT-IR) method. The DSC thermal analysis results show that the binary system of PEG-MA in the ratio of 60:40 wt%, 50:50 wt % and 40:60% forms the eutectic mixture with a melting temperature of 58.34, 60.3 and 59.07 °C and the latent heat of fusion is 187.21, 178.05 and 171 J/g, respectively. FT-IR results show that the material is chemically stable as there is not much changes in the functional group of the mixture irrespective of the weight %. These results make the eutectic mixture a potential candidate for heat storage in passive solar heating applications with respect to the climatic conditions.

Keywords Polyethylene glycol · Myristic acid · Phase change materials · Thermal energy storage

A. K. Ansu (✉) · P. Singh · R. K. Sharma
Department of Mechanical Engineering, Manipal University Jaipur,
Jaipur, Rajasthan 303007, India
e-mail: alokansu12341@gmail.com

P. Singh
e-mail: pooja1720@gmail.com

R. K. Sharma
e-mail: ravipvb@gmail.com

1 Introduction

Industrial evolution and population growth in the past few years have resulted in a vast increase in energy demand, and this leads to the depletion of fossil fuels. The exponential increase in energy demand has created an imbalance between energy supply and demand. Renewable energy such as solar energy has played a very important role to bridge the gap between the energy demand and supply. The main constraint in the use of solar energy is the nonuniform and time-dependent nature. The intensity of sunlight varies during the day and does not exist during the night. The energy can be stored in various forms such as thermal, chemical, and mechanical during the day can overcome these problems.

Being an intermittent source of energy, the utilization of solar energy can be more attractive and reliable if it is associated with energy storage system. Since the solar energy supply is variable in daytime and zero at night, considerable amount of solar energy should be stored during the daytime to meet the demands at night. The excess energy can be stored in thermal energy storage (TES) system and can be later used wherever required. Thermal energy storage (TES) is one of the most efficient ways of storing thermal energy [1]. It balances the mismatch between energy demand and supply which in turn improving the system utility. Thermal energy can be stored by three methods, i.e. sensible heat (by heating and cooling a material), latent heat thermal energy storage (by melting and solidifying a material) and chemical heat (by breaking and forming molecular bonds). Out of the three, latent heat thermal energy storage is preferred because it provides much higher storage density, with a smaller temperature difference between storing and releasing heat [2, 3]. Phase change materials (PCMs) in the thermal energy storage have been the key area of research for the last three–four decades. In the recent years, latent heat thermal energy storage system (LHTES) has been mostly used for solar applications such as solar heating, solar drying and in wall of the buildings. The selection of heat storage material as phase change material in LHTES plays an important role from the point of view of thermal efficiency, economic feasibility, and utility life of the system. These materials are very important for thermal protection and optimal utilization of energy. Myristic acid and polyethylene glycol are organic PCMs, and these materials are non-toxic and do not cause any hazard to the environment [4]. The payback period of any thermal energy storage system is approximately between two to two and half years. So, if a PCM can sustain their thermal properties up to this time, it can pay-back the money spent on it and after this, it will be free to use. The organic PCMs have advantage of being non-toxic to use so they possess better thermal and chemical reliability. They can easily be used for five years or more. In most of the cases, the equipment used for building comfort or water/air heating systems can be completely replaced by PCMs. PCMs are mainly classified as organic, inorganic and eutectic. Organic PCMs (OPCMs) consist of paraffins, fatty acids, polyethylene glycol and esters. OPCMs have high energy storage density, no supercooling, less change in volume and approximately negligible change in temperature during phase transition. Inorganic PCMs are salt,

salt hydrates, hydroxides and nitrates. Inorganic PCM has high thermal conductivity as compared to OPCM, and the melting temperature can go up to 1500 °C, but on the other hand, inorganic PCM suffers with congruent melting and supercooling effect. Corrosion can also take place in a sealed container. Eutectics are the mixture of two compounds such as organic–organic, organic–inorganic and inorganic–inorganic. The advantage of eutectic over the organic and inorganic PCM is that it can achieve any desired value of latent heat and melting temperature by varying the weight percentage of the two materials and can be later used in thermal energy storage applications. The expansion of binary and ternary eutectics as new PCMs for heating and cooling thermal energy storage applications has gained substantial interest in current years [5–8]. Literature review shows [9–11] that lauric and palmitic acids have prudent thermal and heat transfer properties and are the promising PCMs for solar applications like solar heating, buildings, solar heater, etc. Kadir et al. [12] prepare a eutectic mixture of lauric and palmitic acid with 69 and 31 wt%. The mixture has a melting temperature and latent heat of 35.2 °C and 166.3 J/g, respectively, which can be used for low temperature solar heating applications such as solar heating and agriculture heating. Lauric acid and myristic acid have high melting point, so Sedat et al. [13] prepare lauric–myristic eutectic mixture and get the suitable melting temperature of 34.28 °C and relatively high latent heat of 166.8 J/g using DSC analysis so that the PCM can be used for low heating energy storage applications. A good number of organic and inorganic PCMs and their mixture have been prepared for thermal energy storage [14–18]. Polyethylene glycol has been used by some of the researchers [3, 19–21], and the materials have proved to be a potential candidate for energy storage. Polyethylene glycol comes with different molecular weight. PEG has a high energy storage density, no supercooling and minimal temperature change during phase transition. The present work shows the preparation and development of eutectic PCM comprising PEG 6000 and myristic acid. The thermal properties such as melting temperature and latent heat of fusion were determined using differential scanning calorimetry (DSC) analysis technique at different weight fraction. Fourier transform infrared radiation technique was also carried out to analyse the chemical stability of the mixture. The results reveal that the mixture can be a promising candidate to be used in a thermal energy storage system.

2 Materials Preparation

Polyethylene glycol 6000 with 98% purity and myristic acid with 98% purity were obtained from Sigma Aldrich Company and were used without any further purification. The commercial cost of these PCMs is about Rs 150 per kilograms. The binary mixture is prepared in different weight combinations by homogeneous mixing of the two materials using simple melt blending method, and after that at room temperature, it was allowed to cool. The thermal properties like latent heat of fusion and phase change temperature were identified using DSC analysis

(Shimadzu DSC-60 Plus) at constant rate of heating 5 °C/min. In a sealed aluminium pan, sample was kept. The latent heat of fusion is obtained by the area under the differential scanning calorimetry curve, and by obtaining intersection point of tangent on highest slope and adjoining the line of onset and end set peaks, the melting point was calculated. By fixing the maximum and minimum temperature of 90 and 30 °C, the complete freezing and melting in DSC have been ensured. The material was kept idle for 3 min on both extreme temperatures for removing thermal histories. The thermal properties of the eutectic were measured for minimum three times, and the average of that was considered for ensuring the accurate results. The chemical stability of the sample was also measured using Fourier transform and infrared (FTIR) analysis (Bruker Alpha-II) between wavenumber 500 and 4000 cm^{-1} with spectral resolution of 2 cm^{-1} .

3 Results and Discussion

3.1 Thermal Properties

The latent heat and melting temperature of PEG6000 and myristic acid binary eutectic mixture were measured by DSC method, and the values are shown in Table 1. The DSC thermogram curve is shown in Fig. 1.

It can be observed from table that the latent heat of fusion of the binary mixture is 187.21 J/g when the weight % of PEG is 60% and MA is 40%, whereas the melting temperature is 58.34 °C. The latent heat decreases to 178.05 J/g when the ratio of each material is 50% and further decreases to 171 J/g when the wt% of myristic acid increases in the mixture. It can be noticed that the melting temperature is maximum when the wt% of the both the materials is equal. The change in melting temperature is very less irrespective of the wt% of the any materials. The latent heat and phase change temperature of all the samples are almost same with little variations. Phase change enthalpies of the studied eutectic samples are indicative of the successful synthesis of composite. The energy release and storage capacity of PCMs deteriorate in sample S3 may be due to the restricted movement of PEGs chains and impurities. In a small temperature range, the PCMs can melt completely and can store its latent heat, and hence, the PCMs having narrow melting temperature range have a better thermal performance.

Table 1 Thermal properties of PEG6000 and myristic acid mixture

Sample	Eutectic composites (PEG 6000: MA, wt%)	Latent heat (J/g)	Melting point (°C)
S-1	60:40	187.21	58.34
S-2	50:50	178.05	60.3
S-3	40:60	171	59.07

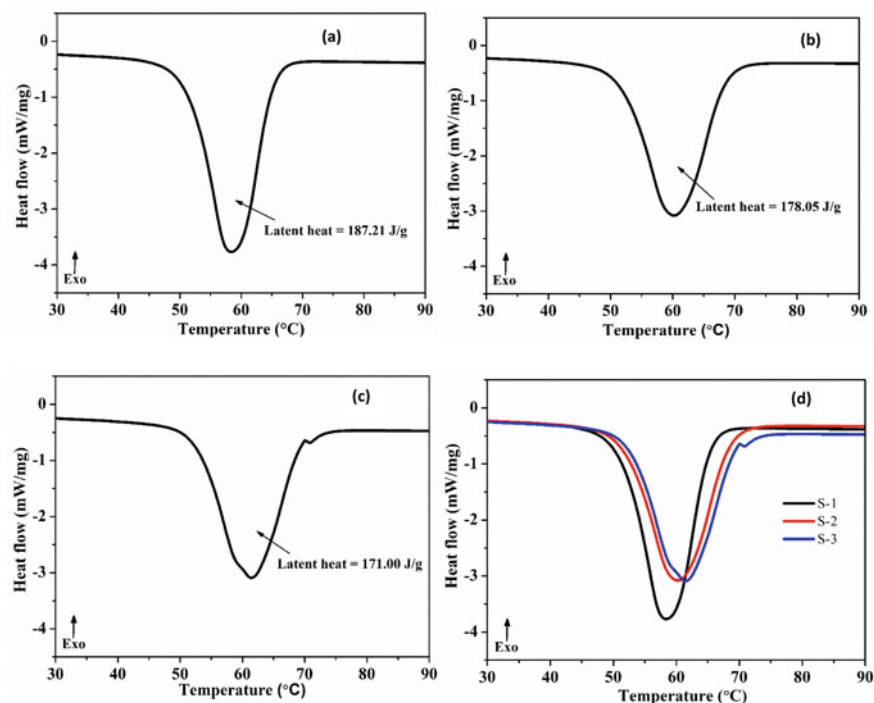


Fig. 1 DSC curve of PEG and myristic acid mixture (a) PEG wt 60% (b) PEG wt 50% (c) PEG wt 40% (d) Combined curve of all sample

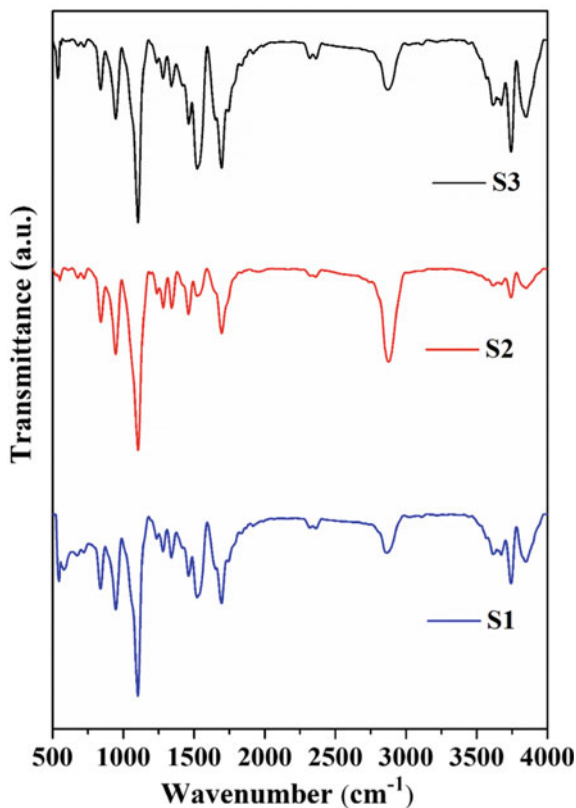
The onset temperature of all the samples is between 51.73 and 52.9 °C, whereas end set temperature lies between 65.28 and 69.29 °C.

3.2 Chemical Reliability

In order to find the chemical stability of the eutectic mixture, FTIR analysis was carried out which is shown in Fig. 2 between the wave number 500–4000 cm^{-1} with spectral resolution of 2 cm^{-1} . An overview of FTIR results obtained from S1 to S3 eutectic composite indicates no significant new peaks were observed other than characteristic peaks of MA/PEG6000 eutectic composite which proves that the interaction between the functional group of MA and PEG is physical in nature. Composite consists of a strong peak at wave number 524 cm^{-1} and 1106 cm^{-1} .

The peak at wave number 1103 cm^{-1} is strong due to C–O stretching vibrations. The absorption peak at 947 cm^{-1} and 840 cm^{-1} represents stretching peak mainly due to –OH swinging and rocking mode which is characteristics of aliphatic chain of myristic acid. The broad bands at different level are associated with stretching and bending vibrations of –OH groups. The strong and medium bands are related

Fig. 2 FTIR spectra of eutectic mixture of varying weight fraction of PEG and myristic acid



with ether groups (H₂C–O–CH₂) of PEGs and carboxyl group (O–C=O) of MA. The strong bands are the signs of the stretching vibrations of –CH₃, –CH₂, –CH groups of synthesized composites. The spectra of the eutectic PCMs include most of the characteristic peaks of both PCM, which confirms that there is no chemical reaction between them. However, slight shift in peak of sample is due to the physical interaction of the functional group between the PEG and myristic acid. It can be concluded that the prepared eutectic composite of organic PCMs has good chemical reliability, which will guarantee the operational stability of eutectic composites in practical TES applications.

4 Conclusion

Eutectic mixture was prepared using simple melt blending method of different weight fractions by using PEGs of molecular weight 2000 and myristic acid. It can be concluded that using DSC analysis the latent heat of fusion ranges from 187.71 to 171.0 J/g and the melting temperature of the mixture varies from 57 to 49.5 °C.

FTIR spectrum shows that not much change in the peaks has occurred with altering the weight fraction of materials. From the DSC thermal analysis, it can be concluded that the PEG—MA eutectic mixtures are attractive PCMs for heat storage in passive solar heating systems like solar water heating, in building wall boards with respect to the climate requirements. The effective utilization of these materials depends upon the development of an efficient and economical thermal energy storage system designed according to suitable climate conditions. However, for further modification of the mixture, thermal cycle testing can be done for the materials for 500, 1000, 1500 cycles to analyse its efficiency and reliability that can be checked for the materials and also for how many years the material can be used.

Acknowledgements The financial support for this research is provided by the Manipal University Jaipur under the grant of the Endowment Fund (EF/2017-18/QE04-04). For characterization facilities, Authors also want to convey their sincere gratitude to the Central Instrumentation Facilities at Jiwaji University Gwalior, India.

References

1. Sharma RK, Ganesan P, Tyagi VV, Metselaar HSC, Sandaran SC (2015) Developments in organic solid–liquid phase change materials and their applications in thermal energy storage. *Energy Convers Manag* 95:193–228
2. Sharma A, Tyagi VV, Chen CR, Buddhi D (2009) Review on thermal energy storage with phase change materials and applications. *Renew Sustain Energy Rev* 13(2):318–345
3. Ansu AK, Sharma RK, Tyagi VV, Sari A, Ganesan P, Tripathi D (2020) A cycling study for reliability, chemical stability and thermal durability of polyethylene glycols of molecular weight 2000 and 10000 as organic latent heat thermal energy storage materials. *Int J Energy Res* 44(3):2183–2195
4. Mehling H, Cabeza LF (2007) Phase change materials and their basic properties. *Therm Energy Storage Sustain Energy Consum*, 257–277
5. Dimaano MNR, Watanabe T (2002) Performance investigation of the capric and lauric acid mixture as latent heat energy storage for a cooling system. *Sol Energy* 72(3):205–215
6. Sari A, Kaygusuz K (2002) Thermal performance of a eutectic mixture of lauric and stearic acids as PCM encapsulated in the annulus of two concentric pipes. *Sol Energy* 72(6):493–504
7. Roxas-Dimaano MN, Watanabe T (2002) The capric and lauric acid mixture with chemical additives as latent heat storage materials for cooling application. *Energy* 27(9):869–888
8. Feldman D, Banu D, Hawes DW (1995) Development and application of organic phase change mixtures in thermal storage gypsum wallboard. *Sol Energy Mater Sol Cells* 36(2):147–157
9. Abhat A (1983) Low temperature latent heat thermal energy storage: heat storage materials. *Sol Energy* 30(4):313–332
10. Hasnain SM (1998) Review on sustainable thermal energy storage technologies, Part I: heat storage materials and techniques. *Energy Convers Manag* 39(11):1127–1138
11. Sari A, Kaygusuz K (2002) Thermal and heat transfer characteristics in a latent heat storage system using lauric acid. *Energy Convers Manag* 43(18):2493–2507
12. Tuncbilek K, Sari A, Tarhan S, Ergüneş G, Kaygusuz K (2005) Lauric and palmitic acids eutectic mixture as latent heat storage material for low temperature heating applications. *Energy* 30(5):677–692

13. Keleş S, Kaygusuz K, Sarı A (2005) Lauric and myristic acids eutectic mixture as phase change material for low-temperature heating applications. *Int J Energy Res* 29(9):857–870
14. Zalba B, Marin JM, Cabeza LF, Mehling H (2003) Review on thermal energy storage with phase change: materials, heat transfer analysis and applications. *Appl Therm Eng* 23(3): 251–283
15. Zhang JJ, Zhang JL, He SM, Wu KZ, Liu XD (2001) Thermal studies on the solid–liquid phase transition in binary systems of fatty acids. *Thermochim Acta* 369(1–2):157–160
16. Zuo J, Li W, Weng L (2011) Thermal properties of lauric acid/1-tetradecanol binary system for energy storage. *Appl Therm Eng* 31(6–7):1352–1355
17. Zuo J, Li W, Weng L (2011) Thermal performance of caprylic acid/1-dodecanol eutectic mixture as phase change material (PCM). *Energy Build* 43(1):207–210
18. Sari A, Sari H, Önal A (2004) Thermal properties and thermal reliability of eutectic mixtures of some fatty acids as latent heat storage materials. *Energy Convers Manag* 45(3):365–376
19. Sharma RK, Ganesan P, Tyagi VV, Mahlia TMI (2016) Accelerated thermal cycle and chemical stability testing of polyethylene glycol (PEG) 6000 for solar thermal energy storage. *Sol Energy Mater Sol Cells* 147:235–239
20. Fu X, Xiao Y, Hu K, Wang J, Lei J, Zhou C (2016) Thermosetting solid–solid phase change materials composed of poly (ethylene glycol)-based two components: flexible application for thermal energy storage. *Chem Eng J* 291:138–148
21. Qi GQ, Liang CL, Bao RY, Liu ZY, Yang W, Xie BH, Yang MB (2014) Polyethylene glycol based shape-stabilized phase change material for thermal energy storage with ultra-low content of graphene oxide. *Sol Energy Mater Sol Cells* 123:171–177

A Review of Natural Gas—Diesel Dual Fuel Engines



Manoj Gwalwanshi  and Gaurav Mittal

Abstract Easy availability and good combustion characteristics of natural gas (NG) make it attractive as an alternative to diesel fuel. The concept of NG–diesel dual fuel engine (NG + Diesel), in which NG serves as the major fuel, while diesel serves as the pilot fuel, is an attractive concept. In this review paper, the concept of NG + Diesel engine and its performance are analyzed. This paper reports the influence of various parameters, such as the amount of pilot fuel injected, NG–diesel proportion, speed of engine, load, fuel injection strategies, and EGR on the performance of NG + Diesel engines. It is noted that the NG + Diesel concept is a very promising low-temperature combustion technique to control NO_x and particulate matter (PM) emissions. However, the emissions of CO and hydrocarbons (HC) depend on various factors and generally exceed the emissions from standard diesel engines.

Keywords Natural gas · NG + diesel · Dual fuel engine

1 Introduction

Diesel is the most popular fuel for C.I. engines [1, 2]. Characteristics such as high compression ratio, high efficiency, adaptability and reliability make diesel engines extremely popular in comparison to all other engines [3–6]. Despite of these advantages of diesel engines, they have limitations due to depleting fuel resources and pollution considerations, particularly NO_x and PM emissions [7–9]. Use of NG as an alternative to diesel can mitigate these limitations. Emissions from combustion of NG have reduced NO_x and almost zero PM [10, 11]. However, its low

M. Gwalwanshi (✉) · G. Mittal
Department of Mechanical Engineering, Graphic Era (Deemed to be University), Bell Road,
Clement Town, Dehradun 248002, Uttarakhand, India
e-mail: manoj.gwalwanshi@geu.ac.in

G. Mittal
e-mail: gauravmittal@geu.ac.in

reactivity as compared to diesel limits the efficiency and power output of NG-operated engines [12]. In order to accelerate combustion in NG engines, diesel-induced ignition is considered. This concept is known as NG + Diesel dual fuel engine concept [13].

2 Natural Gas

NG is obtained as a volatile component of the crude oil, or it can be obtained in dry form from oil gas field, and hence, the composition of NG differs slightly from source to source [14]. It is a mixture of various alkanes (primarily methane) and some other gases [15]. Use of NG in engines can reduce the emission of NO_x by 50–87%, CO_2 by 20–30%, with almost zero smoke and PM [16]. Its high octane number and lower cost have inspired its use in S.I. engines [17, 18]. The concept of NG–diesel engine is, however, still an area of research.

2.1 NG + Diesel in C.I. Engines

As compared to diesel, NG has lower cetane number and is resistant to autoignition [19, 20]. Wei et al. [9] had discussed some methods to resolve this problem, among which one is the dual fuel concept and the other is the high pressure direct injection (HPDI) concept. They differ in the technique used to introduce NG in the engine. In the dual fuel approach, homogeneous mixture of NG and air in combustion chamber is ignited by using diesel injection. In the HPDI mode, a small quantity of diesel is injected at the end of compression and then NG is injected directly. In both cases, the small amount of diesel fuel works as the pilot fuel that initiates combustion of NG. The HPDI mode requires major changes to the engine structure [21]; high cost is also an issue. In contrast, the dual fuel mode is easier to implement [9, 22, 23]. In this mode, NG is considered as the chief fuel while diesel is a secondary pilot fuel [24]. Since the pilot fuel works as an initiator of combustion only, its amount can be decreased to lower than 10% of the entire quantity of the fuel supplied [25]. In the current scenario, the combustion of NG + Diesel is one of the most attractive low-temperature combustion (LTC) techniques for heavy duty engines.

3 Performance Characteristics of NG + Diesel Engines

3.1 Effect of Pilot Fuel Amount

Abd Alla et al. [26] experimentally explored the influence of the amount of pilot fuel on the features of a NG + Diesel engine. The results in Fig. 1 show that the

emissions of unburned hydrocarbon increase with a decrease in the amount of the pilot fuel. It was detected that for very low equivalence ratio, the flame starting from the ignition of pilot fuel was unable to travel throughout the combustion chamber. This leads to incomplete combustion and consequently high concentration of UHC and CO.

It was also noted that the use of larger amount of pilot fuel, while keeping the overall equivalence ratio unchanged, leads to an increase in temperature and thus increases the production of NO_x as depicted in Fig. 1. The variations in power and efficiency with change in the pilot fuel quantity were also investigated by the authors, as depicted in Fig. 1b. It is evident that the use of larger amount of pilot fuel results in higher power output as it leads to successful flame propagation. Higher thermal efficiency is also realized when larger quantity of pilot fuel is used.

Liu et al. [27] also explored the influence of the amount of pilot injection on emissions from a NG + Diesel engine. They presented substantially higher CO

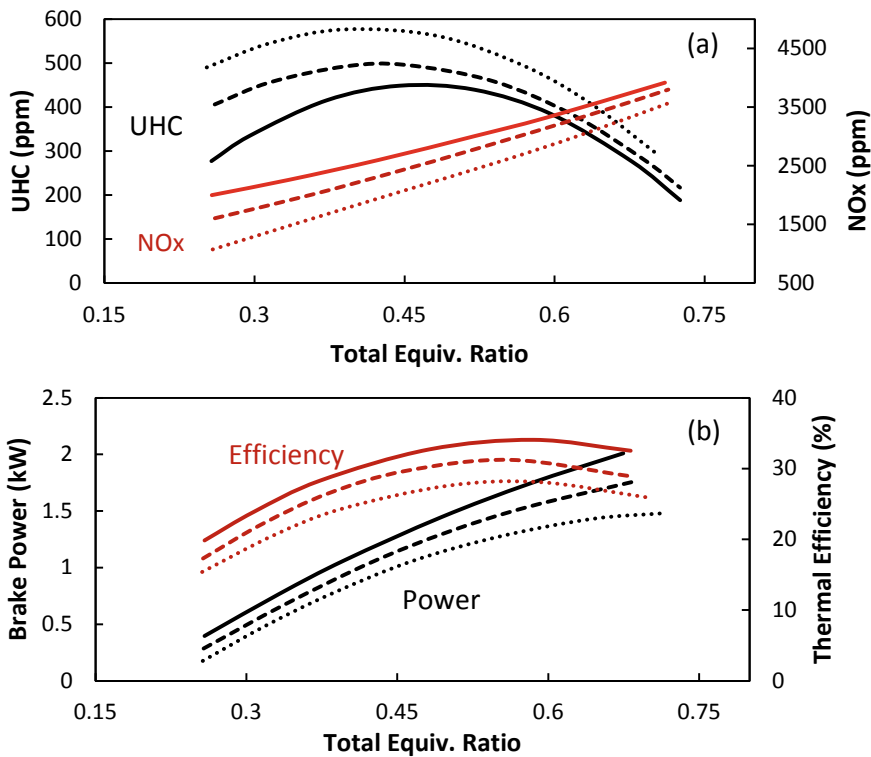


Fig. 1 Variation in (a) UHC and NO_x and (b) brake power and efficiency for different amounts of pilot fuel. Solid line (0.23 kg/h pilot fuel injection), dashed line (0.19 kg/h) and dotted line (0.15 kg/h)

emissions for NG + Diesel combustion in contrast to neat diesel. It was attributed to the existence of flame extinction regions for NG + Diesel, even at high load. At reduced pilot fuel quantity when engine operates at light load, the flame could not even propagate properly due to low local temperature which limited the oxidation reaction of CO. An increase in the pilot fuel quantity at high load resulted in higher temperature, and due to which additional premixed fuel could be completely oxidized. They also found that the quenching due to cold wall can become the main cause of the high CO emissions. The total HC emissions are reduced significantly when higher pilot fuel quantity is employed at high load. These are due to an improvement in the turbulence intensity and an extension of the spray envelope of the pilot fuel. They also reported great reduction in PM emissions with NG + Diesel in comparison to neat diesel. However, with use of larger amount of pilot fuel, the PM emissions also increase as more diesel fuel participates in the diffusion combustion process.

Selim [28] explored the consequences of the pilot fuel quantity variation on the characteristics of NG + Diesel engine. He found that as the pilot fuel quantity is increased, the combustion noise decreases initially, followed by an increase. The engine torque also increases as the pilot fuel quantity is increased.

3.2 Effect of Relative Proportion of NG and Diesel

Papagiannakis et al. [29] experimentally analyzed the influence of the overall ratio of air–fuel on performance and emissions. They took measurements over a speed and load range of 1500–2500 rpm and 1.2–4.9 bar BMEP, respectively. They noted that as diesel fuel supplementary ratio is increased, a reduction in the overall relative air–fuel ratio occurs, which subsequently results in a reduction in the thermal efficiency in comparison to neat diesel engine. The diesel fuel supplementary ratio is defined as the gravimetric ratio of the flow rate of NG to the flow rate of NG + Diesel. They also found that at low and moderate loads efficiency decreases considerably, but improves at higher load and higher diesel supplementary ratios. They observed lower nitric oxide emissions at all speeds and loads as diesel fuel supplementary ratio is increased. In comparison to part load conditions, lower nitric oxide emission was observed at higher load and supplementary ratios. The soot emissions decreased significantly under NG + Diesel operation especially at high load and for near-stoichiometric relative air–fuel ratios. As diesel fuel supplementary ratio was increased, CO emissions also increased and this observation was more marked at low and moderate loads than at high load. Furthermore, higher UHC emissions, compared to diesel engine, were observed. This particular effect was pronounced at part load.

3.3 Effect of Engine Speed

Selim [28] experimentally explored the influence of speed of engine on combustion and efficiency in a NG + Diesel engine. In his experiments, observations were made over a speed range of 900–2000 rpm. It was reported that the rate of pressure rise declines for both NG + Diesel and neat diesel engine when speed is increased. At all engine speeds, NG + Diesel resulted in a higher rate of pressure rise than neat diesel. They also observed a reduction in the rate of heat release with an increase in speed. Selim [30] further discussed the influence of speed on thermal efficiency for NG + Diesel engine. The efficiency of NG + Diesel engine was reported to improve when engine speed was increased.

3.4 Effect of Engine Load

Selim [28] explored the influence of varying engine load on NG + Diesel engine at a speed of 1200 rpm and load from 4 Nm to 23 Nm and found that in comparison to diesel fuel, dual fuel operation leads to higher combustion noise. Combustion noise was also observed to increase for dual fuel as load was increased due to higher rate of pressure rise.

Guo et al. [22] explored the performance and emission of NG + Diesel engine at low and moderate loads. They reported low efficiency at low as well as moderate loads. It was also noted that at low and moderate loads, CO₂ and PM emissions decrease significantly, but the emissions of methane and NO_x increase for NG + Diesel operation in contrast to diesel. CO emissions increased at low load, while for medium load, it increased with an increase in the NG portion first, but started to decrease as NG portion was increased further.

3.5 Effect of NG Injection Approach

You et al. [9] analyzed the influence of NG injection strategies in NG + Diesel engine. An 8.6 L, 6-cylinder, turbocharged, intercooled NG + Diesel engine was employed in experiments. It was shown that the maximum cylinder pressure first increases and then decreases as injection timing of NG is advanced. The reason behind this rise in maximum pressure is the following. As NG is injected earlier, it gets longer time to mix with air, which provides a more uniform mixture. On the contrary, if the injection time is significantly delayed, the mixture uniformity reduces and some NG starts participating in the scavenging process; as a result of this, the maximum pressure decreases. Similarly, if the injection timing is significantly advanced, some NG also takes part in the scavenging process and a small part is concentrated at the bottom of the combustion chamber, making maximum

pressure decrease. The effect of the injection timing of NG on heat release rate was also observed by the authors, and they found that the peak heat release rate first increases and then decreases with advance in NG injection. They also found that with an advance in injection, the emissions of NO_x and CO_2 first increase and then decrease slightly, but the emissions of total HC and CO first decrease and then increase slightly. With too late injection, low CO_2 and NO_x emissions and high total HC and CO emissions were observed.

Yang et al. [7] explored the effect of injection timing of NG for split pilot injection operation. They presented that with retarded NG injection timings, NG premixed combustion stage accelerated substantially and the duration of combustion declined by around 30%. They reported that NO_x emissions increased while that of HC and CO decreased by retarding NG injection timings.

3.6 Effect of Diesel (Pilot Fuel) Injection Timing/Strategies

Yousefi et al. [31] explored the influence of the timing of diesel injection in NG + Diesel engine. The diesel fuel worked as a pilot fuel to ignite the mixture of NG and air. They explored the influence of diesel fuel injection strategy for a range of speed (910–1750 rpm) and load (4.05 bar to 17.6 bar BMEP).

The results obtained from the experiments showed that for low speed—low load and high speed—moderate load operation, methane and CO_2 —equivalent emissions decrease significantly as diesel injection timing is advanced. However, at low speed—moderate to high load operation, methane emissions increase, but the CO_2 —equivalent emissions are not much affected. Their results also showed a decrease in methane and greenhouse gases and an increase in the thermal efficiency when the timing of diesel injection is advanced within the range of traditional diesel engine under low speed—low load and high speed—moderate load operation. Improvement in thermal efficiency was also observed for low speed—moderate to high load operation, but this improvement leads to higher methane emissions which is not desirable.

Shu et al. [32] explored the influence of varying pilot injection timing at low speed and load. They found that with an advance in pilot injection, the start of combustion and CA50 is advanced, which results in an increase in the peak cylinder pressure as well as the rate of heat release. There was a slight decrease in the duration of 10–50% combustion, but the duration for 50–90% combustion increased. The emissions of NO_x and HC were also analyzed in the literature. The authors found that with an advance in pilot fuel injection, the brake-specific NO_x increased significantly, while the brake-specific total HC remained almost unchanged.

3.7 Effect of EGR

Mahla et al. [33] conducted experiments in a naturally aspirated, single-cylinder, air-cooled DI diesel engine. The engine was adapted to operate on both NG + Diesel and only diesel. The results showed that at part loads, the CO and unburnt HC emissions were remarkably higher under the NG + Diesel fuelled operation. They attributed this phenomenon to overall lean mixture and small amount of pilot fuel, which led to incomplete combustion. The authors suggested that the application of cold EGR could overcome these problems. In their investigation, they found that the use of EGR reduced NO_x , CO and smoke significantly. They also showed that the thermal efficiency with NG + Diesel operation is practically similar to diesel engines at higher loads. However, at low loads poor thermal efficiency and increased emissions were observed. The authors suggested use of EGR to improve part load efficiency and emissions of the NG + Diesel engine. It was found that at low loads, the application of hot EGR increased the intake gas temperature, which in turn improved combustion. The authors primarily investigated the effect of cold EGR. It was noted that the brake thermal efficiency rises with the use of EGR, but this method is useful for EGR up to 5%. It was also observed that though the air needed for combustion decreases with an increase in EGR, nonetheless the thermal efficiency decreases by increasing the EGR ratio. However, the use of higher substitution of EGR was found very helpful in lowering NO_x emissions. With increasing EGR ratio, the emissions of CO increase at higher loads mainly due to incomplete combustion. Results also showed that the EGR also affect the peak pressure in the cylinder and ignition delay, and the peak cylinder pressure decreases with 15% EGR and there is an increase in the ignition delay duration.

Paykani et al. [34] examined the combined influence of preheating of incoming air and EGR ratio on efficiency and emissions at part loads. They noted that at part loads, the usage of high levels of EGR was not effective. However, the EGR can slightly increase the thermal efficiency when combined with pre-heating of incoming air, which leads to reduction in the level of emissions of both UHC and NO_x . It was also observed that CO emissions decreased by 24%, while UHC emissions reduced by 31%. The lower combustion temperature was observed when EGR was applied with NG + Diesel operation, and as a result the emission of NO_x reduced. Here, the lower temperature of combustion was attributed to the inert gas inducted by EGR and reduction in oxygen in the cylinder.

4 Conclusions

The concept of NG + Diesel in C.I. engine is a very promising technique to lower the demand for diesel fuel. The following conclusions can be drawn. In NG + Diesel dual fuel engine, diesel serves as the pilot fuel. The quantity of pilot fuel plays a major role, especially at light loads. An increase in the quantity of pilot

fuel leads to (i) increase in thermal efficiency and power, (ii) increase in PM and NO_x and (iii) decrease in UHC and CO. The performance of the NG + Diesel engine is also influenced by NG–diesel proportion. An increase in the diesel fuel supplementary ratio leads to (i) decrease in thermal efficiency, (ii) lower emission of NO_x and (iii) higher CO and UHC emissions. An increase in speed leads to (i) reduction in the rate of pressure rise and (ii) increase in thermal efficiency. An increase in load leads to (i) higher rate of pressure rise and noise, (ii) higher efficiency and (iii) lower CO emissions in comparison to low load.

An advancement in NG injection leads to (i) an initial rise in the peak heat release rate, CO_2 and NO_x emissions followed by a decline (ii) an initial decrease in HC and CO emissions followed by a marginal increase. The effect of pilot fuel (diesel) injection timing is the following. As diesel injection is advanced at low speed - low load and high speed - medium load settings, methane and CO_2 —equivalent emissions decrease significantly. Thermal efficiency, heat release rate and brake-specific NO_x increase with advance of diesel injection timing, while the brake-specific total HC is practically unaffected by advancing pilot fuel injection timing.

References

1. Kalghatgi GT (2014) The outlook for fuels for internal combustion engines. *Int J Engine Res* 15(4):383–398
2. Brownstein AM (2015) *Renewable Motor Fuels: The Past The present and the Uncertain Future*. Butterworth-Heinemann, Oxford, UK
3. Heywood JB (1988) *Internal combustion engine fundamentals*. McGraw-Hill Book Companies, New York
4. Stone R (2012) *Introduction to internal combustion engines*, 4th ed. Palgrave Macmillan, Basingstoke
5. Bayraktar H (2008) An experimental study on the performance parameters of an experimental CI engine fueled with diesel–methanol–dodecanol blends. *Fuel* 87(2):158–164
6. Wei LJ, Yao CD, Wang QG, Pan W, Han GP (2015) Combustion and emission characteristics of a turbocharged diesel engine using high premixed ratio of methanol and diesel fuel. *Fuel* 140:156–163
7. Yang B, Zeng K (2018) Effects of natural gas injection timing and split pilot fuel injection strategy on the combustion performance and emissions in a dual-fuel engine fueled with diesel and natural gas. *Energy Convers Manag* 168:162–169
8. Torregrosa AJ, Broatch A, Garcia A, Monico LF (2013) Sensitivity of combustion noise and NO_x and soot emissions to pilot injection in PCCI diesel engines. *Appl Energy* 104:149–157
9. Wei L, Geng P (2016) A review on natural gas/diesel dual fuel combustion, emissions and performance. *Fuel Process Technol* 142:264–278
10. Pirouzpanah V, Sarai RK (2003) Reduction of emissions in an automotive direct injection diesel engine dual-fuelled with natural gas by using variable exhaust gas recirculation. *Proc Inst Mech Eng D J Automob Eng* 217(D8):719–725
11. Srinivasan KK, Krishnan SR, Qi Y (2014) Cyclic combustion variations in dual fuel partially premixed pilot-ignited natural gas engines. *J Energy Resour Technol Trans ASME* 136(1)
12. Tang Q, Fu J, Liu J, Zhou F, Yuan Z, Xu Z (2016) Performance improvement of liquefied natural gas (LNG) engine through intake air supply. *Appl Therm Eng* 103:1351–1361

13. Papagiannakis RG, Hountalas DT, Rakopoulos CD (2008) Combustion and performance characteristics of a DI diesel engine operating from low to high natural gas supplement ratios at various operating conditions. SAE Technical Paper 2008-01-1392
14. Karim GA (2015) Dual-Fuel Diesel Engines. CRC Press, Boca Raton, USA
15. Demirbas A (2010) Methane gas hydrate: Springer Science & Business Media
16. Semin Bakar RA (2008) A technical review of compressed natural gas as an alternative fuel for internal combustion engines. *Am J Eng Appl Sci* 1(4):302–311
17. Turns SR (2000) *An Introduction to Combustion: Concepts and Applications*. 2nd ed. McGraw-Hill, New York, USA
18. U.S. Department of Energy (2015) Clean Cities Alternative Fuel Price Report
19. Akansu SO, Dulger Z, Kahraman N, Veziroğlu TN (2004) Internal combustion engines fueled by natural gas–hydrogen mixtures. *Int J Hydrog Energy* 29(14):1527–1539
20. Hegab A, Rocca AL, Shayler P (2017) Towards keeping diesel fuel supply and demand in balance: dual-fuelling of diesel engines with natural gas. *Renew Sustain Energy Rev* 70: 666–697
21. Harrington J, Munshi S, Nedelcu C, Ouellette P, Thompson J, Whitfield S (2002) Direct injection of natural gas in a heavy-duty diesel engine, SAE Technical paper 2002-01-1630
22. Guo H, Neill WS, Liko B (2015) An experimental investigation on the combustion and emissions performance of a natural gas—diesel dual fuel engine at low and medium loads. 1, 130–137
23. Karim GA (2003) Combustion in gas fueled compression: ignition engines of the dual fuel type. *J Eng Gas Turbines Power Trans ASME* 125(3):827–836
24. You J, Liu Z, Wang Z, Wang D, Xu Y (2020) Impact of natural gas injection strategies on combustion and emissions of a dual fuel natural gas engine ignited with diesel at low loads. *Fuel* 260:116414
25. Papagiannakis RG, Hountalas DT, Rakopoulos CD (2007) Theoretical study of the effects of pilot fuel quantity and its injection timing on the performance and emissions of a dual fuel diesel engine. *Energy Convers Manag* 48(11):2951–2961
26. Abd Alla GH, Soliman HA, Badr OA, Abd Rabbo MF (2000) Effect of pilot fuel quantity on the performance of a dual fuel engine. *Energy Convers Manag* 41:559–572
27. Liu J, Yang F, Wang H, Ouyang M, Hao S (2013) Effects of pilot fuel quantity on the emissions characteristics of a CNG/diesel dual fuel engine with optimized pilot injection timing. *Appl Energy* 110:201–206
28. Selim MYE (2001) Pressure–time characteristics in diesel engine fueled with natural gas. *Renew Energy* 22:473–489
29. Papagiannakis RG, Rakopoulos CD, Hountalas DT, Rakopoulos DC (2010) Emission characteristics of high speed, dual fuel, compression ignition engine operating in a wide range of natural gas/diesel fuel proportions. *Fuel* 89:1397–1406
30. Selim MYE (2004) Sensitivity of dual fuel engine combustion and knocking limits to gaseous fuel composition. *Energy Convers Manag* 45(3):411–425
31. Yousefi A, Guo H, Birouk M (2019) Effect of diesel injection timing on the combustion of natural gas/diesel dual-fuel engine at low-high load and low-high speed conditions. *Fuel* 235:838–846
32. Shu J, Fu J, Liu J, Zhang L, Zhao Z (2018) Experimental and computational study on the effects of injection timing on thermodynamics, combustion and emission characteristics of a natural gas (NG)-diesel dual fuel engine at low speed and low load. *Energy Convers Manag* 160:426–438
33. Mahla SK, Das LM, Babu MKG (2010) Effect of EGR on Performance and Emission Characteristics of Natural Gas Fueled Diesel Engine. *JJMIE* 4:523–530
34. Paykani A, Saray RK, Tabar MTS, Kousha AM (2012) Effect of exhaust gas recirculation and intake pre-heating on performance and emission characteristics of dual fuel engines at part loads. *J Cent South Univ* 19:1346–1352

Effect of Wall Fin Aspect Ratio in a Suddenly Expanded Micro-Combustor



Arees Qamareen , Shah Shahood Alam,
and Mubashshir Ahmad Ansari

Abstract The present work investigates the performance of micro-combustors with a backward facing step and triangular wall fin with variable aspect ratio (AR). The outer wall temperature distribution was found to be influenced by the aspect ratio of fin with the highest peak observed for $AR = 1$ for the entire velocity range (4–48 m/s). Comparisons were also made with micro-combustors inserted with a triangular block at the centerline. At higher velocities, finned micro-combustors were found to give higher outer wall temperature as compared to the ones with block inserts. Enhancement of heat transfer due to fin attachment at the inner wall results in better performing micro-combustors.

Keywords Micro-combustor · Wall fin · Aspect ratio · Sudden expansion · Recirculation

1 Introduction

Power generating devices [1] of the micro-level are being widely researched for use in micro-gas turbines, portable electric devices such as microthermoelectric (MTE) [2] and micro-photovoltaic devices (MPTV) [3–5] due to the prominent dependencies on micro-electromechanical systems.

Micro-combustors are a vital component of many such energy generating systems due to the high energy densities of hydrocarbon fuels used and longer working hours in comparison with traditional Li-ion batteries. But micro-combustors face many challenges due to their sub-millimeter scales such as higher heat losses from

A. Qamareen (✉) · S. S. Alam · M. A. Ansari
Aligarh Muslim University, Aligarh 202002, India
e-mail: areesq@gmail.com

S. S. Alam
e-mail: sshahood2004@yahoo.co.in

M. A. Ansari
e-mail: mubashshir@zhcet.ac.in

the larger outer surface area causing a reduction in combustion efficiency. Another problem is radical destruction occurring at the gas–solid interface of the combustion chamber apart from the much reduced residence time of the gases. Still these micro-combustor-based power devices are being considered quite promising alternatives for future energy requirements.

Combustion characteristics inside the micro-combustors with bluff bodies [6, 7], ribs [8, 9], baffles [10, 11], porous medium [12, 13], etc., have been researched with an intention to enhance efficiencies. Wan et al. [14, 15] reported that recirculation zones formed in combustor cavities help in flame stabilization and increase the inlet velocity working range.

High combustor wall temperature is much desired for microthermoelectric (MTE) and micro–thermo–photovoltaic systems but lower residence time and high surface-to-volume (cause of large amounts of heat losses) ratio are a big challenge.

In the present study, we report the use of premixed H_2 –air combustion in a micro-combustor with backward facing step and a triangular shaped wall fin to enhance heat transfer from the hot combustion gases to the outer surface of the solid wall. The effect of adding fins of different aspect ratios on the inside surface of the combustor wall at varying inlet velocities is studied, and comparisons are made with the performance of micro-combustors having block insert (at the center line) with same aspect ratios. Also, analysis is made with respect to the basic micro-combustor case having no obstruction, i.e., a simple suddenly expanded combustion chamber.

2 Micro-Combustor Geometrical and Mathematical Model

2.1 Conceptual and Structural Design of Micro-Combustor

The basic concept of a micro-combustor with backward facing step is shown in Fig. 1 where premixed H_2 –air mixture enters the left wall of the combustor and undergoes sudden expansion on entering the combustion chamber. After combustion process, the heat released is transferred through the solid wall and emitted to the ambient in the form of thermal radiation. This thermal energy can be utilized to generate electricity with the help of MTE/MTPV systems [16].

Figure 2 shows the design features of micro-combustors with wall fin and block insert. The geometrical parameters are given in Table 1. The length of the fin/block is a variable while fin/block height and location are kept as constant.

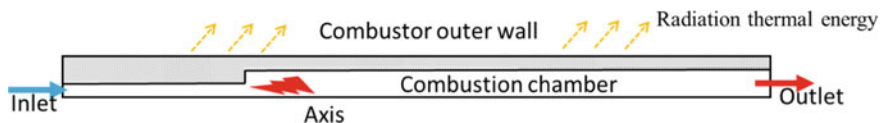


Fig. 1 Micro-combustor design concept

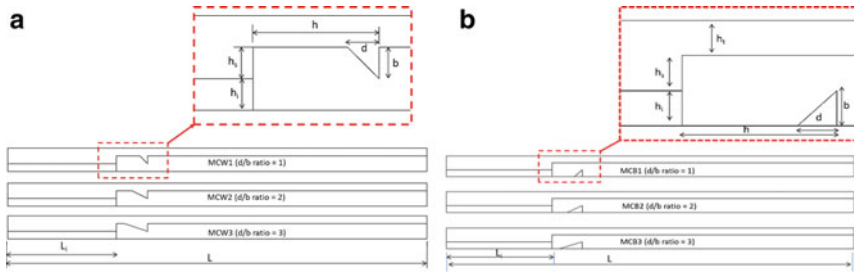


Fig. 2 Geometrical features of micro-combustors (a) with wall fin (b) with block insert

Table 1 Geometrical parameters of micro-combustors

Geometrical parameter	Parameter name	(mm)	Constant/variable
L	Combustor length	27	Constant
L_i	Inlet length	7	Constant
h	Block location	2	Constant
h_i	Inlet height	0.5	Constant
h_s	Step height	0.5	Constant
h_t	Combustor wall thickness	0.5	Constant
AR	Aspect ratio	1, 2, 3	Variable
b	Fin/Block height	0.5	Constant
d	Fin/Block length	$AR \times b$	Variable

Aspect ratio (AR) is defined as the ratio of length (d) to the height (b) of the fin/block.

$$AR \text{ (Aspect Ratio)} = d/b \tag{1}$$

2.2 Mathematical and Computational Model

The governing equations [16] for steady-state combustion were discretized by second-order upwind scheme with the use of commercial CFD software, ANSYS Fluent 16.0. It employs finite volume method for solving the governing equations while SIMPLE pressure correction algorithm is used for pressure-linked equations. Multi-zone quadrilateral mesh (see Fig. 3) with approximately 1.1×10^5 number of nodes was used in the simulation after carrying out the grid independency test (not shown here). Finite rate/eddy dissipation model is used for modeling chemistry–turbulence interaction. Global H_2 –air reaction mechanism is adopted to save the computational time required for modeling detailed mechanism. Though a comparative study was done between the global and detailed mechanisms with respect to experimental results (shown in Fig. 4), the global mechanisms

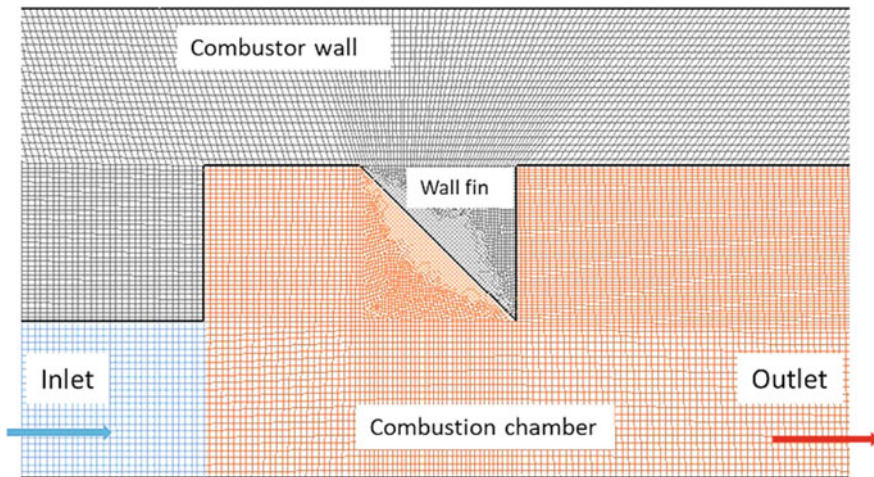


Fig. 3 Multi-zone computational mesh

overpredict the temperatures but trend of the temperature distribution curve is similar. Hence, to get an overview of better performing geometries, we have adopted global mechanism and saved the large amount of computational time required in detailed mechanism based simulation.

Residuals of 10^{-6} are set for convergence of all the equations. The assumptions made for the simulation along with the material properties are taken from the literature of Akhtar et al. [16]. The boundary conditions used are as follows (Table 2).

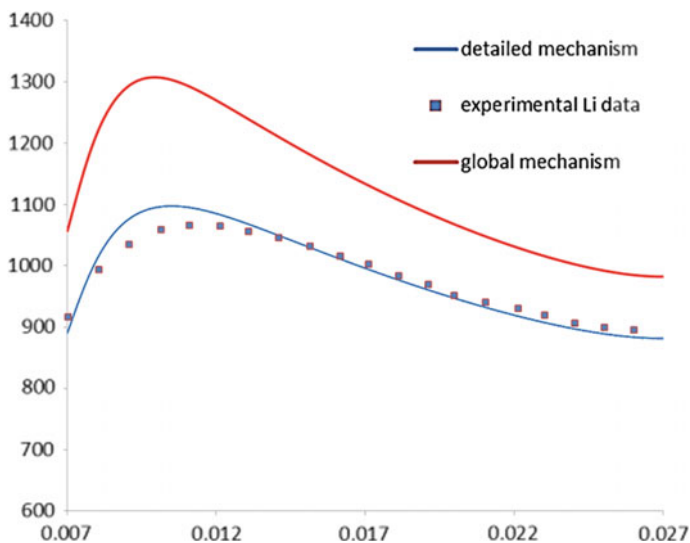


Fig. 4 Validation of the numerical results with the experimental results of Li [17], Outer wall temperature (K) variation with respect to axial displacement (mm)

Table 2 Boundary conditions

Boundary	Conditions applied
Gas–solid interfaces	No-slip condition Zero flux of species Coupled heat transfer
Inlet	Uniform velocity inlet condition [4–48 m/s] Incoming H ₂ –air mixture temperature = 300 K Equivalence ratio of mixture = 0.8
Outlet	Zero gauge pressure
Inlet/outlet walls	Adiabatic
Outer wall	Mixed boundary condition Surface emissivity = 0.6 Ambient heat transfer coefficient = 10 W/m ² -K Ambient temperature = 300 K

3 Results and Discussion

In the present study, we report the use of triangular wall fin in a micro-combustor with backward facing step with variable aspect ratio at different inlet mixture velocity. The fin is added to enhance heat transfer from the hot combustion gases to the outer surface of the solid wall.

In Fig. 5, a narrow zone of the temperature profile is shown and comparisons are made for the micro-combustors with wall fin (MCW—green curves), with block insert (MCB—red curves) and a simple suddenly expanded micro-combustor without any insertion or wall modulation (MC—black curve). For $u = 4$ m/s, there is not much difference in the temperatures for MCWs but MCBs show a higher temperature peak. As the velocity increases, it can be seen that MCWs start reporting a higher maxima for outer wall temperature with the combustor having AR = 1 type of fin having the highest maxima. For higher velocities, i.e., $u \geq 32$ m/s, the difference between maximum temperatures of MCW1 and MC type of combustors is observed as 50 K approximately.

The outer wall temperature is observed quantitatively in the plots as shown in Fig. 6 along with contour plots which help in examining the overall nature of the flow in a single view. It can be seen that the temperature increases from the inlet and reaches a maxima around the center of the combustor length and then decreases toward the outlet side due to heat losses occurring from the combustor wall. For lower velocities, the inlet side temperature is higher due to preheating of the mixture coming in since the residence time of the combustion gases is higher. At higher velocities, the flame shifts downstream but higher amount of heat release occurs due to the larger amount of fuel–air mixture coming in. Temperature contours depict how the high temperature zone gets divided due to the presence of fin at higher velocities.

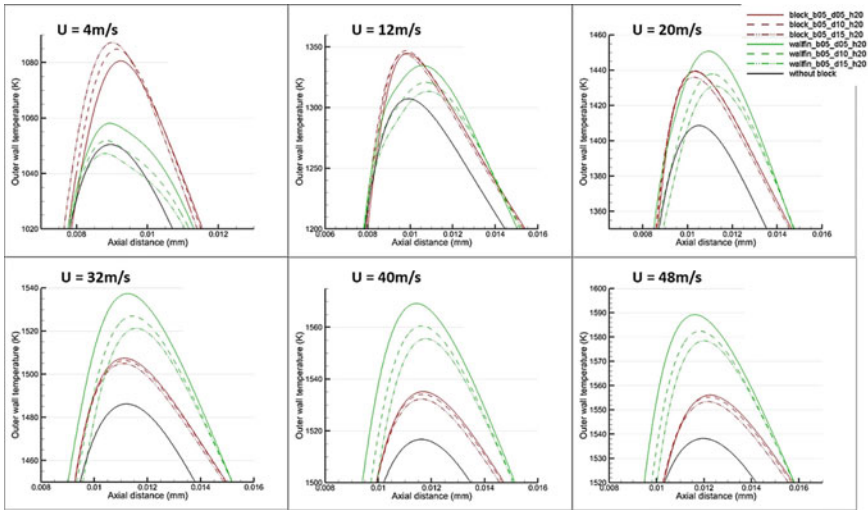


Fig. 5 Comparative representation of the micro-combustors at different inlet velocities

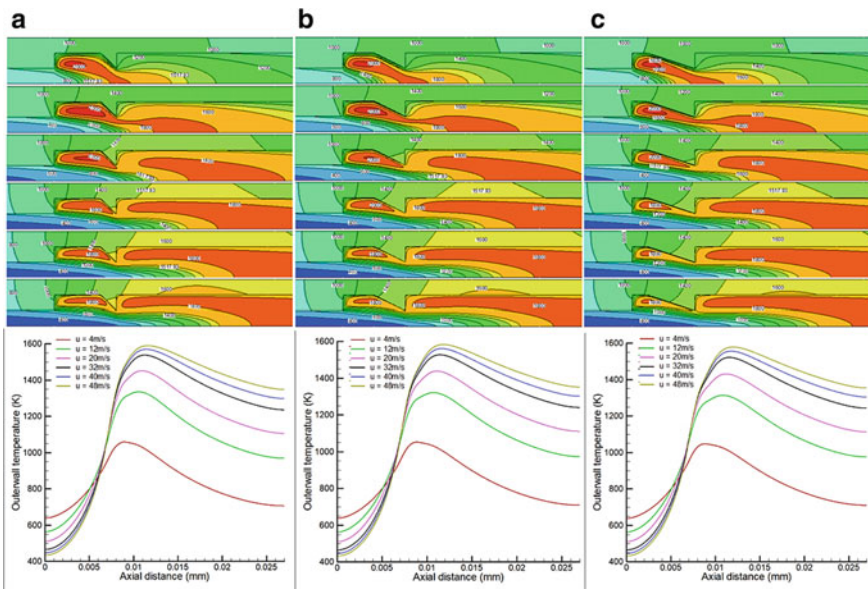


Fig. 6 Temperature contours and outer wall temperature distribution for (a) MCW1, (b) MCW2 and (c) MCW3 micro-combustors

4 Conclusions

The effect of aspect ratio of wall fin on the outer wall temperature in a backward facing stepped micro-combustor was numerically investigated. From the results, it can be concluded that wall fin improves the performance of the combustor as compared to the case without any wall modulation. When compared with micro-combustors inserted with a triangular block at the centerline it was observed that at higher velocities, finned micro-combustors gave higher outer wall temperatures. Enhancement of heat transfer due to inner wall fin attachment resulted in better performing micro-combustors.

References

1. Ju Y, Maruta K (2011) Microscale combustion: Technology development and fundamental research. *Prog Energy Combust Sci* 37:669–715. <https://doi.org/10.1016/j.peecs.2011.03.001>
2. Aravind B, Kumar S (2018) Parametric Studies on Thermo-electric Power Generation Using Micro Combustor. <https://doi.org/10.1007/978-3-319-53556-2>
3. Akhtar S, Khan MN, Kurnia JC, Shamim T (2017) Investigation of energy conversion and flame stability in a curved micro-combustor for thermo-photovoltaic (TPV) applications. *Appl Energy* 192:134–145. <https://doi.org/10.1016/j.apenergy.2017.01.097>
4. Bazooyar B, Darabkhani HG (2019) Analysis of flame stabilization to a thermo-photovoltaic micro-combustor step in turbulent premixed hydrogen flame. *Fuel* 257:115989. <https://doi.org/10.1016/j.fuel.2019.115989>
5. Mansouri Z (2019) Combustion in wavy micro-channels for thermo-photovoltaic applications —Part I: Effects of wavy wall geometry, wall temperature profile and reaction mechanism. *Energy Convers Manag*, 0–1. <https://doi.org/10.1016/j.enconman.2018.12.105>
6. Jia-qiang E, Hai-jiao H, Xiao-huan Z (2016) Numerical investigations on effects of bluff body in flat plate micro thermo photovoltaic combustor with sudden expansion, 975–82. <https://doi.org/10.1007/s11771-016-3145-6>
7. Hosseini SE, Wahid MA (2014) Investigation of bluff-body micro-flameless combustion. *Energy Convers Manag* 88:120–128. <https://doi.org/10.1016/j.enconman.2014.08.023>
8. Wang H, Fang H, Lou B, Abubakar S, Li Y, Meng L (2020) Exploring the benefits of annular rectangular rib for enhancing thermal efficiency of nonpremixed micro-combustor. *J Chem* 9410389:13. <https://doi.org/10.1155/2020/9410389>
9. Zuo W, Jiaqiang E, Liu H, Peng Q, Zhao X, Zhang Z (2016) Numerical investigations on an improved micro-cylindrical combustor with rectangular rib for enhancing heat transfer. *Appl Energy* 184:77–87. <https://doi.org/10.1016/j.apenergy.2016.10.009>
10. Yahagi Y, Sekiguti M, Suzuki K (2007) Flow structure and flame stability in a micro can combustor with a baffle plate. *Appl Therm Eng* 27:788–794. <https://doi.org/10.1016/j.applthermaleng.2006.10.019>
11. Amani E, Alizadeh P, Moghadam RS (2018) ScienceDirect Micro-combustor performance enhancement by hydrogen addition in a combined baffle-bluff configuration. *Int J Hydrogen Energy* 43:8127–8138. <https://doi.org/10.1016/j.ijhydene.2018.03.016>
12. Pan JF, Wu D, Liu YX, Zhang HF, Tang AK, Xue H (2014) Hydrogen/oxygen premixed combustion characteristics in micro porous media combustor. *Energy Procedia* 61:1279–1285. <https://doi.org/10.1016/j.egypro.2014.11.1081>

13. Peng Q, Yang W, Jiaqiang E, Xu H, Li Z, Tay K (2020) Investigation on premixed H₂/C₃H₈/air combustion in porous medium combustor for the micro thermophotovoltaic application. *Appl Energy* 260:114352. <https://doi.org/10.1016/j.apenergy.2019.114352>
14. Wan J, Fan A, Yao H, Liu W (2015) Effect of thermal conductivity of solid wall on combustion efficiency of a micro-combustor with cavities. *Energy Convers Manag* 96:605–612. <https://doi.org/10.1016/j.enconman.2015.03.030>
15. Wan J, Yang W, Fan A, Liu Y, Yao H, Liu W et al (2014) A numerical investigation on combustion characteristics of H₂/air mixture in a micro-combustor with wall cavities. *Int J Hydrogen Energy* 39:8138–8146. <https://doi.org/10.1016/j.ijhydene.2014.03.116>
16. Akhtar S, Kurnia JC, Shamim T (2015) A three-dimensional computational model of H₂-air premixed combustion in non-circular micro-channels for a thermo-photovoltaic (TPV) application. *Appl Energy* 152:47–57. <https://doi.org/10.1016/j.apenergy.2015.04.068>
17. Li J, Chou SK, Yang WM, Li ZW (2009) Experimental and numerical study of the wall temperature of cylindrical micro combustors. *J Micromechanics Microengineering*, 19. <https://doi.org/10.1088/0960-1317/19/1/015019>

Mathematical Modeling of Drying Kinetics of Garlic Clove in Forced Convection Evacuated Tube Solar Dryer



Santanu Malakar and Vinkel Kumar Arora 

Abstract The present research aims to estimate the thermal performances of an evacuated tube solar dryer (ETSD) and analysis of thin-layer drying kinetics of garlic clove. The experiment of the drying was conducted at individual air velocities, viz. 1, 2, and 3 m/s to evaluate the moisture ratio during the drying progression. The solar intensity and collector outlet temperature were increased up to 2 PM and found to be 964 W/m^2 and $85.5 \text{ }^\circ\text{C}$, respectively, and thereafter both are decreased. The maximum drying chamber temperature was noted $76.5 \text{ }^\circ\text{C}$ for drying of the garlic clove. Five thin-layer drying kinetic models were selected and fitted with experimental values of moisture ratio for the identification of the best appropriate drying model. Among the different mathematical models, Weibull model was identified to be best-fitting curve capable for described the drying kinetics at 2 m/s as well as 3 m/s air velocity with highest coefficient of determination (R^2) values, least chi-square (χ^2) and root mean square error (RMSE) values. However, Modified Page model was showed the best-fitted model at 1 m/s air velocity to describe the drying behavior of garlic clove.

Keywords Drying kinetics · ETSD · Moisture ratio · Thin layer drying · Thermal performance

1 Introduction

Renewable energy sources have the potential to provide solutions to the possible energy requirement being faced by developing countries. Solar energy could play a very vital role in the drying of food products and helping to decrease the postharvest

S. Malakar · V. K. Arora (✉)
Department of Food Engineering, National Institute of Food Technology Entrepreneurship
and Management, Sonapat, Haryana, India
e-mail: vinkelarora17@gmail.com

S. Malakar
e-mail: santanuinfo10@gmail.com

losses and thereby increases the availability of food products [1]. The potential application of solar radiation energy in food processing is mostly emphasized on drying operation. Drying is a method of removing moisture content of food materials by virtue of heat as well as mass transfer occurred simultaneously during the process. Garlic clove is highly perishable which can be spoiled due to the presence of a high amount of moisture content [2]. To overcome the spoilage, the garlic clove is dried and its moisture content is reduced up to the desired level for safe storage. Therefore, the reduction of moisture content for safe storage is performed by drying applications. Mainly direct and indirect solar dryers are used to drying of the food materials. Solar energy is absorbed either by flat plate collector (FPC) or evacuated tube collector (ETC) and the energy transfer to the drying chamber for drying of food materials. ETC is higher thermal efficiency in comparison with the normal FPC for drying of food materials [3]. Indirect solar dryer mainly comprises solar collectors, blower assembly and drying chamber, etc.

The drying kinetic behavior of the food materials is a complex heat and mass transport phenomenon that involves the representation of the prediction of the drying process behavior and to the optimization of the drying process parameters [4]. Shringi et al. [5] investigated the thermal profile performance of developed solar dryer and found that the temperature 342 K was achieved at drying chamber, and the efficiency of energy varied from 43.06 to 83.73%. Moreover, it has been found that the Midilli model was finest fitted to experimental values of moisture ratio. The outlet temperature of the solar collector was varying from 47.4 to 91 °C in ETC-based solar drying system, and the efficiency of the dryer was estimated from 26.68 to 54.72% [6]. Page's model was showed the best-fitted model to describing the drying behavior of mango slice dried at ETC-based solar dryer [7].

Thin-layer drying kinetic models were applied to predict the moisture ratio (MR) and drying time for the simplification of drying curves. Limited research in drying characteristics of garlic was reported based on ETSD. The purposes of the research were to investigate thermal performance of ETSD and to study the drying kinetics of garlic cloves to identify the best-fitted model of the thin-layer drying process.

2 Materials and Methods

2.1 Sample Collection

Garlic cloves were procured from the local market Narela, Delhi, India, and separated the cloves from the whole garlic. The cloves were soaked for 5 h in mild hot water to remove the peel for the further drying process. The initial moisture content was determined and found to be 69%, and almost equal size of garlic cloves are selected for the further drying process.

2.2 Drying Equipment and Experiments

The solar dryer based on ETC was considered to evaluate the performance and study the drying kinetics of garlic clove. The experimental setup of ETC-based solar dryer is as shown in Fig. 1. The dryer consists of a series of 15 evacuated tubes mounted on a common manifold, and centrifugal blower of 0.2 hp is attached for airflow through manifold and drying chamber with the dimension of $(0.78 \times 0.70 \times 1.36) \text{ m}^3$.

The experiment was conducted to evaluate the thermal profile of the ETSD during clear sunny days in the month of July, 2019, at NIFTEM, Kundli, India, situated at 28.8676°N , 77.1180°E . The solar dryer was placed in southwest facing at a tilt angle of 45° . The different parameter of thermal profile, viz. solar radiation intensity, drying chamber inlet and outlet temperature, ambient temperature and relative humidity was noted at one-hour interval during 9 AM to 5 PM. The drying experiment was performed at different air flow velocities, viz., 1, 2, and 3 m/s measured by digital Anemometer (± 0.17), to evaluate the changes of moisture ratio throughout the drying process. The moisture ratio data was fitted at different thin layers model equations to identify the best-fitted model of the drying curve.

2.3 Drying Kinetics

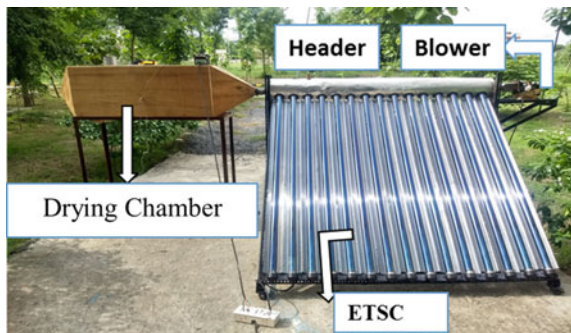
The drying behavior of garlic clove was expressed in terms moisture ratio which is determined based on the initial and final moisture contents and also the equilibrium moisture content (EMC).

The moisture ratio (MR) is expressed as by this equation given below [8].

$$\text{MR} = \frac{M_t - M_e}{M_i - M_e} \tag{1}$$

where M_t is the MC at time t, M_i and M_e are the initial and EMC, respectively.

Fig. 1 Experimental setup of developed ETSD



2.4 Mathematical Modeling of Thin Layer Drying

The moisture ratio of the garlic cloves was estimated experimentally and fitted with different models to identify the best fitted suitable model of drying kinetics of garlic clove in different drying techniques. The following models are considered and were applied to moisture ratio to describe the drying curves and to estimate the different coefficients of the thin-layer model by fitting the data obtained from drying experiments as shown in Table 1.

A non-linear regression modeling was carried out using ‘Origin 18’ (version 2018) to estimate the drying rate constant (k) and various coefficients of the above semi-empirical and empirical models. The identification of best model was done based on the higher value coefficient of determination (R^2), the lowest value of chi-square (χ^2), and RMSE values for identifying the best the drying curve of food materials. These parameters can be calculated by Eqs. 2, 3 and 4 [9]

$$R^2 = 1 - \frac{\sum_{i=1}^N (M \cdot R_{pre,i} - M \cdot R_{exp,i})^2}{\sum_{i=1}^N \left(\frac{\sum_{k=1}^n M \cdot R_{pre,i}}{N} - M \cdot R_{pre,i} \right)^2} \tag{2}$$

$$\chi^2 = \frac{\sum_{i=1}^N (M \cdot R_{exp,i} - M \cdot R_{pre,i})^2}{N - n} \tag{3}$$

$$RMSE = \left[\frac{1}{N} \sum_{i=1}^N (M \cdot R_{pre,i} - M \cdot R_{exp,i})^2 \right]^{1/2} \tag{4}$$

where $MR_{exp, i}$ is the experimental MR of the i^{th} data, $MR_{pre,i}$ is the predicted MR of the i^{th} data, N and n are the number of experimentation and drying constant, respectively.

Table 1 Mathematical models for drying kinetics

Model name	Model equation
Page	$MR = \exp(-kt^n)$
Modified page	$MR = \exp(-kt)^n$
Newton	$MR = \exp(-kt)$
Henderson and Pabis	$MR = a \exp(-kt)$
Weibull	$MR = a - b \exp(-k_o t^n)$

3 Results and Discussion

3.1 Thermal Performance of ETSD

The performance of the solar drying system based on ETC was investigated and represented graphically as shown in Fig. 2. The thermal attributes, viz. solar radiation intensity, collector outlet temperature, relative humidity, drying chamber temperature and atmospheric temperature were noted on an hourly basis throughout the experiment. The solar intensity varied from 606 to 964 W/m² throughout the days. The solar intensity and collector outlet temperature were increased up to 2 PM and found to be 964 W/m² and 85.5 °C, respectively, and thereafter, both decreased with the drying time.

Similarly, the ambient temperature and relative humidity are varied slightly and recorded 30.5–42.5 °C and 42–54%, respectively, during the experimentation. The results of the experiment revealed that the temperature of the collector outlet was raised with the increase of solar radiation intensity. A similar variation of thermal parameters was found by Wang W and Umayal Sundari AR. [7, 10].

3.2 Drying Kinetics of Garlic Clove

The moisture ratio of the garlic cloves was determined at different air flow velocities in an ETSD, and the variations are shown in Fig. 3. The concluding moisture ratio was found 0.195, 0.0483, and 0.101 at 1, 2 and 3 m/s, respectively, at the same drying period. It was noted that the optimum diminishing moisture ratio

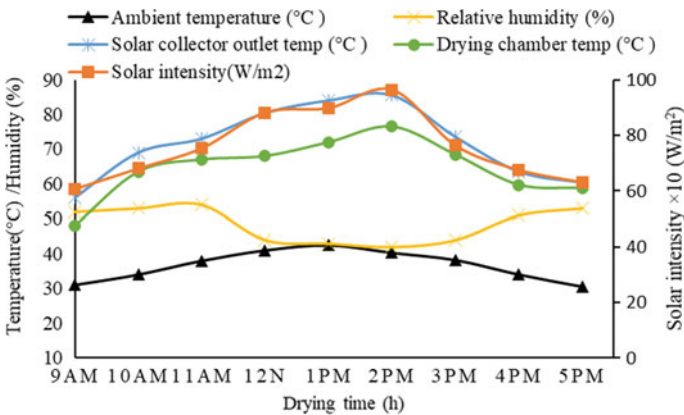


Fig. 2 Variation of thermal attributes of ETSD

was observed at 2 m/s fluid velocity in comparison with the other air velocities. The results showed that the maximum moisture was removed at 2 m/s fluid velocity followed by 3 m/s and 1 m/s velocity of air during the drying process. A similar trend was reported that the moisture ratio declines consistently with drying time [5].

3.3 Mathematic Modeling

The moisture ratio of garlic clove dried at different airflow velocities was described with five various thin-layer drying kinetics models to identify their suitability to describe the drying behavior. The coefficient of determination (R^2) and findings of statistical analyses like chi-square (χ^2), RMSE, and different model coefficient values are obtained from nonlinear regression modelling analysis are given in Table 2. The best-fitted model to describe the drying kinetics of garlic was identified in accordance with the highest value of $R^2 = 0.99891$ and the lower value obtained of $\chi^2 = 0.000258$ and RSME = 0.00093. From the analysis results, it was noted that the Weibull model gave the highest value of R^2 at 2 m/s velocity of air, whereas the χ^2 and RSME values were found lowest during the analysis.

Thus, Weibull model is represented as the best-fitted model for drying kinetic of garlic clove drying at ETSD. Similarly, Modified Page model and Weibull model were identified as the best-fitted models to describe the drying kinetics of garlic clove at 1 and 3 m/s air velocity, respectively. The best-selected-fitted models at different air velocity by plotting the data of the experimental values of moisture ratio with that of the predicted values are displayed in Fig. 4a–c. The experimental values of MR were found to be best aligned to the predicted values with $R^2 = 0.99891$ at 2 m/s and $R^2 = 0.99846$ at 3 m/s described by Weibull model. The experimental values of moisture ratio at 1 m/s are very closed to the predicted value represented by the best suitable Modified Page model with $R^2 = 0.99862$.

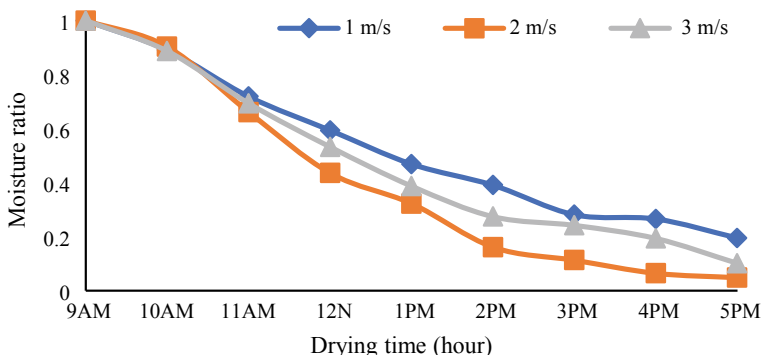


Fig. 3 Moisture ratio changes during the drying time in ETSD

Table 2 Statistical parameters and the coefficients of drying models

Model name	Air velocity (m/s)	R^2	χ^2	RMSE	Estimated parameters			
					a	b	k_o	n
Page	1	0.99762	0.00023	0.00211	–	–	0.00622	1.04145
	2	0.99766	0.00056	0.00175	–	–	0.00856	1.1425
	3	0.99346	0.00075	0.00588	–	–	0.00629	0.8530
Modified Page	1	0.99862	0.00097	0.00117	–	–	0.06488	0.8807
	2	0.99419	0.00023	0.00276	–	–	0.08351	1.0414
	3	0.99602	0.00056	0.00455	–	–	0.09698	1.1425
Newton	1	0.99785	0.00169	0.02518	–	–	0.00421	–
	2	0.99773	0.00097	0.00138	–	–	0.00697	–
	3	0.99792	0.00136	0.00506	–	–	0.00941	–
Henderson and Pabis	1	0.99179	7.70789	0.00547	1.039	–	0.19767	–
	2	0.96428	0.00542	0.03797	1.094	–	0.3147	–
	3	0.98383	0.01322	0.00189	1.059	–	0.24416	–
Weibull	1	0.99792	0.00273	0.00137	0.104	-0.89	0.14687	1.3021
	2	0.99891	0.000258	0.00093	0.034	-0.97	0.13698	1.6432
	3	0.99846	0.00578	0.00289	0.075	-0.93	0.15255	1.4028

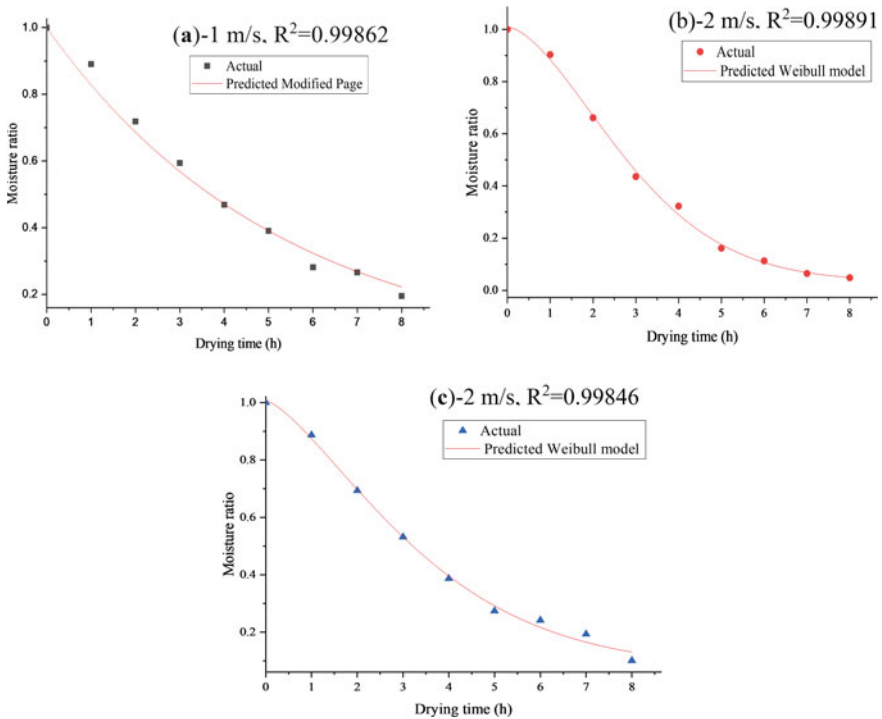


Fig. 4 Curve for best-fitted Weibull model for (a) 1 m/s and (b) 2 m/s and Modified Page model for (c) 3 m/s of thin layer drying kinetics

4 Conclusion

The thermal performance of an ETSD and drying kinetics of the garlic cloves are investigated. The maximum temperature achieved at the solar collector outlet was found to be 85.5 °C at 2 PM; afterward it reduced with the drying time. The moisture ratio curve was less diminishing at airflow velocity of 2 m/s followed by 3 and 1 m/s. The Modified Page model was found to be the best-fitted model of air velocity at 1 m/s. The Weibull model showed the best fit through higher coefficient of determination R^2 at 0.998 with low χ^2 and RSME value both at 2 m/s as well as 3 m/s air velocity during the drying process of garlic clove.

References

1. Chauhan YB, Rathod PP (2018) A Comprehensive Review on Solar Dryer. *Int J Ambient Energy* 41(3):1–28
2. Singh A (2014) Effect of Drying Characteristics of Garlic-A Review. *J. Food Process. Technol.* 05(04):1–6
3. Chopra K et al (2018) Global advancement on experimental and thermal analysis of evacuated tube collector with and without heat pipe systems and possible applications. *Appl Energy* 228 (June):351–389
4. Velić D et al (2004) Influence of airflow velocity on kinetics of convection apple drying. *J Food Eng* 64(1):97–102
5. Shringi V et al (2014) Experimental investigation of drying of garlic clove in solar dryer using phase change material as energy storage. *J Therm Anal Calorim* 118(1):29–41
6. Venkatesan N, Arjunan TV (2014) An experimental investigation and performance analysis of a solar drying of bitter gourd using an evacuated-tube air collector. *Int J ChemTech Res* 6 (14):5510–5518
7. Wang W et al (2018) Thermal performance of indirect forced convection solar dryer and kinetics analysis of mango. *Appl Therm Eng* 134:310–321
8. Mehta P et al (2018) Design and performance analysis of a mixed mode tent-type solar dryer for fish-drying in coastal areas. *Sol Energy* 170(May):671–681
9. Chayjan RA et al (2013) Modeling moisture diffusivity, activation energy and specific energy consumption of squash seeds in a semi fluidized and fluidized bed drying. *J Food Sci Technol* 50(4):667–677
10. Umayal Sundari AR et al (2013) Performance evaluation of a forced convection solar drier with evacuated tube collector for drying amla. *Int. J. Eng. Technol.* 5(3):2853–2858

Numerical Analysis of Regenerator for Pulse Tube Refrigerator



Sahil Variya, Dhruvil Joshi, Nikunj Rohit, Rutvik Brahmhatt,
and Chetan O. Yadav

Abstract The Stirling-type pulse tube cryocoolers (STPTC) consist of regenerator as a key component of the system. Regenerator is a heat exchanger consisting matrix material, in which during pressurization and depressurization cycle, cooling and heating occur within the system. The key parameters for modelling of the regenerator are frequency, mass flow rate, phase angle, diameter and length, porosity of matrix material, hydraulic diameter and charge pressure. The numerical software used for modelling of regenerator is a mathematical tool named REGEN 3.3 developed by National Institute of Standards and Technology (NIST). In present research paper, parametric study of regenerator is conducted. Simulations were performed with fixed diameter, length, porosity of matrix material and hydraulic diameter and factors like mass flow rate, frequency and phase angle were varied to analyse their effects on the system to obtain optimum coefficient of performance (COP). Numerical analysis using REGEN 3.3 and analytical study using phasor analysis of regenerator are carried out, and their results are compared.

Keywords Regenerator · REGEN 3.3 · Phasor analysis · Stirling · Pulse tube

S. Variya · D. Joshi (✉) · N. Rohit · R. Brahmhatt · C. O. Yadav
Sardar Vallabhbhai Patel Institute of Technology (SVIT), Vasad, India
e-mail: dbnd.joshi9@gmail.com

S. Variya
e-mail: variyaahil@gmail.com

N. Rohit
e-mail: nikunjrohit007@gmail.com

R. Brahmhatt
e-mail: rutvikbrahmhatt5@gmail.com

C. O. Yadav
e-mail: coyadav@gmail.com

1 Introduction

There has been rapid growth in the field of miniaturizing the cryocoolers for various applications such as space technology, medical, cooling of IR sensors. STPTC is one of the first choices for the space technologies. Xiaoqin Yang et al. had presented the hydraulic losses and its effect on the system [1]. N. Almtireen et al. carried out analytical and numerical study related to the phase shift mechanism and its effect on the performance of the system [2]. Thota Srikanth et al. had designed a stirling-type pulse tube cryocooler by using component-level software REGEN 3.3 and system-level software SAGE [3]. S. Rotundo et al. in their paper have explained about the practical approach to the system [4]. Ray Radebaugh et al. had studied the effect of geometry and frequency on the system performance [5].

REGEN 3.3 numerical model is used to design the regenerator at the component level, and phasor analytical model is used to design at the system level. This paper represents numerical one-dimensional analysis based on solving mass, energy and momentum equations, and then same parameters are used in the first-order phasor analysis. The obtained results in terms of cooling power were compared and represented at the end. Along with that the variation in cooling power and COP with different gas cross-sectional area has been studied.

It is seen from phasor analysis that with the increase in the volume of components the phase angle increases. Gas volume in the regenerator, conservation of mass requires that flow at the warm end will lead the flow at the cold end and is given by,

$$m_h = m_c + \frac{PV_{rg}}{RT_r} \quad (1)$$

m_c is the flow rate at the cold end, V_{rg} is the gas volume in the regenerator, R is the gas constant, T_r is the mean temperature of the regenerator and P is the rate of change of pressure in the regenerator, given by

$$P = i_2\pi fp \quad (2)$$

where i imaginary unit and p is the dynamic pressure [6].

2 Regenerator

The regenerator is the most important part of regenerative-type cryocoolers. The purpose of regenerator is to transmit acoustic or PV power from the compressor to the cold end of the regenerator with a minimum loss. A regenerative heat exchanger consists of a high heat capacity material with high surface area with which the fluid periodically exchanges energy. In stirling type of refrigerators, the gas oscillates periodically through a single fixed matrix. During compression stroke, the heat

from the gas is stored in the matrix material. Thus, low temperature gas is obtained at cold end of regenerator and during reverse (expansion) stroke the gas receives the heat stored in matrix material and returns to original state. Wire mesh screens and spheres are used as matrix material to store and release heat in regenerator. There exists an optimum ratio between the hydraulic diameter and the length of the regenerator that offers the maximum net refrigeration [1]. The other governing factors for performance of regenerator are frequency, mass flow rate, average pressure, pressure ratio, hot end temperature, cold end temperature, phase angle between mass flow rate at cold end and pressure, matrix material, porosity of matrix material and thermal penetration depth of matrix material.

2.1 Numerical Model of Regenerator and Analysis

The one-dimensional numerical analysis of regenerator is carried out on software named REGEN 3.3. It is the mathematical modelling software developed by NIST. It is used for carrying numerical analysis of only regenerator and not whole system, with Helium-3 or Helium-4 as working fluid. The model finds the numerical solution for one-dimensional equation for flow of helium gas through porous matrix. The solution is carried out by model by dividing the regenerator into small cells based on input value entered. Gas temperature, matrix temperature, mass flux and pressure in the gas are computed at each of these cells. The REGEN 3.3 model uses the equation of conservation of mass, momentum and energy for one-dimensional flow of gases in an open tube by adding friction factor and heat transfer factor in momentum equation and energy equation, respectively, to take into account effect of porous medium. They also take into account the effects of thermal capacity of matrix and heat transfer between matrix and gas.

Thus, following are the conservation equations for regenerator [7]

$$\frac{\partial \rho}{\partial t} + \frac{\partial(\rho v)}{\partial x} = 0 \tag{3}$$

$$\frac{\partial \rho v}{\partial t} + \frac{\partial(\rho v^2 + p)}{\partial x} - f(\rho, T, v) = 0 \tag{4}$$

$$\frac{\partial \emptyset A E}{\partial t} + \frac{\partial(\emptyset A(E + p)V)}{\partial x} - \frac{\partial \emptyset A k_g \frac{\partial T}{\partial x}}{\partial x} - \emptyset A q(p, T, T_m, v) = 0 \tag{5}$$

$$\frac{\partial D}{\partial T} + \emptyset A q(p, T, T_m, v) - \frac{(1 - \emptyset) A k_m \frac{\partial T_m}{\partial x}}{\partial x} = 0 \tag{6}$$

where matrix thermal content term is defined by

Table 1 Fixed parameters for optimization of regenerator on REGEN 3.3

Hot end temperature (K)	Cold end temperature (K)	Diameter (m)	Porosity	Hydraulic diameter (m)	Average pressure (Pa)	Pressure ratio
320	223	0.020	0.647	3.84E-04	1.00E+05	1.298

$$D(x, T) = \int_{T_{min}}^T (1 - \emptyset) A c_m(x, T) dT \quad (7)$$

Heat transfer term is given by

$$q(p, T, T_m, v) = 4H(p, T, v) (T_m - T/D_h) \quad (8)$$

The numerical analysis of regenerator was conducted on REGEN 3.3. More than 1000 test runs were carried out to find the best results for regenerator. During this analysis, mesh number points were selected as 41 and time steps per cycle were selected as 80. The iterations were carried out for 10,000 cycles. Method chosen was selected as 1. Boundary condition was chosen as 2 and so the input parameters were phase between mass flow and pressure at cold end, average pressure and pressure ratio.

During analysis for obtaining the optimum COP with fixed diameter of regenerator, mass flux at cold end, length, phase angle and frequency were varied. During analysis with fixed frequency for a given phase angle, different values of mass flow rate were used. Once all mass flow rates were tested, then another value of phase angle was entered. In this manner for entire range of frequency, mass flow rate, length and phase angle test runs were conducted to obtain the optimum COP and corresponding to that values of frequency, mass flow rate and phase angle.

3 Results and Discussion

Figure 1 shows the effect of COP at a different length of regenerator. It is observed from the figure that for a fixed parameters, i.e. diameter, pressure ratio and phase angle, the COP increases with the increase in the length upto 0.07 m, afterwards it decreases. The maximum COP of the system is observed at the length of 0.07 m, and the ratio of D/L for the regenerator is selected for the design and operating parameters.

Figure 2 shows the variation of COP for a three charge pressure values. From the figure, it is observed that the COP of the system decreases with the increase in inverse mass flux for all the three charge pressures. The system performance is higher at 0.20 MPa over a range of inversion mass flux. The maximum COP of the system is 0.5571 at 0.20 MPa. The figure reveals that system dimensions can be reduced with the increase in charge pressure.

Fig. 1 COP versus Length

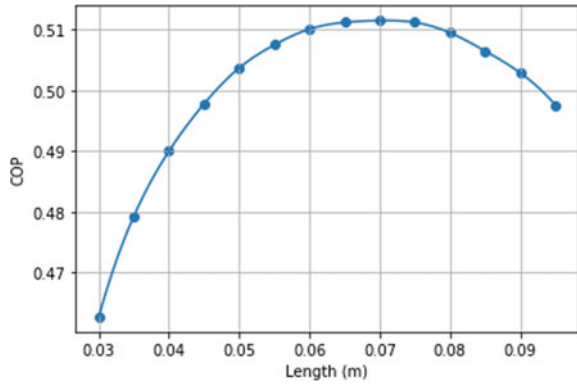


Fig. 2 COP versus A_g/\dot{m}_c

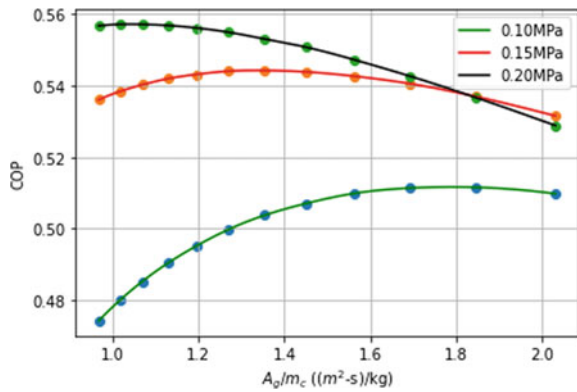
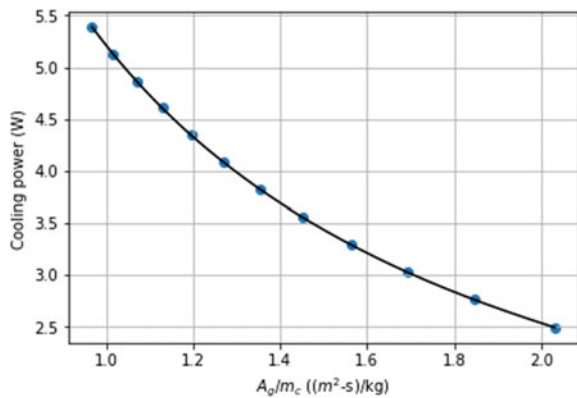


Fig. 3 Cooling power versus A_g/\dot{m}_c



From Fig. 3, it is observed that the cooling power reduces with the increase in inverse mass flux. Due to increase in gas cross-sectional area and reduced mass flow rate, there is a reduction in the heat transfer interaction and thus reduces the cooling power. The final dimension of the regenerator obtained by combining the

Fig. 4 COP versus Phase angle

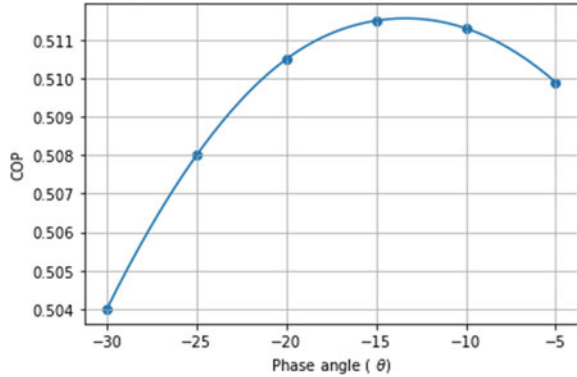
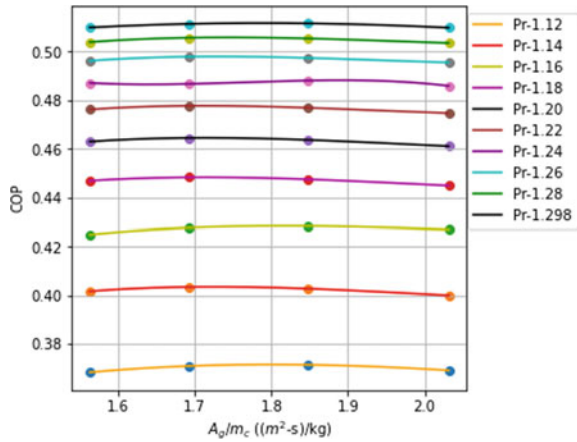


Fig. 5 COP versus A_g/\dot{m}_c



output result of Figs. 1, 2, and 3 is diameter, 0.02 m, length, 0.07 m, at charge pressure of 0.1 MPa and inverse mass flux, 1.84689.

Figure 4 shows the COP vs Phase angle for a regenerator. The maximum COP of 0.5115 for the regenerator is obtained at -15° .

Figure 5 shows variation of COP against inverse mass flux for 10 different pressure ratios. It is observed from figure that with increase in pressure ratio the cooling power is increased and simultaneously work required for the compressor decreases, and thus, the net effect observed is the increase in the COP. The maximum COP 0.5115 is obtained at pressure ratio 1.298.

Figures 6a and b and 7 are the plots of REGEN 3.3. From Fig. 6a, it is observed that the temperature of gas and matrix falls linearly as pressure drop and enthalpy drops along the length of regenerator.

From Fig. 6b, it is observed that mass flux deviates largely from mean value compared to pressure deviation. Also, there exists a phase difference between mass flux at hot and cold ends.

Fig. 6 (a) Average gas and matrix temperature along length of regenerator a— Average gas temperature, b— Average matrix temperature (b) Variation of pressure, mass flux at cold end, mass flux at hot end over one cycle, a—Pressure at cold end, b— Mass flux at hot end, c—Mass flux at cold end

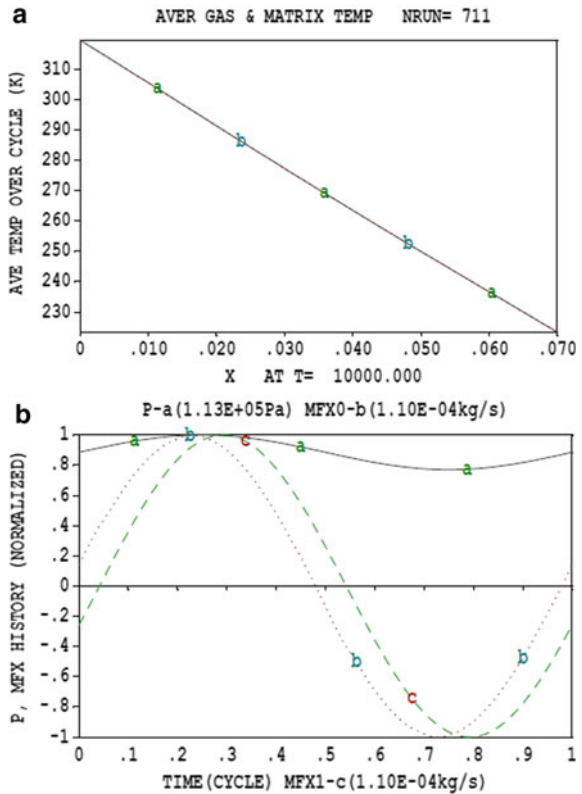
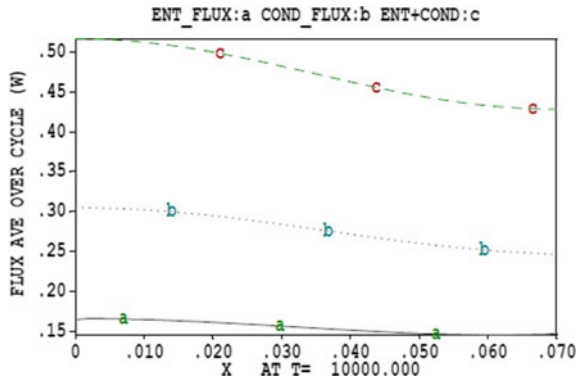


Fig. 7 Variation of enthalpy flux, conduction flux, sum of enthalpy flux and conduction flux along length of regenerator, (a) Enthalpy flux of gas, (b) Conduction flux of matrix, (c) Summation of a & b



From Fig. 7, enthalpy of gas decreases along the length of regenerator which results in decrease of conductive flux which reduces enthalpy of matrix too. Hence, sum of enthalpies decreases (Table 2).

Table 2 Comparison between numerical and analytical results

Sr. no.		Regen	Phasor
<i>Input parameters</i>			
1	Charge pressure (Pa)	10^5	10^5
2	Frequency (Hz)	20	20
3	Working gas ($\gamma=1.66$)	Helium	Helium
4	Hot end temperature (K)	320	320
5	Cold end temperature (K)	223	223
6	Diameter (m)	0.02	0.02
7	Pressure ratio	1.298	1.298
<i>Output—Regenerator</i>			
1	Length (mm)	70	–
2	Mass flow at hot end (Kg/sec)	1.098×10^{-4}	1×10^{-3}
3	Mass flow at cold end (Kg/sec)	1.1×10^{-4}	5.244×10^{-4}
4	Net cooling effect (W)	2.755	8.691

4 Conclusion

- Maximum COP of 0.5115 is obtained for the regenerator at an optimum value of regenerator diameter to length ratio of 0.2857. The thermal and pressure losses were minimum at the obtained regenerator dimension.
- Maximum COP of 0.5115 is observed at phase angle -15 degree due to minimum viscous dissipation effect and friction losses.
- There exists an optimum inversion mass flux for fixed operating pressure ratio. With the decrease in gas cross-sectional area, the gas is not able to lift sufficient heat due to limited heat transfer between regenerator matrix and fluid which adversely affects the performance of the system. Such trend is observed for at all the system charge pressure and pressure ratio.

Acknowledgements Authors would like to thank ‘Student Start-up and Innovation Policy Cell (SSIP)’ of our institute for providing financial aid and support for the development of the system. Authors would also like to thank all industry personnel involved in the fabrication of system.

References

1. Xiaoqin Yang, JN Chung (2005) Size effects on miniature Stirling cycle cryocooler. *Cryogenics* 45(8):537–545
2. Almtireen N, Brandner JJ, Korvink JG (2020) Pulse Tube Cryocooler: Phasor Analysis and One-Dimensional Numerical Simulation. *J Low Temp Phys* 199:1179–1197

3. Thota S, Gurudath CS, Amrit A, Basavaraj S, Dinesh K (2016) Design of High Frequency Pulse Tube Cryocooler for Onboard Space Applications. In: Iop Conference Series: Material Science and Engineering, vol. 171. IOP Publishing Ltd., New Delhi, India, pp 1–8
4. Rotundo S, Hughel G, Rebarchak A, Lin Y, Farouk B (2007) Design, Construction and Operation of a Traveling-Wave Pulse Tube Refrigerator. In: SD Miller, Editor RG Ross (Eds), Jr. International Cryocooler Conference, Inc. 2007, Cryocoolers 14, vol 14, pp 149–156. International Cryocooler Conference, Inc., Boulder, CO
5. Radebaugh R, O’Gallagher A (2005) Regenerator Operation at very high frequencies for microcryocoolers. In: JG Weisend II (Editor), Advances in Cryogenic Engineering: Transactions of Cryogenic Engineering Conference—CEC, Vol. 823, pp 1919–1928. American Institute of Physics, Colorado
6. Vanapalli S, Lewis M, Gan ZH, Radebaugh R (2007) 120 Hz pulse tube cryocooler for fast cooldown to 50 K. AIP Applied Physics Letters 90(7):1–3
7. Gary J, O’Gallagher A. Regen3.3: User manual, National Institute of Standards and Technology. <https://math.nist.gov/archive/regen/>. Last accessed 6 July 2020

Waste Heat Management in Hybrid Vehicles for Cabin Cooling



George Hawkins, Meeta Sharma, and Anoop Kumar Shukla

Abstract Hybrid electric vehicles are gaining popularity nowadays due to their superior fuel efficiency and benefits to the environment. As such a clear thermodynamic study on the hybrid vehicles in order to further improve the efficiency/fuel economy of the vehicle. This paper studies the effect of a vapor absorption cooling system for cabin cooling purposes. The heat required for the powering of the generator was taken from a low-grade heat source, from waste heat. Since the waste heat from the battery is insufficient for powering a cooling system, the heat from the exhaust was used. This is a low-grade heat source. A lithium-bromide (Li-Br-H₂O)-based vapor absorption system is used for the work as this has better output from a low-grade heat source. A waste heat output of 14.2 KW is generally available under city conditions. The thermodynamic analysis of the proposed system was performed, and under this, a coefficient of performance of 0.721 was observed. The thermodynamic first law is used to analyze the effects of various input parameters. Input parameters considered for the analysis are the mass flow rate of the pump, the input to the generator, input to the evaporator. The system was found to be a feasible option in increasing the performance of a hybrid electric vehicle.

Keywords Hybrid electric vehicle · Waste heat management · Cabin cooling · Vapor absorption refrigeration system

Nomenclature

Li-Br Lithium bromide

NH₃ Ammonia

H₂O Water

G. Hawkins · M. Sharma (✉) · A. K. Shukla
Amity University Uttar Pradesh, Noida, India
e-mail: msharma15@amity.edu

G. Hawkins
e-mail: georgehawkinsp@gmail.com

A. K. Shukla
e-mail: shukla.anoophbti@gmail.com

m	Mass flowrate (kg/sec)
h	Enthalpy (kW/kg)
Q_c	Heat transfer in condenser (kW)
P_c	Condenser pressure (KPa)
Q_e	Heat transfer in evaporator (kW)
P_e	Evaporator pressure (KPa)
m_{ss}	Mass flowrate of strong solution (kg/sec)
m_{ws}	Mass flowrate of weak solution (kg/sec)
ξ	Mass fraction
Q_a	Heat transfer in absorber (kW)
Q_{HX}	Heat transfer in heat exchanger (kW)
Q_g	Heat input to generator (kW)
COP	Coefficient of performance

Subscripts

$Ef_{(Ab)}$	Efficiency of absorber
$Ef_{(Con)}$	Efficiency of condenser
$Ef_{(Gen)}$	Efficiency of generator
$Ef_{(Ev)}$	Efficiency of evaporator
Eff_{HX}	Effectiveness of heat exchanger
T (Gen{in})	Generator inlet temperature
T (Chilled water)	Temperature of chilled water
m [1]	Mass flowrate of the pump

Acronyms

IC	Internal combustion
VAR	Vapor absorption refrigeration
EES	Engineering equation solver
HEX 1	Heat exchanger 1
HEX 2	Heat exchanger 2

1 Introduction

A hybrid vehicle is a means of transmission which uses an electric drive in addition to an IC engine as seen in conventional vehicles. The additional electric power train is provided for the two reasons: to increase fuel efficiency and to increase performance. Hybrid vehicles usually have a much smaller internal combustion engine than most conventional vehicles; this engine will also be much lighter. These vehicles also tend to be a lot more aerodynamic than most conventional vehicles.

The typical modern automobile has a coefficient of drag of 0.30–0.35. The Honda Insight, Toyota Prius, and Honda Civic Hybrid have coefficient of drag of 0.25, 0.26, and 0.28, respectively. Hybrid electric vehicles are in addition to this, environment friendly as they make use of an electric motor to be powered during requirements of high power thus reducing the higher amount of carbon dioxide emissions which would have been the case if conventional fuel had been used during high power applications. Thus, they reduce the carbon footprint on the earth. Hybrid vehicles are slightly more performance oriented than common commercial vehicles so any methods to improve the already high performance of these vehicles would be ideal. Seeing as to how performance oriented these vehicles are already, it would be natural to focus attention on how to further improve the performance of these vehicles. Managing the waste heat output of these vehicles is the most effective way to improve already impressive performance figures of these vehicles. Therefore, the two main sources of waste heat in a hybrid electric vehicle are from the engine and from the battery. The heat that can be obtained from the battery though is not significant enough to be converted into anything useful. A low-grade heat source is typically defined as any heat source which has a maximum temperature less than 250 °C. The exhaust of a car is a low-grade heat source. This heat source can be used to power a vapor absorption system. A Li-Br-H₂O vapor absorption system is proposed in this study to provide cabin cooling in these vehicles. There has been a lot of studies been done on hybrid vehicles, especially the thermodynamic aspect of them. There have also been studies done on the recovery of waste heat in vehicles and different ways to obtain them. Considerable work has been done on the modes of heat loss in commercial vehicles as well. Other studies have looked at different types of cooling systems that can be used, whereas more research has been done on how these systems could be implemented. Studies have also been done seeing which cooling system was the better suited for different purposes.

On the basis of the search conducted, some patents/publications were found to be the most relevant were: Dincer et al. [1] had performed a study on vehicle fuel consumption and found out that there was an increase of 20% when the air conditioning was turned on. This means that there is a possibility of increasing the fuel efficiency by 20% in this particular paper. Dincer et al. had also found out that the negative environmental impacts were greatly reduced with increase in fuel efficiency. There are three main ways in which waste heat can be utilized in a vehicle which was studied by Smith et al. [2] and those are: generating electricity, heating, and the cooling of the cabin. Johnson et al. [3] determined the different cooling approaches and prospects in commercial automobiles. Study of thermoelectric cooling systems powered by the waste heat in exhausts for the purposes of cabin cooling was discussed by Hsiao et al. [4]. The more conventional vapor compression system for cooling can deliver cabin cooling, but with mechanical compressor which uses electricity to pressurize the fluid refrigerant. Lambert and Jones [5] had done work on their paper in which they determine how for a normal mid-sized commercial vehicle this means that the compressor uses 12–17% of the power available. Low-grade heat sources are used in this study for useful energy.

A low-grade heat source is a low temperature heat source or a secondary heat source. In the case of the commercial vehicles, it is the heat from the exhaust. Absorption systems in low-grade (low temperature) heat sources and solar cooling systems have been investigated by Ezzine N et al. [6] Javani et al. [7] conducted a study on a vapor absorption system that recovers waste heat from vehicles. They had used a single effect vapor absorption system using NH_3 as the refrigerant. Meng Wang et al. [8] performed a study of a double effect vapor absorption system on fishing vessels in which two NH_3 was used as the refrigerant. Several studies reported the detailed analysis related to waste heat recovery, and combined cooling and heating of power systems [9–12].

The aim of the current work is to integrate a single effect vapor absorption system in vehicles in order to recover waste heat for cooling purposes by using a Li-Br- H_2O absorption system. Florides et al. [13] had accomplished a study on absorption systems in which it was identified that Li-Br- H_2O was a better system when the heat source that was available was from a low-grade heat source. The operating temperature of the Li-Br- H_2O vapor absorption system lies usually from 90 to 150 °C in the generator temperature. And since the exhaust is a low-grade heat source, a vapor absorption system with the working fluid as Li-Br- H_2O will be used for cabin cooling purposes. This working fluid has not been used in a vapor compression system used for cabin cooling and as such this is a novel idea. Reference [14] performed energy and exergy analysis for Li-Br vapour absorption system and investigate the COP for single effect and double effect system. Reference [15] discussed about the exhaust power adsorption air conditioners.

Exhaust gas heat recovery systems are used in some vehicles to accelerate coolant heat up time. This gives faster heat up of the engine coolant which in turn heats up the engine faster. Less fuel is used giving reduced emissions. The current work involves cabin cooling and as cooling of the cabin is required more and more these days due to global warming, the results obtained in this study will be of help in the future.

2 System Description

The Li-Br- H_2O system is used for this vapor absorption system. Figure 1 shows the schematic diagram of the proposed system. The schematic was prepared using microsoft word software. H_2O is the refrigerant and Li-Br is the absorbent. Refrigerant (H_2O) is absorbed by the absorber (Li-Br). There is a high pressure chamber (Generator/Condenser) and a low pressure chamber (Absorber/Evaporator). The H_2O needs to be evaporated at low temperature, which is why there is a low pressure chamber. The H_2O from the evaporator moves to the absorber due to slight pressure difference between them. Absorber contains Li-Br which absorbs the H_2O and forms a weak mixture. Weak Li-Br solution will pass through the pump and through the heat exchanger to reach the generator. In the

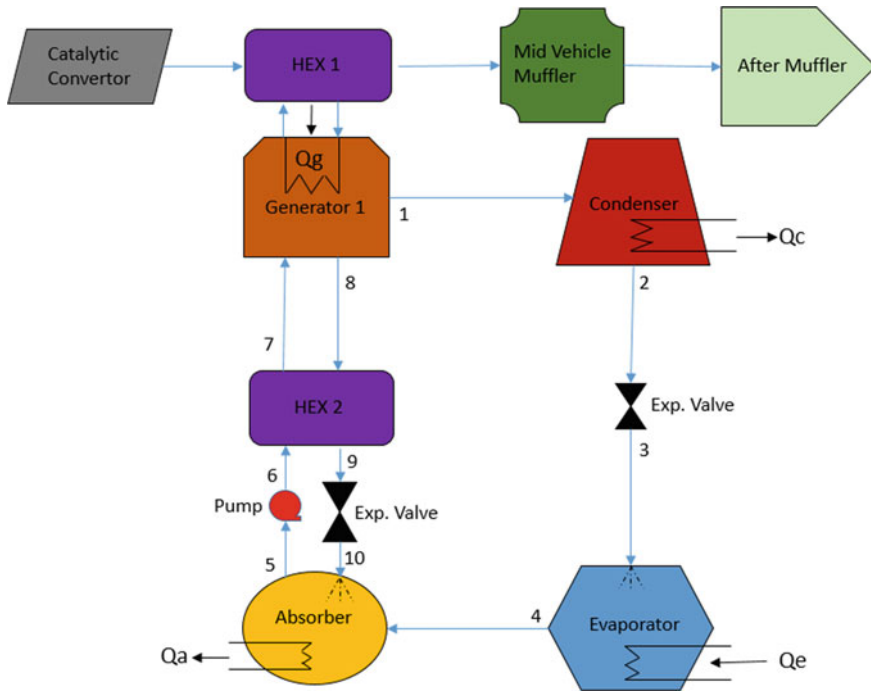


Fig. 1 Proposed system for waste heat management

generator, the heat is supplied. Since H_2O has a lower boiling point than Li-Br, it gets evaporated and the vapor goes to the condenser. Strong solution of Li-Br goes back through the heat exchanger to the absorber. The heat exchanger helps in increasing the heat of the solution going into the generator thus reducing the generator work. A cooling H_2O circuit is provided to cool the strong Li-Br entering the absorber and also to condense the H_2O in the condenser. A pressure reducing valve is used to reduce the pressure difference between the high pressure and low pressure areas. This will provide the cooled H_2O which becomes available in the evaporator. The heat used to heat the fluid in the generator comes from a heat exchanger which is kept after the catalytic converter which can reach temperatures up to $400\text{ }^\circ\text{C}$. The heat exchanger 1 draws heat from the catalytic converter.

3 Mathematical Modeling

The mathematical model for the major components of the proposed system for waste heat recovery (for vapor absorption systems) is given below. The assumptions for the listed components are:

- A steady state condition is assumed for the entire system.
- The heat exchanger effectiveness is kept constant.
- The process in the expander is assumed to be isentropic.
- At the exit of the evaporator, the refrigerant is assumed to be in saturated state.
- During the flow of the fluid, the pressure losses are assumed to be nonexistent.
- The heat losses to the environment from the system are also assumed to not exist.
- The steady state refrigerant is pure H_2O .
- The flow restrictors are assumed to be adiabatic.

3.1 Condenser Model

Since the mass flowing into the condenser and out of the condenser has only one inlet and outlet each both are equal.

There is an enthalpy difference between points 1 and 2. The heat released by the condenser is given in Eq. 1

$$m_1 = m_2 = m$$

$$Q_c = m(h_1 - h_2) \quad (1)$$

where Q_c is the heat removed at the condenser pressure P_c .

3.2 Refrigerant Expansion Valve

In the refrigerant expansion valve too the inlet is the exit of the condenser and there is only one outlet, so the mass flow rate across it remains the same.

The specific enthalpy remains the same across the expansion valve.

$$m_2 = m_3 = m$$

$$h_2 = h_3 \quad (2)$$

3.3 Evaporator Model

There is only one exit and inlet to the evaporator and so just like in the case of the condenser, the mass flow rate remains the same.

There is an enthalpy change from points 3 and 4. The heat absorbed by the evaporator is given by Eq. 3.

$$\begin{aligned} m_3 &= m_4 = m \\ Q_e &= m(h_4 - h_3) \end{aligned} \quad (3)$$

where Q_e shows the heat absorbed by the evaporator at evaporator pressure P_e .

3.4 Absorber Model

The absorber has two inlets, one which comes from the evaporator and the other which comes from the solution expansion valve. The solution coming from the expansion valve is a strong solution. The solution leaving the absorber through the pump is the weak solution.

From total mass balance:

$$\begin{aligned} m + m_{ss} &= m_{ws} \\ m_{ss} &= \lambda m \rightarrow m_{ws} = (1 + \lambda)m \end{aligned} \quad (4)$$

From mass balance for pure H₂O:

$$m + (1 - \xi_{ss})m_{ss} = (1 - \xi_{ws})m_{ws} \quad (5)$$

Combining both:

$$\lambda = \frac{\xi_{ws}}{\xi_{ss} - \xi_{ws}} \quad (6)$$

The heat released by the absorber is estimated as:

$$Q_a = mh_4 + \lambda mh_{10} - (1 + \lambda)mh_5$$

Or

$$Q_a = m[(h_4 - h_5) + \lambda(h_{10} - h_5)] \quad (7)$$

The first term in the above equation represents the enthalpy change of H₂O as changes its state from vapor at state 4 to liquid at state 5. The second term represents the sensible heat transferred as solution at state 10 is cooled to solution at state 5.

3.5 Heat Exchanger Model

The heat exchanger has two inlets and two exits, one inlet comes from the pump and exits to the generator and the other inlet comes from the generator and exits to the solution expansion valve. So there are two mass balance equations for the heat exchanger, one for the weak solution and one for the strong solution.

$$m_6 = m_7 = m_{ws}$$

$$m_8 = m_9 = m_{ss}$$

The heat of the heat exchanger is given by the following equation:

$$Q_{HX} = (1 + \lambda)m(h_7 - h_6) = \lambda m(h_8 - h_9) \quad (8)$$

where Q_{HX} the heat transfer in the heat exchanger and h_8 and h_9 are specific enthalpies at points 8 and 9.

3.6 Generator Model

The generator has one inlet and two outlets. The inlet is from the heat exchangers while the exit is to the condenser and to the heat exchanger. The mass balance is given by the equation below:

$$m_7 = m_8 + m$$

Heat input

$$Q_g = mh_1 + \lambda mh_8 - (1 + \lambda)mh_7$$

Or

$$Q_g = m[(h_1 - h_7) + \lambda(h_8 - h_7)] \quad (9)$$

In the above equation, the 1st term on the right-hand side represents energy required to generate H₂O vapor at state 1 from solution at state 7 and the 2nd term represents the sensible heat required to heat the solution from state 7 to state 8.

3.7 Solution Expansion Valve

The solution expansion valve has an exit toward the absorber and an inlet from the generator. The mass balance is given below. The enthalpy for the points 7 and 8 also remains same.

$$m_9 = m_{10} = m_{ws}$$

$$h_9 = h_{10}$$

3.8 Coefficient of Performance

The coefficient of performance (COP) of a refrigerating system is defined as the ratio of the heat absorbed to the heat supplied. The heat is absorbed in the evaporator and the heat is supplied in the generator. So the equation for COP would be:

$$COP = \frac{Q_e}{Q_g} \tag{10}$$

4 Results and Discussions

Before the starting of the analysis, some assumptions which are quite acceptable for a theoretical study needs to be taken into consideration. The following baseline parametric conditions are chosen for the proposed system and are mentioned in Table 1.

The different driving conditions at which different output of recovered heat are given below. For calculations, the city driving conditions of a mid-sized car were taken the value for recovered heat for this was 14.2KW. The heat source temperature of 120 degrees was obtained from this heat (Table 2).

The solution obtained is shown in Table 3. As can be seen, the COP obtained was 0.721 which is a sufficiently good value to be obtained. The values of the effectiveness of different components were also obtained. Along with the heat values of the different components, the properties at various state points are shown in Table 4. These are computed numerically by EES.

Table 1 Baseline parameters chosen for the analysis

Parameter	Value taken (Unit)
Heat source temperature	120 °C
Condenser operating temperature	46 °C
Absorber operating temperature	40 °C
Chilled H ₂ O outlet temperature	7 °C
Ambient temperature	25 °C
Flow rate at point 1	0.05 kg/sec
High pressure area	7.35 kPa
Effectiveness of heat exchanger	0.64
Ambient pressure	101.325 kPa

Table 2 Heat available for different vehicles

	Sub-compact	Compact	Mid-size
Highway:	14.6 kW	20.3 kW	29.2 kW
City:	9.1 kW	14.2 kW	18.2 kW

Table 3 Solution under the above starting conditions

COP	Ef _(Ab)	Ef _(Con)	Ef _(Gen)	Ef _(Ev)	Q _(hx) (kW)	Q _a (kW)	Q _c (kW)	Q _g (kW)	Q _e (kW)
0.721	0.609	0.641	0.150	0.738	3.06	14	11.2	12	10.6

Table 4 Properties at different state points

Point	h (kW/kg)	m (kg/sec)	P (kPa)	T (C)	X (% Li-Br)
1	85.8	0.0500	0.680	32.9	56.7
2	85.8	0.0500	7.357	32.9	56.7
3	147.0	0.0500	7.357	63.2	56.7
4	221.2	0.0455	7.357	89.4	62.4
5	153.9	0.0455	7.357	53.3	62.4
6	153.9	0.0455	0.680	44.7	62.4
7	2643.8	0.0045	7.357	76.8	0
8	167.2	0.0045	7.357	39.9	0
9	167.2	0.0045	0.680	1.5	0
10	2503.6	0.0045	0.680	1.5	0

4.1 Effect of Variation in Different Parameters

The following parameters such as heat exchanger effectiveness are investigated, and their effects are analyzed below.

The graphical representation in Fig. 2 shows the variation of the COP of the system with the variation in heat exchanger effectiveness. The effectiveness of a heat exchanger is the ratio of actual heat transferred to the max possible heat transfer. This cannot go beyond 1. As can be seen from this graph, the system without a heat exchanger, i.e. when the effectiveness is 0, has a COP of 0.6. This is the minimum obtainable COP. When a heat exchanger is added to the system, the COP increases almost linearly. The effectiveness of heat exchanger used for calculations was 0.64 and this gives a COP of 0.72.

The graphical representation in Fig. 3 shows the variation evaporator output with the variation in generator inlet temperature. The inlet temperature to the evaporator indicates the heat source temperature. From this, it can be seen that the evaporator output surges with the rise in heat source temperature. It can also be noted that after the temperature increases from 80 °C, the evaporator output reaches its highest values.

Fig. 2 COP verses heat exchanger effectiveness

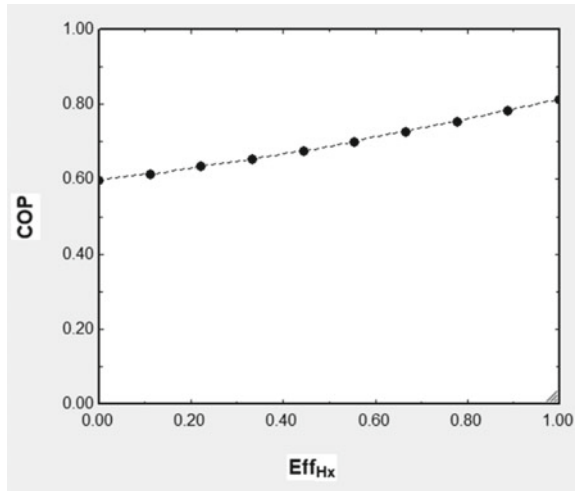
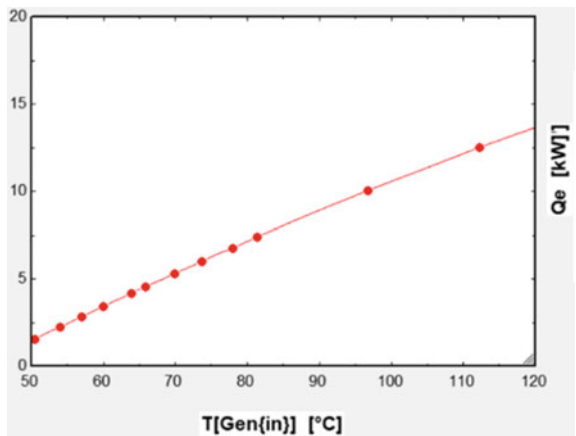


Fig. 3 Generator inlet temperature verses evaporator output



The graphical representation in Fig. 4 shows the variation of the high and low pressure values with the variation of the generator inlet temperature. The generator inlet temperature signifies the heat source temperature. There is always high pressure and low pressure areas for every vapor absorption cycle. As can be seen, the high pressure of the Li-Br solution increases more drastically with rise in heat source temperature. This is expected as the high pressure areas of the system are the condenser and the generator. And since the generator is directly connected to the heat source, this trend is expected. Note that the low pressure values decrease with increase in heat source temperature.

The graphical representation in Fig. 5 shows the variation of the heat values of different components with the variation of heat source temperature. The absorber and condenser releases heat while the evaporator and generator takes in heat. It is

Fig. 4 Generator inlet temperature verses pressure

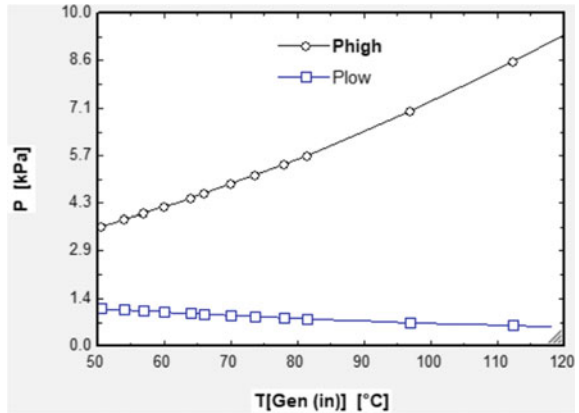
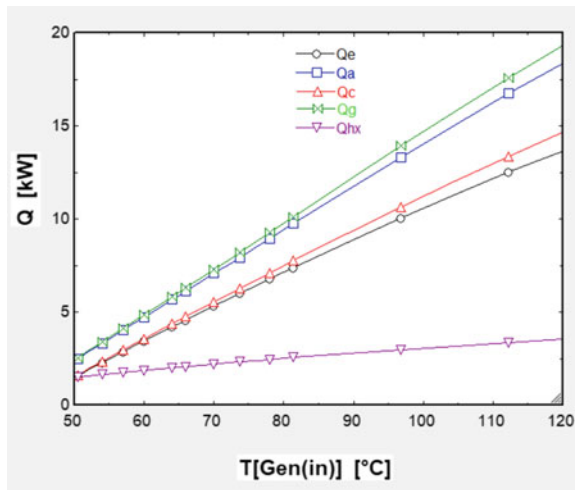


Fig. 5 Generator inlet verses heat values of major components



observed from the graphical result that the values for heat for the different components increase linearly with the increase in heat source temperature.

The graphical representation in Fig. 6 shows the variation in COP and the evaporator heat with variation in the temperature of the chilled H₂O used in the evaporator. The temperature of the chilled H₂O indicates the cabin temperature if the vehicle. As expected, the trend shows that as the evaporator heat which is represented by the blue curve increases with increase in temperature of the chilled H₂O. This means that the evaporator absorbs more heat if it is at a higher temperature. The COP only varies slightly.

Figure 7 shows the variation in the values of heat for the different components used in the system with the variation in temperature of chilled H₂O in the evaporator. As can be seen from the graph, with increase in temperature of chilled H₂O, the heat absorbed or released by different components increases linearly, except for

Fig. 6 Temperature of chilled H₂O versus COP and evaporator heat

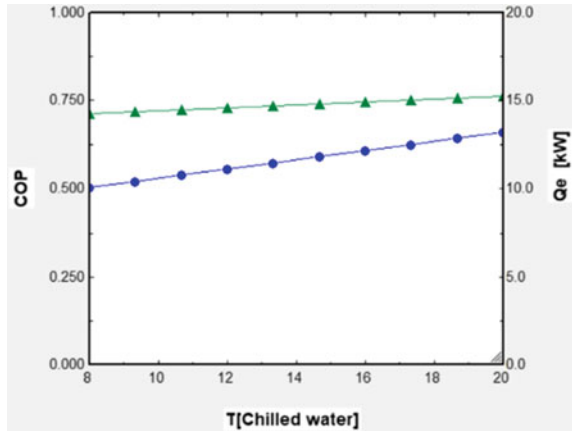
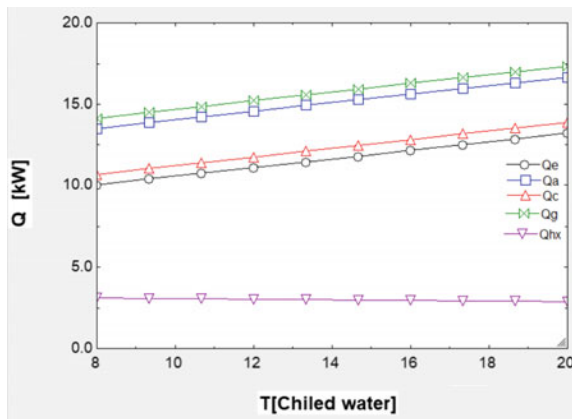


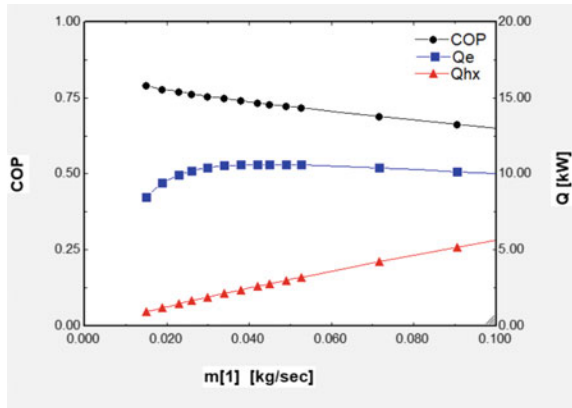
Fig. 7 Temperature of chilled H₂O versus heat of major components



the heat exchanger. The heat exchanger helps in increasing the heat of the solution going into the generator from the absorber. So when the temperature of chilled H₂O increases, this also increases the temperature of the solution going into the generator, thus reducing the work done by the heat exchanger.

The graphical representation in Fig. 8 shows the variation of the COP, evaporator heat value, and heat exchanger work output with the variation in the flow rate of the pump. Increasing flow rate adversely affects the COP of the system. This is due to the more work required by the pump to increase the flow rate. As can be observed from the graph, the heat exchanger work is also increasing while the evaporator heat absorbed is slightly decreasing. From this, it can be incurred that a mass flow rate of 0.02 kg/sec is optimal.

Fig. 8 Flow rate versus COP, heat values of evaporator, and heat exchanger



5 Validation and Discussion

The validation of the results was done based on a paper by S.C. Kaushik, Akhilesh Arora [14]. In the above-mentioned paper, the author had used similar conditions as the starting conditions used in this paper. The validation results are shown in Table 5.

This shows that the results of this work are validated. The slight variation in the results could be due to slight variation in the fluid properties in the software. In order to increase our knowledge in hybrid vehicles, a thorough study was needed to be conducted. In this paper though, the focus on the waste heat management of the Hybrid Electric Vehicles [HEVs] in order to further improve the efficiency of these vehicles. The aim was to use the waste heat output to power a cooling system which can be used to cool the vehicle cabin. The results show that this system for cooling the cabin can be completely possible for use in hybrid electric vehicles. The different ranges of COPs achievable for some different operating conditions are shown in Table 6.

This is a table that shows the different values of COP attained with varying values of heat source temperature and chilled H₂O temperature. From the entire study, however it can be seen that this is an effective system under varying conditions. The optimal conditions though would be if the heat exchanger has the

Table 5 Validation of the results

Name of component	Reference [14] (KW)	Present work (KW)	% error
Absorber	13.9	14	0.72
Condenser	11.3	11.2	0.89
Evaporator	10.5	10.6	0.95
Generator	12.2	12	1.6
Heat exchanger	3.05	3.06	0.33

Table 6 Range of COP and operating conditions

Heat source temperature (°C)	Chilled H ₂ O temperature (°C)	COP
105	8	0.700
95	10	0.730
85	16	0.745
75	20	0.739

best effectiveness as possible and when the heat source temperature is near the range of 120 degree C. It can also be seen that the best pump flow rate would be no more than 0.02 kg/sec. Thus, the Li-Br-H₂O vapor absorption system for cabin cooling was studied and was found to be feasible.

There are some considerable challenges associated with the actual implementation of this system in commercial vehicles. For starters, the economic aspect of the system has not been studied and also its viability while mass production is taken into consideration is also an area that needs to be looked into. Implementation of these systems into non-hybrid vehicles can also be studied. One more area that can be looked into is the maintenance and life of the entire system, since a lot of assumptions were made during the conduction of this analysis. A practical study considering the possible pressure losses and heat losses also needs to be done. Since hybrid vehicles are going to be the norm in the near future, considerable study needs to be invested into their constant improvement and evolution.

6 Conclusion

This paper studied the effect of a vapor absorption cooling system for cabin cooling purposes. The heat required for the powering of the generator was taken from a low-grade heat source. Since high-grade sources are not available in commercial vehicles, and since the waste heat from the battery was not sufficient for powering a cooling system, the heat from the exhaust was used. A Li-Br-H₂O system was used as this had better output from a low-grade heat source. A waste heat output of 14.2 KW is generally available under city conditions. Under this, a COP of 0.721 was obtained. The energy analysis for the system was also done. Effects of various parameters on the output of the cooling system were also found out. The system was found to be a feasible option in increasing the performance of a hybrid electric vehicle, especially under city conditions.

References

1. Dincer I (2007) Environmental and sustainability aspects of hydrogen and fuel cell systems. *Int J Energy Res*
2. Smith K, Thornton M (2007) Feasibility of thermoelectric for waste heat recovery in hybrid vehicles. National Energy Research Lab (NREL)
3. Johnson Valerie H (2002) Heat-generated cooling opportunities in vehicles. National Renewable Energy Laboratory (NREL)
4. Hsiao YY, Changb WC, Chena SL (2010) A mathematic model of thermoelectric module with applications on waste heat recovery from automobile engine *Energy*
5. Lambert MA, Jones BJ (2006) Automotive adsorption air conditioner powered by exhaust heat. part 1: conceptual and embodiment design. *Proceedings of the Institution of Mechanical Engineering*, July
6. Ezzine N, Barhoumi M, Mejbri K, Chemkhi S, Bellagi A (2004) Solar cooling with the absorption principle: first and second law analysis of an ammonia-water double-generator absorption chiller. *Desalination*
7. Javani N, Dincer I (2012) Thermodynamic analysis of waste heat recovery for cooling systems in hybrid and electric vehicles
8. Wang M, Becker TM (2018) Ammonia/ionic liquid based double-effect vapor absorption refrigeration cycles driven by waste heat for cooling in fishing vessels
9. Sharma A, Sharma M, Shukla AK, Negi N (2019) Evaluation of Heat Recovery Steam Generator for Gas/Steam Combined Cycle Power Plants. In: *Advances in Fluid and Thermal Engineering* (pp 189–200). Springer, Singapore
10. Sharma M, Singh O (2017) Energy and exergy investigations upon tri-generation based combined cooling, heating, and power (CCHP) system for community applications. In: *ASME 2017 Gas Turbine India Conference*. American Society of Mechanical Engineers Digital Collection
11. Shukla AK, Sharma A, Sharma M, Mishra S (2018) Performance improvement of simple gas turbine cycle with vapor compression inlet air cooling. *Materials Today: Proceedings* 5 (9):19172–19180
12. Shukla AK, Singh O (2017) Impact of inlet fogging on the performance of steam injected cooled gas turbine based combined cycle power plant. In: *Gas Turbine India Conference* (vol 58509, p V001T03A004). American Society of Mechanical Engineers
13. Florides GA, Kalogirou SA (2009) Design and construction of a LiBr–water absorption machine
14. Kaushik SC, Arora A (2009) Energy and exergy analysis of single effect and series flow double effect water–lithium bromide absorption refrigeration systems. *Int J Refrig* 32 (6):1247–1258
15. Lambert MA, Jones BJ (2006) Automotive adsorption air conditioner powered by exhaust heat. part 2: detailed design and analysis. *Proceedings of the Institution of Mechanical Engineers*
16. Chen Q, Prasad RC (2008) Simulation of a vapour-compression refrigeration cycle using HFC-134a and CFC-12. *International Communications in Heat and Mass Transfer*

Effect on Performance and Emission of IC Engine Using Mahua Oil and Yellow Grease—A Simulation-Based Study Using Diesel-RK



Shiv Kumar Sonkar, Pushyamitra Mishra, and Prashant V. Baredar

Abstract In the present scenario, biodiesel is known to be the best replacement of fossil fuels like diesel used in automotive industries. Biodiesel can be obtained from different sources like animal oil, vegetables, and plants and can fulfill the required need to industry. In the current study, different biodiesel blends are used in the simulation study with the use of Diesel-RK Software. Various IC engine performance parameters were studied under this simulation which resulted in the improvement in the performance of IC engine with less emission of toxic gases using biofuel.

Keywords Biodiesel • Simulation • Diesel-RK • Fuel emission • IC engine

1 Introduction

In the current scenario, diesel used as a fuel is on the gradual way of getting depleted so in order to save these fossil fuels a numerous biodiesel are coming into existence for providing better performance in vehicles with reduction in toxic gases [1]. With this thought of preserving the fossil fuels, current study has been carried out using different biofuels which can act as a replacement for fossil fuels [2]. Though biofuels show less efficiencies as compared to pure diesel but are highly useable as they also contribute in saving the environment by emitting less toxic

S. K. Sonkar (✉)

Department of Electrical and Electronics, SIRTS, Bhopal, India
e-mail: shiv.sonkar19@gmail.com

P. Mishra

Department of Mechanical Engineering, MANIT, Bhopal, India
e-mail: 2010pinkumishra@gmail.com

P. V. Baredar

Department of Energy, Energy Centre, MANIT, Bhopal, India
e-mail: prashant.baredar@gmail.com

gases. In the present study, yellow grease and mahua oil are used for the study purpose using the DIESEL-RK simulation software. DIESEL-RK being the software provides virtual environment for performing the simulations using different parameters and fuels [3]. The fast data processing speed has allowed DIESEL-RK to solve optimization tasks well, including optimizing the crown piston shape and fuel injection system to achieve low NO_x and smoke emissions. Almost simulation-based studies for engine performance and calculation for optimization can be done very quickly with small costs in Diesel-RK.

Use of DIESEL-RK also results in cost saving as compared to experimental works carried out using the real test rig [4]. Commonly used biofuels like Karanja biodiesel are used in a Bharat Stage IV with variable compression ratio [5].

2 Biodiesel—Extraction Processes

As the world is pounding for an alternative fuel to be used instead of diesel in compression ignition engine, biodiesel has come across research scholars which tend to provide and deliver similar properties and outcomes without any bigger mechanical modification when compared to diesel [1]. Biodiesel extraction process varies based on their feedstock and origin [2]. The different types of techniques and synthesis process of biodiesel are described below.

2.1 Pyrolysis

Pyrolysis is also known as thermal cracking [3]. The term thermal cracking itself describes the process of transforming a substance to another with the help of heating, and catalyst may or may not take part. This type of heating is done in the absence of air or oxygen to break the chemical bond and produce smaller molecules [4].

2.2 Transesterification Process

Transesterification process delivers huge conversion rate as well as reaction rate in the given amount of time [2]. It is a chemical process in which transesterification of triglycerides of fatty acids happens and converts it into biodiesel with the help of methanol or ethanol as catalyst. In this, glycerin is produced as a by-product of this reaction [5].

2.3 Biochemical Process

Biochemical process is in which a substance is broken down and converted through a biological process such as fermentation of sugars in biomass crops to alcohol [6]. Organic compounds are broken by several enzymes and microorganisms and organic compounds gets converted into biomass feedstock into alcohols and bio-fuels [7].

3 Simulation (Diesel-RK)

For the simulation purpose, Diesel-RK Software is utilized for obtaining the performance using two different biofuels (mahua oil and yellow grease). Further, the results obtained using these biofuels are compared with results of diesel as a fuel. In RK-model of combustion, the spray is classified into seven regions, as shown in Fig. 1. Each region had a separate condition of evaporation and burning [4]. These are:

- 1) Free spray core.
- 2) Front of the free spray.
- 3) Outer sleeve of the spray.
- 4) Near wall flow (NWF) nucleus.
- 5) NWF on the piston surface.
- 6) The dense front of the NWF and
- 7) NWF outer zone.

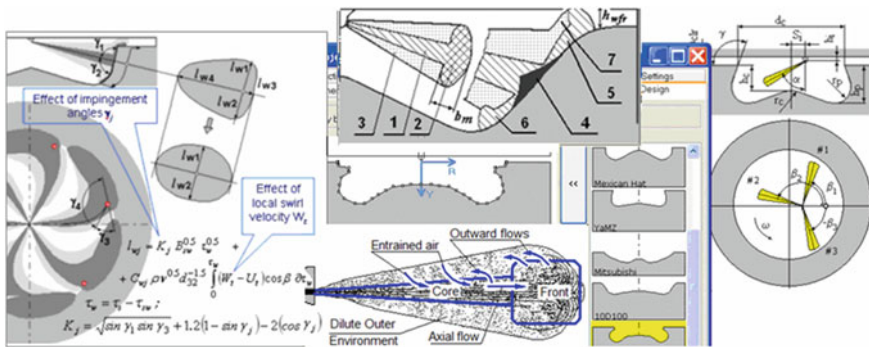


Fig. 1 Spray regions in Diesel-RK Software [7]

Table 1 Specifications used in the simulation

Engine make	Kirloskar TAF 1
Engine type	4-Stroke, Diesel engine
Number of cylinders	1
Bore	87.5
stroke	110 mm
Cylinder capacity	0.66 L
Compression ratio	17.5
Rated power	4.4 kW, 1500 rpm
Orifice diameter	0.15 mm
Injection pressure	220 bar

3.1 Model Used for Simulation

For the simulation study, Kirloskar TAF 1 model was selected in DIESEL-RK software and further specifications were used as shown in Table 1. First the virtual environment for engine simulation was prepared in the software, and different results were evaluated in the final stage of simulation and are further represented in the form of tables.

3.2 Material Property

For the study on engine performance, different blends were prepared using different percentage of mahua oil and yellow grease. These prepared blends were simultaneously tested in DIESEL-RK software with their properties to provide an effect on engine performance and further evaluation (Tables 2 and 3).

Table 2 Material properties of Mahua oil

Property	Pure diesel	10% MO	20% MO	30% MO	40% MO	100% MO
Density (Kg/m ³)	830	829	835	841	847	882
Viscosity (mm ² S)	2.72	2.4	2.7	2.8	3.0	4.2
Cetane number	48	51.6	52.2	52.8	53.4	57
Flash point (°C)	67.7	64	76	88	100	170
Calorific value (KJ/Kg)	42.5	41.55	41.35	40.9	40.65	38.5

Table 3 Material properties of yellow grease

Property	Pure diesel	10% YGO	20% YGO	30% YGO	40% YGO	100% YGO
Density (Kg/m ³)	830	839	841	844	852	885
Viscosity (mm ² S)	2.72	3.2	3.3	3.45	3.6	4.6
Cetane number	48	47.32	48.68	49.07	49.37	51.3
Flash point (°C)	67.7	76	80	84	91	170
Calorific value (KJ/Kg)	42.5	41.37	41.18	40.46	39.48	36.22

4 Results

After the simulation process using DIESEL-RK, different values of piston engine power (KW), brake torque, efficiency of piston engine, indicated efficiency, mechanical efficiency, maximum cylinder pressure, Bosch smoke number, CO₂ g/kWh, NO g/kWh, SO₂.

From Table 4, it can be seen that different values of piston engine power, brake torque, maximum cylinder, and maximum temperature were obtained for diesel as a fuel and different blend with different percent as a fuel used for the simulation. The obtained values of piston engine power are observed that blend with 30% mahua oil showed the maximum values, i.e., 5.5115 KW. From the values obtained for piston engine power, it is seen that initially increasing the percentage of biodiesel increase the engine power and after reaching the maximum point, it again decreases with further addition of biodiesel. Although addition of the biodiesel to the diesel fuel decreases its heating value, higher power was obtained in the simulation. Similarly in the case of brake torque, maximum values were obtained with 30%, i.e., 35.090 of mahua oil, and further, addition of mahua oil further decreases the brake torque. Maximum cylinder pressure and maximum temperature in case of mahua oil are shown in 20% blend with a value of 94.678 bar and 1931.9 K, respectively.

Table 4 Mahua oil engine performance-based result comparison

Parameters	Pure diesel	10 M	20 M	30 M	40 M	100 M
Piston engine power (kW)	5.4220	5.4341	5.4691	5.5115	5.4594	5.2551
Brake torque	34.520	34.597	34.820	35.090	34.758	33.457
Maximum cylinder pressure, bar	90.070	94.467	94.678	89.254	88.712	87.035
Maximum cylinder temperature (K)	1872.3	1900.7	1921.9	1850.0	1843.1	1798.1

Table 5 Yellow grease engine performance-based result comparison

Parameters	Pure diesel	10 YG	20 YG	30 YG	40 YG	100 YG
Piston engine power (kW)	5.4220	5.4415	5.6162	5.3832	5.2391	5.0114
Brake torque	34.520	34.644	35.756	34.273	33.356	31.905
Maximum cylinder pressure, bar	90.070	89.090	93.687	88.470	87.102	77.539
Maximum cylinder temperature (K)	1872.3	1839.7	1917.4	1824.4	1806.5	1660.0

From Table 5, it can be seen that different values of piston engine power, brake torque, maximum cylinder, and maximum temperature were obtained for diesel as a fuel and different blend with different percent as a fuel used for the simulation. The obtained values of piston engine power are observed that blend with 20% yellow grease showed the maximum values, i.e., 5.6152 KW. From the values obtained for piston engine power, it is seen that initially increasing the percentage of biodiesel increase the engine power, and after reaching the maximum point, it again decreases with further addition of biodiesel. Although addition of the biodiesel to the diesel fuel decreases its heating value, higher power was obtained in the simulation. Similarly in the case of brake torque, maximum values were obtained with 30%, i.e., 35.756 of mahua oil, and further, addition of mahua oil further decrease the brake torque. Maximum cylinder pressure and maximum temperature in case of mahua oil are shown in 20% blend with a value of 93.687 bar and 1917.4 K, respectively (Tables 6 and 7)

On comparing different efficiency of biodiesel with different blend percent of mahua oil and yellow grease, no significant changes were obtained only of variation of very less fraction has been observed in all the cases. While comparing the results obtained for different efficiencies, it is observed that for piston engine efficiency maximum results were obtained with diesel as a fuel when compared with different blends of mahua oil and yellow grease. For indicated efficiency, maximum

Table 6 Mahua oil efficiency comparison

Parameters	Pure diesel	10 M	20 M	30 M	40 M	100 M
Efficiency of piston engine	0.35807	0.34594	0.34676	0.35004	0.34848	0.34501
Indicated Efficiency	0.42884	0.43223	0.43310	0.43432	0.43417	0.43273
Mechanical Efficiency	0.85956	0.82767	0.82786	0.83057	0.82936	0.82501

Table 7 Yellow grease efficiency comparison

Parameters	Pure diesel	10 YG	20 YG	30 YG	40 YG	100 YG
Efficiency of piston engine	0.35807	0.35297	0.35377	0.35211	0.34931	0.33818
Indicated efficiency	0.42884	0.42232	0.42196	0.42220	0.42059	0.40823
Mechanical efficiency	0.85956	0.85937	0.86168	0.85839	0.85538	0.85287

Table 8 Mahua oil result for emission

Parameters	Pure diesel	10 M	20 M	30 M	40 M	100 M
Bosch smoke number	2.7674	1.5454	1.3772	1.7265	1.7504	1.8486
CO ₂ (g/kWh)	770.70	762.08	756.85	753.17	759.99	791.11
NO (g/kWh)	12.283	13.900	14.962	12.173	11.923	10.304
SO ₂	0.00946	0.00946	0.00940	0.00935	0.00943	0.00982

Table 9 Yellow grease result for emission

Parameters	Pure diesel	10 YG	20 YG	30 YG	40 YG	100 YG
Bosch smoke number	2.7674	2.3043	2.2420	2.2777	2.3037	2.9968
CO ₂ (g/kWh)	770.70	764.43	736.12	772.90	793.93	841.55
NO (g/kWh)	12.283	9.2990	11.322	8.7594	8.0753	8.5817
SO ₂	0.00946	0.00786	0.00491	0.00765	0.01075	0.02939

efficiency is seen in blend with 30% mahua oil, whereas for mechanical efficiency maximum values were obtained for yellow grease, i.e., with 20% blend (Tables 8 and 9).

Biodiesel also has some emissions benefits, which can result in reduction of toxic gases produced at the time of combustion in engine. In the study with different blend percentages of mahua oil and yellow grease as a biofuel, it was observed that minimum values for mahua oil were obtained in 20% mahua oil blend, whereas in case of yellow grease 20% yellow grease showed the minimum values. In terms of CO₂ emission, 30% mahua oil showed the minimum emission, whereas in yellow grease 20% yellow grease showed the minimum emission. For NO prediction, mahua oil showed the minimum release with the values of 11.923 g/KWH whereas in yellow grease blends, blend with 40% yellow showed the 8.0753 g/KWH values.

SO₂ is also placed under the category of toxic emissions where minimum values were obtained at 30% mahua oil and in case of yellow grease 20% yellow grease showed the least values of SO₂ emission.

5 Conclusion

From the overall study, it can be concluded that both yellow grease and mahua oil can be used as a biodiesel for the engine as a fuel as both of these materials showed overall better performance than pure diesel. Biodiesel blends showed greater significance in decreasing the emission of toxic gases as compared to pure biodiesel. Overall, from this study it can be concluded that replacement of diesel which is a fossil fuel and is on the stage of getting exhausted can be replaced with different biodiesels which will benefit both industrially and environmentally.

References

1. Costa M, Piazzullo D (2018) Biofuel Powering of Internal Combustion Engines: Production Routes, Effect on Performance and CFD Modeling of Combustion. *Front Mech Eng* 4 (August):1–14. <https://doi.org/10.3389/fmech.2018.00009>
2. Balamurugan T, Arun A, Sathishkumar GB (2018) Biodiesel derived from corn oil – A fuel substitute for diesel. *Renew Sustain Energy Rev* 94(March):772–778. <https://doi.org/10.1016/j.rser.2018.06.048>
3. Pham VV (2019) Research on the application of diesel-RK in the calculation and evaluation of technical and economic criteria of marine diesel engines using the unified ULSD and biodiesel blended fuel. *J Mech Eng Res Dev* 42(2):87–97. <https://doi.org/10.26480/jmerd.02.2019.87.97>
4. Al-dawody MF, Bhatti SK (2013) Optimization strategies to reduce the biodiesel NO_x effect in diesel engine with experimental verification. *Energy Convers Manag* 68:96–104. <https://doi.org/10.1016/j.enconman.2012.12.025>
5. Rajak U, Nashine P, Verma TN (2020) Effect of spirulina microalgae biodiesel enriched with diesel fuel on performance and emission characteristics of CI engine. *Fuel* 268(January), p 117305. <https://doi.org/10.1016/j.fuel.2020.117305>
6. Al-Dawody MF, Jazie AA, Abdulkadhim Abbas H (2019) Experimental and simulation study for the effect of waste cooking oil methyl ester blended with diesel fuel on the performance and emissions of diesel engine. *Alexandria Eng J* 58(1), pp 9–17. <https://doi.org/10.1016/j.aej.2018.05.009>
7. Diesel-rk, “Software for engine simulation and optimization,” *Softw. engine Simul. Optim*
8. Gonca G, Dobrucali E (2016) Theoretical and experimental study on the performance of a diesel engine fueled with diesel-biodiesel blends. *Renew. Energy* 93:658–666. <https://doi.org/10.1016/j.renene.2016.03.037>
9. Yan J, Yan Y (2017) *Biodiesel Production and Technologies*, vol 3. Elsevier
10. Hoekman SK, Robbins C (2012) Review of the effects of biodiesel on NO_x emissions. *Fuel Process Technol* 96:237–249. <https://doi.org/10.1016/j.fuproc.2011.12.036>
11. Tan YH, Mujawar MN, Kansedo J (2019) Biodiesel Synthesis using Natural Solid Catalyst Derived from Biomass Waste—A Review. *J Ind Eng Chem*. <https://doi.org/10.1016/j.jiec.2019.09.022>

12. Y. Demirel (2018) Biofuels, vol 1
13. Lawan I et al (2020) Synthesis, properties and effects of a multi-functional biodiesel fuel additive. Fuel Process Technol 198(September), p 106228. <https://doi.org/10.1016/j.fuproc.2019.106228>
14. Abou-shanab R (2015) Green renewable Energy for Sustainable socio-economic development, September

Comparative CFD Analysis of Straight and Helical-Shaped Earth Air Pipe Heat Exchanger (EAPHE) System



Mahendra Kumar Verma and Vikas Bansal

Abstract With the gradual changes in the environment due to the increasing greenhouse effect, numerous techniques are being adopted and are coming into existence to improve the prevailing circumstances. In the present study, three different designs of tubes used in the EAPHE system are considered for the study purpose to identify the effects of different designs on the performance of the EAPHE System. Also, different velocities were considered at the inlet to find the optimum velocity required for the maximum benefits in EAPHE Systems. From the overall study, it is determined that minimum velocity considered in the study, i.e., 5 m/s showed the best output for temperature release in combination with a helical shape pipe. Also, a relation between Nusselt number and velocity has been established using this study.

Keywords EAPHE · Heat transfer · Velocity · Nusselt number

1 Introduction

As fossil fuels are exhausted, the present conditions in the region confront a shortage of resources. We, therefore, have to find sustainable energy renewable energy sources that can meet the increasing wants and expectations of the nation's future source. Unusual renewable technologies are stronger, bigger, and consume more powerful, not effectively unlimited that can be more easily controlled in the

M. K. Verma (✉) · V. Bansal

Department of Mechanical Engineering, Rajasthan Technical University-Kota, Kota, Rajasthan, India

e-mail: vermamv81@gmail.com

V. Bansal

e-mail: bansal_vikas1@yahoo.com

M. K. Verma

Department of Mechanical Engineering, Amity School of Engineering and Technology, Amity University, Noida, Uttar Pradesh, India

© The Author(s), under exclusive license to Springer Nature Singapore Pte Ltd. 2021

B. S. Sikarwar et al. (eds.), *Advances in Fluid and Thermal Engineering*,

Lecture Notes in Mechanical Engineering,

https://doi.org/10.1007/978-981-16-0159-0_76

world's environment [1]. Air conditioning has been most commonly used in homes and commercial computing devices. CFCs that cause damage to the environment and the ecosystem by a greenhouse gas and seem to be the most commonly used refrigerants when combusted. In order to eliminate the huge issue and problem, technology is explored and is developing environmentally sustainable cold infrastructures. Researchers and professionals develop the technology of alternative forms of energy, such as the use of energy of excellent quality, to reduce power consumption. EAPHE has been one of the best options.

Because of the significance of the structure of the earth tunnel, various researchers carried out multiple studies on parametric studies of EAHE and greenhouse. The effects of buried pipe length, pipe diameter, mass flow rate, soil depth and soil types on the greenhouse air temperatures, are present in [2]. Tests of different thermal conductivities of Soil were used to test the effect of soil properties on soil temperature. The soil effects on the ground temperature have been calculated using soil thermal conductivity testing [3, 4] studied the mainly hot and dry climate in Ajmer in India with the experimental and measured fluid dynamics modeling and the effect on the thermal performance of EATHE on the continuous operating time and also the thermal conductivity of the soil under transient conditions. The results of this study showed that the temporary therapeutic performance of EATHE is dependent on thermal conductivity and soil life. The EATHE system has developed a CFD interface simulation model for CFX12.0 studies [5]. Scientific findings on the setup of experiments in Bhopal (Central India) confirmed the results of the study. The effects have been reached. The results were evaluated and comparative research was carried out [6]. This overall experimental study showed that each country has a difference in the levels of heat dissipation and thermal saturation affecting the efficiency of EATHE for a continuous 12 h operation in terms of temperature drop, heat transfer rate, and EATHE system COP.

Various improvements have originated from previous work on EAPHE systems [7]. Conducted an experiment of air cooling research project and reached the conclusion that the internal temperature decrease in a room where the evaporator of a system was placed. Some other findings in this study also indicated that these systems are highly effective in the summer months [8, 9] also demonstrated that the use of such design in summer indicates a different temperature deviation, decreased relative humidity. Artificial neural network studies have been used [10] optimize earth air cooling systems parameters [11] used the EAPHE system's genetics-based algorithms program. The virtual performance of EAPHE systems with results on several parameters which were difficult to consider in the experimental studies was demonstrated by the modeling-based studies [12]. And besides, one can consider the definition of success made in earth's air cooling from the analysis of previous research [13, 14].

2 System Description and Simulation Setup

In order to investigate the effect of the U-shapes, helical and spiral piping on EAPHE system thermal performance and system efficiency, CFD computation and commercial use of Fluent 19.0 CFD were performed and used with Catia V5 geometric modeling software. FLUENT software (version 19.0) was used in this analysis to transform ruling equations by using a finite-volume method into numerically resolvable ordinary differential equations. The $k-\epsilon$ model turbulent model is selected for the problem because the flow is turbulent. The energy equation was maintained using a simple solver algorithm as a heat transfer model. The empirical analysis was emphasized by the following conclusions (Tables 1, 2, and 3; Fig. 1):

Table 1 Geometrical and simulation parameters

Parameters	Unit	Value
U-shaped pipe length	mm	6000
U-shaped pipe inner diameter	mm	100
U-shaped pipe outer diameter	mm	103
spiral-shaped pipe length	mm	6000
spiral-shaped pipe inner diameter	mm	100
spiral-shaped pipe outer diameter	mm	103
Surrounding soil diameter	m	2–3

Table 2 Material properties

Material	Density (Kg/m ³)	Specific heat (J/KgK)	Thermal conductivity (W/mK)	References
PVC	1380	900	1.16	[6]
Air	1.225	1006.43	0.0242	[15]
Soil	2050	1840	0.52	[16]

Table 3 Boundary conditions [6]

Boundaries	Unit	Value
Air inlet velocity	ms ⁻¹	5, 10, 12
Air inlet temperature	°C	46.2
Soil temperature	°C	27
Pipe temperature	°C	27

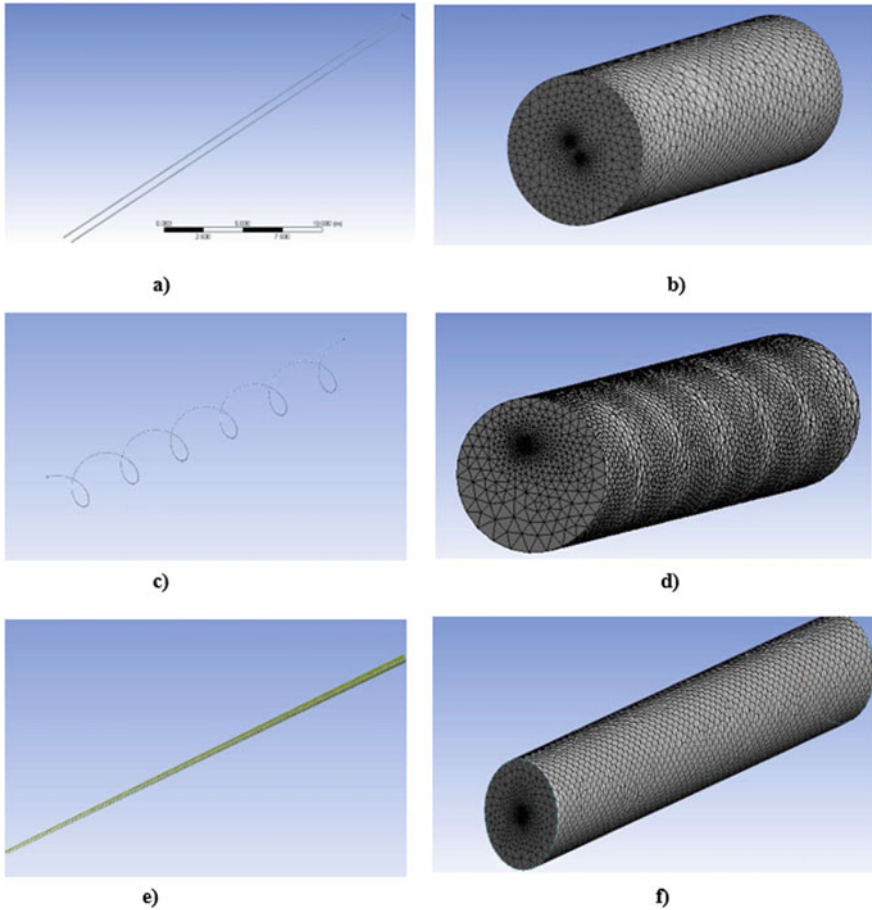


Fig. 1 (a) U-shaped model, (b) meshing of U-shaped model, (c) helical-shaped model, (d) meshing of helical-shaped model (e) spiral-shaped model, (f) meshing of spiral-shaped model

1. The thermal and physical characteristics of solid-fluid may be changed when the input parameter is used at varying velocities.
2. There are certain variations with EAPHE pipes using various design geometries.

2.1 Boundary Conditions

At the inlet of the EAPHE tube system, it was necessary to specify air velocity, V (m/s), and air dynamic loads and variable temperature, t_{in} ($^{\circ}\text{C}$). At the condensed changeable air temperature at the pipe, the dynamical thermal properties (frequency, volume, and



Fig. 2 Temperature contours of U-shaped pipe

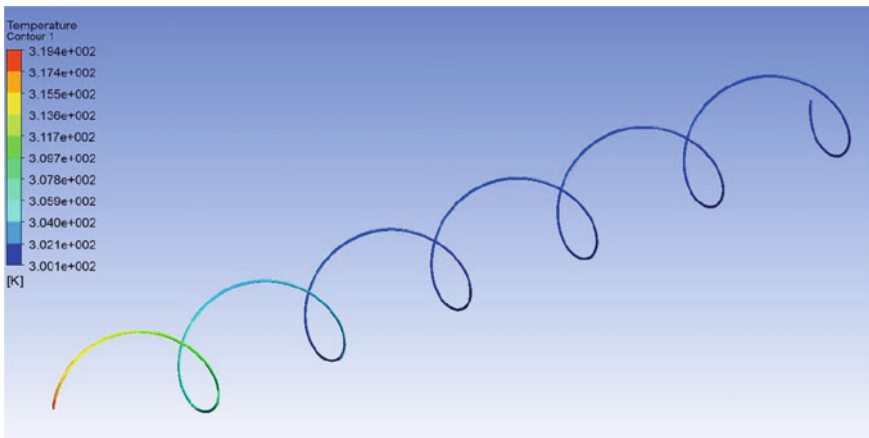


Fig. 3 Temperature contours of helical shaped pipe

coefficient of thermal expansion along with specific heat capacity) and the air transport properties (heat conduction) should be characterized and defined.

Almost the corresponding volume at the EAPHE pipe outlet was defined and represented as zero atm under supersonic flow characteristics and its different conditions.

The average temperature of the pipe system (wall) was homogeneously uniformly longitudinal direction and deceptively equal to the rough average global temperature (27 °C). There has been no slip circumstance on the inside of the pipe with a smooth wall (Figs. 2, 3, and 4; Table 4).

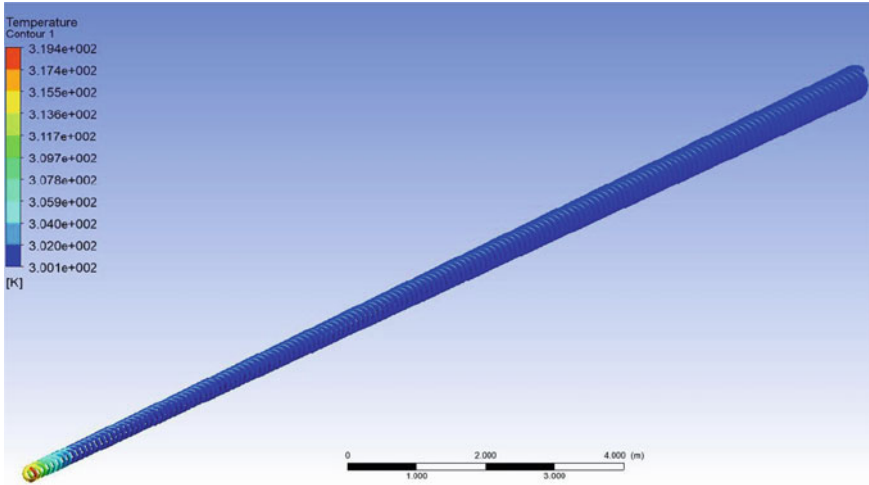


Fig. 4 Temperature contours of spiral-shaped pipe

3 Results

3.1 *Effect of Velocity on Temperature of Different Designs Used in the Present Study*

From the Fig. 5, it is shown that the temperature profile for the velocity = 5 m/s is at the lower part of the two profiles, which clearly demonstrates that the rate of cooling is successful at 5 m/s in comparison with the majority of the two velocities, even though in this particular circumstance the fluid moves at a lower velocity, that further will provide sufficient time for the exposure of the air to the natural environment so that the cooling is rapid in the atmosphere. It thus clearly shows that it is desirable for the efficient transfer of heat at low inlet speeds.

From the Fig. 6, it is shown that the temperature profile for the velocity = 5 m/s is at the lower part of the two profiles, which clearly demonstrates that the rate of cooling is successful at 5 m/s in comparison with the majority of the two velocities, even though in this particular circumstance the fluid moves at a lower velocity, that further will provide sufficient time for the exposure of the air to the natural environment so that the cooling is rapid in the atmosphere. It thus clearly shows that it is desirable for the efficient transfer of heat at low inlet speeds.

From the Fig. 7, it is shown that the temperature profile for the velocity = 5 m/s is at the lower part of the two profiles, which clearly demonstrates that the rate of cooling is successful at 5 m/s in comparison with the majority of the two velocities, even though in this particular circumstance the fluid moves at a lower velocity, that further will provide sufficient time for the exposure of the air to the natural environment so that the cooling is rapid in the atmosphere. It thus clearly shows that it is desirable for the efficient transfer of heat at low inlet speeds.

Table 4 Temperature obtained in different design models used in the study at varying velocities (5, 10 and 12 m/s)

Models	For U-shaped model			For helical model			For spiral model		
	V = 5 m/s	V = 10 m/s	V = 12 m/s	V = 5 m/s	V = 10 m/s	V = 12 m/s	V = 5 m/s	V = 10 m/s	V = 12 m/s
Pipe Length									
0	319.35	319.35	319.35	319.35	319.35	319.35	319.35	319.35	319.35
5	317.65	317.25	317.15	316.45	317.05	315.95	317.15	316.75	316.65
10	310.45	309.95	308.85	306.25	305.75	304.65	306.95	306.45	305.35
20	304.15	303.65	302.55	302.95	302.85	302.35	304.65	304.15	303.05
30	302.85	302.35	301.85	301.65	301.15	300.55	302.35	301.85	300.75
40	301.95	301.55	301.05	301.35	300.85	300	302.05	301.55	300.35
50	301.55	301.12	300.45	300.65	300.25	299.95	301.65	301.15	299.95
55	301.35	300.95	299.85	299.95	299.85	299.74	300.95	300.55	299.35

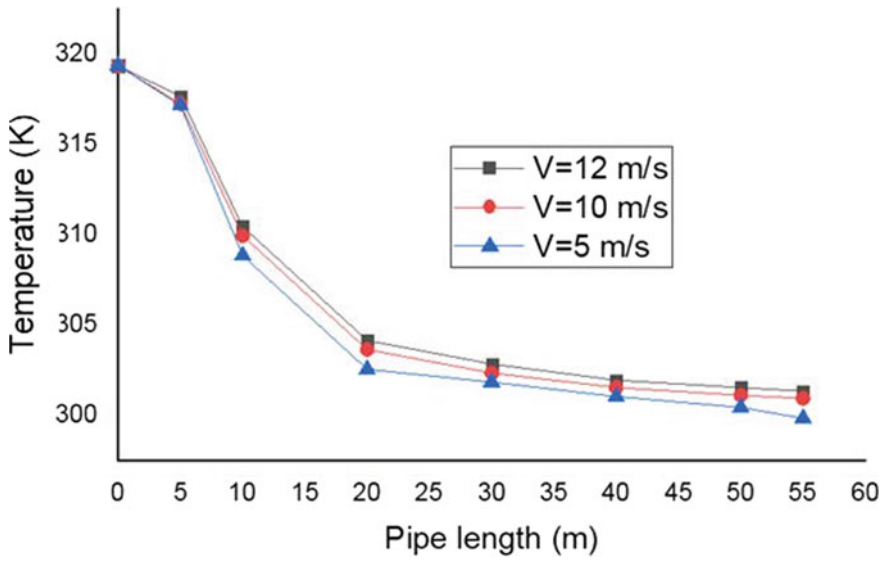


Fig. 5 Temperature versus pipe length graph at different velocity of U-shaped pipe

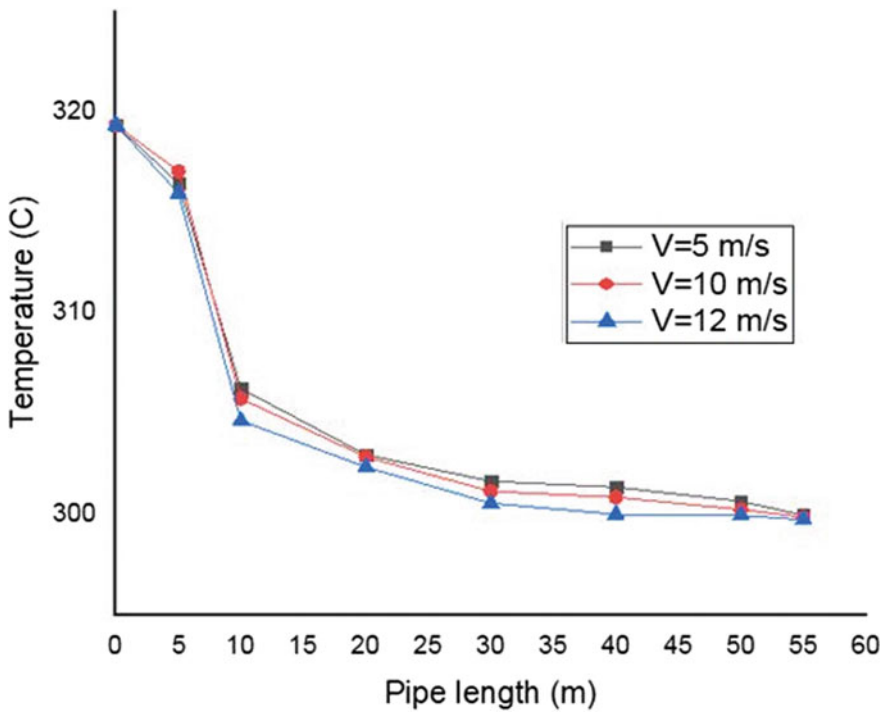


Fig. 6 Temperature versus pipe length graph at different velocity of helical shaped pipe

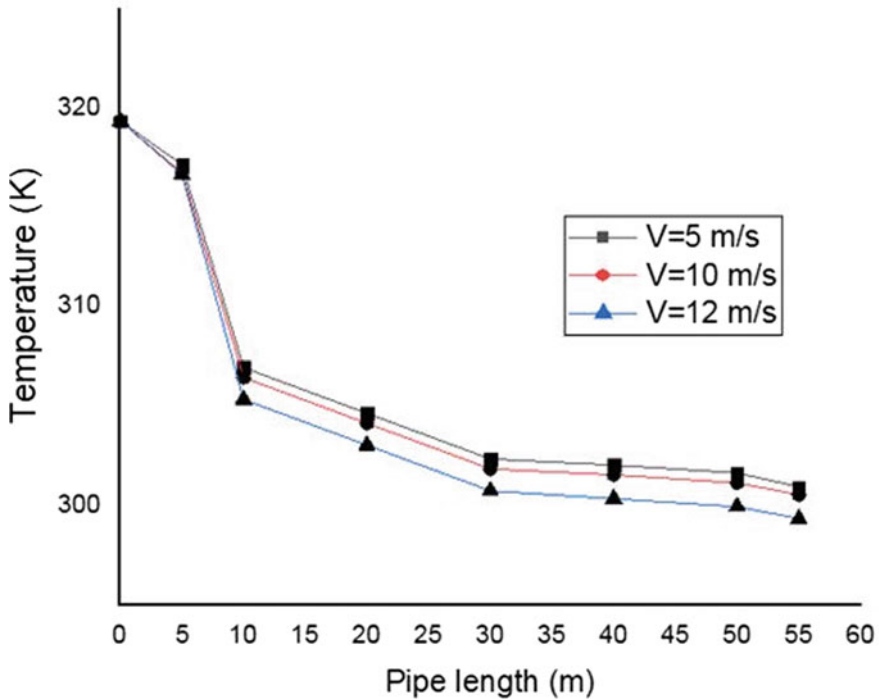


Fig. 7 Temperature versus pipe length graph at different velocity of spiral-shaped pipe

It is evident from the graph above that the helical-shaped tubing has the maximum Nusselt number in all three characteristics, which means that the helical is particularly suited for the air distribution in EAPHE. Because when the velocity is increased with reference to the acceleration, the Nusselt number also increases.

Figure 8 represents the length versus temperature of all three tube models (U-shaped, helical and spiral tube) and helical displayed the gradual drop in temperature, as the air distribution is increased along its tube length. The helical-shaped pipe showed the maximum performance of all three profiles, which means that the helical is particularly suited for the earth air pipe heat exchanger.

It is seen from Fig. 9 that as the velocity increases the Nusselt number also increases giving a proportional relation among velocity and Nusselt number.

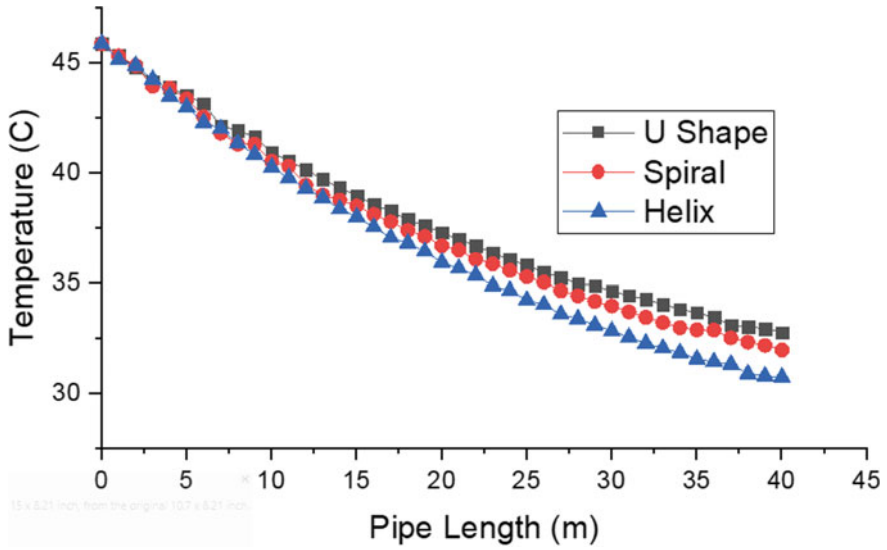


Fig. 8 Graph of temperature versus pipe length for U-shaped, helical and spiral pipe designs

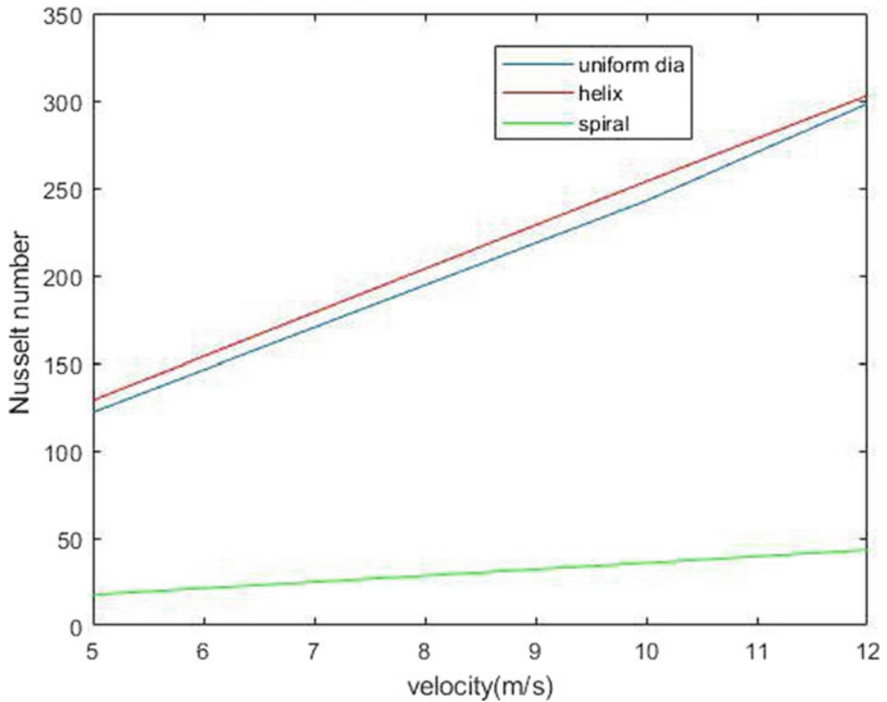


Fig. 9 Graph between Nusselt and velocity for U-shaped, helical and spiral pipe designs

4 Conclusion

In the present study, three different models of pipe are used in the earth pipe air heat exchanger system for identifying the possible outcomes and improvements with these designs. Different velocities were utilized at inlet to find the optimum velocity from EAPHE Systems. Among the overall study it is seen that the spiral pipe showed the maximum heat transfer and improvement in temperature as compared to other designs used in the study. Also 5 m/s velocity came to be the optimum velocity for improved heat transfer among other velocities used for the simulation study. In future, work can be done on the modeling of soil to improve the performance of EAPHE system.

References

1. Bansal V, Mathur J (2009) Performance enhancement of earth air tunnel heat exchanger using evaporative cooling. *Int J Low-Carbon Technol* 4(3):150–158. <https://doi.org/10.1093/ijlct/ctp017>
2. Ghosal MK, Tiwari GN (2006) Modeling and parametric studies for thermal performance of an earth to air heat exchanger integrated with a greenhouse. *Energy Convers Manag* 47(13–14):1779–1798. <https://doi.org/10.1016/j.enconman.2005.10.001>
3. Ben Jmaa Derbel H, Kanoun O (2010) Investigation of the ground thermal potential in Tunisia focused towards heating and cooling applications. *Appl Therm Eng* 30(10):1091–1100. <https://doi.org/10.1016/j.applthermaleng.2010.01.022>
4. Misra R, Bansal V, Das Agrawal G, Mathur J, Aseri T (2013) Transient analysis based determination of derating factor for earth air tunnel heat exchanger in summer. *Energy Build* 58(February):103–110. <https://doi.org/10.1016/j.enbuild.2012.11.001>
5. Bisoniya TS, Kumar A, Baredar P (2015) Heating potential evaluation of earth-air heat exchanger system for winter season. *J Build Phys* 39(3):242–260. <https://doi.org/10.1177/1744259114542403>
6. Mathur A, Srivastava A, Mathur J, Mathur S, Agrawal GD (2015) Transient effect of soil thermal diffusivity on performance of EATHE system. *Energy Reports* 1:17–21. <https://doi.org/10.1016/j.egy.2014.11.004>
7. Thanu NM, Sawhney RL, Khare RN, Buddhi D (2001) An experimental study of the thermal performance of an earth-air-pipe system in single pass mode. *Sol Energy* 71(6):353–364. [https://doi.org/10.1016/S0038-092X\(01\)00072-X](https://doi.org/10.1016/S0038-092X(01)00072-X)
8. Sodha MS, Buddhi D, Sawhney RL (1993) Optimization of pipe parameters of an underground air pipe cooling system. *Energy Convers Manag* 34(6):465–470. [https://doi.org/10.1016/0196-8904\(93\)90077-N](https://doi.org/10.1016/0196-8904(93)90077-N)
9. Mihalakakou G, Santamouris M, Asimakopoulos D (1994) Modelling the thermal performance of earth-to-air heat exchangers. *Sol Energy* 53(3):301–305. [https://doi.org/10.1016/0038-092X\(94\)90636-X](https://doi.org/10.1016/0038-092X(94)90636-X)
10. Kumar R, Kaushik SC, Garg SN (2006) Heating and cooling potential of an earth-to-air heat exchanger using artificial neural network. *Renew. Energy* 31(8):1139–1155. <https://doi.org/10.1016/j.renene.2005.06.007>
11. Kumar R, Sinha AR, Singh BK, Modhukalya U (2008) A design optimization tool of earth-to-air heat exchanger using a genetic algorithm. *Renew Energy* 33(10):2282–2288. <https://doi.org/10.1016/j.renene.2008.01.006>

12. Agrawal KK, Misra R, Bhardwaj M, Das Agrawal G, Mathur A (2019) Computational Fluid Dynamics Simulation Based Comparison of Different Pipe Layouts in an EATHE System for Cooling Operation 11(5)
13. Ghosal MK, Tiwari GN, Srivastava NSL, Sodha MS (2004) Thermal modelling and experimental validation of ground temperature distribution in greenhouse. *Int J Energy Res* 28 (1):45–63. <https://doi.org/10.1002/er.950>
14. Tiwari GN, Akhtar MA, Shukla A, Emran Khan M (2006) Annual thermal performance of greenhouse with an earth-air heat exchanger: An experimental validation. *Renew Energy* 31 (15):2432–2446. <https://doi.org/10.1016/j.renene.2005.11.006>
15. Bansal V, Mishra R, Das Agarwal G, Mathur J (2012) Performance analysis of integrated earth—air-tunnel-evaporative cooling system in hot and dry climate. *Energy Build* 47:525–532. <https://doi.org/10.1016/j.enbuild.2011.12.024>
16. Mathur A, Srivastava A, Agrawal GD, Mathur S (2015) CFD analysis of EATHE system under transient conditions for intermittent operation. *Energy Build* 87:37–44. <https://doi.org/10.1016/j.enbuild.2014.11.022>

Application of Taguchi Method and ANOVA in Parameters Optimization for Fluidization Characteristic of Pine Needles in Fluidized Bed



Vishal Sharma and Rajeev Kamal Sharma

Abstract Pine needle is most occurring commonly available conifer forestry residue in the Himalayan regions that can be used as the feedstock (fuel). A proper understanding of the physiochemical properties of pine needle, for the proper utilization. The current study provides the database for engineering properties such as particles size and density. It would be used for future thermal applications like fluidized beds. To understand the fluidization of pine needles, minimum fluidization velocity (U_{mf}) are the compulsory parameters to ensure the optimal execution of cold fluidized bed in the conversion system. For this, a series of experiments have been carried out on the controlled parameters, were examined to investigate the fluidization behavior of pine needle, by using Taguchi method (L_{16} orthogonal array). It is revealed from the results that the voidage and diameter have a significant effect on the U_{mf} . The analysis suggests for U_{mf} that the length of 5 mm, diameter of 0.23 mm, voidage of 0.11, sphericity of 0.435, and density of 155.67 kg/m^3 ; maximize the SN ratio and give the robust set of parameters.

Keywords Pine needles · Engineering properties · Conifer forest · Himalayan · Taguchi method · Optimization · ANOVA · Thermochemical conversion

V. Sharma (✉)

Chitkara University Institute of Engineering and Technology, Chitkara University,
Punjab, India

e-mail: thevishsharma@gmail.com

R. K. Sharma

Chitkara College of Applied Engineering, Chitkara University, Punjab, India

e-mail: rajeev.sharma@chitkara.edu.in

© The Author(s), under exclusive license to Springer Nature Singapore Pte Ltd. 2021

B. S. Sikarwar et al. (eds.), *Advances in Fluid and Thermal Engineering*,

Lecture Notes in Mechanical Engineering,

https://doi.org/10.1007/978-981-16-0159-0_77

1 Introduction

The energy is the essential component of the global economy and is a primary input required for economic growth of the nation. At present most of the energy comes from conventional sources from a long time [1]. These energy sources are being used extensively in such a manner that their well-known stocks have diminished to an alarming level. Shafiee and Topal [2] estimated that the reservoirs of these sources will get exhausted within a few decades, and their future accumulation may take hundreds of year [2]. And at that time, it will be so difficult to explore and exploit new energy sources. Many researchers suggested the non-conventional energy sources can be the better alternative to reduce stress on conventional sources and can also provide the backup to increasing energy demand [3]. Among all non-conventional energy sources, biomass is the third largest primary energy resource and provides the best solution of almost all the environmental problems. Primary biomass mainly of two kinds: agricultural and forestry waste. Most of the research is carried out on the agricultural biomass, i.e., baggase, cotton stalk, etc. [4]. On the other hand, limited research is carried on the forestry waste such as unused surplus from particular forest, reserved forest, private forest, unclassified forest, and other forest managed. Out of all forest, the most coniferous forest have high potential of pine trees (*Pinus roxiburghii*) grow over the altitude varying from 350 to 3700 m. The huge amount of pine needles litter off from the pine tree in the middle of March to onset of rain in the month of July. It lounges unutilized on the pinewood floor for a more extended period. It prevents natural growth of forest flora and also has relatively poor biodegradability due to high lignin content [5]. The use of pine needles for energy source is progressively gaining the attention of researchers in energy generation [6]. Moreover, dried pine needles are the main source of forest fires in summer season destroy the flora and fauna of forest. Also, the forest fire intercept the seedlings due to preopening of cones abolish the mature or immature seeds when exposed to fire and generate the adverse living conditions [7]. On the other hand, pine needle use is limited to cattle bedding, space heating, and other domestic purpose. But, this quantity is far less than the amount that persist on the forest floor every year [8, 9]. This unutilized pine needles covering is burnt (control burning method) in an open environment to avoid the furious wildfire. A noticeable ecological and economical concerns regarding the disposal of pine needles, emphasizing the crucial need for its effective utilization. Conversion of pine needles into another useful form reducing the chance of forest fires and regulate the ecological system [10]. Fluidized bed technique provides the necessary window to easily handle operating conditions by studying the cold fluidized bed characteristics of particles [11]. The cold fluidized study widely used to understand the physical characteristics and particle behavior. As its performance depends upon the different physical properties of particles, there is the crucial need to optimize its process parameter for constant development. It is considering the novelty of the present work, which not only increase the performance of the combustor (small or large scale), but also save the time to perform the large number of experiments.

The present study is generally preferred to optimize the primary parameters of cold fluidized bed using the Taguchi method, is providing the basic knowledge for efficient fluidization.

2 Methodology

2.1 *Pine Needle Collection*

Pine needle sample is collected (Approximately 15 kg) from Hamirpur and Solan forest range, Himachal Pradesh, India during April–May 2019. The pine needle samples are dried in the domestic box-type solar cooker for 7–8 h to remove interstitial moisture content.

2.1.1 Anatomical and Morphological Structure of Pine Needle

Pine needle typically have needle-shaped leaves and it is arranged in bundles called fascicles. Generally, pine needle length varied from 12 to 20 cm are mainly of two parts (1) scale and (2) foliage. Figure 1 displays the microscopic image, SEM image, pictorial view of pine needle [12, 13].

2.2 *Physiochemical Properties*

2.2.1 Particle Size

Physical parameters (length, width, thickness, and weight) of pine needles are measured for designing the handling, storage, and processing units. The length and diameter measurements were based on the random selection of 50 samples of pine needles. About 33% of pine needle length ranged in between 12 and 17 cm, about 52% of needles length ranged in 8–11 cm, and rest below 8 cm. The measured average diameter of the pine needles is ranged between 494 and 745 μm . Further, the pine needle samples were chopped into different size (3–12 mm). The bulk density of chopped pine needles was ranged from 95 to 106 kg/m^3 . The chopped pine needle sample porosity value varies from 0.675 to 0.96.

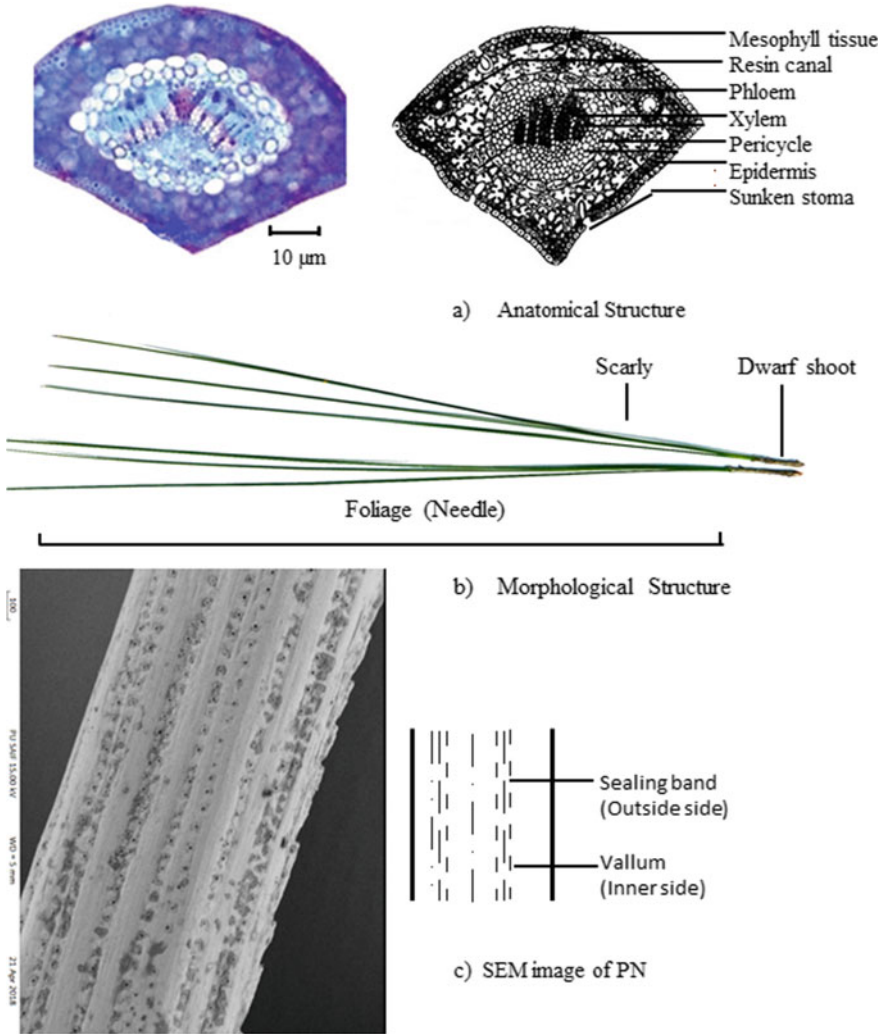


Fig. 1 (a) Microscopic image and schematic diagram of pine needle [12]; (b) Pictorial view of freshly harvested pine needle; (c) SEM image and diagram of pine needle [13]

2.3 Design of Experiments and Approach

Many engineering problems are allowed to be analyzed by applying the Taguchi method without a high amount of experimentations. It is the robust design method that assumes orthogonal array (i.e., fractional factorial experimental design) under permissive reliability. It consists of a set of experiments, in which the results are varied evenly. Before experimentation, some important steps that are involved in Taguchi’s method to identify:

- Main function,
- Testing conditions,
- Objective function,
- Factor and their level,
- Appropriate orthogonal array.

Here, fluidization characteristic of pine needles is the main function. Table 1 shows the operating experiment conditions. Objective function is taken: nominal-the-better, is calculated through the S/N ration Eq. 3. Further, the important step to identify the noise factor (adverse impact on system performance), control factors (significant impact on the performance), and other operating conditions. Identified control factors which going to influence or affect the fluidization are needles length (A), diameter (B), voidage (C), sphericity (D), and density (E). Some other factors (noise factors) are vibration, setup condition, temperature variation, equipment variation. After the experiments have been conducted, the optimal test parameter configuration within the experiment design is to be determined symmetrically in selected orthogonal array. A standard orthogonal array is created in the Taguchi method to find out the effects of selected control parameters on the outcomes in an impartial way. The experimental results are analyzed, gives the optimized conditions.

Further, Taguchi method is applicable to optimize fluidization behavior of pine needles. Here, fluidization can be calculated by Eq. 1 [14].

Table 2 shows the list of factors that influence the fluidization process has identified as control factors along with their levels. These factors help to construct the matrix for the experimentation. Rest factors are considered as noise factors. The experimentations are conducted on the fluidizing bed and the corresponding outcomes of fluidizing parameters (L_{16}) are shown in Table 3. Figure 2 shows the

Table 1 Test conditions

Sr. No.		Test Conditions
1	Pine needles	Diameter range = 494–745 μm Chopped length = 3, 6, 9, 12 mm
2	Distributor plate	Orifice = Round 60° staggered Considered plate inclination angle = 0°
3	Fluidizing medium	Fluid = air Fluidizing velocity range = 0.1–3.0 m/sec

Table 2 Control factors and their levels

Factors	Levels			
	1	2	3	4
Needle length mm (A)	3	6	9	12
Diameter mm (B)	0.23	0.54	0.86	1.15
Voidage ϵ (C)	0.10	0.24	0.45	0.54
Sphericity ϕ (D)	0.69	0.60	0.51	0.43
Density kg/m^3 (E)	303.3	255	184.7	155.6

Table 3 Measured value of the U_{mf} orthogonal array table (L_{16}) with control factors

Trial no.	Factors					U_{mf} (m/sec)	SN Ratio for U_{mf}
	A	B	C	D	E		
1	1	1	1	1	1	3.3E-05	19.98
2	1	2	2	2	2	0.00189	7.40
3	1	3	3	3	3	0.021	2.78
4	1	4	4	4	4	0.046	1.76
5	2	1	2	4	3	0.0001	15.10
6	2	2	1	3	4	5.20E-05	18.35
7	2	3	4	2	1	0.098	1.01
8	2	4	3	1	2	0.096	1.02
9	3	1	3	2	4	0.001	7.53
10	3	2	4	1	3	0.03	2.27
11	3	3	1	4	2	0.0001	14.45
12	3	4	2	3	1	0.007	4.55
13	4	1	4	3	2	0.004	5.62
14	4	2	3	4	1	0.01	3.98
15	4	3	2	1	4	0.003	5.82
16	4	4	1	2	3	0.0003	11.61

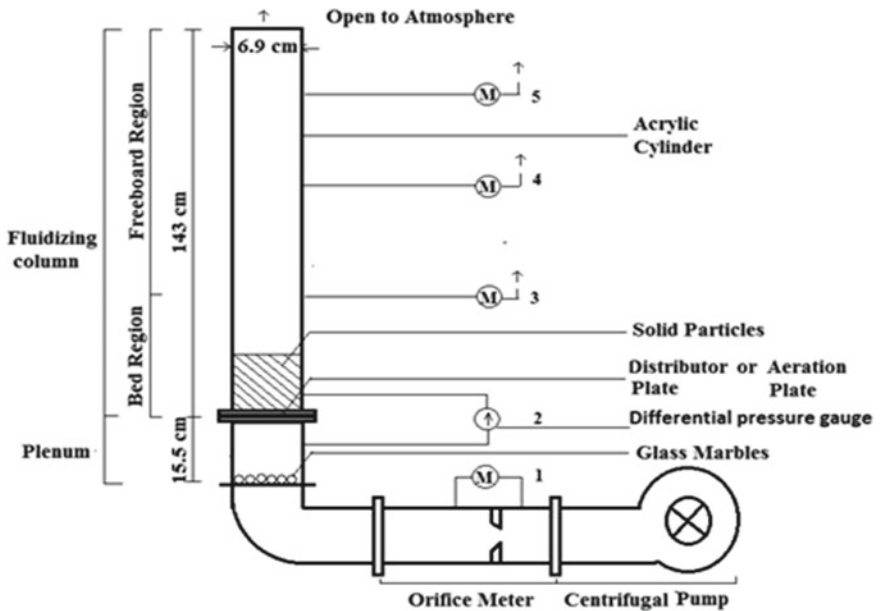


Fig. 2 Experimental apparatus

schematic diagram of experimental apparatus and evaluation of fluidizing characteristics of pine needles in the fluidizing bed.

$$\Delta P = \frac{150(1 - \varepsilon^2) \mu_f U_{mf}}{\varepsilon^3 \phi^2 dp^2} + \frac{1.75(1 - \varepsilon) \rho_f U_{mf}^2}{\varepsilon^3 \phi dp} \tag{1}$$

From Eq. 1, U_{mf} is calculated as

$$U_{mf} = \frac{d_p^2 (\rho_p - \rho_f) g (\phi^2 \varepsilon_{mf}^3)}{150 \mu_f (1 - \varepsilon_{mf})} \tag{2}$$

For calculating the SN ratio for U_{mf} the objective function, “nominal-the-better” type SN ratio was used as shown in Eq. 3:

$$SN \text{ ratio} = 10 \log_{10} \frac{\text{Square of mean}}{\text{Variance}} \tag{3}$$

Analysis of the influence of each control factors (A, B, C, D, and E) on the fluidization behavior of pine needles has been performed with SN ratio response is shown in Table 4. The effect of each control factors can be clearly presented with SN ratio response graphs (Fig. 3). The graph reveals the selected levels for the fluidization, as well as the relative effect of each parameter is on SN ratio. The slope of the

Table 4 SN ratio response for U_{mf}

Factors					
Level	A	B	C	D	E
1	31.92	48.23	64.39	29.09	29.52
2	35.48	32.00	32.87	27.55	28.49
3	28.80	24.06	15.31	31.30	31.76
4	27.03	18.94	10.66	35.29	33.46
Delta	8.45	29.29	53.73	7.74	4.97
Rank	3	2	1	4	5

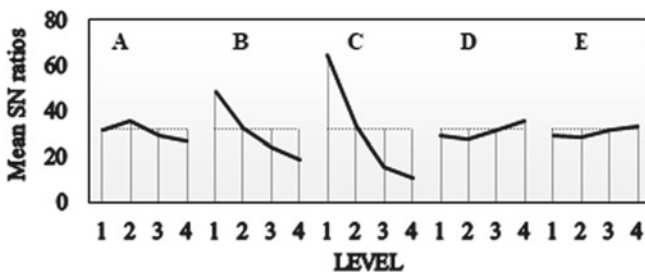


Fig. 3 Effects of selected control factors on the SN ratio for U_{mf}

lines and connects between the levels demonstrates the power of influence of each control factor. Especially the voidage (C), diameter (B), and needle length (A) have a strong effect on the U_{mf} and its SN ratio. The density (E) and sphericity (D) have lower effect as evidenced by the shallow shape of lines. The optimal solution of U_{mf} is obtained by the Taguchi method, and the optimum level of the fluidization parameter are tabulated in Table 5. The Taguchi method acknowledged that the voidage has a more significant impact on the U_{mf} . The slope of the SN ratio graph for voidage is very sharp. The other considerable parameters for pine needles are length and diameter, while sphericity and density have lower effect as shown in Fig. 3.

3 Analysis of Variance (ANOVA) and Its Significant

Analysis of variance (ANOVA) is used to evaluate the percentage response magnitude of each parameter consider in the orthogonal experiments as shown in Table 6 for U_{mf} . It identifies and quantifies the data set of different trial results of experimentation. ANOVA help to find the uncertainty in mean and variance of individual variable and residuals, by considering the degree of freedom of each parameter.

Table 5 Optimum values of factors and their levels for U_{mf}

Parameters	Optimum values (U_{mf})
Needles length mm (A)	5
Diameter mm (B)	0.23
Voidage ϵ (C)	0.104
Sphericity ϕ (D)	0.435
Density kg/m^3 (E)	155.67

Table 6 Sum of squares of all deviations for U_{mf}

Source	DOF	SS	MS	F-test	% contribution
A	3	0.0046	0.0015	387.72	28.83
B	3	0.0034	0.0011	286.09	21.27
C	3	0.0058	0.0019	482.89	35.90
D	3	0.0008	0.0002	66.60	4.95
E	3	0.0014	0.0004	121.68	9.05
Residual	5	2.0E-05	4.1E-06		
Total	20	0.0163		1345	100

4 Conclusion

The engineering properties of pine needles are characterized to be used as a raw material for the energy conversion processes. The engineering parameters considered an application of the Taguchi method for examining the effects of fluidizing parameters on the U_{mf} in fluidization of pine needles. These characteristics of pine needles are selected taking into consideration according to fluidizing results of S/N and ANOVA. Therefore, on the behalf of SN ratio and ANOVA analysis, the optimal fluidizing parameters for U_{mf} is $A_2 B_1 C_1 D_4 E_4$ i.e. $A_2= 5$ mm, $B_1= 0.23$ mm, $C_1= 0.104$, $D_4= 0.435$, $E_4= 155.67$ kg/m³. The following are the conclusion derived from the present study:

- Analytical findings for U_{mf} show that the needles length (A), Diameter (B), and voidage (C) affect the velocity by 28.83, 21.27, and 35.90% in the fluidized bed of pine needles, respectively.
- The U_{mf} for pine needles is varied from 0.1 to 0.96 m/sec calculated as by Taguchi's optimization method.

Present study confirms the experiments for fluidizing velocities has shown that Taguchi process parameter design method can successfully validate the optimum fluidization of pine needles. The above results evident that the accurate measurements are really needed to obtain sufficient desirable accuracy of the fluidized bed. The Taguchi and ANOVA can provide the easy, organized and precise way to select the parameters which allow a reliable determination to handle the controlled factors over the fluidization.

References

1. Balat M, Ayar G (2005) Biomass energy in the world, use of biomass and potential trends. *Energy Sources* 27:931–940. <https://doi.org/10.1080/00908310490449045>
2. Shafiee S, Topal E (2009) When will fossil fuel reserves be diminished? *Energy Policy* 37:181–189. <https://doi.org/10.1016/j.enpol.2008.08.016>
3. Hartmann B, Talamon A, Sugár V (2017) Renewable Energy Potentials in the Administrative Regions of Hungary. *Strateg Plan Energy Environ* 37:33–57. <https://doi.org/10.1080/10485236.2017.11907881>
4. Kumar A, Kumar N, Baredar P, Shukla A (2015) A review on biomass energy resources, potential, conversion and policy in India. *Renew Sustain Energy Rev* 45:530–539. <https://doi.org/10.1016/j.rser.2015.02.007>
5. Lal PS, Sharma A, Bist V (2013) Pine Needle - An Evaluation of Pulp and Paper Making Potential. *J For Prod Ind* 2:42–47
6. Nunes LJR, Matias JCO, Catalão JPS (2016) Biomass combustion systems: A review on the physical and chemical properties of the ashes. *Renew Sustain Energy Rev* 53:235–242. <https://doi.org/10.1016/j.rser.2015.08.053>
7. Zhu X, Liu W, Chen H, Deng Y, Chen C, Zeng H (2019) Effects of forest transition on litterfall, standing litter and related nutrient returns: Implications for forest management in tropical China. *Geoderma* 333:123–134. <https://doi.org/10.1016/j.geoderma.2018.07.023>

8. Dhaundiyal A, Tewari PC (2015) Comparative analysis of pine needles and coal for electricity generation using carbon taxation and emission reductions. *Acta Technol Agric* 18:29–35. <https://doi.org/10.1515/ata-2015-0007>
9. Sharma V, Sharma RK (2020) Pine needle energy potential in conifer forest of western himalayan. *Environ Nat Resour J* 18:55–65. <https://doi.org/10.32526/enrj.18.1.2020.06>
10. Gonzalez-Benecke CA, Zhao D, Samuelson LJ, Martin TA, Leduc DJ, Jack SB (2018) Local and general above-ground biomass functions for *pinus palustris* trees. *Forests* 9:1–17. <https://doi.org/10.3390/f9060310>
11. Sharma V, Sharma RK (2020) Fluidization and combustion characteristics of pine needles in fluidized bed combustor: An experimental investigation. *Test Eng Manag* 83:5177–5189
12. Garrido MA, Conesa JA, Garcia MD (2017) Characterization and Production of Fuel Briquettes Made from Biomass and Plastic Wastes. <https://doi.org/10.3390/en10070850>
13. Monedero E, Lapuerta M, Pazo A, Díaz-Robles LA, Pino-Cortés E, Campos V, Vallejo F, Cubillos F, Gómez J (2019) Effect of hydrothermal carbonization on the properties, devolatilization, and combustion kinetics of Chilean biomass residues. *Biomass Bioenerg* 130:105387. <https://doi.org/10.1016/j.biombioe.2019.105387>
14. Noda K, Uchida S, Makino T, Kamo H (1986) Minimum fluidization velocity of binary mixture of particles with large size ratio. *Powder Technol* 46:149–154. [https://doi.org/10.1016/0032-5910\(86\)80021-3](https://doi.org/10.1016/0032-5910(86)80021-3)

A Study on Agglomeration Behaviour of Cotton Stalk Under Fluidized Bed Conditions



Rajeev Kamal Sharma, Rajneesh Kaushik, and Rajesh Kumar

Abstract In this work, agglomeration behaviour of cotton stalk under conditions similar to fluidized bed has been studied. Fuel samples of cotton stalk, bed material (silica sand), bed ash and agglomerate were collected from 7.5 MW FBC-based thermal power plant located at Sri Muktsar Sahib, Punjab, India. Samples of cotton stalk ash mixed with silica sand are heated in a perforated bowl at three different temperatures viz. 700, 800 and 900 °C in a muffle furnace. SEM images of the samples showed that ash viscosity decreases with increase in temperature leading to increase in ash coated sand particle stickiness. Formation of gas holes and cracks was observed at surfaces due to release of gaseous products. On completion of combustion, solidification of low-melting-point alkali silicates takes place leading to the formation of agglomerates. Agglomeration index of cotton stalk is found to be 4.31, indicating high agglomeration tendency of cotton stalk. An agglomeration mechanism has also been proposed for cotton stalk.

Keywords Fluidized bed · Cotton stalk · Agglomeration · Agglomeration index

1 Introduction

Energy generation industries using coal as fuel are facing many challenges related to emission, efficiency, continuous supply of clean fuel, operational difficulties, etc. Utilization of biomass as a clean and sustainable fuel in fluidized bed combustor (FBC) is the solution for many of such problems up to some extent [1–3]. But agglomeration in combustor makes use of biomass as fuel very limited. Formation of large agglomerates leads to defluidization and shut down of plant. As the temperature in the bed is quite high, this process may take number of days to restart the combustor causing a loss to the thermal power plant. Control or elimination of agglomeration from biomass-based fluidized bed combustor is very difficult as

R. K. Sharma (✉) · R. Kaushik · R. Kumar
Chitkara College of Applied Engineering, Chitkara University, Punjab, India
e-mail: rajeev.sharma@chitkara.edu.in

different biomass fuels contain different proportions of agglomeration enhancing elements. The high fraction of reactive elements like potassium, calcium and magnesium in biomass ash is the major contributor to this phenomenon [4, 5]. In addition to agglomeration, ash produced during biomass burning gets deposited over heat exchange surfaces and bed materials. Ash deposition on heat exchange surfaces causes decrease in heat transfer rate due to increased thermal resistance. Also unwanted reaction of chlorine with K and Na, result in a variety of severe ash-related problems such as alkali-induced slagging, silicate melt-induced slagging (ash fusion), and agglomeration, etc. [6]. Due to the problems associated with agglomeration, the use of fluidized bed combustors at wide scale is inhibited [7, 8]. At low bed temperatures, some components in the biomass ash react with the bed material. This makes the bed material particles stick with each other. The size of agglomerate increases and fluidizing air drag force becomes insufficient to support the mass of the agglomerate. The agglomerate falls down on the distributing plate, thus interrupting the fluidizing airflow. Agglomeration causes slagging, fouling and finally, defluidization of the bed. The large size agglomerates which are harmful to FBC components lead to bed defluidization which further eliminates the sole purpose of fluidization. The operation of the fluidized bed is stopped and it requires removal of affected bed materials. The fresh bed materials reloading is required to restart FBC operation. Preventing agglomeration in thermal power plants can avoid emergency shutdown. Agglomeration reasons and its prevention methods are still unclear and need more research.

In literature, many authors predicted the agglomeration characteristics of different biomass materials [4, 9–17]. However, limited work has been reported on the study of agglomeration behaviour of cotton stalk in fluidized bed combustors. The present work contributes to the study of agglomeration behaviour of cotton stalk with silica sand as bed material under fluidized like conditions has been analysed. The experimental results have been compared with cotton stalk agglomerate collected from a 7.5 MW biomass-based power plant. Further, these agglomerates are investigated experimentally to predict their behaviour at high temperature.

2 Mechanism of Agglomeration

Agglomeration mechanism is a complicated phenomenon and Mettanant et al. [18], describes three agglomeration mechanisms of bed particles in FBC, viz. defluidization-induced agglomeration, coating-induced agglomeration and melt-induced agglomeration.

2.1 *Defluidization Induced Agglomeration*

Biomass fuels have irregular shapes, rough surfaces and large abrasive texture. During combustion of such fuel particles, fluidization may become non-uniform and sometimes defluidization may occur at some local points. The mobility of fuel and bed particles at these local points becomes restricted. Heat transfer to bed from these regions of local defluidization decreases, leading to increase in temperature at some specific locations. In case, the temperature becomes more than the melting or softening temperature of ash or bed material, small agglomerates may be formed in these regions. If the drag force of fluidizing gas and surrounding particles is large enough, these agglomerates may break. Alternatively, the agglomerate size may increase and lead to defluidization of entire fluidized bed. Such agglomerates are generally weak and can be broken if the fluidization velocity is increased beyond minimum fluidization velocity. Defluidization-induced agglomeration is a function of ash chemical composition, particle size and hydrostatic pressure exerted by fluidizing gas on particles. In comparison with deeper beds, shallower beds are less susceptible to defluidization-induced agglomeration.

2.2 *Melt-Induced Agglomeration*

Although biomass ash has varying compositions, but potassium, calcium, sodium and silicon are its major inorganic components with a little amount on aluminium (in some biomass ashes) [19]. At higher bed temperatures, these inorganic biomass ash components react with bed material like sand to form eutectic mixture [20].

Alkali + silica = Eutectic mixture of silicate



The eutectic mixture of sodium and potassium melts at 875 °C and 754 °C respectively, whereas the silica sand (SiO_2) melts at temperature above 1450 °C. Bed material is covered with low-melting eutectic mixture of silicates of inorganic components of ash and at higher temperature coating melts and bed material particles fuse with each other as shown in Fig. 1. This mechanism of agglomeration has been named as melt-induced agglomeration and is shown in Fig. 2.

2.3 *Coating Induced Agglomeration*

It is the most common agglomeration formation mechanism found in FBC. Bed particles are covered and are attached to each other with a very thin sticky layer (Fig. 3). Sticky layer on the bed particles is formed by three processes, viz. (i) fuel

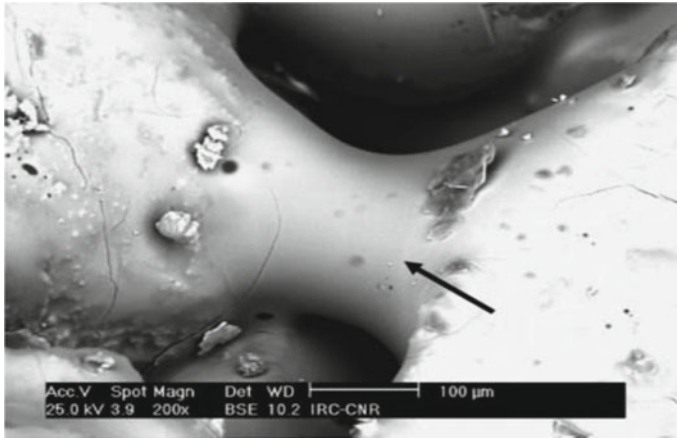
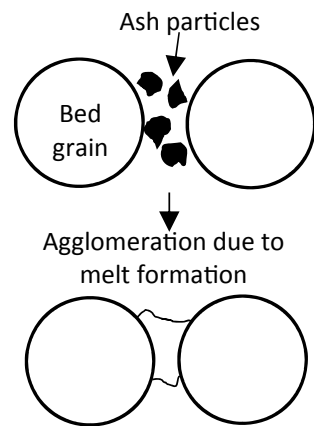


Fig. 1 Two sand particles fuse with each other through molten coating [20]

Fig. 2 Mechanism of melt-induced agglomeration [21]



ash particles attached to bed particle surfaces, (ii) condensate formed during condensation of gaseous alkali compounds such as KCl , K_2SO_4 , KOH and K and (iii) gaseous alkali compounds reacting with bed particle at its surface [22]. Sticky layer grows outward due to first two processes and it grows inward due to the third process. With the passage of time, contributions to sticky layer growth due to first two processes increases and due to third process decreases, as the already developed layer acts as a barrier between gaseous alkali compounds and bed material surface.

Potassium (K) and Sodium (Na) contribute towards agglomeration, whereas presence of calcium (Ca) reduces the tendency of agglomeration. Sometimes, $[\text{Ca}/(\text{Na} + \text{K})]$ ratio (known as agglomeration index) of a fuel is used to predict the agglomeration behaviour of a biomass. A higher value means lower agglomerate formation probability. Hulkkonen et al. [23] proposed that agglomeration tendency is higher when constituents of fuel exceed the following limits:

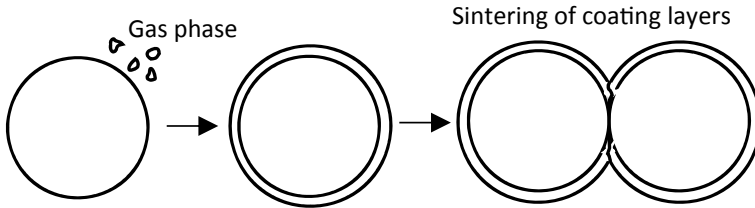


Fig. 3 Mechanism of coating induced agglomeration [21]

$$\frac{(K_2O + Na_2O)}{SiO_2} > 1 \quad (2)$$

3 Methods of Reducing Agglomeration

Agglomeration can be avoided to a certain extent by using agglomeration resistant bed materials, additives, pre-treating the biomass fuels and reducing the bed operating temperature.

3.1 Agglomeration Resistant Bed Materials

Silica is the most common bed material but it is more prone to agglomeration as it forms eutectics and silicates which have low melting points. Alumina (Al_2O_3), feldspar, limestone ($CaCO_3$), ferric oxide (Fe_2O_3), dolomite ($CaCO_3 \cdot MgCO_3$) and magnesite ($MgCO_3$), blast furnace slag (BFS) are the alternate bed materials which are less prone to agglomeration [24, 25].

3.2 Additives

Alumina (Al_2O_3), limestone ($CaCO_3$), dolomite ($CaCO \cdot MgCO_3$), calcium oxide (CaO), magnesium oxide (MgO) and kaolin ($Al_2Si_2O_5(OH)_4$) are the materials which can be used as additives to increase the biomass ash melting temperature. Adding 10% of kaolin in FBC using quartz bed material, burning bark and wheat straw increased agglomeration temperatures from 988 to 1000 °C for bark and from 739 to 885 °C for wheat straw [26]. While burning mixture of bone meal, meat and refuse-derived fuel in a FBC, agglomeration temperature increases from 830 to 890 °C with dolomite as additive and from 830 to 905 °C with kaolin as additive [27].

3.3 Using Coarse Bed Material

Large-size bed material particles have more inertia in comparison with small-size bed particles and their collisions are more energetic. The probability of agglomerate formation is low with such bed material particles. Chirone et al. [28] found that while using sand of size 600–850 μm approximately take twice the time to defluidize as taken by sand particles of size 212–400 μm . It has also been reported that adding 30% of coarse bed particles is the optimum ratio for avoiding agglomeration [29].

3.4 Using Fuels Having High Agglomeration Temperature

Almost all types of biomass fuels have same melting temperatures, but they have different agglomeration temperatures. So wherever possible, the fuels with high initial agglomeration temperatures must be used to avoid agglomeration. Fuels with high amount of calcium have high agglomeration temperature and fuels with high amount of potassium have low agglomeration temperature [22]. Out of cane trash, bagasse, rice husk, olive fresh and bagasse, rice husk and bagasse are found to have higher agglomeration temperatures ($>1000\text{ }^\circ\text{C}$) and are more suitable as fuel for FBC [30].

3.5 Co-combustion

Co-combustion of biomass fuels with high ash containing fossil fuels can reduce the agglomerate formation in fluidized bed combustors [31]. Fossil fuels have kaolin-ites and alumino-silicates which acts as sorbents and reduces the concentration of sodium or potassium in the biomass ash. Using 20% coal (containing 40% ash) with coffee husk reduced concentration of potassium to 13.5% from 43.8% [24].

4 Agglomeration Study of Cotton Stalk

4.1 Materials and Methods

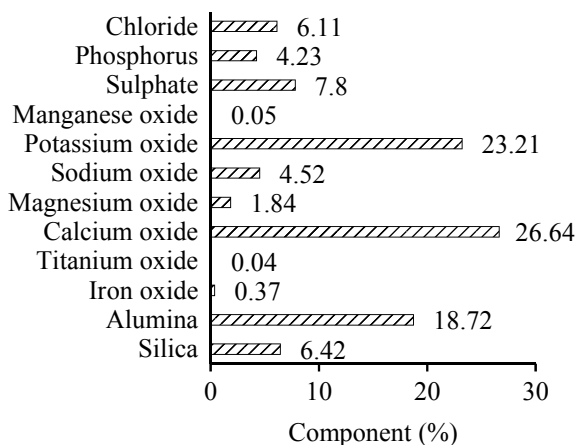
To study the agglomerate behaviour of cotton stalk, the sample of fuel (cotton stalk), bed material (silica sand), bed ash and agglomerate were collected from 7.5 MW FBC plant at Sri Muktsar Sahib. Cotton stalk is one of the agricultural waste and has a potential for energy generation [32]. It is observed that cotton stalk has high volatile matter and less calorific value (13.7 MJ/kg), whereas very less

Table 1 Properties of CS on dry basis

Proximate analysis (wt%)				Ultimate analysis (wt%)					HHV (MJ/kg)
Moisture	Ash	Volatile matter	Fixed carbon	C	H	N	O	S	
8	4	65.89	22	43	4	0.4	35	0.14	13.7

Table 2 Composition of silica sand (wt %)

Components	Weight (%)
SiO ₂	98.89
MgO	0.008
Fe ₂ O ₃	0.04
Al ₂ O ₃	0.14
CaO	0.02
Others	0.902

Fig. 4 Chemical analysis of ash sample collected from plant (%)

amount of sulphur and nitrogen (Table 1). The composition of the silica sand is shown in Table 2. Chemical analysis results of the ash sample collected from the plant site at the time of agglomeration are given in Fig. 4. The agglomerate sample collected from Malwa Power Plant Limited (MPPL) Sri Muktsar Sahib is shown in Fig. 5a. The size of agglomerates formed at plant site was very large and agglomerates were also too hard to be broken with hand.

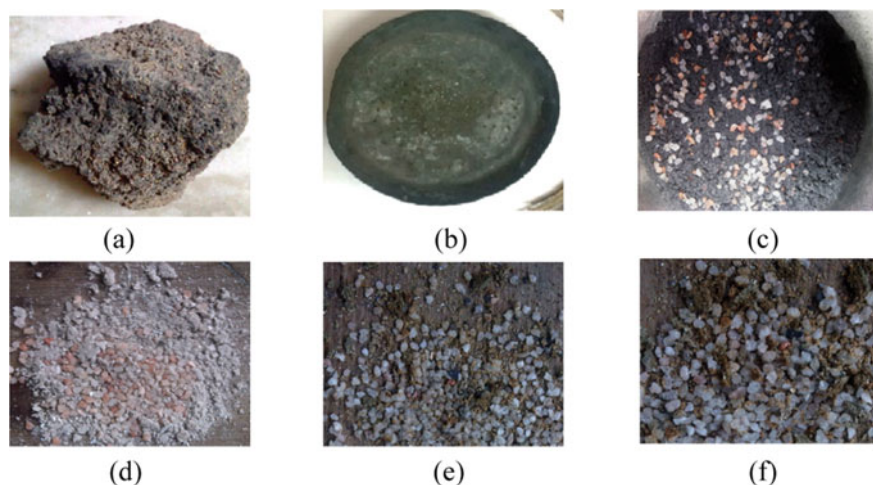


Fig. 5 (a) Agglomerate collected from MPPL, Sri Muktsar Sahib (b) steel bowl with holes. (c–f) Cotton stalk ash and silica sand mixture at room temperature and elevated temperatures. (c) room temperature (d) 700 °C (e) 800 °C (f) 900 °C

4.2 Experimental Procedure

A steel bowl (Fig. 5b) of 6 cm diameter with 1 mm diameter holes (50 in numbers) at the bottom was used for the analysis. Holes were provided to achieve the conditions similar to that in fluidized bed combustor with distributor plate at the bottom of the combustor. 50 g of cotton stalk was taken in the steel bowl and was heated in a muffle furnace at 800 °C for 20 min. Cotton stalk ash was mixed with silica sand. Samples of cotton stalk ash and silica sand mixture were heated for 15 min in steel bowl with holes at three different temperatures, viz. 700, 800 and 900 °C. The bowl was allowed to cool. Results obtained from combustion test at 700, 800 and 900 °C are shown in Fig. 5d–f, respectively.

4.3 Results and Discussions

The scanning electronic microscopy (SEM) test has been done on agglomeration samples collected from plant site and prepared from the combustion test. SEM test has been conducted at Sophisticated Analysis and Instrumentation Laboratory, Thapar Institute of Engineering and Technology, Patiala. Much difference is not observed in SEM test results at 700 and 800 °C, but significant changes have been observed at 700 and 900 °C. SEM test results are shown in Fig. 6. It can be

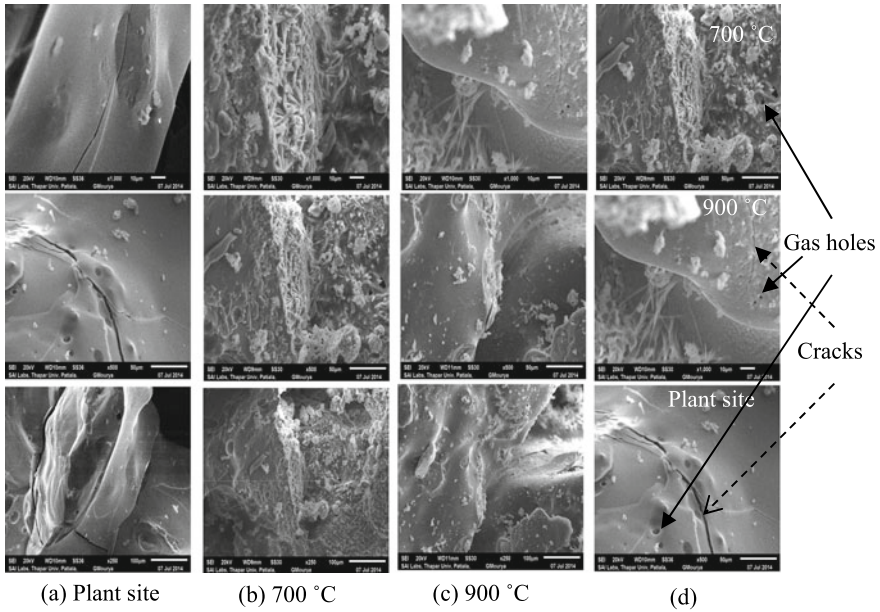


Fig. 6 SEM images of (a) Agglomerate sample collected from plant site (b) Agglomerate produced during combustion test at 700 °C (c) Agglomerate produced during combustion test at 900 °C (d) Agglomerate at 700, 900 °C and from plant site

observed from Fig. 6b that at 700 °C, burning cotton stalk particles stick to the sand surface. The melting rate of ash particles increases with increase in bed temperature to 900 °C. This leads to decrease in the ash viscosity. It increases the ash-coated sand particle stickiness thus accelerating defluidization process.

During molten material combustion, gases are released in the fuel ash forming cracks and gas holes on the surfaces (Fig. 6d). These molten materials are alkali silicates with low-melting point. In this case, agglomeration index = 4.31; hence agglomeration tendency is high when cotton stalk is used as fuel.

Based on this study, the following agglomeration mechanism is proposed: The bed temperature is the major reason for agglomeration and defluidization of fluidized bed combustor using cotton stalk. With increase in the bed temperature, fuel particles burn and generate low-melting-point alkali silicates. These low-melting alkali silicates stick to the sand particle surface. The burning cotton stalk particles adhere to sand surface. On completion of combustion, solidification of low-melting-point alkali silicates takes place leading to the formation of agglomerates.

5 Conclusion

1. During combustion, sand gets coated with the low-melting eutectic mixture and fuses with other particles by forming bridges between sand particles.
2. Ash melting rate increases and its viscosity decreases with rise in bed temperature leading to increase in ash-coated sand particle stickiness. This accelerates defluidization in FBC.
3. Gas holes and cracks are formed on surfaces due to gases released during combustion of low-melting-point alkali silicates.
4. The gaseous combustion products are released from the molten material in the fuel ash, which leads to the formation of gas holes and cracks on the surfaces.
5. Higher value of agglomeration index (4.31) indicates that an elevated fluidized bed temperature, cotton stalk can lead to agglomeration.

References

1. Kumar R, Singh RI (2016) An investigation in 20 kWth oxygen-enriched bubbling fluidized bed combustor using coal and biomass. *Fuel Process Technol* 148:256–268. <https://doi.org/10.1016/j.fuproc.2016.02.037>
2. Singh RI, Kumar R (2016) Current status and experimental investigation of oxy-fired fluidized bed. *Renew Sustain Energy Rev* 61:398–420. <https://doi.org/10.1016/j.rser.2016.04.021>
3. Sharma RK, Mohapatra SK (2016) Thermo-economic analysis of a biomass-fired bubbling fluidised bed thermal power plant. *Int J Exergy* 21:1–20. <https://doi.org/10.1504/IJEX.2016.078504>
4. Mlonka-mędrala A, Magdziarz A, Gajek M, Nowińska K (2020) Alkali metals association in biomass and their impact on ash melting behaviour. *Fuel* 261:116421. <https://doi.org/10.1016/j.fuel.2019.116421>
5. Yao X, Hu Y, Ge J, Ma X, Mao J, Sun L, Xu K, Xu K (2020) A comprehensive study on influence of operating parameters on agglomeration of ashes during biomass gasification in a laboratory-scale gasification system. *Fuel* 276:118083. <https://doi.org/10.1016/j.fuel.2020.118083>
6. Niu Y, Tan H (2016) Ash-related issues during biomass combustion: Alkali-induced slagging, silicate melt-induced slagging (ash fusion), agglomeration, corrosion, ash utilization, and related countermeasures. *Prog Energy Combust Sci* 52:1–61. <https://doi.org/10.1016/j.peccs.2015.09.003>
7. McIlveen-Wright DR, Huang Y, Rezvani S, Wang Y (2007) A technical and environmental analysis of co-combustion of coal and biomass in fluidised bed technologies. *Fuel* 86:2032–2042. <https://doi.org/10.1016/j.fuel.2007.02.011>
8. Scala F, Chirone R, Salatino P (2003) The influence of fine char particles burnout on bed agglomeration during the fluidized bed combustion of a biomass fuel. *Fuel Process Technol* 84:229–241. [https://doi.org/10.1016/S0378-3820\(03\)00108-5](https://doi.org/10.1016/S0378-3820(03)00108-5)
9. Taylor P, Liu H (2010) Energy Sources, Part A : Recovery, Utilization, and Environmental Effects Study of the Bed Agglomeration in the Straw-fired Fluidized Bed Study of the Bed Agglomeration in the Straw-fired Fluidized Bed. *Energy Procedia*, 37–41. <https://doi.org/10.1080/15567030902756113>

10. Taylor P, Mansaray KG, Ghaly AE (2007) Agglomeration Characteristics of Alumina Sand-Rice Husk Ash Mixtures at Elevated Temperatures Agglomeration Characteristics of Alumina Sand-Rice Husk Ash Mixtures at Elevated Temperatures, *Energy Sources*, 37–41. <https://doi.org/10.1080/00908319708908905>
11. Mansaray KG, Ghaly AE (2007) Agglomeration Characteristics of Silica Sand-Rice Husk Ash Mixtures at Elevated Temperatures Agglomeration Characteristics of Silica Sand-Rice Husk Ash Mixtures at Elevated Temperatures, *Energy Sources*, 37–41. <https://doi.org/10.1080/00908319808970083>
12. Chaivatamaset P, Tia S (2015) The characteristics of bed agglomeration during fluidized bed combustion of eucalyptus bark. *Appl Therm Eng* 75:1134–1146. <https://doi.org/10.1016/j.applthermaleng.2014.10.046>
13. Chaivatamaset P, Sricharoon P, Tia S (2011) Bed agglomeration characteristics of palm shell and corncob combustion in fluidized bed. *Appl Therm Eng* 31:2916–2927. <https://doi.org/10.1016/j.applthermaleng.2011.05.021>
14. Sun Z, Shen J, Jin B, Wei L (2010) Combustion characteristics of cotton stalk in FBC. *Biomass Bioenergy* 34:761–770. <https://doi.org/10.1016/j.biombioe.2010.01.019>
15. Sun Z, Jin B, Zhang M, Liu R, Zhang Y (2008) Experimental studies on cotton stalk combustion in a fluidized bed. *Energy* 33:1224–1232. <https://doi.org/10.1016/j.energy.2008.04.002>
16. Kumar R, Singh RI (2017) An investigation of co-combustion municipal sewage sludge with biomass in a 20 kW BFB combustor under air-fired and oxygen-enriched condition. *Waste Manag* 70:114–126. <https://doi.org/10.1016/j.wasman.2017.09.005>
17. Namkung H, Lee Y, Park J, Song G, Choi J, Kim J, Park S, Park J, Kim H, Choi Y (2019) Influence of herbaceous biomass ash pre-treated by alkali metal leaching on the agglomeration/sintering and corrosion behaviors. *Energy* 187:115950. <https://doi.org/10.1016/j.energy.2019.115950>
18. Mettanant V, Basu P, Butler J (2009) Agglomeration of Biomass Fired Fluidized Bed Gasifier and Combustor. *Can J Chem Eng* 87:656–684. <https://doi.org/10.1002/cjce.20211>
19. Lin W, Dam-johansen K, Frandsen F (2003) Agglomeration in bio-fuel fired fluidized bed combustors. *Chem. Eng. Tech.* 96:171–185. <https://doi.org/10.1016/j.cej.2003.08.008>
20. Basu P (2006) Combustion and gasification in fluidized beds. CRC Press
21. Visser HJM, Hofmans H, Huijnen H, Kastelein R, Kiel JHA (2001) Biomass ash - bed material interactions leading to agglomeration in fluidised bed combustion and gasification. In: *Progress in Thermochemical Biomass Conversion*, 272–286. <https://doi.org/10.1002/9780470694954.ch20>
22. Skrifvars B, Backman R, Hupa M (2000) Bed Agglomeration Characteristics during Fluidized Bed Combustion of Biomass Fuels. *Energy Fuels* 14:169–178. <https://doi.org/10.1021/ef990107b>
23. Hulkkonen S, Fabritius M, Enestam S (2003) Application of BFB technology for biomass fuels: Technical discussion and experiences from recent projects, in: *Fluid. Bed Combust. Proc FBC2003 17TH Int Fluid Bed Combust Conf*, 1–9
24. Werther J, Saenger M, Hartge E, Ogada T, Siagi Z (2000) Combustion of agricultural residues. *Prog Energy Combust Sci* 26:1–27
25. Brus E, Marcus O, Nordin A, Bostro D, Hedman H, Eklund A (2004) Bed Agglomeration Characteristics of Biomass Fuels Using Blast-Furnace Slag as Bed Material. *Energy Fuels* 18:1187–1193. <https://doi.org/10.1021/ef034095c>
26. Nordin A (2000) The Role of Kaolin in Prevention of Bed Agglomeration during Fluidized Bed Combustion of Biomass Fuels. *Energy Fuels* 14:618–624. <https://doi.org/10.1021/ef990198c>
27. Hedman H, Lundberg M (2003) Ash transformations during Combustion of Meat-, Bonemeal, and RDF in a (bench-scale) Fluidized Bed. *Energy Fuels* 17:1153–1159. <https://doi.org/10.1021/ef020273a>

28. Chirone R, Miccio F, Scala F (2006) Mechanism and prediction of bed agglomeration during fluidized bed combustion of a biomass fuel: Effect of the reactor scale. *Chem Eng J* 123:71–80. <https://doi.org/10.1016/j.cej.2006.07.004>
29. Alavi SM, Mirmomen L, Saleh K (2007) Experimental study and particle population modeling of coating in a jet-fluidized bed. *Adv Powder Technol* 18:311–327. <https://doi.org/10.1163/156855207780860228>
30. Abra MG, Ordin AN, Illedahl TL, Ao ANR (1998) Experimental determination of bed agglomeration tendencies of some common agricultural residues in fluidized bed combustion and gasification. *Biomass Bioenerg* 15:163–169. [https://doi.org/10.1016/S0961-9534\(98\)00015-4](https://doi.org/10.1016/S0961-9534(98)00015-4)
31. Shao Y, Wang J, Preto F, Zhu J, Xu C (2012) Ash deposition in biomass combustion or co-firing for power/heat generation. *Energies* 5(12):5171–5189. <https://doi.org/10.3390/en5125171>
32. Sharma RK, Mohapatra SK (2016) Study of particle size distribution and oxygen mass balance in a bubbling fluidizing combustor using cotton stalk. *Asia-Pac J Chem Eng* 11:187–199. <https://doi.org/10.1002/apj>

Effect of Fuel Composition on Thermoacoustic Instability in a Turbulent Combustor



Nikhil A. Baraiya and Satyanarayanan R. Chakravarthy

Abstract An experimental investigation is done to study thermoacoustic characterization of syngas fuels for different compositions of syngas, and this was compared with synthesis natural gas. The laboratory scaled bluff body type combustor was fabricated with a power rating of 30KW. The chemical composition of syngas was varied from CO/H₂ ratio from 0 to 95% of CO in a step of 5%. For the chosen cases, simultaneous pressure and time-resolved OH* chemiluminescence were recorded. Further, OH* chemiluminescence fluctuations are qualitatively analyzed to compare the acoustic characteristics of H₂-CH₄ and H₂-CO. The mean flame structure was investigated to study the difference in the combustion instability mechanism due to fuel composition.

Keywords Combustion instability • Fuel-flexible • Bluff-body combustor

1 Introduction

Renewable source of energy has the potential to meet the globally growing demand for energy. Modern combustors are powered by syngas, biomass, and other oxy-fuels, which are possible sustainable fuels. But the use of such fuels is questioning due to its reliability and its complex combustion characteristics due to highly non-linear interaction between flame and flow. The stable operating condition for combustion is required to be carried out by adopting recent computational fluid dynamics and experiments.

The fuel flexibility leads to significant variation in the combustion fundamental properties like reactivity, laminar flame speed, and flammability as these will

N. A. Baraiya (✉)

Sardar Vallabhbhai National Institute of Technology Surat, Surat, India

e-mail: nikhil@med.svnit.ac.in

S. R. Chakravarthy

Indian Institute of Technology Madras, Chennai, India

e-mail: src@iitm.ac.in

© The Author(s), under exclusive license to Springer Nature Singapore Pte Ltd. 2021

B. S. Sikarwar et al. (eds.), *Advances in Fluid and Thermal Engineering*,

Lecture Notes in Mechanical Engineering,

https://doi.org/10.1007/978-981-16-0159-0_79

influence the key combustion characteristics such as flame shape, flashback, and blowoff. Other primary criteria are the flame stabilization, flammability range, and propagation of flame. Therefore, a database of experimental and computational is required for enhancing the efficiency of plants and preventing the plant from hazardous failure due to thermoacoustic instability.

Syngas is highly fuel-flexible due to its various sources, coal type, process of extraction, etc. Hydrogen and carbon monoxide are primary constituents of syngas. Along with this, sometimes, there could be a little amount of nitrogen, methane, and carbon monoxide. Thus syngas combustion characteristics are very complex as fuel flexibility leads to changes in various combustion properties.

Therefore, the motivation of present work is to experimentally study acoustic instability of syngas and synthesis natural gas fuels in a turbulent bluff-body combustor. Thermoacoustic response with respect to fuel flexible condition is very important to study as from the literature survey; we will see that it is not much explored. Combustion instability is triggered by the satisfaction of Rayleigh criterion [1], which states that when heat release rate oscillations and pressure fluctuations are in phase, it adds energy to the system and makes the system unstable. This unstable system sometimes gives rise to very high-pressure amplitudes leading to fatigue failure of combustors as well. So this has to be avoided.

From literature studies, we can see many prior studies dedicated to the variation in combustion fundamental properties due to the composition of syngas. Natrajan et al. [2] reported the effect of pressure, initial temperature, dilution of CO_2 on the combustion properties like laminar flame speeds of H_2/CO mixtures. As the exothermicity, reactivity, and the diffusivity are a function of laminar flame speed, is the reason for its being the primary combustion property. The effect of fuel composition on the flashback, auto ignition, blowout, and autoignition has been reported by Lieuwen et al. [3]. They observed the remarkable differences in the combustion characteristics across the fuel compositions. They also noted that the behavior of the fuel mixtures is completely different when compared to its pure form. They have also studied when hydrogen is present in the fuel; it shows much uniqueness in behavior due to significantly different transport properties and flame speed compared with other gases. Figura et al. [4] reported the fuel composition effect on the flame structure and acoustic instability for a lean-premixed combustor. They approximated the flame to point source, referring it to as the center of heat release in the flame, due to the variation in laminar flame speed, the center of heat release rate location changes. The convective time scale from flame inflection point was changed, which resulted in the modulation of the pressure and heat release rate fluctuations. So these studies provide and evidence that combustion stability characteristics are a function of fuel composition as well along with other operation parameters [5].

Ferguson et al. [6] illustrated that the heating value to be the function of fuel composition, which could be related to the combustion characteristics. The interchangeable factor Wobbe index was used to co-relate the acoustic response of the combustor to the fuel composition. But it was found that it is poorly co-related. Baraiya et al. [7–12] have developed an n -tau model to model the transition in combustion instability characteristics for syngas combustion.

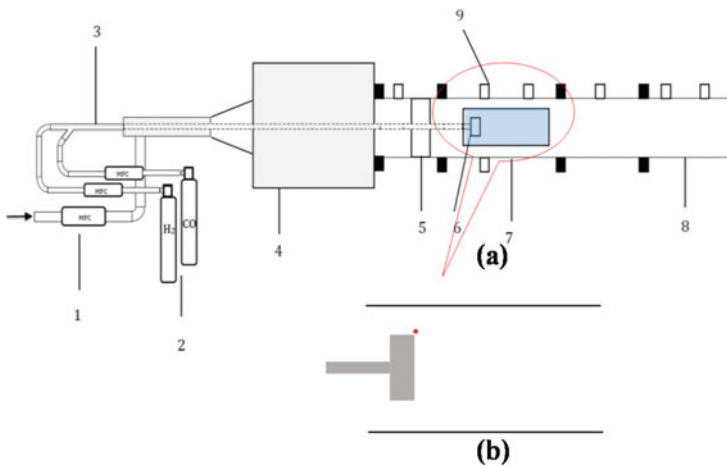
Thus from the literature survey, we could see that much work is yet to be done in correlating the fuel flexibility and stable combustion characteristics. The present work is aimed to study the effect of the composition of fuel on the combustion dynamics of high hydrogen fuels such as syngas and synthesis gas combustion. And the effort was made to understand the different combustion instability mechanisms driving triggering due to the variation in fuel. Such a study has relevance to the industrial implication for the development of fuel-flexible engines.

2 Experimental Details

2.1 Experimental Setup and Measurements

Figure 1 shows the schematic of the lab-scale experimental setup of a turbulent bluff-body combustor. As shown in Fig. 1, the experimental setup is primarily consisting of settling chamber, primary combustor with an optical window, extension ducts, and fuel and air supply lines. The setup is designed for a maximum power rating of 30 KW.

The main combustor consists of a $60 \times 60 \text{ mm}^2$ steel ducts. The total length of the combustor ducts along with the extension ducts is 1440 mm. The primary



1. Air-line, 2. fuel cylinders, 3. fuel-line, 4. settling chamber, 5. flow straightener, 6. flame-holder, 7. main combustor, 8. extension ducts and 9. pressure Transducer

Fig. 1 (a) Schematic of the experimental setup and (b) schematic of the bluff body assembly to demonstrate the flame anchoring point or the origin point of shear layer vortices (in red), which modulates the flame. Bluff body in gray, black solids lines is combustor walls

combustor has two optical access window made up of quartz of 160×60 mm. One side of the primary combustor is attached to the settling chamber. Another end of the combustor is open to the atmosphere—the inlet ducts between the settling chamber and primary combustor houses the honeycomb for flow straightening. The air is supplied to the settling chamber by air supply line through a mass flow controller of range 4000 SLPM (manufactured by Alicat, of the uncertainty of 0.8% of full-scale reading $\pm 0.2\%$ of measured reading). Fuel line made up of stainless steel pipe having inner diameter 9 mm and outer diameter 12 and 2500 mm long. One side of the fuel line is fastened with the circular disk-shaped bluff-body. The bluff-body is 30 mm in diameter and step height of 15 mm. It has 16 equally spaced holes of 1.5 mm on its periphery for the fuel injection to the primary combustor. Another end of the fuel supply line is fastened with Y-joint, which is connected with hydrogen and carbon monoxide cylinders. The mass flow controllers (manufactured by Alicat, of the uncertainty of 0.8% of full-scale reading $\pm 0.2\%$ of measured reading) are used to control the fuel and air supply to the combustor. Acoustic decouplers are used to decouple the fuel source and air source with the chamber to avoid the perturbation travel to the upstream source. There is seven pressure tap along the length of combustor from where acoustic pressure has been recorded by piezoelectric pressure transducer manufactured by PCB; this analog output is acquired by NI 6351 data acquisition system. OH* chemiluminescence imaging was done with phantom high speed. UV lens of 100 mm focal length fastened with OH* filter is attached to the Phantom camera through Lambert intensifier to the camera.

2.2 Operational Condition and Procedure

The equivalence ratio is varied by varying airflow rate was from 500 SLPM to 3000 SLPM in the step of 500 SLPM. For a given airflow rate, the chemical composition of syngas was changed by changing CO/H₂ ratio from 0 to 95% of CO in a step of 5%. For comparison, 75% H₂–25%CO is taken, and based on the combustion behavior, the airflow rate is varied in the range of 250 SLPM—700 SLPM with a step size of 50 SLPM. The pressure data for the bifurcations runs was recorded at 9 kHz for 3 s. For the simultaneous pressure and OH* chemiluminescence, the data were recorded at 4 kHz over a duration of 1 s.

3 Results and Discussion

The objective of the present study is to study the effect of fuel composition on acoustic instability.

3.1 Acoustic Characterization

Figures 2 and 3 show the acoustic characterization of a bluff-body combustor for two different fuels (H_2 -CO and H_2 -CH₄). Syngas being the primary concern and less explored, the composition of the syngas is varied over a range of 0–95% of CO as at 100% CO conditions the flame could not be stabilized.

Figure 2a shows the pressure amplitudes variation across the syngas composition variation by keeping the flow rate of fuel constant. These pressure amplitudes are corresponding to the dominant acoustic frequency shown in Fig. 2b. It is very peculiar to see that beyond 75% of CO in syngas, the pressure amplitudes are increasing for the almost entire range of the airflow rates. The highest pressure amplitudes have been recorded for the airflow rates of 1500 slpm, indicating the

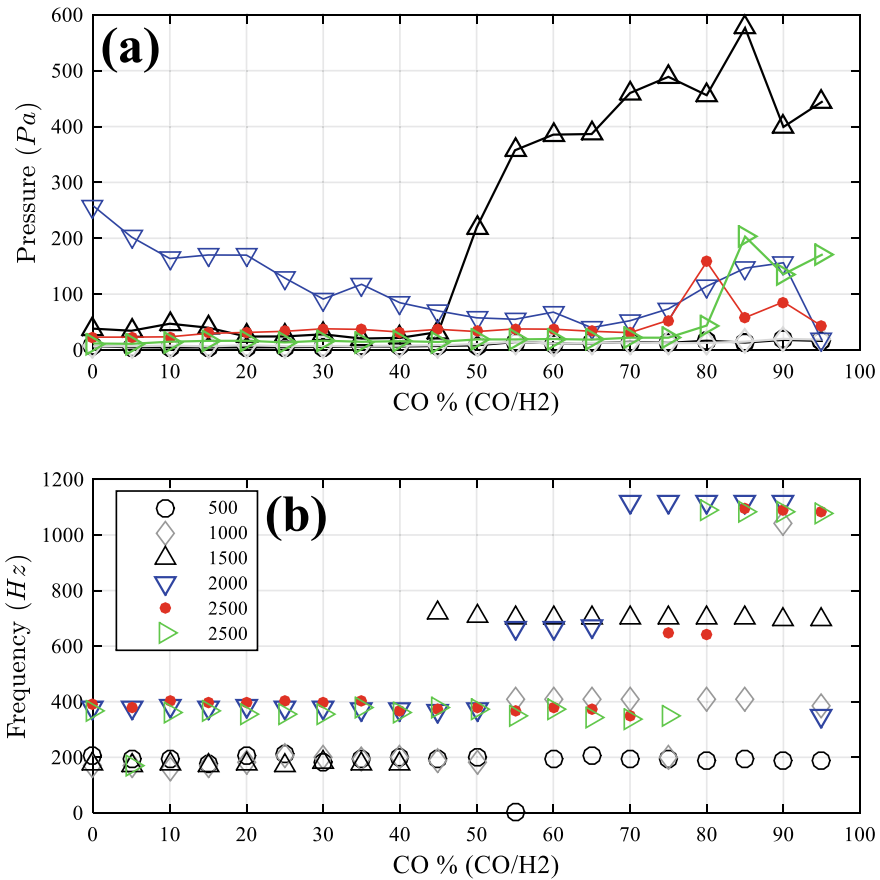


Fig. 2 Variation of (a) pressure amplitudes and (b) dominant frequency with different CO/H₂ ratio for different flow rates

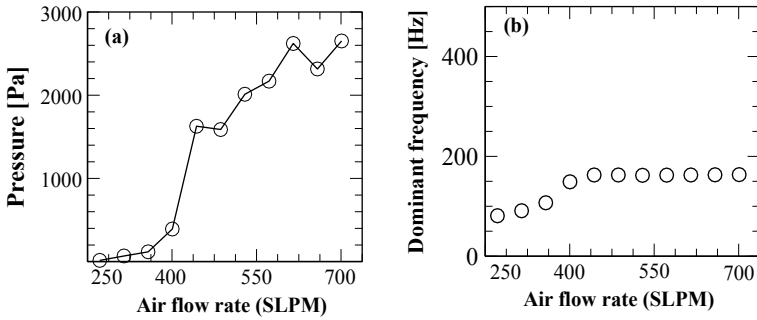


Fig. 3 Variation of (a) pressure amplitudes and (b) dominant frequency with different flow rates for 75% H₂-25% CH₄

possibility of the combustor attaining combustion instability. On analyzing the pressure time series (not shown), the combustor attains the pure limit cycle oscillation for 1500 slpm air flow rate as this could be the condition where it meets the Rayleigh criterion [1]. Also, another interesting observation from this analysis was that for other compositions either combustor is attaining stable, intermittent or quasi-periodic instability. They were so restricting our study to the pure combustion instability the 75% H₂-25% CO is considered for further studies. For getting further insight into the effect of the fuels on thermoacoustic instability, another set of fuel combinations was chosen to be 75% H₂-25% CH₄. Such a combination is chosen as this fuel, also called synthesis natural gas has many industrial applications. Also many time from the coal gasification along with the hydrogen and carbon monoxide the traces of methane is also present.

Figure 2b shows that till 50% of CO across the airflow rate all fuels show similar frequency jumps, which is traditional from fundamental mode to 1st harmonics. However, beyond 50% of CO the frequency jump is seen to be highly non-linear that is from that is to the 4th or 6th harmonics. But pressure amplitudes are very low except for the frequency of 700 Hz, which is oscillating acoustic frequency.

The variation of pressure amplitudes and dominant acoustic frequency with respect to the change in airflow rate is shown in Fig. 3 for H₂-CH₄. From pressure trends (Fig. 3a) it is seen that with the increase in the airflow rate, the pressure amplitudes increase as well, and beyond 600 slpm of air, it almost remains constant. As when compared to H₂-CO case, we could see the pressure amplitudes attained by H₂-CH₄ are highest. But frequency trends show the locking at fundamental mode beyond 450 slpm. Such phenomena are called acoustic lock-on [13]. Thus from the acoustic characterization of the combustor, we could say that acoustic behavior is a function of fuel composition and type of fuels. Next, we would like to analyze the response of the flame to such perturbations.

3.2 Flame Fluctuation

The red point which is shown in Fig. 1b shows the point of the emergence of the shear layer vortices, which could be the reason for such high-frequency modulations. So to study that, the time series from OH* chemiluminescence images is extracted at these pixels. And this time series and its corresponding frequency spectra are demonstrated in Figs. 4 and 5. From Fig. 4a, we could depict the time traces are closely packed, which is the sign of the high-frequency instability. Also, we could see the intensity is fluctuating between the range -0.5 and $0.5-1 \times e4$. To get a clear picture of this, the FFT was done on the pressure time trace. Figure 4b shows the sharp peak in frequency spectra at ~ 700 Hz for H₂-CO. This frequency also matches the frequency of pressure amplitudes. Thus from this, we could say that the flame drives the acoustics instability. Also, the Rayleigh criteria are being satisfied, and the combustor attained the pure limit cycle oscillation states. From this, we could also guess that there is a possibility of the instability driven by the shear layer, which can be depicted from the order of the flame fluctuating frequency.

A similar exercise has been repeated for H₂-CH₄ case shown in Fig. 5. On comparing its pressure-time traces with H₂-CO, we could see that they are not much closely packed indicating the larger time period hence, the lower frequency rate. Another interesting observation from this is fluctuations are closer two to three folds higher compared to H₂-CO, indicating that flame would be going very high flame modulation. This could be the reason for the highest pressure amplitudes observed in Fig. 3a. The frequency spectra of H₂-CH₄ (Figure 5b) shows the intensity peaking around 180 Hz, which is the fundamental modes of the duct for H₂-CH₄. These peaks corroborate with the peak seen in Fig. 3b which confirms the flame as driver of acoustic instability. Another important observation from Fig. 5 can be

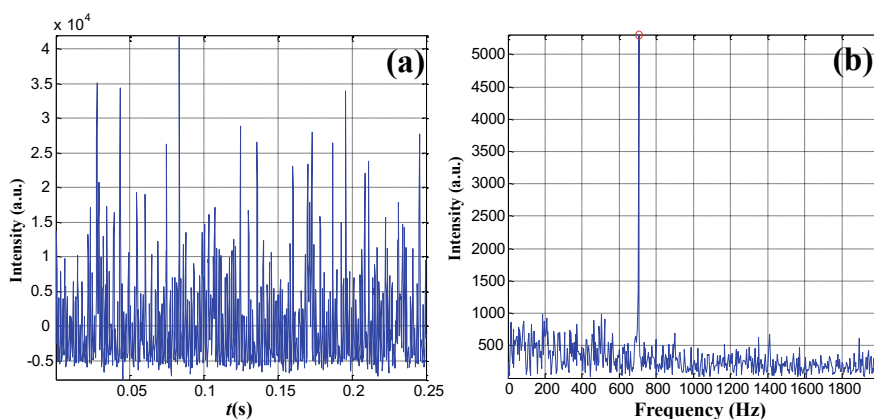


Fig. 4 OH* chemiluminescence intensity fluctuations (a) time series and (b) frequency spectra for H₂-CH₄

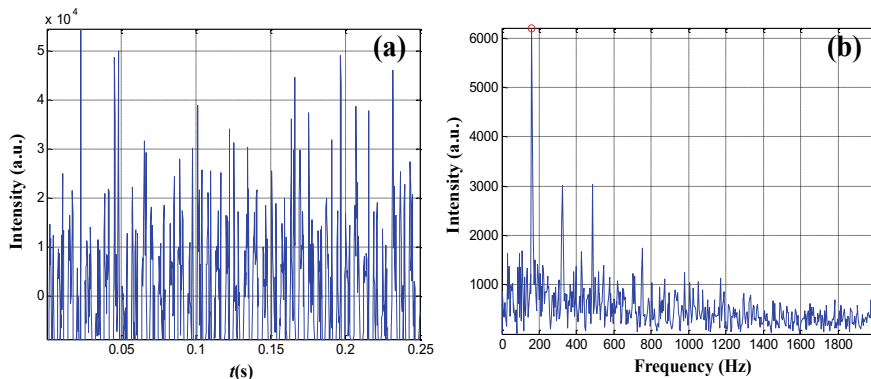


Fig. 5 OH* chemiluminescence intensity fluctuations (a) time series and (b) FFT of the time series for H₂-CH₄

drawn that the mechanism governing the instability of H₂-CO and H₂-CH₄ is different. This can be predicted from the values of the flame fluctuating frequency. But to clarify this, the flame images are to be analyzed.

3.3 Mean Flame Structure

Figure 6 shows the time-averaged OH* chemiluminescence images for two fuels (H₂-CH₄ and H₂-CO). The time average images are indicative of the flame anchoring point, which governs the combustion driving mechanism [14]. From Fig. 6a, it is observed that the right patch of the flame is seen at the shoulder of the bluff-body. In addition, the brightness of the flame is a direct representative of the velocity, which indicates that the density to be lower at the shoulder of the bluff-body and to be the highest in the wake region of the bluff-body. So due to the Baroclinic torque, the flame could not enter the wake of the bluff-body but gets anchored in the shear layer of the bluff-body. Therefore, the combustion instability of H₂-CO fuel is driven by small-scale structures (Shear layer).

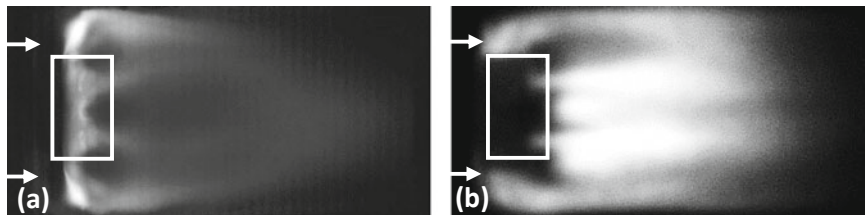


Fig. 6 Mean OH* chemiluminescence for (a) H₂-CO and (b) H₂-CH₄. White arrow shows the flow direction from left to right. The white rectangle shows the location of the bluff-body

Now from Fig. 6b, we could see the bright patch in the wake of the bluff-body and correspondingly dark patch at the shoulder of the bluff-body, which is exactly the reverse case compared to H_2 -CO. Due to this, the Baroclinic torque results into the flame anchoring in the wake of the bluff-body. Thus, the H_2 - CH_4 flame undergoes very high flame modulation; this is the reason for high-amplitudes and low-frequency instability. Thus the acoustic of the H_2 - CH_4 is driven by large-scale structure in contrast to the H_2 -CO.

4 Summary

The combustion dynamics depend upon the chemical composition of the fuel. With the change in the chemical composition of the fuel, the fundamental combustion properties like flame speed, reactivity, and flammability as these will influence the key combustion characteristics such as flame shape, flashback, and blowoff, which could be the huge challenge in fuel flexible engine.

The acoustic characterization of the lab-scale combustor shows that H_2 - CH_4 combustion exhibits low-frequency instability whereas as H_2 -CO combustion shows the high-frequency instability. From the OH^* chemiluminescence intensity fluctuations, it was observed that the H_2 - CH_4 shows the highest intensity fluctuation and hence the highest heat release rate fluctuation compared to H_2 -CO. From the mean flame structure analysis; it was seen that for both the fuels, the combustion driving mechanism is different. For H_2 - CH_4 , the combustion instability is driven by large-scale structures resulting in huge flame modulation, and hence the low-frequency instability with the highest pressure amplitudes is observed, whereas for H_2 -CO, the combustion instability is driven by small-scale structures resulting in very high-frequency instability.

Thus, the difference in the fuel compositions and fuel type results in different combustion characteristics and the combustion instability is seen to be a function of combustion instability.

Acknowledgements The National Centre for Combustion R & D was supported by the Science and Engineering Research Board.

References

1. Rayleigh L (1878) Theory of Sound, vol 2. Dover, New York, p 226
2. Natarajan J, Lieuwen T, Seitzman J (2007) Laminar flame speeds of H_2/CO mixtures: Effect of CO_2 dilution, preheat temperature, and pressure. Combust Flame 151(1-2):104-119
3. Tim Lieuwen et al. (2008) Fuel Flexibility Influences on Premixed Combustor Blowout, Flashback, Autoignition, and Stability. Journal of Engineering for Gas Turbines and Power, vol 130

4. Figura L et al. (2007) The Effects of Fuel Composition on Flame Structure and Combustion Dynamics in a Lean Premixed Combustor. In: vol 2: Turbo Expo. ASME (2007), pp 181–187
5. Huang Y et al (2009) Dynamics and stability of lean-premixed swirl-stabilized combustion. *Prog Energy Combust Sci* 35(4):293–364
6. Ferguson D, Richard GA, Straub D (2008) Fuel Interchangeability for Lean Premixed Combustion in Gas Turbine Engines. In Volume 3: Combustion, Fuels and Emissions, Parts A and B. ASME, pp 973–981
7. Baraiya NA, Chakravarthy SR (2020) Syngas Combustion Dynamics in a Bluff-Body Turbulent Combustor. In: *Dynamics and Control of Energy Systems*. Springer, Singapore, pp 239–263
8. Baraiya NA, Chakravarthy SR (2019) Excitation of high frequency thermoacoustic oscillations by syngas in a non-premixed bluff body combustor. *Int J Hydrogen Energy* 44 (29):15598–15609
9. Baraiya NA, Chakravarthy SR (2019) Effect of syngas composition on high frequency combustion instability in a non-premixed turbulent combustor. *Int J Hydrog Energy* 44(12): 6299–6312
10. Baraiya NA, Chakravarthy SR (2019) The role of mean flame anchoring on the stability characteristics of syngas, synthesis natural gas, and hydrogen fuels in a turbulent non-premixed bluff-body combustor. ASME Turbo Expo 2019, June
11. Baraiya NA, Chakravarthy SR (2018) Effect of chemical composition of syngas on combustion dynamics inside bluff-body type turbulent syngas combustor. In: ASME Turbo Expo 2018, June
12. Baraiya NA, Nagarajan B, Chakravarthy SR (2017) Experimental investigation of combustion dynamics in a turbulent syngas combustor. In ASME Turbo Expo 2017, June
13. Chakravarthy SR, Sivakumar R, Shreenivasan OJ (2007) Vortex-acoustic lock-on in bluff-body and backward-facing step combustors. *Sadhana* 32:145–154
14. Shanbhogue SJ, Sanusi YS, Taamallah S, Habib MA, Mokheimer EMA, Ghoniem AF (2016) Flame macrostructures, combustion instability and extinction strain scaling in swirl-stabilized premixed CH₄/H₂ combustion. *Combust Flame* 163:494–507

Experimental Investigation of Combustion Instability in Syngas Turbulent Combustor



Nikhil A. Baraiya and Satyanarayanan R. Chakravarthy

Abstract In the gas–turbine combustion system when the pressure and heat release rate oscillations are in phase, it can make combustor unstable due to satisfaction of Rayleigh criterion. Such unstable conditions are highly nonlinear and undesirable as it can cause catastrophic failure to engine. The experimental investigation was done to study the combustion dynamics response of a turbulent combustor to the parameters such as the location of the bluff–body, composition of the fuel, and global equivalence ratio. For this study, the circular shape bluff–body is used as a flame holder. bluff–body is when held closer to the air inlet, and the higher-pressure amplitudes were noted to be higher in contrast to when it is in much downstream. The combustion stability map was mapped for the global equivalence ratio, the primary combustion parameter. Lastly, the effect of varying syngas composition by CO/H₂ ratios on acoustic oscillation was studied. The higher-pressure amplitudes and frequency oscillation were achieved at a higher concentration of CO.

Keywords Syngas combustion · Thermoacoustic instability · bluff–body combustor

1 Introduction

Renewable sources of energy have the potential to meet the demand for energy in the modern world. One such renewable fuel is syngas, which is nowadays subject of prime interest due to its renewability and abundance. Generally, syngas is produced from the gasification of the coal, which is an efficient way to use the coal. It can also be produced from biomass, etc. It mainly consists of hydrogen and carbon dioxide.

N. A. Baraiya (✉)

Sardar Vallabhbhai National Institute of Technology Surat, Surat, India

e-mail: nikhil@med.svnit.ac.in

S. R. Chakravarthy

Indian Institute of Technology Madras, Chennai, India

e-mail: src@iitm.ac.in

© The Author(s), under exclusive license to Springer Nature Singapore Pte Ltd. 2021

901

B. S. Sikarwar et al. (eds.), *Advances in Fluid and Thermal Engineering*,

Lecture Notes in Mechanical Engineering,

https://doi.org/10.1007/978-981-16-0159-0_80

So in this paper, we have adopted these two primary components of syngas as representative of it.

Though stable operation, there is always a chance of fluctuations in pressure in the industrial gas–turbine system. The fluctuation may exist in the form of classical acoustic motions, which are small amplitude oscillations. Usually, some type of perturbations can provide energy to the unsteady motions and increase their amplitudes. The resultant organized pressure fluctuations, with the amplitudes, exceed 5% of the mean chamber pressure, are regarded as combustion instabilities.

Coupling between acoustics and heat release rate drives the instability in the chamber. Rayleigh [1] was the first one to demonstrate such a coupling phenomenon. In a flame holder like bluff–body or backward-facing step combustor, the difference in the velocity of streams results in the shear layer vortices and also the generation of the wakes in the dump plane of the combustor. Renard et al. [2] have illustrated the interaction between flame and vortex. Rogers and Marble [3] have reported that the acoustic field initiate vortex shedding could generate heat release rates that are periodic in nature, which was in phase with the acoustic field and consequently served as a source to it. Culick [4] found that vortex shedding as a possible mechanism for combustion instabilities. Hence, the vortex shedding plays an important role in the cause of combustion instabilities, and it is to be studied. Lieuwen and Zinn [5] studied that the significant increase in perturbing ϕ as mean ϕ decreases results into oscillations of reaction rate. Even small changes in the equivalence ratio can introduce large variations in reaction rate near a lean flammability limit, leading to great changes in the flame characteristics such as flame speed, flame temperature, and chemical reaction time, which can excite combustion instability if a positive feedback loop exists between combustion process and acoustics. Recently, Baraiya et al. [6–11] have shown that the two heat release rate zones resulting in high-frequency acoustic instability.

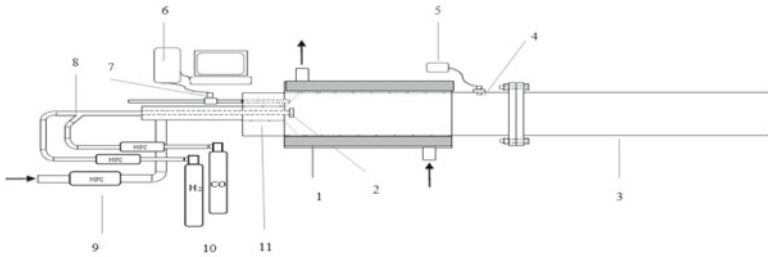
The aim of the present work is to study the effect of bluff–body location, equivalence ratio, and chemical composition of fuel on combustion dynamics of synthesis gas combustion.

2 Experimental Details

2.1 *Experimental Setup and Measurements*

Figure 1 shows the schematic diagram of the lab-scale bluff–body combustor. The combustor consists of three main parts: 1. primary combustor, 2. fuel and air supply line, and 3. extension or tail ducts. The combustion chamber is designed for a fixed power rating of 30 KW.

The combustor setup consists of three concentric pipes. The innermost pipe is the fuel line. It is 19 mm in diameter and around 2 meters long made of stainless steel. One end of the pipe is fastened with the circular disk-shaped bluff–body.



1. Primary combustor with water cooling jacket in gray color, 2. bluff-body, 3. water cooling jacket, 4.tail pipe, 5.spark plug, 6. ignition transformer, 7. NI-DAQ, 8. pressure transducer, 9. fuel line, 10. mass flow controller, 11. hydrogen and carbon monoxide cylinders, 12. Air-line

Fig. 1 Schematic of the experimental setup

bluff-body is having a height of 20 mm and a diameter of 40 mm, having 16 equally spaced holes of 2 mm on its periphery. These holes are used for the fuel injection to the primary combustor. Another end of the fuel pipe is fastened with the Y-shaped adapter providing inlet and connection to two fuel holes. The fuel is supplied to combustor from the fuel cylinders, and it is controlled by mass flow controllers (manufactured by Alicat, of the uncertainty of 0.8% of full-scale reading $\pm 0.2\%$ of measured reading). Acoustic decoupler is used to ensure the perturbation-free supply of fuel to the combustor by dissipating the acoustic wave traveling to the upstream. The fuel line and bluff-body assembly are held in the center of the combustion chamber with the help of the three screws in the body of the air supply line. The rack and pinion mechanism is used to adjust the axial movement of the bluff-body. The primary combustor is at the center between the fuel pipe and water cooling jackets. The primary combustor is made of stainless steel pipe as it is a place where the flame is located, and it is the highest temperature region in the combustor. For long combustor runs, the water cooling jackets are used. The size of the primary combustor is 750 mm long and 110 mm inner diameter. One side of the combustor pipe is connected with the tailpipe of length 750 mm. Another side of the combustor has an opening of fuel and air supply lines. The air supply line is 50 mm in diameter and 600 mm long. The air supply opens into the combustor, with the divergent part having a semi cone angle of 45 degrees. The divergent passage is having pressure tap opening to the combustor from where acoustic pressure is measured by piezoelectric pressure transducer manufactured by PCB; this analog output is acquired by NI 6351 data acquisition system.

Table 1 List of operating conditions

Variable parameter	Min step size (min–max)	Fixed parameter
bluff–body location(l_b) (mm)	1 (1–15)	Ma = 1417 slpm, MH ₂ = 145, Mco = 10.5
Air flow rate (SLPM)	50 (600–2000)	MH ₂ = 145, Mco = 10.5
CO/H ₂ (%)	5 (0–95)	$\phi = 0.5$

2.2 Experimental Conditions and Procedure

The test matrix for the acoustic characterization of the turbulent combustor is shown in Table 1. The parametric study was done for the variation of the parameters like the location of bluff–body (l_b), fuel composition (CO/H₂ ratio), and the global equivalence ratio on the combustion characteristics of the combustor. The bluff–body location is varied from 0 to 15 mm in a step of 1 mm. The airflow rates are varied from 600 SLPM to 2000 SLPM in the step of 50 SLPM at 3 mm and 6 mm bluff–body location, to study the effect of variation of equivalence ratio on acoustic field. The fuel composition was varied by CO/H₂ ratio from 0% of CO to 95% of CO in the step of 5% at two different bluff–body locations(3 mm and 6 mm) by keeping equivalence ratio constant equal to 0.5. In all the experiments, data is acquired at a sampling frequency of 9000 Hz for 3 s. The acquired data is Fourier transformed to get frequency domain.

3 Results and Discussion

The effect of bluff–body position and the ratio of carbon monoxide to hydrogen on equivalence ratio on combustion instability are studied in a turbulent combustor.

3.1 Effect of Bluff–Body Location (l_b)

Figure 2 shows the increase in the dominant acoustic frequency with an increase in the axial gap between sudden expansion plane and bluff–body, and eventually, it decreases. The trends depicted from the figures are linear increase in frequency till 9 mm with few steps bands at 50 Hz, ~300 Hz, ~650 Hz. Beyond 9 mm again, the frequency reduces to 50 Hz. This different shift in the frequency could be the change in different modes of the frequency, such as from fundamental mode of the frequency to higher harmonics or from fundamental longitudinal modes to tangential modes or slant modes [6]. Such a shift in the mode of frequency is maybe a result of variation in vortex shedding frequency of variation of bluff–body location

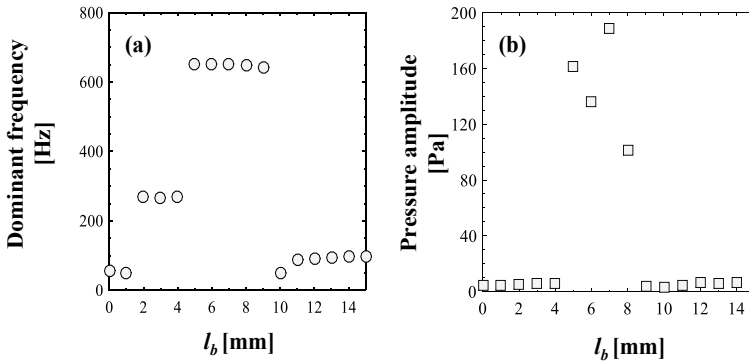


Fig. 2 Variation of (a) dominant frequency and (b) pressure amplitudes with l_b at $\dot{m}_a = 1471$ SLPM, $\dot{m}_{H_2} = 145$ SLPM, $\dot{m}_{CO} = 10.5$ SLPM, $\phi = 0.5$

axially. Balachandran et al. [12] have also reported the shift in frequency to higher modes due to variation in the location of the bluff-body, which is due to a shift of vortex shedding frequency. The shift in modes of frequency due to fuel injection location was also in our earlier work for different configurations (rectangular combustor geometry with optical access window) [6].

Figure 2b shows the pressure amplitudes corresponding to dominant acoustic frequency (shown in Fig. 2a) with the variation in the bluff-body location. The bell shape trend is exhibited by the pressure and the l_b . The pressure amplitude increases suddenly when the bluff-body is at 5 mm, and it reaches a maximum at 7 mm and starts decreasing after that and remains constant for the further downstream location of the bluff-body. Thus, it is clear from this that the combustor attains unstable combustion state when the bluff-body is located at 7 mm with the highest pressure amplitudes. At these points, the time series oscillations show the periodic oscillation (not shown). Thus, combustor becomes unstable at a frequency of 750 Hz due to satisfaction Rayleigh criteria.

3.2 Effect of Fuel Composition (CO/H₂)

The fuel-flexible engine is very critical to design due to the drastic difference in the combustion characteristics. In this section, the fuel composition is varied, and correspondingly acoustic frequency variation is shown in Fig. 3 at the fixed bluff-body location and global equivalence ratio. It is interesting to see that the frequency almost locks and remains constant at around 250 Hz till 50% of CO at both the bluff-body locations (3 and 6 mm). Around 50% CO at 6 mm bluff-body location, the jump in the frequency is noted from 350 Hz to 700 Hz, which is the first harmonics of the fundamental mode, but after that, it remains constant for all increase in CO %. This shows the sensitivity of the combustor in the mid-range of

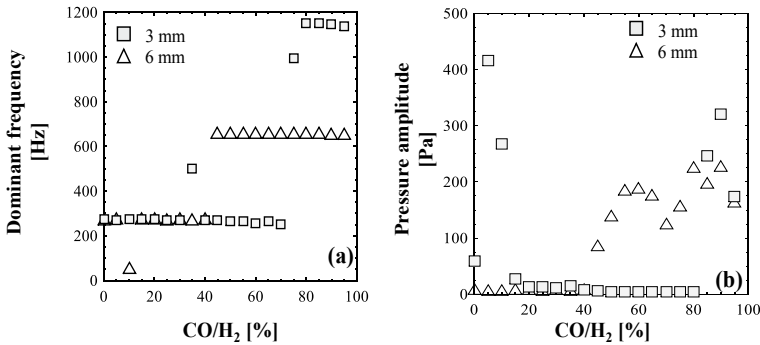


Fig. 3 Variation of (a) acoustic dominant frequency and (b) pressure amplitudes with different CO/H₂ ratio at $\phi = 0.5$ and at 3 mm and 6 mm bluff-body location

CO% when the bluff-body located much downstream where the velocities are lower compared to the upstream location (at 3 mm). Whereas at 3 mm bluff body location, the shift in frequency is seen from fundamental mode to 2nd harmonics by skipping first harmonics. Such behavior is seldom reported in the literature [6], and this type of behavior is due to the existence of the nodal point of the pressure and non-satisfaction of the Rayleigh criteria at such operating conditions.

Figure 3b shows the pressure corresponding to the dominant acoustic frequency shown in Fig. 3a. As clearly expected from the results of the frequency variation, the highest pressure amplitude is observed low CO and high CO for 3 mm bluff-body location. However, the highest peaks for 6 mm l_b are seen closer to higher CO content. Such drastic variation is due to the bluff-body shoulder velocity. As the location of the bluff-body is changed, the shoulder velocity of the bluff-body is changed, which in turn changes the mixing and hence local equivalence ratio. The combustion characteristics are very sensitive to the mixing. This also affects the vortex roll-up and vortex shedding frequency resulting in such a disparity in the behavior of combustor with the fuel composition and l_b combined. Such phenomena are highly complex in nature and nonlinear, which required very tedious diagnostics and analysis.

3.3 Effect of Global Equivalence Ratio

The acoustic characterization of the combustor is done by sweeping the airflow rate hence the equivalence ratio. As the mass flow rate of the air is increased by keeping the fuel flow rate constant, the equivalence ratio of the fuel reduces. From Fig. 4, the frequency amplitude increases first till 700 slpm to ~1150 Hz; further increase in this results into a reduction in it. These reduction trends are peculiar as for 6 mm l_b the reduction is traditional behavior, which is from 4th harmonics; it jumps

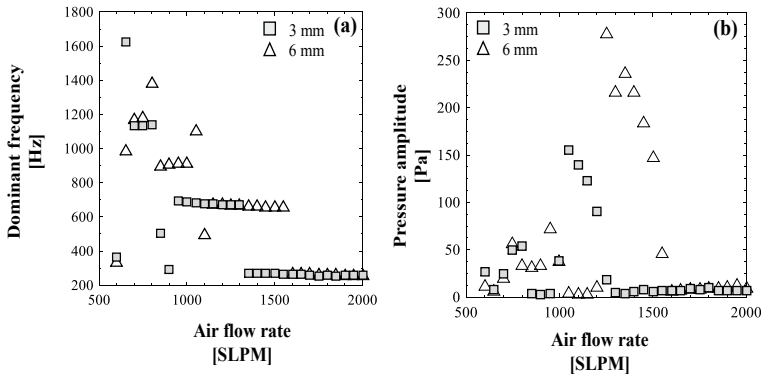


Fig. 4 Variation of (a) dominant frequency (b) pressure amplitudes, with global equivalence ratio (air flow rates), at 3 mm and 6 mm bluff-body location

to 3rd, and from 3rd it jumps to 2nd harmonics and from 2nd it directly jumps to the fundamental mode by skipping the fundamental mode. Whereas for 3 mm lb, the frequency jumps from 4th harmonics to 2nd harmonics by skipping 3rd harmonics, and from 3rd harmonics, it jumps to fundamental modes directly as seen for the 6 mm case. Such behavior is due to the combined effect of change in vortex shedding frequency due to the bluff-body location and equivalence ratio.

Figure 4b shows the pressure amplitudes corresponding to the dominant frequency (shown in Fig. 4a). The bell shape trend is observed for both the bluff-body location with a peak in the mid-range of the airflow rate. From this, we could note two things: 1. the peak for 6 mm lb is highest and 2. The peak for 3 mm lb occurs littler earlier (around 1100 slpm), which is 200 slpm lesser than $l_b = 6$ mm. This is due to the higher velocity resulting in higher turbulence and making the dynamical system earlier than expected. Such behavior is due to a strong affinity of the combustion dynamics toward inlet turbulence [13].

4 Summary

The experimental investigation was done to study the dynamic combustion response to the changes in the location of the bluff-body, fuel composition, and global equivalence ratio. The shift in the frequency from fundamental modes to higher harmonics is observed with variation in all three parameters. But the frequency trends with respect to the location of the bluff-body show the traditional behavior, i.e., linear. Whereas for fuel composition and global equivalence ratio variation cases, the behavior is highly nonlinear. The occurrence of the pressure nodes and not the satisfaction of the Rayleigh criteria results in steady behavior at these conditions.

Thus, we can conclude that the acoustic oscillations are the function of bluff-body location, global equivalence ratio, and chemical composition of the fuel. Combustion diagnostics is required to be done to explore more physics behind the behavior of acoustic oscillation with different parameters.

Acknowledgements The National Centre for Combustion R & D was supported by the Science and Engineering Research Board.

References

1. Rayleigh L (1878) *Theory of Sound*, Vol 2, Dover, New York, p 226
2. Renard PH, Thévenin D, Rolon JC, Candel S (2000) Dynamics of Flame/Vortex Interactions. *Prog Energy Combust Sci* 26:225–282
3. Rogers DE, Marble FE (1956) A mechanism for high frequency oscillations in ramjet combustors and afterburners, *Jet Propulsion*, pp 456-462
4. Culick FEC (1989) Combustion Instabilities in Propulsion Systems, *Combustion Instabilities Driven by Thermo-Chemical Acoustic Sources*, ASME Heat Transfer Div, vol 128, ASME, New York, pp 33–52
5. Lieuwen T, Zinn BT (1997) The Role of Chemical Kinetics in Driving Acoustic Instabilities in Lean Premixed Combustors. In: proceedings of the 16th international colloquium on the dynamics of explosions and reactive systems, Crocow, Poland, August
6. Baraiya NA, Chakravarthy SR (2019) Excitation of high frequency thermoacoustic oscillations by syngas in a non-premixed bluff-body combustor. *Int J Hydrogen Energy* 44 (29):15598–15609
7. Baraiya NA, Chakravarthy SR (2019) Effect of syngas composition on high frequency combustion instability in a non-premixed turbulent combustor. *Int J Hydrog Energy* 44 (12):6299–6312
8. Baraiya NA, Chakravarthy SR (2019) The role of mean flame anchoring on the stability characteristics of syngas, synthesis natural gas, and hydrogen fuels in a turbulent non-premixed bluff-body combustor. *ASME Turbo Expo 2019*, June
9. Baraiya NA, Chakravarthy SR (2018) Effect of chemical composition of syngas on combustion dynamics inside bluff-body type turbulent syngas combustor. In: *ASME Turbo Expo 2018*, June
10. Baraiya NA, Nagarajan B, Chakravarthy SR (2017) Experimental investigation of combustion dynamics in a turbulent syngas combustor. *ASME Turbo Expo 2017*, June
11. Baraiya NA, Chakravarthy SR (2020) Syngas Combustion Dynamics in a bluff-body Turbulent Combustor. In: *Dynamics and Control of Energy Systems*. Springer, Singapore, pp 239–263
12. Balachandran R, Chakravarthy SR, Sujith RI (2008) Characterization of an Acoustically Self-Excited Combustor for Spray Evaporation. *J Propul Power* 24(6):1382–1389
13. Nagarajan B, Baraiya NA, Chakravarthy SR (2019) Effect of inlet flow turbulence on the combustion instability in a premixed backward-facing step combustor. *Proc Combust Inst* 37 (4):5189–5196